

Sotiris Nikoletseas  
Yuanyuan Yang  
Apostolos Georgiadis *Editors*

# Wireless Power Transfer Algorithms, Technologies and Applications in Ad Hoc Communication Networks

# Wireless Power Transfer Algorithms, Technologies and Applications in Ad Hoc Communication Networks

Sotiris Nikoletseas · Yuanyuan Yang  
Apostolos Georgiadis  
Editors

# Wireless Power Transfer Algorithms, Technologies and Applications in Ad Hoc Communication Networks



Springer

*Editors*

Sotiris Nikoletseas  
Department of Computer Engineering  
and Informatics  
University of Patras and Computer  
Technology Institute and Press  
“Diophantus” (CTI)  
Patras  
Greece

Apostolos Georgiadis  
School of Engineering and Physical Sciences  
Heriot-Watt University  
Edinburgh  
UK

Yuanyuan Yang  
Department of Electrical and Computer  
Engineering  
Stony Brook University  
Stony Brook, NY  
USA

ISBN 978-3-319-46809-9  
DOI 10.1007/978-3-319-46810-5

ISBN 978-3-319-46810-5 (eBook)

Library of Congress Control Number: 2016955310

© Springer International Publishing AG 2016

This work is subject to copyright. All rights are reserved by the Publisher, whether the whole or part of the material is concerned, specifically the rights of translation, reprinting, reuse of illustrations, recitation, broadcasting, reproduction on microfilms or in any other physical way, and transmission or information storage and retrieval, electronic adaptation, computer software, or by similar or dissimilar methodology now known or hereafter developed.

The use of general descriptive names, registered names, trademarks, service marks, etc. in this publication does not imply, even in the absence of a specific statement, that such names are exempt from the relevant protective laws and regulations and therefore free for general use.

The publisher, the authors and the editors are safe to assume that the advice and information in this book are believed to be true and accurate at the date of publication. Neither the publisher nor the authors or the editors give a warranty, express or implied, with respect to the material contained herein or for any errors or omissions that may have been made.

Printed on acid-free paper

This Springer imprint is published by Springer Nature  
The registered company is Springer International Publishing AG  
The registered company address is: Gewerbestrasse 11, 6330 Cham, Switzerland

*To my beloved daughter Nonika*

—Sotiris Nikoletseas

*To my beloved husband Jianchao Wang*

—Yuanyuan Yang

*To my daughter Ariadne*

—Apostolos Georgiadis

# Preface

This book is the first systematic exposition on the emerging domain of wireless power transfer in ad hoc communication networks. It selectively spans a coherent, large spectrum of fundamental aspects of wireless power transfer, such as mobility management in the network, combined wireless power and information transfer, energy flow among network devices, joint activities with wireless power transfer (routing, data gathering and solar energy harvesting), safety provisioning through electromagnetic radiation control, as well as fundamental and novel circuits and technologies enabling the wide application of wireless powering.

Wireless Power Transfer (WPT) has recently evolved as a very active research subject in the field of ad hoc communication networks, as well as a topic of rapid technological progress and emerging practical development and application activities. However, a solid foundational, systemic, and applied background seems still necessary for wireless power transfer to achieve its full potential. The provisioning of relevant abstract models, algorithmic design and analysis methods, networking principles, circuit and system design, and application methodologies is a challenging task.

Several such models, algorithms, circuits, systems, and applications for WPT have already appeared, in relevant journals, conferences, and workshops. This book aims to reinforce the emergence of a critical mass of algorithmic and applied foundations by bringing together, for the first time in a systematic way, high-quality research contributions (in the form of invited book chapters) by leading experts worldwide, relevant to important algorithmic, systematic, and technological WPT applications in ad hoc communication networks.

The content is organized into six thematic parts, covering respective common aspects, issues, and methodologies: Technologies, Communication, Mobility, Energy Flow, Joint Operations, and Electromagnetic Radiation Awareness. Because of the inherent relations of different topics, layers, and problems, many chapters could have been associated with more than one theme, and the themes themselves could have been chosen in a different manner. Still, we hope that the chosen structure will be methodologically useful for the reader. In total, 27 chapters are included, contributed by leading relevant experts worldwide.

We now briefly describe each theme. The first one discusses characteristic key circuits and technologies for wireless power transfer in communication networks and briefly presents several regulations. The second theme presents several applications for achieving efficient communication in wirelessly powered networks and identifies relevant performance trade-offs. The next theme concerns basic efficient solutions for mobility management in WPT networks, both distributed and centralized. Mobile nodes and chargers, effective traversal strategies, cost minimization of mobile elements, and the use of cutting-edge technologies like UAVs are some of the proposed approaches. The fourth theme covers the concept of energy flow, a major challenge in wirelessly powered networks. Different aspects of energy flow are addressed, such as collaborative mobile charging, hierarchy assignment, use of resonant repeaters, and energy balance in populations of mobile peers. Different networking operations that can be combined with WPT are addressed in the fifth theme, such as routing, data gathering, and solar energy harvesting. The book concludes with a recent combination of research between wireless power transfer and electromagnetic radiation awareness. In particular, two algorithmic approaches, which apply radiation control methods to ensure human safety without sacrificing effectiveness, are presented.

We hope that this book will be helpful to its readers and contribute to a solid foundation and deeper understanding of the fascinating and rapidly evolving research area of wireless power transfer. The intended audience includes researchers, engineers, educators, and advanced graduate students interested in the area of wireless power transfer in ad hoc communication networks. In addition to use as a text for advanced university courses and research seminars, the book may also be used as a supplement to academic courses on algorithmic applications, wireless protocols, distributed computing, and networking.

## Acknowledgments

We wish to first warmly thank all authors of this book for their high-quality contributions; the willingness of these worldwide leading researchers to participate in this effort was vital to its success and a great honor for us.

We wish to thank Springer for publishing this book. In particular, we thank Alfred Hofmann for a long cooperation and his persistent willingness to encourage high-quality publications in emerging research topics. Also, we thank Senior Editor Ronan Nugent, for a fruitful cooperation in realizing this volume. Many thanks go to Theofanis Raptis (with whom the first editor envisioned this endeavor together) and Adelina Madhja, two brilliant Ph.D. students at the University of Patras and CTI, Greece, for integrating the volume material so timely and efficiently.

The work of Sotiris Nikoletseas was supported by the EU/FIRE IoT Lab project-STREP ICT-610477. The work of Yuanyuan Yang has been supported by the US National Science Foundation under Grant No. ECCS-1307576. The work of Apostolos Georgiadis was supported by the European Union Horizon 2020

Research and Innovation Programme under the Marie Skłodowska-Curie Grant Agreement No 661621.

Apostolos Georgiadis and Sotiris Nikoletseas would also like to acknowledge the European Union COST Action IC1301 WiPE (Wireless Power Transmission for Sustainable Electronics).

Patras, Greece

Stony Brook, USA

Edinburgh, UK

July 2016

Sotiris Nikoletseas

Yuanyuan Yang

Apostolos Georgiadis

# Contents

## Part I Technologies

|   |     |
|---|-----|
| <b>1 Non-radiative Wireless Power Transmission: Theory and Applications</b> . . . . .                         | 3   |
| Giuseppina Monti, Mauro Mongiardo, Franco Mastri,<br>Alessandra Costanzo, Laura Corchia and Luciano Tarricone |     |
| <b>2 Wireless Power Transfer Based on Metamaterials</b> . . . . .   | 31  |
| Bingnan Wang, William Yerazunis and Koon Hoo Teo  |     |
| <b>3 Optimal Array Beamforming for Microwave Power Transmission in Complex Environment</b> . . . . .          | 55  |
| Ce Zhang, Bingnan Wang, Akira Ishimaru and Yasuo Kuga   |     |
| <b>4 Far-Field Wireless Power Transfer for IoT Sensors</b> . . . . .  | 85  |
| Hubregt J. Visser, Hans W. Pflug and Shady Keyrouz  |     |
| <b>5 Wireless Power Transfer: Discrete Rectifier Modeling and Analysis</b> . . . . .                          | 111 |
| Hans W. Pflug and Hubregt J. Visser   |     |
| <b>6 Unconventional Waveform Design for Wireless Power Transfer</b> . . . . .                                 | 137 |
| Alirio Boaventura, Nuno Borges Carvalho<br>and Apostolos Georgiadis   |     |
| <b>7 Regulations and Standards for Wireless Power Transfer Systems</b> . . . . .                              | 161 |
| Christos Kalialakis, Ana Collado and Apostolos Georgiadis   |     |

## Part II Communication

|  |     |
|--|-----|
| <b>8 Trade-Offs in Wireless Powered Communications</b> . . . . . | 185 |
| Panagiotis D. Diamantoulakis and George K. Karagiannidis         |     |

|           |   |     |
|-----------|---|-----|
| <b>9</b>  | <b>Simultaneous WPT and Wireless Communication with TDD Algorithm at Same Frequency Band . . . . .</b>                                  | 211 |
|           | Naoki Shinohara   |     |
| <b>10</b> | <b>Asymptotically Optimal Power Allocation for Wireless Powered Communication Network with Non-orthogonal Multiple Access . . . . .</b> | 231 |
|           | Nikola Zlatanov, Zoran Hadzi-Velkov and Derrick Wing Kwan Ng  |     |
| <b>11</b> | <b>Energy-Efficient Cooperative Transmission for SWIPT in Wireless Sensor Networks . . . . .</b>  | 253 |
|           | Songtao Guo, Yuanyuan Yang and Hongyan Yu   |     |

### **Part III Mobility**

|           |  |     |
|-----------|--|-----|
| <b>12</b> | <b>Using Mobile Nodes in Wireless Sensor Networks with Wireless Power Transfer . . . . .</b>                           | 285 |
|           | Xiaobing Wu  |     |
| <b>13</b> | <b>Strategies for Wireless Recharging in Mobile Ad-Hoc Networks . . . . .</b>  | 305 |
|           | Constantinos Marios Angelopoulos, Julia Buwaya, Orestis Evangelatos and José Rolim                                     |     |
| <b>14</b> | <b>Recharge Scheduling with Multiple Mobile Chargers. . . . .</b>  | 331 |
|           | Cong Wang, Ji Li, Fan Ye and Yuanyuan Yang   |     |
| <b>15</b> | <b>Distributed Coordination Protocols for Wireless Charging in Sensor Networks . . . . .</b>                           | 355 |
|           | Adelina Madhja, Sotiris Nikoletseas and Theofanis P. Raptis  |     |
| <b>16</b> | <b>Minimizing the Service Cost of Mobile Chargers While Maintaining the Perpetual Operations of WRSNs . . . . .</b>    | 389 |
|           | Wenzheng Xu and Weifa Liang  |     |
| <b>17</b> | <b>Unmanned Aerial Vehicle-Based Wireless Charging of Sensor Networks . . . . .</b>                                    | 433 |
|           | Carrick Detweiler, Michael Eiskamp, Brent Griffin, Jennifer Johnson, Jinfu Leng, Andrew Mittleider and Elizabeth Basha |     |
| <b>18</b> | <b>Wireless Power Transfer in Sensor Networks with Adaptive, Limited Knowledge Protocols . . . . .</b>                 | 465 |
|           | Constantinos Marios Angelopoulos, Sotiris Nikoletseas and Theofanis P. Raptis  |     |

**Part IV Energy Flow**

- 19 Collaborative Mobile Charging . . . . .** 505  
Sheng Zhang and Jie Wu
- 20 Assigning Hierarchy to Collaborative Mobile Charging  
in Sensor Networks . . . . .** 533  
Adelina Madhja, Sotiris Nikoletseas and Theofanis P. Raptis
- 21 Improve Charging Distance with Resonant Repeaters . . . . .** 561  
Cong Wang, Ji Li, Fan Ye and Yuanyuan Yang
- 22 Interactive Wireless Charging for Energy Balance . . . . .** 585  
Sotiris Nikoletseas, Theofanis P. Raptis  
and Christoforos Raptopoulos

**Part V Joint Operations**

- 23 Charging and Routing Activity Scheduling to Prolong  
Sensor Network Lifetime . . . . .** 607  
Yang Peng, Wensheng Zhang and Daji Qiao
- 24 Joint Design of Solar Energy Harvesting with Wireless  
Charging . . . . .** 645  
Cong Wang, Ji Li, Fan Ye and Yuanyuan Yang
- 25 Joint Mobile Energy Replenishment with Wireless Power  
Transfer and Mobile Data Gathering in Wireless  
Rechargeable Sensor Networks . . . . .** 667  
Miao Zhao, Ji Li and Yuanyuan Yang

**Part VI Electromagnetic Radiation Awareness**

- 26 Radiation Constrained Charging Utility Optimization  
for Human Safety . . . . .** 703  
Haipeng Dai, Guihai Chen, Yunhuai Liu and Tian He
- 27 Efficient Wireless Power Transfer Under Radiation  
Constraints in Wireless Distributed Systems . . . . .** 727  
Sotiris Nikoletseas, Theofanis P. Raptis  
and Christoforos Raptopoulos

# Contributors

**Constantinos Marios Angelopoulos** Bournemouth University, Bournemouth, UK

**Elizabeth Basha** Department of Electrical and Computer Engineering, University of the Pacific, Stockton, USA

**Alirio Boaventura** Instituto de Telecomunicacoes, Universidade de Aveiro, Aveiro, Portugal

**Julia Buwaya** University of Geneva, Geneva, Switzerland

**Nuno Borges Carvalho** Instituto de Telecomunicacoes, Universidade de Aveiro, Aveiro, Portugal

**Guihai Chen** State Key Laboratory for Novel Software Technology, Nanjing University, Nanjing, China

**Ana Collado** Heriot-Watt University, School of Engineering and Physical Sciences, Edinburgh, UK

**Laura Corchia** Department of Innovation Engineering, University of Salento, Lecce, Italy

**Alessandra Costanzo** Department of Electrical, Electronic and Information Engineering “Guglielmo Marconi”, University of Bologna, Bologna, Italy

**Haipeng Dai** State Key Laboratory for Novel Software Technology, Nanjing University, Nanjing, China

**Carrick Detweiler** Nebraska Intelligent MoBile Unmanned Systems (NIMBUS) Lab, Department of Computer Science and Engineering, University of Nebraska-Lincoln, Lincoln, USA

**Panagiotis D. Diamantoulakis** Aristotle University of Thessaloniki, Thessaloniki, Greece

**Michael Eiskamp** Department of Electrical and Computer Engineering, University of the Pacific, Stockton, USA

**Orestis Evangelatos** University of Geneva, Geneva, Switzerland

**Apostolos Georgiadis** School of Engineering and Physical Sciences, Institute of Sensors, Signals and Systems, Heriot-Watt University, Edinburgh, UK

**Brent Griffin** Department of Electrical Engineering and Computer Science, University of Michigan, Ann Arbor, MI, USA

**Songtao Guo** The College of Electronic and Information Engineering, Southwest University, Chongqing, People's Republic of China

**Zoran Hadzi-Velkov** Ss. Cyril and Methodius University, Skopje, Macedonia

**Tian He** Computer Science and Engineering, University of Minnesota, Minneapolis, MN, USA

**Akira Ishimaru** Department of Electrical Engineering, University of Washington, Seattle, WA, USA

**Jennifer Johnson** Department of Electrical and Computer Engineering, University of the Pacific, Stockton, USA

**Christos Kalialakis** Centre Tecnologic de Telecomunicacions de Catalunya (CTTC), Castelldefels, Barcelona, Spain

**George K. Karagiannidis** Aristotle University of Thessaloniki, Thessaloniki, Greece

**Shady Keyrouz** Eindhoven University of Technology, Eindhoven, The Netherlands

**Yasuo Kuga** Department of Electrical Engineering, University of Washington, Seattle, WA, USA

**Jinfu Leng** Nebraska Intelligent MoBile Unmanned Systems (NIMBUS) Lab, Department of Computer Science and Engineering, University of Nebraska-Lincoln, Lincoln, USA

**Ji Li** Department of Electrical and Computer Engineering, State University of New York, Stony Brook, NY, USA

**Weifa Liang** Research School of Computer Science, The Australian National University, Canberra, Australia

**Yunhuai Liu** Third Research Institute of Ministry of Public Security, Shanghai, China

**Adelina Madhja** Department of Computer Engineering and Informatics, University of Patras and Computer Technology Institute and Press "Diophantus" (CTI), Patras, Greece

**Franco Mastri** Department of Electrical, Electronic and Information Engineering “Guglielmo Marconi”, University of Bologna, Bologna, Italy

**Andrew Mittleider** Nebraska Intelligent MoBile Unmanned Systems (NIMBUS) Lab, Department of Computer Science and Engineering, University of Nebraska-Lincoln, Lincoln, USA

**Mauro Mongiardo** Department of Engineering, University of Perugia, Perugia, Italy

**Giuseppina Monti** Department of Innovation Engineering, University of Salento, Lecce, Italy

**Derrick Wing Kwan Ng** University of New South Wales, Sydney, Australia

**Sotiris Nikoletseas** Department of Computer Engineering and Informatics, University of Patras and Computer Technology Institute and Press “Diophantus” (CTI), Patras, Greece

**Yang Peng** University of Washington Bothell, Bothell, WA, USA

**Hans W. Pflug** Holst Centre/Imec, Eindhoven, The Netherlands

**Daji Qiao** Iowa State University, Ames, IA, USA

**Theofanis P. Raptis** National Research Council, Italy and, University of Patras, Greece

**Christoforos Raptopoulos** Department of Computer Engineering and Informatics, University of Patras & Computer Technology Institute and Press “Diophantus” (CTI), Greece

**José Rolim** University of Geneva, Geneva, Switzerland

**Naoki Shinohara** Kyoto University, Kyoto, Japan

**Luciano Tarricone** Department of Innovation Engineering, University of Salento, Lecce, Italy

**Koon Hoo Teo** Mitsubishi Electric Research Laboratories, Cambridge, MA, USA

**Hubregt J. Visser** Holst Centre/Imec, Eindhoven University of Technology, Eindhoven, The Netherlands

**Bingnan Wang** Mitsubishi Electric Research Laboratories, Cambridge, MA, USA

**Cong Wang** Department of Electrical and Computer Engineering, State University of New York, Stony Brook, NY, USA

**Jie Wu** Department of Computer and Information Sciences, Temple University, Philadelphia, PA, USA

**Xiaobing Wu** Wireless Research Centre, University of Canterbury, Christchurch, New Zealand

**Wenzheng Xu** College of Computer Science, Sichuan University, Chengdu, People's Republic of China

**Yuanyuan Yang** Department of Electrical and Computer Engineering, State University of New York, Stony Brook, NY, USA

**Fan Ye** Department of Electrical and Computer Engineering, State University of New York, Stony Brook, NY, USA

**William Yerazunis** Mitsubishi Electric Research Laboratories, Cambridge, MA, USA

**Hongyan Yu** The College of Electronic and Information Engineering, Southwest University, Chongqing, People's Republic of China

**Ce Zhang** Department of Electrical Engineering, University of Washington, Seattle, WA, USA

**Sheng Zhang** State Key Laboratory for Novel Software Technology, Nanjing University, Nanjing, China

**Wensheng Zhang** Iowa State University, Ames, IA, USA

**Miao Zhao** Department of Computing, The Hong Kong Polytechnic University, Hong Kong, China

**Nikola Zlatanov** Monash University, Melbourne, Australia

# **Part I**

## **Technologies**

# Chapter 1

## Non-radiative Wireless Power Transmission: Theory and Applications

**Giuseppina Monti, Mauro Mongiardo, Franco Mastri,  
Alessandra Costanzo, Laura Corchia and Luciano Tarricone**

**Abstract** Non-radiative Wireless power transfer (NR-WPT) is currently receiving considerable attention in very different application scenarios. To design optimum solutions, a systematic approach based on circuit theory is needed and not yet available in the literature. In this chapter, by using a network formalism, the WPT link is modeled as a two-port network and a methodology to derive an equivalent circuit is proposed. This allows to compute in a rigorous and general way the maximum achievable performance for any given WPT link. The latter can be expressed in terms of either maximum power transfer efficiency (MPTE), or maximum power delivered to the load (MPDL), or by any suitable combination of the two. This chapter provides a comprehensive theoretical and general framework to predict such performance for both inductive and capacitive coupled links. In order to facilitate a practical implementation, both impedance and admittance matrix representations are discussed and computational examples are provided.

---

G. Monti (✉) · L. Corchia · L. Tarricone

Department of Innovation Engineering, University of Salento, Lecce, Italy  
e-mail: giuseppina.monti@unisalento.it

L. Corchia  
e-mail: laura.corchia@unisalento.it

L. Tarricone  
e-mail: luciano.tarricone@unisalento.it

M. Mongiardo  
Department of Engineering, University of Perugia, Perugia, Italy  
e-mail: mauro.mongiardo@unipg.it

F. Mastri · A. Costanzo  
Department of Electrical, Electronic and Information Engineering “Guglielmo Marconi”,  
University of Bologna, Bologna, Italy  
e-mail: franco.mastri@unibo.it

A. Costanzo  
e-mail: alessandra.costanzo@unibo.it

## 1.1 Introduction

In recent years, NR-WPT is gaining a growing interest [3, 4, 11, 13, 15, 16], as a promising technology for energy autonomous systems (intended as electronic devices and systems able to perform their functions without having on board batteries or being connected to a power grid). In its simplest formulation, the desired goal of any NR-WPT system is to transfer energy, at a given operating frequency, with no wires, from a transmitter in position  $A$  to a receiver in position  $B$  located in the near-field of each other. The basic configuration can be implemented by realizing between the transmitting and the receiving device a mere capacitive or inductive coupling. However, several experimental and theoretical studies have demonstrated that the performance of the NR-WPT link can be significantly improved by using a resonant scheme, i.e., by designing the receiver and the transmitter as synchronous resonators. In this regard, the attention has been focused on mid-range WPT links realized by using inductively coupled resonators [2, 8, 9, 12, 14, 18]. In fact, with respect to an inductive coupling, the use of a capacitive coupling has the disadvantage of being more sensitive to the surrounding environment; additionally, it is limited to applications characterized by a small gap distance between the transmitting and the receiving device. However, in this latter case capacitive WPT represents a competitive alternative to inductive WPT [7, 17].

Accordingly, depending on the specific application, the best choice for implementing the NR-WPT can be either based on a capacitive or on an inductive coupling using appropriate compensating elements (inductances or capacitances) realizing the resonance condition at the operating frequency of the link.

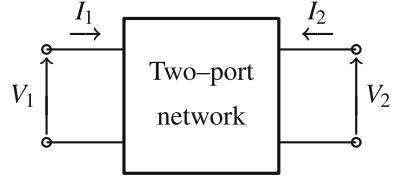
Another key point is the optimization of the parameters of the link for performance maximization. In this regard, two different design approaches can be of interest [10]: (1) maximization of the power transfer efficiency defined as the ratio between the power delivered to the load and the power provided by the source, (2) maximization of the power delivered to the load. In this chapter, by using a network formalism for describing a generic single transmitter-single receiver NR-WPT link, both approaches are introduced and discussed. Useful design formulas are derived and two examples of applications referring to an inductive and a capacitive WPT link are illustrated.

## 1.2 Two-Port Network Representation of a WPT Link

### 1.2.1 Statement of the Problem

We refer to a linear reciprocal link for wireless power transmission from a generator to a load. By using a network formalism, the WPT link can be modeled as a reciprocal two-port network. In order to introduce the variables of interest, it is assumed that a generator is on port 1 and that a load  $Z_L$  is on port 2. With reference to Fig. 1.1, the

**Fig. 1.1** Two-port network modeling a WPT link



active input power delivered from the generator to the two-port network,  $p_{in}$ , can be expressed as

$$p_{in} = \frac{1}{2}V_1I_1^*, \quad (1.1)$$

where the asterisk, ‘\*’, denotes the complex conjugate. Similarly, the active power on the load,  $p_L$ , can be expressed as

$$p_L = \frac{1}{2}V_2I_2^*. \quad (1.2)$$

With regard to the use of the two-port network for WPT applications, two different solutions are of interest

- the solution aiming at maximizing the active power delivered to the load (MPDL solution);
- the solution aiming at maximizing the power transfer efficiency (MPTE solution),  $\eta$ , defined as

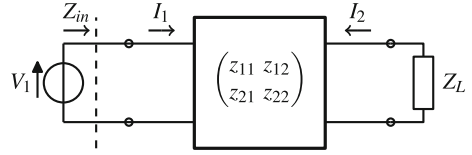
$$\eta = \frac{p_L}{p_{in}}. \quad (1.3)$$

In the following part of this section, closed form analytical formulas to compute the loads that realize the MPDL and the MPTE solutions will be derived. In particular, taking into account that, depending on the network topology, an impedance or admittance matrix can be more suited to model the two-port network, both representations will be adopted and discussed.

### 1.2.2 Impedance Matrix Modeling of a WPT Link

In this subsection the case of a reciprocal two-port network modeled by its impedance matrix, and realizing a WPT link is considered [10]. According to the impedance matrix representation, it is assumed that port 1 is connected to a voltage generator, while port 2 is terminated on a load impedance  $Z_L = R_L + jX_L$  (see Fig. 1.2). With reference to Fig. 1.2, the two-port network can be represented by the following relation:

**Fig. 1.2** Impedance matrix modeling a WPT link: it is assumed that port 1 is connected to a voltage generator, and that a load impedance  $Z_L$  is on port 2



$$\mathbf{V} = \mathbf{Z}\mathbf{I}, \quad (1.4)$$

where  $\mathbf{V}$  is the vector of port voltages,  $\mathbf{I}$  is the vector of port currents and  $\mathbf{Z}$  is the impedance matrix of the network:

$$\mathbf{Z} = \begin{pmatrix} z_{11} & z_{12} \\ z_{21} & z_{22} \end{pmatrix}, \quad (1.5)$$

with elements  $z_{ij} = r_{ij} + jx_{ij}$ , ( $i, j = 1, 2$ ), and, for the hypothesis of reciprocity,  $z_{12} = z_{21}$ . With reference to Fig. 1.2, by denoting with  $Z_{in}$  the input impedance at port 1

$$Z_{in} = R_{in} + jX_{in} = z_{11} - \frac{z_{12}^2}{z_{22} + Z_L}. \quad (1.6)$$

the active power delivered by the voltage generator to the network can be expressed as:

$$p_{in} = \frac{R_{in}}{2|Z_{in}|^2} |V_1|^2, \quad (1.7)$$

similarly, the active power delivered to the load is

$$p_L = \frac{R_L}{2|Z_L|^2} |V_2|^2. \quad (1.8)$$

It is convenient to define the parameters

$$\chi_z^2 = \frac{x_{12}^2}{r_{11}r_{22}} \quad (1.9)$$

$$\xi_z^2 = \frac{r_{12}^2}{r_{11}r_{22}} \quad (1.10)$$

and

$$\mu_z = \frac{x_{11}}{r_{11}} \quad (1.11)$$

$$\nu_z = \frac{x_{22}}{r_{22}}. \quad (1.12)$$

It is also advantageous to introduce the following definitions:

$$\theta_{r,z} = \sqrt{1 + \chi_z^2} \sqrt{1 - \xi_z^2}, \quad (1.13)$$

$$\theta_{x,z} = \chi_z \xi_z. \quad (1.14)$$

Accordingly, the impedance matrix of the two-port network can be written as

$$\mathbf{Z} = \begin{pmatrix} r_{11} (j \mu_z + 1) & \sqrt{r_{11} r_{22}} (\xi_z + j \chi_z) \\ \sqrt{r_{11} r_{22}} (\xi_z + j \chi_z) & r_{22} (j v_z + 1) \end{pmatrix} \quad (1.15)$$

The inverse of the impedance matrix is readily written as

$$\mathbf{Y} = \frac{1}{\Delta_z} \begin{pmatrix} r_{22} (j v_z + 1) & -\sqrt{r_{11} r_{22}} (\xi_z + j \chi_z) \\ -\sqrt{r_{11} r_{22}} (\xi_z + j \chi_z) & r_{11} (j \mu_z + 1) \end{pmatrix} \quad (1.16)$$

with  $\Delta_z$  being defined as

$$\Delta_z = r_{11} r_{22} [(j \mu_z + 1) (j v_z + 1) - (\xi_z + j \chi_z)^2]. \quad (1.17)$$

For this case, by adopting the two-port network for WPT applications, we address the problem of determining the optimum values of the load impedance  $Z_L = R_L + j X_L$ . Analytical formulas will be derived for both the MPDL ( $Z_L^p = R_L^p + j X_L^p$ ) and the MPTE cases ( $Z_L^e = R_L^e + j X_L^e$ ).

### 1.2.2.1 Maximum Power Delivered to the Load Solution

With reference to Fig. 1.2, the load impedance that realizes the maximum power condition is the complex conjugate of the input impedance ( $Z_{2,sc}$ ) seen at port 2 when the generator is short-circuited

$$Z_{2,sc} = \frac{V_2}{I_2}_{|V_1=0} = \frac{1}{y_{22}} = r_{22} (1 + j v_z) - \frac{r_{22} (\xi_z + j \chi_z)^2}{(1 + j \mu_z)} \quad (1.18)$$

As a consequence, the MPDL solution is

$$Z_L^p = R_L^p + j X_L^p \quad (1.19)$$

$$R_L^p = r_{22} \frac{(\mu_z^2 + \chi_z^2 + 1 - \xi_z^2 - 2 \chi_z \mu_z \xi_z)}{\mu_z^2 + 1} \quad (1.20)$$

$$X_L^p = r_{22} \frac{(\chi_z^2 \mu_z - \mu_z \xi_z^2 + 2 \chi_z \xi_z - \mu_z^2 v_z - v_z)}{\mu_z^2 + 1} \quad (1.21)$$

The active power on the load is given by

$$p_L^p = \frac{1}{2} |I_2|^2 R_L \quad (1.22)$$

where  $I_2$  can be calculated by using Thevenin's theorem. In particular, it can be easily verified that Thevenin's generator (i.e., the open circuit voltage at port 2) is given by

$$V_{th} = \frac{z_{12}}{z_{11}} V_1, \quad (1.23)$$

while the series equivalent resistance is  $Z_{2,sc}$ . Accordingly, the expression of the current  $I_2$  is

$$I_2 = \frac{1}{Z_L^p + (Z_L^p)^* \frac{z_{12}}{z_{11}}} V_1. \quad (1.24)$$

Assuming that the internal resistance of the generator at port 1 is  $r_{11}$ , the available active power is

$$P_0 = \frac{|V_1|^2}{8r_{11}}. \quad (1.25)$$

By using (1.20), (1.21) and (1.24), the active power delivered to the load, normalized with respect to  $P_0$ , is

$$P_L^p = \frac{(\xi_z^2 + \chi_z^2)}{(1 - \xi_z^2 - 2\chi_z\mu_z\xi_z + \mu_z^2 + \chi_z^2)} \quad (1.26)$$

By equating to zero the derivative of (1.26) with respect to  $\mu_z$ , we obtain that  $\mu_z$  must satisfy the following relation:

$$\mu_z = \theta_{x,z} \quad (1.27)$$

or equivalently,

$$x_{11} = x_{12} \frac{r_{12}}{r_{22}}. \quad (1.28)$$

Condition (1.28) can be satisfied by adding in series to port 1 a compensating reactance  $X_{c1}$  (see Fig. 1.5)

$$X_{c1} = x_{12} \frac{r_{12}}{r_{22}} - x_{11}. \quad (1.29)$$

When  $X_{c1}$  is added to the network,  $\mu_z$  satisfies (1.27) and the following expression can be derived for the MPDL solution

$$Z_L^p = R_L^p + jX_L^p \quad (1.30)$$

$$R_L^p = r_{22} \frac{\theta_{r,z}^2}{\theta_{x,z}^2 + 1} \quad (1.31)$$

$$X_L^p = -x_{22} + r_{22}\theta_{x,z} + r_{22} \frac{\theta_{x,z}\theta_{r,z}^2}{1 + \theta_{x,z}^2}. \quad (1.32)$$

Additionally, when (1.27) is satisfied, from (1.6) it can be easily verified that the input impedance of the network is purely resistive and is given by

$$R_{in}^p = 2r_{11} \frac{\theta_{r,z}^2}{1 + \theta_{r,z}^2 + \theta_{x,z}^2}. \quad (1.33)$$

According to (1.33), the input power, normalized to  $P_0$  as defined in (1.25), is

$$P_{in}^p = 2 \frac{1 + \theta_{r,z}^2 + \theta_{x,z}^2}{\theta_{r,z}^2}, \quad (1.34)$$

while the normalized active power on the load is

$$P_L^p = \frac{\chi_z^2 + \xi_z^2}{\theta_{r,z}^2}. \quad (1.35)$$

Finally, the expression of the efficiency corresponding to the MPDL solution given in (1.30)–(1.32) is

$$\eta^p = \frac{1}{2} \frac{\chi_z^2 + \xi_z^2}{1 + \theta_{r,z}^2 + \theta_{x,z}^2}. \quad (1.36)$$

It is worth observing that, when  $r_{12} = 0$  the MPDL solution simplifies as follows:

$$Z_L^p = R_L^p + jX_L^p \quad (1.37)$$

$$R_L^p = r_{22}\theta_{r,z}^2 \quad (1.38)$$

$$X_L^p = -x_{22}. \quad (1.39)$$

In this case, the expression for the efficiency becomes

$$\eta^p = \frac{\chi_z^2}{2(2 + \chi_z^2)} \quad (1.40)$$

which asymptotically, for  $\chi_z \rightarrow \infty$ , provides an efficiency value of  $\eta_\infty^p \rightarrow 1/2$ . For this case, the normalized active power on the load is given by

**Fig. 1.3** Normalized power with respect to  $\chi_z$  when  $\xi_z = 0$ . The *black line* refers to the MPDL solution (1.41), while the *red line* refers to the MPTE solution (1.65)

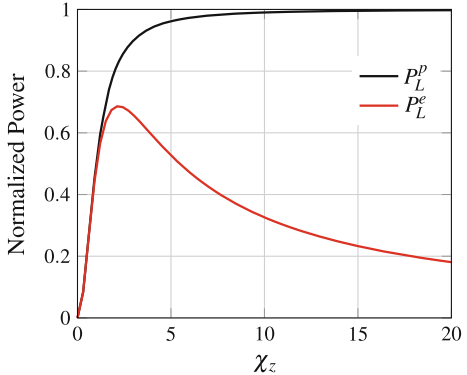
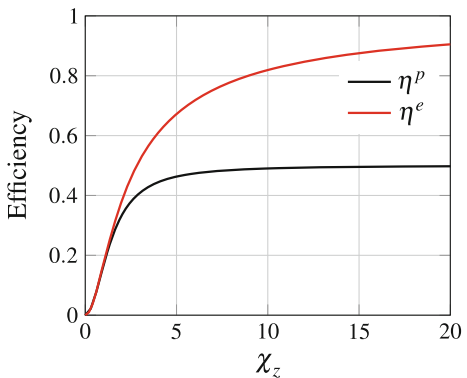


**Fig. 1.4** Efficiency with respect to  $\chi_z = x_{12}/\sqrt{r_{11}r_{22}}$  when  $\xi_z = r_{12}/\sqrt{r_{11}r_{22}} = 0$ . The *black line* refers to MPDL solution (1.40), while the *red line* refers to the MPTE solution (1.56)



$$P_L^p = \frac{\chi_z^2}{(1 + \chi_z^2)} \quad (1.41)$$

which asymptotically, for  $\chi_z \rightarrow \infty$ , gives  $P_L^p \rightarrow 1$ . Assuming that  $r_{11}$  is the generator resistance, the power on the load approaches the generator available power as  $\chi_z \rightarrow \infty$ . For this solution, the dependence on  $\chi_z$  of  $P_L^p$  and of  $\eta^p$  is illustrated in Fig. 1.3 and in Fig. 1.4, respectively. From Fig. 1.3 it can be seen that the maximum of the normalized output power increases monotonically with  $\chi_z$  approaching its maximum value (i.e., 1), corresponding to the case where all the power available for the source is delivered to the load. Conversely, from Fig. 1.4, it can be seen that, although also the efficiency increases monotonically with  $\chi_z$ , in this case the asymptotic value is 0.5, and thus lower than the maximum achievable value of 1.

### 1.2.2.2 Maximum Power Transfer Efficiency (MPTE)

As already seen, the power transfer efficiency  $\eta$  is expressed as the ratio between the active power delivered to the load (i.e., the power dissipated on the load impedance

$Z_L$ ) and the active power delivered to the network by the generator. By using (1.7)–(1.8), the efficiency of the two-port network can be expressed as follows:

$$\eta = \frac{p_L}{p_{in}} = \frac{R_L}{R_{in}} \frac{|Z_{in}|^2}{|Z_L|^2} \frac{|V_2|^2}{|V_1|^2}. \quad (1.42)$$

The voltage  $V_2$  can be expressed as follows:

$$V_2 = z_{12}I_1 + z_{22}I_2 \quad (1.43)$$

where the currents  $I_1$  and  $I_2$  are given by:

$$I_1 = \frac{V_1}{Z_{in}} \quad (1.44)$$

$$I_2 = -\frac{V_2}{Z_L}. \quad (1.45)$$

By substituting (1.44)–(1.45) in (1.43), the following expression can be obtained for the voltage at port 2:

$$V_2 = \frac{z_{12}Z_L}{Z_{in}(z_{22} + Z_L)} V_1 \quad (1.46)$$

accordingly, the efficiency of the network is given by

$$\eta = \frac{R_L}{R_{in}} \left| \frac{z_{12}}{z_{22} + Z_L} \right|^2. \quad (1.47)$$

The value of the MPTE solution can be obtained by solving the following system of equations:

$$\begin{aligned} \frac{\partial \eta}{\partial R_L} &= 0 \\ \frac{\partial \eta}{\partial X_L} &= 0 \end{aligned} \quad (1.48)$$

By solving (1.48), the following expression is obtained for the MPTE solution:

$$Z_L^e = R_L^e + jX_L^e \quad (1.49)$$

$$R_L^e = r_{22}\theta_{r,z} \quad (1.50)$$

$$X_L^e = r_{22}\theta_{x,z} - x_{22} \quad (1.51)$$

By comparing (1.49)–(1.51) with (1.30)–(1.32), it is evident that the MPTE solution has both the real and the imaginary parts different from the ones corresponding to the MPDL solution.

By substituting (1.49)–(1.51) into (1.47), the expression for the efficiency corresponding to the MPTE solution (i.e.,  $\eta^e$ ) is obtained:

$$\eta^e = \frac{\xi_z^2 + \chi_z^2}{(\theta_{r,z} + 1)^2 + \theta_{x,z}^2} \quad (1.52)$$

It is worth observing that, when  $r_{12} = 0$ , the MPTE solution reduces to

$$Z_L^e = R_L^e + jX_L^e \quad (1.53)$$

$$R_L^e = r_{22}\theta_{r,z} \quad (1.54)$$

$$X_L^e = -x_{22} \quad (1.55)$$

By comparing (1.53)–(1.55) with (1.37)–(1.39), it can be noticed that for  $r_{12} = 0$  the MPTE and the MPDL solutions have the same imaginary part. In this case, the expression of the efficiency given in (1.52) becomes

$$\eta^e = \frac{\chi_z^2}{(1 + \sqrt{1 + \chi_z^2})^2}. \quad (1.56)$$

which asymptotically, for  $\chi_z \rightarrow \infty$ , provides an efficiency value of  $\eta_\infty^e \rightarrow 1$  (see Fig. 1.4).

The input impedance  $Z_{in}^e$  at port 1 when port 2 is terminated by  $Z_L^e$  is given by

$$Z_{in}^e = r_{11}\theta_{r,z} - j(r_{11}\theta_{x,z} - x_{11}). \quad (1.57)$$

The active input power  $P_{in}^e$  normalized to  $P_0$  corresponding to this solution is

$$P_{in}^e = \frac{4\theta_{r,z}}{(\theta_{x,z} - \mu_z)^2 + \theta_{r,z}^2}, \quad (1.58)$$

The active power on the load  $P_L^e$ , always normalized to  $P_0$ , is expressed as

$$P_L^e = 4 \frac{\theta_{r,z} (\xi_z^2 + \chi_z^2)}{\left((\theta_{x,z} - \mu_z)^2 + \theta_{r,z}^2\right) \left((\theta_{r,z} + 1)^2 + \theta_{x,z}^2\right)} \quad (1.59)$$

It is evident that both  $P_{in}^e$  and  $P_L^e$  are maximized when the following condition is satisfied:

$$\mu_z = \theta_{x,z} \quad (1.60)$$

or explicitly

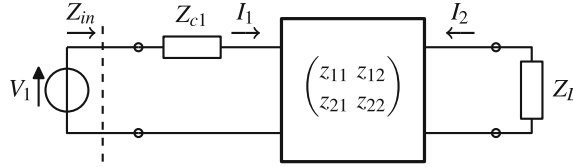


**Fig. 1.5** Two-port network with added impedance  $Z_{c1} = R_{c1} + jX_{c1}$ . The value of  $X_{c1}$  is given in (1.29), while  $R_{c1} = 0$  for both the maximum efficiency and maximum power transfer approach

$$x_{11} = x_{12} \frac{r_{12}}{r_{22}}. \quad (1.61)$$

As already seen for the MPDL case, condition (1.61) can be satisfied by adding a compensating reactance  $X_{c1}$  in series to port 1 (see Fig. 1.5), of value

$$X_{c1} = x_{12} \frac{r_{12}}{r_{22}} - x_{11}. \quad (1.62)$$

By comparing (1.62) and (1.29) it is evident that the same compensating reactance is necessary for the MPTE and the MPDL solution.

When  $X_{c1}$  as given by (1.62) is added, the condition (1.61) is realized and from (1.58) we have the following expressions for the normalized input power:

$$P_{in}^e = \frac{4}{\theta_{r,z}} \quad (1.63)$$

and for the power on the load

$$P_L^e = \frac{4\eta^e}{\theta_{r,z}} \quad (1.64)$$

When  $\xi_z = 0$ , (1.64) reduces to the following expression:

$$P_L^e = \frac{4\chi_z^2}{\sqrt{1 + \chi_z^2} (1 + \sqrt{1 + \chi_z^2})^2} \quad (1.65)$$

which, asymptotically, for  $\chi_z \rightarrow \infty$ , gives a behavior of the type  $P_L^e \rightarrow P_0/\chi_z$ , as shown in Fig. 1.3. As a consequence, for the MPTE solution, when the efficiency tends to one the output power reduces to zero.

As a simple example of application of (1.61), let us consider the case of two coupled inductors  $L_1, L_2$  with the following impedance matrix:  $z_{11} = r_1 + j\omega L_1$ ,  $z_{12} = j\omega M$  and  $z_{22} = r_2 + j\omega L_2$ . In this case we have  $X_{c1} = -x_{11} = -j\omega L_1$ . Therefore, at the frequency of interest  $\omega_0$ , a series capacitance  $C_1$  of value  $C_1 = 1/(\omega_0^2 L_1)$  realizes the sought  $X_{c1}$ . Table 1.1 summarizes all the relevant formulas which allow maximizing either the power on the load or the efficiency of a WPT link described by its impedance matrix.

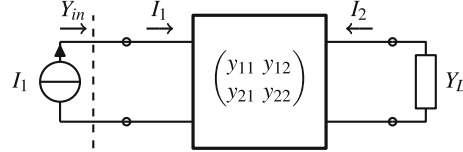


**Fig. 1.6** Admittance matrix modeling a WPT link: it is assumed that port 1 is connected to a current generator, and that a load admittance  $Y_L$  is on port 2

### 1.2.3 Admittance Matrix Modeling of a WPT Link

Let us now consider the case of a reciprocal two-port network modeled by its admittance matrix. According to the admittance matrix representation, it is assumed that port 1 is connected to a current generator, while port 2 is terminated on a load admittance  $Y_L = G_L + jB_L$ . With reference to Fig. 1.6, the two-port network can be represented by the following relation:

$$\mathbf{I} = \mathbf{Y}\mathbf{V}, \quad (1.66)$$

where  $\mathbf{V}$  is the vector of port voltages,  $\mathbf{I}$  is the vector of port currents and  $\mathbf{Y}$  is the admittance matrix of the network:

$$\mathbf{Y} = \begin{pmatrix} y_{11} & y_{12} \\ y_{21} & y_{22} \end{pmatrix}, \quad (1.67)$$

with elements  $y_{ij} = g_{ij} + jb_{ij}$ , ( $i, j = 1, 2$ ), and, for the hypothesis of reciprocity,  $y_{12} = y_{21}$ . With reference to Fig. 1.6, by denoting with  $Y_{in}$  the input admittance of the network at port 1

$$Y_{in} = G_{in} + jB_{in} = y_{11} - \frac{y_{12}^2}{y_{22} + Y_L}, \quad (1.68)$$

the active power delivered by the current generator to the network can be expressed as

$$p_{in} = \frac{G_{in}}{2|Y_{in}|^2} |I_1|^2, \quad (1.69)$$

similarly, the active power delivered to the load is

$$p_L = \frac{G_L}{2|Y_L|^2} |I_2|^2. \quad (1.70)$$

For this case, we address the problem of determining suitable values for the load admittance  $Y_L = G_L + jB_L$ , for realizing wireless power transfer. In particular, closed form analytical formulas will be derived for the MPDL solution,  $Y_L^p = G_L^p + jB_L^p$ , and the MPTE solution,  $Y_L^e = G_L^e + jB_L^e$ .

It is convenient to define the parameters

$$\chi_y^2 = \frac{b_{12}^2}{g_{11}g_{22}} \quad (1.71)$$

$$\xi_y^2 = \frac{g_{12}^2}{g_{11}g_{22}} \quad (1.72)$$

and

$$\mu_y = b_{11}/g_{11} \quad (1.73)$$

$$\nu_y = b_{22}/g_{22} . \quad (1.74)$$

It is also advantageous to introduce the following definitions:

$$\theta_{r,y} = \sqrt{1 + \chi_y^2} \sqrt{1 - \xi_y^2}, \quad (1.75)$$

$$\theta_{x,y} = \chi_y \xi_y . \quad (1.76)$$

According to the above definitions the admittance matrix of the two-port network can be written as

$$\mathbf{Y} = \begin{pmatrix} \frac{g_{11} (j \mu_y + 1)}{\sqrt{g_{11} g_{22}} (\xi_y + j \chi_y)} & \frac{\sqrt{g_{11} g_{22}} (\xi_y + j \chi_y)}{g_{22} (j \nu_y + 1)} \\ -\frac{g_{22} (j \nu_y + 1)}{\sqrt{g_{11} g_{22}} (\xi_y + j \chi_y)} & \frac{-\sqrt{g_{11} g_{22}} (\xi_y + j \chi_y)}{g_{11} (j \mu_y + 1)} \end{pmatrix} \quad (1.77)$$

The inverse of the admittance matrix is

$$\mathbf{Z} = \frac{1}{\Delta} \begin{pmatrix} \frac{g_{22} (j \nu_y + 1)}{\sqrt{g_{11} g_{22}} (\xi_y + j \chi_y)} & -\frac{\sqrt{g_{11} g_{22}} (\xi_y + j \chi_y)}{g_{11} (j \mu_y + 1)} \\ -\frac{g_{11} (j \mu_y + 1)}{\sqrt{g_{11} g_{22}} (\xi_y + j \chi_y)} & \frac{-\sqrt{g_{11} g_{22}} (\xi_y + j \chi_y)}{g_{22} (j \nu_y + 1)} \end{pmatrix} \quad (1.78)$$

with  $\Delta$  being defined as

$$\Delta = g_{11} g_{22} \left[ (j \mu_y + 1) (j \nu_y + 1) - (\xi_y + j \chi_y)^2 \right] . \quad (1.79)$$

### 1.2.3.1 Maximum Power Delivered to the Load Solution

With reference to Fig. 1.6, the load admittance which realizes the maximum power transfer condition is the complex conjugate of the input admittance ( $Y_{2,oc}$ ) seen at port 2 when the generator on port 1 is replaced with an open circuit

$$Y_{2,oc} = \frac{I_2}{V_2|_{I_1=0}} = \frac{1}{z_{22}} = g_{22} (1 + j \nu_y) - \frac{g_{22} (\xi_y + j \chi_y)^2}{(1 + j \mu_y)} \quad (1.80)$$

According to (1.80), the MPDL solution,  $Y_L^p = G_L^p + jB_L^p$ , is

$$Y_L^p = G_L^p + jB_L^p$$

$$G_L^p = g_{22} \frac{(\mu_y^2 + \chi_y^2 + 1 - \xi_y^2 - 2\chi_y\mu_y\xi_y)}{\mu_y^2 + 1} \quad (1.81)$$

$$B_L^p = g_{22} \frac{(\chi_y^2\mu_y - \mu_y\xi_y^2 + 2\chi_y\xi_y - \mu_y^2\nu_y - \nu_y)}{\mu_y^2 + 1} \quad (1.82)$$

Assuming that the generator on port 1 has a conductance  $g_{11}$ , the active available power is

$$P_0 = \frac{|I_1|^2}{8g_{11}}. \quad (1.83)$$

By using (1.81), the active power on the load normalized with respect to  $P_0$  is

$$P_L^p = \frac{(\xi_y^2 + \chi_y^2)}{(1 - \xi_y^2 - 2\chi_y\mu_y\xi_y + \mu_y^2 + \chi_y^2)} \quad (1.84)$$

By deriving (1.84) with respect to  $\mu_y$  and setting to zero the derivative, the following condition can be obtained:

$$\mu_y = \chi_y\xi_y. \quad (1.85)$$

Condition (1.85) is equivalent to

$$b_{11} = b_{12} \frac{g_{12}}{g_{22}}. \quad (1.86)$$

This condition can be satisfied by adding a parallel susceptance  $B_{c1}$  at port 1 (see Fig. 1.7)

$$B_{c1} = b_{12} \frac{g_{12}}{g_{22}} - b_{11}. \quad (1.87)$$

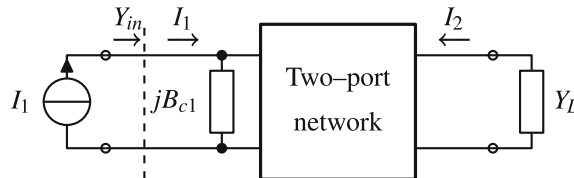


**Fig. 1.7** Two-port network modeled by its admittance matrix: a susceptance  $Y_{c1} = jB_{c1}$  is added for realizing the MPDL and the MPTE solution. The value of  $B_{c1}$  is given in (1.87) for both the maximum efficiency (MPTE) and maximum power transfer (MPDL) approach

When  $B_{c1}$  is added to the network, the following expressions can be obtained for the MPDL solution:

$$Y_L^p = G_L^p + jB_L^p \quad (1.88)$$

$$G_L^p = g_{22} \frac{\theta_{r,y}^2}{\theta_{x,y}^2 + 1} \quad (1.89)$$

$$B_L^p = -b_{22} + g_{22}\theta_{x,y} + g_{22} \frac{\theta_{x,y}\theta_{r,y}^2}{1 + \theta_{x,y}^2}. \quad (1.90)$$

When (1.85) is fulfilled, the input admittance is expressed by

$$G_{in}^p = 2g_{11} \frac{\theta_{r,y}^2}{1 + \theta_{r,y}^2 + \theta_{x,y}^2}. \quad (1.91)$$

It is noted that the input admittance is purely resistive. The input power, normalized to  $P_0$  of (1.83) is easily computed as

$$P_{in}^p = 2 \frac{1 + \theta_{r,y}^2 + \theta_{x,y}^2}{\theta_{r,y}^2}, \quad (1.92)$$

while the normalized active power on the load is

$$P_L^p = \frac{\chi_y^2 + \xi_y^2}{\theta_{r,y}^2}. \quad (1.93)$$

Finally, the expression for the efficiency is recovered as

$$\eta^p = \frac{1}{2} \frac{\chi_y^2 + \xi_y^2}{1 + \theta_{r,y}^2 + \theta_{x,y}^2}. \quad (1.94)$$

When  $g_{12} = 0$ , we obtain the following expression for the efficiency:

$$\eta^p = \frac{\chi_y^2}{2(2 + \chi_y^2)} \quad (1.95)$$

which asymptotically, for  $\chi_y \rightarrow \infty$ , provides an efficiency value of  $\eta_\infty^p \rightarrow 1/2$ . For this case we can express the normalized active power on the load as

$$P_L^p = \frac{\chi_y^2}{(1 + \chi_y^2)} \quad (1.96)$$

which asymptotically, for  $\chi_y \rightarrow \infty$ , gives  $P_L^p \rightarrow 1$ . Assuming that  $g_{11}$  is the generator resistance, the power on the load approaches the generator available power as  $\chi_y \rightarrow \infty$ . Note that the maximum power on the load, for this solution, increases monotonically with  $\chi_y$ .

### 1.2.3.2 Maximum Power Transfer Efficiency (MPTE)

By using (1.68), the following expression can be obtained for the efficiency of the network:

$$\eta = \frac{P_L}{p_{in}} = \frac{G_L}{G_{in}} \left| \frac{y_{12}}{y_{22} + Y_L} \right|^2. \quad (1.97)$$

For a given two-port network the efficiency  $\eta$  is maximized when the following relations are satisfied

$$\frac{\partial \eta}{\partial G_L} = 0 \quad (1.98)$$

$$\frac{\partial \eta}{\partial B_L} = 0. \quad (1.99)$$

By solving (1.98)–(1.99) for the MPTE the following results can be obtained [1]:

$$Y_L^e = G_L^e + j B_L^e \quad (1.100)$$

$$G_L^e = g_{22}\theta_r \quad (1.101)$$

$$B_L^e = g_{22}\theta_x - x_{22}. \quad (1.102)$$

The expression of the efficiency corresponding to the MPTE solution is

$$\eta^e = \frac{\xi_y^2 + \chi_y^2}{(\theta_{r,y} + 1)^2 + \theta_{x,y}^2} \quad (1.103)$$

Noticeably, when  $g_{12} = 0$ , (1.103) reduces to:

$$\eta^e = \frac{\chi_y^2}{(1 + \sqrt{1 + \chi_y^2})^2}. \quad (1.104)$$

which asymptotically, for  $\chi_y \rightarrow \infty$ , provides an efficiency value of  $\eta_\infty^e \rightarrow 1$ . Similarly, also for  $\xi_y \rightarrow 1$  we have  $\eta^e \rightarrow 1$ .

The input admittance  $Y_{in}^e$  at port 1 when port 2 is terminated by  $Y_L$  is given by

$$Y_{in}^e = g_{11}\theta_r - j(r_{11}\theta_{x,y} - x_{11}). \quad (1.105)$$

We can express the active input power  $P_{in}^e$  normalized to  $P_0$  as

$$P_{in}^e = \frac{4\theta_{r,y}}{(\theta_{x,y} - \mu_y)^2 + \theta_{r,y}^2}, \quad (1.106)$$

The active power on the load  $P_L^e$ , always normalized to  $P_0$ , is expressed as

$$P_L^e = 4 \frac{\theta_{r,y} (\xi_y^2 + \chi_y^2)}{(\theta_{x,y} - \mu_y)^2 + \theta_{r,y}^2} \left( (\theta_{r,y} + 1)^2 + \theta_{x,y}^2 \right) \quad (1.107)$$

It is evident that both  $P_{in}^e$  and  $P_L^e$  are maximized when the condition (1.86), or equivalently the condition (1.85), derived for the MPDL case is satisfied. Consequently, as already seen for the MPDL solution, the MPTE solution can be realized by adding in parallel to port 1 the susceptance  $B_{c1}$  given in (1.87).

When  $B_{c1}$  is added, the condition (1.86) is realized and from (1.106) we have the following expressions for the normalized input power:

$$P_{in}^e = \frac{4}{\theta_{r,y}} \quad (1.108)$$

and for the power on the load

$$P_L^e = \frac{4\eta^e}{\theta_{r,y}} \quad (1.109)$$

When  $\xi_y = 0$  (1.109) reduces to the following expression:

$$P_L^e = \frac{4\chi_y^2}{\sqrt{1 + \chi_y^2} \left( 1 + \sqrt{1 + \chi_y^2} \right)^2} \quad (1.110)$$

which, asymptotically, for  $\chi_y \rightarrow \infty$ , gives a behavior of the type  $P_L^e \rightarrow P_0/\chi_y$ . Thus, for the solution that maximizes the efficiency, when the efficiency tends to one the output power reduces to zero. Table 1.2 summarizes the relevant formulas for maximizing either the power on the load or the efficiency of a WPT link described by its admittance matrix.

### 1.3 Application of Theory: The Case of Two Coupled Inductances

The simplest case of WPT that can be conveniently described by an impedance matrix approach is provided by two coupled inductors. With reference to Fig. 1.8, the mutual inductance is denoted with  $M$ :

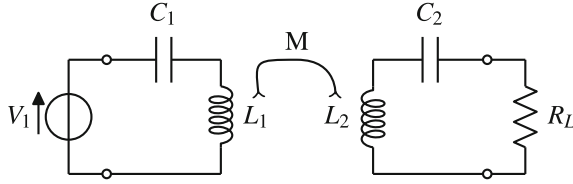


**Fig. 1.8** Matching network for coupled inductances. Note that  $L_i C_i = 1/\omega_0^2$ ,  $i = 1, 2$  at the operating angular frequency  $\omega_0$ . The value of  $R_L$  is provided in Table 1.3

$$M = k\sqrt{L_1 L_2}, \quad (1.111)$$

where  $k$  is the magnetic coupling coefficient. When a particular configuration is chosen the nominal coupling coefficient for that configuration will be denoted by  $k_0$ . The impedance matrix of the two coupled inductors is

$$\begin{bmatrix} z_{11} & z_{12} \\ z_{21} & z_{21} \end{bmatrix} = \begin{bmatrix} r_1 + j\omega L_1 & j\omega M \\ j\omega M & r_2 + j\omega L_2 \end{bmatrix}. \quad (1.112)$$

Assuming that the WPT link operates at the angular frequency  $\omega_0$ , it is convenient to introduce the following parameters:

$$\omega = u \omega_0 \quad (1.113)$$

$$L_1 = \frac{X_0}{\omega_0} \quad (1.114)$$

$$L_2 = L_1 N^2 \quad (1.115)$$

$$M = L_1 N k \quad (1.116)$$

$$r_1 = \frac{X_0}{Q_1} \quad (1.117)$$

$$r_2 = \frac{X_0 N^2}{Q_2}. \quad (1.118)$$

The parameter  $u$  is the frequency normalized with respect to the operating frequency of the link. The parameter  $N^2$  is the ratio between  $L_2$  and  $L_1$ . The resistances are expressed in terms of the quality factors  $Q_1$  and  $Q_2$ . According to these definitions, (1.112) becomes

$$\mathbf{Z} = \begin{bmatrix} \frac{X_0}{Q_1} + j X_0 & j k_0 X_0 N \\ j k_0 X_0 N & \frac{X_0 N^2}{Q_2} + j X_0 N^2 \end{bmatrix} \quad (1.119)$$

With reference to Table 1.1, since  $r_{12} = 0$ , for the parameters  $\chi_z$ ,  $\xi_z$ ,  $\theta_{r,z}$  and  $\theta_{x,z}$ , the following simplified expressions can be derived

$$\chi_z^2 = k_0^2 Q_1 Q_2 \quad (1.120)$$

**Table 1.1** Impedance matrix representation of a two-port WPT link: a summary of the parameters' values for the approaches that maximize efficiency and power. The parameters have the following meanings:  $\chi_z = x_{12}/\sqrt{r_{11}r_{22}}$ ,  $\xi_z = r_{12}/\sqrt{r_{11}r_{22}}$ ,  $\theta_{r,z} = \sqrt{1 + \chi_z^2}\sqrt{1 - \xi_z^2}$ ,  $\theta_{x,z} = \chi_z\xi_z$ . The power has been normalized w.r.t.  $P_0 = |V_1|^2/(8r_{11})$

| Parameter | Maximum efficiency  | Maximum power  |
|-----------|---|--|
| $R_L$     | $r_{22}\theta_{r,z}^2$  | $r_{22}\theta_{r,z}^2/(\theta_{x,z}^2 + 1)$  |
| $X_L$     | $r_{22}\theta_{x,z} - x_{22}$   | $-x_{22} + r_{22}\theta_{x,z} + r_{22}\theta_{x,z}\theta_{r,z}^2/(\theta_{x,z}^2 + 1)$ |
| $R_{c1}$  | 0   | 0  |
| $X_{c1}$  | $x_{12}r_{12}/r_{22} - x_{11}$  | $x_{12}r_{12}/r_{22} - x_{11}$   |
| $R_{in}$  | $r_{11}\theta_{r,z}$  | $2r_{11}\theta_{r,z}^2/(1 + \theta_{r,z}^2 + \theta_{x,z}^2)$                          |
| $X_{in}$  | 0   | 0  |
| $P_{in}$  | $4/\theta_{r,z}$  | $2(1 + \theta_{r,z}^2 + \theta_{x,z}^2)/\theta_{r,z}^2$                                |
| $P_L$     | $4\eta^e/\theta_{r,z}$  | $(\xi_z^2 + \chi_z^2)/\theta_{r,z}^2$  |
| $\eta$    | $\eta^e = (\xi_z^2 + \chi_z^2)/((1 + \theta_{r,z}^2)^2 + \theta_{x,z}^2)$ | $(\xi_z^2 + \chi_z^2)/(2(1 + \theta_{r,z}^2 + \theta_{x,z}^2))$                        |

**Table 1.2** Admittance matrix representation of a two-port WPT link: a summary of the parameters' values for the approaches that maximize efficiency and power. The parameters have the following meanings:  $\chi_y = b_{12}/\sqrt{g_{11}g_{22}}$ ,  $\xi_y = g_{12}/\sqrt{g_{11}g_{22}}$ ,  $\theta_{r,y} = \sqrt{1 + \chi_y^2}\sqrt{1 - \xi_y^2}$ ,  $\theta_{x,y} = \chi_y\xi_y$ . The power has been normalized w.r.t.  $P_0 = |I_1|^2/(8g_{11})$

| Parameter | Maximum efficiency  | Maximum power  |
|-----------|---|--|
| $G_L$     | $g_{22}\theta_r$  | $g_{22}\theta_{r,y}^2/(\theta_{x,y}^2 + 1)$  |
| $B_L$     | $g_{22}\theta_{x,y} - b_{22}$   | $-b_{22} + g_{22}\theta_{x,y} + g_{22}\theta_{x,y}\theta_{r,y}^2/(\theta_{x,y}^2 + 1)$ |
| $G_{c1}$  | 0   | 0  |
| $B_{c1}$  | $b_{12}g_{12}/g_{22} - b_{11}$  | $b_{12}g_{12}/g_{22} - b_{11}$   |
| $G_{in}$  | $g_{11}\theta_{r,y}$  | $2g_{11}\theta_{r,y}^2/(1 + \theta_{r,y}^2 + \theta_{x,y}^2)$                          |
| $B_{in}$  | 0   | 0  |
| $P_{in}$  | $4/\theta_{r,y}$  | $2(1 + \theta_{r,y}^2 + \theta_{x,y}^2)/(\theta_{r,y}^2)$                              |
| $P_L$     | $4\eta^e/\theta_{r,y}$  | $(\xi_y^2 + \chi_y^2)/\theta_{r,y}^2$  |
| $\eta$    | $\eta^e = (\xi_y^2 + \chi_y^2)/((1 + \theta_{r,y}^2)^2 + \theta_{x,y}^2)$ | $(\xi_y^2 + \chi_y^2)/(2(1 + \theta_{r,y}^2 + \theta_{x,y}^2))$                        |

$$\xi_z^2 = 0 \quad (1.121)$$

$$\theta_{r,z} = \sqrt{1 + \chi_z^2} \quad (1.122)$$

$$\theta_{x,z} = 0. \quad (1.123)$$

Accordingly, it can be easily derived that the matching element  $X_{c1}$  is given by

$$X_{c1} = -X_0 = -x_{11} = -\omega L_1 \quad (1.124)$$

**Table 1.3** A summary of the parameters' values for the approaches that maximize efficiency and power for coupled inductors. The parameters have the following meanings:  $\chi_z^2 = \alpha = k_0^2 Q_1 Q_2$  and  $R_0 = X_0 N^2 / Q_2$ . Note that the quantities  $P_{in}$ ,  $P_L$ , are normalized w.r.t.  $P_0 = |V_1|^2 / (8r_{11})$ . In the present case we have  $r_{11} = X_0 / Q_1$

| Parameter | Maximum efficiency  | Maximum power                        |
|-----------|---|--------------------------------------|
| $R_L$     | $\sqrt{\alpha + 1} R_0$                                     | $R_0(1 + \alpha)$                    |
| $X_L$     | $-X_0 N^2$  | $-X_0 N^2$                           |
| $X_{c1}$  | $-X_0$  | $-X_0$                               |
| $R_{in}$  | $X_0 \sqrt{1 + \alpha} / Q_1$                               | $2X_0(1 + \alpha) / (2Q_1 + \alpha)$ |
| $X_{in}$  | 0   | 0                                    |
| $P_{in}$  | $4/\sqrt{\alpha + 1}$                                       | $2(\alpha + 2) / (1 + \alpha)$       |
| $P_L$     | $4\alpha / ((1 + \sqrt{\alpha + 1})^2 (\sqrt{1 + \alpha}))$ | $\alpha / (1 + \alpha)$              |
| $\eta$    | $\alpha / (1 + \sqrt{\alpha + 1})^2$                        | $\alpha / (2(\alpha + 2))$           |

consequently, as illustrated in Fig. 1.8,  $X_{c1}$  is realized by a capacitance  $C_1$  of value  $C_1 = 1 / (\omega_0^2 L_1)$ . Similarly, the reactive part of the load impedance of both the MPDL and the MPTE solution, is given by:

$$X_L = X_L^p = X_L^e = -X_0 N^2 = -x_{22} = -\omega L_2 \quad (1.125)$$

Accordingly,  $X_L$  is realized by a capacitance  $C_2$  of value  $C_2 = 1 / (\omega_0^2 L_2)$ . These results are highlighted in Table 1.3, where all the relevant quantities of interest for both the MPDL and the MPTE solution are summarized.

It is worth observing that, in the MPTE solution the active power on the load decreases as the parameter  $\alpha$  is increased. In fact, from Table 1.3 it can be seen that asymptotically, for  $\alpha \rightarrow \infty$ , the behavior of the power on the load is  $P_L^e \rightarrow P_0 / \sqrt{\alpha}$ . Therefore, even when selecting coils with high quality factor and relatively high nominal coupling  $k_0$  and thus obtaining high values of  $\alpha$ , the power delivered to the load will be modest, even if the efficiency is close to 1. Conversely, in the case of the MPDL solution, asymptotically, for  $\alpha \rightarrow \infty$ , the behavior of the output power on the load, which also represents the available output power of the WPT system, is  $P_L^p \rightarrow P_0$ . These considerations are highlighted in Fig. 1.9, where the ratio between the output power provided by the MPTE ( $P_L^e$ ) and by the MPDL ( $P_L^p$ ) is reported. The corresponding efficiencies are reported in Fig. 1.10. It can be observed that, as the figure of merit  $\alpha$  is increased,  $P_L^e$  becomes a smaller fraction of the available power.

**Fig. 1.9** Ratio between output power corresponding to the MPTE solution (i.e.,  $P_L^e$ ) and maximum output power (i.e.,  $P_L^p$ ) as a function of the figure of merit  $\alpha$

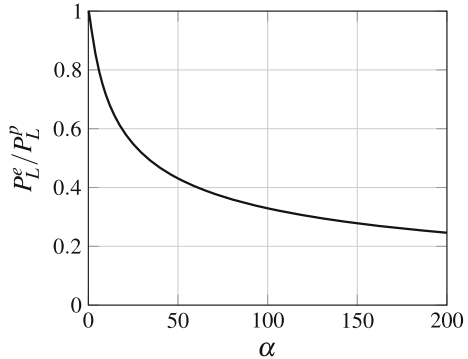
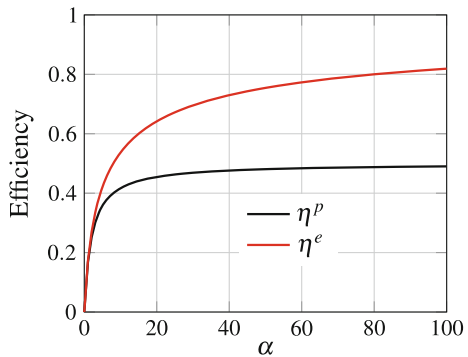


**Fig. 1.10** Efficiency: the black line corresponds to the solution maximizing the power on the load; the red line corresponds to the solution maximizing the efficiency



### 1.3.1 Coupled Inductances with a Capacitive T Network on the Primary Side

In this section the network analyzed in [5, 6] and realizing a  $1 : n$  transformer is discussed. The corresponding schematic is illustrated in Fig. 1.11, it consists of two coupled inductances modeled by an impedance inverter with a capacitive T network on the primary side. According to the analysis developed in [5], a  $1 : n$  transformer can be realized by choosing

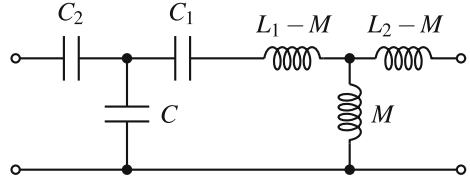
$$C = \frac{n}{N} \frac{1}{\omega_0^2 k_0 L_1} \quad (1.126)$$

$$C_1 = C \frac{k_0}{\frac{n}{N} - k_0} \quad (1.127)$$

$$C_2 = C \frac{k_0}{\frac{N}{n} - k_0} . \quad (1.128)$$

It is convenient to derive the impedance matrix of the network from the ABCD matrix that can be easily computed as the product of the ABCD matrix of the capac-

**Fig. 1.11** Coupled inductors with a capacitive T added on the primary side



itive T network and the one of the impedance inverter. The following expressions can be obtained for the elements  $z_{ij}$

$$\begin{aligned} z_{11} &= \frac{(X_0 Q_1 u^2 - j X_0 u + (k_0^2 - 1) X_0 Q_1) N^2}{j Q_1 n^2 u^3 + n^2 u^2 - j Q_1 n^2 u} \\ z_{12} &= \frac{k_0 X_0 Q_1 k u N^2}{j Q_1 n u^2 + n u - j Q_1 n} \\ z_{22} &= \frac{[(X_0 Q_1 Q_2 k_0^2 - X_0 Q_1 Q_2) u^3 + (j X_0 Q_2 + j X_0 Q_1) u^2 + (X_0 Q_1 Q_2 + X_0) u - j X_0 Q_1] N^2}{j Q_1 Q_2 u^2 + Q_2 u - j Q_1 Q_2} \end{aligned} \quad (1.129)$$

Accordingly, at the nominal frequency  $u = 1$  and for the nominal coupling  $k = k_0$ , we obtain

$$\mathbf{Z} = \begin{bmatrix} \frac{(k_0^2 X_0 Q_1 - j X_0) N^2}{n^2} & \frac{k_0^2 X_0 Q_1 N^2}{Q_2} \\ \frac{k_0^2 X_0 Q_1 N^2}{n} & \frac{x_0 (k_0^2 Q_1 Q_2 + j Q_2 + 1) N^2}{Q_2} \end{bmatrix} \quad (1.130)$$

It is worth observing that, differently from the previous case of mutually coupled inductors, in this case,  $r_{12} \neq 0$  although  $x_{12} = 0$ . From (1.130), by introducing the parameter  $\alpha$  defined as  $\alpha = k_0^2 Q_1 Q_2$  the following expressions are obtained:

$$\chi_z^2 = 0 \quad (1.131)$$

$$\xi_z^2 = \frac{k_0^2 Q_1 Q_2}{k_0^2 Q_1 Q_2 + 1} = \frac{\alpha}{1 + \alpha} \quad (1.132)$$

$$\theta_{r,z} = \frac{1}{\sqrt{1 + \alpha}} \quad (1.133)$$

$$\theta_{x,z} = 0. \quad (1.134)$$

The expressions for the parameters of interest can be readily computed and are summarized in Table 1.4. By comparing Table 1.4 with Table 1.3, it can be seen that the expressions of the active power on the load are different; however, the efficiencies are identical and, also the ratio between  $P_L^e$  and  $P_L^p$  is the same. Hence the results shown in Figs. 1.9 and 1.10 hold in this case, too.

From Table 1.4 it can be also seen that the reactive part of the load impedance  $X_L$  corresponds to a capacitance of value:

$$C_L = \frac{1}{\omega_0^2 L_2}, \quad (1.135)$$

as in the case of two coupled inductances, while the matching reactance  $X_{c1}$  corresponds to an inductance of value  $L_1 N^2/n^2$ . In this regard, it is worth noticing that the circuit can be simplified by replacing the series of the compensating inductance corresponding to  $X_{c1}$  and the capacitor  $C_2$  with an equivalent single inductance of value

$$L_{eq} = k_0 L_1 \frac{N}{n}, \quad (1.136)$$

### 1.3.1.1 The Coupling Independent MPDL Solution

From Table 1.4, it can be seen that for the network illustrated in Fig. 1.11 the optimum load,  $Z_L = R_L + jX_L$ , does not depend on the magnetic coupling coefficient  $k_0$ . Accordingly, the active power on the load (not normalized)

$$p_L = P_L \cdot P_0 = \frac{|V_1|^2}{8} \frac{n^2}{R_0} = \frac{|V_1|^2}{8} \frac{n^2}{N^2} \frac{Q_2}{X_0}, \quad (1.137)$$

does not depend on the coupling  $k_0$ . As a consequence, as long as the losses on the capacitive T are negligible, we can theoretically achieve the same maximum power for different values of the coupling.

Finally, it is worth observing that, in the coupled inductors case, the resistance of the MPTE solution is always greater than the resistance of the MPDL solution; in particular, the following optimum range can be derived for  $R_L$ :  $(1 + \alpha)R_0 > R_L > \sqrt{1 + \alpha}R_0$ . On the other hand, for the  $1 : n$  transformer configuration, the resistance of the MPTE solution is always greater than the one of the MPDL solution. In this case the optimum range of operation for  $R_L$  is:  $\sqrt{1 + \alpha}R_0 > R_L > R_0$ . According to these considerations, it is apparent that, depending on the desired value of the load resistance, one of the two configurations may be preferred.

## 1.4 Application of Theory: The Case of a Capacitive WPT Link

In this section, in order to provide an example of application of the admittance matrix representation introduced in Sect. 1.2.3, a WPT link based on a capacitive coupling will be analyzed.

We consider the lossy capacitive WPT link illustrated in Fig. 1.12, described by its admittance matrix

**Table 1.4** A summary of the parameters' values for the approaches that maximize efficiency and power in the case of a capacitive T on the primary side. The parameters have the following meanings:  $\alpha = k_0^2 Q_1 Q_2$  and  $R_0 = X_0 N^2 / Q_2$ . Note that the quantities  $P_{in}$ ,  $P_L$ , are normalized w.r.t.  $P_0 = V_1^2 / (8r_{11})$ . In the present case we have  $r_{11} = R_0 \alpha / n^2$

| Parameter | Maximum efficiency                                       | Maximum power                      |
|-----------|--|------------------------------------|
| $R_L$     | $\sqrt{\alpha + 1} R_0$                                  | $R_0$                              |
| $X_L$     | $-X_0 N^2$   | $-X_0 N^2$                         |
| $R_{c1}$  | 0  | 0                                  |
| $X_{c1}$  | $X_0 N^2 / n^2$  | $X_0 N^2 / n^2$                    |
| $R_{in}$  | $R_0 \alpha / (n^2 \sqrt{\alpha + 1})$                   | $R_0 2\alpha / (n^2 (\alpha + 2))$ |
| $X_{in}$  | 0  | 0                                  |
| $P_{in}$  | $4\sqrt{\alpha + 1}$                                     | $2(\alpha + 2)$                    |
| $P_L$     | $(4\alpha\sqrt{\alpha + 1}) / (1 + \sqrt{\alpha + 1})^2$ | $\alpha$                           |
| $\eta$    | $\alpha / (1 + \sqrt{\alpha + 1})^2$                     | $\alpha / (2(\alpha + 2))$         |

$$Y = \begin{bmatrix} y_{11} & y_{12} \\ y_{12} & y_{21} \end{bmatrix}, \quad (1.138)$$

where  $y_{ij} = g_{ij} + jb_{ij}$  ( $i, j = 1, 2$ ). The admittance matrix of the Pi equivalent network given in Fig. 1.13 is:

$$Y = \begin{bmatrix} Y_1 + Y_3 & -Y_3 \\ -Y_3 & Y_2 + Y_3 \end{bmatrix}. \quad (1.139)$$

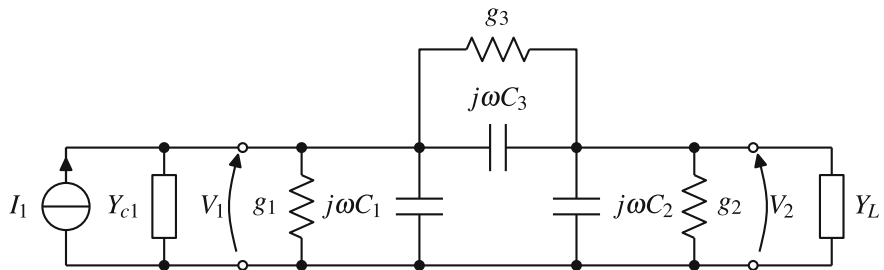
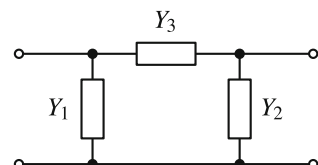


**Fig. 1.12** Network representation of a wireless power transfer system realized with coupled capacitances

**Fig. 1.13** Pi equivalent network representation



According to (1.139), the terms of the admittance of the capacitive link are given by

$$\begin{aligned} y_{11} &= (g_1 + g_3) + j\omega(C_1 + C_3) \\ y_{22} &= (g_2 + g_3) + j\omega(C_2 + C_3) \\ y_{12} &= -g_3 - j\omega C_3. \end{aligned} \quad (1.140)$$

Let us consider the case  $g_3 = 0$  which refers to a lossless dielectric and corresponds to assuming  $g_{12} = 0$ . In this case, referring to Fig. 1.12, from Table 1.2 the following expression can be derived for the compensating admittance  $Y_{c1}$ :

$$Y_{c1} = G_{c1} + jB_{c1} = -jb_{11} = -j\omega(C_1 + C_3) \quad (1.141)$$

As for the load realizing the maximum power transfer solution (i.e., the MPTE solution), it is

$$Y_L = G_L + jB_L, \quad (1.142)$$

$$G_L = g_2 \sqrt{1 + \chi_y^2}, \quad (1.143)$$

$$B_L = -j\omega(C_2 + C_3), \quad (1.144)$$

where the parameter  $\chi_y$ , for the case under analysis is

$$\chi_y^2 = \frac{\omega^2 C_3^2}{g_1 g_2}. \quad (1.145)$$

and represents a figure of merit (f.o.m.) of the system. According to the hypothesis  $g_3 = 0$ , the expressions of the efficiency and of the normalized power delivered to the load for the MPTE solution are

$$\eta^e = \frac{\chi_y^2}{\left(1 + \sqrt{1 + \chi_y^2}\right)^2} \quad (1.146)$$

$$P^e = 4 \frac{\chi_y^2}{\sqrt{1 + \chi_y^2} \left(1 + \sqrt{1 + \chi_y^2}\right)^2} \quad (1.147)$$

The network corresponding to the MPTE solution is illustrated in Fig. 1.14.

Let us now consider the MPDL solution, according to the theory summarized in Table 1.2, the compensating admittance is the same of the MPTE solution and reported in (1.141). As for the load, from Table 1.2 the following expression can be obtained:

$$Y_L = G_L + jB_L = g_2(1 + \chi_y^2) - j\omega(C_2 + C_3). \quad (1.148)$$

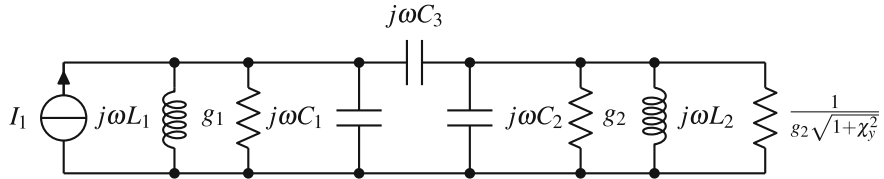


**Fig. 1.14** Maximum efficiency network for a WPT system realized with coupled capacitances; the source is on the *left side* and the load,  $G_L = g_2\sqrt{1 + \chi_y^2}$ , is on the *right side*. The values of the inductances, are  $L_1 = 1/[\omega_0^2(C_1 + C_3)]$  and  $L_2 = 1/[\omega_0^2(C_2 + C_3)]$

it is worth observing that, for the hypothesis  $g_3 = 0$ , the reactive part is the same as calculated for the MPTE solution, while the resistive part is different. The expressions for the efficiency and the active output power are

$$\eta^p = \frac{\chi_y^2}{2(2 + \chi_y^2)}, \quad (1.149)$$

$$P_L^p = P_0 \frac{\chi_y^2}{(1 + \chi_y^2)} \quad (1.150)$$

**Table 1.5** Example of capacitive WPT link. The parameters refer to the networks illustrated in Figs. 1.14 and 1.15

| Parameter     | Maximum efficiency | Maximum power   |
|---------------|--------------------|-----------------|
| Frequency     | 15 MHz             | =               |
| $I_1$         | 1 mA               | =               |
| $C_1 = C_2$   | 6.771 pF           | =               |
| $C_3$         | 0.784 pF           | =               |
| $g_1 = g_2$   | 5.242 $\mu$ S      | =               |
| $L_1 = L_2$   | 14.89 $\mu$ H      | =               |
| $R_L = 1/G_L$ | 13499.65 $\Omega$  | 955.31 $\Omega$ |

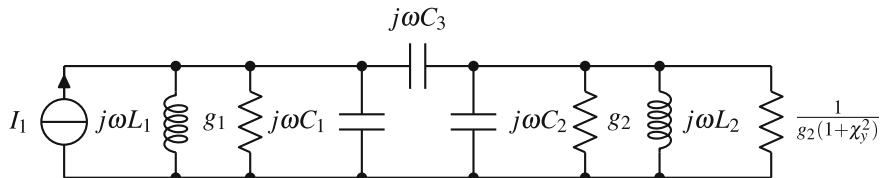


**Fig. 1.15** Network for maximum power transfer; the source is on the *left side* and the load,  $G_L = g_2(1 + \chi_y^2)$ , is on the *right side*. The values of the inductances are the same as in Fig. 1.14

**Fig. 1.16** Output power when a current  $I_1 = 1$  mA is provided by the input generator. The *black line* are the results corresponding to the MPDL solution, while the *red line* are the results obtained for MPTE solution

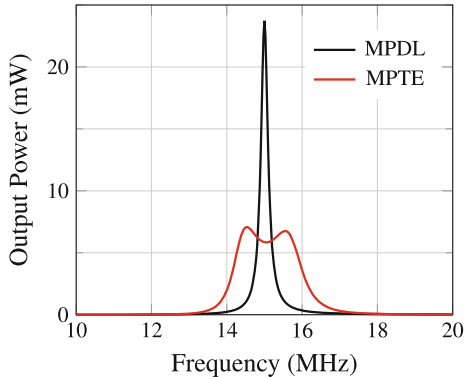
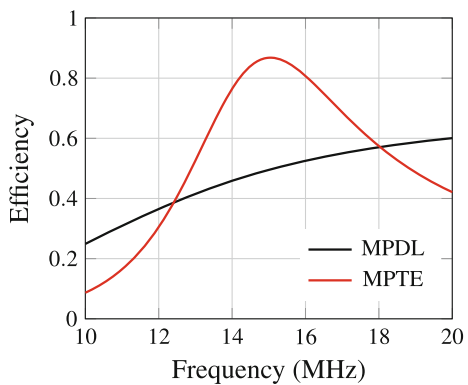


**Fig. 1.17** Comparing efficiency: the MPDL solution generates the *black line*, whilst the *red line* is obtained from the MPTE solution. Note that the maximum power approach provides the limit of 1/2 for the maximum efficiency at the operating frequency (in this case 15 MHz). At other frequencies, the load realizing the maximum power transfer will be, in general, different



As an example of application, let us consider the capacitive WPT link described in Table 1.5, where the parameters refer to the networks illustrated in Figs. 1.14 and 1.15. As it can be seen, the value of  $R_L$  realizing the maximum power condition is  $955.31 \Omega$  and is quite different from the value of  $13499.65 \Omega$  realizing the maximum power transfer efficiency. The frequency behavior of the active power on the load corresponding to both the MPDL and the MPTE solutions is illustrated in Fig. 1.16, while the results obtained for the efficiencies are given in Fig. 1.17. From these figures, it is evident that the two approaches provide very different results. In particular when the MPDL solution is searched, an output power of about 23.73 mW is obtained with a 0.5 efficiency, which is the theoretical maximum. Similarly, the MPTE solution provides a value of 0.87 for  $\eta$  and an active power on the load of about 5.86 mW.

## References

- Bird, T.S., Rypkema, N., Smart, K.W.: Antenna impedance matching for maximum power transfer in wireless sensor networks. *IEEE Sensors* 916–919 (2009)
- Cannon, B.L., Hoburg, J.F., Stancil, D.D., Goldstein, S.C.: Magnetic resonant coupling as a potential means for wireless power transfer to multiple small receivers. *IEEE Trans. Power Electron.* **24**(7), 1819–1825 (2009). doi:[10.1109/TPEL.2009.2017195](https://doi.org/10.1109/TPEL.2009.2017195)
- Chang, Y.C., Yang, C.Y., Li, C.H., Cheng, S.J., Chiu, H.J., Lo, Y.K.: Design and implementation of a contact-less power charger for robot applications. In: 2012 10th IEEE International Conference on Industrial Informatics (INDIN), pp. 827–832 (2012). doi:[10.1109/INDIN.2012.6300832](https://doi.org/10.1109/INDIN.2012.6300832)
- Costanzo, A., Dionigi, M., Masotti, M., Mongiardo, M., Monti, G., Tarricone, L., Sorrentino, R.: Electromagnetic energy harvesting and wireless power transmission: a unified approach. *Proc. IEEE* **102**(11), 1692–1711 (2014). doi:[10.1109/JPROC.2014.2355261](https://doi.org/10.1109/JPROC.2014.2355261)
- Costanzo, A., Dionigi, M., Mastri, F., Mongiardo, M., Russer, J.A., Russer, P.: Rigorous design of magnetic-resonant wireless power transfer links realized with two coils. In: Proceedings of the European Microwave Conference (EuMC), pp. 414–417 (2014)
- Costanzo, A., Dionigi, M., Mastri, F., Mongiardo, M., Russer, J.A., Russer, P.: Design of magnetic-resonant wireless power transfer links realized with two coils: comparison of solutions. *Int. J. Microwave Wirel. Technol.* **7**, 349–359 (2015)
- Dai, J., Ludois, D.C.: A survey of wireless power transfer and a critical comparison of inductive and capacitive coupling for small gap applications. *IEEE Trans. Power Electron.* **30**(11), 6017–6029 (2015)
- Dionigi, M., Mongiardo, M.: Cad of wireless resonant energy links (wrel) realized by coils. In: IEEE MTT-S International Microwave Symposium Digest, pp. 1760–1763 (2010). doi:[10.1109/MWSYM.2010.5516711](https://doi.org/10.1109/MWSYM.2010.5516711)
- Dionigi, M., Mongiardo, M.: Cad of efficient wireless power transmission systems. In: IEEE MTT-S International Microwave Symposium Digest, pp. 1–4 (2011). doi:[10.1109/MWSYM.2011.5972606](https://doi.org/10.1109/MWSYM.2011.5972606)
- Dionigi, M., Mongiardo, M., Perfetti, R.: Rigorous network and full-wave electromagnetic modeling of wireless power transfer links. *IEEE Trans. Microwave Theory Tech.* **63**(1), 65–75 (2015). doi:[10.1109/TMTT.2014.2376555](https://doi.org/10.1109/TMTT.2014.2376555)
- Ghotbi, I., Najjarzadegan, M., Ashtiani, S., Shoaei, O., Shahabadi, M.: 3-coil orientation insensitive wireless power transfer for capsule endoscope. In: 2015 23rd Iranian Conference on Electrical Engineering (ICEE), pp. 1249–1254. IEEE (2015)
- Kurs, A., Karalis, A., Moffatt, R., Joannopoulos, J.D., Fisher, P., Soljacic, M.: Wireless power transfer via strongly coupled magnetic resonances. *Science* **317**(5834), 83–86 (2007). doi:[10.1126/science.1143254](https://doi.org/10.1126/science.1143254)
- Li, J.L.W.: Wireless power transmission: State-of-the-arts in technologies and potential applications. In: Microwave Conference Proceedings (APMC), 2011, pp. 86–89 (2011)
- Low, Z.N., Chinga, R.A., Tseng, R., Lin, J.: Design and test of a high-power high-efficiency loosely coupled planar wireless power transfer system. *IEEE Trans. Ind. Electron.* **56**(5), 1801–1812 (2009). doi:[10.1109/TIE.2008.2010110](https://doi.org/10.1109/TIE.2008.2010110)
- Monti, G., Arcuti, P., Tarricone, L.: Resonant inductive link for remote powering of pacemakers. *IEEE Trans. Microwave Theory Tech.* **63**(11), 3814–3822 (2015). doi:[10.1109/TMTT.2015.2481387](https://doi.org/10.1109/TMTT.2015.2481387)
- Monti, G., Tarricone, L., Dionigi, M., Mongiardo, M.: Magnetically coupled resonant wireless power transmission: An artificial transmission line approach. In: Proceedings of the Microwave Conference (EuMC), pp. 233–236 (2012)
- Russer, J.A., Russer, P.: Design considerations for a moving field inductive power transfer system. In: IEEE International Wireless Power Transfer Conference Perugia WPTC, pp. 1–4 (2013)
- Sample, A.P., Meyer, D.A., Smith, J.R.: Analysis, experimental results, and range adaptation of magnetically coupled resonators for wireless power transfer. *IEEE Trans. Ind. Electron.* **58**(2) (2011). doi:[10.1109/TIE.2010.2046002](https://doi.org/10.1109/TIE.2010.2046002)

# **Chapter 2**

## **Wireless Power Transfer Based on Metamaterials**

**Bingnan Wang, William Yerazunis and Koon Hoo Teo**

**Abstract** Near-field-based wireless power transfer (WPT) technology is promising for many applications from consumer electronics to industrial automation. By utilizing resonant coupling, the power transfer can be made more flexible than conventional inductive WPT. However, the range is still limited. In this chapter, we report research work on near-field wireless power transfer (WPT) based on metamaterials-related ideas, aiming to extend the range and improve the flexibility of a WPT system. In the first part, we show that with a thin slab of meta-material, the near-field coupling between two resonant coils can be enhanced; the power transfer efficiency between coils can also be greatly improved by the meta-material. The principle of enhanced coupling with metamaterials will be discussed; the design process of metamaterial slabs for WPT will be introduced; experimental results on WPT efficiency improvement with metamaterials will also be presented. In the second part, inspired by metamaterials theory, we study the mutual coupling of an array of coupled resonators, and their application for WPT. We show that the range of WPT can be greatly extended with an array of coupled resonators. More importantly, the technology enables wireless power delivery to both static and mobile devices. The principle of this technology will be explained; analytical and numerical models will be introduced to estimate the performance of a WPT system based on an array of coupled resonators; methods for WPT optimization will be discussed and experimental results will be presented.

---

B. Wang (✉) · W. Yerazunis · K.H. Teo

Mitsubishi Electric Research Laboratories, 201 Broadway, Cambridge, MA 02139, USA

e-mail: bwang@merl.com

W. Yerazunis

e-mail: yerazunis@merl.com

K.H. Teo

e-mail: teo@merl.com

© Springer International Publishing AG 2016

S. Nikoletseas et al. (eds.), *Wireless Power Transfer Algorithms, Technologies and Applications in Ad Hoc Communication Networks*,  
DOI 10.1007/978-3-319-46810-5\_2

## 2.1 Introduction

Wireless power transfer (WPT) has a long history of over 100 years that dates back at least to Tesla in 1893. In recent years, WPT research and product development is reemerging due to rapidly increasing demands in new applications. For example, WPT technology is being deployed to provide wireless charging solutions for batteries of electronic devices including smart phones and wearable devices, which require frequent recharging, and where a mechanical charging socket may wear out in normal use. WPT is promising in many areas with different power levels, from implantable medical devices (usually on the order of milliwatts) to electric vehicles (a few kilowatts to tens of kilowatts). Although each application has specific requirements such as transfer distance, device size, power, and packaging, most of them rely on one of the following fundamental technologies: microwave power transmission, inductive coupling, and resonant coupling.

Microwave power transmission uses directed microwave beams to send energy from transmitting antenna to a receiving antenna. The technology requires accurate alignment and clear line-of-sight and was primarily developed for solar power satellite applications with very high power level, very long distance, and very large investment [1]. It was not typically considered suitable for low power consumer electronics devices charging until recently [2].

In short distance WPT applications, inductive and resonant coupling are two dominating technologies. Inductive method utilizes the inductive coupling between transmitting and receiving coils to transfer power. The efficiency of such a system depends strongly on the coupling coefficient of transmitting and receiving coils. To achieve efficient power transfer, the two coils need to be positioned such that most of the magnetic flux generated by the transmitting coil goes through the receiving coil. Thus inductive coupling-based WPT has a limited power transfer range of a few centimeters and requires precise alignment between transmitting and receiving coils [3–5].

Resonant coupling occurs when the transmitting and receiving coils are tuned to the same resonant frequency. With resonant coupling, the effective transfer distance of a WPT system can be greatly extended [6–12]. Although resonant coupling-based WPT has a long history [6, 7], the application has been very limited. In 2007, Kurs et al. demonstrated that WPT based on resonant coupling can be used to transfer 60 W power over a distance of up to 2 m [8]. This work has since inspired many researchers around the world toward the understanding, analysis, improvement, and application of WPT based on resonant coupling technology (see, for example, Refs. [9–12]).

Using resonance, the system can work efficiently even when the coupling coefficient between transmitting and receiving coils is very small (generally  $<0.2$ , while in the case of inductive coupling, the coupling coefficient is typically  $>0.9$ ). The efficiency  $\eta$  of a resonant coupling-based WPT system depends on two important factors: the quality factor  $Q$  of resonant coils, and the coupling coefficient  $k$  between transmitting and receiving coils. Higher  $Q$ , which means smaller loss rate in the energy exchange, and higher  $k$ , which means higher coupling rate, can both lead to

higher efficiency  $\eta$  [8]. Since the coupling coefficient is directly related to the distance and alignment between transmitting and receiving coils, being able to operate at lower  $k$  essentially enables the system to operate at larger distance and in the case of coil misalignment. WPT to a single [8] or multiple [13] receiving devices have been demonstrated at “mid-range” distance, which is several times the characteristic size of the transmitting coil. However, the efficiency still drops rapidly as distance is increasing. It is also desirable to achieve the highest possible efficiency at a given distance for WPT technologies to compete with wired solutions. Since the power receiving devices need to be close to the transmitting device, the mobility is very limited.

In this chapter, we report research on metamaterials for wireless power applications, and show the potential of metamaterials to improve the range and flexibility of WPT systems. In particular, power transfer efficiency improvement using metamaterials, and WPT to mobile devices using array of resonators will be introduced. With a metamaterial slab, the coupling between transmitting and receiving coils can be enhanced, and the efficiency can be subsequently improved [14–19]. In the next section, we will give a brief introduction to metamaterials, their applications to WPT, and a review of recent theoretical and experimental work in this area. With an array of resonators, the range of power transfer can be greatly extended, and dynamic power transfer to mobile devices can be achieved [20–22]. In Sect. 2.3, we will give an introduction to this technology and report experimental development on WPT with arrays of coupled resonators.

## 2.2 Metamaterials for WPT

Metamaterials are a class of artificially engineered materials which can achieve unique properties that cannot be obtained with natural materials. Metamaterials are typically made from periodic arrangement of structures with unit cell size much smaller than the wavelength at the operating frequency. The properties in response to electromagnetic waves are derived from those engineered structures, instead of the base materials used to build the structures. In the last decade, unique wave phenomena such as negative refractive index and evanescent wave enhancement have been predicted and realized in metamaterials [27–29]. Since the first experimental demonstration of negative index of refraction [28], metamaterials have been shown to be powerful and flexible in achieving desirable electromagnetic properties from radio frequencies to optical frequencies. Numerous applications based on metamaterials have been developed, such as superlens imaging devices [30], invisible cloaking devices [31], and novel antennas [32].

### 2.2.1 Metamaterials and Superlens

The building blocks of metamaterials are engineered structures, typically much smaller in size than the working wavelength, so that metamaterials can be treated as effective media. The electromagnetic properties of a metamaterial are obtained from these building blocks, rather than the composition materials. Macroscopic parameters, such as relative permittivity  $\epsilon$ , relative permeability  $\mu$ , and chirality  $\kappa$  can be used to describe the electromagnetic properties of metamaterials. More importantly, we can design for a special set of effective parameters by playing with the shape, geometry, and size of the artificial structures, as these bulk material electromagnetic parameters are determined by those structures in metamaterials. Extraordinary electromagnetic properties, such as negative index of refraction  $n$ , which are not readily available in natural materials, have been discovered in metamaterials. Metamaterials have become a powerful tool leading to numerous new discoveries. In 2000, Pendry studied theoretically the wave propagation properties in a negative-index material, and showed that a negative  $n$  can be achieved having both  $\epsilon$  and  $\mu$  negative in a metamaterial [27]. Negative refraction occurs at the interface between a regular medium of positive  $n$  and a negative  $n$  metamaterial.

Moreover, while evanescent components decrease exponentially in air or other dielectric media, they can propagate and even be enhanced in a  $n < 0$  material. Pendry showed that with a flat slab of metamaterial having the property of relative permittivity and permeability parameters  $\epsilon = -1$  and  $\mu = -1$ , both the far-field propagating waves and the near-field evanescent waves of an object can be restored. This is how the so-called “super lens” is constructed with theoretically unlimited resolution [27]. Although in reality the ideal condition of  $\epsilon = -1$  and  $\mu = -1$  does not exist, metamaterials designed with physical parameters and low material losses can still achieve imaging resolutions beyond the diffraction limit.

The applications of the unique properties of metamaterials, especially evanescent wave amplification, are not limited to imaging devices. For resonant coupling-based WPT, the power is exchanged between resonators via coupling of near-field evanescent waves [8]. At resonance, electromagnetic fields are confined mostly inside the resonators, and the electric and magnetic fields exchange energy periodically. Outside the resonators, the electromagnetic fields decay evanescently and do not carry away energy, unless coupled to the tail of the evanescent wave of a second resonator. It is thus interesting to see if metamaterials can be applied to WPT systems to improve the coupling, and eventually the power transfer efficiency.

### 2.2.2 Metamaterials and WPT

The adoption of a “super-lens” for near-field WPT was proposed in Ref. [14]. A metamaterial slab of  $\epsilon = -1$  and  $\mu = -1$  was placed between transmitting and receiving coils in order to study the effect to the near-field coupling. It was shown

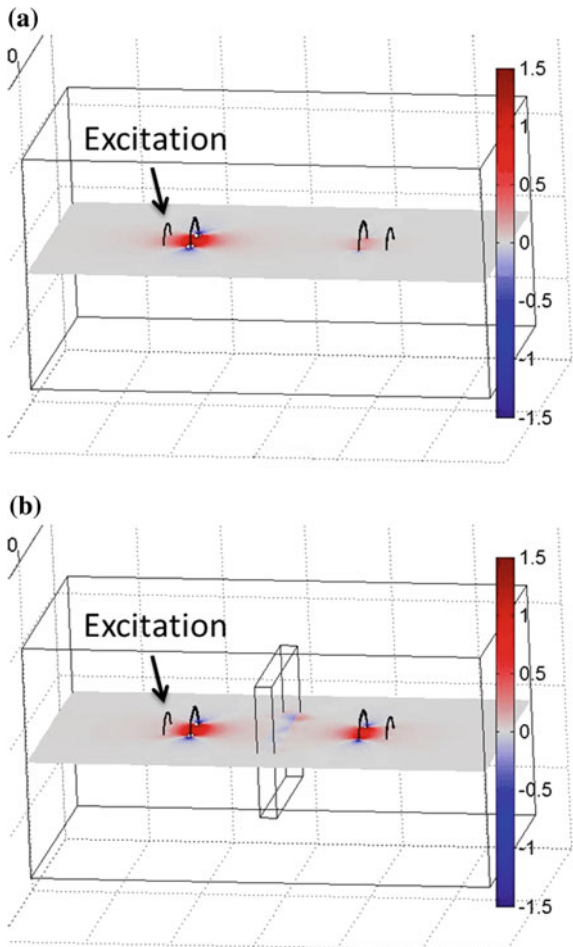
that the metamaterial slab can couple to the near-field evanescent waves, so the effective distance between resonators was reduced, and the coupling coefficient was enhanced. With numerical simulations of a WPT system, it was shown that the power transfer efficiency of the system could also be improved significantly if such a metamaterial slab is used. In Ref. [19], numerical simulations confirmed that the inductive coupling between coils can be enhanced by a metamaterial slab acting as a “super-lens.”

In order to build a “super-lens” metamaterial with negative index for a desired frequency, it is required that both  $\epsilon < 0$  and  $\mu < 0$ . Two sets of artificial structures are typically needed for the metamaterial to achieve such properties, which is relatively complicated in both design and fabrication. Fortunately, the requirements can be simplified for WPT systems, where the wavelength at the operating frequency is on the order of meters and is much larger than the coil size. Indeed, when we are in the deep subwavelength limit, electric and magnetic field decouple, and only one parameter of  $\epsilon$  and  $\mu$  needs to be negative to make a “super lens” [27]. Depending on if the near-field is dominated by electric field or magnetic field, only  $\epsilon < 0$  or  $\mu < 0$  is required. In a WPT system, power is transferred via the coupling of near-field magnetic field, thus a  $\mu < 0$  metamaterial is sufficient to achieve the same effect of efficiency improvement [16].

To demonstrate the idea, a four-coil WPT system [8] was modeled and simulated, as shown in Fig. 2.1. Power is injected through the nonresonant loop antenna on the far left side, which is coupled to a nearby resonant coil. The resonant coil is coupled to the receiving side with another coil of the same resonant frequency, which is then inductively coupled to a nonresonant loop antenna at the far right, which is connected to a resistive load. Figure 2.1a shows the simulated magnetic field distribution of the system. The field intensity is strongest at the resonant coil on the left side, due to the excitation of resonant mode. The magnetic field is coupled to the second resonant coil on the right side, but with weaker intensity, due to the large distance in between. In Fig. 2.1b, a metamaterial slab with  $\mu = -1 + 0.05i$  and  $\epsilon = 1$  is placed in between the two resonant coils, and the field distribution is shown at the same scale as Fig. 2.1a. While the field intensity at the transmitting coil is the same, the field is seen to be enhanced at the metamaterial slab, and the field intensity at the right receiving resonant coil is increased. It indicates that the metamaterial slab can couple to the near-field evanescent waves, such that the effective distance between resonators is reduced, and the coupling is enhanced.

In Ref. [15], theoretical studies were performed based on an analytical model of the coupling between two coils and a homogeneous metamaterial slab. The coils were simplified as point magnetic dipoles, and the metamaterial slab was assumed to be infinitely large. The coupling between two coils was represented by the mutual inductance  $L_{21}$ , and the power transfer was characterized by a simplified circuit model. It was found that the power transfer efficiency from one dipole to the other is proportional to  $|L_{21}|^2$ . The mutual inductance was calculated taking the ratio of the magnetic flux through the second coil generated by the first current carrying coil and the current magnitude of the first coil. That magnetic flux was calculated by solving the field in the system generated by the first coil. A large slab of metamaterial

**Fig. 2.1** Simulated magnetic field distribution of coupled resonators **a** without and **b** with a metamaterial slab. The metamaterial slab has a relative permittivity of  $-1$  and a relative permeability of  $-1$ . The system is excited by a port on the nonresonant loop antenna on the *left side*, and power is transferred to a resistive load connected to the loop antenna on the *right side*



was embedded in the space between the two magnetic dipoles, with the effective  $\varepsilon$  and  $\mu$  assumed to be homogeneous and uniaxial. The presence of the metamaterial modified the field in the system, thus changed the mutual inductance between coils, as well as the self inductance of the coils. With a metamaterial slab acting as a “super lens,” the mutual inductance can be increased significantly depending on the effective parameters of the metamaterial. Consequently the power transfer efficiency can be improved by the metamaterial. It was shown that, with a realistic magnetic loss tangent 0.1 of the metamaterial slab, the power transfer efficiency with the slab can be an order of magnitude greater than efficiency without the slab.

### 2.2.3 Experimental Realization

Previous numerical and analytical studies showed that power transfer efficiency can be improved with metamaterials, through mutual coupling enhancement between coils. However, approximations were used in these studies. In the analytical calculation [15], the coils were assumed to be ideal magnetic dipoles, and the metamaterial slab was considered to be infinitely large and homogeneous. In real systems, the inductance and capacitance of coils are distributed and cannot be treated as magnetic dipoles due to the physical size of coils; the size of metamaterial is finite and the homogeneous parameters are not precise. In the numerical simulation [14], although real coils and finite-sized metamaterial slab were used, the metamaterial parameters were still approximated. It is therefore important to verify the findings with experimental measurements.

In Refs. [16] and [17], experiments on WPT with metamaterial have been done. The metamaterial slab is the essential component for the system. As stated previously, power is transferred via the coupling of near-field magnetic field. Thus a “single-negative” metamaterial with  $\mu < 0$  and  $\epsilon > 0$ , or a magnetic metamaterial was designed.

Magnetic response of physically realizable metamaterials, including secondary effects such as heating and harmonic generation, is an important branch of metamaterial research. Previously, magnetic metamaterials have found applications in areas including new antennas [32] and magnetic resonance imaging systems [33]. However, most of applications of metamaterial before WPT are for information processing, where the required power level is very low, typically on the order of milliwatts. In a WPT system, depending on target applications, the required power level can be anywhere from a few watts to a few kilowatts. Power handling is a major challenge to the metamaterial design. While loss in metamaterial is less sensitive in information processing, it is critical in WPT systems, where the efficiency needs to be as high as possible in order to compete with wired power delivery. For a typical metamaterial, the ratio of operating wavelength to unit cell size  $\lambda/a$  is 10 or less. However, for WPT, the whole system is usually much smaller than the wavelength, producing a  $\lambda/a$  ratio greater than 100. The required fabrication process needs to be simple and low cost for commercial viability. In summary, the metamaterial for WPT needs to be low loss, low cost, compact, and capable of handling high power.

As shown in the inset of Fig. 2.2a, the building block of the metamaterial are two-sided square spirals. The structure is designed to achieve the compact size and low-loss requirements. The 3-turn spirals are printed on Rogers RO4003C circuit boards, with the two sides connected by vias. With a size 6.5 mm by 6.5 mm, the structure gives strong response to external magnetic field around resonant frequency of 24 MHz. The strong response comes from the resonance of the structure, which can be effectively considered as an LC resonator, where the inductance comes from the multi-turn metal wires, and the capacitance comes mainly from the “plate capacitor” formed by the two sides of metal structure on the printed circuit board. The effective inductance and capacitance are much larger than conventional split-ring resonators of

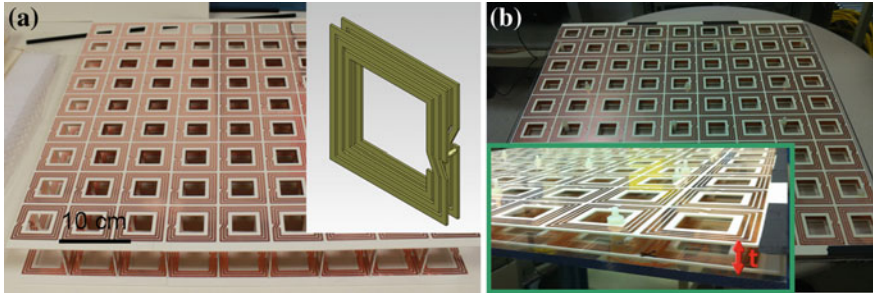


**Fig. 2.2** **a** The fabricated 3d metamaterial, with the unit cell structure shown in the inset. **b** A picture of the planar metamaterial, with inset showing the details.  $t$  is the spacing between two planes

the same size, so much lower resonant frequency is achieved. In terms of wavelength to unit cell ratio  $\lambda/a$ , the double-sided spiral design is about 170, while conventional split-ring resonator is around 10.

A  $\mu$ -negative metamaterial can be constructed by assembling these spirals in cubic lattice [16], as shown in Fig. 2.2a. Above the resonant frequency, the effective  $\mu$  (relative magnetic permeability) of the metamaterial is negative. At our working frequency of 27.12 MHz, this metamaterial has an effective  $\mu$  very close to  $-1.0$  as well as a relatively simple fabrication, low loss, and compact size.

Metamaterial with a different negative effective  $\mu$  can also achieve evanescent wave enhancement. However, when the absolute value of negative  $\mu$  is larger, the frequency gets closer to the resonant frequency of the composing spirals, causing increased Ohmic loss in metallic structures and dielectric loss in the substrate of the metamaterial and less power transfer efficiency improvement.

Other components of a WPT system were also designed and fabricated. This system is intended to work at the ISM band with center frequency of 27.12 MHz. As shown in Fig. 2.3a, two planar coils built with copper wire spirals are used as resonators. Two nonresonant loop antennas are inductively coupled to the resonant coils. RF power is fed to the system by connecting to the loop antenna on the right side. Power is transferred to the left-side resonator and picked up by the second loop antenna, and delivered to a load (an incandescent light bulb).

Experiments were performed to measure the power transfer efficiency of the WPT system at low power [16]. The overall efficiency of the system was measured by an Agilent N5230A vector network analyzer. The two loop antennas were connected to the two ports of the network analyzer, and S-parameters between the two ports were measured. For each measurement, the distances between loop antennas and associated coil resonators were tuned so that the system can be properly matched to the  $50\ \Omega$  ports of the network analyzer for optimal power transfer [12, 13]. When a metamaterial slab is added in the system, the optimal condition needs minor adjustment. The distances between loop antennas and associated coil resonators need to be

**Fig. 2.3** WPT experiment to a 40 W light bulb of system **a** without metamaterials, **b** with the 3D metamaterial slab, and **c** with the anisotropic metamaterial slab. The separation distance is 50 cm for all cases

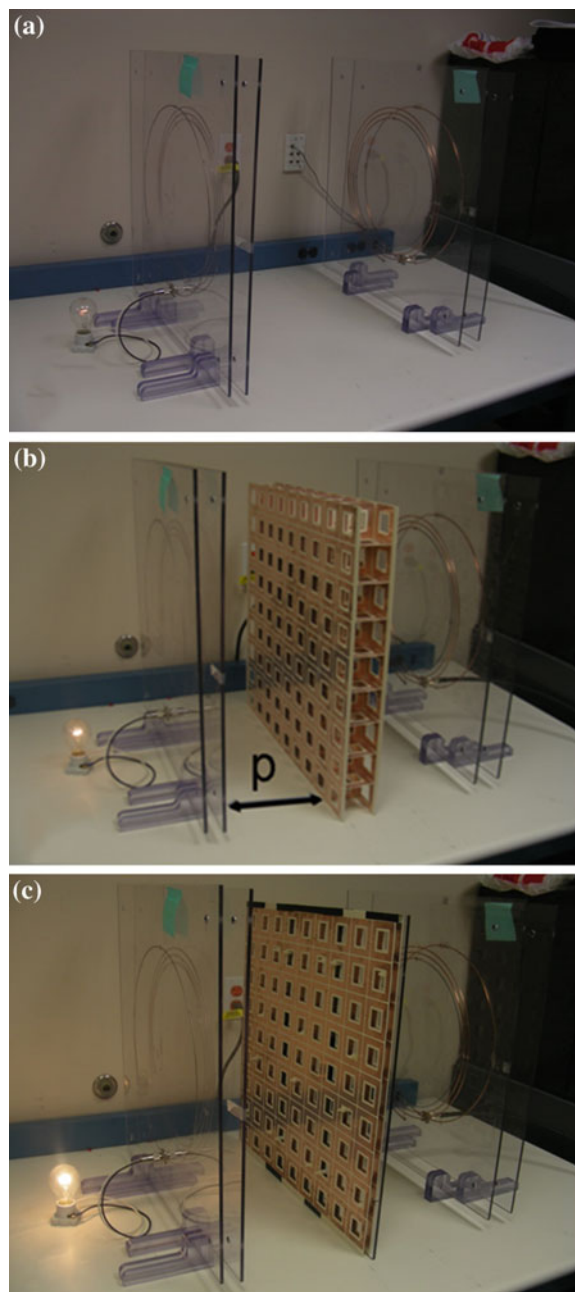
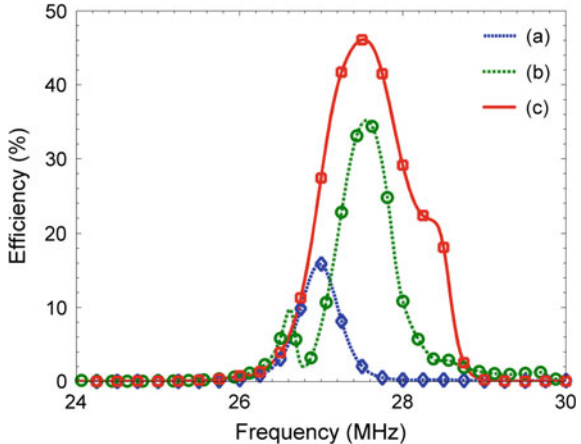


**Fig. 2.4** The measured power transfer efficiency of different system configurations: **a** original system without metamaterials, maximum efficiency is 17 %, **b** with a 3D metamaterial slab, maximum efficiency is 35 %, and **c** with an anisotropic metamaterial slab, maximum efficiency is 47 %



readjusted so that the optimal matching for power transfer is achieved. The reflection parameters  $S_{11}$  and  $S_{22}$  around resonance are both small (around  $-20$  dB), and the change due to the introduction of metamaterial is negligible. Thus the power transfer efficiency of the system can be estimated by  $|S_{21}|^2$ . At a distance of 50 cm between two resonant coils, the efficiency without a metamaterial is 17 %, and is increased to 35 % with the metamaterial slab in the system [16], as shown in Fig. 2.4.

In Ref. [17], the metamaterial slab for WPT was further simplified. Instead of stacking the two-side square spirals in three dimensions, only two flat panels of spirals were used to construct an anisotropic metamaterial, as shown in Fig. 2.2b. The simplification is made because the magnetic field in the WPT system is mainly in the direction along the axis of the spirals. It is sufficient to use a metamaterial having negative magnetic response in this direction, instead of an isotropic metamaterial. The two surfaces are separated by a distance  $t = 2$  cm, optimized to achieve highest power transfer efficiency of the system. With the same method, the efficiency is measured with the anisotropic metamaterial in the WPT system. As shown in Fig. 2.4, the efficiency is increased to 47 % at maximum, comparing to peak efficiency of 17 % without the metamaterial. The achieved efficiency is even higher than the case of isotropic metamaterial, as the loss is lower in the planar metamaterial with unnecessary structures removed. In the anisotropic metamaterial, evanescent wave enhancement is achieved via the excitation of surface waves on the two surfaces. Before WPT, anisotropic metamaterials have been used for near-field imaging [35].

Experiments at higher power level have also been done to the WPT system [16, 17]. Figure 2.3 shows the experimental demonstration of wireless power transfer to a 40 W light bulb. The RF power is provided by a high-frequency transceiver with power amplifier through the input loop antenna. Similar as in the efficiency measurement, the distances between loop antennas and associated resonators are adjusted for optimal matching each time. When a metamaterial slab is inserted in the system, the matching process is repeated to minimize the affect of mismatch. The brightness of

light bulb can thus reflect the amount of power transferred. Figure 2.3a shows the system without metamaterial, where the light bulb barely glows. Figure 2.3b shows the system with the anisotropic metamaterial, and the light bulb is much brighter. This indicates that the efficiency is indeed improved significantly by the metamaterial. The experiment also shows that the metamaterial is capable of handling the high power level.

Later on, the idea on metamaterials for enhanced WPT has been verified by several other studies. In Ref. [23], a “super-lens” metamaterial slab was fabricated for a WPT system, and shown to be capable of increasing the range of power transfer, as well as the power transfer efficiency compared with lensless system. In Ref. [24], improved power transfer efficiency was demonstrated for a short-range telemetry system with a compact metamaterial. The efficiency improvement was achieved with the metamaterial slab placed in close proximity to transmitting or receiving coils. In Ref. [25], the misalignment between transmitting and receiving coils was studied, and it was shown that a metamaterial slab can be applied to mitigate the effect of misalignment and improve the power transfer efficiency. In Ref. [26], a compact metamaterial with adjustable operating frequency between 10 and 30 MHz was designed and fabricated. The metamaterial was applied to a two-coil WPT system and shown to be able to improve the power transfer with less waveform distortion.

## 2.3 Array of Resonators for Mobile Power Transfer

In a resonant coupling-based WPT system, the basic configuration is to have a pair of resonant coils. Wireless power is transferred between the coil pair through coupling of evanescent waves. The resonant coil can be excited through inductive coupling to (as shown in Fig. 2.5a), or directly collected to an excitation source. Although some flexibility in range can be realized, the region of efficient power transfer is still limited to the physical size of the coils. For devices that travel with distance much larger than the physical size of the transmitting coil, the technology is not sufficient to provide wireless power continuously. Examples include the wireless charging for battery-powered vehicles on the road, wireless power for elevators, or wireless power for industrial robots that can travel a long distance. In this section, we introduce a feasible solution to the problem, and show that by utilizing the coupling of an array of resonators, mobile WPT to multiple mobile devices is achievable [20–22]. With this technology, mobile WPT to electric vehicles on road can be realized. By embedding a power transmitting array of resonators under surface of road or track, power can be picked up wirelessly and continuously by vehicles with pre-installed power receivers traveling on the road.

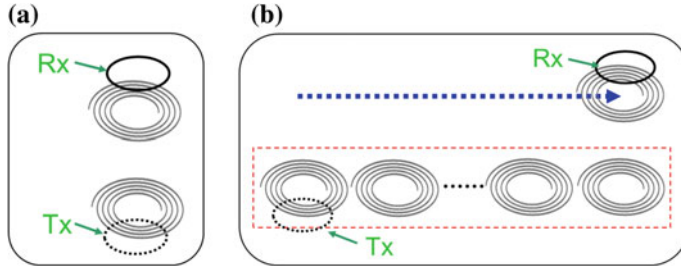


**Fig. 2.5** **a** WPT system with one resonant coil as transmitter and one resonant coil as receiver. **b** WPT system with an array of resonant coils as transmitter and one resonant coil as receiver

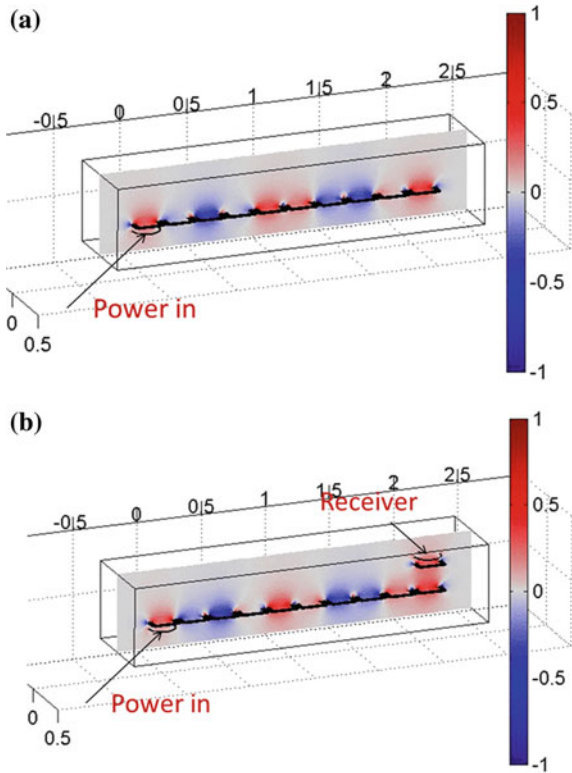
### 2.3.1 Array of Coupled Resonators

An array of coupled resonators can be formed by multiple resonators with same or similar resonant frequencies when each resonator is resonantly coupled to its neighboring resonators. Figure 2.5b shows a simple example of an array in linear shape, which is composed of multiple coils aligned in a straight line. Of course, the resonator design and the shape of the array can both take different forms [20]. For example, the resonators can be arranged in more complex routes with bends and curves. The key is that, when one resonator in the array is excited by an external source, power can be resonantly coupled to its neighboring resonators, then to the next neighbors, then to all resonators in the array. As shown in Fig. 2.5b, power can be distributed in the array by inductively coupling a loop antenna to the first resonator in the array. When a resonant receiver is close to the array and is coupled to any resonator or resonators in the array, power can be transferred to it. The power is distributed and transferred in the system via resonant coupling, thus no electrical connections between resonators are required. The receiver can also be kept a distance away from the array. Two features of the system can be observed. First, the effective power transfer range is greatly extended, as the receiver can now be anywhere along the array, which can be much larger than the physical size of one resonator. Second, the receiver can be attached to a mobile device and travels along the array freely. It is even possible to allow multiple receivers to be powered by the system at the same time, as long as each receiver is coupled to the array.

### 2.3.2 Numerical Simulations and Circuit Analysis

A system similar to the one shown in Fig. 2.5b is modeled and simulated in COMSOL. In the model, the resonators are square spirals of width 20 cm, designed to have a resonant frequency around 25 MHz. A linear array is formed by 10 resonators side-by-side. A loop antenna is aligned to the first resonator in the array and inductively

**Fig. 2.6** Simulated magnetic field distribution of a WPT system with an array of 10 resonators as transmitter: **a** No receiver, and **b** with receiver



couples the energy to the system. With these settings, the magnetic field distribution of the system is calculated and plotted in Fig. 2.6a. A strong field is excited by the nonresonant loop antenna, and localized around resonators in the array. Now we place another resonant coil and a nonresonant loop antenna as receiver and align them with the 10th resonator of the array. As shown in Fig. 2.6b, even though the receiver is very far from the transmitting antenna, a strong field is still seen at the receiver due to resonant coupling between the resonant receiver and the last resonators in the array. Thus efficient WPT can be achieved over a long distance.

As shown in Fig. 2.6, the field is not uniformly distributed along the array. The coupled mode of the resonator system forms a standing wave on the array, with the phase difference between neighboring resonators depending on the operating frequency. It is therefore important to evaluate the power transfer performance of the system when the receiver is at different positions.

As numerical simulations are time consuming, a transmission line model based on circuit analysis and analytical calculations has been developed to quickly evaluate the performance of the array-based system [21]. In the model, each resonator is treated as a tank circuit; capacitive coupling between resonators is neglected and inductive

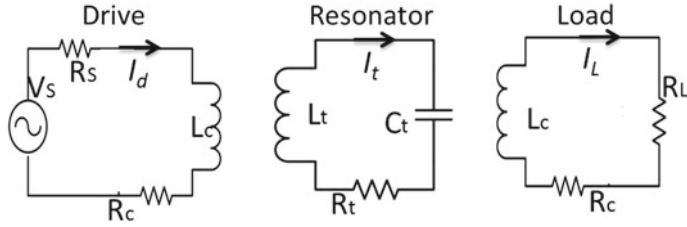


**Fig. 2.7** Circuit model for the nonresonant drive coil, resonator coil in the array and receiver, and nonresonant load coil

coupling is quantified by mutual inductances; nonresonant coils, including the drive and load coil, are also modeled as simple RL circuits, as shown in Fig. 2.7.

The inductance, capacitance, resistance and resonant frequency for resonant coils, the inductance and resistance for nonresonant coils, as well as the mutual inductance between coils are calculated analytically based on the geometry and relative positions of coils. For simplicity, we consider all resonant coils in the array and the resonant receiving coil as identical, thus having the same inductance, capacitance, and resistance values. Similarly, the two nonresonant coils for transmitter and receiver are also identical. Also, we assume the mutual inductance between coils depends only on their separation distance, not on their position in the array system. Thus all nearest neighboring couplings in the array is the same. Finally, we assume that the mutual coupling is reciprocal. With these in mind, we can reduce the circuit elements in the system to those listed in Table 2.1. Referring to Fig. 2.5, the resonant receiving coil and nonresonant load coil moves together linearly along the array of  $N$  resonant coils, and the position is marked as  $x$  relative to the first coil in the array.

The coupled circuits can be represented by a system of equations derived by Kirchhoff's voltage and current laws. The self-impedances for each resonant coil and nonresonant coil are, respectively

$$Z_t = R_t + j(\omega L_t - \frac{1}{\omega C_t}) \quad (2.1)$$

$$Z_c = R_c + j\omega L_c \quad (2.2)$$

For nonresonant drive coil, we have

$$V_s = I_d(Z_c + R_s) + \sum_{m=1}^N j\omega M_{dt}(m)I_m + j\omega M_{dr}(x)I_r + j\omega M_{dL}(x)I_L \quad (2.3)$$

For each resonator in the array, we have an equation of the following form:

$$0 = I_t Z_t + j\omega M_{dt}(t)I_d + \sum_{m=1, m \neq t}^N j\omega M_{tt}(t, m)I_m + j\omega M_{rt}(t, x)I_r + j\omega M_{Lt}(t, x)I_L \quad (2.4)$$

**Table 2.1** Symbols and their meanings in the circuit analysis

| Symbol          | Meaning   |
|-----------------|---|
| $R_t, C_t, L_t$ | Resistance, capacitance, and inductance of a resonant coil  |
| $R_c, L_c$      | Resistance and inductance of a nonresonant coil   |
| $V_S, R_S$      | Voltage source voltage, and resistance  |
| $R_L$           | Load resistance on the load coil  |
| $M_{tt}(m, n)$  | Mutual inductance between coils $m$ and $n$ of the array  |
| $M_{dt}(m)$     | Mutual inductance between drive coil and resonant coil $m$ of the array   |
| $M_{Lr}$        | Mutual inductance between the receiver coil and load coil   |
| $M_{rt}(m, x)$  | Mutual inductance between the receiver coil and resonant coil $m$ of the array when the receiver is at position $x$   |
| $M_{Lt}(m, x)$  | Mutual inductance between the load coil and coil $m$ of the array when the receiver is at position $x$                |
| $M_{dr}(x)$     | Mutual inductance between the receiver coil and the drive coil when the receiver coil is at position $x$              |
| $M_{dL}(x)$     | Mutual inductance between the load coil and the drive coil when the receiver coil is at position $x$                  |
| $I_{d,m,r,L}$   | Current in the drive coil, $m$ -th resonant coil in the array, resonant receiving coil, and the nonresonant load coil |

For the resonant receiving coil, we have

$$0 = I_r Z_t + j\omega M_{Lr} I_L + j\omega M_{dr}(x) I_d + \sum_{m=1}^N j\omega M_{rt}(m, x) I_m \quad (2.5)$$

And for the nonresonant load coil, we have

$$0 = I_L (Z_c + R_L) + j\omega M_{dL}(x) I_d + j\omega M_{Lr} I_r + \sum_{m=1}^N j\omega M_{Lt}(m, x) I_m \quad (2.6)$$

By solving the system of equations, the current in each coil, the transmitted power  $P_t = \frac{1}{2}\Re(V_S \cdot I_t^*)$ , the received power at load  $\frac{|I_L|^2}{2R_L}$ , as well as the power transfer efficiency  $\eta = P_L / P_t$ , can all be obtained.

For an array with 10 resonators, the power transfer efficiency is calculated as a function of receiver position as well as excitation frequency, and plotted in Fig. 2.8. For a fixed excitation frequency, as the receiver moves from one end to the other end, there are highs and lows in efficiency, and different pattern is seen at different frequencies. This is due to the nonuniform field pattern of coupled modes in the array, and different coupled modes of the array are excited at different frequencies. On the other hand, at a fixed receiver position, very different efficiencies can be obtained depending on the excitation frequency.

**Fig. 2.8** Power transfer efficiency (given by circuit analysis) from a 10-resonator array to a receiver, as function of receiver position in unit of lattice size of the array, and the transmitter frequency

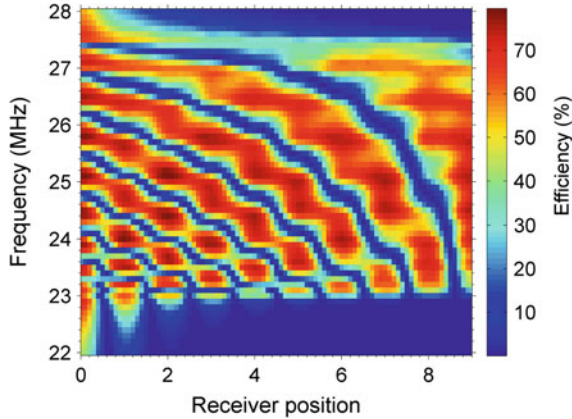
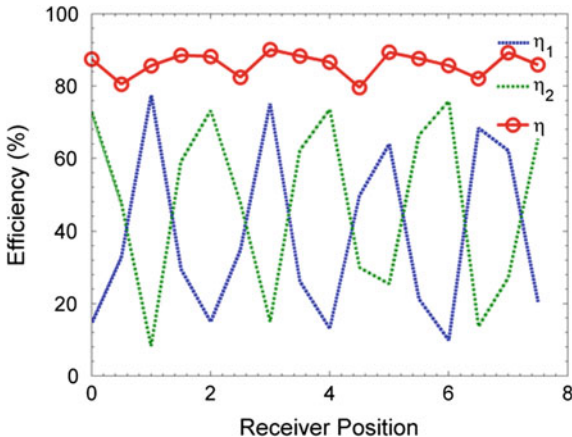


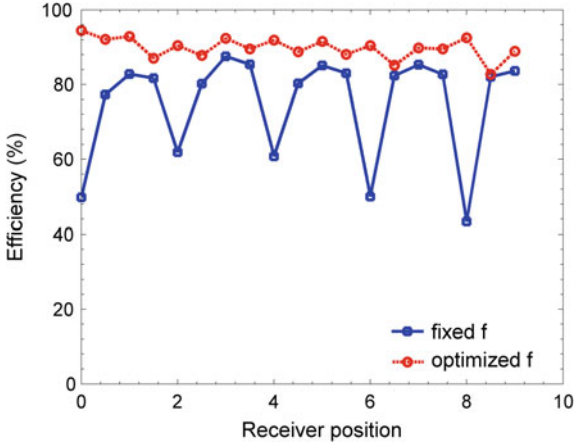
**Fig. 2.9** Simulated power transfer efficiency to two individual receivers and the combined efficiency, as functions of receiver position in unit of lattice size of the array. Operating frequency is fixed



In order to improve power transfer performance, the fluctuation in efficiency as a receiver is moving along the array needs to be reduced. In a WPT system with a single resonant transmitter, it has been discovered that the more receivers in the system, the higher the overall efficiency can be achieved [13]. Similarly, the more receivers we have in the array-based system, the higher the efficiency can be obtained. Moreover, the overall efficiency can be more stable compared with a single-receiver case.

Consider the 10-resonator array system in previous simulations, we now use two resonant receivers that are moving simultaneously along the array, with a lateral distance of 10 cm. In this case, the power at each output port is calculated. The ratio of this output power to the input power is taken as the efficiency to each receiver. The overall efficiency is the sum of the two. They are plotted in Fig. 2.9 as functions of lateral position of the first receiver on the array in unit of the lattice size of the array. Although each receiver has significant fluctuation on the efficiency at different positions, the overall efficiency is much more stable.

**Fig. 2.10** Simulated power transfer efficiency to one receiver as function of receiver position in unit of lattice size of the array, operating at a fixed frequency (blue) and optimized frequency for each position (red)



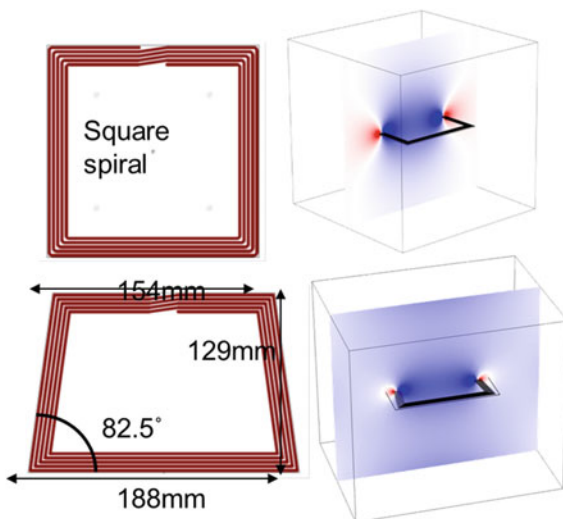
In case of a single receiver, the efficiency fluctuation can be reduced by adjusting the transmitting frequency depending on the position of the receiver. As shown in Fig. 2.8, different efficiencies can be achieved at the same position by changing the frequency. If the frequency is used such that highest efficiency is achieved at each position, the power transfer is optimized for the receiver. Figure 2.10 shows an example of simulated efficiency with a fixed frequency, and optimized frequency for each position, for the same 10-resonator array system used in previous simulations.

To achieve the optimization in real system, a data link can be set up between receiver and transmitter. A monitor can be used on the receiver to detect and send the power transfer status information via the data link back to the transmitter, and the transmitter can then adjust the transmitting frequency depending on the feedback [22].

### 2.3.3 Experiment Demonstration

To demonstrate the flexibility of the array base WPT, we did an experiment with a toy train set running on an oval-shaped track, and built an array of resonators to follow the track and provide power to the train running above. The oval-shaped track has a dimension of 183 cm by 140 cm, and total length of 5.25 m. Planar spirals on circuit board are used for resonator designs in this study for their simple yet reliable fabrication process. For such planar spiral structures, a semi-analytical model has been developed by Ellstein et al. [36] to quickly obtain their resonant frequencies. Two types of resonators are designed for the straight and curved tracks, respectively. As shown in Fig. 2.11, both types are planar 5-turn spirals printed on 0.5 mm Rogers 4350 circuit board, with copper thickness 35  $\mu\text{m}$ , copper strip width 2 mm, spacing between neighboring copper strips 1 mm. The square-shaped

**Fig. 2.11** Design (left) and simulated magnetic field distribution at resonance (right) of planar resonators for the array experiment



resonator has an outer dimension of 15 cm by 15 cm; the trapezoid-shaped resonator has a height of 12.9 cm and side lengths of 15.4 and 18.8 cm. A total of six square-shaped resonators and 24 trapezoid-shaped resonators are used to fill up the oval-shaped track. Square and trapezoid shapes are used in order to have higher coupling coefficient between neighboring resonators by minimizing the distance between the conductors of adjacent resonators. Low-loss substrate is used to reduce power loss in the system, and the resonators are designed and fabricated with standard printed circuit technology for simple and accurate control of the parameters. Both resonators have self-resonant frequency around 25 MHz. The magnetic field distribution of the resonators is also shown in Fig. 2.11, indicating strong field localization due to the high-Q resonances.

Once the resonators are fabricated, they are placed underneath the oval track, with RF power provided to the array via a square antenna inductively coupled to one of the resonators in the array. To receive power, a resonant coil and a nonresonant loop antenna is placed underneath the coal tender of the train set, about 5 cm above the array. The batteries in the coal tender are removed and replaced by circuits for RF to DC conversion. The converted DC power, typically at a voltage varying between 30 and 170 V, is routed to a 40 W light bulb and to a wide-input switching power supply, which produces +5 V for the locomotive's electric motor. A 2 Farad supercapacitor provides a small amount of load leveling.

Figure 2.12 shows the components of the demonstration system. A Kenwood TS-480 transceiver is modified and used as RF power supply [Fig. 2.12a], which is capable of putting out 200 W power with frequency between 3 and 30 MHz. A nonresonant square loop antenna [Fig. 2.12b] is connected to the RF power supply and provides power to the array system via inductive coupling. An additional test receiver consisting of a square resonant coil, inductively coupled to a loop antenna, which

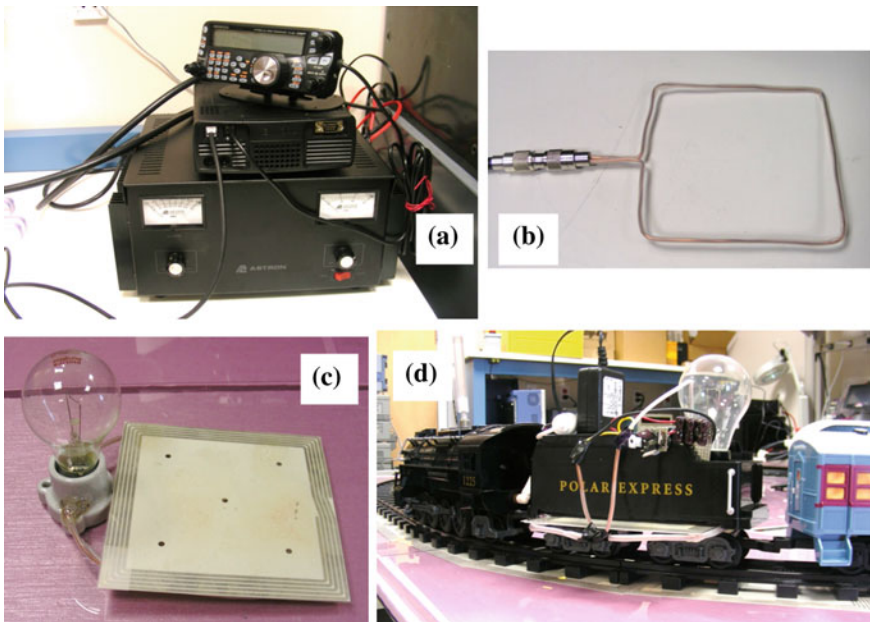


**Fig. 2.12** Components of WPT experiment with array of resonators: **a** RF power transmitter; **b** square antenna to inductively couple power from the RF transmitter to the system; **c** a wireless power receiver composed of a resonant coil, a loop antenna and a 40 W light bulb; **d** a wireless power receiver with a resonant coil and a loop antenna to pick up RF power, a rectifier and regulator to convert RF power to DC, and a motor for the toy train set and a 40 W light bulb as load

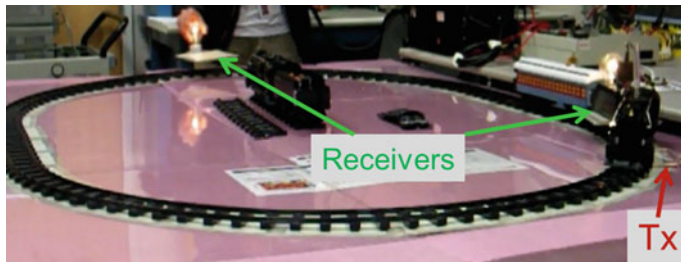


**Fig. 2.13** WPT experiment with array of resonators. The system is used to provide power wireless power to two sets of receivers, one of which is the toy train set moving along the track

is then connected to a 40 W light bulb, is used for power receiving experiment and indicating the transferred power level [Fig. 2.12c]. Figure 2.12d shows the modified train set. The array of resonators under the track is visible in the picture.

The above components were assembled and the WPT system was tested. As shown in Fig. 2.13, the square antenna connected to the RF power supply is coupled to one resonator in the array inductively. With an 80 W power output from the RF power supply, the train set is able to run continuously along the oval track with the

wireless power supply. In addition, the light bulb on the train and the one with a separate receiver are both lit up with wireless power. While the train is traveling along the track, the brightness of the light bulb on the train changes, indicating that the power transferred to the receiver varies. As discussed before, this is a result of resonant coupling in the array. A Bird 4410 wattmeter was used to measure the received power. The fluctuation is significant: the efficiency at peak is about 85 % while efficiency at low is about 15 %.

We observed that at many frequencies, the system does not maintain sufficient voltage to operate the locomotive motor at all points in the loop. This is due both to the node and antinode effect as seen in Fig. 2.8, and also because the loop is closed, so energy circulating clockwise and energy circulating counterclockwise interferes both constructively and destructively. Manually changing the frequency shifts the resonant nodes and antinodes and allows adequate power delivery at all points on the loop. Our hypothesis is that this frequency change can be automated, and yield an improved overall energy delivery.

We then implemented a telemetry system on the train that measured the actual voltage on the high-voltage capacitors at approximately 5 Hz and relayed the value in real time to a host Linux laptop via Bluetooth. We then operated the train set at 100 W nominal power from 23 to 25 MHz (the useful resonance band of our test system) and logged the instantaneous power delivered. The experimental protocol was to test several different automatic frequency tuning strategies and compare them versus fixed-frequency systems. Our tuning strategies were allowed freedom within the same 23–25 MHz band as the fixed-frequency standards, and changed frequencies in steps of either 50 or 100 kHz, either automatically or with feedback via the telemetry system.

As a result, every mode of active tuning operated the train on a continuous loop without failure. There was never a need to manually move the train forward, unlike the case of fixed-frequency testing Ref. [22].

As discussed before, the fluctuation can be reduced with other approaches. A variable capacitor can be used in a receiving coil so that the resonance, and the effective impedance can be tuned electronically. This will change the field distribution on the array, and thus the power coupled to the receiver. When two resonant receivers are used and the received power is combined after rectification, the overall efficiency can be improved with much less fluctuation at different locations on the track.

It is worth to mention that the numerical and experimental study presented in this session were intended for general demonstration. The resonators in this study were not fully optimized. This can be a very flexible and powerful wireless power delivery solution. The resonators in the array does not have to be identical; they can be shaped to allow a curved or even forked track that may have loops or stub ends. With a particular application in mind, the design, size, and other parameters of the resonator array can be further optimized for better wireless power delivery.

## 2.4 Conclusion

In summary, we presented metamaterial-based technologies to improve near-field WPT in range, efficiency, and flexibility in this chapter. Two principal concepts and their implementations were discussed. First, using a properly designed metamaterial slab between two coils, the coupling between coils can be enhanced and the power transfer efficiency can be improved. Studies showed that significant efficiency improvement can still be achieved with reasonable material loss in metamaterials. In experiment, a metamaterial slab has been designed for a WPT system operating at 27 MHz, and the power transfer efficiency when the metamaterial slab is used is almost three times as high as the system without the slab. Second, resonant coupling-based WPT can be extended using an array of coupled resonators. The range of efficient power transfer is significantly increased using multiple coupled resonators in the array system. While conventional WPT technologies are mostly feasible only for static devices, the array-based system can be used to transfer power dynamically to mobile or loosely located devices as well. The array-based system has been studied analytically and numerically; experiment has been done to build an array of 30 resonant coils coupled by a single feeding antenna, and provide wireless power continuously to a train on the move. With the development of these technologies, the capability of near-field coupling-based WPT can be largely expanded, which potentially leads to new application areas.

## References

1. Shimokura, N., Kaya, N., Shinohara, M., Matsumoto, H.: Point-to-point microwave power transmission experiment. *Electr. Eng. Jpn.* **120**(1), 33–39 (1997)
2. Cota (<http://www.ossia.com/cota/>); Energous (<http://www.energous.com/>)
3. Schuder, J.C., Stephenson, H.E., Townsend, J.F.: High-level electromagnetic energy transfer through a closed chest wall. *Inst. Radio Eng. Int. Conv. Rec.* **9**, 119 (1961)
4. Low, Z.N., Chinga, R.A., Tseng, R., Lin, J.: Design and test of a high-power high-efficiency loosely coupled planar wireless power transfer system. *IEEE Trans. Ind. Electron.* **56**, 1801 (2009)
5. Elliott, G.A.J., Raabe, S., Covic, G.A., Boys, J.T.: Multiphase pickups for large lateral tolerance contactless power-transfer systems. *ieee trans. ind. electron.* **57**, 1590 (2010)
6. de Donaldson, N., Perlins, T.A.: Analysis of resonant coupled coils in the design of radio frequency transcutaneous links. *Med. Biol. Eng. Comput.* **21**, 612 (1983)
7. Puers, R., Schuylenbergh, K.V., Catrysse, M., Hermans, B.: Wireless inductive transfer of power and data. In: *Analog Circuit Design*, p. 395. Springer (2006)
8. Kurs, A., Karalis, A., Moffatt, R., Joannopoulos, J.D., Fisher, P., Soljacic, M.: Wireless power transfer via strongly coupled magnetic resonances. *Science* **317**, 83 (2007)
9. Valtchev, S., Borges, B., Brandisky, K., Klaassens, J.B.: Resonant contactless energy transfer with improved efficiency. *IEEE Trans. Power Electron.* **24**(3), 685–699 (2009)
10. Cannon, B.L., Hoburg, J.F., Stancil, D.D., Goldstein, S.C.: Magnetic resonant coupling as a potential means for wireless power transfer to multiple small receivers. *IEEE Trans. Power Electron.* **24**, 1819 (2009)

11. Yuan, Q., Chen, Q., Li, L., Sawaya, K.: Numerical analysis on transmission efficiency of evanescent resonant coupling wireless power transfer system. *IEEE Trans. Antennas Propag.* **58**(5), 1751–1758 (2010)
12. Sample, A.P., Meyer, D.T., Smith, J.R.: Analysis, experimental results, and range adaptation of magnetically coupled resonators for wireless power transfer. *IEEE Trans. Ind. Electron.* **58**, 544 (2011)
13. Kurs, A., Moffatt, R., Soljacic, M.: Simultaneous mid-range power transfer to multiple devices. *Appl. Phys. Lett.* **96**, 044102 (2010)
14. Wang, B., Nishino, T., Teo, K.H.: Wireless power transmission efficiency enhancement with metamaterials. In: Proceedings of the IEEE International Conference on Wireless Information Technology and Systems (ICWITS'10), Honolulu, Hawai'i, 28 Aug–03 Sept 2010
15. Urzhumov, Y., Smith, D.R.: Metamaterial-enhanced coupling between magnetic dipoles for efficient wireless power transfer. *Phys. Rev. B* **83**, 205114 (2011)
16. Wang, B., Teo, K.H., Nishino, T., Yerazunis, W., Barnwell, J., Zhang, J.: Wireless power transfer with metamaterials. In: Proceedings of European Conference on Antennas and Propagation (EuCAP 2011), 11–15 Apr 2011, Rome, Italy
17. Wang, B., Teo, K.H., Nishino, T., Yerazunis, W., Barnwell, J., Zhang, J.: Experiments on wireless power transfer with metamaterials. *Appl. Phys. Lett.* **98**, 254101 (2011)
18. Wang, B., Teo, K.H.: Metamaterials for wireless power transfer. In: Proceedings of IEEE International Workshop on Antenna Technology (iWAT), 5–7 Mar 2012, Tuson, Arizona (2012)
19. Huang, D., Urzhumov, Y., Smith, D.R., Teo, K.H., Zhang, J.: Magnetic superlens-enhanced inductive coupling for wireless power transfer. *J. Appl. Phys.* **111**, 64902 (2012)
20. Wang, B., Teo, K.H., Yamaguchi, S., Takahashi, T., Konishi, Y.: Flexible and mobile near-field wireless power transfer using an array of resonators. IEICE Technical Report, WPT2011-16 (2011)
21. Wang, B., Ellstein, D., Teo, K.H.: Analysis on wireless power transfer to moving devices Based on array of resonators. In: Proceedings of European Conference on Antennas and Propagation (EuCAP) 2012, 26–30 Mar 2012, Prague, Czech Republic
22. Yerazunis, W., Wang, B., Teo, K.H.: Power delivery optimization for a mobile power transfer system based on resonator arrays. In: Proceedings of International Symposium on Antennas and Propagation (ISAP) 2012, 29 Oct–2 Nov 2012, Nagoya, Japan
23. Lipworth, G., Ensworth, J., Seetharam, K., Huang, D., Lee, J.S., Schmalenberg, P., Nomura, T., Reynolds, M.S., Smith, D.R., Urzhumov, Y.: Magnetic metamaterial superlens for increased range wireless power transfer. *Sci. Rep.* **4**, 3642 (2014)
24. Rajagopalan, A., RamRakhiani, A.K., Schurig, D., Lazzi, G.: Improving power transfer efficiency of a short-range telemetry system using compact metamaterials. *IEEE Trans. Microwave Theory Tech.* **62**, 947–955 (2014)
25. Ranaweera, A.L.A.K., Moscoso, C.A., Lee, J.-W.: Anisotropic metamaterial for efficiency enhancement of mid-range wireless power transfer under coil misalignment. *J. Phys. D: Appl. Phys.* **48**, 455104 (2015)
26. Zhang, Y., Tang, H., Yao, C., Li, Y., Xiao, S.: Experiments on adjustable magnetic metamaterials applied in megahertz wireless power transmission. *AIP Adv.* **5**, 017142 (2015)
27. Pendry, J.B.: Negative refraction makes a perfect lens. *Phys. Rev. Lett.* **85**, 3966 (2000)
28. Shelby, R.A., Smith, D.R., Schultz, S.: Experimental verification of a negative index of refraction. *Science* **292**, 77–79 (2001)
29. Smith, D.R., Pendry, J.B., Wiltshire, M.C.K.: Metamaterials and negative refractive index. *Science* **305**, 788 (2004)
30. Fang, N., Lee, H., Sun, C., Zhang, X.: Sub-diffraction-limited optical imaging with a silver superlens. *Science* **308**, 534 (2005)
31. Schurig, D., Mock, J.J., Justice, B.J., Cummer, S.A., Pendry, J.B., Starr, A.F., Smith, D.R.: Metamaterial electromagnetic cloak at microwave frequencies. *Science* **314**, 977 (2006)
32. Engheta, N., Ziolkowski, R.W.: A positive future for double-negative metamaterials. *IEEE Trans. Microw. Theory Tech.* **53**, 1535 (2005)

33. Freire, M.J., Marques, R., Jelinek, L.: Experimental demonstration of a  $\mu = -1$  metamaterial lens for magnetic resonance imaging. *Appl. Phys. Lett.* **93**, 231108 (2008)
34. Smith, D.R., Schultz, S., Markos, P., Soukoulis, C.M.: Determination of effective permittivity and permeability of metamaterials from reflection and transmission coefficients. *Phys. Rev. B* **65**, 195104 (2002)
35. Freire, M.J., Marques, R.: Planar magnetoinductive lens for three-dimensional subwavelength imaging. *Appl. Phys. Lett.* **86**, 182505 (2005)
36. Ellstein, D., Wang, B., Teo, K.H.: Accurate models for spiral resonators. In: Proceedings of European Microwave Week (EuMW 2012), 28 Oct–2 Nov 2012, Amsterdam, Netherlands

# Chapter 3

## Optimal Array Beamforming for Microwave Power Transmission in Complex Environment

Ce Zhang, Bingnan Wang, Akira Ishimaru and Yasuo Kuga

**Abstract** Wireless power transfer (WPT) is a popular research field in recent years and can be categorized into three approaches: inductive coupling, laser beaming, and microwave power transmission (MPT). MPT system operates at the microwave frequency and transfers the energy over more than a few wavelengths. It has its unique advantages of supplying power to non-accessible and mobile receivers. The overall efficiency, which is the ratio between available DC power at the receiver and supplied DC power at the transmitter, depends on both circuit design and wave propagation. As a comprehensive theory of MPT system is not available, this chapter starts with the study of MPT system from the perspectives of mathematical formulation and the experiment in the indoor environment, in Sect. 3.1. The preliminary study leads to the conclusion that highly directional wireless transmitter is very useful in the MPT system for achieving high transmission efficiency. For this reason, phased array antennas with beamforming functionality are usually used to direct the electromagnetic wave toward mobile receivers, and adaptive array algorithms are implemented to enable wireless power focusing in the complex environment. Section 3.3 presents a novel beamforming algorithm, which is proven to give the optimal transmission efficiency and applies to the arbitrarily positioned unequal array based on our problem formulation. To verify this algorithm, Sect. 3.4 validates it with numerical electromagnetic simulation in different cases. The numerical comparison in these examples shows that this algorithm gives higher transmission efficiency over other optimal beamforming algorithms discussed in Sect. 3.2.

---

C. Zhang (✉) · A. Ishimaru · Y. Kuga

Department of Electrical Engineering, University of Washington, Seattle, WA 98195, USA  
e-mail: cezhang2@uw.edu

A. Ishimaru

e-mail: ishimaru@ee.washington.edu

Y. Kuga

e-mail: kuga@ee.washington.edu

B. Wang

Mitsubishi Electric Research Laboratories, 201 Broadway, Cambridge, MA 02139, USA  
e-mail: bwang@merl.com

### 3.1 Microwave Power Transmission System

Microwave power transmission (MPT) is a promising technology for its capability of supplying energy to receivers over a long range, so it is also called long distance wireless power transmission in [9]. MPT has a variety of applications such as powering ubiquitous sensor nodes at low power level [19], and transferring energy to electrical vehicle [13, 15], unmanned aerial vehicles (UAV) and high altitude platforms (HAPs) at high power level [5, 12]. In addition, MPT has also been proposed and implemented in the very high-power transmission from the space to earth, which is called “Solar Power Satellite” (SPSs) [10].

The estimation of MPT system efficiency with high accuracy is a challenging task, as there is no theory available for accurately modeling the electromagnetic wave radiation and reception. We start this section with the general formulation of the MPT, which clarifies the efficiencies of different building blocks in MPT system. Then, we study the transmission efficiency from the different perspectives. If the gain of the transmit and receive antenna is known, the quick estimation of transmission efficiency is easy but its accuracy is highly limited. If the channel transfer matrix between the transmit and receive array and impedance matrix of transmit array can be measured with the built-in hardware in the RF system, a more accurate and dynamic transmission efficiency can be found with our proposed model in this section. Following the theoretical study, an experiment has been carried out in the lab environment with clutters, such as equipment and furniture. The measurement data is analyzed with the help of simulation data and gives us an insight into the power loss contribution of the MPT system. The experiment shows that the propagation loss contributes to the most significant percentage of system loss, given the highly efficient wireless power transmitter and receiver.

#### 3.1.1 Problem Formulation

In the MPT system, the DC power is modulated with RF carrier and radiated from transmitting antenna onto “rectenna”, which collects and converts the impinging power of microwave to available DC power. As shown in [9], five efficiencies are defined respectively to evaluate the efficiency of these five building blocks (Fig. 3.1). The overall efficiency (end-to-end efficiency) is the ratio between available DC power at receiver and supplied DC power at the transmitter, which is the product of these five efficiency values from each building block.

Antenna is a transducer to bridge circuit theory and field theory. Since the excitation weight of antenna array is normally controlled by circuit elements and transmission efficiencies are evaluated at the circuit level, the powers are expressed in terms of voltage and current vectors. The definitions of power are first clarified in this section so that we can clearly set an optimization goal.

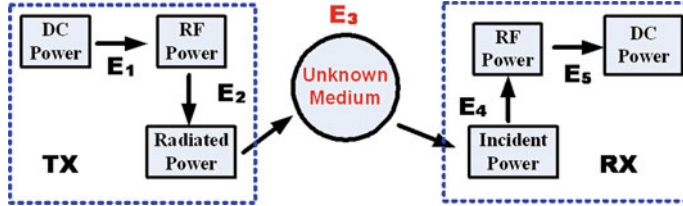


**Fig. 3.1** Microwave power transmission system:  $E_1$  to  $E_5$  are power transfer efficiencies

In antenna array system, each array elements is not independent and the radiated fields interfere to form the radiation pattern. In this way, in the far field, the array is treated as a single antenna and propagated in a spherical coordinate with the array at the origin. The total radiated power ( $P_{rad}$ ) can be expressed in terms of the current fed to each port ( $\mathbf{I}$ ) and mutual impedance matrix ( $\mathbf{Z}$ ). The real part of  $\mathbf{Z}$  corresponds to the radiated energy while the imaginary part corresponds to the reactive energy stored in near field region.

$$P_{rad} = \frac{1}{2} \mathbf{V}^H \mathbf{I} = \frac{1}{2} \mathbf{V}^H \Re\{\mathbf{Z}_A^{-1}\} \mathbf{V} \quad (3.1)$$

The total power ( $P_{\Omega}$ ) can also be computed by taking the integral over the enclosing sphere with the antenna at the center. Moreover, the power focused at the angular region  $\Psi$  given by receive aperture ( $P_{\Psi}$ ) is also defined for the beamforming optimization. These expressions can be similarly simplified into the product of vectors [14].

$$P_{\Omega} = \int_{\Omega} W_n dS \quad (3.2)$$

$$P_{\Psi} = \int_{\Psi} W_n dS \quad (3.3)$$

where  $W_n$  is Poynting flux density.

By energy conservation, the radiated power ( $P_{rad}$ ) is equal to the power enclosed by the sphere ( $P_{\Omega}$ ), and is related to the input power by reflection coefficient ( $\Gamma$ ) of antenna ports:  $P_{rad} = (1 - |\Gamma|^2)P_{in}$ . Normally the antenna impedance is matched to the port impedance so the reflection coefficient is approximately equal to 0 (in this condition,  $P_{rad} = P_{in}$ ).

The incident power with matched load is summed up at the receiver side, as the incident field induces RF currents at each port of receive antenna. The transmission efficiency ( $E_3$ ) in Fig. 3.1, which connects the transmit and receive array, is therefore optimized in power beamforming.

$$E_3 \triangleq \frac{P_{inc}}{P_{rad}} \quad (3.4)$$

In array synthesis theory, the beam collection efficiency (BCE) is usually used to evaluate the ability to shape the total power ( $P_Q$ ) toward the targeted angular region ( $P_\psi$ ) [14]. The overall efficiency is defined as the ratio between the total available RF power ( $P_{L,tot}$ ) and the total input power at transmit array ( $P_{in,tot}$ ), which includes the efficiency of transmit antenna ( $E_2$ ), transmission efficiency ( $E_3$ ) and receive antenna ( $E_4$ ).

$$BCE \triangleq \frac{P_\psi}{P_Q} = \frac{P_\psi}{P_{rad}} \quad (3.5)$$

$$\eta \triangleq E_2 E_3 E_4 = \frac{P_{out}}{P_{in}} \quad (3.6)$$

Since BCE is proportional to the transmission efficiency ( $E_3$ ), BCE is usually the optimization goal instead of the transmission efficiency for the simplicity of mathematical formulation with array factor (AF). However, in the scenario with multipath and high-absorbing or reflection obstacles, the AF and BCE are not valid for optimization as the line-of-sight (LOS) is not available.

### 3.1.2 Transmission Efficiency Based on Antenna Parameters

The electromagnetic field radiated from the antenna can be described as plane wave propagation in the far field, where the power of radiation decays as the square of the distance. In most of the wireless applications, the antenna operates in the region of far field and the transmission efficiency is computed in the way of link budget calculation with the help of the well-known Friis transmission equation. The complete version of Friis transmission equation is usually expressed as (3.7) in terms of antenna gain.

$$\frac{P_{rx}}{P_{tx}} = G_t G_r \left( \frac{\lambda}{4\pi R} \right)^2 (1 - |\Gamma_t|^2) (1 - |\Gamma_r|^2) |\hat{a}_t \cdot \hat{a}_r^*|^2 \quad (3.7)$$

where  $G_t$  denotes the gain of the transmit antenna and  $G_r$  denotes the gain of the receive antenna.  $R$  is the distance between the transmit antenna and the receive antenna.  $|\Gamma_t|$  and  $|\Gamma_r|$  are the reflection coefficient of the transmit and the receive antenna, respectively.  $\hat{a}_r$  denotes the polarization vector of the receive antenna while  $\hat{a}_t$  denotes the incident electric field vector or the polarization vector of the transmit antenna in LOS propagation. The term  $|\hat{a}_t \cdot \hat{a}_r^*|^2$  represents the polarization conversion loss in converting the incident wave into RF power available at the antenna port. The antenna gain is proportional to the effective aperture size of antenna,

$$G = \frac{4\pi}{\lambda^2} A_{eff} = \frac{4\pi}{\lambda^2} \eta_{ap} A_{phy} \quad (3.8)$$

where  $A_{eff}$  is the effective aperture size and the  $A_{phy}$  is the effective physical size.  $\eta_{ap}$  is the aperture efficiency of the antenna. The aperture efficiency relates the physical

aperture to the effective aperture area and can be treated as constant for a given array element geometry.

$$\begin{aligned}\eta_{far} &= \frac{P_{rx}}{P_{tx}} = \frac{A_{eff,tx}A_{eff,rx}}{c^2} \left(\frac{f}{R}\right)^2 \\ &= \eta_{ap,tx} \eta_{ap,rx} \frac{A_{phy,tx}A_{phy,rx}}{c^2} \left(\frac{f}{R}\right)^2\end{aligned}\quad (3.9)$$

After rearranging the Friis transmission equation (Eq. (3.7)), a more intuitive expression can be expressed in terms of physical size and operation frequency in (3.9), assuming no polarization loss and negligible mismatch loss. This expression gives the design guideline of the phased array antenna. Given the range of propagation and the limitation of the array size, the higher frequency of operation leads to higher transmission efficiency. This conclusion contradicts our normal intuition in link budget calculation of wireless communication, that the lower frequency gives lower path loss. The reason for this contradictory conclusion is that, given the fixed physical size of an array antenna, the number of antenna elements increased as with the decrease of wavelength instead of using the single antenna as in wireless communication. Besides, for the use of consumer electronics, the receiver of wireless power is mobile and has to be as small as possible so the demand of smaller size receive array can be compensated by the larger size of transmit array from the observation of this equation.

However, the Friis equation is defined in the region of the far field that is given by  $R > \frac{2D^2}{\lambda}$ , where D is the dimension of array aperture. It implies that, in most cases, the array antenna operates in the Fresnel near field region and incident wave is spherical wave instead of plane wave, if we attempt to achieve the higher transmission efficiency by increasing the frequency of operation and the larger size of transmit array. Another expression for estimating the transmission efficiency in the intermediate near field region is given in [1, 20]. This expression is more accurate when the aperture size of transmit array is very large and more comparisons can be found in the book [20].

$$\eta_{near} = \frac{P_{rx}}{P_{tx}} = 1 - e^{-\tau^2} \quad (3.10)$$

where  $\tau = \eta_{far}$  is equal to the Friis equation.

### 3.1.3 Transmission Efficiency Based on Channel Transfer Function

This subsection presents a general model in terms of the channel transfer equation and mutual impedance matrix. The microstrip patch antenna is taken as an example in our formulation and simulation, which is the most popular planar antenna because it is relatively inexpensive to manufacture and integrate with printed circuit design. In Fig. 3.3, the input voltage at the port of  $n_{th}$  patch antenna is denoted by  $V_{in,n}$  and the

voltage at the radiating slot of this patch is the transmitted wave  $V_n = (1 - \Gamma_n)V_{in,n}$ , where  $\Gamma_n = (Z_A - Z_0)/(Z_A + Z_0)$ .

From the model in [2], the electric field, at any point  $\mathbf{r}$ , given by the  $n_{th}$  patch antenna of transmit array at  $\mathbf{r}_n$ , is expressed in terms of the locations, dimensions of patch and the voltage at radiating slots as Fig. 3.2. The microstrip antenna is a rectangular patch with width of  $W$  and length of  $L$  and the substrate thickness is  $h$  (Fig. 3.3).

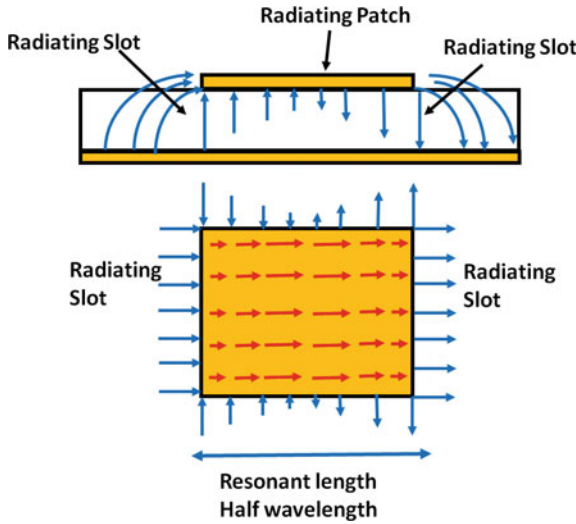


**Fig. 3.2** Radiation of the patch antenna in  $TM_{10}$  mode: blue arrow is electric field and red arrow is current flow

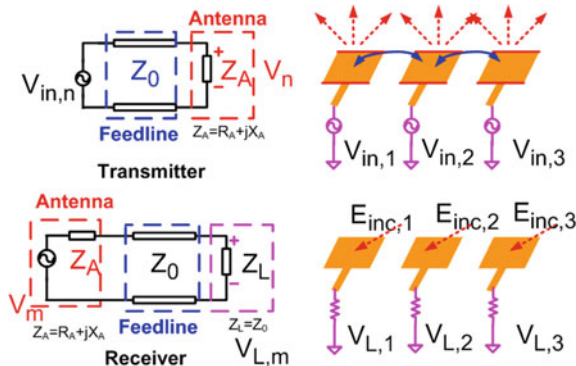


**Fig. 3.3** Transmit and receive patch antenna array:  $E_{inc,n}$  is the incident electric field onto the  $n_{th}$  receive antenna elements;  $V_{in,n}$  is the input voltage at the port of  $n_{th}$  transmit antenna;  $Z_A$  is the impedance of transmit/receive antenna;  $V_{L,n}$  is the available voltage at the load of antenna;  $Z_L$  is the load impedance of the receive antenna

$$\mathbf{E}(\mathbf{r}, \mathbf{r}_n) = \frac{-jV_n k_0 W e^{-jk_0 R}}{\pi R} F(\theta, \phi) \quad (3.11)$$

$$\mathbf{E}(\mathbf{r}, \mathbf{r}_n) = \kappa V_n G(R) \mathbf{F}(\theta, \phi) \quad (3.12)$$

where  $R = |\mathbf{r} - \mathbf{r}_n|$ ,  $\kappa = (-jk_0 W)/\pi$  and  $G = e^{-jk_0 R}/R$ .

$\theta$  and  $\phi$  are the spherical angles corresponding to the location  $\mathbf{r}_n$ . In the directivity pattern  $\mathbf{F}(\theta, \phi)$ , the origin of spherical angles for different patch elements should be the geometric center of the corresponding patch. However, since we have the far field approximation  $\theta_1 \cong \dots \cong \theta_M \cong \theta$  and  $\phi_1 \cong \dots \cong \phi_M \cong \phi$ , the values of  $\theta$  and  $\phi$  corresponding to every transmit element can be approximated by the angle from the phase center of array to the observation point.

The directivity pattern  $\mathbf{F}(\theta, \phi)$  has two orthogonal components  $\mathbf{F}_\theta$  and  $\mathbf{F}_\phi$ .

$$\begin{aligned} \mathbf{F}(\theta, \phi) &= \hat{\theta} F_\theta + \hat{\phi} F_\phi \\ \mathbf{F}(\theta, \phi) &= [\hat{\phi} \cos \theta \sin \phi - \hat{\theta} \cos \phi] \cos(kh \cos \theta) \\ &\quad \frac{\sin(\frac{k_0 W}{2} \sin \theta \sin \phi)}{\frac{k_0 W}{2} \sin \theta \sin \phi} \cos(\frac{k_0 L}{2} \sin \theta \cos \phi) \end{aligned} \quad (3.13)$$

The electric field in Eq. (3.12) can be constructed coherently in space to cancel out the power flow in undesirable direction. Since the electric field is governed by the law of linear superposition, the incident electric field at the  $m_{th}$  receive patch antenna ( $\mathbf{r}_m$ ) is denoted by the sum of electric fields due to input voltage at all M transmit elements.

$$\mathbf{E}_{inc}(\mathbf{r}_m) = \sum_{n=1}^N \kappa V_n G(|\mathbf{r}_m - \mathbf{r}_n|) \mathbf{F}(\theta, \phi) \quad (3.14)$$

By introducing the vector effective length  $\mathbf{L}_{eff}(\theta_m, \phi_m)$  [16], the induced voltage at the  $m_{th}$  receive element is simply the dot product between incident field and effective length.

$$\begin{aligned} V_m &= \mathbf{E}_{inc}(\mathbf{r}_m) \cdot \mathbf{L}_{eff}(\theta_m, \phi_m) \\ &\approx \sum_{n=1}^N \kappa V_n G(|\mathbf{r}_m - \mathbf{r}_n|) [\mathbf{F}(\theta, \phi) \cdot \mathbf{L}_{eff}(\theta', \phi')] \end{aligned} \quad (3.15)$$

It is noted that, in the far field approximation, the angles  $\theta_m$  and  $\phi_m$  can be referred to the geometric center of receive array and the effective length of all the receive elements are approximately equal from the equal incident angles  $\theta'$  and  $\phi'$ . In addition, since there is no widely accepted theory to calculate the exact efficiency of power absorption at receive antennas [17], the effect of scattering or reradiation is not discussed in this chapter and its effect is simply included into the polarization mismatch of incident field and the impedance mismatch at the load impedance.

Hence, the transfer function from the input port to output load, which is actually the S parameters in numerical simulations, can be formulated as follows.

$$\begin{aligned} H_{mn} &= \frac{V_{out,m}}{V_{in,n}}|_{V_{in,j}=0 \text{ for } j \neq n} \\ &= \kappa(1 - \Gamma_n)G(|\mathbf{r}_m - \mathbf{r}_n|) \\ &\quad [\mathbf{F}(\theta_n, \phi_n) \cdot \mathbf{L}_{eff}(\theta_m, \phi_m)] \frac{Z_0}{Z_0 + Z_A} \end{aligned} \quad (3.16)$$

At transmitter side,  $(1 - \Gamma_n)$  denotes the reflection at the input port of transmit antenna. At receiver side,  $[\mathbf{F}(\theta_n, \phi_n) \cdot \mathbf{L}_{eff}(\theta_m, \phi_m)]$  is the polarization factor while  $Z_0/(Z_0 + Z_A)$  is mismatch factor [16].

$G(|\mathbf{r}_m - \mathbf{r}_n|)$  is the Green's function, which represents the wave propagation from the transmit element to the receive element. In free space, it can be simply taken as its simplest form  $G = e^{-jk_0R}/R$  while, in complex medium, this function has to be modified to a different expression of Green's function accordingly [7].

The total RF power deliverable to the load can be added up over all the receive elements incoherently.

$$\begin{aligned} P_{out} &= \sum_{m=1}^M \frac{V_{out,m} V_{out,m}^*}{2Z_L} \\ &= \frac{1}{2Z_L} \sum_{m=1}^M \sum_{n=1}^N (V_{in,n} H_{mn})(V_{in,n} H_{mn})^* \\ &= \frac{1}{2Z_L} \mathbf{V}_{in} \mathbf{H} \mathbf{H}^H \mathbf{V}_{in}^H \end{aligned} \quad (3.17)$$

The total input power can also be computed at the circuit level in terms of mutual impedance matrix in (3.1) and reflection coefficient  $P_{in} = P_{rad}/(1 - |\Gamma|^2)$ . Hence, the overall RF transmission efficiency, which includes the efficiencies due to the transmit antenna, the receive antenna, and the wave propagation in the medium, is computed as follows ( $\eta = E_2 E_3 E_4$ ).

$$\begin{aligned} \eta &= \frac{P_{out}}{P_{in}} = \frac{(1 - |\Gamma|^2)}{Z_L} \frac{\mathbf{V}_{in} \mathbf{H} \mathbf{H}^H \mathbf{V}_{in}^H}{\mathbf{V}_{in} \Re\{\mathbf{Z}^{-1}\} \mathbf{V}_{in}^H} \\ &\sim \frac{\mathbf{V}_{in} \mathbf{H} \mathbf{H}^H \mathbf{V}_{in}^H}{\mathbf{V}_{in} \Re\{\mathbf{Z}_A^{-1}\} \mathbf{V}_{in}^H} \end{aligned} \quad (3.18)$$

### 3.1.4 Experiment Study of Indoor MPT

Since the accuracy of the aforementioned models is to be validated, a wireless power transmission experiment is carried out in our lab environment with two array placed

face-to-face with each other. To obtain the insight into the MPT in such a scenario, the complete MPT system is built with the detailed analysis of link budget.

Firstly, the indoor experiment is carried out with two standard gain horn antennas with the realized gain of 14 dB and the measured  $S_{21}$  (deembeded to the plane of antenna port) is tabulated as follows when the two antennas are facing with each other accurately. Moreover, it is noted that the dimension of the horn antenna is approximately  $D = 0.2\text{ m}$  so the far field condition is  $R > \frac{2D^2}{\lambda} \approx 1.54\text{ m}$  while the near field condition is  $R > 0.62\sqrt{\frac{D^3}{\lambda}} \approx 0.24\text{ m}$ . This implies that the system operates in the Fresnel near field region, where the radiation pattern or spatial distribution of electromagnetic field varies significantly with the distance.

From the Table 3.1, it is found that the far field equation gives a closer estimation of transmission efficiency while the estimation error of near field equation is much larger. The reason for this is that the receiver is closer to the far field boundary than near field boundary. The general rule of determining which equation is stated in [20] as that the near field efficiency is more accurate when the value of  $\tau$  is larger than 1.

Next, the prototype of MPT system including both transmitter and receiver is also built to study the contribution of real system losses. As shown in Fig. 3.4, the full system includes the signal generator, power divider, transmit and receive antenna array, RF rectifier with load resistor, and high power amplifier.

**Table 3.1** Measurement with horn antenna versus distance. The  $S_{21}$  reflects the power ratio at the network analyzer so the cable loss is extracted to deembed the reference to the antenna ports. The path loss is computed from Friis equation with unity antenna gain assuming the transmission with isotropic radiator

| Distance (m)                    | 0.6 | 1.2 | 1.8 | 2.4 | 3   |
|---------------------------------|-----|-----|-----|-----|-----|
| Deembeded $S_{21}$ (dB)         | -22 | -27 | -30 | -31 | -32 |
| Path loss (dB)                  | -50 | -55 | -58 | -59 | -60 |
| Near field equation (3.10) (dB) | -30 | -42 | -49 | -54 | -58 |
| Far field equation (3.9) (dB)   | -15 | -21 | -25 | -27 | -29 |

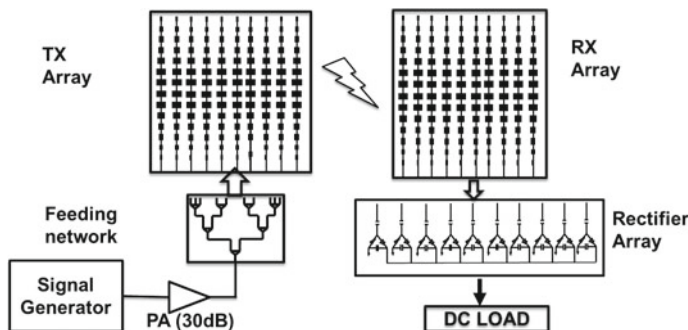


**Fig. 3.4** Experimental configuration of the full MPT system

The transmit and receive antenna array are the same series-fed microstrip antenna array, which has 14 elements connected in series governed by the Chebyshev distribution of width tapering and operates in the resonant mode. In the other dimension, 10 input ports are connected in parallel with the spacing of half free space wavelength. At the transmitter side, the 10 parallel input ports are fed with a 10-way broadband power divider, which is made up of the cascaded two-way Wilkinson power dividers and three-way dividers. Therefore, the 10 ports of power divider are weighted rather than equally distributed. This feeding network can reduce the side-lobe level (SLL) to some extent while achieving broadband power combining at the cost of increased insertion loss. The antenna array and the power divider are fabricated on two separate FR-4 printed circuit board (PCB). The antenna array gives the simulated realized gain of 25 dB, and the broadband power divider gives the measured  $-6.96$  dB insertion loss of power division. Therefore, the total array with the power divider at the transmitter gives realized gain of approximately 19 dB. The power amplifier is a broadband high power amplifier by Mini-Circuits with typical power added efficiency (PAE) of 30 % at 5.8 GHz and can output up to 1 W RF signal without distortion.

At the receiver side, the RF rectifier array is implemented with the single stage charge pump topology and converts the RF signal to DC power. The diode in the rectifier is the HSMS-286x surface mount Schottky detector diode by Avago Technology, which gives the low series resistance of  $6\ \Omega$ . The single rectifier unit achieves up to 73 % conversion efficiency with this low loss diode. The rectifier array employs the hybrid of series and parallel power combining at DC, and is optimized to 20–40 % conversion efficiency with the DC load of  $150\ \Omega$  and the input signal of 0 dBm sinusoidal wave at 5.8 GHz, which is the case in our measurement. It is noted that the efficiency of rectifier varies with the input power level, input signal frequency, the way of DC power combining and DC load present to the rectifier, so the conversion efficiency keeps changing with the experimental condition.

The full system measurement is carried out with the separation distance of 3 m between the transmitter and receiver. To find out the contribution of the system loss, each component of the whole system must be measured one by one and, when the signal generator outputs the RF power of 0 dBm, the link budget can be estimated as in Fig. 3.5. To analyze the reason for a low efficiency, the total system losses are dissected in the view of a pie chart as shown in Fig. 3.6.

From the analysis of system losses, it can be found that, because the total DC power at the transmitter is almost equal to the DC power consumption of power amplifier, the upper limit of power loss is set by the PAE of power amplifier (PA) and the amount of this loss is fixed. Though the second and third largest power loss is contributed by the feeding network and RF cable as Fig. 3.6, these losses can be effectively reduced using the spatial power combining technique.

However, in spite of the high efficiency circuit design, the radiation loss will dominate the system loss and is hard to suppress. The degradation of efficiency is more serious when the LOS propagation is not available. When the LOS channel is blocked in the experiment, the loss of the fixed beam array increases by more than

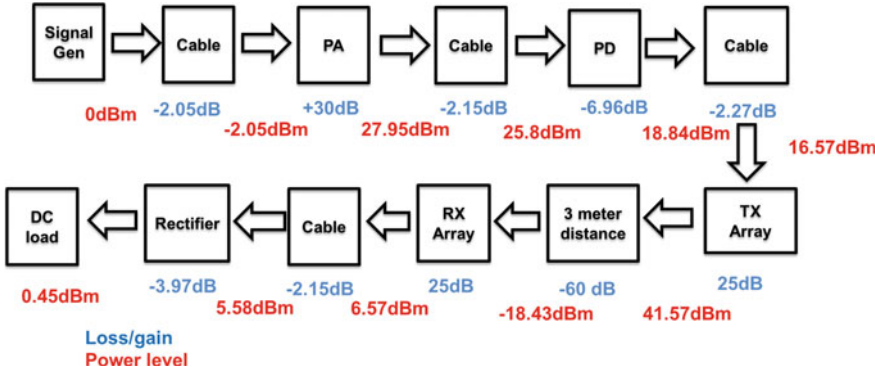
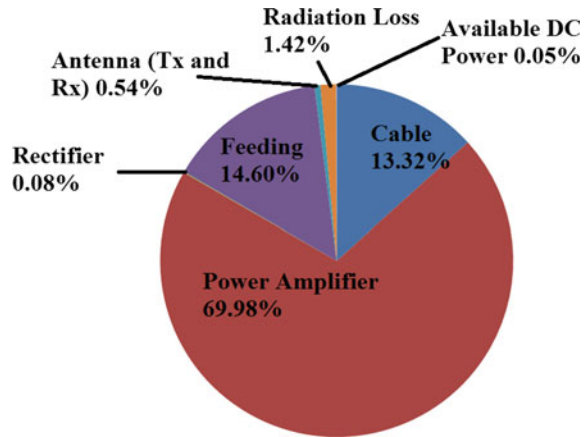


**Fig. 3.5** The link budget of prototype system. The PAE of power amplifier is taken as 30 % as given by the device specification while the conversion efficiency of rectifier array is taken as 40 %. The distance between transmitter and receiver it taken as 3 m. The path loss excluding antenna gain is estimated using the measurement in Table 3.1 and the radiation into wave propagation medium is labeled as radiation loss

**Fig. 3.6** Contribution of system losses: the measured output DC power is consistent with the estimated link budget in Fig. 3.5. The total DC to DC transmission efficiency is computed as 0.068 %



20 dB according to our experiment. The only possible solution to high transmission efficiency is adaptive beamforming array. Techniques for adaptive array will be discussed in the following Sect. 3.2.

## 3.2 Review of Optimal Beamforming Techniques

The antenna beamforming is achieved through the coherent operation of antenna elements so the excitation weight of each element determines the performance of beamforming.

### 3.2.1 Array Factor Optimization

In traditional beamforming based on AF synthesis, the antenna elements are assumed to be have the same radiation pattern and accurately positioned. The steering vector  $\mathbf{v}_s = [e^{ik(ux_n+vy_n)}]$  is used to yield the AF  $F(u, v) = \sum_{n=1}^N w_n e^{ik(ux_n+vy_n)}$ , where  $(u, v)$  identifying the angular region. Since the power of AF is proportional to the spatial distribution of the radiated power, BCE is expressed in terms of power of AF and a closed form expression of BCE is derived for the planar array case by Oliveri et al. [14].

$$BCE = \frac{\int \sum_{n=1}^N w_n e^{ik(ux_n+vy_n)}}{\int \sum_{n=1}^N w_n e^{ik(ux_n+vy_n)}_{\Omega}} = \frac{\mathbf{w}^H \mathbf{A} \mathbf{w}}{\mathbf{w}^H \mathbf{B} \mathbf{w}} \quad (3.19)$$

where  $B_{mn} = 4\pi \text{sinc}(k\sqrt{(x_m - x_n)^2 + (y_m - y_n)^2})$  and  $A_{mn} = 4\pi u_0 v_0 \text{sinc}(k(x_m - x_n)) \text{sinc}(k(y_m - y_n))$

This approximation greatly reduces the computation time at the cost of accuracy. However, for other structures and spacings of array, the closed form expression is not available and the numerical integral of powers has to be performed, which may take a long time to approach an optimal solution. In reality, the radiation pattern of array element is never the same due to mutual coupling, edge effect and manufacturing process. More importantly, this technique is not valid for power optimization if the array is not regular shape with known position [14].

### 3.2.2 Retrodirective Array/Phase Conjugate Array

Retrodirective Array is the array to reflect the incident plane wave toward the source direction without any prior information on the source location. The retrodirective array works in the following way: the receive array/interrogate antenna out a probing signal and then transmit array retransmits the amplified signal toward the receiver by taking phase conjugate of the observed probing signal. Since the phase conjugating functionality can be implemented at RF frequency with hardware, its popularity arises from the automatic beam steering without any computational algorithm (i.e., digital signal processing hardware). Although this technique is also adaptive to the propagation channel, it only works for a fixed frequency. The array calibration becomes problematic, depending on the hardware design.

### 3.2.3 Adaptive Array Digital Beamforming

Digital beamforming is more powerful and flexible than conventional phased array at the expense of hardware complexity and cost. However, if the estimation of channel characteristics is enabled by the additional receive antennas, the adaptive signal processing results in a more powerful beamforming transmitter and flexible beamforming formulation regardless of array shape and position. Digital beamforming based on the channel estimation is also an important technique to enhance the signal-to-interference ratio (SIR), signal-to-noise ratio (SNR), and the intersymbol interference (ISI) in the MISO or MIMO communication.

The time reversal (TR) technique has been studied extensively in wireless communication by many researchers [11], as this scheme can improve SNR greatly in multipath and rich scattering environment. The receivers send a probing signal to transmitter for channel estimation and the transmitters convolve the time-reversed channel impulse response  $h(-t)$  with the transmitted signal  $s(t)$ . The received signal will be equal to the convolution between the transmitted signal  $s(t)$  and the autocorrelation of the channel impulse response. Equation (3.20) indicates that the energy will be spatially focused at the target receiver in any environment. When the receiver has multiple antennas, this TR beamforming technique is not valid for energy focusing.

$$y(t) = s(t) * h(-t) * h(t) = s(t) * R(t) \quad (3.20)$$

The eigen-beamforming is an optimal scheme for maximizing the average SNR [24] in the narrowband MIMO. Nevertheless, the optimization of SNR happens at the output of matched filter instead of the summed power at the receiver. Besides, it is noted that the maximization is implemented with the coding scheme, which results in the spectrum spread. For this reason, this technique is not applicable for adaptive beamforming in MPT, which requires the continuous wave transmission.

$$SNR = \frac{E\{\mathbf{h}^H \mathbf{C}^H \mathbf{Chs}\}}{E\{\mathbf{h}^H \mathbf{C}^H \mathbf{n} \mathbf{n}^H \mathbf{Ch}\}} \quad (3.21)$$

where  $\mathbf{h}$  is the matrix of channel impulse response in time domain and  $\mathbf{C}$  is the coding scheme of eigen-beamforming.  $\mathbf{n}$  is the Gaussian noise and  $s$  is the baseband signal carrying information.

Furthermore, the time reversal scheme is analyzed using the model of Green's function in the frequency domain [6, 8], as the time-reversed signal is equivalent to the complex conjugate in frequency domain. The papers [6, 8] demonstrate that the communication efficiency can be improved with the proposed beamforming scheme in theory and in the experiment, respectively. To our knowledge, the specific application of adaptive beamforming for WPT has not been reported yet.

### 3.3 Time Reversal Eigenmode Beamforming

The classic array synthesis technique is developed based on the model of AF with the assumption of equal element pattern. As is widely known by antenna designer, the mutual coupling leads to the unequal pattern, especially for the edge element. For the array with unequal element and arbitrary location, the AF is no longer valid and the adaptive array processing has to be employed for the array synthesis using the knowledge of probing channel characteristics. However, the previous studies of adaptive beamforming are developed for improving the signal-to-noise (SNR) ratio or channel capacity based on MIMO wireless communication and no discussions on how to devise an adaptive algorithm for MPT. This section presents a modified algorithm for MPT based on the time reversal signal processing techniques. Besides, it will also be proved as a new optimal array synthesis method without the prior knowledge of element spacing and positions.

#### 3.3.1 *Pseudo Transmission Efficiency*

To implement the adaptive optimization of transmission efficiency, we propose the pseudo transmission efficiency (PTE) as an alternative optimization goal. PTE is the ratio between the total RF power available at the receive array and incoherent sum of the input power over all transmit elements.

The incoherent sum of radiated power takes the sum of input power at each radiator independently and is only physical for special case that the mutual impedance matrix is diagonal matrix ( $P_{sum,in} \neq P_{in}$ ). However, the incoherent power is used in communication society for the evaluation of power in wireless communication by neglecting the mutual coupling effect. Similarly, the incoherent sum of radiated power is related to input power ( $P_{sum,rad} = (1 - |\Gamma|^2)P_{sum,in}$ ).

$$P_{sum,rad} = \frac{\mathbf{V}^H \mathbf{V}}{2R_{rad}} = \frac{1}{2} \mathbf{V}^H \Re\{\text{diag}[\mathbf{Z}_A^{-1}]\} \mathbf{V} \quad (3.22)$$

$$PTE \triangleq \frac{P_{out}}{P_{sum,in}} \quad (3.23)$$

PTE is not a physical efficiency, but the difference between PTE and  $\eta$  (Eq. (3.18)) is negligible if the real part of mutual coupling impedance terms are sufficiently small. When the adjacent antenna elements are weakly coupled to each other, the transmit channels are uncorrelated with each other. The correlation between transmit channels are expected to be low in both MPT and MIMO communication. While the envelope correlation coefficient (ECC) is an indicator of the MIMO antenna design, the independency of MPT array is reflected by the ratio between the radiated power and the coupled power dissipation in the following Eq. (3.24). It is noted that this

correlation power factor is related to the complex excitations of the array elements and the power ratio  $R$  increases as with the improved isolation between adjacent elements.

$$R(\mathbf{V}_{in}) \triangleq \frac{\sum_{i=1}^N v_i \Re\{y_{ii}\} v_i^*}{\sum_{j=1}^N \sum_{i=1, i \neq j}^N v_i \Re\{y_{ij}\} v_j^*} \quad (3.24)$$

To verify this assumption quantitatively, a simple  $2 \times 2$  rectangular array is simulated in Ansys HFSS and the exported Y parameter is used to compute the correlation power factor with several complex excitation combinations. These five excitation vectors have the uniform magnitude but random linear phase progression. Figure 3.7 shows that the exact value of correlation power factor is dependent on the excitation vector but the average increases with the array element spacing, which is equivalent to the isolation between two elements. The improvement of mutual coupling can also be implemented by the techniques of enhancing ECC in MIMO antenna design.

In Fig. 3.8, the error between incoherent power sum ( $P_{sum,in}$ ) and physical input power ( $P_{in}$ ) is defined as  $Error \triangleq |(P_{sum,in} - P_{in})/P_{sum,in}|$  and the error is plotted for different excitations as in Fig. 3.7. The average of the five excitations shows that the average error is well below 5 % when the array spacing is greater than the half free space wavelength. In summary, the plots in Figs. 3.7 and 3.8 quantitatively justify why the PTE gives a good estimation of transmission efficiency for weakly coupled array.

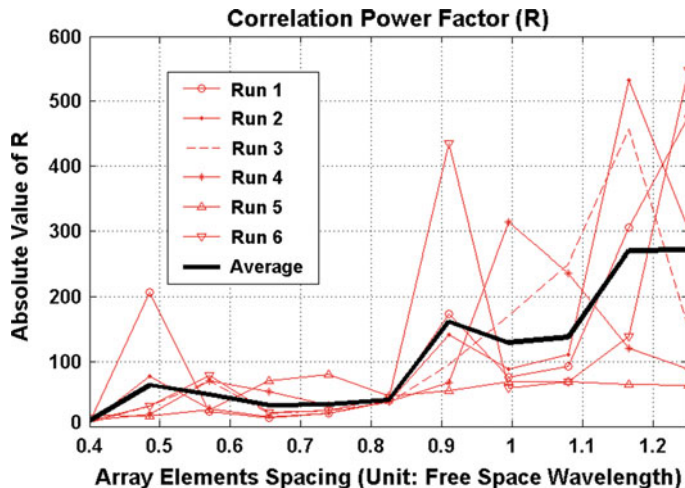


**Fig. 3.7** Correlation power factor (R): the average correlation power factor increases as with the increase of element spacing

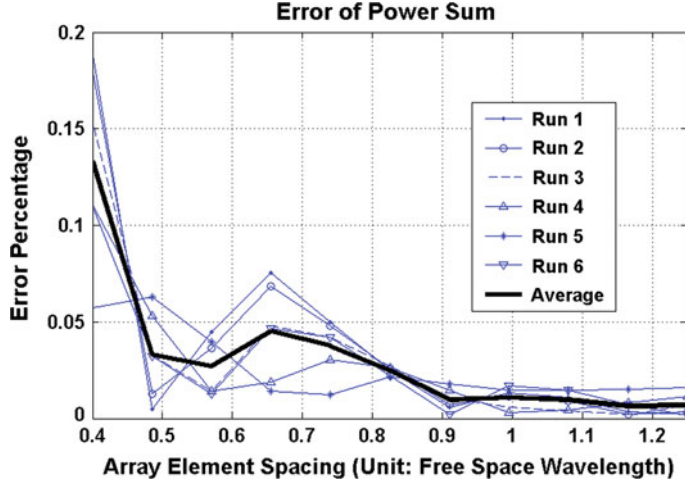


**Fig. 3.8** Error percentage of incoherent sum: the average error decreases as with the increase of element spacing

### 3.3.2 Transmission Efficiency Optimization

Since the correlated power is sufficiently low in most array setup, this chapter will discuss the optimization of PTE instead of either  $\eta$  or BCE. If the PTE is rearranged, Eq. (3.23) can be simplified as in (3.25).

$$\begin{aligned}
 PTE &= \frac{P_{out}}{P_{sum,in}} = \frac{(1 - |\Gamma|^2)}{Z_L} \cdot \frac{\mathbf{V}_{in} \mathbf{H} \mathbf{H}^H \mathbf{V}_{in}^H}{\Re\{\mathbf{Z}_{rad}^{-1}\} \mathbf{V}_{in} \mathbf{V}_{in}^H} \\
 &\sim \frac{\mathbf{V}_{in} \mathbf{H} \mathbf{H}^H \mathbf{V}_{in}^H}{\mathbf{V}_{in} \Re\{diag(\mathbf{Z}_A)^{-1}\} \mathbf{V}_{in}^H} \\
 &\sim \frac{\mathbf{V}_{in} \mathbf{H} \mathbf{H}^H \mathbf{V}_{in}^H}{\mathbf{V}_{in} \mathbf{V}_{in}^H}
 \end{aligned} \tag{3.25}$$

From Eqs. (3.18) and (3.25), it is clear that the ultimate goal of achieving optimal transmission efficiency is to solve the eigenvalue problem  $\mathbf{R}_Z \mathbf{P} \mathbf{V}_{in} = \lambda \mathbf{V}_{in}$ , where  $\mathbf{P} = \mathbf{H}^H \mathbf{H}$  and  $\mathbf{R}_Z = \Re\{\mathbf{Z}\}$ .  $\mathbf{V}_{in}$  is the input voltage, which also corresponds to the eigenvector of this problem. This is a Rayleigh Quotient and the eigenvalues of  $\mathbf{R}_Z \mathbf{P}$  give the possible range of the transmission efficiency  $\eta$ . From Min–Max Theorem, it is known that the dominant eigenvector (the eigenvector corresponding to the largest eigenvalue) maximizes the transmission efficiency  $\eta$ .

$$\mathbf{V}_{in,opt} = \arg \left[ \max_{\mathbf{V}_{in}} \frac{\mathbf{V}_{in} \mathbf{V} \mathbf{V}^H \mathbf{V}_{in}^H}{\mathbf{V}_{in} \Re\{\mathbf{Z}^{-1}\} \mathbf{V}_{in}^H} \right] \tag{3.26}$$

However, the mutual impedance matrix can only be estimated from measurements but the measurement is difficult if the number of array elements are very large so finding the matrices in this eigenvalue problem is a difficult task.

$$\mathbf{V}_{in,opt} = \arg \left[ \max_{\mathbf{V}_{in}} \frac{\mathbf{V}_{in} \mathbf{H} \mathbf{H}^H \mathbf{V}_{in}^H}{\mathbf{V}_{in} \mathbf{V}_{in}^H} \right] \quad (3.27)$$

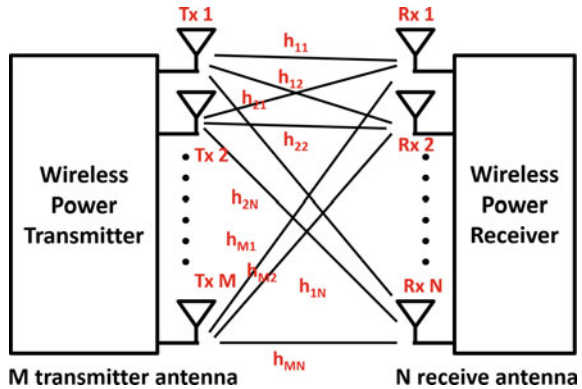
Therefore, as discussed above, we may think of optimizing the PTE as an alternative goal because it can be computed from the signal levels observed at the input ports. This method is validated in Fig. 3.8 as the error between  $\eta$  and PTE is expected to be negligibly small for the array with large spacing. In this way, another eigenvalue problem is formulated  $\mathbf{P}\mathbf{V}_{in} = \lambda \mathbf{V}_{in}$ . The Min-Max Theorem is also applicable for this as Eq. (3.27). In most cases, the maximization of PTE yields the maximal values of transmission efficiencies. Hence, the next challenge is how to devise an algorithm to approach this optimal eigenvector excitation.

### 3.3.3 Time Reversal Eigenmode Beamforming

Time reversal signal processing technique is derived from the research on acoustic focusing effect with time reversal mirror (TRM) by Fink [3, 4]. This principle focuses the energy thanks to the reciprocity of wave equation: the TR (using a negative time) of the wave functions's solution is also a solution to this equation as long as the media is slowly varying, reciprocal, and linear. When the TRM emits the plane wave toward a passive scatterer and observes the scattered signal, the emitted energy by TRM can be focused to this scatterer by retransmit a time reversed copy of observed signal. If the process is iterated, the energy become more and more focused on this passive target. This technique has been developed into applications including wireless communication and radar imaging in cluttered and complex medium with computational iterative process [7, 8, 18, 22].

If the channel transfer function between transmit and receive antenna can be measured in real time, the iterated time reversal process can be performed with a simple eigen decomposition process as discussed in [7]. Thus, the proposed method requires the probing of channel transfer matrix and digital beamforming architecture. Basically, the RF hardware of MPT system is similar to the massive MIMO communication as in Fig. 3.9 [21]. In such a power transmission system, the communication module is integrated with the power delivery module and used to probe the channel characteristics as MIMO communication. Given a transmit array of N elements and a receive array of M elements, the process of the proposed technique is stated as follows.

**Fig. 3.9** Time reversal eigenmode beamforming system



- **Measurement of transfer matrix  $\mathbf{H}$  (M-by-N)**

The probing signal is an impulse waveform  $s_n(t)$  spanning over the power transmission band and sent from each receive array elements one-by-one. The observed signal is recorded simultaneously at all the transmit elements and the recorded transient signal  $y_m(t)$  is transformed to frequency domain  $Y_m(\omega)$  through Fourier Transform. Then, the recorded signal is normalized to the probing signal as  $h_{mn}(\omega) = Y_m(\omega)/S_n(\omega)$ .  $h_{mn}(\omega)$  is defined as the channel transfer function in frequency domain between the  $n_{th}$  element of transmit array and  $m_{th}$  element of receive array.

- **Construction of transfer power matrix  $\mathbf{P}$  (N-by-N)**

The transfer functions  $h_{mn}$  at the frequency of  $\omega$  are rearranged into the matrix format as  $\mathbf{H}(\omega)$ .

$$\mathbf{H}(\omega) = \begin{bmatrix} h_{11} & h_{12} & h_{13} & \dots & h_{1N} \\ h_{21} & h_{22} & h_{23} & \dots & h_{2N} \\ \vdots & \vdots & \vdots & \ddots & \vdots \\ h_{M1} & h_{M2} & h_{M3} & \dots & h_{MN} \end{bmatrix} \quad (3.28)$$

The transfer matrix is used for the computation of the transfer power matrix ( $\mathbf{P}(\omega)$ ).

$$\mathbf{P}(\omega) = \mathbf{H}(\omega)^H \mathbf{H}(\omega) \quad (3.29)$$

- **Calculation of dominant eigenvectors (corresponding to largest eigenvalue)**

The eigenvector of the transfer power matrix can be found through the numerical eigenvalue decomposition of measured data. As discussed before, the eigenvector that corresponding to the largest eigenvalue leads to the maximization of PTE and will be used for beamforming.

$$\mathbf{P}\mathbf{V}_{in,1} = \lambda_1 \mathbf{V}_{in,1} \quad (3.30)$$

- **Power delivery according to dominant eigenvector**

Each element in the eigenvector  $\mathbf{V}_1$  corresponds to the complex excitation of one antenna element. Since, in most cases, the single tone signal is used for wireless power transmission, the sinusoidal wave at the frequency of  $\omega$  is weighted with the dominant eigenvector as follows.

$$y_m(t) = \mathfrak{F}^{-1}\{v_{1m}(\omega)\} = |v_{1m}(\omega)|\sin(\omega t + \angle v_{1m}(\omega)) \quad (3.31)$$

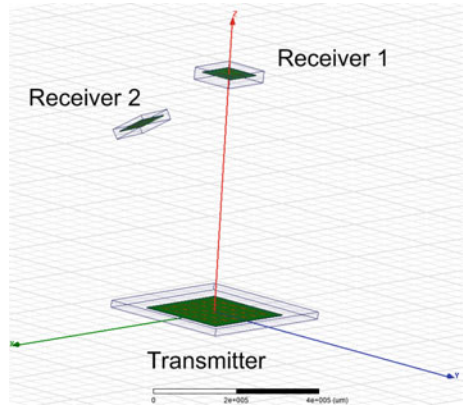
The proposed scheme is implemented with the digital beamforming architecture so the synchronized transmitters synthesize the desired transmit signal  $y_m(t)$  with analog-to-digital convertor (ADC) and feed into each transmit elements for power beamforming. It is noted that, in the real scenario of MPT, the available frequency of power transmission spans over a bandwidth of hundreds of megahertz while only a single carrier frequency is needed. In order to maximize the transmission efficiency, the eigenvalues of transfer power matrix over the available bandwidth can be compared to find at which frequency the power transmission has lowest propagation loss for the given environment.

The TR eigenmode technique has a drawback that is the susceptibility to interfering source. When there are multiple receivers requesting power transmission, the transmitter has to characterize the propagation channel corresponding to these receivers one-by-one and determine which frequencies are allocated to these receivers based on the frequency dependent eigenvalues corresponding to the receivers. After having determined the complex excitations, the simultaneous power transmission can be implemented by superimposing two signals at the baseband. For example, the  $m_{th}$  transmitter directly synthesizes the signal which simultaneous power transmission to two receives as  $y_m(t) = |v_{1m}^1(\omega_1)|\sin(\omega_1 t + \angle v_{1m}^1(\omega_1)) + |v_{1m}^2(\omega_2)|\sin(\omega_2 t + \angle v_{1m}^2(\omega_2))$ . In this way, the transmitter generates dual beams at two different frequencies pointing toward two receivers.

### 3.4 Numerical Examples

The paper [14] reports that the BCE can be up to 99 % by evaluating the power of AF. However, as discussed in Sect. 3.2 the efficiency derived from AF is not valid when the element pattern is not equal. To compare the effectiveness of different beamforming technique, the numerical simulation in different experiment setup is carried out in Ansys HFSS. The experimental verification of transmission efficiency and channel transfer function is extremely challenging and costly for large scale array beamforming. In this chapter, the electromagnetic simulation is carried out in HFSS-IE, which is a new module based on Method of Moment-Integral Equation (MoM-IE) and designed for electrically large simulations.

**Fig. 3.10** Simulation in HFSS-IE. The rectangular patch array antennas are used for both receiver and transmitter. The positions of transmit elements are randomized



As shown in Fig. 3.10, the microstrip rectangular patch antenna is chosen for the investigation as a representative of directive antenna rather than isotropic radiator. In HFSS, each antenna is placed on the planar Duroid 5870 substrate so each element has an image due to ground plane. Its radiation pattern of each antenna is modeled in the previous formulation. The field distribution on the virtual spherical air box is shown in Fig. 3.13 to illustrate the power distribution in space. The amplitude and phase of excitation is modified in the postprocessing function of HFSS according to the calculation of our proposed formulation.

Due to the intensive computation cost and limitation of computer memory, the 6-by-6 microstrip array is examined to make comparison with our theoretical model and the power transfer frequency is taken at 5.8 GHz in HFSS simulation. In the postprocessing, the excitations at each port can be specified with both amplitude and phase and the resultant beam pattern is observed in far field. The followings are several examples to show the advantages of the proposed scheme with the aid of comparison table and figures.

### 3.4.1 Arbitrary Array Beamforming in Free Space

In the first example, the beamforming techniques are evaluated in free space in terms of several transmission efficiencies ( $\eta$ ,  $\eta_{near}$ ,  $\eta_{far}$  and PTE) and spatial distribution of electric field. Four beamforming techniques are chosen for investigation: uniform excitation, phase conjugate (same as retrodirective array), the proposed method, and AF synthesis technique described in [14].

In the HFSS simulation setup, the transmit array is arbitrarily positioned 6-by-6 antenna array as in Fig. 3.11, the inset of which shows the resultant arbitrary array for beamforming. The random spacing is generated by the normal distribution function of Matlab with the mean of  $0.65\lambda_0$ . The receive array is 3-by-3 rectangular array with the spacing of  $0.65\lambda_0$  in both x and y direction. The receiver is located

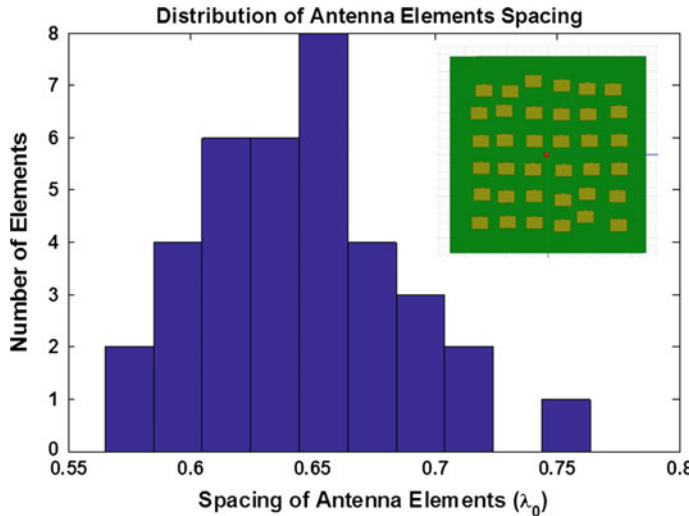


**Fig. 3.11** Spacing distribution of randomly positioned antenna array: the mean of element spacings is  $0.65\lambda_0$

at a distance 0.5 m from the center of transmit array and takes the angular area of  $0.1 \times 0.1$  receive aperture, which is defined as  $-\arcsin(0.1/2) \leq \theta \leq \arcsin(0.1/2)$  and  $-\arcsin(0.1/2) \leq \phi \leq \arcsin(0.1/2)$  in spherical coordinate. It is noted that, in this case, the receive array is located in the Fresnel near field region because the distance between receiver and transmitter is between the far field ( $\frac{2D^2}{\lambda} \approx 2.18$  m) and near field boundary ( $0.62\sqrt{\frac{D^3}{\lambda}} \approx 0.31$  m). As the exact position of arbitrary array is not available, the mean spacing is taken for the formulation of AF. Therefore, the degradation of beamforming is expected due to the random phase error.

To compute the beamforming efficiency, the power density can be integrated over angular regions ( $\Psi$ ) to obtain the power focused into the target area. It is noted that, when we compute the spatial power flow, the transmit antenna is simulated without the receive antenna with finite element method (FEM) only and enclosed with a upper hemisphere of radius 0.5 m. Then the BCE (Eq. (3.5)) is computed to evaluate ability of shaping power beam into angular regions of  $0.1 \times 0.1$  receive aperture. Besides, the received power and transmitted power are computed from mutual impedance matrix and S parameters are used to evaluate the transmission efficiency (Eq. (3.6)). For comparison, the incoherent sum of transmitted power is obtained from simulation and used for the computation of PTE as Eq. (3.6).

FEM simulation solves the far field antenna pattern with different complex excitations as in Fig. 3.12. The max antenna gains can be read from radiation pattern as 165.82, 177.16, 193.35, and 193.41 (in linear scale) for the techniques of phase conjugate array, TR eigenmode, uniform excitation, and AF synthesis, respectively. These four beamforming techniques gives the effective aperture for the calculation

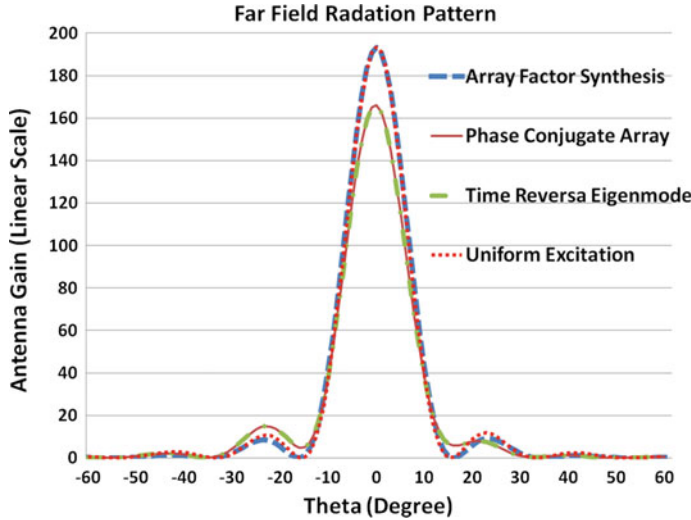


**Fig. 3.12** Far field radiation pattern of transmit array with different beamforming techniques: max array gain in linear scale can be read from radiation pattern as 165.82, 177.16, 193.3, and 193.41 for the techniques of phase conjugate array, TR eigenmode, uniform excitation, and AF synthesis, respectively

in Eqs. (3.9) and (3.10). The AF synthesis technique and uniform excitation give much higher gain and narrower beamwidth. From the models based on antenna parameters, it implies that these two techniques give higher transmission efficiency with the specific equations. However, the HFSS-IE simulation shows a contradictory results. The AF synthesis and uniform excitation result in the significant leakage of the real power flow (Fig. 3.13) if the spatial electric field distribution is plotted on the enclosing hemisphere. The phase conjugate and TR eigenmode techniques have lower far field gain but focuses most of power into the region of receive aperture. For this reason, Table 3.2 shows that the model-based estimation (either  $\eta_{near}$  or  $\eta_{far}$ ) overestimates the efficiency if it is compared with the simulated efficiency. The discrepancy is attributed to the wide main beam at the cost of lower gain so that the adaptive beamforming directs more integrated power into the targeted area.

Futhermore, Table 3.2 shows that either phase conjugate array or time reversal eigenmode technique leads to higher transmission efficiency  $\eta$  especially in the case that the position of antenna elements is not available. It also verifies that the assumption of negligible correlated power dissipation is valid in adaptive beamforming and shows their advantages over the classic array synthesis.

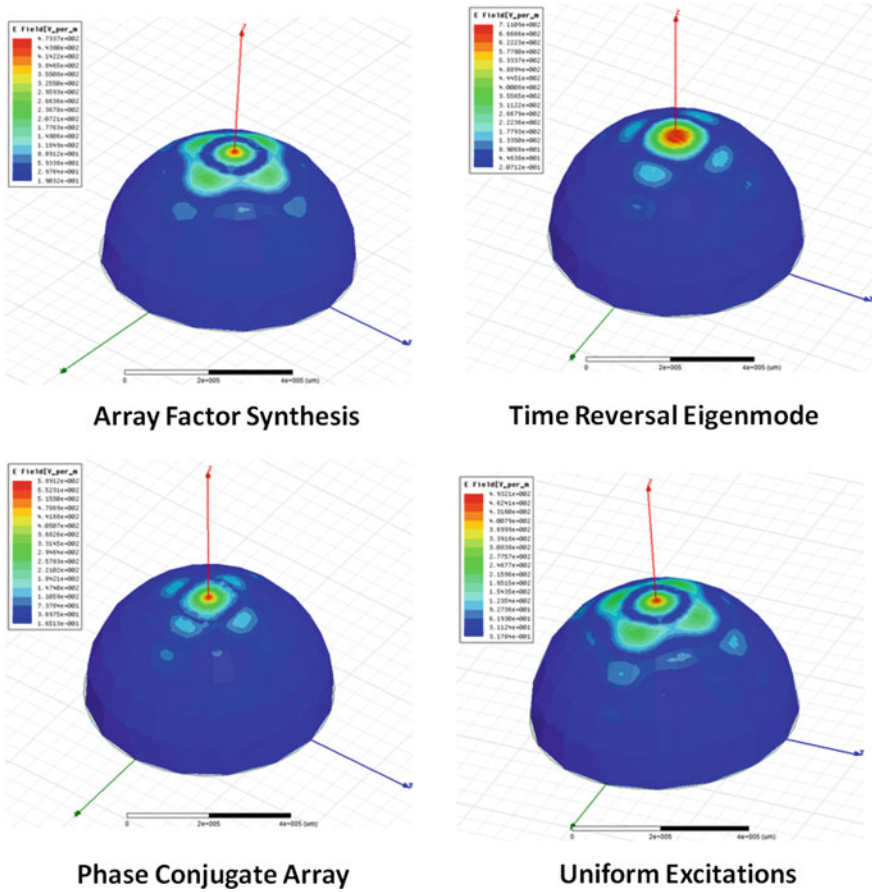


**Fig. 3.13** Spatial power distribution from different beamforming methods: significant amount of power leakage appears for the AF synthesis and uniform excitations. The enclosing sphere shows the spatial distribution of the real power flow in the region of Fresnel near field region

**Table 3.2** Comparison of different optimization techniques for MPT in free space

| Beamforming method | BCE<br>( $0.1 \times 0.1$ ) (%) | PTE (%) | $\eta$ (%) | $\eta_{near}$ (%) | $\eta_{far}$ (%) | Gain<br>(linear) |
|--------------------|---------------------------------|---------|------------|-------------------|------------------|------------------|
| Uniform            | 21.37                           | 34.18   | 18.50      | 50.64             | 70.59            | 193.41           |
| Phase conjugate    | 33.05                           | 45.82   | 25.14      | 45.47             | 60.65            | 177.16           |
| TR eigenmode       | 33.22                           | 45.86   | 25.22      | 45.41             | 70.59            | 165.82           |
| AF synthesis       | 22.64                           | 36.58   | 18.91      | 50.63             | 60.52            | 193.35           |

### 3.4.2 Arbitrary Array Beam Steering

The previous section demonstrates the potential of maximizing transmission efficiency when the receive array at the scan angle of  $0^\circ$ . At this scan angle, the transmit array gives the largest gain and the consequent transmission efficiency over any other beam pointing angles. In our analytical model, although the propagation channel is irrelevant with the location of scan angle, the synthesized beam by adaptive technique has the beam pointing error in some cases as discussed by [23]. Therefore, it is worthy of studying the impact of steering the beam away from the center.

In this subsection, the positions of transmit array elements are the same as last section while the receive array is rotated along the x axis to create different receiving angles. Figure 3.14 shows the beam steering toward the receive array based on the time reversal eigenmode technique. The main beam is steered to the angular region without the grating lobe where the receiver is until the scan angle is greater than  $30^\circ$ . The limited scan angle is due to array spacing of  $0.65\lambda_0$ . According to the array theory, the maximum scan angle can be computed from the array spacing as  $\theta_{max} = \arcsin(d/\lambda_0 - 1) = \arcsin(0.538) = 32.57^\circ$ . It is noted that, for the scan angle of  $45^\circ$ , most of power flows toward to the direction of receive array with the significant grating lobe at the symmetric location. However, when the scan angle moves further to  $60^\circ$ , the main beam cannot be steered to the direction of receiver any more. In fact, this phenomenon is attributed to the scan blindness due to surface wave and can be mitigated by the proper antenna elements design with cavity backing and so on. The beam scanning pattern given by the adaptive array technique also presents

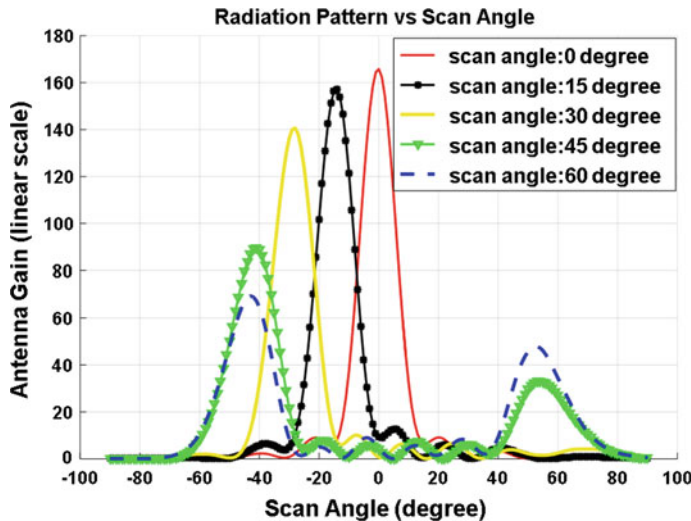


**Fig. 3.14** Antenna pattern over different scan angles: grating lobe becomes large for the scan angle of  $\theta = 45^\circ$  and  $60^\circ$ ; for the scan angle of  $60^\circ$ , the main beam cannot be steered to the direction of receive aperture

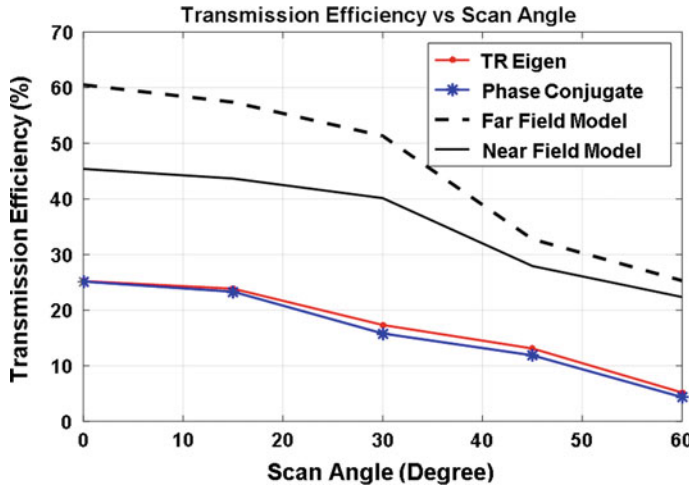


**Fig. 3.15** Transmission efficiency over different scan angles. The near field and far field models overestimate the transmission efficiency while the PTE has much better accuracy

the degradation of array gain, which is called the scan loss. The simulated gains at the angle of  $0^\circ$ ,  $15^\circ$ , and  $30^\circ$ , are 165.8, 157.3, and 140.6, respectively. The gain degradation is close to the scan loss equation  $\cos(\theta)$  ( $\theta$  is scan angle).

From the aforementioned analysis, it can be found that the beam scanning leads to the drop of array gain, which is also predicated by the model of AF. As a consequence, Fig. 3.15 shows that the transmission efficiency also drops as with the increase of scan angle. Given a fixed channel transfer matrix, the TR eigenmode technique gives a maximization of PTE and the consequent transmission efficiency  $\eta$ . However, the maximum value of  $\eta$  is limited by the array setup and propagation medium, no matter what complex excitation vector is. The limitation of array beam scanning is discussed using the model of Plane wave impulse response Element Pattern in [23].

### 3.4.3 Arbitrary Array Beamforming in Multipath Environment

In this subsection, an obscured propagation channel is studied to demonstrate the advantages of TR eigenmode technique in the multipath environment. In this numerical example, a PEC (perfect electric conducting) spherical obstacle is inserted (Fig. 3.16) with a diameter equal to the diagonal length of receive aperture. This example has also been formulated and discussed for the application of wireless communication in [6, 8].

The PTE and transmission efficiency are tabulated as Table 3.3 for four different techniques. In this case, if the array synthesis and uniform excitation techniques are

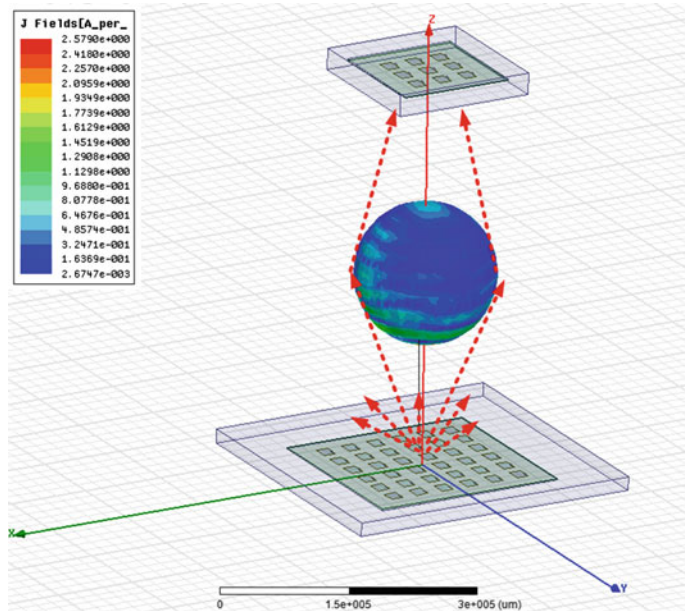


**Fig. 3.16** Wireless power transfer behind PEC spherical obstacle. No LOS propagation path is available

**Table 3.3** Comparison of different optimization techniques for MPT behind PEC spherical obstacle

| Beamforming method | Uniform (%) | Phase conjugate (%) | TR eigenmode (%) | AF synthesis (%) |
|--------------------|-------------|---------------------|------------------|------------------|
| $\eta$             | 2.23        | 5.22                | 5.85             | 2.44             |
| PTE                | 3.12        | 5.96                | 6.39             | 3.33             |

not well-defined and shown for the purpose of comparison. Because the receiver is located in the region shadowed by the obstacle and no direct beam can be formed toward the receiver, the shaping of the main beam toward any direction leads to a large amount of backward scattering. Nevertheless, the advantage of phase conjugate and TR eigenmode stands out in the comparison table. These two techniques give several times greater efficiencies (both  $\eta$  and BCE) over the other two techniques. Given the same norm of input power, the eigenmode method has approximately 10 % higher efficiencies over the phase conjugate method (Table 3.3). It can be expected the improvements in efficiency from TR-Eigenmode method will be even more significant as with the increase of propagation channel due to multipath environment.

In Fig. 3.17a, b, the far field pattern from TR eigenmode and phase conjugate technique is computed with the results from FEM in HFSS. The reason why TR eigenmode technique is better than phase conjugate technique is shown apparently

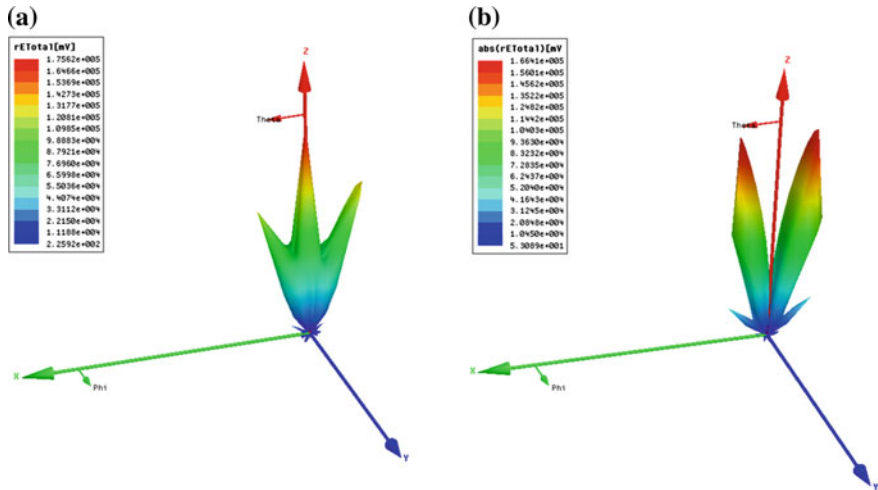


**Fig. 3.17** Array beamforming with the presence of spherical obstacle: **a** radiation pattern from phase conjugate, **b** radiation pattern from time reversal eigenmode. A significant main lobe exists in (a) and results in the propagation loss

in Fig. 3.17. Instead of one main beam in traditional beamforming technique, two beams are generated by the eigenvector excitations. The dual-beam maximizes the diffracted wave toward receiver while it minimizes the reflection by the obstacle. The phase conjugate technique, on the other hand, still maintains a main beam in the direction of LOS, apart from two side beams. Therefore, a portion of power is reflected back due to the existence of main beam. In Fig. 3.16, the induced surface current in MoM-IE method gives an implication of how the two side beam makes use of diffractions.

In short, the TR eigenmode method is the best adaptive array synthesis technique for MPT in the channel with multipath.

### 3.5 Conclusion

In this chapter, the wireless power transmission system is formulated in terms of the circuit theory and the field theory. The clarification of definitions on powers and efficiencies implies the challenges of estimating the transmission efficiency. For this reason, the classic model of transmission efficiency based on antenna parameter is reviewed while another transmission equation is presented in terms of the channel transfer function and mutual impedance matrix. Then, the experimental study of transmission efficiency is carried out in an indoor environment, which is a rich scattering and multipath environment. The quantitative study of transmission efficiency

in experiment shows that the adaptive array beamforming is demanded to improve the MPT in a complex environment.

Furthermore, the exact transmission efficiency is approximated with pseudo transmission equation (PTE) as the coupled power dissipation is sufficiently small if the array spacing is greater than half wavelength. Based on this approximation, an optimal method is derived from time reversal signal processing technique. As the iterative TR process achieves spatial focusing effect through the automatic probing the channel characteristics, this property enlightens us with its application in the wireless power transmission. Then the iterative process is implemented computationally with eigen decomposition process since the channel transfer matrix can be measured and processed. Based on this principle, the time reversal eigenmode technique is proposed and validated with numerical examples. The MoM-Integral Equation was employed to demonstrate the advantages of the proposed techniques due to the prohibitive cost of large phased array. From the simulation results, it has been shown that the proposed scheme gives an optimal transmission efficiency for an array with unequal element pattern and arbitrary position. Moreover, the simulation also shows that this method is applicable for the receivers located in either far field or near field region while conventional array synthesis assumes the far field propagation. Most importantly, we have shown that the TR eigenmode technique can improve the transmission efficiency in the complex environment.

## References

1. Brown, W.C.: Adapting microwave techniques to help solve future energy problems. In: 1973 IEEE G-MTT International Microwave Symposium, pp. 189–191 (1973)
2. Carver, K., Mink, J.: Microstrip antenna technology. *IEEE Trans. Antennas Propag.* **29**(1), 2–24 (1981)
3. Fink, M.: Time reversal of ultrasonic fields. I. Basic principles. *IEEE Trans. Ultraso. Ferroelectr. Freq. Control* **39**(5), 555–566 (1992)
4. Fink, M.: Time-reversal mirrors. *J. Phys. D: Appl. Phys.* **26**(9), 1333 (1993)
5. Gavan, J., Tapuch, S.: Microwave wireless power transmission to high altitude platform systems. *Radio Sci. Bullet.* **344**, 25–42 (2010)
6. Ishimaru, A., Jaruwatanadilok, S., Kuga, Y.: Wireless communications through unknown obscuring media by using time-reversal technique. *IEEE AP Communications* (2005)
7. Ishimaru, A., Zhang, C., Stoneback, M., Kuga, Y.: Time-reversal imaging of objects near rough surfaces based on surface flattening transform. *Waves Random Complex Media* **23**(3), 306–317 (2013)
8. Jaruwatanadilok, S., Ishimaru, A., Kuga, Y.: Optimum wireless communication through unknown obscuring environments using the time-reversal principle: theory and experiments. In: Ultra-Wideband Short-Pulse Electromagnetics, vol. 8, pp. 105–112. Springer (2007)
9. Massa, A., Oliveri, G., Viani, F., Rocca, P.: Array designs for long-distance wireless power transmission: state-of-the-art and innovative solutions. *Proc. IEEE* **101**(6), 1464–1480 (2013)
10. McSpadden, J.O., Mankins, J.C.: Space solar power programs and microwave wireless power transmission technology. *IEEE Microw. Mag.* **3**(4), 46–57 (2002)
11. Nguyen, H.T., Andersen, J.B., Pedersen, G.F.: The potential use of time reversal techniques in multiple element antenna systems. *IEEE Commun. Lett.* **9**(1), 40–42 (2005)

12. Oda, Y., Yamaguchi, T., Komurasaki, K., Kajiwara, K., Takahashi, K., Sakamoto, K.: An experimental study on high power millimeter wave beam transmission for microwave beaming propulsion. In: Microwave Workshop Series on Innovative Wireless Power Transmission: Technologies, Systems, and Applications (IMWS), 2011 IEEE MTT-S International, pp. 181–184. IEEE (2011)
13. Oida, A., Nakashima, H., Miyasaka, J., Ohdoi, K., Matsumoto, H., Shinohara, N.: Development of a new type of electric off-road vehicle powered by microwaves transmitted through air. *J. Terramech.* **44**(5), 329–338 (2007)
14. Oliveri, G., Poli, L., Massa, A.: Maximum efficiency beam synthesis of radiating planar arrays for wireless power transmission. *IEEE Trans. Antennas Propag.* **61**(5), 2490–2499 (2013)
15. Oman, H.: Electric car progress. *IEEE Aerosp. Electr. Syst. Mag.* **17**(6), 30–35 (2002)
16. Orfanidis, S.J.: Electromagnetic waves and antennas. Rutgers University (2002)
17. Pozar, D.: Scattered and absorbed powers in receiving antennas. *IEEE Antennas Propag. Mag.* **46**(1), 144–145 (2004)
18. Prada, C., Manneville, S., Spoliansky, D., Fink, M.: Decomposition of the time reversal operator: detection and selective focusing on two scatterers. *J. Acoust. Soc. Am.* **99**, 2067 (1996)
19. Shams, K.M., Ali, M.: Wireless power transmission to a buried sensor in concrete. *IEEE Sens. J.* **7**(12), 1573–1577 (2007)
20. Shinohara, N.: Wireless Power Transfer via Radiowaves. Wiley (2014)
21. Vieira, J., Malkowsky, S., Nieman, K., Miers, Z., Kundargi, N., Liu, L., Wong, I., Owall, V., Edfors, O., Tufvesson, F.: A flexible 100-antenna testbed for massive mimo. In: Globecom Workshops (GC Wkshps), 2014, pp. 287–293. IEEE (2014)
22. Zhang, C., Ishimaru, A., Kuga, Y.: Time-reversal and music imaging of objects near rough surface based on surface flattening transform. In: Radio Science Meeting (USNC-URSI NRSM), 2013 US National Committee of URSI National. URSI (2013)
23. Zhao, D., Jin, Y., Wang, B.Z., Zang, R.: Time reversal based broadband synthesis method for arbitrarily structured beam-steering arrays. *IEEE Trans. Antennas Propag.* **60**(1), 164–173 (2012)
24. Zhou, S., Giannakis, G.B.: Optimal transmitter eigen-beamforming and space-time block coding based on channel mean feedback. *IEEE Trans. Signal Process.* **50**(10), 2599–2613 (2002)

# **Chapter 4**

## **Far-Field Wireless Power Transfer for IoT Sensors**

**Hubregt J. Visser, Hans W. Pflug and Shady Keyrouz**

**Abstract** For employing large IoT wireless sensor networks, powering the sensors by cabling or primary batteries is not feasible. Using radiated fields seems to be a possible alternative. However, the expected power densities from ambient radio frequency (RF) sources (Global System for Mobile communication (GSM), digital television (DTV), WiFi) are too small for a practical use. Using dedicated transmitters in a wireless power transfer setup, using the (power-restricted) license-free ISM frequency bands will increase the levels by an order of magnitude. Then through a careful co-design of the rectifier, receive antenna and the power management, the powering of low-power, duty-cycled wireless IoT sensors becomes feasible. The models employed for the rectifier are outlined. Then working from the core (the rectifier) toward both extremes (the antenna and the power management circuit), the design procedure for a rectifying antenna or rectenna is outlined. Future perspectives for increasing the rectenna's efficiency and the amount of power being received are outlined, using transient arrays and multisine signals.

---

H.J. Visser (✉)

Holst Centre/imec and Eindhoven University of Technology,  
Eindhoven, The Netherlands  
e-mail: huib.visser@imec-nl.nl

H.W. Pflug

Holst Centre/imec, P.O. Box. 8550, 5605 KN Eindhoven, The Netherlands  
e-mail: hans.pflug@imec-nl.nl

S. Keyrouz

Eindhoven University of Technology, Building Flux, P.O. Box. 513,  
5600 MB Eindhoven, The Netherlands  
e-mail: s.keyrouz@tue.nl

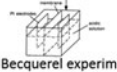
## 4.1 Introduction

In the “Internet of Things” (IoT) [1], devices and vehicles are connected using electronic sensors and the internet. The IoT opens up the possibility for creating so-called Smart Buildings. Smart Buildings are the buildings able to react to the environment and/or human activities in an adaptive way.

In its most basic form, a large network of sensors would monitor the presence of people and the lighting and heating conditions throughout a building. The gathered information can then be used to fine-tune the buildings heating and lighting, e.g., switching off heating and lighting in areas where nobody is present. When properly employed, this will result in a huge reduction in energy consumption. At present, 40% of the energy consumed is used for heating, ventilation, and air conditioning (HVAC), and 30% is used for lighting [2].

However, employing a large network of miniature wireless sensors poses a powering challenge. The use of cabling excludes retrofit solutions. But even for new buildings, the cost of cabling is too high. Cabling an average office unit or a four bed house is estimated at €7,000–11,000 (\$9,000–15,000) [3]. Although using batteries may severely reduce these cabling costs, the maintenance issues associated with using primary batteries in a large wireless sensor network—i.e., locating batteries to be replaced, replacing these batteries and disposing of the old ones—will not be tolerated by the market.

An alternative way of powering may be looked for in the energy harvesting technology. Energy harvesting is the process by which energy is derived from (unintentional) external sources. Known energy harvesting sources are movement, piezoelectricity, temperature gradients, and light, see Fig. 4.1.

|                         |   |
|-------------------------|---|
| <b>Movement</b>         |  →  →  |
| <b>Piezoelectricity</b> |  →  →  |
| <b>Temperature</b>      |  →  →  |
| <b>Light</b>            |  →  →  |

**Fig. 4.1** Sources and history of energy harvesting

The potential energy harvesting sources as shown in Fig. 4.1 are not the most promising ones for Smart Building applications. Neither movement and vibration nor large temperature gradients will be present. Light will not be always and everywhere available. Then, what remains is the use of radio waves for wireless power transfer (WPT).

As will be discussed in more detail in the remainder, the power densities of ambient RF signals will, in general, be too low for practical applications. Therefore, dedicated RF sources need to be brought into the system. This will change the wireless energy harvesting concept into the special case of wireless power transfer (WPT).<sup>1</sup>

In WPT we distinguish two techniques: near-contact WPT and far-field WPT.

#### 4.1.1 Near-Contact WPT

Near-contact WPT is mostly employed in inductive WPT systems, wherein a transmitting and a receiving coil are brought in each others vicinity. The coils are lined up coaxially so that the receiving coil encompasses most of the magnetic flux generated by the transmit coil. When the axial distance between both coils is less than the smallest coil diameter, and the transmit and receive coil are well-aligned, a power transfer efficiency well above 90 % may be achieved [4]. The introduction of resonant coupling, in which the coils are made resonant through the use of capacitors [7], allows the transmitter and receiver coils to be separated a few times the smallest coil diameter. Also the coaxial lining up requirements can be relaxed a bit.

#### 4.1.2 Far-Field WPT

In far-field WPT, use is made of radiating fields [5, 6]. A transmit antenna excites propagating electromagnetic waves in free space. At a substantial distance (i.e., in the far-field region of the transmit antenna), a receive antenna intercepts a part of the transmitted radiowaves and a connected rectifier converts this part into usable DC power. The combination of rectifier and antenna is known as *rectenna*, a contraction of *rectifier* and *antenna*.

### 4.2 Far-Field WPT Basics

The core of any far-field WPT system is the rectenna, see Fig. 4.2. Before discussing the details of the rectenna, we need to look at the system as a whole. We need to establish the limits on what is physically possible concerning the obtainable DC power levels.

---

<sup>1</sup>Strictly speaking, the correct term should be Wireless *Energy* Transfer. However, since WPT is by now a generally accepted term, we will stick to the use of WPT.

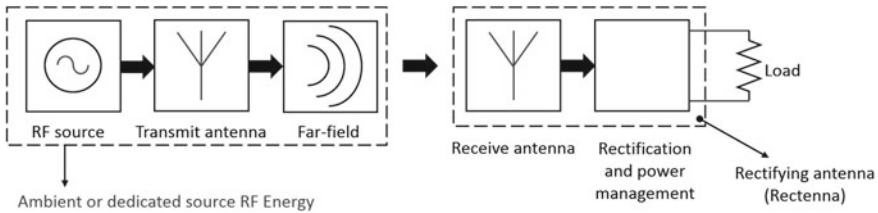


**Fig. 4.2** Far-field wireless power transfer. An ambient or dedicated (intentional) source is connected to a transmit antenna that radiates in free space. The antenna of the rectenna intercepts a part of the radiated signal and the connected rectifier converts it into usable DC power

### 4.2.1 Power Density

If the power accepted by the transmit antenna from the source is  $P_T$  and if the antenna would be a lossless, uniform radiator, the power density  $S$  at a distance  $r$  from the transmit antenna would follow from the spherical spreading of the radiated power:

$$S = \frac{P_T}{4\pi r^2}. \quad (4.1)$$

Uniform radiators do not exist. A real-life antenna will radiate more than a uniform radiator in certain directions and less in other directions. The amount an antenna can radiate more than a (hypothetical) uniform radiator is expressed in the gain  $G$  of the antenna. If we assume that the transmit antenna is positioned in such a way that the maximum radiation is in the direction of the rectenna (the receiver), the power density becomes

$$S = \frac{P_T G_T}{4\pi r^2}, \quad (4.2)$$

where  $G_T$  is the gain of the transmit antenna. With this equation we can find limits on the power density at a distance  $r$  for the situation where a dedicated source is being used (WPT) and compare this situation with the situation where we take energy from unintentional sources (the ambient).

### 4.2.2 Wireless Power Transfer

The product of  $P_T$  and  $G_T$  is known as the *Effective Isotropic Radiated Power* (EIRP), which is subject to legal restrictions in the license-free frequency bands for industry, science, and medicine (ISM) [8].<sup>2</sup> In Fig. 4.3, the power density as a function of distance from the source is shown for two EIRP limits.

<sup>2</sup>That means that using a highly directive transmit antenna (large  $G_T$ ) needs to be compensated by lowering the power injected into the antenna (decreasing  $P_T$ ).

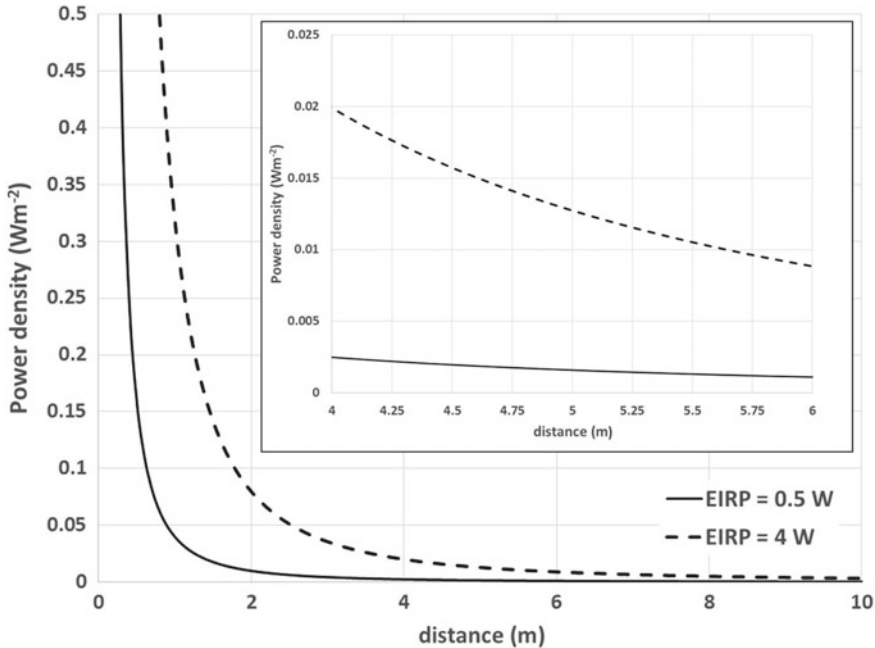


**Fig. 4.3** Power density (in  $\text{Wm}^{-2}$ ) as a function of distance from the source (in m) for an Effective Isotropic Radiated Power level of 0.5 W (solid line) and 4 W (dashed line). Inset Power density for the range 4–6 m

The figure clearly shows the rapid decay of the power density with distance from the source (inversely proportional to the distance squared). At distances around 5 m from the source, we may expect to be able to realize RF power densities in the order of  $0.01 \text{ Wm}^{-2}$  ( $1 \mu\text{W cm}^{-2}$ ). It is interesting to compare this value with the value we may expect when we harvest RF energy from the ambient.

#### 4.2.3 RF Harvesting from the Ambient

When we want to harvest RF energy from the ambient, i.e., from non-intentional sources, we first need to identify possible radiating sources. We will restrict ourselves to sources radiating at ultra high frequencies (UHF, 300 MHz–1 GHz [9]) and microwave frequencies (300 MHz–300 GHz [10]). This restriction will keep the dimensions of the receive antenna within bounds that are practical for miniature applications.

As shown in [11], the most powerful RF sources available in the urban environment within these frequency ranges can be found for digital television (DTV, 470–610 MHz), mobile telephony GSM900 (925–960 MHz), mobile telephony GSM1800

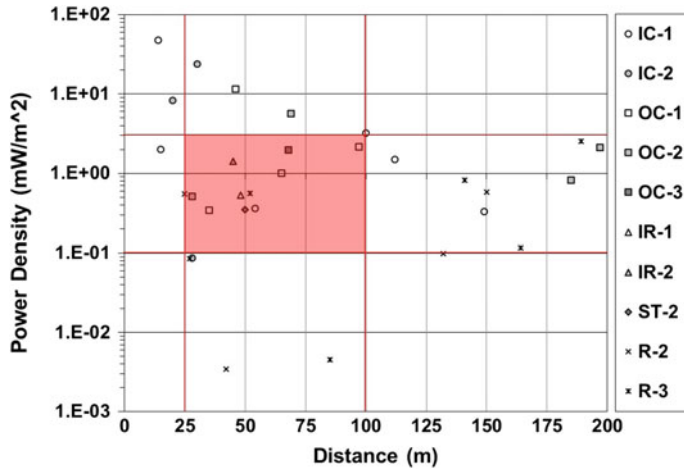


**Fig. 4.4** Measured summed power density levels of GSM900 base stations as a function of the distance to the base station. Data taken from [13]. IC = inner city, OC = outer country, IR = industrial area, ST = small town, R = rural or countryside area. 1 = outdoors on roof, terrace or balcony, 2 = indoors, close to windows, 1.5 m or less, 3 = indoors not close to windows

(1805–1880 MHz), 3G (2110–2170 MHz), and WiFi (2400–2500 MHz). The frequencies within the parentheses are for the base station transmit situations that generate the highest power density levels. Also shown in [11] is that GSM900 is providing the highest power density in a survey conducted in the vicinity of London underground stations.

Expanding these GSM900 findings to a broader range of areas, the data gathered within COST<sup>3</sup> action 244 bis “Biomedical Effects of Electromagnetic Fields” is being used [12]. Figure 4.4 shows summed GSM900 peak power density levels as a function of distance to the nearest base station for different situations (indoor, outdoor, country side, inner city, etc.)

In between 25 and 100 m from a GSM900 base station, we may expect, indoors everywhere or outdoors on an elevated level, a power density level between 0.001 and  $0.1 \mu\text{W cm}^{-2}$  [12]. The Figure reveals that the summed power density (integrating over the downlink frequencies) results in power density levels between 0.01 and  $0.3 \mu\text{W cm}^{-2}$  ( $0.1\text{--}3 \text{ mW m}^{-2}$ ), values about an order of magnitude lower than what may be obtained by applying WPT in the ISM frequency bands with a dedicated source within 5 m distance.

Understanding now the power density levels to expect, we can start looking at the rectenna in more detail. We do so by first looking at the core of the rectenna, i.e., the rectifier.

<sup>3</sup>COST = Cooperation in Science and Technology.

### 4.3 Rectifier

Since we are dealing with low-power density levels, it is of paramount importance that the power intercepted by the receive antenna is delivered completely to the rectifier. In other words, we need a perfect, or at least very good, impedance match between the rectifier and the antenna. To accomplish this, we need to be able to determine the—in general complex—input impedance of the rectifier circuit.

The simplest rectifying circuit is a half-wave rectifier, consisting of one discrete diode. Due to the frequency range chosen, we will use a Schottky diode. A Schottky diode is known for its fast switching capability. Figure 4.5 shows the rectifying circuit and the equivalent circuit for the packaged diode in the circuit.

In the circuits, the choke inductance parallel over the source with generator voltage  $V_g$  and internal resistance  $R_g$  is positioned there to ensure a DC current path in the circuit.

The current  $i_d$  through the diode  $d$  is described by the Shockley equation [14]

$$i_d = I_s \left( e^{\frac{q}{nkT} v_d} - 1 \right), \quad (4.3)$$

wherein  $I_s$  is the saturation current,  $q$  is the electron charge amplitude ( $1.60217662 \times 10^{-19}$  C),  $k$  is the Boltzmann constant ( $1.38064852 \times 10^{-23}$  m $^2$  kg s $^{-2}$  K $^{-1}$ ),  $T$  is the temperature in Kelvin,  $n$  is the ideality factor of the diode, and  $v_d$  is the voltage over the diode. The values for  $I_s$  and  $n$  can be found in the datasheet of the specific diode used.

For the equivalent circuit, shown on the right of Fig. 4.5, the diode is expanded with a junction capacitance  $C_j$ , which is related to  $v_d$  through [15]

$$C_j(v_d) = \frac{C_{j0}}{\sqrt{1 - \frac{v_d}{\Phi}}}. \quad (4.4)$$

In the above equation,  $C_{j0}$  is the zero-bias differential barrier capacitance and  $\Phi$  is the barrier potential of the diode. Values for both parameters can be found in the datasheet of the diode used.  $R_s$  represents the losses in the diode's substrate and can also be found in the diode's datasheet.  $L_p$  and  $C_p$  are the packaging parasitic

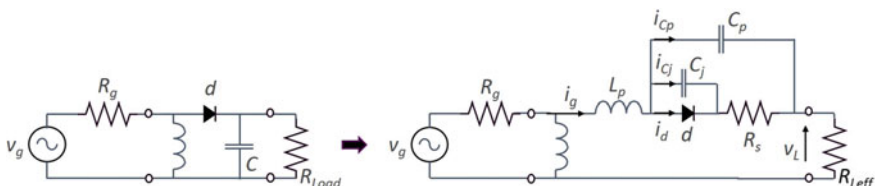


**Fig. 4.5** Half-wave rectifier with a single (Schottky) diode. *Left*: Basic circuit. *Right*: Same circuit with an equivalent circuit for the packaged diode

inductance and capacitance, respectively, the values of which can also be found in the datasheet.

In the equivalent circuit at the right in Fig. 4.5, we have left out the load capacitor  $C$ . We assume a large value for this capacitor and therefore a constant output DC voltage at steady state. The capacitor then behaves as an open circuit and may be left out in the steady state circuit analysis.

The load resistance  $R_{Load}$  has been replaced by an equivalent load resistance  $R_{L_{eff}}$ . The value of this equivalent load resistance is obtained through a harmonic current analysis. This analysis will be discussed later. First, we will discuss the analysis of the equivalent circuit.

### 4.3.1 Equivalent Circuit Analysis

Applying the Kirchhoff laws to the equivalent circuit in Fig. 4.5 leads to

$$v_g = |v_g| \cos(\omega t), \quad (4.5)$$

$$v_g = R_g i_g + L_p \frac{di_g}{dt} + V_{C_p} + V_L, \quad (4.6)$$

$$v_{C_p} = v_d + v_{R_s}, \quad (4.7)$$

$$v_{R_s} = R_s i_{R_s} = R_s (i_{C_j} + i_d), \quad (4.8)$$

$$i_{C_j} = C_j \frac{dv_d}{dt}, \quad (4.9)$$

$$i_d = I_s \left( e^{\frac{q}{nkT} v_d} - 1 \right), \quad (4.10)$$

$$i_g = i_d + i_{C_j} + i_{C_p}, \quad (4.11)$$

$$i_{C_p} = C_p \frac{dv_{C_p}}{dt}, \quad (4.12)$$

$$v_L = R_{L_{eff}} i_g. \quad (4.13)$$

From these equations, we obtain the following set of of coupled first-order ordinary differential equations:

$$v_g = (R_g + R_{L_{eff}}) i_g + L_p \frac{di_g}{dt} + v_d + R_s C_j \frac{dv_d}{dt} + R_s I_s \left( e^{\frac{q}{nkT} v_d} - 1 \right), \quad (4.14)$$

$$i_g = I_s \left( e^{\frac{q}{nkT} v_d} - 1 \right) + C_j \frac{dv_d}{dt} + C_p \frac{dv_g}{dt} - C_p (R_g + R_{L_{eff}}) i_x - C_p L_p \frac{di_x}{dt}, \quad (4.15)$$

where

$$\frac{di_g}{dt} = i_x. \quad (4.16)$$

This last equation has been introduced to avoid the occurrence of second-order derivatives. Now the remaining set of coupled first-order ordinary differential equations can be cast in a form wherein every unknown derivative is expressed in terms of known parameters:

$$\frac{dv_d}{dt} = \frac{1}{R_s C_j} \left[ v_g - (R_g + R_{L\text{eff}}) i_g - L_p i_x - v_d - R_s I_s \left( e^{\frac{q}{nkT} v_d} - 1 \right) \right], \quad (4.17)$$

$$\frac{di_x}{dt} = \frac{1}{L_p C_p} \left[ I_s \left( e^{\frac{q}{nkT} v_d} - 1 \right) + C_j \frac{dv_d}{dt} + C_p \frac{dv_g}{dt} - C_p (R_g + R_{L\text{eff}}) i_x - i_g \right], \quad (4.18)$$

$$\frac{di_g}{dt} = i_x. \quad (4.19)$$

Solving this set of equations gives us the voltage over the diode  $v_d$  and substituting that value in Eq. (4.10) gives us the current  $i_d$ . Then, by applying a fast Fourier transform (FFT) we will find the diode impedance for each harmonic of the working frequency:

$$Z_{d_f} = \frac{V_{d_f}}{I_{d_f}}. \quad (4.20)$$

In the past, we have solved this set of ordinary differential equations (ODEs) using a time-stepping algorithm [16] for a load resistance equal to zero [16]. This choice prevented the set of ODEs to become ‘stiff’ [17], but restricted the application of the rectenna to low-impedance loads.

To overcome this restriction and allow the use of non-zero loads, ODE solvers for stiff equations are being employed [18].

Having a method now to solve for the rectifier input impedance having a non-zero load, we need to find an expression for the equivalent load resistor  $R_{L\text{eff}}$  that differs from the actual load resistance  $R_{Load}$ .

### 4.3.2 Harmonic Current Analysis

To get an expression for  $R_{L\text{eff}}$ , we will start by analyzing the voltages and currents through a diode, using a commercially available harmonic balance simulator. We will use an Avago HSMS2850 Schottky diode [19] and apply a sinusoidal signal at 900MHz coming from a source with an internal resistance of  $R_g = 50 \Omega$ . The maximum available power  $P_{in}$  equals  $-10 \text{ dBm}$  ( $0.1 \text{ mW}$ ). The generator voltage is related to the maximum available power through

$$P_{in} = \frac{|v_g|^2}{8R_g}. \quad (4.21)$$

**Fig. 4.6** Generator voltage, DC output voltage, and diode current as a function of time for an Avago HSMS2850 Schottky diode excited by a 900 MHz sinusoidal signal.  $P_{in} = -10 \text{ dBm}$ ,  $R_g = 50 \Omega$ ,  $R_{Load} = 10 \text{k}\Omega$ ,  $C_L = 10 \mu\text{F}$

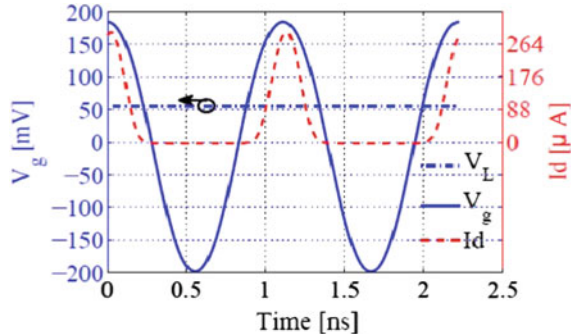
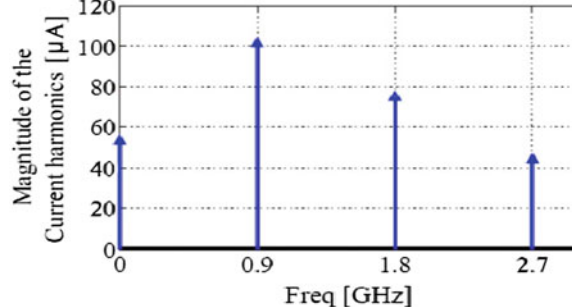


**Fig. 4.7** Current harmonics for an Avago HSMS2850 Schottky diode excited by a 900 MHz sinusoidal signal.  $P_{in} = -10 \text{ dBm}$ ,  $R_g = 50 \Omega$ ,  $R_{Load} = 10 \text{k}\Omega$ ,  $C_L = 10 \mu\text{F}$



The load resistor  $R_{Load}$  equals  $10 \text{k}\Omega$  and the load capacitor is  $10 \mu\text{F}$ .

The generator voltage as a function of time is shown as the solid blue curve in Fig. 4.6. In the same Figure, the constant DC output voltage  $v_L$  is shown as a blue dashed line. The current through the diode,  $i_d$  is shown as a dashed red curve.

By taking the Fourier transform of the current through the diode, the amplitudes of the diode's current harmonics are found. The first four harmonics are displayed in Fig. 4.7.

The most important harmonics are  $i_0$  at zero frequency and the fundamental one  $i_g$  at 900 MHz.

The current through the diode  $i_d(t)$ , i.e., the red dashed curve in Fig. 4.6, may be expressed as the following Fourier series [20]:

$$i_d(t) = a_0 + \sum_{n=1}^{\infty} a_n \cos(n\omega t) + \sum_{n=1}^{\infty} b_n \sin(n\omega t). \quad (4.22)$$

$a_0$ , the DC coefficient of the Fourier series is the average of the diode current  $i_d(t)$ , where the average is most conveniently taken over one period  $T = \frac{1}{f_0}$  with  $f_0$  being the operational frequency (in the shown example 900 MHz).

$$a_0 = i_0 = \frac{1}{T} \int_0^T i_d(t) dt. \quad (4.23)$$

The Fourier coefficients for the fundamental frequency  $f_0 = \frac{\omega}{2\pi}$  are:

$$a_1 = \frac{2}{T} \int_0^T i_d(t) \cos(\omega t) dt, \quad (4.24)$$

$$b_1 = \frac{2}{T} \int_0^T i_d(t) \sin(\omega t) dt. \quad (4.25)$$

Assuming that the current through the diode  $i_d(t)$  during conduction is a positive cycle of a truncated cosine waveform, see also Fig. 4.6, it may be shown [21, 22] that the amplitude of the current at the fundamental frequency  $i_g$  is approximately twice the amplitude of the DC current  $i_0$

$$i_g \approx 2i_0, \quad (4.26)$$

so that

$$v_L = R_{Load}i_0 = R_{Leff}i_g, \quad (4.27)$$

and

$$R_{Leff} = \frac{R_{Load}}{2}. \quad (4.28)$$

This value for the effective load resistor is being substituted in the ODEs of the previous section. Results of the analysis, compared to measurements, will be shown together with results for cascaded rectifiers that will be discussed next.

## 4.4 Cascaded Rectifiers

In general, the DC output voltage of a single Schottky diode will not be sufficient to drive any application, see also Fig. 4.6. Instead of immediately trying to find our refuge in applying a DC-to-DC boost converter to increase the output voltage, we might consider to cascade several diodes. This should not be seen as a means to increase the DC voltage up to a level that applications can be driven directly. It could provide a means of lowering the required dynamic range of the DC-to-DC boost converter, thus increasing the latter's power conversion efficiency.

A much used cascaded (Schottky) diode rectifier circuit is based on the Dickson's charge pump circuit [23], see Fig. 4.8. The cascaded rectifier consists of  $n$  identical Schottky diodes.

For determining the input impedance of the cascaded rectifier, we consider the capacitors as short circuits at  $f_0$ . All diodes are then connected in an antiparallel circuit. The input impedance is then equal to the input impedance of a single diode divided by the number of diodes.

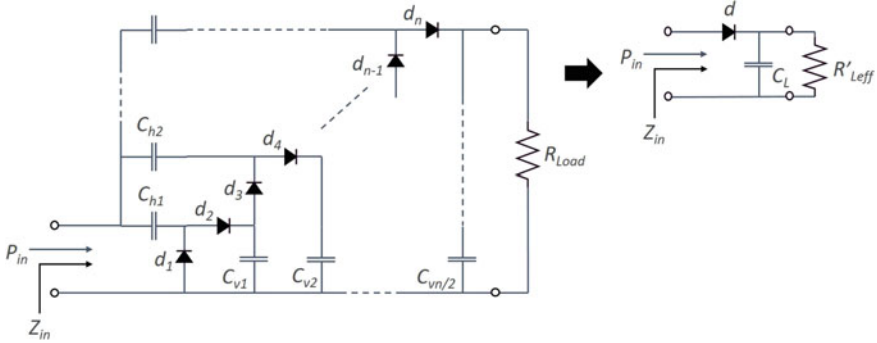


**Fig. 4.8** Multistage, cascaded rectifier based on the Dickson's charge pump circuit and the equivalent circuit

$$Z_{in} = \frac{Z_d}{n}. \quad (4.29)$$

This means that we can replace the cascaded rectifier circuit with an equivalent circuit as shown in Fig. 4.8.

To determine the equivalent load resistor  $R'_{Load}$ , we start by assuming that the cascaded diode network is lossless. Then we assume that the DC output voltage  $v_L$  consists of  $n$  identical contributions  $v_1$  from all the diodes:

$$v_L = nv_1. \quad (4.30)$$

The DC output power may also be regarded as being constructed from  $n$  added contributions

$$P_{out} = \frac{v_L^2}{R_{Load}} = n \frac{v_1^2}{R'_{Load}}. \quad (4.31)$$

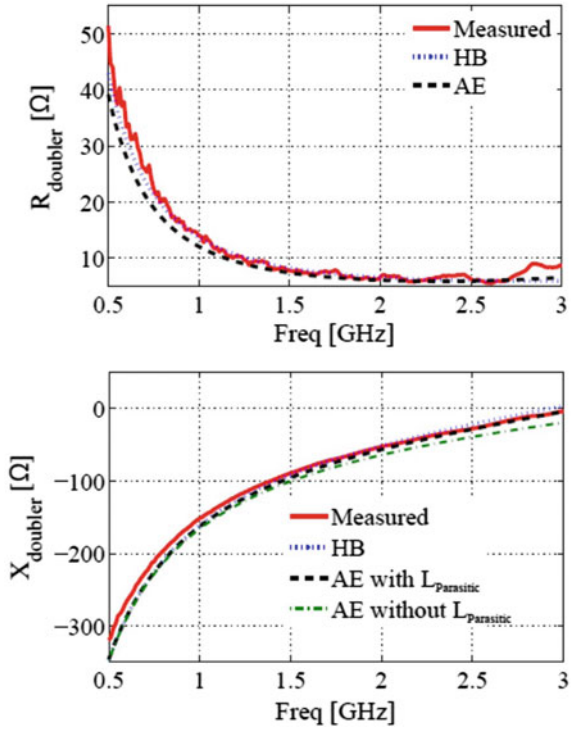
Substitution of Eq. (4.30) in Eq. (4.31), followed using Eq. (4.28) leads to

$$R'_{Load} = \frac{R_{Load}}{n} = \frac{R_{Load}}{2n}. \quad (4.32)$$

So the input impedance of a cascade of  $n$  half-wave rectifiers is analyzed through using the equivalent circuit shown in Fig. 4.8, where the input impedance is calculated according to Eq. (4.29) where for the single diode an equivalent load resistance as given in Eq. (4.32) is used.

As an example, Fig. 4.9 shows the calculated and measured real and imaginary part of the input impedance for an available power level of  $P_{in} = -20$  dBm (0.01 mW) of a voltage doubler ( $n = 2$ ) configuration based on the Avago HSMS2850 Schottky diode as a function of frequency.

**Fig. 4.9** Simulated and measured real part (top) and imaginary part (bottom) of the input impedance voltage doubling ( $n = 2$ ) rectifier, loaded with  $R_{Load} = 5\text{ k}\Omega$  and excited with  $P_{in} = -20\text{ dBm}$  at  $f_0 = 900\text{ MHz}$



In the Figure, HB stands for harmonic balance, a simulation performed with a commercially available circuit simulation software and AE stands for analytical equations, i.e., the solving of the ODE's as discussed here.

For determining the output voltage, we refer to [24] from which combining Eqs. (4.2) and (4.6) leads to:

$$\frac{q}{nkT} v_L - N \ln \left[ \frac{I_0 \left( \frac{q}{nkT} v_g \right)}{1 + \frac{1}{2\pi} \int_{-\pi}^{\pi} \left( e^{\frac{q}{nkT} [v_g \cos \theta - v_L]} - 1 \right) d\theta} \right] = 0, \quad (4.33)$$

from which  $v_L$  can be found through, for example, a bisection method.

In the above equation,  $n$  is the diode ideality factor and  $N$  is the number of cascaded diodes.  $I_0$  is a modified Bessel function of the first kind and order zero.

## 4.5 Receive Antenna

With the rectifier input impedance known, we can now choose or design the receive antenna and impedance match the antenna to the rectifier. Concerning the receive antenna, we are challenged with different choices.

### **4.5.1 Antenna Input Impedance**

The use of a ‘standard’  $50 \Omega$  antenna has the benefit that it can be employed for different rectifiers, input power levels, and load conditions. A general impedance matching network can be applied. Only the component values need to change for different applications. The drawback is that the impedance matching network necessary for matching this antenna to the rectifier occupies space and can become a size-limiting factor. Using an antenna that is directly (complex conjugately) matched to the antenna requires special antenna design skills.

### **4.5.2 Antenna Integration Level**

Directly related to the input impedance of the antenna is the integration level. Will we use a separate antenna—to be connected to the rectifier through a (coaxial) transmission line—or will we use a printed circuit board (PCB) trace antenna or will we use a ceramic chip antenna?

The benefits of using a separate antenna is that it is easy to realize or select a high gain and high radiation efficiency and that antennas can be selected from a vendor’s catalog. The drawback is that the size of the whole rectenna will become large and this may not comply with a wish for employing small-sized wireless autonomous IoT sensors.

The benefits of using a PCB trace antenna is that it results in a thin antenna that is easy to produce and connects directly to the rectenna electronics. The drawback may be that additional PCB area is needed—added to the area needed for the electronics—to house the antenna. Furthermore, to prevent a substantial decrease in antenna radiation efficiency, it may be necessary to use a low-loss, microwave-specific PCB material. This will increase the costs of the rectenna.

The use of ceramic chip antennas at first glance seems to overcome the above-mentioned problems. These antennas are physically very small due to combining a helix, patch, or meandered mono- or dipole antenna with a high permittivity, low-loss ceramic material. However, the radiation efficiencies are typically in the range of 10–50 % which is rather low for rectenna use where we have to deal with low input power levels and cannot compensate for these low efficiency values. The input impedance, even though specified as being  $50 \Omega$  in general needs additional matching [25]. Then, special care must be taken with respect to the manufacturer’s specifications regarding footprint, ground areas, mounting of the chip antenna and guaranteeing the keep out area around the antenna. All in all, ceramic chip antennas may be small by themselves but may occupy a substantial PCB area. The antenna performance in general is mediocre. Therefore, we will not consider this antenna type for rectenna applications.

### 4.5.3 Antenna Shielding

Especially for miniaturized antennas to be integrated with the rectenna, shielding may become an important issue. With shielding we mean the characteristic that the antenna is not being influenced by the carrier, it is placed upon or by the electronics of the device being powered by the rectenna. In practice, this means that the antenna needs to be realized on a conducting ground plane. This ground plane will act as the shielding device. However, standard shielded antennas like, e.g., the microstrip patch antenna cannot easily be miniaturized using standard PCB or PCB-like materials. A dedicated design for a miniature, shielded antenna is required.

### 4.5.4 Miniaturized Complex Conjugately Matched Antenna

From the above we may conclude that ideally, the antenna of a rectenna for a small-sized wireless autonomous IoT sensor should be physically small, directly matched to the rectifier and be shielded from the electronics of the device it is powering or the material it is positioned upon. On top of that, the manufacturing costs should be close to nothing.

Meeting nearly all these requirements is accomplished using the printed loop-like antenna [26] as shown in Fig. 4.10.

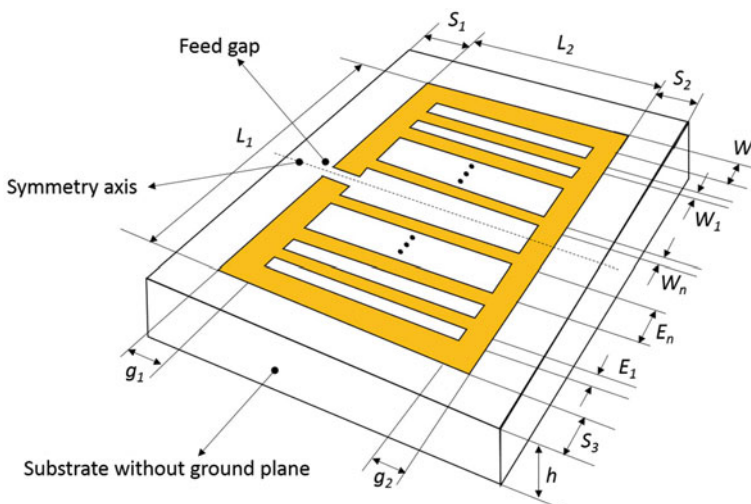


**Fig. 4.10** Printed loop-like antenna and definition of the dimensions. The loop is filled with two times  $n$  short-circuiting strips as shown

The antenna is specifically designed for being used with a voltage doubling rectifier of the type AVAGO HSMS-2852. The input impedance of this rectifier  $Z_{rect,in}$  at a frequency of 868 MHz for a load resistor of  $5\text{ k}\Omega$  and an available input power level of  $-20\text{ dBm}$  can be read from Fig. 4.9 as being approximately  $Z_{rect,in} \approx (12 - j175)\Omega$ . For an input power level of  $-10\text{ dBm}$  and a load resistance of  $10\text{ k}\Omega$ , the input impedance is  $Z_{rect,in} = (7.1 - j240)\Omega$  [26]. For both situations we see that the imaginary part of the rectifier's input impedance is capacitive. So, if we want to connect an antenna directly, without having to employ an impedance matching network, the antenna needs to be inductive. Hence, we choose for a printed loop antenna. Next, we see that the real part of the input impedance is much lower than  $50\Omega$ . A small resistive part of an antenna's input impedance may be realized by employing an antenna that is much smaller than the wavelength used [27].

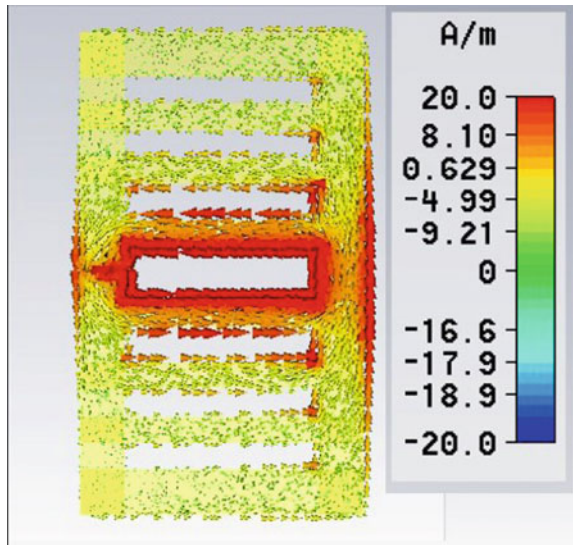
So, for an antenna that is complex conjugately matched to the rectifier at 868 MHz for an available RF input power to the rectifier of  $-10\text{ dBm}$ , and the rectifier being loaded with  $10\text{ k}\Omega$ ,<sup>4</sup> we need an electrically (and physically) small loop antenna. The additional short-circuiting arms shown in Fig. 4.10 are introduced to lead the current through different paths, and thus provide a means of tuning the antenna's input impedance to the desired value.

Figure 4.11 shows the simulated [28] peak surface current density over the antenna surface at a frequency of 868 MHz and for dimensions as stated in the caption of the Figure. The input impedance of the antenna is  $Z_{ant,in} = (7 + j240)\Omega$ .

This antenna, directly connected to a voltage doubling rectifying circuit has led to the smallest, most efficient UHF rectenna [26]. One drawback of this antenna

**Fig. 4.11** Simulated peak surface current density at 868 MHz for the antenna shown in Fig. 4.10 for the following dimensions.

$n = 3$ ,  $h = 1.6\text{ mm}$ ,  $\epsilon_r = 2.2$ ,  
 $W_1 = W_2 = W_3 = E_1 =$   
 $E_2 = 3\text{ mm}$ ,  $E_3 = 4\text{ mm}$ ,  
 $W = g_1 = g_2 = 5\text{ mm}$ ,  
 $L_2 = 32\text{ mm}$ ,  $L_1 = 54\text{ mm}$ ,  
 $S_1 = 10\text{ mm}$ ,  $S_2 = 7\text{ mm}$ ,  
 $S_3 = 8\text{ mm}$



<sup>4</sup>The reason that we choose for a  $10\text{ k}\Omega$  load is that later we will connect the rectifier to a power management IC with voltage boost functionality. The input impedance of this IC is close to  $10\text{ k}\Omega$ .

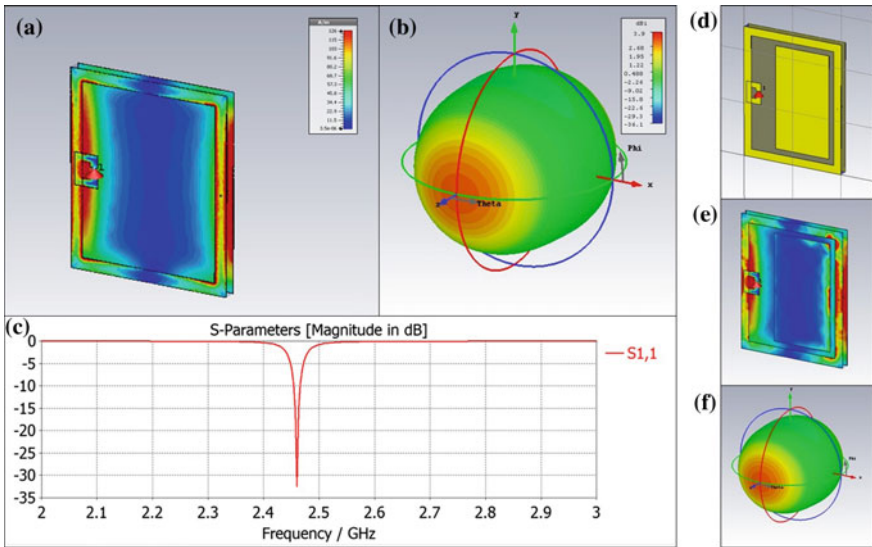


**Fig. 4.12** Miniature shielded antenna, ground plane radiation. **a** Simulated peak current density at 2.45 GHz. **b** Simulated radiation pattern at 2.45 GHz. **c** Simulated reflection coefficient as a function of frequency. **d** Antenna with electronics for rectenna. **e** Simulated peak current density for antenna with electronics at 2.45 GHz. **f** Simulated radiation pattern for antenna with electronics at 2.45 GHz

however is that it needs to be positioned in free space. Positioning it flush to a (metal) carrier will deteriorate the radiation characteristics. Other means of antenna design are needed to create a miniature shielded antenna.

#### 4.5.5 Miniature Shielded Antenna

One possible way to design a shielded miniature antenna is to not start with the antenna, but with the electronics and then let the PCB ground plane—after some fine tuning—resonate at the desired frequency. The theory of characteristic modes (TCM) will be of great benefit in the design process [29]. The addition of a bezel or printed loop to tune the antenna characteristics might help in miniaturizing the antenna [30].

Figure 4.12 shows a miniature 2.45 GHz  $50\ \Omega$  antenna meant for a rectenna and the simulated current densities, radiation patterns and reflection coefficient as a function of frequency. The antenna measures 2 cm by 2.5 cm by 1.6 mm.

The loop on top of the multilayer PCB is connected through a via with the ground plane on the bottom of the PCB. Figure 4.12a shows the peak current density at 2.45 GHz. The excitation (balanced in the small loop on the left) excites a vertically polarized dipole mode in the ground plane and large loop. The radiation pattern is

shown in Fig. 4.12b. Figure 4.12c shows the reflection coefficient—relative to  $50\Omega$ —as a function of frequency. The electronic circuitry of the rectenna is meant to be placed on the inside of the loop on the top of the PCB. To account for the PCB layout for this electronic circuit, a metal area is added, as shown in Fig. 4.12d. Figure 4.12e, f show the peak current density and the radiation pattern at 2.45 GHz for this structure.

The design of the antenna, especially through the connected loop on the top of the PCB, ensures that – when the PCB is placed on a metal carrier – the current density remains within the bounds of the rectenna’s ground plane. Therefore, the antenna will hardly detune when placed on a (metal) carrier.

## 4.6 Rectenna

For a practical rectenna, we need—next to a receive antenna and a rectifying circuit—some form of power management circuitry. This power management circuitry takes the varying DC output voltage of the rectifier, up-converts it to store the energy in a rechargeable battery or a capacitor and uses a buck converter to supply the loading circuit with a lower and constant output voltage.

### 4.6.1 Power Management

The power management needed for the rectenna may be based on discrete solutions originally developed for photovoltaic (PV) cells [31] or commercially available integrated solutions may be applied. Although PV cells are basically current sources<sup>5</sup> and rectennas behave more like voltage sources, for the low-power input levels we are dealing with the difference is not really of importance.

For our low-power rectennas, we have chosen to use the Texas Instruments TI BQ25570 Power Management IC [32]. The IC incorporates a DC-to-DC boost converter that requires microwatts of power to begin operating. The boost converter can start from an input voltage as low as 330 mV, and once started can continue with an input voltage going down to 100 mV. The boost converter stores energy in a rechargeable battery or a capacitor. The IC also incorporates a highly efficient, nano-power buck converter for providing a constant voltage to the application that needs to be powered. The IC further comprises a programmable Maximum Power Point Tracking (MPPT) sampling network to optimize the transfer of power into the device.

---

<sup>5</sup>Power management circuits therefore need an input voltage regulation to prevent collapsing.

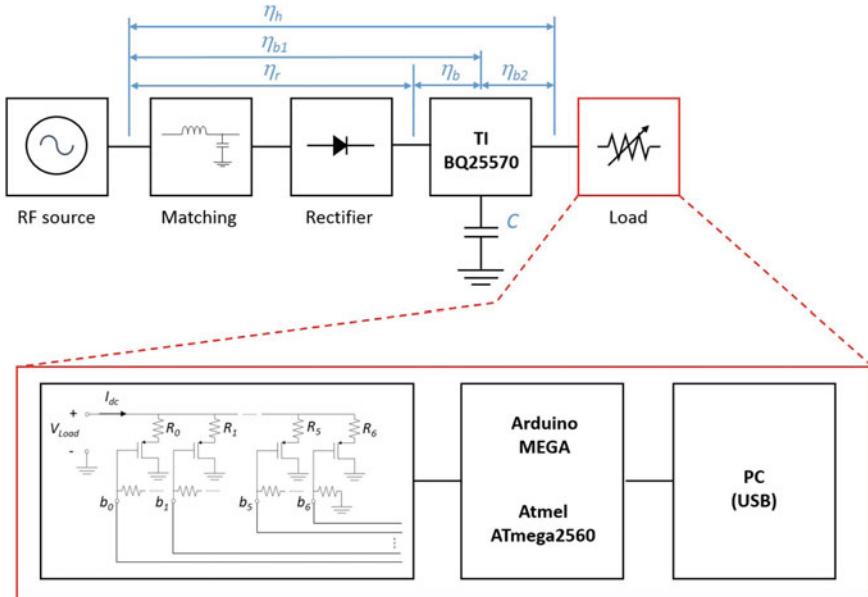


**Fig. 4.13** Rectifier connected to a loaded power management circuit and excited by a matched source. Energy is stored in capacitor  $C$ . the different power conversion efficiencies  $\eta$  are explained in the text

#### 4.6.2 Efficiency Evaluation

The output of a voltage doubling rectifier (based on the Avago HSMS2850 Schottky diode) has been connected to the TI BQ25570 power management IC. The input of the rectifier is connected—through an impedance matching network—to a 868 MHz signal source. This source replaces the antenna and ensures a stable and repeatable signal, necessary for evaluating the rectifier and power management circuits. The configuration is shown in Fig. 4.13.

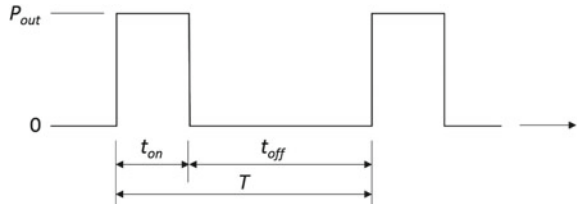
The power management circuit is loaded with a dynamic load. This dynamic load consists of seven resistors  $R_i$ ,  $i = 0, 1, \dots, 6$ ,<sup>6</sup> selectable by BS170 FETs that are controlled using an Atmel ATmega2560 microcontroller on an Arduino MEGA board [33], see Fig. 4.13. The Arduino MEGA board is controlled by a PC through a USB connection.

Using the PC, a sequence of different resistor combinations can be cycled in time, see Fig. 4.14, thus mimicking a duty-cycled IoT sensor node load.

The system consisting of rectifier, power management, energy storage ( $C$ ), and load are tested for a duty cycle that is such that the system is in energy equilibrium [33].

<sup>6</sup> $R_0 = 750 \Omega$ ,  $R_1 = 360 \Omega$ ,  $R_2 = 180 \Omega$ ,  $R_3 = 91 \Omega$ ,  $R_4 = 47 \Omega$ ,  $R_5 = 22 \Omega$ ,  $R_6 = 11 \Omega$ .

**Fig. 4.14** Time diagram of the DC power consumption of a dynamic load for a periodic load having period  $T$ .



The efficiencies evaluated are shown in Fig. 4.13. In this figure,  $\eta_r$  is the RF-to-DC power conversion efficiency of the rectifier combined with the impedance matching network. The overall efficiency  $\eta_h$  is defined as

$$\eta_h = \frac{P_{out_{avg}}}{P_{RF}}, \quad (4.34)$$

where  $P_{RF}$  is the power generated by the signal generator and  $P_{out_{avg}}$  is the time-averaged output DC power dissipated in the dynamic load. The power conversion efficiency  $\eta_{b1}$  is the power conversion efficiency of the chain consisting of impedance matching network, rectifier, and boost converter of the TI BQ25570 IC. This value can be determined as

$$\eta_{b1} = \frac{1}{2} C \frac{V_{C_{max}}^2 - V_{C_{min}}^2}{T \cdot P_{RF}}, \quad (4.35)$$

where  $V_C$  is the voltage over storage capacitor  $C$ , see Fig. 4.13, and  $V_{C_{min}}$  and  $V_{C_{max}}$  are the minimum and maximum values of this voltage, respectively. The maximum value is determined by the IC and the minimum value is determined by the capacitor value  $C$  and the on-time  $t_{on}$ , see Fig. 4.14 [33].

With  $\eta_r$ ,  $\eta_h$  and  $\eta_{b1}$  known, the remaining power conversion efficiencies shown in Fig. 4.13 are found to be

$$\eta_b = \frac{\eta_{b1}}{\eta_r}, \quad (4.36)$$

$$\eta_{b2} = \frac{\eta_h}{\eta_{b1}}. \quad (4.37)$$

These efficiencies are measured as a function of input power  $P_{RF}$  and are shown in Fig. 4.15.

We do observe a rather high power conversion efficiency from the IC's boost converter and buck converter. The power conversion efficiency of the input-matched rectifier (optimized for  $P_{RF} = -10$  dBm) is still fair but lower than the IC's converter efficiencies. This results in an overall efficiency of 23 % for  $P_{RF} = -10$  dBm.

The time-averaged DC output power is then  $P_{out_{avg}} = 23 \mu\text{W}$ . To give an impression what this means for a practical, duty-cycled IoT wireless sensor: For a period  $T = 8.7$  s, this yields 20 mW DC power during 10 ms.

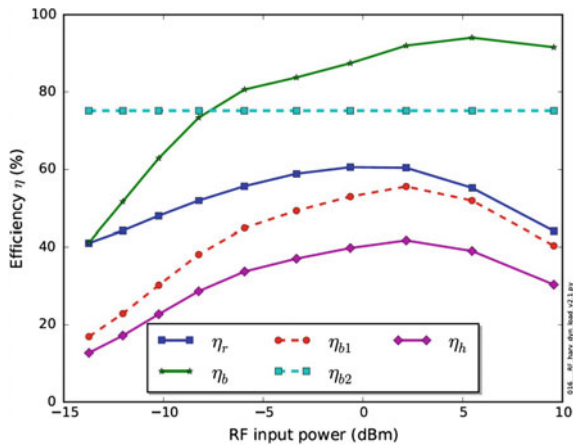


**Fig. 4.15** Efficiencies of the different sections in the rectifier plus power management setup shown in Fig. 4.13

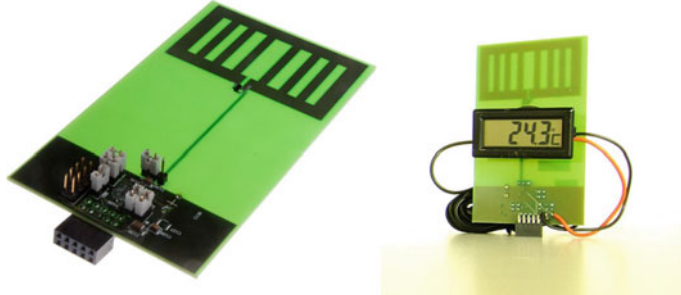


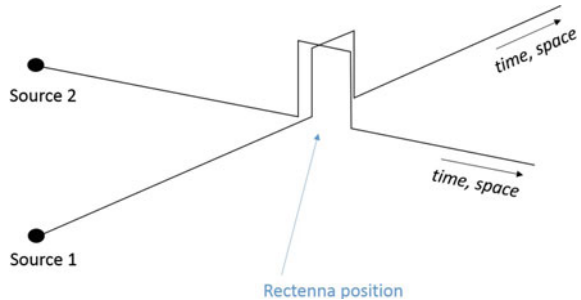
**Fig. 4.16** Rectenna (left) and the same rectenna powering a thermometer with Liquid Crystal Display (LCD)

### 4.6.3 Complete Rectenna

The system consisting of an antenna, complex conjugately matched to a voltage doubling rectifying circuit that is connected to a TI BQ25570 power management circuit is integrated on a single PCB measuring  $6\text{ cm} \times 10\text{ cm} \times 1.6\text{ mm}$  and is shown in Fig. 4.16.

The rectenna has been designed for a frequency of 915 MHz. Excited by a 3W EIRP transmitter, it produces  $P_{out\_avg} \approx 30\mu\text{W}$  at a distance up to 5 m from the source, which is sufficient to continuously power a Commercially Of The Shelf (COTS) thermometer with Liquid Crystal Display (LCD), see Fig. 4.16.

**Fig. 4.17** Combining pulsed waveforms to locally increase the received power



## 4.7 Future Developments

Through a careful co-design of antenna and rectifier, considering the load of the rectifier (power management circuit), efficient rectennas may be realized. To further increase the efficiency, it has recently been demonstrated that an optimization of the transmitted waveform is needed [34–36]. The use of a multisine signal will increase the rectifier’s RF-to-DC power conversion efficiency.

An intermittent continuous wave (ICW) signal, i.e., a CW signal modulated by a rectangular pulse train is a special form of a multisine signal [36]. Therefore, we can not only use rectangular pulses to increase the rectenna’s efficiency, but if we combine pulses coming from different directions, we can also create pockets of energy in space and time and thus further increase the received power, see Fig. 4.17.

As an example, we consider a linear array of thin-wire dipole antennas positioned along the  $x$ -axis and parallel to the  $z$ -axis in a rectangular  $x, y, z$  coordinate system, see Fig. 4.18. The far electric field emitted by such a dipole antenna is given by [37]

$$E(r, t) = \frac{\mu_0 c}{2\pi r \sin \vartheta} \left\{ I_s \left( t - \frac{r}{c} \right) + I_s \left( t - \frac{r}{c} - \frac{2h}{c} \right) - I_s \left( t - \frac{r}{c} - \frac{h}{c} [1 - \cos \vartheta] \right) - I_s \left( t - \frac{r}{c} - \frac{h}{c} [1 + \cos \vartheta] \right) \right\}. \quad (4.38)$$

In the above equation,  $\mu_0$  is the free space permeability,  $c$  is the free space velocity of light,  $r$  is the distance from the antenna,  $h$  is the half-length of the antenna, and  $\vartheta$  is the angle between the vector to the observation point and the dipole axis, see Fig. 4.18.

We assume that the current  $I_s(t)$  is a sinusoidal signal at frequency  $f_0$ , modulated by a rectangular pulse train having amplitude  $A$ , Pulse Repetition Frequency (PRF)  $f_p$  and duty cycle  $D$ :

$$I_s(t) = A \cdot D \cos(2\pi f_0 t) + A \cdot D \sum_{n=1}^N \frac{\sin(n\pi D)}{(n\pi D)} \{ \cos[2\pi (f_0 - nf_p) t] + \cos[2\pi (f_0 + nf_p) t] \}. \quad (4.39)$$

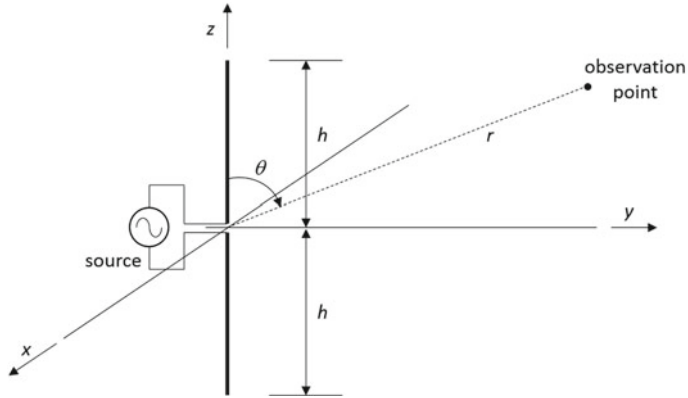
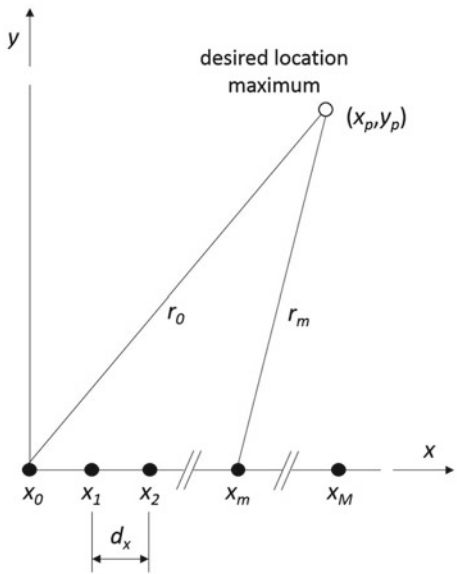


**Fig. 4.18** Thin-wire dipole antenna of half-length  $h$ , positioned in the origin and along the  $z$ -axis of a rectangular  $x, y, z$  coordinate system

**Fig. 4.19** A linear array of  $M + 1$  antenna elements, equidistantly positioned on the  $x$ -axis of a rectangular  $x, y, z$  coordinate system for creating an electric field maximum at  $(x, y) = (x_p, y_p)$



By applying time-delays between the pulse trains transmitted by the antennas, energy can be concentrated in time and space. The time-delays are easily calculated from the differences in the path lengths between the dipole elements and the desired energy maximum position, see Fig. 4.19.

As an example, in Fig. 4.20 the transmitted power distribution in the  $x, y$ -plane is shown for four time instances. The used parameters are:  $M = 4$ ,  $x_p = 6$  m,  $y_p = 18$  m,  $h = 0.31$  m,  $f_0 = 2.45$  GHz,  $\vartheta = \pi/2$ ,  $N = 100$ ,  $f_p = 10$  MHz,  $D = 0.01$ ,  $d_x = 2$  m.

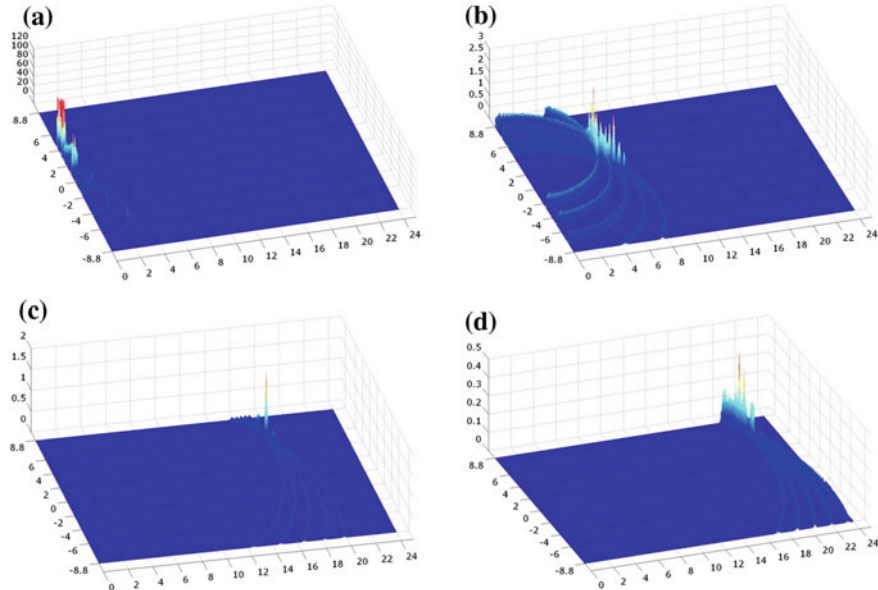


**Fig. 4.20** Transmitted power distribution in the  $x$ ,  $y$ -plane for a linear array of dipole antennas on the  $x$ -axis, parallel to the  $z$ -axis.  $M = 4$ ,  $x_p = 6$  m,  $y_p = 18$  m,  $h = 0.31$  m,  $f_0 = 2.45$  GHz,  $\vartheta = \pi/2$ ,  $N = 100$ ,  $f_p = 10$  MHz,  $D = 0.01$ ,  $d_x = 2$  m. a.  $t = t_0 + 10$  ns, b.  $t = t_0 + 30$  ns, c.  $t = t_0 + 68$  ns, d.  $t = t_0 + 80$  ns

The Figure clearly shows how the pulses are transmitted from the five antenna elements and add up in power after 68 ns at the position  $(x_p, y_p) = (6\text{m}, 18\text{m})$ . Afterwards, the fields diffuse and decay, as expected.

## 4.8 Conclusions

For employing large IoT wireless sensor networks, powering the sensors by cabling or primary batteries is not feasible. For networks employing large numbers of miniature wireless sensors alternative power sources are needed. Energy harvesting from sources like light, vibration, temperature gradients, or ambient RF radiation will not always be possible, especially not for IoT sensor networks for smart houses. Far-field wireless power transfer has shown to be a good alternative for low average power, duty-cycled sensors. For transmitters operating in the license-free ISM frequency bands, being restricted in EIRP, it is possible to obtain tens of microwatts average DC power. To realize this, a careful co-design is needed of receive antenna, rectifying circuit, and power management circuit into a so-called rectifying antenna

or rectenna. To further increase the rectenna's efficiency, future work on transmitted waveform optimization is needed. This can be combined with transient array antenna technology to not only increase the efficiency but also increase the transferred power level without violating EIRP restrictions.

## References

1. Internet of Things Global Standards Initiative. International Telecommunication Union. <http://www.itu.int/en/ITU-T/gsi/iot/Pages/default.aspx>. Accessed 04 Mar 2016
2. Intelligent buildings—a holistic perspective on energy management. Electrical Rev. <http://www.electricalreview.co.uk/features/6495-118645>. Accessed 04 Mar 2016
3. Wiring a Building. <http://www.macktez.com/2004/wiring-a-building/>. Accessed 04 Mar 2016
4. Waffenschmidt, E., Staring, T.: Limitation of inductive power transfer for consumer applications. In: European Conference on Power Electronics, p. 10 (2009)
5. Sample, A.P., Yeager, D.J., Powledge, P.S., Mamishev, A.V., Smith, J.R.: Design of an RFID-based battery-free programmable sensing platform. IEEE Trans. Instrum. Measur. **57**(11), 2608–2615 (2008)
6. Hemour, S., Wu, K.: Radio-frequency rectifier for electromagnetic energy harvesting: development path and future outlook. Proc. IEEE **102**(11), 1667–1691 (2014)
7. Karalis, A., Joannopoulos, J.D., Soljacic, M.: Efficient wireless non-radiative mid-range energy transfer. Ann. Phys. **323**(1), 34–48 (2008)
8. International Telecommunication Union. Radio Regulations (2012). <http://www.itu.int/dms-pub/itu-s/oth/02/02/S02020000244501PDFF.PDF>. Accessed 04 Mar 2016
9. IEEE. IEEE Standard Letter Designators for Radar-Frequency Bands. IEEE Std 521-2002 (2002)
10. Pozar, D.M.: Microwave Engineering, 4th edn. Wiley, New York (2012)
11. Pinuela, M., Mitcheson, P.D., Lucyszyn, S.: Ambient RF energy harvesting in urban and semi-urban environments. IEEE Trans. Microw. Theor. Tech. **61**(7), 2715–2726 (2013)
12. Visser, H.J., Vullers, R.J.M.: RF energy harvesting and transport for wireless sensor network applications: principles and requirements. Proc. IEEE **101**(6), 1410–1423 (2013)
13. Bergqvist, U., Friedrich, G., Hamerius, Y., Martens, L., Neubauer, G., Thuroczy, G., Vogel, E., Wiart, J.: Mobile Telecommunication Base Stations—Exposure to electromagnetic Fields, COST-244bis Short term Mission on Base Station Exposure (2000)
14. Shockley, W.: The theory of  $p - n$  junctions in semiconductor and  $p - n$  junction transistors. Bell Syst. Tech. J. **28**, 435–489 (1949)
15. Fleri, D.A., Cohen, L.D.: Nonlinear analysis of the Schottky-barrier mixer diode. IEEE Trans. Microw. Theor. Tech. **21**(1), 39–43 (1973)
16. Hubregt, J.: Visser Approximate Antenna Analysis for CAD. Wiley, Chichester, UK (2009)
17. Shampine, L., Gear, C.: A user's view of solving stiff ordinary differential equations. SIAM Rev. **21**(1), 1–17 (1979)
18. Shampine, L., Reichelt, M.: The matlab ODE suite. SIAM J. Sci. Comput. **18**(1), 1–22 (1997)
19. Avago Technologies. HSMS-285x Series: Surface Mount Zero Bias Schottky Detector Diodes, 29 May 2009
20. Shepherd, W., Zand, P.: Energy Flow and Power Factor in Nonsinusoidal Circuits, Cambridge University Press (1979)
21. Barnett, R., Liu, J., Lazar, S.: A RF to DC voltage conversion model for multi-stage rectifiers in UHF RFID transponders. IEEE J. Solid-State Circ. **44**(2), 354–370 (2009)
22. Barnett, R., Lazar, S., Liu, J.: Design of multistage rectifiers with low-cost impedance matching for passive RFID tags. In: IEEE Radio Frequency Integrated Circuits (RFIC) Symposium (2006)
23. Dickson, J.: On-chip high voltage generation in NMOS integrated circuits using an improved voltage multiplier technique. IEEE J. Solid-State Circ. **11**(3), 374–378 (1976)

24. de Carli, L., Juppa, Y., Cardoso, A., Galup-Montoro, C., Schneider, M.: Maximizing the power conversion efficiency of ultra-low voltage CMOS multi-stage rectifiers. *IEEE Trans. Circ. Syst. I Regul. Pap.* **62**(4), 967–975 (2015)
25. Freescale Semiconductor Inc.: Comapct integrated antennas, designs and applications for the MC1321X, MC1322X, MC1323X and MKW40/30/20. Application Note, Document Nr. AN2731, September 2015
26. Visser, H.J., Keyrouz, S., Smolders, B.: Optimized rectenna design. *Wirel. Power Transf.* **2**(1), 44–50 (2015)
27. Hubregt, J.: Visser Antenna Theory and Applications. Wiley, Chichester, UK (2012)
28. <https://www.cst.com/Products/CSTMWS>. Accessed 04 Mar 2016
29. Cabedo-Fabres, M., Antonino-Daviu, E., Valero-Nogueira, A., Bataller, M.F.: The theory of characteristic modes revisited: a contribution to the design of antennas for modern applications. *IEEE Antennas Propag. Mag.* **49**(5), 52–68 (2007)
30. Miers, Z., Li, H., Lau, B.K.: Design of bezel antennas for multiband MIMO terminals using charactersitic modes. In: European Conference on Antennas and Propagation, pp. 2556–2560 (2014)
31. Visser, H.J., Pop, V., Op het Veld, B., Vullers, R.J.M.: Remote RF battery charging. In: PowerMEMS Conference, 4pp. (2010)
32. <http://www.ti.com/product/BQ25570>. Accessed 05 Mar 2016
33. Pflug, H.W., Visser, H.J., Keyrouz, S.: Practical applications of radiative wireless power transfer. In: Wireless Power Transfer Conference, 4pp. (2015)
34. Boaventura, A.S., Carvalho, N.B.: Maximizing DC power in energy harvesting circuits using multisine excitation. In: International Microwave Symposium, 4pp. (2011)
35. Boaventura, A., Carvalho, N.B., Georgiadis, A.: The impact of multi-sine tone separation on RF-DC efficiency. In: Asia-Pacific Microwave Conference, pp. 606–609 (2014)
36. Boaventura, A., Belo, D., Fernandes, R., Collado, A., Georgiadis, A., Carvalho, N.B.: Boosting the efficiency. *IEEE Microw. Mag.* 87–96, Apr 2015
37. Smith, G.S., Hertel, T.W.: On the transient radiation of energy from simple current distributions and linear antennas. *IEEE Antennas Propag. Mag.* **43**(3), 49–63 (2001)

# Chapter 5

## Wireless Power Transfer: Discrete Rectifier Modeling and Analysis

Hans W. Pflug and Hubregt J. Visser

**Abstract** An accurate equivalent circuit model to predict the Power Conversion Efficiency (PCE) of a Schottky Barrier Diode (SBD) is presented in this chapter. By making use of good insight into the used SBD models and careful analysis of circuit behavior, more efficient rectifier circuits have been identified. An increase in circuit efficiency of 18–25 % is shown compared to state of the art, resulting in 20–180 % more available energy from the rectifying circuit. Also the accuracy of simulation results has increased significantly due to the proposed model usage and analysis technique. All the simulations in this chapter are performed in a conjugately matched environment, which allows for an objective comparison of different Schottky diodes and rectifier topologies. The simulation results show a near-perfect match with measured data.

### 5.1 Introduction

In recent years, the Internet of Things (IoT) concept has emerged, in which physical objects are connected to the Internet without the need for human interaction [11]. Key in this concept is a long term, self-sustainable operation for a rapid growing amount of devices. Energy aware devices are preferred, capable of harvesting their required energy from ambient sources. Far-field Wireless Energy Harvesting (WEH) is one of the most promising techniques for its ease of implementation and availability, among other methods [8]. A logical step toward WEH is Wireless Energy Transfer (WET)—commonly known as Wireless Power Transfer (WPT), making use of intentional

---

H.W. Pflug (✉)

Holst Centre and imec, High Tech Campus 31, 5656 AE Eindhoven, The Netherlands  
e-mail: hans.pflug@imec.be

H.W. Pflug

Holst Centre and imec, imec, Kapeldreef 75, 3001 Leuven, Belgium

H.J. Visser

Holst Centre/imec, Eindhoven University of Technology, Eindhoven, The Netherlands  
e-mail: huib.visser@imec-nl.nl

RF transmitting energy sources. Once the consuming devices' energy consumption drops low enough and the WPT circuitry becomes efficient enough, IoT can switch to WEH usage. Typical IoT applications span a wide range of fields including smart buildings, healthcare, transportation, agriculture, and surveillance [1]. Supplying energy to this rapid growing system is a dominant implementation barrier. WPT is seen as a promising approach for IoT.

WPT works by rectifying a RF signal, received by an antenna, into a usable dc component. To achieve a high Power Conversion Efficiency (PCE) of the WPT circuitry, objective topology comparison is required. This calls for realistic circuit models and an objective analysis technique.

Both are investigated in this work: first the diode modeling topic will be covered in Sect. 5.2, showing a significant improvement of the model that has been used for decades. Section 5.3 discusses an objective analysis technique, making use of adaptive source power and a time trajectory technique. These two sections provide the means for proper topology comparison, which is discussed in Sect. 5.4.

## 5.2 Rectifier Modeling

Schottky Barrier Diodes (SBD) are typically used as a building blocks for WPT rectifiers as they exhibit, apart from a relative low voltage drop, a small junction capacitance. A draw-back of the SBD is the relative large reverse leakage current [9].

The *p-i-n* diode (or PIN diode), shows a lower series resistance (around  $0.6\ \Omega$ ) but has a higher junction capacitance (around  $1\text{ pF}$ ), which makes this type less useful for WPT rectification. The low series resistance becomes significant for efficiency at higher input power levels (above  $0\text{ dBm}$ ) [10].

For decades, these SBDs have been used as mixers and video detectors [5]. These applications are not significantly impacted by the reverse leakage current. This is different for the WPT case where this leakage current corresponds to a loss of stored energy, reducing the rectifier PCE. The PCE is a main design goal for WPT systems [27, 30]. In this chapter a global optimization of the PCE will be investigated.

It will be shown that, under impedance matched conditions, a low saturation current will lead to a high PCE. This is related to the fact that the reverse leakage current is directly proportional to the diode saturation current.

This insight makes the modeling of the SBD reverse bias region important. In most work, e.g. [9, 20], the SBD is modeled using the SPICE (Simulation Program with Integrated Circuit Emphasis [15]) built-in *p-n* junction diode model, which appears to be far from realistic for a significant range of biases. Figure 5.1 provides more insight.

Next to this, measurements reveal an inaccurate SBD current–temperature relationship in the SPICE-based diode models. Both findings resulted in a new SBD macro model, discussed in Sect. 5.2.2. Diode models used in Keysight ADS provide additional parameters to model the nonidealities, which can not be filled in from the diode data-sheet. They should be extracted from measurements.

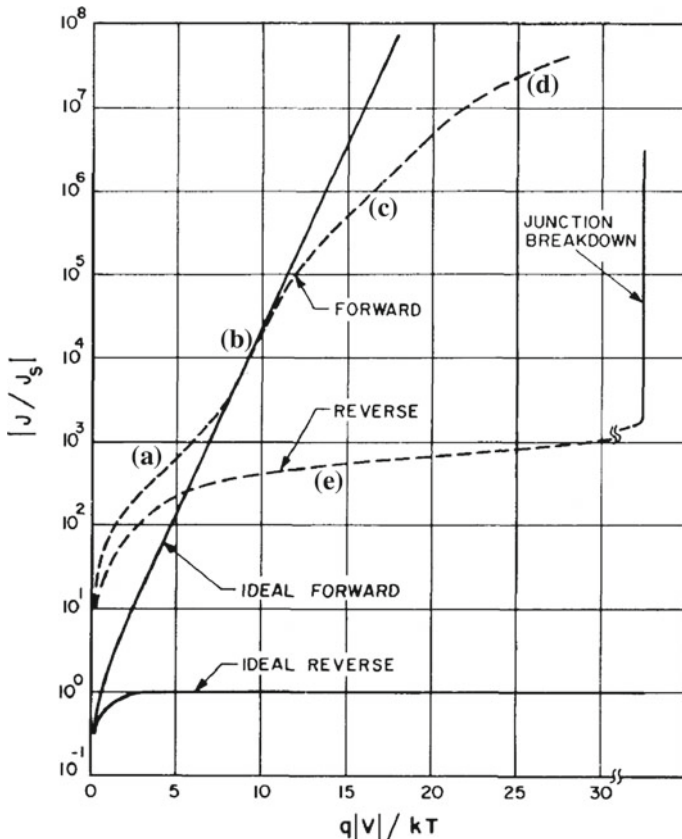


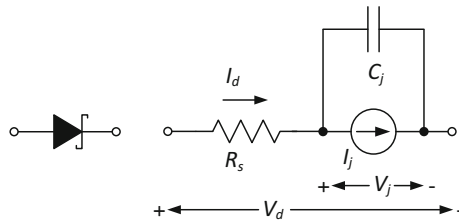
**Fig. 5.1** Current-voltage characteristics of a practical (dashed) and ideal (straight) Si diode: **a** generation-recombination current region, **b** diffusion current region, **c** high-injection region, **d** series resistance effect, **e** reverse leakage current due to generation–recombination and surface effect. (after [24])

Both the junction diode and the Schottky barrier diode can be modeled using an equivalent model as shown in Fig. 5.2 [14, 31]. The model consists of a voltage dependent current source, parallel to a junction and diffusion capacitance, the combination being in series with a resistor  $R_s$ .  $C_j$  represents the charge storage in the semiconductor junction.  $I_j$  accounts for the impedance of the barrier layer itself and is both  $V_j$  and temperature dependent [4].

### 5.2.1 I-V Relationship

Different semiconductor physics theories exist to model the SBD current. The single thermionic emission–diffusion theory by Crowell and Sze combines the isothermal

**Fig. 5.2** Schottky Barrier Diode symbol and equivalent diode model



thermionic emission theory by Bethe [25] and the isothermal diffusion theory by Schottky [22], and describes the total current density as [24]:

$$J_d = J_s (e^{V_j/nV_T} - 1), \quad \text{with } V_j > -3V_T, \quad (5.1)$$

similar to the Shockley equation [23] for *p-n* junctions, with  $J_s$  being the saturation current density ( $\text{A}/\text{m}^2$ ),  $V_j$  the diode junction voltage (V),  $n$  the emission coefficient,  $V_T = kT/q$  the thermal voltage (V),  $q$  the elementary charge ( $1.60218 \times 10^{-19}$  C),  $k$  Boltzmann's constant ( $1.38065 \times 10^{-23}$  J/K), and  $T$  the physical temperature (K). In the reverse bias domain, the diode current density saturates at  $-J_s$  for the ideal SBD.

The saturation current density is described by

$$J_s = A^* \cdot T^2 e^{-\phi_B/V_T} \quad (5.2)$$

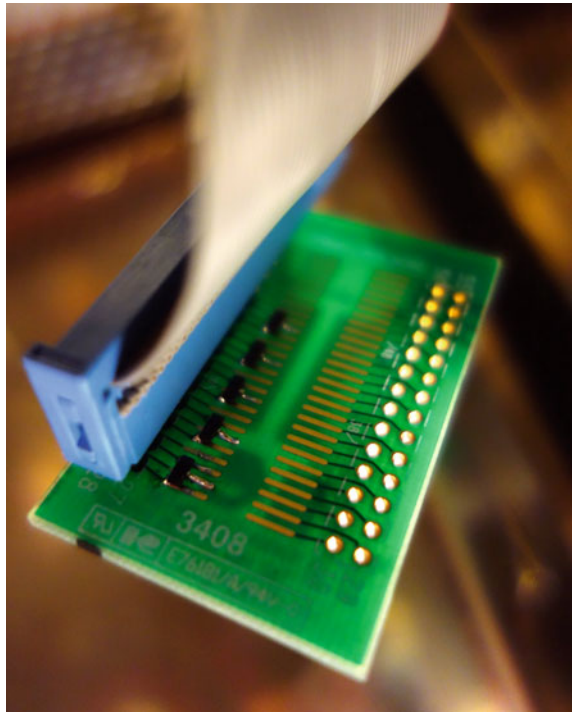
with  $A^*$  being the effective Richardson constant ( $\text{A}/\text{m}^2/\text{K}^2$ ) and  $\phi_B$  the Schottky junction potential (V).  $A^*$  is not dependent on temperature but on the typical semiconductor being used and the crystal orientation.

The SPICE *p-n* junction diode model makes use of a different equation to model the reverse bias region [14], compared to the physical SBD relationship provided by [24]. Both an equation defined device model and a macro model [6, 32], are compared. The latter one—used in this work—uses two SPICE *p-n* junction diode models with measurement-based parameter values and simulates ten times faster, with similar accuracy. The former one is a user-defined equation-based nonlinear component based on the physical SBD equations. In Keysight ADS, these components are named Symbolically-Defined Devices (SDD).

### 5.2.1.1 I-V Measurement

To validate the diode current–voltage (I-V) model, a measurement is carried out on five Avago HSMS-2852 and five Skyworks SMS7621 diode pairs (for forward and reverse biasing). Using multiple diodes, insight in component to component variation is provided. The limited amount of 10 diodes for each type was chosen for practical reasons. The manual selection of diodes, when using a temperature chamber, sets the practical boundary for the number of diodes used. Figure 5.3 shows the used

**Fig. 5.3** Test PCB with 5 Avago HSMS-2852 pairs, used inside a climate test cabinet to measure their I-V characteristics. At a later stage, the Skyworks SMS7621 diodes were added on the *right side* of the board



test structure. For accurate current–voltage measurements, an Agilent (Keysight) B1500A Semiconductor Device Analyzer is used together with a CTS climatic test cabinet (series C) to control the environmental temperature. For each of the diodes, both the forward and reverse DC I-V characteristic is measured by applying a voltage between the anode and cathode and measuring the resulting diode current. This is done at a temperature of  $-40$ ,  $0$ ,  $26.85$ ,  $40$ , and  $80^{\circ}\text{C}$ .

The measured SMS7621 reverse- and forward-bias currents are shown for  $26.85^{\circ}\text{C}$  in Figs. 5.4 and 5.5.

### 5.2.2 Macro Model

The diode macro model consists of a reverse diode parallel to a forward diode, see Fig. 5.6. This model makes use of the SPICE *p-n* junction diode model, with measurement-based parameter values. Compared to the single SPICE diode model, this model has four extra *reverse* parameters for the series resistance  $R_{sr}$ , emission coefficient  $n_r$ , saturation current  $I_{sr}$ , and temperature coefficient  $p_{ir}$ . The reverse diode zero-bias junction capacitance  $C_{j0}$  is set to zero as this capacitance is modeled by the forward diode. All other parameters have the same values as in the forward

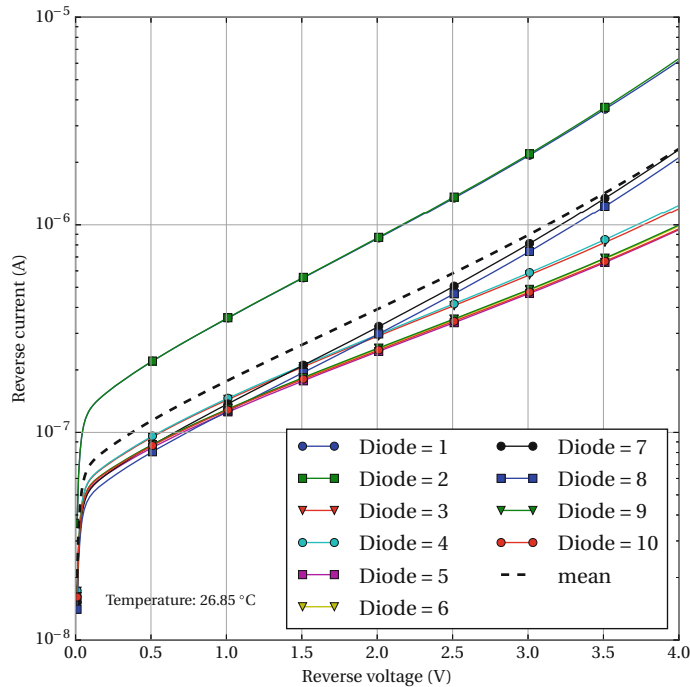


**Fig. 5.4** Skyworks SMS7621 reverse current measurement on 10 devices against reverse bias voltage at 26.85 °C, together with mean response (dashed line)

diode model. The easy employment in different circuit simulators is an advantage of this model, compared to the equation defined model.

### 5.2.2.1 Model Extraction

Different techniques can be applied to obtain a proper model, being a representation of the real world within acceptable margins. In this work, the first Russell method [21] (three-point I-V method) is used for the forward bias region model (Fig. 5.7).

The obtained error between the modeled diode current  $I_{d,\text{model}}$  and the measured diode current  $I_{d,\text{meas}}$ , is calculated using a Normalized Root Mean Square Error (NRMSE). This function is defined as

$$E_{I_d} = \sqrt{\frac{\sum |\varepsilon_i|^2}{N}}, \quad (5.3)$$

with  $N$  being the number of data-points and  $|\varepsilon_i|$  being the normalized error at the  $i$ -th measured data-point. This error is defined as

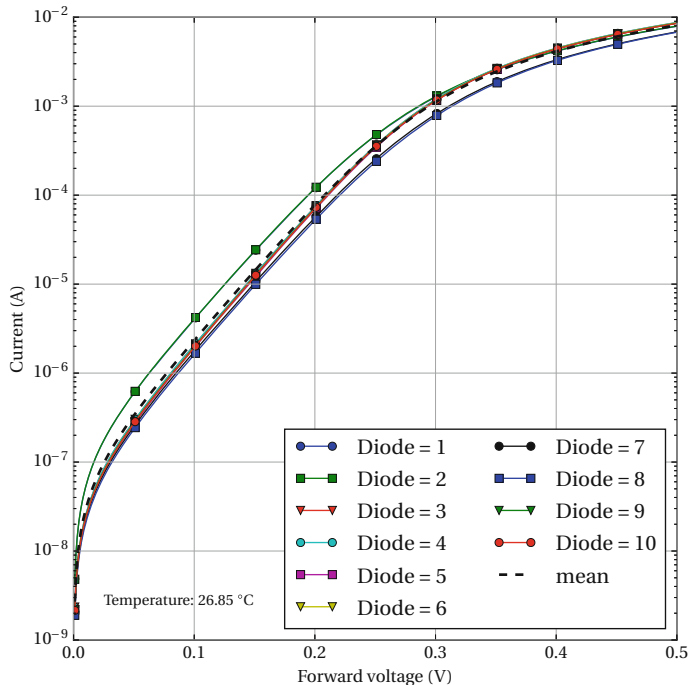
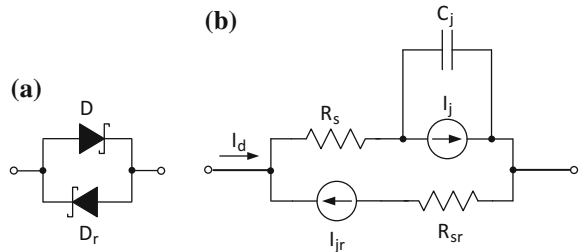


**Fig. 5.5** Skyworks SMS7621 forward current measurement on 10 devices against forward bias voltage at  $26.85^{\circ}\text{C}$ , together with mean response (dashed line)

**Fig. 5.6** Schematic of the diode macro model with forward and reverse bias elements: **a** macro model with forward diode  $D$  and reverse diode  $D_r$ , **b** detailed diode macro model



$$\varepsilon_i = \frac{I_{d,\text{model}} - I_{d,\text{meas}}}{I_{d,\text{meas}}}. \quad (5.4)$$

### 5.2.2.2 Reverse Bias Model

For the reverse bias model, the ideal  $p$ - $n$  junction diode model does not fit the measured values. As mentioned before, a macro model is used in which the second (reverse) diode serves the reverse bias region. The advantage of this model is the

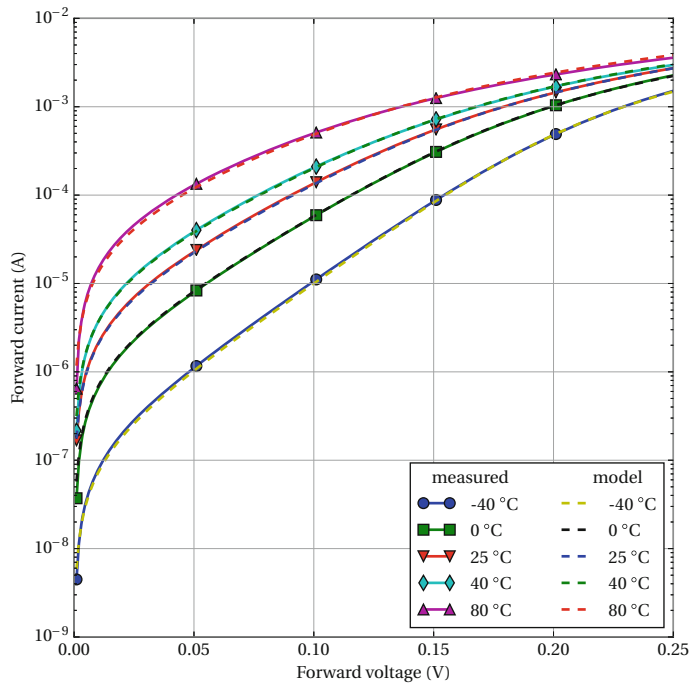


**Fig. 5.7** Nominal (diode D3) Avago HSMS2852 forward I-V measurement at a temperature of  $-40$ ,  $0$ ,  $40$ , and  $80$  °C together with the model

usage of a normal standard SPICE *p-n* junction diode model, only having a few odd parameter values. Figure 5.6 shows the schematic of the reverse bias diode model. The breakdown region is still modeled by the forward diode *D*. The reverse diode has special values for the series resistance  $R_{sr}$ , the emission coefficient  $n_r$ , the saturation current  $I_{sr}$ , and its temperature coefficient  $p_{ir}$ . The reverse diode zero-bias junction capacitance  $C_{j0}$  is set to zero as this capacitance is modeled by the forward diode. All other parameters have the same values as in the forward diode model.

The comparison between this model and the typical (D3) HSMS-2852 measurement is shown in Figs. 5.7 and 5.8. The model provides a better match compared to the current ideal model implemented in the simulator Qucs. The reverse current model NRSME for the nominal HSMS-2852 diode, equals  $E_{I_d,\text{rev}} = 20.4\%$ .

An overview of the resulting HSMS-2852 and SMS7621 SPICE diode parameters (including the new introduced reverse model parameters) is provided in Tables 5.1 and 5.2, together with the data-sheet values provided by the manufacturer. A comparison between the different  $E_{I_d}$  values shows the improvement obtained by the macro model.

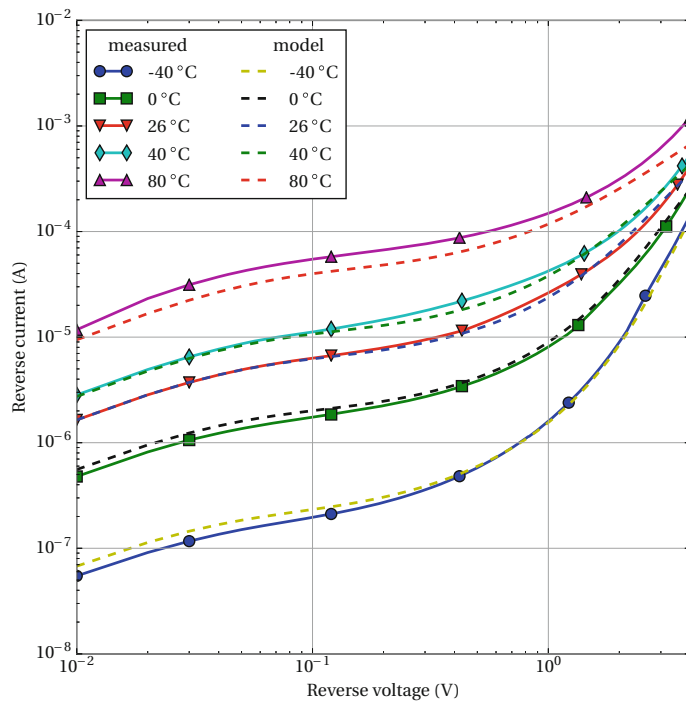


**Fig. 5.8** Nominal (diode D3) Avago HSMS2852 reverse I-V measurement at a temperature of  $-40$ ,  $0$ ,  $26$ ,  $40$ , and  $80^\circ\text{C}$  together with the macro model result

**Table 5.1** HSMS-2852 SPICE p-n junction-based SBD macro model and data-sheet SPICE model parameters

| Parameter             | Minimal | Nominal | Maximal | Data-sheet         | Unit             |
|-----------------------|---------|---------|---------|--------------------|------------------|
| $R_s$                 | 26.2    | 24.0    | 21.0    | 25                 | $\Omega$         |
| $n$                   | 1.130   | 1.141   | 1.141   | 1.06               |                  |
| $I_s$                 | 4.96    | 5.57    | 6.55    | 3.00               | $\mu\text{A}$    |
| $\psi'$               | 0.32    | 0.31    | 0.31    | 0.69               | eV               |
| $R_{sr}$              | 3.50    | 2.80    | 1.42    | —                  | $\text{k}\Omega$ |
| $n_r$                 | 31.1    | 30.2    | 30.0    | —                  |                  |
| $I_{sr}$              | 6.9     | 8.0     | 11.97   | —                  | $\mu\text{A}$    |
| $p_{ir}$              | 415     | 368     | 320     | —                  |                  |
| $E_{I_d,\text{forw}}$ | 4.28    | 4.35    | 5.30    | 77.44 <sup>a</sup> | %                |
| $E_{I_d,\text{rev}}$  | 19.99   | 20.37   | 19.73   | 143.8 <sup>a</sup> | %                |
| Diode                 | D10     | D3      | D5      |                    |                  |

<sup>a</sup>Compared with nominal diode D3

**Table 5.2** SMS7621 SPICE p-n junction-based SBD macro model and data-sheet SPICE model parameters.

| Parameter             | Minimal | Nominal | Maximal | Data-sheet         | Unit      |
|-----------------------|---------|---------|---------|--------------------|-----------|
| $R_s$                 | 26      | 17      | 40      | 12                 | $\Omega$  |
| $n$                   | 1.055   | 1.068   | 1.081   | 1.05               |           |
| $I_s$                 | 51.6    | 55.0    | 121     | 40                 | nA        |
| $\psi'$               | 0.465   | 0.460   | 0.404   | 0.69               | eV        |
| $R_{sr}$              | 3.6     | 42      | 10      | —                  | $k\Omega$ |
| $n_r$                 | 48      | 47      | 48      | —                  |           |
| $I_{sr}$              | 42      | 43.4    | 200     | —                  | nA        |
| $p_{ir}$              | 860     | 862     | 730     | —                  |           |
| $E_{I_d,\text{forw}}$ | 5.26    | 3.88    | 7.16    | 72.48 <sup>a</sup> | %         |
| $E_{I_d,\text{rev}}$  | 19.36   | 17.52   | 23.34   | 126.3 <sup>a</sup> | %         |
| Diode                 | D5      | D6      | D2      | —                  |           |

<sup>a</sup>Compared with nominal diode D6

### 5.2.3 Integrated Equivalent

When integrating rectifier circuits, typically diode-connected Metal-Oxide-Semiconductor (MOS) Field-Effect Transistors (FET) are used. These devices also have a reverse bias leakage current, which is especially significant for low-threshold voltage and zero-threshold voltage devices. For the latter category, the leakage current easily reaches several  $\mu\text{A}$  for reverse voltages below  $-0.1$  V [33].

### 5.2.4 SPICE Model

The equations and variables used for the diode model in SPICE are fixed and not easily modified. The accuracy resulting from a SPICE simulation of a diode therefore depends on the precise extraction of its model parameters. Looking at the difference between real diode behavior and the SPICE diode model shows:

- The saturation current  $I_s$  is constant and not a function of the reverse bias voltage, up to the breakdown voltage.
- The series resistance  $R_s$  is constant and not a function of voltage or current. The resistance of the bulk neutral semiconductor regions of a real diode actually increases for high-level injection.
- The  $R_s$  has no temperature coefficient. The temperature coefficient of the bulk neutral semiconductor regions of a real diode is positive, producing a positive voltage temperature coefficient at high-level injection.
- The emission coefficient  $n$  is constant and cannot model the change in slope of the I-V characteristics between the extreme low-level and low-level injection regions.

**Table 5.3** Diode SPICE parameters

| Symbol   | Name | Parameter                                      | Unit     | Default             |
|----------|------|--|----------|---------------------|
| $I_s$    | IS   | Saturation current                             | A        | $1 \times 10^{-14}$ |
| $R_s$    | RS   | Parasitic resistance                           | $\Omega$ | 0                   |
| $n$      | N    | Emission coefficient                           | —        | 1                   |
| $\tau_d$ | TT   | Transit time                                   | s        | 0                   |
| $C_{j0}$ | CJO  | Zero-bias junction capacitance                 | F        | 0                   |
| $\phi_0$ | VJ   | Junction potential                             | V        | 1                   |
| $m$      | M    | Junction grading coefficient <sup>a</sup>      | —        | 0.5                 |
| $\psi$   | EG   | Energy gap <sup>b</sup>                        | eV       | 1.11                |
| $p_i$    | XTI  | $I_s$ temperature exponent <sup>c</sup>        | —        | 3.0                 |
| $k_f$    | KF   | Flicker noise coefficient                      | —        | 0                   |
| $a_f$    | AF   | Flicker noise exponent                         | —        | 1                   |
| FC       | FC   | Forward bias depletion capacitance coefficient | —        | 0.5                 |
| BV       | BV   | Breakdown voltage                              | V        | $\infty$            |
| IBV      | IBV  | Current at breakdown voltage                   | A        | $1 \times 10^{-3}$  |
| $T_0$    | TNOM | Parameter specification temperature            | °C       | 27                  |

<sup>a</sup>Linearly graded junction: 0.33, abrupt junction: 0.5

<sup>b</sup>Si: 1.11 eV, Ge: 0.67 eV, Schottky: 0.69 eV(Al-Si), 0.85 eV(Al-GaAs), 0.3 eV(Al-InP)

<sup>c</sup>*p-n* junction: 3.0, Schottky: 2.0

- The reverse breakdown characteristics of a real diode tend to be soft; the reverse leakage current gradually increases toward the breakdown current as the reverse bias voltage increases. The SPICE model has a hard breakdown characteristic with parameter IS being constant up to the breakdown point.

#### 5.2.4.1 Diode SPICE Parameters

The SPICE *p-n* junction diode model parameters are listed in Table 5.3. These are typically specified by the manufacturer on a diode data-sheet.

Spice circuits have two global temperature parameters: TEMP and TNOM, which can both be altered. They can also be swept in DC analysis by referring to them as temp or tnom. TEMP and TNOM are given in degrees Celsius. They are internally stored in Kelvin. TEMP is the circuit temperature and TNOM is the temperature at which the given model parameters are valid. If TEMP differs from TNOM, model parameters are internally recalculated to reflect the temperature dependence of the simulated devices.

**Table 5.4** Commercial Schottky barrier diode SPICE model parameters

| ID <sup>a</sup> | Part       | IS ( $\mu$ A) | RS ( $\Omega$ ) | N    | CJ0 (pF) | VJ (V) | M    | FC  | BV (V) | IBV ( $\mu$ A) |
|-----------------|------------|---------------|-----------------|------|----------|--------|------|-----|--------|----------------|
| A0              | HSMS-2822x | 0.022         | 6.0             | 1.08 | 0.7      | 0.65   | 0.5  |     | 15     | 100            |
| A1              | HSMS-285x  | 3             | 25              | 1.06 | 0.18     | 0.35   | 0.5  |     | 3.8    | 300            |
| A2              | HSMS-286x  | 0.05          | 6.0             | 1.08 | 0.18     | 0.65   | 0.5  |     | 7.0    | 10             |
| S1              | CDB7620    | 0.04          | 4               | 1.20 | 0.15     | 0.495  | 0.35 | 0.5 | 10     | 10             |
| S2              | CDF7621    | 0.09          | 6               | 1.10 | 0.11     | 0.510  | 0.30 | 0.5 | 2.5    | 10             |
| S3              | CDB7619    | 0.03          | 30              | 1.04 | 0.11     | 0.540  | 0.32 | 0.5 | 3.0    | 10             |
| S4              | CDC7623    | 0.11          | 5               | 1.10 | 0.20     | 0.510  | 0.30 | 0.5 | 2.5    | 10             |
| S5              | SMS1546    | 0.3           | 4               | 1.04 | 0.38     | 0.51   | 0.36 | 0.5 | 3      | 10             |
| S6              | SMS7621    | 0.04          | 12              | 1.05 | 0.10     | 0.51   | 0.35 | 0.5 | 3      | 10             |
| S7              | SMS7630    | 5             | 20              | 1.05 | 0.14     | 0.34   | 0.40 | 0.5 | 2      | 100            |
| S8              | SMS7621-   | 0.026         | 10.3            | 1.01 | 0.13     | 0.51   | 0.35 | 0.5 | 3      | 10             |
| S8              |            | 0.060         |                 |      |          |        |      |     |        |                |
| M1              | MSS20-141  | 3.5           | 20              | 1.3  | 0.08     |        |      |     |        |                |

<sup>a</sup>An = Avago Technologies, Sn = Skyworks Solutions, Mn = Metelics

For all diodes: TT = 10 ps, EG = 0.69 eV, XTI = 2

### 5.2.4.2 Commercial Diode Examples

An overview of some commercial available Schottky barrier diodes is provided in Table 5.4. In the last years, the Avago HSMS-2852 type has been used often in WPT rectifiers. In this work, the Skyworks SMS7621 is identified as a better choice for its lower saturation current and junction capacitance. The higher series resistance (compared to e.g. the Avago HSMS-286x family) does not play a role at input power levels below 0 dBm.

Manufacturers sell the diodes typically packaged. As these packages introduce extra parasitic elements (e.g., bondwires for connecting the diode to the package pins introduce inductance), a model can be made for each type of package. Suppliers often provide these models, normally based on lumped components for easy insertion in (time domain) simulations.

Different types of packages exist. Consumer and commercial applications require low cost packages, which are easy to assemble. The JEDEC standard surface mount package SOT-23 is a plastic package with tin/lead plated leads, suited for various soldering processes and is a good low cost example. A disadvantage is the inherently long bondwire ( $L_B = 1.0 \text{ nH}$ ) inside the package and the bent leads ( $L_L = 0.5 \text{ nH}$  each). Figure 5.9 shows the SOT-23 package drawing and Fig. 5.10 gives an idea of a single diode SOT-23 packaging, showing the parasitic inductance elements [3].

Figure 5.11 shows the Avago supplied model for the SOT23 plastic package [2], which model is valid up to 3 GHz and can be used both for the double diode series configuration package as for the single diode package. The component values are listed in Table 5.5. For the Skyworks SOT-23 diode package, the same model is used.

Schottky barrier diodes are made as *n*-type and *p*-type silicon versions, resulting in different characteristics and are intended for different applications. Other design considerations are also made: for example the *n*-type Avago HSMS-282x family of diodes are designed for low variation in characteristics using a minimal amount of process steps. The HSMS-285x family is of the *p*-type silicon, showing significant more series resistance  $R_s$  and two orders of magnitude more saturation current  $I_s$  compared to the *n*-type HSMS-282x and also the HSMS-286x families.

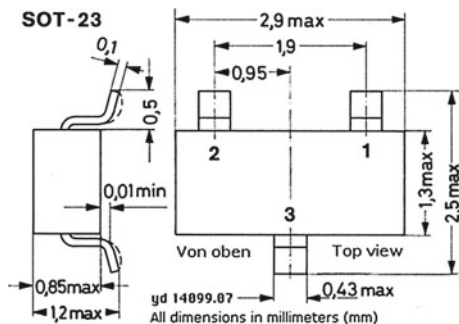


**Fig. 5.9** Plastic SOT-23 package outline

**Table 5.5** Avago SOT23 package model component values, corresponding to the model shown in Fig. 5.11

| Element | Description           | Value | Unit |
|---------|-----------------------|-------|------|
| $L_L$   | Leadframe inductance  | 0.50  | nH   |
| $C_L$   | Leadframe capacitance | 0     | pF   |
| $C_P$   | Package capacitance   | 0.080 | pF   |
| $C_C$   | Coupling capacitance  | 0.060 | pF   |
| $L_B$   | Bondwire inductance   | 1.0   | nH   |

### 5.3 Circuit Analysis Techniques

For the design and optimization of electrical circuits, it's key to make use of the right models. All available methods will use circuit models, in which each component can be represented by one or more mathematical equations. These describe, with a certain accuracy, the electrical behavior of the circuit element. A resistor is modeled with a linear equation using Ohm's law  $V_R = I_R R$ . A capacitor is described by a differential equation  $I_C = C \frac{dV}{dt}$ . A diode can be modeled using several equations, as shown in the previous section. The main one being the Shockley ideal diode equation (5.1).

When combining these circuit elements, a system of Ordinary Differential Equations (ODEs) has to be solved, to obtain the electrical behavior. For that, the transient analysis tool SPICE is commonly used. This provides a time-domain large-signal solution of nonlinear differential algebraic equations. In this work, usage of SPICE is made, resulting in discrete-time voltage and current values. These results will be referred to as 'simulation' results. Figure 5.12 shows an overview of the different

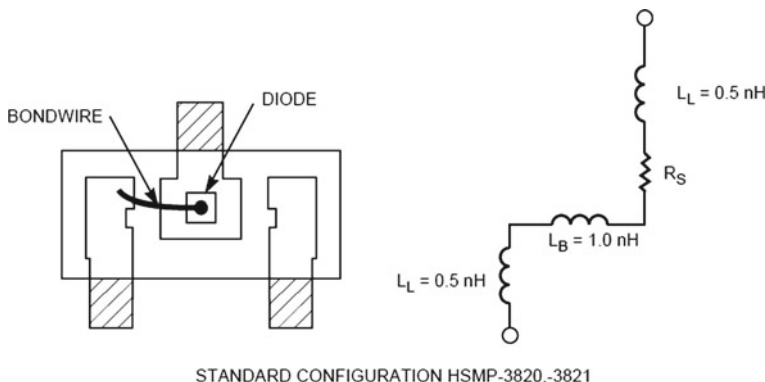


**Fig. 5.10** An Avago SOT-23 package construction showing the parasitic inductances of bondwire and bent leads on the *left side* and a corresponding first order model on the *right side* [3]

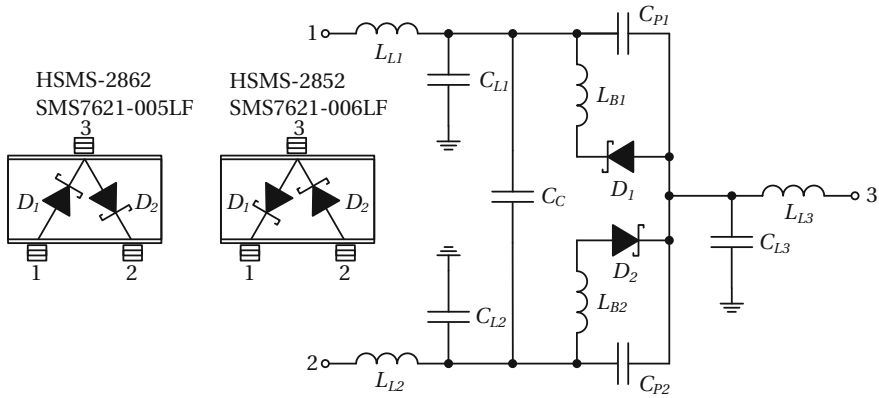


**Fig. 5.11** Second order model of the Avago SOT-23 plastic diode package, valid up to 3 GHz, and also used for the Skyworks SMS7621 in this work. A single diode version is also available. In that case only diode  $D_1$  is mounted. The HSMS-2852 and HSMS-2862 have a different configuration as shown in the figure *left side*. The equivalent circuit model represents the HSMS-2852 version. In this work, the HSMS-2852 and SMS7621-006LF are used

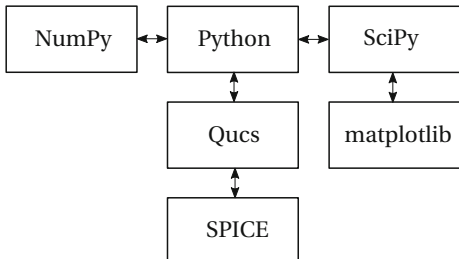
tools used in this work for circuit calculations. Other software tools used next to SPICE, will be briefly discussed below.

### 5.3.1 Software Tools

#### 5.3.1.1 Python

The high-level programming language Python [26] is used to control the circuit calculations performed using SPICE, with Qucs (Quite universal circuit simulator) being the interfacing tool [18]. The SPICE results are post-processed using Python as well. This post-processing results in, e.g., reflection coefficient and impedance information.

**Fig. 5.12** Overview of the different open-source tools used in this work. NumPy is a matrix and array extension to Python, SciPy is a scientific computing extension to Python and matplotlib is a plotting library for Python



### 5.3.1.2 Qucs

To interface with SPICE, the open-source electronics circuit simulator Qucs [18] is chosen. The simulator backend, i.e., the text-mode of Qucs, is used mainly. The operation of the simulation back-end is controlled via a text file (called netlist), which describes the circuit to be simulated and the kind of simulation to perform. By using Python to control this process, additional flexibility is introduced. Algorithms creating, e.g., simulation-loops to adapt signal source power level, can easily be implemented as will be shown later.

### 5.3.2 Time Trajectory Technique

A technique is introduced to analyze the time-variant behavior of nonlinear circuit elements, like diodes. These components possess a time-varying impedance, which has a significant impact on the behavior, especially at higher signal power levels.

This dynamic behavior is also a reason for not using a *harmonic balance* simulation technique as that is based on a steady-state assumption. A *transient* simulator is needed for analyzing dynamic signals. In this work we only take constant envelope signals into account. The time trajectory technique is validated for a steady-state situation with a Keysight ADS harmonic balance simulation of a voltage doubler.

Figure 5.13 provides a result of the time trajectory technique, showing a peak detector circuit input reflection coefficient, both in a time average and in a continuous time representation. When measured with a standard Vector Network Analyzer (VNA), this circuit would show a very good input reflection coefficient of  $-30.7$  dB, corresponding to the  $\Gamma_{in}$  point in the figure. In reality, the circuit constantly possesses a mismatch due to its nonlinear nature. This mismatch is made visible by the time-varying  $\gamma_{in}(t)$  curve and reveals that the input reflection coefficient is only  $-10.1$  dB with a mismatch loss of  $0.47$  dB. This means that  $10\%$  of the energy is not entering the circuit, although one would expect a much higher percentage from the (single frequency) VNA measurement result.

### 5.3.3 Adaptive Input Power Algorithm

In WPT, we want to transfer available energy with the highest possible efficiency from one point to another point. Therefore, on the receiving side, a maximum energy transfer between the input (receiving antenna) and the following circuitry needs to be accomplished. A typical rectifier circuit used has an input impedance far from  $50\Omega$ , the value used for a standard receiving antenna. For a maximum energy transfer, an impedance matching network is typically inserted between the antenna and

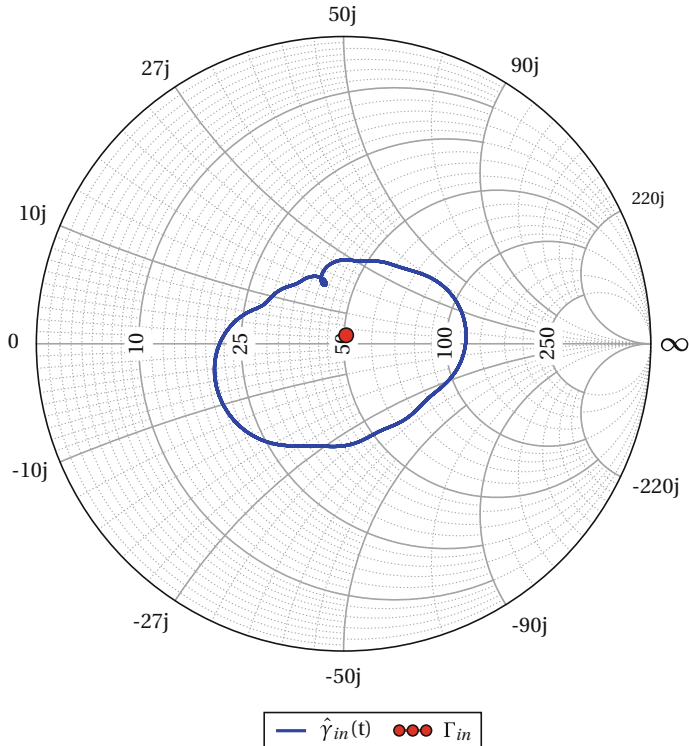


**Fig. 5.13** Smith-chart showing both the time-average input reflection coefficient  $\Gamma_{in}$  and the time-varying version  $\gamma_{in}(t)$  of a peak detector using a bare Avago HSMS-2850 (i.e. without package) at 915 MHz, +10 dBm input power and matched to  $50 \Omega$ .

the rectifier. The optimal matching circuit varies with the circuit input impedance, which varies with circuit input power, operating frequency, possible bias current, and temperature.

As the input reflection coefficient at the rectifier input  $\Gamma_{in}$  is dependent on the input power level  $P_g$ , its determination from diode simulations is an iterative process. An adaptive input power algorithm is implemented, obtaining a quasi conjugate impedance matched circuit simulation with a specified circuit input power level (see Algorithm 1 below). This enables an objective circuit comparison, as the matching circuit is taken out of the equation. An example of its usage is shown in Fig. 5.14.

**Algorithm 1:** Adaptive Input Power (variables in dB or dBm)

---

**Data:**  $P_{in0}$  - specified circuit input power level  
**Result:**  $P_g$  - adapted source power level to reach  $P_{in0}$  at circuit input  
with  $M_c[n]$  mismatch loss

```

1  $P_g[0] \leftarrow P_{in0};$                                 /*  $P_g$  initiation */
2  $M_c[0] \leftarrow 0 \text{ dB};$                           /*  $M_c$  initiation */
3  $\text{tol}_{M_c} \leftarrow 0.001 \text{ dB};$                 /*  $M_c$  tolerance */
4  $n \leftarrow 30;$                                      /* max iterations */

5 for  $i \leftarrow 1$  to  $n$  do
6    $(V, I)(t) \leftarrow \text{sim-circuit}(P_g[i - 1]);$       /* sim circuit */
7    $(\Gamma_{in}, M_c[i]) \leftarrow (V, I)(t);$               /* calc  $\Gamma$ ,  $M_c$  */
8    $\max_{\Delta M_c} \leftarrow 16/2^i;$                       /* max  $M_c$  step-size */
9   if  $|M_c[i] - M_c[i - 1]| > \max_{\Delta M_c}$  then
10    | if  $M_c[i] - M_c[i - 1] > 0$  then
11     | |  $M_c[i] \leftarrow M_c[i - 1] + \max_{\Delta M_c};$         /* limit  $M_c+$  step */
12    | else
13     | |  $M_c[i] \leftarrow M_c[i - 1] - \max_{\Delta M_c};$         /* limit  $M_c-$  step */
14    | end if
15   end if
16   if  $|M_c[i] - M_c[i - 1]| < \text{tol}_{M_c}$  then
17     | |  $M_c[n] \leftarrow M_c[i];$                             /* final  $M_c$  */
18     | |  $P_g[n] \leftarrow P_g[i - 1];$                          /* final  $P_g$  */
19     | | break out of for loop;
20   end if
21    $P_g[i] \leftarrow P_{in0} - M_c[i];$                       /* adapt  $P_g$  */
22 end for
```

---

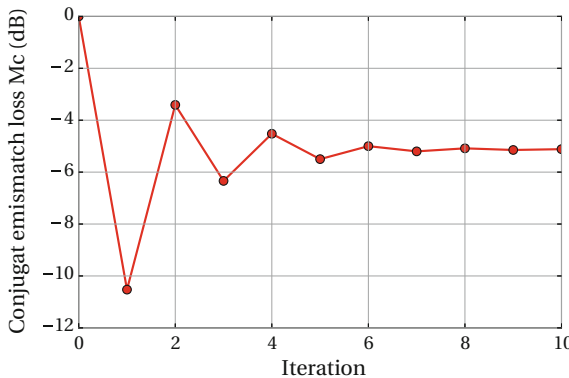


**Fig. 5.14** An example of the source power adaptation algorithm, showing simulated conjugate mismatch loss  $M_c$  against iteration number. The source power level is scaled accordingly to obtain a quasi complex conjugate matched situation. In this case,  $P_{in} = -10 \text{ dBm}$  was used with a single diode attached. Nine iterations were required to obtain a stable value (using  $\text{tol}_{M_c} = 0.001 \text{ dB}$ ), after which the result is copied to the last ( $n = 30$ ) iteration

The algorithm starts with a specified circuit input power level  $P_{in0}$ , an initial source power level  $P_g[0]$ , an initial mismatch loss  $M_c[0]$ , and the required tolerance or accuracy on  $M_c$ ,  $\text{tol}_{M_c}$ . Also the maximum number of iterations  $n$  is defined. For each iteration, the circuit is simulated with the updated source power level. The resulting voltage and current time-domain values are translated into the time-average circuit input reflection coefficient  $\Gamma_{in}$  and the time-average mismatch loss  $M_c$ . The current  $M_c$  value is compared with the previous iteration value and the maximum step-size is limited by  $\max_{\Delta M_c}$ . If the step-size is within the specified tolerance  $\text{tol}_{M_c}$  the iteration process is stopped and the resulting values are available. Otherwise the source power level is updated with the latest  $M_c$  value and a next iteration is done.

### 5.3.4 Steady-State Algorithm

The simulation work in this chapter is based on time-domain behavior, using Qucs' transient simulator. When steady-state results are required, it is important to ensure that the circuit has reached a stable state. Circuits containing capacitance and inductance models always require a certain time before reaching a steady-state situation. This duration is typically dependent on elements like the capacitance value, available signal levels, resistance values, etc.

The steady-state algorithm is used to ensure that the circuit state is close enough to a steady-state situation. This is implemented by varying the starting point in time  $T_{st}$ . The time-domain simulation produces an output voltage over a certain number of cycles, determined by the time duration  $T_d$ . The difference in the mean load voltage of the first and last cycle in this time window is  $\Delta V_L$ . This is an indication of steady-state level. If the value is not below a specified maximum tolerance  $\max_{\Delta V_L}$ , the starting point of the analysis is doubled in time. The algorithm is shown in Algorithm 2 below.

---

#### Algorithm 2: Steady-state

---

**Data:**  $\max_{\Delta V_L}$  - max load voltage variation,  $T_{st}$  - time start,  $T_d$  - time duration

**Result:**  $T_{st}$  - steady-state time start

```

1 while True do
2    $T_{sp} \leftarrow T_{st} + T_d;$                                 /* stop time */
3    $\Delta V_L \leftarrow \text{sim-circuit}(T_{st} \dots T_{sp});$       /* VL variation */
4   if  $\Delta V_L \leq \max_{\Delta V_L}$  then
5     | break out of while loop;
6   end if
7    $T_{st} \leftarrow 2T_{st};$                                     /* increase time start */
8 end while

```

---

As an example of the steady-state algorithm, Table 5.6 shows the result of simulations done using a single diode peak detector circuit.

**Table 5.6** Steady-state algorithm example, showing start time  $T_{st}$ ,  $V_L$  variation  $\Delta V_L$ , and conversion efficiency  $\eta_c$ , using a peak detector circuit at  $P_{in} = -10$  dBm and  $f_c = 915$  MHz

| $T_{st}$ (ns) | $\Delta V_L$ (V)      | $\eta_c$ (%) |
|---------------|-----------------------|--------------|
| 27.3          | $3.00 \times 10^{-2}$ | 19.725       |
| 54.6          | $9.75 \times 10^{-3}$ | 47.912       |
| 109.3         | $1.07 \times 10^{-3}$ | 69.268       |
| 218.6         | $1.30 \times 10^{-5}$ | 72.419       |
| 437.2         | $1.91 \times 10^{-6}$ | 72.461       |
| 874.3         | $9.54 \times 10^{-7}$ | 72.460       |
| 1748.6        | $1.43 \times 10^{-6}$ | 72.463       |

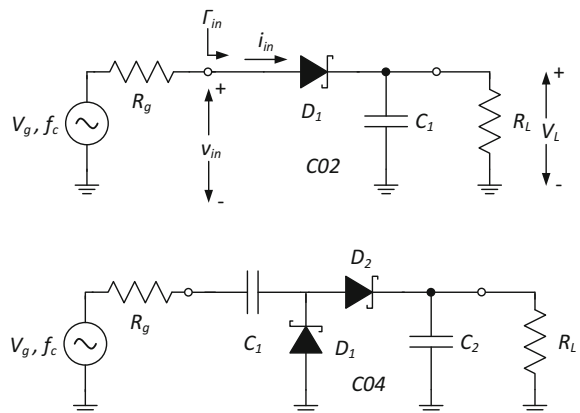
## 5.4 Comparing Topologies

The method used to compare different circuit topologies, makes use of the adaptive input power algorithm. Optimizing the load resistance at the output of the rectifier circuit, for each input power level using the time trajectory technique, ensures that proper efficiency values are calculated.

The Greinacher dual diode voltage doubler rectifying circuit topology [7] is used often in published work, for generating a higher output voltage compared to the single diode topology; both shown in Fig. 5.15. Using the obtained diode models and analysis techniques established in this work, the voltage doubler (in this work named C04) is compared to a single diode rectifier topology (named C02). Figure 5.16 shows the PCE versus input power results.

The comparison shows two things: first, a clear advantage of using the single diode C02 topology over the dual diode C04 topology. This is in line with what is previously reported in [16], where it is recommended to use a single stage rectifying circuit for low power levels. Second, the use of a Skyworks SMS7621 low  $I_s$  diode shows a better efficiency compared to the Avago HSMS-2852 diode. Combining

**Fig. 5.15** Different rectifier topologies: Single diode peak detector circuit (C02), including source and load, and Greinacher voltage doubler (C04).



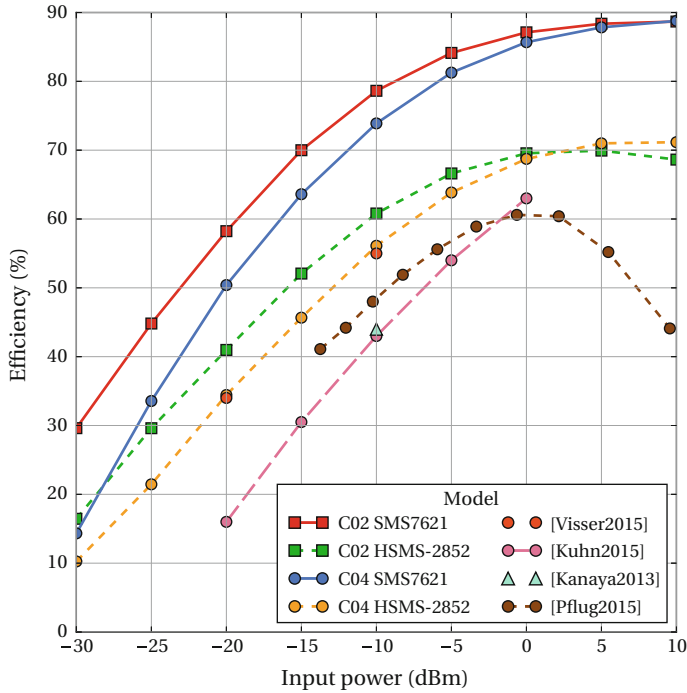


**Fig. 5.16** Comparison between the single diode C02 topology (square) and the twin diode voltage doubler Greinacher C04 topology (circle). Shown is the maximum available conversion efficiency  $\eta_c$  versus  $P_{act}$ , both for the Avago HSMS-2852 (dash) and the Skyworks SMS7621 (solid) diodes, including the SOT23 package and using the adaptive input power algorithm, with a constant envelope input signal at 915 MHz and 26.85 °C. Also shown is measured data from literature: Kanaya2013, Kuhn2015, Pflug2015, and Visser2015, [12, 13, 17, 29] with even a four diode (triangle up) configuration. The circuit in [13] uses Metelics MSS20-141 diodes (long dash). The circuits [13, 17] are 50 Ω matched at their input side, therefore showing overall efficiency  $\eta_o$  versus  $P_g$

the two elements results in an efficiency increase of 18–25 % for the SMS7621 C02 circuit over the C04 topology with the HSMS-2852 diodes, being equivalent to a increase in available power of 20–180 %. The corresponding output voltages show a factor 1.6–3.9 improvement (see Fig. 5.17a). The SMS7621 doubler circuit provides about 50 % higher output voltage for input power levels above –25 dBm, but shows less maximum available efficiency compared to the single diode version. Also shown in the figure is measured data from literature with conjugate matched topologies [12, 29] and 50 Ω matched circuits [13, 17]. The Metelics MSS20-141 diode in [13] is a 3.5 μA saturation current type, similar to the HSMS-2852. The predicted HSMS-2852 C04 PCE matches the conjugate matched measurement [29] very well. When using the data-sheet SPICE parameters with a standard  $p$ - $n$  junction diode model, the PCE is predicted about 15 % too high, mainly due to inaccurate reverse bias region modeling.

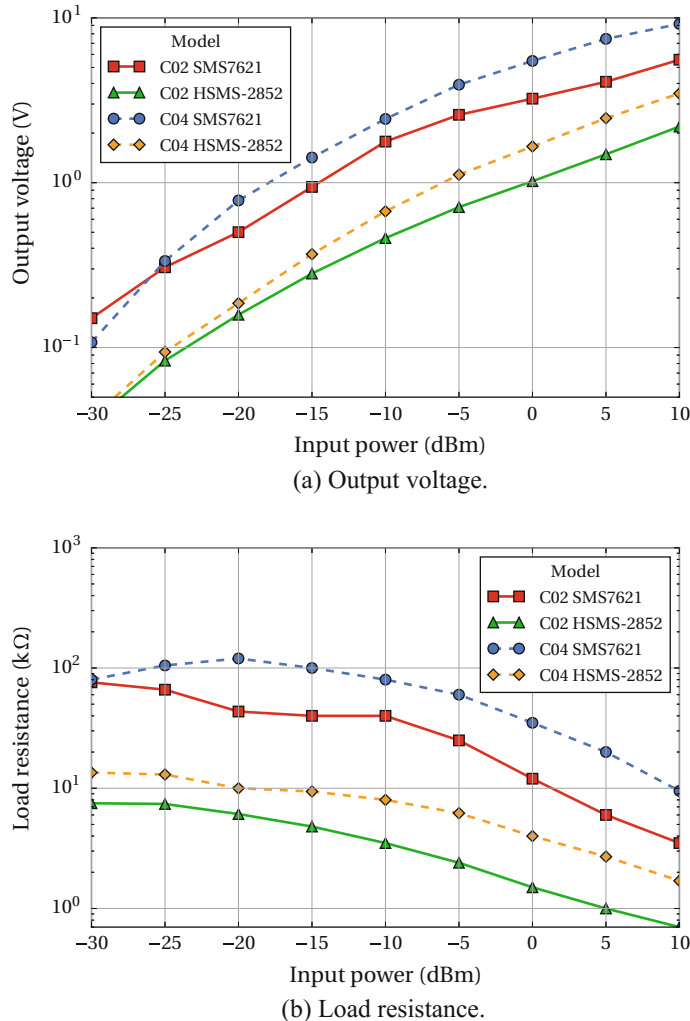


**Fig. 5.17** Comparison between the single diode C02 topology (solid) and the twin diode voltage doubler Greinacher C04 topology (dashed). Shown is the average output voltage (a) and the used load resistance  $R_L$  (b), both for the Avago HSMS-2852 (triangle/diamond) and the Skyworks SMS7621 (square/circle) diodes, including the SOT23 package and using the adaptive input power algorithm, with a constant envelope input signal at 915 MHz and 26.85 °C

In Fig. 5.17b the different optimal (for efficiency) load resistances are shown for the different topologies. The SMS7621 diode results in a roughly one order of magnitude larger resistance value compared to the HSMS-2852 diode.

### 5.4.1 Definition of Efficiency

The rectifier RF to dc power *conversion*-efficiency (PCE) can be defined as

$$\eta_c = \frac{P_{dc}}{P_{act}}, \quad (5.5)$$

with  $P_{act}$  being the RF power entering the circuit. The instantaneous power entering the circuit, can be calculated using the instantaneous voltage  $v_{in}(t)$  and current  $i_{in}(t)$  as

$$p_{in}(t) = v_{in}(t) \cdot i_{in}(t). \quad (5.6)$$

The active power  $P_{act}$  is the power entering the circuit during one period  $T$  of the input signal:

$$P_{act} = \frac{1}{T} \int_0^T p_{in}(t) dt \quad (5.7)$$

The dc power consumed from the output of the circuit is calculated from the average dc output voltage  $V_L$  as  $P_{dc} = V_L^2/R_L$ . A possible mismatch between source and circuit is not taken into account in this efficiency. Another efficiency can be defined, named the *overall*-efficiency, as

$$\eta_o = \frac{P_{dc}}{P_g}, \quad (5.8)$$

with  $P_g$  the available source power. From circuit theory [19, 28] the maximum available power from the source can be defined as

$$P_g = \frac{|V_g|^2}{8 \operatorname{Re}(Z_g)} \quad (5.9)$$

with  $V_g$  being the source voltage.<sup>1</sup> This efficiency takes into account the mismatch between source and circuit if present and therefore we can state

$$\eta_o \leq \eta_c. \quad (5.10)$$

With the adaptive source power analysis, the circuit efficiency  $\eta_c$  is used. In the input impedance matched case, the overall efficiency  $\eta_o$  makes sense to be used. As an example, for the comparison of the ‘C04 HSMS-2852’ curve in Fig. 5.16 with the impedance matched- and measured case curve [17], the  $\eta_o/\eta_c$  ratio varies between the value 0.84 at -15 dBm and 0.89 at -5 dBm, going down to 0.60 at +10 dBm. This shows that the matching network accounts for 11 % extra loss on  $\eta_c$ , being

---

<sup>1</sup>In [19, 28], rms values are used for voltages and currents. In this work, peak values are used.

optimal around an input power level of  $-5$  dBm. At lower and higher input power levels, the lower  $\eta_o/\eta_c$  values are a result of extra loss due to impedance mismatch.

Having an ideally matched rectifier circuit (perfect impedance match using a lossless matching network), the efficiency  $\eta_c$  is determined by the diode series resistance  $R_s$ , the diode junction capacitance  $C_j$  and the diode's characteristics like breakdown voltage  $BV$  and its junction potential  $\phi_0$  [27].

The practical impedance matched rectifier circuit shows an overall efficiency  $\eta_o$  with extra loss due to the nonideal matching circuit and impedance mismatch. This loss can be reduced by using a complex conjugate impedance matched antenna, which does not require the addition of a matching network.

**Acknowledgements** The authors would like to thank Shady Keyrouz of the Eindhoven University of Technology for his contribution in the validation of the time trajectory technique.

## References

1. Andreev, S., Galinina, O., Pyattaev, A., Gerasimenko, M., Tirronen, T., Torsner, J., Sachs, J., Dohler, M., Koucheryavy, Y.: Understanding the IoT connectivity landscape: a contemporary M2M radio technology roadmap. *IEEE Commun. Mag.* **53**(9), 32–40 (2015). doi:[10.1109/MCOM.2015.7263370](https://doi.org/10.1109/MCOM.2015.7263370)
2. Avago Technologies: Linear Model for Diode Surface Mount Packages. In: Application Note 1124 (2010)
3. Avago Technologies: Low Cost Surface Mount Power Limiters. In: Application Note 1050 (2010)
4. Bardeen, J.: On the theory of the A-C. Impedance of a contact rectifier. *Bell Syst. Tech. J.* **28**, 428–434 (1949)
5. Cowley, A., Sorensen, H.: Quantitative comparison of solid-state microwave detectors. *IEEE Trans. Microw. Theory Tech.* **14**(12), 588–602 (1966). doi:[10.1109/TMTT.1966.1126337](https://doi.org/10.1109/TMTT.1966.1126337)
6. Deveney, M.: A temperature dependent SPICE macro-model for Zener and avalanche diodes. In: Proceedings of the 34th Midwest Symposium on Circuits and Systems, 1991, vol. 2, pp. 592–596 (1991). doi:[10.1109/MWSCAS.1991.252092](https://doi.org/10.1109/MWSCAS.1991.252092)
7. Greinacher, H.: Das Ionometer und seine Verwendung zur Messung von Radium- und Rontgenstrahlen. *Physikalische Zeitschrift* **15**, 410–415 (1914)
8. Hemour, S., Wu, K.: Radio-frequency rectifier for electromagnetic energy harvesting: development path and future outlook. *Proc. IEEE* **102**(11), 1667–1691 (2014). doi:[10.1109/JPROC.2014.2358691](https://doi.org/10.1109/JPROC.2014.2358691)
9. Hemour, S., Zhao, Y., Lorenz, C., Houssameddine, D., Gui, Y., Hu, C.M., Wu, K.: Towards low-power high-efficiency RF and microwave energy harvesting. *IEEE Trans. Microw. Theory Tech.* **62**(4), 965–976 (2014). doi:[10.1109/TMTT.2014.2305134](https://doi.org/10.1109/TMTT.2014.2305134)
10. Hewlett Packard: Hermetic PIN Diodes for Stripline / Microstrip Switches / Attenuators. In: Technical Data 5965-8882E
11. Kamalinejad, P., Mahapatra, C., Sheng, Z., Mirabbasi, S., Leung, V., Guan, Y.L.: Wireless energy harvesting for the internet of things. *IEEE Commun. Mag.* **53**(6), 102–108 (2015). doi:[10.1109/MCOM.2015.7120024](https://doi.org/10.1109/MCOM.2015.7120024)
12. Kanaya, H., Tsukamaoto, S., Hirabaru, T., Kanemoto, D., Pokharel, R., Yoshida, K.: Energy harvesting circuit on a one-sided directional flexible antenna. *IEEE Microw. Wirel. Compon. Lett.* **23**(3), 164–166 (2013). doi:[10.1109/LMWC.2013.2246779](https://doi.org/10.1109/LMWC.2013.2246779)
13. Kuhn, V., Lahuec, C., Seguin, F., Person, C.: A multi-band stacked RF energy harvester with RF-to-DC efficiency up to 84%. *IEEE Trans. Microw. Theory Tech.* **63**(5), 1768–1778 (2015). doi:[10.1109/TMTT.2015.2416233](https://doi.org/10.1109/TMTT.2015.2416233)

14. Massobrio, G., Antognetti, P.: Semiconductor Device Modeling with SPICE. McGraw-Hill (1988)
15. Nagel, L.W., Pederson, D.: Spice (simulation program with integrated circuit emphasis). Tech. Rep. UCB/ERL M382, EECS Department, University of California, Berkeley. <http://www.eecs.berkeley.edu/Pubs/TechRpts/1973/22871.html> (1973)
16. Nintanavongsa, P., Muncuk, U., Lewis, D., Chowdhury, K.: Design optimization and implementation for RF energy harvesting circuits. *IEEE J. Emerg. Sel. Topics Circuits Syst.* **2**(1), 24–33 (2012). doi:[10.1109/JETCAS.2012.2187106](https://doi.org/10.1109/JETCAS.2012.2187106)
17. Pflug, H.W., Visser, H.J., Keyrouz, S.: Practical applications of radiative wireless power transfer. In: Wireless Power Transfer Conference (WPTC), 2015 IEEE, pp. 1–4. doi:[10.1109/WPTC.2015.7140131](https://doi.org/10.1109/WPTC.2015.7140131) (2015)
18. Qucs homepage: <http://qucs.sourceforge.net/>. [Online] <http://qucs.sourceforge.net/> (2015)
19. Rahola, J.: Power waves and conjugate matching. *IEEE Trans. Circuits Syst. II: Express Briefs* **55**(1), 92–96 (2008). doi:[10.1109/TCSII.2007.905420](https://doi.org/10.1109/TCSII.2007.905420)
20. Roberg, M., Reveyrand, T., Ramos, I., Falkenstein, E., Popovic, Z.: High-efficiency harmonically terminated diode and transistor rectifiers. *IEEE Trans. Microw. Theory Tech.* **60**(12), 4043–4052 (2012). doi:[10.1109/TMTT.2012.2222919](https://doi.org/10.1109/TMTT.2012.2222919)
21. Russell, H.T.: The SPICE Diode Model (1991). Chapter 3 from Rectifier Applications Handbook, Motorola
22. Schottky, W.: Vereinfachte und erweiterte Theorie der Randschichtgleichrichter. *Zeitschrift für Physik* **118**(9–10), 539–592 (1942)
23. Shockley, W.: The theory of p-n junctions in semiconductor and p-n junction transistors. *Bell Syst. Tech. J.* **28**, 435–489 (1949)
24. Sze, S.M.: Physics of Semiconductor Devices. Wiley (1969)
25. Torrey, H., Whitmer, C.: Crystal Rectifiers. McGraw-Hill (1948)
26. van Rossum, G.: Python website. <https://www.python.org/>. [Online] <https://www.python.org/>
27. Valenta, C.R., Durgin, G.D.: Harvesting wireless power: survey of energy-harvester conversion efficiency in far-field, wireless power transfer systems. *IEEE Microw. Mag.* **15**(4), 108–120 (2014). doi:[10.1109/MMM.2014.2309499](https://doi.org/10.1109/MMM.2014.2309499)
28. Vendelin, G.D., Pavio, A.M., Rohde, U.L.: Microwave Circuit Design Using Linear and Non-linear Techniques, 1st edn. Wiley-Interscience (1992)
29. Visser, H.J., Keyrouz, S., Smolders, A.B.: Optimized rectenna design. *Wirel. Power Transf.* **2**, 44–50 (2015). doi:[10.1017/wpt.2014.14](https://doi.org/10.1017/wpt.2014.14)
30. Visser, H.J., Vullers, R.J.M.: RF energy harvesting and transport for wireless sensor network applications: principles and requirements. *Proc. IEEE* **101**(6), 1410–1423 (2013). doi:[10.1109/JPROC.2013.2250891](https://doi.org/10.1109/JPROC.2013.2250891)
31. Vladimirescu, A.: The SPICE Book. Wiley (1994)
32. Wong, S., Hu, C.M.: SPICE macro model for the simulation of zener diode I-V characteristics. *IEEE Circuits Devices Mag.* **7**(4), 9–12 (1991). doi:[10.1109/101.134564](https://doi.org/10.1109/101.134564)
33. Yi, J., Ki, W.H., Tsui, C.Y.: Analysis and design strategy of UHF micro-power cmos rectifiers for micro-sensor and RFID applications. *IEEE Trans. Circuits Syst. I: Regul. Pap.* **54**(1), 153–166 (2007). doi:[10.1109/TCSI.2006.887974](https://doi.org/10.1109/TCSI.2006.887974)

# Chapter 6

## Unconventional Waveform Design for Wireless Power Transfer

Alirio Boaventura, Nuno Borges Carvalho and Apostolos Georgiadis

**Abstract** Continuous wave RF signals have been traditionally used in wireless power transmission systems. This chapter considers RF signals with a time varying envelope and specifically multi-sine signals, and investigates the effect on the obtained RF-dc conversion efficiency of wireless power transmission. The time-varying envelope characteristic of such signals leads to a peak-to-average-power ratio (PAPR) greater than 1 (0 dB) and can have a profound effect in the RF-dc conversion efficiency performance. The chapter begins with a presentation of typical RF-dc converter circuits and modeling of the nonlinear rectifier circuit used to convert RF power in dc electrical power. A description of multi-sine signals and their characteristics is then provided, followed by a theoretical analysis of the rectification process of such signals. Finally, a circuit rectifier prototype is presented and measurements of the RF-dc conversion efficiency are shown demonstrating the fact that it is possible under certain load conditions to obtain an improved efficiency performance over continuous wave signals of the same average power, which increases with higher PAPR.

### 6.1 Introduction

Traditionally, WPT has been carried out using constant envelope continuous wave (CW) signals. However, it has been shown recently that high peak-to-average-power (PAPR) waveforms can improve the efficiency of existing rectifying circuits,

---

A. Boaventura (✉) · N.B. Carvalho  
Instituto de Telecomunicacoes, Universidade de Aveiro, Aveiro, Portugal  
e-mail: a34422@ua.pt

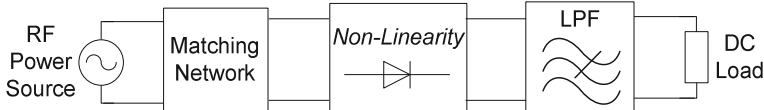
N.B. Carvalho  
e-mail: nbcarvalho@ua.pt

A. Georgiadis  
School of Engineering and Physical Sciences, Institute of Sensors, Signals and Systems,  
Heriot-Watt University, Edinburgh EH14 4AS, UK  
e-mail: apostolos.georgiadis@ieee.org

especially at low average power levels. This can potentially increase the reading range of passive-backscatter systems. Curiously, the first electromagnetic signals successfully generated, transmitted and detected by Heinrich Hertz were damped waveforms with nonconstant envelope [11], which were utilized for many years in wireless telegraphy and also in some wireless power transfer (WPT) experiments conducted by Tesla [17]. However, due to large spectrum occupancy, dumped waves were banned later and were replaced with CW signals (first generated by Ernst Alexanderson in 1902 [12]) which have been adopted for power transfer since Brown's microwave power transmission (MPT) experiments in the 1960s. The theoretical analysis of CW radio path shows that, unlike conventional wireless communication systems, which are mainly limited by noise and receiver sensitivity, passive-backscatter systems are primarily limited by the downlink power, i.e., in radio frequency identification (RFID) systems the reader-to-transponder energy transfer. This was theoretically predicted in [13, 16], and confirmed by practical experiments in [9], where a far RFID listener device was used to capture the signal backscattered from a tag while being interrogated by a closer principal RFID reader. In that experiment, the RFID listener was able to receive and decode the uplink/backscattered signal 35 m away from the tag, a distance well beyond the maximum attainable range of current RFID systems (up to 10 m). This shows that the more stringent limitation on range is in fact imposed by downlink. A closer look reveals that the downlink limitation lies on the reduced RF-dc conversion efficiency of existing energy harvesting circuits at low power level regime. Because Schottky diodes and CMOS devices commonly used in rectifier circuits exhibit a nonzero turn-on voltage, a certain amount of energy is needed to overcome the electrical barrier of the device and thereby the RF-dc conversion efficiency at low input power levels is degraded. In order to maximize the RF-dc conversion efficiency, circuit level optimization is conventionally carried out. Alternatively, the RF-dc conversion efficiency can be boosted by selecting properly formatted waveforms, such as high PAPR in-phase multi-sine (MS) signals, that are capable of efficiently surpassing the turn-on voltage of rectifying devices at low average power levels. A survey on the use non-conventional waveforms for WPT, including chaotic signals, intermittent CW, ultra-wideband (UWB) signals, multi-carrier signals, harmonic signals, modulated signals and white noise is presented in [3].

## 6.2 RF-dc Power Conversion Basics

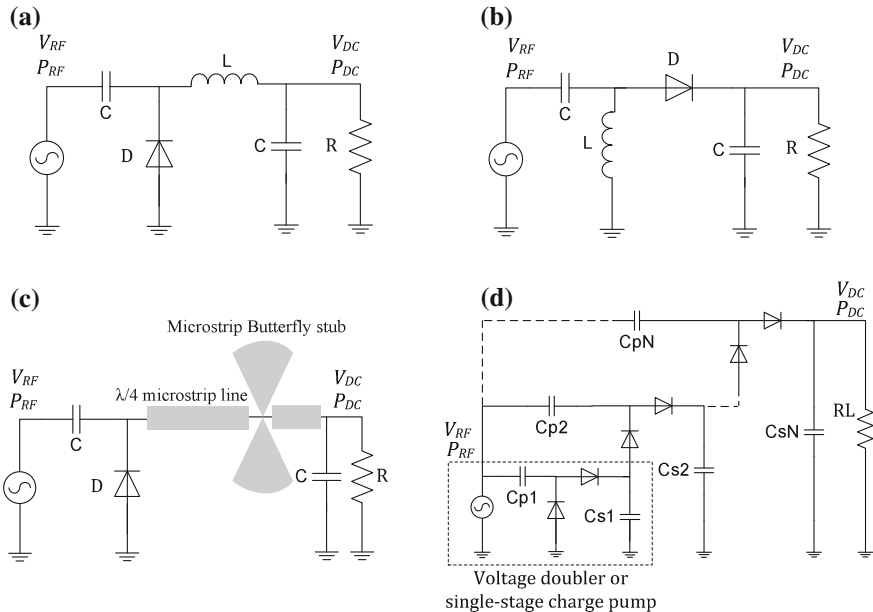
Figure 6.1 depicts the block diagram of an RF-dc converter system, composed of an RF power source, a matching circuit to allow maximum power transference, a nonlinear rectifying device, that is the main component of the circuit, followed by a low-pass filter and a dc load. The nonlinear device transforms the input AC signal at frequency  $f_0$  into a dc component plus fundamental and harmonic components:  $y_{out} = NL[x_{in}] = Y(dc) + Y(f_0) + Y(2f_0) + Y(3f_0) + \dots + Y(nf_0)$ . In order to select only the dc component, a low-pass filter is used to remove the ac components of the rectified signal.



**Fig. 6.1** Basic blocks of an RF–dc conversion circuit

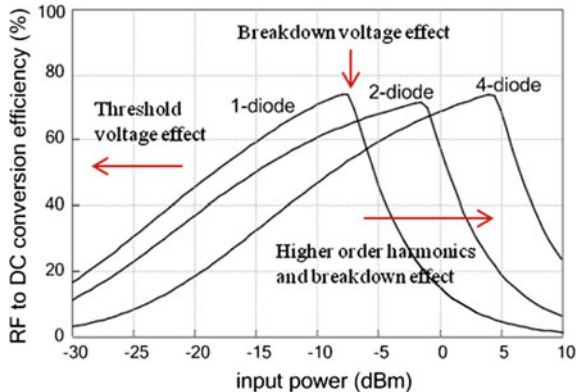
### 6.3 Typical RF–dc Converter Topologies

Figure 6.2 depicts the most popular harvester topologies, namely the shunt diode rectifier (Fig. 6.2a), the series diode rectifier (Fig. 6.2b), and the  $N$ -stage Dickson voltage multiplier or charge pump (Fig. 6.2d) [10]. Charge pumps are typically employed in passive RFID tags and single diode rectifiers, especially the microwave version of the shunt rectifier, are commonly used for EM ambient energy harvesting and MPT applications. The voltage doubler or single-stage charge pump (dashed circuit in Fig. 6.2d), which is the cell unit of a Dickson charge pump, is composed of a pumping capacitor at the input, a shunt diode, a series diode and a storage capacitor at the output. It operates as follows: when the capacitors are uncharged and the input signal with peak amplitude  $V_p$  is in the negative cycle, the series diode is cut and the pumping capacitor is charged with a voltage  $-V_p$  through the shunt diode; when



**Fig. 6.2** Typical energy harvesting circuit topologies. **a** Shunt diode rectifier. **b** Series diode rectifier. **c** Shunt diode rectifier using microstrip  $\lambda/4$  stubs. **d**  $N$ -stage Dickson voltage multiplier

**Fig. 6.3** Typical efficiency curves of different rectifying circuits



the input waveform swings to its positive cycle, the shunt diode is cut, the series diode conducts, and the peak amplitude of the input signal,  $+V_p$ , is summed to the pre-charged voltage, yielding a voltage of  $2V_p$  in the output storage capacitor. The charge pump has a similar operation, being the dc output of each voltage doubler stage used as a reference level for the next stage, such that the maximum voltage at the output of the  $N$ -th stage is given by  $(2N - 1)(V_p - 2V_D)$ , where  $N$  is the number of stages,  $V_p$  is the peak amplitude of the AC signal and  $V_D$  is the voltage drop in the diodes. Typical efficiency curves of different RF–dc converter circuits are presented in Fig. 6.3, from which two main conclusions can be drawn. First, the efficiency depends on the selected circuit topology, and the lower the number of devices, the higher the efficiency. This is explained because of the need for a minimum amount of input power to switch on the rectifying devices and also due to the increase in parasitic losses as the number of devices increases. Nevertheless, the higher the number of stages, the higher the collected dc voltage. For this reason, charge pumps are used in RFID tags to boost the output dc to a level compliant with tag electronics. Second, the efficiency depends on the available power at the input of the circuit: for low power levels the efficiency is low because the rectifying device is not completely switched on. As the input power increases the efficiency increases and reaches a maximum value right before the input amplitude reaches the diode breakdown voltage. After this point, diode reverse current starts to be significant and the efficiency starts to drop. Losses due to higher order harmonics also increase with the increase in the input power level.

## 6.4 Rectifying Device Characterization and Modeling

The Schottky diode is the key component of many rectifying circuits. Its circuit model (Fig. 6.4) comprehends a nonlinear junction current source  $i_j(v_j)$ , shunted by a nonlinear junction capacitance  $C_j(v_j)$  and a series parasitic resistance  $R_S$ . Packaged diodes also include a parasitic package capacitance ( $C_p$ ) and inductance ( $L_p$ ).

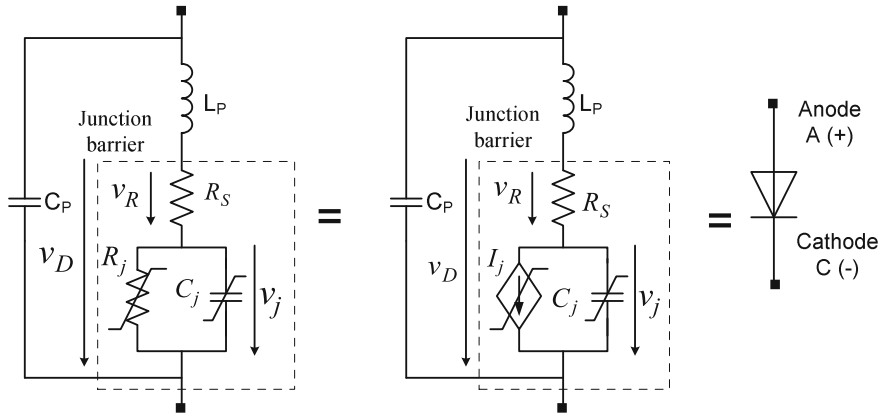


**Fig. 6.4** Physical model of a Schottky diode

The nonlinear forward and reverse breakdown I–V characteristics ( $I_f$  and  $I_{br}$ ) of the junction barrier can be described respectively by (6.1) [14] and (6.2) [1], and the total diode current is given by (6.3).

$$I_f = I_s (e^{\frac{qV_j}{\eta kT}} - 1) = I_s (e^{\frac{V_j}{\eta V_t}} - 1) = I_s (e^{\frac{V_d - R_s I_f}{\eta V_t}} - 1) \quad (6.1)$$

$$I_{br} = I_{BV} e^{-\frac{V_j + V_{br}}{V_t}} = -I_{BV} e^{\frac{V_d - R_s I_f + V_{br}}{\eta V_t}} \quad (6.2)$$

$$I_D = I_f + I_{br} \quad (6.3)$$

where  $I_s$  is the diode reverse saturation current,  $k = 1.3806488 \times 10^{-23} \text{ m}^2 \text{ kg s}^{-2} \text{ K}^{-1}$  is the Boltzmann constant,  $V_t = kT/q$  is the thermal voltage ( $\approx 26 \text{ mV}$  @ room temperature),  $T$  is the junction temperature in Kelvin (room temperature = 298 K),  $q = 1.60217657 \times 10^{-19} \text{ Cb}$  is the electron charge,  $\eta$  is the diode ideality factor, used to model imperfections in the junction,  $V_j$  is the voltage across the junction barrier, which is equal to an external voltage applied to the diode,  $V_D$ , minus the voltage drop in the parasitic series resistor  $R_s$ ,  $V_{bi}$  is the built-in junction potential,  $V_{br}$  is the reverse breakdown voltage and  $I_{BV}$  is the breakdown saturation current. Figure 6.5 shows the typical I–V characteristic curve described by Eqs. (6.1)–(6.3). According to (6.1), at low forward (positive) current, the voltage drop across the parasitic series resistance is insignificant and the diode behavior is dominated by the nonlinear resistance of the Schottky barrier. At very high positive bias levels, the ohmic resistance  $R_s$  dominates, and the I–V curve assumes a linear relationship. For negative bias levels above the breakdown voltage, the exponential terms in (6.1) and (6.2) are negligible and the total diode current (6.3) approximates a constant value equal to  $-I_s$ . Below the breakdown voltage, Eq. (6.2) governs the diode behavior. Depending on the input power level, the zero-bias Schottky detector operates in dif-

**Fig. 6.5** Typical dc I–V curve of a Schottky diode and respective operating regions

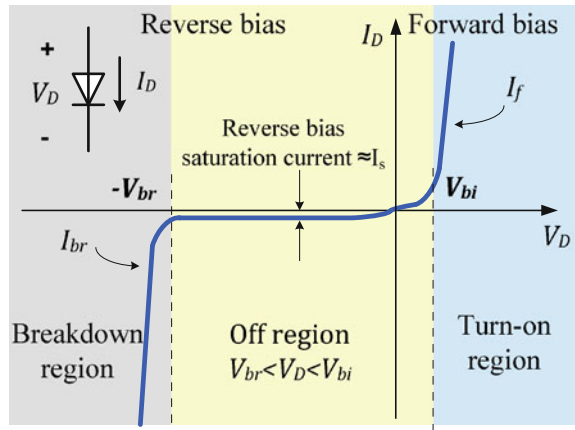
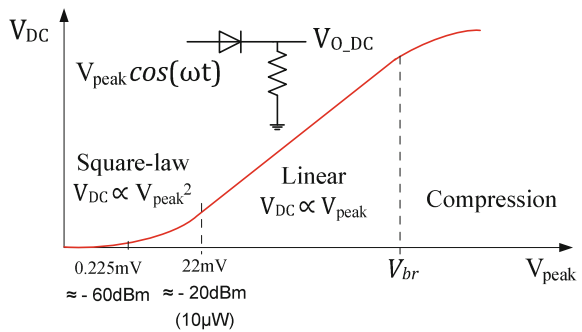


**Fig. 6.6** Typical RF–dc characteristic of a detector circuit, illustrating the operation in square-law, linear and compression regions



ferent regimes as illustrated in Fig. 6.6: at very low power level (typically bellow  $-20\text{ dBm}$ ,  $20\text{ mV}$ ), the diode operates in the square-law region where it produces an average dc output proportional to the average input power [19]. Above  $0\text{ dBm}$  ( $> 300\text{ mV}$ ), the diode enters into forward conduction in each positive cycle of the carrier, and the peak RF voltage is held by the output smoothing capacitor (see Fig. 6.7a). In this regime, known as linear, the rectifier behaves as a peak or envelope detector, and the output dc is proportional to the input peak amplitude minus the voltage drop across the diode. The region between  $-20$  and  $0\text{ dBm}$  is said to be a transition region. At very high input power levels, the dc output compresses due to the breakdown effect (described next).

## 6.5 CW Envelope Detection

The rectification of a single RF carrier in an envelope detector (linear regime) is illustrated in Fig. 6.6: in the positive cycle of the input signal  $v_i(t)$ , whenever the

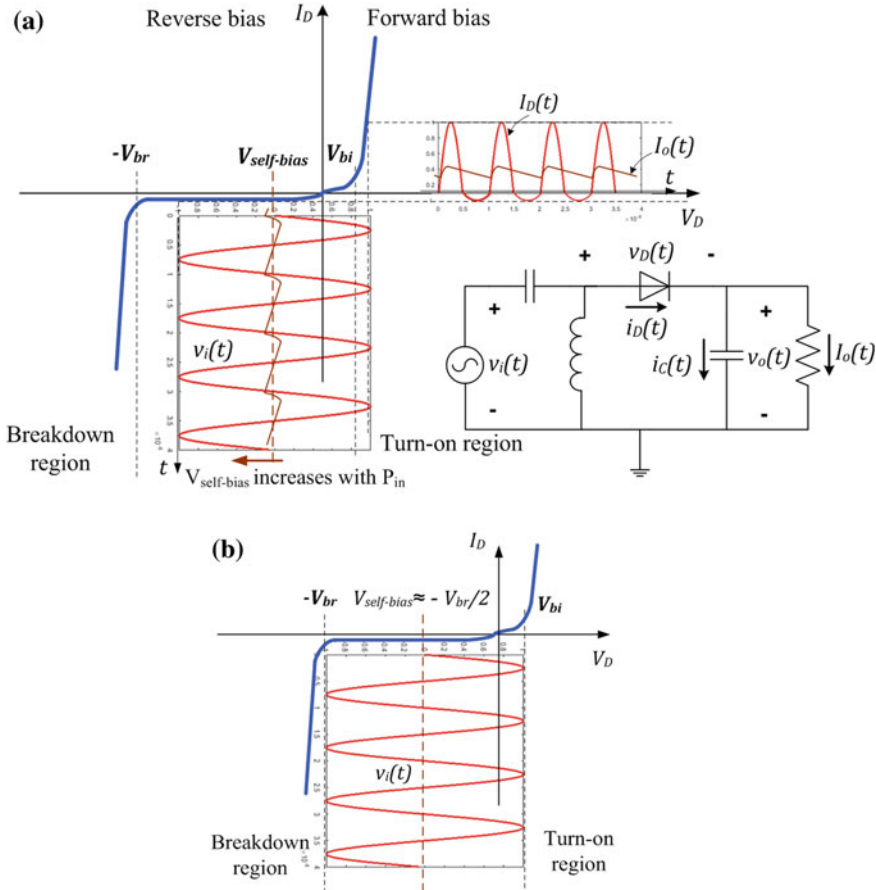


**Fig. 6.7** **a** Illustration of single-carrier rectification in a series diode detector. **b** Breakdown effect

total signal across the diode  $v_D(t)$  (input signal minus the generated dc output) is larger than the diode turn-on voltage ( $v_D(t) > V_{bi}$ ), the output capacitor is charged through the diode and the peak RF voltage (minus the drop in the diode) is held by the output smoothing capacitor. In the negative cycles of the input signal ( $v_D(t) < V_{bi}$ ), the charge stored in the output capacitor bleeds thorough the load resistance. The low-pass filter, formed of the output capacitor and load resistance, ideally filters out all the RF components generated in the rectification process, allowing only the dc component to reach the load.

### 6.5.1 Self-biasing and Breakdown Effects

Although the rectifying devices used in WPT applications are not intentionally biased (since a local dc source is not available in battery-less applications), diode rectifiers present a self-biasing mechanism via the dc voltage collected from the RF signal. Initially, the output capacitor is uncharged, the diode is zero-biased and the total signal  $V_D(t)$  applied to the diode is solely due to the input signal  $v_i(t)$ . When the input signal satisfies the turn-on condition, the output capacitor starts charging and the total voltage applied to the diode becomes equal to  $v_D(t) = v_i(t) + V_{self-bias}$ , where  $V_{self-bias}$  is the self-bias voltage, which is given by the mean value of the signal across the diode (6.4):

$$V_{self-bias} = \langle v_D(t) \rangle = \frac{1}{2\pi} \int_0^{2\pi} (v_i - V_{DC}) d\phi = -V_{DC} \quad (6.4)$$

where the operator  $\langle \rangle$  denotes the average over time, and  $V_{DC}$  is the output dc voltage produced by the rectifier. Note that the diode is biased with a voltage symmetrical to its own generated dc.

If the turn-on condition maintains ( $v_i(t) + V_{self-bias} > V_{bi}$ ) and the input signal continue to increase, then the dc output and thereby the self-bias will continue to increase (Fig. 6.7). Once the amplitude of the signal across the diode reaches the diode threshold voltage  $V_{br}$ , a significant amount of reverse current will start to flow through the diode in the negative cycles of the input signal, which contributes to decrease the average current across the diode and to degrade the RF–dc efficiency as the input signal increases (see Fig. 6.7). From this point on, regardless of any increase in the input signal, the generated dc voltage will be fixed to a maximum value of approximately  $V_{br}/2$ . Therefore, the maximum dc power produced by a single diode rectifier is limited by (6.5).

$$P_{DC\_MAX} = \frac{V_{br}^2}{4R_L} \quad (6.5)$$

## 6.6 High PAPR Signal Rectification

High PAPR waveforms are able to enhance the RF–dc conversion efficiency of energy harvesting circuits, especially at low input power level. This is due to their greater ability to overcome the built-in potential of the rectifying devices when compared to constant envelope CWs. In order to evaluate the impact of the high PAPR feature in an envelope detector circuit, an analytical-numerical model [based on the diode equations (6.1)–(6.3)] is derived in [2]. The model uses a pulsed signal with a variable amplitude and duty-cycle to mimic a general high PAPR signal. Given the input signal amplitude and duty-cycle (which determine the signal's PAPR) and the diode parameters, the model was used to predict the output dc voltage, RF–dc conversion

efficiency and efficiency gain, as functions of input average power and PAPR. The following general conclusions concerning high PAPR signals were drawn from the preliminary model results in [2]:

- (1) At low power levels, as the PAPR increases, the RF–dc conversion efficiency increases, which is attributed to the greater ability to overcome the built-in potential of the diode.
- (2) For higher power levels, however, the increase in PAPR degrades the efficiency. This effect is due to an increased voltage drop across the diode series resistance and consequent resistive loss.
- (3) Moreover, as the PAPR increases, the breakdown is reached earlier and the maximum efficiency is significantly decreased. In the next experiments, the high PAPR feature is achieved by constructively summing several sinusoidal carriers to form a time-domain waveform with high peaks and low average power level. The rectification of such MS signal is discussed in the next section. Although the model presented in [2] considers a general high PAPR signal, the conclusions drawn from that model are also valid for high PAPR MS signals.

## 6.7 Using Multi-sines for Wireless Power Transfer

### 6.7.1 MS Signal Definition

A MS signal results from the sum of several sine waves each with a given amplitude, phase and frequency. In order to create a high PAPR signal, the sine waves must be constructively combined in phase. In this case, the higher the number of subcarriers, the higher the PAPR and the higher the signal bandwidth. A MS signal can be expressed in the time-domain as

$$S_{MS}(t) = \sum_{n=1}^N V_n e^{j[(\omega_{min} + (n-1)\Delta\omega)t + \phi_n]} \quad (6.6)$$

where  $V_n$ ,  $\omega_{min} + (n-1)\Delta\omega$ , and  $\phi_n$  are respectively the amplitude, frequency and phase of the individual subcarriers,  $\omega_{min}$  is the lowest frequency component,  $N$  is the number of subcarriers, and  $\Delta\omega$  is the frequency spacing between them. The total signal bandwidth, the maximum peak amplitude ( $V_{peakMAX}$ ), the peak and average power, and the maximum PAPR of the MS signal are affected by the number of subcarriers, their amplitudes, phases and frequency spacing, and are given respectively by:

$$B_\omega = (N - 1)\Delta\omega$$

$$V_{peakMAX} = NV_n$$

$$\begin{aligned}
 P_{peak} &= \frac{1}{R_L} N^2 V_n^2 \\
 P_{AV} &= \frac{1}{2R_L} N V_n^2 \\
 PAPR &= \frac{P_{peak}}{P_{AV}} = 2N \Rightarrow PAPR(dB) = 10 \log_{10}(2N)
 \end{aligned} \tag{6.7}$$

It may be convenient to design the MS with the same average power as a given CW signal. This can be done by making  $V_1 \dots V_N = V_{CW}/\sqrt{N}$ , where  $V_{CW}$  is the peak amplitude of the CW signal and  $N$  is the number of subcarriers of the MS signal. The top of Fig. 6.8 shows a 4-tone MS signal with a random phase arrangement (left) and a 4-tone MS with 0 phase arrangement overlapped with an average power-equivalent CW (right). The respective frequency spectra are depicted on the bottom of Fig. 6.8. Notice the higher peak amplitudes of the MS in the time-domain waveform, which implies the spreading of the spectrum with respect to a CW with the same average power. Note also that, although the 0 phase arrangement provides the highest PAPR, the random phase arrangement is still overpassing the CW in terms of PAPR.

### 6.7.2 Multi-sine Rectification

The rectification of a high PAPR MS signal is illustrated in Fig. 6.9. In comparison with a CW signal with the same average power, the high PAPR MS signal provides higher time-domain peaks. As a consequence, for low average power levels, the MS can more easily overpass the device turn-on voltage and force it into a more efficient regime than a CW with the same average power would do.

### 6.7.3 Memoryless Model to Describe MS RF–dc Conversion

In the forthcoming analysis, the Schottky diode current is approximated by a memoryless Taylor polynomial expansion around a quiescent bias point ( $V_{bias}, I_{bias}$ ) as done in [4]. Although simple, this model is useful to understand the general nonlinear behavior of the rectifier under CW and MS signals, and also to assess the impact of MS parameters such as phase arrangement. The current across the diode is given by:

$$i_D(t) \approx \sum_{i=0}^N k_i (u_D(t) - V_{bias})^i = \sum_{i=0}^N k_i (u_i(t) - u_o(t) - V_{bias})^i \tag{6.8}$$

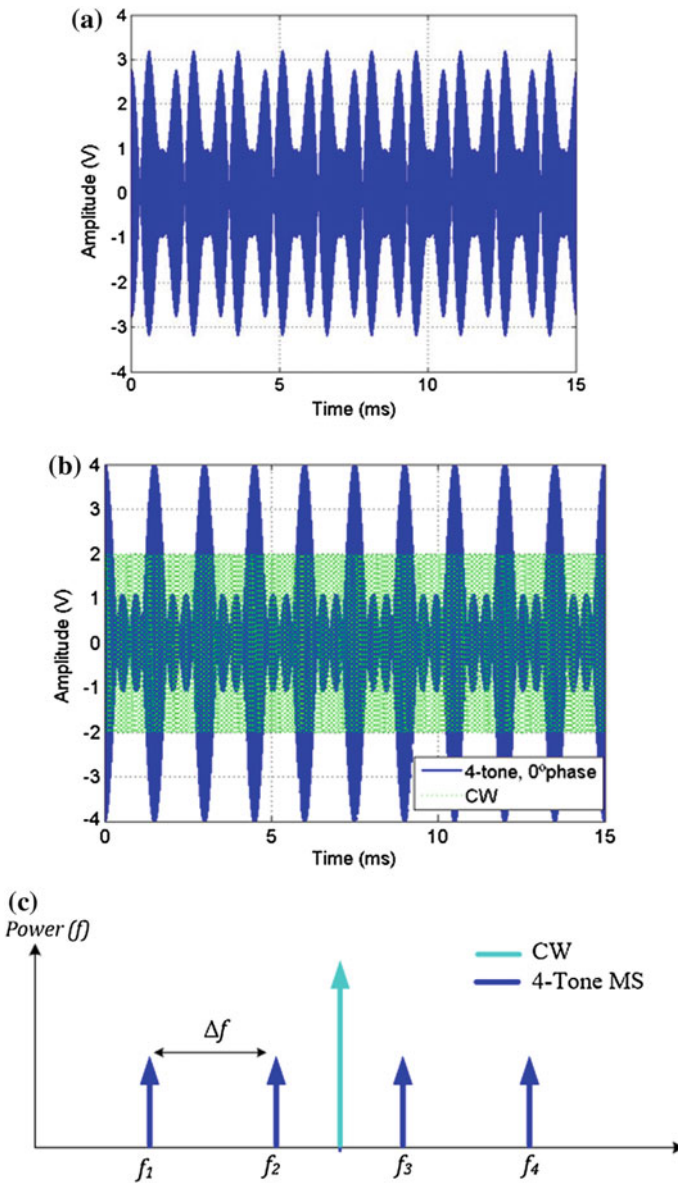


**Fig. 6.8** **a** Time-domain waveform of a 4-tone MS with random phase arrangement. **b** 4-tone MS with 0 phase arrangement (blue signal) overlapped with a CW with same average power (green signal). **c** frequency spectrum of a CW and MS signal

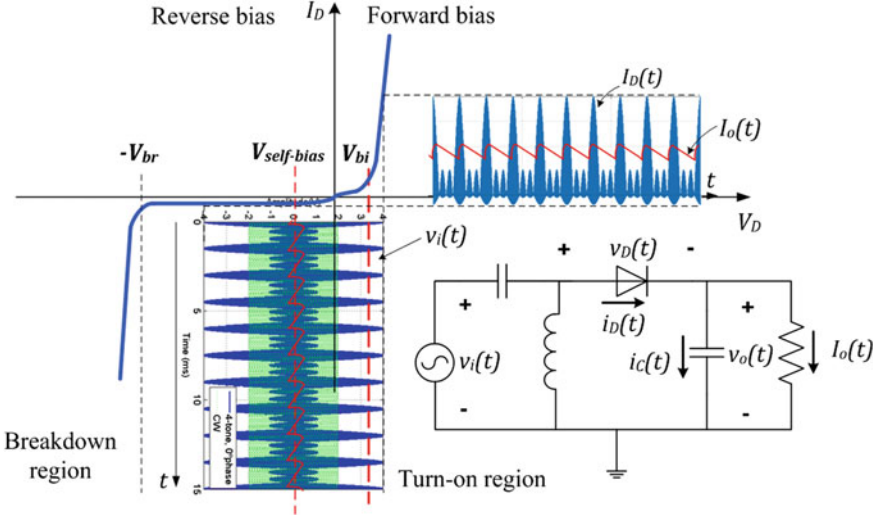


**Fig. 6.9** CW (green signal) versus MS (blue signal) rectification

where  $v_D(t) = v_i(t) - v_o(t)$ , the bias point is taken as the self-bias voltage as given by Eq. (6.4), and  $k_0, k_1, \dots, k_N$  are the coefficients of the Taylor model, which are obtained from the successive derivatives of the diode current with respect to the diode voltage, taken at the bias point [14]:

$$k_0 = I_{bias} = I_S(e^{\frac{V_{bias}}{\eta V_t}} - 1); \dots; k_i = \frac{1}{i!} \frac{\partial^i I_D}{\partial V_D^i} |_{V_D=u_{bias}} = \frac{I_S}{i!} \frac{e^{\frac{V_{bias}}{\eta V_t}}}{(\eta V_t)^i} \quad (6.9)$$

By assuming that the output capacitor is high enough such that the steady-state output voltage is constant [ $v_o(t) = V_{dc}$ ], and by taking the self-bias quiescent point ( $V_{bias} = -V_{dc}$ ), it follows that,

$$i_D(t) = I_S(e^{\frac{-V_{dc}}{\eta V_t}} - 1) + \frac{I_S}{1!} \frac{e^{\frac{-V_{dc}}{\eta V_t}}}{(\eta V_t)^1} u_i(t) + \frac{I_S}{2!} \frac{e^{\frac{-V_{dc}}{\eta V_t}}}{(\eta V_t)^2} u_i^2(t) + \dots + \frac{I_S}{3!} \frac{e^{\frac{-V_{dc}}{\eta V_t}}}{(\eta V_t)^3} u_i^3(t) + \frac{I_S}{4!} \frac{e^{\frac{-V_{dc}}{\eta V_t}}}{(\eta V_t)^4} u_i^4(t) + \dots + \frac{I_S}{i!} \frac{e^{\frac{-V_{dc}}{\eta V_t}}}{(\eta V_t)^i} u_i^i(t) \quad (6.10)$$

For finding the output dc using the model (4.10), only the even order terms are considered ( $i = 0, 2, 4, 6 \dots$ ), as the odd order ones do not contribute to the dc component. Considering the first even terms up to the fourth order, and exciting the system (6.10) with a single tone signal with frequency  $\omega_1$ , amplitude  $V_A$  and phase  $\phi_1$ ,

$$u_i(t) = V_A \cos(\omega_1 t + \phi_1) \quad (6.11)$$

the following output current is produced:

$$\begin{aligned} i_D(t) = & k_0 + \frac{1}{2}V_A^2k_2 + \frac{3}{8}V_A^4k_4 + \dots \\ & \frac{1}{2}V_A^2k_2 \cos(2\omega_1 t + 2\phi_1) + \frac{1}{2}V_A^4k_4 \cos(2\omega_1 t + 2\phi_1) + \frac{1}{8}V_A^4k_4 \cos(4\omega_1 t + 4\phi_1) \end{aligned} \quad (6.12)$$

Recalling the assumption of constant dc output imposed by the output low-pass filter, the current components at RF frequencies, namely at  $\omega_1$  and  $4\omega_1$ , are eliminated, and the remaining term is a pure dc component that gives the average value of the diode current:

$$I_{DC} \approx k_0 + \frac{1}{2}V_A^2k_2 + \frac{3}{8}V_A^4k_4 = \frac{V_{DC}}{R_L} \quad (6.13)$$

At low power regime (square-law), the second order term  $k_2$  dominates, and the output dc can be approximated by  $1/2V_A^2k_2$ , which provides power information since it is proportional to the square of the input amplitude. This is the key rule for average power measurements at low power levels. Now, in order to evaluate the system (6.10) under MS excitation, consider an evenly spaced 4-tone MS signal (6.14) whose individual subcarriers have amplitudes  $V_1 = V_2 = V_3 = V_4 = V_B$ , relative phases  $\phi_1$ ,  $\phi_2$ ,  $\phi_3$  and  $\phi_4$ , and evenly spaced frequencies  $\omega_1$ ,  $\omega_2 = \omega_1 + \Delta\omega$ ,  $\omega_3 = \omega_1 + 2\Delta\omega$  and  $\omega_4 = \omega_1 + 3\Delta\omega$ , where  $\Delta\omega$  is a constant subcarrier frequency spacing:

$$u_i(t) = V_B \cos(\omega_1 t + \phi_1) + V_B \cos(\omega_2 t + \phi_2) + V_B \cos(\omega_3 t + \phi_3) + V_B \cos(\omega_4 t + \phi_4) \quad (6.14)$$

Substituting (6.14) in (6.10), and after low-pass filtering, the following output dc component is obtained:

$$\begin{aligned} I_{DC}(\phi_1, \phi_2, \phi_3, \phi_4) \approx & k_0 + \frac{1}{2}(4V_B^2k_2 + 21V_B^4k_4 + 3V_B^4k_4 \cos(2\phi_3 - \phi_2 - \phi_4) + \dots \\ & 3V_B^4k_4 \cos(-2\phi_2 + \phi_1 - \phi_2) + 6V_B^4k_4 \cos(\phi_1 - \phi_2 - \phi_3 - \phi_4)) \end{aligned} \quad (6.15)$$

In order to set MS signal to be the same average power as the single-carrier, we make  $V_B = V_A/\sqrt{N}$ , where  $N = 4$  is the number of tones. Accordingly, (6.15) can be rewritten as:

$$\begin{aligned} I_{DC}(\phi_1, \phi_2, \phi_3, \phi_4) \approx & k_0 + 0.5V_A^2k_2 + 0.65625V_A^4k_4 + \dots \\ & 0.09375V_A^4k_4 \cos(2\phi_3 - \phi_2 - \phi_4) + \dots \\ & 0.09375V_A^4k_4 \cos(-2\phi_2 + \phi_1 - \phi_2) + \dots \\ & 0.1875V_A^4k_4 \cos(\phi_1 - \phi_2 - \phi_3 - \phi_4) \end{aligned} \quad (6.16)$$

The following conclusions can be drawn from the previous analysis:

- (1) The phase-independent component in (6.16) is greater than (6.13).
- (2) The phase-dependent term can be maximized by choosing an optimal phase arrangement.
- (3) Considering the same input average power for the CW and MS signals, (6.16) provides a higher output dc level than that provided by (6.13), guaranteed that (2) is fulfilled.

#### **6.7.4 Waveform Optimization: MS Phase Arrangement Optimization**

In order to maximize (6.16), the arguments of all the three cosines must be simultaneously set to zero.

$$\begin{aligned} Arg1 &= 2\phi_3 - \phi_2 - \phi_4 \\ Arg2 &= -2\phi_2 + \phi_1 - \phi_2 \\ Arg3 &= \phi_1 - \phi_2 - \phi_3 - \phi_4 \end{aligned} \quad (6.17)$$

As stated in [4], the most trivial phase arrangement that equals equations (6.17) to zero and maximizes equation (6.16) is  $\phi_1 = \phi_2 = \phi_3 = \phi_4 = 0$ . In fact, this is a particular case; in general, (6.16) can be maximized by imposing a constant phase progression, as in the case of the phase-locked antenna array presented in [7]:

$$\phi_{i+1} - \phi_i = \Delta\phi \quad (6.18)$$

where  $\Delta\phi$  is a constant phase value. Considering (6.18) and taking the phase of the first subcarrier ( $\phi_1$ ) as the reference ( $\phi_2 = \phi_1 + \Delta\phi$ ;  $\phi_3 = \phi_1 + 2\Delta\phi$ ;  $\phi_4 = \phi_1 + 3\Delta\phi$ ), the zero condition for all the three arguments (6.17) can be simultaneously satisfied:

$$\begin{aligned} Arg1 &= 2(\phi_1 + 2\Delta\phi) - (\phi_1 + \Delta\phi) - (\phi_1 + 3\Delta\phi) = 0 \\ Arg2 &= -2(\phi_1 + \Delta\phi) + \phi_1 + (\phi_1 + 2\Delta\phi) = 0 \\ Arg3 &= \phi_1 - (\phi_1 + \Delta\phi) - (\phi_1 + 2\Delta\phi) + (\phi_1 + 3\Delta\phi) = 0 \end{aligned} \quad (6.19)$$

The general condition stated by (6.18) as well as the 0 phase condition in [4] are consistent, as they also provide the MS signal with the maximum PAPR. Subcarriers' amplitudes may also be optimized as in [18].

## 6.8 Defining a Figure-of-Merit (FOM) to Evaluate the Efficiency Gain

In order to evaluate the improvements obtained with the MS signals, compared to CWs, a FOM is defined, namely the RF–dc efficiency gain ( $G_\eta$ ), which relates the dc power collected from a single-carrier with the dc power obtained with a MS waveform with the same average power ( $P_{RF(CW)} = P_{RF(MS)}$ ).

$$\begin{aligned} G_\eta(dB) &= 10 \log_{10} \left( \frac{\eta_{MS}}{\eta_{CW}} \right) = 10 \log_{10} \left( \frac{P_{DC(MS)}/P_{RF(MS)}}{P_{DC(CW)}/P_{RF(CW)}} \right) \\ &= 10 \log_{10} \left( \frac{P_{DC(MS)}}{P_{DC(CW)}} \right) = 20 \log_{10} \left( \frac{V_{DC(MS)}}{V_{DC(CW)}} \right) \end{aligned} \quad (6.20)$$

where,  $\eta_{CW}$  and  $\eta_{MS}$  are the efficiency of the CW and MS signal respectively,  $P_{dc(CW)}$  and  $P_{dc(MS)}$  refer to the output dc power obtained in a rectifier circuit when using respectively a CW and a MS signal at its input. Note that the second part of (6.20) is valid when the average input power level and the output dc load are the same for the CW and MS signals.

## 6.9 Simulations

The circuit of Fig. 6.10a is used in Keysight ADS simulator to evaluate the RF–dc conversion using CW and MS signals. For this purpose, two situations were simulated using multi-frequency Harmonic Balance (HB). In the first case, a CW was used as the input signal, and in the second, an evenly spaced  $N$ -tone MS signals with zero phase shift between the subcarriers was applied. The average power of the MS signals was set to the same value as the CW average power by doing  $P_{CW} = P_{\omega 1} + P_{\omega 2} + \dots + P_{\omega N}$ , where  $P_{CW}$  (in dBm) is the average power of the CW signal, and  $P_{\omega 1}, P_{\omega 2}, \dots, P_{\omega N}$ , are the power levels of the individual MS subcarriers. A central frequency and tone spacing of 2.4 GHz and 1 MHz respectively was considered. For the sake of an efficient HB simulation, the frequency mapping of Fig. 6.10b was used, allowing to evaluate the CW and all the MS signals in a single HB run.

Figure 6.11 depicts the input and output time-domain waveforms corresponding to a CW, a 2-tone and a 4-tone MS input signals. First, it can be observed that the output ripple follows the envelope of the input signal and it is strongly dependent on the time constant of the output filter. In the CW case, the output ripple is insignificant (blue curves), as the RF signal period ( $T_{RF} = 1/f_{RF} \approx 0.4$  ns) is very small compared to the time constant of the output RC filter ( $\tau = RC = 4.7$  ms). On the other hand, the 2-tone and 4-tone MS signals are affected by a considerably larger output ripple (red and green curves). This is due to the much slower envelope of the MS signal, whose periodicity is related to the frequency spacing between the subcarriers ( $T_{env} = 1/\Delta\omega$ ). Therefore, the output filter has to be optimized to account for the MS envelope

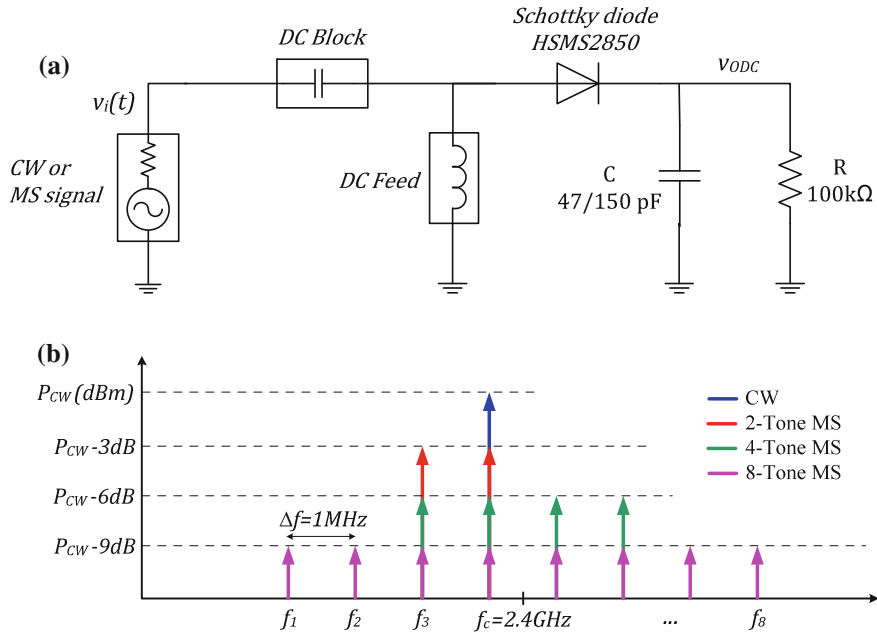


**Fig. 6.10** **a** Simple series diode rectifier used in ADS HB simulations. **b** Frequency mapping of the input signals used in the HB simulations

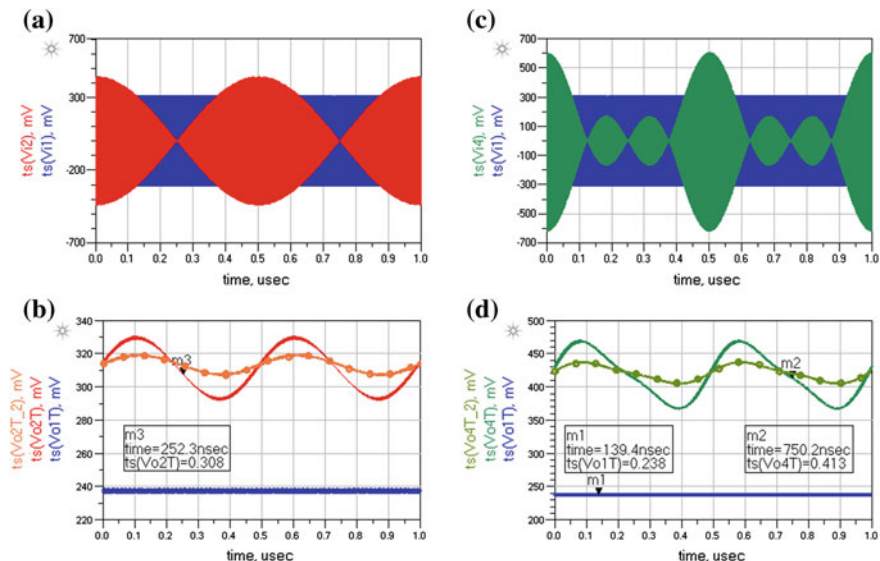
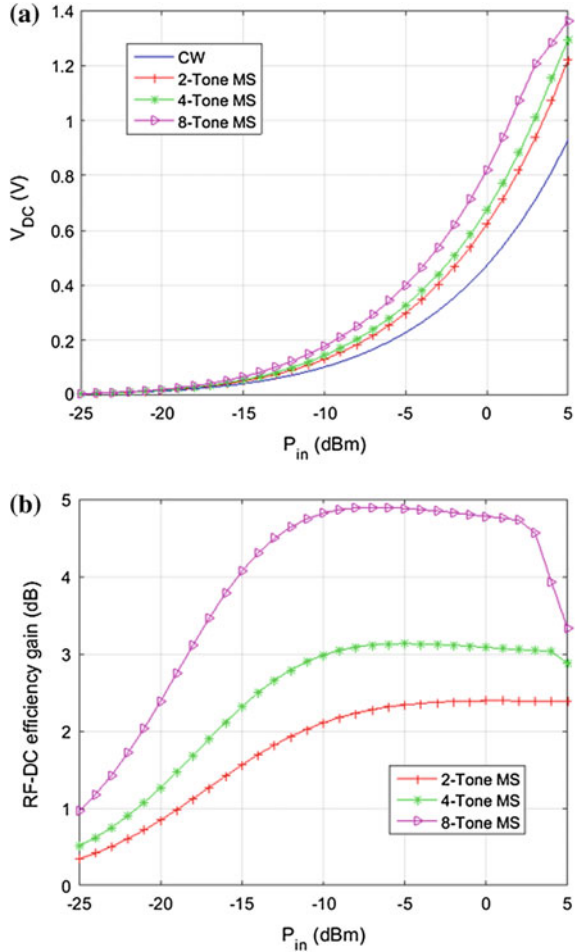


**Fig. 6.11** Time-domain waveforms obtained in the HB simulations. **a** Input 2-tone MS signal overlapped with a CW signal with the same average power, and **b** respective output waveform. **c** Input 4-tone MS signal overlapped with a CW signal with the same average power, and **d** respective output waveform. In **b** and **d**, the constant curve (blue) corresponds to the CW signal and the rippled waveforms (red and green) corresponds to the MS signals

**Fig. 6.12** **a** Simulated dc voltage as a function of average input power for several input excitation signals. **b** Efficiency gain as a function of average input power



frequency rather than the RF frequency. As seen in Fig. 6.11b, d, by increasing the time constant of the output filter (e.g., increasing  $C$  from 47–150 pF), it is possible to reduce the output ripple (curve with circles). The simulated output dc voltages and efficiency gains as given by Eq. (6.20) are depicted respectively in Fig. 6.12a, b, as a function of the input average power. A maximum gain of 5 dB is obtained for a 8-tone MS for the series diode configuration tested here, and a similar gain was obtained in [4] for a shunt diode simulated at 5.8 GHz.

## 6.10 Measurements

A set of measurements was conducted to evaluate the efficiency gains obtained in two RF–dc converter circuits under several MS signal excitations. For this purpose, a single diode detector operating at 2.3 GHz (see Fig. 6.13a) and a five-stage charge pump voltage multiplier working at 866 MHz (see Fig. 6.13b) were tested. The respective simulated and measured return losses of the circuits under test are also depicted in Fig. 6.13. In order to evaluate the performance under several excitation signals, both rectifying circuits were first fed with a CW signal and then with a MS signal with the same average power as the CW. This was done over a range of input power, input signal bandwidth and MS phase arrangements. Figures 6.14 and 6.15 present the dc output voltages and efficiency gains as defined by Eq.(6.20). The measurement results support the initial premise that MS signals can provide an efficiency gain over CW signals. This is valid for the single diode rectifier (both series and shunt configurations) which showed an efficiency gain up to 6 dB, as well as for the charge

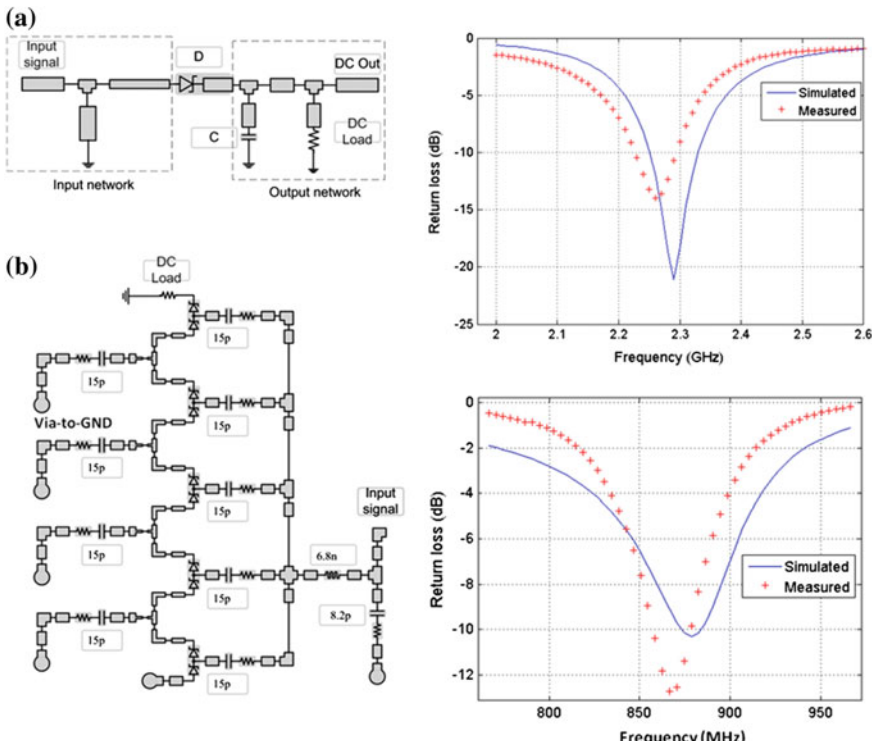


**Fig. 6.13** Rectifying circuits used in the cabled measurements and respective input return loss (simulated and measured). **a** Single diode detector operating at 2.3 GHz band. **b** Charge pump rectifier with 866 MHz center frequency

**Fig. 6.14** **a** Measured dc output voltage of the single diode detector, as a function of average input power. **b** Efficiency gain of the single diode detector, as a function of average input power. Except for the 64-tone MS, as the number of tones and the PAPR increase, the gain also increases. **c** Output dc voltage as a function of the input signal bandwidth. It is also visible that there is an optimal MS bandwidth that produces a maximum output dc

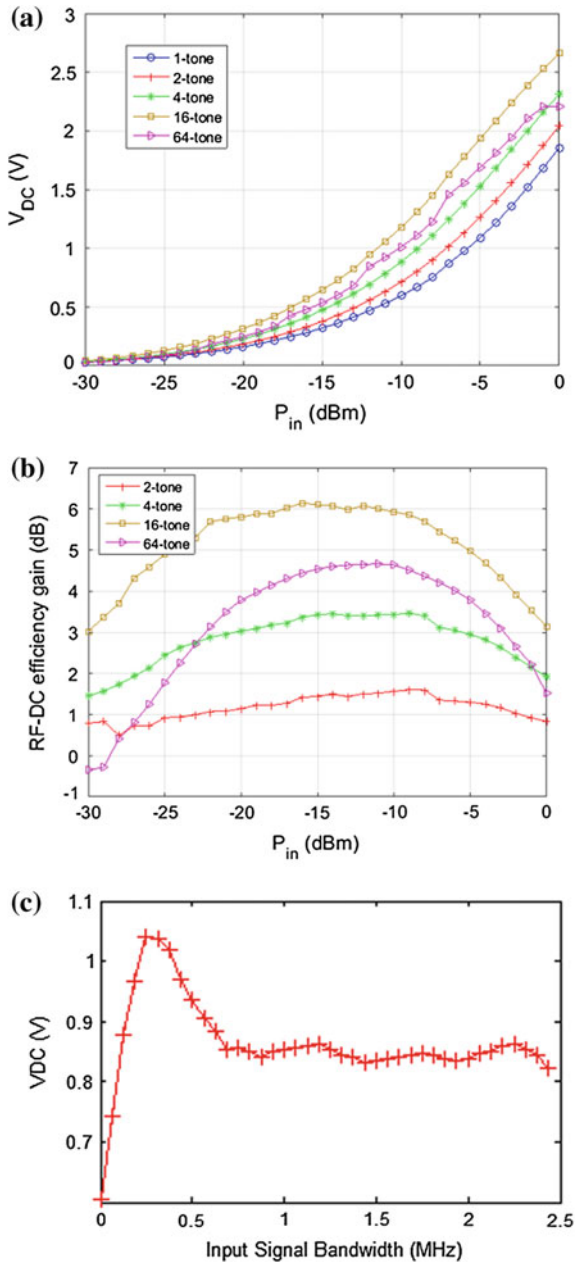
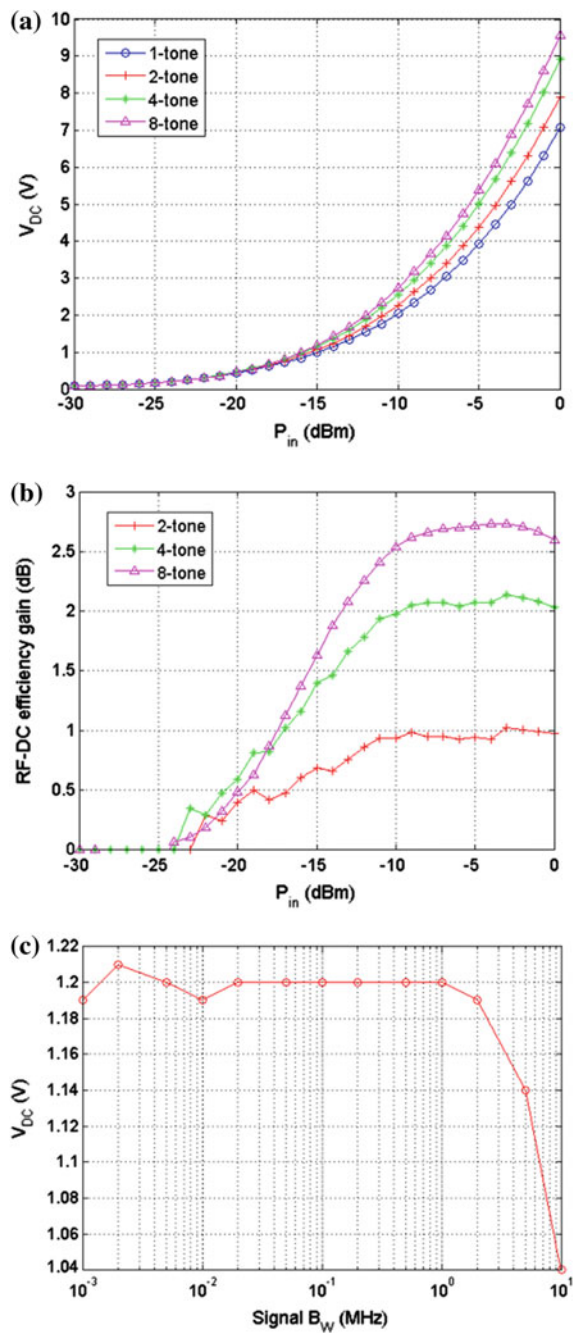


**Fig. 6.15** **a** Measured dc output voltage of the charge pump, as a function of average input power. **b** Efficiency gain of the charge pump, as a function of average input power. **c** Output dc voltage as a function of the input signal bandwidth



pump circuit which exhibited a gain up to 2.75 dB. These results suggested that this scheme could potentially extend the range of passive RFID systems. This subject was evaluated in [2, 5, 6].

### 6.10.1 The Impact of Input Signal Statistics

The circuits under test were also evaluated using different input amplitude statistics, including a 16-tone MS with 0 phase, normal amplitude distribution and uniform amplitude distribution. A similar experimental study was also done in [8]. To achieve the given amplitude distribution, the algorithm outlined in [15] was used to synthesize MS signals from noise signals with the desired amplitude statistics. The algorithm returns the phases of a MS with the same amplitude statistics as the reference noise signal. The Probability Density Functions (PDF) of the noise and MS with normal and uniform distributions are depicted in Fig. 6.16. Figure 6.17 shows the measured output dc voltage of the charge pump, for a CW signal, and a 16-tone MS with 0 phase arrangement, normal and uniform amplitude distributions. As can be seen in Fig. 6.17, the 0 phase MS provides the best performance, followed by the MS with normal amplitude distribution. A similar result is obtained for the single diode detector.

**Fig. 6.16** Probability density functions of noise and synthesized MS signals.  
**a** Normal distribution.  
**b** Uniform distribution

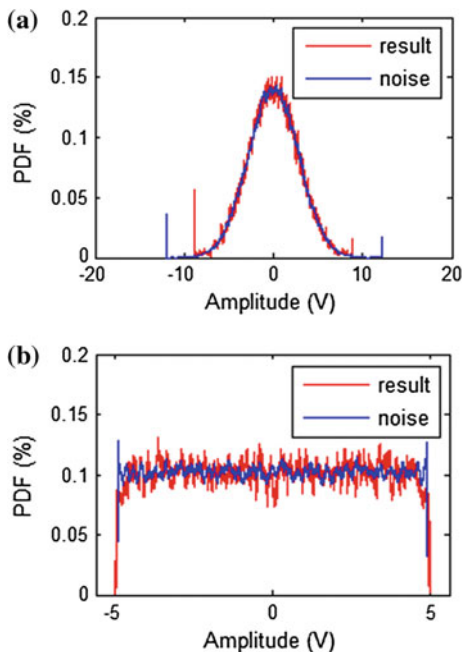
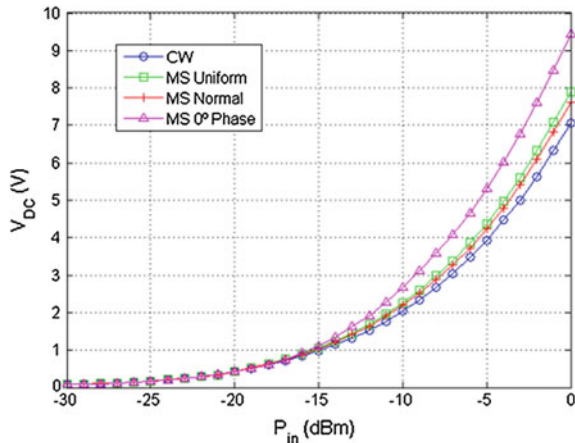


**Fig. 6.17** Measured dc output voltage of the charge pump, for a CW signal, and a 16-tone MS with uniform and normal amplitude distributions, and with 0° phase arrangement



## 6.11 Conclusion

The main conclusions can be summarized as follows:

When compared to conventional CWs, high PAPR signals are able to more efficiently overpass the turn-on voltage of existing rectifying devices, especially at low power levels, yielding an improved RF–dc conversion efficiency. High PAPR MS signals provide higher dc power compared to a CW with the same average power level. This results in an efficiency gain which increases with the increase in PAPR at low average power. However, for very high PAPR values, as predicted by the model in [2], the efficiency is significantly degraded.

The MS time-domain waveform is impacted by the phase arrangement, number of tones and their frequency domain distribution. If the subcarriers are phase-synchronized, the higher the number of tones, the higher the PAPR and the higher the efficiency gain at low power levels. The peak repetition rate in time-domain is inversely proportional to the tone separation in the frequency domain, and thus, a decrease in tone separation imposes an increase in the output ripple. On the other hand, a very large tone separation may cause the total MS bandwidth to exceed the input bandwidth of the circuit, resulting in an efficiency drop. Therefore, an optimal tone separation should be selected.

Contrary to the cabled measurements conducted in this chapter, in which we have full control over the MS parameters, in open-air experiments, we lose control over the subcarrier phases and amplitudes, especially due to multi-path fading. Nevertheless, measurements show that even with a random phase arrangement, the MS signal can outperform the CW signal.

While the output filter design is not critical for CW operation (as a relatively small output capacitor is sufficient to smoothen the output ripple), for MS operation, the output filter design is important and should take into account the MS signal envelope.

The output ripple follows the MS envelope, and the average output dc depends on the time constant of the output filter.

Not less important, the use of a MS transmitter represents an increased complexity and the amplification of high PAPR signals is challenging because it may occur nonlinear distortion (amplitude clipping, spectrum regrowth) and efficiency degradation. For this reason, space power combining has been proposed in [2, 7] as an efficient way to create and radiate high PAPR MS signals.

## References

1. Ansoft: Application note: pin diode model parameter extraction from manufacturers (1997)
2. Boaventura, A.: Efficient wireless power transfer and radio-frequency identification systems. Ph.D. thesis, University of Aveiro (2016)
3. Boaventura, A., Belo, D., Fernandes, R., Collado, A., Carvalho, N.B., Georgiadis, A.: Unconventional waveform design for efficient wireless power transfer. *IEEE Microw. Mag.* **16**(3), 87–96 (2015)
4. Boaventura, A., Carvalho, N.: Maximizing DC power in energy harvesting circuits using multisine excitation. In: IEEE (ed.) IEEE MTT-S International Microwave Symposium. Baltimore (2011)
5. Boaventura, A., Carvalho, N.: Extending reading range of commercial RFID readers. *IEEE Trans. Microw. Theory Tech.* **61**(1) (2013)
6. Boaventura, A., Carvalho, N.: A software-defined radio RFID reader with multi-sine capability for improved wireless power transfer. *IEEE Trans. Microw. Theory Tech.* (submitted for publication, 2016)
7. Boaventura, A., Collado, A., Carvalho, N.B.: Spatial power combining of multi-sine signals for wireless power transmission applications. *IEEE Trans. Microw. Theory Tech.* **62**(4), 1022–1030 (2014)
8. Collado, A., Georgiadis, A.: Optimal waveforms for efficient wireless power transmission. *IEEE Microw. Wirel. Compon. Lett.* **24**(5), 354–356 (2014)
9. De Donno, D., Ricciato, F., Tarricone, L.: Listening to tags: uplink RFID measurements with and open-source software-defined radio tool. *IEEE Trans. Instrum. Meas.* **62**(1), 109–118 (2013)
10. Dickson, J.: Voltage Multiplier Employing Clock Gated Transistor Chain (1980)
11. Huerdeman, A.A.: The Worldwide History of Telecommunications. Wiley, Hoboken (2003)
12. Network, I.G.H.: Biography of ernst f. w. alexanderson
13. Nikitin, P., Rao, K.: Performance limitations of passive UHF RFID systems. In: IEEE (ed.) IEEE Antennas and Propagation International Symposium, pp. 1011–1014 (2006)
14. Pedro, J., Carvalho, N.: Intermodulation Distortion in Microwave and Wireless Circuits. Artech House, Norwood (2003)
15. Pedro, J., Carvalho, N.: Designing band-pass multisine excitations for microwave behavioral model identification. In: IEEE (ed.) IEEE MTT-S International Microwave Symposium (2004)
16. Pursula, P.: Analysis and design of UHF and millimetre wave radio frequency identification. Ph.D. thesis, VTT Technical Research Centre of Finland (2008)
17. Tesla, N.: The Transmission of Electric Energy Without Wires. The Thirteenth Anniversary Number of the Electrical World and Engineer. McGraw-Hill, New York (1904)
18. Trotter Jr., M., Griffin, J., Durgin, G.: Power-optimized waveforms for improving the range and reliability of RFID systems. In: IEEE (ed.) IEEE International Conference on RFID (2009)
19. USA, W.T.G.: Principles of power measurement, a primer of RF and microwave power measurement (2011)

# Chapter 7

## Regulations and Standards for Wireless Power Transfer Systems

Christos Kalialakis, Ana Collado and Apostolos Georgiadis

**Abstract** A survey of the regulatory framework pertinent to Wireless Power Transfer systems is given. Both technical (power and frequency) considerations along with health safety radiation compliance are examined. A primer on regulatory processes is also included to facilitate the understanding of the developments. The current state is analyzed and ongoing regulatory activities across the globe are discussed. Furthermore, a review of recent radiation safety studies of WPT systems is included.

### 7.1 Introduction

Wireless power transfer (WPT) systems are becoming increasingly important for several applications; telecoms, automotive industries, medical electronics, sensors [1–6]. Presently, the most attractive WPT function is wireless charging [7]. Regulations and standard is an unavoidable and necessary prerequisite for any new wireless technology. On one hand, the regulatory compliance imposes limitations on the technical characteristics of the devices but on the other hand facilitates market adoption and mitigates consumer concerns about radiation.

The regulatory regime is in general quite complex because regulations and standards are delivered by a multitude of organization with the interdisciplinary nature of WPT adding to the complexity. The main target audience is academics who conduct research in the field of WPT. Sections of the chapter also aim to professionals

---

C. Kalialakis (✉)  
Centre Tecnologic de Telecomunicacions de Catalunya-CTTC,  
08860 Castelldefels, Barcelona, Spain  
e-mail: christos.kalialakis@cttc.es

A. Collado · A. Georgiadis  
School of Engineering and Physical Sciences, Institute of Sensors, Signals and Systems,  
Heriot-Watt University, Edinburgh EH14 4AS, UK  
e-mail: ana.collado@ieee.org

A. Georgiadis  
e-mail: apostolos.georgiadis@ieee.org

engaged in regulatory and standard work which seek a source a map of developments. Very few studies have appeared that review regulatory and standardization developments. In [8] activities with a focus on Japan were presented. In [9] some radiation safety compliance regulations were reviewed and in [10] a similar brief review discussion about radiation safety for emerging technologies including far-field systems was presented. This chapter builds on our previous work on the subject [11].

In Sect. 7.2, some terminology on WPT systems including top-level descriptions is provided. In Sect. 7.3, basic notions on regulatory process and standards are presented in order to facilitate a deeper understanding of current developments deployed in the next sections. The relation between standards and regulations is explained. In Sect. 7.4, the current status of WPT pertinent regulations is analysed and ongoing regulatory activities are surveyed. Conclusions are drawn in Sect. 7.5.

## 7.2 Wireless Power Transfer Systems

WPT systems can be classified based on the way the electromagnetic field is exploited, i.e., coupling for near field and radiation in the far-field case.

Wireless charging systems that operate in the near field are spatially confined. They are brought in the close vicinity (up to a few cm) of the device to be charged. Usual frequencies of operation start from as low as 20 kHz up to 13.56 MHz [1, 7]. Such systems are practically cordless chargers.

Besides the low frequency systems, WPT systems operate in GHz or RF frequency range using the radiative far field. The system that needs to receive energy is already placed in a fixed position and access is not easy or possible. For the purposes of this work, WPT-NF will denote a near-field system and a far-field WPT will be denoted explicitly as WPT-FF.

As mentioned in the introduction, the dominant WPT function is wireless battery charging which finds applications most notably in

- Electric Vehicles
- Mobile Communications Devices
- Implantable Medical Devices
- Building Automation Sensors

A note should be made about a subclass of WPT-FF systems, called Energy Harvesting systems. These are passive systems in the sense that they only receive ambient energy from all the available sources [12–19]. Because of their expected widespread use in quite different sensor systems [2, 20] interoperability is important. This topic is examined further in Sect. 7.5. Another notable application of WPT-FF is the Space Solar system where power is collected by satellites and then transmitted via microwaves to earth stations [21, 22]. Medical devices always generate a huge interest. The need to avoid batteries and power wirelessly implantable devices has given WPT a lead as a solution [3–6].

### 7.3 Basic Concepts of Regulations and Standards

Regulation is a necessary function common in any market, transparent to the consumer. This function is exercised by regulatory institutions which are usually organizations created by governments. Regulation targets on supporting market development without sacrificing the state and the consumer interests. The industry, as a stakeholder, is frequently initiating matters at the regulatory level. Therefore, wireless power transfer systems also need to operate within regulatory boundaries. Focusing on WPT systems as a case of wireless technology, at least two technical parameters must be defined. These parameters are the frequency and the power. Regulations can also impose limitations on other device characteristics. For example, compliance may be required on

- Electrical Power limitations (such as the European Union Low Voltage Directive [23])
- Manufacturing considerations such as the RoHS directive [24] which prohibits the use of lead and other materials in PCB (Printed Circuit Boards)
- Heat/Noise Limits
- Electromagnetic Compatibility and Immunity (EMC/EMI)

At this point, it is instructive to classify regulatory bodies using two main criteria; first, the geographic coverage and second the technical focus. Geographically speaking, three ranks can be recognized (Fig. 7.1).

Organizations that emanate from global collaboration generate regulations which are general. In a regional level, i.e., Europe, the regulations must be further adapted. Nevertheless, the regulations are not legally binding before they reach the national level. Each sovereign state decides for the adoption or not of the regulation as national legislation. This harmonization process is not without problems which is quite apparent in adoption of frequency bands of operation. In principle, frequencies are

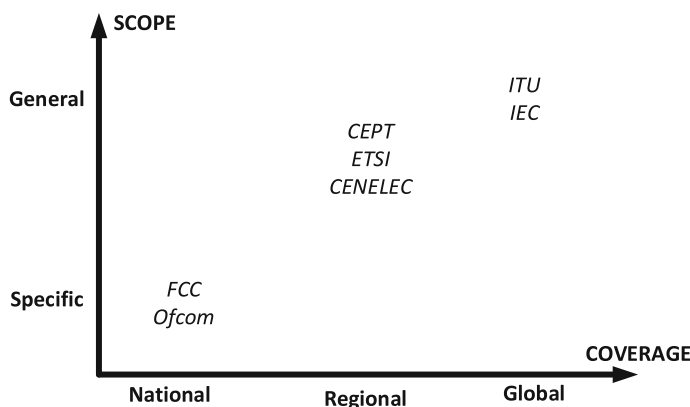


**Fig. 7.1** Relation of the regulations scope with the geographical area of influence

harmonized but in practice there is quite a difference from region to region. Sometimes a technical parameter such as the transmitted power can be regulated not on technological grounds only but also on perceived risks as in the case of human exposure radiation safety limits.

Each regulatory body is responsible for specific sectors. In response to sector activities that are regulated, three major areas can be distinguished.

- Telecommunications. The most important technical parameters that are regulated are frequency and power. The frequency is allocated through a frequency coordination process dictated by ITU procedures. In this procedure, power is usually known by EMC/EMI considerations, radiation limits, and industry standards. In some cases, devices are also expected to meet other equipment type approvals as noted above.
- Electrical. This is most commonly related to EMC/EMI standards and thus includes a larger number of devices and systems since they are not limited to radio devices only.
- Health & Safety. The emphasis is on human radiation exposure and safety rules.

In Table 7.1 all the related organizations that are active in the WPT are shown. It is apparent that a lot of organizations exist and the boundaries between them are not always clear-cut. It is often that strong connections exist among them which take the form of liaison statements or even attendance of the activities of one organization by representatives of the other organization.

At this point, an elucidation on the difference between standardization and regulation is deemed necessary. Regulations have legal power and they are adopted by an authority in a national context. Standards are documents that are developed and approved by a recognized body.

**Table 7.1** Regulatory bodies

| Organization | Geographical influence | Sector                     | Notes                     |
|--------------|------------------------|----------------------------|---------------------------|
| APT Regional | Telecoms               | Asia                       | Pacific Region            |
| CENELEC      | Global                 | Electrical                 |                           |
| CEPT/ECC     | Regional               | Telecoms                   | Europe                    |
| CISPR        | Global                 | Electrical                 |                           |
| ETSI         | Regional               | Telecoms                   | Europe                    |
| FCC          | National               | Telecoms                   | USA                       |
| ICNIRP       | Global                 | Health                     |                           |
| IEC          | Global                 | Electrical                 |                           |
| IEEE         | Global                 | Telecoms/Electrical/Health | Professional Organization |
| ISO          | Global                 | General                    |                           |
| ITU          | Global                 | Telecoms                   |                           |

Standards provide for repeated use, guidelines and characteristics for systems or devices [25]. Technical regulations, a subclass of regulations that provide technical compliance requirements, are always standard driven, either directly or indirectly. As such, there is quite a close collaboration among these bodies. Standards could be broadly described as compliance and application oriented. Compliance standards are always connected with a technical regulation. Application standards on the other hand are design specifications that aim more toward interoperability and open technical details such as the data structure or components characteristics' usually without resorting to implementation. Application standards are not necessarily connected with technical regulations but they are frequently invoked as a reference. The difference is somehow subtle resulting in the use of the terms standards and regulations interchangeably in the open literature. It must be stressed out that regulation and standardization are not done in the absence of industry. Industry contributes significantly to the activities of these bodies and most often takes the initiative when new technologies appear. In order to speed up interaction, companies that work in the same field form representative bodies that focus on specific topics. These organizations come by the terms forum, alliance, or initiative. In the WPT-NF area (Table 7.2), there are several international forums, the Wireless Power Consortium [26], the AirFuel Alliance which advocates on Loosely Coupled WPT [27, 28] and the Open Dots Alliance [29]. More on these industry forums are given in Sect. 7.7. These organizations are also active in application standards through the issue of design specifications. Another forum, called ENOCEAN should also be mentioned [30] which represents companies from the building and automation sector. There are also established industry alliances in the area of WPT-NF, in countries where there is a large automotive industry such as Japan, US, and Korea [31, 32] (see Table 7.2).

**Table 7.2** Industry-related organizations active in WPT standards development

| No  | Organization                                      | Notes                                   |
|-----|---|---|
| 1.  | Wireless Power Consortium                         | Qi Specification, Near-Field Technology |
| 2.  | AirFuel Alliance                                  | Near-Field Technology                   |
| 3.  | Open Dots Alliance                                | Focused on cars                         |
| 4.  | ENOCEAN Alliance                                  | Energy Harvesting Sensors               |
| 4.  | Consumer Electronics Association                  | USA Companies                           |
| 6.  | Underwriters Laboratories                         | USA Testing House                       |
| 7.  | Society of Automotive Engineers                   | USA Professional Organization           |
| 8.  | ARIB—Association of Radio Industries and Business | Japanese Companies                      |
| 9.  | Broadband Wireless Forum                          | Japanese Companies                      |
| 10. | Wireless Power Management Consortium              | Japanese Companies                      |
| 11. | Telecommunications Technology Association         | Korean Companies                        |
| 12. | Korea Wireless Power Forum                        | Korean Companies                        |

Considering the multitude of organizations, the overlap and work duplication is highly probable. In order to cover the imperative need for efficient information exchange, an organized and formal way of interface between most of these organizations has been established; the Global Standards Collaboration (GSC). GSC takes the form of an annual meeting with ITU hosting the repository [33] and ETSI the web presence [34].

### 7.3.1 *Radiation Safety Regulations*

As far as radiation safety is concerned, the 1998 Guidelines by the International Commission on Non-Ionizing Radiation Protection (ICNIRP) [35], as amended in 2010 for frequencies up to 100 kHz [36], have been globally recognized as the de facto standard, although other guidelines are possible both internationally, i.e., IEEE [37] or nationally. In fact, several national legislations (Belgium, Switzerland, and Greece being typical examples) impose more stringent limitations based on political decisions rather than scientific data. It is worth noting ICNIRP and not the IEEE is usually referenced in national legislations.

Specific Absorption Rate (SAR) is the most well-known metric that due to the widespread adoption for assessing safety radiation limits of mobile telephones [38]. SAR at a given position can be evaluated using

$$\text{SAR} = \frac{\sigma E_{inc}^2}{\rho} \quad (7.1)$$

where  $\sigma$  is the tissue conductivity,  $\rho$  the tissue material density,  $E_{inc}$  the incident electric field. In most cases SAR requires integration over a volume (1 g or 10 g in weight) which is exposed for the measurement time. In these cases, the above quantities become functions of position and time. SAR is related to the tissue heating and is applied from frequencies 100 kHz to 10 GHz. SAR on humans can be computed from simulations or alternatively by phantoms that emulate human bodies [39]. However, because WPT systems and especially near-field systems operate in lower frequencies, there are other metrics that must concurrently be used. In Table 7.3 the frequency bands where WPT systems exist and the corresponding metrics with limit values are noted.

Other adverse health effects are possible in frequencies from 1 kHz to 10 MHz such as nerve and muscle stimulation. Retinal phosphene is such an effect where electromagnetic waves can induce the sensation of light in the retina without light actually entering the eye. In this frequency band current density limits also apply (see Table 7.3). In common frequencies, i.e., from 100 kHz to 10 MHz both SAR and current density limits must be met.

Additional limitations apply for RF contact currents up to a frequency of 110 MHz. These should not exceed 20 mA [35, 39].

**Table 7.3** Basic ICNIRP maximum exposure limits for WPT frequency bands

| Frequency band | Current density<br>(mA/m <sup>2</sup> ) | SAR for whole<br>body (W/kg) | SAR (head and<br>trunk) (W/kg) | SAR (limbs)<br>(W/kg) |
|----------------|---|------------------------------|--------------------------------|-----------------------|
| 1–100 kHz      | $f(\text{Hz})/500$                      | X                            | X                              | X                     |
| 100 kHz–10 MHz | $f(\text{Hz})/500$                      | 0.08                         | 2                              | 4                     |
| 10 MHz–10 GHz  | X                                       | 0.08                         | 2                              | 4                     |

### 7.3.2 Regulatory Processes for New Technologies

New technologies are continuously introduced which must be framed in a regulatory environment. This process brings two major questions;

- can the new technology be used in existing spectrum or does it require new spectrum bands to be allocated on a primary or secondary basis.
- Is the interference potential great which entails frequency coordination with other technologies in other parts of the spectrum, i.e., does it need to be recognized as a new service.

How to answer these questions can be illustrated with the following examples:

*Example* When GSM-type cellular communications technology was introduced a new frequency band allocation was needed. Furthermore, due to the long distance nature of the system, interference potential was great leading to the fact that GSM telephony had to be characterized as a service with exclusive usage rights in its 900 MHz band. The rights did not come without obligations. Every cellular operator had to pay a frequency license fee which was a sizeable amount of money.

*Example* The fixed service corresponds to a wireless point-to-point communications link between two set locations. The existence of a network is not a prerequisite for a technology to be a service. A fixed service realization is the connection of a broadcasting studio with the transmission sites can be done with a radio link. This radio link operates on a frequency that is licensed with a small fee and it needs to be coordinated with other radio links and other services in neighboring bands.

*Example* RFID technology operates in a short range and low power context, i.e., its interference potential is in general small in several frequency bands. RFID use is permitted without protection from interference as an SRD (Short Range Device). Consequently, RFID is not categorized as a service and carries no obligation for a frequency license fee.

A notable exception in the spectrum use is the ISM (Industrial Scientific and Medical) band. In reality ISM Bands are spread along the spectrum. These bands do not require a license fee and thus no protection from interference can be claimed from the regulator. For example, a Wi-Fi system can be used to create a radio link based fixed service. ISM bands devices are mandated to follow EMC/EMI regulations that

are region specific such as the FCC Part 15 [40] in the case of US or the EMC Directive [41] in European Union. These points should be born in mind when the WPT case is discussed below in Sects. 7.5–7.7.

All international regulatory (and standardization) bodies tackle new technologies in a well-organized manner as shown in Fig. 7.2. A decision is made usually in administration (political) level and the required technical work is assigned to groups of experts who provide feedback in documents with predefined structure so a decision can be reached. The diagram of Fig. 7.2 can be applied to every standardization and regulatory organization.

For instance, in ITU for radiocommunications issues, a proper decision body such as the Radiocommunications assembly issues a formal statement called Question. A Question can belong to one of several categories depending on its urgency and relation with assemblies that take decisions. This Question is tackled by groups of regulatory and industry experts who are organized in technical groups, called Study Groups (SG) in ITU context, under the guidance of ITU staff engineers. Each Study group divides its work in several subgroups called Working Parties that carry a designation that denotes the SG. Thus WP1A means the first working party of SG1 that deals with spectrum engineering. The products of SG are usually two kinds of formal documents,

- Recommendations are binding documents that form part of Radio Regulations and are embodied in national legislations. Recommendations are formally structured texts with the bare minimum required technical detail.
- Reports are documents that contain much more detailed technical information on a topic. It is usually the technical background related to a recommendation, although stand-alone reports are feasible.

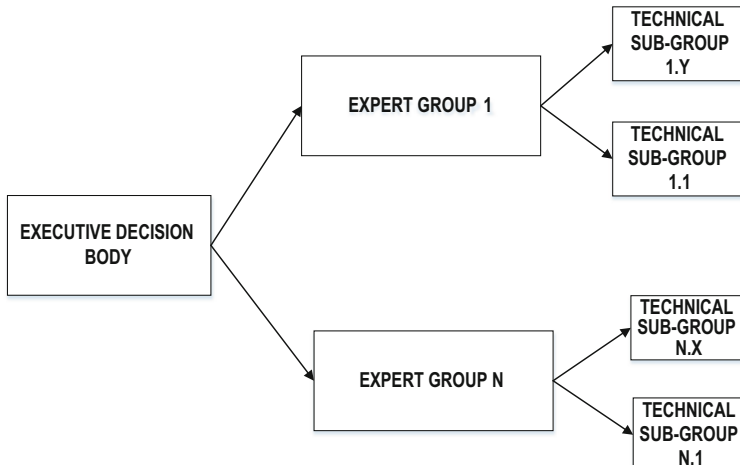


**Fig. 7.2** Work allocation in a regulatory level to cope with technical issues

In a similar way, in standardization organizations, like ETSI for example, technical reports and standards are produced by the technical groups.

## 7.4 WPT Regulations in International Level

In light of the discussion in Sect. 7.3, regulations and standardization are required to address in the WPT context the following questions;

- How WPT should be classified? As a device only or as a service? Can WPT coexist with other technologies in the same spectrum?
- Are current radiation safety limits adequate? If yes, are standardized measurement procedures adapted for such devices?

Currently no specific frequency band for WPT is allocated. Many WPT-NF systems operate in the ISM Bands 6.78 and 13.56 MHz. As analysed in the previous section, these bands do not need license fee and EMC/EMI compliance is required. Still the issue of the human safety radiation limits must be resolved. A further issue of high KW power at 13.56 MHz is the potential compatibility problem in locations where radio telescopes operate between 13.36 and 13.41 MHz. In the case of RFID systems, no realistic scenario was found [42], yet this exercise might have to be repeated for high-power WPT.

The USA regulatory authority FCC treats WPT devices as general equipment that intentionally radiates and therefore requires compliance with Parts 15 [38] and Part 18 [43]. Specific frequency allocation goes through ITU first, although national specific regulations are possible in some neutral parts of the spectrum. Usually radio regulations on a system without communication are quite different from those on a communication system. A decision has not been made yet if WPT is a subcategory of a communication system, although it contains a transmitting part and a receiving part.

Energy Harvesting Systems (EHS) as receivers require Electromagnetic Immunity compliance from a regulatory point of view. As far as interoperability is concerned, the ENOCEAN Alliance was instrumental in the creation of the ISO/IEC standard [44]. An interesting question is that if EHS should be allowed to operate in any band. For example, are EHS in large numbers able to produce disruption in areas, whereas GSM type networks have marginal coverage? Perhaps, EHS could be limited to bands where excess energy is abundant, i.e., close to high-power transmitters or close to microwave ovens.

Regardless of the exotic nature of the Space Solar Power application, this application must conform to regulations which exist for space too! At the moment no specific regulatory activities have been initiated. However, in this case additional regulations will apply for the satellite part. Most notable is the extra requirement of orbital position and the difficulty of getting such an approval by ITU due to the large size of the collecting satellite. Furthermore, further restrictions apply to space activities [45].

As far as medical electronics are concerned, the regulatory process must include regulatory approval by the related authority. In USA, for example where much of this research is carried out, FDA (Food and Drug Administration) approval must be met before market submission [46], although the RF part is not regulated by FDA.

In terms of health and safety regulations, no need is seen to put new limits. For the moment existing procedures can be used for the assessment of radiation limits as in the case of far field of mobile devices [47].

There is an array of significant activities in progress by many of the regulatory and standardization bodies shown in Table 7.1. These ongoing activities are analysed below. Apart from efforts in the international stage, two notable contributors in the national level, Korea and Japan, are examined.

#### **7.4.1 ITU**

A Question was recently updated (see Sect. 7.3.2 above on ITU procedures), that is, handled by Study Group 1 and its subgroup called WP1A. The WPT Question [48] falls in category S3, i.e., required studies which expect to facilitate the development of radiocommunications.

The question is usually considered resolved when a Report and a Recommendation are finalized. According to the proceedings in progress of the meetings [49], the first major outcome is that WPT devices are classified as **non-beam WPT** which corresponds to near field and **beam WPT corresponding** to WPT-FF. A recent ITU report SM.2303-1 reviews frequency bands and out-of-band radiation levels for non-beam devices [50]. Moreover, a draft recommendation is in progress with major inputs from Korea and Japan. The recommendation is expected to be completed in 2016.

#### **7.4.2 ETSI**

WPT systems in ETSI are covered by EMC and Radio Spectrum Matters (ERM) technical group. They are currently aiming in the revision of standard EN 300 330 [51] to include wireless charging and an update of the 13.56 MHz RFID mask. An early draft revision is already available [52]. The work is based on a revision of Technical Report TR 103 059 which is in the publication stage. The revision is about the spectrum mask requirements for narrowband but long-range and wideband but short-range RFID systems. Furthermore, ETSI has assigned the ERM technical group TG28 to prepare material on inductive wireless charging for inclusion in EN 300 330. The task is to clarify the type of WPT-NF systems, the technical requirements and possible interference scenarios to existing SRD devices. The work concentrates on frequencies below 30 MHz. The task includes the revision of the guidelines for Notified Bodies and Test houses which carry out the EMC/EMI compliance procedures [53]. ERM

also discussed the interference potential from wireless chargers that use power from 100 W to many kW. Some products proposed are intended to operate in recognized ISM bands. Other products intend to operate in bands already allocated to radio communication services. The interference potential of such equipment would need to be assessed separately in ITU. In order to facilitate this process, the ERM is in liaison with CEPT/TCAM and ITU [54].

#### 7.4.3 *CEPT/ECC*

CEPT/ECC is involved in WPT through two technical groups; the SE (Spectrum Engineering) and FM(Frequency management). As noted above, there is a close collaboration between these Groups and ETSI [54–56]. The revision of ETSI EN 300 330 [48] is being carried out in consultation with CEPT technical subgroup designated SE24 [54].

#### 7.4.4 *IEC and ISO*

IEC (International Electrotechnical Commission) has initiated work through two technical groups. IEC Technical Committee 69 [57] works on Electric vehicle WPT-NF systems in order to produce the forthcoming standard IEC/TS 61980 “Electric vehicle wireless power transfer (WPT-NF) systems.” The standard will be composed of the following three parts:

- Part 1: General requirements
- Part 2: specific requirements for communication between electric road vehicle (EV) and infrastructure with respect to wireless power transfer (WPT-NF) systems
- Part 3: specific requirements for the magnetic field power transfer systems.

At this stage, the standards are in very early draft status. The full standard is expected to be released in 2017, although parts of the standard will be available by 2015. Furthermore, Technical Committee TC100 [58] has launched activities with a time horizon of 2017 on creating IEC 62827- Wireless Power Transfer - Management which is more general and not limited to vehicles. It is composed by the following parts:

- Part 1: Common Components
- Part 2: Multiple devices control management
- Part 3: Multiple sources control management

ISO has initiated since early 2014 activities on a new standard under the code 19363 [59]. Subcommittee TC22/SC2 “Road Vehicles-Electrically propelled Road Vehicles” and in specific its working group WG 1(Vehicle operation conditions, vehicle safety and energy storage installation) is responsible for drafting.

A joint IEC/ISO technical committee on Information Technology Standards (JTC 1) has included information technology issues that are related to wireless power transfer such as wireless communication support, interoperability with NFC (Near-Field Communications), convergence with RFID and security for WPT [60]. The creation of the ISO/IEC standard on interoperability is also noted [44].

#### 7.4.5 CISPR

The International Special Committee on Radio Interference (CSIPR) works under the auspices of IEC but is operating separately from the other IEC Technical committees. CISPR is working to develop emission limits below 30 MHz for wireless power transfer. The primary effort is occurring in its Subcommittee B, CIS-B [61] which deals with interference relating to industrial, scientific and medical radiofrequency apparatus, to other heavy industrial equipment, to overhead power lines. Similar requirements will be applied to multimedia equipment once the limits and test methods are well founded.

#### 7.4.6 CENELEC

European standardization body CENELEC has been initiated to follow up work on the IEC work. Technical committee CLC/TC 69X [62] is working on a European standard in accordance with the IEC forthcoming standard described above in Sect. 7.4.4. The standard will carry the same code number as the IEC work, i.e., EN.61980-1:2013. Part 1 is in the voting stage.

### 7.5 Selected National Level WPT Regulations

#### 7.5.1 Activities in Japan

In Japan the WPT activities have attracted a lot of interest by both communications and automotive industries [8, 63]. The activities were initiated by the Ministry of Internal Affairs and Communication which formed a working group on WPT in June 2013 [63] to establish specific regulatory procedures. The communication industry efforts are led by BWF. The working group WPT-WG has developed guidelines for the use of wireless power transmission technologies which have reached ver.2.0 [64]. The guidelines concern ISM band systems. An interesting feature of these guidelines are safety measures for heating which occur due to induction. The use of the international standard IEC- 60335-1, “Household and similar electrical

appliances-Safety-Part 1 General requirements” is suggested. The absence of a near-field SAR measurement method below 30 MHz is noted too.

The BWF through a technical working group WPT/WG has commenced standardization activities through a subgroup called the Standard Development Group (SDG). The intention is that the developed standard will be submitted to the Association of Radio Industries and Businesses (ARIB) Standards Assembly. Note that ARIB participates in the GSC [34].

A related industry body Japan Electronics and Information Technology Industries Association (JEITA) has formed a group called The Wireless Feeding Project Group. JEITA is participating in the work of IEC/TC100 which was discussed above in Sect. 7.4.4.

As far as the automotive industry is concerned, the Japan Automobile Research Institute (JARI) has also assigned a technical team to work on the subject, namely the Inductive Wireless Charging Subworking Group (SWG). Its work is supplemented by the Society of Automotive Engineers of Japan (JSOE) through its Wireless Charging System Technical Committee [8]. The JARI/SWG is the national voting member in the corresponding IEC and ISO standards (i.e., JPT61980 in IEC TC69 and ISO 19363 in ISO TC22).

### 7.5.2 Activities in Korea

In Korea, the activities are led by the Telecommunications Technology Association (TTA) [65]. Three technical subgroups have been established;

- Project Group 709 (PG709) established in March 2011 and has already produced a series of national standards in 2011 and 2012 (see Table 7.4). The work is based on cellular and low-power WPT
- Project Group (PG309) works on EMI/EMC
- Project Group (PG422) concentrates on high-power, especially electric vehicles.

The need for coordination has been solved by a liaison team among the three groups [66]. A particular note should be made about the standard TTAE.KO-06.0303 which deals with the practical issue of control signaling.

It must also be noted that TTA is very active in the GSC [66] and ITU level [49]. Moreover, considering the interest by Japan as analysed in Sect. 7.5.1, a regional collaboration group was formed with Korea. China also joined the collaboration which has been named CJK (China Japan Korea) and has started to become an active player in ITU level [49].

**Table 7.4** Recent Korean standards on wireless power transfer

| No  | Std number      | Title  |
|-----|-----------------|--|
| 1.  | TTAR-06.0112    | Evaluation methodology on candidate technologies for wireless power transfer                                   |
| 2.  | TTAR-06.0109    | Requirements for wireless power transfer (Technical Report)  |
| 3.  | TTAR-06.0108    | Use case for wireless power transfer (Technical Report)  |
| 4.  | TTAR-06.0107    | Service scenario for wireless power transfer (Technical Report)  |
| 5.  | TTAR-06.0113    | Definition on efficiency of wireless power transfer for Mobile devices   |
| 6.  | TTAE.KO-06.0304 | Interface definition for highly resonant wireless power transfer   |
| 7.  | TTAE.KO-06.0303 | Control protocol of wireless power transfer  |
| 8.  | TTAK.KO-10.0571 | Guideline for functional receiver components of wireless power transfer system via coupled magnetic resonances |
| 9.  | TTAK.KO-10.0590 | System control sequence of resonant wireless power transmission  |
| 10. | TTAK.KO-10.0632 | Evaluation method of ultrasonic receiver efficiency for wireless power transmission                            |

### 7.5.3 Activities in USA

The Society of Automotive Engineers has initiated standardization work through a task force called J2954 on wireless charging for vehicles [67]. Furthermore UL is working on safety aspects [68]. Procedures for Electric Vehicle Wireless Charging procedures, under UL 2750 have been developed [69]. It should also be noted that IEEE Industry Standards Technology Organization had the initiative of founding the Wireless Power Consortium program [70]. IEEE Standards has commenced pre-standardization activities on Electric Vehicle Wireless Power Transfer with a focus on in-motion wireless charging [71, 72].

## 7.6 Selected Radiation Safety Studies in WPT

The prevailing opinion is that current radiation safety limits standards are in general adequate. However, there is a need to further and better understand at a cellular and molecular level the mechanisms of interaction with the electromagnetic fields on humans [73]. The anticipated deeper understanding does not necessarily imply a change on the current standards.

SAR calculations based on phantoms should be carefully chosen since height does affect substantially absorption through human body resonances [74]. The phantom models are potentially different for each gender. This agrees also with the directive of the European Commission in the framework of the Horizon 2020 [75] that encourages gender analysis in R&D activities. With the WPT still not mature, it seems that specific standardized procedures for measuring WPT [76–80] are required. In any case, considering the capability of kW operation in close range to humans, radiation hazard safety should be integrated in the engineering design process for better results [9]. In the open literature, several cases have been demonstrated that WPT systems do not violate the radiation limits when humans are located in some distance on the order of cm from the charging device [81–93]. In [94] a magnetic field value that exceeded the maximum field strength was found locally. It is to be noted that in comparison, the RF dosimetry studies in the RF region are vast in number comparing to such studies for frequency up to 10 MHz [76].

In Table 7.5, a list of exposure studies in WPT-NF and WPT-FF systems that have been recently published are given. Both computational studies and experimental approaches are mentioned. For easier identification the first author of the study and the reference number is used. A very interesting application of these studies is the optimization of the WPT frequency range with respect to compliance with exposure safety guidelines. In [81] it was shown that the optimal range is for operation between 1 and 2.5 MHz. For the kHz region, in [88] it was shown that a frequency of 450 kHz is optimal. Safety studies can be also quite important in determining experimentally the power rating that results in exposure beyond the limits. The harmonics is another parameter that can cause concerns. In [95] the presence of harmonics decreased the allowable transmitting power by almost 40 %.

A surprising omission from all the studies is the estimation of uncertainty. Uncertainty is even more important in the case of outdoor measurements where more uncontrollable conditions may appear compared to a laboratory. In general a radiation limits conformity study should include uncertainty assessments [39]. Probably, the reason is that in general the exposure is orders of magnitude away from the limit alleviating in partly the need for an uncertainty budget.

## 7.7 Industry Initiatives and De Facto Application Standards

There are some industry initiatives which are analysed in this section. These industry alliances provide certifications of conformance to certain proposed technologies. These certifications are acting as de facto application standards.

**Table 7.5** Recent exposure studies in WPT systems

| No  | System               | Frequency (MHz) | Power (W)   | Simulation | Experiment | References      |
|-----|----------------------|-----------------|-------------|------------|------------|-----------------|
| 1.  | Magnetic resonant    | 0.1             | 5           | Yes        | Yes        | Chen [81]       |
| 2.  | Magnetic resonant    | 8–15            | 200         | Yes        | No         | Misuno [82]     |
| 3.  | Magnetic resonant    | 1.8, 5.78       | 1           | Yes        | No         | Hong [83]       |
| 4.  | Magnetic resonant    | 0.085           | 3300, 20000 | Yes        | No         | Ombach [84]     |
| 5.  | Magnetic resonant    | 5               | 10,000      | Yes        | No         | Yuan [85]       |
| 6.  | Evanescence coupling | 2440            | 11.2        | Yes        | Yes        | Noda [86]       |
| 7.  | Magnetic resonant    | 6.74            | 1           | Yes        | No         | Mun [87]        |
| 8.  | Loosely coupled      | 0.468, 6.78     | Variable    | Yes        | NO         | Nadakuduti [88] |
| 9.  | Magnetic resonant    | 10              | 1           | Yes        | No         | Park [89]       |
| 10. | Magnetic resonant    | 0.020           | 153         | Yes        | Yes        | Cruciani [90]   |
| 11. | Magnetic resonant    | 0.1–10          | Variable    | Yes        | No         | Chen [91]       |
| 12. | Magnetic resonant    | 10              | 1           | Yes        | No         | Sunohara [92]   |
| 13. | Magnetic resonant    | 0.030           | 3000        | Yes        | No         | Ding [74]       |
| 14. | Magnetic resonant    | 0.140           | 1           | Yes        | No         | Sunohara [93]   |
| 15. | Magnetic resonant    | 0.150           | Variable    | Yes        | No         | Song [96]       |
| 16. | Magnetic resonant    | 10              | Variable    | Yes        | No         | Hirata [97]     |

### 7.7.1 Airfuel Alliance

The Airfuel alliance was formed with the merger of Alliance for Wireless Power (AW4P) and Power Matters Alliance (PMA). The intended application domain covers consumer, industrial, medical, and military applications. Furthermore, it aims at coping with different power requirements such as simultaneous charging of a laptop and smartphone. The Alliance classifies the devices according to power ratings

possibilities in five Classes. Airfuel focuses on 6.78 MHz that belongs to the first ISM band and is a WPT-NF technology that utilizes inductive, resonant, and Uncoupled.

### 7.7.2 *Wireless Power Consortium*

Qi is a certification pushed forward by the Wireless Power Consortium (see Table 7.2). It is also focusing on a near-field approach utilizing resonant induction. The consortium has issued a detailed set of specifications [98].

### 7.7.3 *Open Dots Alliance*

Another interesting alliance on WPT matters is the Open Dots Alliance [29] mainly initiated by the car industry. It is called “Open” because the specifications and compliance information is available to the public. It is called “Dots” because products employing the standard use a distinctive pattern of contact “dots” to transfer power. The Alliance claims transfer of up to 160 Watts. The major difference of this technology is that it is a wire-free approach but conductive. The contact requirement limits this technology to cordless charging [99].

## 7.8 Conclusions

A review of regulations and standards related to WPT systems has been presented. WPT devices are still not classified as a separate category with many of them operating in ISM bands. There is a considerable amount of ongoing work in all related international organizations, the majority of which focuses on the near-field WPT and corresponding EMC/EMI issues. Important efforts are also noted in Korea, Japan and USA, and in some cases national standards in the case of near-field devices have been prepared that guide international efforts. Radiation safety studies indicate conformity to the general limits and could be used as a supplementary tool to select some frequencies over other available frequencies. As many technological solutions appear for WPT systems, the need for more radiation safety studies becomes greater.

In terms of regulations, WPT in the near field can be dealt as a new device that should conform to EMC/EMI standards. Usually EMC/EMI difficulties occur when the transmission power is getting higher and higher. Furthermore, radiation safety regulations impose additional power limits. WPT in the far field must be additionally coordinated in frequency with other systems and could be classified according to range as a short range device or a completely new application such as cellular telephony. It is to be noted that ITU has recognized the necessity to treat

WPT devices that operate in the near field differently than the ones which operate in the far field.

**Acknowledgments** The work was supported by the EU COST Action IC1301 WiPE (Wireless Power Transmission for sustainable Electronics) and by the EU Horizon 2020 Research and Innovation Programme under the Marie Skłodowska-Curie Grant Agreement No 654734. The authors would like to thank Dr. Konstantinos Prokopidis for help with the preparation of the L<sup>A</sup>T<sub>E</sub>X files.

## References

1. Carvalho, N.B., Georgiadis, A., Costanzo, A., Rogier, H., Collado, A., García, J., Lucyszyn, S., Mezzanotte, P., Kracek, J., Masotti, D., Boaventura, A., de las Nieves Ruiž Lavín, M., Pinuela, M., Yates, D., Mitcheson, P., Mazanek, M., Pankrac, V.: IEEE Trans. Microwave Theory Tech. **62**(4), 1031 (2014). doi:[10.1109/TMTT.2014.2303420](https://doi.org/10.1109/TMTT.2014.2303420)
2. Visser, H., Vullers, R.: Proc. IEEE **101**(6), 1410 (2013). doi:[10.1109/JPROC.2013.2250891](https://doi.org/10.1109/JPROC.2013.2250891)
3. Ho, J.S., Yeh, A.J., Neofytou, E., Kim, S., Tanabe, Y., Patlolla, B., Beygui, R.E., Poon, A.S.Y.: Proc. Natl. Acad. Sci. **111**(22), 7974 (2014). doi:[10.1073/pnas.1403002111](https://doi.org/10.1073/pnas.1403002111)
4. Laughner, J.I., Marrus, S.B., Zellmer, E.R., Weinheimer, C.J., MacEwan, M.R., Cui, S.X., Nerbonne, J.M., Efimov, I.R.: PLoS ONE **8**(10), e76291 (2013). doi:[10.1371/journal.pone.0076291](https://doi.org/10.1371/journal.pone.0076291)
5. Xu, Q., Gao, Z., Wang, H., He, J., Mao, Z.H., Sun, M.: IEEE Microwave Mag. **14**(2), 63 (2013). doi:[10.1109/MMM.2012.2234640](https://doi.org/10.1109/MMM.2012.2234640)
6. Tang, T., Smith, S., Flynn, B., Stevenson, J., Gundlach, A., Reekie, H., Murray, A., Renshaw, D., Dhillon, B., Ohtori, A., Inoue, Y., Terry, J., Walton, A.: Nanobiotechnology. IET **2**(3), 72 (2008). doi:[10.1049/iet-nbt.20080001](https://doi.org/10.1049/iet-nbt.20080001)
7. Musavi, F., Eberle, W.: Power electronics. IET **7**(1), 60 (2014). doi:[10.1049/iet-pel.2013.0047](https://doi.org/10.1049/iet-pel.2013.0047)
8. Shoki, H.: Proc. IEEE **101**(6), 1312 (2013). doi:[10.1109/JPROC.2013.2248051](https://doi.org/10.1109/JPROC.2013.2248051)
9. Jiang, H., Brazis, P., Tabaddor, M., Bablo, J.: 2012 IEEE Symposium on Product Compliance Engineering (ISPCE) (2012), pp. 1–6. doi:[10.1109/ISPCE.2012.6398288](https://doi.org/10.1109/ISPCE.2012.6398288)
10. Taki, M.: Proceedings of 2013 URSI International Symposium on Electromagnetic Theory (EMTS), pp. 3–4 (2013)
11. Kalialakis, C., Georgiadis, A.: Wirel. Power Transf. **1**, 108 (2014). doi:[10.1017/wpt.2014.13](https://doi.org/10.1017/wpt.2014.13)
12. Pinuela, M., Yates, D., Mitcheson, P., Lucyszyn, S.: 2013 7th European Conference on Antennas and Propagation (EuCAP), pp. 2839–2843 (2013)
13. Parks, A., Sample, A., Zhao, Y., Smith, J.R.: 2013 IEEE Topical Conference on Biomedical Wireless Technologies, Networks, and Sensing Systems (BioWireleSS), pp. 154–156 (2013)
14. Hagerty, J., Helmbrecht, F., McCalpin, W., Zane, R., Popovic, Z.: IEEE Trans. Microwave Theory Tech. **52**(3), 1014 (2004). doi:[10.1109/TMTT.2004.823585](https://doi.org/10.1109/TMTT.2004.823585)
15. Vyay, R., Cook, B., Kawahara, Y., Tentzeris, M.: IEEE Trans. Microwave Theory Tech. **61**(6), 2491 (2013). doi:[10.1109/TMTT.2013.2258168](https://doi.org/10.1109/TMTT.2013.2258168)
16. Pinuela, M., Mitcheson, P., Lucyszyn, S.: IEEE Trans. Microwave Theory Tech. **61**(7), 2715 (2013). doi:[10.1109/TMTT.2013.2262687](https://doi.org/10.1109/TMTT.2013.2262687)
17. Kawahara, Y., Tsukada, K., Asami, T.: Antennas and Propagation Society International Symposium, APSURSI'09, pp. 1–4. IEEE (2009). doi:[10.1109/APS.2009.5171785](https://doi.org/10.1109/APS.2009.5171785)
18. Visser, H., Reniers, A., Theeuwes, J.: Microwave Conference, 2008. EuMC 2008. 38th European, pp. 721–724 (2008). doi:[10.1109/EUMC.2008.4751554](https://doi.org/10.1109/EUMC.2008.4751554)
19. Guenda, L., Santana, E., Collado, A., Niotaki, K., Carvalho, N.B., Georgiadis, A.: Trans. Emerg. Telecommun. Technol. **25**(1), 56 (2014). doi:[10.1002/ett.2768](https://doi.org/10.1002/ett.2768)
20. EnOcean Alliance, Energy Harvesting Wireless Technology for Home and Building Automation. [http://www.enocean-alliance.org/en/enocean\\_technology/](http://www.enocean-alliance.org/en/enocean_technology/)

21. Sasaki, S.: IEEE Spectrum **51**(5), 46 (2014). doi:[10.1109/MSPEC.2014.6808461](https://doi.org/10.1109/MSPEC.2014.6808461)
22. Jaffe, P., McSpadden, J.: Proc. IEEE **101**(6), 1424 (2013). doi:[10.1109/JPROC.2013.2252591](https://doi.org/10.1109/JPROC.2013.2252591)
23. European Union. Low Voltage Directive (LVD) 2006/95/EC
24. European Union. Directive on the restriction of the use of certain hazardous substances (RoHS) in electrical and electronic equipment 2011/65/EU
25. ISO/IEC Guide 2:2004, standardization and related activities—general vocabulary
26. Wireless Power Consortium. <http://www.wirelesspowerconsortium.com/>
27. Airfuel Alliance. <http://airfuel.org/home/about-us-2>
28. Grajski, K., Tseng, R., Wheatley, C.: Microwave Workshop Series on Innovative Wireless Power Transmission: Technologies, Systems, and Applications (IMWS), 2012 IEEE MTT-S International, pp. 9–14 (2012). doi:[10.1109/IMWS.2012.6215828](https://doi.org/10.1109/IMWS.2012.6215828)
29. Open Dots Alliance. <http://opendotsalliance.org/>
30. EnOcean Alliance. <http://www.enocean-alliance.org/en/home/>
31. Korean Wireless Power Forum. <http://kwpf.org/eng/html/main.html>
32. Wireless Power Management Consortium. <http://wpm-c.com/>
33. Global Standards Collaboration Repository. <http://www.itu.int/en/ITU-T/gsc/Pages/meetings.aspx>
34. Global Standards Collaboration. [www.gsc.etsi.org](http://www.gsc.etsi.org)
35. Guideline, ICNIRP, Health Phys. **74**(4), 494 (1998)
36. Guideline, ICNIRP, Health Phys. **99**(6), 818 (2010)
37. International Committee on Electromagnetic Safety, The Institute of Electrical and Electronics Engineers. IEEE Std C95.1-2005, Safety Levels with Respect to Human Exposure to Radio frequency Electromagnetic Fields, 3 kHz to 300 GHz (2005)
38. FCC. Specific absorption rate (SAR) for cellular telephones. <http://www.fcc.gov/encyclopedia/specific-absorption-rate-sar-cellular-telephones>
39. Grudzinski, E., Trzaska, H.: Electromagnetic Field Standards and Exposure Systems. SciTech Publishing (2014)
40. FCC. Title 47 of the Code of Federal Regulations, Part 15 RF Devices
41. European Union. EMC Directive 2004/108/EC on the approximation of the laws of the Member States relating to electromagnetic compatibility and repealing Directive 89/336/EEC
42. ERC Report 074, Compatibility between radio frequency identification devices (RFID) and the radioastronomy service at 13 MHz (1999)
43. FCC. Title 47 of the Code of Federal Regulations, Part 18 ISM
44. ISO/IEC 14543-3-10:2012, Information technology—home electronic systems (HES)—Part 3–10: Wireless short-packet (WSP) protocol optimized for energy harvesting—architecture and lower layer protocols
45. Ernst, D.: Review of European. Comp. Int. Environ. Law **22**(3), 354 (2013). doi:[10.1111/reel.12041](https://doi.org/10.1111/reel.12041)
46. Center for Devices and Radiological Health. Radio frequency wireless technology in medical devices—guidance for industry and food and drug administration staff (2013)
47. ECC Recommendation, Determination of the radiated power through field strength measurements in the frequency range from 400 MHz to 6000 MHz, ECC/REC/(12)03
48. ITU. QUESTION ITU-R 210-3/1 Wireless Power Transfer (2012)
49. ITU. Working party 1a, contributions on question: 210-3/1. <https://www.itu.int/md/meetingdoc.asp?lang=en&parent=R12-WP1A-C&question=210-3/1>
50. ITU. ITU-R Report SM.2303-1, Wireless power transmission using technologies other than radio frequency beam (2015). <http://www.itu.int/pub/R-REP-SM.2303-1-2015>
51. Standard EN 300 330—radio equipment in the frequency range 9 kHz to 25 MHz and inductive loop systems in the frequency range 9 kHz to 30 MHz
52. EN 300 330-1. <http://portal.etsi.org/portal/server.pt/community/ERM/306?tbId=584>
53. ETSI, radio and spectrum matter. <http://portal.etsi.org/tb.aspx?tbid=584&SubTB=584>
54. CEPT Reference ETSI Liaison ECC(13)089\_ ETSI report to ECC#35
55. FM(14)003\_Response LS ETSI TC ERM on status of EN 302 291 on SRD at 13.56 MHz
56. SE(13)114\_ETSI Progress report

57. IEC, TC 69: Electric road vehicles and electric industrial trucks. [http://www.iec.ch/dyn/www/f?p=103:23:0::::FSP\\_ORG\\_ID,FSP\\_LANG\\_ID:1255,25](http://www.iec.ch/dyn/www/f?p=103:23:0::::FSP_ORG_ID,FSP_LANG_ID:1255,25)
58. IEC, TC 100, audio, video and multimedia systems and equipment. [http://www.iec.ch/dyn/www/f?p=103:23:0::::FSP\\_ORG\\_ID,FSP\\_LANG\\_ID:1297,25](http://www.iec.ch/dyn/www/f?p=103:23:0::::FSP_ORG_ID,FSP_LANG_ID:1297,25)
59. ISO/AWI PAS 19363, electrically propelled road vehicles—magnetic field wireless power transfer—safety and interoperability requirements. [http://www.iso.org/iso/home/store/catalogue\\_tc/catalogue\\_detail.htm?csnumber=64700](http://www.iso.org/iso/home/store/catalogue_tc/catalogue_detail.htm?csnumber=64700)
60. ISO/IEC JTC, on going work. [http://jtc1info.org/?page\\_id=541](http://jtc1info.org/?page_id=541)
61. CISPR, CIS/B. [http://www.iec.ch/dyn/www/f?p=103:30:0::::FSP\\_ORG\\_ID,FSP\\_LANG\\_ID:1412,25](http://www.iec.ch/dyn/www/f?p=103:30:0::::FSP_ORG_ID,FSP_LANG_ID:1412,25)
62. CLC/TC 69X electrical systems for electric road vehicles. [ftp://ftp.cencenelec.eu/CENELEC/EP/BP\\_TC\\_69X.pdf](ftp://ftp.cencenelec.eu/CENELEC/EP/BP_TC_69X.pdf)
63. Sasaki, K.: EVTeC and APE Japan 2014 Conference. Yokohama, Japan (2014)
64. Broadband Wireless Forum Japan. Guidelines for the use of wireless power transmission/transfer technologies, technical report, tr-01 edition 2 (2013). <http://bwf-yrp.net/english/update/docs/guidelines.pdf>
65. Telecommunications technology association, standardization. [http://www.tta.or.kr/English/new/standardization/eng\\_ttstd\\_main.jsp](http://www.tta.or.kr/English/new/standardization/eng_ttstd_main.jsp)
66. Lee, H.: 17th Global Standards Collaboration meeting (GSC-17). Jeju, Korea (2013)
67. Schneider, J.: SAE J2954 overview and path forward. [http://www.sae.org/smartgrid/sae-j2954-status\\_1-2012.pdf](http://www.sae.org/smartgrid/sae-j2954-status_1-2012.pdf)
68. UL. Safety considerations of wireless charger for electric vehicles a review (2013)
69. UL. Connecting to electric vehicle infrastructure (2014). [http://newscience.ul.com/wp-content/uploads/sites/30/2014/04/Powering\\_the\\_New\\_Generation\\_of\\_Electric\\_Vehicles.pdf](http://newscience.ul.com/wp-content/uploads/sites/30/2014/04/Powering_the_New_Generation_of_Electric_Vehicles.pdf)
70. IEEE ISTO, wireless power consortium program. <http://www.ieee-isto.org/member-programs/wireless-power-consortium>
71. IEEE Standards. Electric Vehicle Wireless Power Transfer. [http://standards.ieee.org/about/sasb/iccom/IC13-002-03\\_Electric\\_Vehicle\\_Wireless\\_Power\\_Transfer\\_0313.pdf](http://standards.ieee.org/about/sasb/iccom/IC13-002-03_Electric_Vehicle_Wireless_Power_Transfer_0313.pdf)
72. Gil, A., Taiber, J.: A Literature Review in Dynamic Wireless Power Transfer for Electric Vehicles: Technology and Infrastructure Integration Challenges. Springer (2014)
73. Miyakoshi, J.: Proc. IEEE **101**(6), 1494 (2013). doi:[10.1109/JPROC.2013.2248111](https://doi.org/10.1109/JPROC.2013.2248111)
74. Ding, P.P., Bernard, L., Pichon, L., Razek, A.: IEEE Trans. Magn. **50**(2), 1037 (2014). doi:[10.1109/TMAG.2013.2284245](https://doi.org/10.1109/TMAG.2013.2284245)
75. European Commission. Vademecum on gender equality in horizon 2020 (2014)
76. Christ, A., Douglas, M., Nadakuduti, J., Kuster, N.: Proc. IEEE **101**(6), 1482 (2013). doi:[10.1109/JPROC.2013.2245851](https://doi.org/10.1109/JPROC.2013.2245851)
77. Lin, J.: IEEE Antennas Propag. Mag. **55**(2), 250 (2013). doi:[10.1109/MAP.2013.6529362](https://doi.org/10.1109/MAP.2013.6529362)
78. Lin, J.: IEEE Microwave Mag. **14**(5), 18 (2013). doi:[10.1109/MMM.2013.2259409](https://doi.org/10.1109/MMM.2013.2259409)
79. Lin, J.C.: Wireless battery—charging technology or energy harvesting to power mobile phones or other mobile communication devices, and health effects. URSI Radio Sci. Bull. **344**, 34–36 (2013)
80. Kuster, N.: Microwave Conference Proceedings (APMC), 2012 Asia-Pacific, pp. 708–710 (2012). doi:[10.1109/APMC.2012.6421711](https://doi.org/10.1109/APMC.2012.6421711)
81. Chen, X.L., Umenei, A., Baarman, D., Chavannes, N., De Santis, V., Mosig, J., Kuster, N.: IEEE Trans. Electromagn. Compat. **56**(5), 1027 (2014). doi:[10.1109/TEMC.2014.2308013](https://doi.org/10.1109/TEMC.2014.2308013)
82. Mizuno, K., Miyakoshi, J., Shinohara, N.: Microwave Workshop Series on Innovative Wireless Power Transmission: Technologies, Systems, and Applications (IMWS), 2012 IEEE MTT-S International, pp. 79–82 (2012). doi:[10.1109/IMWS.2012.6215824](https://doi.org/10.1109/IMWS.2012.6215824)
83. Hong, S.E., Cho, I.K., Choi, H.D., Pack, J.K.: 2014 IEEE Wireless Power Transfer Conference (WPTC), pp. 216–219 (2014). doi:[10.1109/WPT.2014.6839587](https://doi.org/10.1109/WPT.2014.6839587)
84. Ombach, G.: 2014 Ninth International Conference on Ecological Vehicles and Renewable Energies (EVER), pp. 1–4 (2014). doi:[10.1109/EVER.2014.6844157](https://doi.org/10.1109/EVER.2014.6844157)
85. Yuan, Q., Ishikawa, T.: 2013 IEEE Wireless Power Transfer (WPT), pp. 238–241 (2013). doi:[10.1109/WPT.2013.6556927](https://doi.org/10.1109/WPT.2013.6556927)

86. Noda, A., Shinoda, H.: ICCAS-SICE, 2009, pp. 1105–1109 (2009)
87. Mun, J.Y., Seo, M.G., Kang, W.G., Jun, H.Y., Park, Y.H., Pack, J.K.: PIERS Proceedings, pp. 322–324. Russia, Moscow (2012)
88. Nadakuduti, J., Lu, L., Guckian, P.: 2013 IEEE Wireless Power Transfer (WPT), pp. 234–237 (2013). doi:[10.1109/WPT.2013.6556926](https://doi.org/10.1109/WPT.2013.6556926)
89. Park, S.W., Wake, K., Watanabe, S.: IEEE Trans. Microwave Theory Tech. **61**(9), 3461 (2013). doi:[10.1109/TMTT.2013.2274053](https://doi.org/10.1109/TMTT.2013.2274053)
90. Cruciani, S., Maradei, F., Feliziani, M.: 2013 IEEE International Symposium on Electromagnetic Compatibility (EMC), pp. 259–264 (2013). doi:[10.1109/ISEMC.2013.6670420](https://doi.org/10.1109/ISEMC.2013.6670420)
91. Chen, X.L., Santis, V.D., Umenei, A.E.: Phys. Med. Biol. **59**(13), 3453 (2014). <http://stacks.iop.org/0031-9155/59/i=13/a=3453>
92. Sunohara, T., Laakso, I., Chan, K.H., Hirata, A.: Proceedings of 2013 URSI International Symposium on Electromagnetic Theory (EMTS), pp. 831–833 (2013)
93. Sunohara, T., Hirata, A., Laakso, I., Onishi, T.: Phys. Med. Biol. **59**(14), 3721 (2014). <http://stacks.iop.org/0031-9155/59/i=14/a=3721>
94. Laakso, I., Hirata, A.: Phys. Med. Biol. **58**(21), 7583 (2013). <http://stacks.iop.org/0031-9155/58/i=21/a=7583>
95. Sunohara, T., Hirata, A., Laakso, I., Santis, V.D., Onishi, T.: Phys. Med. Biol. **60**(20), 8129 (2015). <http://stacks.iop.org/0031-9155/60/i=20/a=8129>
96. Song, H.J., Shin, H., Lee, H.B., Yoon, J.H., Byun, J.K.: IEEE Trans. Magn. **50**(2), 1041 (2014). doi:[10.1109/TMAG.2013.2282364](https://doi.org/10.1109/TMAG.2013.2282364)
97. Hirata, A., Ito, F., Laakso, I.: Phys. Med. Biol. **58**(17), N241 (2013). <http://stacks.iop.org/0031-9155/58/i=17/a=N241>
98. Wireless Power Consortium, The Qi Specification. <http://www.wirelesspowerconsortium.com/downloads/wireless-power-specification-part-1.html>
99. Open Dots Alliance, Open Dots 101. <http://opendotsalliance.org/technical-information/open-dots-101/>

## **Part II**

# **Communication**

# Chapter 8

## Trade-Offs in Wireless Powered Communications

Panagiotis D. Diamantoulakis and George K. Karagiannidis

**Abstract** We investigate trade-offs that are created in wireless powered communication networks. To this end, we take into account throughput maximization, energy efficiency, and fairness and we present and discuss the solution of several optimization problems, considering different scenarios for the network consistence, the adopted protocol, and the energy arrival knowledge. We show that all optimization problems can be solved using convex optimization, and, thus the provided solutions can be efficiently used in practical implementations.

### 8.1 Introduction

Untethered communication equipments are limited by the finite battery capacity, since devices operate for a finite duration, only as long as the battery lasts [29]. In this context, energy harvesting (EH), which refers to harnessing energy from the environment or other energy sources and converting to electrical energy, is regarded as a disruptive technological paradigm to prolong the lifetime of energy-constrained wireless networks. Apart from offering a promising solution for energy sustainability of wireless nodes in communication networks [9], EH also reduces considerably the operational expenses [29].

Among the energy harvesting techniques, simultaneous wireless information and power transfer (SWIPT) is the most challenging, as it presupposes the efficient design of systems in order to support SWIPT [13, 31]. In this framework, nodes use the power by the received signal to charge their batteries [24], or to transmit the information to a base station (BS) [15]. However, in practice, nodes cannot harvest energy and receive/transmit information simultaneously [15, 17, 20, 36]. In order to overcome this difficulty, two strategies have been proposed, i.e., *power-splitting* and

---

P.D. Diamantoulakis (✉) · G.K. Karagiannidis  
Aristotle University of Thessaloniki, 54124 Thessaloniki, Greece  
e-mail: padiaman@auth.gr

G.K. Karagiannidis  
e-mail: geokarag@auth.gr

*time-sharing* [17, 39]. The idea of SWIPT has been reported in various case studies, such as one source destination pair [24], multiple-input multiple-output (MIMO) communications systems [19, 30, 33, 34, 40], orthogonal frequency division multiple access (OFDMA) [26], cooperative networks [6, 10, 16], and cognitive radio networks [18, 23].

Among the proposed SWIPT applications, this chapter focuses on the joint design of downlink energy transfer and uplink information transfer in multiuser communications systems, which has been initially investigated in [15, 21]. Taking into account the time-sharing technique, the authors in [15] have proposed a novel protocol referred to as *harvest-then-transmit*, where the users first harvest energy, and then they transmit their independent messages to the BS by using the harvested energy.

### 8.1.1 Motivation

The harvest-then-transmit protocol infers several interesting trade-offs that have considerably attracted the research interest [4, 14, 15, 35, 39]. First, there is a nontrivial trade-off between the time dedicated for energy harvesting and that for information transmission [15, 19]. A solution to this trade-off depends on both the available channel state information and the knowledge of the energy arrival rate. To this end, three cases have been considered in the literature:

- The deterministic case, where the energy harvesting rate is known in advance [35].
- The stochastic case, where the energy harvesting rate is unknown and only its statistical properties are available [35].
- The multiple timeslots approach, where in each timeslot the BS has perfect knowledge of the instantaneous fading gains and the energy arrival rate [14].

Beyond this trade-off, in the multiple users scenario, there is a trade-off between performance and decoding complexity, which depends on the utilized multiple access scheme [7, 8, 33]. More specifically, two well-known multiple access schemes have been explored in the context of wireless powered communications networks, namely time division multiple access (TDMA) and non-orthogonal multiple access (NOMA) [11, 12, 28]. NOMA is substantially different from the traditional orthogonal multiple access schemes (i.e., time/frequency/code), since its basic principle is to achieve multiple access by exploiting the power domain [11, 22]. For this reason, the decoder needs to implement a joint processing technique, such as successive interference cancellation (SIC), which increases the decoding complexity. However, when utilized in wireless powered communication networks, NOMA proves to increase the minimum throughput and fairness, since the throughput region is different compared to that of TDMA. Note that the implementation of NOMA in the uplink is not a burden for the users, since the encoding complexity at the users' side is not affected, while their synchronization is usually simpler than the case of TDMA.

Moreover, there is an interesting trade-off between performance and fairness. In general, when the sum-throughput is maximized, fairness is considerably reduced, due to the “*double near-far*” problem. This phenomenon appears when a user far from the BS receives a smaller amount of wireless energy than a nearer user, while it needs to transmit with more power [15]. In this case, in order to achieve fairness the following three schemes can be used [15]:

- The *weighted sum-throughput maximization*, which aims to maximize the scaled sum of the users throughputs.
- The *rate profile*, which aims to maximize the sum-throughput under the constraint that each user’s throughput is proportional to the sum-throughput. In this method, a predetermined proportionality parameter is utilized, which ensures a minimum level of fairness.
- The *common throughput maximization*, which guarantees equal throughput allocations to all users and simultaneously maximizes their sum-throughput.

Note that the level of fairness of each scheme has a direct impact on the achieved sum-throughput.

Finally, although most of the research focuses on throughput maximization and fairness improvement, there is also an interesting trade-off between throughput and energy efficiency, which was studied in [32]. Because of the rapidly rising energy costs and the tremendous carbon footprints of existing systems, energy efficiency (EE) is gradually accepted as an important design criterion for future communication systems. Moreover, in wireless powered communication networks, significant amount of energy may be consumed during energy harvesting, in order to combat the channel attenuation, which makes the consideration of EE even more interesting [25, 32].

### 8.1.2 Contribution

This chapter provides useful insights into the main trade-offs that have been explored in the literature, in the context of wireless powered communications. Besides, an interesting dependence between throughput, fairness, complexity, and energy efficiency is revealed. Extended simulations illustrate that

- The increase of the energy arrival rate reduces the portion of time that is allocated to energy harvesting.
- Stochastic knowledge of the energy rate arrival only slightly reduces the throughput compared to the deterministic case.
- NOMA can be efficiently used to increase fairness.
- Sophisticated optimization methods can be also used to improve fairness, at the expense of sum-throughput.
- The maximization of the sum-throughput reduces considerably the achieved energy efficiency.

## 8.2 System Model

We consider the uplink in a wireless network, consisting of  $N$  EH users, one BS, and one power beacon (PB). We assume that PB supplies wireless energy to the users and does not participate in the information transmission. However, it is assumed that the PB is empowered with the functionality of a communication entity, and is capable of performing tasks such as channel estimation [37, 38]. We also assume that all nodes are equipped with a single antenna, while they share the same frequency band.

The communication is divided into timeslots of unitary duration unitary. Hereinafter, the notation  $(\cdot)[i]$  and  $(\cdot)_n$  will be used to denote the value of the variable  $(\cdot)$  during the  $i$ -th timeslot and for the  $n$ -th user, respectively. Besides,  $\mathcal{N}$  will denote the set of all users, while  $(\cdot)^*$  will be utilized to denote optimality. Note that when the provided analysis focuses to a single timeslot,  $[i]$ , and a single user  $n$ ,  $(\cdot)[i]$  and  $(\cdot)_n$  will be omitted, respectively.

We assume that users cannot receive and transmit simultaneously. For this purpose, the harvest-the-transmit protocol is employed and there are the following two distinct phases during a timeslot:

- *Phase 1*: The users harvest energy in order to charge their batteries. The duration of this phase is denoted by  $T[i]$ .
- *Phase 2*: The remaining amount of time, i.e.,  $1 - T[i]$  is assigned to the users, in order to transmit their messages.

### 8.2.1 Phase 1

The energy received by the  $n$ -th user is denoted by  $\tilde{Y}_n[i]$ . The harvested energy,  $Y_n$  is

$$Y_n[i] = \eta \tilde{Y}_n[i], \quad (8.1)$$

where  $\eta$  is the efficiency of the energy harvester. Assuming that users harvest energy solely from the signals transmitted by the a dedicated PB, the received energy is given by

$$\tilde{Y}_n = \tilde{\gamma}_n[i] P_0 T[i], \quad (8.2)$$

where  $\tilde{\gamma}_n[i] = |\tilde{h}_n[i]|^2 \tilde{L}_n[i]$ , with  $\tilde{h}_n[i]$ ,  $|\tilde{h}_n[i]|^2$ , and  $\tilde{L}[i]$  being the channel coefficient, the channel power gain, and the path loss factor from the PB to the  $n$ -th user, respectively. Also,  $P_0$  denotes the power transmitted by the PB during the first phase. At the special case that the users harvest energy solely from the signals transmitted by the BS, i.e., when the BS has the power beacon functionality during the first phase,  $\tilde{\gamma}_n$ ,  $\tilde{h}_n[i]$  and  $\tilde{L}_n[i]$  can be replaced by  $\gamma_n$ ,  $h_n[i]$  and  $L_n[i]$ , where  $h_n[i]$  and  $L_n[i]$  denote the channel coefficient and the path loss factor from the BS to the  $n$ -th user, respectively. It is assumed that the channel conditions remain constant during a timeslot, and their exact values are known by the coordinator of the network, e.g., the BS.

### 8.2.2 Phase 2

Assuming channel reciprocity, the channel coefficient and the path loss factor from the  $n$ -th user to the BS are given by  $h_n$  and  $L_n$ , respectively, while  $N_0$  is used to denote the power of the additive white gaussian noise (AWGN). Moreover, let  $R_n[i]$  denote the achievable throughput of the  $n$ -th user during the  $i$ -th timeslot,  $P_n[i]$  the power of the signal that is transmitted by the  $n$ -th user, and  $\tau_n[i]$  the time that is allocated to the  $n$ -th user, in order to transmit its information. Since we have assumed that users cannot receive and transmit simultaneously, it must hold that

$$\tau_n[i] \leq 1 - T[i]. \quad (8.3)$$

Finally, it is considered that wireless power transfer is the sole energy source and, unless otherwise stated, all nodes consume energy only for transmission.

## 8.3 Trade-Off Between Information Transmission and Energy Transfer

This section focuses on the trade-off between the time that is allocated to energy transfer and information transmission. More specifically, it is shown that the achieved throughput is strongly affected by the time that is allocated to each phase, while for simplicity, a single user is considered. The achievable throughput in each timeslot is given by [35]

$$R = \tau \log_2 \left( 1 + \frac{P\gamma}{N_0} \right). \quad (8.4)$$

Since given  $T$ ,  $R$  is an increasing function of  $\tau$ , it can be written as

$$R = (1 - T) \log_2 \left( 1 + \frac{P\gamma}{N_0} \right). \quad (8.5)$$

### 8.3.1 Single Timeslot Approach

In this subsection, we focus on a single timeslot, i.e., we assume that in each timeslot the user only uses the energy that was harvested during the first phase. Taking into account that  $R$  is an increasing function with respect to  $P$ , it can be replaced by  $\frac{\gamma}{1-T}$ . Thus, the achievable throughput in each timeslot is given by [35]

$$R = (1 - T) \log_2 \left( 1 + \frac{XT}{(1 - T)} \right), \quad (8.6)$$

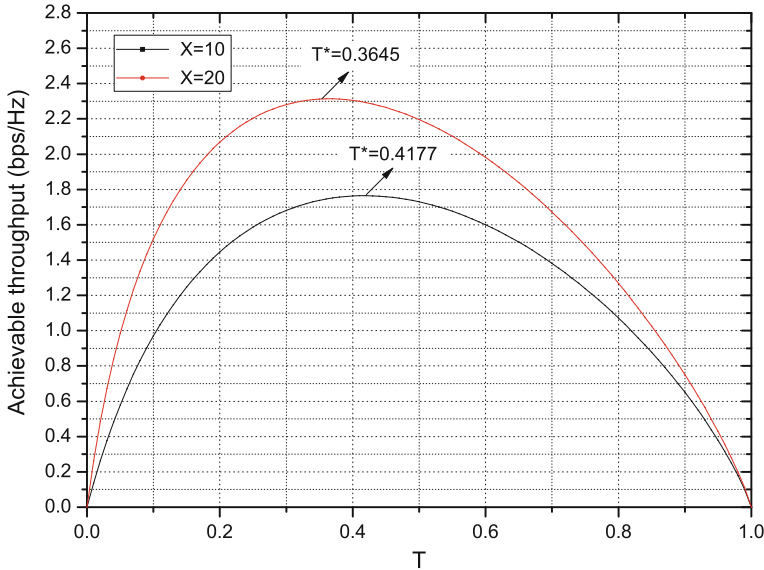


**Fig. 8.1** Throughput versus the time allocated to energy harvesting

where

$$X = \frac{Y\gamma}{N_0 T}. \quad (8.7)$$

Figure 8.1 shows the throughput given in (8.6) for  $X = 10$  and  $X = 20$  versus the time allocated to energy harvesting. It is observed that the throughput is zero when  $T = 0$ , as well as when  $T = 1$ . Also, it is illustrated that the achievable throughput has one global maximum, i.e., it first increases when  $T < T^*$ , while it decreases when  $T > T^*$ . This can be explained as follows. With small  $T$ , the amount of energy harvested by the user is small. As the user harvests more energy with increasing  $T$ , i.e., more energy is available for the information transmission, the throughput increases with  $T$  [15]. However, as  $T$  becomes larger than  $T^*$  the throughput is decreased due to the reduction in the time allocated to information transmission. Also, it is observed that when  $X = 10$ ,  $T^* = 0.4177$ , while when  $X = 20$ ,  $T^* = 0.3645$ . Thus, it can be concluded that when  $X$  increases the optimal time allocated to energy harvesting decreases. This is because when the user has enough energy to transmit, its sensitivity to the resource of time dedicated to information transmission increases [7, 8].

### 8.3.1.1 Deterministic Energy Arrival

Assuming that  $X$  can be perfectly estimated, the achievable throughput maximization problem can be written as [35]

$$\max_T R \quad (8.8) \\ \text{C : } 0 < T < 1.$$

It can easily be proved that  $R$  is strictly concave with respect to  $T$  in  $(0, 1)$ ,  $\forall X$ , since it holds that [35]

$$\frac{d^2R}{dT^2} = -\frac{-X^2}{\ln(2)(1-T)((X-1)T+1)^2} < 0. \quad (8.9)$$

Thus, the optimal value for  $T$  in  $(0, 1)$  that maximizes  $R$  is unique and can be obtained through

$$\frac{dR}{dT} = 0. \quad (8.10)$$

After some mathematical manipulations, the optimal value can be expressed as [35]

$$T^* = \frac{X-1-W\left(\frac{X-1}{e}\right)}{(X-1)\left(W\left(\frac{X-1}{e}\right)+1\right)}, \quad (8.11)$$

where  $(\cdot)^*$  denotes a solution value and  $W(x)$  returns the principal branch of the Lambert W function, also called omega function or product logarithm. This function is defined as the set of solutions of the equation  $x = W(x)e^{W(x)}$  [5]. Note that  $W(x)$  can be easily evaluated since it is a built-in function in most of the well-known mathematical software packages as MATLAB, Mathematica, etc [9].

### 8.3.1.2 Energy Harvesting Source with Stochastic Energy Arrival

When the energy harvesting rate is nondeterministic, the appropriate metric to optimize is the long-term expectation of the achievable throughput, which is denoted by  $\tilde{R}$ . Next, it is assumed that  $X$  follows a Gamma distribution, i.e.,  $X \sim \Gamma(k, z)$ , where  $k, z > 0$  refer to the shape parameter, because Gamma distribution can model accurately the energy harvesting rate [21]. Note that the channel condition between the user and the BS, described by  $\gamma$ , is assumed to be invariable within each timeslot, thus  $\gamma$  is considered as constant coefficient of energy harvesting rate. The corresponding maximization problem of the expected achievable throughput is given by

$$\max_T \tilde{R} \quad (8.12) \\ \text{C : } 0 < T < 1.$$

Considering the signal-to-noise ratio (SNR), there are two asymptotic cases:

- *Low SNR Approximation:* Under a low SNR condition, i.e., when  $\frac{XT}{1-T} \ll 1$ ,  $\tilde{R}$  is given by [35]

$$\tilde{R} = \frac{T}{\ln(2)} E[X]. \quad (8.13)$$

Apparently, in this case,  $\tilde{R}$  is maximized when  $T \rightarrow 1$ .

- *High SNR Approximation:* Assuming a high SNR condition,  $\tilde{R}$  can be expressed as [35]

$$\tilde{R} = \frac{1-T}{\ln(2)} \left( \psi(k) + \ln \left( \frac{T}{1-T} z \right) \right), \quad (8.14)$$

where  $\psi(\cdot)$  denotes the digamma function, defined by

$$\psi(x) = \frac{d}{dx} \ln (\Gamma(x)). \quad (8.15)$$

The second derivative of  $\tilde{R}$  can be expressed as

$$\frac{d^2 \tilde{R}}{dT^2} = -\frac{1}{\ln(2)} \left( \frac{1}{T(1-T) + \frac{1}{T^2}} \right). \quad (8.16)$$

Apparently, it holds that  $\frac{d^2 \tilde{R}}{dT^2} < 0$ , for  $0 < T < 1$  and, thus, the optimization problem in (8.12) is concave and has a unique solution. Finally, by setting  $\frac{d\tilde{R}}{dT} = 0$  and after some mathematic manipulations, the value of  $T$  which corresponds to the solution of (8.12), for the high SNR approximation, is given by [35]

$$\tilde{T}^* = \frac{1}{W(z e^{\psi(k)-1}) + 1}. \quad (8.17)$$

Note that the derived solution is suboptimal, i.e., it does not necessarily maximize the throughput in (8.6).

### 8.3.1.3 Comparison Between the Deterministic and the Stochastic Case

Next, the stochastic and the deterministic case are compared in terms of time dedicated to energy harvesting and average throughout versus the parameter  $k$ , assuming that  $k = z$ . Note that lower value of  $k$  implies lower average  $X$ . For reference, the throughput when  $T = 0.5$ , i.e., the *half-half* case, is also depicted.

As it is shown in Fig. 8.2 the solution of the optimization problem in (8.12), which corresponds to the stochastic case, usually leads to the selection of lower value of  $T$  than the optimal one that is selected when the optimization problem in (8.8) is solved. Therefore, as it can be observed in Fig. 8.3, the deterministic case slightly outperforms the stochastic case for all values of  $k$ . This is reasonable, since in the former one the optimal save-ratio can be exactly derived, in contrast to the second one, where only the expected optimal choice can be made.

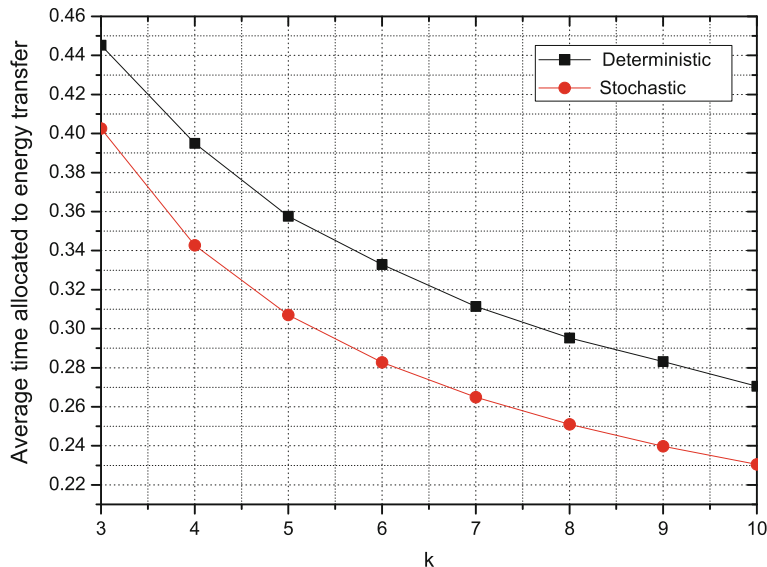


**Fig. 8.2** Comparison of the deterministic and stochastic case in terms of time allocated to energy harvesting

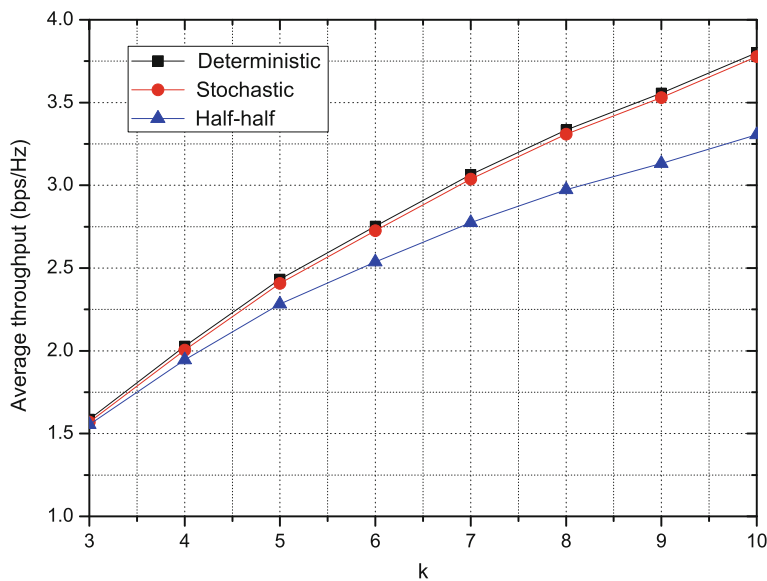


**Fig. 8.3** Comparison of the deterministic and stochastic case in terms of throughput

On the other hand, both the deterministic and stochastic cases outperform the half-half, which validates that both schemes can efficiently use the level of knowledge of the energy harvesting rate in order to maximize the throughput [35].

### 8.3.2 Multiple Timeslots Approach

Let us consider  $M \rightarrow \infty$  timeslots. For simplicity, it is assumed that the user harvests energy solely from the signals transmitted by the BS, i.e., during the first phase the BS has the PB functionality. The average throughput can be written as [14, 27]

$$R_{\text{av}} = \frac{1}{M} \sum_{i=1}^M (1 - T[i]) \log_2 \left( 1 + \frac{\eta \rho_0[i] g[i] T[i]}{1 - T[i]} \right). \quad (8.18)$$

where  $\rho_0[i] = \frac{P_0[i]}{N_0}$  and  $g[i] = \gamma [i]^2$ .

Next, a scheme for jointly optimal allocation of  $\rho_0[i]$  and  $T[i]$  is discussed, which aims to the maximization of the average throughput. This scheme is feasible if, in each timeslot  $i$ , the BS has perfect CSI. The corresponding optimization problem can be written as

$$\begin{aligned} & \max_{\bar{T}, \bar{\rho}} R_{\text{av}} \\ \text{s.t. } & C_1 : 0 < T[i] < 1, \\ & C_2 : 0 \leq \rho_0[i] \leq P_{\text{max}}, \\ & C_3 : \frac{1}{M} \sum_{i=1}^M \rho_0[i] T[i] \leq P_{\text{avg}}, \end{aligned} \quad (8.19)$$

where  $P_{\text{max}}$  and  $P_{\text{avg}}$  are the (normalized by the AWGN power) maximum and average available BS transit power, respectively, with  $\bar{T}$  and  $\bar{\rho}$  being the vectors with elements  $T[i], \forall i$  and  $\rho[i], \forall i$ .

The optimization problem in (8.19) can be easily be transformed to a convex one by utilizing the change of variables  $\varepsilon[i] = \rho_0[i]T[i]$ . The transformed problem is given by [14]

$$\begin{aligned} & \max_{\bar{T}, \bar{\varepsilon}} \bar{R}_{\text{av}} \\ \text{s.t. } & C_1 : 0 < T[i] < 1, \\ & \bar{C}_2 : 0 \leq \varepsilon[i] \leq P_{\text{max}} T[i], \\ & \bar{C}_3 : \frac{1}{M} \sum_{i=1}^M \varepsilon[i] \leq P_{\text{avg}}, \end{aligned} \quad (8.20)$$

where  $\varepsilon$  is the vector with elements  $\varepsilon[i], \forall i$ . In the above,  $\bar{R}_{\text{av}}$  is given by

$$\bar{R}_{\text{av}} = \frac{1}{M} \sum_{i=1}^M \tilde{R}_{\text{in}}[i], \quad (8.21)$$

where

$$\tilde{R}_{\text{in}}[i] = (1 - T[i]) \log_2 \left( 1 + \frac{\eta g[i] \varepsilon[i]}{1 - T[i]} \right). \quad (8.22)$$

The convexity of (8.20) can be easily proved since its objective function is the summation of concave functions and all the constraints are linear. Note that the terms,  $\tilde{R}_{\text{in}}[i]$ , are concave because the eigenvalues,  $\phi_j[i]$ ,  $j = \{1, 2\}$ , of their Hessian matrices,  $\mathcal{H}[i]$ , are both nonpositive. These are given by  $\phi_1[i] = 0$  and

$$\phi_2[i] = \frac{g[i]^2 \eta^2 (\varepsilon[i]^2 + (T[i] - 1)^2)}{(1 + g[i] \eta \varepsilon[i] - T[i])^2 (T[i] - 1) \ln(2)} < 0. \quad (8.23)$$

Thus,  $\mathcal{H}[i]$  is negative semi-definite for all  $i$ .

The Lagrangian of the transformed problem is given by [14]

$$L(\lambda, \mu, \mathbf{T}, \bar{\mathbf{e}}) = \bar{R}_{\text{av}} - \sum_{i=1}^M \mu[i] (\varepsilon[i] - P_{\max} T[i]) - \lambda \left( \frac{1}{M} \sum_{i=1}^M \varepsilon[i] - P_{\text{avg}} \right), \quad (8.24)$$

where the nonnegative Lagrange multipliers (LMs)  $\mu[i]$  and  $\lambda$ , and are associated with the right side of the constraints  $\bar{C}_2$  and  $\bar{C}_3$ , respectively. Note that the constraint  $C_1$  and the left side of the constraint  $C_2$  will be absorbed in the Karush–Kuhn–Tucker (KKT) conditions. Using the KKT conditions,  $\rho_0^*[i]$  is given by [14]

$$\rho_0^*[i] = \begin{cases} P_{\max}, & \eta g[i] > \lambda, \\ 0, & \text{otherwise,} \end{cases} \quad (8.25)$$

where  $T[i]^*$  is the root of the following equation [14]

$$\log_2 \left( 1 + \frac{\eta g[i] T^*[i] P_{\max}}{1 - T^*[i]} \right) + \lambda P_{\max} = \frac{\eta g[i] P_{\max}}{1 - T^*[i] + \eta g[i] P_{\max} T^*[i]}. \quad (8.26)$$

Finally, constant  $\lambda$  is estimated by an iterative algorithm such as bisection method.

## 8.4 Trade-Off Between Decoding Complexity and Performance

Next, we assume multiple users, while we focus on a single epoch, and we consider two multiple access schemes, namely TDMA and NOMA. After maximizing the sum-throughput, we further compare the considered schemes in terms of performance and fairness.

### 8.4.1 TDMA Protocol

In this subsection, we assume that the users transmit their independent information to the BS by TDMA. Considering the amount of time that is allocated to each user [15],

$$\sum_{n=1}^N \tau_n \leq 1 - T. \quad (8.27)$$

#### 8.4.1.1 User Throughput

Taking into account (8.6), the achievable throughput of the  $n$ -th user can be written as [15]

$$R_n = \tau_n \log_2 \left( 1 + \frac{g_n P_n}{N_0} \right) = \tau_n \log_2 \left( 1 + \frac{\eta \rho_0 T g_n}{\tau_n} \right). \quad (8.28)$$

#### 8.4.1.2 Sum-Throughput Maximization

The sum-throughput of all users is given by [15]

$$R_{\text{sum}} = \sum_n^N R_n, \quad (8.29)$$

and the corresponding sum-throughput maximization problem can be formulated as [15]

$$\begin{aligned} & \max_{T, \tau} R_{\text{sum}}, \\ & \text{C}_1 : T + \sum_{n=1}^N \tau_n \leq 1, \\ & \text{C}_2 : T > 0, \\ & \text{C}_n : \tau_n \geq 0, \forall n \in \mathcal{N}. \end{aligned} \quad (8.30)$$

The eigenvalues of the Hessian matrix of  $R_n$  denoted by  $\phi_i$ ,  $i \in \{1, 2\}$  are given by  $\phi_1 = 0$  and

$$\phi_2 = -\frac{g_n^2 \eta^2 \rho_0^2 (\tau_n^2 + T^2)}{\tau_n (\tau_n + g_n \eta \rho_0 T)^2 \ln(2)} < 0, \quad (8.31)$$

i.e., they are both nonpositive. Thus,  $R_n$  is jointly concave with respect to  $T$  and  $\tau_n$ , since its Hessian matrix has nonpositive eigenvalues and, thus, it is negative semi-definite. Therefore, since  $R_{\text{sum}}$  is the summation of concave functions, i.e.,  $R_n$ , it is also concave [2]. Besides, all the constraints are linear. Consequently, the optimization problem in (8.30) can be also solved by using convex optimization

techniques. Next, this problem is solved using dual decomposition. For this reason, the Lagrangian of (8.30) is needed which is given by

$$L(\lambda, \tau, T) = R_{\text{sum}} - \lambda \left( T + \sum_{i=1}^N \tau_n - 1 \right), \quad (8.32)$$

where  $\lambda$  is the LM that corresponds to the constraint  $C_1$  and  $\tau$  the vector with elements  $\tau_n$ .

Using the KKT conditions, the optimal time allocated to EH and information transmission by the  $n$ -th is given by [15]

$$T^* = \frac{z^* - 1}{A + z^* - 1} \quad (8.33)$$

and

$$\tau_n^* = \frac{\eta \rho_n g_n}{A + z^* - 1}, \quad (8.34)$$

where  $z^*$  is the unique solution of the following equation:

$$z \ln(z) - z - A + 1 = 0 \quad (8.35)$$

and  $A = \eta \rho \sum_{n=1}^N g_n$ .

### 8.4.2 NOMA Protocol

In this subsection, we assume that the users transmit their independent information to the BS utilizing NOMA [7, 8]. NOMA is substantially different compared to TDMA, since the power domain is used to achieve multiple access, while SIC is carried out at the BS [1, 11, 33].

#### 8.4.2.1 User Throughput

Next, the user throughput is defined assuming that the users' messages are decoded in an increasing order of their indices. It is worth pointing out that different decoding order does affect individual rates, and this will be discussed in the next subsection. Therefore, for decoding the first user's message ( $n = 1$ ), interference is created due to all other users  $n = 2, \dots, N$ , while on the second user's message, interference is created due to users  $n = 3, \dots, N$ , and so on. Then, the throughput of the  $n$ -th user,  $1 \leq n \leq (N - 1)$ , is given by [1, 7]

$$\begin{aligned} R_n &= (1 - T) \log_2 \left( 1 + \frac{P_n g_n}{\sum_{j=n+1}^N (P_j g_j) + N_0} \right) \\ &= (1 - T) \log_2 \left( 1 + \frac{\frac{\eta \rho T g_n}{1-T}}{\frac{\eta \rho T \sum_{j=n+1}^N g_j}{1-T} + 1} \right), \end{aligned} \quad (8.36)$$

while the throughput of the  $N$ -th user is

$$R_N = (1 - T) \log_2 \left( 1 + \frac{\eta \rho T g_N}{1 - T} \right). \quad (8.37)$$

#### 8.4.2.2 Sum-Throughput Maximization

Interestingly, the decoding order does not affect the system throughput in NOMA uplink, and any arbitrary decoding order can be assumed to define the system throughput. Thus, taking into account (8.36) and (8.37) the system throughput achieved by NOMA is [7, 8]

$$\begin{aligned} R_{\text{sum}} &= \sum_{n=1}^N R_n = \\ &(1 - T) \sum_{n=1}^{N-1} \left( \log_2 \left( \eta \rho \sum_{i=n}^N g_i + \frac{1 - T}{T} \right) - \log_2 \left( \eta \rho \sum_{i=n+1}^N g_i + \frac{1 - T}{T} \right) \right) + \\ &(1 - T) \left( \log_2 \left( \eta \rho g_N + \frac{1 - T}{T} \right) - \log_2 \left( \frac{1 - T}{T} \right) \right) = (1 - T) \log_2 \left( 1 + \frac{A}{\frac{1-T}{T}} \right). \end{aligned} \quad (8.38)$$

The corresponding optimization problem, which aims at maximizing the system throughput, can be written as

$$\max_T R_{\text{sum}} \quad (8.39)$$

$\text{C : } 0 < T < 1.$

Similarly to (8.9), it can easily be proved that  $R_{\text{sum}}$  is strictly concave with respect to  $T$  in  $(0, 1)$ . Thus, the optimal value for  $T$  in  $(0, 1)$  that maximizes  $R_{\text{sum}}$  is unique and can be obtained through

$$\frac{dR_{\text{sum}}}{dT} = 0. \quad (8.40)$$

After some mathematical manipulations, it can be easily shown that  $T^*$  is given by (8.33).

### 8.4.3 Comparison Between TDMA and NOMA in Terms of Fairness

In order to compare TDMA and NOMA, we assume two users which are located at different distances from the BS. It is assumed that the path loss is given by  $L_n = 10^{-3}d_n^{-2}$  [15], where  $d_n$  is the distance between the  $n$ -th user and the BS. We further assume that  $d_1 = 5$  m,  $d_2 = 10$  m, and  $N_0 = -114$  dBm. All statistical results are averaged over  $10^5$  random realizations. The main focus of the simulation results is the comparison of the two schemes in terms of fairness.

In Fig. 8.4 the average minimum throughput achieved by both TDMA and NOMA is illustrated. For reference, the normalized sum-throughput (i.e., the sum-throughput divided by the number of users,  $\frac{R_{\text{sum}}}{N}$ ) is also depicted. It is evident that both NOMA and TDMA achieve the same normalized sum-throughput, however, the application of NOMA results in a notable increase of the minimum throughput for the whole range of  $P_0$ . Thus is because the throughput region achieved by NOMA is different from conventional rate region achieved by TDMA [7, 8].

Also, in order to fairly compare the two schemes in Fig. 8.5, we use the Jain's fairness index, which is given by [1]

$$J = \frac{\left(\sum_{n=1}^N R_n\right)^2}{N \sum_{n=1}^N R_n^2}. \quad (8.41)$$

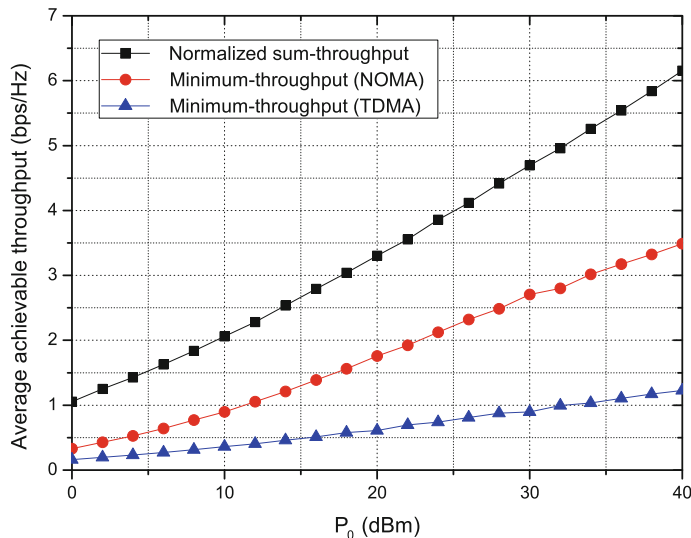


**Fig. 8.4** Comparison of NOMA and TDMA in terms of minimum throughput

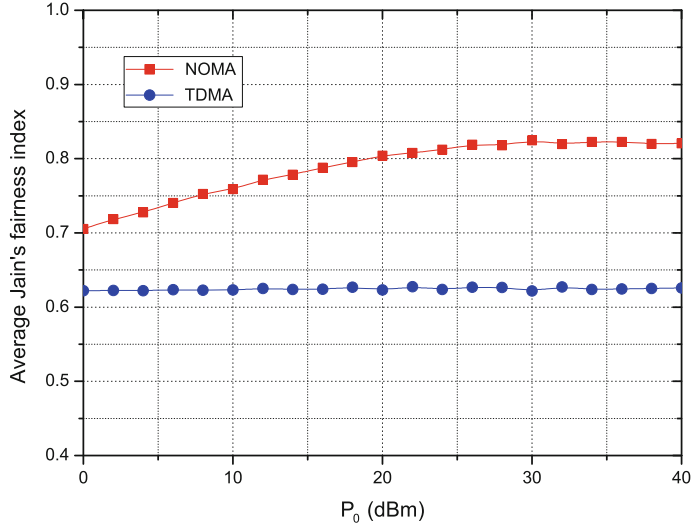


**Fig. 8.5** Jain's fairness index comparison

Note that  $J$  is bounded between 0 and 1, with unitary value indicating equal users throughputs. It is evident from Fig. 8.5 that NOMA provides more fairness compared to TDMA. Consequently, taking into account that NOMA increases the decoding complexity, there is a clear trade-off between fairness and decoding complexity. However, it should be noted that the implementation of NOMA in the uplink is not a burden for the users, since the encoding complexity at the users' side is not affected, while their synchronization is usually simpler than the case of TDMA. Thus, employing NOMA is an efficient possible solution in order to increase fairness in wireless powered communication networks.

## 8.5 Trade-Off Between Fairness and Performance

In this section, we focus on methods that can be used to increase the fairness among users when TDMA is used. Note that similar methods can be also adopted in the case of NOMA, which, however, is out of the scope of this chapter. The interested readers are referred to [7, 8] for further information.

### 8.5.1 Weighted Sum-Throughput

In order to consider fairness, the weighted sum-throughput can be used and maximized, which is given by

$$R_w = \sum_{n=1}^N a_n R_n. \quad (8.42)$$

In the above, higher  $d_n$  implies higher  $a_n$ , however the exact values of  $a_n$  depend on the specific application. The formulation and the solution of the corresponding optimization problem is similar to the one in (8.30). An alternative to the maximization of the weighted sum-throughput is the rate-profile method, which will be further discussed in the following subsection.

### 8.5.2 Rate-Profile Method

In order to realize the rate-profile method, the rate-profile vector needs to be introduced, which is denoted by  $\mathbf{b} = \{b_1, b_2, \dots, b_N\}$  and defined as

$$b_n = \frac{R_n}{R_{\text{sum}}}, \quad (8.43)$$

where  $R_n$  denotes the required throughput of the  $n$ -th user and is given by (8.28). Note that the vector  $\mathbf{b}$  is specified by the specific application. For example, if  $b_n > b_m$  it means that the  $n$ -th user requires higher rate than the  $m$ -th user.

The corresponding fairness aware optimization problem can be written as

$$\begin{aligned} \max_T \min\left(\frac{R_1}{b_1}, \frac{R_2}{b_2}, \dots, \frac{R_N}{b_N}\right) \\ C_1 : T + \sum_{n=1}^N \tau_n \leq 1, \\ C_2 : T > 0, \\ C_3 : \tau_n \geq 0, \forall n \in \mathcal{N}. \end{aligned} \quad (8.44)$$

The objective function of the optimization problem in (8.44) is not a purely analytical expression. For this purpose, (8.44) is transformed into its epigraph form by utilizing the auxiliary variable  $\bar{R}$ . Therefore, it can now be written as [15]

$$\begin{aligned} \max_{T, \tau} \bar{R} \\ C_1 : T + \sum_{n=1}^N \tau_n \leq 1, \\ C_2 : T > 0, \\ C_3 : \tau_n \geq 0, \forall n \in \mathcal{N}, \\ C_4 : \frac{R_n}{b_n} \geq \bar{R}. \end{aligned} \quad (8.45)$$

Note that the optimization problem in (8.45) is concave and, thus, it can also be solved by dual decomposition. Its Lagrangian is given by

$$L(\mu, \lambda, \tau, T, \bar{R}) = \bar{R} - \mu \left( T + \sum_{n=1}^N \tau_n - 1 \right) + \sum_{n=1}^N \lambda_n \left( \frac{R_n}{b_n} - \bar{R} \right), \quad (8.46)$$

where  $\lambda_n$  and  $\mu$  are the LMs that correspond to the constraints  $C_4$  and  $C_1$ , respectively.

The dual problem is given by

$$\min_{\mu, \lambda} \max_{T, R_{\text{eq}}} L(\mu, \lambda, \tau, T, \bar{R}), \quad (8.47)$$

where  $\lambda$  is the LM vector with elements  $\lambda_n$ . Considering the parts of the Lagrangian related to  $\bar{R}$ , it holds that

$$\max_{\bar{R}} \left( 1 - \sum_{n=1}^N \lambda_n \right) \bar{R} = \begin{cases} 0 & \text{if } \sum_{n=1}^N \lambda_n = 1, \\ \infty & \text{otherwise.} \end{cases} \quad (8.48)$$

Thus, the dual problem in (8.47) is bounded if and only if  $\sum_{n=1}^N \lambda_n = 1$ . By setting

$$\lambda_N = 1 - \sum_{n=1}^{N-1} \lambda_n \quad (8.49)$$

in (8.46), the variable  $\bar{R}$  vanishes and the dual problem in (8.47) is simplified to

$$\min_{\lambda} \max_{T, \tau} \tilde{L}(\mu, \lambda, \tau, T). \quad (8.50)$$

where  $\tilde{L}(\mu, \lambda, \tau, T) = L(\mu, \lambda, \tau, T, \bar{R})|_{(8.49)}$ .

According to the KKT conditions, given  $\lambda^*$ , the optimal  $\tau$  and  $T$  are given by

$$T^* = \frac{1}{1 + \sum_{n=1}^N \frac{\eta \rho g_n}{z_n^*}}, \quad (8.51)$$

$$\tau_n^* = \frac{\frac{\eta \rho g_n}{z_n^*}}{1 + \sum_{n=1}^N \frac{\eta \rho g_n}{z_n^*}}, \quad (8.52)$$

where  $z_n^*, \forall n \in \mathcal{N}$  is the solution of the following set of equations:

$$\ln(1 + z_n) - \frac{z_n}{1 + z_n} = \frac{b_n}{\lambda_n} \sum_{n=1}^N \frac{\lambda_n g_n}{b_n(1 + z_n)} \quad (8.53)$$

Since the dual function in (8.50) is differentiable, it can be solved iteratively. In each iteration,  $T$  and  $\tau$  are calculated for a fixed LM vector, using (8.51) and (8.52), while  $\lambda$  is then updated using the gradient method as follows [2, 3]

$$\lambda_n[t+1] = \left[ \lambda_n[t] - \hat{\lambda}_n[t] \left( \frac{\tau_n}{b_n} \log_2 \left( 1 + \frac{\eta \rho_n g_n T}{\tau_n} \right) - \frac{\tau_N}{b_N} \log_2 \left( 1 + \frac{\eta \rho_N g_N T}{\tau_N} \right) \right) \right]_{\mathcal{U}_n}^+, \quad \forall n \in \{1, \dots, N-1\}, \quad (8.54)$$

where  $t$  is the iteration index,  $\hat{\lambda}_n$ ,  $n \in \{1, \dots, N-1\}$  are positive step sizes,  $[\cdot]^+ = \max(\cdot, 0)$ , and  $\mathcal{U}_n$  denotes the projection operator on the feasible set

$$\mathcal{U}_n = \{\lambda_n \mid \sum_{n=1}^N \lambda_n = 1\}. \quad (8.55)$$

The projection can be simply implemented by a clipping function  $[\lambda_n]_0^{1-\sum_{i=1}^{n-1} \lambda_i}$  and  $\lambda_N$  can be obtained from (8.49). Since Problem 1 is concave, it is guaranteed that the iterations between the two layers converge to the optimal solution if the size of the chosen step satisfies the infinite travel condition [3]

$$\sum_{t=1}^{\infty} \hat{\lambda}_n[t] = \infty, \quad n \in \{1, \dots, N-1\}. \quad (8.56)$$

Finally, the optimal  $\bar{R}$  can be evaluated by

$$\bar{R}^* = \min_{n \in \mathcal{N}} \left( \frac{\tau_n^*}{b_n} \log_2 \left( 1 + \frac{\eta \rho_n g_n T^*}{\tau_n^*} \right) \right), \quad (8.57)$$

where  $T^*$  is given by (8.51). This is because  $\bar{R}^*$  is actually limited by the most stringent constraint.

### 8.5.3 Common Throughput Maximization

The common throughput approach corresponds to the rate-profile method with parameters  $b_n = \frac{1}{N}, \forall n \in \mathcal{N}$  [15]. This approach guarantees equal throughput allocations to all users, while it maximizes the sum-throughput, which now is defined as  $R_{\text{sum}} = N\bar{R}$ . Notice that the sum-throughput maximization in (8.30) and the common throughput maximization deal with two extreme cases of throughput allocation to the users in a wireless powered communication network where the fairness is completely ignored and a strict equal fairness is imposed, respectively.

### 8.5.4 Comparison of Fairness Aware Schemes

Next, we compare the three aforementioned fairness aware approaches, i.e., the weighted sum-throughput maximization, the rate-profile method, and the common throughput maximization, in terms of performance and fairness. To this end, in Fig. 8.6 the sum and the minimum throughput are illustrated when  $T$  and  $\tau$  are set according to each one of the aforementioned methods. The simulation parameters are set according Sect. 8.4.3. Besides, we assume that  $a_1 = 1$ ,  $a_2 = 2$  and  $b_1 = 2/3$ ,  $b_2 = 1/3$  for the rate-profile method and the weighted sum-throughput maximization, respectively. This means that for the sum-throughput maximization the user with  $d_n = 10$  m has double weight than the user with  $d_n = 5$  m, while for the rate-profile method the user with the longer distance from the BS must achieve at least half the throughput that the other user achieves. As one can observe, there is a trade-off between the sum-throughput and the minimum throughput. The rate-profile method achieves a good balance between the sum and the minimum throughput, while for the high region of  $P_0$ , it outperforms the weighted sum-throughput maximization both in terms of throughput and fairness. On the other hand, the common throughput maximization achieves the highest minimum throughput and the lowest sum-throughput. Consequently, it should be selected when it is critical for the users to transmit with equal rate, such as when only symmetrical rates are permitted.

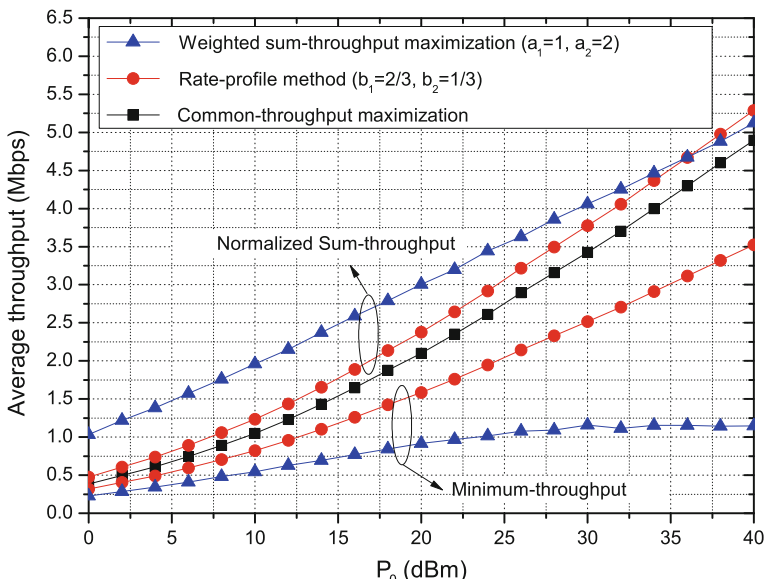


Fig. 8.6 Comparison among fairness aware schemes

## 8.6 Trade-Off Between Energy Efficiency and Throughput

Next, we focus on the energy efficiency optimization when TDMA is utilized, while we consider two different cases: (i) negligible processing cost, (ii) nonnegligible processing cost.

### 8.6.1 Negligible Processing Cost

Assuming that energy is consumed only for transmission, the efficiency of the energy transmitted by the BS, denoted by  $U_{\text{eff}}$ , and defined as the ratio of the sum-throughput and the consumed energy

$$U_{\text{eff}} = \frac{R_{\text{sum}}}{P_0 T}. \quad (8.58)$$

It can easily be shown that  $U_{\text{eff}}$  is maximized when  $T \rightarrow 0$ .

In Fig. 8.7 the EE versus  $P_0$  is depicted when  $T$  and  $\tau$  are chosen in order to maximize the sum-throughput, i.e., by solving (8.30) or (8.39). The simulation parameters are set according to Sect. 8.4.3. As it can be observed, the EE is decreased considerably when the value of  $P_0$  is increased. On the other hand, as it has already been illustrated in Fig. 8.4, the sum-throughput increases as  $P_0$  increases. Consequently, there is a clear trade-off between achievable throughput and EE. More details about this trade-off have been presented in [32], where a detailed power consumption model

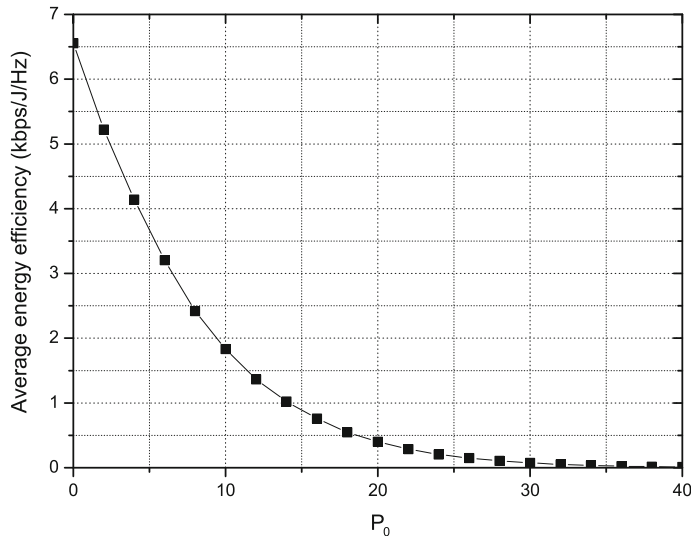


**Fig. 8.7** Average energy efficiency when the sum-throughput is maximized

has been considered, taking into account the circuit power consumed for hardware processing. Part of this work will be discussed in the next subsection.

### 8.6.2 Nonnegligible Processing Cost

The EE maximization problem when the processing cost is nonnegligible can be expressed as [32]

$$\begin{aligned} \max_{T, \tau, \rho_0, \rho} & \frac{\sum_{n=1}^N \log_2(1+\rho_n \gamma_n)}{N_0 \left( \rho_0 T \left( \frac{1}{\zeta} - \sum_{n=1}^N \eta \gamma_n \right) + p' T + \sum_{n=1}^N \left( \frac{\rho_n}{\zeta} T + p'' \tau_n \right) \right)} \\ C_1 : & \rho_n \leq P_{\max}, \\ C_2 : & T + \sum_{n=1}^N \tau_n \leq 1, \\ C_3 : & \frac{\rho_n}{\zeta} + p'' \tau_n \leq \eta \rho_0 T \gamma_n, \forall n \in \mathcal{N} \\ C_4 : & T > 0, \tau_n \geq 0, \forall n \in \mathcal{N}, \\ C_5 : & \rho_0 \geq 0, \rho_n \geq 0, \forall n \in \mathcal{N}, \end{aligned} \quad (8.59)$$

where  $\rho$  is the vector with elements  $\rho_n, \forall n$ ,  $\rho_n = \frac{P_n}{N_0}$ ,  $\zeta$  and  $\varsigma$  are the efficiency of the power amplifiers of the BS and the users, respectively. Also,  $p'$  and  $p''$  denote the constant circuit power consumption (normalized by the AWGN power) of the BS and the users, respectively.

Using once more the dual decomposition and KKT conditions, the optimal power and time allocation can be expressed as [32]

$$\rho_n^* = \left[ \frac{1}{N_0 e e_n^* \ln(2)} - \frac{1}{\gamma_n} \right]^+, \quad (8.60)$$

$$T^* = \frac{1}{1 + \eta P_{\max} \sum_{n=1}^N \frac{N_0 \gamma_n e e_n^*}{\log_2 \left( \frac{\varsigma \gamma_n}{N_0 e e_n^* \ln(2)} \right)}}, \quad (8.61)$$

$$\tau_n^* = \eta P_{\max} T \frac{N_0 \gamma_n e e_n^*}{\log_2 \left( \frac{\varsigma \gamma_n}{N_0 e e_n^* \ln(2)} \right)}, \quad (8.62)$$

where  $e e_n^*$  is the maximum EE of user  $n$  and can be easily obtained using the bisection method [2].

## 8.7 Conclusions

In this chapter, we have reviewed several trade-offs in wireless powered communication networks, when the harvest-then-transmit protocol is adopted. More specifically, we have focused on the dependence between harvested energy, achieved throughputs,

fairness, decoding complexity, and energy efficiency. Extensive simulations have shown, among others, that the increase of the energy arrival rate reduces the portion of time that is allocated to energy harvesting, and that NOMA can be used to increase fairness. Finally, they reveal an interesting trade-off among efficiency, sum-throughput, and fairness.

## References

1. Al-Imari, M., Xiao, P., Imran, M.A., Tafazolli, R.: Uplink non-orthogonal multiple access for 5G wireless networks. In: Proceedings 11th International Symposium on Wireless Communications Systems (ISWCS), pp. 781–785 (2014). doi:[10.1109/ISWCS.2014.6933459](https://doi.org/10.1109/ISWCS.2014.6933459)
2. Boyd, S., Vandenberghe, L.: Convex Optimization. Cambridge University Press (2009)
3. Boyd, S., Xiao, L., Mutapcic, A.: Subgradient Methods. Lecture Notes of EE392o Stanford University Autumn (2003–2004)
4. Chen, H., Li, Y., Rebelatto, J.L., Ucha-Filho, B.F., Vucetic, B.: Harvest-Then-Cooperate: wireless-powered cooperative communications. *IEEE Trans. Signal Process.* **63**(7), 1700–1711 (2015). doi:[10.1109/TSP.2015.2396009](https://doi.org/10.1109/TSP.2015.2396009)
5. Corless, R.M., Gonnet, G.H., Hare, D.E.G., Jeffrey, D.J., Knuth, D.E.: On the LambertW function. *Adv. Comput. Math.* **5**(1), 329–359 (1996). doi:[10.1007/BF02124750](https://doi.org/10.1007/BF02124750)
6. Diamantoulakis, P.D., Ntoumi, G.D., Pappi, K.N., Karagiannidis, G.K., Sharif, B.S.: Throughput maximization in multicarrier wireless powered relaying networks. *IEEE Wireless Commun. Lett.* **4**(4), 385–388 (2015). doi:[10.1109/LWC.2015.2424237](https://doi.org/10.1109/LWC.2015.2424237)
7. Diamantoulakis, P.D., Pappi, K.N., Ding, Z., Karagiannidis, G.K.: Wireless Powered Communications with Non-Orthogonal Multiple Access. *IEEE Trans. on Wireless Commun.* (2015). **99**, pp. 1 doi:[10.1109/TWC.2016.2614937](https://doi.org/10.1109/TWC.2016.2614937)
8. Diamantoulakis, P.D., Pappi, K.N., Ding, Z., Karagiannidis, G.K.: Optimal Design of Non-Orthogonal Multiple Access with Wireless Power Transfer. In: Proceedings IEEE International Conference on Communications (ICC), Kuala Lumpur, pp. 1–6 (2016). doi:[10.1109/ICC.2016.7510866](https://doi.org/10.1109/ICC.2016.7510866)
9. Diamantoulakis, P.D., Pappi, K.N., Karagiannidis, G.K., Poor, H.V.: Autonomous energy harvesting base stations with minimum storage requirements. *IEEE Wireless Commun. Lett.* **4**(3), 265–268 (2015). doi:[10.1109/LWC.2015.2406711](https://doi.org/10.1109/LWC.2015.2406711)
10. Ding, Z., Perlaza, S.M., Esnaola, I., Poor, H.V.: Power allocation strategies in energy harvesting wireless cooperative networks. *IEEE Trans. Wireless Commun.* **13**(2), 846–860 (2014). doi:[10.1109/TWC.2013.010213.130484](https://doi.org/10.1109/TWC.2013.010213.130484)
11. Ding, Z., Yang, Z., Fan, P., Poor, H.V.: On the performance of non-orthogonal multiple access in 5G systems with randomly deployed users. *IEEE Signal Process. Lett.* **21**(12), 1501–1505 (2014). doi:[10.1109/LSP.2014.2343971](https://doi.org/10.1109/LSP.2014.2343971)
12. Ding, Z., Peng, M., Poor, H.V.: Cooperative non-orthogonal multiple access in 5G systems. *IEEE Commun. Lett.* **19**(8), 1462–1465 (2015). doi:[10.1109/LCOMM.2015.2441064](https://doi.org/10.1109/LCOMM.2015.2441064)
13. Grover, P., Sahai, A.: Shannon Meets Tesla: wireless information and power transfer. In: Proceedings IEEE International Symposium on Information Theory Proceedings (ISIT), pp. 2363–2367 (2010). doi:[10.1109/ISIT.2010.5513714](https://doi.org/10.1109/ISIT.2010.5513714)
14. Hadzi-Velkov, Z., Nikoloska, I., Karagiannidis, G., Duong, T.: Wireless networks with energy harvesting and power transfer: joint power and time allocation. *IEEE Signal Process. Lett.* **23**(1), 50–54 (2016). doi:[10.1109/LSP.2015.2500340](https://doi.org/10.1109/LSP.2015.2500340)
15. Ju, H., Zhang, R.: Throughput maximization in wireless powered communication networks. *IEEE Trans. Wireless Commun.* **13**(1), 418–428 (2014). doi:[10.1109/TWC.2013.112513.130760](https://doi.org/10.1109/TWC.2013.112513.130760)

16. Krikidis, I.: Simultaneous information and energy transfer in large-scale networks with/without relaying. *IEEE Trans. Commun.* **62**(3), 900–912 (2014). doi:[10.1109/TCOMM.2014.020914.130825](https://doi.org/10.1109/TCOMM.2014.020914.130825)
17. Krikidis, I., Timotheou, S., Nikolaou, S., Zheng, G., Ng, D.W.K., Schober, R.: Simultaneous wireless information and power transfer in modern communication systems. *IEEE Commun. Mag.* **52**(11), 104–110 (2014). doi:[10.1109/MCOM.2014.6957150](https://doi.org/10.1109/MCOM.2014.6957150)
18. Lee, S., Zhang, R.: Cognitive wireless powered network: spectrum sharing models and throughput maximization. *IEEE Trans. Cogn. Commun. Netw.* **PP**(99), 1–1 (2015). doi:[10.1109/TCCN.2015.2508028](https://doi.org/10.1109/TCCN.2015.2508028)
19. Liu, L., Zhang, R., Chua, K.C.: Multi-antenna wireless powered communication with energy beamforming. *IEEE Trans. Commun.* **62**(12), 4349–4361 (2014). doi:[10.1109/TCOMM.2014.2370035](https://doi.org/10.1109/TCOMM.2014.2370035)
20. Liu, Y., Wang, L., Elkashlan, M., Duong, T., Nallanathan, A.: Two-way relaying networks with wireless power transfer: policies design and throughput analysis. In: Proceedings IEEE Global Communications Conference (GLOBECOM), pp. 4030–4035 (2014). doi:[10.1109/GLOCOM.2014.7037438](https://doi.org/10.1109/GLOCOM.2014.7037438)
21. Luo, S., Zhang, R., Lim, T.J.: Optimal save-then-transmit protocol for energy harvesting wireless transmitters. *IEEE Trans. Wireless Commun.* **12**(3), 1196–1207 (2013). doi:[10.1109/TWC.2013.012413.120488](https://doi.org/10.1109/TWC.2013.012413.120488)
22. Marshoud, H., Kapinas, V.M., Karagiannidis, G.K., Muhaidat, S.: Non-orthogonal multiple access for visible light communications. *IEEE Photon. Technol. Lett.* **28**(1), 51–54 (2016). doi:[10.1109/LPT.2015.2479600](https://doi.org/10.1109/LPT.2015.2479600)
23. Mohjazi, L., Dianati, M., Karagiannidis, G.K., Muhaidat, S., Al-Qutayri, M.: RF-powered cognitive radio networks: technical challenges and limitations. *IEEE Commun. Mag.* **53**(4), 94–100 (2015). doi:[10.1109/MCOM.2015.7081081](https://doi.org/10.1109/MCOM.2015.7081081)
24. Ng, D., Lo, E., Schober, R.: Energy-efficient power allocation in OFDM systems with wireless information and power transfer. In: Proceedings IEEE International Conference on Communications (ICC), pp. 4125–4130 (2013). doi:[10.1109/ICC.2013.6655208](https://doi.org/10.1109/ICC.2013.6655208)
25. Ng, D.W.K., Lo, E., Schober, R.: Energy-efficient Power allocation in OFDM systems with wireless information and power transfer. In: Proceedings IEEE International Conference on Communications (ICC), pp. 4125–4130 (2013). doi:[10.1109/ICC.2013.6655208](https://doi.org/10.1109/ICC.2013.6655208)
26. Ng, D.W.K., Lo, E.S., Schober, R.: Wireless information and power transfer: energy efficiency optimization in OFDMA systems. *IEEE Trans. Wireless Commun.* **12**(12), 6352–6370 (2013). doi:[10.1109/TWC.2013.103113.130470](https://doi.org/10.1109/TWC.2013.103113.130470)
27. Nikoloska, I., Hadzi-Velkov, Z., Cingoska, H.: Future Access Enablers for Ubiquitous and Intelligent Infrastructures, chap. Resource Allocation in Energy Harvesting Communication Systems, pp. 292–298. Springer International Publishing (2015)
28. Saito, Y., Benjebbour, A., Kishiyama, Y., Nakamura, T.: System-level performance evaluation of downlink non-orthogonal multiple access (NOMA). In: Proceedings IEEE 24th International Symposium on Personal Indoor and Mobile Radio Communications (PIMRC), pp. 611–615 (2013). doi:[10.1109/PIMRC.2013.6666209](https://doi.org/10.1109/PIMRC.2013.6666209)
29. Sudevalayam, S., Kulkarni, P.: Energy harvesting sensor nodes: survey and implications. *IEEE Commun. Surveys Tutorials* **13**(3), 443–461 (2011). doi:[10.1109/SURV.2011.060710.00094](https://doi.org/10.1109/SURV.2011.060710.00094)
30. Timotheou, S., Krikidis, I., Zheng, G., Ottersten, B.: Beamforming for MISO interference channels with QoS and RF energy transfer. *IEEE Trans. Wireless Commun.* **13**(5), 2646–2658 (2014). doi:[10.1109/TWC.2014.032514.131199](https://doi.org/10.1109/TWC.2014.032514.131199)
31. Varshney, L.R.: Transporting Information and energy simultaneously. In: Proceedings IEEE International Symposium on Information Theory (ISIT), pp. 1612–1616 (2008). doi:[10.1109/ISIT.2008.4595260](https://doi.org/10.1109/ISIT.2008.4595260)
32. Wu, Q., Tao, M., Ng, D., Chen, W., Schober, R.: Energy-efficient resource allocation for wireless powered communication networks. *IEEE Trans. Wireless Commun.* **PP**(99), 1–1 (2015). doi:[10.1109/TWC.2015.2502590](https://doi.org/10.1109/TWC.2015.2502590)
33. Wu, X., Xu, W., Dong, X., Zhang, H., You, X.: Asymptotically optimal power allocation for massive MIMO wireless powered communications. *IEEE Wireless Commun. Lett.* **5**(1), 100–103 (2016). doi:[10.1109/LWC.2015.2502939](https://doi.org/10.1109/LWC.2015.2502939)

34. Xiang, Z., Tao, M.: Robust beamforming for wireless information and power transmission. *IEEE Wireless Commun. Lett.* **1**(4), 372–375 (2012). doi:[10.1109/WCL.2012.053112.120212](https://doi.org/10.1109/WCL.2012.053112.120212)
35. Yin, S., Zhang, E., Li, J., Yin, L., Li, S.: Throughput optimization for self-powered wireless communications with variable energy harvesting rate. In: Proceedings Wireless Communications and Networking Conference (WCNC), pp. 830–835 (2013). doi:[10.1109/WCNC.2013.6554671](https://doi.org/10.1109/WCNC.2013.6554671)
36. Zhong, C., Suraweera, H., Zheng, G., Krikidis, I., Zhang, Z.: Wireless information and power transfer with full duplex relaying. *IEEE Trans. Commun.* **62**(10), 3447–3461 (2014). doi:[10.1109/TCOMM.2014.2357423](https://doi.org/10.1109/TCOMM.2014.2357423)
37. Zhong, C., Chen, X., Zhang, Z., Karagiannidis, G.K.: Wireless-powered communications: performance analysis and optimization. *IEEE Trans. Commun.* **63**(12), 5178–5190 (2015). doi:[10.1109/TCOMM.2015.2488640](https://doi.org/10.1109/TCOMM.2015.2488640)
38. Zhong, C., Zheng, G., Zhang, Z., Karagiannidis, G.K.: Optimum wirelessly powered relaying. *IEEE Signal Process. Lett.* **22**(10), 1728–1732 (2015). doi:[10.1109/LSP.2015.2428812](https://doi.org/10.1109/LSP.2015.2428812)
39. Zhou, X., Zhang, R., Ho, C.K.: Wireless information and power transfer: architecture design and rate-energy tradeoff. *IEEE Trans. Commun.* **61**(11), 4754–4767 (2013). doi:[10.1109/TCOMM.2013.13.120855](https://doi.org/10.1109/TCOMM.2013.13.120855)
40. Zhu, G., Zhong, C., Suraweera, H.A., Karagiannidis, G.K., Zhang, Z., Tsiftsis, T.A.: Wireless information and power transfer in relay systems with multiple antennas and interference. *IEEE Trans. Commun.* **63**(4), 1400–1418 (2015). doi:[10.1109/TCOMM.2015.2398862](https://doi.org/10.1109/TCOMM.2015.2398862)

# Chapter 9

## Simultaneous WPT and Wireless Communication with TDD Algorithm at Same Frequency Band

Naoki Shinohara

**Abstract** A wireless sensor network is considered a game changing technology. Currently, the power of the sensors is limited by the limits of the batteries. This chapter investigated wireless power transfer (WPT) via radio wave or microwave for a batteryless and wireless sensor network. In this study, a WPT assisted ZigBee was proposed as a low power wireless sensor. In particular, to suppress the interference between the WPT and the wireless communication, a time division duplex WPT (TDD-WPT) was proposed to enable the coexistence of WPT and ZigBee on the same frequency band. A scheduled TDD-WPT that can automatically transmit wireless power between the wireless communication devices was suggested and examined through an experiment.

### 9.1 Introduction

Wireless sensor networks are increasingly attracting significant attention for applications in monitoring systems such as energy conservation systems for buildings and houses, traffic management systems, and environment monitoring. Several wireless sensor terminals are scattered over a wide area, and send and receive monitoring information through an ad hoc network. The collected information is utilized to actively control various infrastructures, such as electric power consumption.

A critical issue of the wireless sensor network is the method of supplying electric power to sensor terminals. Although the power consumption of the sensor terminals is quite small, primary batteries must be changed periodically. Thus, the running costs of the wireless sensor network are expensive. Wired power supply can provide stable operation of the sensor terminals. However, it confines the installation location and burdens the wireless sensor network with wired cost. Natural energy utilization

---

N. Shinohara (✉)  
Kyoto University, Kyoto, Japan  
e-mail: shino@rish.kyoto-u.ac.jp

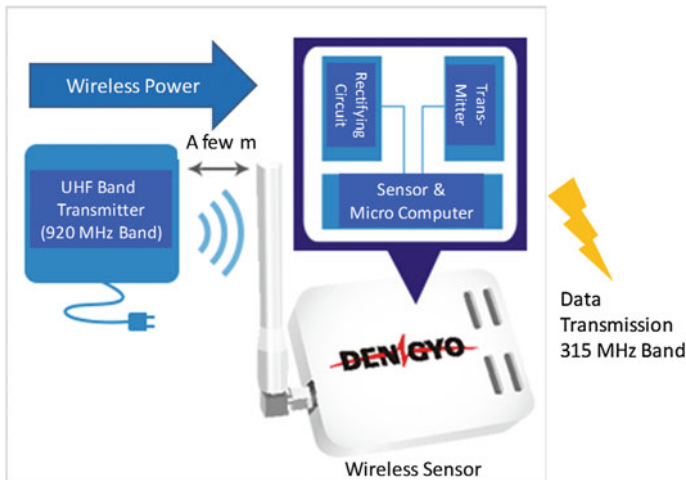


**Fig. 9.1** Commercial wireless sensor using WPT in the 920 MHz band

like solar cells with a charging system can drive the sensor terminal permanently. Nevertheless, as they have unstable natural energies, their installation locations and regular operations are limited.

We, therefore, suggest wireless power supply to the sensor terminals by a wireless power transfer via microwaves (microwave power transfer: MPT), to realize a fruitful wireless sensor network. The MPT is able to provide stable power for the sensor terminals. It transmits power for long distances, simultaneously supplies power for multiple terminals, and drives the terminals without batteries [1]. Hence, the utilization of MPT for the wireless sensor network allows the provision of new applications of the wireless sensor network in addition to the traditional applications. The DENGYO corporation in Japan provided a commercial wireless sensor using WPT in the 920 MHz band (Fig. 9.1, [2]). The application distance is less than 5 m. The RF-DC conversion efficiency is approximately 60 %. The proposed application of the wireless sensor includes sensing in high temperature environments (85C120C), sensing on a rotating or moving object, and sensing in severe environments such as outdoor or marine environments. The DENGYO corporation developed a high efficiency rectenna, rectifying antenna with a RF-DC conversion efficiency of approximately 86 % at 2.45 GHz, and 7 W [3].

A wireless sensor network system for disaster relief, as shown in Fig. 9.2 is a good example of the application of the sensor system. Wireless sensor terminals located in different places normally sleep. However, they work in emergency situations by receiving the power from vehicles or helicopters via long range MPT. The activated terminals can collect and send disaster information via short-range wireless communication. On July, 2015, the Japanese WPT consortium of Wireless Power Transfer Consortium for Practical Applications (WiPoT [4]) conducted a WPT assisted sensor experiment with a small drone (Fig. 9.3). The drone carried a microwave power trans-

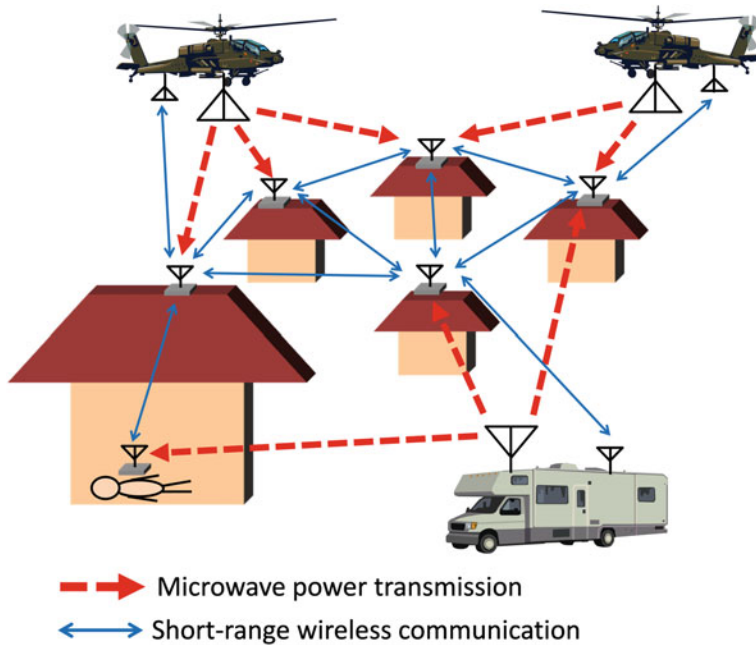


**Fig. 9.2** Conceptual image of a wireless sensor network system for disaster relief

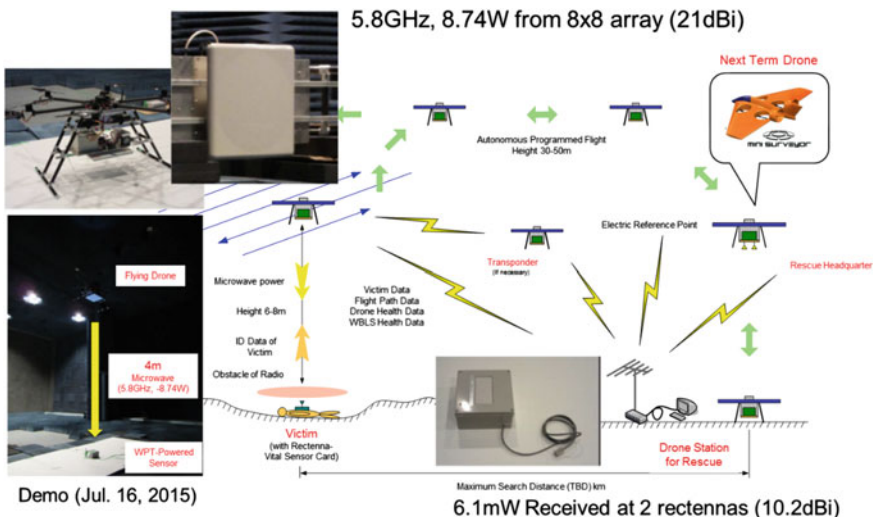


**Fig. 9.3** WPT assisted batteryless sensor experiment with a drone at Kyoto University (July 16, 2015)

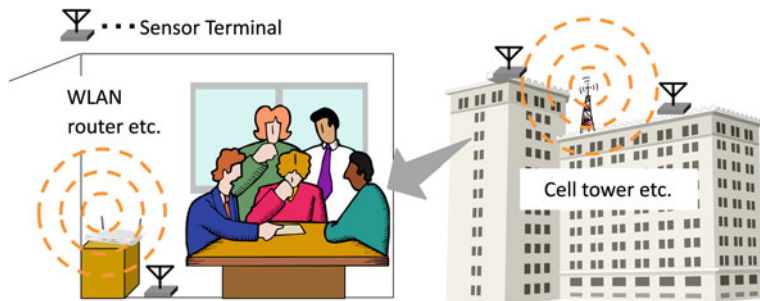


**Fig. 9.4** Conceptual image of energy harvesting through radio communications in the microwave band

mitter and a transmitting antenna to provide the microwave power to the sensors on the ground. A proposed application was to find a victim by using the batteryless positioning and vital sensor. Another application involved using the batteryless sensor to measure an active volcano even when the volcano was buried by volcanic ash. In the experiment, 8.74 W of microwave power was provided over 5.8 GHz frequency from a flying drone at 4 m height. The sensor received and rectified the microwave power to 6.1 mW direct current. A WiFi radio wave was used by the sensor to transmit thermal data to a base station.

The batteryless sensor can be driven by both the transmitted microwave power and wireless communication radio wave if the sensor does not require high power. This technology is known as “energy harvesting” from radio communication [5]. As shown in Fig. 9.4 mobile communication systems and wireless local area network systems are potential candidates for energy harvesting sources in the microwave band. In 2009, energy harvesting systems that received VHF or UHF energy from TV towers were reported [6]. University of Washington group proposes WISP (Wireless Identification and Sensing Platform) system with the WPT and the energy harvesting. They have developed “PoWiFi” system, energy harvesting from WiFi, for temperature sensor, battery-free camera, and Li-Ion Battery Charger [7]. European group proposes hybrid energy harvester from radio wave and from solar [8] or heat [9] or additional WPT [10] to increase harvesting energy.

Typically, a nonmodulated and continuous microwave is used for the MPT. Hence, a wave spectrum for the MPT is relatively pure as shown in Fig. 9.5. However, the power of the MPT is usually higher than that of a wireless communication because of user requirement such as a sensor. Different frequencies like the 5.8 GHz band for the MPT and WiFi for the wireless communication are normally used in order to suppress an interference between the WPT and the wireless communication and allow their coexistence. Unfortunately, there are no radio wave regulations for the WPT and the MPT, and there is no specified frequency for the MPT. These issues are still under discussion. The MPT experiments in previous studies were performed with ISM (industry, scientific, and medical) bands such as 2.45 and 5.8 GHz. Currently, WiFi

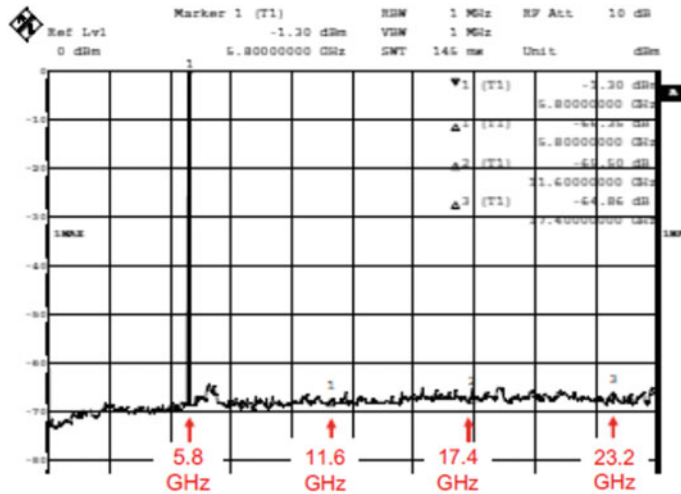


**Fig. 9.5** Typical wave spectrum for MPT (by GaN HPA developed by Mitsubishi Electric. and Kyoto University)

and the other wireless communication applications are on the ISM band. Thus, it is important to consider the coexistence of the MPT and the wireless communication in various ways.

## 9.2 Time Division Duplex WPT (TDD-WPT)

### 9.2.1 TDD-WPT Assisted ZigBee

The MPT continues to use ISM bands such as 2.45 and 5.8 GHz. Presently, the WiFi and the other wireless communications use the ISM band, and there is no special frequency band for the MPT. Hence, time division duplex WPT (TDD-WPT) was proposed to enable the coexistence of the MPT and the wireless communication. For example, as shown in Table 9.1, ZigBee requires very low power. Therefore, ZigBee is considered as a suitable sensor device with the WPT. The ZigBee uses a 2.45 GHz frequency band for the wireless communication. ZigBee device transmits information intermittently between a router and an end device as shown in Fig. 9.6. Thus, interference will be suppressed if the wireless power is transmitted between the intermittent ZigBee wireless communications even at the same frequency band (2.45 GHz band). Moreover, the MPT and ZigBee can coexist at the same frequency band. Hence, the TDD-WPT for the ZigBee as shown in Fig. 9.7 was proposed and experiments were conducted to demonstrate the coexistence of the MPT and the wireless sensor.

**Table 9.1** Average power consumption of ZigBee devices (IEEE802.15.4/ZigBee Evaluation and Development Kit TWE-EK-001)

| Device type | As joined in the network (mW) | As not joined in the network (mW) |
|-------------|-------------------------------|-----------------------------------|
| End device  | 9.46                          | 61.8                              |
| Router      | 57.4                          | 57.1                              |

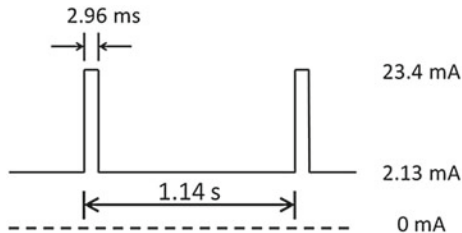


**Fig. 9.6** Typical ZigBee wireless communication timing

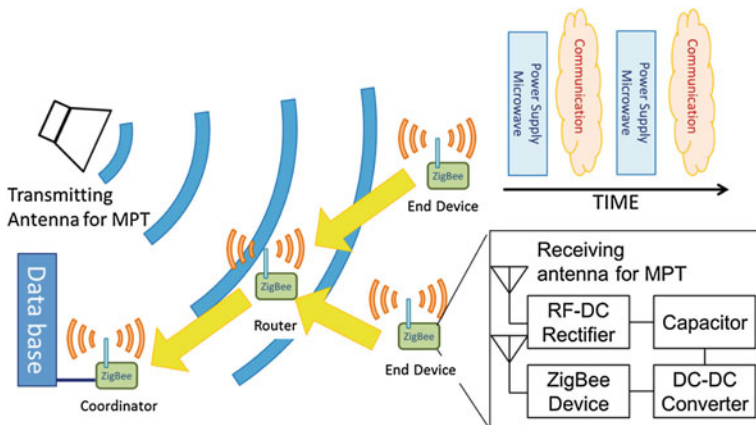


**Fig. 9.7** Image of TDD-WPT assisted ZigBee sensor

In this study, IEEE802.15.4/ZigBee Evaluation and Development Kit TWE-EK-001 produced by Tokyo Cosmos Electric Company (TOCOS) was used as a ZigBee device. The devices were driven by a range of direct currents from 2.7 to 3.6 V. JN-AN-1122 produced by NXP Semiconductors were also installed in the devices as applications of the ZigBee sensor network.

A coordinator, a router, and an end device configured the ZigBee network. The coordinator was simply a device in a network that coordinated the network. The router relayed data and sensing information from other routers and end devices. As the functions of the end device are limited to sending data and sleeping (when no data is sent), its power consumption is lower than the others. However, as the end device is not part of a network, it requires a large amount of power temporarily for

joining a network. The MPT in this study supplies the end device in the form of a sensor device. The router and the end device woke up after sleeping for 1 s. They were awake for 0.14 s, and sent data for approximately 2 ms of the 0.14 s. They took approximately 2 s to scan all channels of the ZigBee communication in 2.4 GHz band, when they attempted to join the network. If the coordinator did not receive data from the routers and end devices for 15 s, then it (the coordinator) dropped them from its network. Once a device was out of the network, it had to go through the necessary steps in order to rejoin the network.

The final goal of this study was to demonstrate a batteryless sensor. Nevertheless, a small battery or a capacitance was also used to reduce microwave power and to increase sustainability of the sensor.

### 9.2.2 Microwave Power Receiver (Rectenna)

A rectenna (rectifying antenna) was required as a receiver of the MPT. The rectenna is a passive element with rectifying diodes that operates without an internal power source. It can receive microwave power and rectify it to produce DC power. A general block diagram of a rectenna is shown in Fig. 9.8. A low-pass filter is installed between the antenna and the rectifying circuit to suppress reradiation of higher harmonics from the diodes. An output filter is used to stabilize the DC current and to increase RF-DC conversion efficiency. Various antennas and rectifying circuits can be applied. Their selection depends on the requirements for a wireless power system and its users. A frequency dependence of a RF-DC conversion efficiency of the rectenna developed in the past is shown in Fig. 9.9. The maximum RF-DC conversion efficiency was approximately 90 % at 2.45 GHz band.

The RF-DC conversion efficiency shown in Fig. 9.9 was obtained with a continuous microwave. However, the TDD-WPT system requires the estimation of the RF-DC conversion efficiency of the rectenna with an intermittent microwave. For the following experiment, a new rectenna was developed. A circular patch antenna was adopted as the receiving antenna in this study. The measured antenna gain was 6.5 dBi. A single-shunt type RF-DC rectifier was developed. The shingle-shunt rectifier could theoretically rectify the microwave by 100 % with a single diode [11]. The Schottky barrier diode (Avago HSMS-2860) was adopted as a rectifier diode. The

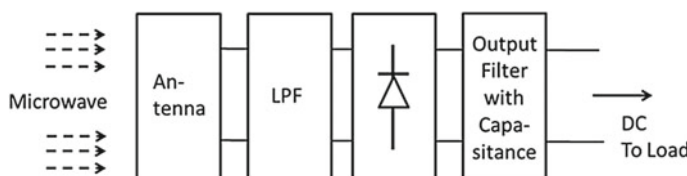


**Fig. 9.8** General block diagram of a rectenna

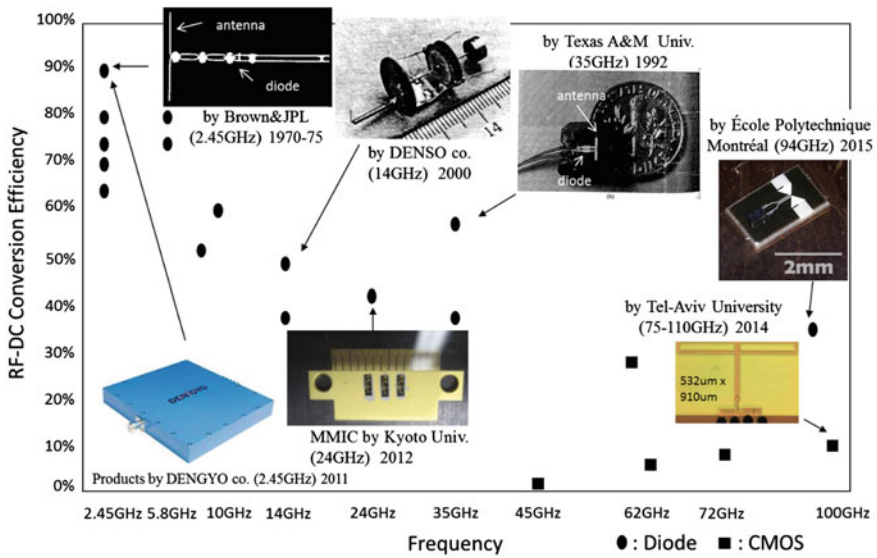
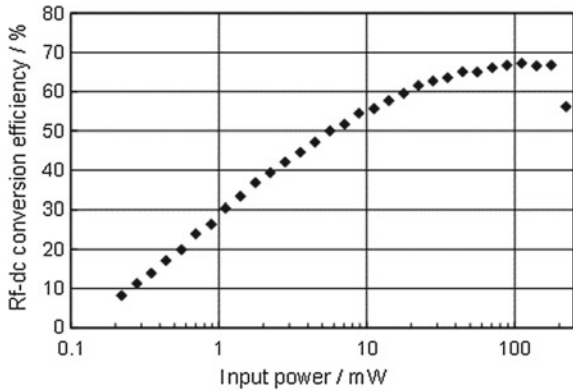


**Fig. 9.9** Frequency dependence of a RF-DC conversion efficiency of the rectenna developed in the past

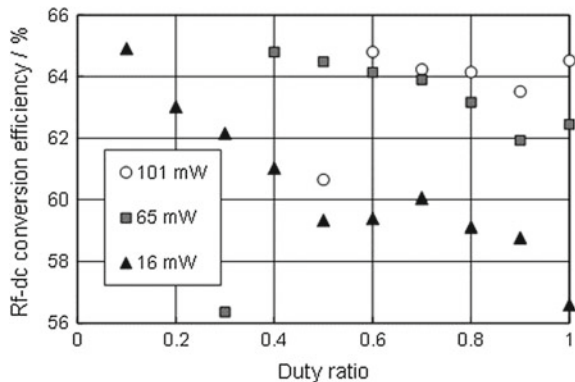
**Fig. 9.10** RF-DC conversion efficiency of the rectifier in the CW microwave case



measurement results of RF-DC conversion efficiency are shown in Fig. 9.10. In the CW microwave case, the rectifier provided the maximum RF-DC conversion efficiency of 65 % at 2.46 GHz when the output load was  $138.1 \Omega$  [12]. The RF-DC conversion efficiency started decreasing at an input power of 180 mW. This decrease in the conversion efficiency was related to the breakdown voltage of the diode.

We also investigated RF-DC conversion efficiency when the intermittent microwave was input to the rectifier. The duty ratio of the intermittent microwave changed from 1 (CW) to 0.1. The pulse frequency was 1 kHz, and the average input powers were 16, 65, and 101 mW. As the average input power was fixed, the peak

**Fig. 9.11** RF-DC conversion efficiency of the rectifier in the intermittent microwave case



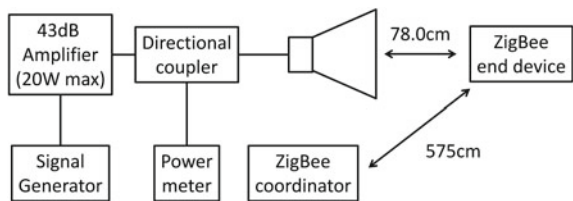
input power was dependent on the duty ratio. The peak input power was equal to the average input power at the duty ratio of 1. In contrast, it was 10 times the average input power at the duty ratio of 0.1. Figure 9.11 shows the measurement results of RF-DC conversion efficiency in the intermittent microwave case. Interestingly, the RF-DC conversion efficiency depended on the peak input power. Even if the average power was small, the maximum RF-DC conversion efficiency could be obtained by adjusting the duty ratio of the intermittent microwave. The RF-DC conversion efficiency decreased at low duty ratios when the average input power was 65 and 101 mW. This was because the peak input power exceeded the input power of 180 mW.

The measurement results indicated that the rectenna output voltage exceeded 4 V at the input microwave power of 180 mW. In comparison, the ZigBee input voltage should be in the range from 2.7 to 3.6 V. Therefore, a step-down DC–DC converter (Texas Instruments TPS62120) was adopted as DC–DC converter. This DC–DC converter provided an efficiency of over 90 % in an output voltage range of approximately 3 V.

### 9.3 Coexistence of MPT and ZigBee uncontrolled-

Experimental measurements of electromagnetic compatibility between MPT and ZigBee were first performed to investigate how the MPT affected the ZigBee [13]. Moreover, the measurements contributed to fix the frequency and maximum transmitting power of MPT in this study. Two indices were evaluated and defined on MPT power density, namely communicable power density (CPD) and joinable power density (JPD). CPD was the threshold of MPT power density that did not affect the ZigBee. That is, when a ZigBee device joined the network, it could communicate with another ZigBee device under the CPD. JPD was the threshold of MPT power density under which a ZigBee device could join in the network. The CPD was generally larger than the JPD.

**Fig. 9.12** Experimental configuration of electromagnetic compatibility between MPT and ZigBee



### 9.3.1 Measurement Setup

Figure 9.12 shows the experimental configuration. The ZigBee frequency was set to 2.46 GHz (22 ch). The network had just two devices, namely, a coordinator and an end device. First, the coordinator, which was put behind the transmitting horn antenna, established communication with the end device. Then, the end device was irradiated with a nonmodulated microwave as an alternative to MPT. The CPD was measured by increasing the nonmodulated microwave power until the communication was disabled. Subsequently, the JPD was measured by reducing the nonmodulated microwave power until the coordinator reestablished communication with the end device.

We investigated two types of nonmodulated microwave irradiation, namely, CW microwave irradiation and intermittent microwave irradiation. The nonmodulated microwave turned on and off under the conditions of a pulse frequency and a duty ratio, during the intermittent microwave irradiation.

### 9.3.2 Measurement Results of CW Microwave Irradiation

The CW microwave irradiation was conducted to a ZigBee end device, by changing the frequency from 2.4 to 2.5 GHz (20 MHz step). The maxima of the CPD and JPD were measured at all the frequency points.

The experimental results of the CPD and JPD are shown in Fig. 9.13. At all the frequency points, the CPDs were lower than  $1 \text{ mW/cm}^2$ . This is the maximum power density determined by International Commission on NonIonizing Radiation Protection (ICNIRP, 1998). The power density of  $5 \text{ pW/cm}$  even interrupted the ZigBee at approximately the ZigBee frequency. These results indicated that it was quite difficult for the CW MPT to be compatible with the ZigBee to wirelessly supply sufficient power for a ZigBee device.

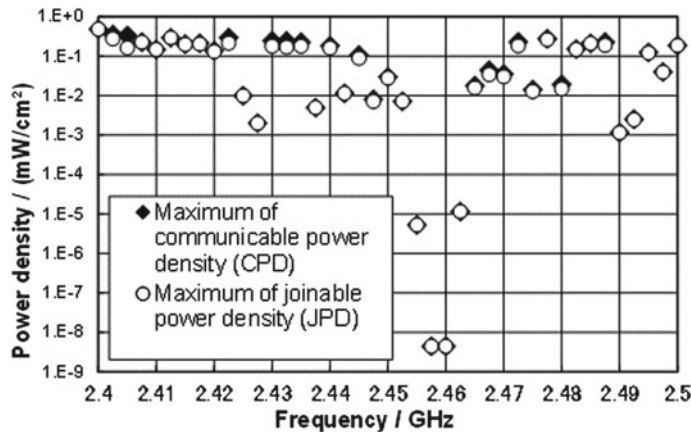


**Fig. 9.13** Measurement results of the CPD and JPD when the ZigBee end device was irradiated with a CW microwave

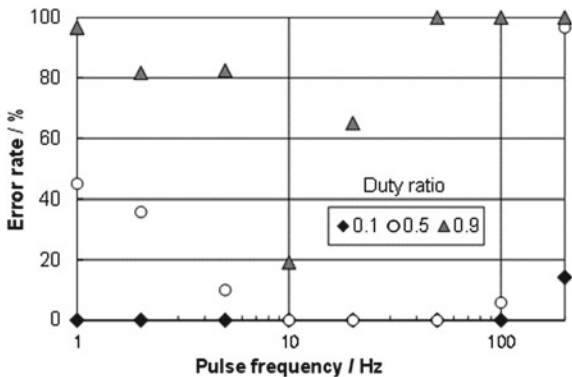
### 9.3.3 Measurement Results of Uncontrolled Intermittent Microwave Irradiation

Under the same conditions as shown in Fig. 9.12, the intermittent microwave irradiation was conducted to a ZigBee end device. The intermittent microwave frequency was fixed at 2.46 GHz. This is the point at which the lowest maximum of the CPD and JPD was obtained in the CW microwave irradiation case. The intermittent microwave irradiation was not synchronized with the ZigBee. The end device was irradiated with the intermittent microwave, within the pulse frequency ranging from 1 to 200 Hz, and the duty ratios of 0.1, 0.5, and 0.9.

As seen in the experimental results, 1.91 mW/cm<sup>2</sup> of the peak power density with any duty ratios allowed the end device to participate in the network and communicate with the coordinator. This implied that when the MPT frequency was the same as the ZigBee frequency, the CPD and JPD of the intermittent microwave was more than 108 times greater than those of CW microwave.

The error rates of ZigBee during the intermittent microwave irradiation were also measured. The experimental results under the peak power density of 1.91 mW/cm<sup>2</sup> are shown in Fig. 9.14. Because the peak power density was fixed in the measurements, the average power density was dependent on the duty ratio as follows: 0.191, 0.955, and 1.72 mW/cm<sup>2</sup> at the duty ratios of 0.1, 0.5, and 0.9, respectively. The experimental results shown in Fig. 9.14 suggested that the ZigBee end device could communicate with the coordinator almost perfectly at the duty ratio of 0.1. Conversely, it was difficult for the ZigBee end device to send data in a stable manner at the duty ratio of 0.9.

**Fig. 9.14** Measurement results of error rates when a ZigBee end device was irradiated with an intermittent microwave under the peak power density of  $1.91 \text{ mW/cm}^2$



In the measurements, interference occurred stochastically because the period of intermittent microwave irradiation was irrelevant to that of ZigBee. Therefore, it was important to build a scheduling rule between the intermittent MPT and ZigBee for a robust wireless sensor network with MPT.

## 9.4 Coexistence of MPT and ZigBee-Scheduled and Single-end Device

As described in the previous section, the MPT and the ZigBee wireless communication could coexist at the same frequency band even if the microwave transmitted continuously. However, the microwave power required to suppress an interference to the ZigBee was not sufficiently large to drive the ZigBee. Hence, a scheduled intermittent MPT to the ZigBee should be considered [14]. In this section, the number of ZigBee end devices was assumed to be one.

Power supply microwave should be transmitted to a ZigBee end device in two states. The first state occurs when a capacitor has no charged energy for the end device to start up and join the network. It is also necessary for the power supply microwave to radiate while the end device is awake in this state. Then, after the device joins the network, the device is allowed to sleep. The power supply microwave must radiate only while the device sleeps for robust communication. This is the second state.

Based on the above points, to save time and effort for finding some settings of the intermittent transmission experimentally, a transmission scheduling was developed for robust communication. The developed algorithm of the transmission scheduling is shown in Fig. 9.15. First, after a coordinator set up its ZigBee network, the transmission scheduling was started. An end device was supplied power to start up and join the network during the time T1. The end device then tried to join in the network while the transmission paused during the time T2. If the device did not join after the time T2 since transmission paused, the scheduling algorithm returned to the step in

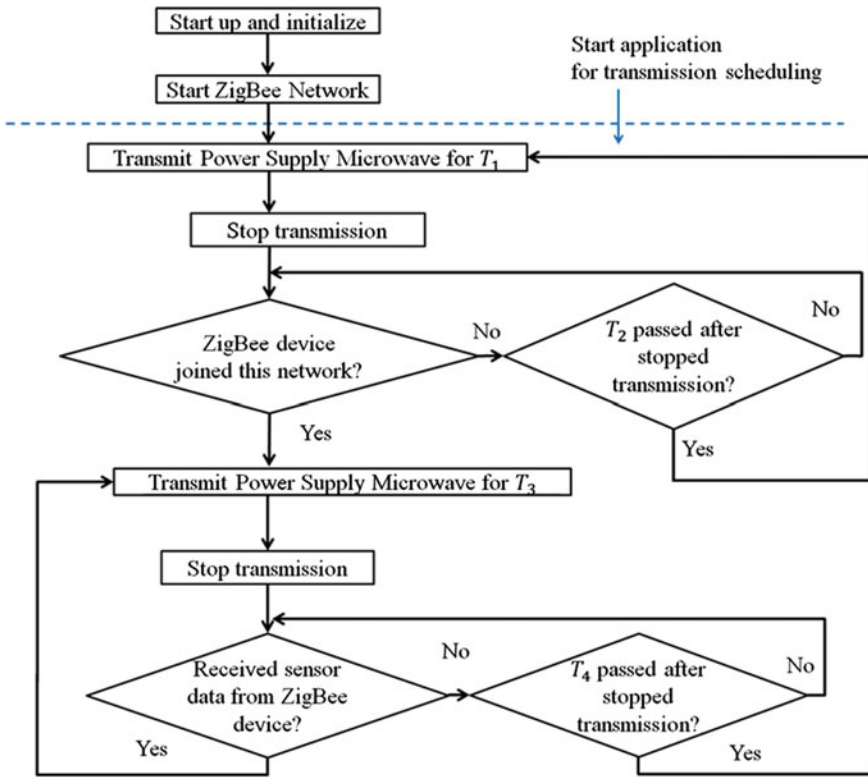


**Fig. 9.15** Algorithm of the transmission scheduling for MPT

which power supply microwave radiates for the end device started. The end device slept when it joined the network. Power transmission restarted and continued for the time  $T_3$ , which was shorter than the time when the end device woke up. Following this, whenever the end device sent data and slept, it was supplied power for the time  $T_3$ . It was determined that if the time  $T_4$  passed without sending data to the end device, then the end device does not work because of insufficient energy stored in the capacitor. In this case, the algorithm returned to the first step. The scheduling algorithm did not require any extra revisions of the ZigBee. The algorithm automatically recognized the timing of the ZigBee wireless communication and the microwave power automatically transmitted between the wireless communications.

The transmission scheduling program was installed in a coordinator besides a program of ZigBee sensor network. Then, an experiment was conducted to confirm that the developed transmission algorithm was compatible with the ZigBee network.

The experimental configuration is shown in Fig. 9.16. The number of times when a ZigBee end device failed to send data for 24 min was measured. A stabilized DC power supply was used as the power source of the end device. The output signal of the ZigBee coordinator determined whether or not the microwave power supply

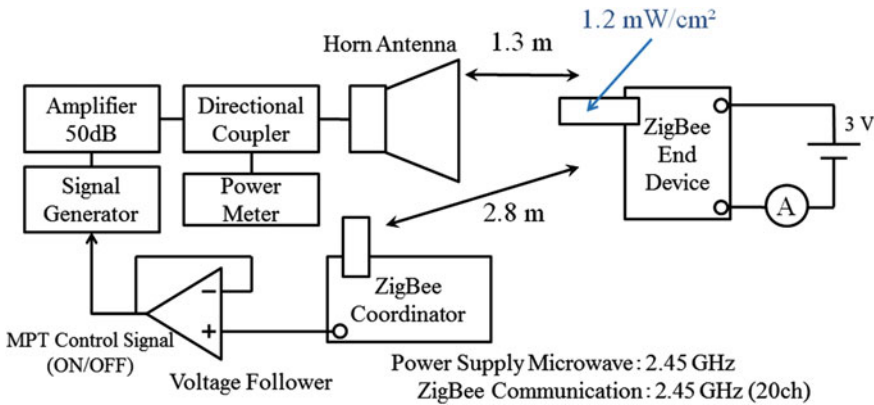


**Fig. 9.16** Experimental configuration of transmission scheduling

**Table 9.2** Values of temporal parameters in the experiment of transmission scheduling

| T1 (s) | T2 (s) | T3 (s) | T4 (s) |
|--------|--------|--------|--------|
| 4      | 3      | 1      | 15     |

microwave radiated. This was the “MPT control signal.” The microwave power supply radiated in the case with the MPT control signal of 0.5 V or more input to a signal generator. Conversely, the microwave power supply paused with a MPT control signal of less than 0.5 V input to the signal generator. Due to the insufficiency in the coordinator’s maximum output current, a voltage follower was also inserted between the coordinator and signal generator. Furthermore, the peak power density of the power supply microwave was  $1.2 \text{ mW/cm}^2$  at the position of the end device. In this configuration, the center frequency of the ZigBee communication was set as 2.45 GHz (20ch), and the frequency of the power supply microwave was also set as 2.45 GHz. The values shown in Table 9.2 were used as the temporal parameters of T1, T2, T3, and T4 for the transmission scheduling.

As indicated by the experimental results, the ZigBee end device did not fail to send data throughout the experiment. That is, the end device succeeded in sending the data approximately 1,260 times. Figure 9.17 shows the waveforms of the power consumption of the end device and the MPT control signal with a transmission time of 2 s during the experiment. Figure 9.17 suggests that the microwave power supply radiated while the end device slept. The microwave also paused when the device was awake. From these results, it was confirmed that the developed transmission scheduling algorithm was compatible with the ZigBee network. Furthermore, the transmission time of T3 could be set to less than 1 s given the success of the experiment with the sleeping time of the device set to the value of T3.

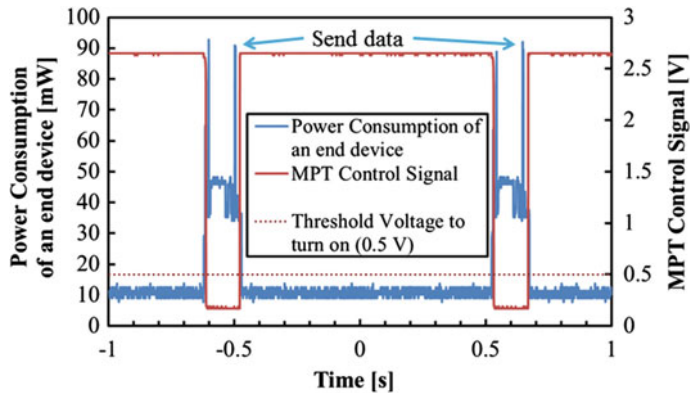


**Fig. 9.17** Waveforms of the power consumption of an end device and MPT control signal of 2 s during the experiment

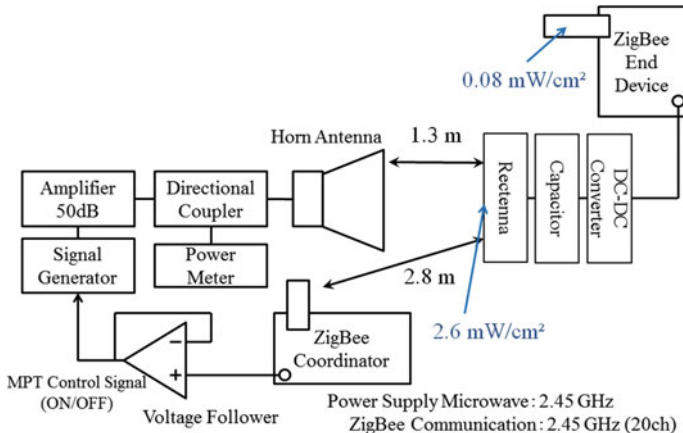


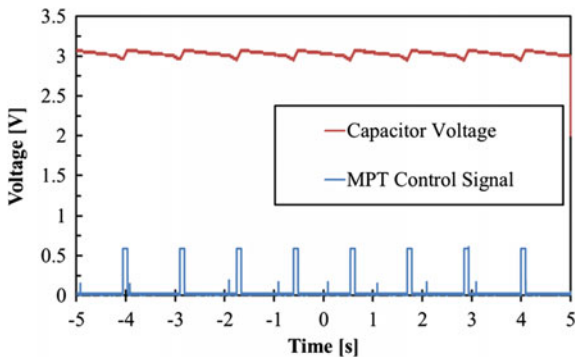
**Fig. 9.18** Experimental configuration of the intermittent MPT demonstration with the transmission scheduling

We conducted an experiment to demonstrate the power supply to a ZigBee end device by intermittent MPT with transmission scheduling. Figure 9.18 shows the demonstration configuration. A RF-DC rectifier circuit with a slave circuit was used as a rectifier. Both the frequencies of MPT and ZigBee communication were set to 2.45 GHz, and the values in Table 9.3 were used as the temporal parameters. The ZigBee end device had no batteries. That is, it was driven by only the intermittent MPT controlled by the transmission scheduling. In this demonstration, we fixed the peak power density of 2.6 mW/cm<sup>2</sup> at the rectenna position. In this configuration, the peak power density at the end device was 0.08 mW/cm<sup>2</sup>. Power supply microwave of this power density prevented the end device from sending data, if the end device

**Table 9.3** Values of the temporal parameters in the scheduled intermittent MPT experiment

| T1 (s) | T2 (s) | T3 (s) | T4 (s) |
|--------|--------|--------|--------|
| 4      | 3      | 0.09   | 15     |

**Fig. 9.19** Waveforms of the capacitor voltage and MPT control signal with a transmission time of 10 s during the demonstration



was awake while the microwave power supply radiated. In addition, the capacitance of a capacitor was 33 mF.

From the demonstration experiment, the end device was driven by the intermittent MPT with the transmission scheduling for 27 min. The experiment was stopped because the end device worked even after 27 min. The end device did not fail to send data throughout the experiment. Figure 9.19 shows the waveforms of the capacitor voltage and MPT control signal with a transmission time of 10 s during the experiment. Findings revealed that the end device worked stably because the capacitor voltage was kept at approximately 3 V.

## 9.5 Coexistence of MPT and ZigBee-scheduled and Multi-end Devices

The scheduling algorithm for a single ZigBee end device is shown in Fig. 9.15. We can expand it for multiple ZigBee end devices. The expanded scheduling algorithm for two ZigBee end devices is shown in Fig. 9.20.

The experimental configuration of the scheduled multi-device TDD-WPT assisted ZigBee is shown in Fig. 9.21. Two ZigBee end devices were used. As shown in Fig. 9.22, MPT control signal was well scheduled between the turning on of two end devices by the algorithm shown in Fig. 9.20. This suggested that the microwave power transmitted as TDD-WPT for the multi-end devices of the ZigBee without interference.

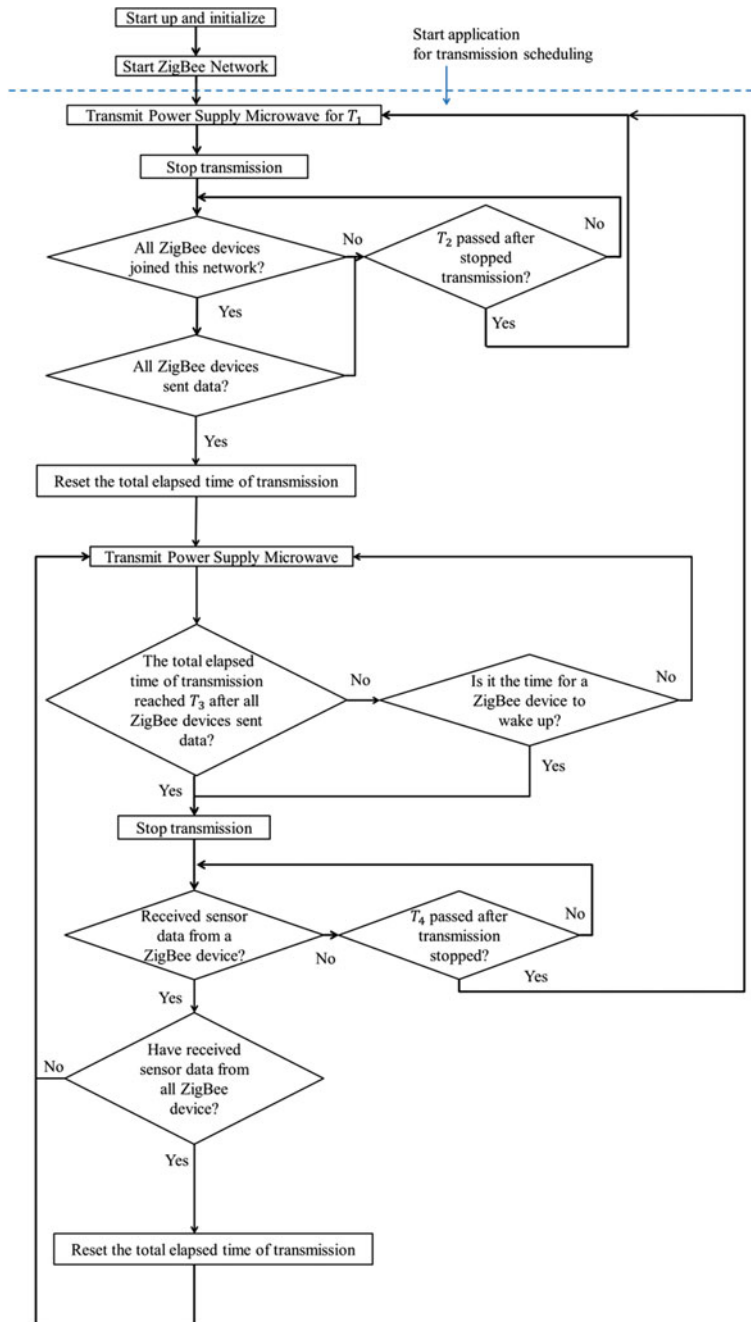


**Fig. 9.20** Algorithm of transmission scheduling for two ZigBee end devices for MPT

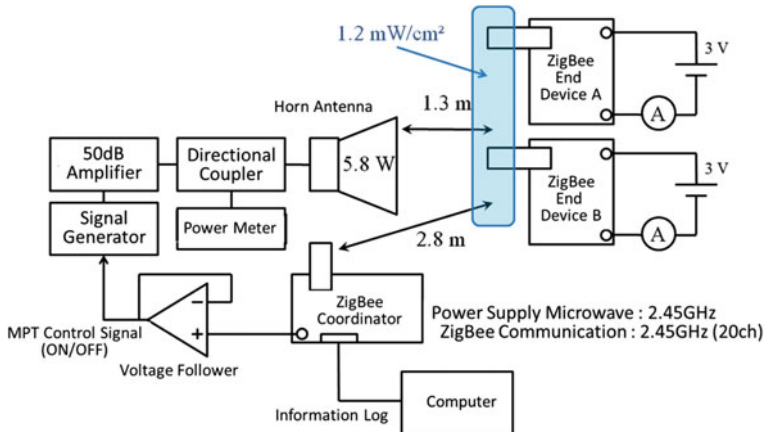
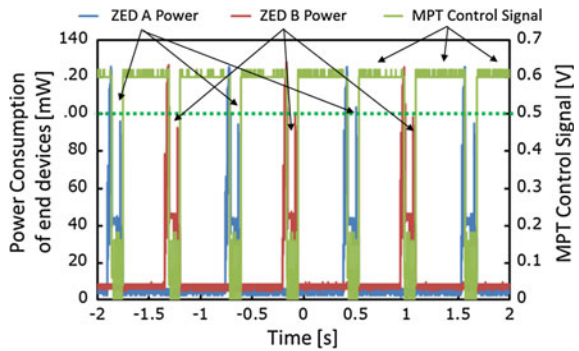


**Fig. 9.21** Experimental configuration of transmission scheduling for two end devices

**Fig. 9.22** Waveforms of the power consumption of two end devices and MPT control signal



## 9.6 Conclusion

To promote the WPT in near future, it is very important to suppress interference between a WPT and a wireless communication. In this study, a time division duplex WPT (TDD-WPT) was proposed to enable the coexistence of the MPT and the wireless communication. A ZigBee sensor network was selected as an application of the TDD-WPT. The maximum power density of the microwave beam to suppress the interference of the ZigBee from the microwave power was estimated. It was concluded that the maximum power, which is provided to the ZigBee, could be increased with a scheduled TDD-WPT, and the interference could be suppressed. In the near future, a new WPT regulation without any interference to a wireless communication will be considered.

## References

1. Shinohara, N.: Wireless Power Transfer via Radiowaves (Wave Series). STE Ltd. and Wiley, Great Britain and USA (2014)
2. DENGYO corporation. [http://www.den-gyo.com/solution/solution10\\_b.html](http://www.den-gyo.com/solution/solution10_b.html)
3. Furukawa, M., Shirato, T.: Efficiency improvement of rectenna for microwave power transmission (in Japanese). IEICE Technical Report, pp. 27–30 (2010)
4. WiPoT consortium. <http://www.wipot.jp/english/>
5. Kawahara, Y., Lakafosis, V., Sawakami, Y., Nishimoto, H., Asami, T.: Design issues for energy harvesting enabled wireless sensing systems. In: 2009 Asia Pacific Microwave Conference, pp. 2248–2251 (2009). doi:[10.1109/APMC.2009.5385431](https://doi.org/10.1109/APMC.2009.5385431)
6. Sample, A., Smith, J.R.: Experimental results with two wireless power transfer systems. In: 2009 IEEE Radio and Wireless Symposium, pp. 16–18 (2009). doi:[10.1109/RWS.2009.4957273](https://doi.org/10.1109/RWS.2009.4957273)
7. Talla, V., Kellogg, B., Ransford, B., Naderiparizi, S., Gollakota, S., Smith, J.R.: Powering the next billion devices with wi-fi (2015). [arXiv:1505.06815](https://arxiv.org/abs/1505.06815)
8. Collado, A., Georgiadis, A.: Conformal hybrid solar and electromagnetic (em) energy harvesting rectenna. IEEE Trans. Circuits Syst. I: Regul. Pap. **60**(8), 2225–2234 (2013). doi:[10.1109/TCSI.2013.2239154](https://doi.org/10.1109/TCSI.2013.2239154)
9. Virili, M., Georgiadis, A., Collado, A., Niotaki, K., Mezzanotte, P., Roselli, L., Alimenti, F., Carvalho, N.B.: Performance improvement of rectifiers for wpt exploiting thermal energy harvesting. Wireless Power Transfer **2**, 22–31 (2015). doi:[10.1017/wpt.2015.4](https://doi.org/10.1017/wpt.2015.4)
10. Belo, D., Georgiadis, A., Carvalho, N.B.: Increasing wireless powered systems efficiency by combining wpt and electromagnetic energy harvesting. In: Wireless Power Transfer Conference (WPTC), 2016 IEEE (2016)
11. Gutmann, R.J., Borrego, J.M.: Power combining in an array of microwave power rectifiers. IEEE Trans. Microw. Theory Tech. **27**(12), 958–968 (1979). doi:[10.1109/TMTT.1979.1129774](https://doi.org/10.1109/TMTT.1979.1129774)
12. Suzuki, N., Mitani, T., Shinohara, N.: Study and development of a microwave power receiving system for zigbee device. In: 2010 Asia-Pacific Microwave Conference, pp. 45–48 (2010)
13. Ichihara, T., Mitani, T., Shinohara, N.: Study on intermittent microwave power transmission to a zigbee device. In: 2012 IEEE MTT-S International Microwave Workshop Series on Innovative Wireless Power Transmission: Technologies, Systems, and Applications (IMWS), pp. 209–212 (2012). doi:[10.1109/IMWS.2012.6215795](https://doi.org/10.1109/IMWS.2012.6215795)
14. Ichihara, T., Mitani, T., Shinohara, N.: Study and development of an intermittent microwave power transmission system for a zigbee device. In: Wireless Power Transfer Conference (WPTC), 2014 IEEE, pp. 40–43 (2014). doi:[10.1109/WPT.2014.6839623](https://doi.org/10.1109/WPT.2014.6839623)

# Chapter 10

## Asymptotically Optimal Power Allocation for Wireless Powered Communication Network with Non-orthogonal Multiple Access

Nikola Zlatanov, Zoran Hadzi-Velkov and Derrick Wing Kwan Ng

**Abstract** In this chapter, we investigate a wireless powered communication network (WPCN) comprised of a power beacon that broadcasts radio frequency (RF) energy to a set of energy harvesting (EH) transmitters equipped with unlimited batteries, which use the harvested energy to transmit information back to the power-beacon in a non-orthogonal multiple access fashion. For this network, we propose a communication scheme which achieves the capacity region. Moreover, we show that the capacity region of the considered WPCN converges to the capacity region of its corresponding non-EH multiple access network, where the non-EH transmitters have specific average power constraints.

### 10.1 Introduction

Wireless sensor networks have been developed for a host of applications, such as surveillance, environmental monitoring, and health care [1]. Wireless sensors are small low-cost devices which are typically powered by a battery. Recharging the batteries of such devices might be too expensive or even impossible if the sensors are deployed in a hostile environment. As a result, alternative approaches for powering low-cost sensors must be investigated. One viable solution for powering wireless sensors is energy harvesting (EH). Thereby, the sensor nodes harvest energy from external sources, such as solar, thermal, and wind energy, and transform the harvested

---

N. Zlatanov (✉)  
Monash University, Melbourne 3800, Australia  
e-mail: nikola.zlatanov@monash.edu

Z. Hadzi-Velkov  
Ss. Cyril and Methodius University, Skopje 1000, Macedonia  
e-mail: zoranhv@feit.ukim.edu.mk

D.W.K. Ng  
University of New South Wales, Sydney 2052, Australia  
e-mail: w.k.ng@unsw.edu.au

energy into electrical energy. However, EH from natural resources is usually location and climate dependent, and may not be suitable for small and mobile wireless sensors. In these cases, wireless power transfer (WPT) of radio frequency (RF) energy to an EH transmitter is an appealing solution for providing a perpetual power supply [17]. For example, using current technology, RF EH circuits embedded in wireless sensors are capable of harvesting microwatt to milliwatt of power over the range of several meters for a transmit power of 1 W and a carrier frequency of less than 1 GHz [3].

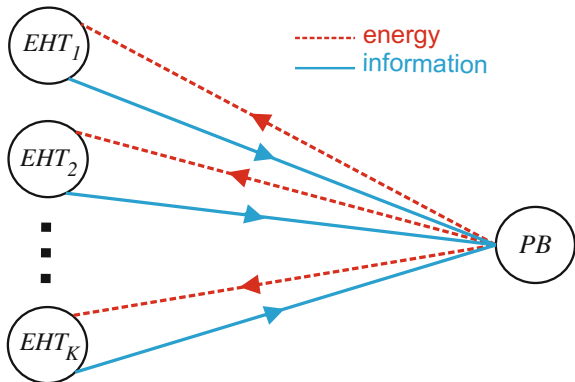
In this chapter, we investigate a wireless powered communication network (WPCN) comprised of a power-beacon that transmits RF energy to a set of EH transmitters, which use the harvested energy to transmit information back to the power-beacon. The considered WPCN is illustrated in Fig. 10.1. In general, the EH transmitters can use different schemes for transmitting information to the power-beacon. For example, each EH transmitter can transmit information to the power-beacon in orthogonal channels, which can be separated either in frequency or in time, and such schemes have been investigated in [8–10]. However, orthogonal multiple access is not optimal in terms of achievable date rates [4]. In particular, in order for the EH transmitters to maximize their data rates, they have to transmit information to the power-beacon non-orthogonally, i.e., at the same time and in the same frequency band. As a result, non-orthogonal multiple access (NOMA) schemes have to be investigated for the considered WPCN. In order to maximize the achievable data rates, NOMA schemes have to involve optimal allocation of the transmit powers of the power-beacon and the EH transmitters. Moreover, optimal selection of the coding schemes and the data rates of the EH transmitters is also necessary. To this end, full-channel channel state information (CSI) is needed at all network nodes. Although full CSI may be impractical, the maximum achievable rates of a NOMA scheme utilizing full CSI can serve as an upper bound for the data rates achieved by more practical multiple access schemes which require only local CSI. As a result, studying a WPCN with NOMA is crucial for understanding the limits on the achievable data rates of WPCN. For the considered WPCN with NOMA, illustrated in Fig. 10.1, we propose a communication scheme which achieves the capacity region. Moreover, we show that the capacity region of the considered WPCN converges to the capacity region of its corresponding non-EH<sup>1</sup> multiple access network, where the non-EH transmitters have specific average power constraints.

Multiple access schemes for EH transmitters have been proposed in [6, 7, 11, 16, 18, 20]. In this chapter, in order to derive optimal NOMA schemes for the considered WPCN, we follow the theoretical framework developed in [6, 19, 20].

---

<sup>1</sup>By non-EH system we mean a communication network that is comprised of nodes which have unlimited power supply that they can use for transmitting information.

**Fig. 10.1** WPCN comprised of a power-beacon (PB) and  $K$  energy harvesting transmitters (EHT)



## 10.2 The Point-to-Point WPT System

In order to introduce the proposed framework for maximizing the achievable rate of WPCN with NOMA, we first present a corresponding framework for a point-to-point channel with WPT, which can be considered as a NOMA scheme for WPCN comprised of a single EH transmitter. This will allow the reader to better understand the proposed framework for a general WPCN comprised of  $K$  EH transmitters which transmit information to the power-beacon employing NOMA. We note that the capacity of the EH additive white Gaussian noise (AWGN) channel with EH from natural resources (i.e., not from a power-beacon), has been derived in [12, 13].

All of the assumptions and definitions that we introduce for the single EH transmitter are also valid for each of the EH transmitters in the WPCN with NOMA introduced in Sect. 10.3.

### 10.2.1 Point-to-Point WPT System Model

We consider an EH transmitter which harvests RF energy from a power-beacon and stores it in its battery. Then, the EH transmitter uses the stored energy to transmit information back to the power-beacon, which also acts as a receiver of information, cf. Fig. 10.2. We assume that the EH transmitter and the power-beacon are both equipped with a single antenna. Furthermore, we assume that the EH transmitter is

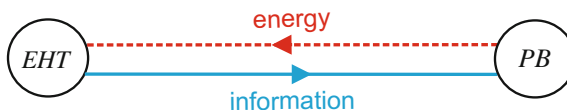


**Fig. 10.2** Point-to-point channel with WPT comprised of a power-beacon (PB) and an energy harvesting transmitter (EHT)

equipped with a battery of unlimited storage capacity. Moreover, we assume that the power-beacon transmits energy in one frequency band and receives information in another (nonoverlapping) frequency band. As a result, the EH transmitter also harvest energy from the power-beacon in one frequency band and transmits information to the power-beacon in another frequency band. We assume that the transmission time is divided into  $N$  time slots, where  $N \rightarrow \infty$ . Moreover, the channels between the EH transmitter and the power-beacon are assumed to be AWGN channels with noise variance  $N_0$ , which are impaired by block fading. Thereby, the channels have constant fading gains during one time slot, and the fading gains change from one time slot to the next.

In time slot  $i$ , let  $x(i)$  denote the power of the fading gain of the channel between the EH transmitter and the power-beacon. Similarly, let  $y(i)$  denote the power of the fading gain of the channel between the power-beacon and the EH transmitter. Let the amount of transmit power<sup>2</sup> that is radiated from the power-beacon in time slot  $i$  be denoted by  $P_0(i)$ . We assume that the power-beacon has an average power constraint, denoted by  $\bar{P}_0$ , and a maximum power constraint, denoted by  $P_{0,\max}$ , i.e.,  $P_0(i), \forall i$ , have to satisfy

$$\lim_{N \rightarrow \infty} \frac{1}{N} \sum_{i=1}^N P_0(i) \leq \bar{P}_0 \quad (10.1)$$

and

$$P_0(i) \leq P_{0,\max}, \forall i. \quad (10.2)$$

Let  $P_{\text{in}}(i)$  denote the amount of harvested power in the battery of the EH transmitter in time slot  $i$ . Then,  $P_{\text{in}}(i)$  can be expressed as a function of the transmit power of the power-beacon as [9]

$$P_{\text{in}}(i) = \eta y(i) P_0(i), \quad (10.3)$$

where  $0 < \eta < 1$  denotes the energy harvesting efficiency. Assuming stationary and ergodic fading, the average harvested power of the EH transmitter, denoted by  $\bar{P}_{\text{in}}$ , can be obtained as

$$\bar{P}_{\text{in}} = \lim_{N \rightarrow \infty} \frac{1}{N} \sum_{i=1}^N P_{\text{in}}(i) = E\{P_{\text{in}}(i)\}, \quad (10.4)$$

where  $E\{\cdot\}$  denotes expectation.

Let  $P_{\text{out}}(i)$  denote the amount of power extracted from the battery in time slot  $i$  and used for the transmission of information to the power-beacon. Moreover, let  $B(i)$  denote the amount of stored power in the battery of the EH transmitter at the

---

<sup>2</sup>We adopt the normalized energy unit Joule-per-second. As a result, we use the terms “energy” and “power” interchangeably.

end of time slot  $i$ . Then, using the harvested power in the battery in time slot  $i$ ,  $P_{\text{in}}(i)$ , and the power extracted from the battery in time slot  $i$ ,  $P_{\text{out}}(i)$ , the amount of stored power in the battery of the EH transmitter at the end of time slot  $i$ ,  $B(i)$ , can be obtained as

$$B(i) = B(i - 1) + P_{\text{in}}(i) - P_{\text{out}}(i), \quad (10.5)$$

where

$$P_{\text{out}}(i) \leq B(i - 1) \quad (10.6)$$

holds due to the energy causality, i.e., in time slot  $i$ , an EH transmitter is unable to extract more power from its battery than the amount of power already stored in the battery in the previous, i.e.,  $(i - 1)$ -th time slot.

Our task in this section is to maximize the achievable data rate of the considered point-to-point system with WPT by optimal power allocation of the transmit powers of the EH transmitter and the power-beacon, as well as optimal selection of the data rates at the EH transmitter. To this end, in the following, we introduce the notion of the *desired amount of power* that the EH transmitter wants to extract from the battery in time slot  $i$ , denoted by  $P_d(i)$ , and then use it for transmission of information. Note that, in contrast to a non-EH system, in an EH system, the desired amount of power that the EH transmitter wants to extract from its battery in time slot  $i$  and the actual amount of power that can be extracted from the battery in time slot  $i$  may not be identical. In particular, if the desired amount of power that the EH transmitter wants to extract from its battery in time slot  $i$ ,  $P_d(i)$ , is smaller than the amount of power already stored in the battery at the end of time slot  $i - 1$ ,  $B(i - 1)$ , then at most the EH transmitter can extract  $B(i - 1)$  units of power. Otherwise, if the desired amount of power that the EH transmitter wants to extract from its battery in time slot  $i$ ,  $P_d(i)$ , is larger than or equal to the amount of power already stored in the battery at the end of time slot  $i - 1$ ,  $B(i - 1)$ , then the EH transmitter transmits with power  $P_{\text{out}}(i) = P_d(i)$ . To simplify<sup>3</sup> the proposed framework, we assume that when  $B(i - 1) < P_d(i)$  holds, i.e., there is not enough desired power stored in the battery in time slot  $i$ , the EH transmitter is silent, i.e.,  $P_{\text{out}}(i) = 0$  holds. Mathematically, the relation between  $P_d(i)$ ,  $P_{\text{out}}(i)$ , and  $B(i - 1)$  can be written as

$$P_{\text{out}}(i) = \begin{cases} P_d(i) & \text{if } B(i - 1) \geq P_d(i) \\ 0 & \text{if } B(i - 1) < P_d(i). \end{cases} \quad (10.7)$$

By introducing a binary indicator variable for time slot  $i$ , denoted by  $q(i)$ , which is defined as

$$q(i) = \begin{cases} 1 & \text{if } B(i - 1) \geq P_d(i) \\ 0 & \text{if } B(i - 1) < P_d(i), \end{cases} \quad (10.8)$$

---

<sup>3</sup>This simplification is without any loss to the average data rate.

the relation in (10.7) can be simplified as

$$P_{\text{out}}(i) = q(i)P_{\text{d}}(i). \quad (10.9)$$

Note that we can obtain the time average of the desired transmit power, denoted by  $\bar{P}_{\text{d}}$ , and the actual transmit power of the EH transmitter, denoted by  $\bar{P}_{\text{out}}$ , as

$$\bar{P}_{\text{d}} = \lim_{N \rightarrow \infty} \frac{1}{N} \sum_{i=1}^N P_{\text{d}}(i) \quad (10.10)$$

and

$$\bar{P}_{\text{out}} = \lim_{N \rightarrow \infty} \frac{1}{N} \sum_{i=1}^N P_{\text{out}}(i) \stackrel{(a)}{=} \lim_{N \rightarrow \infty} \frac{1}{N} \sum_{i=1}^N q(i)P_{\text{d}}(i), \quad (10.11)$$

where (a) follows from (10.9). Moreover, it can be observed that  $\bar{P}_{\text{out}} \leq \bar{P}_{\text{d}}$  always holds.

*Remark 10.1* Note that the transmit power of the EH transmitter in time slot  $i$ ,  $P_{\text{out}}(i)$ , is completely dependent on  $P_{\text{d}}(j)$  and  $P_0(j)$ ,  $\forall j \leq i$ . Hence, in order to find the optimal transmit power of the EH transmitter for time slot  $i$ ,  $P_{\text{out}}(i)$ , we need to find the optimal desired transmit powers,  $P_{\text{d}}(j)$ , and the optimal transmit powers of the power-beacon,  $P_0(j)$ ,  $\forall j \leq i$ . Although this may seem as a complex task at first, we will show that, using the proposed framework, the power allocation solution can be obtained analytically.

### 10.2.2 Maximization of the Average Data Rate

In time slot  $i$ , using power  $P_{\text{out}}(i)$ , the maximum possible data rate that the EH transmitter can achieve, denoted by  $R(i)$ , is given by

$$\begin{aligned} R(i) &= \log_2 \left( 1 + \frac{P_{\text{out}}(i)x(i)}{N_0} \right) \stackrel{(a)}{=} \log_2 \left( 1 + \frac{q(i)P_{\text{d}}(i)x(i)}{N_0} \right) \\ &\stackrel{(b)}{=} q(i) \log_2 \left( 1 + \frac{P_{\text{d}}(i)x(i)}{N_0} \right), \end{aligned} \quad (10.12)$$

where (a) follows from (10.9) and (b) follows since  $\log_2(1) = 0$ . The data rate in (10.12) can be achieved if the EH transmitter uses optimal capacity coding for the AWGN channel, i.e., it transmits codewords which are comprised of infinitely many complex zero-mean Gaussian distributed symbols with variance  $P_{\text{out}}(i) = q(i)P_{\text{d}}(i)$ .

Using (10.12), the average data rate that the EH transmitter can achieve during  $N \rightarrow \infty$  time slots via optimal capacity coding for the AWGN channel, denoted by  $\bar{R}$ , is obtained as

$$\bar{R} = \lim_{N \rightarrow \infty} \frac{1}{N} \sum_{i=1}^N q(i) \log_2 \left( 1 + \frac{P_d(i)x(i)}{N_0} \right). \quad (10.13)$$

Our task is to maximize the average data rate  $\bar{R}$  in (10.13). Due to the proposed framework, the desired powers  $P_d(i)$ ,  $\forall i$ , and the transmit powers of the power-beacon,  $P_0(i)$ ,  $\forall i$ , are the only variables with degrees of freedom in the expression for  $\bar{R}$  in (10.13). In particular,  $q(i)$  in (10.8) depends completely on  $P_0(j)$  and  $P_d(j)$ ,  $\forall j \leq i$ , via  $B(i-1)$ , cf. (10.5). Hence, to maximize the average data rate in (10.13), we need to find the optimal  $P_d(i)$  and  $P_0(i)$ ,  $\forall i$ . To this end, we formulate the following optimization problem for  $N \rightarrow \infty$

$$\begin{aligned} & \underset{P_d(i), P_0(i), \forall i}{\text{Maximize}} : \quad \frac{1}{N} \sum_{i=1}^N q(i) \log_2 \left( 1 + \frac{P_d(i)x(i)}{N_0} \right) \\ & \text{Subject to :} \quad \text{C1 : } B(i) = B(i-1) + P_{\text{in}}(i) - q(i)P_d(i), \\ & \quad \text{C2 : } P_{\text{in}}(i) = \eta y(i)P_0(i), \\ & \quad \text{C3 : } q(i) = \begin{cases} 1 & \text{if } B(i-1) \geq P_d(i) \\ 0 & \text{if } B(i-1) < P_d(i), \end{cases} \\ & \quad \text{C4 : } \frac{1}{N} \sum_{i=1}^N P_0(i) \leq \bar{P}_0, \\ & \quad \text{C5 : } P_0(i) \leq P_{0,\max}, \\ & \quad \text{C6 : } P_0(i) \geq 0, \\ & \quad \text{C7 : } P_d(i) \geq 0. \end{aligned} \quad (10.14)$$

In (10.14), constraint C1 is the expression that describes the input–output relation of the battery, cf. (10.5); constraint C2 describes the relation between the harvested power of the EH transmitter and the transmitted power of the power-beacon, cf. (10.3); constraint C3 is the expression for the binary indicator variable  $q(i)$ , cf. (10.8); constraints C4 and C5 are the average and maximum power constraints of the transmit power of the power-beacon, respectively, cf. (10.1) and (10.2); constraints C6 and C7 constrain the powers  $P_0(i)$  and  $P_d(i)$  to be nonnegative. As can be observed, the maximization problem (10.14) is non-concave, and therefore, very difficult to solve analytically, in general. However, the following lemma will provide us with the necessary tools for solving the maximization problem in (10.14).

**Lemma 10.1** *In the considered point-to-point WPT system, if  $P_d(i) \geq 0$ ,  $\forall i$ , are chosen such that they satisfy*

$$\lim_{N \rightarrow \infty} \frac{1}{N} \sum_{i=1}^N P_d(i) = \bar{P}_{\text{in}}, \quad (10.15)$$

*then the following relations hold*

$$\bar{P}_{\text{in}} = \bar{P}_{\text{out}} \quad (10.16)$$

*and*

$$\lim_{N \rightarrow \infty} \frac{1}{N} \sum_{i=1}^N q(i) = 1. \quad (10.17)$$

*Expression (10.16) means that all of the harvested power is eventually used for the transmission of information, i.e., there is no excess of energy that is kept stored in the battery and not used for the transmission of information. On the other hand, expression (10.17) means that the events  $q(i) = 1$  hold for practically all time slots<sup>4</sup>  $i$ . Conversely, the number of time slots for which  $q(i) = 0$  holds are negligible compared to  $N \rightarrow \infty$ . As a result, these time slots have a negligible contribution to the average data rate and therefore these events can be neglected.*

*Hence, by choosing the values of  $P_d(i) \geq 0$ ,  $\forall i$ , arbitrarily, as long as the constraint in (10.15) holds, we actually choose the values of  $P_{\text{out}}(i)$  arbitrarily for practically all time slots  $i$ .*

*Proof* If  $\bar{P}_d$  is set to  $\bar{P}_d = \bar{P}_{\text{in}}$ , i.e., if (10.15) holds, then the following must hold

$$\bar{P}_{\text{out}} = \lim_{N \rightarrow \infty} \frac{1}{N} \sum_{i=1}^N q(i) P_d(i) \stackrel{(a)}{=} \lim_{N \rightarrow \infty} \frac{1}{N} \sum_{i=1}^N P_d(i) = \bar{P}_d = \bar{P}_{\text{in}}. \quad (10.18)$$

We prove the above claim, i.e., equality (a) in (10.18) by contradiction. Assume that  $\bar{P}_d = \bar{P}_{\text{in}}$  holds, however, equality (a) in (10.18) does not hold and

$$\bar{P}_{\text{out}} = \lim_{N \rightarrow \infty} \frac{1}{N} \sum_{i=1}^N q(i) P_d(i) < \lim_{N \rightarrow \infty} \frac{1}{N} \sum_{i=1}^N P_d(i) = \bar{P}_d = \bar{P}_{\text{in}} \quad (10.19)$$

holds instead. However, since  $\bar{P}_{\text{out}} < \bar{P}_{\text{in}}$  holds, more energy is harvested into the battery than what is extracted from the battery. Since the battery storage capacity is unlimited and since the number of transmit time slots is also unlimited, after some

---

<sup>4</sup>When we say that it holds for practically all time slots, we mean that it holds for all time slots or that it holds for all time slots except for a negligible fraction of them, denoted by  $\Delta$ , which satisfies  $\lim_{N \rightarrow \infty} \Delta/N = 0$ .

negligible transient time, during which  $q(i) = 0$  might occur,  $q(i) = 1$  will hold in all subsequent time slots. In other words, when  $\bar{P}_{\text{out}} < \bar{P}_{\text{in}}$  holds and the battery is unlimited, after some negligible transient time of the start of the transmission, there will always be sufficient power in the battery such that  $B(i-1) \geq P_{\text{d}}(i)$ , i.e.,  $q(i) = 1$  will always hold.<sup>5</sup> Now, since when  $\bar{P}_{\text{out}} < \bar{P}_{\text{in}}$ ,  $q(i) = 1$  will hold for practically all time slots, we obtain

$$\bar{P}_{\text{out}} = \lim_{N \rightarrow \infty} \frac{1}{N} \sum_{i=1}^N q(i) P_{\text{d}}(i) \stackrel{(b)}{=} \lim_{N \rightarrow \infty} \frac{1}{N} \sum_{i=1}^N P_{\text{d}}(i) = \bar{P}_{\text{d}}, \quad (10.20)$$

where (b) holds since  $q(i) = 1$  holds for practically all time slots when  $\bar{P}_{\text{out}} < \bar{P}_{\text{in}}$  holds and the battery is unlimited. Note that (10.20) is a contradiction to (10.19). Due to this contradiction, (10.19) cannot hold and (10.18) must hold instead. This concludes the proof of (10.18).

Now, there is only one possibility for which (10.18) can hold. In particular, the only possibility for which (10.18) can hold is if and only if

$$\lim_{N \rightarrow \infty} \frac{1}{N} \sum_{i=1}^N q(i) = 1 \quad (10.21)$$

holds. On the other hand, if (10.21) holds, then the average data rate in (10.13) can be written as

$$\bar{R} = \lim_{N \rightarrow \infty} \frac{1}{N} \sum_{i=1}^N q(i) \log_2 \left( 1 + \frac{P_{\text{d}}(i)x(i)}{N_0} \right) = \lim_{N \rightarrow \infty} \frac{1}{N} \sum_{i=1}^N \log_2 \left( 1 + \frac{P_{\text{d}}(i)x(i)}{N_0} \right). \quad (10.22)$$

This completes the proof.  $\square$

Using, Lemma 10.1, we now provide a very simple solution to the optimization problem in (10.14). To this end, we first add the constraint in (10.15) into the optimization problem in (10.14) as constraint C8. As a result, we obtain the following optimization problem for  $N \rightarrow \infty$

$$\begin{aligned} \text{Maximize}_{P_{\text{d}}(i), P_0(i), \forall i} \quad & \frac{1}{N} \sum_{i=1}^N q(i) \log_2 \left( 1 + \frac{P_{\text{d}}(i)x(i)}{N_0} \right) \\ \text{Subject to :} \quad & \text{C1 : } B(i) = B(i-1) + P_{\text{in}}(i) - q(i)P_{\text{d}}(i), \\ & \text{C2 : } P_{\text{in}}(i) = \eta y(i)P_0(i), \\ & \text{C3 : } q(i) = \begin{cases} 1 & \text{if } B(i-1) \geq P_{\text{d}}(i) \\ 0 & \text{if } B(i-1) < P_{\text{d}}(i), \end{cases} \end{aligned}$$

---

<sup>5</sup>For a rigorous proof of this claim, please refer to [12, 20].

$$\begin{aligned}
C4 : \frac{1}{N} \sum_{i=1}^N P_0(i) &\leq \bar{P}_0(i), \\
C5 : P_0(i) &\leq P_{0,\max}, \\
C6 : P_0(i) &\geq 0, \\
C7 : P_d(i) &\geq 0, \\
C8 : \frac{1}{N} \sum_{i=1}^N P_d(i) &= \bar{P}_{\text{in}}. \tag{10.23}
\end{aligned}$$

Note that, since the optimization problem in (10.23) has an additional constraint compared to the optimization problem in (10.14), the maximum data rate obtained from (10.23) can only be lower than or equal to the maximum data rate obtained from (10.14). On the other hand, in the optimization problem in (10.23), since constraint (10.15) is satisfied, Lemma 10.1 holds. Therefore, we can consider that  $q(i) = 1$  holds for practically all time slots, i.e., the events for which  $q(i) = 0$  holds have a negligible contribution to the average data rate. As a result, we can set  $q(i) = 1$ ,  $\forall i$ , in (10.23). Now, with  $q(i) = 1$ ,  $\forall i$ , in (10.23), constraints C1 and C3 become unnecessary, and therefore can be removed. Moreover, we can plug in constraint C2 into C8, and thereby obtain the following equivalent optimization problem for  $N \rightarrow \infty$

$$\begin{aligned}
\underset{P_d(i), P_0(i), \forall i}{\text{Maximize}} : \quad & \frac{1}{N} \sum_{i=1}^N \log_2 \left( 1 + \frac{P_d(i)x(i)}{N_0} \right) \\
\text{Subject to : } \quad & C1 : \frac{1}{N} \sum_{i=1}^N P_0(i) \leq \bar{P}_0, \\
& C2 : P_0(i) \leq P_{0,\max}, \\
& C3 : P_0(i) \geq 0, \\
& C4 : P_d(i) \geq 0, \\
C5 : \frac{1}{N} \sum_{i=1}^N P_d(i) &= \frac{1}{N} \sum_{i=1}^N \eta y(i) P_0(i). \tag{10.24}
\end{aligned}$$

The optimization problem in (10.24) is concave and can be easily solved using the Lagrangian method. The solution of (10.24) is given in the following Theorem.

**Theorem 10.1** *The solution of the optimization problem in (10.24), i.e., the optimal power allocation that maximizes the average data of the considered point-to-point system with WPT is given by*

$$P_0(i) = \begin{cases} P_{0,\max} & \text{if } y(i) \geq \mu \\ 0 & \text{if } y(i) < \mu \end{cases} \tag{10.25}$$

and

$$P_d(i) = \left( \frac{1}{\lambda} - \frac{N_0}{x(i)} \right)^+, \quad (10.26)$$

where  $(x)^+ = \max\{0, x\}$ , and  $\mu$  and  $\lambda$  are Lagrange multipliers corresponding to constraints C1 and C5 in (10.24), respectively. The transmit power of the EH transmitter,  $P_{out}(i)$ , can be found by inserting (10.26) into (10.9).

The maximum data rate achieved with the power allocation solution in (10.26) is obtained by inserting (10.26) in (10.22) as

$$\bar{R} = \lim_{N \rightarrow \infty} \frac{1}{N} \sum_{i=1}^N \log_2 \left( 1 + \frac{x(i)}{N_0} \left( \frac{1}{\lambda} - \frac{N_0}{x(i)} \right)^+ \right). \quad (10.27)$$

*Proof* The solutions for  $P_d(i)$  and  $P_0(i)$  can be relatively easily obtained using the Lagrangian method [2]. The exact derivation using this method is shown in [6].  $\square$

*Remark 10.2* In (10.25),  $\mu$  is found such that constraint C1 in (10.24) holds. If  $f_Y(y)$  is the probability distribution function (PDF) of the fading power gain  $y(i)$ , then the constant  $\mu$  can be found as the solution of the following identity

$$P_{0,\max} \int_{\mu}^{\infty} f_Y(y) dy = \bar{P}_0. \quad (10.28)$$

On the other hand, in (10.26),  $\lambda$  is found such that constraint C5 in (10.24) holds, with  $P_0(i)$  given in (10.25). If  $f_X(x)$  is the PDF of the fading power gains  $x(i)$ , then  $\lambda$  can be found as the solution of the following identity

$$\int_{\lambda}^{\infty} \left( \frac{1}{\lambda} - \frac{N_0}{x} \right) f_X(x) dx = \eta P_{0,\max} \int_{\mu}^{\infty} y f_Y(y) dy. \quad (10.29)$$

*Remark 10.3* An interesting consequence arising from Theorem 10.1 is that the maximum average data rate of the considered point-to-point WPT system is identical to the capacity of a non-EH point-to-point AWGN channel with an average power constraint  $\eta E\{y(i)P_0(i)\}$  at the non-EH transmitter, where  $P_0(i)$  is given in (10.25), see [5]. Having in mind that the EH transmitter cannot harvest more power than  $\eta E\{y(i)P_0(i)\}$ , with  $P_0(i)$  given in (10.25), we can conclude that the rate achieved with the power allocation outlined in Theorem 10.1 is also the capacity of the considered WPT system with one EH transmitter. Note that this result is inline with the results in [12, 13], which derive the capacity of the EH AWGN channel with EH from natural resources (i.e., not from a power-beacon).

## 10.3 Wireless Powered Communication Networks with Non-orthogonal Multiple Access

In the following, we generalize the framework developed for the WPT system with one EH transmitter to the case of multiple EH transmitters which transmit information to the power-beacon in a non-orthogonal manner, i.e., we generalize the framework to the WPCN with NOMA.

### 10.3.1 System Model

The WPCN with NOMA is identical to the point-to-point system with WPT investigated in Sect. 10.2, but, instead of a WPCN with one EH transmitter, the system is comprised of  $K$  EH transmitters which transmit information in the same time and in the same frequency band to the power-beacon. On the other hand, the power-beacon broadcasts energy to the  $K$  EH transmitters, which use the harvested energy to transmit information back to the power-beacon, cf. Fig. 10.1. We assume that the channels between the EH transmitters and the power-beacon are independent AWGN channels with noise variance  $N_0$  affected by block fading.

In time slot  $i$ , let  $x_k(i)$  denote the power of the fading gain of the channel between the  $k$ th EH transmitter and the power-beacon. Similarly, let  $y_k(i)$  denote the power of the fading gain of the channel between the power-beacon and the  $k$ th EH transmitter.

Let  $P_{\text{in},k}(i)$  denote the amount of harvested power in the battery of the  $k$ th EH transmitter in time slot  $i$ . Then, considering that the transmit power of the power-beacon in time slot  $i$  is  $P_0(i)$ ,  $P_{\text{in},k}(i)$  can be obtained as

$$P_{\text{in},k}(i) = \eta y_k(i) P_0(i). \quad (10.30)$$

In each time slot, each EH transmitter extracts power from its battery and uses it to transmit information to the power-beacon. Let the transmit power of the  $k$ th EH transmitter in time slot  $i$  be denoted by  $P_{\text{out},k}(i)$ . Moreover, let  $P_{\text{d},k}(i)$  denote the desired power that the  $k$ th EH transmitter wants to extract from its battery in the  $i$ th time slot. Then, similar to the single EH transmitter case,  $P_{\text{out},k}(i)$  and  $P_{\text{d},k}(i)$  are related by

$$P_{\text{out},k}(i) = q_k(i) P_{\text{d},k}(i), \quad (10.31)$$

where  $q_k(i)$  is defined as

$$q_k(i) = \begin{cases} 1 & \text{if } B_k(i-1) \geq P_{\text{d},k}(i) \\ 0 & \text{if } B_k(i-1) < P_{\text{d},k}(i). \end{cases} \quad (10.32)$$

In (10.32),  $B_k(i)$  is the amount of power stored in the battery of the  $k$ th EH transmitter at the end of the  $i$ th time slot, which is given by

$$B_k(i) = B_k(i - 1) + P_{\text{in},k}(i) - P_{\text{out},k}(i), \quad (10.33)$$

where

$$P_{\text{out},k}(i) \leq B_k(i - 1) \quad (10.34)$$

holds. For the  $k$ th EH transmitter, the average transmit power, denoted by  $\bar{P}_{\text{out},k}$ , the average desired transmit power, denoted by  $\bar{P}_{\text{d},k}$ , and the average harvested power, denoted by  $\bar{P}_{\text{in},k}$ , are given by

$$\bar{P}_{\alpha,k} = \lim_{N \rightarrow \infty} \frac{1}{N} \sum_{i=1}^N P_{\alpha,k}(i), \quad \alpha \in \{\text{out, d, in}\}. \quad (10.35)$$

### 10.3.2 Maximization of the Average Data Rate

The achievable average rate region of the considered WPCN with NOMA is given by

$$\begin{aligned} R_{\text{region}} &= \left\{ \bigcup (\bar{R}_1, \bar{R}_2, \dots, \bar{R}_N) : \right. \\ &\quad \sum_{k \in \mathcal{S}} \bar{R}_k \leq \lim_{N \rightarrow \infty} \frac{1}{N} \sum_{i=1}^N \log_2 \left( 1 + \sum_{k \in \mathcal{S}} P_{\text{out},k}(i) x_k(i) \right) \Big\} \\ &\stackrel{(a)}{=} \left\{ \bigcup (\bar{R}_1, \bar{R}_2, \dots, \bar{R}_N) : \right. \\ &\quad \left. \sum_{k \in \mathcal{S}} \bar{R}_k \leq \lim_{N \rightarrow \infty} \frac{1}{N} \sum_{i=1}^N \log_2 \left( 1 + \sum_{k \in \mathcal{S}} q_k(i) P_{\text{d},k}(i) x_k(i) \right) \right\}, \end{aligned} \quad (10.36)$$

where (a) follows from (10.31), and where  $\mathcal{S}$  is any subset of  $\{1, 2, 3, \dots, K\}$  and  $\bar{R}_k$  is the average data rate of the  $k$ th EH transmitter. The boundary surface of region  $R_{\text{region}}$  can be achieved if the data rate of the  $k$ th EH transmitter in each time slot  $i$ , denoted by  $R_k(i)$ , is given by [15]

$$R_k(i) = \log_2 \left( 1 + \frac{P_{\text{out},k}(i) x_k(i)}{1 + \sum_{l < k} P_{\text{out},l}(i) x_l(i)} \right)$$

$$= \log_2 \left( 1 + \frac{q_k(i) P_{d,k}(i) x_k(i)}{1 + \sum_{l < k} q_l(i) P_{d,l}(i) x_l(i)} \right). \quad (10.37)$$

Moreover, for the boundary surface of region  $R_{\text{region}}$  to be achieved, the power-beacon has to decode the transmitted codewords from the EH transmitters in the order  $K, K - 1, \dots, 1$ . In addition, when the power-beacon decodes the information from EH transmitter  $k$ , it should consider all the codewords transmitted from EH transmitters  $l < k$  as noise. Furthermore, once the power-beacon decodes the codeword from EH transmitter  $k$ , it uses successive interference cancellation, i.e., it subtracts the decoded codeword from its received codeword. On the other hand, the data rate in (10.37) can be achieved if all EH transmitters use optimal capacity coding for the AWGN channel, i.e., transmit codewords which are comprised of infinitely many zero-mean complex Gaussian distributed symbols with variance  $P_{\text{out},k}(i) = q_k(i) P_{d,k}(i)$ .

To simplify the proposed framework, without any loss in the average rate region as will be shown later, we propose the  $k$ th EH transmitter to transmit with a rate which is smaller than the rate in (10.37), and given by

$$R_k(i) = \log_2 \left( 1 + \frac{q_k(i) P_{d,k}(i) x_k(i)}{1 + \sum_{l < k} P_{d,l}(i) x_l(i)} \right) = q_k(i) \log_2 \left( 1 + \frac{P_{d,k}(i) x_k(i)}{1 + \sum_{l < k} P_{d,l}(i) x_l(i)} \right). \quad (10.38)$$

Hence, the  $k$ th EH transmitter reduces its rate compared to (10.37) by considering that  $q_l(i) = 1, \forall l < k$ , i.e., all  $l < k$  EH transmitters will have enough power in their batteries to transmit information to the power-beacon. Using (10.38), the average data rate that the EH transmitter can achieve during  $N \rightarrow \infty$  time slots, denoted by  $\bar{R}_k$ , is given by

$$\bar{R}_k = \lim_{N \rightarrow \infty} \frac{1}{N} \sum_{i=1}^N q_k(i) \log_2 \left( 1 + \frac{P_{d,k}(i) x_k(i)}{1 + \sum_{l < k} P_{d,l}(i) x_l(i)} \right). \quad (10.39)$$

To maximize the boundary rate region  $R_{\text{region}}$  in (10.36), similar to the problem formulation for maximizing the boundary rate region of the non-EH multiple access channel described in [14, 15], we need to maximize the weighted sum rate  $\sum_{k=1}^K \nu_k \bar{R}_k$ , where  $\bar{R}_k$  is given by (10.39) and  $\nu_k$  are non-negative constants. More precisely, the maximum boundary rate region  $R_{\text{region}}$  in (10.36) can be obtained by solving the following optimization problem for  $N \rightarrow \infty$

$$\begin{aligned} \text{Maximize : } & \sum_{k=1}^K \nu_k \frac{1}{N} \sum_{i=1}^N q_k(i) \log_2 \left( 1 + \frac{P_{d,k}(i) x_k(i)}{1 + \sum_{l < k} P_{d,l}(i) x_l(i)} \right) \\ \text{Subject to : } & \text{C1 : } B_k(i) = B_k(i-1) + P_{\text{in},k}(i) - q_k(i) P_{d,k}(i), \quad \forall k, \end{aligned}$$

$$\begin{aligned}
C2 : P_{\text{in},k}(i) &= \eta y_k(i) P_0(i), \quad \forall k, \\
C3 : q_k(i) &= \begin{cases} 1 & \text{if } B_k(i-1) \geq P_{\text{d},k}(i) \\ 0 & \text{if } B_k(i-1) < P_{\text{d},k}(i) \end{cases}, \quad \forall k, \\
C4 : \frac{1}{N} \sum_{i=1}^N P_0(i) &\leq \bar{P}_0, \\
C5 : P_0(i) &\leq P_{0,\max}, \\
C6 : P_0(i) &\geq 0, \\
C7 : P_{\text{d},k}(i) &\geq 0, \quad \forall k,
\end{aligned} \tag{10.40}$$

where  $v_k$  are nonnegative constants which have to satisfy<sup>6</sup>  $v_1 \geq v_2 \geq \dots \geq v_K$  and  $\sum_{k=1}^K v_k = 1$ , see [15]. One set of values for the constants  $v_1, v_2, \dots, v_K$  provides one point of the boundary rate region  $R_{\text{region}}$ . By varying the values of  $v_1, v_2, \dots, v_K$ , all of the point of the boundary rate region  $R_{\text{region}}$  can be obtained, see [14, 15]. On the other hand, the constraints C1 to C7 in (10.40) are identical to the constraints C1 to C7 in (10.14), but now have to hold for all  $k = 1, \dots, K$  EH transmitters. Again, the optimization problem in (10.40) is non-concave and is difficult to solve in general. However, similar to the single EH transmitter case, this optimization problem can be easily solved utilizing Lemma 10.1.

To solve the optimization problem in (10.40), we first add the constraint in (10.15) into the optimization problem in (10.14) as constraint C8 which has to hold  $\forall k$ . Thereby, we obtain the following optimization problem for  $N \rightarrow \infty$

$$\begin{aligned}
\text{Maximize}_{P_{\text{d},k}(i), P_0(i), \forall i, k} \quad & \sum_{k=1}^K v_k \frac{1}{N} \sum_{i=1}^N q_k(i) \log_2 \left( 1 + \frac{P_{\text{d},k}(i)x_k(i)}{1 + \sum_{l < k} P_{\text{d},l}(i)x_l(i)} \right) \\
\text{Subject to :} \quad C1 : B_k(i) &= B_k(i-1) + P_{\text{in},k}(i) - q_k(i) P_{\text{d},k}(i), \quad \forall k, \\
C2 : P_{\text{in},k}(i) &= \eta y_k(i) P_0(i), \quad \forall k, \\
C3 : q_k(i) &= \begin{cases} 1 & \text{if } B_k(i-1) \geq P_{\text{d},k}(i) \\ 0 & \text{if } B_k(i-1) < P_{\text{d},k}(i) \end{cases}, \quad \forall k, \\
C4 : \frac{1}{N} \sum_{i=1}^N P_0(i) &\leq \bar{P}_0, \\
C5 : P_0(i) &\leq P_{0,\max}, \\
C6 : P_0(i) &\geq 0, \\
C7 : P_{\text{d},k}(i) &\geq 0, \quad \forall k,
\end{aligned}$$

---

<sup>6</sup>Note that, if a different decoding priory is needed other than  $K, K-1, \dots, 1$ , then, without loss of generality, the EH transmitters can be renumbered such that  $v_1 \geq v_2 \geq \dots \geq v_K$  again holds, where EH transmitter 1 is related to  $v_1$ , EH transmitter 2 is related to  $v_2, \dots$ , and EH transmitter K is related to  $v_K$ , see [15].

$$\text{C8} : \frac{1}{N} \sum_{i=1}^N P_{d,k}(i) = \bar{P}_{\text{in},k}, \quad \forall k. \quad (10.41)$$

Similar to the single EH transmitter case, note that, since the optimization problem in (10.41) has an additional constraint compared to the optimization problem in (10.40), the maximum data rate obtained from (10.41) can only be lower than or equal to the maximum data rate obtained from (10.40). On the other hand, according to Lemma 10.1, since the constraint in (10.15) holds,  $q_k(i) = 1$  holds for practically all time slots, i.e., the events for which  $q_k(i) = 0$  holds have a negligible contribution to the average data rates at the individual EH transmitters. As a result, we can set  $q_k(i) = 1, \forall k, i$ , in (10.41). Now, with  $q_k(i) = 1, \forall k, i$ , in (10.41), constraints C1 and C3 become unnecessary, and therefore can be removed. Moreover, we can plug in constraint C2 into C8, and thereby obtain the following equivalent optimization problem for  $N \rightarrow \infty$

$$\begin{aligned} & \underset{P_{d,k}(i), P_0(i), \forall i, k}{\text{Maximize}} : \quad \sum_{k=1}^K v_k \frac{1}{N} \sum_{i=1}^N \log_2 \left( 1 + \frac{P_{d,k}(i)x_k(i)}{1 + \sum_{l < k} P_{d,l}(i)x_l(i)} \right) \\ & \text{Subject to :} \quad \text{C1} : \frac{1}{N} \sum_{i=1}^N P_0(i) \leq \bar{P}_0, \\ & \quad \text{C2} : P_0(i) \leq P_{0,\max}, \\ & \quad \text{C3} : P_0(i) \geq 0, \\ & \quad \text{C4} : P_{d,k}(i) \geq 0, \quad \forall k, \\ & \quad \text{C5} : \frac{1}{N} \sum_{i=1}^N P_{d,k}(i) = \frac{1}{N} \sum_{i=1}^N \eta y_k(i) P_0(i), \quad \forall k. \end{aligned} \quad (10.42)$$

The optimization problem in (10.42) is concave and can be easily solved using the Lagrangian method. The solution to this problem is given in the following Theorem.

**Theorem 10.2** *The solution to the optimization problem in (10.24), i.e., the optimal power allocation that maximizes the average data of the considered WPCN with NOMA is the following*

$$P_0(i) = \begin{cases} P_{0,\max}, & \sum_{k=1}^K \lambda_k y_k(i) \geq \lambda_0 \\ 0, & \text{otherwise,} \end{cases} \quad (10.43)$$

and

$$\begin{aligned} P_{d,k_1}(i) &= \frac{v_{k_1} - v_{k_2}}{\lambda_{k_1} - \lambda_{k_2} x_{k_1}(i)/x_{k_2}(i)} - \frac{1}{x_{k_1}(i)} \\ &\vdots \end{aligned}$$

$$\begin{aligned}
P_{d,k_m}(i) &= \frac{v_{k_m} - v_{k_{(m+1)}}}{\lambda_{k_m} - \lambda_{k_{(m+1)}} x_{k_m}(i)/x_{k_{(m+1)}}(i)} \\
&\quad - \frac{v_{k_{(m-1)}} - v_{k_m}}{-\lambda_{k_m} + \lambda_{k_{(m-1)}} x_{k_m}(i)/x_{k_{(m-1)}}(i)} \\
&\quad : \\
P_{d,k_l}(i) &= \frac{v_{k_l}}{\lambda_{k_l}} - \frac{v_{k_{(l-1)}} - v_{k_l}}{-\lambda_{k_l} + \lambda_{k_{(l-1)}} x_{k_l}(i)/x_{k_{(l-1)}}(i)} \\
P_{d,s}(i) &= 0, \quad \forall s \notin \{k_1, \dots, k_m, \dots, k_l\},
\end{aligned} \tag{10.44}$$

where  $\lambda_0$  is a Lagrange multiplier correspond to constraint C1 in (10.42) and  $\lambda_k$ , for  $k = 1, \dots, K$ , is the Lagrange multiplier correspond to constraint C5 in (10.42). The numbers  $k_1, k_2, \dots, k_K$  in (10.44) are obtained as follows. Let  $\mathbf{x}(i) = [x_1(i), x_2(i), \dots, x_N(i)]$  denote the fading vector for time slot  $i$ . The space of all possible vectors  $\mathbf{x}(i)$  is divided into  $2^K$  disjoint regions, such that the  $j$ th region is associated with the binary expansion  $\{j_1, j_2, \dots, j_k, \dots, j_K\}$ , where  $j_k = 1$  implies an active EH transmitter  $k$  and  $j_k = 0$  implies a silent EH transmitter  $k$ . If the indices  $j_1 < j_2 < \dots < j_m < \dots < j_l$  denote the positions of 1s in this binary expansion, then  $K - l$  EH transmitters are silent and  $l$  EH transmitters transmit with optimal powers given by (10.44) (see [15] for more details on how the numbers  $j_1, j_2, \dots, j_K$  are obtained.)

The transmit powers  $P_{out,k}(i), \forall k$ , are obtained by inserting the appropriate  $P_{d,k}(i)$  in (10.44) into (10.31).

A point of the maximum achievable rate region is obtained by inserting the appropriate  $P_{d,k}(i)$  in (10.44) into

$$\bar{R}_k = \lim_{N \rightarrow \infty} \frac{1}{N} \sum_{i=1}^N \log_2 \left( 1 + \frac{P_{d,k}(i)x_k(i)}{1 + \sum_{l < k} P_{d,l}(i)x_l(i)} \right) \tag{10.45}$$

for  $k = 1, \dots, K$ .

*Proof* The solutions for  $P_{d,k}(i), \forall k$ , and  $P_0(i)$  can be relatively easily obtained using the Lagrangian method [2]. The exact derivation using this method is shown in [6, 15].  $\square$

*Remark 10.4* When there are only two EH transmitters, the power allocation solution in Theorem 10.2 is simplified significantly as [15]

$$P_0(i) = \begin{cases} P_{0,\max}, & \sum_{k=1}^2 \lambda_k y_k(i) \geq \lambda_0 \\ 0, & \text{otherwise,} \end{cases} \tag{10.46}$$

and

$$P_{d,1}(i) = \begin{cases} 0 & \text{if } x_1/N_0 < \lambda_1/v_1 \\ v_1/\lambda_1 - N_0/x_1(i) & \text{if } x_1(i)/N_0 < \lambda_1/v_1 \text{ and } P_{d,2}(i) = 0 \\ (v_1 - \mu_2)/(\lambda_1 - \lambda_2 x_1(i)/x_2(i)) & \text{if } x_1/N_0 > \lambda_1/v_1 \text{ and } P_{d,2}(i) \neq 0 \end{cases} \quad (10.47)$$

and

$$P_{d,2}(i) = \begin{cases} 0 & \text{if } x_2(i)/(N_0 + x_1(i)P_{d,1}(i)) < \lambda_2/v_2 \\ v_2/\lambda_2 - (N_0 + x_1(i)P_{d,1}(i))/x_2(i) & \text{if } x_2(i)/(N_0 + x_1(i)P_{d,1}(i)) < \lambda_2/v_2. \end{cases} \quad (10.48)$$

*Remark 10.5* An interesting consequence arising from Theorem 10.2 is that the average data rate region of the considered WPCN with NOMA converges to the capacity of a non-EH multiple access network comprised of  $K$  transmitters, where the  $k$ th non-EH transmitter has an average power constraint  $\eta E\{y_k(i)P_0(i)\}$  with  $P_0(i)$  given in (10.43). For the considered WPCN, having in mind that the  $k$ th EH transmitter cannot harvest more average power than  $\eta E\{y_k(i)P_0(i)\}$ , we can conclude that the rate region achieved with the power allocation outlined in Theorem 10.2 is also the capacity of the considered WPCN with NOMA.

## 10.4 Numerical Examples

In the following, we provide numerical examples in which we show the average rate of the point-to-point system with WPT and the WPCN with NOMA for two EH transmitters. To this end, we first outline the system parameters.

We assume Rayleigh fading, where the average power of the fading gains of link  $k$  is found using the standard path loss model as

$$\Omega_k = \left( \frac{c}{f_k 4\pi} \right)^2 d_k^{-\alpha}. \quad (10.49)$$

In (10.49)  $c$  is the speed of light,  $f_k$  is the carrier frequency,  $d_k$  is the distance between the power-beacon and the  $k$ th EH transmitter, and  $\alpha$  is the path loss exponent. For the numerical examples in this section, we assume  $\alpha = 3$  and  $d_k = 10$  meters,  $\forall k$ , and the energy conversion efficiency is set to  $\eta = 0.5$ . Moreover, we assume that the carrier frequency used by the power-beacon to broadcast energy is  $f_c = 2.3999$  GHz, whereas, the carrier frequency used by the EH transmitters to transmit information to the power-beacon is  $f_c = 2.4001$  GHz. The maximum transmit power of the power-beacon is set as  $P_{0,\max} = 5\bar{P}_0$ . The transmit bandwidth is assumed to be  $B = 100$  kHz. Thereby, assuming ideal Nyquist sampling, we have  $2B$  independent symbols per second. Moreover, we assume that the noise power per Hz is  $-160$  dBm, which

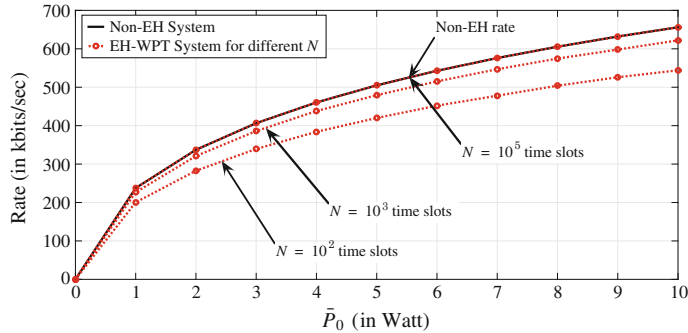


**Fig. 10.3** Average data rate of the point-to-point system with WPT for different time slots  $N$  as a function of  $\bar{P}_0$

leads to a total noise power of  $10^{-19} B$  Watt. Finally, since the derived rates throughout this chapter are in bits/symbol, to plot the rates in bits/sec, we need to multiply the corresponding rate expressions by  $2B$ .

In Fig. 10.3, we show the average data rate,  $\bar{R}$ , of the point-to-point system with WPT for different numbers of time slots  $N$  as a function of the average transmit power at the power-beacon  $\bar{P}_0$ . The figure shows that even for finite  $N$ , the loss in data rate is small compared to the case when  $N = 10^5$ . Moreover, the average data rate achieved by the WPT system for  $N = 10^5$  is almost identical to the AWGN channel capacity with an average power constraint at the non-EH transmitter given by  $\eta E\{y(i)P_0(i)\}$ , where  $P_0(i)$  is given in (10.25).

In Fig. 10.4, we plot the average rate region of the WPCN with NOMA for two EH transmitters ( $K = 2$ ),  $\bar{P}_0 = 5$  Watt, and different numbers of transmission slots,  $N$ . We note that for  $N = 10^5$  the boundary surface of the WPCN with NOMA is identical to the boundary surface of the non-EH network with NOMA for two transmitters, where the  $k$ th non-EH transmitter has an average power constraint  $\eta E\{y_k(i)P_0(i)\}$

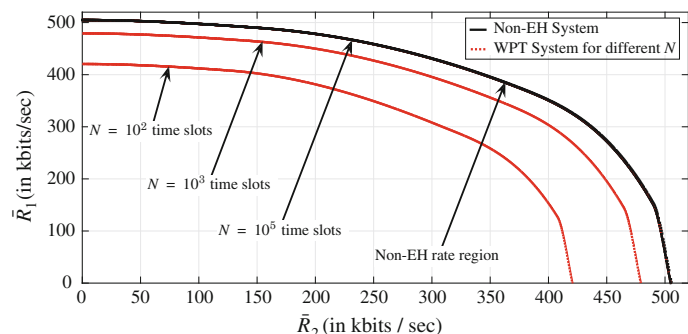


**Fig. 10.4** Average data rate region of the WPCN with NOMA for two EH transmitters,  $\bar{P}_0 = 10$  Watt, and different time slots  $N$

with  $P_0(i)$  given in (10.43). On the other hand, Fig. 10.4 also shows that even for finite  $N$ , the loss in data rate is small compared to the case when  $N = 10^5$ .

## 10.5 Conclusion

We have presented a theoretical framework which provides analytical solutions for the power allocations of a WPCN with NOMA. The power allocation solutions obtained by the theoretical framework are identical to the already available power allocation solutions for a non-EH network with NOMA, where the transmitters have specific average power constraints related to the average harvested power at the corresponding EH transmitters of the WPCN. Moreover, we have shown that the maximum achievable average rate region of the WPCN with NOMA is identical to the capacity rate region of the corresponding non-EH network with NOMA under identical average power constraints at the transmitters.

## References

1. Akyildiz, I., Su, W., Sankarasubramaniam, Y., Cayirci, E.: Wireless sensor networks: a survey. *Comput. Netw.* **38**(4), 393–422 (2002)
2. Boyd, S., Vandenberghe, L.: Convex Optimization. Cambridge University Press (2004)
3. Corporation, P.: RF Energy Harvesting and Wireless Power for Low-Power Applications (2014). <http://www.mouser.com/pdfdocs/Powercast-Overview-2011-01-25.pdf>
4. Cover, T.M., Thomas, J.A.: Elements of Information Theory. John Wiley & Sons (2012)
5. Goldsmith, A., Varaiya, P.: Capacity of fading channels with channel side information. *IEEE Trans. Inf. Theory* **43**, 1986–1992 (1997)
6. Hadzi-Velkov, Z., Zlatanov, N., Schober, R.: Multiple-access fading channel with wireless power transfer and energy harvesting. *IEEE Commun. Lett.* **18**(10), 1863–1866 (2014)
7. Jeon, J., Ephremides, A.: On the stability of random multiple access with stochastic energy harvesting. *IEEE J. Sel. Areas Commun.* **33**(3), 571–584 (2015)
8. Ju, H., Zhang, R.: Optimal resource allocation in full-duplex wireless-powered communication network. *IEEE Trans. Commun.* **62**(10), 3528–3540 (2014)
9. Ju, H., Zhang, R.: Throughput maximization in wireless powered communication networks. *IEEE Trans. Wirel. Commun.* **13**(1), 418–428 (2014)
10. Kang, X., Ho, C.K., Sun, S.: Optimal time allocation for dynamic-TDMA-based wireless powered communication networks. In: Global Communications Conference (GLOBECOM), 2014 IEEE, pp. 3157–3161 (2014)
11. Khuzani, M.B., Mitran, P.: On online energy harvesting in multiple access communication systems. *IEEE Trans. Inf. Theory* **60**(3), 1883–1898 (2014)
12. Ozel, O., Ulukus, S.: Achieving AWGN capacity under stochastic energy harvesting. *IEEE Trans. Inf. Theory* **58**(10), 6471–6483 (2012)
13. Rajesh, R., Sharma, V., Viswanath, P.: Capacity of gaussian channels with energy harvesting and processing cost. *IEEE Trans. Inf. Theory* **60**(5), 2563–2575 (2014)
14. Tse, D.N.C., Hanly, S.V.: Multiaccess fading channels. I. polymatroid structure, optimal resource allocation and throughput capacities. *IEEE Trans. Inf. Theory* **44**(7), 2796–2815 (1998)

15. Vishwanath, S., Jafar, S.A., Goldsmith, A.: Optimum power and rate allocation strategies for multiple access fading channels. *IEEE Veh. Technol. Conf.* **4**, 2888–2892 (2001)
16. Wang, Z., Aggarwal, V., Wang, X.: Iterative dynamic water-filling for fading multiple-access channels with energy harvesting. *IEEE J. Sel. Areas Commun.* **33**(3), 382–395 (2015)
17. Xie, L., Shi, Y., Hou, Y., Lou, A.: Wireless power transfer and applications to sensor networks. *IEEE Wirel. Commun.* **20**(4), 140–145 (2013)
18. Yang, J., Ulukus, S.: Optimal packet scheduling in a multiple access channel with energy harvesting transmitters. *J. Commun. Netw.* **14**(2), 140–150 (2012)
19. Zlatanov, N., Hadzi-Velkov, Z., Schober, R.: Asymptotically optimal power allocation for point-to-point energy harvesting communication systems. In: IEEE Global Communication Conference (GLOBECOM) (2013)
20. Zlatanov, N., Hadzi-Velkov, Z., Schober, R.: Asymptotically optimal power allocation for energy harvesting communication networks. Submitted to a IEEE journal (2015). <http://arxiv.org/abs/1308.2833>

# Chapter 11

## Energy-Efficient Cooperative Transmission for SWIPT in Wireless Sensor Networks

Songtao Guo, Yuanyuan Yang and Hongyan Yu

**Abstract** This work considers applying simultaneous wireless information and power transfer (SWIPT) technique to cooperative clustered wireless sensor networks, where energy-constrained relay nodes harvest the ambient radio frequency (RF) signal and use the harvested energy to forward the packets from sources to destinations. To this end, we first formulate the energy-efficient cooperative transmission (eCotrans) problem for SWIPT in clustered wireless sensor networks as a non-convex constrained optimization problem. Then by exploiting fractional programming and dual decomposition, we develop a distributed iteration algorithm for power allocation, power splitting, and relay selection to solve the non-convex optimization problem. We find that power splitting ratio plays an imperative role in relay selection. Our simulation results illustrate that the proposed algorithm can converge within a few iterations and the numerical analysis provides practical insights into the effect of various system parameters, such as the number of relay nodes, the intercluster distance and the maximum transmission power allowance, on energy efficiency and average harvested power.

### 11.1 Introduction

Maximizing energy efficiency for data transmission becomes one of the most important design considerations in energy-constrained wireless sensor networks (WSNs).

---

S. Guo (✉) · H. Yu

The College of Electronic and Information Engineering, Southwest University,  
Chongqing 400715, People's Republic of China  
e-mail: stguo@swu.edu.cn

H. Yu

e-mail: yhy710502@163.com

Y. Yang

Department of Electrical and Computer Engineering, State University of New York,  
Stony Brook, NY 11794, USA  
e-mail: yuanyuan.yang@stonybrook.edu

Moreover, in a clustered WSN, the relay nodes near cluster heads (CHs) will deplete their energy rapidly due to carrying out heavy tasks of data forwarding. Such nonuniform energy consumption may easily cause the network disconnected. It has been shown in [1] that cooperative transmission is more effective to balance energy consumption among nodes and improve energy efficiency of data transmission in WSNs. Recently, there have been some research efforts on developing cooperative schemes in clustered WSNs [2–5], in which sensors within a cluster relay data packets to nearby clusters using cooperative communication. A key element of cooperative transmission schemes is the selection and coordination of cooperative nodes.

In the meanwhile, energy harvesting technology has also been recognized as a promising cost-effective technique to maximize energy efficiency in WSNs. Unlike the conventional energy harvesting technique, which scavenges energy from the natural sources such as solar, wind and thermal, wireless power transfer (WPT) is an emerging energy harvesting technique, where sensors charge their batteries from electromagnetic radiation [6]. In WPT, green energy can be harvested through either strongly coupled magnetic resonances or radio frequency (RF) signals. The former requires that each sensor as an energy receiver to mount a coil tuned to resonate at exactly the same frequency as the coil on the energy transmitter [7–10]. However, in practice, sometimes it is difficult to mount a resonant coil in a small sensor. Moreover, energy transfer based on magnetic resonances is usually activated by near field induction from more powerful nodes (e.g., base stations and vehicles). Clearly, the application of this technology has some limitations in certain applications where there are no base stations near sensor nodes or the vehicle cannot travel or migrate very close to sensors, such as in wild forests and steep mountains.

On the other hand, compared to strongly coupled magnetic resonances, radio frequency (RF) signal can convey both energy and information simultaneously. Thus, it is a promising energy source of wireless power transfer [11], since it can achieve both wireless information transmission and energy transfer, even in a hostile environment. Recently, a RF-based energy harvesting technique, called simultaneous wireless information and power transfer (SWIPT), becomes very appealing since it utilizes both information and energy carried by RF signals at the same time, and potentially offers great possibility to replenish the energy of sensor nodes. The core idea of SWIPT is that the receiver has two circuits to perform energy harvesting and information decoding separately [12].

SWIPT as an appealing energy harvesting technique has been applied to various types of wireless communication networks [13–21]. In [16], Lee et al. considered the application of SWIPT to cognitive radio networks. SWIPT for multi-antenna systems also attracts much attentions from researchers. In [20], Zhang et al. studied a three-node multiple-input multiple-output (MIMO) broadcasting system with SWIPT. Furthermore, Chen et al. extended the work in [20] by considering SWIPT in large-scale MIMO systems employing energy beamforming. In [19], Xu et al. studied a multiuser multiple-input single-output (MISO) broadcast SWIPT system. In [14], Chen et al. analyzed the tradeoff of wireless energy and information transfer for limited-feedback multi-antenna systems. In the meanwhile, the application of SWIPT in orthogonal frequency division multiple access (OFDMA) systems has gained the attention in academia. The resource allocation algorithm was designed

in [18] for energy-efficient communication in OFDMA systems with SWIPT as an optimization problem. Subsequently, Zhou et al. [21] provided the optimal design for SWIPT in downlink multiuser orthogonal frequency division multiplexing (OFDM) systems.

Energy harvesting in wireless cooperative networks is particularly important as it can enable information relaying. In [17], the problem of SWIPT in an amplify-and-forward (AF) wireless cooperative network was studied. In [15], Ding et al. considered the application of SWIPT to wireless cooperative networks with one source-destination pair and multiple energy harvesting relays. However, these existing works did not consider how to optimally allocate transmit power and provide power splitting ratio to maximize energy efficiency. Compared to existing works in the literature, the contribution of this work is that (i) we address the problem of energy-efficient data transmission between clusters in WSNs by integrating RF-based SWIPT with cooperative relay, and (ii) we provide the optimal solution of power allocation, relay selection and power splitting to maximize system energy efficiency.

In this work, therefore, we consider applying SWIPT to wirelessly charge the relay nodes with low energy in clustered WSNs. The superiority of this scheme lies in two aspects: (i) the network system can enjoy the benefit of cooperative transmission using intermediate sensors as relays in significantly saving energy; (ii) the relay nodes can be powered by the harvested energy as the energy compensation for data forwarding. This work aims at determining the optimal transmission power and relay selection, and finding the optimal power splitting ratio for energy harvesting and information decoding so that the system energy efficiency is maximized.

To this end, we first formulate the energy-efficient cooperative transmission (eCotrans) problem for SWIPT in clustered WSNs as a non-convex optimization problem constrained by the minimum harvested energy, the minimum system data rate, and the maximum transmission power. The non-convex optimization problem is solved by an iteration algorithm, which combines nonlinear fractional programming and dual decomposition via appropriate objective function and optimization variable transformations. It is worth noting that although we employ a similar mathematical method to that in [18, 22] for formulating and solving the energy efficiency maximization problem, our work is significantly different from the work in [18, 22], which aimed at finding optimal policies of power allocation, subcarrier allocation and power splitting for energy efficiency optimization in OFDMA systems, instead of solving the problem of cooperative transmission with relay selection and energy harvesting in clustered WSNs.

Furthermore, we provide a distributed algorithm for power allocation, power splitting, and relay selection. In particular, we find that power splitting ratio plays an imperative role in relay selection and it depends on the minimum harvested energy requirement. Finally, our simulation results demonstrate that the proposed algorithm can converge within a few iterations and its energy efficiency depends on the number of relay nodes and the intercluster distance. More importantly, we observe that the maximum allowed transmission power has a limited impact on average harvested energy. Compared to existing algorithms without adopting energy harvesting

or energy efficiency maximizing, our proposed algorithm can achieve higher energy efficiency and more remaining energy.

The remainder of this chapter is organized as follows. Section 11.2 introduces the system and communication models. Section 11.3 formulates the eCotrans problem and provides an iterative algorithm to solve the problem. Section 11.4 proposes a distributed algorithm for power allocation, power splitting and relay selection. Section 11.5 provides numerical results. Finally, Sect. 11.6 concludes the paper.

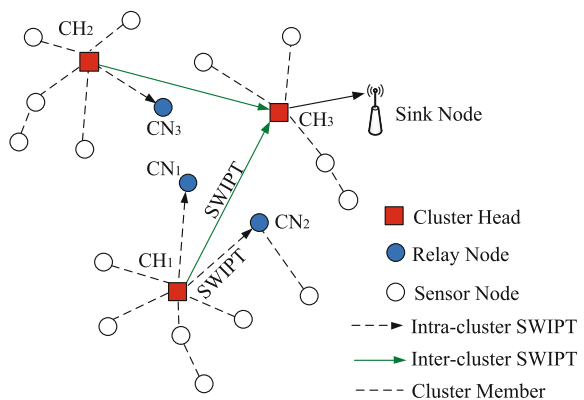
## 11.2 System and Communication Models

In this section, we first introduce the system model and communication model, and then formulate the optimization problem for energy-efficient resource allocation in a clustered WSN with SWIPT.

### 11.2.1 System Model

We consider a wireless sensor network consisting of multiple clusters of sensor nodes and a sink node as shown in Fig. 11.1, where sensor nodes are statically and randomly scattered over the sensing field. Each sensor node has a single antenna. The sink node is responsible for collecting data from all the sensor nodes. The nodes within the same cluster are distributed closely around the cluster head (CH), and can cooperate on signal transmission and/or reception. Suppose that the cluster head (CH) in a cluster (the source) wants to transmit data to the CH of its nearby cluster (the destination). Since the transmission distance is relatively long between clusters, the source can first broadcast the data to the member nodes in the cluster, select the “best” relay from a set of potential cluster member nodes, and then use this relay to aid the source-

**Fig. 11.1** A clustered wireless sensor network with SWIPT consisting of 3 clusters



to-destination communication. Clearly, the transmission is the single-relay-selection cooperative communication scheme. It is worth noting that the destination here refers to the CH of the source's nearby cluster instead of its final data sink node. In general, the CHs of two adjacent clusters can communicate directly or by one-hop relay. If the sink node is far away from the source, it may require multiple hops.

To enable SWIPT, each CH works as both an information transmitter and a power transerrer. While a source CH transmits data to its relay/destination node, in practice, the RF energy is also transferred to the node. The receiver harvests the RF energy from the source CH and uses the energy to replenish its rechargeable battery as a compensation for supporting the energy consumption of forwarding. In particular, to concurrently decode information and harvest energy from the received radio signals, the receiver node is composed of a power splitting unit, an energy harvesting unit, a conventional signal processing core unit and a rechargeable battery, as shown in Fig. 11.2. Since the signal used for decoding the information in the receiver cannot be used for harvesting energy due to hardware circuit limitations [12], we employ a separated information decoding unit and energy harvesting unit.

In this paper, we adopt a practical dynamic power splitting (DPS) scheme, which is implemented by power splitting unit at the receiver, to enable the receiver to harvest energy and decode information from the same received signal at any time. The core idea of the DPS scheme is that a receiver  $i$  dynamically splits the received signal into two power streams in the radio frequency (RF) front end with power splitting ratio  $\rho_i^I$  and  $\rho_i^E$  as shown in Fig. 11.2, which are used for decoding information and harvesting energy, respectively, where  $0 \leq \rho_i^I \leq 1$  and  $0 \leq \rho_i^E \leq 1$ . In order to improve energy efficiency, we adopt the cooperative communication scheme in a decode-and-forward (DF) and time division relaying manner. As shown in Fig. 11.1, the energy harvesting cooperative transmission is carried out in two phase as follows.

*Phase 1:* The intracluster broadcasting transmission. When a CH has data to transmit, it first broadcasts a request-to-send (RTS) message to the cluster member nodes (CNs) within the same cluster to contend for the shared wireless channel. Once receiving the RTS message, the member nodes reply a clear-to-send (CTS) message to show being ready to communicate. These ready CNs also belonging to the receiving cluster form the set of candidate relays. To elaborate, when a source node has data to transmit, it first sends out a request-to-send (RTS) message to contend for the shared wireless channel as in IEEE 802.11 protocol. The destination node

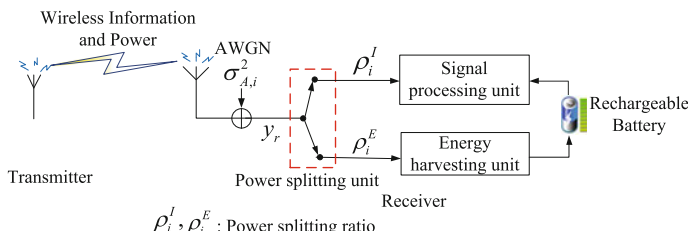


**Fig. 11.2** A block diagram of the receiver model with SWIPT

and the source's cluster member nodes hear this message. Once receiving the RTS message, the destination node and the source's cluster member nodes reply a clear-to-send (CTS) message. Based on the information in CTS, the source node and the destination's cluster nodes estimate the channel gains from them to the destination. After a successful RTS/CTS exchange, all cluster nodes of both the source and the destination become aware of this transmission event and refrain themselves from transmitting data to avoid collisions. After the RTS/CTS exchange, all candidate relay nodes will calculate their priority according to some predefined policies, which will be described in Sect. 11.4.4, based on the available channel state information fed back by RTS/CTS messages. Then they compete with each other within a fixed time window of length  $T_{max}$ , which is called the “relay contention period.” The cluster member node with the higher priority will transmit and “win” the competition to serve as the relay for cooperative data transmission.

*Phase 2:* The intercluster cooperative transmission. After the relay is determined, the source sends out data to the relay/destination. The relay/destination decodes the received data and meanwhile harvests the energy from the received RF signals based on DPS scheme. To elaborate, The relay/destination first tries to direct the received data flow to the signal processing unit to decode and detect whether the minimum targeted data rate is satisfied, following the DPS approach. If the detection is successful and there is some energy left, the remaining signal flows will be directed to the energy harvesting unit, and the harvested energy will be used to support relay transmission. Then the source and relays will simultaneously transmit the packets to the destination (i.e., the CH of the receiving cluster).

The single-relay selection cooperative scheme is fully distributed and easy to implement. The underlying reasons are that it is much simpler than the multi-relay cooperation [5]. The former only selects one “best” relay to forward data, while the latter requires the distributed space-time coding or beamforming. In particular, the selected relay can use the energy harvested to support relay transmission so as to avoid its energy being drained.

### 11.2.2 Communication Model

We consider two types of transmission modes for wireless communications: direct transmission mode (DT) and cooperative relay transmission mode (RT). Depending on whether the relay is helpful, each source may work in either the DT mode or the RT mode. Let  $P_s$  and  $P_r$  be the transmission power of source  $s$  in Phase 1 and relay  $r$  in Phase 2, respectively;  $\mathcal{N}_s$  and  $\mathcal{N}_d$  be the set of cluster member nodes (CNs) of source node  $s$  (the CH in the transmitting cluster) and the destination node  $d$  (the CH of the receiving cluster), respectively. Then the candidate relay set  $\mathcal{N} = \mathcal{N}_s \cap \mathcal{N}_d$ . We assume that all the links are symmetrical, i.e., the channel from node  $i$  to node  $j$  is the same as the channel from node  $j$  to node  $i$ , and the channel from the source to the relay/destination follows quasi-static block fading. The channel is unchanged over the block time  $T$  and independently and identically distributed from one block

to the next, following a Rayleigh distribution. The use of such channels is motivated by prior research [12, 17]. We take a relatively short block duration compared to the minimum coherence time of the channel and interference such that both the channel and interference can be treated as unchanged during each block transmission. Let  $h_{sd}$  and  $h_{sr}$ ,  $r \in \mathcal{N}$ , denote the channel gains between source  $s$  and destination  $d$  and between source  $s$  and its relay  $r$ , respectively,  $h_{rd}$ ,  $r \in \mathcal{N}$ , denote the channel gain from relay  $r$  to destination  $d$ , and  $\sigma_{sd}^2$ ,  $\sigma_{sr}^2$  and  $\sigma_{rd}^2$  denote the variances of the additive white Gaussian noise (AWGN) in the corresponding channels.

It is shown in [23, 24] that it is difficult to obtain perfect channel state information (CSI) due to noisy channel estimation and the unavoidable delay between the time channel estimation is performed and the time the estimation result is used for actual transmission. Therefore, we will consider imperfect CSI in this paper, i.e., the receiver knows the value of CSI, and both the transmitter and the receiver know the distribution of CSI, since transmitting CSI information would lead to extra overhead and considerable additional complexity.

To perform relay selection and power allocation, the source can obtain the channel gains by the feedback of the CTS message in *Phase 1* via the dedicated control channel. To elaborate, in practical implementation, during the training period, i.e., RTS/CTS exchange in *Phase 1*, before data transmission in the first time slot, the source transmits training signals by RTS message so that the relay and the destination measure the SR and SD channels and get the corresponding channel gains, respectively. The relay then transmits training signals in the second time slot to the destination so that the destination measures the RD channel and obtain its channel gain. The measured channel gains can be fed back to the source by CTS message on dedicated reverse control channels. Since all the links are assumed to be symmetrical, the source can obtain the SR and SD channel gains.

The normalized effective channel gains can be represented by  $a_{sd} = |h_{sd}|^2/\sigma_{sd}^2$ ,  $a_{sr} = |h_{sr}|^2/\sigma_{sr}^2$ , and  $a_{rd} = |h_{rd}|^2/\sigma_{rd}^2$ , where  $h_{ij} = \zeta_{ij} L_{ij}^{-\alpha}$ ,  $L_{ij}$  is the distance between transmitter  $i$  and receiver  $j$ ,  $\alpha$  is a constant path loss exponent, and  $\zeta_{ij}$  is a normalization constant depending on the radio propagation properties of the environment. As aforementioned, source  $s$  via direct link would actively transmit data in both time slots while source  $s$  via relay link would only transmit data in the first time slot. Thus, the end-to-end data rate from source  $s$  to destination  $d$  during the two phases is given by

$$R_{sd} = \begin{cases} B \log(1 + \rho_d^l a_{sd} P_s), & \text{DT mode} \\ \frac{B}{2} \min(\log(1 + \rho_d^l a_{sd} P_s + \rho_d^l a_{rd} P_r), \log(1 + \rho_r^l a_{sr} P_s)), & \text{RT mode,} \end{cases} \quad (11.1)$$

where  $B$  denotes the base-band width and the rate is scaled by  $\frac{1}{2}$  since the entire transmission takes two phases. A criterion to decide the working mode of the source in selective DF mode was given in [25], that is, using relay is advantageous when  $\min(\rho_r^l a_{sr}, \rho_d^l a_{rd}) > \rho_d^l a_{sd}$ . Otherwise, the relay keeps inactive in the relay phase.

In particular, the effect of best relay selection on the rate for the RT mode is reflected by the following two aspects. (1) Best relay selection as a single-relay cooperative scheme can avoid the complex mathematical expression for data rate

since compared to multi-relay cooperative schemes, single-relay cooperation requires neither cooperative beamforming nor distributed space-time coding [4]. (2) Best relay selection can ensure that the candidate relay that can provide the maximum data rate is always selected as the actual relay of source  $s$  as shown in relay selection subalgorithm in Sect. 11.4.4. Moreover, the increase of the number of relays will increase the cooperation overhead and degrade the energy efficiency of cooperative communication, i.e., more cooperators may lead to less energy efficiency [26]. This also motivates us to adopt the best relay selection.

We first consider the data rate  $R_{sd}$  in the RT mode. Let  $P_{sd}$  indicate the total transmission power between source  $s$  and destination  $d$  in the two phases. As mentioned in Sect. 11.2.1, the harvested energy from the source is used by the relay as the energy compensation of data forwarding. This means that the harvested energy may not be enough for data forwarding to ensure the minimum data rate requirement, as shown in constraint C5. In this case, the relay has to consume part of its own energy for data forwarding. Therefore, the total consumed power should be the sum of the transmission powers of the source and the relay, i.e.,  $P_{s,d} = P_s + P_r$ . If the harvested energy from the source is sufficient for data forwarding, then  $P_{s,d} = P_s$ . Clearly, the transmission power of relay  $r$ ,  $P_r$ , includes two parts: one is the harvested power, denoted by  $P_{r,\text{harp}}$ , from the source, which is given by  $P_{r,\text{harp}} = \eta \rho_k^E P_s |h_{sk}|^2$  [18], where  $0 < \eta < 1$  is the energy conversion efficiency. The other is the power from the relay itself, denoted by  $P_{r,\text{own}}$ . Therefore, we have  $P_r = P_{r,\text{harp}} + P_{r,\text{own}}$ .

We can observe from (11.1) that the achievable rate is maximized when the amount of decoded information at the relay node is the same as the destination, i.e.,

$$1 + \rho_d^I a_{sd} P_s + \rho_d^I a_{rd} P_r = 1 + \rho_r^I a_{sr} P_s. \quad (11.2)$$

Together with  $P_{sd} = P_s + P_r$  and  $P_r = P_{r,\text{harp}} + P_{r,\text{own}}$ , we obtain

$$\begin{cases} P_s = \frac{\rho_d^I a_{rd}}{\rho_r^I a_{sr} + \rho_d^I a_{rd} - \rho_d^I a_{sd}} P_{sd}, \\ P_{r,\text{own}} = \frac{\rho_r^I a_{sr} - \rho_d^I a_{sd} - \rho_d^I a_{rd} \eta \rho_k^E |h_{sk}|^2}{\rho_d^I a_{rd} + \rho_r^I a_{sr} - \rho_d^I a_{sd}} P_{sd}. \end{cases} \quad (11.3)$$

In the DT mode, we can easily obtain  $P_s = P_{sd}$  and  $P_r = 0$ . Let  $\lambda_{sd}$  be the equivalent channel gain given by

$$\lambda_{sd} = \begin{cases} \frac{\rho_r^I a_{sr} \rho_d^I a_{rd}}{\rho_r^I a_{sr} + \rho_d^I a_{rd} - \rho_d^I a_{sd}}, & \text{RT mode,} \\ \rho_d^I a_{sd}, & \text{DT mode.} \end{cases} \quad (11.4)$$

Accordingly, by introducing a binary indicator  $\vartheta_s$ , which is 1 if source  $s$  transmits data in the DT mode, and 0 in the RT mode, we can unify the data rate as

$$R_{sd} = \frac{B}{2} (1 + \vartheta_s) \log (1 + \lambda_{sd} P_{sd}). \quad (11.5)$$

We can observe from (11.5) that as the equivalent channel gain in (11.4) is directly proportional to power splitting ratio  $\rho^I$ , increasing  $\rho^I$  can improve the unified data rate.

## 11.3 Problem Formulation

In this section, we formulate the SWIPT-based resource allocation optimization problem for cooperative transmission, aiming to maximize system energy efficiency.

### 11.3.1 Network Energy Efficiency

Let  $\mathcal{K}$  denote the set of CHs in the network and  $|\mathcal{K}| = K$ , and  $\mathcal{N}$  denote the candidate relay set for source  $s$  and  $|\mathcal{N}| = N$ . We assume  $t_{s,r}$  is a binary indicator, which is 1 if relay node  $r$  is selected for forwarding data from source  $s$ , and 0 otherwise. Next, we give the definition of the weighted system throughput.

**Definition 11.1** (*Weighted System Throughput*) The weighted system throughput is defined as the weighted sum of the data rates that all the sources deliver to the destinations in the network and is given by

$$U(\mathcal{P}, \rho, \mathcal{T}) = \sum_{s,d=1}^K \sum_{r=1}^N \alpha_r t_{s,r} R_{sd} [\text{bit/s}] \quad (11.6)$$

where  $\mathcal{P} = \{P_{sd} \geq 0, \forall s, d \in \mathcal{K}\}$  is the power allocation policy,  $\rho = \{\rho_i^I, \rho_i^E \geq 0, \forall i \in \mathcal{K} \cup \mathcal{N}\}$  is the power splitting policy and  $\mathcal{T} = \{t_{s,r} \in \{0, 1\}, \forall s \in \mathcal{K}, r \in \mathcal{N}\}$ .

Let  $\alpha_r$  denote a nonnegative weight that accounts for the priorities of different receivers to enforce certain fairness and is specified by the application layer. In practice, proportional fairness and max-min fairness can be achieved by varying the values of  $\alpha_r$  over time [27].

On the other hand, by considering the constant circuit power consumption and the inefficiency of power amplifier, we model the weighted power consumption as

$$U_{TP}(\mathcal{P}, \rho, \mathcal{T}) = K P_{CH} + K N P_{CR} + \sum_{s,d=1}^K \sum_{r=1}^N \varepsilon t_{s,r} P_{sd} \quad (11.7)$$

where  $P_{CH} > 0$  and  $P_{CR} > 0$  denote the constant circuit power consumption in the CH and relay node, respectively. Thus the first two terms indicate the total circuit power consumption in the  $K$  CHs and all relay nodes. The last term is the total power

dissipation in the power amplifiers of all sources and the corresponding relays.  $\varepsilon \geq 1$  is a constant that accounts for the inefficiency of power amplifier in the source and relay nodes.

Next, we give the definition of weighted energy efficiency similar to [18].

**Definition 11.2** (*Weighted Energy Efficiency*) The weighted energy efficiency of the considered system is defined as the total average number of bits successfully conveyed by the sources and relays to the destinations per Joule consumed energy and is given by

$$U_{eff}(\mathcal{P}, \rho, \mathcal{T}) = \frac{U(\mathcal{P}, \rho, \mathcal{T})}{U_{TP}(\mathcal{P}, \rho, \mathcal{T})} \quad (11.8)$$

Compared to the energy efficiency in [18], the harvested energy at the receiver is not taken as the replenishment for the total system power consumption, which is because that from the whole network system point of view, the total energy of the whole system does not get replenished but is recycled and transferred from one node to another so as to achieve energy balance.

### 11.3.2 Optimization Formulation

As aforementioned in Sect. 11.2, the power splitter splits the received signal  $y_r$  in  $\rho_i^I : \rho_i^E$ , such that the portion of the received signal,  $\sqrt{\rho_i^I} y_r$ , is sent to the information decoding unit and the remaining signal strength,  $\sqrt{\rho_i^E} y_r$ , drives the energy harvesting unit. Using the signal received at the input of the energy harvesting unit, similar to [17], the harvested energy at receiver  $k$  from transmitter  $s$  during a half of the block time,  $T/2$ , is given by

$$Q_k = \eta \rho_k^E t_{s,k} P_s |h_{sk}|^2 (T/2) \quad (11.9)$$

where  $0 < \eta < 1$  is the energy conversion efficiency.

In this paper, we aim to provide the optimal power allocation policy  $\mathcal{P}^*$ , power splitting policy  $\rho^*$ , and relay selection policy  $\mathcal{T}^*$  such that the weighted energy efficiency is maximized. To this end, the energy-efficient cooperative transmission (eCotrans) problem for SWIPT in clustered WSNs can be formulated as

$$\textbf{OPT - 1} \quad \max_{\mathcal{P}, \rho, \mathcal{T}} U_{eff}(\mathcal{P}, \rho, \mathcal{T}) \quad (11.10)$$

Subject to

$$C1: Q_k + Q_{C,k} \geq E_k^{\min}, \forall k \in \mathcal{K},$$

$$\begin{aligned}
C2 : \sum_{r=1}^N t_{s,r} P_{sd} &\leq P_{sd}^{\max}, \forall s, d \in \mathcal{K} \\
C3 : P_{CH} + \varepsilon t_{s,r} P_{sd} &\leq E^{\max} \\
C4 : \sum_{s=1}^K \sum_{r=1}^N t_{s,r} R_{sd} &\geq R^{\min}, \forall d \in \mathcal{K}, \\
C5 : \sum_{r=1}^N t_{s,r} R_{sd} &\geq R_d^{\min}, \forall s, d \in \mathcal{K}', \\
C6 : t_{s,r} &\in \{0, 1\}, \forall s \in \mathcal{K}, r \in \mathcal{N}, \\
C7 : \sum_{r=1}^{N_r} t_{s,r} &\leq 1, \forall s \in \mathcal{K}, \quad C8 : \rho_{\min}^E \leq \rho_i^E \leq \rho_{\max}^E \\
C9 : \rho_{\min}^I &\leq \rho_i^I \leq \rho_{\max}^I, \quad C10 : \rho_i^E + \rho_i^I \leq 1, \forall i
\end{aligned}$$

where C1 is energy harvesting constraint, which specifies that the sum of the harvested energy  $Q_k$  and the remaining energy  $Q_{C,k}$  should be bounded by the minimum required energy transferred to receiver  $k$ ,  $E_k^{\min}$ . We assume  $E_k^{\min} \geq Q_{C,k}$  so as to guarantee the harvested energy  $Q_k \geq 0$ . Transmission power constraint C2 ensures that the power radiated by transmitter  $s$  is upper bounded by maximum transmission power  $P_{sd}^{\max}$ . Power consumption constraint C3 restricts the maximum power supplied by the source for supporting the power consumption on its circuit and power amplifier to the maximum battery capacity  $E^{\max}$ . C4 is a quality of service (QoS) constraint for the system that the aggregate network throughput should satisfy the minimum system data rate requirement,  $R_{\min}$ . Note that although  $R_{\min}$  is not an optimization variable in this paper, we can strike a balance between energy efficiency and aggregate system throughput by varying its value. C5 is the minimum required data rate  $R_d^{\min}$  for the delay constrained services of receiver  $d$ , and is specified by the application layer, and  $\mathcal{K}'$  denotes a set of receivers having delay constrained services. C6 and C7 are relay selection constraints which require that each relay node is only allocated to at most one source exclusively. C6 and C7 implicitly impose a fairness constraint, since each relay node is only allocated to at most one source exclusively. In other words, the relay allocated to a source is not allowed to forward the data from other sources. This implies that a weaker source also has a higher chance to be selected as a relay. C8 specifies that the power splitting ratio for harvesting energy is limited by the constant lower bound,  $\rho_{\min}^E$ , and upper bound,  $\rho_{\max}^E$ . These bounds reflect the limited capability of receivers in splitting the received power.  $\rho_{\min}^I$  and  $\rho_{\max}^I$  in C9 denote the constant lower and upper bounds of the power splitting ratio for decoding information, respectively, where  $\rho_{\min}^E + \rho_{\max}^I = 1$  and  $\rho_{\max}^E + \rho_{\min}^I = 1$ . C10 reflects that the power splitting unit as shown in Fig. 11.2 is a passive device and no extra power gain can be achieved during the power splitting process.

The key challenge in solving the optimization problem **OPT-1** in (11.10) is its lack of convexity due to the fractional form of the objective function and the couplings of optimization variables  $\{\mathcal{P}, \rho, \mathcal{T}\}$  in constraints C1–C5 and the objective function.

### 11.3.3 Transformation of Objection Function

We now transform the objective function in **OPT-1** problem in the fractional form into an equivalent one in the subtractive form via nonlinear fractional programming [28]. Without loss of generality, we define the maximum weighted energy efficiency  $q^*$  as

$$q^* = \frac{U(\mathcal{P}^*, \rho^*, \mathcal{T}^*)}{U_{TP}(\mathcal{P}^*, \rho^*, \mathcal{T}^*)} = \max_{\mathcal{P}, \rho, \mathcal{T}} \frac{U(\mathcal{P}, \rho, \mathcal{T})}{U_{TP}(\mathcal{P}, \rho, \mathcal{T})} \quad (11.11)$$

We introduce the following important theorem for solving the **OPT-1** problem in (11.10).

**Theorem 11.1** *The optimal resource allocation policies  $(\mathcal{P}^*, \rho^*, \mathcal{T}^*)$  achieves the maximum energy efficiency  $q^*$  if and only if*

$$\begin{aligned} & \max_{\mathcal{P}, \rho, \mathcal{T}} [U(\mathcal{P}, \rho, \mathcal{T}) - q^* U_{TP}(\mathcal{P}, \rho, \mathcal{T})] \\ &= U(\mathcal{P}^*, \rho^*, \mathcal{T}^*) - q^* U_{TP}(\mathcal{P}^*, \rho^*, \mathcal{T}^*) = 0 \end{aligned} \quad (11.12)$$

for  $U(\mathcal{P}, \rho, \mathcal{T}) > 0$  and  $U_{TP}(\mathcal{P}, \rho, \mathcal{T}) > 0$

*Proof* It follows from (11.6) and (11.7) that  $U(\mathcal{P}, \rho, \mathcal{T}) > 0$  and  $U_{TP}(\mathcal{P}, \rho, \mathcal{T}) > 0$  are satisfied and  $U_{eff}(\mathcal{P}, \rho, \mathcal{T})$  is well defined. The remaining proof can be completed by following a similar approach to that in [22, Appendix A].

Theorem 11.1 reveals that for any optimization problem with an objective function in fractional form, there exists an equivalent objective function in subtractive form, e.g.,  $U(\mathcal{P}, \rho, \mathcal{T}) - q^* U_{TP}(\mathcal{P}, \rho, \mathcal{T})$  in the considered case, such that both problem formulations lead to the same optimal resource allocation policy.

### 11.3.4 Iterative Algorithm for Energy Efficiency Maximization

We now propose an iterative algorithm based on the Dinkelbach method [28] for solving the optimization problem **OPT-1** in (11.10) with the equivalent objective function  $U(\mathcal{P}, \rho, \mathcal{T}) - q^* U_{TP}(\mathcal{P}, \rho, \mathcal{T})$ . The proposed algorithm is described in Algorithm 3.

**Algorithm 3:** Iterative algorithm for **OPT-1** problem**Require:**

$Iter_{\max}$ : maximum number of iterations;  
 $\varepsilon$ : an infinitesimal number;  
 $q$ : energy efficiency;  
 $j$ : iterative index;

**Ensure:**

$\{\mathcal{P}^*, \rho^*, \mathcal{T}^*\}$ : optimal resource allocation policy;  
 $q^*$ : maximum energy efficiency;

- 1:  $j \leftarrow 1, q \leftarrow 0$ ;
- 2: **while**  $j \leq Iter_{\max}$  **do** {Main Loop}
- 3: Solve the optimization problem in (11.13) for a given  $q$  and obtain resource allocation policies  $\{\mathcal{P}, \rho, \mathcal{T}\}$
- 4: **if**  $U(\mathcal{P}, \rho, \mathcal{T}) - qU_{TP}(\mathcal{P}, \rho, \mathcal{T}) < \varepsilon$  **then**
- 5:   **return**  $\{\mathcal{P}^*, \rho^*, \mathcal{T}^*\} = \{\mathcal{P}, \rho, \mathcal{T}\}$  and  $q^* = \frac{U(\mathcal{P}, \rho, \mathcal{T})}{U_{TP}(\mathcal{P}, \rho, \mathcal{T})}$
- 6:   **else**
- 7:     Set  $q = \frac{U(\mathcal{P}, \rho, \mathcal{T})}{U_{TP}(\mathcal{P}, \rho, \mathcal{T})}$  and  $j = j + 1$
- 8:   **end if**
- 9: **end while**

Algorithm 3 can be described briefly as follows. In each iteration of the main loop, we solve the transformed **OPT-2** problem in (11.13) for a given parameter  $q$  via dual decomposition and obtain an alternative optimal policy  $(\mathcal{P}, \rho, \mathcal{T})$  of power allocation, power splitting and relay selection. Then we update parameter  $q$  and use it to solve the main loop problem in the next iteration until the condition  $U(\mathcal{P}, \rho, \mathcal{T}) - qU_{TP}(\mathcal{P}, \rho, \mathcal{T}) < \varepsilon$  is satisfied, which implies that the iterative algorithm converges and the obtained allocation policy achieves optimum, i.e.,  $(\mathcal{P}, \rho, \mathcal{T}) \rightarrow (\mathcal{P}^*, \rho^*, \mathcal{T}^*)$ .

The transformed problem (**OPT-2**) for given energy efficiency  $q$  can be given by

$$\text{OPT - 2} \quad \max_{\mathcal{P}, \rho, \mathcal{T}} U(\mathcal{P}, \rho, \mathcal{T}) - qU_{TP}(\mathcal{P}, \rho, \mathcal{T}) \quad (11.13)$$

Subject to constraints C1-C10.

Next, we verify the convergence of the iterative algorithm in Algorithm 3.

**Theorem 11.2** *The proposed algorithm of energy efficiency maximization in Algorithm 3 converges to the optimal energy efficiency if the optimization problem (11.13) can be solved in each iteration.*

*Proof* We employ a similar approach to that in [22, 28] to prove the convergence of Algorithm 3. We first introduce two propositions to demonstrate the properties of the equivalent objective function in (11.13). For the sake of notational simplicity, we define  $\mathcal{F}$  as the set of feasible points of the optimization problem in (11.10) and let  $F(q) = \max_{\mathcal{P}, \rho, \mathcal{T}} U(\mathcal{P}, \rho, \mathcal{T}) - qU_{TP}(\mathcal{P}, \rho, \mathcal{T})$ .

**Proposition 11.1** [22]  $F(q)$  is a strictly monotonically decreasing function with respect to (w.r.t)  $q$ , i.e.,  $F(q') > F(q)$  if  $q' > q$ .

**Proposition 11.2** [22] Let  $\{\mathcal{P}', \rho', \mathcal{T}'\} \in \mathcal{F}$  be an arbitrary feasible solution and  $q' = \frac{U(\mathcal{P}', \rho', \mathcal{T}')}{U_{TP}(\mathcal{P}', \rho', \mathcal{T}')}$ . Then  $F(q') > 0$ .

Next, we prove the convergence of Algorithm 3. This proof includes two parts: the first part is to prove that energy efficiency  $q$  increases with the number of iterations; the second part is to prove that if the number of iterations is large enough, then energy efficiency  $q$  converges to the optimal  $q^*$  such that it satisfies the optimality condition in Theorem 11.1, i.e.,  $F(q^*) = 0$ .

Let  $\{\mathcal{P}_n, \rho_n, \mathcal{T}_n\}$  be the optimal resource allocation policies in the  $n$ -th iteration. We assume  $q_n \neq q^*$  and  $q_{n+1} \neq q^*$  represent the energy efficiency of the system in iterations  $n$  and  $n + 1$ , respectively. By Proposition 11.2, we have  $F(q_n) > 0$  and  $F(q_{n+1}) > 0$ . On the other hand, in the proposed Algorithm 3, we calculate  $q_{n+1}$  as  $q_{n+1} = \frac{U(\mathcal{P}_n, \rho_n, \mathcal{T}_n)}{U_{TP}(\mathcal{P}_n, \rho_n, \mathcal{T}_n)}$ . Thus we can compute  $F(q_n)$  by

$$\begin{aligned} F(q_n) &= U(\mathcal{P}_n, \rho_n, \mathcal{T}_n) - q_n U_{TP}(\mathcal{P}_n, \rho_n, \mathcal{T}_n) \\ &= q_{n+1} U_{TP}(\mathcal{P}_n, \rho_n, \mathcal{T}_n) - q_n U_{TP}(\mathcal{P}_n, \rho_n, \mathcal{T}_n) \\ &= U_{TP}(\mathcal{P}_n, \rho_n, \mathcal{T}_n)(q_{n+1} - q_n) \end{aligned}$$

Since  $F(q_n) > 0$  and  $U_{TP}(\mathcal{P}_n, \rho_n, \mathcal{T}_n) > 0$ , it is not difficult to obtain  $q_{n+1} > q_n$ . That completes the proof of the first part.

By  $q_{n+1} > q_n$  and Proposition 11.1, we can obtain that  $F(q_n)$  will eventually approach zero and satisfy the optimality condition in Theorem 11.1. That completes the proof of the second part.

In fact, the transformed objective function has an interesting pricing interpretation from the economy point of view.  $U(\mathcal{P}, \rho, \mathcal{T})$  indicates the system profit due to data cooperative transmission, while  $U_{TP}(\mathcal{P}, \rho, \mathcal{T})$  represents the associated cost due to energy consumption. The optimal value of  $q$  indicates a scaling factor for balancing profit and cost.

Although the transformed optimization problem (**OPT-2**) has an equivalent objective function in subtractive form which is easier to handle, there are still two obstacles in tracking the problem. First,  $\rho_i^I$  and  $\rho_i^E$  are coupled with the power allocation variables in both the objective function and constraints C1, C4 and C5, which complicates the solution. Second, the binary constraint C6 on relay selection variables creates a disjoint feasible solution set and makes constraints C1-C5 become the combinatorial constraints, which is a hurdle for solving the **OPT-2** problem.

In order to strike a balance between solution tractability and computational complexity, we handle the above issues in following two steps. In the first step, due to the integer constraint  $t_{s,r} \in \{0, 1\}$ , problem **OPT-1** is a mixed integer programming problem, which is in general non-convex and NP-hard. Thus, we first adopt the time-sharing relaxation technique that has been employed in [18, 29–32] to guarantee the convexity and tractability of the optimization problem. We relax the relay selection

variable  $t_{s,r}$  in C6 to a real number between 0 and 1, i.e.,  $0 \leq t_{s,r} \leq 1$ . Then  $t_{s,r}$  can be interpreted as a time-sharing factor for the  $K$  sources to utilize relay node  $r$ .

In the second step, we introduce a new auxiliary variable  $\tilde{P}_{sd}$ , which is defined as  $\tilde{P}_{sd} = t_{s,r} P_{sd}$  and represents the actual transmitted power from source  $s$  to its destination  $d$  through relay node  $r$ . In addition, we assume that the power splitting ratio for information decoding at relay  $r$  is the same as that at the corresponding destination  $d$ , i.e.,  $\rho_r^I = \rho_d^I$ . This is justified since if  $\rho_r^I \neq \rho_d^I$ , it can be observed from (11.4) that the update of  $\rho_r^I$  at relay node  $r$  depends on the update of  $\rho_d^I$  at its destination  $d$  in the proposed power splitting subalgorithm, and vice versa, which greatly increases the computation complexity and consumes much more energy for exchanging a large number of intermediate computation messages.

As for the suboptimality caused by the assumption, let  $\rho_d^{I*}$  and  $\rho_d^{I**}$  denote the suboptimal and optimal power splitting ratios for information decoding at destination  $d$ , respectively, and we can obtain  $\frac{\rho_d^{I*}}{\rho_d^{I**}} = \frac{\rho_r^I a_{sr}}{\rho_r^I a_{sr} + \rho_d^I (a_{rd} - a_{sd})}$  for RT mode and  $\rho_d^{I*} = \rho_d^{I**}$  for DT mode. The latter is because the channel gain  $\lambda_{sd}$  is not related to  $\rho_r^I$ . Clearly, for RT mode, when  $a_{rd} \rightarrow a_{sd}$ ,  $\rho_d^{I*}$  will approximately equal  $\rho_d^{I**}$ . In practice, this case occurs frequently since the relay usually lies in the middle between the source and the destination, and the channel gain  $a_{rd}$  between the relay and the destination is close to the channel gain  $a_{sd}$  between the source and the destination.

Based on this assumption, we follow the approach in [18] and approximate the data rate as

$$\tilde{R}_{sd} = \frac{B}{2} (1 + \vartheta_s) \log (\rho_d^I \tilde{\lambda}_{sd} \tilde{P}_{sd} / t_{s,r}) \quad (11.14)$$

which is a tight approximation for high SINR, i.e.,  $\lambda_{sd} P_{sd} \gg 1$ . Indeed, high SINR can be guaranteed since a minimum required system data rate  $R^{\min}$  is set to guarantee a desired system data rate.  $\tilde{\lambda}_{sd}$  is defined as

$$\tilde{\lambda}_{sd} = \begin{cases} \frac{a_{sr} a_{rd}}{a_{sr} + a_{rd} - a_{sd}}, & \text{RT mode,} \\ a_{sd}, & \text{DT mode.} \end{cases} \quad (11.15)$$

To remove the associated non-convexity, we can rewrite constraint C1 as

$$C1' : \eta t_{s,k} P_s |h_{sk}|^2 (T/2) + \frac{Q_{C,k}}{\rho_k^E} \geq \frac{E_k^{\min}}{\rho_k^E}, \quad (11.16)$$

Next, we explore the convexity of the transformed **OPT-2** problem with approximate data rate  $\tilde{R}_{sd}$  and auxiliary variable  $\tilde{P}_{sd}$ .

**Theorem 11.3** *The transformed **OPT-2** problem with constraints C1' – C10 is convex with respect to (w.r.t) the optimization variables  $\tilde{P}_{sd}$ ,  $\rho_d^I$ ,  $\rho_d^E$  and  $t_{s,r}$ .*

*Proof* We first prove that the transformed objective function  $U(\mathcal{P}, \rho, \mathcal{T}) - q U_{TP}(\mathcal{P}, \rho, \mathcal{T})$  is jointly concave w.r.t. the optimization variables  $\tilde{P}_{sd}$ ,  $\rho_d^I$ ,  $\rho_d^E$  and  $t_{s,r}$ . Then we show the convexity of constraints C1'–C10.

The concavity of the transformed objective function can be proved by the following steps. First, we consider the concavity of function  $U(\mathcal{P}, \rho, \mathcal{T})$  based on a relay selection w.r.t. the optimization variables  $\tilde{P}_{sd}$ ,  $\rho_d^I$  and  $\rho_d^E$ .

For notational simplicity, we define a vector  $\mathbf{x}_{sd} = [\tilde{P}_{sd}, \rho_d^I, \rho_d^E]$  and a function  $f_{sd}(\mathbf{x}_{sd}) = \frac{B}{2}(1 + \vartheta_s)\alpha_r \log_2(\rho_d^I \tilde{\lambda}_{sd} \tilde{P}_{sd})$ . Then we use  $\mathbf{H}(f_{sd}(\mathbf{x}_{sd}))$  and  $\tau_1, \tau_2$  and  $\tau_3$  to denote the Hessian matrix of function  $f_{sd}(\mathbf{x}_{sd})$  and eigenvalues of  $\mathbf{H}(f_{sd}(\mathbf{x}_{sd}))$ , respectively. The Hessian matrix of function  $f_{sd}(\mathbf{x}_{sd})$  is given by

$$\mathbf{H}(f_{sd}(\mathbf{x}_{sd})) = \begin{bmatrix} \tau_1 & 0 & 0 \\ 0 & \tau_2 & 0 \\ 0 & 0 & \tau_3 \end{bmatrix}$$

where  $\tau_1 = -\frac{B(1+\vartheta_s)\alpha_r}{2 \ln 2 (\tilde{P}_{sd})^2}$ ,  $\tau_2 = -\frac{B(1+\vartheta_s)\alpha_r}{2 \ln 2 (\rho_d^I)^2}$  and  $\tau_3 = 0$ . Since  $\tau_i \leq 0, i \in \{1, 2, 3\}$ ,  $\mathbf{H}(f_{sd}(\mathbf{x}_{sd}))$  is a negative semi-definite matrix. In other words, function  $f_{sd}(\mathbf{x}_{sd})$  is jointly concave w.r.t.  $\tilde{P}_{sd}$ ,  $\rho_d^I$  and  $\rho_d^E$ .

Then we can take the perspective transformation on  $f_{sd}(\mathbf{x}_{sd})$ , which is given by

$$u_{sd}(\mathbf{x}_{sd}) = \frac{B}{2}(1 + \vartheta_s)t_{s,r}\alpha_r \log_2\left(\rho_d^I \tilde{\lambda}_{sd} \tilde{P}_{sd} / t_{s,r}\right) = \alpha_r t_{s,r} \tilde{R}_{sd}$$

It is shown in [33] that the perspective transformation preserves the concavity of the function. Thus, function  $u_{sd}(\mathbf{x}_{sd})$  is jointly concave w.r.t.  $\tilde{P}_{sd}$ ,  $\rho_d^I$ ,  $\rho_d^E$  and  $t_{s,r}$ . Function  $U(\mathcal{P}, \rho, \mathcal{T})$  is the sum of  $u_{sd}(\mathbf{x}_{sd})$  over indices  $s, d$  and  $r$ , which preserves the concavity of the function [33].

In the following, we prove the convexity of function  $U_{TP}(\mathcal{P}, \rho, \mathcal{T})$ . Since the function  $U_{TP}(\mathcal{P}, \rho, \mathcal{T})$  is an affine function of the variable  $\tilde{P}_{sd}$ , the function is convex w.r.t the variable  $\tilde{P}_{sd}$ . Therefore, it is not difficult to obtain that the transformed objective function  $U(\mathcal{P}, \rho, \mathcal{T}) - qU_{TP}(\mathcal{P}, \rho, \mathcal{T})$  is jointly concave w.r.t. the optimization variables  $\tilde{P}_{sd}$ ,  $\rho_d^I$ ,  $\rho_d^E$  and  $t_{s,r}$ .

Now, we verify the convexity of constraints C1'–C10. The left term of constraint C1' is linear, which implies that it is both convex and concave, and its right term is convex. Therefore, constraint C' is convex. Since all the inequalities in constraints C2 and C3 are linear function of variable  $\tilde{P}_{sd}$ , clearly, the constraints C2–C3 are convex. The relaxed constraint C6 and constraints C7–C10 span a convex feasible set. As for constraints C4 and C5, it is easy to show that the constraints are convex due to the concavity of function  $U(\mathcal{P}, \rho, \mathcal{T})$ .

As a result, the transformed **OPT-2** problem is a convex optimization problem w.r.t.  $\tilde{P}_{sd}$ ,  $\rho_d^I$ ,  $\rho_d^E$  and  $t_{s,r}$ .

Theorem 11.3 reveals that the transformed **OPT-2** problem in (11.13) has a zero-duality gap and satisfies the Slater's constraint qualification. The zero-duality-gap result provides an avenue to obtain the optimal solution of the primal problem in (11.13) derived from its corresponding dual problem as will be seen later.

## 11.4 Distributed Algorithm for eCotrans Problem

In this section, we solve the transformed **OPT-2** problem with the approximated data rate  $\tilde{R}_{sd}$  in (11.14), relaxed constraint C4 and constraint  $C1'$ .

### 11.4.1 Dual Problem Formulation

The resource allocation policy is derived via solving the dual problem of (11.13) with the approximated data rate function. For this purpose, we first give the Lagrangian function of the primal problem (11.13) by

$$\begin{aligned}
 & L(w, \eta, \mu, \nu, v, \phi, \varphi, \mathcal{P}, \rho, \mathcal{T}) \\
 &= \sum_{s,d=1}^K \sum_{r=1}^{N_r} \alpha_r t_{s,r} \tilde{R}_{sd} - q(P_T + \sum_{s,d=1}^K \sum_{r=1}^{N_r} \varepsilon \tilde{P}_{sd}) \\
 &\quad + \sum_{s,d=1}^K \sum_{r=1}^{N_r} w_s \left( H_T t_{s,r} P_s + \frac{Q_{C,d}}{\rho_d^E} - \frac{E_d^{\min}}{\rho_d^E} \right) \\
 &\quad - \sum_{s,d}^K \mu_{sd} (\tilde{P}_{sd} - P_{sd}^{\max}) - \sum_{s,d=1}^K \nu_{sd} (P_{CH} + \varepsilon \tilde{P}_{sd} - E^{\max}) \\
 &\quad + v \left( \sum_{s,d}^K \sum_{r=1}^{N_r} t_{s,r} \tilde{R}_{sd} - R^{\min} \right) - \phi \left( \sum_{r=1}^{N_r} t_{s,r} - 1 \right) \\
 &\quad + \sum_{s,d=1}^K \sum_{r=1}^{N_r} \eta_d (t_{s,r} \tilde{R}_{sd} - R_d^{\min}) - \varphi \sum_{d=1}^K (\rho_d^E + \rho_d^I - 1)
 \end{aligned} \tag{11.17}$$

where  $P_T = K P_{CH} + \sum_{s=1}^K \sum_{r=1}^{N_r} P_{CR}$ ,  $H_T = \eta |h_{sd}|^2 (T/2)$ . Lagrangian multiplier  $w = [w_s, s = 1, \dots, K]^T$  is for the inequalities of energy harvesting constraint  $C1'$ , which denote the prices for the individual minimum transferred power of harvested energy in C1. Lagrangian multiplier  $\mu = [\mu_{sd}, s, d = 1, \dots, K]^T$  corresponds to transmission power constraint C2, which represents the price for the individual maximum transmission power.  $\nu = [\nu_{sd}, s, d = 1, \dots, K]^T$  is Lagrangian multiplier for power consumption constraint C3, which indicates the price for the individual maximum power consumption. Lagrangian multiplier  $v$  is for QoS constraint C4, representing the price for the minimum data rate requirement  $R_{\min}$  of the system. Lagrangian multiplier  $\eta = [\eta_b, b = 1, \dots, K]^T$  is for the minimum required data rate constraint C5.  $\phi$  is Lagrangian multiplier for relay selection constraint C7, denoting the price for a relay corresponding to at most one source. Lagrangian multiplier  $\varphi$  is for power splitting ratio constraint C10, reflecting the price for no extra power gain during power splitting process. On the other hand, the boundary constraints C8

and C9 on optimization variables are captured by the Karush–Kuhn–Tucker (KKT) conditions when deriving the resource allocation solution later.

The dual problem for the primal problem (11.13) is given by

$$\min_{w, \eta, \mu, \nu, v, \phi, \varphi} \max_{\mathcal{P}, \rho, \mathcal{T}} L(w, \eta, \mu, \nu, v, \phi, \varphi, \mathcal{P}, \rho, \mathcal{T}) \quad (11.18)$$

Based on zero-duality-gap result, we know that the solution of the **OPT-2** problem in (11.13) can be derived from its dual problem in (11.18).

We use an iterative approach to solving the dual problem (11.18) as follows. In each iteration, given dual variables  $w, \eta, \mu, \nu, v, \phi$  and  $\varphi$ , we first calculate the primal variables  $\mathcal{P}, \rho$  and  $\mathcal{T}$  by applying the KKT conditions; Then by using the primal variables, we update the dual variables via the subgradient method. In the following, we give the corresponding distributed subalgorithms for power allocation, power splitting and relay selection.

### 11.4.2 Power Allocation Subalgorithm

Power allocation subalgorithm aims to determine the optimal transmission power at the source in Phase I and at the relay in Phase II, satisfying the constraints of maximum power consumption and minimum data rate requirement (QoS requirement). Using standard convex optimization techniques and the KKT conditions [33], for a given  $q$ , in each iteration of the Dinkelbach method, the power allocation policy is given by

$$P_{sd}^* = \left[ \frac{(\alpha_r + v + \eta_d)B(1 + \vartheta_s)}{2 \ln 2(\Phi_{sd,r})} \right]_0^{P_{sd}^{max}} \quad (11.19)$$

where  $\Phi_{sd,r} = q\varepsilon + \mu_{sd} + \nu_{sd}\varepsilon - w_s H_T$ , and  $H_T = \eta |h_{sd}|^2 (T/2)$ . Here operator  $[x]_a^b$  is defined as  $[x]_a^b = \max(a, \min(x, b))$ . If source  $s$  and  $P_{sd}^{max}$  can be considered as a water vessel and its maximum water level, respectively, it is clear that different sources have different maximum water levels, and the power allocation in (11.19) has the form of multilevel water-filling, which can be interpreted as adaptively allocating transmission power according to a certain law and channel state. Usually, the link with good channel gain will always be allocated more power, that is, be filled more water up to its maximum water level in the vessel, in order to maximize transmission rate. However, the power allocation in (11.19) is not exactly multilevel water-filling since the water level in allocating power on source  $s$ , i.e.,  $\frac{(\alpha_r + v + \eta_d)B(1 + \vartheta_s)}{2 \ln 2(\Phi_{sd,r})}$ , is not only directly proportional to the priority of the source via variable  $\alpha_r$ , but also depends on the channel gains among the source, relay and destination.

### 11.4.3 Power Splitting Subalgorithm

Power splitting subalgorithm aims at determining the optimal power splitting ratio at the receiver so as to guarantee that the harvested energy at the receiver is no less than the minimum required power transfer while the aggregated data rate is no less than the minimum system data rate requirement. In practice, the power split for energy harvesting and that for information decoding contradict with each other, that is, the increase of  $\rho_d^E$  will lead to the decrease of  $\rho_d^I$ . The optimal power splitting policy can be obtained by solving the following maximization problem:

$$\max_{\rho_d^E, \rho_d^I} (\alpha_r + v + \eta_d) t_{s,r} \tilde{R}_{sd} - w_s \frac{\varpi_d}{\rho_d^E} - \varphi (\rho_d^E + \rho_d^I) \quad (11.20)$$

Subject to

$$C8 : \rho_{\min}^E \leq \rho_d^E \leq \rho_{\max}^E,$$

$$C9 : \rho_{\min}^I \leq \rho_d^I \leq \rho_{\max}^I,$$

where  $\varpi_d = E_d^{\min} - Q_{C,d}$ .

By the KKT conditions [33], for a given  $q$ ,  $\rho_d^{I*}$  and  $\rho_d^{E*}$  are given by

$$\rho_d^{I*} = \left[ \frac{B(1 + \vartheta_s)(\alpha_r + v + \eta_d)}{2 \ln 2 \varphi} \right]_{\rho_{\min}^I}^{\rho_{\max}^I} \quad (11.21)$$

$$\rho_d^{E*} = \left[ \sqrt{\frac{w_s(E_d^{\min} - Q_{C,d})}{\varphi}} \right]_{\rho_{\min}^E}^{\rho_{\max}^E} \quad (11.22)$$

We can observe from (11.21) that the power splitting ratio for information decoding,  $\rho_d^I$ , is also a water-filling scheme and depends on the priority of the receiver via  $\alpha_r$ , which implies that the receiver with high priority has to increase  $\rho_d^I$  to improve its data rate. Besides, Lagrange multiplier  $v$  forces the receiver to split larger ratio of power used to decode information in order to ensure that the aggregated network throughput satisfies the minimum system data rate requirement. On the other hand,  $E_d^{\min}$  and  $w_s$ , require the receiver to increase the power splitting ratio for energy harvesting,  $\rho_d^E$ , so as to meet the constraint of  $E_d^{\min}$ .

### 11.4.4 Relay Selection Subalgorithm

The goal of the relay selection subalgorithm is to provide a relay selection criterion by which all overhearing nodes calculate their priority. The node with the highest

priority will be selected as the relay node that cooperatively delivers data from the source. Thus, using the standard convex technique [33] to solve the dual problem (11.18), relay node  $r$  is assigned to source  $s$  when the following selection criterion is satisfied

$$t_{s,r}^* = \begin{cases} 1, & \text{if } r = \arg \max_j M_{s,j} \\ 0, & \text{otherwise} \end{cases} \quad (11.23)$$

where

$$M_{s,r} = \frac{B}{2} (\alpha_r + v + \eta_d) \log (\rho_r^{I*} \tilde{\lambda}_{sr} P_{sr}^*) - \phi \quad (11.24)$$

$M_{s,r}$  can be regarded as the marginal benefit provided to the system when relay  $r$  is assigned to source  $s$ . In other words, relay  $r$  is selected to cooperatively forward the data of source  $s$  if it can provide the maximum marginal benefit to the system, which implies that relay  $r$  has the highest priority to be selected among all candidate relay nodes of source  $s$ . Besides, if relay  $r$  has a high priority, it will have a large value of  $\alpha_r$  and the resource allocator at the transmitter will have a higher preference to select relay  $r$ . On the other hand, we can observe from (11.23) that although constraint relaxation is used in constraint C6 for facilitating the design of the resource allocation algorithm, the relay selection policy on each relay for the relaxed problem remains Boolean.

#### 11.4.5 Lagrange Multiplier Update

In this subsection, we will solve the minimization problem at the high level in (11.18) by using the subgradient method which leads to the following Lagrange multiplier update

$$w_s(t+1) = \left[ w_s(t) - \delta(t) \left( H_{sd} \tilde{P}_{sd} + \frac{Q_{C,d} - E_d^{\min}}{\rho_d^E} \right) \right]^+ \quad (11.25)$$

$$\eta_b(t+1) = [\eta_b(t) + \delta(t) (t_{s,r} \tilde{R}_{sd} - R_d^{\min})]^+ \quad (11.26)$$

$$\mu_{sd}(t+1) = [\mu_{sd}(t) + \delta(t) (\tilde{P}_{sd} - P_{sd}^{\max})]^+ \quad (11.27)$$

$$\nu_{sd}(t+1) = [\nu_{sd}(t) + \delta(t) (P_{CH} + \varepsilon \tilde{P}_{sd} - E^{\max})]^+ \quad (11.28)$$

$$v(t+1) = \left[ v(t) - \delta(t) \left( \sum_{s,d=1}^K \sum_{r=1}^{N_r} t_{s,r} \tilde{R}_{sd} - R^{\min} \right) \right]^+ \quad (11.29)$$

$$\varphi(t+1) = [\varphi(t) + \delta(t) (\rho_d^E + \rho_d^I - 1)]^+ \quad (11.30)$$

where  $H_{sd} = H_T A_{sd,r}$ , index  $t \geq 0$  is the iteration index, and  $\delta(t)$  is positive diminishing step size. Updating  $\phi$  is not necessary as it has the same value for all nodes and does not affect the power splitting in (11.21) and (11.22) and the relay selection

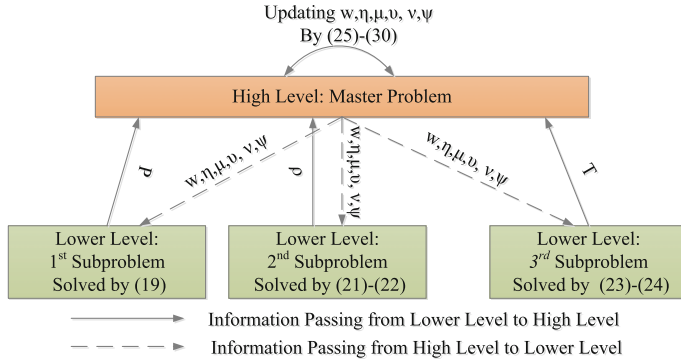


**Fig. 11.3** Dual decomposition of **OPT-2** problem into a two-level problem in each main loop iteration

in (11.23). Therefore, we can simply set  $\phi = 0$  in each iteration. Indeed, in each iteration for solving the main loop problem, the master problem at the high level adjusts the Lagrange multipliers by (11.25)–(11.30). On the other hand, each subproblem at the lower level adjusts the water levels of (11.19), (11.21) and (11.22) and relay selection metric (11.23) by using the updated Lagrange multipliers. The procedure is repeated until convergence is achieved or the number of iterations reaches a predefined maximum number of iterations for the main loop, as shown in Fig. 11.3.

We now analyze the time complexity of the proposed iterative algorithm in Algorithm 3. It consists of two nested loops. The outer loop is to update the parameter  $q$  and can be proved to have a linear time complexity. On the other hand, the inner loop optimization problem is proved to be convex in Theorem 11.3, in other words, solving the inner loop optimization problem requires only a polynomial time complexity, i.e., the complexity is  $O(K \times N)$ . As a result, the proposed algorithm has a polynomial time complexity, i.e.,  $O(\text{Iter}_{\max} \times K \times N)$ .

## 11.5 Simulation and Discussions

In this section, we first verify the convergence of the proposed eCotrans algorithm. Furthermore, we compare and evaluate the performance of our solution for different parameters.

We assume that 50 cluster member nodes (CNs) are randomly located within a circular area within a radius of 120 m. Here, we only use LEACH algorithm as an example to organize the clusters. Note that many other clustering protocols can also be used in our algorithm. We let  $\alpha = 2$ ,  $\varepsilon = 5$  and  $\zeta_{ij} = 1$ . The channel gains are generated according to a Rayleigh fading model. Without loss of generality, we assume that all receivers have the same priority  $\alpha_r = 1$ , and all nodes have the same circuit power consumption, i.e.,  $P_{CH} = P_{CR} = 10 \text{ dBm}$ . We let  $\rho_{\min}^E =$

**Table 11.1** Parameter settings

| Parameter       | Value    | Parameter       | Value  |
|-----------------|----------|-----------------|--------|
| $B$             | 3MHz     | $P_{sd}^{\max}$ | 40 dBm |
| $K$             | 100      | $T$             | 10 s   |
| $N$             | 8        | $\eta_i$        | 0.4    |
| $\sigma_{sd}^2$ | -130 dBm | $E_d^{\min}$    | 0 J    |
| $\sigma_{sr}^2$ | -120 dBm | $E^{\max}$      | 100 J  |
| $\sigma_{rd}^2$ | -110 dBm | $\varepsilon$   | 0.001  |
| $R^{\min}$      | 2 Mbps   | $iter_{\max}$   | 20     |

$\rho_{\min}^I = 0$  and  $\rho_{\max}^E = \rho_{\max}^I = 1$ . Moreover, to ensure fast convergence, the iteration step size adopted in Lagrange multiplier updates is optimized via backtracking line search [33]. Other system parameters are listed in Table 11.1.

### 11.5.1 Convergence and Performance Analysis

In this subsection, we study the convergence of the proposed eCotrans algorithm. Figure 11.4 illustrates the evolution of energy efficiency for different maximum transmit power allowance  $P^{\max}$ , and the number of relays  $N$  in a cluster. By analyzing the results in Fig. 11.4, we can see that the energy efficiency increases with the number of iterations and then converges within 12 iterations in every considered scenario. Note that the number of iterations in Fig. 11.4 indicates only the main loop iterations for the Dinkelbach method, but not that for the gradient method. Another important observation is that the energy efficiency is directly proportional to  $P^{\max}$ . This is justifiable since a higher transmit power allowance leads to the larger transmit power and data rate.

### 11.5.2 Impact of Relay Nodes on Energy Efficiency

In this subsection, we evaluate the impact of the number of candidate relay nodes in a cluster on energy efficiency under the DT and RT modes, respectively. To reflect the DT and RT modes, we let  $\rho_r^I = \rho_d^I$  and  $a_{sr} \geq a_{rd}$ , which implies that if  $a_{rd} > a_{sd}$ , the CH works at the RT mode, otherwise, it works at the DT mode. We define  $INR = a_{rd}/a_{sd}$  and let  $INR$  be 0.5, 0.8, 1.2 and 1.5. Clearly, the first two ratio values indicate the DT mode is valid while the latter two values imply that the RT mode is available. We observe from Fig. 11.5 that compared to the DT mode, the energy efficiency of the proposed algorithm at the RT mode increases remarkably with the number of candidate relay nodes. However, the increase of energy efficiency

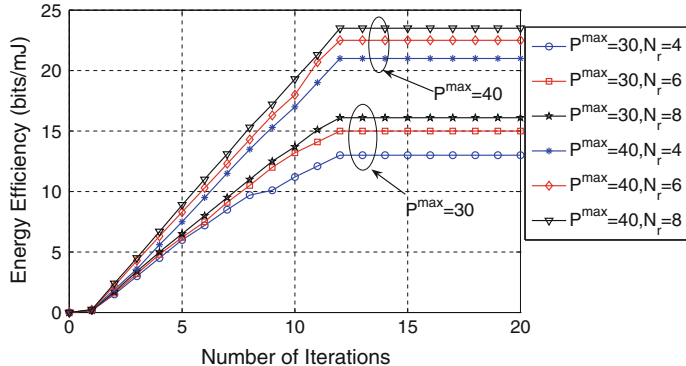
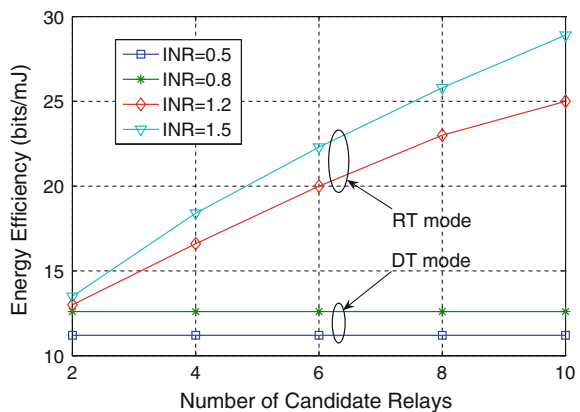


**Fig. 11.4** Energy Efficiency (bits/mJ) versus the number of iterations for  $P^{max} = 30$  and  $40$  dBm, and  $N = 4, 6, 8$

**Fig. 11.5** Energy Efficiency (bits/mJ) versus the number of relay nodes for  $INR = 0.5, 0.8, 1.2, 1.5$ , and  $N = 2, 4, 6, 8, 10$

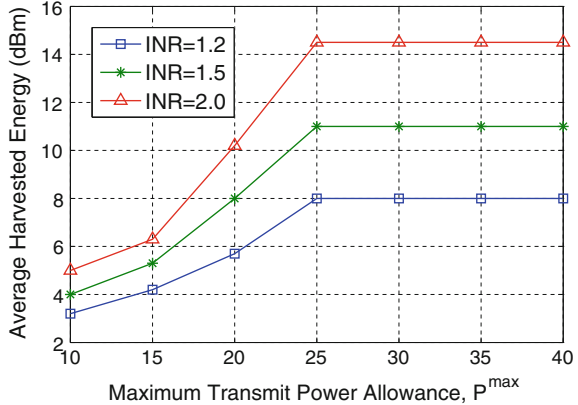


becomes slower and finally stable with further increase of the number of relays. This is mainly due to that (i) it induces more collisions and energy consumption of all control messages such as RTS/CTS; (ii) the relay selection subalgorithm has to traverse more candidate relays and execute more iterations to find the optimal relay. Another important observation is that for the same transmission mode, the energy efficiency is directly proportional to the normalized effective channel gain.

### 11.5.3 Impact of Power Allowance on Average Harvested Energy

In this subsection, we explore the impact of the maximum allowed transmit power  $P^{max}$  on the average harvested energy for different INR levels. Figure 11.6 depicts

**Fig. 11.6** Average harvested energy (dBm) versus maximum transmit power allowance,  $P^{\max}$  for different  $INR$  levels and  $N = 8$

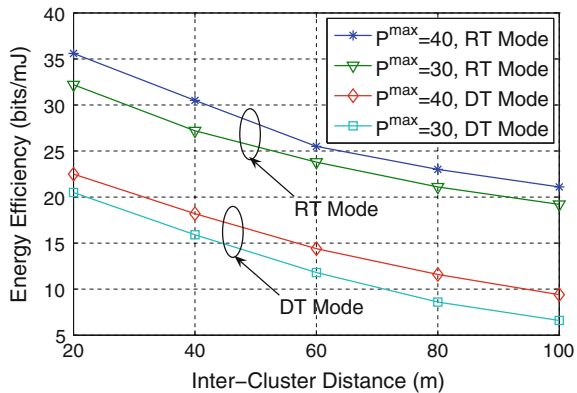


the average harvested energy at the CH versus the maximum power allowance for different  $INR$  levels. We set  $INR$  to be 1.2, 1.5, and 2.0, which means that the CH works at the RT mode. It can be observed from Fig. 11.6 that in lower  $P^{\max}$ , only a small portion of received energy is harvested by the CH for energy efficiency maximization. This is due to the fact that for small values of the transmit power allowance, the received power of the desired signal at the receivers may not be sufficiently large for simultaneous information decoding and energy harvesting. On the contrary, for the higher level of the transmit power allowance, the receiver has a higher tendency to split a larger proportion of the received power for energy harvesting until the amount of average harvested energy is saturated. This is because that once the constraints on the minimum required energy transfer to receiver  $k$ ,  $E_k^{\min}$ , and the minimum system data rate requirement,  $R_{\min}$ , are satisfied, the transmitter stops increasing the transmit power for energy efficiency maximization. On the other hand, we can observe that a higher amount of energy is harvested by the receiver when the  $INR$  level increases. As a result, splitting more received power for energy harvesting can enhance the system energy efficiency.

#### 11.5.4 Impact of Intercluster Distance on Energy Efficiency

In this subsection, we discuss how the distance  $L_{ij}$  between the CH  $i$  and the CH  $j$  affects the energy efficiency under the different maximum transmit power allowance. In this case, we set the number of CN nodes in a cluster as  $N = 8$  and let  $P^{\max}$  be 30dBm and 40dBm. Figure 11.7 reflects the evolution of energy efficiency with intercluster distance. It can be seen in Fig. 11.7 that when the intercluster distance  $L_{ij}$  increases, the energy efficiency decreases, correspondingly. This is justified since when  $L_{ij}$  increases, the proposed algorithm needs more sensor nodes to participate in cooperation to reach long transmitting distance for a given  $P^{\max}$ , which leads to more energy consumption. Another observation is that the energy efficiency at the

**Fig. 11.7** Energy Efficiency (bits/mJ) versus the intercluster distance for  $N = 8$  and  $P^{\max} = 30\text{ dBm}$ , 40 dBm



RT mode is always larger than that at the DT mode as  $L_{ij}$  increases. This is because that the long transmitting distance will hinder the direct transmission between the two CHs and even make the direct transmission invalid.

### 11.5.5 Comparison on Energy Efficiency and Remaining Energy

In this subsection, we compare the performance of the proposed eCotrans algorithm and several existing cooperative schemes, such as the eCocom scheme in [4], the coCoalition scheme in [3], the eCooperation algorithm in [2], and the coNetspa scheme in [15] in terms of energy efficiency and remaining energy for different maximum allowed transmit powers. The eCocom is an energy-efficient selective single-relay cooperative scheme with physical layer power control. The coCoalition is a cooperative communication scheme based on coalition formation game in clustered WSNs. The eCooperation is an energy-efficient cooperative transmission strategy using cooperative multiple-input and multiple-output (CMIMO) technique. The coNetspa scheme is an energy harvesting cooperative scheme for wireless information and power transfer in cooperative networks with spatially random relays. The first three schemes are energy-efficient cooperative schemes, but without energy harvesting, while the coNetspa scheme involves the application of SWIPT to wireless cooperative networks, but it does not consider energy efficiency maximization.

In the simulation, we let  $N = 8$  and  $INR = 1.5$ . We consider the scenario that all cluster member nodes (CNs) have the same amount of data to be sent and the same initial remaining energy. Figure 11.8 illustrates the comparison of energy efficiency between the proposed eCotrans algorithm and the existing schemes. It can be observed that all the cooperative schemes have an increasing energy efficiency with the maximum transmit power allowance until the achieved energy efficiency gain attains its maximum in the high transmit power allowance region. However,

**Fig. 11.8** Energy Efficiency (bits/mJ) versus maximum allowed transmit power for different cooperative schemes

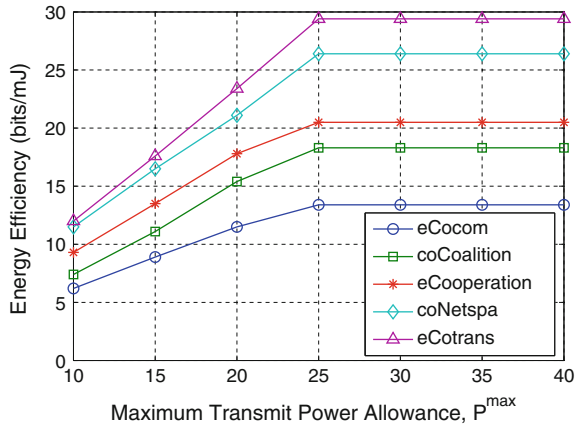
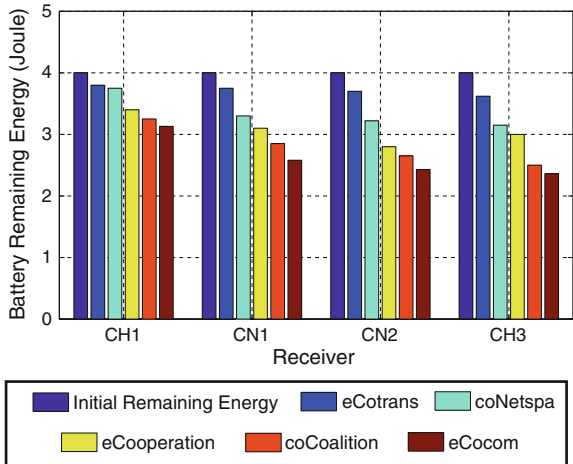


**Fig. 11.9** Remaining energy in the battery versus receivers for different cooperative schemes



our proposed eCotrans algorithm achieves the highest energy efficiency. This is justified since we employ the energy harvesting cooperative transmission, combining the optimal cooperative relay selection with the optimal power control and power splitting at the physical layer.

Figure 11.9 depicts the remaining energy in the battery for receivers CH1, CN1, CN2 and CH3 as shown in Fig. 11.1 after transmitting the same amount of data by different cooperative schemes. It is observed that the proposed eCotrans algorithm has more remaining energy in the batteries of all receivers while also having the best remaining energy balance among receiver nodes. In particular, for the receivers CN1 and CN2, the superiority of the eCotrans algorithm is more obvious. The reason is that using eCotrans algorithm, the receivers are able to harvest the energy from the received signals and replenish the harvested energy in the battery while forwarding the data from their upstream nodes. More importantly, although the CH3 node has

more data to forward from its neighbor nodes as shown in Fig. 11.1, it still has more remaining energy in its battery. This is because the CH3 node is capable of harvesting the energy of ambient RF signals from the transmitters.

## 11.6 Conclusions

In this paper, we consider applying SWIPT to cooperative clustered WSNs, where energy-constrained relay nodes avail the ambient RF signal and simultaneously harvest energy and process information to prolong their lifetime. Our goal is to provide the optimal policies for power allocation and relay selection and determine the optimal power splitting ratio so that the system energy efficiency is maximized. To achieve this goal, we formulate the eCotrans problem as a non-convex constrained optimization problem. Furthermore, we propose a distributed iteration algorithm with closed-form transmission power, power slitting ratio and relay selection by exploiting dual decomposition. In particular, we find that power splitting ratio plays an imperative role in relay selection, however, it depends on the minimum harvested energy requirement. Our simulation results demonstrate that the proposed iterative algorithm converges within a small number of iterations. Compared to existing algorithms without energy harvesting or energy efficiency maximizing, our proposed iterative algorithm can achieve higher energy efficiency and more remaining energy.

## References

1. Siam, M.Z., Krunz, M., Younis, O.: Energy-efficient clustering/routing for cooperative mimo operation in sensor networks. In: INFOCOM 2009, pp. 621–629. IEEE (2009). doi:[10.1109/INFCOM.2009.5061969](https://doi.org/10.1109/INFCOM.2009.5061969)
2. Li, B., Li, H., Wang, W., Yin, Q., Liu, H.: Performance analysis and optimization for energy-efficient cooperative transmission in random wireless sensor network. IEEE Trans. Wireless Commun. **12**(9), 4647–4657 (2013). doi:[10.1109/TWC.2013.072313.121949](https://doi.org/10.1109/TWC.2013.072313.121949)
3. Wu, D., Cai, Y., Zhou, L., Wang, J.: A cooperative communication scheme based on coalition formation game in clustered wireless sensor networks. IEEE Trans. Wireless Commun. **11**(3), 1190–1200 (2012). doi:[10.1109/TWC.2012.012712.111049](https://doi.org/10.1109/TWC.2012.012712.111049)
4. Zhou, Z., Zhou, S., Cui, J.H., Cui, S.: Energy-efficient cooperative communication based on power control and selective single-relay in wireless sensor networks. IEEE Trans. Wireless Commun. **7**(8), 3066–3078 (2008). doi:[10.1109/TWC.2008.061097](https://doi.org/10.1109/TWC.2008.061097)
5. Zhou, Z., Zhou, S., Cui, S., Cui, J.H.: Energy-efficient cooperative communication in a clustered wireless sensor network. IEEE Trans. Veh. Technol. **57**(6), 3618–3628 (2008). doi:[10.1109/TVT.2008.918730](https://doi.org/10.1109/TVT.2008.918730)
6. Krikidis, I., Timotheou, S., Nikolaou, S., Zheng, G., Ng, D.W.K., Schober, R.: Simultaneous wireless information and power transfer in modern communication systems. IEEE Commun. Mag. **52**(11), 104–110 (2014). doi:[10.1109/MCOM.2014.6957150](https://doi.org/10.1109/MCOM.2014.6957150)
7. Guo, S., Wang, C., Yang, Y.: Joint mobile data gathering and energy provisioning in wireless rechargeable sensor networks. IEEE Trans. Mob. Comput. **13**(12), 2836–2852 (2014). doi:[10.1109/TMC.2014.2307332](https://doi.org/10.1109/TMC.2014.2307332)

8. Li, J., Wang, C., Ye, F., Yang, Y.: Netwrap: An NDN based real time wireless recharging framework for wireless sensor networks. In: 2013 IEEE 10th International Conference on Mobile Ad-Hoc and Sensor Systems (MASS), pp. 173–181 (2013)
9. Yang, Y., Wang, C.: Wireless Rechargeable Sensor Networks. Springer (2015)
10. Zhao, M., Li, J., Yang, Y.: A framework of joint mobile energy replenishment and data gathering in wireless rechargeable sensor networks. *IEEE Trans. Mob. Comput.* **13**(12), 2689–2705 (2014). doi:[10.1109/TMC.2014.2307335](https://doi.org/10.1109/TMC.2014.2307335)
11. Varshney, L.R.: Transporting information and energy simultaneously. In: IEEE International Symposium on Information Theory, ISIT 2008, pp. 1612–1616. IEEE (2008)
12. Zhou, X., Zhang, R., Ho, C.K.: Wireless information and power transfer: Architecture design and rate-energy tradeoff. *IEEE Trans. Commun.* **61**(11), 4754–4767 (2013)
13. Chen, X., Wang, X., Chen, X.: Energy-efficient optimization for wireless information and power transfer in large-scale mimo systems employing energy beamforming. *IEEE Wireless Commun. Lett.* **2**(6), 667–670 (2013)
14. Chen, X., Yuen, C., Zhang, Z.: Wireless energy and information transfer tradeoff for limited-feedback multiantenna systems with energy beamforming. *IEEE Trans. Veh. Technol.* **63**(1), 407–412 (2014)
15. Ding, Z., Krikidis, I., Sharif, B., Poor, H.V.: Wireless information and power transfer in cooperative networks with spatially random relays. *IEEE Trans. Wireless Commun.* **13**(8), 4440–4453 (2014)
16. Lee, S., Zhang, R., Huang, K.: Opportunistic wireless energy harvesting in cognitive radio networks. *IEEE Trans. Wireless Commun.* **12**(9), 4788–4799 (2013)
17. Nasir, A.A., Zhou, X., Durrani, S., Kennedy, R.A.: Relaying protocols for wireless energy harvesting and information processing. *IEEE Trans. Wireless Commun.* **12**(7), 3622–3636 (2013)
18. Ng, D.W.K., Lo, E.S., Schober, R.: Wireless information and power transfer: energy efficiency optimization in ofdma systems. *IEEE Trans. Wireless Commun.* **12**(12), 6352–6370 (2013)
19. Xu, J., Liu, L., Zhang, R.: Multiuser miso beamforming for simultaneous wireless information and power transfer. *IEEE Trans. Signal Process.* **62**(18), 4798–4810 (2014)
20. Zhang, R., Ho, C.K.: Mimo broadcasting for simultaneous wireless information and power transfer. *IEEE Trans. Wireless Commun.* **12**(5), 1989–2001 (2013)
21. Zhou, X., Zhang, R., Ho, C.K.: Wireless information and power transfer in multiuser ofdm systems. *IEEE Trans. Wireless Commun.* **13**(4), 2282–2294 (2014)
22. Ng, D.W.K., Lo, E.S., Schober, R.: Energy-efficient resource allocation for secure ofdma systems. *IEEE Trans. Veh. Technol.* **61**(6), 2572–2585 (2012)
23. Ng, D.W.K., Lo, E.S., Schober, R.: Robust beamforming for secure communication in systems with wireless information and power transfer. *IEEE Trans. Wireless Commun.* **13**(8), 4599–4615 (2014)
24. Xiang, Z., Tao, M.: Robust beamforming for wireless information and power transmission. *IEEE Wirel. Commun. Lett.* **1**(4), 372–375 (2012)
25. Liu, Y., Chen, W.: Limited-feedback-based adaptive power allocation and subcarrier pairing for ofdm df relay networks with diversity. *IEEE Trans. Veh. Technol.* **61**(6), 2559–2571 (2012)
26. Zhou, Z., Zhou, S., Cui, S., Cui, J.H.: Energy-efficient cooperative communication in clustered wireless sensor networks. In: Proceedings of the 2006 IEEE conference on Military communications, pp. 1292–1298. IEEE Press (2006)
27. Ma, Y., Leith, A., Alouini, M.S., Shen, X.: Weighted-snr-based fair scheduling for uplink ofdma. In: Global Telecommunications Conference, GLOBECOM 2009, pp. 1–6. IEEE (2009)
28. Dinkelbach, W.: On nonlinear fractional programming. *Manage. Sci.* **13**(7), 492–498 (1967)
29. Liu, L., Zhang, R., Chua, K.C.: Wireless information and power transfer: a dynamic power splitting approach. *IEEE Trans. Commun.* **61**(9), 3990–4001 (2013)
30. Liu, L., Zhang, R., Chua, K.C.: Wireless information transfer with opportunistic energy harvesting. *IEEE Trans. Wireless Commun.* **12**(1), 288–300 (2013)
31. Ng, D.W.K., Lo, E.S., Schober, R.: Energy-efficient resource allocation in ofdma systems with large numbers of base station antennas. *IEEE Trans. Wireless Commun.* **11**(9), 3292–3304 (2012)

32. Yu, W., Lui, R.: Dual methods for nonconvex spectrum optimization of multicarrier systems. *IEEE Trans. Commun.* **54**(7), 1310–1322 (2006)
33. Boyd, S., Vandenberghe, L.: Convex Optimization. Cambridge university press (2004)

## **Part III**

# **Mobility**

# Chapter 12

## Using Mobile Nodes in Wireless Sensor Networks with Wireless Power Transfer

Xiaobing Wu

**Abstract** In this chapter, we introduce works on using mobile nodes in wireless sensor networks with wireless power transfer ability. The mobile nodes here can be mobile chargers or mobile sensor nodes. There are works discussing the energy provision problem considering mobility of sensors in the network although most works focus on the scenario where only chargers are mobile. We classify the works into two categories, namely, centralized approach and distributed approach. The former one refers to that the proposed method is centrally controlled and relies on global information of the network, and the latter one refers to that the proposed scheme works based on limited local information. As for centralized approach, we introduce several popular topics such as mobile charger planning, joint mobile charging and data gathering, using minimum mobile chargers, etc. As for the distributed approach, we present topics including on-demand charging, planning for a single mobile charger and coordination of multiple mobile chargers. There are more works on centralized approach than on distributed approach. Finally we conclude this chapter.

### 12.1 Introduction

In traditional wireless sensor networks (WSNs), the sensors are powered by battery and the networks are usually deployed in remote areas where it is difficult for people to replace the battery. The network lifetime of WSNs is defined as the duration from the time when the network starts to operate till the time when the first node in the network depletes its energy. A lot of research has been conducted on how to improve the network lifetime of WSNs. Wireless power transfer (WPT) technology can help to overcome the energy problem of traditional WSNs. Using mobile nodes in WSNs enabled by wireless power transfer brings both opportunities and challenges. Many

---

X. Wu (✉)

Wireless Research Centre, University of Canterbury, Christchurch 8140, New Zealand  
e-mail: barry.wu@canterbury.ac.nz

research efforts have been put in this field. In this chapter, we introduce the latest progress in regarding to using mobile nodes in WSNs enabled by wireless power transfer.

## 12.2 Centralized Approach

A typical wireless-power-transfer-enabled rechargeable sensor network is usually composed of a base station, one or multiple mobile chargers and many sensors as illustrated in Fig. 12.1. The base station can serve as a dual role of data sink for the sensor nodes and energy refilling station for the mobile rechargers. Usually the mobile charger and base station are different nodes, but we will introduce some works on co-located mobile charger and mobile base stations. The mobile charger roams in the network according to some traveling path which is computed a priori or on-site. It is usually assumed that the chargers have higher capacities than the ordinary nodes in terms of energy, mobility and communications. Using centrally controlled mobile chargers means that the network operator can design and plan the operation of the mobile charger a priori based on global network information. Centralized approach always brings higher system efficiency since less coordination is involved. We will introduce some of the most important works in this area in the following subsections. The topics include planning of single mobile charger, joint

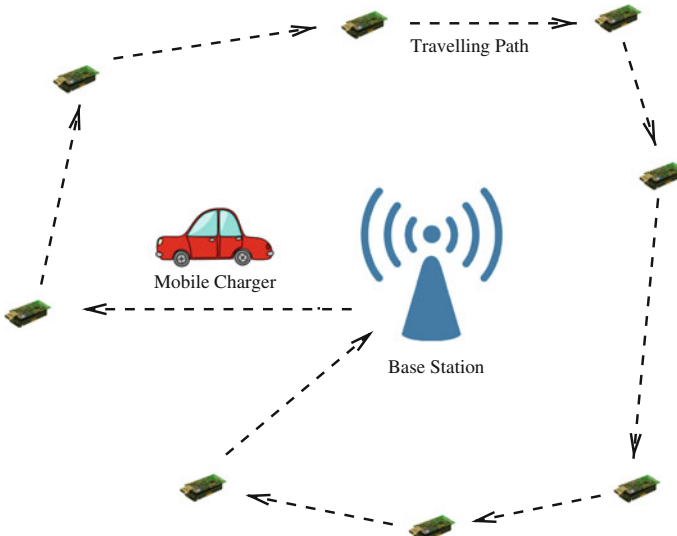


**Fig. 12.1** Illustration of a typical wireless rechargeable sensor network which consists of a base station, one/multiple mobile chargers and many sensor nodes

mobile charging and data gathering, using minimum mobile chargers, collaborative mobile charging, localization with mobile chargers, etc.

### 12.2.1 Planning of Mobile Charger

In wireless ad hoc networks with wireless power transfer, the wireless charger is usually a more advanced device compared to ordinary nodes. Accordingly, it is more expensive in terms of device cost. Using a mobile charger to travel in the network instead of deploying multiple static chargers is an effective method to reduce the device cost. We need consider several technical issues when we consider using a mobile charger in the network. In particular, one needs to consider the trajectory, moving speed, sojourn points, sojourn of the mobile chargers. All these factors can influence the charging efficiency of a mobile charger. Here we introduce two important works in the literature.

#### 12.2.1.1 Trajectory of Mobile Charger

Xie, Shi, Hou and Sherali [23] assume that there are sensors and a static sink in the network and a mobile charger that travels inside the network and charges the sensors. Initially, every node is fully charged and has an energy reserve of  $E_{max}$ . The node stops working once its remained energy goes below  $E_{min}$ . The mobile charger starts from a service station and moves at a speed of  $V$ . It will stop at a node  $i$  for a duration of  $\tau_i$ . It is assumed that the mobile charger has unlimited supply of energy. The mobile charger returns to the service station after it visits every node in the network. The time between two tours is called vacation time of the mobile charger,  $\tau_{vac}$ . Here a tour is defined as the process that the charger starts from the service station and return to it. In order to improve the charging efficiency, we need to maximize the ratio of vacation time to the whole tour time  $\tau$ . It is also assumed that the data flow routing in the network does not change over time. The energy level of every node in this network under these assumptions is periodic and goes to a high level when the mobile charger comes in its vicinity and drops to a lower level before the mobile charger comes again. The authors call the periodic energy level renewable if it starts and ends with the same energy level over the tour period of the mobile charger and it never falls below  $E_{min}$ . The following theorem has been proved.

**Theorem 12.1** ([23]) *The mobile charger needs to travel along the shortest Hamiltonian cycle covering all ordinary nodes and the service station in order to maximize the vacation ratio  $\tau_{vac}/\tau$ .*

Based on Theorem 12.1, now it is enough if we can figure out the flow routing and charging time for each sensor node. The authors propose an optimization formulation for the joint flow routing and charging time problem. It is however non-linear and

NP-hard in general. They resort to approximation for a near-optimal final solution. The following lemma states the performance guarantee of the near-optimal solution.

**Lemma 12.1** *The proposed approximation algorithm guarantees that the performance difference between the feasible solution and the optimal one is no greater than  $U \cdot \tau_{TSP}/\{4m^2(E_{max} - E_{min})\}$ .*

Here  $m$  is the number of piecewise linear segments to approximate the quadratic curve of the original problem.  $\tau_{TSP}$  is the tour duration of the shortest Hamiltonian cycle.

### 12.2.1.2 Velocity of Mobile Charger

In [17], Shu, Yousefi, Cheng, et al., consider the velocity control problem of the mobile charger in a wireless rechargeable sensor network. It is assumed that the trajectory of the mobile charger is given a priori and the time for one tour is bounded. The aim of the proposed scheme is to maximize the minimum charged energy among all the nodes in the network. In particular, it is assumed that the charger moves at  $v(t)$  with acceleration of  $a(t)$  at time  $t$  within each charging trip duration  $T$ . The aim of this problem can be formulated as follows [17],

$$\max \min_i \left( \int_0^T P_i(t) dt - \gamma_i T \right), \quad (12.1)$$

where the first part in the min function is the integrated charged energy for node  $i$  and the second part is the energy consumption during the time  $T$ . The first part can be calculated via multiplication of charging efficiency and distance between the node and the mobile charger. Usually the charging efficiency is an exponentially decreasing function of the distance between the charger and the node.

It is in fact hard to solve the problem since the function (12.1) is non-convex due to the non-linear continuous change of the distance between the charger and the node. The authors propose to use both temporal and spatial discretization to approximately solve the problem. Here temporal discretization refers to that the speed can change only at discrete time. Spatial discretization means that the pre-defined trajectory is divided into multiple segments where for each segment, the charging power is approximated by the lowest charging power when the mobile charger moves along the segment. With the discretization, the authors present an algorithm outputting the velocity profile for each segment for the single-node scenario. The authors have also proved the performance guarantee of their algorithm as follows.

**Theorem 12.2** ([17]) *The velocity profile output by the proposed algorithm enables that the node is charged at least  $E^*/(1 + \varepsilon)$ .*

Here  $E^*$  is the charged energy by the optimal solution and  $\varepsilon$  is the approximation parameter.

For multiple nodes scenario with given arbitrary 2D trajectory, the authors first prove the NP-hardness of the problem by reduction from the Multi-Objective Shortest Path problem. A heuristic algorithm is given with theoretical bounds.

### **12.2.2 Joint Mobile Charging and Data Gathering**

In traditional wireless sensor networks, using mobile sink for data collection has been regarded as an effective method for achieving longer network lifetime. The reason behind this is that the nodes near to the sink usually consume their energy faster and the energy consumption of all the nodes can be more balanced if the nodes around the sink change all the time. At the same time, using a mobile charger can save the deployment cost since wireless charger is always more expensive. Zhao, Li and Yang propose to combine the data collection function with wireless power transfer ability into one mobile node in their pioneering work [25].

#### **12.2.2.1 A Two-Step Approach for the Joint Optimization**

In the journal version [26] of the work [25], the authors elaborate on a two-step approach for the joint optimization of data gathering and mobile charging. The first step of the proposed design is to periodically select a set of anchor points where the mobile sink and charger will visit them and charge the sensors located there in sequence and collect data from all sensors nearby. The second step is for the sensors around the mobile charger to adjust their data rates, link scheduling and flow routing according to their energy replenishing status. In this work, the authors assume that the charging happens in a one-to-one fashion. There are two types of tours, namely, recharging tour (R-tour) and data gathering tour (D-tour). The R-tour is used mainly for scenarios where energy is consumed quickly. The D-tour is used mainly for scenarios where energy depletes slowly. Different strategies are used when performing the anchor points selection. For R-tours, the selection criterion is to find a subset of sensors with energy reserve below a threshold and the tour length is upper bounded. On the contrary, for D-tours, the selection criterion is to find a subset of nodes with energy lever higher than a threshold and the tour length is also upper bounded. Within a time interval guaranteed for bounded data collection latency, the system can perform at least one R-tour ensuring that the network is operational and  $q$  D-tours ensuring an efficient data collection. Here  $q$  is a system parameter and it is tunable for the balance of energy charging and data collection. The next step is how to plan the data collection trip when the anchor points are decided regardless of either R-tour or D-tour. The authors treat it as a utility maximization problem. A DAG (Directed Acyclic Graph) is set up over all the anchor points and the mobile charger. For other nodes not included in the DAG, it finds its shortest path towards

an anchor point using Dijkstra algorithm. The weight of outgoing edge can be set to the reciprocal of the residual energy at the node for simplicity. The utility function has been defined as strictly concave, increasing and twice-differentiable with respect to the data gathered from a specific sensor during a specific time interval. The aim of this optimization is to maximize the total network utility which is the sum of all utilities of all sensors. There are three types of constraints considered in this formulation. Flow constraints state that the equality between outgoing flow rates and incoming flow rates plus local data rate. Energy constraints ensure that energy consumed for data receiving and transmitting is less than the remained energy at the node. Capacity constraint enforces that the flow rate allocated on a link for an anchor point is feasible. Node exclusive interference model is employed to model the interference among links.

### 12.2.2.2 From Time-Dependency to Spatial-Dependency

Xie, Shi, Hou, Lou et al. [22] study the scheme for minimizing the energy consumption while ensuring a long-run wireless sensor network with a mobile charger behaving as a mobile data collector as well. Along a pre-defined path, the mobile charger can travel at a constant speed and make stops in the network and collect data via multiple hops. It is equivalent to maximize the ratio of mobile charger's vacation time to the whole trip duration, i.e.  $\tau_{vac}/\tau$ . Here  $\tau_{vac}$  is the idle period during the whole trip time  $\tau$ . The authors propose formal problem formulation for maximizing  $\tau_{vac}/\tau$ , with time, flow and energy constraints. This problem is generally difficult to solve since the variables are time-dependent. The authors then consider a special case where data flow routing and energy consumption only depend on the mobile charger's location. That is to say, as long as the mobile charger visits some point along the path, the data flow routing and energy depletion will not change in spite of the time when the mobile charger visits the point. In essence, this special case comes based on the observation that the mobile charger moves at a constant velocity. The following theorem has been proved.

**Theorem 12.3** ([22]) *The optimal value of the spatial-dependent only problem formulation is the same as the general time-dependent problem formulation.*

The spatial-dependent only problem formulation is still hard to solve since the path has infinite number of points. The authors resort to approximation method based on discretizing the path, treating a segment as a logical point. The proposed approximation method achieves a  $(1-\varepsilon)$ -optimal solution. The basic idea is to model the energy consumption of a sensor node corresponding to a logical point (in fact a segment) as the worst case to that point. Then the lower bound of  $\tau_{vac}/\tau$  can be calculated. The authors have proved that the low bound is sufficient for achieving the  $(1-\varepsilon)$  near-optimal solution.

### 12.2.2.3 Stochastic Analysis and Battery-Aware Charging

Wang, Yang and Li [21] observe that most schemes proposed in the literature are predetermined in terms of which sensor to charger and in which order. The authors assume that sensor nodes are placed on a virtual grid and time is slotted. The mobile charger follows a random walk mobility model. In order to ensure that the network can operate forever without depleting any node's energy, it is assumed that every node is forced to sleep once its energy reserve goes below the sleep threshold  $L$ . At the same time, the mobile charger usually does not charge the sensor to its full capacity since it takes too long for keeping other nodes alive. They propose to use the Markov Chain to model the wireless recharge process. Each sensor works with probability  $p$  and sleeps with probability  $1 - p$ . In the model, the state represents the energy level of a sensor node. A node transfers from state  $i$  to state  $i + R$  in one step if it gets recharged, where  $R$  is the energy received from the mobile charger in a time slot. It is also possible to generate the transition matrix for this Markov Chain model based on the above information. Generally, the steady state probabilities of all the states can be obtained through eigen decomposition. Here it is hard to do eigen decomposition since the variable  $R$  is changing. The authors propose a recursive algorithm to solve this problem based on the fact that the Markov Chain forms an  $R$ -th order linear recurrence equation. Then the steady state probability that a sensor is in mandatory sleep mode ( $\pi_L$ ) can be derived and the percentage of inactive nodes and failed nodes can be calculated as well. These two rates can be used for network planning.

The authors further propose two algorithms for sensor activation and recharging. The linear adaptation and prioritized recharge algorithm (LAPR) is used to adjust the working probability for the sensors. The working probability increases and decreases according to its state in the last time slot. The probability resets to the ratio of  $R$  to the node full capacity  $M$  whenever it get recharged by a mobile charger. The mobile charger can enquiry the battery level of sensor nodes and moves towards the area with lower battery level. The battery-aware sensor activation and  $k$ -step selective recharge algorithm (BSR) is similar to LAPR except that this algorithm does not consider the last  $k$  nodes which have been recharged by the mobile charger.

### 12.2.2.4 Tradeoff Between Data Latency and Charging Efficiency

Wang, Li and Yang [18] raise the mismatch issue of charging latency versus data collection latency. With the current charging technology, charging takes up to 90 minutes but data collection costs only several minutes. It is possible that data become obsolete when the mobile charger returns to the base station after finishing its charging. The authors propose to use a dedicated mobile sink for data collection so as to reduce the data collection latency. Besides the mobile sink, multiple mobile chargers are used in the network to charge the nodes, ensuring no node dies out of energy. It is assumed that sensor nodes are deployed uniformly randomly in the field. The network will be organized into clusters. The mobile sink visits every cluster head to

collect data and deliver them to the static sink when it returns. The mobile charger charges the sensor node based on its current energy level. The information on energy level of sensor can be gathered through the scheme proposed in [19]. The authors try to answer two questions. The first one is how many clusters are needed to cover the whole network to minimize the data collection latency. The second one is how many mobile chargers are needed to guarantee that no sensor node runs out of energy. As for the first question, the authors believe that it is equivalent to finding a complete coverage of the sensing field with minimum number of circles of radius  $r = kd_r$ . Here  $k$  is the biggest hop number a cluster head can cover and  $d_r$  is the transmission range of a sensor node. The following theorem gives the lower bound of number of circles (clusters).

**Theorem 12.4** ([18]) *The number of circles with radius  $r$  to cover a square area with side length  $L$  should be greater than  $2\sqrt{3}(L^2 - 2\pi r^2)/9r^2$ .*

As for the second question, the authors have the following result.

**Theorem 12.5** ([18]) *The minimum number of mobile chargers for forever network operation is  $\lceil(2.33\sigma_c + \mu_c n_c - E_0)T_r/(C_s T)\rceil$ .*

Here  $n_c$  is the lower bound of the number of clusters.  $\mu_c = \sigma_c^2$  is the average energy consumption in a cluster in time  $T$ .  $E_0$  is the total initial energy of sensor nodes in the network.  $T_r$  is the time required for a charger to fully charge a sensor node to its capacity  $C_s$ . These two theoretical results serve as good guidelines for network planning when we want a balance between data collection delivery and charging efficiency.

The scheme proposed in [20] is used for scheduling the mobile charger. The intuitive behind this scheme is to cluster nodes according to their energy demands and locations to avoid charging nodes back and forth. Also the scheme ensures that node in emergency of energy gets higher priority when being charged.

### 12.2.3 Using Minimum Mobile Chargers

Using multiple mobile chargers is necessary since a single mobile charger is usually capacity-limited. For large-scale wireless sensor networks, using multiple mobile chargers has been proposed to keep the network running. A natural question is how to charge the whole network with minimum mobile chargers. Dai, Wu and Xu et al. [8] examine this problem and present interesting theoretical results. The minimum number of mobile chargers problem is proved to be NP-hard and approximation algorithms are given. Hu and Wang [11] propose a two-step approach to solve this problem. The first step is to divide a Hamilton tour into sub-tours and the second is to assign these sub-tours to minimum number of mobile chargers in a greedy fashion. Numerical results indicate that the proposed heuristic performs quite close to the optimum.

### 12.2.3.1 Hardness and Approximation

Dai, Wu and Xu et al. [8, 9] study the minimum number of mobile chargers for keeping a rechargeable sensor network immortal. The authors assume that multiple mobile chargers are dispatched by the sink to charge the sensors periodically. Each mobile charger visits and charges a subset of sensor nodes and then returns to the sink to be refilled. The mobile charger repeats its schedule after a period. This period includes traveling time, charging time and vacation time which is the time duration when charger stays idle at the sink. Different mobile chargers have different periods so no one needs to wait for the others. A weighted complete graph is used to represent the network. For an edge connecting node  $i$  and  $j$ , the edge weight  $w(i, j)$  is the traveling time for a mobile charger to move from one node to the other. It is assumed that the edge weights are symmetric and form a metric space. The minimum mobile chargers problem (MinMCP) has been formally defined as: To find a minimum number of mobile chargers starting from the sink and charging all the sensor nodes, ensuring that no nodes depletes its energy.

MinMCP is proved to be NP-hard by reduction from Distance Constrained Vehicle Routing Problem (DVRP). Accordingly, the authors propose to solve a relaxed version of MinMCP where the linear constraint over the traveling time of mobile chargers is removed. An approximation algorithm is proposed for the relaxed MinMCP. The algorithm is based on  $\gamma$ -Constant Transformation, DVRP algorithm and Nearest Neighbour Algorithm for TSP (Travelling Salesman Problem).  $\gamma$ -Constant Transformation is a metric-retained adjustment of edge weights of a graph. Then a feasible solution for MinMCP is possible by considering the linear constraint again. The authors present theoretical results in terms of approximation ratio for the proposed solution for the original MinMCP.

### 12.2.3.2 A Two-Step Approach

A two-step approach is described in [11] to solve the minimum mobile chargers problem for wireless rechargeable sensor networks. Heuristics are used due to the hardness of the problem. The two steps are tour construction and tour assignment. The first one is to construct minimum number of tours to exactly cover all the nodes in the network. Here the tour refers to a sequence of nodes which can be charged by a single mobile charger and none of them runs out of energy. It has been proved that the minimum tour construction is NP-hard. Accordingly, a Hamilton tour (traversing all nodes including the sink) is constructed by using the Lin-Kernighan algorithm. Then the Hamilton tour will be cut into several sub-tours. Each sub-tour is maximal in terms of number of nodes which can be charged by a single mobile charger and none of them will use up their energy. The second step is to assign these sub-tours to a minimum number of mobile chargers. It is referred to as tour assignment problem which is proved to NP-hard by reduction from the set-partition problem. Note that a single mobile charger might cover several sub-tours. The authors propose a heuristic to assign the sub-tours to mobile chargers. Numerical results indicate that

the proposed solution achieves an approximation ratio less than 1.1 in comparison to the lower bound of minimum number of mobile chargers.

### **12.2.4 Collaborative Mobile Charging**

Zhang, Wu and Lu [24] propose the idea of collaborative charging for the first time. In collaborative charging, mobile chargers can charge each other as well. Accordingly, energy can be transferred among mobile chargers. This is a brand new paradigm for wireless power transfer. They propose different protocols for different scenarios, starting from the simplest case where sensors are deployed along a line. Madhja, Nikoletseas and Raptis propose to use two layers of mobile chargers in [15]. The upper layer of mobile chargers are called super chargers. The lower layer of chargers are ordinary mobile chargers. The super chargers charge mobile chargers and the ordinary mobile chargers charge sensor nodes. They propose heuristics for different cases depending on how much network information is available and whether the coordination among super chargers is centralized or distributed.

#### **12.2.4.1 Homogeneous Collaborative Mobile Charging**

In [24] Zhang, Wu and Lu first propose the concept of collaborative charging among mobile chargers for wireless rechargeable sensor networks. Collaborative charging among mobile chargers means that besides charging the ordinary sensor nodes, mobile chargers can charge each other as well. In this work, the authors assume different charging efficiencies for charging sensors and for charging mobile chargers. Energy consumption for traveling and energy loss during charging are overhead energy. The final energy received by the sensors is called payload energy. Then the ratio of payload energy over all the energy consumed is defined as energy usage effectiveness. The authors propose different schemes to optimize the energy usage effectiveness for different scenarios from the basic linear network to two-dimensional network. For the simplest case where every sensor in a line has the same recharging cycle (the longest period a fully charged sensor can last), the charging efficiency is ideally 100 %. Since there is no charging loss during charging, either charging ordinary sensor nodes or mobile chargers, minimizing the traveling distance can maximize the energy usage effectiveness. The proposed solution is to let as few mobile chargers as possible to carry all the residual energy of all mobile chargers to charge the sensors, thus saving traveling distances. A more complex case is the energy loss during charging. The authors find that in this case it is better to exploit the collaborative charging wisely. Particularly, no collaborative charging is needed if it covers no less sensor nodes than using collaborative charging because collaboration among mobile chargers increases overhead energy. The strategy without collaborative charging use a single mobile charger for each sensor node and tunes the traveling distance of each mobile charger such that the residual energy reduces to zero when it

returns to the base station. Collaborative charging can be used for those sensor nodes not covered by non-collaborative charging. For other cases, the authors also present efficient collaborative charging schemes. All these schemes are combination of the schemes for the aforementioned schemes for the simple cases.

#### 12.2.4.2 Hierarchical Collaborative Mobile Charging

Madhja, Nikoletseas and Raptis [15] propose to use two layers of mobile chargers. The lower layer of mobile chargers charge ordinary sensor nodes and the higher layer of mobile chargers charge lower layer chargers. Initially, each mobile charger takes care of a group of sensors and each higher layer charger (super charger) charges a group of mobile chargers. The super chargers may cooperate with each other to improve the charging efficiency. The authors propose a coordination decision problem (CDP) and prove that it is NP-complete by reduction from Bin Packing Decision Problem. The CDP deals with whether there is a partition of mobile chargers such that every super charger can charge them to their full capacity. Accordingly, heuristics are proposed. Depending on how much network information is available, whether there is coordination among the super chargers and the coordination is distributed or centralized, the authors propose four kinds of protocols for different scenarios. Extensive simulations have been done to evaluate the performance of the proposed protocols. Results indicate that with two-layer network knowledge and centralized coordination among super chargers, the network performance in terms of network life time has been improved greatly. These protocols serve as good guidelines for deploying different types of chargers in the network.

#### 12.2.5 Localization with Mobile Chargers

Localization in wireless sensor networks has been investigated for many years. The basic methods can be classified into two categories, range-based localization and range-free localization. Range-based localization needs the ranging between the target node and the anchor node. Such methods includes those of Angle of Arrival (AoA), Time of Arrival (ToA), Time Difference of Arrival (TDOfA) and Received Signal Strength Index(RSSI). The range-free methods rely on the connectivity information among nodes to infer the location information. Usually range-based localization methods need extra hardware, although they provide higher precision. Range-free methods have no such requirement but their precision is lower. Shu, Cheng, Gu, Chen and He [16] propose to use the time of charging (ToC) in localization in wireless rechargeable sensor networks with a mobile charger. ToC can be used to measure the distance between the mobile charger and the target node. Here the mobile charger serves as an anchor node for localization and charges the nodes at the same time. ToC-based localization therefore belongs to the range-based category. Their work assumes the use of an omnidirectional antenna. Chang, Wu, Wang and Chen design

two methods for localization with mobile charger with directional antenna in wireless rechargeable sensor networks in [4]. The current available charging devices always use directional antenna due to its higher charging efficiency.

### 12.2.5.1 Using Omnidirectional Antenna

In [16], Shu, Cheng, Gu, Chen and He propose the concept of time of charging (ToC) for the first time for localization in wireless rechargeable sensor networks. It is observed that there is an obvious correlation between the charging time and the distance between the chargers and the sensor node. Use of ToC can help localize the nodes in the networks. The basic idea of the proposed scheme is to gradually reduce the potential area where the target node could be when the mobile charger moves in the network. In particular, two region dividing schemes are proposed in this work. The first one, Inter-Node Division, divides the feasible region into two parts with the perpendicular of the line connecting the two stops of the mobile charger. Depending on which one of the stops is closer to the target node, Inter-Node Division can decide which part is the narrowed down potential region for the target node. The other one, Inter-Area Division, makes use of the charging range of the mobile charger. The basic idea is to further reduce the feasible region of the target node by reducing it to the intersection or difference of the original feasible region and the circular coverage of the mobile charger. The authors discuss how to optimize the stops of mobile chargers in order to localize the target node. For both one node and multiple nodes scenarios, the intuition behind is to cut the original feasible regions into two parts such that the length of its diagonal is minimized after division. A smaller diagonal of the feasible region means smaller localization error.

### 12.2.5.2 Using Directional Antenna

Chang, Wu, Wang and Chen [4] observe that the current available COTS (Commercial off-the-shelf) energy chargers usually use a directional antenna instead of an omnidirectional one. They propose to make use of the angular property of the directional mobile charger. Two schemes are proposed, namely, Angle Division and Grid Division. As for the angle division, the feasible region can be reduced to the intersection of the original feasible region and the sector area of the mobile charger if the target node is covered. The angle division is designed for deployment field of convex polygon shape. As for the grid division, it is efficient when the nodes are distributed uniformly and the area is approximate to a rectangle. The basic idea of grid division is to use the chords of the angular coverage of the mobile charger to partition the field into grids. Exploitation of time of charge can further speed up the localization and improve precision. The authors conduct experiments and simulations to evaluate the performance of the proposed schemes.

### 12.2.6 Stochastic Event Capture with Mobile Chargers

Wireless sensor network technology can be applied to event monitoring scenarios. There are quite a few interesting problems when event monitoring application meets wireless charging. The basic question is how to schedule the mobile charger and how to activate the sensors such that the quality of monitoring (QoM) is optimized. Cheng, He, Jiang, Gu and Chen [5] first notice this problem. The results on moving speed and charging time of the mobile charger, and the duty cycle of sensors are interesting and insightful although simplified assumptions are used to make the problem solvable. Dai, Jiang and Wu et al. [7] make generalization over their work and prove that the problem is NP-hard. Accordingly they present useful approximation algorithms.

#### 12.2.6.1 Moving Speed, Charging Time and Duty Cycle

Cheng, He, Jiang, Gu and Chen investigate this problem for the first time in [5]. It is assumed that the mobile charger charges the sensor nodes when moving in the network. Each sensor node monitors a point of interest (PoI). The metric QoM is defined as ratio of captured events over all events in the long run. Due to the random appearance of events and the on-off working style of sensors, it is reasonable that not all events can be captured. The authors analyze QoM of three scenarios: (1) the mobile charger moves at constant speed to recharge the sensors and the sensors consume energy at their best effort; (2) the mobile charger stops to charge sensor nodes for a duration and sensor nodes deplete energy as much as possible; (3) the mobile charger stops to charge the sensor node and the sensor nodes work in duty cycle. For the first scenario, the authors have the following result.

**Theorem 12.6** ([5]) *In order to achieve the maximum QoM, it is necessary that the mobile charger moves at its maximum speed.*

In essence, this theorem states that if the charger charge the nodes on the run and the sensor node consumes its energy as much as possible, the mobile charger needs to move as fast as possible for higher QoM.

For second scenario, the authors assume that the charger stays at each sensor for a constant duration of time. The authors present the following theorem.

**Theorem 12.7** ([5]) *All of the sensors can work constantly if the number of sensors is not greater than  $\tau / (\beta^2 P_{act})$  and the charging duration is no less than  $(P_{act}L - 2Ar)\beta^2 / ((\tau - N P_{act}\beta^2)v)$ , where  $A = 2\tau r / (\beta(r + \beta))$ .*

Here  $\tau$ ,  $\beta$  and  $r$  are system parameters related to charging efficiency;  $P_{act}$  is the power consumption for activating a sensor;  $L$  is the length of the traveling path of the mobile charger;  $N$  is the number of sensors;  $v$  is the moving speed of the mobile charger. For the third scenario, the authors have the following theorem regarding to the maximization of QoM.

**Theorem 12.8** ([5]) Given the moving speed  $v$  and the charging duration  $t$  of the mobile charger, the QoM is maximized (1) with no duty cycle if  $1/\alpha \leq \Delta E/(P_{act} - P_{slp})$ ; (2) with a specific duty cycle if otherwise.

Here  $1/\alpha$  is the expected event staying time;  $\Delta E$  is the extra energy consumption when the sensor wakes up from sleeping.  $P_{slp}$  is the sleeping power of the sensor node. This theorem states essentially that the sensor needs to be active (without duty cycle) if the event stays shorter than a threshold and it can work with duty cycle if otherwise.

### 12.2.6.2 Generalization and Approximation

Dai, Jiang and Wu et al. [7] generalize the work by Cheng, He, Jiang, Gu and Chen [5] and present approximation algorithms. They assume that a single PoI (Point of Interest) can be monitored by multiple sensors, the charging duration for every sensor can be different and a utility function for measuring the quality of monitoring (QoM) is used. The problem in this work is formally defined as the maximum QoM charging and scheduling problem (MQCSP). The objective of MQCSP is  $\text{Max } \sum_{i=1}^n w_i Q(i)$ , subject to time, charging and energy constraints. Here  $w_i$  is the weight associated with the  $i$ -th PoI and  $Q(i)$  is the QoM at the  $i$ -th PoI. MQCSP is quite challenging since it involves optimization over factors such as traveling time, charging duration, sensor activation and the calculation of QoM. The authors propose to solve a relaxed version R-MQCSP in which the traveling time of the mobile charger is neglected. In fact, the traveling time could be much less than the charging time. However, even R-MQCSP is proved to be NP-hard via restriction to a known NP-hard problem Maximum Coverage Problem. Then the authors show that R-MQCSP can be converted into a monotone submodular maximization function, assuming that the utility function is concave. An approximation algorithm specially tailored for the original MQCSP is proposed based on proposed algorithm for R-MQCSP. The following theorem states the property of the algorithm.

**Theorem 12.9** ([7]) The proposed algorithm for MQCSP achieves  $\frac{1}{6}(1 - \frac{\tau_{TSP}(V) + \max\{c_i\}}{\tau_w})$ -approximation.

Here  $\tau_{TSP}(V)$  is the traveling time of the mobile charger which moves along a specified TSP route traversing all nodes in the set  $S$ .  $\tau_w$  is the total maximum working time of the charging schedule, including the travel overhead and the charging time of all selected sensors.  $c_i$  is the required charging time for the charger to fulfill enough energy to the sensor node such that it can work for one time slot.

### 12.2.7 Energy Provision for Mobile Nodes

In [10] and its extension [6], the energy provision problem with mobile nodes in terms of moving velocity and battery capacity is discussed. This work is quite interesting

because the authors assume that there are one or multiple static chargers deployed in the network while the ordinary sensor nodes are mobile which is in contrast to the most of the existing works with mobile chargers. The quality of energy provision (QoEP) metric is used in this work. Before a formal definition of QoEP, the instantaneous quality of energy provisioning (IQoEP) of a node at time  $t$  is defined as,

$$IQoEP(t) = \frac{p_r(t)}{p_s}, E_{re}(t) = 0 \wedge p_r(t) < p_s.$$

Here  $p_r(t)$  is the cumulative charging power the node received at time  $t$ ;  $E_{re}(t)$  is the remained energy of the node;  $p_s$  is the constant power consumption when the node is working. Then the QoEP is defined as,

$$QoEP = \lim_{t \rightarrow \infty} \frac{1}{t - t_0} \int_{t'=t_0}^t IQoEP(t') dt'.$$

This definition of QoEP captures the expected portion of time in the long run that the node can operate normally. It is however time-dependent. The authors further define a spatial-dependent QoEP as follows. Quality of energy provision at location  $x$  ( $LQoEP(x)$ ) of a node is the expected proportion of cumulative time that the node maintains normal operation to the duration the node stays at the location  $x$ .

$$LQoEP(x) = \lim_{t \rightarrow \infty} \frac{\int_{t'=t_0}^t IQoEP(t') I(t', x) dt'}{\int_{t'=t_0}^t I(t', x) dt'},$$

where  $I(t', x)$  equals to 1 if a node stays at location  $x$  at time  $t'$ , and 0 otherwise. Then QoEP can be rewritten as

$$QoEP = \int_{\Omega} LQoEP(x) f_{dis}(x) dx.$$

Here  $f_{dis}(x)$  is the spatial distribution function at location  $x$ . Now QoEP depends only on spatial information provided that  $LQoEP(x)$  exists. The authors first drive theoretical bound of the QoEP in 1D case with a single source in the following theorem.

**Theorem 12.10** ([6]) *The QoEP in 1D case with a single energy source is no greater than  $QoEP_{min} + 2 \frac{\min\{\Lambda_c^{opt}(\Omega_o), \Lambda_h^{opt}(\Omega_i)\}}{p_s}$ .*

Here it is assumed that the energy source is located at the origin point and the whole line is divided into two parts.  $\Omega_i$  is the part close to the energy source where a node receives power no less than  $p_s$ .  $\Omega_o$  is the remained part.  $\Lambda_h^{opt}(\Omega_i)$ ,  $\Lambda_c^{opt}(\Omega_o)$  are the maximum expected received energy for the part  $\Omega_i$  and the maximum expected energy consumption rate for part  $\Omega_o$ , respectively.  $QoEP_{min}$  is the derived lower

bound for 1D case with a single energy source which is only related to the spatial distribution of the nodal moving trace.

As for the 2D case with multiple energy sources, the following result is given.

**Theorem 12.11** ([6]) *The QoEP is at least  $\int_{\Omega} f_{dis}(x, y) J(\frac{p_r(x,y)}{p_s}) dx dy$  for 2D case with multiple sources, where  $J(x) = x$  for  $0 \leq x \leq 1$  and  $J(x) = 1$  for  $x > 1$ .*

Here  $f_{dis}(x, y)$  is the spatial distribution of the moving trace  $\Omega$  of the node and  $p_r(x, y)$  is the energy received by the node at location  $(x, y)$ .

## 12.3 Distributed Approach

Most works related to using mobile chargers or mobile nodes in wireless rechargeable sensor networks adopt a centralized approach. The proposed problems are mostly NP-hard and the authors resort to heuristics. Usually, a centralized approach assumes the availability of global information about the network. In spite of this, there are some works concentrating on distributed schemes for mobile charger scheduling and planning. Dai, Jiang, Wu and Chen [12] propose the idea of on-demand scheduling of mobile chargers where the mobile charger charges the sensor nodes based on the received requests from the nodes. Angelopoulos, Nikoletseas and Raptis [1] also propose the idea of using distributed and reactive schemes for mobile charger planning. Madhja and Nikoletseas and Raptis [13, 14] further propose the coordination schemes for multiple mobile chargers.

### 12.3.1 On-Demand Mobile Charger Scheduling

Using mobile chargers for wireless charging in sensor networks is an economic way compared to deployment of static chargers. Most works about mobile chargers assume that the traveling path of the mobile charger is pre-calculated. Obviously the pre-calculation needs a priori information (e.g. the energy status of all nodes). Dai, Jiang, Wu and Chen [12] propose the idea of on-demand scheduling of mobile chargers based on no a priori knowledge. The sensor nodes can send energy charging requests and the mobile charger decides where to move on receiving the energy requests. The authors consider an event monitoring application where sensors are dispersed in the field to cover a few PoIs (Point of Interest). The mobile charger will travel in the network and charge the sensors based on its received energy requests. At any time  $t$ , the coverage utility is defined as the ratio of the number of covered PoIs currently to the number of PoIs that can be covered by all the sensors. Note that some sensors might be turned off not to cover a PoI. The authors prove that the maximum covering utility charging scheduling (MCUCS) problem is NP-complete by reduction from the geometric TSP problem. Here the MCUCS problem is to find whether there is a feasible schedule for the mobile charger to visit the sensors such

that all events will be captured. Three heuristics are proposed. The first one is to meet the energy request with maximum marginal coverage utility; The second one is to satisfy the energy request with maximum coverage utility gain over its service time. Here the service time includes traveling time and charging time. The intuition behind this is that some energy requests are less preferable if the nodes are far away although they might bring more utility gain.

### **12.3.2 Planning for Single Mobile Charger**

In [1], Angelopoulos, Nikoletseas and Raptis propose the idea of using distributed and reactive schemes for the planning of mobile charger. They notice that most centralized schemes are of high computational complexity. They propose to consider two related issues: (1) how much each sensor needs to be charged; (2) the trajectories the mobile charger should follow. They propose to use a new metric to measure the importance of each node, i.e. node criticality, which is related to the traffic passing the node and the energy consumed by the node. A node with higher traffic and low residual energy is usually of higher priority to be recharged. Three protocols are evaluated through simulations. The first protocol is one relying on global knowledge of the network. This protocol assigns priorities according to the criticality of the node and the distance between the mobile charger and the node. The higher is the criticality and the nearer is the node, the higher is its priority. In the protocol with limited global knowledge, the sink collects information about some representative nodes across the network and informs the mobile charger. In the protocol with local knowledge, the mobile charger moves along a set of concentric circles.

They further elaborate their idea in [2]. Node criticality is improved to energy/flow criticality which is the multiplication of flow passing the node and energy consumption at the node. The protocols with global network knowledge, limited network knowledge and local knowledge are evaluated extensively and thoroughly.

Angelopoulos, Nikoletseas and Raptis et al. [3] propose the so-called charger dispatch decision problem (CCDP) where given the network information including energy capacity of every node, distance among nodes and charging information of the mobile charger, they need to decide whether there is a feasible schedule of the mobile charger to charge the sensors and no data is lost due to deficit of energy. This problem is proved to be NP-complete. The authors find that instead of always charging the nodes to their full capacity, the strategy of partial charging is more efficient. Five trajectories for the mobile charger are discussed: (1) In the global knowledge traversal strategy the mobile charger move first to the node minimize  $(1 + \frac{E_{curr}}{E_{init}})(1 + \frac{dist_{curr}}{2R})$ . Here  $E_{curr}$ ,  $E_{init}$ ,  $dist_{curr}$ ,  $R$  refer to the current energy, initial energy, distance of the sensor and the radius of the field, respectively; (2) In the spiral traversal strategy the mobile charger starts from the sink and travels around circles with increasing radii. This strategy covers the whole network but is not adaptive; (3) In the diameter traversal strategy, the mobile charger first moves to the perimeter of the network and moves along the perimeter for a certain degree once it reaches the perimeter;

and then it moves towards the other side of the network along a diameter; (4) In random walk traversal strategy, the mobile charger staying at a node turns to one of its neighbors with equal probability; (5) In the proposed adaptive circular traversal protocol, the mobile charger starts from the sink and travels along concentric circles with increasing radii; it keeps its moving direction if it is moving towards energy-hungry areas but changes its direction if it is entering energy-rich areas. Whether the area is energy-hungry or energy-rich is decided by a comparison between the current energy profile and the historical energy profile.

### ***12.3.3 Coordinating Multiple Mobile Chargers***

In [13], Madhja and Nikoletseas and Raptis propose the concept of distributed coordination among multiple mobile chargers. The extended version of [13] appears in [14]. It is assumed that there are multiple mobile chargers deployed in the network to charge all the static sensor nodes. The authors consider two critical issues: (1) how can these mobile chargers coordinate with each other such that the network performance is optimized; (2) what kind of trajectories the mobile chargers should follow. It is assumed that the network is deployed in a circular area and the network is divided into several sectoral areas. The mobile charger can charge at most one sensor and the data rate at different sensors are different (drawn from uniform distribution). In the proposed scheme, the charging process consists of two phases, coordination phase and charging phase. The mobile chargers might have different energy reserve after serving the network for a while since the data rates of sensor nodes are different. In coordination phase, mobile chargers with less energy can be assigned to smaller areas. The coordination among chargers can be finished in a centralized or distributed way. The mobile chargers might have quite a few choices of trajectories depending on how much information on the network they own in the charging phase.

Specifically, the authors present five coordination and charging protocols. The first one is the distributed coordination (DC) protocol. In its coordination phase, neighboring mobile chargers coordinate with each other to either enlarge or shrink the charging area depending on the energy information. In the charging phase, the mobile charger moves across the whole network to cover all sensor nodes. The second one is the centralized coordination (CC) protocol. In its coordination phase, each mobile charger is assigned to a sector proportional to its energy reserve. The trajectory of mobile charger can be a scanning scheme to visit all nodes in its charging area. The third one is the distributed coordination local knowledge (DCLK) protocol. Its coordination phase is similar to that of DC protocol. The local knowledge the mobile charger acquires in the charging phase is the information on the residual energy of the nodes in its charging area. Accordingly, the mobile charger can charge some sub-areas first. The fourth one is the centralized coordination reactive knowledge (CCRK) protocol. The coordination information is exchanged through the sink node. The mobile charger puts priorities to nodes according the distance to travel and the residual energy at the node. The fifth one is the centralized coordination global

knowledge (CCGK) protocol. Different from the coordination phase in CC protocol, CCGK's coordination is based on the clustering of nodes and clusters are assigned to mobile chargers, although it is also centralized. In its charging phase, the mobile charger moves first to the node of its cluster which minimizes  $(1 + \frac{dist_{ij}}{2R})(1 + \frac{E_i}{E_{max}})$ . Here  $dist_{ij}$  is the traveling distance from mobile charger  $j$  to sensor node  $i$ ;  $E_i$  and  $E_{max}$  are the residual energy and capacity of node  $i$ .

## 12.4 Conclusion

In this chapter, we review the representative works and present interesting results in using mobile nodes in wireless ad hoc networks with wireless power transfer in this chapter. As for centralized approach we cover topics such as joint data gathering and mobile charging, planning of a single mobile charger or multiple chargers. Most related problems are proved to be NP-hard and heuristics have been proposed. As for the distributed approach, we discuss on-demand mobile charging and planning for one or more multiple chargers. Distributed approach is reactive and relies on no or limited network information.

## References

1. Angelopoulos, C.M., Nikoletseas, S., Raptis, T.P.: Efficient wireless recharging in sensor networks. In: IEEE International Conference on Distributed Computing in Sensor Systems (2013)
2. Angelopoulos, C.M., Nikoletseas, S., Raptis, T.P.: Wireless energy transfer in sensor networks with adaptive, limited knowledge protocols. Comput. Netw. (2013)
3. Angelopoulos, C.M., Nikoletseas, S., Raptis, T.P., Raptopoulos, C., Vasilakis, F.: Improving sensor network performance with wireless transfer. Int. J. Ad Hoc Ubiquitous Comput. (2013)
4. Chang, Z., Wu, X., Wang, W., Chen, G.: Localization in wireless rechargeable sensor networks using mobile directional charger. In: IEEE Global Communications Conference (GlobeCom) (2015)
5. Cheng, P., He, S., Jiang, F., Gu, Y., Chen, J.: Optimal scheduling for quality of monitoring in wireless rechargeable sensor networks. IEEE Trans. Wirel. Commun. (2013)
6. Dai, H., Chen, G., Wang, C., Wang, S., Wu, X., Wu, F.: Quality of energy provisioning for wireless power transfer. IEEE Trans. Parallel Distrib. Syst. (2015)
7. Dai, H., Jiang, L., Wu, X., Yau, D.K., Chen, G., Tang, S.: Near optimal charging and scheduling scheme for stochastic event capture with rechargeable sensors. In: IEEE International Conference on Mobile Ad hoc and Sensor Systems (MASS) (2013)
8. Dai, H., Wu, X., Chen, G., Xu, L., Lin, S.: Minimizing the number of mobile chargers for large-scale wireless rechargeable sensor networks. Comput. Commun. (2014)
9. Dai, H., Wu, X., Xu, L., Chen, G., Lin, S.: Using minimum mobile chargers to keep large-scale wireless rechargeable sensor networks running forever. In: International Conference on Computer Communication and Networks (ICCCN) (2013)
10. Dai, H., Xu, L., Wu, X., Dong, C., Chen, G.: Impact of mobility on energy provisioning in wireless rechargeable sensor networks. In: IEEE Wireless Communications and Networking Conference (WCNC) (2013)

11. Hu, C., Wang, Y.: Minimizing the number of mobile chargers in a large-scale wireless rechargeable sensor network. In: IEEE Wireless Communications and Networking Conference (WCNC) (2015)
12. Jiang, L., Dai, H., Wu, X., Chen, G.: On-demand mobile charger scheduling for effective coverage in wireless rechargeable sensor networks. In: Annual International Conference on Mobile and Ubiquitous Systems: Computing, Networking and Services (MobiQuitous) (2013)
13. Madhja, A., Nikoletseas, S., P.Raptis, T.: Efficient, distributed coordination of multiple mobile chargers in sensor networks. In: ACM International Conference on Modeling, Analysis and Simulation of Wireless and Mobile Systems (MSWiM) (2013)
14. Madhja, A., Nikoletseas, S., Raptopoulos, C., Vasilakis, F.: Distributed wireless power transfer in sensor networks with multiple mobile chargers. *Comput. Netw.* (2015)
15. Madhja, A., Nikoletseas, S., Raptis, T.P.: Hierarchical collaborative wireless charging in sensor networks. In: IEEE Wireless Communications and Networking Conference (WCNC) (2015)
16. Shu, Y., Cheng, P., Gu, Y., Chen, J., He, T.: Toc: Localizing wireless rechargeable sensors with time of charge. In: IEEE International Conference on Computer Communications (INFOCOM) (2015)
17. Shu, Y., Yousefi, H., Cheng, P., Chen, J., Gu, Y., He, T., Shin, K.G.: Near-optimal velocity control for mobile charging in wireless rechargeable sensor networks. *IEEE Trans. Mob. Comput.* (2015)
18. Wang, C., Li, J., Yang, Y.: Low-latency mobile data collection for wireless rechargeable sensor networks. In: IEEE International Conference on Communications (ICC) (2015)
19. Wang, C., Li, J., Ye, F., Yang, Y.: Multi-vehicle coordination for wireless energy replenishment in sensor networks. In: IEEE International Parallel and Distributed Processing Symposium (IPDPS) (2013)
20. Wang, C., Li, J., Ye, F., Yang, Y.: Recharging schedules for wireless sensor networks with vehicle movement costs and capacity constraints. In: IEEE International Conference on Sensing, Communication and Networking (SECON) (2014)
21. Wang, C., Yang, Y., Li, J.: Stochastic mobile energy replenishment and adaptive sensor activation for perpetual wireless rechargeable sensor networks. In: IEEE Wireless Communications and Networking Conference (WCNC) (2013)
22. Xie, L., Shi, Y., Hou, Y.T., Lou, W., Sherali, H.D., Midkiff, S.F.: Bundling mobile base station and wireless energy transfer: modeling and optimization. In: IEEE International Conference on Computer Communications (INFOCOM) (2013)
23. Xie, L., Shi, Y., Hou, Y.T., Sherali, H.D.: Making sensor networks immortal: an energy-renewal approach with wireless power transfer. *ACM/IEEE Trans. Netw.* (2012)
24. Zhang, S., Wu, J., Lu, S.: Collaborative mobile charging. *IEEE Trans. Comput.* (2015)
25. Zhao, M., Li, J., Yang, Y.: Joint mobile energy replenishment and data gathering in wireless rechargeable sensor networks. In: 23rd International Teletraffic Congress (ITC) (2011)
26. Zhao, M., Li, J., Yang, Y.: A framework of joint mobile energy replenishment and data gathering in wireless rechargeable sensor networks. *IEEE Trans. Mob. Comput.* **13**(12) (2014)

# Chapter 13

## Strategies for Wireless Recharging in Mobile Ad-Hoc Networks

Constantinos Marios Angelopoulos, Julia Buwaya, Orestis Evangelatos and José Rolim

**Abstract** In this chapter we investigate the problem of wireless power transfer in mobile ad-hoc networks. In particular, we investigate which traversal strategy should a Mobile Charger follow in order to efficiently recharge agents that are randomly and dynamically moving inside an area of interest. We first formally define this problem as the Charger Traversal Decision Problem and prove its computational hardness. We then define a weighting function which evaluates several network parameters in order to prioritize the nodes during the charging process. Based on this function we define three traversal strategies for the MC; a global-knowledge strategy that uses an Integer Linear Program to optimize its trajectory; a global-knowledge strategy which tessellates the network area and prioritizes the charging process over each tile; a local-knowledge strategy that uses local network information collected and ferried distributively by the moving agents. We also evaluate two naive zero-knowledge strategies; a space-filling deterministic one in which the MC systematically sweeps the network area and a randomized one in which the MC performs a blind random walk. We evaluate these strategies both in homogeneous and heterogeneous agent distributions and for various network sizes with respect to number of alive nodes over time, energy distribution among the nodes over time and charging efficiency over distance traveled. Our findings indicate that network agnostic strategies are sufficient in small networks. However, as the network scales the use of local distributed network information achieves good performance-overhead trade-offs.

---

C.M. Angelopoulos (✉)  
Bournemouth University, Bournemouth, UK  
e-mail: mangelopoulos@bournemouth.ac.uk

J. Buwaya · O. Evangelatos · J. Rolim  
University of Geneva, Geneva, Switzerland  
e-mail: Julia.Buwaya@unige.ch

O. Evangelatos  
e-mail: Orestis.Evangelatos@unige.ch

J. Rolim  
e-mail: Jose.Rolim@unige.ch

### 13.1 Introduction

In principle, the theoretical and technological know-how regarding wireless power transfer has been known since the beginning of the 20th century. However, only recently the corresponding technology has become mature enough so as to be used in practice and to be commercialized. In particular, in [1] it has been shown that through strongly coupled magnetic resonances, the efficiency of transferring 60 watts of power over a distance in excess of 2 meters is as high as 40 %. Industrial research has also demonstrated that it is possible to improve transferring 60 watts of power over a distance of up to two to three feet with efficiency of 75 % [2]. As technology constantly improves, commercial products utilizing wireless power transfer have been available on the market such as those in [3] and [4]. The potential of this technology has led to the establishment of corresponding industrial standardization bodies such as the Rezence Alliance for Wireless Power [5] and the Wireless Power Consortium (WPC) [6] that seek to maximize the use of Wireless Power Transfer.

In parallel, significant research effort is conducted in the context of this technological advance. In the field of ad-hoc networks, a new paradigm has emerged; the Wireless Rechargeable Sensor Networks (WRSN). In WRSNs sensor motes are equipped with fast rechargeable batteries [7] and with specialized hardware components called wireless power receivers. There also exist special mobile entities called Mobile Chargers (MC), that are able to wirelessly transfer power to the sensor motes while traversing the network area. The existence of the MCs enables the detailed and efficient energy management of the network while it also renders obsolete the need for complex and computationally intense energy management algorithms that infer significant computational and communication overhead to the network. However, as hand-held mobile devices demonstrate high acceptance rates by the general public, we believe that research efforts in Wireless Power Transfer should not be restricted only to WRSNs but should also address mobile ad-hoc networks in general.

**The Problem.** We consider a set of mobile agents deployed in an area of interest. The agents abstract moving people that carry portable autonomous devices, such as smartphones, smart-watches or sensor motes, that are capable of wirelessly receiving power and fast charging their batteries. The type of motion of the agents is considered to be diverse and unpredictable. Finally, we consider a single, special purpose mobile entity, called the Mobile Charger (MC), that traverses the network area of interest and is capable of wirelessly recharging devices that lie in its vicinity.

The problem we study is which traversal strategy should the Mobile Charger follow in order to efficiently recharge the moving agents of the network. We focus on the process of efficiently transferring energy from the MC to the network and therefore the strategies we design and evaluate are agnostic to any underlying, energy consuming tasks.

*Remarks.* We note that, although the wireless charging problem might look similar to other related research problems (such as aggressive data collection via mobile sinks), it admits special features that necessitate a direct approach, while the optimization of concrete trade-offs and the fine-tuning of design alternatives that arise

in wireless charging necessitate the distinct investigation of special protocol design parameters. Finally, we note that Mobile Charger optimization problems are (inherently) computationally hard e.g. in [8] we have formulated the wireless charging problem as the Charger Dispatch Decision Problem—CDDP, and showed that it is NP-complete (via reduction from the Geometric Travelling Salesman Problem, G-TSP; see e.g. [9], p. 212).

**Our Contribution.** Our contribution can be summarized as follows: (a) We formally define the Charger Traversal Decision Problem (CTDP) and prove its computational hardness. (b) We identify four network parameters that affect the MC in choosing its trajectory; the energy needs of the nodes, their energy dissipation rates, their mobility level and their distance from the MC. We define a corresponding weighting function used to prioritize the nodes during the charging process. (c) Based on this weighting function, we design three traversal strategies for the MC; a global-knowledge strategy that uses an Integer Linear Program, to compute the MC’s trajectory, a global-knowledge strategy that tessellates the network area and prioritizes each tile based on its aggregated weight, and a local-knowledge strategy that uses local network information collected and ferried distributively by the moving agents. (d) We evaluate the designed strategies along with two naive zero-knowledge ones; one space-filling deterministic strategy and one in which the MC performs a blind random walk. In our evaluation we use several performance metrics and simulate various network sizes and densities. Our findings indicate that in small networks network agnostic strategies are sufficient. However, as the network scales the use of local distributed network information achieves good performance-overhead trade-offs.

## 13.2 Related Work and Comparison

There has been much research effort in WRSNs; in particular for the case where the charged entities (e.g. sensors) are *static*. In [10, 11] authors study the cases where a Mobile Charger traverses the network area where a set of static sensors is deployed. In each work, authors focus on some particular aspect of the network (e.g. on the ratio of the MC’s vacation time over the cycle time) and provide methods in order to compute corresponding optimal charging tours. In [12], the authors formulate an energy-constrained wireless charging problem, which maximizes the number of sensors wirelessly charged by a Mobile Charger. The paper proposes heuristic solutions based on the meta-heuristics of Particle Swarm Optimization. However, the model assumes the charger has an extensive knowledge on the network and the performance evaluation is limited to simulations of small-scale networks.

In a previous work of our group [8], we study the impact of the charging process to the network lifetime for selected routing protocols. They propose a mobile charging protocol that locally adapts the circular trajectory of the Mobile Charger to the energy dissipation rate of each sub-region of the network. They compare this protocol against several other trajectories via a detailed experimental evaluation. The derived findings

demonstrate performance gains, but are *limited to uniform network deployments*, in contrast to our approach in this chapter which also considers heterogeneous node distributions.

Alternative versions of the problem have also attracted important research attention. In [13–15] the authors consider the wireless recharging problem, using multiple Mobile Chargers. In this case, several other interesting aspects emerge, such as the minimum number of chargers that suffice to cover the network area, inter-charger coordination, etc.

Few research efforts have also taken into consideration settings in which the charged entities are *mobile*. In [16] authors study the throughput of an energy-constrained mobile network where MCs recharge the battery of each mobile node. However, they do not focus on the traversal of the MC *per se* as they consider it to perform only a random walk. Also, they assume a naive mobility model for the mobile nodes (they assume identically distributed random processes). In [17] authors also consider mobile nodes and propose a novel metric, the Quality of Energy Provisioning (QoEP, to characterize the expected portion of time that a node sustains normal operation by taking into account node speed and battery capacity. In [18] authors consider a small scale network of mobile robots in which the MC needs to rendezvous with the robots in order to recharge them. Authors provide a centralized solution while considering direct-contact charging technologies.

Although these efforts successfully identify and address fundamental aspects of wireless power transfer in ad-hoc networks, they significantly differ from our approach in this chapter. They mostly consider networks with low dynamics, where the sensor motes are static or small scale networks. Also, motivated by the characteristics of the wireless power transfer via conductive charging technologies that operate efficiently in very small distances (in the order of few centimeters), in most of the previous efforts the charging model considered is point-to-point. On the contrary, we envision a wireless power transfer scheme that is based on *inductive charging*; i.e. the MC is able to simultaneously charge devices that lie inside its charging radius by creating an electromagnetic field [19].

### 13.3 The Model

In our model we consider two types of entities: the set of  $n$  *mobile agents*  $\mathcal{A} = \{A_i \mid i : 1 \leq i \leq n\}$ , that abstracts autonomous devices carried by people (such as smartphones, smart-watches and sensor motes) and a *Mobile Charger* (MC) which is a special purpose entity capable of wirelessly transferring power to devices located in its vicinity while traversing the network area  $\Omega$ . We discuss below the mobility and energy aspects of our model.

### 13.3.1 Mobility Models

We consider a planar area of interest  $\Omega$  in which the set of mobile agents  $\mathcal{A}$  is initially uniformly at random deployed. The speed at which each agent traverses the network is modelled as a random variable following the Poisson distribution. The corresponding mean value  $s_i$  capturing the *average speed* of agent  $A_i$  is drawn uniformly at random from a set of four indicative values corresponding to four distinct mobility levels  $\mathcal{M}_x^i$  ( $x \in \{\text{work; walk; bic; veh}\}$ ). Each mobility level captures a different kind of activity such as moving in an office environment, walking, riding the bicycle and moving by using a vehicle. As a result, a diverse population of agents is created in terms of mobility in  $\Omega$ . In order to model the particular *type of motion* of each  $A_i$  we use two mobility models, each one leading to a different agent distribution over  $\Omega$ .

*The Random Walk Mobility Model—RWMM.* According to this model, the agents are initially deployed uniformly at random inside  $\Omega$ . Then each agent  $A_i$  performs a random walk independently of the other agents. The motion of each agent in this model consists of consecutive movements of a constant time duration  $\Delta t$ . We refer to these intervals as rounds. In particular, each agent  $A_i$  given its current position and its mobility level  $\mathcal{M}_x^i$ , moves to a new location by randomly choosing a *direction* in which to travel from  $[0, 2\pi]$ ; if the agent lies close to the borders of  $\Omega$ , then the interval is properly adjusted so as the agents to always remain inside  $\Omega$ . From a broad point of view, this model over time results in a uniform distribution of agents over  $\Omega$ , while at the same time local minima and maxima emerge in the density of the agents.

Although similar mobility models to the RWMM (e.g. the well-known Random Waypoint Model) have been proven not so efficient in capturing particular characteristics of human mobility (note we assume that agents abstract people carrying electronic devices), we choose to use this model for its simplicity that helps us focus and highlight the qualitative characteristics of each traversal strategy during the evaluation process.

*The extended Random Walk Mobility Model—eRWMM.* To better address the intrinsic social aspects of human mobility, we take into consideration the notion of *social attraction*. Social attraction comes from the field of social network theory and is broadly used in mobility models for Mobile Social Networks [20]. In particular, it is used in *community-based* mobility models in order to capture in a more realistic way the aspects of human mobility [21]. Social attractivity is defined as the aggregate attraction among the agents as well as towards physical locations inside the area of interest. Real-life examples would include the commercial mall of a city or a cafeteria in a university campus.

Towards more heterogeneous and dynamic placements, we expand the RWMM by adding *social hotspots* inside area  $\Omega$ , that attract the agents during their network traversal. More specifically, in this extended model each agent randomly chooses a new direction in  $[0, 2\pi]$  not uniformly but with a bias factor  $b$  towards the hotspots. The value of  $b$  affects the impact of the hotspot on the network; higher values result to

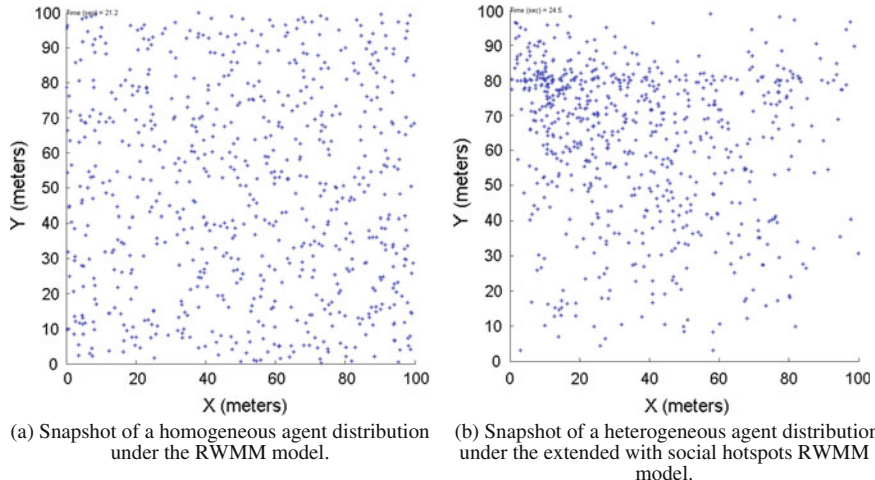


**Fig. 13.1** Example snapshots of homogeneous and heterogeneous agent distributions

denser hotspots and thus in more heterogeneous agent distributions in  $\Omega$ . Figure 13.1a depicts a snapshot of a network following the RWMM model while Fig. 13.1b depicts a network following the eRWMM model.

### 13.3.2 Energy Model

We denote with  $E_i^t$  the amount of energy reserves of agent  $A_i$  on time  $t$  and with  $E_{max}$  the maximum amount of energy each agent may have; i.e. when an agent is *fully charged*. Initially each agent is assumed to be fully charged; i.e.  $E_i^0 = E_{max}, \forall A_i \in \mathcal{A}$ . We also assume that the amount of energy each agent  $A_i$  dissipates during a time interval  $\Delta t$ , i.e. a round, follows a Poisson distribution with mean value  $\lambda_i$ . For each agent,  $\lambda_i$  is constant and is chosen uniformly at random from  $[\lambda_{min}, \lambda_{max}]$ . Intuitively, small values of  $\lambda_i$  correspond to users that mainly perform light activities with their devices (e.g. taking pictures or chatting), while larger values correspond to users that tend to perform more intense activities (e.g. high definition video streaming or GPS navigation).

### 13.3.3 Charging Model

We assume that the Mobile Charger uses inductive charging technology thus being able to wirelessly transmit energy in an omnidirectional way and to simultaneously recharge multiple devices that lie in its vicinity. We identify two *charging zones*

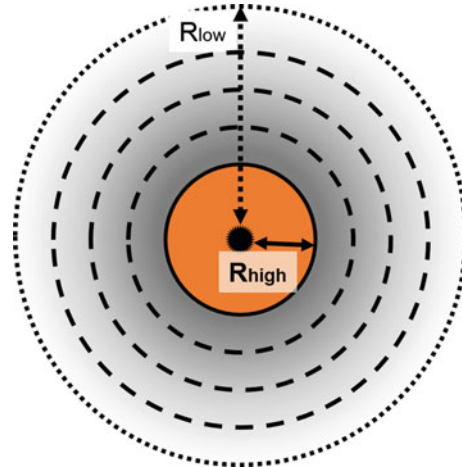


**Fig. 13.2** Graphical representation of the charging zones around the mobile charger. Over all zones, the efficiency of the power transfer reduces sub-quadratically to the distance from the mobile charger. However, for distance  $d \leq R_{high}$  (central zone) the efficiency of charging is sufficiently high for the MC to fully charge agents in a single round. In distances  $d > R_{low}$ , efficiency is so low, that effectively no charging takes place

around the MC (Fig. 13.2). The first one extends up to a radius  $R_{high}$  around the MC. Inside this zone the charging process is conducted at such a high efficiency that the corresponding agents can be fully charged during a single round. The second zone lies in distances greater than  $R_{high}$  and smaller than  $R_{low}$ . In this zone although the devices are being charged, this happens with a lower efficiency and therefore an agent may end-up being only partially recharged after a single round (depending of course on its residual energy at the beginning of the round). For distances greater than  $R_{low}$ , although energy is still emitted, we assume that charging efficiency is so low that effectively no charging takes place.

Based on the specifications of commercially available wireless chargers (such as those in [3]), we assume that the amount of energy each agent receives and eventually stores in its battery per round is inversely proportional to the square of its euclidean distance from the MC. In fact, in order to estimate the amount of the received power, industrial manufacturers make use of the Friis transmission equation. Figure 13.3 shows the theoretical received power rates from the specifications of a 3 Watt Powercast transmitter [3]. In fact, the actual power that can be received by the battery of the receiver is about 50 % less than the power its antenna receives in distances up to 6 m and more than 70 % less in distances further than that. This is due to the RF-to-DC energy conversion efficiency.

We consider the energy reserves of the MC to be significantly bigger than those of the agents' or to be easily and continuously replenished during network traversal; e.g. via energy harvesting from the environment (like solar panels) or via more

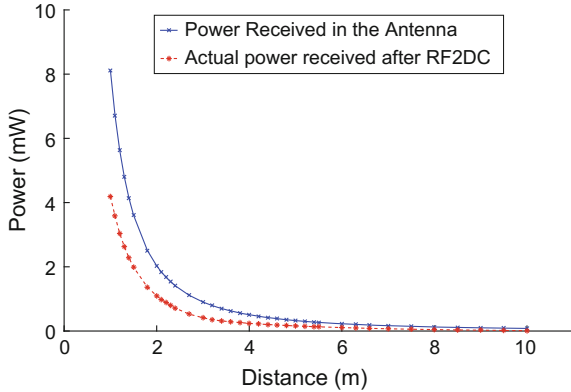


**Fig. 13.3** Received power using a 3 Watt powercast charger (transmitter)

conventional means such as having the charger draw energy from the vehicle it is attached on. Therefore, in this work we consider the energy reserves of the MC to be infinite.

## 13.4 The Charger Traversal Decision Problem

Based on the model presented in the latter section, we formally define the Charger Traversal Decision Problem and prove its NP-completeness.

**Definition 13.1** (*CTDP*) Suppose that we are given a set  $\{A_i \mid i = 1, \dots, n\}$  of mobile agents with positions  $(x_i^t, y_i^t)$  at times  $t = 0, \dots, T$ . We assume that at initial time  $t = 0$  all agents are charged up to their maximum energy level of  $E_{max}$  energy units. The energy dissipation units  $EU_i^t$  in time windows  $[t - 1, t]$  are known for all agents and times  $t = 1, \dots, T$ . Furthermore, we are given a Mobile Charger MC which charges all agents in its range up to radius  $R_{high}$  in one time unit up to their maximum energy level. All agents with distances greater than  $R_{high}$  up to  $R_{low}$  are charged following a rule such that the amount of energy units received by an agent is reversely proportional to the square of its distance from the MC. The additional amount of energy units the agent eventually stores is limited such that the maximum energy level of the agent is not exceeded. The Charger Traversal Decision Problem (*CTDP*) is to determine whether there is a feasible schedule for the MC to visit points in the plane such that no agent falls below sufficient energy level at any time.

**Theorem 13.1** *The CTDP is  $\mathcal{NP}$ -complete.*

*Proof* Given a schedule  $S$  of the MC visiting positions in the plane, we can verify whether all agents have sufficient energy at all times in polynomial time. Let  $E_i^t$  denote the residual energy of agent  $A_i$  at time  $t$ . For all times  $t > 0$ , we compute the

euclidean distances  $d_i^t$  of the agents to the MC. Let  $E_i^{rec}(d_i^t)$  denote the additional energy units an agent  $A_i$  receives reversely proportional to the square of its distance  $d_i^t$ . From  $d_i^t$  we can infer the residual energy of agent  $i$  which equals to  $E_i^{t-1} - EU_i^t$ , if  $d_i^t > R_{low}$ ; equals to the max{ $E_{max}$ ,  $E_i^{t-1} - EU_i^t + E_i^{rec}(d_i^t)$ }, if  $R_{low} \geq d_i^t > R_{high}$ ; or else equals to  $E_{max}$ . Note that the value of  $E_i^{rec}(d_i^t)$  can be computed in polynomial time in  $d_i^t$ . Therefore CTDP  $\in \mathcal{NP}$ .

Now consider the subclass of CTDP problem instances where the positions of the agents are static; i.e. there exists  $x_i, y_i$  such that  $x_i^t = x_i$  and  $y_i^t = y_i$  for all  $i = 1, \dots, n$  and  $t = 0, \dots, T$ . Let us denote this subclass by  $CTDP^{stat}$ . To prove completeness, we reduce the Charger Dispatch Decision Problem (CDDP), introduced and proved to be  $\mathcal{NP}$ -complete in [8], to the  $CTDP^{stat}$  in polynomial time. In the CDDP, we are given a set of sensors  $S$  with a maximum energy deposit of discrete energy units and information of distances between every two sensors in the form of a distance matrix. These sensor motes are the agents in our corresponding  $CTDP^{stat}$  instance. Now in the CDDP, for every sensor  $s \in S$ , we have a list  $L_s$  of pairs  $(t_s^j, e_s^j)$ ,  $j \geq 1$  in which  $t_s^j$  corresponds to the time that the  $j$ -th message of  $s$  was generated and  $e_s^j$  to the energy that the sensor used to transmit it. In the corresponding  $CTDP^{stat}$ , we consider these values by setting the energy dissipation units of the agents as  $EU_s^t = \sum_{j:t_s^j=t} e_s^j$  (i.e., we are summing up the transmission energy of node  $s$  for messages send at time  $t_s^j$ ). In the CDDP, a charger which can charge a sensor in one time unit to its initial (maximum) energy is given. In order to create the same setting, we increase distances between nodes by a constant factor such that the smallest distance between two nodes is larger than  $R_{low}$ . In this way, the corresponding charger in the  $CTDP^{stat}$  can charge at most one node per time unit as well. The CDDP is to determine whether there is a feasible schedule for the charger to visit the sensors so that no message is lost due to insufficient energy. This corresponds to the decision problem of the  $CTDP^{stat}$  for the created instance. An answer to the  $CTDP^{stat}$  would provide an answer to the CDDP, hence the  $CTDP^{stat}$  is  $\mathcal{NP}$ -complete. Since all instances of the  $CTDP^{stat}$  are in the CTDP, the CTDP is  $\mathcal{NP}$ -complete.  $\square$

Note that the CTDP and CDDP differ particularly in the mobility of agents and in the charging range enabling the MC in the CTDP to charge several agents at the same time. In addition, in the CTDP we consider energy dissipation of agents independently of their precedent actions while in the CDDP energy is considered in relation to message transmission.

Distinguishing our work from previous related works, in this chapter we focus on the investigation of tackling the mobility of nodes in an ad-hoc network while recharging it. In real-life settings a MC would have limited local knowledge about the decentralized mobile ad-hoc network it traverses; i.e. the charger will only have information on agents it encounters and no exact information on future events. Therefore, our goal is to define traversal strategies that are applicable in such local knowledge online settings.

Ensuing from the CTDP, let us consider the associated NP-hard problem of optimizing the network life time in terms of maximizing the number of agents alive over time. We go directly over to its online problem with global information about the

agents and their attributes at the current time only. Further investigation of the offline version of the problem in order to obtain an upper bound for the results of the online optimization is not presented here due to lack of space. In fact, we intent to provide such a solution in our future work. However, we note that experimental results extracted from our detailed simulation study demonstrate that our online heuristics have sufficiently high performance (see Sect. 13.7). In addition, the consideration of the online problem offers valuable insights on optimization aspects when information on the future positions of agents is missing. This insight is then used to define a distributed local knowledge strategy which also has to act online.

### 13.5 The Weighting Function

As the MC traverses the network area, it needs a way to prioritize the agents in terms of visiting them for recharging. This prioritization will take into consideration several network aspects that affect the evolution of the network over time. For mobile ad-hoc networks we identify these aspects to be:

1. the *energy need*  $E_i^{need} := E_{max} - E_i$  (with  $E_i$  indicating residual energy) of each agent  $A_i$
2. the mean energy *dissipation* rate  $\lambda_i$  of each agent  $A_i$
3. the *mobility* level  $\mathcal{M}_{x(i)}^i$  of each agent  $A_i$
4. the euclidean *distance*  $d_i$  of each agent  $A_i$  from the MC

However, each one of these aspects is measured in different units and has different ranges. Therefore, the *Weighting Function* (see below) considers their normalized values. We multiply by the factor 100 in order to simplify arithmetics as these values will be used as basis for exponents (see below).

- we normalize the *energy needs* over the maximum energy an agent may store; i.e.  $\bar{E}_i^{need} := \frac{E_{max}-E_i}{E_{max}} \cdot 100$
- we normalize the *dissipation rates* over  $\lambda_{max}$ ; i.e.  $\bar{\lambda}_i := \frac{\lambda_i}{\lambda_{max}} \cdot 100$
- we normalize the *mobility levels* over the maximum mobility level  $\mathcal{M}_{max}$ ; i.e.  $\bar{\mathcal{M}}_{x(i)}^i := \frac{\mathcal{M}_{x(i)}^i}{\mathcal{M}_{max}} \cdot 100$
- we normalize the *distances* over the maximum distance possible in the network area  $d_{max}$  (e.g. if  $\Omega$  is a rectangle then  $d_{max}$  is its diagonal); i.e.  $\bar{d}_i := \frac{d_i}{d_{max}} \cdot 100$

Given these normalized values, the MC will assign a weight to each agent via a *Weighting Function*  $W^*$  whose generic form is defined as:

$$W^* : \mathcal{A} \rightarrow \mathbb{R}_0^+; \quad W_i^* \mapsto (\bar{E}_i^{need})^\alpha (\bar{\lambda}_i)^\beta (\bar{\mathcal{M}}_{x(i)}^i)^\gamma (\bar{d}_i)^\delta \quad (13.1)$$

The higher the weight assigned to an agent, the higher priority it will have during the charging traversal of the MC. The use of the exponents enables us to fine-tune the significance of each network aspect by adjusting the value of the corresponding

exponent. The monotony of  $W_i^*$  with respect to each network aspect will help us define the sign of each exponent. In this context we denote that

1. the higher the current *energy need*  $\bar{E}_i^{need}$  of agent  $A_i$ , the higher the value of  $W_i^*$
2. the higher the mean energy *dissipation*  $\bar{\lambda}_i$ , the higher  $W_i^*$
3. the higher the *mobility* level  $\tilde{\mathcal{M}}_{x(i)}^i$  of agent  $A_i$ , the smaller  $W_i^*$
4. the higher the distance  $\bar{d}_i$  of  $A_i$ , the smaller the value of  $W_i^*$ .

While the rationale for relations 1 and 2 is intuitively straight forward, rules 3 and 4 capture the abilities of the MC to react in a timely manner to spatio-temporal dynamics of the network. In the online problem even if the MC has global knowledge, we assume that it cannot infer the exact future positions of the agents; instead the MC has to make decisions based on a “snap shot” of the network at the current time. Rule 3 supports the idea that the smaller the mobility level of an agent the more likely that in the near future the agent will still be in close vicinity to its current positions. Hence, the incentive for the charger to start travelling towards the direction of such an agent is to be successful in actually reaching the agent and charging it. A similar motivation can be used to reason on rule 4 concerning the distance of an agent to the charger; the closer an agent is, the more likely that the MC will reach the agent in the near future.

In the light of the previous discussion the final generic form of the *Weighting Function* (assuming that all exponents are positive) is:

$$W : \mathcal{A} \rightarrow \mathbb{R}_0^+; \quad W_i \mapsto \frac{(\bar{E}_i^{need})^\alpha (\bar{\lambda}_i)^\beta}{(\tilde{\mathcal{M}}_{x(i)}^i)^\gamma (\bar{d}_i)^\delta} \quad (13.2)$$

As mentioned before, the exponents in the generic form of  $W$  enable us to investigate the relationship and importance of individual attributes with respect to the charging process. In order to define the exact numerical values for each exponent, in this chapter we adopt the One-Factor-At-A-Time (OFAT) methodological approach (see e.g. [22]); i.e. varying the value of the exponent of one of the attributes at the time, while fixing the others to a base value in order to evaluate the impacts on the performance of the MC.

Experimental findings indicate that the uniform consideration of all network aspects (i.e., all exponents equal to one) already lead to good results in our MC traversal strategies (see details in Sect. 13.7). Fine tuning via more sophisticated methods would only further increase the already high efficiency of the proposed traversal strategies.

## 13.6 Traversal Strategies for the Mobile Charger

We now discuss five traversal strategies for the Mobile Charger that are qualitatively different in terms of the assumed level of knowledge that the MC has on the network. The first one is a zero-knowledge deterministic space-filling strategy. The second

one is a zero-knowledge randomized strategy. The third and fourth ones are online, complete-knowledge centralized strategies integrating the node *Weighting Function* defined above. The last strategy is a reactive one that is based on local network information gathered by the agents in a distributed way.

In terms of network knowledge, complete-knowledge strategies are the most powerful strategies for the MC. At any given moment, the MC is aware of the exact distribution of the agents over the area  $\Omega$  and is therefore able to choose its trajectory accordingly towards maximizing the number of nodes alive over time while considering the delay between the time of computing positions and the arrival time of the MC in the online setting. Such recharging schemes have the strong assumption that the agents are able to periodically propagate data regarding their position and energy needs to the MC; e.g. over the Internet. The MC is assumed to have the required computational power in order to be able to perform the necessary calculations.

### **13.6.1 The Space-Filling Strategy (SPF)**

This zero-knowledge deterministic traversal strategy consists in having the MC to systematically sweep the network area in such a way that no overlaps occur. In particular, according to this strategy the MC is moving along the one dimension of  $\Omega$  until it reaches its border. Then, it takes a U-turn shifted by a distance of  $2R_{low}$  along the second direction. When the entire network area has been covered the process is repeated. This traversal strategy guarantees that eventually all network sub-regions will be covered by the MC and in uniform agent distributions it is expected to have a satisfactory performance. However, in heterogeneous distributions where big numbers of agents are located in confined sub-regions (i.e. the social hotspots) significant latencies in inter-charging times are expected.

### **13.6.2 The Random Walk Strategy (RAND)**

This is a zero-knowledge randomized traversal strategy for the MC. Given its current position, the MC chooses the direction of its next move uniformly at random from  $[0, 2\pi]$  and the distance to be covered uniformly at random from  $[0, 2R_{low}]$ . This strategy assumes zero-knowledge on the network and the distribution of the agents. Therefore, like the SPF, it is characterized by the absence of any overhead as the agents maintain a passive role, simply waiting to encounter the MC in order to be recharged. Moreover, this strategy probabilistically guarantees that eventually all the sub-regions of the network will be visited by the MC, although it may infer long waiting periods for the agents among consecutive charges, particularly for highly heterogeneous topologies.

### 13.6.3 Global Knowledge ILP Strategy (GK-ILP)

Initially the Mobile Charger is placed at a random position in the network area  $\Omega$ . At each round, given the current positions of all the agents in  $\Omega$  and the current values of their network attributes (i.e.  $E_i^{need}$ ,  $\bar{\lambda}_i$ ,  $\bar{M}_{(x)}^i$ ,  $\bar{d}_i$ ), the MC is able to compute the exact location it should visit (or move towards to) at the current time. The MC could do so by finding the center of the circle of radius  $R_{low}$  which encircles the agents that cumulatively have the highest node weights with respect to the *Weighting Function*. By the design of the *Weighting Function*, the cumulation of the node weights correctly prioritizes the various areas with respect to demand for being charged. The corresponding non-linear problem formulation is as follows:

$$\max_{x, y, \beta_i, d_i} \sum_i W_i \beta_i \quad (13.3a)$$

$$d_i = (\sqrt{(x_i - x)^2 + (y_i - y)^2})^{1/2} \quad \forall i \quad (13.3b)$$

$$R_{low} + (1 - \beta_i) \cdot \mathbf{M} \geq d_i \quad \forall i \quad (13.3c)$$

$$\beta_i \in \{0, 1\} \quad \forall i \quad (13.3d)$$

In the problem formulation the  $i$ 's are the indices of the agents  $A_i \in \mathcal{A}$ ,  $W_i$  indicate their weights,  $\beta_i$  are binary decision variables,  $d_i$  the distance of the agents to the MC at position  $(x, y)$ ,  $x_i$  and  $y_i$  are the position coordinates of the agents, and  $\mathbf{M}$  is a very large constant. In (13.3b) we compute the distances of the agents to the MC. In (13.3c) we make sure that if  $\beta_i = 1$  (i.e., if the weight of agent  $A_i$  is considered in the objective function) then  $R_{low} \geq d_i$ .

To create an ILP, we approximate  $d_i$ . Instead of a circle with radius  $R_{low}$ , we look for a rectangle whose sides are at most of length  $R_{low}$  and whose center  $(x, y)$  is the position of the MC:

$$\max_{x, y, \beta_i, d_i} \sum_i W_i \beta_i \quad (13.4a)$$

$$d_i \geq |x_i - x| \quad \forall i \quad (13.4b)$$

$$d_i \geq |y_i - y| \quad \forall i \quad (13.4c)$$

$$R_{low} + (1 - \beta_i) \cdot \mathbf{M} \geq d_i \quad \forall i \quad (13.4d)$$

$$\beta_i \in \{0, 1\} \quad \forall i \quad (13.4e)$$

In the above equations the constraints (13.4b) can be replaced by linear equations  $d_i \geq x_i - x$  and  $d_i \geq -(x_i - x)$ . Corresponding replacements can be made for (13.4c) resulting in an ILP. By solving this ILP, the MC is able to identify the rectangle that maximizes demands and move towards its center. The MC is updating its directions using the ILP with updated information at each time step.

Note that even for relatively big and dense network instances the ILP can be solved in reasonable amount of time.

### 13.6.4 Global Knowledge Tessellation Strategy (GK-TS)

In this traversal strategy the MC is initially deployed at a random position inside the network area  $\Omega$ . First, the MC virtually tessellates the network area in square tiles of the same size. In order to minimize overlaps in the charging areas the pivot of the tessellation is chosen to be equal to  $2R_{low}$ . Then on each round, given the current positions of all the agents in the  $\Omega$  and the current values of their attributes, the MC assigns weights to each agent via the *Weighting Function* and computes the aggregated weight for each tile by summing the weights of the agents located in that tile. Finally, the MC chooses to move towards the center of the tile with the highest cumulative weight.

### 13.6.5 The Reactive Local Knowledge Strategy (RLK)

This is a local knowledge traversal strategy that exploits local information collected distributively. The agents overtake an active role in collecting local network information and informing the MC on the current demands of their neighbourhood (we assume that  $R_{low}$  and the communication range of the agents, although not equal, are of the same order). This way the MC is able to identify and serve stressed areas of the network as well as to react to changes of the network topology under a more realistic and efficient distributed scheme.

More specifically, each agent periodically collects information regarding the network attribute values of its neighbouring agents; i.e. each agent poles its one-hop neighbours on their energy needs, their average energy dissipation rate and their mobility levels. Then this information is used to assign to each neighbour a weight via a modified *Weighting Function* that does not take in consideration the distance to the MC. This is due to the fact that the agent is unaware of the actual location of the MC. Instead, the agent associates the assigned weights to its current position for future reference. The modified *Weighting Function* applied by an agent in the GK-TS strategy is the following:

$$\bar{W} : \bar{A} \rightarrow \mathbb{R}_0^+; \quad \bar{W}_i \mapsto \frac{\bar{E}_i^{need} \bar{\lambda}_i}{\bar{\mathcal{M}}_{x(i)}^i} \quad (13.5)$$

Eventually, the agent stores in its memory and ferries a tuple consisting of the cumulative weight of its current neighbourhood and the coordinates of the position where this weight was measured. As each agent is moving inside the network area, the quality (in terms of accuracy) of the measurements degrade over time due to the dynamics of the network, such as the mobility of the agents. In order to address this issue we introduce the following ageing mechanism. At every round each agent updates the carried tuples by multiplying the stored aggregated weight with a constant  $q \in [0, 1]$ . Therefore, after  $T$  rounds the corresponding value will have been

**Table 13.1** Structure of the tuple each agent maintains.

| Variable name | Description                                 |
|---------------|---|
| tuple.x       | % X coordinates of the measurement location |
| tuple.y       | % Y coordinates of the measurement location |
| tuple.weight  | % Modified weight of the measured location  |

multiplied by a factor of  $q^T$  and will be a percentage of the initial weight. The lower the value of  $q$  is set, the more aggressive the reduction over time of the weight stored in the tuple.

On another aspect, as the agent traverses the network, it periodically collects local network information and stores them in tuples in its memory. As new tuples are being created, at each round the agent re-evaluates the already existing ones and compares them to the new tuples. Low weight entries are replaced by higher weight entries once the storage space limit of the agent has been reached. An agent carries stored tuples and opportunistically delivers it to the MC once it encounters it. Table 13.1 shows the structure of the tuple that each agent maintains.

The MC is initially placed at a randomly chosen position inside  $\Omega$ . As the MC traverses the network, it receives and saves tuples from each agent it encounters. Then, the MC uses the information provided in order to solve the ILP introduced in the latter subsection thus adjusting its trajectory correspondingly at each time step.

The presented reactive, local knowledge traversal strategy introduces a communication overhead to the network as the agents need to exchange information with each other. However, this overhead is rather small, thus not yielding significant energy consumption for the agents. Further, we note that information regarding network areas with high agent density and/or high energy needs (such as social hotspots) will be carried by the agents for a longer time period and will traverse a longer distance into the network. Finally, the distributed nature of this strategy makes it scalable and applicable in more realistic settings.

## 13.7 Performance Evaluation

### 13.7.1 Simulation Set-Up

We evaluate the performance of the five traversal strategies by conducting extensive simulation studies in Matlab 2015. We conduct simulations with three different sizes for  $\Omega$ ; (a)  $50 \times 50$  and (b)  $100 \times 100$  where in each setting 100 agents are deployed. We make this choice as it provide us with qualitatively different sizes and densities of the network in which the agents are distributed enabling us to better study the performance of each heuristic. In terms of speed of movement, we set the mean agent speed for each mobility level to be (all numbers are in space units over time units)

$\mathcal{M}_{work} = 2$ ;  $\mathcal{M}_{walk} = 4$ ;  $\mathcal{M}_{bic} = 8$ ;  $\mathcal{M}_{veh} = 16$  and the speed of the MC  $MC_{sp} = 10$ . Mobility levels are assigned to the agents u.a.r., thus leading each one to correspond to approximately 25 % of the population. We also set the maximum and initial energy for each agent to be  $E_{max} = 3000$  units of Energy. At each round of simulation, the amount of energy that each agent dissipates follows a Poisson distribution whose mean value for each agent is chosen independently and u.a.r. in [20, 80] units of Energy. We study both homogeneous and heterogeneous placements. In the heterogeneous placements three social hotspots are considered each on in different network subregion with a bias factor of: 0.45; 0.15; 0.15 accordingly. Note that the agents are *attracted* towards the hotspots; they do not move directly to them. For each setting we simulate the network for 500 rounds. Each simulation is repeated for 60 iterations and we compute the mean values for each metric; results demonstrate strong concentration around the mean (evaluated via the standard error over the mean).

### 13.7.2 Preliminary Evaluation of the Weighting Function

Before running the simulations for the evaluation of each strategy we turn to the task of finding appropriate parameter settings for the attribute exponents in the *Weighting Function* introduced in Sect. 13.5. We employ the simple One-Factor-At-A-Time (OFAT) methodology: varying the parameter values of the exponent of one of the attributes while fixing the others to a base value in order to evaluate the impacts on the simulation outputs (see e.g. [22]). OFAT has the advantage of being relatively easily conducted and, as it will turn out, over relatively few trials will provide settings which result in sufficiently high performance. We will leave a more sophisticated analysis of the exponent parameter settings for future work claiming that this would only ameliorate the our findings. For the evaluation of the exponents we measure the performance of varying parameter settings when employing the *Global Knowledge ILP Strategy* as this strategy employs the base version of the *Weighting Function* and in terms of adjusting the traversal strategy of the MC may, out of all of the presented strategies, best exploit the added value of *Weighting Function*.

We first evaluated different values for the  $E^{need}$  exponent with values ranging from 1 to 10 (keeping the other exponents at 0). Figure 13.4a shows the percentage of alive nodes over the number of rounds for different exponents of  $E^{need}$  in a  $50 \times 50$  area with a homogeneous agent distribution. We observe that the more we increase the value of the  $E^{need}$  exponent the less alive nodes we have in the area. Similar results are achieved for  $100 \times 100$  area and  $150 \times 150$  area. This can be explained by how the *Weighting Function* assigns values with respect to the exponents: the higher the exponent of  $E^{need}$  is, the higher the weight distance between two agents, even if their actual energy needs are similar. For instance, for value 10, consider two nodes: one with energy need equal to 2 and one with energy need 2.5. These would end up in receiving weights 1024 versus 9537. In a network with several nodes the MC integrating the *Weighting Function* with high exponents might focus too much on some few individual nodes.

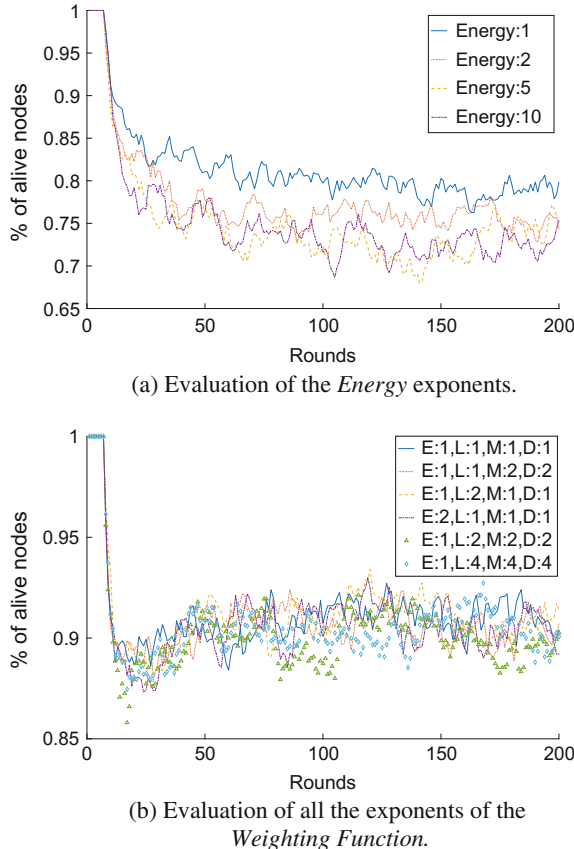


**Fig. 13.4** Evaluation of exponents using the *GLK-ILP* strategy

As  $E^{need}$  is the indicative factor for the survivability of an agent, we conducted tests for evaluating the exponents of pairs of  $\{E^{need}\} \times \{Dissipation, Mobility, Distance\}$ . Similarly to the tests on using only the  $E^{need}$  exponent, the results were changing with respect to changes of the  $E^{need}$  exponent only. As such we run tests for evaluating all the exponents by keeping the  $E^{need}$  exponent at 1. The results can be seen in Fig. 13.4b. Considering the relatively high performance, we used for our strategies evaluation the exponents in a uniform manner (i.e. all exponents equal to 1).

### 13.7.3 Evaluation of Traversal Strategies

#### 13.7.3.1 Evaluation Metrics

**Percentage of Alive Nodes.** In this metric we examine the percentage of alive agents each traversal strategy is able to achieve in a given amount of rounds. We note here

that a fully charged agent with highest possible dissipation rate in the absence of the MC will die in 12 rounds. This metric is a good indicator of whether a strategy manages to provide energy to the network where and when is needed.

**Energy Distribution.** In this metric we examine the energy distribution to the agents by the MC in percentiles over time. In particular, we tessellate the percentage of agents that have residual energy in the ranges of: (0–20 %), (20–40 %), (40–80 %), (80–100 %). We take some samples of the network in terms of energy distribution and we examine the % of the agents that lie in each of the ranges.

**Distance Coverage.** In this metric we examine the cumulative distance covered by the MC in the network. This metric although it is not directly correlated with the operation of the network itself, it can lead to useful conclusions regarding the charging process and the efficiency of the route that the MC is following. In addition, this metric is associated to relevant movement costs of the MC.

### 13.7.3.2 Results for Percentage of Alive Nodes

**Homogeneous Agent Distribution.** Figure 13.5 depicts the percentage of alive nodes (*survivability of the network*) in an homogeneous agent distribution for a (a)  $50 \times 50$  and (b)  $100 \times 100$  area  $\Omega$ . We observe in the subfigure (a) that the *GK-ILP* strategy outperforms the other ones, as expected. This is due to the knowledge the Mobile Charger has and its ability to best exploit the *Weighting Function*. The second best strategy is the *Random Walk* of the Mobile Charger and this is due to the nature of the homogeneous area and the fact that the random walk probabilistically will eventually visit the entire area. Comparing the *RAND* to the *Space-Filling* strategy, it distributes “more evenly” the probabilities of visiting all the subareas. The *SPF* strategy comes third since the MC is sweeping the network and thus some sub-areas are left without being charged until the MC will revisit them in the next iteration. The *GLK-TS* performs even worse. This may be explained by the limitation of the positions the MC can visit when this strategy is applied, i.e. it may only visit the centres of the tiles of the tessellation. In the case where nodes are positioned towards

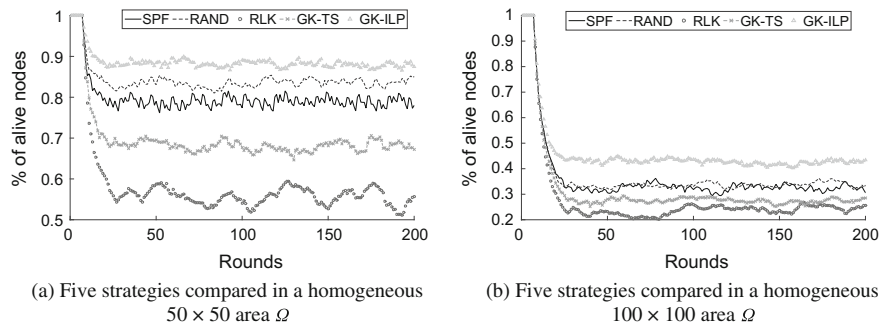


**Fig. 13.5** Percentage of alive nodes over 200 rounds in homogeneous setting

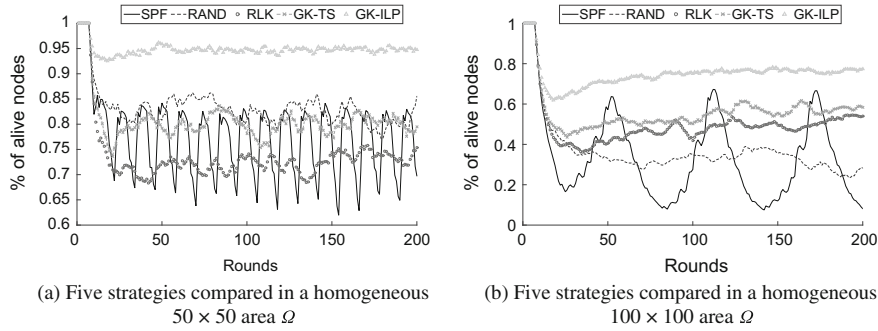


**Fig. 13.6** Percentage of alive nodes over 200 rounds in heterogeneous setting

the edges of the tiles, the MC will not have the chance to fully charge these nodes in one round. We observe that in the homogeneous set-up, the *RLK* strategy has the poorest performance: the MC has limited information about the agents and they are equally distributed over the area  $\Omega$ . We observe that in all settings of  $50 \times 50$  and  $100 \times 100$ , the strategies follow the same trend. The differences of the strategies in comparison to the topologies lie in the absolute values of % of alive nodes they are able to achieve. In a bigger area with the same MC the distances are longer thus the MC does not have enough speed and sufficient time to keep a high % of overall alive nodes.

**Heterogeneous Agent Distribution.** Figure 13.6 depicts the % of alive nodes in an heterogeneous agent distribution for a (a)  $50 \times 50$  area  $\Omega$  and (b)  $100 \times 100$  area  $\Omega$ . In the heterogeneous setting the *GLK-ILP* strategy is again clearly the best in all topologies, as expected. In the  $50 \times 50$  area the *GK-TS* and the *RAND* have almost identical behaviour but in the  $100 \times 100$  area the *RAND* performs much worse. This is explained as follows: since the distribution of the agents in the area is done in a heterogeneous manner and there are three hotspots, when the overall area is small, the MC manages to cover a sufficient area thus charging a relative high number of agents. On the contrary, when the area is relatively big, the random walk of the MC does not manage to cover sufficiently neither the whole area nor the hotspots. The *RLK* strategy in the  $50 \times 50$  area performs weaker again, even though much better in relation to all of the other strategies and much better than the *SPF* strategy in terms of maintaining the agents alive. However in a larger area, its performance increases quite significantly, i.e. in the  $100 \times 100$  area the *RLK* strategy performs similarly well as the *GK-TS* although it is only employing local knowledge collected while traversing the network. At the same setting the performances of both zero-knowledge strategies, *SPF* and *RAND*, drop significantly. Lastly, we observe that the *SPF* strategy maintains the least number of agents alive in both topologies and specifically it is following a “wave charging” every time it is passing through the hotspots.

### 13.7.3.3 Results for Energy Distribution

**Homogeneous Agent Distribution.** Figures 13.7 and 13.8 show the energy distribution in percentiles in the homogeneous  $50 \times 50$  and  $100 \times 100$  areas. In general we observe that the performance of all the strategies is stable over time. In the  $50 \times 50$  area the *GK-ILP* performs clearly better than all the other protocols, not only with respect to number of nodes alive, but also regarding the percentage of nodes with high energy level. Regarding the performance w.r.t. energy distribution, *GK-ILP* is followed by *RAND*, than *GK-TS* and than *SFP*. The reactive protocol *RLK* is outperformed by the other protocols and has the highest number of nodes with relatively low energy level. This is due to *RLK* focusing on nodes with highest needs to be recharged first. While traversing the network it also charges other nodes on the way, but its main goal is to successfully keep as many as possible nodes alive. When looking at the  $100 \times 100$  area, we note that even though the *GK-ILP* performance in terms of number of alive nodes is much better than the other strategies, its energy distribution percentiles are only slightly better. The *SFP*, *RAND* and *GK-ILP* have relatively high values for nodes with energy levels higher than 40 % .

**Heterogeneous Agent Distribution.** Figures 13.9 and 13.10 show the energy distribution in percentiles in the heterogeneous  $50 \times 50$  and  $100 \times 100$  areas respectively. In the  $50 \times 50$  area, again the *GK-ILP* performs best, followed by *RLK*, *GK-TS* and *RAND* which here perform all similar like with more than 60 % of the nodes having energy level equal or higher than 40 %. The *SFP* protocol performs worst with up to about 60 % of nodes with less than 40 % energy level for 500 rounds. For the  $100 \times 100$  area, we observe that the *GK-ILP* manages to both keep a high number of nodes alive and hold a relatively even distribution over them. The *RAND* has a performance similar to the homogeneous setting but compared to the non-naive strategies, it performs much worse. Moreover, we observe that similarly to the performance of the number of alive nodes, the *RLK* and *GK-TS* perform equally good; i.e. both are being successful in keeping a relatively high number of nodes at high energy levels.

### 13.7.3.4 General Findings

Conclusively, for a homogeneous distribution of agents, our simulation results suggest that when the knowledge of the MC is limited, as in most real world applications for mobile ad-hoc networks, it may be advisable to employ a naive, low-cost *Random Walk* strategy. In the heterogeneous setting, experimental results suggest an outstanding suitability of our local knowledge *RLK* strategy when the area of interest

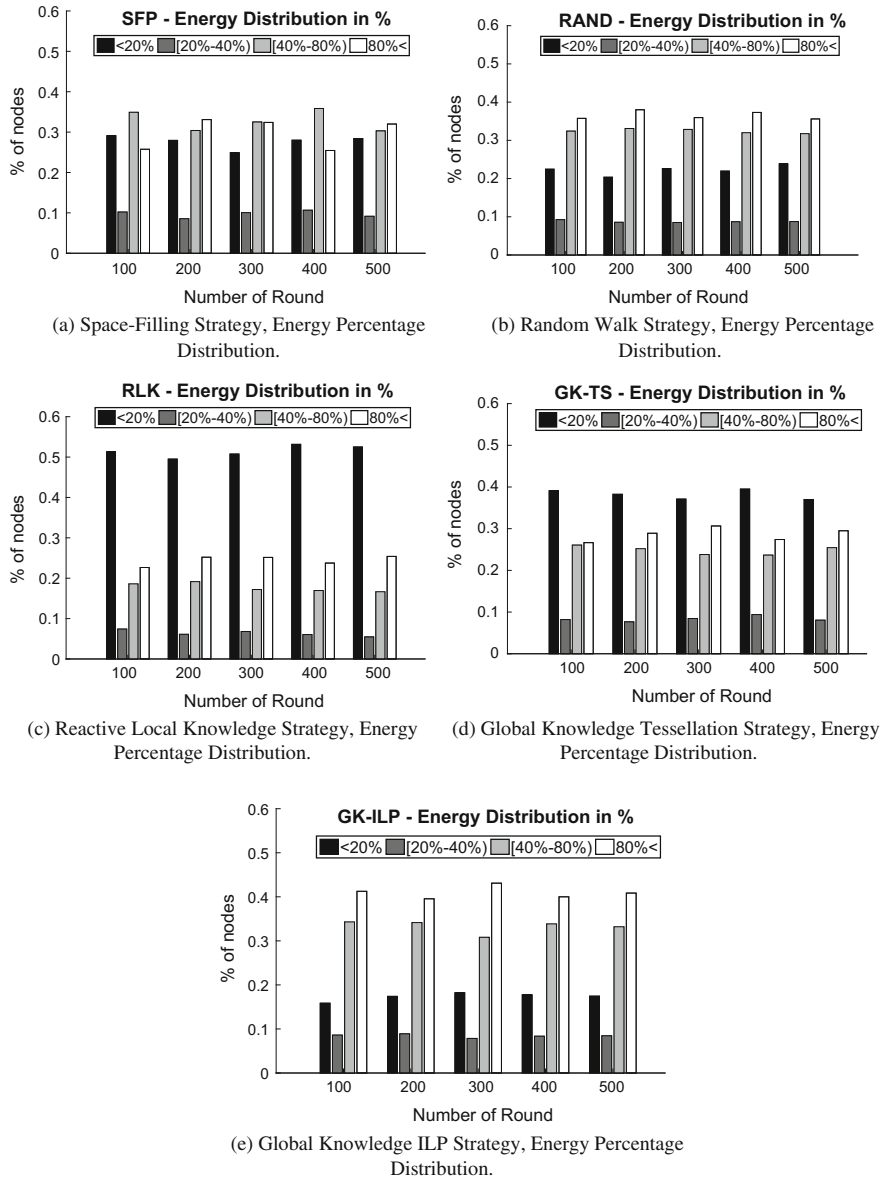


**Fig. 13.7** Energy distribution in homogeneous setting in a  $50 \times 50$  area  $\Omega$

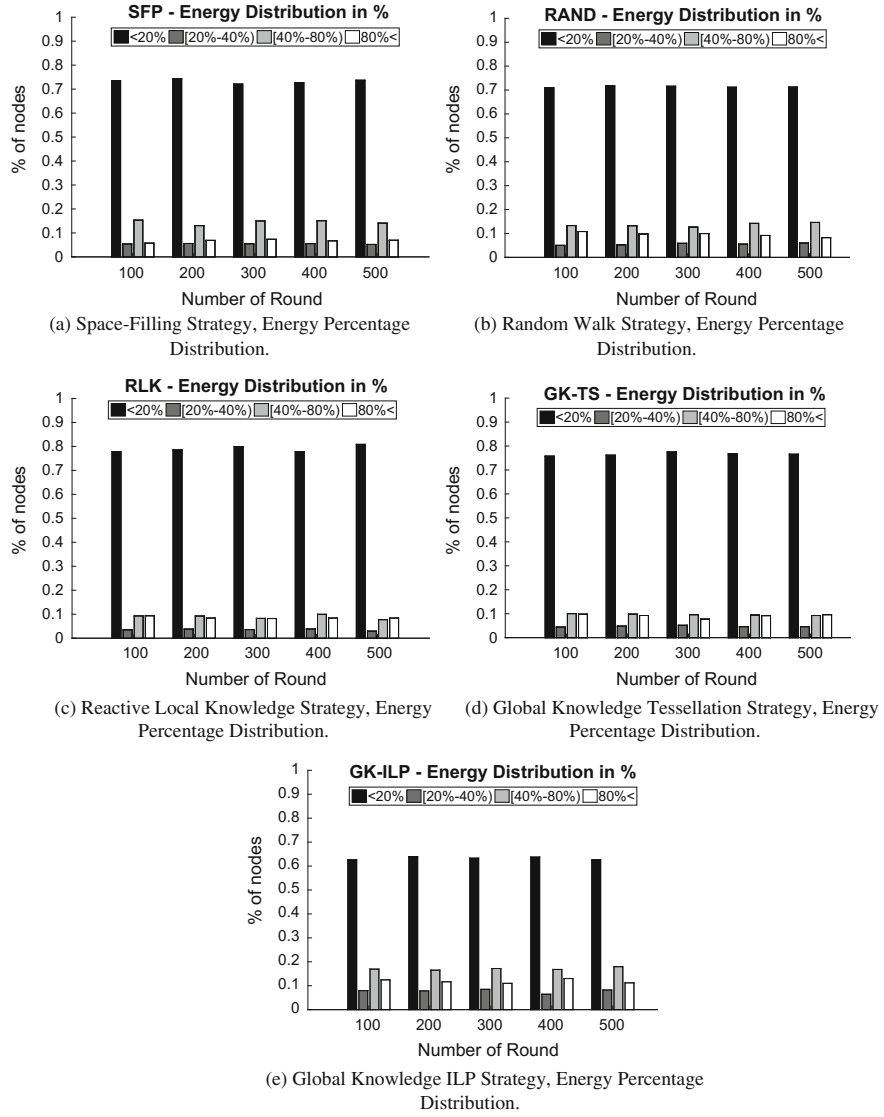


**Fig. 13.8** Energy distribution in homogeneous setting in a  $100 \times 100$  area  $\Omega$

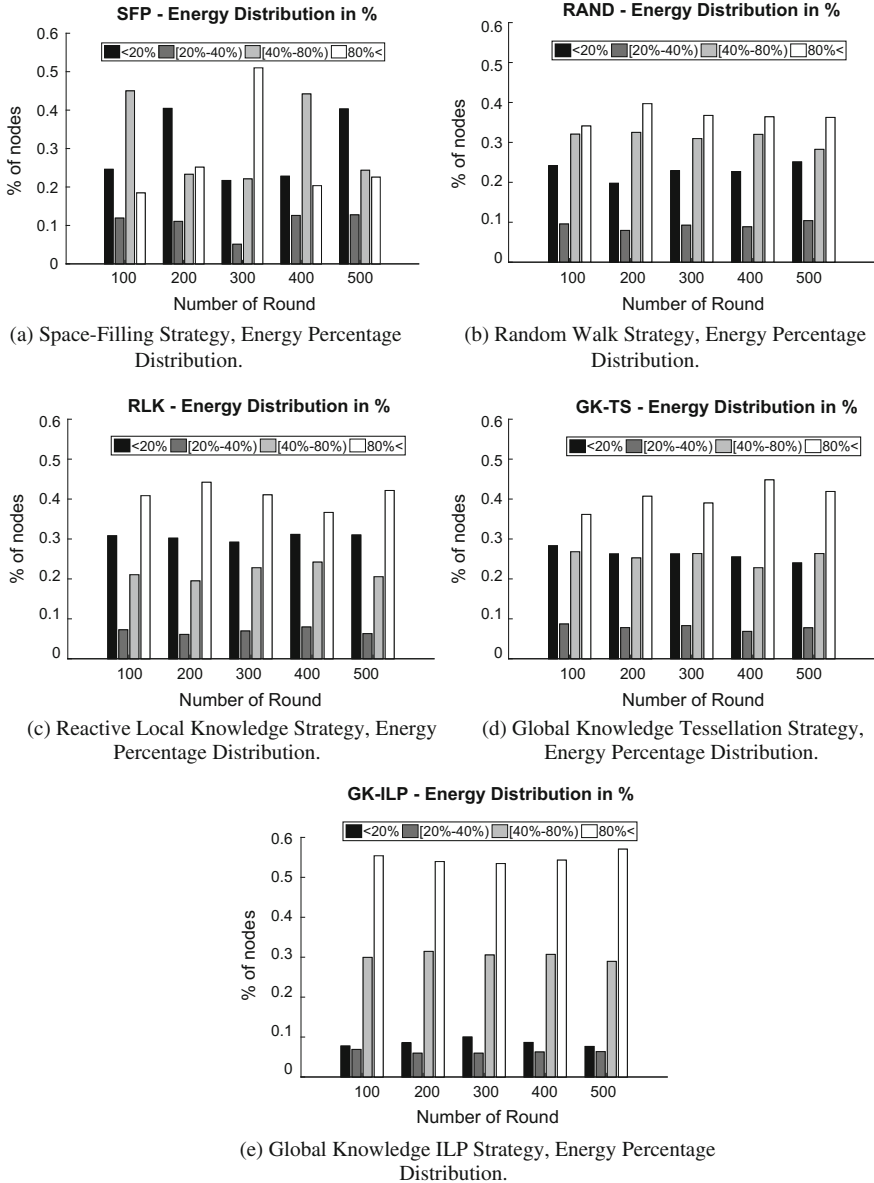


**Fig. 13.9** Energy distribution in heterogeneous setting in a  $50 \times 50$  area  $\Omega$

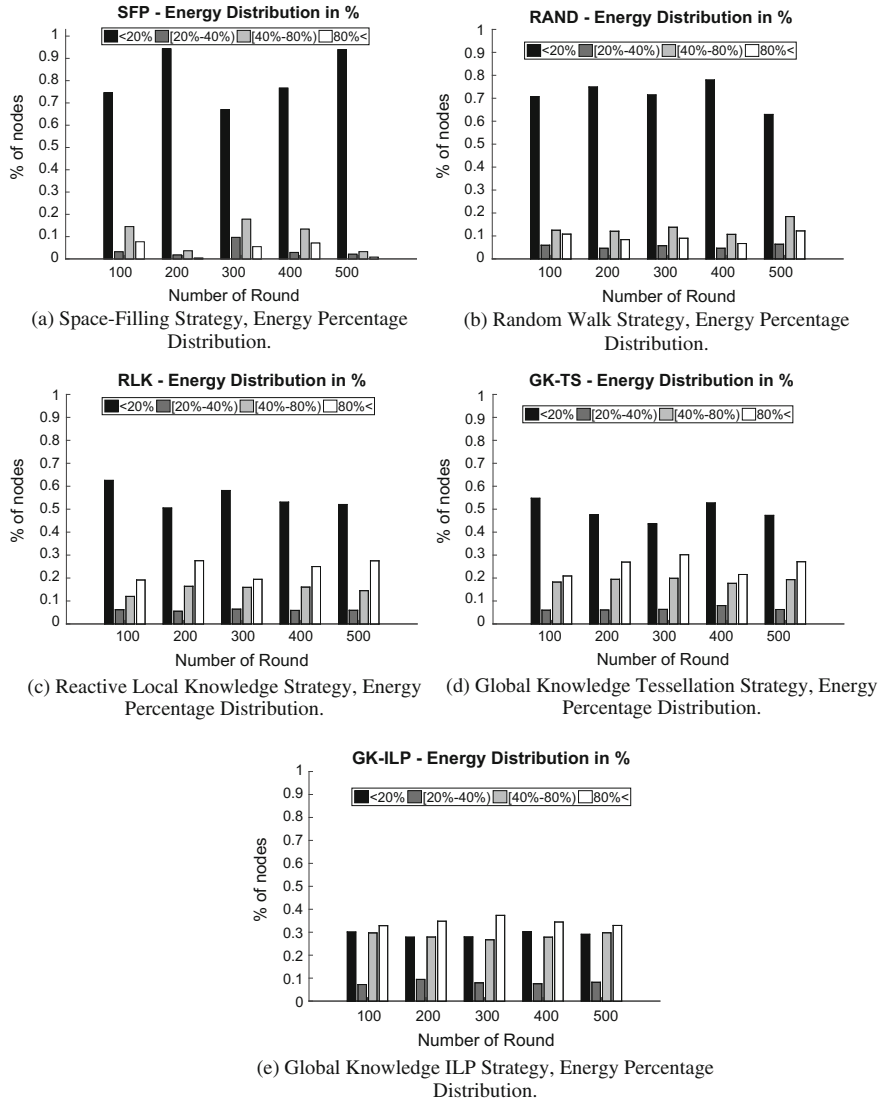


**Fig. 13.10** Energy distribution in heterogeneous setting in a  $100 \times 100$  area  $\Omega$

**Table 13.2** Cumulative distance (units of space) covered by the MC in 500 rounds in  $100 \times 100$  area  $\Omega$ 

| Strategy | Homogeneous | Heterogeneous |
|----------|-------------|---------------|
| SPF      | 10800       | 10800         |
| RAND     | 12000       | 12000         |
| RLK      | 4271        | 2982          |
| GLK-TS   | 6553        | 5387          |
| GLK-ILP  | 10692       | 8933          |

is relatively large. In addition, Table 13.2 shows the cumulative distance traveled by the MC in a  $100 \times 100$  area  $\Omega$  over 500 Rounds in homogeneous and heterogeneous setting. We observe that the MC, in our *RLK* strategy both in homogeneous and in heterogeneous setting, is traveling the least distance. This is a significant result given that *RLK* performs also very well in terms of keeping the a high number of agents alive.

## 13.8 Conclusions

In this chapter we addressed the Wireless Recharge Problem in mobile ad-hoc networks characterized by diverse and unpredictable spatio-temporal dynamics. First, we defined the charging model and then utilized the notion of social attraction in order to better capture human mobility in our mobility model. We evaluated the performance of five qualitatively different traversal strategies for the MC; a zero-knowledge deterministic space-filling strategy, a zero-knowledge randomized strategy, two complete-knowledge centralized strategies and a local distributed knowledge reactive strategy. Our findings indicate that in homogeneous topologies the added value of the network information is degraded. However, in heterogeneous topologies strategies utilizing local network knowledge can outperform more powerful schemes if they efficiently exploit their knowledge.

In future research we aim at investigating more diverse topologies of the network area, more accurate mobility models as well as coordination schemes among multiple Mobile Chargers. In fact, our aim will be to efficiently coordinate the Mobile Chargers so as their effect on the network to be at least super-linear with respect to their number. Finally, we will also employ more detailed evaluation methods for further fine tuning the *Weighting Function*.

## References

1. Kurs, A., Karalis, A., Moffatt, R., Joannopoulos, J.D., Fisher, P., Soljacic, M.: Wireless power transfer via strongly coupled magnetic resonances. *Science* **83** (2007)
2. Intel: Wireless resonant energy link (wrel) demo. <http://software.intel.com/en-us/videos/wireless-resonant-energy-link-wrel-demo/>. Accessed 2015
3. Powercast. <http://www.powercastco.com/>. Accessed 2015
4. Murata manufacturing. <http://www.murata.com/>. Accessed 2015
5. Rezence alliance for wireless power. <http://www.rezence.com/>. Accessed 2015
6. The wireless power consortium. <http://www.wirelesspowerconsortium.com/>. Accessed 2015
7. Kang, B., Ceder, G.: Battery materials for ultrafast charging and discharging. *Nature* **458**, 190–193 (2009)
8. Angelopoulos, C.M., Nikoletseas, S., Raptis, T.P., Raptopoulos, C., Vasilakis, F.: Efficient energy management in wireless rechargeable sensor networks. In: ACM International Conference on Modeling, Analysis and Simulation of Wireless and Mobile Systems, (MSWiM) (2012)
9. Garey, M.R., Johnson, D.S.: Computers and Intractability. W.H. Freeman and Company (1979)
10. Fu, L., Cheng, P., Gu, Y., Chen, J., He, T.: Optimal charging in wireless rechargeable sensor networks. *IEEE Trans. Veh. Technol.* (2015)
11. Xie, L., Shi, Y., Hou, Y.T., Sherali, H.D.: Making sensor networks immortal: An energy-renewal approach with wireless power transfer. *IEEE/ACM Trans. Network.* (2012)
12. Li, K., Luan, H., Shen, C.C.: Qi-ferry: Energy-constrained wireless charging in wireless sensor networks. In: IEEE Wireless Communications and Networking Conference, (WCNC) (2012)
13. Madhja, A., Nikoletseas, S., Raptis, T.P.: Distributed wireless power transfer in sensor networks with multiple mobile chargers. *Elsevier Computer Networks*, pp. 89–108 (2015)
14. Wang, C., Li, J., Ye, F., Yang, Y.: Multi-vehicle coordination for wireless energy replenishment in sensor networks. In: International Parallel and Distributed Processing Symposium, (IPDPS) (2013)
15. Zhang, S., Wu, J., Lu, S.: Collaborative mobile charging for sensor networks. In: IEEE International Conference on Mobile Ad hoc and Sensor Systems, (MASS) (2012)
16. Ko, S.W., Yu, S.M., Kim, S.L.: The capacity of energy-constrained mobile networks with wireless power transfer. *IEEE Commun. Lett.* (2013)
17. Dai, H., Chen, G., Wang, C., Wang, S., Wu, X., Wu, F.: Quality of Energy Provisioning for Wireless Power Transfer. *IEEE Transaction Parallel Distribution, Syst* (2015)
18. He, L., Cheng, P., Gu, Y., Pan, J., Zhu, T., Liu, C.: Mobile-to-mobile energy replenishment in mission-critical robotic sensor networks. In: Proceedings—IEEE INFOCOM, pp. 1195–1203 (2014)
19. Kurs, A., Moffatt, R., Soljacic, M.: Simultaneous mid-range power transfer to multiple devices. *Appl. Phys. Lett.* (2010)
20. Musolesi, M., Hailes, S., Mascolo, C.: An ad hoc mobility model founded on social network theory. In: ACM International Conference on Modeling, Analysis and Simulation of Wireless and Mobile Systems, (MSWiM) (2004)
21. Vastardis, N., Yang, K.: An enhanced community-based mobility model for distributed mobile social networks. *J. Ambient Intell. Humanized Comput.* **5** (2014)
22. Wu, C.J., Hamada, M.S.: Experiments: Planning, Analysis, and Optimization, vol. 552. Wiley (2011)

# Chapter 14

## Recharge Scheduling with Multiple Mobile Chargers

Cong Wang, Ji Li, Fan Ye and Yuanyuan Yang

**Abstract** This chapter studies the important research scheduling problem for wireless charging in wireless sensor networks. We first present a distributed protocol that can collect energy information from the network on demand. For scalability, the protocol divides the network into hierarchical levels, selects head nodes on each level and establishes routing paths to the heads. *Mobile Chargers* (MC) send recharge requests to reveal their current locations. Energy information messages then utilize the established routing paths to get back to the MCs. Based on the gathered energy information, our objective is to minimize energy cost for the MCs during movements and make sure no sensor depletes battery energy. We formulate the problem into an optimization problem by capturing both battery capacity from the MCs and dynamic lifetime from sensors. Since the problem is NP-hard, we present a three-step adaptive algorithm. The algorithm first partitions energy requests according to their locations. Then it constructs *Capacitated Minimum Spanning Trees* to capture charger's battery capacities. Finally, the algorithm calculates recharge routes for each tree based on node's lifetime. Simulation evaluations have demonstrated that the algorithm can successfully maintain perpetual operation of the network.

---

C. Wang (✉) · J. Li · F. Ye · Y. Yang

Department of Electrical and Computer Engineering, State University of New York,  
Stony Brook, NY 11794, USA  
e-mail: cong.wang@stonybrook.edu

J. Li  
e-mail: ji.li@stonybrook.edu

F. Ye  
e-mail: fan.ye@stonybrook.edu

Y. Yang  
e-mail: yuanyuan.yang@stonybrook.edu

## 14.1 Introduction

Equipped with wireless charging coils, mobile chargers (MCs) can move around sensing the field and recharge nodes via wireless energy transfer [1–9]. An important problem of recharge scheduling—when and which MCs should recharge which nodes and in what order—critically impacts the lifetime and performance of the network. Since it takes nontrivial time (60–80 mins) to recharge a commercial Ni-MH battery [10], a sequence of a few hundreds of nodes may take several days. The energy information gathered prior to a recharge tour may be outdated so it is necessary for the MCs to request updated energy information during operation. Thus, for effective recharge schedules, the timely, efficient, and scalable gathering of energy information from nodes and its delivery to MCs are challenging problems. Instead of letting nodes report their energy to the base station only after a long time, a scalable energy information aggregation protocol enables the MCs to gather energy status information continuously from sensors on demand. Since the MCs are moving among different locations, successful delivery of energy information to the MCs requires building routing paths in run-time. We first propose a distributed communication protocol for the MCs to request energy information on demand.

In the second step, based on the latest energy information collected, we present an adaptive recharge scheduling algorithm for multiple MCs. It contains the following steps: (1) partition energy requests according to their location distributions using the *k-means* algorithm [11] (2) build *Capacitated Minimum Spanning Tree (CMST)* [12] to capture MCs' battery capacities and (3) improve recharge routes by classifying nodes based on their lifetimes. It is worth mentioning that location-based partitioning of energy requests can make sure that the MCs only move in confined regions, so long distance movement back and forth through the entire field can be avoided. For the second step, construction of CMST ensures that the total energy demands are within MC's recharge capacity. It also forms a subset of nodes that are closer to each other to facilitate the computation of recharge routes. In the last step, for nodes in each tree, we first compute an initial route using any algorithm for the Traveling Salesmen Problem. Then we iteratively insert nodes with limited lifetime into the route and make sure node's lifetime constraint is not violated for each insertion. Next, let us present the energy information gathering protocol first.

## 14.2 Related Work

Extensive research efforts that apply wireless charging to renovate traditional design of battery-powered WSNs are sought in [1–9]. In [6], the impact from wireless charging on routing and sensor deployment is studied. In [4], a greedy algorithm is designed to find a recharge sequence to maximize the lifetimes of sensor nodes. In [3], a joint consideration of wireless charging and message routing in the network is considered to improve network utility and lifetime. In [9], an MC is used for both

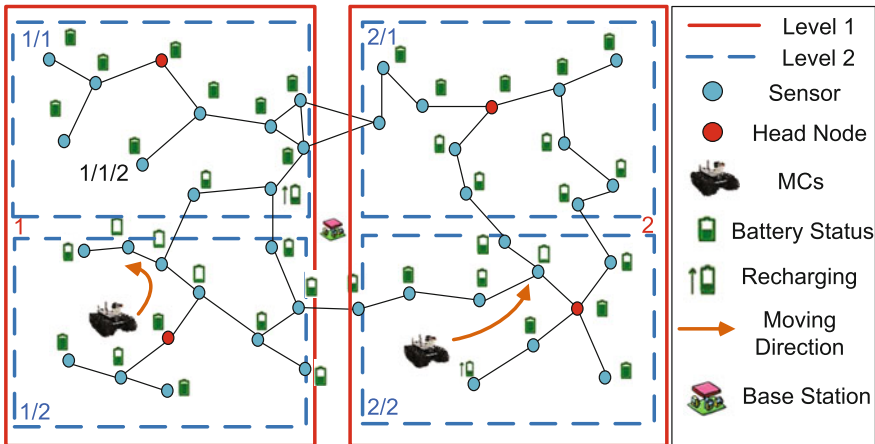


**Fig. 14.1** Illustration of network components and divisions

wireless charging and data collection to reduce system cost. A utility maximization problem is formulated and cross-layer optimization is performed. In [5], a near-optimal solution that utilizes one MC to recharge all sensor nodes is provided. In [7], an online algorithm is developed to schedule multiple MCs to recharge sensor nodes. In [8], the recharge capacity and actual moving cost of the MCs are considered in the recharge scheduling problem. In [1], batteries are allowed to be partially filled and various recharging schemes that require different levels of knowledge are explored. In [2], deployment problems of wireless chargers are studied to extend network lifetime. These works are the pioneering steps to adopt wireless charging in WSNs. In the following sections, we build such a wireless rechargeable sensor network from scratch and describe various components in the network.

## 14.3 Energy Information Gathering Protocol

### 14.3.1 Network Division

For scalability and efficiency, the network is divided into several *areas* and each area is further divided recursively as shown in Fig. 14.1. In practice, the division can be based on geographical coordinates or connectivity among nodes. For simplicity, we use geographical coordinates for determining the boundaries of different areas here in this chapter. Some new *subareas* are generated by each division which also increases the number of *levels* in the network. The process continues till the bottom-level subareas are small enough (contains several tens of nodes or less). Figure 14.1 gives an example of a two-level network with two areas (solid lines). Each area is

further split into two subareas (dashed lines), where each subarea on the second level contains 10–20 sensor nodes.

Then we assign network address prefix for different subareas in a hierarchical manner. Figure 14.1 shows an example of assignments for different subareas. The first level areas are “1” and “2,” and the second level areas are “1/1,” “1/2,” “2/1,” “2/2.” Each subarea is identified by its unique hierarchical address. Nodes have IDs which are identified by the addresses of their bottom-level subareas plus identifiers. For example, “1/1/2” is node “2” in subarea “1/1.” Note that nodes beyond the intended subarea will not receive message propagation. That is, as an example, for messages in the second-level subareas, nodes in area “1/1” will not receive messages from “1/2.” In this way, we can confine the scope of message propagation rather than flood messages in the entire network to reduce overhead.

### 14.3.2 Head Election

After the network areas and their addresses have been configured, the first step is to elect a head node for each area. The election starts from the bottom level and propagates all the way up to the top level. For robustness, node with the highest energy level should be elected as the head node. Since nodes have about the same energy level at initialization, any one of them can become a head node. Although it is trivial to do in a centralized manner (simply select a random node as the head), head election in distributed wireless sensor networks may require a little more efforts. It is done by generating a random number  $x$  at each sensor  $i$ . If  $x$  is larger than a predetermined number threshold, the node will send out a *head election* message in its subarea with the field of maximum value  $x_{max}$  set to  $x$ , and  $ID_{max}$  pointed to its own ID. Then it waits for *head election* messages from other nodes in the area.

A node receiving such a *head election* message compares the  $x_{max}$  in the message with  $x_{max}$  at its local memory. If its local record is larger, the message is discarded. Otherwise, the sensor updates its local record to the  $x_{max}$  in the message, sets  $ID_{max}$  to that in the message, and forwards the message to its neighbors except the node that sent this message. As the propagation finishes, the node with the maximum random number  $x$  wins the head election and all the nodes in this subarea record the node as the head.

After the head elections on the bottom-level are over, new heads then contend to become heads on the  $(l - 1)$ -th level (for a network of  $l$  levels). Similarly, they send out new *head election* messages in the  $(l - 1)$ -th level subareas with their generated random number  $x$  and IDs. Nodes receiving the messages conduct the same comparisons as the bottom-level nodes and forward the messages to their neighbors. After the head nodes are elected at the  $(l - 1)$ -th level, the process continues to the  $(l - 2)$ -th level and so on until the top-level head node is elected.

Different from the bottom-level, starting from the  $(l - 1)$ -th level to the top, nodes do not discard messages with  $x$  smaller than their local copies. For building intermediate routing tables through the subareas, these messages are propagated

in the respective subareas. Each node will have an entry for the child-head in its subarea by pointing to the neighboring node where the head election message has come first. Any duplicate copies arrive later will be discarded. The purpose of this step is to establish routing entries for *energy request* messages to reach lower level child-heads. For the top-level head nodes, the head election messages are propagated throughout the entire network. Later on, when energy information is requested by the MCs, the intermediate nodes will use these routing entries to reach the destined head node.

In summary, head nodes form a head hierarchy throughout all network levels. Note that such network-wide message propagation is performed only at the initialization stage. During operations, head nodes are responsible for managing activities, energy information of their designated subareas. Since they usually handle more traffic loads and computations, they may consume energy faster than other nodes. Once a head node is about to deplete its battery energy, a new head node should be elected to maintain operations of the head hierarchy, which will be discussed later in this section.

### 14.3.3 Energy Request Propagation

After the head hierarchy is constructed, the MCs send *energy request* messages to poll sensors that need wireless charging. In contrast to head elections, energy request is propagated in a top down manner. The MCs perform recharge of a subarea by sending out energy request. For example, an MC can request all the energy information from subarea “1/2” by properly setting the destination address to “1/2” for the energy request. Upon receiving an energy request, the intermediate nodes use the routing entries established during top-level head election and forward it to the designated top-level head nodes. At the same time, an intermediate node also sets up a routing entry pointing to the neighbor where the energy request message is received. These entries can be used later on for guiding the returning energy information messages back to the MCs.

To reduce traveling cost of the MCs and maximize their utility, we need to avoid duplicate selections of nodes in the same subarea from different MCs. Since propagation of energy information also consumes energy, we let the MC with the least number of hop count to receive a head node’s energy information. A field that records the number of hop count is set in the energy request message and is increased by one after each intermediate node. If more than one energy request messages are received at the top-level, an intermediate node updates its routing entry to the neighbor that carries the smallest hop count. Then the aggregated energy information from the head can follow these directions to reach the requested MCs. Since the MCs’ locations are constantly changing after each recharge, the routing entries should be updated each time by new energy request messages. After an intermediate node forwards energy information in the top-level area, it deletes corresponding routing entries.

After the top-level head receives an energy request message, it looks up the destination address and generates a new energy request message to its destined child-heads. For example, if the requested subarea is “1/2,” the top-level head sends out a new energy request to its child-head in subarea “2.” If the requested area is the entire subarea of “1,” it sends out new energy requests to all its child-heads in the subordinate subareas. Similarly, these messages can follow the routing entries set up earlier during head selections to reach the destined child-heads. Intermediate nodes also establish returning routing entries for directing energy information from child-heads to their parent heads. This process is repeated down the head hierarchy until the heads at bottom-level are reached. Different from the upper-levels, heads on the bottom-level flood their respective subareas with energy request messages. In this way, all the nodes in the requested areas will receive the energy request from the MCs.

#### 14.3.4 Energy Information Propagation

Once a sensor node (not head node) receives a bottom-level energy request, it responds with its *energy information* by including its ID and estimated lifetime in the message. Using the routing entries established during the head election, such energy information messages are aggregated at the bottom-level heads.

To reduce redundancy, we can delegate the head nodes some responsibilities to filter out nodes that do not need recharge. A recharge threshold (e.g., 20%) is pre-configured at the head nodes so that any nodes reported with energy higher than the threshold will not be aggregated toward the upper level. If a node’s energy is less than the recharge threshold, its energy information along with ID and lifetime are stored into an aggregated energy message and sent to its parent head. The parent head may have requested energy from several subareas so it waits until receiving all the energy information messages from its child-heads, aggregates all the information and forwards to its parent head. The process is repeated recursively until the requested MC at the top-level is reached. Then the MC examines all the energy information and follows the recharge scheduling algorithm to perform wireless charging.

To keep track of real-time energy status in the network, the MCs may send out new energy requests after it finishes recharging every node. However, it also increases the overhead, delay and energy consumptions in the network. Therefore, we can relax this constraint by reducing the frequencies of such energy request, i.e., send out energy request only at the time when energy on sensors has changed dramatically (e.g., after charging a few tens of nodes). Figure 14.2 gives a pictorial illustration of a network with two levels. After an energy request message is sent by an MC, energy information from the requested area is converged from the bottom level and forwarded to the MC.

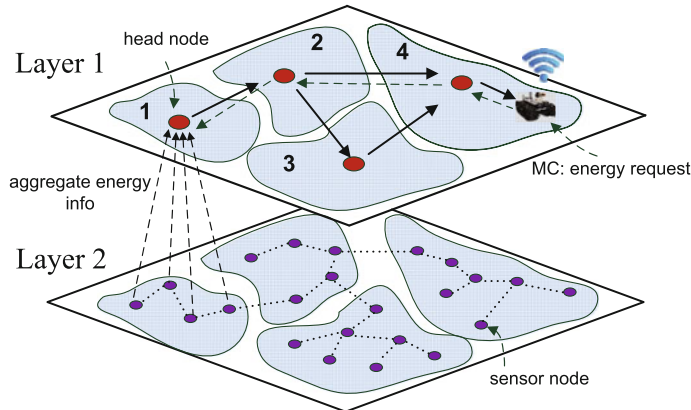


**Fig. 14.2** Propagation of energy request and information in the network

### 14.3.5 Maintenance of Head Hierarchy

We have mentioned earlier that a head node may deplete its energy faster than other nodes due to more traffic loads and computations. In this case, a new head is needed immediately. During each round of energy information gathering, the head node aggregates energy information from all its subordinate subareas so it knows local energy situations and which node has the highest energy. In fact, since head nodes on the upper-levels are elected among the bottom-level head nodes, any head node is always the head of its own bottom-level subarea. We do not need to initiate the head election process again. Instead, we can simply appoint the node with the highest energy as the new head by sending out a *head appointment* message in the bottom levels. Then the new head will flood a *head declaration* message in its subarea to establish routing entries. The new head on the bottom-level then triggers a new head election process in the  $(l - 1)$ -th level subarea. New *head selection* messages with current energy levels from the heads are sent. Node with the maximum energy is elected as a new head for the  $(l - 1)$ -th level subarea. In case if it is the same head, the process stops. Otherwise, a new process of head selection is triggered in its upper level subarea until either the same head is selected or the top level is reached.

### 14.3.6 Summary

We now summarize how the protocol routes different messages briefly. First, routing entries are established during the head election process so that the *energy request* messages can be sent from parent head nodes to child ones. Second, the propagation of *energy request* messages from the MCs, or from parents to child-heads, establishes relevant routing entries for later return of *energy information* messages from top-level

heads or child-heads. In the next section, we describe how to schedule several MCs for wireless charging efficiently.

## 14.4 Recharge Scheduling with Multiple Mobile Chargers

After discussing the protocol that can help the MCs gather energy information efficiently, in this section, we schedule multiple MCs for recharge. Our objective is to maintain perpetual operation of sensors. In other words, no sensor will deplete its battery energy. In addition, a set of practical constraints should be considered. The first constraint comes from the energy cost of the MC itself because it also consumes energy for wireless charging and moving. An oversight of such constraint may cause impractical schedules where the MCs deplete energy en route, become stranded and unable to return the base station. Further, it overestimates MC's recharge capability and node's lifetime since it also takes time for the MCs to return and replace their batteries. The second constraint is imposed by nodes' dynamic battery lifetime. The MCs should follow an effective schedule to resolve all energy requests before their battery deadlines expire. In the meanwhile, the MCs should also save as much moving energy as possible to keep the energy overhead low. Therefore, an interesting question here is that under limited battery capacity, which nodes should the MCs recharge in what order and how to coordinate recharge among different MCs efficiently such that all the sensors are alive?

After some analysis, we can see that the difficulty of the problem lies in achieving conflicting goals. On one hand, the goal to keep the network running pushes the MCs to recharge as many sensors as possible which may cause a significant amount of energy expenditures during movement. On the other hand, the desire to reduce cost requires the MCs to minimize traveling distances in order to save energy cost. An ideal solution should achieve a good balance between these two aspects. Next we show that the recharge scheduling problem can be formulated into a *Vehicle Routing Problem with Capacity and Battery Deadlines* (VRP-CBD) [13]. The *Vehicle Routing Problem* (VRP) is a combinatorial optimization problem that finds an optimal set of routes for a fleet of vehicles to traverse through a set of customer locations and satisfy their demands.

### 14.4.1 Problem Formulation

The recharge scheduling problem is defined in the following. Given a set of MCs  $\mathcal{S} = \{1, 2, \dots, m\}$  and a set of energy requested for recharge  $\mathcal{N} = \{1, 2, \dots, n\}$  ( $n$  is the total number of energy requests), we formalize the problem in the following. Consider a graph  $G = (V, E)$ , where  $V_i$  ( $i \in \mathcal{N}$ ) is the location of node  $i$  to be visited by an MC, and  $E$  is the set of edges. We add a vertex  $V_0^a$  as the starting position of vehicle  $a$ . Each edge  $E_{ij}$  is associated with a traveling energy cost  $c_{ij}$ ,

which is proportional to the distance between nodes  $i$  and  $j$ . During operations, MCs have recharge capacity  $C_a$  which is less than or equal to full capacity  $C_h$  and it determines the maximum number of nodes that can be recharged in each round. Each sensor node  $i$  has lifetime  $L_i$  and energy demand  $d_i$  (demand equals sensor's battery capacity  $C_b$  minus its residual energy).  $A_i$  specifies the arrival time for an MC at sensor node  $i$ .

We introduce two additional decision variables  $x_{ij}^a$  for edge  $E_{ij}$  and  $y_{ia}$  for vertex  $V_i$ . The decision variable  $x_{ij}^a$  is 1 if an edge is visited by MC  $a$ . Otherwise, it is 0. The decision variable  $y_{ia}$  is 1 if and only if node  $i$  is recharged by MC  $a$ . Otherwise, it is 0.  $u_i$  is the position of node  $i$  in the recharging path. Our objective is to minimize the total traveling cost of sensors while guaranteeing either the recharge capacities of MCs are not exceeded or no sensor node depletes battery energy.

$$\mathbf{P1 :} \quad \min \sum_{a=1}^m \sum_{i=1}^n \sum_{j=1}^n c_{ij} x_{ij}^a \quad (14.1)$$

### Subject to

$$\sum_{j=1}^n x_{0j}^a = 1; a \in \mathcal{S} \quad (14.2)$$

$$\sum_{i=1}^n x_{ik} = \sum_{j=1}^n x_{kj} = 1; k \in \mathcal{N} \quad (14.3)$$

$$\sum_{i=1}^n d_i y_{ia} + \sum_{i=1}^n \sum_{j=1}^n c_{ij} x_{ij}^a \leq C_a; a \in \mathcal{S} \quad (14.4)$$

$$\sum_{a=1}^m y_{ia} = 1; i \in \mathcal{N} \quad (14.5)$$

$$A_i \leq L_i; i \in \mathcal{N} \quad (14.6)$$

$$x_{ij}^a \in \{0, 1\}; i, j \in \mathcal{N}, a \in \mathcal{S} \quad (14.7)$$

$$y_{ia} \in \{0, 1\}; i \in \mathcal{N}, a \in \mathcal{S} \quad (14.8)$$

$$1 \leq u_i \leq n_r; i \in \mathcal{N} \quad (14.9)$$

$$u_i - u_j + (n_r - m)x_{ij} \leq n_r - m - 1; i, j \in \mathcal{N}, i \neq j \quad (14.10)$$

In the above formulation, constraint (14.2) states that the recharge tour starts at initial location 0 for each MC.<sup>1</sup> Constraint (14.3) ensures the connectivity of the path and every sensor is visited only once. Constraints (14.4) and (14.5) guarantee MC's recharge capacity is not exceeded and each sensor is visited by only one MC.

---

<sup>1</sup>The initial locations are usually the last node visited in the previous recharge tour. If the MC has returned to the base station for battery replacement. The initial location is the base station.

Constraint (14.6) guarantees an MC arrives at a sensor node before its battery deadline expires (within lifetime). Constraints (14.7) and (14.8) impose decision variables  $x_{ij}$  and  $y_{ia}$  to be 0–1 valued. Constraints (14.9) and (14.10) eliminate the subtour in the recharge routes, which are formulated according to [14].

Obviously, the problem is NP-hard if we consider the original Vehicle Routing Problem [13] as a special case with unlimited vehicle capacity as well as unspecified visiting deadlines. A direct solution to the problem is not very common so we review some of the previous works that have partially solve the problem.

A great amount of research efforts have been devoted in the context of Vehicle Routing Problem with either vehicle capacity or battery deadline constraints. The Capacitated Vehicle Routing Problem states that a number of vehicles with a fixed capacity start from a depot to visit client locations and the objective is to minimize the total traveling distance of the vehicles [15]. In [16], the Vehicle Routing Problem with Time Windows is studied. For each client location, there is an associated time window such that the vehicle should visit the location within the interval governed by the start and end of the time window. A local search algorithm based on  $k$ -exchange mechanism is proposed and computation for checking feasibility of the time constraint is also studied. Although these works have tried to solve the problem by considering only a single constraint from Eq. (14.4) or (14.6), combining them together is definitely more challenging and makes the problem much more complicated.

The nature of the problem makes any attempt to use standard optimization techniques [17] not practical in a wireless environment. This is because these methods usually deal with datasets from static inputs and the optimization is done offline by a one-time effort. Nevertheless, in wireless sensor networks, the pattern of energy consumptions is usually dynamic which depends on tasks, duty cycles, communications, or even external events. As a result, the input to our optimization problem is more dynamic than that most existing works have considered. Finally, the existing techniques require high computation power from a central controller whereas energy information is gathered by MCs in a distributed manner. It is more desirable to implement online calculations on the MCs. Therefore, our objective is to develop an algorithm that is suitable to the wireless environment. Next, we design an adaptive algorithm step by step to address all the issues in problem formulations.

#### **14.4.2 Recharge Scheduling Algorithm—An Adaptive Algorithm**

##### **14.4.2.1 Adaptive Network Partitioning**

In the first step, an MC requests sensor nodes for energy information based on the protocol discussed in Sect. 14.3. Then based on the locations of energy requests, the

MC partitions the network into  $m$  regions. The partitioning requests are disseminated to other MCs via long range radios (e.g., 802.16 WiMax).

For efficient network partitioning, we use the well-known *K-means* algorithm [11]. The K-means algorithm can adaptively organize the subsets of nodes into different regions and minimize their square sums of distances regarding to the centroid of each region. After the partition, MCs only need to take care of energy requests in their selected regions. In this way, MCs will move within confined scope in the network and avoid long distance movements.

For each region, the K-means algorithm minimizes the intra-region square sum of internode distance,

$$S = \sum_{j=1}^m \sum_{i=1}^n \|n_i^{(j)} - \mu^{(j)}\|^2 \quad (14.11)$$

in which  $\|n_i^{(j)} - \mu^{(j)}\|^2$  is the square of distance between a node  $n_i$  in region  $j$  to the region's centroid  $\mu^{(j)}$  (represented by the mean of  $x$ ,  $y$  coordinates from all the nodes in the region). The process of partitioning is described in the following.

First, the MC selects a number of  $m$  sensor nodes with the minimum lifetime from all the nodes to be the initial centroid. Note that since the number of regions is equivalent to the number of MCs  $m$ . The initial number of centroids is set to  $m$  here. Then we assign each node to its closest centroid till all the nodes have been associated with a centroid. The next step is to update the centroid locations, so we recalculate their coordinates by taking the mean from all the  $x$  and  $y$  coordinates. This process is repeated until the centroids no longer change. The final centroid of each region represents a virtual point that has the minimal square sum of distances to all the nodes in the region. Then the MCs can use this point as the starting location for the recharging route.

#### 14.4.2.2 Capacitated Minimum Spanning Trees

After the first step,  $m$  regions are generated and each MC only works within its region to resolve energy requests. In the second step, we further look for a subset of nodes such that all their energy demands plus the moving cost among them do not exceed MC's recharge capacity (Eq. 14.4). In the meanwhile, since our objective is to minimize traveling cost for the MCs, we want to find subsets of nodes that are closer to each other. It suggests find the Capacitated Minimum Spanning Tree (CMST) [12] in which the MC's recharge capacity is reflected by the capacity of the tree and constructing minimum spanning trees can facilitate finding minimal moving cost. In other words, CMST makes sure that sensor nodes close to each other are placed in the same tree which will be covered by the same recharge route.

The optimal solution of CMST requires examinations of all possible trees and pick the one with the lowest cost. The size of the problem grows exponentially with the number of nodes. An efficient algorithm proposed by Esau-Williams (EW) finds a suboptimal solution very close to optimality in polynomial time [12]. The EW

algorithm falls into the category of “saving algorithms” that is similar to the well-known *Clarke–Wright algorithm* [18] for the Vehicle Routing Problem. In principle, the EW algorithm merges any two subtrees when there is a “saving” in the total cost of two merged trees.

However, there are some challenges to apply the original EW algorithm directly in our problem. First, while determining whether two subtrees can be merged, only energy demands from sensors are accounted whereas the traveling costs are not. Second, multiple CMST could be generated depending on the energy of the MCs. Which trees should the MCs pick? We extend the original EW algorithm to overcome these limitations.

To solve the first problem, we utilize a deterministic upper bound developed in [19] for the shortest path problem. For a rectangle of side length  $a, b$  and  $n$  nodes, a loose upper bound is  $\sqrt{2(n-2)ab} + 2(a+b)$ . If the sensing field is a square with side length  $L$  and MC’s moving cost  $e_c$  J/m, the moving energy of  $n$  nodes is bounded by  $(\sqrt{2(n-2)} + 4)L e_c$ . For the second extension, when several trees are generated, the tree with maximal ratio of total energy demand to edge cost is selected. In this way, we can maximize the utility of limited resources on MCs by improving energy efficiency in the network.

Next, we explain the extended EW algorithm. A distance matrix is introduced to maintain costs of tree nodes and facilitate the computation process. Each MC computes CMST independently in its region by updating its own distance matrix. Denote recharge subset  $\mathcal{N}_a$  with  $n_a$  nodes for MC  $a$  ( $\bigcup_{a=1}^m \mathcal{N}_a = \mathcal{N}$ ). In the EW algorithm, an important *trade-off function*  $t_i$  for each node in its recharge set  $\mathcal{N}_a$  is defined as,  $t_i = \min(c_{ij}^{(a)}) - c_{0i}^{(a)}$  and  $j \in P_i$ , where  $P_i$  is the neighboring set of node  $i$ ,  $\min(c_{ij}^{(a)})$  finds the minimum cost from node  $i$  to its neighbor  $j$  in  $P_i$  and  $c_{0i}^{(a)}$  is the cost from node  $i$  to the MC’s starting position. Recall that we can set the starting locations to be the centroid output from the K-means algorithm, which is also the root of the CMST. The trade-off function evaluates whether it has more cost savings to merge subtrees of nodes  $i$  and  $j$ . Positive  $t_i$  indicates that the MC enjoys less cost to directly travel from the root to node  $i$ . In this case, merging subtrees of nodes  $i$  and  $j$  is not preferred. The value of negative  $t_i$  indicates how much it can be saved by merging subtrees of  $i$  and  $j$ . In each iteration, the most negative trade-off value yields the most savings.

After all the trade-off values have been computed, we search through all  $t_i$  ( $\forall i = 1, \dots, n_a$ ) and look for the most negative trade-off value. Assume  $t_k$  is the most negative trade-off and  $j$  is  $k$ ’s minimum cost neighbor. To capture the constraint in Eq. (14.4), if the sum of energy demands from the subtrees of  $k$  and  $j$  plus upper bound of their traveling costs is less than MC’s energy, we merge the subtrees of  $k$  and  $j$  since we can cover the subtrees of  $k$  and  $j$  without violating the capacity constraint. Since merging  $k$  and  $j$  has resulted in a lower total traveling cost to  $k$ , direct connection from the root to reach  $k$  has higher cost and should be avoided. So we remove the edge from node  $k$  to the root by setting  $c_{0k}^{(a)}$  in the distance matrix to  $\infty$ .

The next step is to update the minimum cost of the newly merged tree to the root. It is done by updating the minimum cost in the distance matrix from the tree to the root by setting the value to  $\min(c_{0i}^{(a)})$ , where  $i$  is the node in the newly merged tree.

If merging subtrees of  $k$  and  $j$  violates MC's recharge capacity, we need to restrict any further actions to merge  $j$  to  $k$  and these two trees should be covered by the MC in two separate runs. Then we recompute the trade-off function  $t_k$  to search for the next neighboring node that results in minimum trade-off until the next valid neighboring node  $j$  is found and merged to the existing trees. The iteration continues until all the trade-offs become nonnegative. That is, no more saving can be made.

After the CMST has been generated, the MC selects a tree with the highest ratio between energy demand and sum of tree's edge cost. Then it will utilize the route improvement algorithm to form the shortest recharging path among the tree nodes. After an MC finishes recharging nodes in a tree, it checks whether its energy falls below an energy threshold. If so, it returns to the base station for battery replacement. Algorithm 4 summarizes the extended EW algorithm.

---

**Algorithm 4:** Extended Esau-Williams algorithm

---

**Input :** recharging node set  $\mathcal{N}_r$ , distance matrix  $D^{(a)}$ , recharge capacity  $C_a$ , demand of nodes  $d_i, i \in \mathcal{N}_a$ .

**Output:** CMST nodes need to recharge.

- 1 Initialize  $t^{(a)} < 0$ , weight of tree,  $C^{(a)} = 0$ ;
- 2 **while**  $t^{(a)} < 0$  **do**
- 3     Find neighbor  $m_i$  of  $i$  results min cost,  $\min_{m_i} D^{(a)}(i, m_i)$ . Compute trade-off value list  $t_i^{(a)} = D^{(a)}(i, m_i) - D^{(a)}(1, i)$ ;
- 4     Find  $k$  and  $j$  resulting most negative trade-off value,  
 $k \leftarrow \min_i(t^{(a)}), j \leftarrow m_k$ ;
- 5     **while** ( $N_{new}$  is not accepted) and (all  $t_i^{(a)} < 0$ ) **do**
- 6         Add new nodes  $N_{new} \leftarrow k + j$  if not exist in current trees;
- 7         **if** weight of merging subtree of  $N_{new} < C_a$  **then**
- 8             Add  $N_{new}$  to corresponding tree  $i$ , update cumulative weight of corresponding tree  $i$ ,  $C_i^{(a)}$ . Declare  $N_{new}$  is accepted.
- 9         **else**
- 10             update  $D^{(a)}(k, j) \leftarrow \infty$ . Search for next min cost neighbor for  $k$ ,  
 $m_k \leftarrow \min_{m_k} D^{(a)}(k, m_k)$ ;
- 11             Recompute trade-off for  $k$ ,  $t_k^{(a)} = D^{(a)}(k, m_k) - D^{(a)}(1, k)$ . Declare  $N_{new}$  rejected.
- 12         **end if**
- 13     **end while**
- 14 **end while**
- 15 Select a tree results maximum energy efficiency.

---

### 14.4.2.3 Improve Recharge Routes

Based on the CMST obtained in each region, next we want to further improve the recharge routes and make sure the MCs arrive before sensors' battery deadlines. It is not difficult to see that the total time span for recharging all the nodes in the CMST is bounded by the sum of their recharge time. A trivial case is that all the nodes have lifetime much larger than such time span (total recharge time). We can simply use an algorithm for the Traveling Salesman Problem to find the shortest route. During operation, there could be some nodes with lifetime less than the total recharge time. If we disregard their lifetime and still use the shortest route, they might deplete their battery energy before an MC arrives. Therefore, we need to expedite their recharge by placing these nodes at advantageous positions in the recharge sequence. The details of the algorithm design are explained in the following.

Let us denote the nodes from CMST by a recharge node set  $\mathcal{N}_r^{(a)}$  ( $\mathcal{N}_r^{(a)} \subseteq \mathcal{N}_a$ ). First, we classify nodes into two categories according to their lifetimes. If a node's lifetime is larger than the total recharge time, we claim this node to be feasible and form a *feasible node set*  $\mathcal{N}_f^{(a)}$ . These nodes can be placed anywhere in the recharge sequence. Otherwise, a node requires expedited service to meet its battery deadline. We denote such a set of nodes as a prioritized set  $\mathcal{N}_p^{(a)}$  ( $\mathcal{N}_f^{(a)} \cup \mathcal{N}_p^{(a)} = \mathcal{N}_r^{(a)}$ ).

Second, we use a Traveling Salesman Problem algorithm to find the shortest route as the initial sequence  $\Psi$  among nodes in the feasible set  $\mathcal{N}_f^{(a)}$ . For example, the  $\mathcal{O}(n^2)$  nearest neighbor heuristic algorithm is easy to implement, where  $n$  is the number of nodes. Then we insert nodes from the prioritized set  $\mathcal{N}_p^{(a)}$  into  $\Psi$  one by one. For each insertion, we make sure the lifetime constraints in Eq. (14.6) for all the nodes in the prioritized set still hold. We sort the nodes in  $\mathcal{N}_p^{(a)}$  in a descending order of residual lifetimes and denote the sorted sequence as  $\Omega$ . We insert these nodes starting from the first node  $\Omega_1$  with the maximal lifetime. Let  $A_i$  denote the arrival time of the MC at the  $i$ -th node in the shortest path  $\Psi$ ,  $i = \{1, 2, \dots, n_f^{(a)}\}$ .

To insert the  $j$ -th node  $\Omega_j$  from  $\Omega$  into  $\Psi$ , we first find position  $m_t$  in  $\Psi$  such that  $A_{m_t} \leq l_{\Omega_j}$  and  $A_{m_t+1} > l_{\Omega_j}$ , where  $l_{\Omega_j}$  is  $\Omega_j$ 's lifetime. We call  $m_t$  the *temporary maximum position* to insert  $\Omega_j$ . It indicates the maximum number of nodes in  $\Psi$  that can be recharged before node  $\Omega_j$  depletes its battery.

Then we need to further narrow down the maximum position to insert  $\Omega_j$  by considering the remaining  $|\Omega| - j$  nodes. Because it is possible that all the remaining nodes are inserted before  $\Omega_j$ , we look for a position to accommodate all possible insertions such that  $\Omega_j$  can still meet its battery deadline. We look for the *maximum position*  $m$  such that  $A_m \leq A_{m_t} - \sum_{i=j+1}^{n_p^{(a)}} t_i$  and  $A_{m+1} > A_{m_t} - \sum_{i=j+1}^{n_p^{(a)}} t_i$ , where  $t_i$  is the recharge time of  $\Omega_j$ . At this point, the maximum position  $m$  represents the rightmost position  $\Omega_j$  can be inserted in an extreme case if all remaining nodes are later inserted before  $\Omega_j$ . For  $\Omega_j$ , we can find a position for minimal cost insertion up to position  $m$  in the recharge sequence. This position is selected as the final insertion position for  $\Omega_j$  and a new sequence  $\Psi$  is generated. We remove  $\Omega_j$  from  $\Omega$  and consider the next node in  $\Omega$  until  $\Omega$  is exhausted. During insertion, it is also possible that there is no position available to insert a node from  $\Omega$  to  $\Psi$ . It means

no matter where the node is placed in the sequence, it will still deplete its battery. In this case, we can insert the node at the beginning of the recharge sequence to minimize the time duration when nodes are not functional. Table 5 gives a summary of the recharge route improvement algorithm.

---

**Algorithm 5:** Route improvement algorithm

---

**Input :** CMST  $\mathcal{N}_r^{(a)}$ , lifetime  $l_i$  and recharge time  $t_i$ ,  $i \in \mathcal{N}_r^{(a)}$ , distance matrix  $D^{(a)}$ , feasible set  $\mathcal{N}_f^{(a)}$ .

**Output:** Resultant recharge sequence  $\Psi$ .

- 1 Compute shortest path in the feasible set,  $\Psi \leftarrow \text{TSP}(\mathcal{N}_f^{(a)})$ . Sort  $\mathcal{N}_p^{(a)}$  in a descending order of lifetime as  $\Omega$ ;
- 2 Initialize  $i \leftarrow 1$ , last step node position  $k \leftarrow \infty$ ;
- 3 **while**  $\Omega \neq \emptyset$  **do**
- 4   Find temporary max position  $m_t$  in  $\Psi$  such that  $A_{m_t} \leq l_{\Omega_i}$  and  $A_{m_t+1} > l_{\Omega_i}$ ;
- 5   Find the max insertion position  $m$  such that  $A_m \leq A_{m_t} - \sum_{k=i+1}^{n_p^a} t_k$  and  $A_{m+1} > A_{m_t} - \sum_{k=i+1}^{n_p^a} t_k$ ;
- 6   **if** Cannot find  $m \geq 0$  **then**
- 7     | Insert node  $\Omega_i$  at the beginning of  $\Psi$
- 8   **else**
- 9     | Set minimum cost  $c_{min} \leftarrow \infty$ ;
- 10    | **for**  $x$  from 0 to  $m$  **do**
- 11      | Insert node  $\Omega_i$  into  $\Psi$ , get temporary sequence  $\Psi_t$ . Calculate cost  $c \leftarrow \sum_{j=1}^{|\Psi_t|-1} D^a(j, j+1)$ ;
- 12      | **if**  $c < c_{min}$  **then**
- 13       | |  $\Psi \leftarrow \Psi_t$ ,  $c_{min} \leftarrow c$ ,  $k \leftarrow x$ .
- 14      | **end if**
- 15    | **end for**
- 16   **end if**
- 17   |  $i \leftarrow i + 1$ , update  $\Omega \leftarrow \Omega - i$ ;
- 18 **end while**
- 19 Return recharge sequence  $\Psi$ , minimum cost  $c_{min}$ ;

---

#### 14.4.2.4 Complexity Analysis

Finally, we analyze the complexity of our algorithms. The K-means algorithm requires  $\mathcal{O}(mnc)$  time in which  $c$  represents the number of iterations until convergence [11]. For calculating the CMST, in the worst case, there is only one MC to handle all  $n$  nodes. For the extended EW algorithm, finding the minimum trade-off value requires  $(n^2 + 2n)$  iterations at the outer loop. In the inner loop, the worst case is that for a node with the minimum trade-off value, every minimum cost neighbor is rejected due to capacity violations so a total number of  $n$  iterations are required. Thus, the time complexity is  $\mathcal{O}(n^3)$ .

For the route improvement algorithm, a typical TSP algorithm such as nearest neighbor requires  $\mathcal{O}(n^2)$  time. Sorting nodes' lifetimes requires  $\mathcal{O}(n \log n)$  time. Inserting nodes into the established route requires  $\mathcal{O}(n^2)$  time. Hence, the total time complexity of route improvement algorithm is  $\mathcal{O}(n^2)$ . In sum, the total time complexity of the adaptive algorithm  $\mathcal{O}(mnc + n^3)$  time. For  $n$  much larger than  $m$  and  $c$ , the time complexity is dominated by  $\mathcal{O}(n^3)$ .

#### 14.4.3 A Running Example of the Algorithm

We show an example of the algorithm in Figs. 14.3, 14.4, 14.5, and 14.6. During operation, a snapshot of energy requests is presented in Fig. 14.3 and three MCs

**Fig. 14.3** Snapshot of energy requests

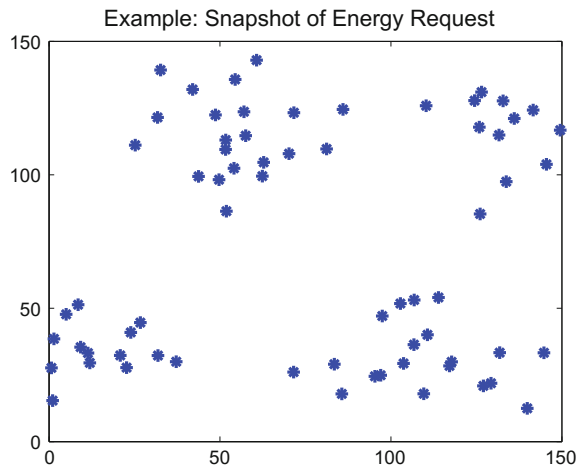


**Fig. 14.4** Adaptive network partition of energy requests

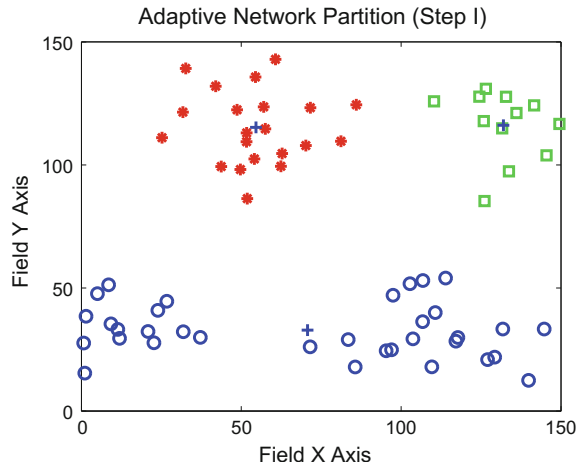


**Fig. 14.5** Generate capacitated minimum spanning trees

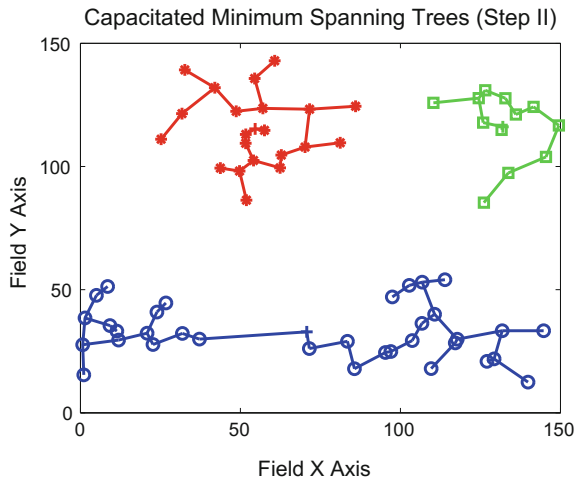
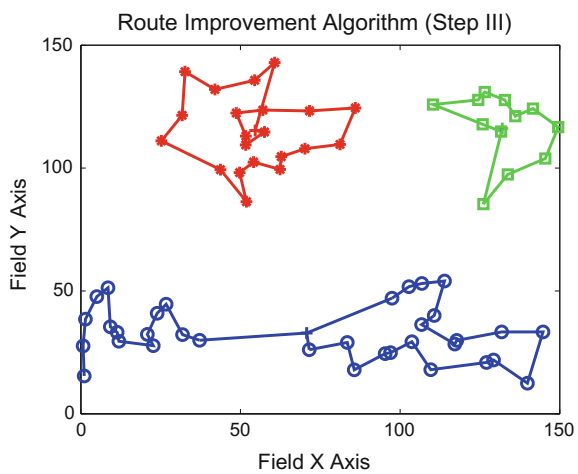


**Fig. 14.6** Improved recharge routes for MCs



cooperate to recharge these nodes. Figure 14.4 shows an adaptive partition of the network into three regions using the K-means algorithm. Then each MC computes its CMST in a distributed fashion as shown in Fig. 14.5. Next, each MC calculates an improved recharge route on the selected tree shown in Fig. 14.6.

## 14.5 Performance Evaluation

The adaptive algorithm is evaluated in a discrete event-driven simulator. A number of  $N = 500$  sensor nodes are uniformly randomly deployed over a square sensing field with side length  $L = 150$  m. All sensors transmit at the same power level with

fixed transmission range  $d_r = 15$  m. The total battery recharge time is 78 mins as modeled from [10]. Each MC is equipped with a 12 V battery. At the speed of 1 m/s, the current draws from the battery is 4 Ah. Thus, the moving energy consumption is  $e_s = 48$  J/m. We vary the number of MCs  $m$  from 2 to 5. The simulation is set to run for 4 months time.

For comparison, we compare the performance of the adaptive algorithm with the simplest approach we can think of, which is a greedy algorithm. The algorithm basically directs the MCs to their next available node with the closest distance. When the MC's energy falls below a predetermined threshold, it returns to the base station for battery replacement and then resumes recharge in the same fashion.

### 14.5.1 Nonfunctional Nodes

First, we evaluate the number of nonfunctional nodes in Figs. 14.7 and 14.8. When a sensor node depletes its battery energy, it becomes nonfunctional until recharged.

Let us examine the performance of the greedy algorithm first. When  $m = 2$ , the number of nonfunctional nodes surges dramatically around 18 days to nearly 90% until it decreases and stabilizes between 20 and 30% at 40 days. Similar phenomenon is observed for  $m = 3$ . This is because nodes at the closest locations may not be those that require immediate recharge. For  $m = 2\text{--}5$ , it is observed that there is persistently more than 5% nonfunctional nodes. In contrast, the adaptive algorithm has more stability. When  $m = 2, 3$ , the huge spike disappeared. For  $m = 5$ , the adaptive algorithm can maintain perpetual network operation by reducing the nonfunctional nodes to zero. This is because of the additional step in our algorithm to capture sensors' battery deadlines.

**Fig. 14.7** Evolution of nonfunctional nodes using the greedy algorithm

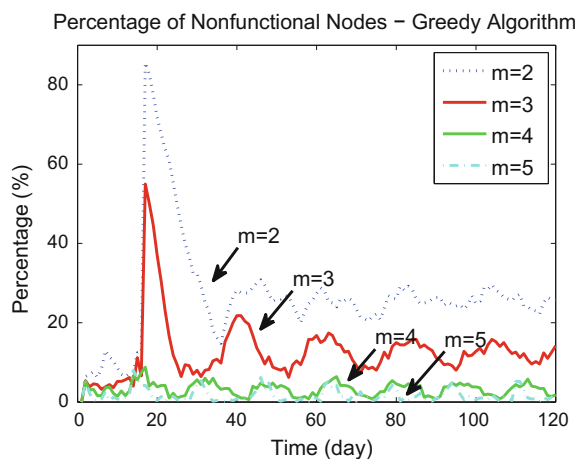
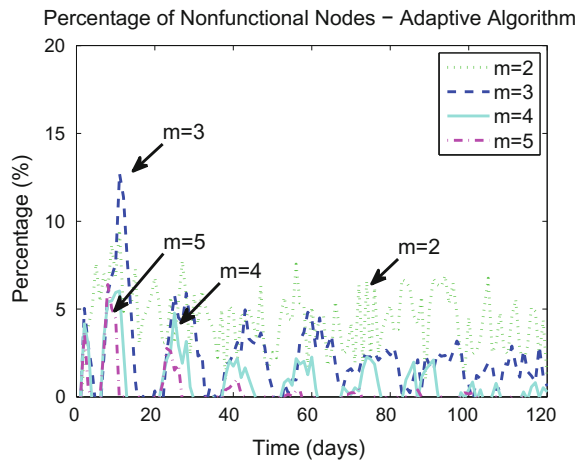


**Fig. 14.8** Evolution of nonfunctional nodes using the adaptive algorithm



### 14.5.2 Energy Consumption and Replenishment

Next, we present the evolution of energy consumption versus replenishment to gain some insights of energy evolution in the network. We illustrate the energy changes using the adaptive algorithm in Fig. 14.9 and trace the evolution of energy consumed and replenished when  $m = 2, 4$ . From the previous results, we can tell  $m = 2$  cannot sustain network operations. Thus some nodes continuously deplete battery and no longer consume energy, which causes the drop in energy consumption at the very beginning. Since the recharge capability from the two MCs has put an upper limit on the energy consumption, the two curves reach an equilibrium and converge after 30 days. For  $m = 4$ , we also observe that when there is a drop in energy consumption,

**Fig. 14.9** Trace of energy evolution for energy consumption and replenishment

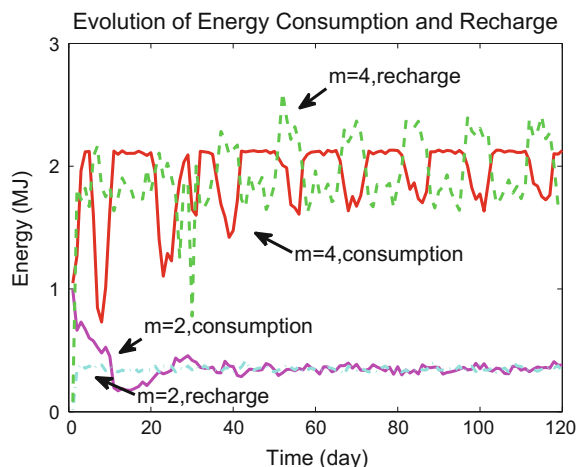
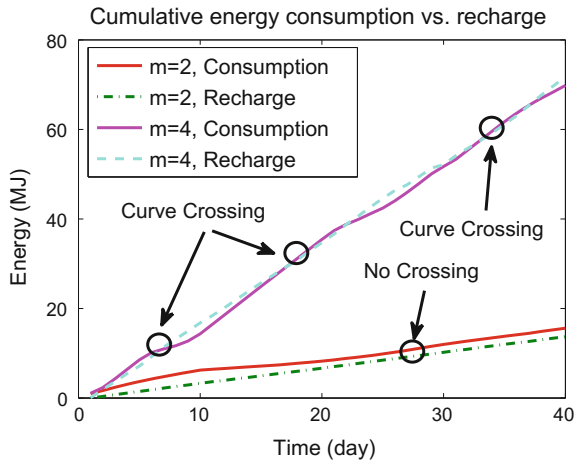


**Fig. 14.10** Trace of cumulative energy consumption and replenishment



whereas the energy replenishment correspondingly jumps up, which represents MCs acting effectively in response to battery depletions.

We also show the cumulative energy evolution in Fig. 14.10. For better observations of the gaps and intersections between curves, we plot simulation time for 40 days. If the energy replenishment curve is above the consumption curve, more energy has been refilled into the network than consumed, and vice versa. For  $m = 2$ , the energy consumption curve is above the energy replenishment curve. A gap is observed at the first 10 days, indicating energy replenishment can barely keep up with consumptions and we have perceived similar results in Fig. 14.7.

In contrast, with  $m = 4$ , the energy consumption curve stays above replenishment until the two curves first cross each other around 6 days. This is because from the very beginning, more energy is consumed than replenished. Around 6 days, a few nodes have depleted energy and stopped consuming more, which brings down the consumption curve. The replenishment curve stays above the consumption curve until the next crossing around 20 days. Therefore, the evolution of network energy shows that  $m = 4$  here is a threshold case since energy consumption and replenishment are almost equivalent to each other in the network.

#### 14.5.2.1 Nonfunctional Durations

Figures 14.11 and 14.12 compare the percentage of duration that nodes are nonfunctional regarding their locations. For the greedy algorithm, the peak value of 20 % time in nonfunctional status is observed whereas the adaptive algorithm yields much less results (around 6 %). The adaptive algorithm also spreads nonfunctional durations across the field while the spikes of the greedy algorithm are highly concentrated

**Fig. 14.11** Durations for nonfunctional nodes when  $m = 4$  for the greedy algorithm

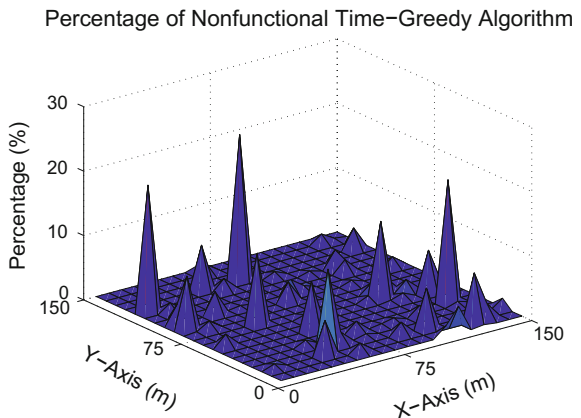
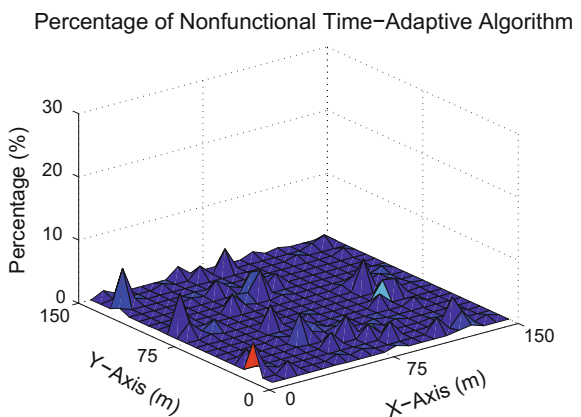


**Fig. 14.12** Durations for nonfunctional nodes when  $m = 4$  for the adaptive algorithm

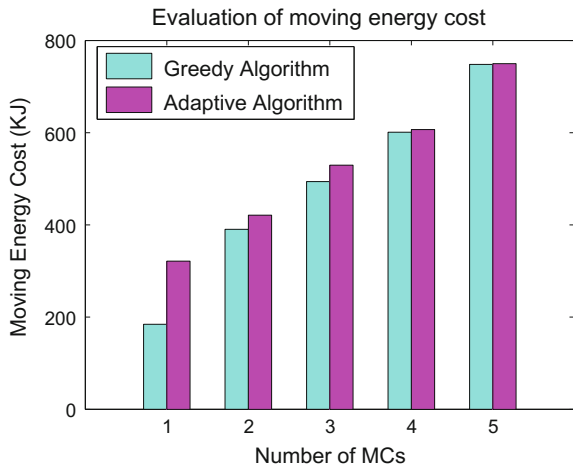


around cluster head areas. This is because nodes close to cluster heads consume energy much faster whereas the greedy algorithm only recharges the nearest node in each step and has no measure for battery deadlines. In contrast, the adaptive algorithm considers battery deadlines explicitly so its duration of nonfunctional nodes is significantly less than that of the greedy algorithm.

### 14.5.3 Operating Energy Cost

Finally, we evaluate the moving energy cost of MCs. Figure 14.13 compares the average moving cost of each MC for the greedy and adaptive algorithms. When  $m = 1\text{--}3$ , the adaptive algorithm consumes more energy on the MCs. This is because it takes care of nodes that require recharging more actively whereas the greedy algorithm only searches for the nearest nodes for recharging. When  $m = 4\text{--}5$ , network partition

**Fig. 14.13** Comparison of moving cost between greedy and adaptive algorithms



is more effective with smaller divided regions so movements of the MCs are confined in smaller regions. This brings down the movement energy of MCs for the adaptive algorithm to the same level as the greedy algorithm.

## 14.6 Conclusions

In this chapter, we consider the important recharge scheduling problem of multiple MCs. We first propose a communication protocol to realize distributed energy information gathering on demand. Based on the energy information collected, we formulate recharge scheduling problem into a Vehicle Routing Problem with Capacity and Battery Deadline constraints, which is NP-hard. We propose a three-step adaptive algorithm that systematically captures the recharge capacity and battery deadlines while minimizing traveling costs. Finally, we evaluate and compare the proposed algorithm to a trivial greedy algorithm by extensive simulations. The results indicate that the adaptive algorithm provides much better stability by reducing the number of nonfunctional nodes and has similar energy cost compare to the greedy approach.

## References

1. Angelopoulos, C.M., Nikoletseas, S., Raptis, T.P., Raptopoulos, C., Vasilakis, F.: Efficient energy management in wireless rechargeable sensor networks. In: Proceedings of the 15th ACM International Conference on Modeling, Analysis and Simulation of Wireless and Mobile Systems, MSWiM '12, pp. 309–316. ACM, New York, NY, USA (2012). doi:[10.1145/2387238.2387291](https://doi.org/10.1145/2387238.2387291)
2. He, S., Chen, J., Jiang, F., Yau, D.K.Y., Xing, G., Sun, Y.: Energy provisioning in wireless rechargeable sensor networks (2013). doi:[10.1109/TMC.2012.161](https://doi.org/10.1109/TMC.2012.161)
3. Li, Z., Peng, Y., Zhang, W., Qiao, D.: J-roc: A joint routing and charging scheme to prolong sensor network lifetime (2011). doi:[10.1109/ICNP.2011.6089076](https://doi.org/10.1109/ICNP.2011.6089076)
4. Peng, Y., Li, Z., Zhang, W., Qiao, D.: Prolonging sensor network lifetime through wireless charging (2010). doi:[10.1109/RTSS.2010.35](https://doi.org/10.1109/RTSS.2010.35)
5. Shi, Y., Xie, L., Hou, Y.T., Sherali, H.D.: On renewable sensor networks with wireless energy transfer. In: INFOCOM, 2011 Proceedings IEEE, pp. 1350–1358 (2011). doi:[10.1109/INFCOM.2011.5934919](https://doi.org/10.1109/INFCOM.2011.5934919)
6. Tong, B., Li, Z., Wang, G., Zhang, W.: How wireless power charging technology affects sensor network deployment and routing (2010). doi:[10.1109/ICDCS.2010.61](https://doi.org/10.1109/ICDCS.2010.61)
7. Wang, C., Li, J., Ye, F., Yang, Y.: Multi-vehicle coordination for wireless energy replenishment in sensor networks. In: 2013 IEEE 27th International Symposium on Parallel Distributed Processing (IPDPS), pp. 1101–1111 (2013). doi:[10.1109/IPDPS.2013.22](https://doi.org/10.1109/IPDPS.2013.22)
8. Wang, C., Li, J., Ye, F., Yang, Y.: Recharging schedules for wireless sensor networks with vehicle movement costs and capacity constraints. In: 2014 Eleventh Annual IEEE International Conference on Sensing, Communication, and Networking (SECON), pp. 468–476 (2014). doi:[10.1109/SAHCN.2014.6990385](https://doi.org/10.1109/SAHCN.2014.6990385)
9. Zhao, M., Li, J., Yang, Y.: A framework of joint mobile energy replenishment and data gathering in wireless rechargeable sensor networks (2014). doi:[10.1109/TMC.2014.2307335](https://doi.org/10.1109/TMC.2014.2307335)
10. Panasonic ni-mh battery handbook. [http://www2.renovaar.ee/userfiles/panasonic\\_ni-mh\\_handbook.pdf](http://www2.renovaar.ee/userfiles/panasonic_ni-mh_handbook.pdf)
11. MacQueen, J.: Some methods for classification and analysis of multivariate observations. In: Proceedings of the Fifth Berkeley Symposium on Mathematical Statistics and Probability, Volume 1: Statistics, pp. 281–297. University of California Press, Berkeley, California (1967). <http://projecteuclid.org/euclid.bsmsp/1200512992>
12. Esau, L.R., Williams, K.C.: On teleprocessing system design, part ii: a method for approximating the optimal network. IBM Syst. J. **5**(3), 142–147 (1966). doi:[10.1147/sj.53.0142](https://doi.org/10.1147/sj.53.0142)
13. Christofides, N., Mingozzi, A., Toth, P.: Exact algorithms for the vehicle routing problem, based on spanning tree and shortest path relaxations. Math. Program. **20**(1), 255–282 (1981). doi:[10.1007/BF01589353](https://doi.org/10.1007/BF01589353)
14. Gavish, B.: The formulation of the m-salesman traveling salesman problem. Manage. Sci. **22**(6), 704–705 (1976). doi:[10.1287/mnsc.22.6.704](https://doi.org/10.1287/mnsc.22.6.704)
15. Chandran, B., Raghavan, S.: Modeling and solving the capacitated vehicle routing problem on trees, pp. 239–261. Springer US, Boston, MA (2008). doi:[10.1007/978-0-387-77778-8\\_11](https://doi.org/10.1007/978-0-387-77778-8_11)
16. Savelsbergh, M.W.P.: Local search in routing problems with time windows. Ann. Oper. Res. **4**(1), 285–305 (1985). doi:[10.1007/BF02022044](https://doi.org/10.1007/BF02022044)
17. Desrochers, M., Lenstra, J.K., Savelsbergh, M.W., Soumis, F.: Vehicle routing with time windows: optimization and approximation. In: Vehicle routing: Methods and studies, vol. 16, pp. 65–84 (1988)
18. Clarke, G., Wright, J.W.: Scheduling of vehicles from a central depot to a number of delivery points. Oper. Res. **12**(4), 568–581 (1964)
19. Jaillet, P.: Probabilistic traveling salesman problems. Ph.D. thesis, Massachusetts Institute of Technology (1985)

# Chapter 15

## Distributed Coordination Protocols for Wireless Charging in Sensor Networks

Adelina Madhja, Sotiris Nikoletseas and Theofanis P. Raptis

**Abstract** In this chapter, we investigate the problem of efficient wireless power transfer in wireless sensor networks where special mobile entities called Mobile Chargers, traverse the network and wirelessly replenish the energy of sensor nodes. The methods we present are distributed and use limited network information. More specifically, we propose four new protocols for efficient wireless charging while addressing key issues such as the identification of what are good coordination procedures and what are good trajectories for the Mobile Chargers. Two of our protocols (DC, DCLK) perform distributed, limited network knowledge coordination and charging, while two others (CC, CCGK) perform centralized, global network knowledge coordination and charging. As detailed simulations demonstrate, one of our distributed protocols outperforms a known state-of-the-art method, while its performance gets quite close to the performance of the powerful centralized global knowledge method.

### 15.1 Introduction and Contribution

As wireless and portable mobile devices become pervasive, charging batteries for these devices has become a critical problem. Current battery charging technologies are dominated by wired technology, which requires a wired power plug to be connected to an electrical wall outlet. Existing wireless sensor networks are constrained

---

A. Madhja (✉) · S. Nikoletseas · T.P. Raptis

Department of Computer Engineering and Informatics, University of Patras and  
Computer Technology Institute and Press “Diophantus” (CTI), Patras, Greece  
e-mail: madia@ceid.upatras.gr

S. Nikoletseas  
e-mail: nikole@cti.gr

T.P. Raptis  
Institute of Informatics and Telematics, National Research Council, Moruzzi Str 1,  
56124 Pisa, Italy  
e-mail: theofanis.raptis@iit.cnr.it

by limited battery energy at a sensor node and can only remain operational for a limited amount of time. To prolong network lifetime, there have been many research efforts at all layers, from topology control, physical, MAC, and all the way up to the application layer. Despite these intensive efforts, the lifetime of a wireless sensor network remains a performance bottleneck and is perhaps the key factor that hinders its wide-scale deployment.

The technology of wireless power transfer lead the way towards *a new paradigm* for wireless sensor networks; the Wireless Rechargeable Sensor Networks. Such networks consist of sensor nodes that may be either stationary or mobile, as well as few mobile nodes with high energy supplies. The latter, using wireless power transfer technologies are capable of charging sensor nodes. This way, the highly constrained resource of energy can be managed in great detail and more efficiently. Another important aspect is the fact that energy management in Wireless Rechargeable Sensor Networks can be performed passively from the perspective of sensor nodes and without the computational and communicational overhead introduced by complex energy management algorithms. Finally, Wireless Rechargeable Sensor Networks allow energy management to be studied and designed independently of the underlying routing protocol used for data propagation.

**The Problem.** Let a Wireless Rechargeable Sensor Network comprised of *stationary* sensor nodes and *special mobile entities called the Mobile Chargers*. The Mobile Chargers have significant (yet finite) energy supplies, that are much larger than those of each sensor node, and are thus capable of charging the sensors in the network. We design and evaluate efficient protocols for the Mobile Chargers' coordination and charging procedures that improve energy efficiency, prolong the lifetime of the network and also improve important network properties (such as the quality of network coverage and the robustness of data propagation).

In particular, we view the Mobile Chargers' coordination as a distinct procedure, on top of the sensor nodes charging mechanism. Unlike other methods in the state of the art, we do not couple the Mobile Chargers' coordination neither with the sensor nodes charging process nor with the underlying network energy information data propagation. Actually, we perform efficient coordinated wireless power transfer in a way which is agnostic of the network energy status, via adaptive techniques that *implicitly (based on the Mobile Chargers' status) adapt to the network's energy evolution*.

*Remark.* We note that, although the wireless charging problem might look similar to other related research problems (such as aggressive data collection via mobile sinks), it admits special features that necessitate a direct approach, while the optimization of concrete trade-offs and the fine-tuning of design alternatives that arise in wireless charging necessitate the distinct investigation of special protocol design parameters.

Finally, we note that Mobile Charger optimization problems are (inherently) computationally hard, e.g. in [3] we have formulated the wireless charging problem as the Charger Dispatch Decision Problem—CDDP, and showed that it is  $\mathcal{NP}$ -complete (via reduction from the Geometric Traveling Salesman Problem, G-TSP; see e.g. [6], p. 212).

**Our Contribution.** While interesting research has been lately contributed to the wireless charging problem and particularly to the scheduling of a single Mobile Charger, most methods so far necessitate significant (in many cases even global) network knowledge (e.g. it is assumed that the Mobile Charger knows the energy levels of all sensors in the network) and the solutions are centralized. On the contrary, our methods are *distributed, and use (at most) local network information*. Also, unlike other multiple Mobile Chargers state-of-the-art approaches that opt for integration and coupling of the coordination and charging procedures, our methods distinguish the network operations in three separate levels: *the coordination procedure, the charging process and the routing mechanism*. We identify the necessity of this demarcation as an efficient approach to the design of more detailed and better fine-tuned charging protocols.

In particular, we propose and evaluate selected *alternative strategies for efficient charging* in stationary Wireless Rechargeable Sensor Networks via multiple Mobile Chargers. Our design provides concrete, different solutions to some *key issues (and the associated trade-offs)* of wireless charging which we identify, most notably

1. assuming a number of Mobile Chargers in the network, *in what way should they coordinate,*
2. given that the Mobile Chargers have coordinated, *what are good trajectories for the Mobile Chargers to follow.*

More specifically, (a) we first distinguish two fundamental network operations, *Mobile Chargers' coordination* and *node charging* (b) taking into account the capability of *both centralized and distributed processing* we design selected Mobile Chargers' coordination alternatives that efficiently split the network area and assign subregions to the Mobile Chargers (c) assuming *different levels of network knowledge* we design different charging traversal strategies employed by the Mobile Chargers in their region of interest.

We provide four new coordination and charging protocols based on their network knowledge (from global to local and to the absence of knowledge) and their processing ability (from distributed to centralized). The CC and DC protocols perform centralized and distributed coordination respectively with no network knowledge, the DCLK protocol performs distributed coordination with local knowledge and the CCGK protocol performs centralized coordination with global knowledge. Actually, we view the CCGK protocol as a kind of performance upper bound to which the two distributed, partial knowledge protocols are compared with.

## 15.2 Related Work and Comparison

Recently there has been much research effort in the field of Wireless Rechargeable Sensor Networks using *a single Mobile Charger*. In [11], the authors build a proof-of-concept prototype using a wireless power charger installed on a robot and sensor nodes equipped with wireless power receivers and carry out experiments on the prototype to evaluate its performance in small-scale networks of up to ten nodes. In [13], the authors introduce the necessary and sufficient conditions such that the wireless

charging problem can be studied as an optimization problem, with the objective of maximizing the ratio of the Mobile Charger's vacation time over the network traveling time. In [2, 3], the authors study the impact of the charging process to the network lifetime for selected routing alternatives by proposing protocols that locally adapt the trajectory of the Mobile Charger to several network properties. In [17], the authors co-locate the mobile base station on the Mobile Charger and minimize the energy consumption of the entire system while ensuring none of the sensor nodes runs out of energy. All above works are advancing the topic, but do not address the capability of a network to support more than one Mobile Chargers. Such a capability could be vital for the lifetime prolongation of large networks that consist of several thousand nodes (and thus their maintenance is not feasible using one single Mobile Charger).

On the other hand, in the field of Wireless Rechargeable Sensor Networks using *multiple Mobile Chargers* there has been limited research effort. In [18] the authors introduce collaborative mobile charging, where Mobile Chargers are allowed to charge each other (in our case, the model is different since we do not address Mobile Chargers charging each other). They investigate the problem of scheduling multiple Mobile Chargers which collaboratively charge nodes over one-dimensional wireless sensor networks, to maximize the ratio of the amount of payload energy to overhead energy, such that no sensor runs out of energy but in contrast to our work, they restrict their algorithms only in line-graphs. In [4], the authors consider the minimum number of Mobile Chargers problem in a general two-dimensional network so as to keep the network running forever. They partition the sensor nodes in subsets such that any Mobile Charger, at each own period, visits its corresponding sensors, charges them and then gets back to the base station to charge its own battery. In [9], the authors use Mobile Chargers for energy replenishment of robots in robotic sensor networks. Observing the discrepancy between the charging latency of robots and charger travel distance, they propose a tree-based charging schedule for the charger, which minimizes its travel distance without causing the robot energy depletion. They evaluate its performance and show its closeness to the optimal solutions. In [10] and [15] the authors nicely leverage concepts and mechanisms from NDN (Named Data Networking) to design energy monitoring protocols that deliver energy status information to Mobile Chargers in an efficient manner. They interestingly study how to minimize the total traveling cost of multiple Mobile Chargers while ensuring no node failure and derive theoretical results on the minimum number of mobile vehicles required for perpetual network operations. They present a sophisticated heuristic algorithm and conduct simulations to demonstrate the effectiveness and efficiency of the proposed design but in contrast to our approach, they propose only one charging scheme of simple charger coordination and node selection procedures, i.e. they do not really elaborate on the coordination aspect. Also, unlike our work, in both above approaches, the chargers' coordination is performed centrally and not distributively. That may not be considered realistic in large-scale networks as it introduces high communication overhead (i.e. every charger has to propagate its status over large distances) and does not scale well with network size. We have chosen to compare with the protocol presented in [15], for comparison fairness in terms of similar model assumptions.

### 15.3 The Model

Our model features three types of devices: stationary sensors, Mobile Chargers and one stationary Sink as illustrated in Fig. 15.1. We assume that there are  $N$  sensors of wireless communication range  $r$  distributed at random in a circular area (we investigate two cases, uniform distributions and nonuniform distribution)  $\mathcal{A}$  of radius  $R$  and  $K$  Mobile Chargers initially deployed at the center of their area, i.e. at coordinates

$$(x, y) = \left( \frac{R}{2} \cos \left( \frac{\pi}{K} (2j - 1) \right), \frac{R}{2} \sin \left( \frac{\pi}{K} (2j - 1) \right) \right)$$

of the circular area (dots in Fig. 15.2a), where  $j = 1, 2, \dots, K$ . Since the protocols run for a long time and the initialization happens only once, the initial position of the Mobile Chargers is not a crucial parameter, i.e. it could be the center of the circular area as well. The Sink lies at the center of the circular area. In our model we assume that the Mobile Chargers do not perform any data gathering process.

We denote by  $E_{total}$  the total available energy in the network. Initially,

$$E_{total} = E_{sensors} + E_{MC}(t_{init})$$

where  $E_{sensors}$  is the amount of energy shared among the sensor nodes and  $E_{MC}(t_{init})$  is the total amount of energy that the Mobile Chargers have and may deliver to the network by charging sensor nodes. The maximum amount of energy that a single node and a single Mobile Charger may store is  $E_{sensor}^{max}$  and  $E_{MC}^{max}$  respectively. Energy is split among the sensor nodes and the Mobile Chargers as follows:

$$E_{sensor}^{max} = \frac{E_{sensors}}{N} \quad \text{and} \quad E_{MC}^{max} = \frac{E_{MC}(t_{init})}{K}$$

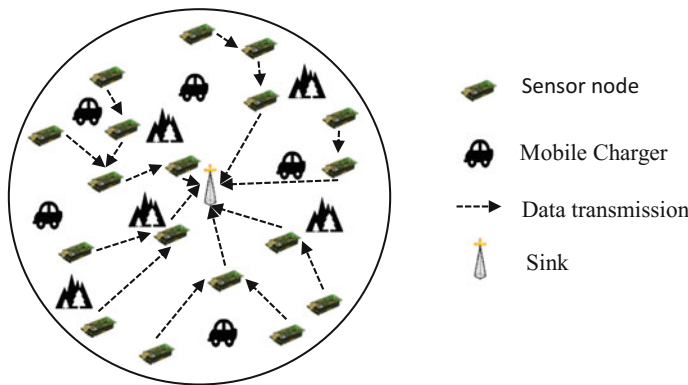


**Fig. 15.1** The network

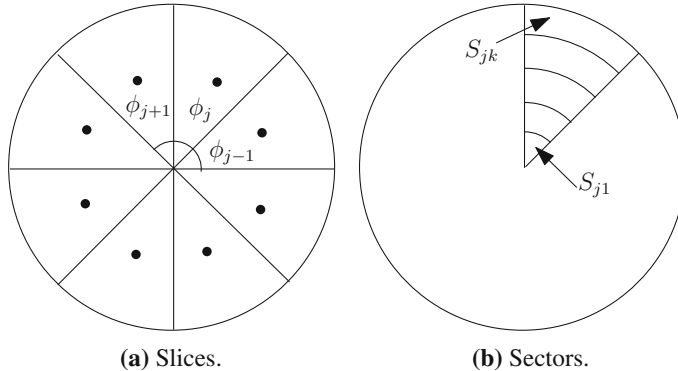


**Fig. 15.2** Network division in Slices and Sectors (in DCLK)

In our model, the charging is performed point-to-point, i.e. only one sensor may be charged at a time from a Mobile Charger by approaching it at a very close distance so that the charging process has maximum efficiency. The time that elapses while the Mobile Charger moves from one sensor to another is considered to be very small when compared to the charging time; still the trajectory followed (and particularly its length) is of interest to us, since it may capture diverse cost aspects, like gas or electric power needed for Mobile Charger's movement. We assume that the charging time is equal for every sensor and independent of its battery status.

We assume a quite heterogeneous data generation model. Each sensor node chooses independently a relative data generation rate  $\lambda_i \in [a, b]$  (where  $a, b$  constant values) according to the uniform distribution  $\mathcal{U}[a, b]$ . Values of  $\lambda_i$  close to  $a$  imply low data generation rate and values close to  $b$  imply high data generation rate. The routing protocol operates at the network layer, so we are assuming appropriate underlying data-link, MAC and physical layers. We refer to [5, 7] for greedy, single path, underlying routing protocol.

To transmit a  $k$ -bit message, the radio expends  $E_t(k) = \varepsilon_{trans} \cdot k$  and to receive a  $k$ -bit message, the radio expends  $E_R(k) = \varepsilon_{recv} \cdot k$  where  $\varepsilon_{trans}$  and  $\varepsilon_{recv}$  are constants. As usual, the power needed to transmit a message at distance  $d$  is roughly  $d^c$  where  $2 \leq c \leq 6$  is a constant; for simplicity we take  $c = 2$ .

**Placement heterogeneity.** We virtually divide the network into  $2R/r$  co-centric rings and  $2\pi/\phi$  Slices. A Sector is defined as the intersection of a specific ring and Slice. For example, in Fig. 15.2a the network is divided into eight Slices ( $\phi = \pi/4$ ) and Fig. 15.2b illustrates the separation of a Slice into Sectors. In this figure, the Slice contains five Sectors, resulting in a total of 40 Sectors in the network. We consider random instances of the following quite *general model of nonuniform deployment*: Denote by  $S_{ij}$  the Sector corresponding to the intersection of Slice  $i$  and ring  $j$  as shown in Fig. 15.2b. Let  $b > 1$  be an arbitrary constant. Each Sector  $S_{ij}$  chooses independently a number  $\delta_{ij} \in [1, b]$  according to the uniform distribution  $\mathcal{U}[1, b]$ . We will refer to the number  $\delta_{ij}$  as the relative density of Sector  $S_{ij}$ . Values of  $\delta_{ij}$

close to 1 imply low relative density and values close to  $b$  imply high relative density. By combining the knowledge about the total number of sensors in the network  $N$ , together with the relative density  $\delta_{ij}$  and the area  $A_{ij}$  of every Sector, we compute the number of nodes  $n_{ij}$  deployed in Sector  $S_{ij}$  by the following formula:

$$n_{ij} = \frac{N}{\sum_{i',j'} \frac{A_{i'j'}}{A_{ij}} \frac{\delta_{i'j'}}{\delta_{ij}}}$$

where  $N = \sum_{i,j} n_{ij}$ . Finally, we scatter  $n_{ij}$  nodes in the area corresponding to Sector  $S_{ij}$ . The fraction of the actual densities of two Sectors  $S_{ij}$  and  $S_{i'j'}$  is exactly

$$\frac{A_{i'j'}}{A_{ij}} \frac{\delta_{ij}}{\delta_{i'j'}}.$$

Furthermore, if all Sectors have the same relative density (i.e.  $\delta_{ij} = \delta_{i'j'}$ , for all  $i', j'$ ), we get the uniform deployment. An example of nonuniform network deployment is shown in Fig. 15.13.

## 15.4 Demarcated Protocol Phases

In contrast to other known works, we split the charging process in two phases, the *coordination phase* and the *charging phase*. The demarcation of the Mobile Chargers' operations in phases allows us to focus on each aspect separately and fine-tune the protocols more precisely.

**Coordination Phase.** A Mobile Charger's energy is consumed as it replenishes the energy of the sensor nodes. The energy dissipation rate among Mobile Chargers may not be the same, since the nonuniform generation rate of events can eventually lead to stressed network regions and burden some Mobile Chargers more than others. For this reason, the Mobile Chargers periodically communicate with each other and deal out their charging regions fairly (for example, a weaker Mobile Charger in terms of energy should be assigned to a smaller network region). This coordination process can be achieved either in a *centralized* or a *distributed* manner.

In the centralized case, the coordination is performed using information from all  $K$  Mobile Chargers. We assume that the calculations for this type of coordination are performed by a computationally powerful network entity, e.g. the Sink. Centralized coordination is generally more powerful than distributed coordination, thus centralized protocols' performance serves as an upper bound on performance which the distributed methods are compared to. In the distributed case, a Mobile Charger is informed about the status of its neighboring Mobile Chargers resulting in a more secluded coordination between close Mobile Chargers.

**Charging Phase.** Charging traversal alternatives have been widely studied in the case of a single Mobile Charger. In our approach, where the Mobile Charger's operation is dual, we give emphasis to the *amount of knowledge* possessed by protocols

in terms of locality. In order to appropriately design the charging phase of a protocol we distinguish the protocol's knowledge amount among *global knowledge*, *local knowledge*, *no knowledge* and *reactive knowledge*.

In the case of global knowledge, we suppose that a Mobile Charger can use information from all over the network (sensor nodes and other Mobile Chargers). Such an amount of knowledge makes the Mobile Charger powerful but it may be unrealistic in large networks and do not scale well with network size. On the contrary, in the more realistic case of local knowledge, a Mobile Charger is allowed to use limited information derived from its neighborhood. We consider a Mobile Charger to be “blind” when it has no knowledge on the network and thus cannot use a sophisticated charging method. The reactive knowledge is a special case of real-time acquisition of global knowledge, by receiving messages from a subset of nodes while the information refers to all set of nodes. Note that the amount of knowledge can also be diversified in the coordination phase, among the Mobile Chargers.

## 15.5 The Protocols

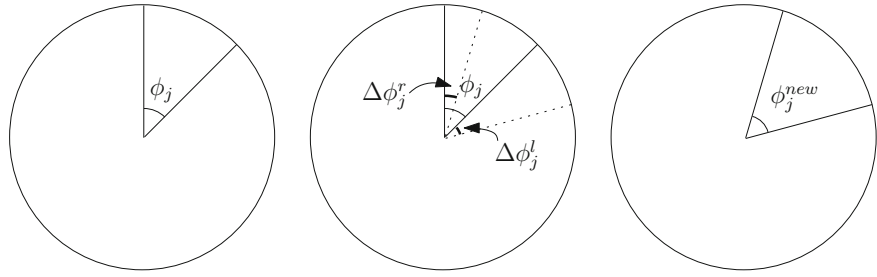
We present four new Mobile Chargers protocols and another, state-of-the-art protocol ([15]) that we compare with. Protocol's details are presented in short in Table 15.1.

### 15.5.1 *Distributed Coordination Protocol DC*

**Coordination phase.** The DC protocol performs distributed coordination among Mobile Chargers and assumes no network knowledge. We split the network area in Slices as shown in Fig. 15.2a and assign one Slice per charger. Angle  $\phi_j$  corresponds to the central angle of  $j$ th Mobile Charger's Slice. The Mobile Chargers distributively define their Slice boundaries (i.e. the two radii that define the Slice), according to the size of the region each one can handle, w.r.t. their energy status. Each Mobile Charger can shift its right and left Slice boundaries resulting in either a widening or a shrinkage of the region of interest. This task is performed distributively and each region boundaries change is determined through a cooperation of each pair of adjacent Mobile Chargers. A boundary change of  $j$ 's region is expressed as a change of  $\phi_j$ .

**Table 15.1** Protocol phase details

| Protocol  | Coordination Phase | Charging Phase     |
|-----------|--------------------|--------------------|
| DC        | Distributed        | No knowledge       |
| CC        | Centralized        | No knowledge       |
| DCLK      | Distributed        | Local knowledge    |
| CCRK [15] | Centralized        | Reactive knowledge |
| CCGK      | Centralized        | Global knowledge   |



(a) Before the coordination. (b) During the coordination. (c) After the coordination.

**Fig. 15.3** Distributed coordination

Figure 15.3 depicts the coordination procedure. More specifically, Fig. 15.3a depicts the region of the Mobile Charger  $j$  before the coordination phase. Figure 15.3b depicts the angle's change after the communication with the left and right neighbors ( $\Delta\phi_j^l$  and  $\Delta\phi_j^r$ , respectively) during the coordination phase. Figure 15.3c depicts the new angle i.e. the new region of the Mobile Charger after the coordination phase.

The coordination process uses two critical Mobile Chargers' parameters for definition of the region of interest, the Mobile Charger's current energy level  $E_j$  and the Mobile Charger's energy consumption rate since the last coordination  $\rho_j$ . The changes  $\Delta\phi_j^l$  and  $\Delta\phi_j^r$  of  $\phi_j$  for the Slice's left boundary and for the Slice's right boundary are defined by the Algorithms 6 and 7 respectively.

---

**Algorithm 6:** The change  $\Delta\phi_j^l$  of  $\phi_j$  for the Slice's left boundary

---

```

Input :  $E_{j-1}, E_j, \rho_{j-1}, \rho_j$ 
1 if  $\min\{E_j, E_{j-1}\} = E_j$  then
2    $\Delta\phi_j^l = -\phi_j \cdot \frac{|\rho_{j-1} - \rho_j|}{\max\{\rho_{j-1}, \rho_j\}}$ 
3 else
4    $\Delta\phi_j^l = \phi_{j-1} \cdot \frac{|\rho_{j-1} - \rho_j|}{\max\{\rho_{j-1}, \rho_j\}}$ 
5 end if
Output:  $\Delta\phi_j^l$ 
```

---

The new angle (denoted by  $\phi'_j$ ) is computed as  $\phi'_j = \phi_j + \Delta\phi_j^l + \Delta\phi_j^r$ . Note that, between two adjacent Mobile Chargers  $j_1$  and  $j_2$ , the change of their common Slice boundary (i.e. the common radii) is  $\Delta\phi_{j_1}^r = -\Delta\phi_{j_2}^l$  so that the Mobile Charger with the lower energy level provides its neighbor with a portion of its region of interest. Also, it is their energy level that determines which charger should reduce its region of interest and the energy consumption rate that determines the size of the reduced area. The size of the angle change is not computed by considering the energy levels of the two chargers because energy consumption rate shows how quickly will this energy level be reduced. For example, if  $\rho_j$  is high then  $j$ 's Slice is critical, causing a rapid

**Algorithm 7:** The change  $\Delta\phi_j^r$  of  $\phi_j$  for the Slice's right boundary

---

```

Input :  $E_j, E_{j+1}, \rho_j, \rho_{j+1}$ 
1 if  $\min\{E_j, E_{j+1}\} = E_j$  then
2    $\Delta\phi_j^r = -\phi_j \cdot \frac{|\rho_j - \rho_{j+1}|}{\max\{\rho_j, \rho_{j+1}\}}$ 
3 else
4    $\Delta\phi_j^r = \phi_{j+1} \cdot \frac{|\rho_j - \rho_{j+1}|}{\max\{\rho_j, \rho_{j+1}\}}$ 
5 end if
Output:  $\Delta\phi_j^r$ 
```

---

reduction of  $E_j$ , independently of its current level. The above angle computations are performed simultaneously by all Mobile Chargers.

**Charging phase.** During this phase, Mobile Charger  $j$  traverses the network region it is assigned to (Slice defined by angle  $\phi_j$ ) and charges the corresponding sensor nodes. The CC protocol assumes no knowledge on the network. For this reason the path followed by the Mobile Charger is restricted to several naive alternatives (some presented in [3]). In our approach we use a “blind” scanning of the region where the Mobile Charger starts from the Sink and traverses an exhaustive path until it reaches the boundaries of the network area. The advantage of this movement is that due to its space filling attributes, the Mobile Charger covers the whole Slice and almost every node is charged, until the energy of the Mobile Charger is totally depleted. On the other hand, due to lack of knowledge, this movement is not adaptive, i.e. it does not take into account differences of the energy depletion rates of the network area caused by the underlying message propagation.

### 15.5.2 Centralized Coordination Protocol **CC**

The CC protocol performs centralized coordination among the Mobile Chargers and assumes no knowledge on the network. In particular, the coordination process is able to use information from all Mobile Chargers (energy status, position, etc.), but is agnostic of the underlying network and sensor nodes attributes (energy status, position, etc.). This approach virtually partitions the network elements in two completely separate levels, the Mobile Chargers level and the sensor nodes level.

**Coordination phase.** Each Mobile Charger is assigned to a network region. Since the initial Mobile Charger’s deployment coordinates are

$$(x, y) = \left( \frac{R}{2} \cos \left( \frac{\pi}{K} (2j - 1) \right), \frac{R}{2} \sin \left( \frac{\pi}{K} (2j - 1) \right) \right)$$

where  $j = 1, 2, \dots, K$ , we can split the network area in Slices, as shown in Fig. 15.2a (example for  $K = 8$  Mobile Chargers), with one charger assigned to each Slice. When the coordination process is initialized, the region of each charger is

computed. Each Mobile Charger should be assigned to a region of size analogous to its current energy level, so that the energy dissipation among the Mobile Chargers is balanced. In order to compute the size of the region of Mobile Charger  $j$ , it suffices to compute the central angle  $\phi_j$  corresponding to the Mobile Charger's Slice. In particular

$$\phi_j = 2\pi \cdot \frac{E_j}{\sum_{j=1}^K E_j}, \quad \text{where} \quad \sum_{j=1}^K \phi_j = 2\pi.$$

**Charging phase.** Since this protocol operates under the no knowledge assumption, the charging phase follows the same pattern with the DC protocol (Slice scanning).

### 15.5.3 *Distributed Coordination Local Knowledge Protocol DCLK*

The DCLK protocol performs a distributed coordination phase and uses local knowledge to perform the charging phase.

**Coordination phase.** The coordination phase follows the same pattern with the coordination phase of DC protocol (distributed  $\phi_j$  angle computation).

**Charging phase.** The DCLK protocol operates with local knowledge assumption. The Slice corresponding to Mobile Charger  $j$  is divided into  $k$  Sectors  $S_{jk}$  of the same width as shown in Fig. 15.2b. Mobile Charger  $j$  prioritizes its Sectors w.r.t. high number of sensor nodes with low level of residual energy.

**Definition 15.1**  $E_{jk}^{\min}$  is the lowest nodal residual energy level in the Sector  $S_{jk}$ .

**Definition 15.2**  $E_{jk}^{\min+\Delta}$  is an energy level close to  $E_{jk}^{\min}$ :

$$E_{jk}^{\min+\Delta} = E_{jk}^{\min} + \delta \cdot \frac{E_{\text{sensor}}^{\max}}{E_{jk}^{\min}}, \quad \delta \in (0, 1).$$

**Definition 15.3**  $N(S_{jk})$  is the number of nodes in Sector  $S_{jk}$  with residual energy between  $E_{jk}^{\min}$  and  $E_{jk}^{\min+\Delta}$ :

$$N(S_{jk}) = \sum_{e=E_{jk}^{\min}}^{E_{jk}^{\min+\Delta}} N(e)$$

where  $N(e)$  is the number of nodes with energy level  $e$ .

Charger  $j$  charges Sector  $S_{jk}$  which maximizes the product

$$\max_{S_{jk}} \{N(S_{jk}) \cdot (E_{\text{sensor}}^{\max} - E_{jk}^{\min})\}.$$

The intuition behind this charging process is the grouping of nodes in each Slice and the selection of a critical group. A critical group is a Sector containing a large number of sensor nodes that require more energy than other nodes throughout the network.

#### **15.5.4 Centralized Coordination Reactive Knowledge Protocol CCRK ([15])**

The CCRK protocol acquires global knowledge in exchange for some in-network message aggregation. The Mobile Chargers obtain the most up-to-date energy information from sensor nodes and make decisions in real time. The energy information is aggregated by several special nodes in the network that act as representatives of partitioned network regions. We denote by  $S$  the number of the representative nodes.

**Coordination phase.** Mobile Chargers communicate with each other to know their positions. To avoid conflicts where multiple Mobile Chargers choose the same node for charge, the Sink stores and updates the availability of each node. The procedure is similar to that for shared memory access in operating systems, e.g. see [14], p. 125. The Sink maintains a  $0 - 1$  valued node list. Once a sensor node is chosen, its value is set to 1 (locked). Otherwise, it is 0. The value should be changed back from 1 to 0 when a Mobile Charger finishes charging that node. A Mobile Charger can simply communicate with the Sink, exclude nodes already selected by other Mobile Chargers, and notify the Sink of the status of nodes it chooses.

**Charging phase.** Two important metrics impact the charging order between node  $i$  and node  $i'$ : the traveling time between node  $i$  to node  $i'$ , and their residual lifetime  $L_i$  and  $L_{i'}$ . If node  $i'$  has a small  $L_{i'}$  such that it would be dead if a Mobile Charger charges node  $i$  first, node  $i'$  should be visited first. In this protocol we use a weighted sum of traveling time from current node  $i$  to next node  $i'$  and the residual lifetime of node  $i'$ ,

$$w_{ii'} = \beta \cdot t_{ii'} + (1 - \beta) \cdot L_{i'}.$$

$w_{ii'}$  is used to decide which node  $i'$  to charge next. A sensor node with a smaller weighted value should be visited at a higher priority. When  $\beta = 1$ , the algorithm reduces to nearest node selection that the Mobile Chargers always charge the closest node first regardless of battery deadlines; when  $\beta = 0$ , it picks the node with the earliest battery deadline first regardless of the traveling distance.

#### **15.5.5 Centralized Coordination Global Knowledge Protocol CCGK**

The CCGK protocol, similar to the CC protocol, performs centralized coordination. However, the assumption of global knowledge on the network further extends the

Mobile Chargers' abilities. For this reason, it is expected to outperform all other strategies that use only local information, thus somehow representing a performance bound. The global knowledge assumption would be unrealistic for real large-scale networks, as it introduces large communication overhead (i.e. nodes and Mobile Chargers have to propagate their status over large distances).

**Coordination phase.** Instead of using the same coordination process with the CC protocol, we integrate the global knowledge assumption in the coordination phase. As a result, the network is not partitioned in two separate levels (Mobile Chargers, sensor nodes) and the Mobile Chargers are allowed to use network information during this phase. Each Mobile Charger is assigned to a network region. The region of interest of Mobile Charger  $j$  is a cluster of nodes. Node  $i$  belongs to the cluster of Mobile Charger

$$j' = \arg \min_j \left\{ \left( 1 + \frac{dist_{ij}}{2R} \right) \cdot \left( 2 - \frac{E_j}{E_{MC}^{max}} \right) \right\}$$

where  $dist_{ij}$  is the distance between node  $i$  and Mobile Charger  $j$  and  $E_j$  the residual energy of Mobile Charger  $j$  ( $E_j > 0$ ). In other words, a node selects a Mobile Charger which is close and has high amount of energy. If a Mobile Charger's energy level is low, it may not be able to charge the node. Also, if the distance between the node and the Mobile Charger is long, then the Mobile Charger will waste a lot of energy for movement. Moreover, because of long distance, the traveling time is long too and thus, the node may die before the Mobile Chargers arrives to its position.

The two factors of the product are normalized. That is to avoid elimination of the product from one possible zero factor, which may result in prioritizing the wrong Mobile Charger. For example, for a node  $i$  if there is a Mobile Charger  $j$  that has no energy then the factor  $\frac{E_j}{E_{MC}^{max}}$  would be zero and the node would choose to belong to its cluster (since it chooses the Mobile Charger with min product). In contrast, when the factor is of the normalized form  $2 - \frac{E_j}{E_{MC}^{max}}$ , then the value of the factor would be 2 (maximized) and thus the node would avoid this Mobile Charger. For the distance factor the normalization is used in order to avoid the product to be eliminated as well. Thus, between two Mobile Chargers that are close to the node, the latter should choose the Mobile Charger with higher battery supplies.

Note that the centralized computation of the Mobile Charger's region in the CCGK protocol is more powerful compared to other methods, since it uses information about the distance among every Mobile Charger with every node.

**Charging phase.** The global knowledge charging phase that we suggest uses energy and distance in a ranking function. In each round the Mobile Charger moves to the sensor in the corresponding cluster, that minimizes the product of each node's energy times its distance from the current position of the Mobile Charger. More specifically, in each moving step the Mobile Charger  $j$  charges node

$$i' = \arg \min_{i \in C_j} \left\{ \left( 1 + \frac{dist_{ij}}{2R} \right) \cdot \left( 1 + \frac{E_i}{E_{sensor}^{max}} \right) \right\}$$

where  $E_i$  is the residual energy of sensor node  $i$ . In other words, this protocol prioritizes nodes with low energy and small distance to the Mobile Charger. Both of the two factors have the same weight in the product, i.e. there is no any dominant factor. The Mobile Charger computes the product for each node (in its cluster) and selects to charge the one which minimizes the product.

## 15.6 Cost Analysis

There are three kind of costs that are responsible for energy dissipation of the Mobile Chargers, the movement cost, the charging cost and the communication cost.

### 15.6.1 Movement Cost

Movement cost refers to the amount of energy that Mobile Chargers dissipate for movement in order to charge sensor nodes. We assume that Mobile Chargers have only one energy pool which is used both for movement and for charging.

In our simulations, we have not taken into account the movement cost directly, i.e. we do not calculate how much energy is spent for movement but we have calculated how much distance has each Mobile Charger traveled, which provides an estimation of the cost. More specifically, using the same assumptions for the Mobile Chargers with that in [16] (i.e. they carry high density battery packs (12A, 5V) and weight 20lbs) and the battery calculator in [1] we provide in Fig. 15.4 an estimation of the energy spent for the Mobile Chargers' movement throughout the network for all

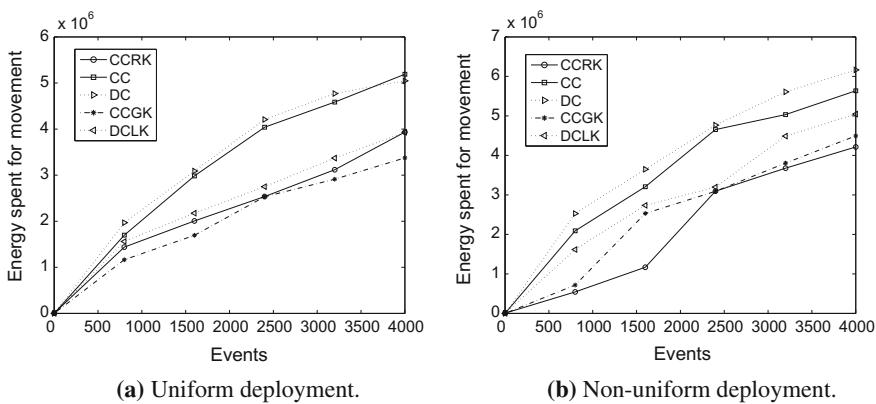


**Fig. 15.4** Energy spent for Mobile Chargers' movement over time

protocols for both uniform and nonuniform network deployment. The DC and CC protocols which have a naive charging phase (slice scanning) spend high amount of energy for movement. In contrast, the CCGK and CCRK protocols which minimize the distance traveled also minimize the movement cost.

### **15.6.2 *Charging Cost***

Charging cost refers to the amount of energy dissipated to charge sensor nodes. This cost can be distinguished in two kinds, the beneficial charging cost which is the energy obtained by sensor nodes and the wasted charging cost which is the energy wasted because of losses due to wireless power transfer technology. In this work we assume that there is no any energy loss during the charging procedure and the charging cost equals to beneficial energy cost.

### **15.6.3 *Communication Cost***

Communication cost refers to the amount of energy dissipated by a Mobile Charger in order to get informed about the energy status of the sensor nodes. This cost depends on two quantities. The first one is the number of messages that Mobile Chargers send and receive and the second one is the distances between the sensor nodes and the Mobile Chargers since the message transmission cost is analogous to the square of their distance.

The communication cost is based both on coordination and on charging procedure. An analysis of the communication cost of our proposed protocols is provided below.

#### **15.6.3.1 *Communication Cost Analysis of CCGK protocol***

**Coordination phase.** The Mobile Chargers are informed about the energy status of all sensor nodes. In this case, the number of messages of each Mobile Charger is  $O(N)$  and the total number of messages is  $O(KN)$ . Also, the transmission distances between a Mobile Charger and a node may vary ( $\in [0, 2R]$ ) A relevant small-scale example of eight nodes and eight Mobile Chargers is depicted in Fig. 15.5a.

**Charging phase.** Each Mobile Charger receives messages about energy status of each node that belong to its group and thus, the total number of messages is  $O(N)$ . The transmission distances are relatively small, since it is a factor that affects the cluster construction. Figure 15.5b depicts an example according to the charging phase of the protocol.

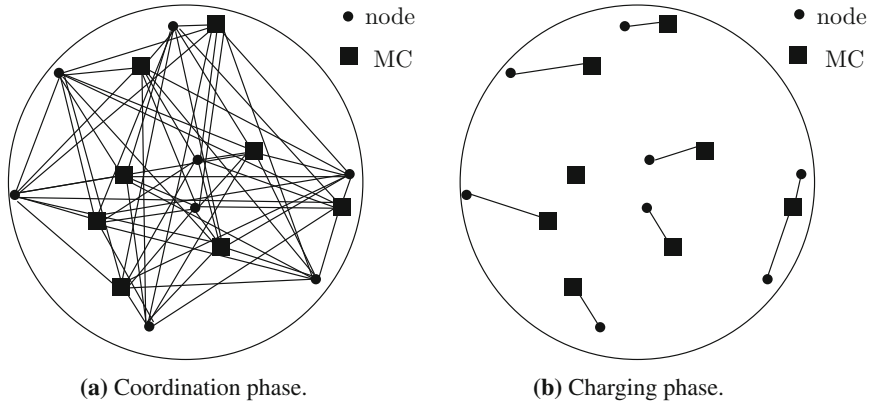


**Fig. 15.5** Messages of CCGK protocol

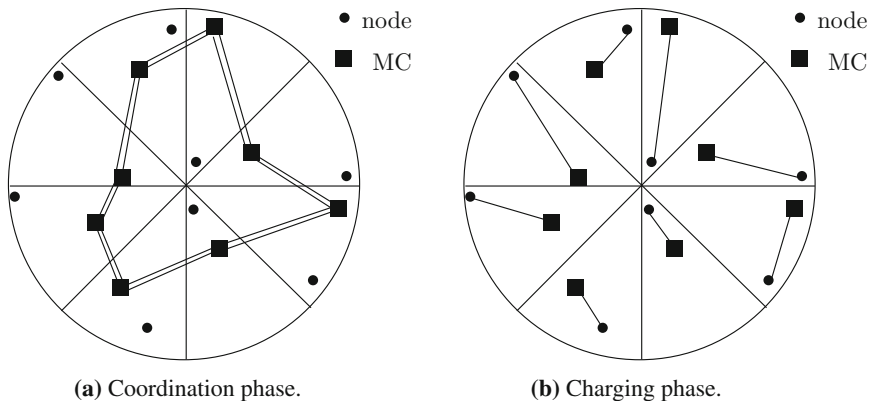


**Fig. 15.6** Messages of DCLK protocol

### 15.6.3.2 Communication Cost Analysis of DCLK protocol

**Coordination phase.** Each Mobile Charger communicate with its two adjacent Mobile Chargers. Thus, the total number of transmitted messages is  $O(K)$ . Also, the distances between the adjacent Mobile Chargers are relatively small as depicted in Fig. 15.6a.

**Charging phase.** Each Mobile Charger is informed about the energy status of the sensor nodes that belong to its Slice at each time period. The expected amount of nodes in each Slice is  $\frac{N}{K}$  since there are  $K$  Slices, one for each Mobile Charger. Thus, the total number of messages is  $O(K \frac{N}{K}) = O(N)$ . However, this number of messages is not transmitted at each time slot as in CCGK but at each time period. In order to provide local knowledge, Slice size should be small enough. Considering that the network radius is  $R$ , we assume that in local knowledge the distance between

a node and a Mobile Charger should exceed this value. Since there are  $K$  Slices, each Slice has an central angle  $A = \frac{2\pi}{K}$  (in radians). The length of an arc of a central angle  $A$  is  $\ell = \frac{2\pi R A}{2\pi} = RA$ . Thus, the distance is  $\ell = R \frac{2\pi}{K}$ . In order to ensure that the maximum node-charger distance in each Slice is at most  $R$ , the following inequality should hold:

$$\ell \leq R \Rightarrow R \frac{2\pi}{K} \leq R \Rightarrow K \geq 2\pi.$$

As a result, the distances in local knowledge are in  $[0, R]$ . Figure 15.6b depicts the communication distances between the nodes and the Mobile Chargers in charging phase.

### 15.6.3.3 Communication Cost Analysis of CC protocol

**Coordination phase.** Each Mobile Charger sends to the Sink its available energy and receives the value of its angle. The number of messages is  $O(K)$  and the distances are in  $[0, R]$ .

**Charging phase.** The Mobile Chargers obtain no network knowledge and perform “blind” scanning. Thus there is not any communication cost.

### 15.6.3.4 Communication Cost Analysis of DC protocol

**Coordination phase.** Each Mobile Charger communicates with its two adjacent Mobile Chargers. Thus, the number of transmitted messages is  $O(K)$ . Also, the distances between the adjacent Mobile Chargers are relatively small.

**Charging phase.** The Mobile Chargers obtain no network knowledge and perform “blind” scanning. Thus there is not any communication cost.

### 15.6.3.5 Communication Cost Results

It is clear that the lower the knowledge level is, the lower the communication cost becomes, since both the number of messages and the distances between nodes and Mobile Chargers are reduced. Thus, in our simulation results we can make useful conclusions about protocols, e.g. if two protocols achieve the same performance on a specific metric, the protocol with lower knowledge level is considered more efficient.

We conducted simulations to verify the above analysis on the number of messages that are sent and received by the Mobile Chargers. Figure 15.7 depicts the amount of messages that are spent by all Mobile Chargers throughout our simulations for both uniform and nonuniform network deployment. As shown in this figure, the DC and CC protocols which use no network knowledge achieve the lower number of messages sent throughout the simulation. The CCGK protocol achieves higher number of messages than the DCLK protocol since each Mobile Chargers communicates with each sensor node in the coordination phase. Also, the cost of each message is higher because the distances between nodes and chargers are larger.

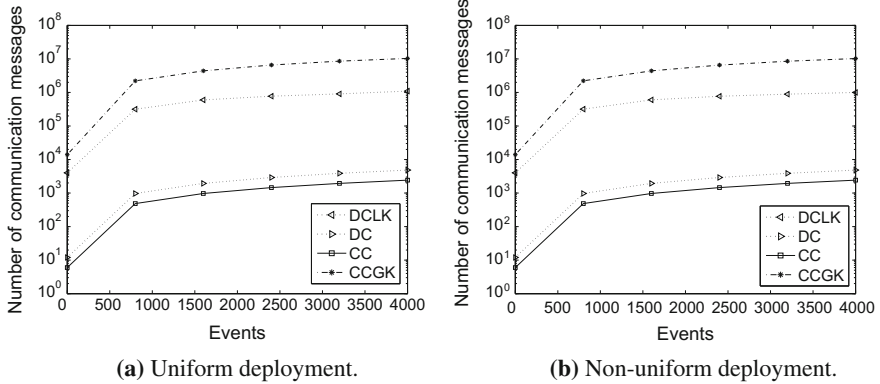


**Fig. 15.7** Number of messages over time

## 15.7 Experimental Evaluation

The simulation environment for conducting the experiments is Matlab 7.11. The Sink is placed at the center  $(x, y) = (0, 0)$  of the circular deployment area. The number of sensors is set to 2000 and the number of Mobile Chargers to 6. We simulate experiments of 4000 generated events. For statistical smoothness, we apply several times the deployment of nodes in the network and repeat each experiment 100 times. For each experiment we simulate large numbers of data propagations and the average value is taken. The statistical analysis of the findings (the median, lower and upper quartiles, outliers of the samples) demonstrate very high concentration around the mean, so in the following Figures we only depict average values. Since the  $N$  sensors are uniformly distributed in the circular area  $\mathcal{A}$  of radius  $R$ , we apply a well-known connectivity threshold, in order to maximize the probability that the produced random instances are connected. More strictly, since  $\mathcal{A} \subset \mathbb{R}^2$ , an instance of the *random geometric graphs model*  $\mathcal{G}(\mathcal{X}_N; r)$  is constructed as follows: select  $N$  points  $\mathcal{X}_N$  uniformly at random in  $\mathcal{A}$ . The set  $V = \mathcal{X}_N$  is the set of vertices of the graph and we connect two vertices if their Euclidean distance is at most  $r$ . In [8, 12] it is shown that the connectivity threshold for  $\mathcal{G}(\mathcal{X}_N; r)$  is

$$r_c = \sqrt{\frac{\ln N}{\pi N}}.$$

We consider random instances of  $\mathcal{G}(\mathcal{X}_N; r)$  of varying density, by selecting

$$r = \sqrt{\frac{c \ln N}{\pi N}}$$

for different values of  $c > 1$ , which guarantees that the produced random instance is connected with high probability.

We focus on the following performance metrics: (a) **alive nodes over time**, that is the number of nodes with enough residual energy to operate, during the progress of the experiment, (b) **connected components over time** which indicates the number of strongly connected components of the network graph throughout the experiment (c) **routing robustness** and **average routing robustness**, in terms of the nodes' average alive neighbors during the progress of the experiment, (d) **coverage aging**, that is the average coverage number (number of sensors having the point in their range) of 1000 randomly selected points in the network over time and (e) **distance traveled** per Mobile Charger and **total distance traveled** by all Mobile Chargers.

We design energy efficient protocols for both uniform and nonuniform network deployments. Our main goal is to manage the available energy efficiently. In all simulations that are performed in this section, we assume that the energy is dissipated only for charging purposes, i.e. we do not take into consideration the movement and communication cost. The total energy of the Mobile Chargers is transferred to sensor nodes through our proposed recharging protocols.

### **15.7.1 Uniform Network Deployment**

#### **15.7.1.1 Protocols' Impact on Network Properties**

(i) The application of charging protocols results in a great reduction in the overall death rate of the network (in terms of **alive nodes over time**), as shown in Fig. 15.8a. The CCGK as expected outperforms all other protocols and rather serves as an upper bound of their performance. The power of CCGK comes from the great amount of knowledge it assumes and from the robust centralized coordination of the Mobile Chargers. The DCLK protocol, with limited network knowledge is an efficient distributed alternative, since it manages to achieve a performance close to the upper bound and outperform the reactive CCRK protocol. CC and DC protocols which assume no network knowledge are outperformed by other protocols. Note that the upward curve of the DC protocol after 1500 generated events indicates a temporary starvation, after which the Mobile Chargers revive some of the dead nodes when passing by areas with high amounts of dead nodes.

The CCGK protocol achieves the lowest death rate since it computes which node to charge next based on both its distance from the node and on the energy status of the node. In contrast, CC and DC protocols use just the distance property for the relevant choice, so the weak nodes that are also far away from the Mobile Charger may deplete their energy. DCLK protocol separates each Slice into Sectors and the Mobile Charger chooses to charge the nodes of the most critical Sector. This procedure may incur higher traveling distance since it may change Sectors more often than the CCGK protocol which minimizes the covered distance each time (see Fig. 15.12).

(ii) **Routing robustness** is critical for wireless sensor networks, as all data collected have to be sent to the Sink. Path breakage occurs frequently due to node failure, mobility or channel impairments, so the maintenance of a path from each node to

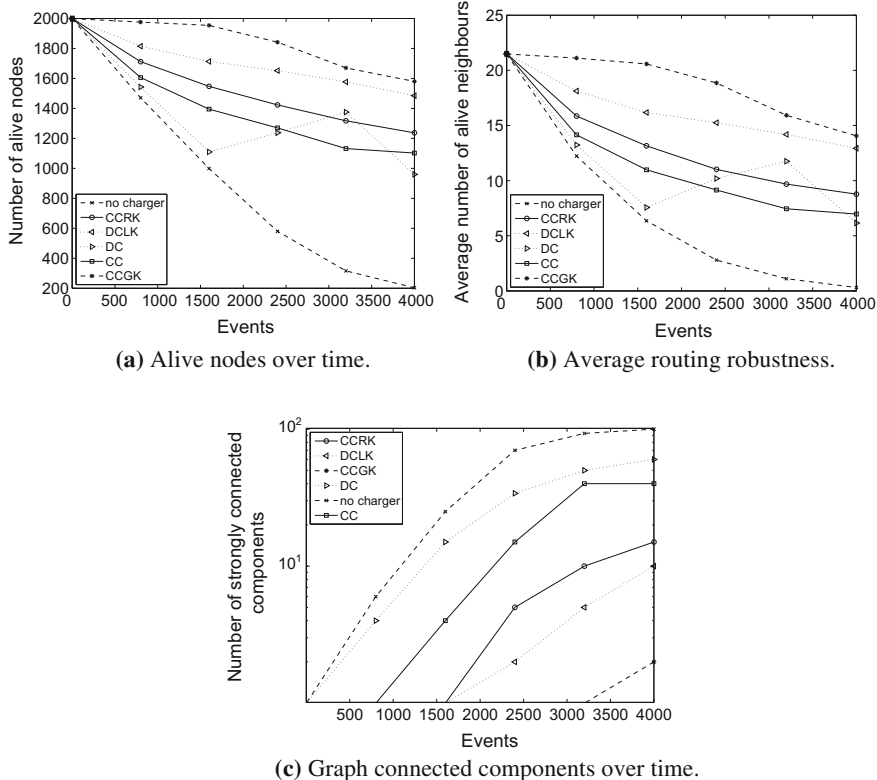


**Fig. 15.8** Various metrics for uniform deployments

a control center is a challenging task. A way of addressing the routing robustness of a wireless sensor network is by counting the number of its alive neighbors over time for each node. This can be seen as an implicit measure of network connectivity. For our protocols, the average number of alive neighbors is depicted in Fig. 15.8b. A more detailed evolution of the network's routing robustness is depicted in Fig. 15.9. The average routing robustness follows the same pattern as the death rate of nodes in the network. This is natural, since more dead nodes in the network result in loss of neighbors for each node. In Fig. 15.9 we can see that in the no charger case the black bar (representing number of neighbors  $<7$ ) is increasing, while the white bar (number of alive neighbors  $>16$ ) is rapidly decreasing. On the other hand, CCGK, CCRK and DCLK protocols achieve reliable routing robustness.

(iii) Similar to the routing robustness, the number of **strongly connected graph components** is an overall measure of connectivity quality in a wireless sensor network. Disconnected components are unable to communicate with each other and support efficient data propagation, resulting in high data delivery failures. A strategy of improving data delivery latency is the maintenance of a small number of connected components in the network. High numbers of components may lead to isolation of

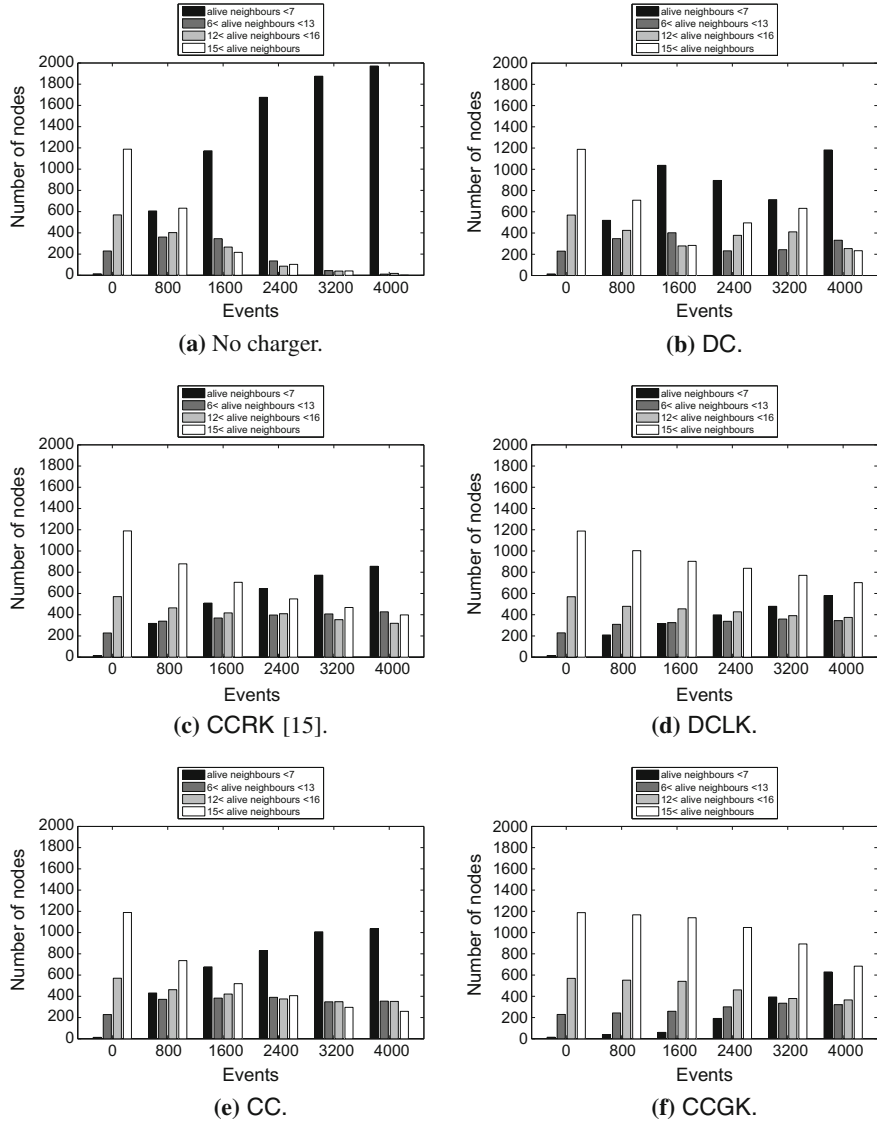


**Fig. 15.9** Routing robustness for uniform deployments

critical nodes, thus loss of important information. Figure 15.8c depicts the evolution of the number of network components throughout the experiments. As we noted earlier, DC and CC protocols lead to a higher node death rate in comparison to CCRK and DCLK protocols, a fact that results in early disconnections and sharp increase of connected components. The powerful CCGK maintains a single strongly connected component for much longer.

(iv) **Point coverage** problem regards the assurance that some selected points in the network are covered by an adequate number of sensors and is an important aspect in numerous wireless sensor networks functionalities (e.g. localization, tracking, etc.). A point that is covered by  $k$  sensors is called  $k$ -covered. In Fig. 15.10 we can see the coverage aging of 1000 randomly selected points scattered throughout the network. We examine how many points are  $<2$ -covered, 2-covered, 3-covered and  $>3$ -covered

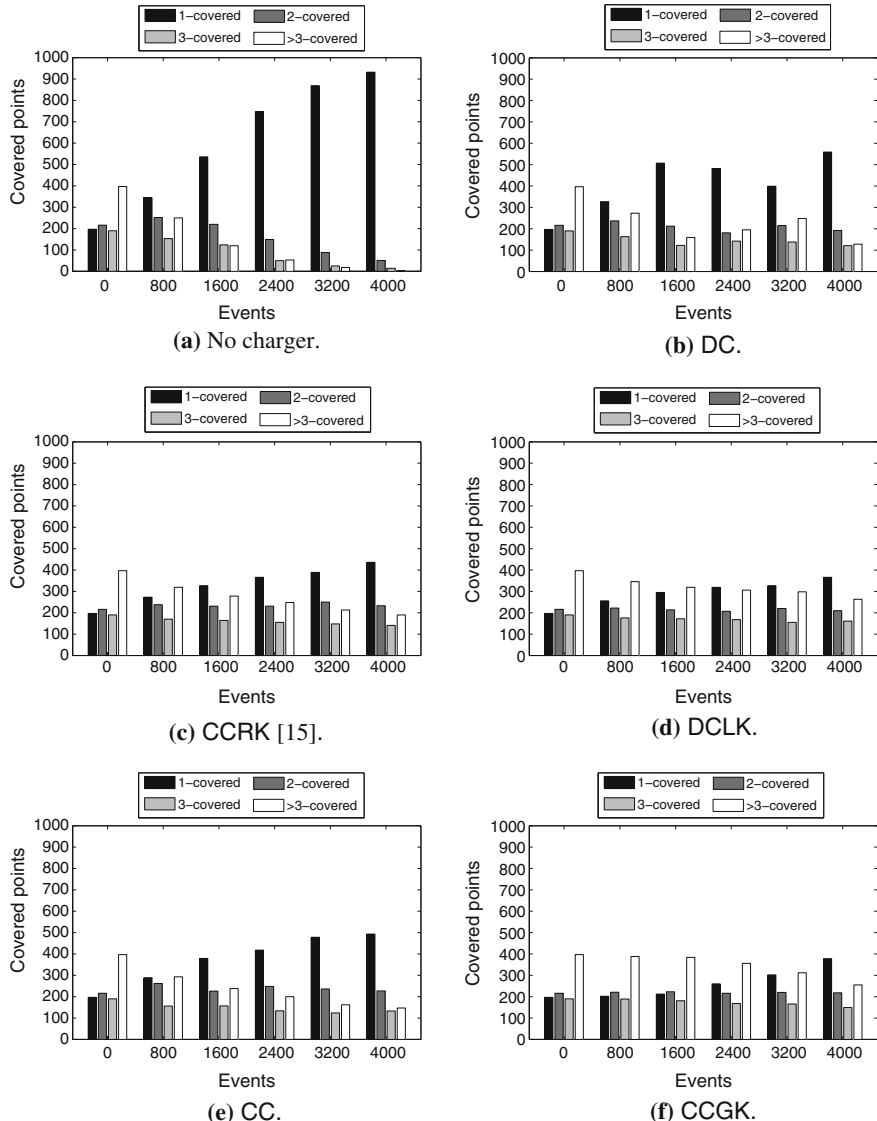


**Fig. 15.10** Coverage aging for uniform deployments

for 4000 generated events. Each bar in the plot represents a number of the covered points. In the no charger case, the number of  $<2$ -covered points is increasing in contrast to the number of  $>3$ -covered points that is decreasing. CCGK, DCLK and CCRK protocols improve the network coverage by reducing the rate that the coverage of  $>3$ -covered points is decreasing. The absolute difference of the number of  $<2$ -covered and  $>3$ -covered points, between different time instances, is not increasing quickly, compared to the no charger case.

### 15.7.1.2 The Impact of Knowledge

An important fact that comes up from the observation of the aforementioned metrics is that the CC and DC protocols are outperformed by their improved alternatives, CCGK and DCLK. The CC protocol, which uses a strong, centralized computation in order to calculate the regions of interest for the Mobile Chargers, is outperformed even by the DCLK protocol that employs distributed computation (but assumes more knowledge on the network). This leads to the conclusion that the nature of the coordination procedure is less significant than the design of the charging traversal, when the latter relies on a greater amount of knowledge. Of course, when assuming the same amount of knowledge, the coordination procedure is still important (e.g. CC vs. DC).

Also, the comparison between CCGK and CCRK protocols enlightens us about the size of the impact for acquiring knowledge on the network w.r.t. energy cost. The CCRK protocol is provided with global knowledge on the network but (in contrast to CCGK) the information maintenance relies on an underlying message propagation mechanism which is dissipating node and charger energy. As shown by the experimental evaluation, the degradation from global knowledge to local knowledge assumption (DCLK) is more efficient than a costly acquisition of global knowledge. This is why, although in our simulations we do not calculate the communication cost between the Mobile Chargers and the nodes, we calculate the cost of the node-to-node communication. This cost is similar to the one introduced by the underlying routing protocol that is used by the nodes for data propagation. However, in the CCRK protocol, the representative nodes communicate with the nodes in their group more frequently, in order to collect their important status information and thus, they are dissipating their energy with a higher rate. This may lead to a higher node death rate, higher number of connected components, etc. This communication overhead is the reason of the worse CCRK performance compared to DCLK.

### 15.7.1.3 Traveling Distance

Traveling distance of the Mobile Chargers indirectly reflects the efficiency of the coordination procedure and the charging process. Although the investigation of traveled distance does not display the impact on crucial network parameters, it can lead to useful conclusions about the balance of the Mobile Chargers activity.

Also, traveling distance can be associated with relevant cost for movement as presented in Sect. 15.6.1.

Figure 15.12 depicts the total distance traveled by all (six) Mobile Chargers in the network. It is clear that CCGK, CCRK and DCLK protocols achieve the required charging process by traveling less distance than DC and CC protocols. Figure 15.11 is comprised of five piecharts, one per protocol. A piechart consists of Slices, the size of which is proportional to the distance traveled by the corresponding Mobile Charger. We observe that in contrast to DC and CC protocols, CCGK, CCRK and DCLK protocols achieve balanced distribution of traveled distance among the Mobile Chargers.

## 15.7.2 Nonuniform Network Deployment

We examine the performance of our protocols in networks where the deployment of the sensor nodes is nonuniform (follows the heterogeneous placement described in Sect. 15.3). This scenario is more realistic in large scale, real-life, sensor networks. The protocol's performance over the various metrics share some similarities with the uniform case.

### 15.7.2.1 Protocol's Impact on Network Properties

(i) **Alive nodes over time.** As shown in Fig. 15.14a, the most powerful protocol, CCGK, still outperforms all other protocols. Furthermore, the number of alive nodes in the DCLK protocol decreases with a very low rate indicating that the protocol's charging process that partitions the Slices into Sectors and charges the nodes of the most critical Sector, achieves a balanced energy consumption between the sensor nodes. The DC protocol, which assumes no network knowledge and has a distributed coordination procedure, achieves the worst performance, which in the nonuniform case is even worse, since it is quite close to the no charger protocol. Also, the number of alive nodes in the CC protocol is much higher than in the DC protocol. Since both protocols are not using any knowledge, the difference in their performance is due to the coordination procedure, which in CC is centralized and in DC is distributed.

(ii) **Routing Robustness.** The average routing robustness, as shown in Fig. 15.14b, follows the same pattern with the lifetime of the network, indicating that the higher the level of knowledge is, the more reliable the provided routing robustness becomes. In Fig. 15.15, a detailed evolution of the routing robustness is provided. The no charger case results in the worst performance (the black bar increases rapidly) as the number of generated events is increasing. In contrast, the CCGK protocol achieves the best performance since it maintains high robustness. DCLK and CCRK protocols also achieve high robustness by maintaining a high number of alive neighbors ( $> 12$ -alive neighbors as well as  $> 16$ -alive neighbors) and a low increase on black bar (which represents  $< 7$ -alive neighbors).

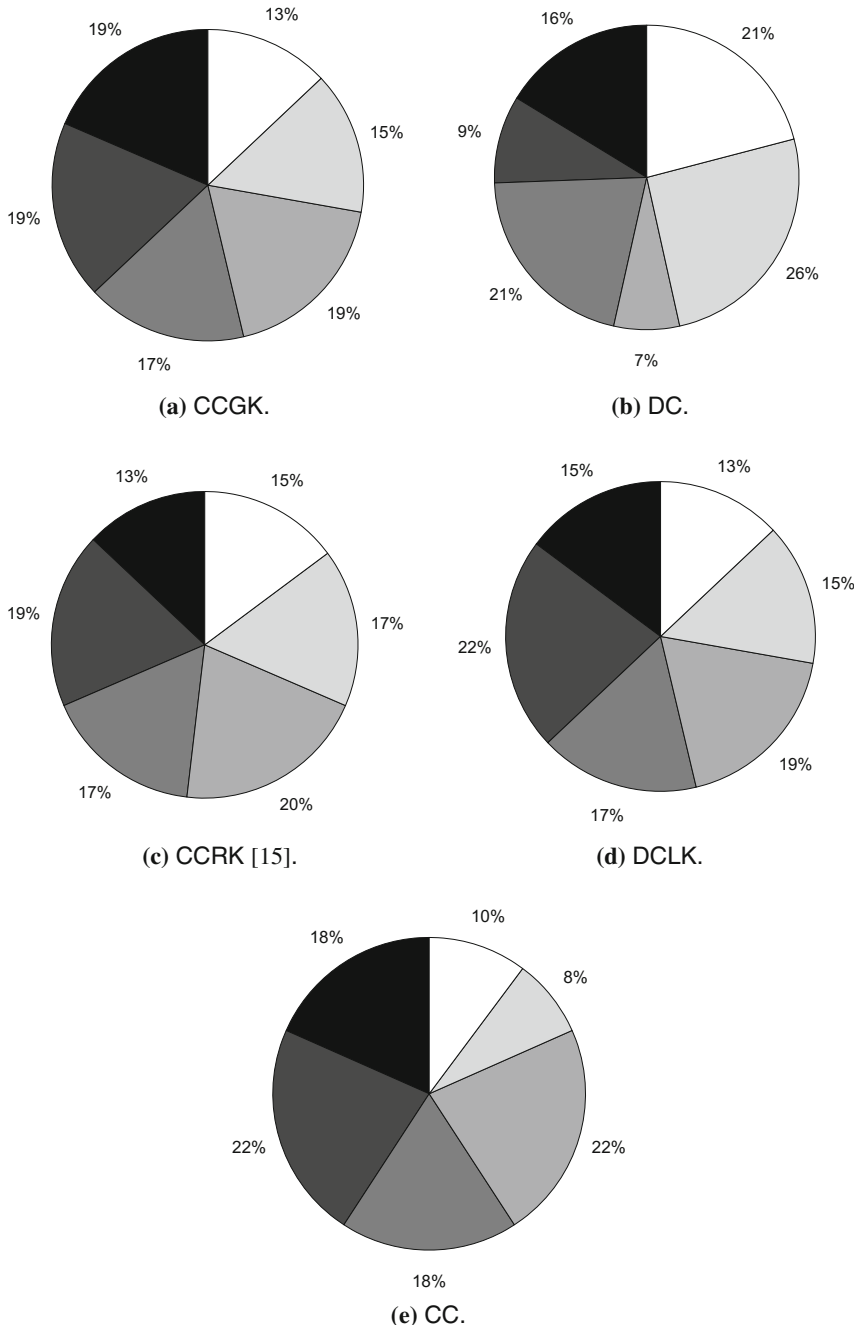


**Fig. 15.11** Distance traveled per Mobile Charger for uniform deployments

**Fig. 15.12** Distance traveled by Mobile Chargers for uniform deployments

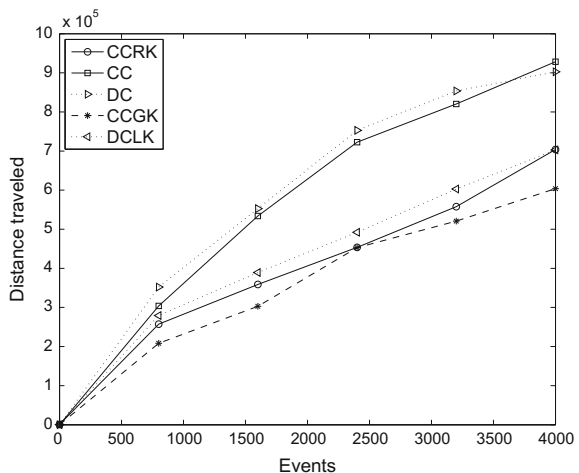
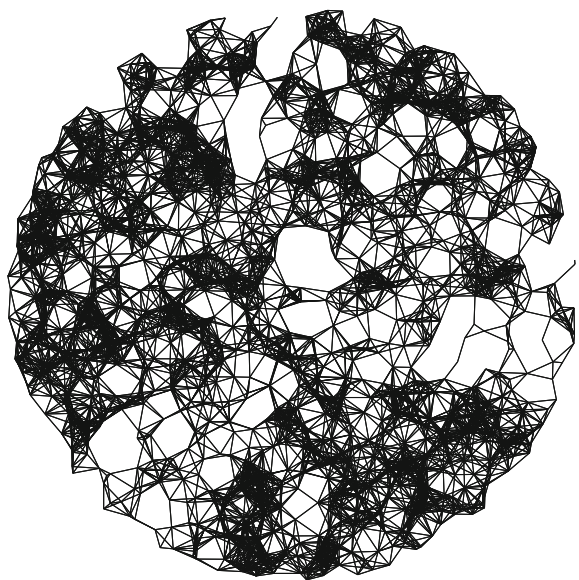


**Fig. 15.13** Nonuniform deployment



(iii) **Strongly connected components.** This metric is the one affected the most by the nonuniform node deployment. As shown in Fig. 15.14c, the difference between the protocols' performance is similar to the uniform case, i.e. the order of the protocols based on their performance is the same. Four of the protocols begin to increase the number of connected components after some time (and not earlier as in the uniform case) but they achieve similar number of components at the end of the simulation. This indicates that the number of components increases with higher rate. Also, the CCGK, CCRK and DCLK protocols begin to increase the number of components earlier than in the uniform case (and with a higher rate).

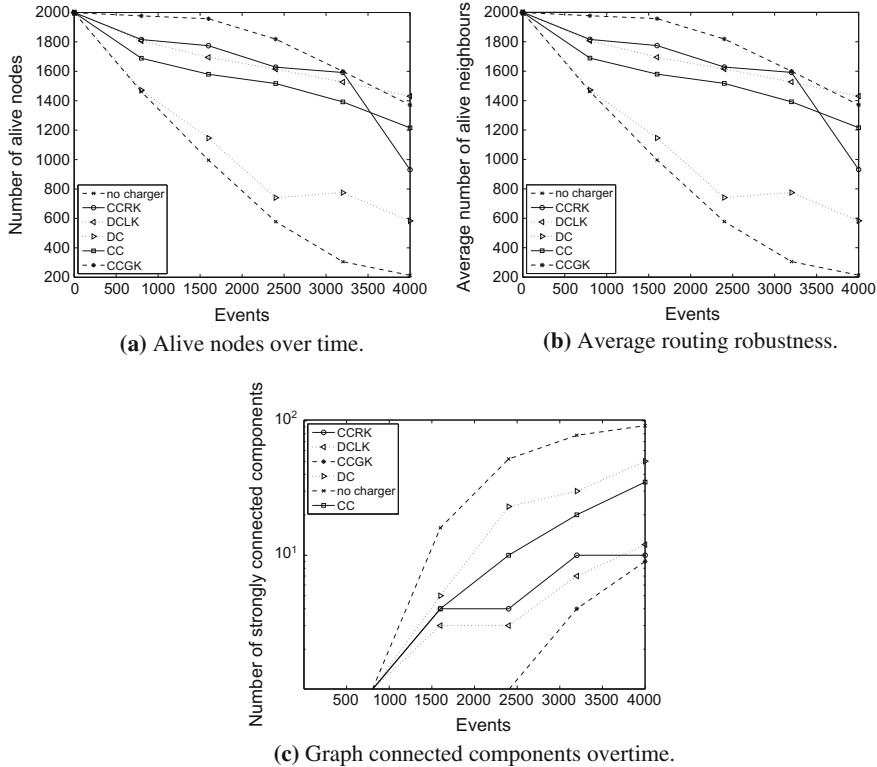


**Fig. 15.14** Various metrics for nonuniform deployments

(iv) **Point coverage.** In the nonuniform network deployment, there may be some parts of the network that are more sparse than others and the points belonging in these areas will be uncovered earlier, i.e. there will not be any alive nodes to collect their generated data. As shown in Fig. 15.16, the three protocols that assume large amount of network knowledge, manage to keep a high point coverage level, i.e. the black bar depicting the number of points covered by  $< 7$  nodes is not increasing with a high rate. More specifically, the CC and CCRK achieve better performance than in the uniform case. In contrast, DC and no charger are not able to maintain good coverage levels and increase the black bar rapidly. The increase on the DC protocol is higher than the corresponding increase in the uniform case.

### 15.7.2.2 Impact of Knowledge

The following observation in the uniform case is also valid in the nonuniform case. The higher the amount of knowledge is, the better the protocol's performance achieved (for the same coordination procedure). This is natural since protocols with higher knowledge amounts exploit more efficiently the network resources.

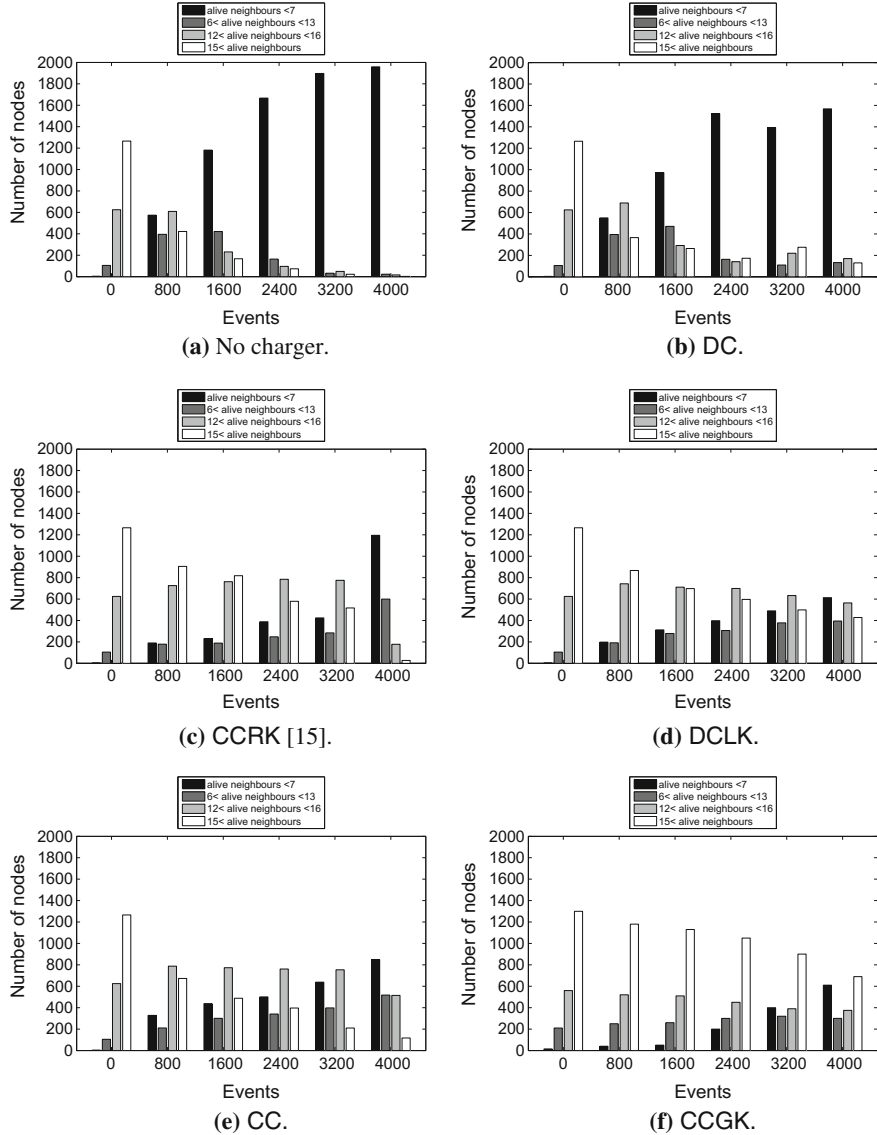


**Fig. 15.15** Routing robustness for nonuniform deployments

### 15.7.2.3 Traveling Distance

In the nonuniform case, (similarly to the uniform), when using the CC and DC protocols that are not exploiting any network knowledge, there are some Mobile Chargers that cover much longer distance than others. As shown in Fig. 15.17 the total distance

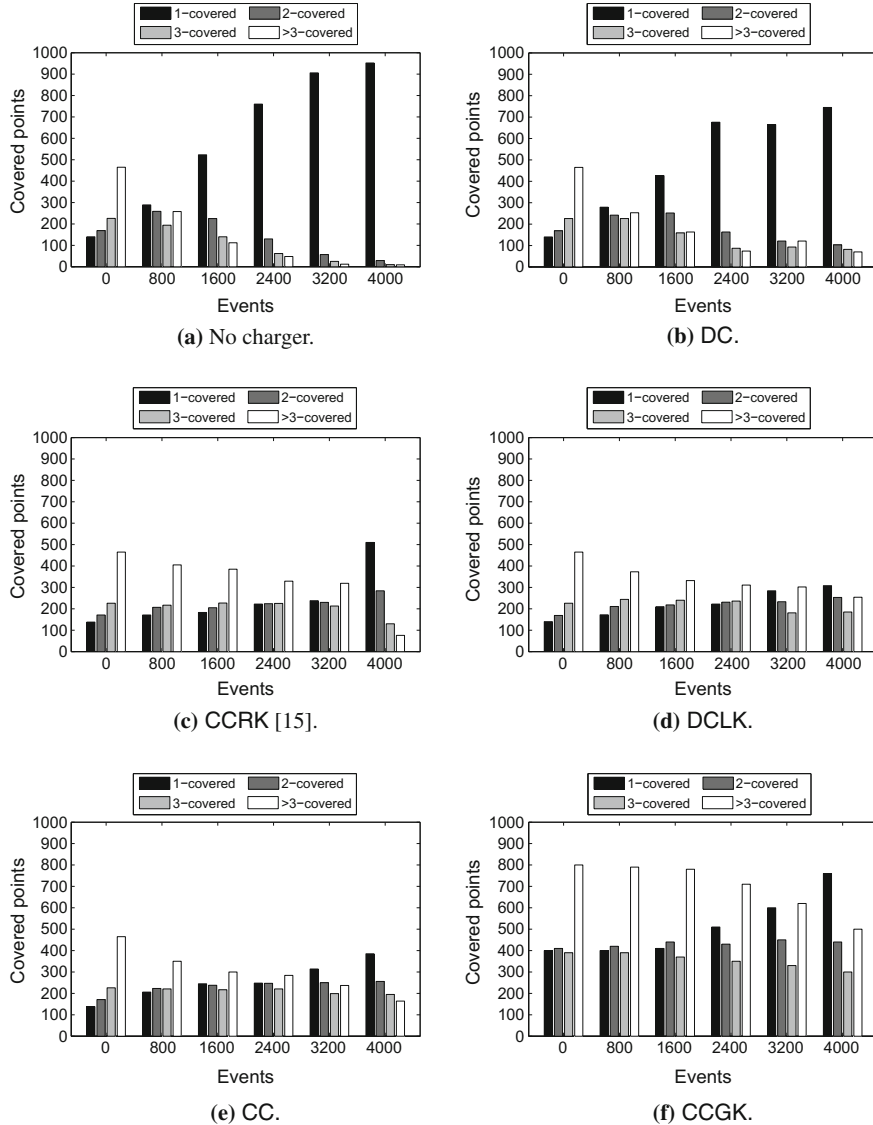
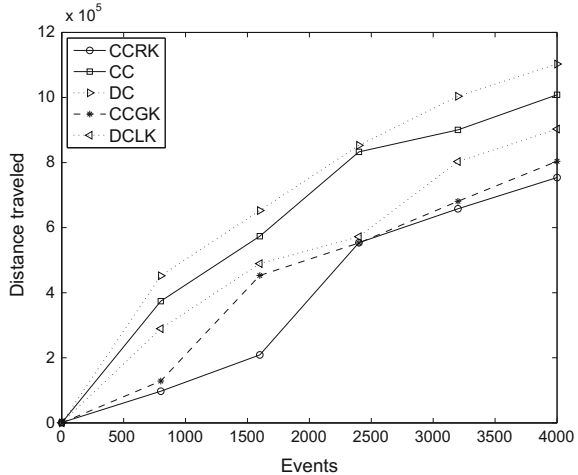


**Fig. 15.16** Coverage aging for nonuniform deployments

traveled by all Mobile Chargers for each protocol, is higher than the corresponding distance traveled in the uniform network deployment. Despite the fact that the nodes are nonuniformly deployed, the distribution of the total distance traveled among all Mobile Chargers is quite similar to the corresponding distribution of the uniform case. As is shown in Fig. 15.18, the CCGK, CCRK and DCLK protocols perform a more balanced distribution of total traveled distance between the Mobile Chargers

**Fig. 15.17** Distance traveled per Mobile Charger for nonuniform deployments



than the CC and the DC protocols. As we can see, CC and DC not only lead to an unbalanced distribution of traveled distance among the Mobile Chargers (Fig. 15.18) but also have larger traveled distance compared to other protocols (Fig. 15.17).

#### 15.7.2.4 Summary of Differences Between Impact on Uniform and Nonuniform Node Deployment

We compared the protocols both on networks with uniform node deployment and on networks with nonuniform node deployment. The simulation results demonstrated that the protocols' performance on the various metrics on the two networks have a lot of similarities. In general, in most metrics the ordering of the protocols by their performance is the same. Differences exist mostly on the exact values of the metrics. More specifically, the differences in each metric are the following. In the *alive nodes over time* metric, the CCRK protocol achieves better performance in the nonuniform case than in the uniform one throughout almost the whole experiment. After that, the death rate is very high. Also, in this time interval it outperforms the DCLK protocol while in the uniform case the DCLK always achieves a better performance. In the *average routing robustness* metric, the differences are the same as with the previous metric since these two metrics are related. In the *routing robustness* metric, the DC, DCLK and CC protocols show great differences. In the nonuniform case, the DC and DCLK achieve inefficient routing robustness while the CC achieves better performance. In *strongly connected components* metric (nonuniform case), the no charger and DC protocols improve their performance since they keep one connected component for long time. In contrast, in the uniform case, the same protocols increase the number of connected components since the beginning of the experiment. Unlike the above protocols, the CCGK, CCRK and DCLK protocols, start to increase the

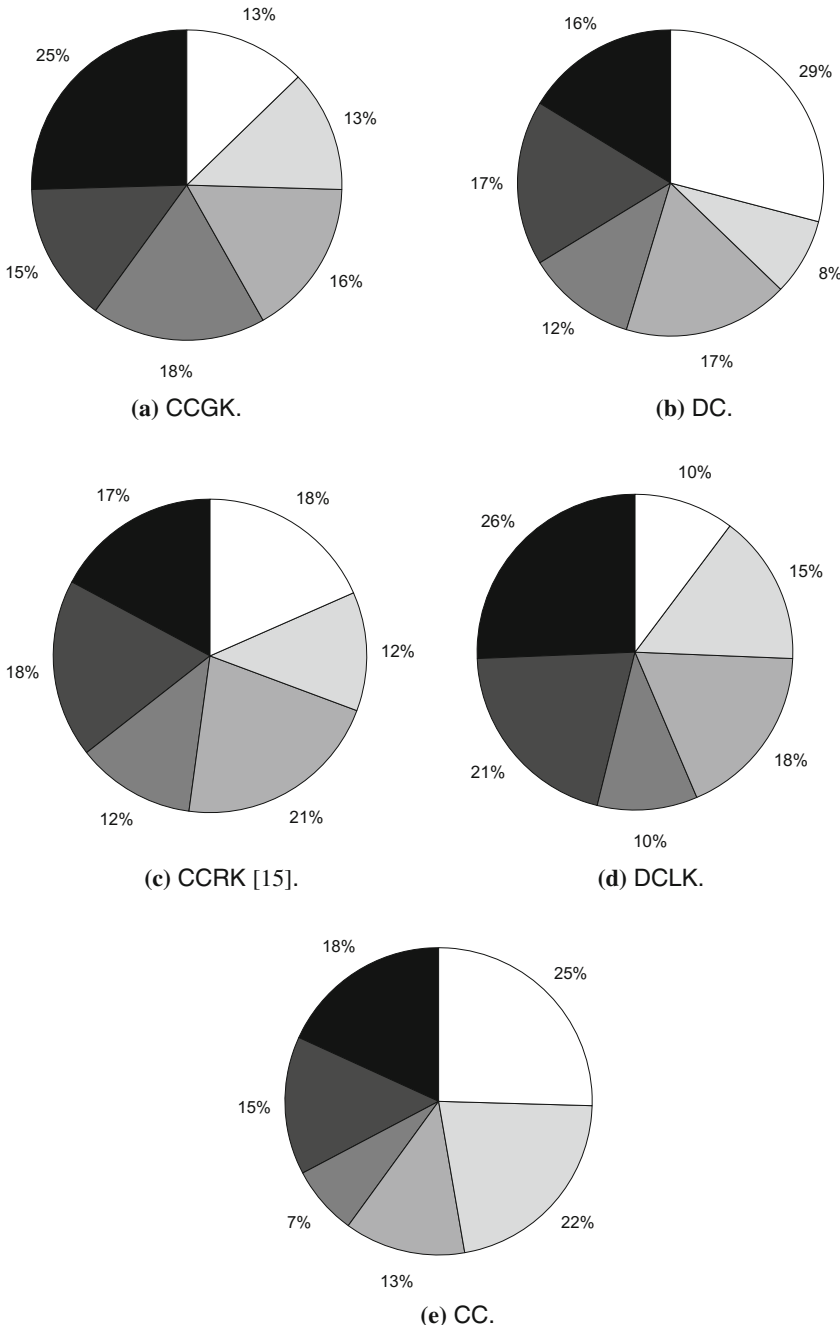


**Fig. 15.18** Distance traveled per Mobile Charger for nonuniform deployments

number of components earlier than in the uniform case. Furthermore, in the *point coverage* metric, in the nonuniform case, the DC protocols increase the uncovered points with a higher rate compared to the uniform case. On the contrary, the CC and CCRK protocols, manage to keep more nodes alive to cover the points than in the uniform case. Comparing the *distance traveled* metric, in the nonuniform case all protocols cover longer distance than that in the uniform case. Also, in the uniform case the CCGK protocol has covered the shortest distance while in the nonuniform case the CCRK has the shortest traveled distance. Finally, on the distribution of total traveled distance between Mobile Chargers there is not any remarkable difference between the performance on the two types of node deployment.

### 15.7.3 Conclusion

In this work we have studied the problem of efficient wireless power transfer in Wireless Rechargeable Sensor Networks. In such networks, Mobile Chargers traverse the network and wirelessly replenish the energy of sensor nodes. We first identify and investigate some critical issues and trade-offs of the Mobile Chargers configuration (i) what are good coordination procedures for the Mobile Chargers to perform and (ii) what are good trajectories for the Mobile Chargers to follow. In contrast to most current approaches, we envision methods that are distributed and use limited network information. We propose four new protocols for efficient charging assuming different levels of network knowledge (from global to local and no network knowledge), and different processing (from centralized to distributed).

## References

1. Battery calculator. [http://www.evsource.com/battery\\_calculator.php/](http://www.evsource.com/battery_calculator.php/)
2. Angelopoulos, C.M., Nikoletseas, S., Raptis, T.P.: Wireless energy transfer in sensor networks with adaptive, limited knowledge protocols. *Comput. Netw.* **70**, 113–141 (2014)
3. Angelopoulos, C.M., Nikoletseas, S., Raptis, T.P., Raptopoulos, C., Vasilakis, F.: Improving sensor network performance with wireless energy transfer. *Int. J. Ad Hoc Ubiquitous Comput.* (2014). Inderscience Publishers
4. Dai, H., Wu, X., Xu, L., Chen, G., Lin, S.: Using minimum mobile chargers to keep large-scale wireless rechargeable sensor networks running forever. In: Proceedings of the 22nd International Conference on Computer Communications and Networks (ICCCN), pp. 1–7 (2013)
5. Efstathiou, D., Koutsopoulos, A., Nikoletseas, S.: Analysis and simulation for parameterizing the energy-latency trade-off for routing in sensor networks. In: Proceedings of the 13th ACM International Conference on Modeling, Analysis and Simulation of Wireless and Mobile Systems (MSWiM) (2010)
6. Garey, M.R., Johnson, D.S.: Computers and intractability. W. H. Freeman and Company (1979)
7. Gnawali, O., Fonseca, R., Jamieson, K., Moss, D., Levis, P.: Collection tree protocol. In: Proceedings of the 7th ACM Conference on Embedded Networked Sensor Systems (SenSys) (2009)

8. Gupta, P., Kumar, P.: Critical power for asymptotic connectivity in wireless networks. In: Stochastic Analysis, Control, Optimization and Applications (1998)
9. He, L., Cheng, P., Gu, Y., Pan, J., Zhu, T., Liu, C.: Mobile-to-mobile energy replenishment in mission-critical robotic sensor networks. In: Proceedings of the 33rd IEEE International Conference on Computer Communications (INFOCOM) (2014)
10. Li, J., Wang, C., Ye, F., Yang, Y.: Netrap: An NDN based real time wireless recharging framework for wireless sensor networks. In: Proceedings of the 10th IEEE International Conference on Mobile Ad-Hoc and Sensor Systems (MASS), pp. 173–181 (2013)
11. Peng, Y., Li, Z., Zhang, W., Qiao, D.: Prolonging sensor network lifetime through wireless charging. In: Proceedings of the 31st IEEE Real-Time Systems Symposium (RTSS) (2010)
12. Penrose, M.: Random Geometric Graphs. Oxford University Press (2003)
13. Shi, Y., Xie, L., Hou, Y.T., Sherali, H.D.: On renewable sensor networks with wireless energy transfer. In: Proceedings of the 30th IEEE International Conference on Computer Communications (INFOCOM) (2011)
14. Tanenbaum, A.: Modern Operating Systems, 3rd edn. Prentice Hall (2007)
15. Wang, C., Li, J., Ye, F., Yang, Y.: Multi-vehicle coordination for wireless energy replenishment in sensor networks. In: Proceedings of the 27th IEEE International Parallel & Distributed Processing Symposium (IPDPS) (2013)
16. Wang, C., Li, J., Ye, F., Yang, Y.: Recharging schedules for wireless sensor networks with vehicle movement costs and capacity constraints. In: Proceedings of the 11th IEEE International Conference on Sensing, Communication, and Networking (SECON), pp. 468–476. IEEE (2014)
17. Xie, L., Shi, Y., Hou, Y.T., Lou, W., Sherali, H.D., Midkiff, S.F.: Bundling mobile base station and wireless energy transfer: Modeling and optimization. In: Proceedings of the 32nd IEEE International Conference on Computer Communications (INFOCOM) (2013)
18. Zhang, S., Wu, J., Lu, S.: Collaborative mobile charging for sensor networks. In: Proceedings of the 9th IEEE International Conference on Mobile Ad-Hoc and Sensor Systems (MASS) (2012)

# Chapter 16

## Minimizing the Service Cost of Mobile Chargers While Maintaining the Perpetual Operations of WRSNs

Wenzheng Xu and Weifa Liang

**Abstract** The wireless energy transfer technology based on magnetic resonant coupling has been emerging as a promising technology for lifetime prolongation of wireless sensor networks, by providing controllable yet perpetual energy to sensors. As a result, we can employ mobile chargers (i.e., charging vehicles) to charge sensors with wireless energy transfer when the mobile charger approach lifetime-critical sensors. It is however very costly to dispatch mobile chargers to travel too long to charge sensors since their mechanical movements are energy-consuming too. To minimize the operational cost of wireless sensor networks, in this chapter we study the deployment of multiple mobile chargers to charge sensors in a large-scale wireless sensor network so that none of the sensors will run out of energy and aim to minimize the service cost of the mobile chargers. Specifically, we study the problem of minimizing the total traveling distance of mobile chargers for a given monitoring period, and the problem of deploying the minimum number of mobile chargers to replenish a set of lifetime-critical sensors while ensuring that none of the sensors will run out of energy, respectively. For the former, we propose a novel approximation algorithm with a guaranteed approximation ratio, assuming that the energy consumption rate of each sensor does not change for the given monitoring period. Otherwise, we devise a heuristic algorithm through modifications to the approximation algorithm. Simulation results show that the proposed algorithms are very promising. For the latter, we develop an approximation algorithm with a provable performance guarantee, and experimental results demonstrate that the solution delivered by the proposed approximation algorithm is fractional of the optimal one.

---

W. Xu

College of Computer Science, Sichuan University,  
Chengdu 610065, People's Republic of China  
e-mail: wenzheng.xu3@gmail.com

W. Liang (✉)

Research School of Computer Science, The Australian National University,  
Canberra 0200, Australia  
e-mail: wliang@cs.anu.edu.au

## 16.1 Introduction

The limited battery capacities of sensors obstruct the large-scale deployment of wireless sensor networks (WSNs). Although there are many energy-aware approaches developed in the past decade to reduce sensor energy consumptions or balance energy expenditures among sensors [1–8], the lifetime of WSNs remains a main performance bottleneck in their real deployments, since wireless data transmission consumes substantial sensor energy. The wireless energy transfer technology based on magnetic resonant coupling has been emerging as a promising technology for wireless sensor networks, by providing controllable yet perpetual energy to sensors [9]. In this chapter, we employ multiple mobile chargers (i.e., charging vehicles) to replenish sensor energy in a large-scale WSN for a given monitoring period  $T$  so that none of the sensors will run out of energy, where each sensor can be charged by a mobile charger in its vicinity with the wireless power transfer technique. Since each sensor consumes energy on data sensing, data transmission, data reception, etc., the sensor may need to be charged multiple times during the monitoring period of  $T$  to avoid its energy depletion. It is however very costly to dispatch mobile chargers to travel too long to charge sensors since their mechanical movements are very energy-consuming, or deploy too many mobile chargers to replenish sensors. To minimize the network operational cost, in this chapter we study the deployment of multiple mobile chargers to charge sensors in a large-scale wireless sensor network so that none of the sensors will run out of energy, and aim to minimize the service cost of mobile chargers. Specifically, we investigate two charging optimization problems: the problem of minimizing the traveling distance of mobile chargers for a given monitoring period [10, 11]; and the problem of deploying the minimum number of mobile chargers to replenish a set of lifetime-critical sensors while ensuring that none of the sensors will run out of energy, respectively [12, 13].

Most existing studies on sensor charging scheduling employ mobile chargers to charge all sensors periodically [14–16], or charge only the sensors that will run out of energy very soon [12, 13, 17–22]. One major disadvantage of these studies is that the total traveling distance of the mobile chargers in the entire monitoring period can be very long, which may not be necessary, as the energy consumption rates of different sensors usually are significantly different. For example, the sensors near to the base station have to relay data for other remote sensors, their energy consumption rates thus are much higher than that of the others [23]. Therefore, the naive strategy of charging all sensors per charging tour will significantly increase the total traveling distance of the mobile chargers. Similarly, the charging strategy that schedules the mobile chargers to charge only the life-critical sensors also suffers from the same problem as these life-critical sensors may be far away from each other in the monitoring area.

The long total traveling distance of mobile chargers can result in prohibitively high energy consumptions of mobile chargers on their mechanical movements. It is reported that the most fuel-efficient vehicle has an energy consumption of 600 kJ per km (i.e., 27 kWh per 100 miles) [24] while the energy capacity of a regular sensor

battery is 10.8 kJ [14]. This implies that the amount of energy consumed by the vehicle traveling for one kilometer is equivalent to the amount of energy used for charging as many as 55 ( $\approx \frac{600 \text{ kJ}}{10.8 \text{ kJ}}$ ) sensors. Since WSNs usually are deployed for long-term environmental sensing, target tracking, and structural health monitoring [25–28], the monitoring area of a WSN can be very large (e.g., several square kilometers) [26, 29], the mobile chargers by the existing studies consume a large proportion of their energy on traveling, rather than on sensor charging, thereby leading to a very high cost of network operations.

Unlike existing studies that ignore the energy consumption of mobile chargers on traveling for charging sensors, in this chapter we develop efficient charging scheduling algorithms to dispatch multiple mobile chargers for sensor charging in a large-scale WSN for a long-term monitoring period  $T$ , so that not only none of the sensors runs out of energy but also the total traveling distance of all the mobile chargers for the monitoring period of  $T$  is minimized. As energy consumption rates of different sensors may significantly vary, different sensors have different charging frequencies during the period  $T$ , this poses great challenges for scheduling the mobile chargers, which include

- (1) when should we activate a charging round to dispatch the mobile chargers to replenish sensor energy?
- (2) which sensors should be included in each charging round?
- (3) given a set of to-be-charged sensors, which sensors should be charged by which mobile charger?
- (4) what is the charging order of the sensors assigned to each mobile charger?

In this chapter, we will tackle these challenges by first formulating a novel optimization problem, and then devising an efficient approximation algorithm with a performance guarantee and a heuristic algorithm for the problem, depending on whether the energy consumption rate of each sensor is fixed or not for the given monitoring period. On the other hand, most existing studies assumed that one mobile charging vehicle will have enough energy to charge all sensors in a WSN, and the proposed algorithms for vehicle charging scheduling thus are only applicable to small-scale WSNs [10, 11, 14, 15, 22, 30, 31]. However, in a large-scale sensor network, the amount of energy carried by a single mobile charging vehicle may not be enough to charge all nearly expired sensors, as there are a large proportion of life-critical sensors to be charged. Thus, multiple mobile charging vehicles instead of a single one are needed to be employed. In this chapter, we will study the use of minimum numbers of mobile charging vehicles to replenish energy to sensors for a large-scale wireless sensor network such that none of the sensors will run out of energy. We will adopt a flexible on-demand sensor charging paradigm that decouples sensor energy-charging scheduling from the design of sensing data routing protocols, and dispatch multiple mobile charging vehicles to charge life-critical sensors in an on-demand way. Specifically, we assume that each mobile charging vehicle can carry only a limited, rather than infinite, amount of energy. We will study a fundamental sensor charging problem. That is, given a set of life-critical sensors to be charged and the energy capacity constraint on each mobile charging vehicle, what is the

minimum number of mobile charging vehicles needed to fully charge these sensors in order to reduce the operational cost of the WSN, while ensuring that none of the sensors runs out of energy? To address this problem, not only should the number of charging vehicles be determined but also the charging tour of each mobile charging vehicle needs to be found so that all life-critical sensors can be charged prior to their expirations, where each vehicle consumes energy on charging sensors in its tour and its mechanical movement along the tour.

There are two closely related studies on minimizing the number of deployed charging vehicles [32, 33]. Specifically, Nagarajan and Ravi studied *the distance constrained vehicle routing problem* (DVRP), in which given a set of nodes in a metric graph, a depot, and an integral distance bound  $D$ , the problem is to find the minimum number of tours rooted at the depot to cover all nodes such that the length of each tour is no more than  $D$  [33]. For the DVRP problem, they presented a  $(O(\log \frac{1}{\varepsilon}), 1 + \varepsilon)$ -bicriteria approximation algorithm for any constant  $\varepsilon$  with  $0 < \varepsilon < 1$ , i.e., the algorithm finds a set of tours that the length of each tour is no more than  $(1 + \varepsilon)D$ , while the number of deployed vehicles is no more than  $O(\log \frac{1}{\varepsilon})$  times the minimum number of vehicles. On the other hand, Dai et al. investigated the problem of deploying the minimum number of charging vehicles to fully charge the sensors, by making use of the approximation algorithm in [33], assuming that all sensors have identical energy consumption rates [32]. There are however two essential differences between these two mentioned studies and the work in this chapter. First, the cost of each found tour by the algorithms in [32, 33] may violate the travel distance constraint on the mobile vehicles. In contrast, in this chapter the total energy consumption of each mobile charging vehicle per tour cannot exceed its energy capacity  $IE$ . Otherwise, the vehicle cannot return to the depot for recharging itself. Also, a constant approximation algorithm for the minimum number of mobile chargers deployment problem is devised. Second, the study in [32] assumed that all sensors have identical energy consumption rates. Contrarily, this chapter does not require that all sensors have identical energy consumption rates and the energy consumption rates of different sensors may be significantly different. Therefore, the proposed algorithms in the two mentioned studies cannot be applicable to the problem in this chapter. New approximation algorithms need to be devised, and new algorithm analysis techniques for analyzing the approximation ratio need to be developed, too.

The main contributions of this chapter can be summarized as follows. We first formulate a novel service cost minimization problem of finding a series of charging scheduling of multiple mobile chargers such that the total traveling distance of the mobile chargers for sensor charging is minimized. We also formulate a minimum number of mobile chargers deployment problem while maintaining the perpetual operations of sensors for a given monitoring period, subject to the energy capacity constraint on each mobile charger. We third propose an approximation algorithm for the service cost minimization problem with a provable approximation ratio if energy consumption rates of sensors are fixed during the monitoring period. Otherwise, we devise a heuristic solution through modifications to the approximate solution. Furthermore, we develop an approximation algorithm with a provable performance guarantee for the minimum number of mobile chargers deployment problem. We

finally conduct extensive experiments by simulations to evaluate the performance of the proposed algorithms. Experimental results demonstrate that the proposed algorithms are very promising. To the best of our knowledge, they are the first approximation algorithms for scheduling multiple mobile chargers to charge sensors within a given monitoring period for the service cost minimization problem and the minimum number of mobile chargers deployment problem.

The rest of this chapter is organized as follows. Section 16.2 introduces preliminaries. Sections 16.3 and 16.4 propose efficient approximation and heuristic algorithms for the service cost minimization problem and the minimum number of mobile chargers deployment problem, respectively. Sections 16.5 and 16.6 evaluate the performance of the proposed algorithms. Section 16.7 concludes this chapter.

## 16.2 Preliminaries

In this section, we first introduce the network and energy consumption models, then introduce notations and notions, and finally define the problems precisely.

### 16.2.1 Network Model

We consider a wireless sensor network consisting of  $n$  sensors, which are randomly deployed in a two-dimensional space. Let  $V$  be the set of sensors. Each sensor  $v_i \in V$  generates sensing data with a rate of  $b_i(t)$  (in bps) at time  $t$ , and it is powered by a rechargeable battery with energy capacity  $B_i$ . There is one stationary base station in the network. We assume that there is a routing protocol for sensing data collection that relays sensing data from sensors to the base station through multihop relays. For example, each sensor uploads its sensing data to the base station via the path with the minimum energy consumption. Figure 16.1 illustrates such a wireless sensor network. Assume that the entire monitoring period is  $T$  ( $T$  typically is quite long, e.g., several months, even years). Since each sensor consumes energy on data sensing, processing, transmission and reception, it requires to be charged multiple times for the period of  $T$  to avoid its energy depletion.

We employ  $q$  wireless mobile chargers to replenish energy to sensors in the network, where mobile charger  $l$  is located at depot  $r_l$ ,  $1 \leq l \leq q$ . Without loss of generality, let  $R = \{r_1, r_2, \dots, r_q\}$  be the set of depot locations of the  $q$  mobile chargers. To determine charging trajectories of the  $q$  mobile chargers, we define a weighted, undirected graph  $G = (V \cup R, E; w)$ , where for any two distinct nodes (sensors or depots)  $u$  and  $v$  in  $V \cup R$ , there is an edge  $e = (u, v) \in E$  between them with their Euclidean distance being the weight  $w(e)$  of edge  $e$ . Assume that each mobile charger has a full energy capacity  $IE$  and a charging rate  $\mu$  for charging a sensor, and the charger travels at a constant speed  $s$ . We further assume that the mechanical movement of the charger is derived from its energy as well. Let  $\eta$  be the energy consumption rate of each charger on traveling per unit length. Each time mobile charger  $l$  is dispatched to charge some sensors, it always starts from and ends at its depot  $r_l$  for recharging

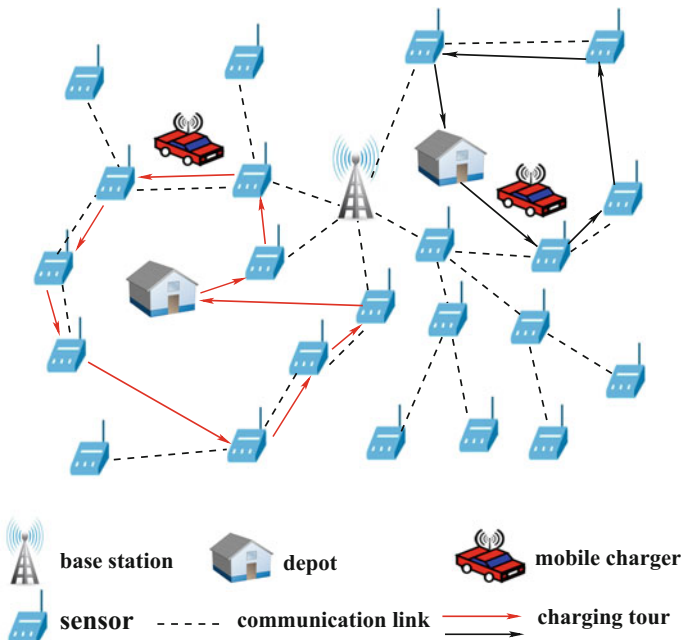


**Fig. 16.1** A rechargeable wireless sensor network

itself or refuelling its petrol. In other words, each charging tour of a mobile charger  $l$  in  $G$  is a *closed tour* including depot  $r_l$ . For any closed tour  $C$  in  $G$ , denote by  $w(C)$  the weighted sum of the edges in  $C$ , i.e.,  $w(C) = \sum_{e \in E(C)} w(e)$ . We consider a point-to-point charging, i.e., to efficiently charge a sensor by a mobile charger, the mobile charger must be in the vicinity of the sensor [34] and the sensor will be charged to its fully capacity.

We assume that the duration of the  $q$  mobile chargers per charging round that includes the time for charging sensors and their traveling time is several orders of magnitude less than the lifetime of a fully charged sensor. The rationale behind the assumption is as follows. Once a sensor is fully charged, its lifetime can last from several weeks to months until its next charging, since the sensor energy can be well managed through various existing energy conservation techniques, e.g., duty cycling [35]. On the other hand, the  $q$  mobile chargers can collaboratively finish a charging round within a few hours, since sensor batteries can be made with ultra-fast charging battery materials [36]. For example, in 2009, scientists from MIT implemented an ultra-fast charging, in which a battery can be fully charged within a few seconds [36]. We thus envision that ultra-fast charging batteries will be commercialized in the near future and will be widely used for smartphones, sensors, electric vehicles, etc. Therefore, we ignore the time spent by the  $q$  mobile chargers per charging round. Note that [22, 37, 38] also adopted the similar assumption.

### 16.2.2 Energy Consumption Models

Each sensor will consume energy on data sensing, data transmission, and data reception, and the energy consumption models for these three components are shown in Eqs. (16.1), (16.2), and (16.3), respectively [23].

$$P_{sense} = \lambda \times b_i, \quad (16.1)$$

$$P_{Tx} = (\beta_1 + \beta_2 d_{ij}^\alpha) \times b_i^{Tx}, \quad (16.2)$$

$$P_{Rx} = \gamma \times b_i^{Rx}, \quad (16.3)$$

where  $b_i$  (in  $bps$ ) is the data sensing rate of sensor  $v_i$ ,  $b_i^{Tx}$  and  $b_i^{Rx}$  are the data transmission rate and the reception rate of sensor  $v_i$ , respectively,  $d_{ij}$  is the Euclidean distance between sensors  $v_i$  and  $v_j$ ,  $\alpha$  is a constant that is equal to 2 or 4, and the values of other parameters are as follows [23].

$$\begin{aligned} \lambda &= 60 \times 10^{-9} J/b, \\ \beta_1 &= 45 \times 10^{-9} J/b, \\ \beta_2 &= 10 \times 10^{-12} J/b/m^2, \text{ when } \alpha = 2, \\ \text{or } \beta_2 &= 1 \times 10^{-15} J/b/m^4, \text{ when } \alpha = 4, \\ \gamma &= 135 \times 10^{-9} J/b. \end{aligned}$$

The residual lifetime of each sensor  $v_i \in V$  at time  $t$  is defined as  $l_i(t) = \frac{RE_i(t)}{\rho_i(t)}$ , where  $RE_i(t)$  and  $\rho_i(t)$  are the amounts of residual energy and energy consumption rate of  $v_i$  at time  $t$ , respectively. The base station keeps a copy of the energy depletion rate  $\rho_i(t)$  and the residual energy  $RE_i(t)$  of each sensor  $v_i \in V$ .

We assume that each sensor is able to monitor its residual energy  $RE_i(t)$  and estimate its energy consumption rate  $\rho_i(t)$  in the near future through some prediction techniques such as linear regressions. We further assume that the energy consumption rate of each sensor does not change within a charging round, or such minor changes can be neglected as the duration of a charging round usually is short (e.g., a few hours). But the energy consumption rate of each sensor is allowed to change at a different charging round. Thus, each sensor can estimate its residual lifetime  $l_i(t)$  prior to the next charging round. Recall that for each sensor  $v_i \in V$ , there is a record of its energy consumption rate  $\rho_i(t)$  at the base station, and this value is subject to be updated if the energy consumption profile of the sensor in the future will experience significant changes. To accurately measure the energy consumption rate of each sensor, each sensor adopts a lightweight prediction technique to estimate its energy consumption rate in the near future, e.g., a sensor can make use of a linear regression,  $\hat{\rho}_i(t) = \omega \rho_i(t-1) + (1 - \omega) \hat{\rho}_i(t-1)$ , where  $\hat{\rho}_i$  is the estimation and  $\rho_i$  is the actual value at that moment and  $\omega$  is a weight between 0 and 1 [39]. Let  $\theta > 0$  be a small given threshold. For each sensor  $v_i \in V$ , the updating of its energy consumption rate is as follows. If  $|\hat{\rho}_i(t) - \hat{\rho}_i(t-1)| \leq \theta$ , no updating report from sensor  $v_i$  will be forwarded to the base station; otherwise, the updated energy consumption rate and

its residual energy of  $v_i$  that will be sent to the base station through a charging request is issued by  $v_i$ . The base station then performs the updating accordingly.

### 16.2.3 Notations and Notions

A *charging scheduling* of  $q$  mobile chargers is to dispatch each of the  $q$  mobile chargers from its depot to collaboratively visit a set of to-be-charged sensors in the current round, and each charger will return to its depot after finishing its charging tour. Assume that at time  $t_j$ , let closed tours  $C_{j,1}, C_{j,2}, \dots, C_{j,q}$  be the charging tours of the  $q$  mobile chargers, where tour  $C_{j,l}$  of mobile charger  $l$  contains its depot  $r_l$  and  $1 \leq l \leq q$ . Let  $\mathcal{C}_j = \{C_{j,1}, C_{j,2}, \dots, C_{j,q}\}$  be the set of the  $q$  tours at time  $t_j$ . Notice that it is likely that some tours  $C_{j,l}$ s may contain none of the sensors, and if so,  $V(C_{j,l}) = \{r_l\}$  and  $w(C_{j,l}) = 0$ . For the sake of simplicity, we represent each charging scheduling by a 2-tuple  $(\mathcal{C}_j, t_j)$ , where all sensors in tour  $C_{j,l} \in \mathcal{C}_j$  will be charged to their full energy capacities by mobile charger  $l$ , all the  $q$  mobile chargers are dispatched at time  $t_j$ , and  $0 < t_j < T$ . Denote by  $V(C_{j,l})$  and  $V(\mathcal{C}_j)$  the set of nodes in  $C_{j,l}$  and  $\mathcal{C}_j$ , respectively. Then,  $V(\mathcal{C}_j) = \bigcup_{l=1}^q V(C_{j,l})$ .

The *charging cycle* of a sensor  $v_i \in V$  is the duration between its two consecutive chargings, and its *maximum charging cycle*  $\tau_i$  is the maximum duration in which it will not run out of its energy. Since different WSNs adopt different sensing and routing protocols, different sensors may have different energy consumption rates and different maximum charging cycles. If the energy consumption rate of each sensor  $v_i \in V$  does not vary for the period of  $T$ , denote by  $\rho_i$  and  $\tau_i$  its energy consumption rate and maximum charging cycle, then  $\tau_i = \frac{B_i}{\rho_i}$ , where  $B_i$  is the energy capacity of sensor  $v_i$  and the energy consumption rate  $\rho_i$  of sensor  $v_i$  usually is determined by the data generation rate of the sensor and the sum of data rates from other sensors that the sensor must forward to the base station [35]. It is obvious that sensors with shorter maximum charging cycles need to be charged more frequently than sensors with longer maximum charging cycles. Since each time the  $q$  mobile chargers are dispatched to charge a set of sensors, they will consume their electricity or petrol, thereby incurring a service cost. We thus define the *service cost* of the  $q$  mobile chargers as the *sum of their travel distances* for charging sensors in the period of  $T$ .

### 16.2.4 Problem Definitions

In this chapter, we investigate the problem of minimizing the traveling distance of mobile chargers for a given monitoring period, and the minimum number of mobile chargers deployment problem, which are precisely defined as follows.

### 16.2.4.1 The Service Cost Minimization Problem

We note that not every sensor must be replenished in each charging round as the energy consumption rates of different sensors may be significantly different. Therefore, a naive strategy of charging all sensors per round will increase the service cost substantially. Also, as some to-be-charged sensors and their nearest depots in a large-scale sensor network can be far away from each other, it is crucial to schedule the  $q$  mobile chargers, by taking into account both the maximum charging cycles and the geographical locations of the sensors. We assume that each of the  $q$  mobile chargers has enough energy to charge the sensors assigned to it in each charging tour [14–16, 30].

Given a metric complete graph  $G = (V \cup R, E)$  with  $q$  mobile chargers located at  $q$  depots in  $R$ , a distance function  $w : E \mapsto \mathbb{R}^+$ , a monitoring period  $T$ , and a maximum charging cycle function  $\tau : V \mapsto \mathbb{R}^+$ , assume that the location coordinates  $(x_i, y_i) \in (X, Y)$  of each sensor  $v_i \in V$  are given. The *service cost minimization problem with fixed maximum charging cycles* in  $G$  is to find a series of charging scheduling  $(\mathcal{C}_1, t_1), (\mathcal{C}_2, t_2), \dots, (\mathcal{C}_p, t_p)$  of the  $q$  mobile chargers such that the total length of all closed tours (or the service cost) is minimized, where  $p$  is a positive integer to be determined by the algorithm. Specifically, the problem can be mathematically formulated as follows.

$$\text{minimize} \quad \sum_{j=1}^p w(\mathcal{C}_j) = \sum_{j=1}^p \sum_{l=1}^q w(C_{j,l}), \quad (16.4)$$

subject to the following conditions: That is, for each sensor  $v_i \in V$ , we have

1. the time gap between its any two consecutive charging scheduling  $(\mathcal{C}_{j_1}, t_{j_1})$  and  $(\mathcal{C}_{j_2}, t_{j_2})$  is no more than its maximum charging cycle  $\tau_i$  (assuming that  $t_{j_1} < t_{j_2}$ ), i.e.,  $t_{j_2} - t_{j_1} \leq \tau_i$ , where sensor  $v_i$  is contained in both charging scheduling  $\mathcal{C}_{j_1}$  and  $\mathcal{C}_{j_2}$  and there is no charging scheduling  $(\mathcal{C}_j, t_j)$  such that sensor  $v_i$  is contained in  $\mathcal{C}_j$  and  $t_{j_1} \leq t_j \leq t_{j_2}$ ;
2. the duration from its last charging to the end of period  $T$  is no more than  $\tau_i$ ,

where  $\mathcal{C}_j = \{C_{j,1}, C_{j,2}, \dots, C_{j,q}\}$ ,  $C_{j,l}$  is the charging tour of mobile charger  $l$  located at depot  $r_l$ ,  $1 \leq l \leq q$ , and  $0 < t_1 < t_2 < \dots < t_p < T$ .

For this problem, we not only need to determine the number of rounds  $p$  to schedule mobile chargers for sensor charging but also to decide which sensors to be charged in which rounds and by which chargers. Intuitively, during the period of  $T$ , if more rounds are scheduled, then there are less number of sensors to-be-charged in each round. On the other hand, if less number of rounds is scheduled, there are more sensors to-be-charged in each round. Our objective is to minimize the total traveling distance of the  $q$  mobile chargers for the  $p$  charging rounds. The challenge of this optimization problem is to determine both  $p$  and the set of to-be-charged sensors in each round in order to minimize the total traveling distance of  $q$  mobile chargers. The

service cost minimization problem is NP-hard, by a reduction from the well-known NP-hard problem—traveling Salesman Problem (TSP), omitted.

So far, we have assumed that the maximum charging cycle of each sensor  $v_i \in V$  in the entire period  $T$  is fixed. However, in reality, it may experience significant changes over time, since the data rates of different sensors usually depend on the specific application of a WSN, some sensors may be required to increase their data rates for better monitoring the area of these sensors at some time while the others may be required to reduce their data rates for saving their energy. For this general setting, we define *the service cost minimization problem with variable maximum charging cycles* as follows. Given a wireless sensor network  $G$ , a period  $T$ ,  $q$  mobile chargers located at  $q$  depots, the maximum charging cycle  $\tau_i(t)$  of each sensor  $v_i$  that varies with time  $t$ , the problem is to find a series of charging scheduling of the  $q$  mobile chargers such that the service cost of them is minimized, subject to that none of the sensors runs out of energy for the period of  $T$ .

We finally define a  *$q$ -rooted TSP problem*, which will be used as a subroutine for the problems of concern. Assume that there is a set of to-be-charged sensors  $V^c \subseteq V$  at some time point. Given a subgraph  $G^c = (V^c \cup R, E^c; w)$  of  $G$  with  $|R| = q \geq 1$  and  $q$  mobile chargers, the problem is to find  $q$  closed tours  $C_1, C_2, \dots, C_q$  in  $G^c$  such that the total length of the  $q$  tours,  $\sum_{l=1}^q w(C_l)$ , is minimized, subject to that these  $q$  tours cover all sensors in  $V^c$ , i.e.,  $V^c \subseteq \bigcup_{l=1}^q V(C_l)$ , and each of the  $q$  tours contains a distinct depot in  $R$ . The  $q$ -rooted TSP problem is NP-hard as the classical TSP problem is a special case of it when  $q = 1$ .

#### 16.2.4.2 The Minimum Number of Mobile Chargers Deployment Problem

We notice there is no need that every sensor must be charged at each round. Also, sensor charging tours are not necessarily periodic, instead sensors should be charged in an on-demand fashion. The rationale behind this is that in some applications such as event detections, if there are no events happening in a monitoring area, sensors usually perform duty cycling to save energy, thus they can run much longer than keeping in wake up statuses. When an event does occur, the sensors within the event region will keep in wake up statuses to capture the event and report their sensing results to the base station, while for the sensors not in the event region, they continue maintaining their wakeup-and-sleep duty cycling statuses, thus consuming much less energy. It can be seen from this case that not all sensors in the network need to be charged in each energy-charging round, only the sensors in the regions where the event happened are needed to be charged.

Let  $l_{max}$  be the longest duration of a mobile vehicle tour for charging all sensors in the network. Consider that all sensors in the network will be charged by only one mobile charger. Then,  $l_{max}$  should be no more than the sum of the time spent on traveling and the time spent on charging sensors on its tour by a mobile charging vehicle. Thus, the value of  $l_{max}$  is upper bounded as  $l_{max} \leq \frac{L_{TSP}}{s} + \frac{\min\{IE, \sum_{v_i \in V_S} B_i\}}{\mu}$ ,

where  $L_{TSP}$  is the length of a TSP tour including all sensors and the depot which can be approximately found by applying Christofides' algorithm [40],  $s$  is the travel speed of the charging vehicle,  $IE$  is the battery capacity of the vehicle,  $B_i$  is the battery capacity of sensor  $v_i$ , and  $\mu$  is the charging rate for sensors. In other words, to ensure that none of the sensors fail due to its energy expiration, a sensor should be charged when its residual lifetime is no greater than  $l_{max}$ .

We define the *critical time point* of a sensor as the time point that the sensor can survive for the next  $l_{max}$  time units. We say that a sensor  $v_i$  at time  $t$  is in a *critical lifetime interval* if  $l_{max} \leq l_i(t) \leq \alpha \cdot l_{max}$  with a given constant  $\alpha \geq 1$ , where  $l_i(t)$  is the residual lifetime of sensor  $v_i$  at time  $t$ . Following the definition of the critical lifetime interval, only the sensors within their critical lifetime intervals need to be charged to avoid running out of their energy completely. Without loss of generality, in the rest of this section, we assume that  $V$  is the set of sensors within their critical lifetime intervals, i.e.,  $V_s = \{v_i \mid v_i \in V, l_{max} \leq l_i(t) \leq \alpha \cdot l_{max}\}$ , where  $l_i(t)$  is the residual lifetime of sensor  $v_i$  at time  $t$ . Clearly,  $V_s \subseteq V$ .

We propose a flexible on-demand sensor energy-charging paradigm as follows. We assume that there is only one depot  $r$  in the monitoring region, where there are a number of mobile vehicles available to meet sensor charging demands. Each sensor will send an energy-charging request to the base station for its energy replenishment when its residual lifetime is below the critical lifetime  $l_{max}$ . The energy-charging request contains the identity, the amount of residual energy, and the energy consumption rate of the sensor. Once the base station receives a set of such requests from the sensors, it then performs a scheduling to dispatch a number of mobile charging vehicles to charge the sensors in the set, where a sensor  $v_i$  at time  $t$  is in its critical lifetime interval if  $l_{max} \leq l_i(t) \leq \alpha \cdot l_{max}$ . Hence, the result of each scheduling consists of the number of mobile charging vehicles needed, a closed tour for each of the mobile vehicle, and the charging duration at each to-be-charged sensor node along the tour. Finally, the mobile charging vehicles are dispatched from the depot to perform charging tasks.

Given a rechargeable sensor network  $G = (V, E)$  consisting of sensors, one stationary base station, and a depot with multiple mobile vehicles, following the on-demand sensor energy-charging paradigm, assume that at a specific time point, the base station receives charging requests from the sensors within their critical lifetime intervals. The base station then starts a new round scheduling by dispatching a certain number of mobile charging vehicles to charge these sensors so that none of sensors will run out of energy. Let  $V_s$  be the subset of sensors in  $G$  to-be-charged (within their critical lifetimes) in the next round ( $V_s \subseteq V$ ). Assume that for each sensor  $v_i \in V_s$ , its energy consumption rate  $\rho_i$  does not change during each charging round (or such changes are marginal and can be ignored), and its residual energy  $RE_i$  is given (at the base station), the *minimum number of mobile chargers deployment problem* is to find a scheduling of mobile charging vehicles to fully charge the sensors in  $V_s$  by providing a closed tour for each vehicle, such that the number of mobile vehicles deployed is minimized, subject to the energy capacity constraint  $IE$  on each mobile vehicle. The minimum number of mobile chargers deployment problem is NP-hard, through a reduction from the well-known NP-hard Traveling Salesman Problem (TSP).

The rest is to define the  $p$ -optimal closed tour problem, which will serve as a subroutine of the proposed algorithms for the minimum number of mobile chargers deployment problem. Given a node and edge weighted complete metric graph  $G_s = (V_s, E_s; h, w)$ , a root node  $r \in V_s$ , and an integer  $p \geq 1$ , where  $h : V_s \mapsto \mathbb{R}^{\geq 0}$  and  $w : E_s \mapsto \mathbb{R}^{>0}$  (i.e., the node weight  $h(v)$  of each sensor node  $v \in V_s$  is the amount of energy to be charged to sensor  $v$ , and the edge weight  $w(u, v)$  of each edge  $(u, v) \in E_s$  represents the amount of energy consumed by a mobile vehicle traveling along the edge), *the  $p$ -optimal closed tour problem* in  $G_s$  is to find  $p$  node-disjoint closed tours covering all nodes in  $V_s$  except the root  $r$  that appears in each of the tours such that the maximum total cost among the  $p$  closed tours is minimized, where *the total cost* of a closed tour is the weighted sum of nodes and edges in it.

## 16.3 Algorithms for the Service Cost Minimization Problem

In this section, we devise efficient algorithms for the service cost minimization problem. We first devise an algorithm for a  $q$ -rooted TSP problem in Sect. 16.3.1, which will be served as a subroutine of the proposed algorithms. We then propose an approximation algorithm in Sect. 16.3.2 and a heuristic algorithm in Sect. 16.3.3 for the problem under fixed and variable sensor energy consumption rates, respectively.

### 16.3.1 Algorithm for the $q$ -rooted TSP Problem

We propose a 2-approximation algorithm for the  $q$ -rooted TSP problem, which will serve as a subroutine of the approximation algorithm for the service cost minimization problem.

The basic idea of the algorithm for the  $q$ -rooted TSP problem is that we first find  $q$ -rooted trees with the minimum total cost, and we then show that the total cost of the  $q$ -rooted trees is a lower bound on the optimal cost of the  $q$ -rooted TSP problem. We finally convert each of the trees into a closed tour with the cost of the tour no more than twice the cost of the tree.

We start with *the  $q$ -rooted minimum spanning forest ( $q$ -rooted MSF) problem*: given a graph  $G^c = (V^c \cup R, E^c; w)$ ,  $q = |R|$ , and  $w : E^c \mapsto \mathbb{R}^+$ , the problem is to find  $q$  trees  $T_1, T_2, \dots, T_q$  spanning all nodes in  $V^c$  with each tree containing a distinct depot in  $R$  such that the total cost of the  $q$  trees,  $\sum_{l=1}^q w(T_l)$ , is minimized.

For the  $q$ -rooted MSF problem, an exact algorithm is given as follows. We start by constructing an auxiliary graph  $G_r = (V^c \cup \{r\}, E_r; w_r)$  from  $G^c = (V^c \cup R, E^c; w)$  by contracting the  $q$  depots in  $R$  into a single root  $r$ : (i) remove the  $q$  depots in  $R$  and introduce a new node  $r$ ; (ii) for each  $r_l \in R$ , introduce an edge  $(v, r) \in E_r$  for each edge  $(v, r_l) \in E^c$ , where  $v \in V^c$ ; (iii)  $w_r(v, r) = \min_l \{w(v, r_l)\}$ . We then find an MST  $T$  of  $G_r$ . We finally break  $T$  into  $q$  disjoint trees  $T_1, T_2, \dots, T_q$  by uncontracting the roots in  $R$ . This uncontraction means that an edge  $(v, r)$  is mapped to an edge  $(v, r_l)$ , where  $w_r(v, r) = w(v, r_l)$ . Note that each tree  $T_l$  roots at depot  $r_l$ . The detailed algorithm is presented in Algorithm 8.

---

**Algorithm 8:** *q*-rooted MSF

---

**Input:**  $G^c = (V^c \cup R, E^c; w)$ ,  $w : E^c \mapsto \mathbb{R}^+$ , and  $q = |R|$ .**Output:** a solution for the *q*-rooted MSF problem

- 1 Construct a graph  $G_r = (V^c \cup \{r\}, E_r; w_r)$  from  $G^c$  by contracting the *q* depots in  $R$  into a single root  $r$ ;
  - 2 Find an MST  $T$  in  $G_r$ ;
  - 3 Decompose the MST  $T$  into *q* disjoint rooted trees  $T_1, T_2, \dots, T_q$  by uncontracting depots in  $R$ ;
- 

**Lemma 16.1** *There is an algorithm for the *q*-rooted MSF problem, which delivers an optimal solution and takes  $O(n^2)$  time, where  $n = |V^c \cup R|$ .*

*Proof* Assume that trees  $T_1^*, T_2^*, \dots, T_q^*$  form an optimal solution to the *q*-rooted MSF problem. We show that the solution consisting of trees  $T_1, T_2, \dots, T_q$ , delivered by Algorithm 8, is optimal. On one hand, since the *q* trees  $T_1, T_2, \dots, T_q$  form a feasible solution, then  $\sum_{l=1}^q w(T_l^*) \leq \sum_{l=1}^q w(T_l)$ . On the other hand, as each tree  $T_l^*$  contains a depot  $r_l \in R$ , we can construct a spanning tree  $T'$  in graph  $G_r$  by contracting the *q* depots into a single root  $r$ , and  $w(T') = \sum_{l=1}^q w(T_l^*)$ . As the MST  $T$  is the minimum one, we have  $w(T) \leq w(T')$ . Since  $\sum_{l=1}^q w(T_l) = w(T)$ ,  $\sum_{l=1}^q w(T_l) = w(T) \leq w(T') \leq \sum_{l=1}^q w(T_l^*)$ . Therefore,  $\sum_{l=1}^q w(T_l) = \sum_{l=1}^q w(T_l^*)$ , i.e., the found trees  $T_1, T_2, \dots, T_q$  form an optimal solution to the problem. The time complexity of Algorithm 8 is analyzed as follows. Constructing graph  $G_r$  takes time  $O(E^c) = O(n^2)$ . Finding the MST  $T$  in  $G_r$  takes  $O(n^2)$  time, while uncontracting the MST  $T$  also takes time  $O(E^c) = O(n^2)$ . Algorithm 8 thus runs in  $O(n^2)$  time.  $\square$

With the help of the exact algorithm for the *q*-rooted MSF problem, we now devise a 2-approximation algorithm for the *q*-rooted TSP problem in Algorithm 9.

---

**Algorithm 9:** *q*-rooted TSP

---

**Input:**  $G^c = (V^c \cup R, E^c; w)$ ,  $w : E^c \mapsto \mathbb{R}^+$ , and  $q = |R|$ .**Output:** A solution  $\mathcal{C}$  for the *q*-rooted TSP problem

- 1 Find *q* optimal trees  $T_1, T_2, \dots, T_q$  for the *q*-rooted MSF problem in  $G^c$  by calling Algorithm 8;
  - 2 For each tree  $T_l$ , double the edges in  $T_l$ , find a Eulerian tour  $C_l'$ , and obtain a less cost closed tour  $C_l$  by shortcutting repeated nodes in  $C_l'$ . Let  $\mathcal{C} = \{C_1, C_2, \dots, C_q\}$ ;
- 

We show that Algorithm 9 delivers a 2-approximate solution.

**Theorem 16.1** *There is a 2-approximation algorithm for the *q*-rooted TSP problem, which takes time  $O(|V^c \cup R|^2)$ .*

*Proof* Assume that closed tours  $C_1^*, C_2^*, \dots, C_q^*$  form an optimal solution to the *q*-rooted TSP problem in  $G^c$ . For each tour  $C_l^*$ , we can obtain a tree  $T_l'$  by removing any edge in  $C_l^*$ . Then,  $w(T_l') \leq w(C_l^*)$ ,  $1 \leq l \leq q$ . It is obvious that trees  $T_1', T_2', \dots, T_q'$

form a feasible solution to the  $q$ -rooted MSF problem. As trees  $T_1, T_2, \dots, T_q$  form the optimal solution by Lemma 16.1,  $\sum_{l=1}^q w(T_l) \leq \sum_{l=1}^q w(T'_l) \leq \sum_{l=1}^q w(C_l^*)$ . Also, we can see that the total cost of each found tour  $C_l$  is no more than twice the total cost of tree  $T_l$ , i.e.,  $w(C_l) \leq 2w(T_l)$ . Therefore,  $\sum_{l=1}^q w(C_l) \leq \sum_{l=1}^q 2w(T_l) \leq 2 \sum_{l=1}^q w(C_l^*)$ . The time complexity analysis is straightforward, omitted.  $\square$

### 16.3.2 Approximation Algorithm with Fixed Maximum Charging Cycles

In this subsection, we devise an approximation algorithm for the service cost minimization problem, assuming that each sensor has a fixed maximum charging cycle. We start with the basic idea behind the algorithm. We then present the approximation algorithm, and we finally analyze the approximation ratio of the proposed approximation algorithm.

#### 16.3.2.1 Overview of the Approximation Algorithm

Given a maximum charging cycle function:  $\tau : V \mapsto R^+$  and a monitoring period  $T$ , if there is a series of mobile charger schedulings for  $T$  such that no sensor depletes its energy, then we say that these schedulings form a *feasible solution* to the service cost minimization problem, i.e., for each sensor  $v_i \in V$ , the maximum duration between its any two consecutive chargings is no more than  $\tau_i$ . A *series of feasible charging schedulings* of the  $q$  mobile chargers is an *optimal solution* if the service cost of the solution is the minimum one.

The basic idea behind the proposed approximation algorithm is to construct another charging cycle function  $\tau'(\cdot)$  for the sensors based on the maximum charging cycle function  $\tau(\cdot)$ , by exploring the combinatorial property of the problem. We construct a very special charging cycle function  $\tau'(\cdot)$  such that charging cycles of the  $n$  sensors will form a geometric sequence as follows.

Let  $\tau_1, \tau_2, \dots, \tau_n$  be the maximum charging cycles of sensors  $v_1, v_2, \dots, v_n$  in the network. Assume that  $\tau_1 \leq \tau_2 \leq \dots \leq \tau_n$ . Let  $\tau'_1, \tau'_2, \dots, \tau'_n$  be the charging cycles of the sensors and  $\tau'_i \leq \tau'_j$  if  $\tau_i \leq \tau_j$ . We construct  $\tau'(\cdot)$  as follows. We partition the set  $V$  of the sensors into  $K + 1$  disjoint subsets  $V_0, V_1, \dots, V_K$ , where  $K = \lfloor \log_2 \frac{\tau_n}{\tau_1} \rfloor$ , and sensor  $v_i \in V$  with its maximum charging cycle  $\tau_i$  is contained in  $V_k$  if  $2^k \tau_1 \leq \tau_i < 2^{k+1} \tau_1$ . Then,  $k = \lfloor \log_2 \frac{\tau_i}{\tau_1} \rfloor$ . Let  $\tau'_i = 2^k \tau_1$ . We assign each sensor in  $V_k$  with the identical charging cycle  $2^k \tau_1 = 2^k \tau_i$ . Consequently, the charging cycles of sensors in  $V_0, V_1, \dots, V_K$  are  $\tau_1, 2\tau_1, \dots, 2^K \tau_1$ , respectively. We can see that the assigned charging cycle  $\tau'_i$  of sensor  $v_i$  is no less than the half its maximum charging cycle  $\tau_i$ , since

$$\tau'_i = 2^{\lfloor \log_2 \frac{\tau_i}{\tau_1} \rfloor} \tau_1 > 2^{\log_2 \frac{\tau_i}{\tau_1} - 1} \tau_1 = \frac{\tau_i}{2}, \quad \forall v_i \in V. \quad (16.5)$$

### 16.3.2.2 Approximation Algorithm

Given the charging cycle function  $\tau'(\cdot)$ , we can see that  $\tau'_j$  is divisible by  $\tau'_i$  for any two sensors  $v_i$  and  $v_j$  if  $\tau_i \leq \tau_j$  and  $1 \leq i < j \leq n$ . For simplicity, assume that the monitoring period  $T$  is divisible by the maximum assigned charging cycle  $\tau'_n$ , let  $T = 2m\tau'_n = 2m2^K\tau_1$ , where  $m$  is a positive integer. Furthermore, we assume that each sensor is fully charged at time  $t = 0$ . The solution delivered by the proposed algorithm consists of a series of schedulings of the  $q$  mobile chargers. Specifically, we first find a sequence of schedulings for a period  $\tau'_n$ . Then, we repeat the found schedulings for the next time period of  $\tau'_n$ , and so on. We repeat the scheduling sequence for period  $T$  no more than  $\lfloor T/\tau'_n \rfloor - 1 = 2m - 1$  times.

In the following, we construct a series of schedulings for a period  $\tau'_n = 2^K\tau_1$ . Recall that we have partitioned the sensor set  $V$  into  $K + 1$  disjoint subsets  $V_0, V_1, \dots, V_K$ , and the charging cycle of each sensor in  $V_k$  is  $2^k\tau_1$ ,  $0 \leq k \leq K$ . We further partition the period  $\tau'_n$  into  $2^K$  *equal time intervals* with each interval lasting  $\tau_1$ , and label them from the left to right as the 1st, 2nd, ..., and the  $2^K$ th time interval. Clearly, all sensors in  $V_0$  must be charged at each of these  $2^K$  time intervals; all sensors in  $V_1$  must be charged at every second time interval; and all sensors in  $V_k$  must be charged at every  $2^k$  time interval,  $0 \leq k \leq K$ . That is,

At time  $\tau_1$ , charge the sensors in  $V_0$ .

At time  $2\tau_1$ , charge the sensors in  $V_0 \cup V_1$ .

At time  $3\tau_1$ , charge the sensors in  $V_0$ .

At time  $4\tau_1$ , charge the sensors in  $V_0 \cup V_1 \cup V_2$ .

$\vdots$

At time  $j\tau_1$ , charge the sensors in  $\bigcup_{(j \bmod 2^k)=0} V_k$  where  $0 \leq k \leq K'$ ,  $K' = \lfloor \log_2 j \rfloor$ , and  $1 \leq j \leq 2^K$ .

$\vdots$

At time  $2^K\tau_1$ , charge the sensors in  $\bigcup_{i=0}^K V_i = V$ .

There are  $2^K$  charging schedulings of the  $q$  mobile chargers and one charging scheduling is dispatched at each time interval. Let  $\mathcal{C}_j = \{C_{j,1}, C_{j,2}, \dots, C_{j,q}\}$  be the set of closed tours of the  $q$  mobile chargers at time interval  $j$ , where  $1 \leq j \leq 2^K$ . Furthermore, it can be seen that in the  $2^K$  charging schedulings, there are  $2^{K-1}$  identical charging schedulings with each only containing the sensors in  $V_0$ , there are  $2^{K-2}$  identical charging schedulings with each containing the sensors only in  $V_0 \cup V_1$ . In general, there are  $2^{K-1-k}$  identical charging schedulings with each containing the sensors only in  $V_0 \cup V_1 \dots \cup V_k$ ,  $0 \leq k \leq K - 1$ . Finally, there is one charging scheduling containing the sensors in  $V_0 \cup V_1 \dots \cup V_K = V$ . Denote by  $\mathcal{D}_k = \{D_{k,1}, D_{k,2}, \dots, D_{k,q}\}$  the set of  $q$  closed tours for the  $q$ -rooted TSP problem in the induced graph  $G[R \cup V_0 \dots \cup V_k]$ , which is delivered by Algorithm 9.

The series of charging schedulings for a period  $\tau'_n$  thus is  $(\mathcal{C}_1, \tau_1), \dots, (\mathcal{C}_j, j\tau_1), \dots, (\mathcal{C}_{2^K}, 2^K\tau_1)$ , where the 2-tuple  $(\mathcal{C}_j, j\tau_1)$  represents that the  $q$  mobile chargers are dispatched at time  $j\tau_1$  and the set of to-be-charged sensors is  $\cup_{C_{j,i} \in \mathcal{C}_j} V(C_{j,i}) = \cup_{(j \bmod 2^k)=0} V_k$ ,  $0 \leq k \leq K'$ ,  $K' = \lfloor \log_2 j \rfloor$ , and  $1 \leq j \leq 2^K$ . As a result, there are  $p = 2m \cdot 2^K - 1$  charging schedulings found for a period of  $T = 2m\tau'_n$  as follows.

$$\begin{aligned} & (\mathcal{C}_1, \tau_1), \dots, (\mathcal{C}_{2^K-1}, (2^K-1)\tau_1), (\mathcal{C}_{2^K}, 2^K\tau_1), \\ & (\mathcal{C}_1, \tau'_n + \tau_1), \dots, (\mathcal{C}_{2^K-1}, \tau'_n + (2^K-1)\tau_1), (\mathcal{C}_{2^K}, \tau'_n + 2^K\tau_1), \\ & \vdots \\ & (\mathcal{C}_1, (2m-1)\tau'_n + \tau_1), \dots, (\mathcal{C}_{2^K-1}, (2m-1)\tau'_n + (2^K-1)\tau_1). \end{aligned}$$

Note that we do not perform a charging scheduling at time  $T = 2m\tau'_n$  as there is no such need at the end of period  $T$ . The proposed algorithm is described in Algorithm 10.

---

**Algorithm 10:** MinDis

---

```

Input:  $G = (V \cup R, E; w)$ , maximum charging cycles  $\tau : V \mapsto \mathbb{R}^+$ ,  $q$  chargers, and a monitoring period  $T$ .
Output: A series of charging schedulings  $\mathcal{C}$  for period  $T$ 
1 Let  $\tau_1, \tau_2, \dots, \tau_n$  be the sorted maximum charging cycles of sensors  $v_1, v_2, \dots, v_n$  in ascending order;
2 For each sensor  $v_i$ , let  $\tau'_i = 2^{\lfloor \log_2 \frac{\tau_i}{\tau_1} \rfloor}$ ;
3 Partition sensors in  $V$  into  $K + 1$  disjoint subsets  $V_0, V_1, \dots, V_K$ , where sensor  $v_i \in V_k$  if  $2^k\tau_1 = 2^{\lfloor \log_2 \frac{\tau_i}{\tau_1} \rfloor}\tau_1$ ,  $0 \leq k \leq K$ , and  $K = \lfloor \log_2 \frac{\tau_n}{\tau_1} \rfloor$ . All sensors in  $V_k$  have the same charging cycle  $2^k\tau'_1$ ;
4 for  $k \leftarrow 0$  to  $K$  do
5   | Find  $q$  charging tours  $\mathcal{D}_k = \{D_{k,1}, D_{k,2}, \dots, C_{j,q}\}$  in the induced subgraph  $G[R \cup V_0 \dots \cup V_k]$  by applying Algorithm 9;
6 end for
7  $\mathcal{C} \leftarrow \emptyset$ ; /* the solution */
8 /* Construct schedulings  $(\mathcal{C}_1, \tau_1), \dots, (\mathcal{C}_{2^K}, 2^K\tau_1)$  */
9 for  $j \leftarrow 1$  to  $2^K$  do
10  | /* Find the charging scheduling  $\mathcal{C}_j$  of the  $q$  mobile chargers at time  $t_j = j\tau_1$  */;
11  | Let  $\mathcal{C}_j = \mathcal{D}_k$ , where  $k$  is the largest integer so that  $j \bmod 2^k = 0$ , where  $0 \leq k \leq K'$  and  $K' = \lfloor \log_2 j \rfloor$ ;
12  |  $\mathcal{C} \leftarrow \mathcal{C} \cup \{(\mathcal{C}_j, t_j)\}$ ;
13 end for
14 for  $m' \leftarrow 2$  to  $\lfloor T/\tau'_n \rfloor$  do
15  | for  $j \leftarrow 1$  to  $2^K$  do
16  |   |  $\mathcal{C} = \mathcal{C} \cup \{(\mathcal{C}_j, m' \cdot \tau'_n + t_j)\}$ ;
17  | end for
18 end for
19 return  $\mathcal{C}$ .

```

---

### 16.3.2.3 Algorithm Analysis

In the following, we dedicate ourselves to analyzing the approximation ratio of the proposed approximation algorithm. We start by showing that Algorithm 10 delivers a feasible solution to the service cost minimization problem by Lemma 16.2. We then provide a lower bound on the minimum cost of the problem by Lemma 16.3. We finally derive the approximation ratio of Algorithm 10 based on the lower bound in Theorem 16.2.

**Lemma 16.2** *Algorithm 10 delivers a feasible solution to the service cost minimization problem.*

*Proof* It is obvious that the solution delivered by Algorithm 10 is feasible, as the charging cycle  $\tau'_i$  of each sensor  $v_i \in V$  in the solution is no more than its maximum charging cycle  $\tau_i$ , i.e.,  $\tau'_i \leq \tau_i$ . Thus, no sensors will die in the period  $T$ .  $\square$

The following lemma provides a lower bound on the optimal service cost, which bounds the service cost of the solution delivered by Algorithm 10.

**Lemma 16.3** *Given the sensor set partitioning  $V_0, V_1, \dots, V_K$  based on the maximum charging cycles of sensors, each sensor in  $V_k$  is assigned with the same charging cycle  $2^k \tau_1$ ,  $0 \leq k \leq K$ . Let  $OPT$  be the service cost of an optimal solution to the service cost minimization problem. Denote by  $\mathcal{D}_k^* = \{D_{k,1}^*, D_{k,2}^*, \dots, D_{k,q}^*\}$  the optimal  $q$  closed tours for the  $q$ -rooted TSP problem in the induced graph  $G[R \cup V_0 \cup V_1 \cup \dots \cup V_k]$ , then  $OPT \geq m2^{K-k} \cdot w(\mathcal{D}_k^*)$ , assuming that  $T = 2m\tau'_n$ , where  $w(\mathcal{D}_k^*) = \sum_{l=1}^q w(D_{k,l}^*)$ ,  $K = \lfloor \log_2 \frac{\tau_n}{\tau_1} \rfloor$ , and  $0 \leq k \leq K$ .*

*Proof* To show that  $OPT \geq m2^{K-k} \cdot w(\mathcal{D}_k^*)$ , we partition the entire period  $T = 2m\tau'_n = 2m \cdot 2^K \tau_1$  into  $m \cdot 2^{K-k}$  time intervals with each lasting time  $t_k = 2^{k+1} \tau_1$ . Let  $(0, t_k], (t_k, 2t_k], \dots, ((j-1)t_k, jt_k], \dots, ((m2^{K-k}-1)t_k, m2^{K-k}t_k]$  be these  $m \cdot 2^{K-k}$  intervals, where time interval  $j$  is the interval  $((j-1) \cdot t_k, j \cdot t_k]$ ,  $1 \leq j \leq m \cdot 2^{K-k}$ . Note that  $m2^{K-k}t_k = m2^{K-k}2^{k+1}\tau_1 = T$ .

In the following, we first show that there is at least one time interval among the  $m2^{K-k}$  time intervals such that (i) the service cost of charging schedulings within the interval is no more than  $\frac{1}{m2^{K-k}}$  of the service cost  $OPT$  in the optimal solution; (ii) each sensor in  $\bigcup_{i=0}^k V_i$  must be charged at least once in this interval; and (iii) the service cost within this interval in the optimal solution is no less than the cost  $w(\mathcal{C}_k)$  of a feasible solution  $\mathcal{C}_k$  to the  $q$ -rooted TSP problem in graph  $G[R \cup V_0 \cup \dots \cup V_k]$ . Since  $\mathcal{D}_k^*$  is the optimal solution to the  $q$ -rooted TSP problem,  $w(\mathcal{D}_k^*) \leq w(\mathcal{C}_k) \leq \frac{OPT}{m2^{K-k}}$ .

Assume that an optimal solution consists of  $p$  charging schedulings  $(\mathcal{C}_1^*, t_1^*), (\mathcal{C}_2^*, t_2^*), \dots, (\mathcal{C}_p^*, t_p^*)$  with  $0 < t_1^* \leq \dots \leq t_p^* < T$ . Recall that  $OPT$  is the sum of lengths of the  $p$  charging schedulings i.e.,  $OPT = \sum_{s=1}^p w(\mathcal{C}_s^*) = \sum_{s=1}^p \sum_{l=1}^q w(C_{s,l}^*)$ . We partition the  $p$  charging schedulings into  $m2^{K-k}$  disjoint groups according to their dispatching times, the charging scheduling  $\mathcal{C}_s^*$  is in group  $j$  if its dispatching time  $t_s^*$  is within time interval  $j$ , i.e.,  $t_s^* \in ((j-1)t_k, jt_k]$ , where  $1 \leq s \leq p$  and

$1 \leq j \leq m2^{K-k}$ . Denote by  $\mathcal{G}_j$  and  $w(\mathcal{G}_j)$  the set of charging schedulings in group  $j$  and the cost sum of charging schedulings in  $\mathcal{G}_j$ , respectively, i.e.,  $w(\mathcal{G}_j) = \sum_{\mathcal{C}_s^* \in \mathcal{G}_j} w(\mathcal{C}_s^*)$ ,  $1 \leq j \leq m2^{K-k}$ . Then,  $\sum_{j=1}^{m2^{K-k}} w(\mathcal{G}_j) = OPT$ . Among the  $m2^{K-k}$  groups, there must be a group  $\mathcal{G}_j$  whose service cost  $w(\mathcal{G}_j)$  is no more than  $\frac{1}{m2^{K-k}}$  of the optimal cost  $OPT$ , i.e.,

$$w(\mathcal{G}_j) \leq \frac{OPT}{m2^{K-k}}. \quad (16.6)$$

We then show that each sensor in  $\bigcup_{i=0}^k V_i$  must be charged at least once by the charging schedulings in  $\mathcal{G}_j$  by contradiction. Assume that there is a sensor  $v_i \in \bigcup_{i=0}^k V_i$  which will not be charged by any charging scheduling in  $\mathcal{G}_j$ . Since  $v_i \in \bigcup_{i=0}^k V_i$ , its maximum charging cycle  $\tau_i$  must be strictly less than  $2 \cdot 2^k \tau_1 = 2^{k+1} \tau_1$  by inequality (16.5), i.e.,  $\tau_i < 2^{k+1} \tau_1$ . On the other hand, as  $v_i$  will not be charged by any charging scheduling in  $\mathcal{G}_j$  while it is still survived, this implies that its maximum charging cycle must be no less than the length  $t_k$  of the time interval, i.e.,  $\tau_i \geq t_k = 2^{k+1} \tau_1$ , this results in a contradiction. Thus,  $v_i$  must be charged by at least one charging scheduling in  $\mathcal{G}_j$ .

We finally construct a feasible solution  $\mathcal{C}_k = \{C_{k,1}, C_{k,2}, \dots, C_{k,q}\}$  to the  $q$ -rooted TSP problem in graph  $G[R \cup V_0 \cup \dots \cup V_k]$  based on the charging schedulings in  $\mathcal{G}_j$  such that the service cost  $w(\mathcal{C}_k)$  is no more than  $w(\mathcal{G}_j)$ . Since each closed tour in  $\mathcal{G}_j$  contains a depot  $r_l \in R$ , we partition the closed tours in  $\mathcal{G}_j$  by the depot that each tour contains. To this end, we partition tours in  $\mathcal{G}_j$  into  $q$  disjoint subgroups  $\mathcal{G}_{j,1}, \mathcal{G}_{j,2}, \dots, \mathcal{G}_{j,q}$ , where subgroup  $\mathcal{G}_{j,l}$  includes all closed tours in  $\mathcal{G}_j$  that contains depot  $r_l$ ,  $1 \leq l \leq q$ . For each subgroup  $\mathcal{G}_{j,l}$ , since each tour contains depot  $r_l$ , the union of all close tours in  $\mathcal{G}_{j,l}$  forms a connected Eulerian graph. Then, we can derive a Eulerian circuit  $C'_{k,l}$  from this Eulerian graph and  $w(C'_{k,l}) = w(\mathcal{G}_{j,l})$ . We further obtain a closed tour  $C_{k,l}$  including only nodes in  $R \cup V_0 \cup \dots \cup V_k$  once from  $C'_{k,l}$ , by the removal of the nodes not in  $R \cup V_0 \cup \dots \cup V_k$  and the nodes with multiple appearances, and performing path shortcutting. Since edge weights satisfy the triangle inequality, we have

$$w(C_{k,l}) \leq w(C'_{k,l}) \leq w(\mathcal{G}_{j,l}), \quad 1 \leq l \leq q. \quad (16.7)$$

As each sensor in  $\bigcup_{i=0}^k V_i$  will be charged at least once by the charging schedulings in  $\mathcal{G}_j$ , and tour  $C_{k,l}$  contains depot  $r_l$ , we have  $\bigcup_{i=0}^k V_i \subseteq \bigcup_{l=1}^q V(C_{k,l})$ . Then, all tours in  $\mathcal{C}_k$  form a feasible solution to the  $q$ -rooted TSP problem in graph  $G[R \cup V_0 \cup \dots \cup V_k]$ . Let  $\mathcal{D}_k^* = \{D_{k,1}^*, D_{k,2}^*, \dots, D_{k,q}^*\}$  be the optimal  $q$  tours. Then,

$$\sum_{l=1}^q w(D_{k,l}^*) \leq \sum_{l=1}^q w(C_{k,l}). \quad (16.8)$$

By combining inequalities (16.6), (16.7), and (16.8), the lemma then follows.  $\square$

According to Lemmas 16.2 and 16.3, we show the approximation ratio of Algorithm 10 by the following theorem.

**Theorem 16.2** *There is a  $2(K + 2)$ -approximation algorithm for the service cost minimization problem with fixed maximum charging cycles, which takes time  $O(\lfloor \log \frac{\tau_{\max}}{\tau_{\min}} \rfloor n^2 + \frac{T}{\tau_{\min}} n)$ , where  $\tau_{\max} = \max_{i=1}^n \{\tau_i\}$ ,  $\tau_{\min} = \min_{i=1}^n \{\tau_i\}$ , and  $K = \lfloor \log_2 \frac{\tau_n}{\tau_1} \rfloor$ .*

*Proof* By Lemma 16.2, Algorithm 10 delivers a feasible solution. The rest is to analyze its approximation ratio. Recall that the charging schedulings delivered by Algorithm 10 for period  $T = 2m\tau'_n$  are:  $(\mathcal{C}_1, \tau_1), \dots, (\mathcal{C}_{2^K}, 2^K\tau_1), (\mathcal{C}_1, \tau'_n + \tau_1), \dots, (\mathcal{C}_{2^K}, \tau'_n + 2^K\tau_1), \dots, (\mathcal{C}_1, (2m-1)\tau'_n + \tau_1), \dots, (\mathcal{C}_{2^K-1}, (2m-1)\tau'_n + (2^K-1)\tau_1)$ . The total service cost during  $T$  then is

$$(2m-1) \sum_{j=1}^{2^K} w(\mathcal{C}_j) + \sum_{j=1}^{2^K-1} w(\mathcal{C}_j) \leq 2m \sum_{j=1}^{2^K} w(\mathcal{C}_j). \quad (16.9)$$

Recall that  $\mathcal{D}_k = \{D_{k,1}, D_{k,2}, \dots, D_{k,q}\}$  is the set of  $q$  closed tours for the  $q$ -rooted TSP problem in graph  $G[R \cup V_0 \cup \dots \cup V_k]$  delivered by Algorithm 9. Let  $\mathcal{C}(\tau'_n) = \{(\mathcal{C}_1, \tau'_1), (\mathcal{C}_2, \tau'_2), \dots, (\mathcal{C}_{2^K}, \tau'_n)\}$ .

From the construction of  $\mathcal{C}(\tau'_n)$ , we can see that there are  $2^{K-1-k}$  identical charging schedulings in  $\mathcal{C}(\tau'_n)$  with each only containing the nodes in  $R \cup V_0 \cup V_1 \dots \cup V_k$ . Denote by  $w(\mathcal{D}_k)$  the cost of the charging scheduling  $\mathcal{D}_k$ , where  $0 \leq k \leq K-1$ . And there is one charging scheduling in  $\mathcal{C}(\tau'_n)$  containing the nodes in  $R \cup V_0 \cup \dots \cup V_K = R \cup V$ , denote by  $w(\mathcal{D}_K)$  the cost of the charging scheduling  $\mathcal{D}_K$ . We then rewrite the upper bound on the service cost in Inequality (16.9) as

$$2m \sum_{j=1}^{2^K} w(\mathcal{C}_j) = 2m(w(\mathcal{D}_K) + \sum_{k=0}^{K-1} 2^{K-1-k} w(\mathcal{D}_k)). \quad (16.10)$$

Denote by  $\mathcal{D}_k^* = \{D_{k,1}^*, D_{k,2}^*, \dots, D_{k,q}^*\}$  the set of the optimal  $q$  closed tours for the  $q$ -rooted TSP problem in graph  $G[R \cup V_0 \cup \dots \cup V_k]$ . Since  $\mathcal{D}_k$  is an approximate solution by Theorem 16.1,  $w(\mathcal{D}_k) \leq 2w(\mathcal{D}_k^*)$ ,  $0 \leq k \leq K$ . Also, by Lemma 16.3,  $w(\mathcal{D}_k^*) \leq \frac{OPT}{m2^{K-k}}$ . We have

$$\begin{aligned} & 2m(w(\mathcal{D}_K) + \sum_{k=0}^{K-1} 2^{K-1-k} w(\mathcal{D}_k)) \\ & \leq 4m\left(\frac{OPT}{m} + \sum_{k=0}^{K-1} 2^{K-1-k} \frac{OPT}{m2^{K-k}}\right) = 2(K+2)OPT. \end{aligned} \quad (16.11)$$

The time complexity analysis is straightforward, omitted.  $\square$

### 16.3.3 Heuristic Algorithm with Variable Maximum Charging Cycles

So far we have developed an approximation algorithm for the service cost minimization problem, assuming that the maximum charging cycle of each sensor is fixed for the given monitoring period. This assumption however sometimes may be restrictive and unrealistic in some applications. In this subsection we devise a novel heuristic algorithm by removing this assumption.

#### 16.3.3.1 Heuristic Algorithm

Within the period  $T$ , the energy consumption rates of sensors may dynamically change over time, resulting in the changes of sensor maximum charging cycles eventually. Recall that the base station maintains the updated energy information of each sensor, including its residual energy and energy consumption rate. Also, the sensor sends an updating request of its energy information to the base station if the variation of its maximum charging cycle is beyond a predefined threshold.

Assume that the base station receives the maximum charging cycle updatings from some sensors at time  $t$ , this implies that the charging schedulings based on the previous maximum charging cycles of these sensors may not be applicable any more, otherwise these sensors will deplete their energy prior to their next chargings. For example, assume that a sensor has changed its maximum charging cycle from a longer one to a shorter one, it might be dead if the sensor is still charged according to its previous longer charging cycle since the sensor now can last for only a shorter cycle once it is fully charged.

The basic idea of the heuristic algorithm is as follows. When the base station receives maximum charging cycle updatings, it checks whether the previous schedulings are still applicable for these updated maximum charging cycles. If so, nothing needs to be done. Otherwise, it recomputes a new series of schedulings, by first applying the approximation algorithm based on the updated maximum charging cycles, followed by modifications to the solution delivered by the approximation algorithm.

Assume that the previous maximum charging cycle of sensor  $v_i$  is  $\hat{\tau}_i(t-1)$  and it was charged at a charging cycle  $\hat{\tau}'_i(t-1)$  in the previous series of schedulings. At time  $t$ , the base station receives the maximum charging cycle updating of sensor  $v_i$ , which changes from  $\hat{\tau}_i(t-1)$  to  $\hat{\tau}_i(t)$ . The base station then checks the feasibility of the previous schedulings as follows. If  $\hat{\tau}'_i(t-1) \leq \hat{\tau}_i(t) < 2\hat{\tau}'_i(t-1)$ , the previous schedulings are still feasible as sensor  $v_i$  will be charged with a charging cycle  $\hat{\tau}'_i(t-1)$  no more than its current maximum charging cycle  $\hat{\tau}_i(t)$ . Otherwise ( $\hat{\tau}_i(t) < \hat{\tau}'_i(t-1)$  or  $\hat{\tau}_i(t) \geq 2\hat{\tau}'_i(t-1)$ ), we recompute a new series of schedulings based on the updated maximum charging cycles since the previous schedulings are not feasible any more (i.e.,  $\hat{\tau}_i(t) < \hat{\tau}'_i(t-1)$ ), or though the schedulings still are feasible, they are not optimal in terms of the service cost (i.e.,  $\hat{\tau}_i(t) \geq 2\hat{\tau}'_i(t-1)$ ). In the following, we recompute a new series of schedulings.

We first invoke the proposed approximation algorithm based on the updated maximum charging cycles. Let  $\hat{\tau}_1(t), \hat{\tau}_2(t), \dots, \hat{\tau}_n(t)$  be the updated maximum charging cycles of the  $n$  sensors. Assume that residual lifetimes of the  $n$  sensors are  $\hat{l}_1(t), \hat{l}_2(t), \dots, \hat{l}_n(t)$ , respectively. We further assume that the solution delivered by the approximation algorithm based on the updated maximum charging cycles consists of

$$\begin{aligned} & (\mathcal{C}_1, t + \hat{\tau}_1(t)), (\mathcal{C}_2, t + 2\hat{\tau}_1(t)), \dots, (\mathcal{C}_{2^K}, t + 2^K\hat{\tau}_1(t)), \\ & (\mathcal{C}_1, t + \hat{\tau}'_n(t) + \hat{\tau}_1(t)), (\mathcal{C}_2, t + \hat{\tau}'_n(t) + 2\hat{\tau}_1(t)), \dots, (\mathcal{C}_{2^K}, t + \hat{\tau}'_n(t) + 2^K\hat{\tau}_1(t)), \\ & \vdots \\ & (\mathcal{C}_1, t + x\hat{\tau}'_n(t) + \hat{\tau}_1(t)), \dots, (\mathcal{C}_y, t + x\hat{\tau}'_n(t) + y\hat{\tau}_1(t)), \end{aligned}$$

where  $t + x\hat{\tau}'_n(t) + y\hat{\tau}_1(t) < T$ ,  $t + x\hat{\tau}'_n(t) + (y+1)\hat{\tau}_1(t) \geq T$ , and  $x$  and  $y$  are positive integers. The most updated charging cycles of the  $n$  sensors in the solution are  $\hat{\tau}'_1(t), \hat{\tau}'_2(t), \dots, \hat{\tau}'_n(t)$ , where  $\hat{\tau}'_i(t) = 2^{\lfloor \log_2 \frac{\hat{\tau}_i(t)}{\hat{\tau}_1(t)} \rfloor} \hat{\tau}_1(t)$ .

Note that the solution delivered may not be feasible as different sensors may have different amounts of residual energy. This violates the condition of applying the approximation algorithm, that is, all sensors must be fully charged initially. The residual energy in some sensor  $v_i$  may not support its operation until its next charging time  $t + \hat{\tau}'_i(t)$ , i.e.,  $\hat{l}_i(t) < \hat{\tau}'_i(t)$ . Denote by  $V^a$  the set of sensors with  $\hat{l}_i(t) < \hat{\tau}'_i(t)$ . We then schedule the mobile chargers to replenish sensors in  $V^a$  to avoid their energy depletion, through adding a new charging scheduling  $(\mathcal{C}'_0, t)$  and modifying the first  $2^K$  scheduling from  $(\mathcal{C}_1, t + \hat{\tau}_1(t)), (\mathcal{C}_2, t + 2\hat{\tau}_1(t)), \dots, (\mathcal{C}_{2^K}, t + 2^K\hat{\tau}_1(t))$  to  $(\mathcal{C}'_1, t + \hat{\tau}_1(t)), (\mathcal{C}'_2, t + 2\hat{\tau}_1(t)), \dots, (\mathcal{C}'_{2^K}, t + 2^K\hat{\tau}_1(t))$ . Also, the charging scheduling delivered by the heuristic algorithm after the first  $2^K$  scheduling are the same as them delivered by the approximation algorithm. The rest is to construct the first  $2^K + 1$  charging scheduling.

Let  $V_t^a = \{v_i | v_i \in V^a \text{ & } \hat{l}_i(t) < \hat{\tau}_1(t)\}$ , which implies that the residual lifetime of each sensor in  $V_t^a$  is less than  $\hat{\tau}_1(t)$  and  $V_t^a \subseteq V^a$ . We construct a scheduling  $(\mathcal{C}_0, t)$ , in which all sensors in  $V_t^a$  will be charged at time  $t$ . We then, like the node set partition in the approximation algorithm, partition the set  $V^a \setminus V_t^a$  into  $K+1$  disjoint sets  $V_0^a, V_1^a, \dots, V_K^a$  according to their residual lifetimes, where  $K = \lfloor \log_2 \frac{\hat{\tau}_n(t)}{\hat{\tau}_1(t)} \rfloor$  and a sensor  $v_i \in V^a \setminus V_t^a$  is contained in  $V_k^a$  if  $2^k\hat{\tau}_1(t) \leq \hat{l}_i(t) < 2^{k+1}\hat{\tau}_1(t)$ . Note that the residual lifetime  $\hat{l}_i(t)$  of each sensor  $v_i$  in  $V_k^a$  at time  $t$  is no less than  $2^k\hat{\tau}_1(t)$  but no greater than its charging cycle  $\hat{\tau}'_i(t)$ , i.e.,  $2^k\hat{\tau}_1(t) \leq \hat{l}_i(t) < \hat{\tau}'_i(t)$ . To avoid the energy depletion of sensor  $v_i$ , we can add it into any one of the scheduling:  $\{(\mathcal{C}_0, t), (\mathcal{C}_1, t + \hat{\tau}_1(t)), (\mathcal{C}_2, t + 2\hat{\tau}_1(t)), \dots, (\mathcal{C}_{2^K}, t + 2^K\hat{\tau}_1(t))\}$ . However, to minimize the service cost, we add sensor  $v_i$  into a nearest scheduling  $\mathcal{C}_j$ . The detailed construction of the  $2^K + 1$  scheduling is as follows.

We construct the  $2^K + 1$  scheduling by iteratively invoking Algorithm 8 for the  $q$ -rooted minimum spanning forest problem. Denote by  $V(\mathcal{C}_j^{(k)})$  and  $V(\mathcal{C}_j^{(k+1)})$  the constructed node sets of scheduling  $\mathcal{C}_j'$  before and after iteration  $k$ , respectively, where  $0 \leq k \leq K$ . Note that  $\mathcal{C}_j^{(k)} = \{C_{j,1}^{(k)}, \dots, C_{j,q}^{(k)}\}$  and  $V(\mathcal{C}_j^{(k)}) = \bigcup_{l=1}^q V(C_{j,l}^{(k)})$ . After

$K + 1$  iterations, we let  $V(\mathcal{C}'_j) = V(\mathcal{C}_j^{(K+1)})$ . We finally obtain scheduling  $\mathcal{C}'_j$  by applying Algorithm 9 for the  $q$ -rooted TSP problem in the induced graph  $G[V(\mathcal{C}'_j)]$ . Consequently, each sensor in  $V_t^a \cup V_0^a \cup \dots \cup V_K^a = V^a$  will be charged in time. Initially, let  $V(\mathcal{C}_0^{(0)}) = V_t^a \cup R$  and  $V(\mathcal{C}_j^{(0)}) = V(\mathcal{C}_j)$ , where  $1 \leq j \leq 2^K$ . At iteration  $k$  ( $0 \leq k \leq K$ ), we first construct an auxiliary graph  $G^{(k)} = (V_k^a \cup R^{(k)}, E^{(k)}; w^{(k)})$  based on node sets  $V_k^a$  and  $V(\mathcal{C}_0^{(k)})$ ,  $V(\mathcal{C}_1^{(k)})$ ,  $\dots$ ,  $V(\mathcal{C}_{2^k}^{(k)})$ , where there is a root  $r_j^{(k)}$  in  $R^{(k)}$  representing node set  $V(\mathcal{C}_j^{(k)})$ ,  $0 \leq j \leq 2^k$ , and  $E^{(k)} = V_k^a \times V_k^a \cup V_k^a \times R^{(k)}$ . Then,  $|R^{(k)}| = 2^k + 1$ . For each edge  $(u, v) \in V_k^a \times V_k^a$ ,  $w^{(k)}(u, v)$  is the Euclidean distance between nodes  $u$  and  $v$ . For each edge  $(u, r_j^{(k)}) \in V_k^a \times R^{(k)}$ ,  $w^{(k)}(u, r_j^{(k)})$  is the smallest Euclidean distance between node  $u$  and nodes in  $V(\mathcal{C}_j^{(k)})$ . We then obtain  $2^k + 1$  minimum cost rooted trees  $T_0^{(k)}, T_1^{(k)}, \dots, T_{2^k}^{(k)}$ , by invoking Algorithm 8 on  $G^{(k)}$ , where tree  $T_j^{(k)}$  contains root  $r_j^{(k)}$  and  $0 \leq j \leq 2^k$ . Note that each sensor in  $V_k^a$  is contained in a tree  $T_j^{(k)}$  and  $V_k^a = V(T_0^{(k)}) \cup V(T_1^{(k)}) \cup \dots \cup V(T_{2^k}^{(k)}) - R^{(k)}$ . Then, the sensors in tree  $T_j^{(k)}$  will be charged in scheduling  $(\mathcal{C}'_j, t + j\hat{\tau}_1(t))$ . To this end, we let  $V(\mathcal{C}_j^{(k+1)}) = V(\mathcal{C}_j^{(k)}) \cup V(T_j^{(k)}) - \{r_j^{(k)}\}$  if  $0 \leq j \leq 2^k$ , otherwise ( $2^k + 1 \leq j \leq 2^K$ ),  $V(\mathcal{C}_j^{(k+1)}) = V(\mathcal{C}_j^{(k)})$ . We refer to this heuristic algorithm as *MinDis-var*.

**Theorem 16.3** *There is a heuristic algorithm for the service cost minimization problem with variable maximum charging cycles, which takes  $O(\frac{\tau_{\max}}{\tau_{\min}}n^2 + \frac{T}{\tau_{\min}}n + \frac{\tau_{\max}^2}{\tau_{\min}^2})$  time, where  $n = |V|$ ,  $\tau_{\max} = \max_{i=1}^n \{\tau_i\}$ , and  $\tau_{\min} = \min_{i=1}^n \{\tau_i\}$ .*

## 16.4 Approximation Algorithm for the Minimum Number of Mobile Chargers Deployment Problem

In this section, we propose a novel approximation algorithm for the minimum number of mobile chargers deployment problem. We first detail a 5-approximation algorithm for the optimal  $p$ -closed tour problem in Sect. 16.4.1, which serves as a subroutine of the proposed algorithm. We then present the approximation algorithm in Sect. 16.4.2.

### 16.4.1 Algorithm for the $p$ -optimal Closed Tour Problem

In this subsection, we devise a 5-approximation algorithm for the  $p$ -optimal closed tour problem in a node and edge weighted metric graph  $G_s(V_s, E_s; h, w)$ . This algorithm will be used as a subroutine for the minimum number of mobile chargers deployment problem in Sect. 16.4.2. As a special case of the  $p$ -optimal closed tour problem when  $p = 1$  is the well-known TSP problem which is NP-hard, the  $p$ -optimal closed tour problem is NP-hard, too. In the following, we start by introducing a

popular technique to transform a tree into a closed tour in  $G_s$ . We then introduce a novel tree decomposition. We finally present an approximation algorithm for the problem based on the tree decomposition.

#### 16.4.1.1 A Closed Tour Derived from a Tree

We first introduce the technique that transforms a tree in  $G_s$  to a closed tour by the following lemma.

**Lemma 16.4** *Given a node and edge weighted metric graph  $G_s = (V_s, E_s; h, w)$  with sets  $V_s$  and  $E_s$  of nodes and edges,  $h : V_s \mapsto \mathbb{R}^{\geq 0}$  and  $w : E_s \mapsto \mathbb{R}^{> 0}$ , and the edge weight follows the triangle inequality, let  $T = (V_s, E_T; h, w)$  be a spanning tree of  $G_s$  rooted at  $r$ . Let  $C$  be the traveling salesman tour of  $G_s$  derived from  $T$  through performing the preorder traversal on  $T$  and pruning, then the total cost  $WH(C)$  of  $C$  is no more than twice the total cost  $WH(T)$  of  $T$ , i.e.,  $WH(C) \leq 2WH(T) = 2(\sum_{v \in V_s} h(v) + \sum_{e \in E_T} w(e))$ .*

*Proof* Let  $H(X)$  be the weighted sum of nodes in  $X$  and  $W(Y)$  the weighted sum of edges in  $Y$ . As the weighted sum  $W(C)$  of the edges in  $C$  is no more than  $2\sum_{e \in E_T} w(e)$ , and the weighted sum  $H(C)$  of nodes in  $C$  is the same as the one in  $T$ . Thus, the total cost of  $C$  is  $WH(C) = W(C) + H(C) \leq 2W(T) + H(T) \leq 2(W(T) + H(T)) = 2WH(T)$ .  $\square$

#### 16.4.1.2 Tree Decomposition

Given a metric graph  $G_s = (V_s, E_s; h, w)$ , let  $T = (V_s, E_T; h, w)$  be a spanning tree in  $G_s$  rooted at node  $r$  and  $\delta \geq \max_{v \in V_s} \{h(v), 2w(v, r)\}$  a given value, then, both the node weight  $h(v)$  of any node  $v \in V_s$  and the edge weight  $w(e)$  of any edge  $e \in E_T$  in tree  $T$  are no more than  $\delta$ , i.e.,  $h(v) \leq \delta$  and  $w(e) \leq \delta$ . We decompose the tree into a set of subtrees such that the total cost of each subtree is no more than  $2\delta$  as follows.

Let  $(u, v)$  be a tree edge in  $T$ , where  $u$  is the parent of  $v$  and  $v$  is a child of  $u$ . Also, let  $T_v$  be a subtree of  $T$  rooted at node  $v$ . We perform a depth-first search on  $T$  starting from the tree root  $r$  until the total cost of the leftover tree rooted at  $r$  is no less than  $2\delta$ , i.e.,  $WH(T_r) < 2\delta$ . Figure 16.2 demonstrates an example of the tree decomposition procedure. Assume that node  $v$  is the node that is currently visited, we distinguish into the following four cases.

Case 1. If  $WH(T_v) < \delta$  and  $WH(T_v) + w(u, v) < \delta$ , no action is needed, and the tree decomposition procedure continues.

Case 2. If  $WH(T_v) < \delta$  and  $WH(T_v) + w(u, v) \geq \delta$ . Then, we must have  $WH(T_v) + w(u, v) < 2\delta$ , since the weight  $w(u, v)$  of edge  $(u, v)$  is no more than  $\delta$ . A new tree  $T_v \cup \{(v, u')\}$  is created with a virtual node  $u'$  with  $h(u') = 0$ . Split the subtree  $T_v \cup \{(v, u')\}$  from the original tree, see Fig. 16.2b.

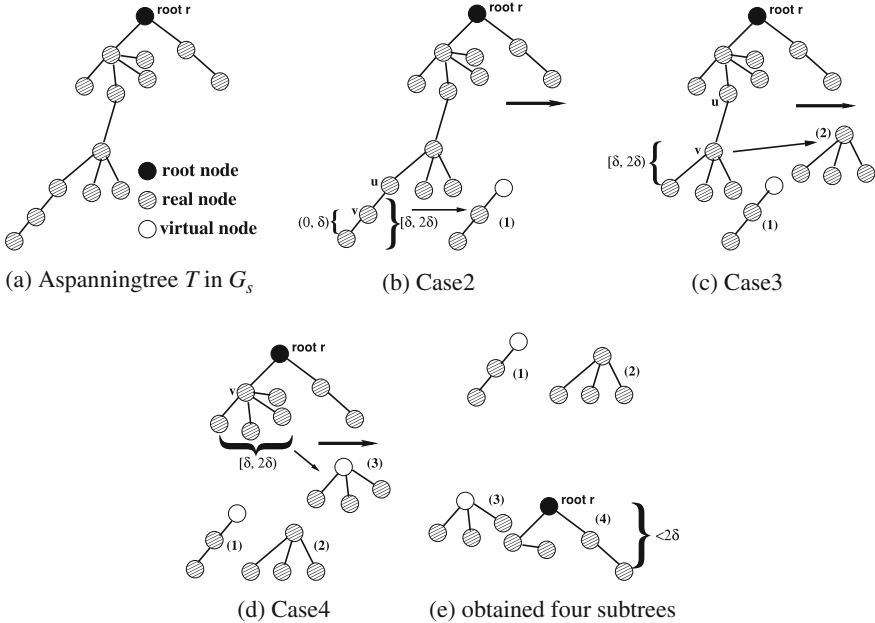


**Fig. 16.2** An illustration of the tree decomposition

Case 3. If  $\delta \leq WH(T_v) < 2\delta$ , split the subtree  $T_v$  from the original tree and remove edge  $(u, v) \in E_T$  from the original tree, see Fig. 16.2c.

Case 4. Let  $v_1^c, v_2^c, \dots, v_k^c$  be the  $k$  children of  $v$ . Let  $l$  be the maximum children index so that  $\delta \leq \sum_{j=1}^l (WH(T_{v_j^c}) + w(v_j^c, v)) < 2\delta$  with  $1 \leq l \leq k$ , then, a new subtree  $\cup_{j=1}^l (T_{v_j^c} \cup \{(v_j^c, v')\})$  rooted at the virtual node  $v'$  is created, which consists of these subtrees with  $h(v') = 0$ . Split off this subtree from the original tree, see Fig. 16.2d.

As a result, a set of subtrees is obtained by the tree decomposition on  $T$ , see Fig. 16.2e. The number of subtrees is bounded by the following lemma.

**Lemma 16.5** *Given a spanning tree  $T = (V_s, E_T; h, w)$  of a graph  $G_s = (V_s, E_s; h, w)$  with the total cost  $WH(T)$  and a value  $\delta \geq \max_{v \in V_s} \{2w(r, v), h(v)\}$ , the tree  $T$  can be decomposed into  $p$  subtrees  $T_1, T_2, \dots, T_p$  with  $WH(T_i) < 2\delta$  by the proposed tree decomposition procedure,  $1 \leq i \leq p$ . Then,  $p \leq \lfloor \frac{WH(T)}{\delta} \rfloor$ .*

*Proof* Following the tree decomposition on  $T$ , subtrees with the total cost in  $[\delta, 2\delta)$  are split away from  $T$  until the total cost of the leftover tree including root  $r$  is less than  $2\delta$ . Suppose that  $T_1, T_2, \dots, T_p$  are the split trees with  $p \geq 2$ . From the subtree construction, we know that  $\delta \leq WH(T_i) < 2\delta$  for each  $i$  with  $1 \leq i \leq p - 1$ . The only subtree with the total cost less than  $\delta$  is  $T_p$ . Note that prior to splitting  $T_{p-1}$ , the total cost of the remaining tree is at least  $2\delta$ . Therefore, the average total cost of  $T_{p-1}$

and  $T_p$  is no less than  $\delta$ . That is, the average total cost of all  $T_i$  is at least  $\delta$ . Thus,  $p \cdot \delta \leq WH(T)$ , i.e.,  $p \leq \frac{WH(T)}{\delta}$ . Since  $p$  is an integer,  $p \leq \lfloor \frac{WH(T)}{\delta} \rfloor$ .  $\square$

### 16.4.1.3 Algorithm for Finding $p$ -optimal Closed Tours

Given a metric graph  $G_s = (V_s, E_s; h, w)$  with root  $r$  and a positive integer  $p$ , we now devise an approximation algorithm for the  $p$ -optimal closed tour problem in  $G_s$  as follows.

Let  $T$  be a minimum spanning tree (MST) of  $G_s$  rooted at  $r$ . The basic idea of the proposed algorithm is that we first perform a tree decomposition on  $T$  with  $\delta = \max_{v \in V_s} \{WH(T)/p, 2w(v, r) + h(v)\}$  and we later show that  $\delta$  is a lower bound on the optimal cost of the  $p$ -optimal closed tour problem. As a result,  $p'$  subtrees are derived from such a decomposition, and  $p'$  closed tours are then derived from the  $p'$  subtrees. We finally show that  $p' \leq p$  and the maximum total cost of any closed tour among the  $p'$  closed tours is no more than  $5\delta$ .

Specifically,  $T$  is decomposed into no more than  $p'$  edge-disjoint subtrees, excepting the root node  $r$  which appears in one of these subtrees. Let  $T_1, T_2, \dots, T_{p'}$  be the  $p'$  trees obtained by decomposing  $T$ . It can be observed that each  $T_i$  contains at least one real node and at most one virtual node, where a node  $v$  is a *real node* if  $h(v) \neq 0$ ; otherwise, it is a virtual node. As a result, a forest  $\mathcal{F}$  consisting of all the trees is found through the tree decomposition, and the number of trees in  $\mathcal{F}$  is  $p' \leq \lfloor WH(T)/\delta \rfloor$  and the total cost of each subtree is no more than  $2\delta$  by Lemma 16.5.

For each  $T_i \in \mathcal{F}$ , if it does not contain the root  $r$ , then, a tree  $T'_i = T_i \cup \{(v_i, r)\}$  rooted at  $r$  is obtained by including node  $r$  and a tree edge  $(v_i, r)$  into  $T_i$ , where node  $v_i$  is a node in  $T_i$  and  $w(v_i, r) = \min_{v \in T_i} \{w(v, r)\}$ . The total cost  $WH(T'_i)$  of  $T'_i$  is

$$WH(T'_i) = WH(T_i) + w(v_i, r) \leq 2\delta + w(v_i, r) \leq 2.5\delta, \text{ as } w(v_i, r) \leq \delta/2.$$

Otherwise ( $T_i$  contains node  $r$ ),  $T'_i = T_i$  and  $WH(T'_i) = WH(T_i) \leq 2\delta$ . We thus obtain a forest  $\mathcal{F}' = \{T'_1, T'_2, \dots, T'_{p'}\}$ . From the trees in  $\mathcal{F}'$ ,  $p'$  edge-disjoint closed tours with each containing the root  $r$  can be derived. Let  $\mathcal{C}' = \{C'_1, C'_2, \dots, C'_{p'}\}$  be the set of  $p'$  closed tours obtained, by transforming each tree in  $\mathcal{F}'$  into a closed tour. For each  $C'_i$ , we have that  $WH(C'_i) \leq 2 \cdot WH(T'_i) \leq 5\delta$  by Lemma 16.4. As there are some  $C'_i$ 's containing virtual nodes that are not part of a feasible solution to the problem, a feasible solution can be derived through a minor modification to the closed tours in  $\mathcal{C}'$ . That is, for each  $C'_i$ , if it contains a virtual node (as each  $C'_i$  contains at most one virtual node), a closed tour  $C_i$  with a less total cost than that of  $C'_i$  is obtained, by removing the virtual node and the two edges incident to the node from  $C'_i$  through shortcircuiting, then  $WH(C_i) \leq WH(C'_i)$  as the edge weight follows the triangle inequality. Otherwise,  $C_i = C'_i$ . Clearly, each of the  $p'$  closed tours  $C_1, C_2, \dots, C_{p'}$  roots at  $r$ . The detailed algorithm is described in Algorithm 11.

---

**Algorithm 11:** Finding closed tours rooted at  $r$  with each having the bounded total cost

---

- Input:** A metric graph  $G_s = (V_s, E_s; h, w)$ , a root  $r \in V_s$ , and a given value  $\delta \geq \max_{v \in V_s} \{h(v), 2w(v, r)\}$ .
- Output:** a set of node-disjoint closed tours covering all nodes in  $V_s$  with the shared root  $r$  so that the total cost of each tour is no more than  $5\delta$ .
- 1 Let  $T$  be an MST of  $G_s$  and  $WH(T)$  be the total cost of  $T$ ;
  - 2 Let  $\mathcal{T} = \{T_1, T_2, \dots, T_{p'}\}$  be the forest obtained by performing the tree decomposition on  $T$  with the given value  $\delta$ ;
  - 3 Let  $\mathcal{T}' = \{T'_1, T'_2, \dots, T'_{p'}\}$  be a forest, where  $T'_i = T_i \cup \{(r, v_i)\}$  is derived by adding root  $r$  and an edge with the minimum edge weight between a node  $v_i$  in  $T_i$  and  $r$  if  $r$  is not in  $T_i$ ; otherwise  $T'_i = T_i$ , where  $1 \leq i \leq p'$ ;
  - 4 Let  $\mathcal{C}' = \{C'_1, C'_2, \dots, C'_{p'}\}$ , where closed tour  $C'_i$  is derived from  $T'_i$ ;
  - 5 Let  $\mathcal{C} = \{C_1, C_2, \dots, C_p\}$  be a set of closed tours, where  $C_i$  is derived by removing the virtual node from  $C'_i \in \mathcal{C}'$  if it does contain a virtual node. Otherwise,  $C_i = C'_i$ ;
  - 6 **return**  $\mathcal{C}$ .
- 

#### 16.4.1.4 Algorithm Analysis

In the following, we show that Algorithm 11 delivers a 5-approximate solution. Specifically, we first show that Algorithm 11 delivers a feasible solution to the  $p$ -optimal closed tour problem. We then show that the total cost of each closed tour in the solution is no more than  $5\delta$ . We thirdly show that  $\delta (= \max_{v \in V_s} \{WH(T)/p, 2w(v, r) + h(v)\})$  is a lower bound on the optimal cost of the problem. Then, the total cost of each closed tour in the solution delivered by Algorithm 11 is no more than  $5\delta \leq 5OPT$ . We finally analyze the time complexity of Algorithm 11.

**Theorem 16.4** *Given a metric graph  $G_s = (V_s, E_s; h, w)$  and an integer  $p \geq 1$ , there is a 5-approximation algorithm for finding  $p$ -optimal closed tours. The time complexity of the proposed algorithm is  $O(|V_s|^2)$ .*

*Proof* We first show that Algorithm 11 delivers a feasible solution to the  $p$ -optimal closed tour problem. Recall that  $T$  is an MST of  $G_s$ . Since  $\delta = \max_{v \in V_s} \{WH(T)/p, 2w(v, r) + h(v)\}$ ,  $\delta \geq \max_{v \in V_s} \{2w(v, r), h(v)\}$ . A solution  $\mathcal{C}$  which consists of  $p'$  closed tours rooted at  $r$  can be obtained, by applying Algorithm 11 on  $T$ , and

$$\begin{aligned} p' &\leq \lfloor WH(T)/\delta \rfloor \leq WH(T)/\delta \\ &= \frac{WH(T)}{\max_{v \in V_s} \{WH(T)/p, 2w(v, r) + h(v)\}} \leq \frac{WH(T)}{WH(T)/p} = p, \end{aligned} \quad (16.12)$$

by Lemma 16.5. Thus,  $\mathcal{C}$  is a feasible solution.

We then show that the total cost of each closed tour in  $\mathcal{C}$  is no more than  $5\delta$ . As each  $C_i \in \mathcal{C}$  is derived from a  $C'_i \in \mathcal{C}'$ , we have  $WH(C_i) \leq WH(C'_i) \leq 2WH(T'_i) \leq 2 \cdot 2.5\delta = 5\delta$  by Lemma 16.4.

We thirdly prove that  $\delta$  is a lower bound on the optimal cost of the problem. Given a node and edge weighted metric graph  $G_s = (V_s, E_s; h, w)$  with root  $r$ , an integer

$p \geq 1$ , partition the nodes in  $V_s$  into  $p$  disjoint subsets  $X_1, X_2, \dots, X_p$ , and let  $C_j$  be the closed tour containing all nodes in  $X_j$  and the root  $r$ . The optimal partitioning is a partitioning such that the maximum value  $\max_{1 \leq j \leq p} \{WH(C_j)\}$  is minimized. Let  $OPT$  be the total cost of the maximum closed tour in the optimal solution. We show that  $\delta \leq OPT$  as follows.

Let  $C_1^*, C_2^*, \dots, C_p^*$  be the  $p$  closed tours in the optimal solution with the shared root  $r$ . Then,  $WH(C_i^*) \leq OPT$ . Let  $e_i$  be the maximum weighted edge in  $C_i^*$ . Then, a tree  $T' = \bigcup_{i=1}^p C_i^* \setminus \{e_i\}$  rooted at  $r$  can be obtained by removing  $e_i$  from each tour  $C_i^*$ . We then have

$$WH(T') = \sum_{i=1}^p (WH(C_i^*) - w(e_i)) \leq \sum_{i=1}^p WH(C_i^*) \leq p \cdot OPT. \quad (16.13)$$

It can be seen that  $T'$  is a spanning tree in  $G_s$ . Since  $T$  is an MST of  $G_s$ ,  $WH(T) \leq WH(T')$ . We thus have

$$\frac{WH(T)}{p} \leq \frac{WH(T')}{p} \leq OPT. \quad (16.14)$$

On the other hand, each node  $v \in V_s$  must be contained by one closed tour  $C_i^*$  in the optimal solution. Since tour  $C_i^*$  contains node  $v$  and the depot  $r$ , then the total cost of  $C_i^*$ ,  $WH(C_i^*)$ , is at least  $2w(v, r) + h(v)$ , Thus,

$$2w(v, r) + h(v) \leq WH(C_i^*) \leq OPT, \quad \forall v \in V_s. \quad (16.15)$$

Combing inequalities (16.14) and (16.15), we have

$$\delta = \max_{v \in V_s} \left\{ \frac{WH(T)}{p}, 2w(v, r) + h(v) \right\} \leq OPT. \quad (16.16)$$

The time complexity analysis of Algorithm 11 is straightforward, omitted.  $\square$

### 16.4.2 Approximation Algorithm for the Minimum Number of Mobile Chargers Deployment Problem

In this subsection, we provide an approximation algorithm for the minimum number of mobile chargers deployment problem. As each mobile charger consumes energy on traveling and charging sensors per tour, the total amount of energy consumed by the mobile vehicle is bounded by its energy capacity  $IE$ .

### 16.4.2.1 Algorithm

The basic idea of the proposed approximation algorithm is to reduce the minimum number of mobile chargers deployment problem into a  $p$ -closed tour problem, by bounding the total cost of each closed tour. A solution to the latter in turn returns a solution to the former as follows.

Recall that we assume that the base station knows both the residual energy  $RE_i$  and the energy consumption rate  $\rho_i$  of each sensor  $v_i \in V_s$ , and  $\mu$  is the wireless charging rate of a mobile vehicle. Assume that there are sufficient numbers of fully charged mobile vehicles available at the depot. Then, a mobile vehicle takes  $\tau_i = \frac{B_i - RE_i}{\mu}$  time to charge sensor  $v_i$  to its full capacity  $B_i$  when it approaches the sensor. We thus construct a node and edge weighted metric graph  $G_s = (V_s, E_s; h, w)$ , where  $V_s$  is the set of sensors to be charged in this round. There is an edge in  $E_s$  between any two to-be-charged sensor nodes. For each edge  $(u, v) \in E_s$ , its weight is  $w(u, v) = \eta \cdot d(u, v)$  which is the amount of energy consumed by a mobile vehicle traveling along the edge, where  $\eta$  is the energy consumption rate of a mobile vehicle for traveling per unit length and  $d(u, v)$  is the Euclidean distance between sensor nodes  $u$  and  $v$ .

For each node  $v_i \in V_s$ , its weight  $h(v_i)$  ( $= B_i - RE_i = \mu \cdot \tau_i$ ) is the amount of energy needed to charge sensor  $v_i$  to reach its full capacity  $B_i$ . We assume that  $IE \geq \max_{v \in V_s} \{2w(v, r) + h(v)\}$ ; otherwise, there are no feasible solutions to the problem, which will be shown by Lemma 16.6 later. The detailed algorithm is described in Algorithm 12. We refer to this algorithm as NMV\_without\_Eloss.

---

**Algorithm 12:** Finding the optimal number of mobile vehicles and their closed tours (NMV\_without\_Eloss)

---

**Input:** A metric graph  $G_s = (V_s, E_s; h, w)$ , a root  $r$ , and  $IE$  with  $IE \geq \max_{v \in V_s} \{2w(r, v) + h(v)\}$ .  
**Output:**  $p$ -node-disjoint closed  $r$ -rooted tours  $C_1, C_2, \dots, C_p$  covering all nodes in  $V_s$  such that  $WH(C_i) \leq IE$ .

- 1 Let  $T$  be an MST of  $G_s$ . Denote by  $W(T)$  and  $H(T)$  the total costs of the edges and nodes in  $T$ , respectively;
- 2 **if**  $IE \geq 2 \cdot W(T) + H(T)$  **then**
- 3     One mobile vehicle suffices by Lemma 16.4; EXIT;;
- 4 **end if**
- 5  $A \leftarrow \max_{v \in V_s} \{2w(v, r)\}$ ;
- 6 **if**  $IE/5 \geq A$  **then**
- 7      $\delta \leftarrow IE/5$ ; /\* $\delta$  is the average subtree cost after tree decomposition\*/;
- 8 **else**
- 9      $\delta \leftarrow \frac{IE-A}{4}$ ;
- 10 **end if**
- 11 Perform the tree decomposition using  $\delta$ . If there is a node  $v$  with  $h(v) > \delta$ , then the node itself forms a tree;
- 12 Let  $\mathcal{C} = \{C_1, C_2, \dots, C_p\}$  be the solution by applying Algorithm 11 for the tree decomposition on  $T$  with the given  $\delta$ ;
- 13 **return**  $\mathcal{C}$  as a solution of the problem and  $p = |\mathcal{C}|$ .

---

### 16.4.2.2 Algorithm Analysis

We analyze the approximation ratio of the proposed algorithm, Algorithm 12, and its time complexity as follows. We start by Lemma 16.6, which says that there must be a feasible solution to the problem if and only if  $IE \geq \max_{v \in V_s} \{2w(v, r) + h(v)\}$ ; otherwise, there are no solutions to the problem. Thus, in the rest of our discussions, we assume that  $IE \geq \max_{v \in V_s} \{2w(v, r) + h(v)\}$ .

**Lemma 16.6** *Given a metric graph  $G_s = (V_s, E_s; h, w)$  and an energy capacity  $IE$  of each mobile charging vehicle, there is a feasible solution to the minimum number of mobile chargers deployment problem in  $G_s$  if and only if  $IE \geq \max_{v \in V_s} \{2w(v, r) + h(v)\}$ , where  $r$  is the depot of charging vehicles.*

*Proof* If  $IE \geq \max_{v \in V_s} \{2w(v, r) + h(v)\}$ , we can derive a feasible solution to the problem, by dispatching one charging vehicle to charge only one of the  $n = |V_s|$  sensors. Thus,  $n$  charging vehicles are deployed. On the other hand, assume that there is a feasible solution  $\mathcal{C} = \{C_1, C_2, \dots, C_p\}$  to the problem, where  $p$  charging vehicles are deployed to fully charge the  $n$  sensors and  $C_j$  is the charging tour of the  $j$ -th charging vehicle with  $1 \leq j \leq p$ . It is obvious that  $WH(C_j) \leq IE$  for  $1 \leq j \leq p$ . Consider a sensor  $v_i \in V_s$  such that  $v_i = \arg \max_{v \in V_s} \{2w(v, r) + h(v)\}$ . Let  $C_j$  be the charging tour containing sensor  $v_i$  in the solution. Since tour  $C_j$  must contain sensor  $v_i$  and depot  $r$ , the total cost of the tour,  $WH(C_j)$ , must be no less than  $2w(v_i, r) + h(v_i)$ , i.e.,  $WH(C_j) \geq 2w(v_i, r) + h(v_i)$ . Then,  $IE \geq 2w(v_i, r) + h(v_i) = \max_{v \in V_s} \{2w(v, r) + h(v)\}$ .  $\square$

**Theorem 16.5** *Given a metric graph  $G_s = (V_s, E_s; h, w)$  and the energy capacity  $IE$  of each mobile charging vehicle with  $IE \geq \max_{v \in V_s} \{2w(v, r) + h(v)\}$ , there is an approximation algorithm, Algorithm 12, with an approximation ratio of 8 for the minimum number of mobile chargers deployment problem in  $G_s$  if  $IE \geq 2A$ ; otherwise, the approximation ratio of the algorithm is  $4(1 + \frac{A}{h_{\min}}) = O(1)$ . The algorithm takes  $O(|V_s|^2)$  time, where  $r$  is the depot of charging vehicles,  $A = \max_{v \in V_s} \{2w(r, v)\}$ , and  $h_{\min} = \min_{v \in V_s} \{h(v)\}$ .*

*Proof* We first show that Algorithm 12 can deliver a feasible solution  $\mathcal{C} = \{C_1, C_2, \dots, C_p\}$ . Recall that  $A = \max_{v \in V_s} \{2w(v, r)\}$ , which is the maximum energy consumption of a charging vehicle on one round trip between a sensor  $v$  and the depot  $r$  in the sensor network. We distinguish it into three cases.

Case 1. If  $IE \geq 2 \cdot W(T) + H(T)$ , then there is a closed tour  $C$  including all nodes in  $V_s$  derived from  $T$  and the total cost of  $C$ ,  $WH(C)$  ( $\leq 2 \cdot W(T) + H(T) \leq IE$  by Lemma 16.4), is no more than the energy capacity of a mobile vehicle  $IE$ . Hence, one mobile charging vehicle suffices for charging all nodes in  $V_s$ .

Case 2. If  $IE/5 \geq A$ , then  $\delta = IE/5$ , and the total cost of each closed tour in the solution is no more than  $5\delta = IE$  by Theorem 16.4.

Case 3. ( $IE/5 < A \leq IE$ ). Following Algorithm 12, we set  $\delta = \frac{IE-A}{4}$ . Clearly,  $w(v, r) \leq A/2$  for any node  $v \in V_s$  since  $A = \max_{v \in V_s} \{2w(r, v)\}$ . Then, the total cost of each closed tour  $C$  in the solution is analyzed as follows. (i)  $C$  contains only one sensor node  $v \in V_s$ . The total cost of  $C$  thus is  $WH(C) = 2w(r, v) + h(v) \leq IE$  by Lemma 16.6 and the input condition of the algorithm. (ii)  $C$  consists of multiple sensor nodes and is derived from a tree  $T_i$ . Then, the total cost of tour  $C$  in the solution is  $WH(C) \leq 2 \cdot (2\delta + w(v_0, r)) \leq 4 \cdot \frac{IE-A}{4} + 2w(v_0, r) \leq IE - A + A = IE$ , where  $w(v_0, r) = \min_{v \in T_i} \{w(v, r)\}$  and  $T_i$  is the tree from which  $C$  is derived. Thus, the solution is a feasible solution of the problem.

We then analyze the approximation ratio of the proposed algorithm. Assume that the minimum vehicles needed is  $p_{min}$ . With a similar discussion in Theorem 16.4, a lower bound on the value of  $p_{min}$  is

$$p_{min} \geq \lceil \frac{WH(T)}{IE} \rceil. \quad (16.17)$$

Let  $p$  be the number of vehicles delivered by the proposed algorithm. We show the approximation ratio by the following four cases.

Case 1. If  $IE \geq 2 \cdot W(T) + H(T)$ , only one mobile vehicle suffices, and this is an optimal solution.

Case 2. If  $IE/5 \geq A$ , we have  $\delta = IE/5$ . Then,  $\frac{p}{p_{min}} \leq \frac{\lfloor WH(T)/\delta \rfloor}{\lceil WH(T)/IE \rceil} \leq \frac{WH(T)/\delta}{WH(T)/IE} = IE/\delta = 5$  by Lemma 16.5.

Case 3. ( $IE/5 < A \leq IE/2$ ). We have  $\delta = \frac{IE-A}{4}$ . Then,  $\frac{p}{p_{min}} \leq \frac{\lfloor WH(T)/\delta \rfloor}{\lceil WH(T)/IE \rceil} = \frac{WH(T)/\delta}{WH(T)/IE} = \frac{IE}{\delta} = \frac{4 \cdot IE}{IE-A} = \frac{4}{1-A/IE} \leq \frac{4}{1-A/2A} = 8$ , by Lemma 16.5, Eq. (16.17), and  $IE \geq 2A$ .

Case 4. ( $IE/2 < A < IE$ ). We have  $\delta = \frac{IE-A}{4}$ . Let  $h_{min} = \min_{v \in V_s} \{h(v)\}$ , which is the minimum amount of energy for fully charging an energy-critical sensor  $v$  in the sensor network. Then,  $IE \geq \max_{v \in V_s} \{2w(r, v) + h(v)\} \geq 2w(r, v_i) + h(v_i) = A + h(v_i) \geq A + h_{min}$ , where  $v_i = \arg \max_{v \in V_s} \{2w(r, v)\}$ . The approximation ratio for Case 4 then is  $\frac{p}{p_{min}} \leq \frac{\lfloor WH(T)/\delta \rfloor}{\lceil WH(T)/IE \rceil} \leq \frac{WH(T)/\delta}{WH(T)/IE} = \frac{IE}{\delta} = \frac{4 \cdot IE}{IE-A} = 4(1 + \frac{A}{IE-A}) \leq 4(1 + \frac{A}{A+h_{min}-A}) = 4(1 + \frac{A}{h_{min}}) = O(1)$ , as each of the to-be-charged sensors has consumed a large portion of its energy already and  $h_{min}$  thus is proportional to the battery capacity of each sensor, the ratio  $\frac{A}{h_{min}}$  is usually a constant, where  $A$  is the maximum energy consumption of a charging vehicle on one round trip between a sensor and the depot  $r$  and  $h_{min}$  is the minimum amount of energy for fully charging an energy-critical sensor. Therefore, the approximation ratio for Case 4 is a constant. Notice that Case 4 in practice rarely happens, since the energy capacity of a charging vehicle cannot be used just for its travel without charging sensors, or its energy is only enough to charge one or two sensors per tour.

In summary, the approximation ratio of Algorithm 12 is no more than 8 when  $IE \geq 2A$ ; otherwise ( $\max_{v \in V_s} \{2w(r, v) + h(v)\} \leq IE < 2A$ ), its approximation ratio is  $4(1 + \frac{A}{h_{min}}) = O(1)$ . The dominant time of Algorithm 12 is the invoking of Algorithm 11, which takes  $O(|V_s|^2)$  time by Theorem 16.4.  $\square$

## 16.5 Performance Evaluation of the Algorithms for the Service Cost Minimization Problem

In this section, we evaluate the performance of the proposed algorithms for the service cost minimization problem through experimental simulations. We also study the impact of important parameters on the algorithm performance, including network size, data aggregation, and the ratio of the maximum data generation rate to the minimum data generation rate.

### 16.5.1 Simulation Environment

We consider a WSN consisting of from 100 to 500 sensors in a  $1,000\text{ m} \times 1,000\text{ m}$  square area, in which sensors are randomly deployed. The base station is located at the center of the square. The battery capacity  $B_i$  of each sensor  $v_i$  is 10.8 kJ [14]. The data sensing rate  $b_i$  of each sensor  $v_i$  is randomly chosen from an interval  $[b_{min}, b_{max}]$ , where  $b_{min} = 1\text{ kbps}$  and  $b_{max} = 10\text{ kbps}$  [14]. The coefficient  $\alpha$  in Eq. (16.2) is 2. Furthermore, we assume that each sensor  $v_i$  performs data aggregations on both pass-by traffic and self-sensed data with a data aggregation factor  $\theta$ , i.e., the data transmission rate  $b_i^{Tx}$  of sensor  $v_i$  is  $b_i^{Tx} = \theta \cdot (b_i^{Rx} + b_i)$ , where  $b_i^{Rx}$  and  $b_i$  are the data reception rate and data sensing rate of sensor  $v_i$ , respectively, and  $\theta$  is constant with  $0 < \theta \leq 1$  [23]. The default value of  $\theta$  is 1.

There are 5 depots in the WSN (i.e.,  $q = 5$ ) and there is a mobile charger at each depot. To reduce the total traveling distance of the  $q$  mobile chargers, one depot is colocated with the base station, as the most energy-consuming sensors in a WSN usually are close to the base station for relaying data from other remote sensors. The rest of  $q - 1$  depots are randomly distributed in the area. The entire monitoring period  $T$  is one year, which is partitioned into equal time slots with each lasting  $\Delta T$  ( $\Delta T$  typically is much shorter than  $T$ , e.g.,  $\Delta T$  is one month). We assume that the data sensing rate  $b_i$  of each sensor  $v_i \in V$  does not change within each time slot  $\Delta T$ . Even if it does change within the time slot, the difference can be neglected.

To evaluate the performance of the proposed algorithms MinDis and MinDis-var against the state-of-the-art algorithms, we implement three benchmark algorithms of sensor charging Periodic [14–16, 30], OnDemand, and Partition of [19, 22], which are described as follows. In algorithm Periodic, the base station periodically dispatches the  $q$  mobile chargers to charge every sensor in the network with charging period being  $\tau_{min}$ . The charging tours of the  $q$  chargers will be found by applying Algorithm 9. In algorithm OnDemand, each sensor sends a charging request to the base station when its residual energy is below a given energy threshold. Having received a set of such requests, the base station then dispatches the  $q$  mobile chargers to charge the sensors whose estimated residual lifetimes are less than a given threshold  $\Delta l$  with  $\Delta l = \tau_{min}$ . The charging tours of the  $q$  mobile chargers are finally obtained by applying Algorithm 9 for the  $q$ -rooted TSP problem in the induced graph of the to-be-charged sensors. Finally, in algorithm Partition,

the monitoring region is divided into  $q$  subregions, in other words, the sensors in the network are first partitioned into  $q$  disjoint sets  $V_1, V_2, \dots, V_q$  with each set corresponding to the sensors in its subregion, where a sensor  $v_i$  is contained in set  $V_j$  if depot  $r_j$  is its nearest depot among the  $q$  depots. Then, the sensors in  $V_j$  will be charged by only the mobile charger located at depot  $r_j$ , where  $1 \leq j \leq q$ . Each sensor  $v_i \in V_j$  sends a charging request to the base station when it will deplete its energy soon. Once receiving the request, the base station dispatches the mobile charger at depot  $r_j$  to charge a subset  $V'_j$  of sensors of  $V_j$  with the residual lifetime of each sensor in  $V'_j$  being less than a given threshold  $\Delta l_j$ , i.e.,  $V'_j = \{v_i \mid v_i \in V_j, l_i < \Delta l_j\}$ , and the charging tour of the charger is a shortest closed tour visiting the sensors in  $V'_j$  and depot  $r_j$ , where  $\Delta l_j = \tau_{min}^j$  and  $\tau_{min}^j$  is the shortest maximum charging cycle of sensors in set  $V_j$ , i.e.,  $\tau_{min}^j = \min_{v_i \in V_j} \{\tau_i\}$ .

It must be mentioned that each value in all figures is the average of the results by applying each mentioned algorithm to 100 different network topologies with the same network size.

### 16.5.2 Performance with Fixed Maximum Charging Cycles

We first evaluate the performance of the proposed approximation algorithm `MinDis` against algorithms `OnDemand`, `Partition`, and `Periodic` by varying network size  $n$ , assuming that maximum charging cycles within  $T$  are fixed. Figure 16.3 shows that the service costs delivered by algorithms `MinDis`, `OnDemand`, and `Partition` are much less than that by algorithm `Periodic`. For example, Fig. 16.3 demonstrates that the service cost by algorithm `MinDis` only about from 15 to 25 % of the cost by algorithm `Periodic`, and the costs by algorithms `OnDemand` and `Partition` are from 19 to 28 % of that by algorithm `Periodic`. Also, it can be seen from Fig. 16.3 that the proposed algorithm `MinDis` delivers a solution with the least service cost of mobile chargers, while the service costs delivered by algorithms `OnDemand` and `Partition` are almost identical and the one by algorithm `OnDemand` is only marginal better than that by algorithm `Partition`, ranging from 0.3 to 1.5 % improvement. In the following, we only compare the performance of algorithms `MinDis`, `OnDemand`, and `Partition`, and omit the performance of algorithm `Periodic`, since the service cost delivered by the algorithm is much higher than that by the three algorithms.

We then examine the impact of the data aggregation factor  $\theta$  on the performance of the three algorithms, by decreasing  $\theta$  from 1.0 to 0.1. Figure 16.4 clearly presents that the service costs by algorithms `MinDis`, `OnDemand`, and `Partition` decrease when  $\theta$  becomes smaller and the service costs by the three algorithms are almost identical when  $\theta = 0.1$ . The rationale behind the phenomenon is that the data transmission rates of sensors can be greatly reduced by a small data aggregation factor  $\theta$  while the sensor energy consumption on data transmission is usually the dominant one [23]. As a result, the maximum charging cycles of sensors becomes longer with

**Fig. 16.3** Performance of algorithms MinDis, OnDemand, Partition, and Periodic by varying the network size from 100 to 500 sensors

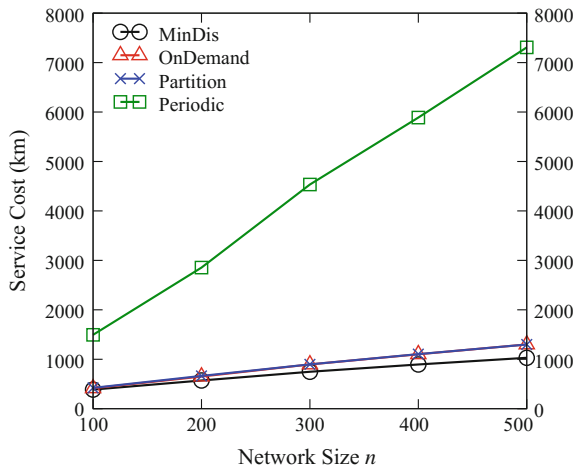
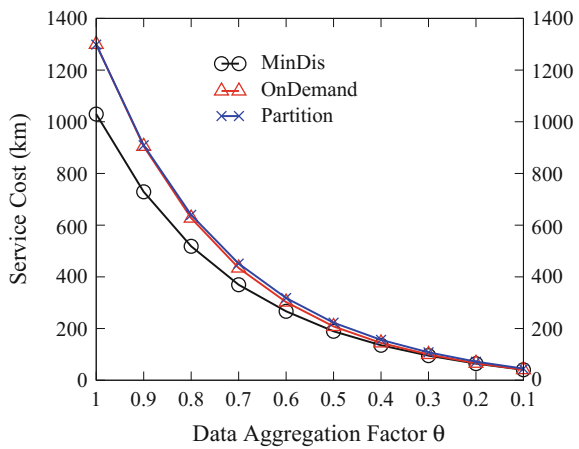


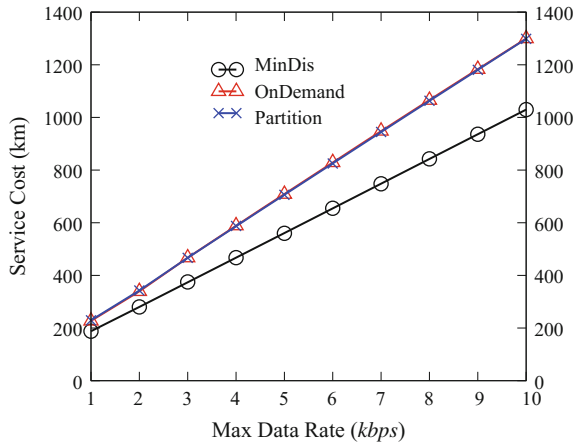
**Fig. 16.4** Performance of algorithms MinDis, OnDemand, and Partition by decreasing the data aggregation factor  $\theta$  from 1.0 to 0.1 when  $n = 500$



a smaller value of  $\theta$  and the service cost of mobile chargers thus is significantly reduced.

We finally study the impact of the maximum data rate  $b_{max}$  on the algorithm performance, by varying  $b_{max}$  from 1 to 10 kbps when  $b_{min} = 1$  kbps. Figure 16.5 demonstrates that the service cost by algorithm MinDis is only from 79 to 82% of the service cost by algorithm OnDemand and their performance gap increases when  $b_{max}$  becomes larger. Furthermore, Fig. 16.5 clearly shows that the service costs by the three algorithms increase with the increase of  $b_{max}$ . This is because that the energy consumption rates of sensors becomes higher when the maximum data rates of sensors  $b_{max}$  increases. As a result, sensors must be charged more frequently, which incurs more service cost of the mobile chargers.

**Fig. 16.5** Performance of algorithms MinDis, OnDemand, and Partition by varying the maximum data rate  $b_{max}$  from 1 to 10 kbps when  $b_{min} = 1$  kbps and  $n = 500$



In the following, we omit the performance of algorithm Partition, since the service costs by algorithms OnDemand and Partition are almost identical, which have already been shown in Figs. 16.3, 16.4, and 16.5.

### 16.5.3 Performance with Variable Maximum Charging Cycles

We first investigate the performance of the proposed heuristic algorithm MinDis-var against algorithm OnDemand with variable maximum charging cycles. Figures 16.6 and 16.7 illustrate the performance of both algorithms, by varying network size  $n$  and the data aggregation factor  $\theta$ , respectively. It can be seen that

**Fig. 16.6** Performance of algorithms MinDis-var and OnDemand by varying the network size when  $\Delta T$  is one month

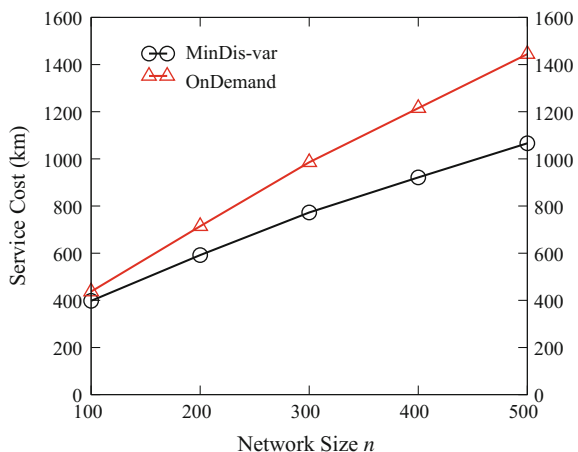
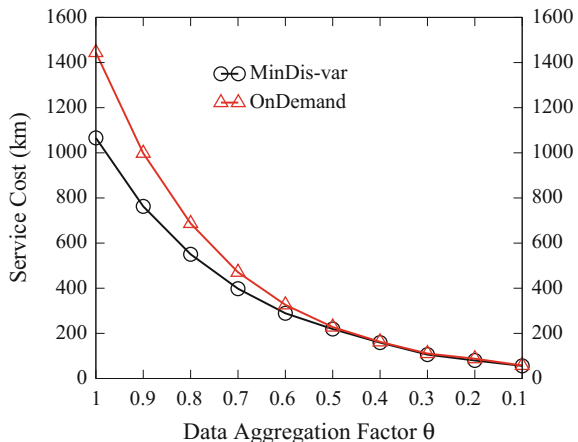


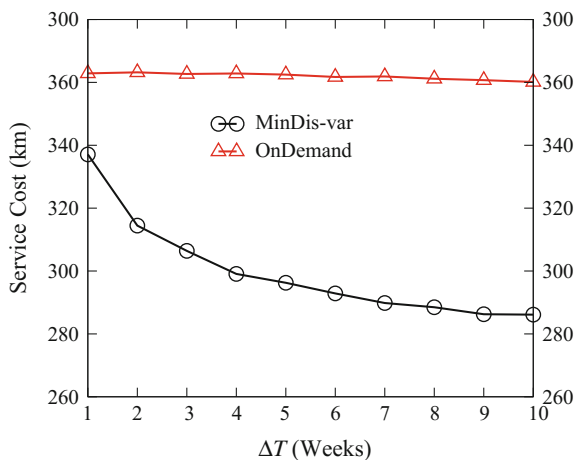
**Fig. 16.7** Performance of algorithms MinDis-var and OnDemand by decreasing the data aggregation factor  $\theta$  from 1.0 to 0.1 when  $\Delta T$  is one month and  $n = 500$



algorithm MinDis-var is still very competitive as it did under fixed maximum charging cycles.

We finally study the impact of the dynamics of maximum charging cycles on the algorithm performance, by varying parameter  $\Delta T$  from 1 week (i.e., extremely dynamic) to 10 weeks (i.e., rather stable). Figure 16.8 shows that the service cost by algorithm MinDis-var decreases with the increase of the stability of the sensor maximum charging cycles (a larger  $\Delta T$ ), while the service cost by algorithm OnDemand almost does not change with the increase of  $\Delta T$ . We also note that algorithm MinDis-var significantly outperforms algorithm OnDemand even when the maximum charging cycles are stable only in a short time slot  $\Delta T$  (e.g.,  $\Delta T =$  one week), which indicates that algorithm MinDis-var can quickly adapt to the changes of maximum charging cycles.

**Fig. 16.8** Performance of algorithms MinDis-var and OnDemand by varying  $\Delta T$  from 1 week to 10 weeks when  $b_{min} = 1$  kbps,  $b_{max} = 2$  kbps, and  $n = 500$



## 16.6 Performance Evaluation of the Algorithm for the Minimum Number of Mobile Chargers Deployment Problem

In this section, we evaluate the performance of the proposed algorithm for the minimum number of mobile chargers deployment problem through experimental simulations. We also investigate the impact of several important parameters on the algorithm performance including the network size  $n$ , the variance of energy consumption rates, the energy capacity  $IE$  of mobile charging vehicles, and the critical lifetime interval parameter  $\alpha$ .

### 16.6.1 Simulation Environment

We consider a wireless rechargeable sensor network consisting of from 100 to 500 sensors that are randomly deployed in a  $500\text{ m} \times 500\text{ m}$  square. The battery capacity  $B_i$  of each sensor  $v_i \in V_s$  is set to be 10.8 kiloJoules (kJ), by referring to a regular *NiMH* battery [14]. A base station is located at the center of the square, and a depot of mobile vehicles is colocated with the base station. The energy capacity of each mobile charging vehicle  $IE$  ranges from 1,000 to 5,000 kJ. We assume that each of them travels at a constant speed of  $s = 5\text{ m/s}$  with energy consumption rate of  $\eta = 0.6\text{ kJ/m}$  [15]. The energy-charging rate of each charging vehicle is  $\mu = 5\text{ W}$  [34]. The default value of  $\alpha$  is 5.

We consider two different distributions of energy consumption rates of sensors: the linear distribution and the random distribution. In *the linear distribution*, the energy consumption rate  $\rho_i$  of sensor  $v_i$  is proportional to its distance to the base station. The nearest and farthest sensors to the base station have the maximum energy consumption rates  $\rho_{max}$  and the minimum energy consumption rates  $\rho_{min}$ , respectively, where  $\rho_{min} = 1\text{ mJ/s}$  and  $\rho_{max} = 10\text{ mJ/s}$ . The linear distribution models the energy consumptions of sensors in WSNs where the main energy consumption of sensors is on the data transmission and relays. Sensors close to the base station must relay the sensing data for other remote sensors, thus consuming much more energy than the others. Furthermore, by adjusting the energy consumption ratio of each sensor from  $\rho_{max}$  to  $\rho_{min}$ , this model can be used to model data aggregations at relay sensor nodes, i.e., a smaller ratio  $\frac{\rho_{max}}{\rho_{min}}$  implies a higher data aggregation. On the other hand, in *the random distribution*, the energy consumption rate  $\rho_i$  of each sensor  $v_i \in V_s$  is randomly chosen from a value interval  $[\rho_{min}, \rho_{max}]$ . The random distribution captures the energy consumption of heterogeneous sensors. For example, video camera sensors in multimedia sensor networks typically consume plenty of energy on image processing [41]. Thus, the energy consumption rates of sensors in such sensor networks do not closely correlated with the distances between the sensors and the base station. We further assume that the energy-charging rate  $\mu$  of each mobile vehicle is several orders of magnitude of the energy depletion rate of sensors, i.e.,

$\mu \gg \max_{v_i \in V} \{\rho_i\}$ . A fully charged sensor can survive from 10 days up to 4 months. We put one year as our monitoring period of the sensor network. Each value in figures is the mean of the results by applying each mentioned algorithm to 50 different network topologies with the same network size.

To evaluate the performance of the proposed algorithms, we have also implemented three benchmarks `LB_optimal`, algorithm `Heuristic`, and algorithm `minMCP` [32, 33], in which *LB\_optimal* is a lower bound on the minimum number of mobile chargers which is an approximate estimation of the optimal solution, i.e.,  $\text{LB\_optimal} = \lceil WH(T)/IE \rceil$  by Eq. (16.17), where  $WH(T)$  is the total cost of the MST  $T$  of the metric graph  $G_s$  induced by the to-be-charged sensors, and  $IE$  is the energy capacity of each mobile charging vehicle. Algorithm `Heuristic` is described as follows. Given  $n$  to-be-charged sensors  $v_1, v_2, \dots, v_n$  indexed by their appearance in the area, we assume that the depot is the origin, and index the sensors in anticlockwise order. Algorithm `Heuristic` assigns the vehicles to the sensors one by one until all sensors are charged. Specifically, assume that the first  $K - 1$  mobile vehicles have been assigned to sensors  $v_1, v_2, \dots, v_{i-1}$  already. We now assign the  $K$ th mobile vehicle to charge the sensors in the sequence  $v_i, v_{i+1}, \dots, v_n$ . Initially,  $K = 1$  and  $i = 1$ . The set of sensors charged by vehicle  $K$  will be  $v_i, v_{i+1}, \dots, v_j$  if the total cost of a shortest closed tour  $C_K$  including depot  $r$  and sensors  $v_i, v_{i+1}, \dots, v_j$  is no more than the energy capacity  $IE$  while the total cost of a shortest closed tour  $C'_K$  including depot  $r$  and sensors  $v_i, v_{i+1}, \dots, v_j, v_{j+1}$  is larger than  $IE$ , i.e.,  $WH(C_K) \leq IE$  and  $WH(C'_K) > IE$ , where  $i \leq j \leq n$ . This procedure continues until all  $n$  sensors are charged.

To compare our work with the two closely related works [32, 33], we adopt a variant of algorithm `minMCP` in [32, 33] since the total energy consumption of some of the closed tours delivered by their algorithms may violate the energy capacity constraint  $IE$ , and the amount of energy consumed on each such a tour can be up to  $IE(1 + \varepsilon)$  with  $\varepsilon > 0$  being a constant. To ensure that the energy consumption of any charging tour is no greater than the energy capacity  $IE$  of each mobile vehicle when applying algorithm `minMCP`, we set the energy capacity of mobile vehicles as  $\frac{IE}{1+\varepsilon}$  when invoking the algorithm. Thus, the total energy consumption of a charging vehicle per tour will be no more than  $\frac{IE}{1+\varepsilon} \cdot (1 + \varepsilon) = IE$ , and we set  $\varepsilon = 0.1$  in all our experiments in the default setting.

### 16.6.2 Performance Evaluation of Algorithms

We evaluate the performance of algorithms `NMV_without_Eloss`, `NMV_with_Eloss`, `Heuristic` and `minMCP` as follows, where algorithm `NMV_without_Eloss` does not take into account the sensor energy consumption during each charging tour, while algorithm `NMV_with_Eloss` does take such sensor energy consumption into consideration.

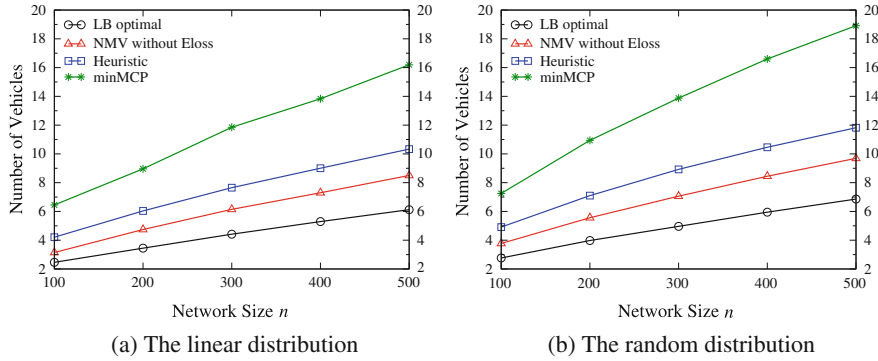
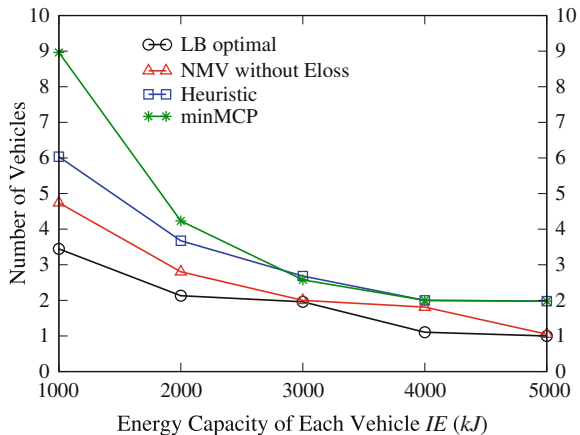


**Fig. 16.9** Performance of algorithms NMV\_without\_Eloss, Heuristic, and minMCP by varying network size under two different distributions of energy consumption rates when  $IE = 1,000 \text{ kJ}$ ,  $\rho_{\min} = 1 \text{ mJ/s}$ , and  $\rho_{\max} = 10 \text{ mJ/s}$

We first evaluate the performance of algorithms NMV\_without\_Eloss, Heuristic, and minMCP under the assumption that sensor energy consumption rates follow linear and random distributions, by varying the network size from 100 to 500 sensors. Figure 16.9a plots their performance curves, from which it can be seen that the solution delivered by algorithm NMV\_without\_Eloss is fractional of the optimal one. Specifically, the number of mobile vehicles delivered by it is around 35 % more than the lower bound LP\_optimal, while the number of mobile vehicles by it is about 20 and 45 % less than that by algorithms Heuristic and minMCP, respectively. The rationale behind is as follows. Given a set of to-be-charged sensors, algorithm Heuristic first sorts the sensors in anticlockwise order, where the depot is the origin. The algorithm then assigns the mobile vehicles to sensors one by one until all sensors are charged. There may be some cases that some sensors charged by a mobile charging vehicle are far away from each other. Then, the charging vehicle consumes more energy on traveling, rather than on charging the sensors. As a result, more charging vehicles are needed. In contrast, the proposed algorithm NMV\_without\_Eloss will schedule a mobile charging vehicle to replenish a set of sensors whose locations are close to each other. Therefore, less charging vehicles are required. Figure 16.9b indicates that the four algorithms have the similar behaviors under both linear and random distributions of energy consumption rates.

We then study the impact of the energy capacity of mobile charging vehicle  $IE$  on the performance of algorithms NMV\_without\_Eloss, Heuristic, and minMCP by varying  $IE$  from 1,000 to 5,000 kJ. Figure 16.10 shows that with the growth of the energy capacity  $IE$ , the number of mobile charging vehicles delivered by algorithm NMV\_without\_Eloss decreases, and the gap between the solution and the lower bound of the optimal solution becomes smaller and smaller, which implies that the performance of algorithm NMV\_without\_Eloss is near-optimal. On the other hand, the number of vehicles delivered by algorithm NMV\_without\_Eloss is up to 50 % less than that by algorithm Heuristic.

**Fig. 16.10** Performance of algorithms NMV\_without\_Eloss, Heuristic, and minMCP by varying the energy capacity of each mobile vehicle  $IE$  when  $n = 200$ ,  $\rho_{min} = 1 \text{ mJ/s}$ , and  $\rho_{max} = 10 \text{ mJ/s}$



We finally investigate the impact of the variance among energy consumption rates of sensors on the performance of algorithms NMV\_without\_Eloss, Heuristic, and minMCP, by varying  $\rho_{max}$  from 1 to 10 mJ/s while fixing  $\rho_{min}$  at 1 mJ/s. Figure 16.11 indicates that the number of mobile vehicles needed by each of the three algorithms NMV\_without\_Eloss, Heuristic, and minMCP decreases, followed by slowly growing. The rationale behind is that when the variance is quite small (i.e., the gap between  $\rho_{max}$  and  $\rho_{min}$  is small), the solution delivered by algorithm NMV\_without\_Eloss will include almost all sensors in each charging round, thus, a large number of mobile vehicles are required. With the increase on the variance, the number of to-be-charged sensors in each charging round significantly decreases. On the other hand, when the maximum energy consumption rate  $\rho_{max}$  becomes large, the average energy depletion rate of the sensors will be faster, the solution by algorithm NMV\_without\_Eloss will include more sensors to be charged per charging round as more sensors are within their critical lifetimes. In the following, we do not compare the performance of algorithm minMCP, since its performance is the worst one among the four algorithms LB\_optimal, NMV\_without\_Eloss, Heuristic, and minMCP, which has been shown in Figs. 16.9–16.11.

### 16.6.3 The Impact of $\alpha$ on Algorithmic Performance

We now evaluate the impact of critical lifetime interval parameter  $\alpha$  on the performance of the proposed algorithms by varying the value of  $\alpha$  from 1 to 7. A smaller  $\alpha$  implies that more frequent scheduling are needed, and less numbers of mobile vehicles are employed per charging round. With the growth of  $\alpha$ , more and more sensors will be included in  $V_s$ , and more sensors will be charged by mobile charging vehicles per charging round. Figure 16.12 implies that with the growth of  $\alpha$ , more charging vehicles are needed by algorithms NMV\_without\_Eloss and Heuristic in

**Fig. 16.11** Performance of algorithms NMV\_without\_Eloss, Heuristic, and minMCP by varying the maximum energy consumption rate  $\rho_{max}$  from 1 mJ/s to 10 mJ/s when  $n = 200$ ,  $IE = 1,000\text{ kJ}$ , and  $\rho_{min} = 1\text{ mJ/s}$

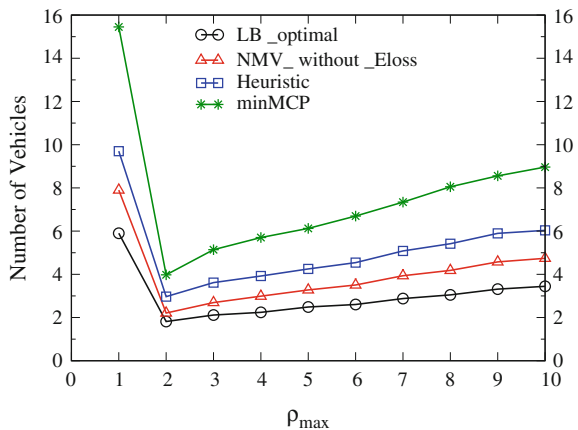
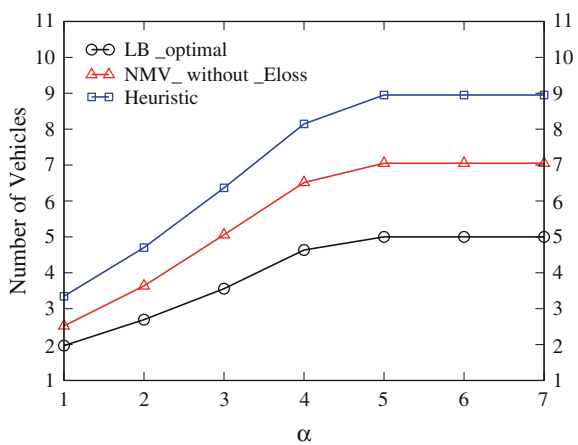


**Fig. 16.12** Performance of algorithms NMV\_without\_Eloss and Heuristic by varying  $\alpha$  when  $n = 200$ ,  $IE = 1,000\text{ kJ}$ ,  $\rho_{min} = 50\text{ mJ/s}$ , and  $\rho_{max} = 100\text{ mJ/s}$



each charging round, as more sensor nodes fall in the defined critical lifetime interval. However, it is interesting to see that no more mobile vehicles are required when the value of  $\alpha$  is greater than 6, since all sensors will be charged in each charging round.

## 16.7 Conclusions

In this chapter, we studied the use of multiple mobile chargers to charge sensors in a wireless sensor network so that none of the sensors will run out of energy for a given monitoring period, for which we first formulated the novel service cost minimization problem of finding a series of charging schedulings of mobile chargers so that the total traveling distance of the mobile chargers for the monitoring period is

minimized, and the problem of using the minimum number of mobile chargers to charge sensors such that none of the sensors will run out of energy, subject to the energy capacity constraint imposed on each mobile charger, while maintaining the perpetual operations of sensors. As these optimization problems are NP-hard, we then devised an approximation algorithm for the service cost minimization problem with a provable approximation ratio if the maximum charging cycle of each sensor is fixed in the given monitoring period. Otherwise, we developed a novel heuristic solution through modifications to the approximate solution. We further devised an approximation algorithm for the minimum number of mobile chargers deployment problem with a provable performance guarantee. We finally evaluated the performance of the proposed algorithms through extensive experimental simulations, and experimental results showed that the proposed algorithms are very promising, and the solutions obtained are fractional of the optimal ones.

**Acknowledgements** It is acknowledged that Wenzheng Xu's work was partially supported by 2016 Basic Research Talent Foundation of Sichuan University (Grant No. 2082204194050), and Weifa Liang's work was partially supported by a research grant funded by the Actew/ActewAGL Endowment Fund, the ACT Government of Australia.

## References

1. Liang, W., Luo, J., Xu, X.: Prolonging network lifetime via a controlled mobile sink in wireless sensor networks. In: IEEE Global Telecommunications Conference (GLOBECOM), pp. 1–6 (2010)
2. Liang, W., Luo, J., Xu, X.: Network lifetime maximization for time-sensitive data gathering in wireless sensor networks with a mobile sink. *Wireless Commun. Mob. Comput.* **13**(14), 1263–1280 (2013)
3. Liang, W., Schweitzer, P., Xu, Z.: Approximation algorithms for capacitated minimum forest problems in wireless sensor networks with a mobile sink. *IEEE Trans. Comput.* **62**(10), 1932–1944 (2013)
4. Ren, X., Liang, W.: Delay-tolerant data gathering in energy harvesting sensor networks with a mobile sink. In: IEEE Global Communications Conference (GLOBECOM), pp. 93–99 (2012)
5. Ren, X., Liang, W.: The use of a mobile sink for quality data collection in energy harvesting sensor networks. In: IEEE Wireless Communications and Networking Conference (WCNC), pp. 1145–1150 (2013)
6. Ren, X., Liang, W., Xu, W.: Use of a mobile sink for maximizing data collection in energy harvesting sensor networks. In: 42nd International Conference on Parallel Processing (ICPP), pp. 439–448 (2013)
7. Ren, X., Liang, W., Xu, W.: Data collection maximization in renewable sensor networks via time-slot scheduling. *IEEE Trans. Comput.* **64**(7), 1870–1883 (2015)
8. Xu, Z., Liang, W., Xu, Y.: Network lifetime maximization in delay-tolerant sensor networks with a mobile sink. In: IEEE 8th International Conference on Distributed Computing in Sensor Systems (DCOSS), pp. 9–16 (2012)
9. Xu, W., Liang, W., Hu, S., Lin, X., Peng, J.: Charging your smartphones on public commuters via wireless energy transfer. In: 2015 IEEE 34th International Performance Computing and Communications Conference (IPCCC), pp. 1–8 (2015)

10. Xu, W., Liang, W., Lin, X., Mao, G.: Efficient scheduling of multiple mobile chargers for wireless sensor networks. *IEEE Trans. Veh. Technol.* to appear
11. Xu, W., Liang, W., Lin, X., Mao, G., Ren, X.: Towards perpetual sensor networks via deploying multiple mobile wireless chargers. In: 43rd International Conference on Parallel Processing (ICPP), pp. 80–89 (2014)
12. Liang, W., Xu, W., Ren, X., Jia, X., Lin, X.: Maintaining sensor networks perpetually via wireless recharging mobile vehicles. In: IEEE 39th Conference on Local Computer Networks (LCN), pp. 270–278 (2014)
13. Liang, W., Xu, W., Ren, X., Jia, X., Lin, X.: Maintaining large-scale rechargeable sensor networks perpetually via multiple mobile charging vehicles. *ACM Trans. Sens. Netw. (TOSN)* **12**(2), 14:1–14:26 (2016)
14. Shi, Y., Xie, L., Hou, Y., Sherali, H.: On renewable sensor networks with wireless energy transfer. In: IEEE The 30th Conference on Computer Communications (INFOCOM), pp. 1350–1358 (2011)
15. Xie, L., Shi, Y., Hou, Y., Lou, W., Sherali, H., Midkiff, S.: Bundling mobile base station and wireless energy transfer: Modeling and optimization. In: IEEE 32nd International Conference on Computer Communications (INFOCOM), pp. 1636–1644 (2013)
16. Xie, L., Shi, Y., Hou, Y.T., Lou, W., Sherali, H.D.: On traveling path and related problems for a mobile station in a rechargeable sensor network. In: The 14th ACM International Symposium on Mobile Ad Hoc Networking and Computing (MobiHoc), pp. 109–118 (2013)
17. Guo, S., Wang, C., Yang, Y.: Mobile data gathering with wireless energy replenishment in rechargeable sensor networks. In: IEEE 32nd International Conference on Computer Communications (INFOCOM), pp. 1932–1940 (2013)
18. Ren, X., Liang, W., Xu, W.: Maximizing charging throughput in rechargeable sensor networks. In: 23rd International Conference on Computer Communication and Networks (ICCCN), pp. 1–8 (2014)
19. Wang, C., Li, J., Ye, F., Yang, Y.: Multi-vehicle coordination for wireless energy replenishment in sensor networks. In: IEEE 27th International Symposium on Parallel Distributed Processing (IPDPS), pp. 1101–1111 (2013)
20. Xu, W., Liang, W., Jia, X., Xu, Z.: Maximizing sensor lifetime in a rechargeable sensor network via partial energy charging on sensors. In: 13th IEEE International Conference on Sensing, Communication and Networking (SECON) (2016)
21. Xu, W., Liang, W., Ren, X., Lin, X.: On-demand energy replenishment for sensor networks via wireless energy transfer. In: 2014 IEEE 25th Annual International Symposium on Personal, Indoor, and Mobile Radio Communication (PIMRC), pp. 1269–1273 (2014)
22. Zhao, M., Li, J., Yang, Y.: Joint mobile energy replenishment and data gathering in wireless rechargeable sensor networks. In: 23rd International Teletraffic Congress (ITC), pp. 238–245 (2011)
23. Li, J., Mohapatra, P.: Analytical modeling and mitigation techniques for the energy hole problem in sensor networks. *Pervasive Mob. Comput.* **3**(3), 233–254 (2007)
24. bmw i3 bev (2014). <http://www.fueleconomy.gov/feg/find.do?action=sbs&id=35207>
25. Akyildiz, I.F., Su, W., Sankarasubramaniam, Y., Cayirci, E.: Wireless sensor networks: a survey. *Comput. Netw.* **38**(4), 393–422 (2002)
26. Kim, S., Pakzad, S., Culler, D., Demmel, J., Fenves, G., Glaser, S., Turon, M.: Health monitoring of civil infrastructures using wireless sensor networks. In: 6th International Symposium on Information Processing in Sensor Networks (IPSN), pp. 254–263 (2007)
27. Lin, K., Yu, J., Hsu, J., Zahedi, S., Lee, D., Friedman, J., Kansal, A., Raghunathan, V., Srivastava, M.: Heliomote: enabling long-lived sensor networks through solar energy harvesting (demo). In: Proceedings of the 3rd ACM International Conference on Embedded Networked Sensor Systems (SenSys), p. 309 (2005)
28. Yick, J., Mukherjee, B., Ghosal, D.: Wireless sensor network survey. *Comput. Netw.* **52**(12), 2292–2330 (2008)
29. Greenorbs: a long-term kilo-scale wireless sensor network system in the forest. <http://www.greenorbs.org>

30. Xie, L., Shi, Y., Hou, Y., Lou, W., Sherali, H., Midkiff, S.: On renewable sensor networks with wireless energy transfer: The multi-node case. In: 9th Annual IEEE Communications Society Conference on Sensor, Mesh and Ad Hoc Communications and Networks (SECON), pp. 10–18 (2012)
31. Xu, W., Liang, W., Lin, X.: Approximation algorithms for min-max cycle cover problems. *IEEE Trans. Comput.* **64**(3), 600–613 (2015)
32. Dai, H., Wu, X., Chen, G., Xu, L., Lin, S.: Minimizing the number of mobile chargers for large-scale wireless rechargeable sensor networks. *Comput. Commun.* **46**(15), 54–65 (2014)
33. Nagarajan, V., Ravi, R.: Approximation algorithms for distance constrained vehicle routing problems. *Networks* **59**, 209–214 (2011)
34. Kurs, A., Karalis, A., Moffatt, R., Joannopoulos, J.D., Fisher, P., Soljačić, M.: Wireless power transfer via strongly coupled magnetic resonances. *Science* **317**(5834), 83–86 (2007)
35. Anastasi, G., Conti, M., Francesco, M.D., Passarella, A.: Energy conservation in wireless sensor networks: a survey. *Ad Hoc Netw.* **7**(3), 537–568 (2009)
36. Kang, B., Ceder, G.: Battery materials for ultrafast charging and discharging. *Nature* **458**(7235), 190–193 (2009)
37. He, L., Cheng, P., Gu, Y., Pan, J., Zhu, T., Liu, C.: Mobile-to-mobile energy replenishment in mission-critical robotic sensor networks. In: IEEE 33rd International Conference on Computer Communications (INFOCOM), pp. 1195–1203 (2014)
38. Zhang, S., Wu, J., Lu, S.: Collaborative mobile charging for sensor networks. In: IEEE 9th International Conference on Mobile Adhoc and Sensor Systems (MASS), pp. 84–92 (2012)
39. Cox, D.R.: Prediction by exponentially weighted moving average and related methods. *J. Roy. Stat. Soc.* **23**, 414–422 (1961)
40. Christofides, N.: Worst-case analysis of a new heuristic for the travelling salesman problem. Technical report, Graduate School of Industrial Administration, CMU (1976)
41. Akyildiz, I.F., Melodia, T., Chowdhury, K.R.: A survey on wireless multimedia sensor networks. *Comput. Netw.* **51**(4), 921–960 (2007)

# Chapter 17

## Unmanned Aerial Vehicle-Based Wireless Charging of Sensor Networks

Carrick Detweiler, Michael Eiskamp, Brent Griffin, Jennifer Johnson,  
Jinfu Leng, Andrew Mittleider and Elizabeth Basha

**Abstract** Sensor networks deployed in remote and hard to access locations often require regular maintenance to replace or charge batteries as solar panels are sometimes impractical. In this chapter, we develop an Unmanned Aerial Vehicle (UAV) that can fly to remote locations to charge sensors using magnetic resonant wireless power transfer. We discuss the challenges of using UAVs to charge sensors wirelessly. We then present the design of a lightweight system that can be carried by a UAV as well as design a localization sensor and algorithm to allow the UAV to precisely align itself with the receiver by sensing the induced field. We also develop a number of algorithms to address the question of which sensors should be charged given a network of sensors. Finally, we experimentally verify algorithms that leverage the sensor network's ability to adapt internal communication and energy consumption patterns to optimize UAV-based wireless charging.

---

C. Detweiler (✉) · J. Leng · A. Mittleider

Nebraska Intelligent MoBile Unmanned Systems (NIMBUS) Lab, Department of Computer Science and Engineering, University of Nebraska-Lincoln, Lincoln 68588, USA  
e-mail: carrick@cse.unl.edu

J. Leng  
e-mail: jinfu.leng@gmail.com

A. Mittleider  
e-mail: amittleider@gmail.com

M. Eiskamp · J. Johnson · E. Basha  
Department of Electrical and Computer Engineering, University of the Pacific,  
Stockton 95211, USA  
e-mail: m\_eiskamp@u.pacific.edu

J. Johnson  
e-mail: j\_johnson31@u.pacific.edu

E. Basha  
e-mail: ebasha@pacific.edu

B. Griffin  
Department of Electrical Engineering and Computer Science, University of Michigan,  
Ann Arbor, MI 48109, USA  
e-mail: griffb@umich.edu

## 17.1 Introduction

Battery life continues to limit long-term deployment of wireless sensor networks for applications such as remote environmental monitoring. Typically, the batteries are charged using solar cells, but these are impractical in numerous applications where the sensors are placed in shady locations (e.g., under bridges for structural monitoring) or when they are embedded in materials (e.g., in agronomy fields for monitoring soil conditions). Wireless recharging of environmental monitoring systems addresses many of these issues, including being able to transfer power through many materials, and does not require the precise physical alignment required for contact-based charging. Getting close enough to the sensors to use medium-range wireless power transfer systems, however, can still be a challenge in many environments (e.g., a sensor under a bridge monitoring structural integrity). In this chapter, we use an Unmanned Aerial Vehicle (UAV) to wirelessly recharge sensor nodes located in hard to access outdoor environments.

Using wireless power transfer systems carried by a UAV to charge sensor nodes poses numerous challenges. First, we need to determine if this system can even be effectively carried on a payload and power-limited UAV. Typical methods for optimizing the quality factor of the power transmission coils may not be best for UAV systems that need to be lightweight and handle minor crashes that can deform coils. In addition, the UAV has specific operating voltages and battery capacities so care must be taken to ensure that sufficient energy is reserved for flight. Solving this requires designing a specialized lightweight wireless system that can be carried by a UAV. Further, GPS alone is insufficient to get close enough to the sensors to charge, so this requires additional systems to align with the sensors for efficient recharging. Second, in a network of many sensors, we need to decide the best order to charge nodes to optimize the overall lifetime of the network.

In this chapter, we solve these challenges with three solutions: (1) a novel wireless recharging system for a UAV to recharge a sensor node, (2) a localization strategy for the UAV to efficiently align with the sensor node for recharging, and (3) algorithms that effectively utilize both systems (the UAV and the sensor network) for recharging. Our first solution is our wireless recharging system, consisting of the UAV transmission system, a sensor node receiving system, and a specialized sensing system for alignment between the two. Our second solution utilizes these systems to develop an algorithm for the UAV to locate a sensor node for recharging. Our final solution develops algorithms to identify the correct node to recharge and recharges that node, using both systems collaboratively.

We demonstrate that it is possible to develop a lightweight wireless power system that can be carried by a UAV. Further, we develop a magnetic resonance sensor that can detect the induced magnetic field. This allows the UAV to localize the sensor network node within 27 cm, which enables efficient wireless power transfer. We then develop a family of heuristic algorithms that address the NP-hard problem of selecting the sequence and amount of energy to transfer to a set of sensor nodes in a network given different levels of knowledge about the network. Further, we leverage the capabilities

of the sensor network to change the routing protocols within the network to shift the energy deficit to a subset of nodes. This enables better algorithms for selecting the node to charge and the UAV can then use this information to optimize its recharging strategy while not requiring full network energy information. We test this on our sensor network platform to confirm operation.

The chapter has the following structure: Section 17.2 outlines related work. Section 17.3 describes the technical challenges in greater detail. Section 17.4 discusses our system implementation while Sect. 17.5 describes the algorithm for efficiently recharging a sensor node. Section 17.6 outlines our use of this information by the UAV to determine recharging strategies; Sect. 17.7 then discusses our work on identifying which node to recharge within the larger sensor network using both systems. Finally, we conclude with Sect. 17.8 that describes our future work.

## 17.2 Related Work

There are a wide range of techniques for wirelessly transmitting energy ranging from directed microwave energy [25] to radio frequency power harvesting [30] (see [23] for an overview of techniques). The concept of using magnetic resonance to transfer power is based on systems developed by Tesla over a century ago [34]. We use magnetic resonance wireless to transfer power from our UAV to sensors. Magnetic resonance power transfer has seen significant advances in the past decade as discussed in the other chapters in this book. We refer readers to those chapters for detailed related work on the development and advances in magnetic resonance-based power transfer. In this chapter, we focus our related work on power transfer and localization systems for UAV-based power transfer and also examine work related to wireless sensor network charging.

### 17.2.1 UAV Power Transfer and Localization

Instead of focusing on improving the efficiency of magnetically resonant wireless power transfer systems, part our research focuses on obtaining precise relative localization between the UAV carrying the power transfer system and the sensor node being charged. Since GPS is not sufficiently accurate for our purposes, we must use another localization technique. There are a number of approaches to obtaining more accurate position information for UAVs outdoors. While it is possible to use a Real Time Kinematic or Differential GPS to obtain decimeter-level accuracy [21], these systems require infrastructure, expensive receivers, and the signals may still be blocked, for instance, under bridges where we wish to operate. Altug et al. used a ground-based camera to track a UAV to provide accurate position information [2]. Optical flow, often fused with inertial measurement unit (IMU) data, has been used on UAVs to provide good position estimates over the course of a UAV mission [15],

[16, 20]. We cannot solely rely on optical flow, however, since we require submeter positioning accuracy and even the best optical flow techniques cannot provide this under all conditions. In our system, we use a velocity estimate from a simulated optical flow camera with 0.2 m/s error, which is moderate accuracy for an optical flow system as explained by Honegger et al. [16].

Simultaneous Localization and Mapping (SLAM) is an alternative approach to optical flow which, unlike optical flow, does not typically suffer from accumulated error. SLAM methods correct for drift by developing a map on which to localize. Weiss et al. used a monocular camera and IMU on a UAV to perform SLAM with only a few centimeters of error over 1 min [38]. Bachrach et al. used a laser scanner on a UAV to perform 2D SLAM inside large buildings [3]. Grzonka et al. perform SLAM in 3D on a UAV while navigating indoors [14]. While SLAM techniques on UAVs have sufficient accuracy for our system, they require significant processing systems that are heavy to carry and would greatly reduce flight time.

Our localization approach is inspired by Moore and Tedrake [27] who use a magnetic field to localize a glider UAV to perch on a power line. They use a standard magnetometer to sense the magnetic field from low-frequency, high-current power lines (40 A). They use a Kalman filter and track the magnetic field and eliminate positional ambiguity in the magnetic field sensors. They conclude that their method of localization is sufficient for a small UAV to perch on a power line; however, their system does not fully close the loop to enable control based on the sensor readings. Our work differs from theirs in a number of ways. First, our system operates at higher frequencies and lower currents so standard magnetometers do not work. Instead we develop a sensor that measures the voltage in a small resonant coil (see Sect. 17.4.2). Second, we are primarily interested in having a final position close enough to transfer power and are less interested in the trajectory during approach, which is critical to enable perching. Thus, we do not need to consider the details of vehicle dynamics, which allows us to easily adapt our approach to new vehicles. Finally, we demonstrate our system and perform full closed-loop control.

Also related to our work is methods for localizing based on radio transmissions [7, 9, 17, 24, 35, 37]. For instance, Tokekkar et al. used bearing and signal strength to locate radio tagged fish with a robotic boat [35]. They use many wireless sensor network nodes equipped with rotatable antenna to locate the fish. First, they map a relationship between the signal strength and the distance from a ground truth measurement. They fit a linear regression model of this data. When the radio strength is at its maximum value, the bearing and radio strength information is sent to a centralized computer. The position of the fish is then triangulated by creating an enclosed polygon with the bearing angles.

While we were one of the first to demonstrate charging of ground sensors from an aerial robot [13, 26], the reverse problem of how to power an aerial vehicle was looked at in 1964 to wirelessly power a flying helicopter [6] and in 2011 was used to enable a 12-h, record-length quadrotor flight [1].

Finally, we also examine the impact of embedding the sensors we are localizing and charging in different materials. Prior work by Seo et al. examined the impact of building materials such as softwood lumber, concrete brick, and drywall with insulation on wireless power transfer [32]. We add to this by also examining common outdoor materials and looking specifically at how these impact our magnetic resonant localization sensor.

### 17.2.2 Wireless Sensor Network Charging

The lifetime of a sensor network remains a performance bottleneck of many wireless sensor network applications. While this chapter focuses on recharging wireless sensor networks with a robot, many researchers take a different approach to eliminating this bottleneck. For example, Coleri et al. introduced the PEDAMACS control scheme, which shows that with an unlimited energy source for an Access Point coupled with clever transmission synchronization using Time Division Multiplexing, they are able to increase the lifetime of some networks by 1–2 years [8, 10]. Feeney et al. identified the complex relationships between energy consumption and transmission speed, transmission range, and node density [11]. This allows researchers to identify energy performance bottlenecks in a variety of wireless sensor networks. Roundy et al. reviewed many potential power sources for wireless sensor networks [29], allowing the lifetime of some networks to be prolonged.

Still, the lifetime of the network can only be lengthened so much using these methods. Recharging the network has the potential to power the network indefinitely. Bing et al. use a mobile robot to replace wireless sensor network nodes [36]. Xie et al. discuss the scenario of periodically charging sensors with a vehicle and created the concept of a renewable circle [39]. Peng and Li [28] proved the concept that wireless power transfer can effectively prolong the lifetime of the sensor network. They used an energy station to monitor the status of the nodes and then guide the behavior of the mobile charger. They also showed that optimally deciding which sensor to recharge and how much energy to recharge is NP-complete via a reduction from the Traveling Salesman Problem. Sheng et al. discussed how to use multiple mobile robots to collaboratively recharge the sensor network and proposed an optimal recharging algorithm for the scenario where nodes are distributed in one dimension [40].

In our prior work, we determined the best sink selection algorithm for improving network lifetime assuming that a UAV can recharge a single sensor node per flight [4, 18]. This work occurred in simulation only. In this chapter, we implement a combined sink selection and recharging algorithm on a sensor network; to the best of our knowledge, it is the only field experiment to do so. In addition to the sensor network implementation, in this chapter, we consider a UAV-centric approach to the problem of finding the best strategy for UAV to recharge these sensor nodes if it can only have one flight out to the network.

### 17.3 Design Consideration and Challenges

In this section, we provide an overview of wireless magnetic resonant power transfer and discuss the specific design challenges associated with UAV-based wireless power transfer systems.

Resonant power transfer has a number of advantages over other techniques. Laser- and microwave-based power transfer systems can transfer high amounts of energy, but cannot operate through materials. RFID-type systems transfer power with radio waves, but have limited power transfer capabilities. Standard inductive power transfer has a very limited transmission range. Resonant power transfer improves upon standard inductive power transfer by including two coupled resonant coils between the driven and loaded inductive coils, as seen in Fig. 17.1. In this configuration, the primary inductive coil, or Drive coil, is driven by an AC power supply. Due to the close proximity between the Drive coil and the first resonant coil, called the Tx resonant coil, oscillations occur and power is transferred to the Tx coil. The Tx coil causes the Rx coil to oscillate with a proportional degree of energy that is dependent on their coupling. The Tx and Rx coils do not have any direct load connected to them to interfere with the resonance. This allows them to couple and resonate over larger distances than is possible without resonant coils. The last coil, the Load coil, inductively receives power from the Rx coil in the same way that the Drive coil transfers energy to the Tx coil, and it applies the voltage that it gains across a load to receive the power.

In this work, we primarily consider two factors that impact resonant wireless power transfer performance: (1) the quality factor ( $Q$ ) of the coils and (2) ensuring that all coils naturally resonate at a similar frequency. The quality factor represents how well a resonant coil can hold energy without losses to heat and is defined as [5]:

**Fig. 17.1** Schematic for resonant power transfer

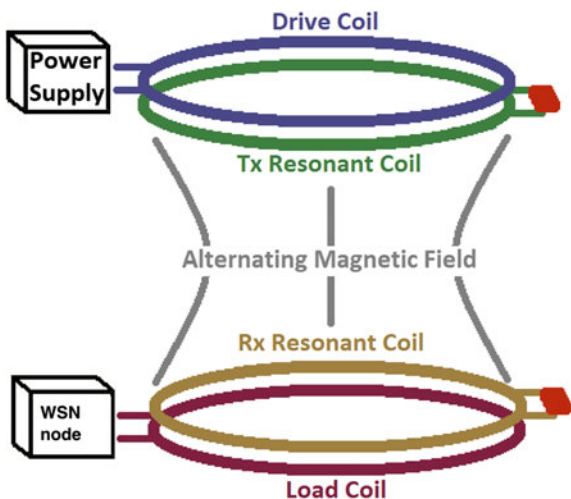
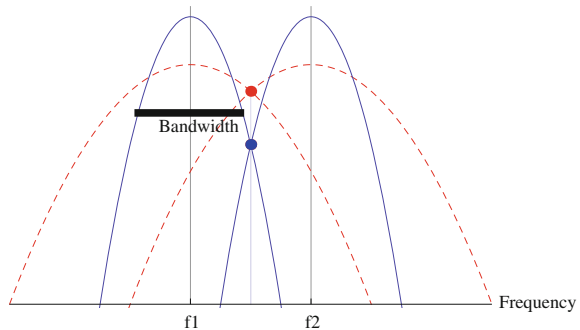


**Fig. 17.2** Coils with high quality factor (*solid blue*) can have lower coupling than those with lower quality factors (*dashed red*) due to manufacturing tolerances



$$Q = \frac{1}{R} \sqrt{\frac{L}{C}}, \quad (17.1)$$

where  $R$  is the resistance of the coil ( $\Omega$ ),  $L$  is the inductance of the coil (H), and  $C$  is capacitance (F). For details on how to compute these parameters, see [12].

Intuitively, the quality factor can be thought of as how much energy a resonant system can hold compared to energy lost during a single cycle. However, as previously stated, while maximizing the quality factor is important when trying to minimize the losses within the coils, a high  $Q$  may have a detrimental effect. In practice, the resonant frequency of all of the coils will be slightly different from each other due to manufacturing imperfections and component tolerances. High  $Q$  factors cause a decrease in the bandwidth of the resonant coil,  $\Delta f$  in Hz, which is defined as  $\Delta f = \frac{f_r}{Q}$ .

If the resonant frequency of one coil is not within the bandwidth range of the other coil, they will couple poorly as shown in Fig. 17.2. The figure represents two sets of resonant coils. The solid blue curves represent coils which have resonant frequencies  $f_1$  and  $f_2$ , respectively, and have a high  $Q$ . The higher the curves intersect on the  $y$ -axis, the higher the power transfer. Notice that the high  $Q$  means that the peak power transfer is higher if they are aligned, but because of the difference in the coils natural resonant frequency (e.g., manufacturing tolerances), they are only able to transfer at about half of the optimal performance. The red, dashed curves show coils with the same resonate at the same frequencies  $f_1$  and  $f_2$ , but lower  $Q$ . If they were precisely aligned, they would have lower overall transfer, but, since they have higher bandwidth, they better tolerate misalignment. Thus, in this configuration, using the coils with lower  $Q$  results in a higher power transfer.

While fixed, ground-based power transfer systems can be precisely tuned, this can be difficult for UAV-based systems or other field robotics applications. For instance, in order to be lightweight, our coils flex significantly during flight and, after rough landings or crashes, their shape becomes distorted. This distortion changes their resonant frequencies so, while having high  $Q$  is typically good, too high of a  $Q$  may reduce performance in many robot systems.

In addition to these considerations, with UAVs, we have to consider the construction and weight of the wireless power transfer system. One of the primary constraints for UAVs is the weight of the payload, since any increase in the payload will decrease the flight time. For low-frequency systems, power transfer systems energy losses are dominated by ohmic losses and high frequency losses by radiative losses [19]. The primary loss in our relatively low-frequency system is ohmic, which causes the coils to heat when high currents move through the slightly resistive wire coils. Ohmic loss can be decreased using a thicker gauge wire, thus decreasing resistance and increasing Q, but this adds weight to the UAV and reduces flight time. Further, a reduction in resistance can cause an increase in the switching losses due to higher currents moving through MOSFETs. Similar trade-offs must be made when adjusting the capacitance and inductance in the system to attempt to maximize the quality factor while minimizing weight.

Finally, a key consideration for designing power transfer systems for UAVs is the battery voltage available on the UAV and how drawing extra power from the UAV will impact flight time. Typically, it is better to directly use the onboard UAV battery as adding an additional battery dedicated to the power transfer system is often impractical due to the added weight. Most UAVs use high-power LiPo batteries, so most batteries can support wireless power transfer systems, although care should be taken to not exceed the maximum current rating for the batteries as the UAV motors also draw high currents. If an existing UAV is used to carry the power transfer system, then the power transfer system must be designed to operate on the specific voltage of the battery, since most UAVs are designed to use a single voltage (e.g., a three-cell LiPo). Adding transformers or step-up regulators can increase the voltage available to the power transfer system, but the weight of these systems typically reduces flight time too much to be practical. If a high or specific voltage is required for the power transfer system, then it is best to choose or design a UAV around this operating voltage.

Now that we have briefly examined the theory behind magnetic resonant wireless power transfer and discussed design considerations, we will look at the specific components of our UAV-based wireless power transfer system and wireless sensor network node.

## 17.4 System Overview

This section describes the hardware of the wireless power transfer system and the UAV. Figure 17.3 shows an overview of the wireless power transfer system on the UAV. The system consists of a UAV, the wireless power transmitter on the UAV, and the receiving wireless sensor node.

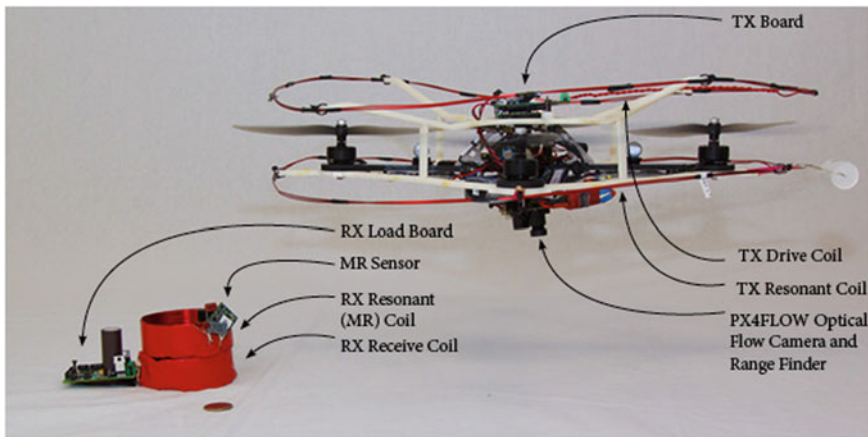


**Fig. 17.3** The wireless power transfer system

#### 17.4.1 UAV Power Transfer System

On the UAV, the TX Drive Board sends an alternating current through the Drive Coil causing an alternating magnetic field that drives the neighboring Tx Resonant Coil. The Tx Resonant Coil serves to focus the field for transmission to the Rx Resonant Coil, which is placed on the sensor network node along with the Load Coil. A magnetic resonant (MR) sensor is connected to the Rx Resonant Coil to detect the Tx system and enable localization. The Load Coil is connected to the receiving board, which draws energy from the Rx Resonant Coil. Finally, the energy from the Load Coil can be stored in the sensor network node. Table 17.1 gives an overview of the specific parameters for the coils we use in our wireless power transfer system.

**Table 17.1** Power transfer system parameters for the UAV and sensor network node coils

| Description      | Variable | Value                           |
|------------------|----------|---------------------------------|
| Coil length      | $l$      | 1.47655 m                       |
| Coil radius      | $r$      | 0.235 m                         |
| Resistance       | $R$      | 0.0143 $\Omega$                 |
| Number of wraps  | $N$      | 2                               |
| Inductance       | $L$      | $5.20068 \times 10^{-6} \Omega$ |
| Capacitance      | $C$      | $1.5 \times 10^{-7} F$          |
| Frequency        | $f_r$    | 167 kHz                         |
| Bundle thickness | $c$      | 0.004 m                         |
| Quality factor   | $Q$      | 411                             |

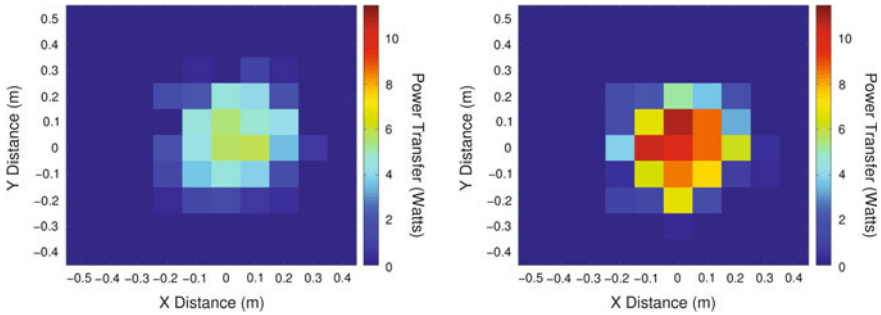


**Fig. 17.4** Power transferred to the sensor node with input voltage of (left) 12 V and (right) 24 V recorded at a constant height roughly 5 cm above the sensor

At the heart of the TX Drive Board is an AD9833 programmable waveform generator that can generate up to a 12.5 MHz signal. This signal is input into an H bridge that generates a high-power alternating current that is driven through the Drive Coil. Typically, we operate with a 9–24 V input range with a current between 1–4 Amps, although the board is designed to support up to 45 V and 8 A with a maximum power rating of up to 100 W. In addition, the TX Board has a processor to control the frequency, enable or disable power transfer, monitor voltage and current, and communicate with the ground sensors and base station with a Zigbee radio.

Figure 17.4 shows the amount of power that can be received by the device attached to the load coil using an input of 12 and 24 V. This figure shows that there is a region with a radius of approximately 30 cm that provides over 3 W of power transfer for 12 V input (our UAV operating voltage). As the distance from the transmitter to receiver increases past this radius, the amount of power transferred drops significantly. In Sect. 17.5, we show that the UAV can consistently localize to within 21 cm of the sensor. While we are less concerned with optimizing the power transfer system, it is important to note that the overall power transfer can be easily increased. Figure 17.4(right) shows that we can double the power transfer, obtaining over 10 W by doubling the input voltage. This can be accomplished using a UAV with higher operating voltage, which is preferable to adding a dedicated power transfer battery as the increased weight would significantly reduce flight time.

#### 17.4.2 Wireless Power Receiver Sensor Node

A node in the sensor network consists of the wireless power receiver board, coils, a magnetic resonant sensor, and any other sensors that are specific to the nodes application, such as vibration, temperature, soil moisture, or pressure sensors. In this chapter, we omit any application-specific sensing system; instead, we focus on the power transfer system and localizing the UAV with the sensor network node

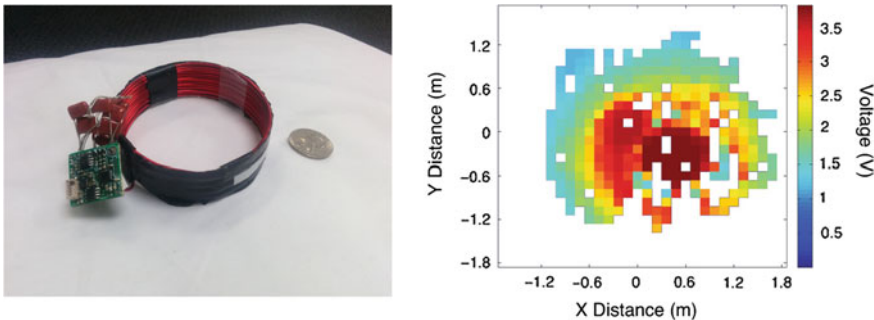


**Fig. 17.5** (left) Magnetic resonant (MR) sensor, which reads the voltage through the resonant coil and (right) a heatmap of the values read 1.0 m above the sensor (white indicates areas of no data)

using the wireless power transfer system. A sensor network node receives about 6.1 W at peak efficiency. With 6.1 W power transfer for 5 min, we nearly charge a typical rechargeable AAA battery, which can operate most types of low-power sensing systems for weeks. As with the transmitter, there is a Rx Resonant Coil in close proximity to the Load Coil. The receiver board draws energy from the Load Coil and may either use this energy directly or may charge batteries or super capacitors.

A Magnetic Resonant (MR) sensor, Fig. 17.5(left), is connected to the Rx Resonant Coil and can detect the presence of the UAV power transfer system. When the Tx system approaches, the voltage in this resonant coil increases significantly and is measured by the MR sensor. The MR sensor detects the power transfer system from three times farther away than the Rx Load Board and is thus the primary input to the localization algorithm discussed in Sect. 17.5. The MR sensor circuit consists of two opamps. The first controls the gain while the second is configured as a precision rectifier to transform the AC signal into a DC value. This value is then read by a microcontroller with a 10-bit analog-to-digital converter (ADC). Figure 17.5(right) visualizes the data returned from the MR sensors. As the transmitter approaches the MR sensor, the voltage values approach a maximum value of about 3.7 V. As the distance between the MR sensor and the transmitter increases, the voltage values approach a minimum of around 1 V.

### 17.4.3 MR Sensing Through Different Materials

We envision that the sensor network nodes charged by the UAV may be embedded in many different materials, for example, underground to monitor soil properties. In this section, we test the effect of common outdoor materials on the MR sensor to ensure it will work for this scenario.

In this experiment, the sensor network node was placed under at least 15 cm of each of the target materials (except for the steel, where it was covered with a single 1 mm sheet). The UAV flew a straight horizontal line directly over the sensor network node

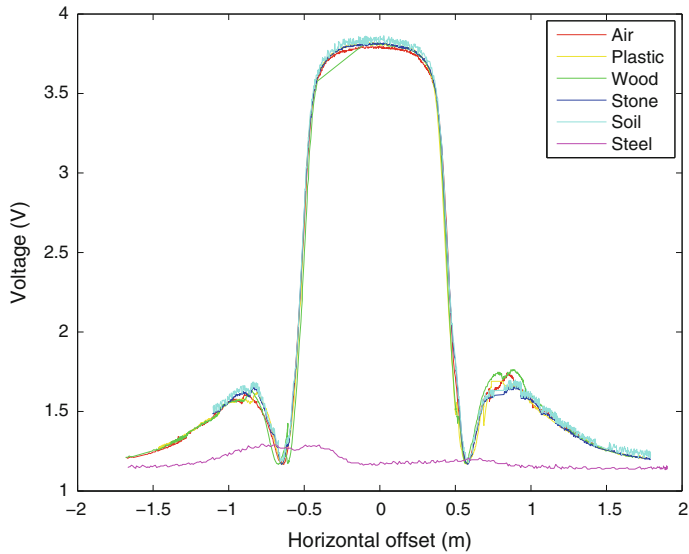


**Fig. 17.6** Voltage readings from an MR sensor which is embedded in different materials

at a constant height of 1 m, and we record the values of the MR sensor. Figure 17.6 compares the voltage through the resonant coil that is embedded in plastic, wood, stone, soil, and steel compared with a baseline measurement of air. The  $x$ -axis is the horizontal distance, which is circularly symmetric around the MR sensor. The voltage on the  $y$ -axis is used for localization and is also directly correlated with the power transfer that the sensor network node receives. As Fig. 17.6 shows, the nonferrous materials have no effect on the reception; however, the steel interferes with reception, as would other metals. This means that the sensors can be embedded in many common materials for long-term deployment.

## 17.5 Localization

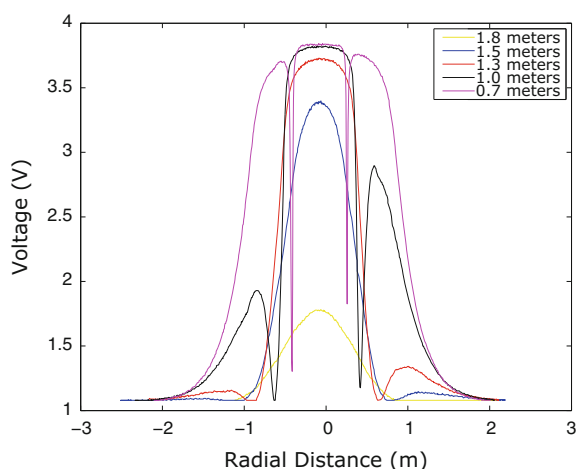
In the prior section, we explored the details of the magnetic resonant power transfer system that is attached to the UAV and the sensor network node. We showed that the system is able to transfer sufficient power to charge a low-powered sensor network node. In this section, we address the problem of using the MR sensor to align the UAV close enough to the sensor network node to improve power transfer. The UAV can use GPS to get near the location of a sensor network node, but GPS has 7.8 m error in a 95 % confidence range [33]. Since the UAV must be within 30 cm to efficiently transfer power, in this section we develop a localization algorithm that uses the sensed magnetic field and dead-reckoning information from an optical flow sensor at the sensor network to aid in localizing the UAV.

### 17.5.1 Converting Measured Voltages to Distance Measurements

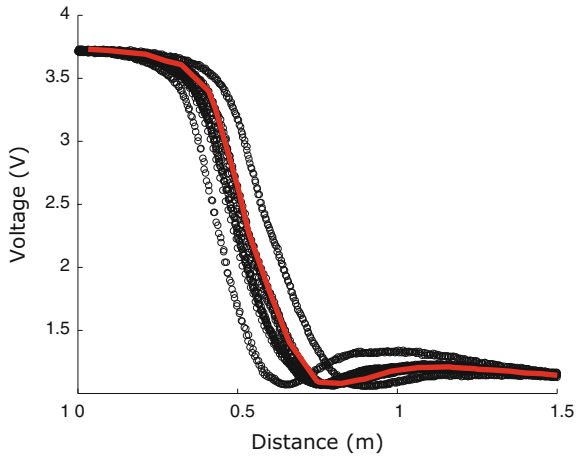
The first step in estimating the position of the UAV is to convert the voltage measurements from the MR sensors into a distance measurement. We experimentally determined this relationship between the voltage and distance. We collected the data by recording the positions of the UAV and the MR sensor readings at 52 Hz (the rate the MR sensors transmit data). The UAV flew in the  $x$  direction directly over the top of the MR sensor while holding  $y$  and  $z$  constant. Figure 17.7 shows curves that represent distances from the sensor for  $z$  values between 70 and 180 cm. These curves are circularly symmetric on any radial axis. The figure shows that, for  $z$  values which are too close to the MR sensor, there are significant lobes in the magnetic field. This may be caused by poor coupling or overcoupling that can cause destructive interference within the resonant coil [31]. The lobes make it difficult to estimate the range of the UAV because one reading may correspond to two possible ranges. However, when the UAV is sufficiently far from the sensor (in the vertical direction), the magnetic field is still strong but there are no lobes. This shows that it is best to fly with a  $z$  distance of roughly 1.3–1.6 m from the sensor, which can be accomplished using the height estimates from the acoustic range finder on our optical flow system.

Figure 17.8 shows the data (black) and model (red) from 10 passes of the UAV over the MR sensor at a height of  $1.3 \text{ m} \pm 5 \text{ cm}$ . The resulting dataset contains 6852 data points. We use this data to create a lookup table to convert the readings to ranges. The maximum range at which the MR sensor can detect the UAV is about 2.2 m; however, the model is the most accurate when the UAV is between 1.3 and 1.5 m of the sensor. We should note that in many environments we can fly within this 20 cm altitude range using the ultrasonic range finder; this may be more challenging in complex environments and is part of our future work.

**Fig. 17.7** Distance versus MR voltage received at various  $z$  values



**Fig. 17.8** MR voltage averaged over multiple runs while at a  $z$  value of 1.3 m



### 17.5.2 Localization Algorithm

Now that we have an estimate of the distance between the UAV and the MR sensor, we develop a localization algorithm for the UAV using this information. Since the MR sensor only provides a range and not direction, we need additional data to provide the direction and aid in localization. Here, we use an optical flow camera, since it can provide accurate motion estimates over short periods of time [20, 38] with higher accuracy and update rates than GPS.

---

#### Algorithm 13: Localization Algorithm

---

```

// Input: coarse position of the sensor
1 Function Localize( $x_{sc}$ ,  $y_{sc}$ )
2   GPSFlyTo( $x_{sc}$ ,  $y_{sc}$ ) // Fly to the coarse position
   // Now switch to Optical Flow + MR sensor control
3   OptFlowFlySquare( $x_{sc}$ ,  $y_{sc}$ , 2);
4   OptFlowFlyTo( $\hat{x}_s$ ,  $\hat{y}_s$ );
5   while True do // Continually refine estimate
6     | OptFlowFlyInCircle(Radius =  $d$ );
7     | OptFlowFlyTo( $\hat{x}_s$ ,  $\hat{y}_s$ );
8   end while
9 end
10 Function OnNewMRreading(Volts)
11   |  $d \leftarrow \text{Volts\_to\_range}(Volts)$ ;
12   |  $X_{uav} \leftarrow \text{Append}(X_{uav}, \hat{x}_{uav})$ ;
13   |  $Y_{uav} \leftarrow \text{Append}(Y_{uav}, \hat{y}_{uav})$ ;
14   |  $D \leftarrow \text{Append}(D, d)$ ;
15   |  $\hat{x}_s, \hat{y}_s \leftarrow \text{ArgMin}(((X_{uav} - \hat{x}_s)^2 + (Y_{uav} - \hat{y}_s)^2 - D)^2)$  // Eq. 17.2
16   | return  $\hat{x}_s, \hat{y}_s$  // The estimated position of the sensor
17 end

```

---

We use a least squares approach to find the location of the sensor network node. We find a location  $(\hat{x}_s, \hat{y}_s)$  that minimizes the difference between the position of the UAV and the range measurements from the MR sensor. Specifically, we minimize the function

$$\arg \min_{\hat{x}_s, \hat{y}_s} \sum_{i=1}^n ((\hat{x}_{uav_i} - \hat{x}_s)^2 + (\hat{y}_{uav_i} - \hat{y}_s)^2 - \hat{d}_i)^2, \quad (17.2)$$

where  $(\hat{x}_{uav_i}, \hat{y}_{uav_i})$  is the estimated position of the UAV given by the simulated optical flow camera and  $\hat{d}_i$  is the distance measurement from the MR sensor. We then find the estimated position of the MR sensor,  $(\hat{x}_s, \hat{y}_s)$ , that minimizes this function over the  $n$  readings. Using  $n$  readings prevents the minimization function from becoming overweighted with areas with dense sampling, producing erroneous position estimates from too few samples, and problems from longer term optical flow position estimation drift.

Minimizing Eq. 17.2 produces accurate position estimates as long as there are sufficient samples within 1 m of the MR sensor (as per Fig. 17.7). Algorithm 13 is the algorithm we develop to ensure good sampling of the area. This localization algorithm first approaches the position of the sensor using GPS alone (line 2). Once the UAV is near the sensor, the algorithm switches to the optical flow camera and MR sensor data. The UAV flies in a square surrounding the estimated position (lines 3 through 8) while simultaneously calculating the minimization function described in Eq. 17.2 (Line 15). After the last waypoint is reached, the UAV flies to the estimated position of the sensor given by the minimization function (line 4). It then enters a loop which continually refines the estimate (lines 5 through 8) until some other action is taken (for example, land, charge, fly home, fly to another node).

To evaluate the localization algorithm, we perform a series of trials where we placed the MR sensor in a random location in a motion capture room. Since our optical flow camera does not work well in the low lighting conditions of our test environment, we simulate the accuracy of an optical flow system through the motion capture system. Honegger et al. have shown that their optical flow system is able to provide velocity estimates to within 0.2 m/s [15]. We induce this level of error as random Gaussian noise.

The results from one experiment are shown in Figs. 17.9 and 17.10. Figure 17.9 shows the flight path in space; Fig. 17.10 shows the range readings compared to ground truth and the power transfer rate over time. During time  $t = 0$  to  $t = 5$ , since the system does not have a valid range estimate, it cannot estimate distance. The UAV continues the scripted flight until  $t = 15$  at which point it flies to the current estimate of the sensor's position. In this experiment, the system found the position within 6 cm of the true location after 24 s. At this distance, the sensor network node receives 5.49 W and the MR sensor is at 100 % of its maximum value.

We perform 20 experiments overall and all successfully found the location of the MR sensor with an average positional error of 27 cm and an average localization

**Fig. 17.9** The flight path of the UAV as it searches for the MR sensor

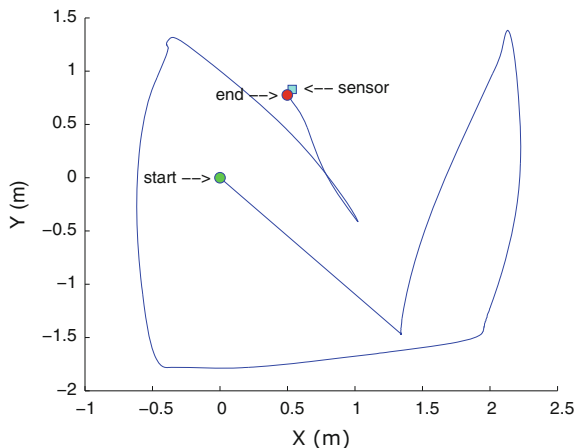
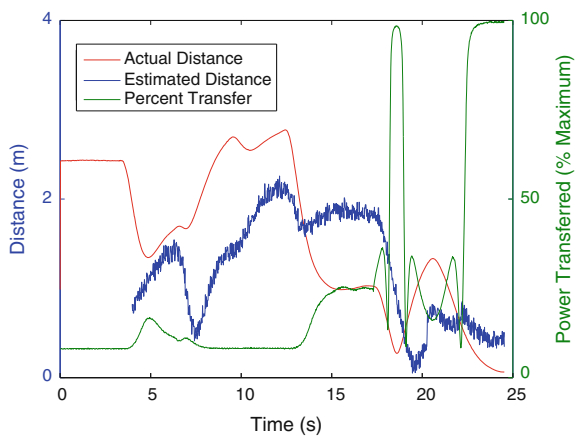


**Fig. 17.10** Localization experiment showing estimated/actual distance from the sensor node



time of 36 s. The maximum positional error is 48 cm. These experiments show that we can localize the UAV to the sensor node for good power transfer using an optical flow camera and an MR sensor.

## 17.6 Sensor Network Recharging with a UAV

With the ability to wirelessly recharge a node and optimize this recharging through localization, we now examine how to use this UAV recharging system in support of an overall sensor network. The problem requires determining the order and how much to charge sensor nodes in order to prolong the sensor network lifetime. Initially, we will examine the problem from the UAV perspective; Sect. 17.7 will then include leveraging the sensor network's processing capabilities. We develop charging

strategies for one flight of one UAV; we would rerun these algorithms for multiple flights of the UAV. We begin by formally describing the problem; then we develop algorithms based on how much information the UAV has about the sensor nodes' energy levels (no knowledge, some knowledge, and complete knowledge).

### 17.6.1 Problem Definition

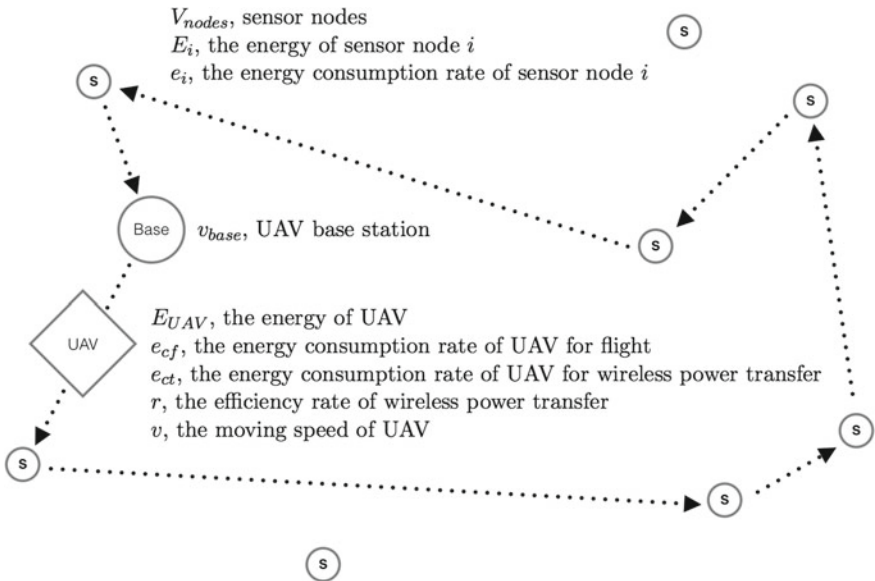
We begin by defining the problem and appropriate variables. We model the system as a graph  $G = (V, E)$ ,  $V = \{v_{base}\} \cup V_{nodes}$ , where  $v_{base}$  is the UAV base station and each vertex of the  $V_{nodes}$  is a sensor node. The set of edges,  $E$ , represent the possible UAV flight paths between the base station and the sensor nodes. These paths are defined by the shortest flight path between vertices. The UAV travels along the edges in  $E$  and stops at nodes in  $V_{nodes}$  to recharge the sensor nodes. In addition to the topology of the system, we define the energy used by the UAV. The UAV consumes energy at a rate of  $e_{cf}$  while flying and  $e_{ct}$  while transferring energy. This total energy consumed by the UAV cannot exceed energy capacity,  $e_{UAV}$ , of the UAV. We also define variables for the wireless recharging and the sensor nodes. All of these variables and notations are summarized in Table 17.2.

Figure 17.11 shows a visual representation of the problem that the algorithm solves. This example has eight sensor nodes in a configuration near the UAV base station. An example route is shown with the UAV leaving the base station, visiting six nodes, and returning to the base stations. As shown, five variables define the UAV, one variable the base station, and three variables the sensor nodes.

We also need to define the behaviors of the system in addition to its properties. The UAV must start at  $v_{base}$  and it must return to  $v_{base}$  before it consumes all of its energy. As the UAV travels through the network, when the UAV is at some sensor

**Table 17.2** Variables in UAVWS problem

| Variables                                 | Description  |
|---|--|
| $G = (V, E)$                              | The graph of the sensor nodes and UAV base station             |
| $v_{base} \in V$                          | UAV base station   |
| $V_{nodes} = V - \{v_{base}\}$            | sensor nodes   |
| $e_{UAV} \in \mathbb{R}_{>0}$             | The energy of UAV  |
| $e_{cf} \in \mathbb{R}_{>0}$              | The energy consumption rate of UAV for flight                  |
| $e_{ct} \in \mathbb{R}_{>0}$              | The energy consumption rate of UAV for wireless power transfer |
| $r \in \mathbb{R}$ and $r \in [0.0, 1.0]$ | The efficiency rate of wireless power transfer                 |
| $v \in \mathbb{R}_{\geq 0}$               | The moving speed of UAV  |
| $e_i \in \mathbb{R}_{>0}$                 | The energy of sensor node $i$                                  |
| $e_{cs\_i} \in \mathbb{R}_{>0}$           | The energy consumption rate of sensor node $i$                 |
| $T \in \mathbb{R}_{\geq 0}$               | The lifetime of the system                                     |



**Fig. 17.11** A representation of the UAV, UAV base station, and sensor nodes along with the different variables used in the definition

node, vertex  $A$ , where  $A \in V$ , it has two types of valid actions. It can move to vertex  $B$ , where  $B \in V$  and edge  $(A, B) \in E$ , or it can stay at  $A$  and charge  $A$ , if  $A \in V_{nodes}$ , for a time of  $t$ , where  $t \in \mathbb{R}^+$ . For the sensor network, at each time interval,  $e_i$  for all sensor nodes in  $V_{nodes}$  will reduce by  $e_{cs\_i}$ . Once any of the sensor nodes' energy is zero, the sensor network system is *dead*; its lifetime is the number of intervals until that occurs.

The problem is to then determine the path and charging sequence for the UAV to maximize the system lifetime. The challenge is that this problem is NP-complete; we can show this through a reduction from the metric version of the traveling salesman problem [22].

### 17.6.2 Path Planning Algorithms and Charging Algorithms

We now want to develop a set of algorithms to solve this problem; since this problem is NP-complete, we focus on heuristic algorithms. We separate the algorithms into three categories based on the UAV's knowledge of the sensor node energy levels: (1) no network energy information is known and the UAV-only discovers an individual node's energy level when it flies to the node (No Knowledge), (2) the network's initial average energy level is known in advance but the UAV-only discovers an individual node's energy level when it flies to the node (Some Knowledge), and (3)

| No Knowledge     |              | Some Knowledge   |          | Complete Knowledge |          |
|------------------|--------------|------------------|----------|--------------------|----------|
| Path Planning    | Charging     | Path Planning    | Charging | Path Planning      | Charging |
| SHORTEST CLOSEST | FULL RND FIX | SHORTEST CLOSEST | AVG      | LEAST              |          |

**Fig. 17.12** An outline of the algorithms evaluated in simulation. By combining a *Path Planning* algorithm and a *Charging* algorithm, we have 6 *No Knowledge*, 3 *Some Knowledge*, and 1 *Complete Knowledge* algorithm

all network energy information is known in advance (Complete Knowledge). All of the algorithms, except for *LEAST* (which has Complete Knowledge), break the problem down into deciding the order to visit nodes (Path Planning) and determining how much energy to transfer (Charging). This results in nine algorithms, six requiring no knowledge (two path planning approaches and three charging approaches), two requiring some knowledge (two path planning and one charging approach), and one requiring complete knowledge. Figure 17.12 outlines the nine algorithms in these three categories. We now describe the details of the algorithms.

**Path Planning:** The *Path Planning* portion of each algorithm schedules the order of nodes to visit. This order includes all nodes in the network independent of the energy required to visit the nodes as that will depend on energy charging levels and environmental conditions. To ensure that the UAV has sufficient energy to return to the base station, as the UAV traverses the network, the UAV tracks its own energy levels. If necessary, the UAV will stop its traversal of the network and return to the base station before visiting all of the sensor nodes; it will not return to visit those nodes in the current time iteration. Alternatively, after visiting all the sensor nodes, the UAV might have energy remaining; in this case, it will restart the traversal with the same path planning schedule.

We examine two path planning algorithms:

- ***SHORTEST*:** This algorithm finds the shortest route that visits each node *at least* once and returns to the base station at the end. This requires knowledge of the network topology in advance.
- ***CLOSEST*:** This greedy algorithm always moves to the closest unvisited sensor node until all the nodes are visited. If each sensor node knows its neighbors, the UAV does not have to know the topology of the network in advance, just the total number of nodes.

**Charging:** The *Charging* algorithm determines the amount of energy to transfer from the UAV to the node. We evaluate four different charging algorithms:

- ***FULL*:** Charge each candidate node to its full capacity. Charging each node to its full capacity means that the UAV may be unable to visit every node in the network due to its own energy limitations.

- **RND:** Charge each candidate node with a random amount of energy from zero to the amount that will completely charge the node.
- **FIX:** Charge each candidate node with a fixed amount of energy up to the amount that will completely charge the node.
- **AVG:** Charge each candidate node to the initial average energy level of the sensor network. If a node is at or above the initial network average, the UAV will not charge that node. This algorithm requires knowledge of the sensor network's average energy level.

**LEAST:** This algorithm requires that the UAV has complete knowledge of all sensor nodes' energy levels. It first visits the sensor node with lowest energy level, then moves to the sensor node with second lowest energy level, and so forth until it has visited all nodes. This does not generate the optimal path, but it makes sure that sensor nodes with low energy levels are charged first. The algorithm then computes the best target energy to charge all nodes while taking into account the energy required for flying, localization, etc. It may only charge a subset of the sensor nodes if this would result in a longer overall network life. Algorithm 14 gives an overview of this algorithm. The helper function `BinarySearchTargetEnergy` uses binary search to narrow the range of optimal target energy until the result satisfies a user-specified minimum accuracy requirement.

---

**Algorithm 14:** Compute Target Energy for LEAST Algorithm

---

```

1 Function ComputeTargetEnergy(nodes, UAV)
2   sn  $\leftarrow$  SortByEnergy(nodes) ;                                // Sorted nodes
3   te  $\leftarrow$  0 ;                                            // Target energy
4   nn  $\leftarrow$  len(sn) ;                                         // Node number
5   for i = 1 to nn do
6     cn  $\leftarrow$  sn[0 : i] ; // Candidate nodes, the first i nodes of the
      sorted nodes
7     te  $\leftarrow$  UAV['energy'] ;                                     // Total energy
8     te  $\leftarrow$  te - FlyingCost(cn, UAV) ;
9     te  $\leftarrow$  te - LocalizationCost(cn, UAV) ;
10    te  $\leftarrow$  te - HoveringCost(cn, UAV) ;
11    ee  $\leftarrow$  te * transferRate ; // Efficient energy for sensor nodes
12    cte  $\leftarrow$  BinarySearchTargetEnergy(ee, cn) ; // Current target energy
13    if i < nn then
14      | cte  $\leftarrow$  min(cte, nodes[i]['energy']) ;
15    end if
16    te  $\leftarrow$  max(te, cte) ;
17  end for
18  return te ;
19 end
```

---

### 17.6.3 Simulation Analysis and Results

We developed a simulation system to evaluate the performance of these nine algorithms. Table 17.3 lists the default values of all parameters used in the simulation; these parameters are based on the capabilities and empirical measurements from our UAV power transfer system. For the system topology, we start with a virtual field where the center of the field is the UAV base station. We then randomly generate a set of sensor node locations within this field. At the start of the simulation, these sensor nodes have a random amount of energy that is between 20 and 60 % of their capacity.

Our goal is to improve the lifetime of the sensor network as much as possible on a single flight of the UAV. Therefore, we use the network's average lifetime as our metric to compare the performance of the nine algorithms. We vary the area of the virtual field and the number of sensor nodes. For each system configuration, we run each algorithm 100 times.

We first vary the area of the virtual field and fix the sensor network size at eight nodes. This network size allows for easy computation of the *SHORTEST* algorithm for comparison purposes. Figure 17.13 shows the performance of algorithms deployed over three different areas: 100 m × 100 m, 200 m × 200 m, and 400 m × 400 m.

The results for each algorithm show nominal differences as the area changes since the energy used for traveling between nodes is minimal as compared to the energy used to charge nodes. Between the algorithms, we see the best lifetime with the *LEAST* algorithm that combines path planning with charging. This approach provides over five additional days of network lifetime compared to the next best

**Table 17.3** Simulation system parameters

| Variables  | Default value           |
|--|-------------------------|
| Field size   | 200 m * 200 m           |
| Number of sensor nodes   | 5                       |
| Energy of UAV: $E_{UAV}$   | 25 WH                   |
| Energy consumption rate of UAV for flight: $e_{cf}$                  | 121.91 W                |
| Energy consumption rate of UAV for hovering: $e_{ch}$                | 92.28 W                 |
| Energy consumption rate of UAV for wireless power transfer: $e_{ct}$ | 20 W                    |
| Efficiency rate of wireless power transfer $r$                       | 0.2                     |
| Moving speed of UAV: $v$   | 7.33 m/s                |
| Sensor localization time   | 36 s                    |
| Energy capacity of sensor node                                       | 2.34 WH                 |
| Energy of sensor node $i$ : $E_i$                                    | 20 % to 60 % of 2.34 WH |
| Energy consumption rate of sensor node $i$ : $e_i$                   | 1.625 mW                |

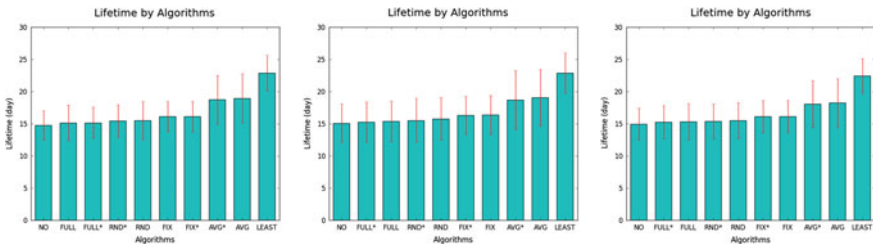


**Fig. 17.13** The performance of algorithms on sensor network of eight sensor nodes and different sizes of field (100 m × 100 m, 200 m × 200 m, and 400 m × 400 m from left to right). Error bar is for the standard error. *NO* means no charge. On default, *CLOSEST* is used for *FULL*, *RND*, *FIX*, *AVG*, and \* means *SHORTEST* is used

algorithm, *AVG*. These results show that, as the system has more information, the decisions do improve the system lifetime. With no information, however, we still can improve the network lifetime; the *FIX* algorithm still is within three days of the network lifetime of the *AVG* algorithm. Finally, among the different algorithms with no information, we do not see a difference between the two path planning algorithms.

We now skew the number of nodes while keeping the area fixed at 200 m × 200 m. Figure 17.14 shows the lifetime of the five charging algorithms as the number of nodes increases from 4 to 12. Since we did not see a difference between the path planning algorithms, we use the *CLOSEST* algorithm as it is the computationally cheapest of our two path planning algorithms. The ordering of the five algorithms based on network lifetime mirrors the earlier results; the more information we have, the better the algorithm performs. This holds across all of the network sizes; although, as Fig. 17.14 shows, the lifetime decreases with the increasing of number of sensor nodes for all algorithms.

These results imply that the UAV spends the majority of its energy on hovering and recharging the nodes, and spends less energy traveling between nodes. We can examine the implications of this for the UAV. Given that the simulation energy capacity of a sensor node is 2.34 WH and that the UAV consumes 20 W to transfer power with an efficiency rate of 0.2, the power transferred to the node is 4 W. At this rate, it would take 35 min to recharge a fully discharged node. While performing this recharging, the UAV hovers near the sensor node; the cost for it to hover is expensive with the result that the energy required to fully recharge one completely discharged node exceeds the energy capacity of the UAV. To improve this, we either need to improve the efficiency of the power transfer system or ensure that the UAV visits before nodes reach a fully discharged state.

These results also indicate the UAV behavior improves given information about the energy status of the network. In the base case, 200 m × 200 m with eight sensor nodes, with no information of the energy level of sensor nodes, the best charging algorithm achieves an 8 % improvement in network lifetime. With information of the initial average energy of sensor nodes, the charging algorithm achieves an 25 % improvement. With information of the energy level of each sensor node, the algorithm

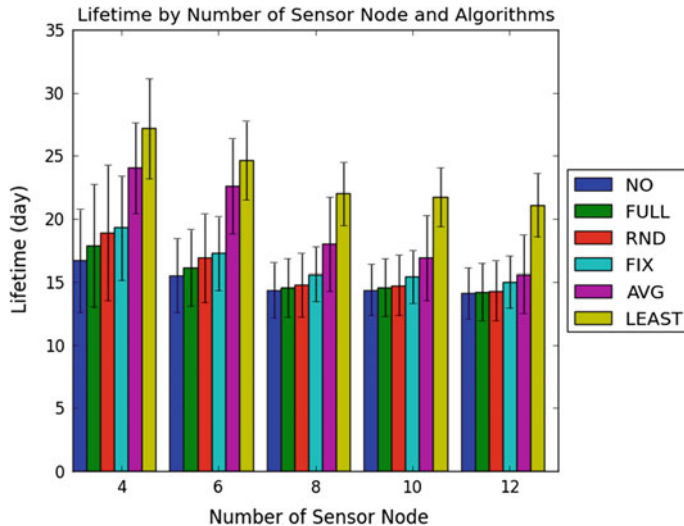


**Fig. 17.14** The performance of algorithms on sensor network of different number of sensor nodes on a 200 m × 200 m field

achieves an 50 % improvement. Therefore, we need to ensure that the UAV has the information about the sensor network; this communication is costly so we will examine methods to reduce communication and better utilize systems next.

## 17.7 Sensor Network Recharging with a UAV and a Sensor Network

As Sect. 17.6 identifies, the UAV needs information about the network to best extend the lifetime. However, this information requires significant communication between nodes and the UAV, which will limit the network's lifetime. In addition, this approach ignores the computational ability of the sensor network. In this section, we develop a combined approach that utilizes the sensor network computation in order to minimize communication. The sensor network determines which node to recharge to maximize the lifetime of the network as well as modifying its routing protocols to shift the energy deficit. The UAV then communicates with the network to gather that information, optimize its flight to that node, and recharge that node. In this section, we outline our algorithmic solutions along with our experiments on real sensor network platforms to validate our solutions.

Determining which node to recharge depends on our sensor network sink policies as that defines the communication patterns of the system. In the sensor network, the sink is the one node that controls the network and to which all other nodes forward their sensed data; this node then sends all of the data out of the network (perhaps

**Table 17.4** UAV recharge amount per grid topology

| Grid topologies | Total number of nodes | Node recharged | UAV recharge amount (%) |
|-----------------|-----------------------|----------------|-------------------------|
| 8 × 8           | 64                    | Lowest Powered | 10                      |
| 8 × 13          | 104                   | Lowest powered | 25                      |
| 8 × 18          | 144                   | Lowest powered | 55                      |
| 11 × 18         | 198                   | Lowest powered | 80                      |
| 14 × 18         | 252                   | Lowest powered | 80                      |
| 17 × 18         | 306                   | Lowest powered | 95                      |
| 20 × 18         | 360                   | Sink           | 30                      |

using the UAV). Since communication dominates power usage in a sensor network and, therefore, defines the network lifetime, nodes that must communicate more will die sooner. The nodes closest to the sink communicate the most (since they receive and forward messages from all other nodes) so the method by which the sink is selected and rotates among the nodes will define the network lifetime.

In our prior work, we examined five different sink selection algorithms to determine which will extend the network lifetime the longest when one node is recharged at each time interval [4, 18]. These algorithms are *Static*, *Random*, *Circles*, *Greedy*, and *Linear Programming*. That work determined recharging policies and sink selection algorithms based on the network size. Table 17.4 describes the recharge amount and node to recharge for which the UAV has the largest impact for each grid topology; these results are shown as a percentage of the initial node's energy. In that table, we choose which node to recharge (either the sink or the node with the lowest power) and the amount that the UAV recharges (as a percentage of the battery). For the recharging algorithm, Sect. 17.6 explored algorithms that try to charge many nodes in a single flight. To extend that work, we instead examine only recharging nodes with multiple flights; as the network size and node recharged change, the amount the UAV has to recharge a node in order to achieve the best network lifetime varies. Using these policies outlined in Table 17.4, Table 17.5 describes our sink algorithm policy for a given grid size. The best performing sink positioning algorithms for the larger three grid sizes are the *Greedy* and *Circles* algorithms.

**Table 17.5** Policy of sink algorithm choice per grid size

| Grid topologies | Number of nodes | Chosen algorithm           |
|-----------------|-----------------|----------------------------|
| 8 × 8           | 64              | All 5 Equal                |
| 8 × 13          | 104             | Static sink, Random and LP |
| 8 × 18          | 144             | Static sink                |
| 11 × 18         | 198             | Static sink                |
| 14 × 18         | 252             | Greedy                     |
| 17 × 18         | 306             | Circles                    |
| 20 × 18         | 360             | Greedy                     |

Based on this work, we implement the algorithms on our sensor network and verify the results through field experiments. We address three key questions: (1) does recharging significantly improve the network lifetime, (2) which node to recharge, and (3) which sink selection algorithm to use. First, we outline implementation details and differences between the simulation and experiments. Then, we discuss and analyze the experiment results.

### 17.7.1 Experiment System Detail and Modifications

We use our sensor nodes described in Sect. 17.4.2. The system consists of nine nodes, communicating via XBee radios. To create easily repeatable experiments, we do not use the recharging system, but simulate recharging. This allows us to ignore the UAV temporarily while analyzing our key questions. Our field experiment recharging uses 0.85 % of the starting node power level instead of the 30 % used in the simulation; this ensures that the network will die and end the experiment within a reasonable time period.

Figure 17.15 shows the control algorithm that each node follows. The process is event driven; the time interval completes once all nodes receive a new sink message from the current sink.

All XBee messages utilize a common packet structure as shown in Table 17.6. Each node can transmit three types of messages: (1) *startSink*, (2) *sendToSink*, and (3) *newSinkSelection*. At the beginning, the sink sends a *startSink* message to the rest

**Fig. 17.15** Sensor node program flow diagram

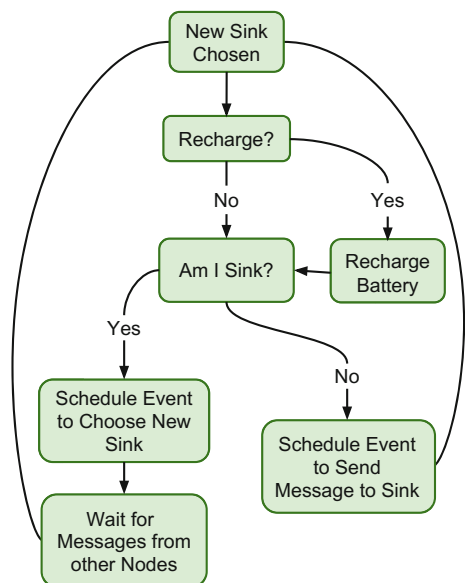


**Table 17.6** XBee packet structure

| Source ID | Destination ID | Message Type | Origin ID | Power level (3 bytes) | Iteration (2 bytes) | Packet terminator (2 bytes) |
|-----------|----------------|--------------|-----------|-----------------------|---------------------|-----------------------------|
|-----------|----------------|--------------|-----------|-----------------------|---------------------|-----------------------------|

of the network. Upon receiving this message, the other nodes schedule a *sendToSink* message. Each node has a specific time window in which its message is sent to prevent interference between the nodes; we use a 200-ms window, which allows for enough time for a single message to propagate through the network and reach the sink. This *sendToSink* message contains the power level of a node in the network and is stored by the sink. At the same time, the sink schedules a *newSinkSelection* message that selects the new sink for the next iteration of the test and broadcasts this message after receiving all *sendToSink* messages.

The *newSinkSelection* messages were not needed in the simulation where all nodes had instant information of the sink. The experiment, then, has a total of  $2 * (\text{number of nodes in network}) - 1$  extra messages transmitted and received at each sink iteration. These extra messages consume energy from the physical network that is not accounted for in the simulated network.

### 17.7.2 Experiment Results

We answer three key questions with three experiments: (1) does UAV recharging increase network lifetime, (2) which node should the UAV recharge at each sink iteration, and (3) how does the combination of the best recharging algorithm and different sink selection algorithm impact the lifetime of the network. We compare all experiment results to the simulation results from Basha et al. [4].

**Recharging Effectiveness:** The first experiment verifies that recharging extends the sensor network lifetime. To test this, we first run the sensor network with the *Static* sink selection algorithm and no recharging. We then run the sensor network with the same *Static* sink selection algorithm and introduce sink recharging of 0.85 % of starting node power. The experiment stops when the first node fails.

Figure 17.16 shows that recharging the sink in the network provides a large increase in the overall network lifetime. Without recharging, the network lives for 112 iterations, with the sink being the first node to die and end the experiment. With recharging, the network lives for 667 iterations, almost six times longer than without recharging. Unlike the first test, recharging the sink allows it to stay alive the entire test. With the other eight nodes consuming an equal amount of power, each has no power remaining at the end of the test.

Comparing the experiment to the network simulation results shown in Table 17.7, we see that the two tests have similar behaviors. The no recharging run lasts almost exactly the same time, 118 versus 112 iteration, with the slight difference due to the

**Fig. 17.16** Recharge algorithm results

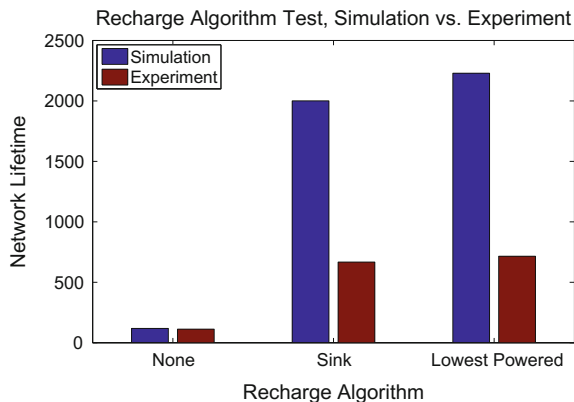


**Table 17.7** Network lifetime for recharging algorithms in simulation and experiment

| Recharge algorithm  | Simulation time | Experiment time |
|---------------------|-----------------|-----------------|
| None                | 118             | 112             |
| Sink                | 2000            | 666             |
| Lowest powered node | 2229            | 715             |

extra message sent by the sink at each time iteration. Similarly, for the recharging run, each of the neighbor nodes transmits and receives two extra messages compared to the one transmit in the simulation; the experiment should last one-third the length of the simulation, which it does at 666 iterations. Based on this, we verify the results of the simulation that determined that UAV recharging does provide a significant increase to the overall network lifetime.

**Node Recharging Selection:** This second experiment compares recharging the sink with recharging the lowest powered node. Since the sink is the node that spends the most energy receiving the messages from all the other nodes in the network, it is likely to die first. The lowest powered node, however, is the node that is most critical to the lifetime of the overall network since, if one node dies, so does the network. In this experiment, we reuse our sink recharging results. We now also run the network with the *Static* sink selection algorithm and 0.85 % recharge value, but now recharge the lowest powered node instead of the sink.

Figure 17.16 shows that the lowest powered node recharging algorithm test lasts for 715 sink iterations. Similar to the sink recharging algorithm, the lowest powered node recharging algorithm lasts significantly shorter in the experiments compared to the simulation due to the extra messages.

We calculate the theoretical maximum number of iteration to expect for the simulation and experiment based on the number of messages being sent and amount of energy added to the network at each sink iteration. In the simulation, the sink receives 8 messages, one from each node, and transmits 9 while each other node transmits

the one message to the sink. Therefore, the simulation transmits or receives a total of 25 messages in each iteration. We then subtract from that the total energy added to the network by the UAV, which is 0.85 % of 2000 or equivalent to 17 messages. Therefore, we compute the total power in the network,  $\frac{9 * 2000}{25 - 17}$ , to determine that the network lives for 2250 iterations maximum. Similarly, for the experiment, the sink receives 8 messages and transmits 10, while the other nodes transmit 2 and receive 1, which equals a total of 42 messages transmitted and received at each sink iteration. We then compute  $\frac{9 * 2000}{42 - 17}$  to get a theoretical maximum of 720 iterations before the network dies. When comparing the results of the simulation and experiment to these theoretical values, both fall just below, supporting the theory behind these results.

Since lowest powered node recharging allows the sensor network to last longer than static sink recharging, it is the best recharging algorithm for this network size. Although both do not provide the same increase in network life time as in the simulation, the percentage increase between lowest powered and static is similar for the simulation and experiment. The simulation of the lowest powered node algorithm provides an 11 % increase in network lifetime over the static algorithm. The experiment on the network shows the lowest powered algorithm providing a 7 % increase in network performance over the static algorithm.

**Sink Selection:** Finally, we find the best combination of sink selection and node recharging algorithms to maximize network lifetime. Using lowest powered node recharging, the best performing from the previous experiment, we test each of the five sink selection algorithms.

Figure 17.17 shows that the *Static* sink algorithm performs the best out of the five, which matches the simulation results. The remaining four algorithms do not follow the same ordering as the simulation, however. In the simulation, *Random* was the next best performing algorithm with *Greedy* performing the worst. In the experiments, the *Greedy* algorithm performs the next best with *Random* and *Circles* performing the worst. This result is due to slight differences in how each selects the sink (Table 17.8).

**Fig. 17.17** Sink algorithm results

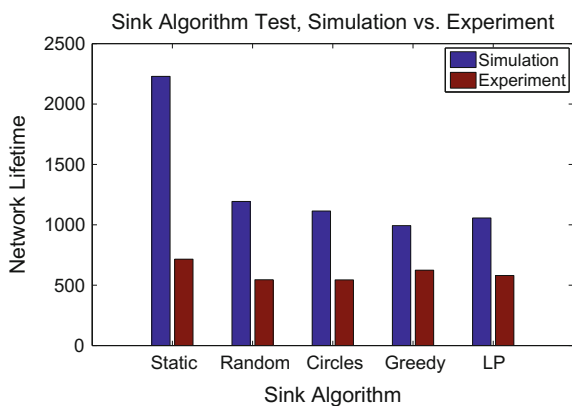


**Table 17.8** Network lifetime for sink algorithms in simulation and experiment

| Sink algorithm            | Simulation time | Experiment time |
|---------------------------|-----------------|-----------------|
| <i>Static</i>             | 2229            | 715             |
| <i>Random</i>             | 1193            | 545             |
| <i>Circles</i>            | 1114            | 544             |
| <i>Greedy</i>             | 993             | 624             |
| <i>Linear programming</i> | 1056            | 580             |

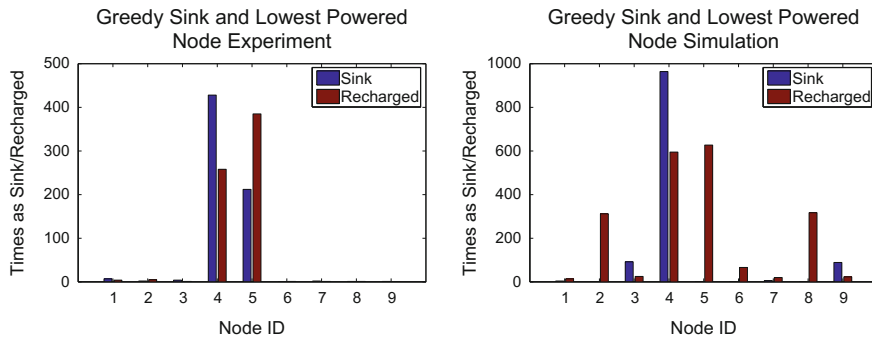
**Fig. 17.18** *Greedy* algorithm times as sink and recharged during experiment (left) and simulation (right)

Figure 17.18(left) shows the number of times the *Greedy* experiment chooses each node as the sink and the number of times the system recharges a node. The experiment selects node four as the sink over 400 times and node five approximately 200 times, while it selects the other nodes only a few times. These two nodes are also the most commonly recharged. With only these two nodes selected as sink, the algorithm requires less messages sent through the network compared to *Random*, *Circles*, or *Linear Programming*.

We now compare this to the simulation. Figure 17.18(right) shows the number of times the simulator selects each node as the sink. The nine nodes share sink duty more than the experiment. Node five is not selected, while node four is selected over 900 times, node three is selected approximately 100 times, and node nine is selected approximately 100 times. During the simulation, there are an average of about 31 messages sent per iteration. The experiment sends less messages per iteration, an average of approximately 27, due to the small differences in sink selection. Since the experiment averages less messages each iteration, the *Greedy* algorithm performs better than in the simulation compared to the other sink selection algorithms.

Calculating the relative lifetime of the network, the four other algorithms last 45 to 54 % of the lifetime of the *Static* algorithm in the simulation. On the physical sensor network, the other algorithms last 77 to 87 % of the lifetime of the *Static* sink selection algorithm, due to the introduction of the new messages sent during the experiments.

Overall, the *Static* sink selection algorithm with the lowest powered node recharging algorithm outperforms the other sink selection and recharging algorithms. With these results, we verify that the simulation accurately represents the behavior of a real sensor network of the size used in our experiments.

The UAV-only experiments of Sect. 17.6 provide path planning algorithms for the UAV to best visit the nodes; this section provides sensor network algorithms to identify the best node to recharge. Moving forward, we want to connect these two pieces together into a complete system and full outdoor field experiments. Some small modifications are needed to achieve this. First, the sensor network algorithms need to identify an number of nodes to recharge instead of just one; this will provide the best information to leverage the UAV algorithms. Second, the UAV and sensor network need a shared communication strategy that optimizes the energy of both while not forcing the UAV to always fly to the sink (which it would not know in advance).

## 17.8 Conclusion and Future Work

This chapter described the development of a UAV-based wireless power transfer and localization system designed to allow the UAV to charge sensor network nodes in remote locations. We discussed the challenges specific to developing UAV-based wireless power transfer systems. We developed a power transfer system that is light-weight enough to be carried by a UAV and meets the other design challenges. In the future, we plan to investigate adaptive systems that actively adjust the frequency and impedance to further optimize power transfer. The localization system we developed can localize the UAV with respect to the sensor node by sensing the induced magnetic field. It can localize to within 30 cm to transfer over 3 W of power to the sensor node. We tested the operation through a variety of materials where sensor network nodes may be embedded. In future, we plan to test the localization system in a variety of outdoor environments to verify functionality when faced with wind and other factors.

We then developed algorithms that define how a UAV equipped with these systems can recharge a network of sensor nodes. First, we considered it from a UAV-only perspective and develop heuristic algorithms to select the order and amount to charge nodes, which is an NP-hard problem. This enables significant improvements to the life of the sensor network with only a single charging flight, but is limited to relatively small networks.

We also developed algorithms that leverage the communication and computation capabilities of the sensor network to shift the energy deficit to a small subset of nodes to allow the UAV to effectively charge those nodes. We verified these algorithms on sensor network hardware and showed that this enables significant sensor network lifetime improvements for larger sensor networks even if only a single sensor node is charged per UAV flight. In the future, we plan to validate the sensor network charge selection algorithms with larger scale field experiments. We also plan to extend the

system to use multiple UAVs recharging the same network and adaptively determine the time intervals in which the UAVs should recharge the network. This work will help extend sensor network lifetimes, providing more complete monitoring information.

**Acknowledgements** This work was partially supported by NSF 1217400, NSF 1217428, and USDA-NIFA 2013-67021-20947.

## References

1. Achtelik, M.C., Stumpf, J., Gurdan, D., Doth, K.M.: Design of a flexible high performance quadcopter platform breaking the mav endurance record with laser power beaming. In: International Conference on Intelligent Robots and Systems (IROS), pp. 5166–5172 (2011)
2. Altug, E., Ostrowski, J., Taylor, C.: Quadrotor control using dual camera visual feedback. Int. Conf. Robot. Autom. (ICRA) **3**, 4294–4299 (2003)
3. Bachrach, A., He, R., Roy, N.: Autonomous flight in unknown indoor environments. Int. J. Micro Air Veh. **1**(4), 217–228 (2009)
4. Basha, E., Eiskamp, M., Johnson, J., Detweiler, C.: Uav recharging opportunities and policies for sensor networks. Int. J. Distrib. Sens. Netw. **10** (2015)
5. Bishop, O.: Electronics—Circuits and Systems. Taylor & Francis (2012)
6. Brown, W.C.: The history of power transmission by radio waves. Trans. Microw. Theory Tech. **32**(9), 1230–1242 (1984)
7. Cliff, O.M., Fitch, R., Sukkarieh, S., Saunders, D.L., Heinsohn, R.: Online localization of radiotagged wildlife with an autonomous aerial robot system. In: Proceedings of Robotics Science and Systems XI, pp. 13–17 (2015). <http://www.roboticsproceedings.org/rss11/p42.pdf>
8. Coleri, S., Puri, A., Varaiya, P.: Power efficient system for sensor networks. In: International Symposium on Computers and Communication, pp. 837–842 (2003)
9. Deyle, T., Reynolds, M.S., Kemp, C.C.: Finding and navigating to household objects with UHF RFID tags by optimizing RF signal strength. In: 2014 IEEE/RSJ International Conference on Intelligent Robots and Systems (IROS 2014), pp. 2579–2586 (2014). doi:[10.1109/IROS.2014.6942914](https://doi.org/10.1109/IROS.2014.6942914)
10. Ergen, S.C., Varaiya, P.: Pedamacs: power efficient and delay aware medium access protocol for sensor networks. Trans. Mob. Comput. **5**(7), 920–930 (2006)
11. Feeney, L.M., Nilsson, M.: Investigating the energy consumption of a wireless network interface in an ad hoc networking environment. Conf. IEEE Comput. Commun. Soc. **3**, 1548–1557 (2001)
12. Griffin, B.: Automated resonant wireless power transfer to remote sensors from an unmanned aerial vehicle. Master's thesis, University of Nebraska—Lincoln, NE (2012)
13. Griffin, B., Detweiler, C.: Resonant wireless power transfer to ground sensors from a UAV. In: Proceedings of IEEE International Conference on Robotics and Automation (ICRA) (2012)
14. Grzonka, S., Grisetti, G., Burgard, W.: A fully autonomous indoor quadrotor. Trans. Rob. **28**(1), 90–100 (2012)
15. Honegger, D., Greisen, P., Meier, L., Tanskanen, P., Pollefey, M.: Real-time velocity estimation based on optical flow and disparity matching. In: International Conference on Intelligent Robots and Systems (IROS), pp. 5177–5182 (2012)
16. Honegger, D., Meier, L., Tanskanen, P., Pollefey, M.: An open source and open hardware embedded metric optical flow cmos camera for indoor and outdoor applications. In: International Conference on Robotics and Automation (IROS) (2013)
17. Hook, J.V., Tokekar, P., Isler, V.: Algorithms for cooperative active localization of static targets with mobile bearing sensors under communication constraints. IEEE Trans. Rob. **31**(4), 864–876 (2015)

18. Johnson, J., Basha, E., Detweiler, C.: Charge selection algorithms for maximizing sensor network life with UAV-based limited wireless recharging. In: Proceedings of IEEE International Conference on Intelligent Sensors, Sensor Networks and Information Processing (ISSNIP) (2013)
19. Karalis, A., Joannopoulos, J.D., Soljačić, M.: Efficient wireless non-radiative mid-range energy transfer. *Ann. Phys.* **323**(1), 34–48 (2008)
20. Kendoul, F., Fantoni, I., Nonami, K.: Optic flow-based vision system for autonomous 3d localization and control of small aerial vehicles. *Robot. Auton. Syst.* **57**(6), 591–602 (2009)
21. LAB, N.J.P.: The global differential gps system. *Science*
22. Leng, J.: Using a uav to effectively prolong wireless sensor network lifetime with wireless power transfer. Master's thesis, University of Nebraska—Lincoln, NE (2014)
23. Lu, X., Wang, P., Niyato, D., Kim, D.I., Han, Z.: Wireless charging technologies: Fundamentals, standards, and network applications (2015)
24. Martinelli, F.: Robot localization using the phase of passive UHF-RFID Signals Under Uncertain Tag Coordinates. *J. Intell. Robot. Syst.* 1–17 (2015)
25. McSpadden, J.O., Mankins, J.C.: Space solar power programs and microwave wireless power transmission technology. *Microwave Mag.* **3**(4), 46–57 (2002)
26. Mittleider, A., Griffin, B., Detweiler, C.: Experimental analysis of a uav-based wireless power transfer localization system. In: Proceedings of International Symposium on Experimental Robotics (ISER) (2014)
27. Moore, J., Tedrake, R.: Magnetic localization for perching uavs on powerlines. In: 2011 IEEE/RSJ International Conference on Intelligent Robots and Systems (IROS), pp. 2700–2707. IEEE (2011)
28. Peng, Y., Li, Z., Zhang, W., Qiao, D.: Prolonging sensor network lifetime through wireless charging. In: RTSS, pp. 129–139 (2010)
29. Roundy, S., Steingart, D., Frechette, L., Wright, P., Rabaey, J.: Power sources for wireless sensor networks. In: Karl, H., Wolisz, A., Willig, A. (eds.) *Wireless Sensor Networks*. Lecture Notes in Computer Science, vol. 2920, pp. 1–17. Springer, Berlin Heidelberg (2004)
30. Sample, A., Smith, J.R.: Experimental results with two wireless power transfer systems. In: Radio and Wireless Symposium, pp. 16–18 (2009)
31. Sample, A.P., Meyer, D.A., Smith, J.R.: Analysis, experimental results, and range adaptation of magnetically coupled resonators for wireless power transfer. *Trans. Industr. Electron.* **58**(2), 544–554 (2011)
32. Seo, Y.S., Hughes, Z., Hoang, M., Isom, D., Nguyen, M., Rao, S., Chiao, J.C.: Investigation of wireless power transfer in through-wall applications. In: Microwave Conference Proceedings (APMC), pp. 403–405 (2012)
33. N.C.O. for Space-Based Positioning NavigationTiming, Global positioning system standard positioning service performance standard 4e. science
34. Tesla, N.: Apparatus for transmitting electrical energy (1914)
35. Tokekar, P., Bhaduria, D., Studenski, A., Isler, V.: A robotic system for monitoring carp in minnesota lakes. *J. Field Robot.* **27**(6), 779789 (2010)
36. Tong, B., Wang, G., Zhang, W., Wang, C.: Node reclamation and replacement for long-lived sensor networks. *IEEE Trans. Parallel Distrib. Syst.* **22**(9), 1550–1563 (2011)
37. Wang, J., Schluntz, E., Otis, B., Deyle, T.: A new vision for smart objects and the Internet of Things: mobile robots and long-Range UHF RFID sensor tags (2015). [arXiv:1507.02373](https://arxiv.org/abs/1507.02373)
38. Weiss, S., Scaramuzza, D., Siegwart, R.: Monocular-slambased navigation for autonomous micro helicopters in gps-denied environments. *J. Field Robot.* **28**(6), 854–874 (2011)
39. Xie, L., Shi, Y., Hou, Y.T., Sherali, H.D.: Making sensor networks immortal: an energy-renewal approach with wireless power transfer. *Trans. Networking* **20**(6), 1748–1761 (2012)
40. Zhang, S., Wu, J., Lu, S.: Collaborative mobile charging for sensor networks. In: International Conference on Mobile Adhoc and Sensor Systems (MASS), pp. 84–92 (2012)

# Chapter 18

## Wireless Power Transfer in Sensor Networks with Adaptive, Limited Knowledge Protocols

Constantinos Marios Angelopoulos, Sotiris Nikoletseas  
and Theofanis P. Raptis

**Abstract** In this chapter, we investigate the problem of efficient wireless power transfer in Wireless Rechargeable Sensor Networks (WRSNs). In such networks a special mobile entity (called the Mobile Charger) traverses the network and wirelessly replenishes the energy of sensor nodes. In contrast to other approaches, we envision methods that are distributed, adaptive and use limited network information. We propose three new, alternative protocols for efficient charging, addressing key issues which we identify, most notably (i) to what extent each sensor should be charged (ii) what is the best split of the total energy between the charger and the sensors and (iii) what are good trajectories the Mobile Charger should follow. One of our protocols (**LRP**) performs some distributed, limited sampling of the network status, while another one (**RTP**) reactively adapts to energy shortage alerts judiciously spread in the network. We conduct detailed simulations in uniform and non-uniform network deployments, using three different underlying routing protocol families. In most cases, both our charging protocols significantly outperform known state of the art methods, while their performance gets quite close to the performance of the global knowledge method (**GKP**) we also provide.

---

C.M. Angelopoulos (✉)  
Bournemouth University, Bournemouth, UK  
e-mail: mangelopoulos@bournemouth.ac.uk

S. Nikoletseas · T.P. Raptis  
Department of Computer Engineering and Informatics, University of Patras and  
Computer Technology Institute and Press “Diophantus” (CTI), Patras, Greece  
e-mail: nikole@cti.gr

T.P. Raptis  
Institute of Informatics and Telematics, National Research Council, Moruzzi Str 1,  
56124 Pisa, Italy  
e-mail: theofanis.raptis@iit.cnr.it

## 18.1 Introduction

The last decade energy harvesting technologies have been effectively integrated into wireless sensor networks. A variety of ambient energy, such as mechanical, thermal, photovoltaic and electromagnetic energy, can be converted into electrical energy to charge sensor batteries. However, as all these energy sources come from the external environment and their spatial-temporal profiles exhibit great variations, the strength of harvested energy is typically low, and especially sensitive to the environmental dynamics. As there is generally a lack of a priori knowledge of energy profiles, such dynamics impose much difficulty on the design of protocols that try to keep sensors from running out of energy.

Wireless power transfer technologies offer new possibilities for managing the available energy in wireless sensor networks and pave the way towards *a new paradigm* for wireless sensor networks; the *Wireless Rechargeable Sensor Networks (WRSNs)*. WRSNs consist of sensor nodes that may be either stationary or mobile, as well as few mobile nodes with high energy supplies. The latter, by using wireless power technologies are capable of fast recharging [10] sensor nodes. This way, the highly constrained resource of energy can be managed in great detail and more efficiently. Another important aspect is the fact that energy management in WRSNs can be performed passively from the perspective of the sensor nodes and without the computational and communicational overhead introduced by complex energy management algorithms. Finally, WRSNs allow energy management to be studied and designed independently of the underlying routing protocol used for data propagation.

**The Problem.** Let a Wireless Rechargeable Sensor Network comprised of *stationary* sensor nodes and *a single, special mobile entity called the Mobile Charger*. The Mobile Charger has significant (yet finite) energy supplies, that are much larger than those of each sensor node, and is thus capable of recharging the sensors in the network.

We aim at designing and evaluating efficient strategies for several critical aspects of the Mobile Charger's configuration in order to improve energy efficiency, prolong the lifetime of the network and also improve important network properties (such as the quality of network coverage, the robustness of data propagation).

We focus on the cases of both *randomly heterogeneous* and *homogeneous* sensor nodes deployment. An underlying routing protocol is taking care of the data propagation from sensors to the Sink. Unlike other methods in the state of the art, *we do not couple the charging process and the data propagation*; actually, we wish to perform efficient wireless energy transfer in a way which is agnostic to the routing protocol, via adaptive techniques that (without knowing the routing protocol) *implicitly adapt to any routing protocol*.

*Remarks.* We note that, although the wireless recharging problem might look similar to other related research problems (such as aggressive data collection via mobile Sinks), it admits special features that necessitate a direct approach, while the optimization of concrete trade-offs and the fine-tuning of design alternatives that arise in

wireless recharging necessitate the distinct investigation of special protocol design parameters (like the extent of wireless recharging at each node, the energy split between the charger and the nodes etc.) mentioned above.

Finally, we note that such charger optimization problems are (inherently) computationally hard, e.g. in [1] we have formulated the wireless recharging problem as the Charger Dispatch Decision Problem (CDDP), and showed that it is *NP*-complete (via reduction from Geometric Travelling Salesman Problem, G-TSP; example [5], p. 212).

**Our contribution.** While interesting research has been contributed to the wireless recharging problem and particularly to the scheduling of the mobile charger, most methods necessitate significant (in many cases even global) network knowledge (e.g. it is assumed that the charger knows the energy levels of all sensors in the network) and the solutions are centralized. On the contrary, the methods we design are *distributed and adaptive, and use only local (or limited) network information*. Also, unlike many state of the art approaches that opt for integration and coupling of the recharging and routing problems, our methods can be used together with *any underlying routing protocol* (since they adapt on it implicitly). Furthermore, our protocols dynamically and distributively *adapt to network diversities, e.g. they cope well with heterogeneous node placement* (while still behaving very well in the homogeneous case too).

In particular, we propose and evaluate selected *alternative strategies for efficient recharging* in stationary WRSNs via a single Mobile Charger. Our design provides concrete, different solutions to some *key issues (and the associated trade-offs)* of wireless recharging which we identify, most notably

- (i) given that the energy the Mobile Charger is finite, *to what extent each sensor should be charged*,
- (ii) what should be the *split of the total available energy* between the charger and the sensors and
- (iii) what are *good trajectories the Mobile Charger should follow* in order to charge the sensor nodes.

More specifically, (a) we first introduce *a new network attribute*, which we call *node criticality*, capturing both the energy consumption at the node over time and the traffic flow served by the node (b) taking the node criticality of each sensor node into account, we suggest *a particular amount of energy the sensor node should be charged* to when visited by the mobile charger (c) for the trajectory followed by the mobile charger, we design *three alternative strategies* (GKP, LRP, RTP) assuming different levels of network knowledge (from global to limited and reactive); actually, we view the global knowledge protocol as a performance upper bound to which the two distributed, partial knowledge protocols are compared with.

One of our protocols (LRP) performs some distributed, limited sampling of the network status, while another one (RTP) reactively adapts to energy shortage alerts judiciously spread in the network. As detailed simulations demonstrate, both protocols significantly outperform known state of the art methods, while their performance gets quite close to the performance of the global knowledge method (GKP) which we also provide.

## 18.2 Related Work and Comparison

Recently, there has been much research effort in WRSNs. In [21] the authors consider a sensor network in which a mobile entity is employed which (in contrast to our approach) serves also as a data collector and as an energy transporter that charges the stationary sensors on its migration tour. They provide a two-step approach: in the first step the mobile entity selects the maximum number of anchor points such that the sensors located in these anchor points hold the least energy and meanwhile the tour length is no more than a threshold. In the second step they formulate a utility maximization problem on a flow-level network model in order to determine how to gather data from sensors. However this algorithm requires global information, thus making it not very practical in even medium-sized sensor networks.

In [12] the authors analyse again the possibility of practical and efficient joint routing and charging schemes. They propose a sensor network in which both a mobile charger and a base station appear. Each sensor sends data hop-by-hop to the Sink periodically using the Collection Tree Protocol. Also, measurements of other local properties such as energy level, consumption rate, etc., are piggybacked along with data and reported to the Sink. Then, the base station, according to sensors information, schedules future charging activities and commands the mobile charger through long-range radio to execute the schedules. Authors show that the network lifetime is prolonged by the mobile charger which mostly moves in energy-minimum paths. However, each sensor has to send more data to the Sink and the charger has to know the location of each sensor *a priori*.

Authors in [16, 19] consider the scenario of a mobile charging vehicle periodically traveling inside the sensor network and charging the battery of each sensor node wirelessly. The necessary and sufficient conditions are introduced and the problem is studied as an optimization problem, with the objective of maximizing the ratio of the wireless charging vehicle's vacation time over the cycle time. Also, in [18], the authors collocate the mobile base station on the Mobile Charger and minimize the energy consumption of the entire system while ensuring none of the sensor nodes runs out of energy. In contrast to our protocols, the models used in the above works use global knowledge.

In [14] the authors build a proof-of-concept prototype by using a wireless power charger installed on a robot and sensor nodes equipped with wireless power receivers, carry out experiments on the prototype to evaluate its performance in small-scale networks of up to ten nodes, and conduct simulations to study its performance in larger networks of up to a hundred nodes. Despite the fact that this paper nicely demonstrates the feasibility of a real, implemented WRSN, the simulations of the proposed heuristics are limited to a small number of sensor nodes in the network, an approach that is not convenient for highlighting the behavior of the charging protocol in large scale networks.

In [11], the authors formulate an energy-constrained wireless charging problem, which maximizes the number of sensors wirelessly charged by a Mobile Charger. The paper proposes heuristic solutions based on the meta-heuristics of Particle Swarm

Optimization but, in contrast to our approach, the model assumes extensive knowledge on the charger and the performance evaluation is limited to simulations on small-scale networks.

In previous work of our group in [1] the authors study the impact of the charging process to the network lifetime for selected routing protocols. They propose a mobile charging protocol that locally adapts the circular trajectory of the mobile charger to the energy dissipation rate of each sub-region of the network. They compare this protocol against several other trajectories by a detailed experimental evaluation. The derived findings demonstrate performance gains, but are *limited to uniform network deployments*, in contrast to our approach which focuses on heterogeneous node distributions.

Alternative versions of the problem have also attracted important research attention. In [13, 17, 20] the authors consider the wireless recharging problem, using multiple mobile chargers. In this case, several other interesting aspects emerge, such as the minimum number of chargers that suffice to cover the network area, inter-charger coordination etc. Another interesting approach is presented in [4], where the charging process is conducted using another, RFID-based technology resulting in the introduction of the charging delay notion and different modeling of the problem.

Overall, in the majority of the above methodologies, the knowledge of the model is much stronger than ours, allowing for offline and/or centralized optimization under high levels of network information. Also, in several of these approaches the charging problem is coupled together with routing, while in our method the charging policy implicitly adapts to any underlying routing policy. For this reason, we have chosen to compare with the protocols presented in [1, 14], in order to be fair in terms of the model assumptions. Our strategies here significantly extend the ones in [1] via also taking into account the traffic served by a node (not just its energy levels). This gives rise to *completely new configurations* of the Mobile Charger (one based on a limited network knowledge and a reactive one) that significantly outperform (especially in heterogeneous settings) the ones in [1]; even in uniform placements, our protocols perform similar or better to the ones in [1].

### 18.3 The Model

We consider a plane sensor network, in which the sensors and the single Sink node are stationary. We abstract the network by a graph  $G(V, E)$ , where  $V = \{v_1, v_2, \dots, v_n\}$  denotes the set of nodes (sensors), while  $E \subseteq V^2$  represents the set of edges (wireless links). An edge between two nodes in the graph exists iff the distance between the corresponding sensors in the network is less than or equal the transmission range  $r$ .

Without loss of generality, we assume that network deployment area is a circle of radius  $D$ . We virtually slice the network into  $M = D/r$  co-centric Rings and  $N = 2\pi/\phi$  Slices. A Sector is defined as the intersection of a specific Ring and Slice. For example, in Fig. 18.1 the network is divided into 12 Slices ( $\phi = \pi/6$ ) where

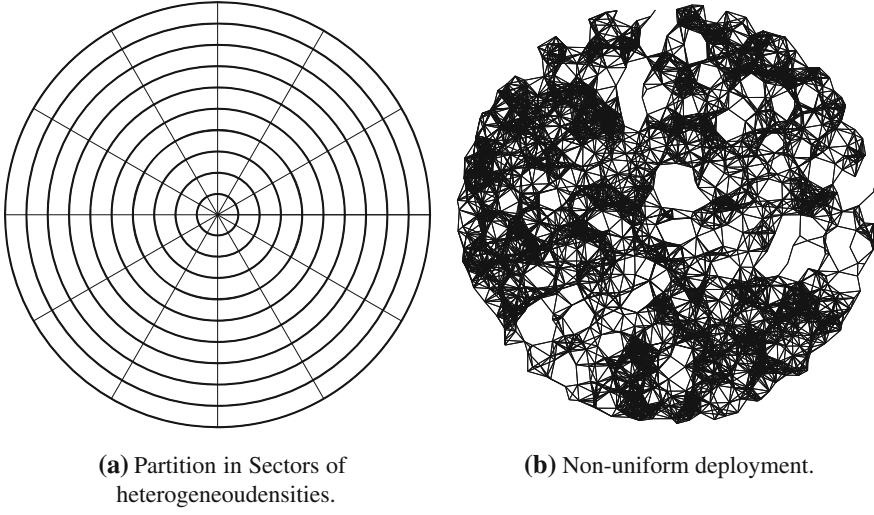


**Fig. 18.1** Network deployment

each Slice contains 10 Sectors, resulting in a total of 120 sectors in the network. An example of non-uniform network deployment is shown in Fig. 18.1.

**Placement heterogeneity.** We consider random instances of the following quite general model of non-uniform deployment: Denote by  $S_{ij}$  the sector corresponding to the intersection of Slice  $i$  and Ring  $j$ . Let  $b > 1$  be an arbitrary constant. Each sector  $S_{ij}$  chooses independently a number  $\delta_{ij} \in [1, b]$  according to the uniform distribution  $\mathcal{U}[1, b]$ . We will refer to the number  $\delta_{ij}$  as the relative density of sector  $S_{ij}$ . Values of  $\delta_{ij}$  close to 1 imply low relative density and values close to  $b$  imply high relative density. By combining the knowledge about the total number of sensors in the network  $n$ , together with the relative density  $\delta_{ij}$  and the area  $A_{ij}$  of every Sector, we compute the number of nodes  $n_{ij}$  deployed in sector  $S_{ij}$  by the following formula:

$$n_{ij} = \frac{n}{\sum_{i',j'} \frac{A_{i'j'}}{A_{ij}} \frac{\delta_{i'j'}}{\delta_{ij}}}$$

where  $n = \sum_{i,j} n_{ij}$ . Finally, we scatter  $n_{ij}$  nodes in the area corresponding to sector  $S_{ij}$ . The fraction of the actual densities of two sectors  $S_{ij}$  and  $S_{i'j'}$  is exactly  $\frac{A_{i'j'}}{A_{ij}} \frac{\delta_{ij}}{\delta_{i'j'}}$ . Furthermore, if all Sectors have the same relative density (i.e.  $\delta_{ij} = \delta_{i'j'}$ , for all  $i', j'$ ), we get the uniform deployment.

Each sensor node knows its location, has a unique ID and belongs to exactly one Sector. Each node can identify in which Slice it belongs to. This information can be disseminated through a setup phase initiated by the Sink during which the position of the Sink and the IDs of the nodes in neighboring Slices is diffused. Our protocols operate at the network layer, so we are assuming appropriate underlying data-link, MAC and physical layers. The nodes' memory is assumed limited and each node

chooses independently a relative data generation rate  $\lambda_i \in [c, d]$  (where  $c, d$  constant values) according to the uniform distribution  $\mathcal{U}[c, d]$ . Values of  $\lambda_i$  close to  $c$  imply low data generation rate and values close to  $d$  imply high data generation rate. We consider two types of data transmission: (a) single-hop transmission (cheap in terms of energy and slow) between two neighboring nodes and (b) direct transmission (expensive in terms of energy and fast) where the node that holds the data transmits directly to the Sink. We assume that the energy spent at a sensor when transmitting data messages is proportional to the square of the transmitting distance and only energy spent during transmissions is counted (for simplicity).

We assume a single, Mobile Charger that traverses the network and wirelessly charges sensor nodes when getting appropriately close to them. We assume that  $E_{total}$  is the total available energy in the network (at the sensors and at the charger). Initially

$$E_{total} = E_{sensors} + E_{MC}(t_{init})$$

where  $E_{sensors}$  is the amount of energy shared among the sensor nodes and  $E_{MC}(t_{init})$  is the total amount of energy that the Mobile Charger may deliver to the network by recharging sensors. At time  $t$  the energy left to the Mobile Charger for sensor charging is denoted as  $E_{MC}(t)$  and the current residual energy of node  $v_i$  as  $E_i(t)$ . The maximum amount of energy that a single sensor may store is denoted as  $E_{sensor}^{max}$  and is the initial energy given to each sensor, i.e.  $E_{sensor}^{max} = \frac{E_{sensors}}{n}$ . In our model the charging is performed point-to-point, i.e. only one sensor may be charged at a time from the Mobile Charger by approaching it at a very close distance so that the charging process has maximum efficiency. The time that elapses while the Mobile Charger moves from one sensor to another is considered to be very small when compared to the charging time; still the trajectory followed (and particularly its length) is of interest to us, since it may capture diverse cost aspects. We assume that the charging time is inversely proportional to the battery level of each sensor.

Regarding the three families of routing protocols we use to investigate the impact of our methods, we refer to [8] for clustering, [2, 6] for greedy, single path routing and [3, 9] for energy balanced data propagation.

## 18.4 Node Criticality: A New Network Attribute

In order to develop efficient protocols for the Mobile Charger and address the corresponding trade-offs, we introduce *a new attribute that captures a node's "importance"* in the network, under any given routing protocol. This new attribute relies on two factors, (a) the *traffic served* by the node and (b) the *energy consumed* by the node.

The need for combining these two factors emerges from the fact that the traffic served by a node captures different aspects than its energy consumption rate. A node may consume a large amount of energy either because it serves a high network flow, or because its transmissions have high cost (e.g. long ranged transmissions) (or both).

The purpose of the attribute is to indirectly prioritize the nodes according to their flow rate and energy consumption; a node serving high traffic and/or having low residual energy should be charged at higher energy level.

We denote as  $c_i(t)$  the *criticality* of node  $v_i$  at time  $t$ , with

$$c_i(t) = f_i(t) \cdot \rho_i(t).$$

Given the time  $t_{MC}$  when the last charging of the node occurred

$$f_i(t) = 1 - \frac{\text{generation rate of node } v_i}{\text{traffic rate of } v_i \text{ since } t_{MC}} = 1 - \frac{\lambda_i}{\lambda_i + \frac{m_i(t)}{t-t_{MC}}}$$

is the *normalized traffic flow* served by node  $v_i$ , where  $m_i(t)$  is amount of traffic (number of messages) that  $v_i$  has processed (received and forwarded) towards the Sink by time  $t$  since time  $t_{MC}$ , and

$$\begin{aligned} \rho_i(t) &= \frac{\text{energy consumed since last charging}}{\text{max node energy since } t_{MC}} \\ &= \frac{E_i(t_{MC}) - E_i(t)}{E_i(t_{MC})} = 1 - \frac{E_i(t)}{E_i(t_{MC})} \end{aligned}$$

is the *normalized energy consumption* by time  $t$ , since the last charging. The criticality is thus a number in  $[0, 1]$  which captures the importance of a given node by taking into account its flow rate, its energy consumption, its possible special role in the network and its influence to the routing protocol; nodes serving high traffic (large  $m_i(t)$ ) and/or having consumed a lot of energy (low  $E_i(t)$ ) have high criticality  $c_i(t)$  at time  $t$  and are “prioritized” by the Mobile Charger.

## 18.5 Mobile Charger Configuration

### 18.5.1 Charging Extent

A straightforward charging policy (such as in [1]) follows the rationale that the amount of energy the Mobile Charger delivers to node  $v_i$  is proportional to the residual charging energy of the Mobile Charger. This approach takes into account the energy dissipation rate of the Mobile Charger but neglects the energy evolution in the network and the fact that some nodes are more important than others, due to their location, generation rate, special role in the network, etc. In other words, by adopting that charging policy, the energy of every node is replenished in the same way, with the absence of any energy levels based on node diversity.

In this work we use the criticality attribute as a measure of the level that a node  $v_i$  should be charged.

**Definition 18.1** Let  $e_{MC}(t) = \frac{E_{MC}(t)}{E_{MC}(t_{init})}$  denote the ratio of the Mobile Charger's residual energy at time  $t$  over the total amount of energy that the Mobile Charger was provided at the network initialization at time  $t_{init}$ .

**Definition 18.2** Let  $\Delta e_i(t) = E_i(t_{MC}) - E_i(t)$  denote the amount of energy that node  $v_i$  has consumed by time  $t$ , since the last charging (occurred at time  $t_{MC}$ ).

Node  $v_i$  will be charged until its energy becomes

$$E_i(t + t_c) = E_i(t) + c_i(t) \cdot e_{MC}(t) \cdot \Delta e_i(t)$$

where  $t_c$  is the time needed (considered negligible) for the charging of  $v_i$  and

$$\begin{aligned} c_i(t) \cdot e_{MC}(t) \cdot \Delta e_i(t) &= \\ &= \left(1 - \frac{\lambda_i}{\lambda_i + \frac{m_i(t)}{t-t_{MC}}}\right) \cdot \frac{E_{MC}(t)}{E_{MC}(t_{init})} \cdot \frac{(E_i(t_{MC}) - E_i(t))^2}{E_i(t_{MC})} \end{aligned}$$

We notice that  $v_i$ 's charging is not a fraction of its maximum or initial energy but a fraction of the consumed energy since the last charging. In other words, a sensor that consumed a lot of energy since its last charging will be charged at a higher level; this level is also higher when the sensor has high criticality and when the energy left at the charger is high.

### 18.5.2 New Protocols

We introduce three protocols for the trajectory followed by the mobile charger. These protocols assume different levels of network knowledge (from global to limited and reactive). Actually, the global knowledge method can not be considered realistic in large scale networks and rather serves as an upper bound on performance which the other methods are compared to.

#### 18.5.2.1 Global Knowledge Protocol GKP

The global knowledge charger we suggest is an online method that uses criticality as a ranking function. In each round the charger moves to the sensor that minimizes the product of the negation of each node's criticality times its distance from the current position of the Mobile Charger. More specifically, in each moving step the GKP minimizes the product

$$\min_i \left\{ (2 - c_i(t)) \cdot \left(1 + \frac{dist_i}{2D}\right) \right\}$$

where  $dist_i$  is the distance of each sensor from the Mobile Charger and  $D$  is the network radius, with the minimum taken over all sensors in the network (or at least a large part of it). In other words, *this protocol prioritizes nodes with high criticality and small distance to the Mobile Charger*. Since this protocol requires *a global knowledge of the state of the network*, it is expected to outperform all other strategies that use only local or limited network information, thus somehow representing an on-line centralized performance upper bound. However, it would not be suitable for large scale networks as it introduces great communication overhead (i.e. every node has to propagate its criticality to the Mobile Charger) and does not scale well with network size.

### 18.5.2.2 Limited Reporting Protocol LRP

The Sink is informed about the status of some representative nodes scattered throughout the network and is able to provide the Mobile Charger with some guidance. In other words, this protocol distributively and efficiently “simulates” the global knowledge protocol. We assume that the Sink can transmit to the Mobile Charger wherever in the network the latter might be. The protocol follows a limited reporting strategy, since it exploits information not from the whole network area but from a limited number of nodes. The nodes of each Slice periodically run a small computation overhead algorithm in order to elect some special nodes, the *reporters* of the Slice; in particular, each node becomes a reporter independently with some appropriate probability (thus, the number of reporters is binomially distributed). The reporters act as the representatives of their Slice and their task is the briefing of the Sink about their criticality.

The *percentage of the nodes that will act as reporters* brings off a trade-off between the representation granularity of the network and the communication overhead on each message propagated in the network. If we set a large percentage of reporters, the Sink will have a more detailed knowledge of each Slice’s overall criticality but the message overhead will highly increase, since each message should carry the Slice reporter’s current criticality. On the contrary, if we set a small percentage of reporters, the overhead will be tolerable, but the representation of a Slice will be less detailed.

In order to maintain *a small set of reporters* for each Slice (for communication overhead purposes) we propose that Slice  $i$  which contains  $n_i$  nodes elects

$$\kappa_i = \frac{n_i}{n} \cdot \kappa_{total}$$

reporters, with the global number of reporters being

$$\kappa_{total} = h \frac{D}{r} \log n, \text{ where } h = 1 - \frac{a}{b}$$

is a network density heterogeneity parameter. Clearly, a highly heterogeneous deployment (large  $b$  compared to  $a$ ) will necessitate a higher number  $\kappa_{total}$  of reporters. Also,  $\kappa_{total}$  must be large in large networks with many sensors. Each node periodically with probability  $p_i$  becomes a reporter. In order to have an expected number of  $\kappa_i$  reporters in Slice  $i$  we need

$$\kappa_i = n_i \cdot p_i \Rightarrow p_i = \frac{\frac{n_i}{n} \cdot \kappa_{total}}{n_i} \Rightarrow p_i = \frac{\kappa_{total}}{n}$$

### 18.5.2.3 Reactive Trajectory Protocol RTP

In this protocol, a node  $v_i$  is propagating an *alert message* to its neighbors each time its energy drops below a set of some crucial limits. The messages are propagated for some hops and are stored at every node passed, in order for a *tree structure* rooted at  $v_i$  to be formed that can be *detected by the Mobile Charger when passing through* some tree node. Every node can root a tree and the strategy followed (towards a small tree management overhead) is the maintenance of a small tree degree with a larger tree depth.

The tree that is formed for each node is gradually growing, in an analogous way to the criticality of the root node, as the gradual increase of a node's criticality is an indication of either high traffic or high energy consumption. We use *criticality as a measure of the gradual expansion of the tree*, since its value depicts both the importance of the node in the network and its energy consumption rate. We propose a strategy of message propagations that aims at covering a relatively large area of the network, while keeping energy consumption due to communication overhead low.

More specifically, each node  $v_i$  can alter among  $\lceil \log(n \frac{D}{r}) \rceil$  alert levels which determine the characteristics of the  $v_i$ 's rooted tree. We denote as  $al_i$  the current *alert level* of node  $v_i$ . The tree rooted at  $v_i$  is formed in a way that the *degree* =  $al_i - 1$  and the *depth* =  $2^{al_i-1} - 1$ . The duration of each successive alert level is increased by a constant ratio from the previous level

$$al_i = \begin{cases} 1 & \text{if } 0 \leq c_i(t) < 0.5 \\ 2 & \text{if } 0.5 \leq c_i(t) < 0.75 \\ \vdots & \vdots \\ \lceil \log(n \frac{D}{r}) \rceil & \text{if } 1 - \frac{1}{2^{\lceil \log(n \frac{D}{r}) \rceil - 1}} \leq c_i(t) < 1 \end{cases}$$

$$= \left\{ \mu \mid \mu \in \left[ 1, 2, \dots, \lceil \log \left( n \frac{D}{r} \right) \rceil \right] \right\}$$

$$\text{with } 1 - \frac{1}{2^{\mu-1}} \leq c_i(t) < 1 - \frac{1}{2^\mu}$$

$$\text{where } 1 - \frac{1}{2^{\mu-1}} = \sum_{j=1}^{\mu-1} \frac{1}{2^j}, 1 - \frac{1}{2^\mu} = \sum_{j=1}^{\mu} \frac{1}{2^j}.$$

The Mobile Charger alters its state between a *patrol mode* and a *charging mode*. When in patrol mode, it follows a spiral patrol trajectory centered at the Sink with gradually increasing radius. The spiral trajectory is a space-filling trajectory that enables the MC to traverse the network area in a systematic way while visiting several sub-regions. During the patrol mode the MC does not charge any nodes until it is notified—via an alert message—that a neighboring subregion is low on energy. When so, the MC will switch to charging mode and will follow a different trajectory towards charging that subregion. If the Mobile Charger detects simultaneously different trees, then by a check on the *depth* of each structure it can decide which is the most critical. After the completion of the charging process the Mobile Charger resumes the patrol mode.

The reactive traversal can be an efficient, adaptive solution for dynamic networks such as networks with varying event generation rate per Slice.

### **18.5.3 Known Protocols**

We also briefly describe two other state of the art protocols, that will be used in our experimental evaluation.

#### **18.5.3.1 Local Knowledge Protocol LKP ([1])**

An intuitive traversal strategy is that the Mobile Charger follows a circular trajectory around the Sink. The radius of the trajectory varies and adapts to the energy depletion rates of each subregion of the network. Starting from the Sink, the mobile charger traverses a path which forms a set of concentric circles, centered around the Sink with varying (increasing or decreasing) radii. In particular, the Mobile Charger charges the sensors inside the ring which contains the corresponding trajectory. The width of each ring is pre-specified and constant.

#### **18.5.3.2 GreedyPlus ([14])**

The algorithm is designed to find a charging sequence with which the lifetime of the network can be prolonged as much as possible while incurring small traveling distance. Sensor nodes estimate their remaining lifetime periodically and an aggregated report of the shortest lifetime nodes is delivered to the Sink. The Sink informs the Mobile Charger about the best charging sequence of those nodes, taking into account the maximum time that can be spent to move to and charge a given node in order to extend its lifetime so that no other node of the sequence dies. We note that the knowledge amount of this protocol is relatively high, since the Mobile Charger knows the exact position and ID of each node. Also, since all nodes participate in the lifetime information aggregation, the protocol is expected to have high overhead due to transmission of messages that keep the Mobile Charger updated.

## 18.6 Experimental Evaluation

### 18.6.1 Experimental Setup

The simulation environment for conducting our experiments is Matlab 7.11.0. For statistical smoothness, we apply the deployment of nodes in the network and repeat each experiment 100 times. For each experiment we simulate large numbers of data propagations and the average value is taken. The statistical analysis of the findings (the median, lower and upper quartiles, outliers of the samples) demonstrate very high concentration around the mean, so in the following figures we only depict average values.

Before we deploy the nodes as described in Sect. 18.3 and in order to come up with a heterogeneous network topology that will be connected with high probability, we deploy a portion of the nodes (defined by the connectivity threshold discussed below) uniformly at random in order to establish connectivity. Since two nodes communicate with each other iff their euclidean distance is at most  $r$ , the generated network topology by this first set of nodes is in fact an instance of the *Random Geometric Graph* model. In [7, 15] it is shown that the connectivity threshold for an instance of the RGG model is  $r_c = \sqrt{\frac{\ln n}{\pi n}}$ . This is the connectivity threshold according to which the initial nodes are deployed.

We focus on the following performance metrics: (a) **alive nodes over time**, that is the number of nodes with enough residual energy to operate, during the progress of the experiment, (b) **connected components over time** which indicates the number of strongly connected components of the network graph throughout the experiment, (c) **network criticality map**, which is a spatial depiction of the whole network in terms of energy dissipation and flow traffic, after the generation of a number of events, (d) **routing robustness** and **average routing robustness**, in terms of the nodes' average alive neighbors during the progress of the experiment, (e) **coverage aging**, that is the average coverage number (number of sensors having the point in their range) of 1000 randomly selected points in the network over time. We provide results for three underlying routing protocol families; energy balance, clustering and hop-by-hop.

### 18.6.2 Protocol Parameters

#### 18.6.2.1 Node Criticality

Our node criticality attribute captures a node's diversity in terms of both energy consumption aspects and flow rate. The LKP, as proposed in [1], uses only the nodes' average energy levels as an indication for its traversal configuration. Intuitively, a change at the charger's traversal decision criterion that replaces energy check with criticality check could provide the charger with a more detailed evaluation of the current network neighborhood. As shown in Fig. 18.2, changing the above criterion

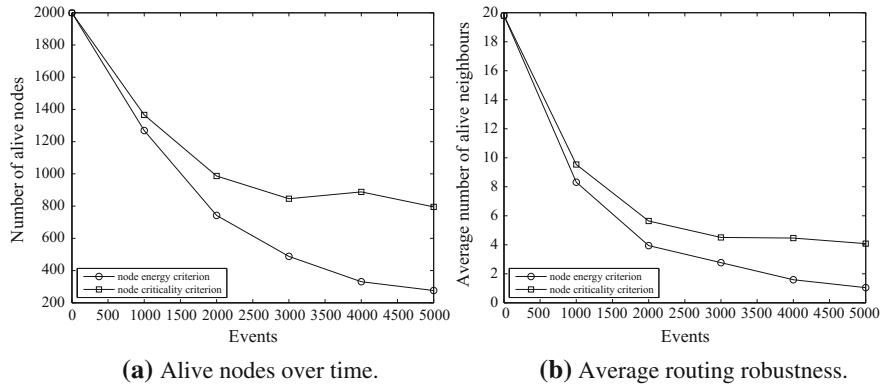


**Fig. 18.2** LKP with energy criterion and with criticality criterion

and using our new one, results in a lifetime extension of the network, as well as in improved routing robustness; the improvements are larger as the number of events increases. This demonstrates the strength of the node criticality attribute which we thus adopt in the sequel.

### 18.6.2.2 Percentage of $E_{total}$ available to the charger

This particular trade-off consists in how much energy (of the total available) should the Mobile Charger be initially equipped with. On the one hand, more energy to the Mobile Charger leads to better on-line management of energy in the network. However, since  $E_{total} = E_{sensors} + E_{MC}(t_{init})$ , more energy to the Mobile Charger also means that the sensor nodes will initially be only partially charged. Therefore, they may run out of energy before the Mobile Charger charges them leading to possible network disconnection and low coverage of the network area.

To investigate this trade-off, we conducted a comparison among several percentages of initial energy given to the charger. More specifically, we investigate the cases of 20, 30, 50, 70, and 80 % of the total energy to be given to the Mobile Charger, both for the LRP and for RTP (Fig. 18.3a, b correspondingly). It is clear that providing the Mobile Charger with more than 30 % of the total energy is negatively affecting the life evolution of the network, in both protocol cases. On the other hand, a smaller percentage of energy at the charger (like 20 %) leads to worse results, since the recharging potential is limited. We thus adopt a 30 % in the following.

### 18.6.2.3 $\kappa_{total}$ of the LRP

The total number of nodes that act as reporters is a fundamental parameter of the LRP. High numbers of reporters provide the Mobile Charger with detailed information

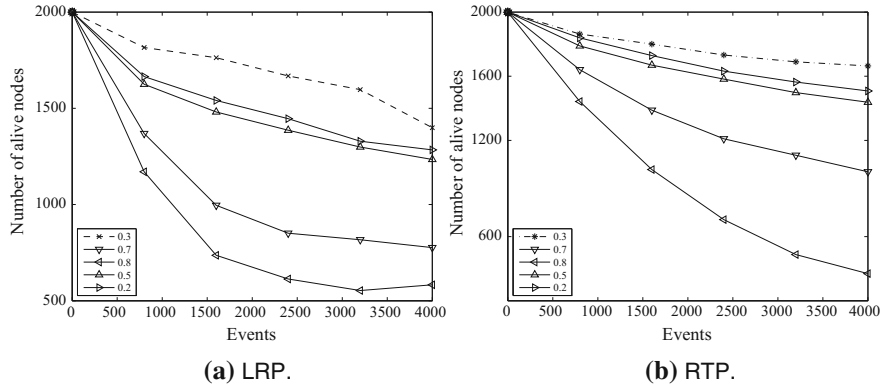


**Fig. 18.3** Various percentages of  $E_{total}$  given to the charger

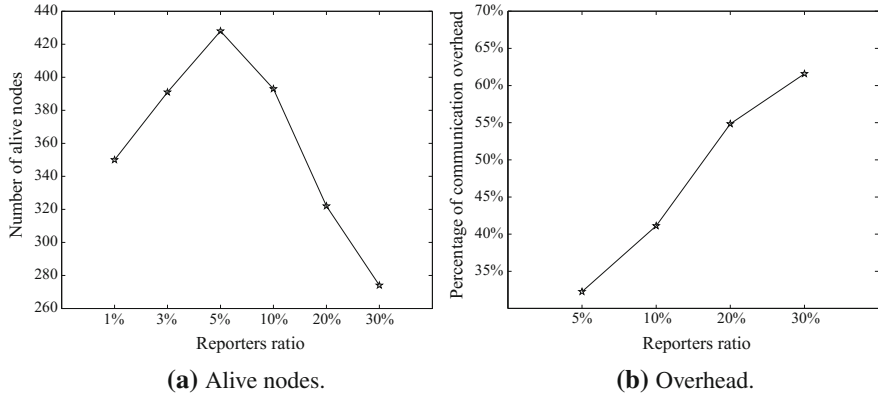


**Fig. 18.4** Alive nodes and communication overhead for various  $\kappa_{total}$  values in LRP, after 6000 generated events

about the current state of the Slices' criticality but require more messages for the propagation of the reporters' state, resulting in higher energy consumption throughout the network. On the other hand, whereas a small number of reporters decreases the number of message exchanges, poor detail of the Slice's representation may disorientate the Mobile Charger and guide it to Slices where the energy to be provided is not truly needed (in comparison to other Slices).

In order to figure out possible good values for  $\kappa_{total}$  that maximize the LRP performance we carry out a comparison operating the protocol between several reporter numbers. Figure 18.4 depicts the number of alive nodes of the network after 6000 events, for various percentages of reporters over the total number of nodes in the network. In the particular setting the formula for  $\kappa_{total}$  yields  $\kappa_{total} = 5\%$ . Then we try to experimentally validate the suitability of this  $\kappa_{total}$  choice. It is obvious that if the protocol defines the number of reporters to be less than 5 % of the network nodes,

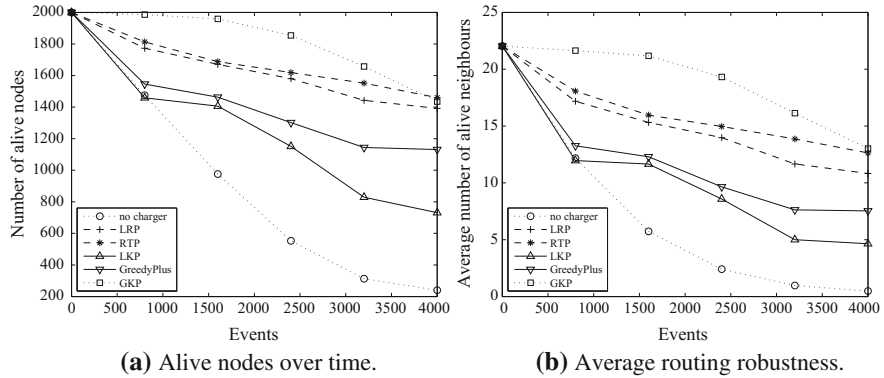


**Fig. 18.5** Various metrics for non-uniform deployments with the  $E_i$  routing protocol

the granularity of the Slice representation is poor, resulting in reduced network lifetime. Similarly, for numbers greater than 5 % of the network nodes, the lifetime is also reduced, due to the higher message exchange overhead (over total traffic) in Fig. 18.4. Thus, we set the reporters to a 5 %.

### 18.6.3 Results in Non-uniform Deployments

We study the effect of our charger strategies, on the number of alive nodes over time, the energy/flow balance of the network, the routing robustness, the coverage aging and the number of strongly connected components over time in non-uniform network deployments. The results with the  $E_i$  energy balance protocol as underlying routing protocol are displayed in Figs. 18.5, 18.8, 18.11, and 18.15, for the Greedy protocol in Figs. 18.6, 18.9, 18.12, and 18.16 for the LEACH protocol in Figs. 18.7, 18.10, 18.13, and 18.17.

#### 18.6.3.1 Alive Nodes over Time

(i)  $E_i$  protocol: The overall death rate (in terms of *alive nodes over time*) of the network is vastly reduced, as shown in Fig. 18.5. The performance of both the LRP and the RTP approaches the performance of the GKP, powerful charger. We note that our traversal strategies outperform both the LKP of [1], which seems to be less adaptive, when used in non-uniform deployments, and the GreedyPlus.

(ii) *Greedy protocol*: In the hop-by-hop routing case we observe that the performance of both the LRP and the RTP approaches the performance of the GKP again (Fig. 18.6). We notice that the LKP of [1], is more adaptive than in the  $E_i$  case and its performance is similar to the LRP. This can be explained by the fact that the greedy message propagation tends to stress the regions closer to the Sink. Thus, since the

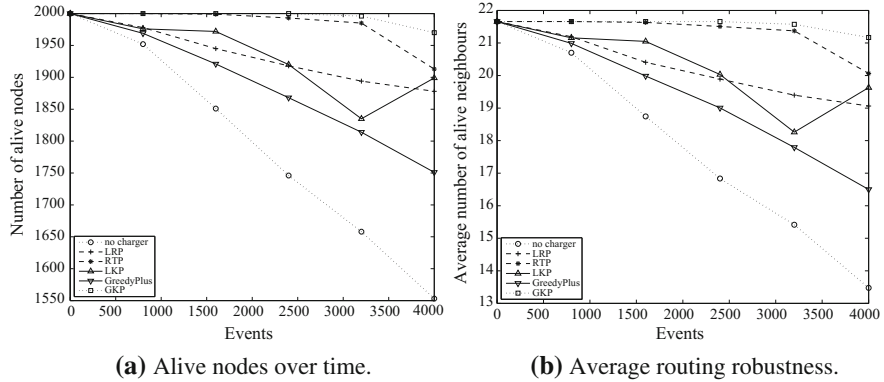


**Fig. 18.6** Various metrics for non-uniform deployments with the Greedy routing protocol

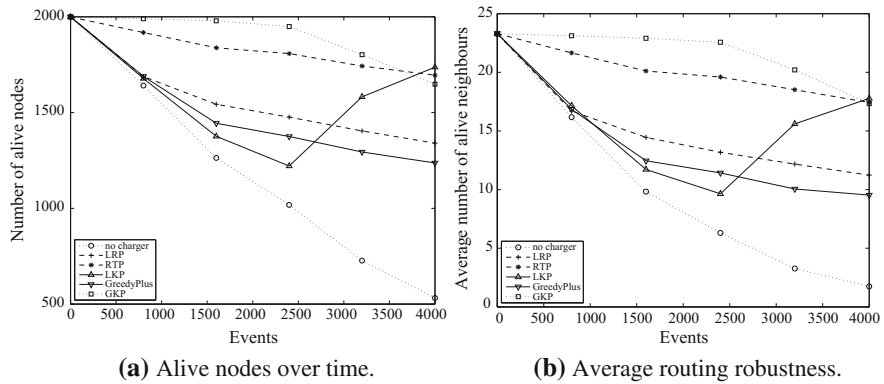


**Fig. 18.7** Various metrics for non-uniform deployments with the LEACH routing protocol

LKP charger does not travel large distances in the network area, it can adjust more effectively its circular trajectory.

(iii) *LEACH protocol*: As shown in Fig. 18.7, the results for the LEACH case are similar to the ones for the  $E_i$  case. The RTP maintains a large number of alive nodes over the network and approaches the performance of the GKP. The LKP, while starting with a relatively inefficient charging behavior, it ends up to a fast regeneration of dead nodes after 2500 events. However, such network starvation phenomena may lead to high percentages of lost messages.

### 18.6.3.2 Criticality Map

(i)  *$E_i$  protocol*: Fig. 18.8 depicts the *criticality map* of the network over time, for each one of the chargers. More specifically, we present graphically the spatial evolution of energy dissipation combined with flow traffic information in the network after 4.000

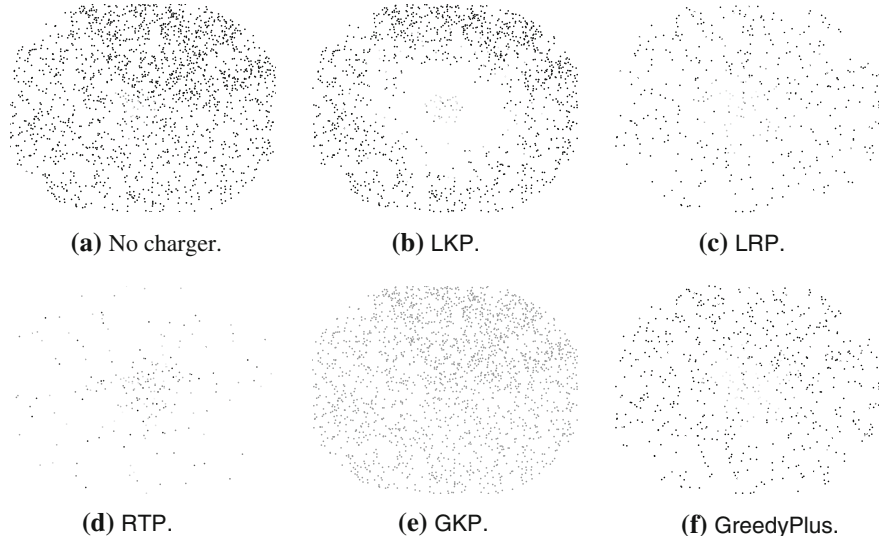


**Fig. 18.8** Criticality map for non-uniform deployments with the  $E_i$  routing protocol

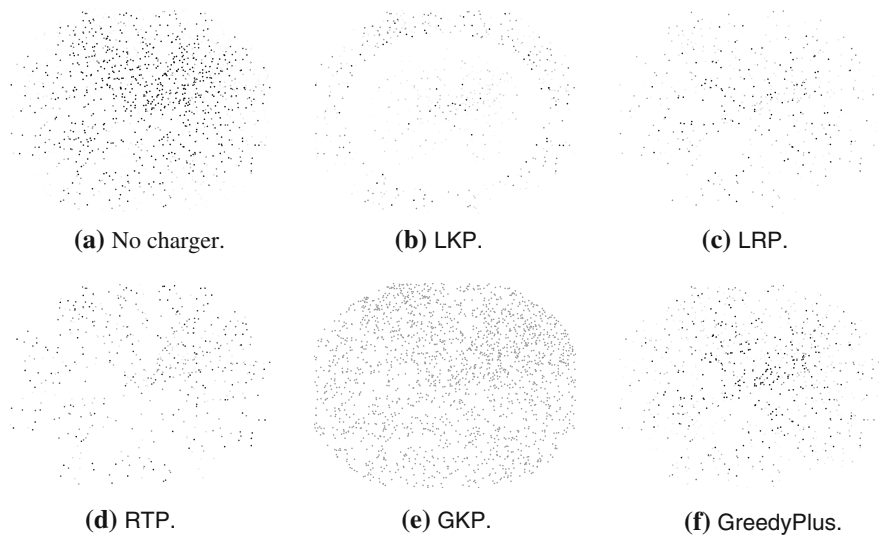


**Fig. 18.9** Criticality map for non-uniform deployments with the Greedy routing protocol

event generations. Nodes with low criticality values are depicted with bright colors. In contrast, nodes with high criticality values are depicted with dark colors. The centralized global knowledge charger **GKP** outperforms all other chargers and achieves a balanced overall network criticality, as expected, while the local knowledge **LKP** of [1] creates a ring consisted of low criticality nodes, since the underlying routing

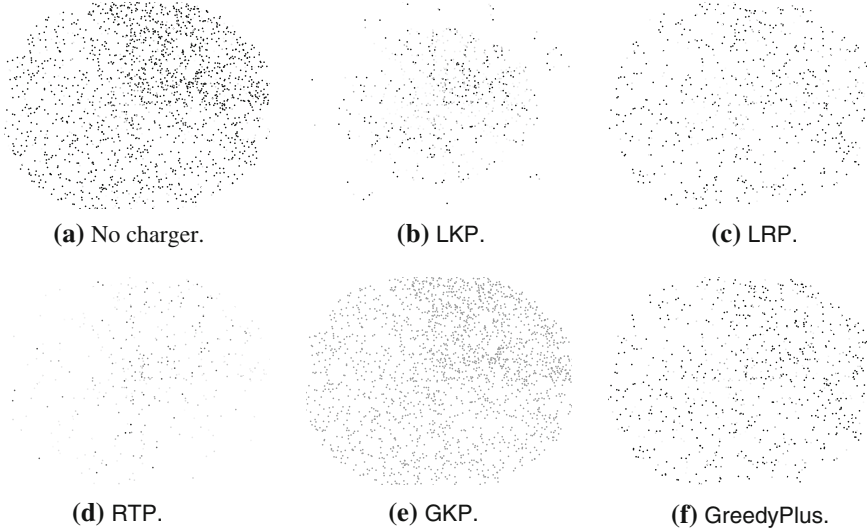


**Fig. 18.10** Criticality map for non-uniform deployments with the LEACH routing protocol

protocol is the energy balance  $E_i$ , where nodes in the middle of the network radius suffer both from long-range transmissions and high flow rate from outer nodes. This ring is a cause of imbalance, in contrast to our proposed charger scheme **LRP** where the overall network criticality is more balanced.

(ii) *Greedy protocol*: Fig. 18.9 displays the *criticality map* of the network over time, for each one of the chargers. Again, we present graphically the spatial evolution of energy dissipation combined with flow traffic information in the network after 4.000 event generations. The centralized global knowledge charger **GKP**, in this case also achieves a balanced overall network criticality followed by the **LRP**, **RTP** and **GreedyPlus**. The ring of **LKP** of [1] consisted of low criticality nodes, in this case, which are spread in a wider area, since the underlying hop-by-hop routing protocol tends to stress the regions closer to the Sink.

(iii) **LEACH protocol**: In Fig. 18.10 we can see the *criticality map* of the network over time, for the clustering-based routing protocol. We present graphically the spatial evolution of energy dissipation combined with flow traffic information in the network after 4.000 event generations. Nodes with low criticality values are depicted with bright colors and nodes with high criticality values are depicted with dark colors. As usual, the **GKP**, outperforms all other chargers and achieves a balanced overall network criticality. In this case, the **LKP** of [1] does not create a low criticality ring, the **LRP** and the **GreedyPlus** of [14] lead to an efficient criticality map and the **RTP** forms a map with a small number of low criticality nodes.

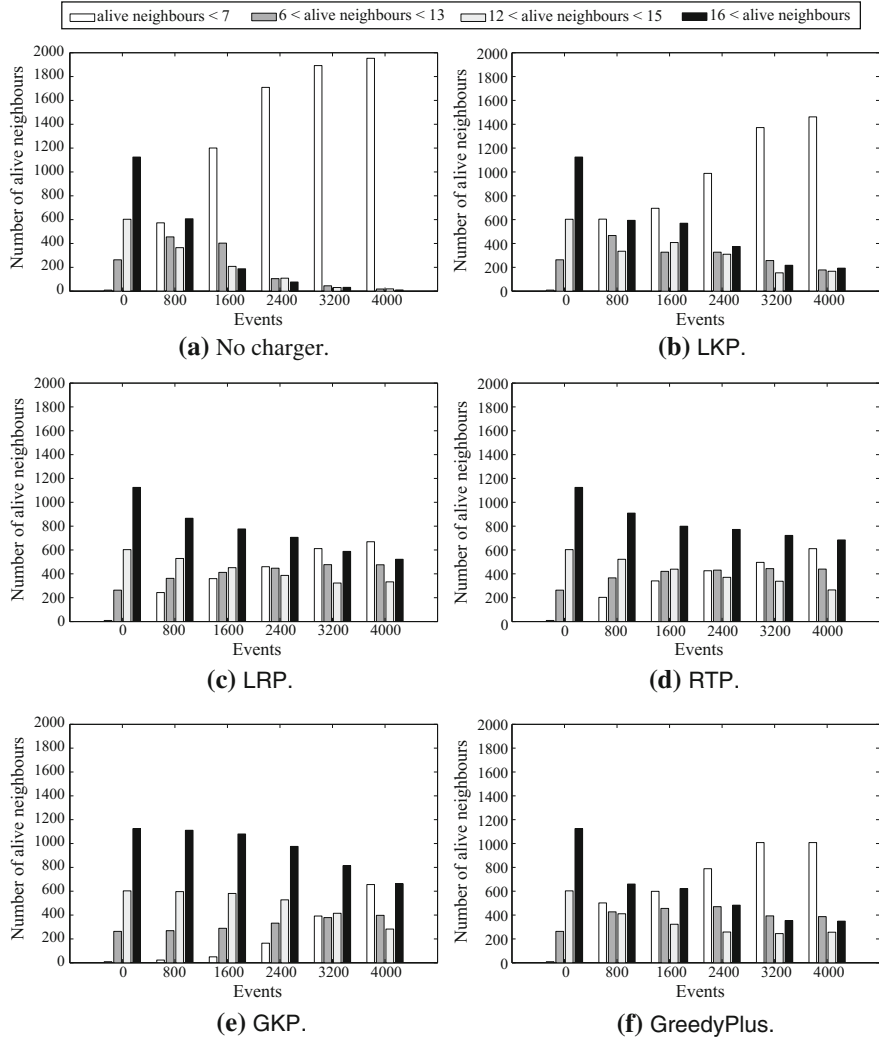


**Fig. 18.11** Routing robustness for non-uniform deployments with the  $E_i$  routing protocol

### 18.6.3.3 Routing Robustness

(i)  $E_i$  protocol: *Routing robustness* is critical for sensor networks, as information collected needs to be sent to remote control centers. Path breakage occurs frequently due to node mobility, node failure, or channel impairments, so the maintenance of a path from each node to a control center is challenging. A way of addressing the routing robustness of a sensor network is by considering for each node the number of its alive neighbors over time, which can be seen as an implicit measure of network connectivity. The average number of alive neighbors is depicted in Fig. 18.5. A more

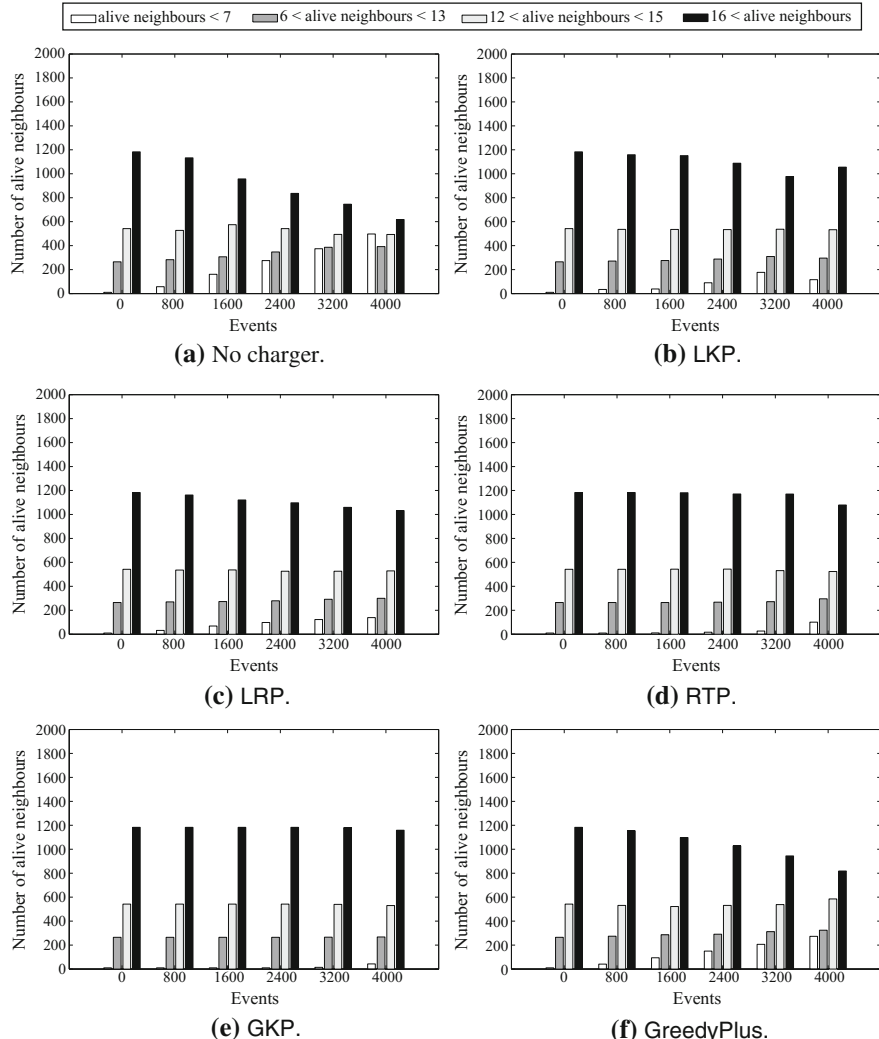


**Fig. 18.12** Routing robustness for non-uniform deployments with the Greedy routing protocol

detailed evolution of the network's routing robustness is shown in Fig. 18.11. Our LRP and our RTP achieve high robustness, outperforming both the LKP and the GreedyPlus and approaching the GKP performance.

(ii) *Greedy protocol:* The average number of alive neighbors is depicted in Fig. 18.6. A more detailed evolution of the network's routing robustness is shown in Fig. 18.12. Again, the LRP and RTP achieve high robustness, outperforming the LKP and GreedyPlus and approaching the GKP performance. We observe that in contrast to the  $E_i$  routing case the number of alive neighbors follows a smoother decrease pattern, since the hop-by-hop message propagation does not include long ranged transmissions.

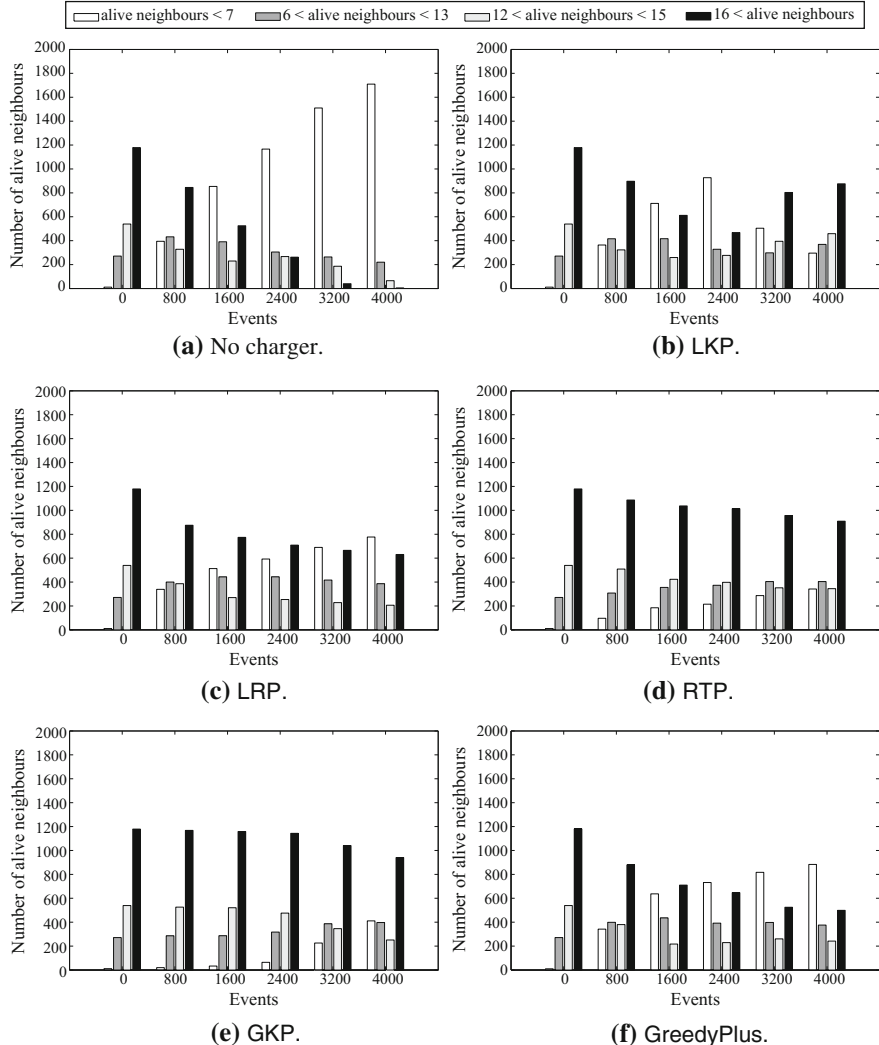


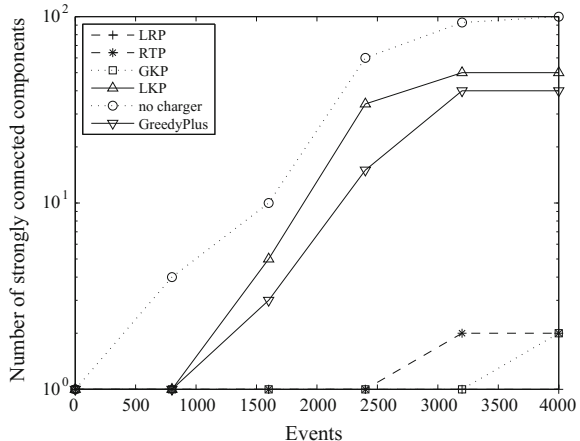
**Fig. 18.13** Routing robustness for non-uniform deployments with the LEACH routing

(iii) *LEACH protocol*: The average number of alive neighbors is depicted in Fig. 18.7. A more detailed evolution of the network's routing robustness is shown in Fig. 18.13. The results are similar to the  $E_i$  routing case.

#### 18.6.3.4 Strongly Connected Graph Components

The number of *strongly connected graph components* is also an overall measure of connectivity quality in a sensor network. Disconnected components are unable to

**Fig. 18.14** Graph connected components over time



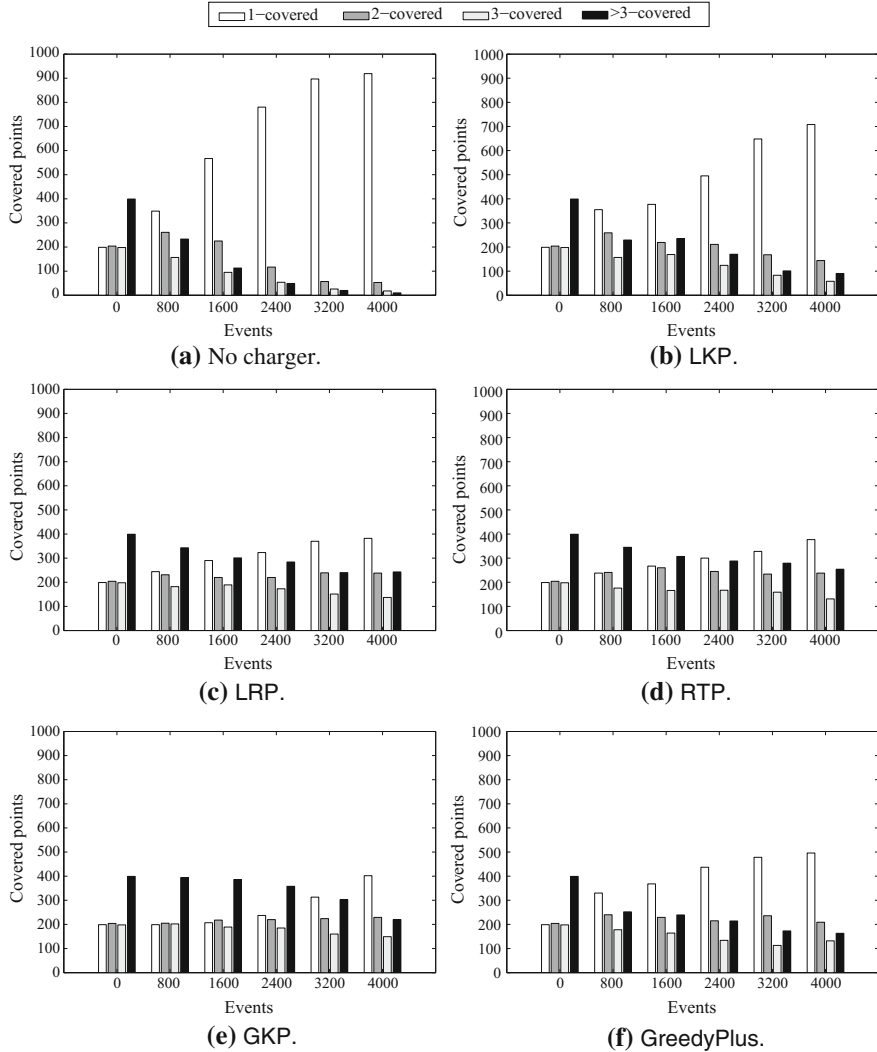
communicate with each other and sometimes even with the Sink, resulting in high data delivery failures. Maintaining a small number of connected components in the network can also improve data delivery latency. High numbers of components may lead to isolation of critical nodes, thus loss of important information. Figure 18.14 depicts the evolution of the number of network components throughout the experiments ( $E_i$  routing protocol). As we noted earlier, the LKP of [1] has a high node death rate, a fact that results in early disconnections and sharp increase of connected components. Our LRP maintains a (single) strongly connected network. The performance of LKP and GreedyPlus is characterized by an increasing number of connected components.

### 18.6.3.5 Point Coverage

(i)  $E_i$  protocol: Point coverage problem is regarding how to ensure that all points in the network are covered by enough sensors. Coverage is an important aspect in sensor networks (e.g. localization, target tracking etc.). A point that is covered by  $k$  sensors is called  $k$ -covered. The coverage aging (evolution of coverage with time) of 1000 randomly selected points in the network is shown in Fig. 18.15. We investigate how many points are  $<2, 2, 3, >3$  covered during an experiment of 4000 generated events. Our LRP and RTP maintain satisfactory levels of coverage.

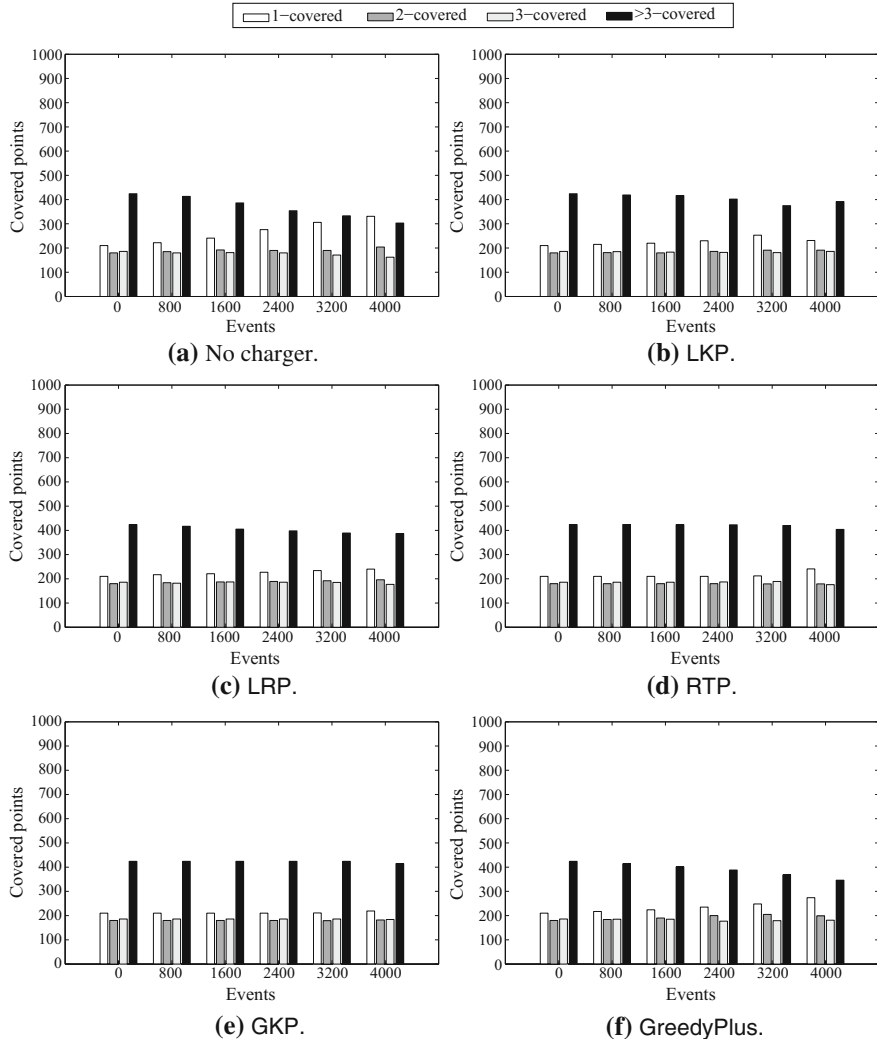
(ii) Greedy protocol: The coverage aging of 1000 randomly selected points in the network is shown in Fig. 18.16. We investigate how many points are  $<2, 2, 3, >3$  covered during an experiment of 4000 generated events. Our LRP and RTP maintain satisfactory levels of coverage. Note that in this case, the LKP charger has a rather unstable impact on the network coverage.

(iii) LEACH protocol: The coverage aging of 1000 randomly selected points in the network is shown in Fig. 18.17. We investigate how many points are  $<2, 2, 3, >3$  covered during an experiment of 4000 generated events. Our LRP and RTP maintain satisfactory levels of coverage, approaching the performance of the GKP.



**Fig. 18.15** Coverage aging for non-uniform deployments with the  $E_i$  protocol

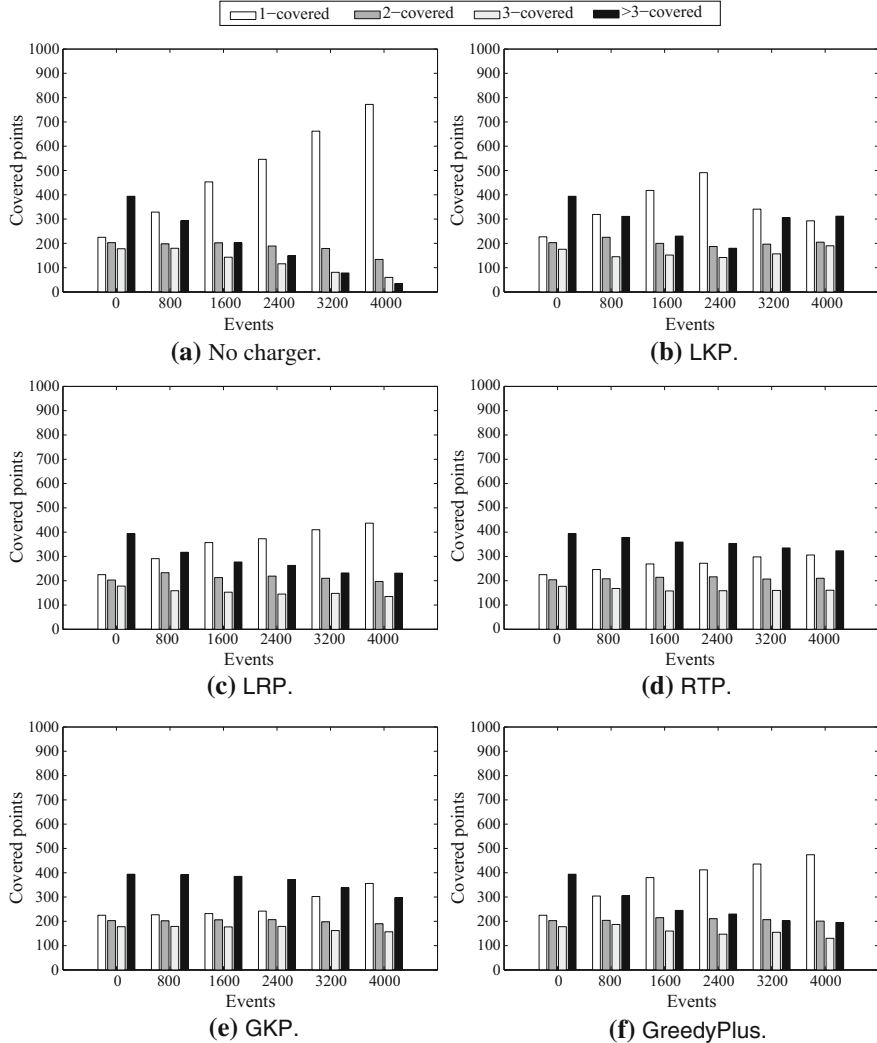
Overall, our proposed protocols extend several network attributes, approach the performance of the global powerful knowledge protocol and significantly outperform the LKP which was designed with a focus on uniform deployments, and the Greedy-Plus in which the Mobile Charger requires frequent updating, hence increased energy consumption due to message transmissions throughout the whole network.



**Fig. 18.16** Coverage aging for non-uniform deployments with the Greedy protocol

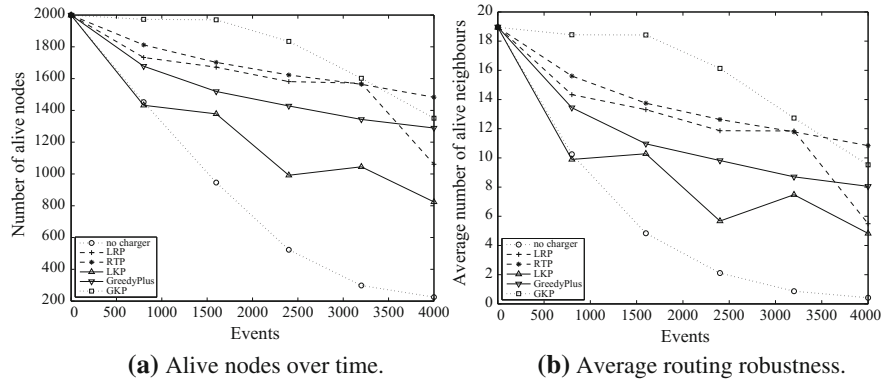
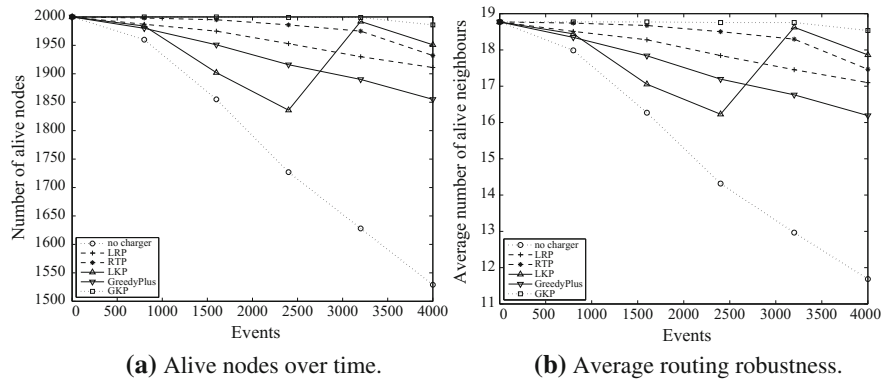
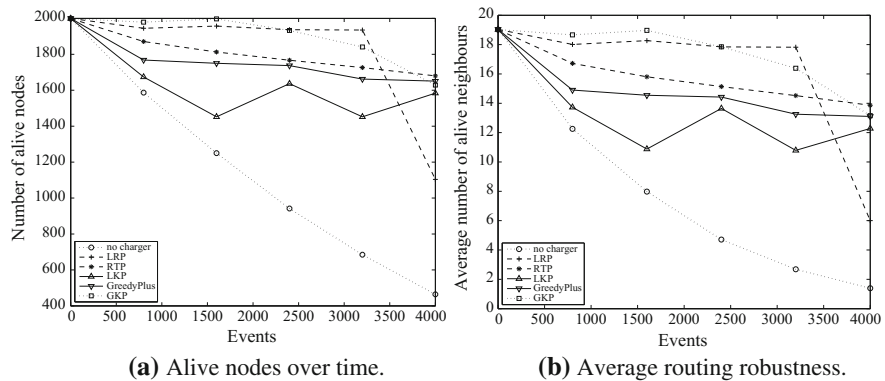
#### 18.6.4 Uniform Deployments

Our protocols achieve performance which approaches the one of the centralized, full knowledge strategy; also, interestingly, their performance is similar or better than the performance of the local protocol of [1] whose design was tailored to uniform deployments. The impact of the charger, in all cases, is lower than the impact on the non-uniform cases, but still greatly improves the no-charger case performance. The alive nodes over time metric for the three routing protocols is shown in Figs. 18.18a,



**Fig. 18.17** Coverage aging for non-uniform deployments with the LEACH protocol

[18.19a](#), and [18.20a](#), criticality map in Figs. [18.21](#), [18.22](#), and [18.23](#), coverage aging in Figs. [18.27](#), [18.28](#), and [18.29](#), and routing robustness in Figs. [18.18b](#), [18.19b](#), [18.20b](#), [18.24](#), [18.25](#), and [18.26](#).

**Fig. 18.18** Various metrics for uniform deployments with the  $E_i$  routing protocol**Fig. 18.19** Various metrics for uniform deployments with the Greedy routing protocol**Fig. 18.20** Various metrics for uniform deployments with the LEACH routing protocol

#### 18.6.4.1 Alive Nodes over Time

(i) *E<sub>i</sub> protocol*: The overall death rate (in terms of *alive nodes over time*) of the network is reduced, as shown in Fig. 18.18a. The performance of both the LRP and the RTP approaches the performance of the GKP. Our traversal strategies outperform both the LKP of [1], which seems to be less adaptive, even in uniform deployments, and the GreedyPlus of [14]. An explanation about the LKP less efficient behavior is that the charger is constantly moving and charging, a fact that may result in energy replenishment of non-vital network regions.

(ii) *Greedy protocol*: In the hop-by-hop routing case, the performance of both the LRP and the RTP approaches the performance of the GKP (Fig. 18.19a). We notice that the LKP, is more adaptive than in the E<sub>i</sub> case and its performance is similar to the LRP and RTP. This is a result of the uniform network deployment in combination with the greedy message propagation that tends to stress the regions closer to the Sink and results in less traveling distance for the LKP.

(iii) *LEACH protocol*: As shown in Fig. 18.20a, both the RTP and the LRP maintain a large number of alive nodes over the network and approach the performance of the GKP. In contrast to the LEACH case in non-uniform network deployments, all chargers follow a smoother behavior throughout the experiment and network starvation phenomena are absent.

#### 18.6.4.2 Criticality Map

(i) *E<sub>i</sub> protocol*: Fig. 18.21 depicts the *criticality map* of the network over time, for each one of the chargers. More specifically, we present graphically the spatial evolution of energy dissipation combined with flow traffic information in the network after 4.000 event generations. Nodes with low criticality values are depicted with bright colors. In contrast, nodes with high criticality values are depicted with dark colors. The centralized global knowledge charger GKP, as expected, outperforms all other chargers and achieves a balanced overall network criticality while the local knowledge LKP of [1] creates a dense ring consisted of low criticality nodes.

(ii) *Greedy protocol*: In Fig. 18.22 we can see the *criticality map* of the network over time, for each one of the chargers. The centralized global knowledge charger GKP, in this case also achieves a balanced overall network criticality followed by the LRP, RTP and GreedyPlus. The ring of LKP of [1] consisted of low criticality nodes in this case is spread in a wider area, since the underlying hop-by-hop routing protocol tends to stress the regions closer to the Sink.

(iii) *LEACH protocol*: In Fig. 18.23 we can see the *criticality map* of the network over time, for the clustering-based routing protocol. We present graphically the spatial evolution of energy dissipation combined with flow traffic information in the network after 4.000 event generations. In this case, the LRP and the GreedyPlus of [14] lead to an efficient criticality map and the RTP forms a map with a small number of low criticality nodes.

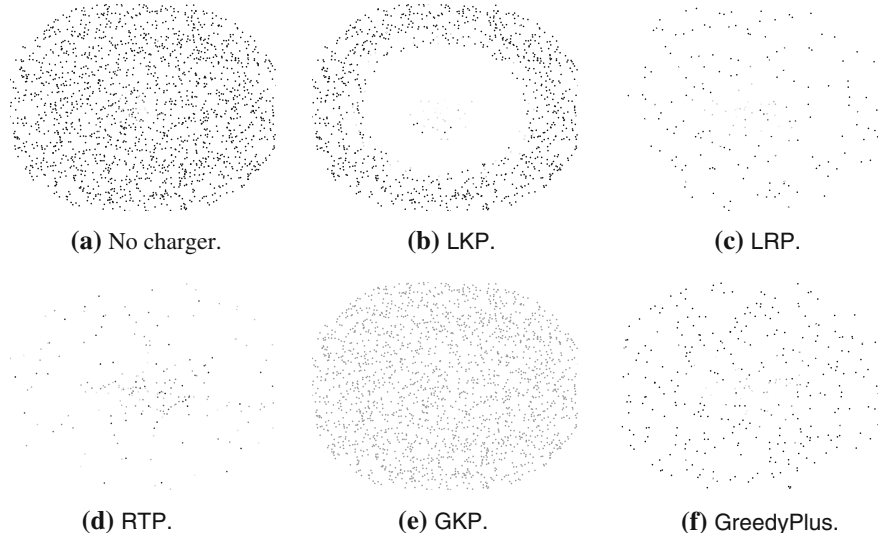


**Fig. 18.21** Criticality map for uniform deployments with the  $E_i$  routing protocol

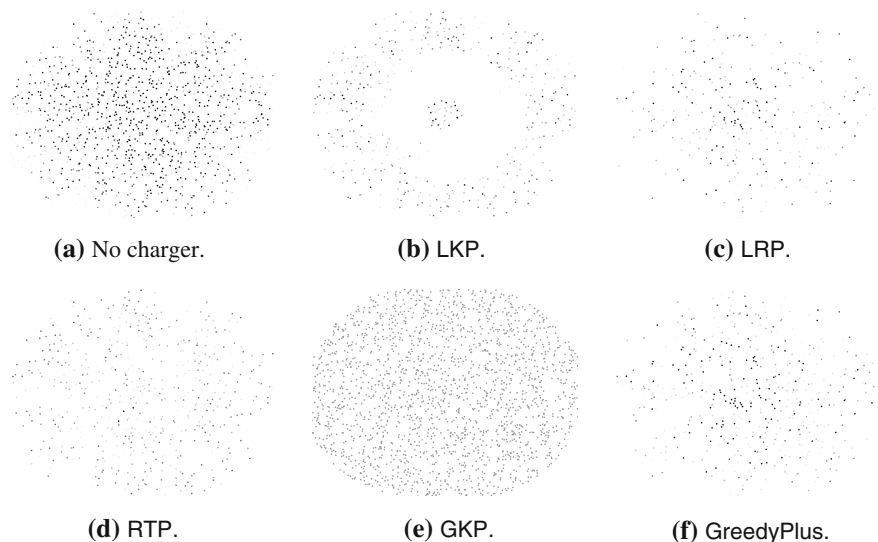


**Fig. 18.22** Criticality map for uniform deployments with the Greedy routing protocol

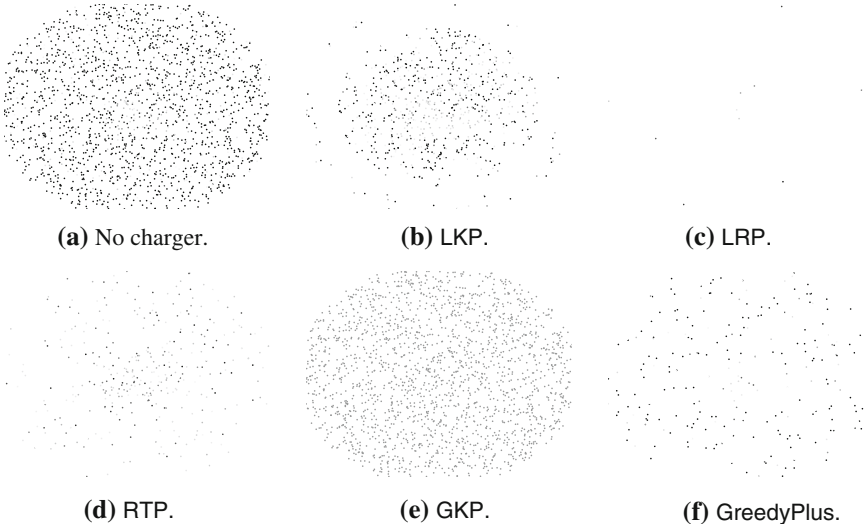


**Fig. 18.23** Criticality map for uniform deployments with the LEACH routing protocol

#### 18.6.4.3 Routing Robustness

(i)  $E_i$  protocol: The average number of alive neighbors is depicted in Fig. 18.18a. A more detailed evolution of the network's routing robustness is shown in Fig. 18.24. Our LRP and our RTP achieve high robustness, outperforming the LKP and Greedy-Plus and approaching the performance of the GKP.

(ii) *Greedy protocol*: The average number of alive neighbors is depicted in Fig. 18.19b. A more detailed evolution of the network's routing robustness is shown in Fig. 18.25. Again, the LRP and RTP achieve high robustness, outperforming the LKP and GreedyPlus and approaching the GKP performance. We observe that in contrast to the  $E_i$  routing case the number of alive neighbors follows a smoother decrease pattern, since the hop-by-hop message propagation does not include long ranged transmissions.

(iii) *LEACH protocol*: The average number of alive neighbors is depicted in Fig. 18.20b. A more detailed evolution of the network's routing robustness is shown in Fig. 18.26. The results are similar to the  $E_i$  routing case, where both hop-by-hop and direct transmissions are used.

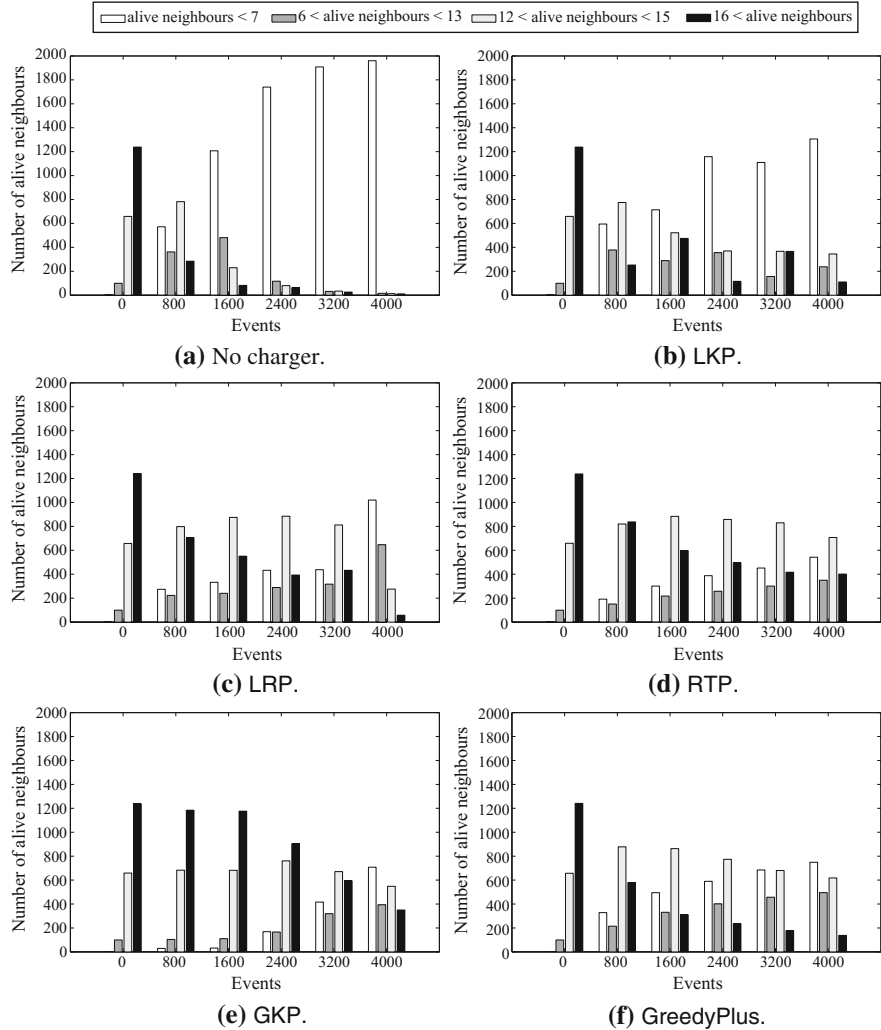


**Fig. 18.24** Routing robustness for uniform deployments with the  $E_i$  routing protocol

#### 18.6.4.4 Point Coverage

(i) *E<sub>i</sub> protocol:* The coverage aging (evolution of coverage with time) of 1000 randomly selected points in the network is shown in Fig. 18.27. We investigate how many points are <2, 2, 3, >3 covered during an experiment of 4000 generated events. Our LRP and RTP maintain satisfactory levels of coverage.

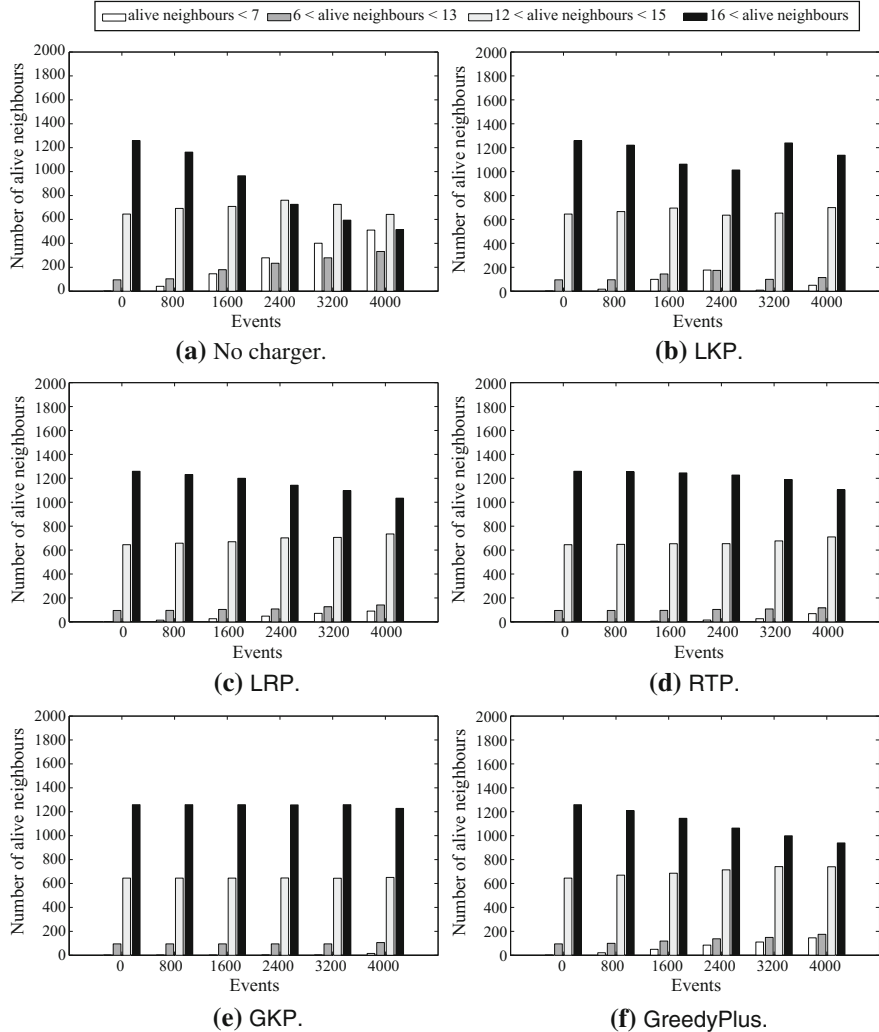


**Fig. 18.25** Routing robustness for uniform deployments with the Greedy routing protocol

(ii) *Greedy protocol*: The coverage aging of 1000 randomly selected points in the network is shown in Fig. 18.28. We investigate how many points are  $<2$ ,  $2$ ,  $3$ ,  $>3$  covered during an experiment of 4000 generated events. Our LRP and RTP maintain satisfactory levels of coverage, approaching the performance of the GKP.

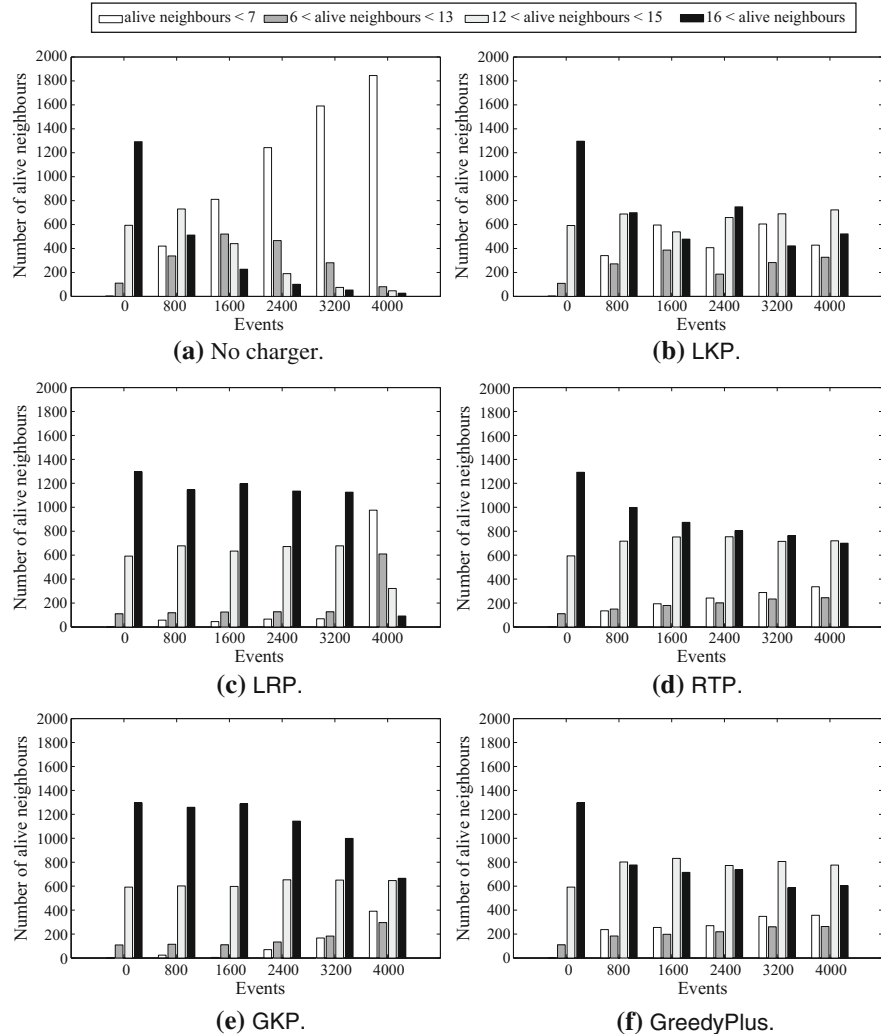


**Fig. 18.26** Routing robustness for uniform deployments with the LEACH routing protocol

(iii) *LEACH protocol*: The coverage aging of 1000 randomly selected points in the network is shown in Fig. 18.29. We investigate how many points are  $<2$ ,  $2$ ,  $3$ ,  $>3$  covered during an experiment of 4000 generated events. The LKP ring is now located at the outer network region. Our RTP achieves satisfactory levels of coverage. We observe that the LRP not only achieves an overall network criticality balance, but also maintains the corresponding criticality values at low levels.

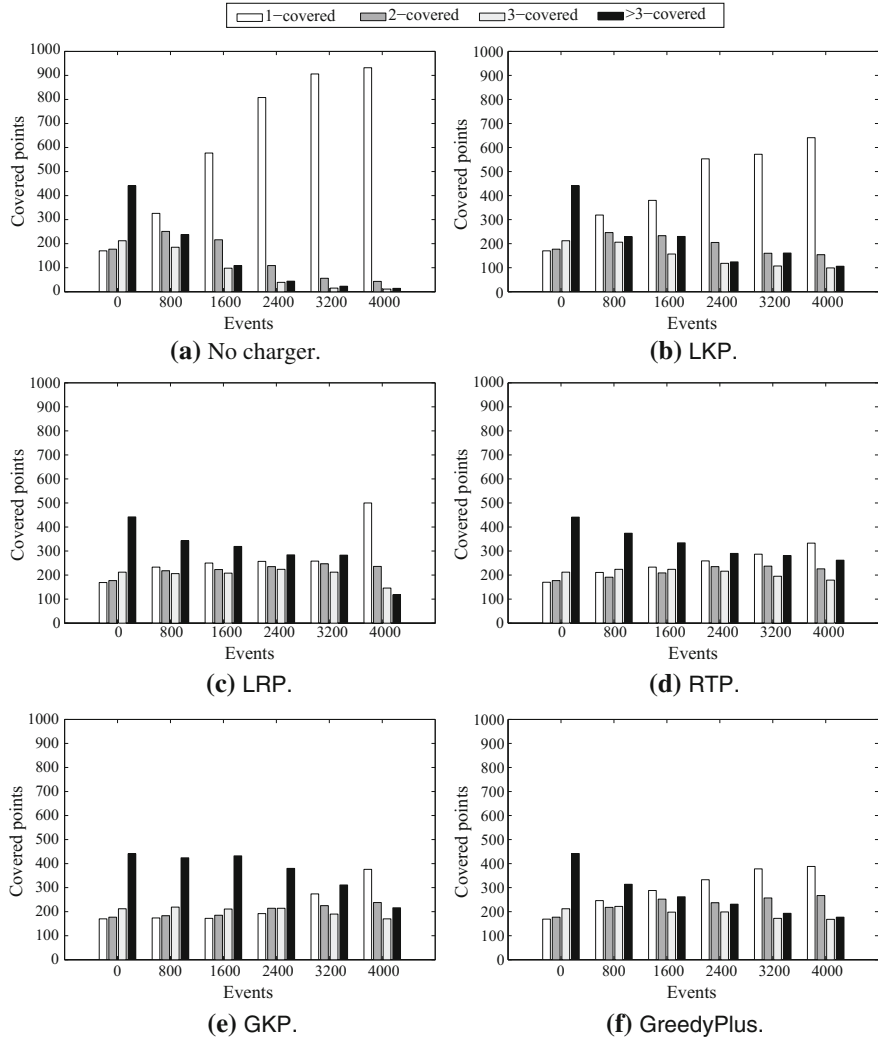


**Fig. 18.27** Coverage aging for uniform deployments with the  $E_i$  protocol

Overall, our proposed protocols extend several network attributes, approach the performance of the global powerful knowledge protocol and significantly outperform the LKP of [1] which was designed with a focus on uniform deployments, and the GreedyPlus of [14] in which the Mobile Charger requires frequent updating, hence increased energy consumption due to message transmissions throughout the whole network.

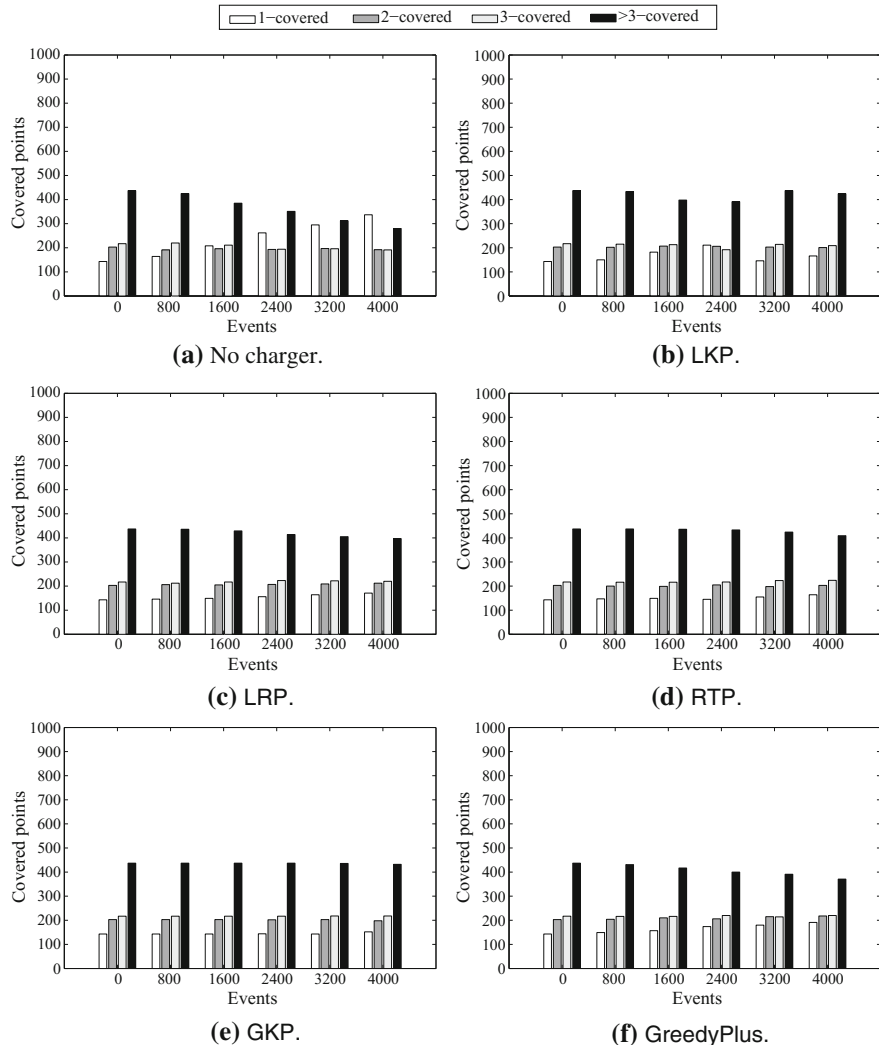


**Fig. 18.28** Coverage aging for uniform deployments with the Greedy protocol

## 18.7 Conclusions

In this chapter we studied the problem of efficient wireless power transfer in Wireless Rechargeable Sensor Networks (WRSNs), in which a Mobile Charger traverses the network and wirelessly replenishes the energy of sensor nodes. We first identify and investigate some critical issues and trade-offs of the Mobile Charger's configuration, such as (i) the energy level each sensor should be charged to (ii) the best split of

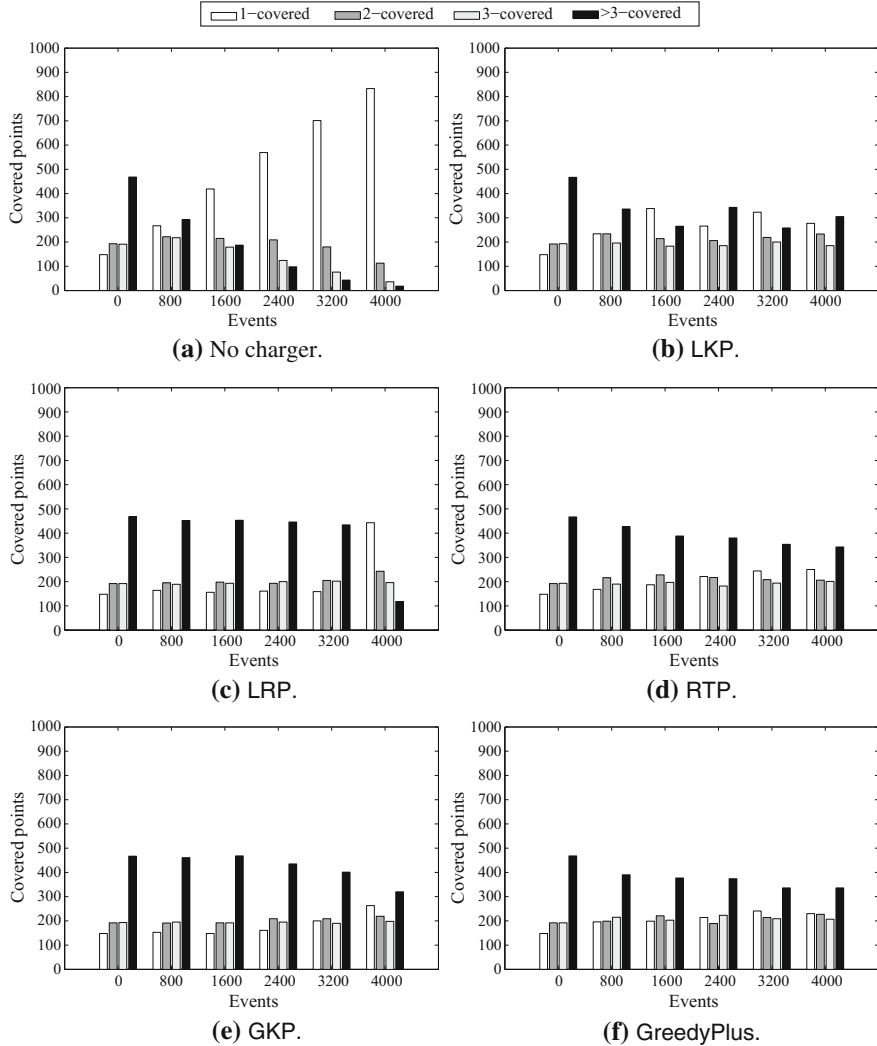


**Fig. 18.29** Coverage aging for uniform deployments with the LEACH protocol

the total available energy between the charger and the sensor nodes and (iii) which trajectories are good for the Mobile Charger to follow.

To capture the diverse dynamics in the network (for both the energy consumption and the traffic flow) we introduce the new network attribute of node criticality; nodes with high criticality are “prioritized” by the charger. This also gives rise to alternative traversal strategies for the charger; in particular, we suggest three new protocols assuming different levels of network knowledge: a centralized global knowledge method, a limited knowledge protocol that performs a distributed sampling of the

network conditions and a reactive method based on the judicious propagation of alert levels in the network. We note that, in contrast to most current approaches, our methods are distributed and adaptive, and use only local (or limited) network information; also, we do not couple recharging with routing, since our methods can be used together with any underlying routing protocol (since they implicitly adapt to it).

For future research, we plan to investigate the case of WRSNs with multiple chargers, where energy transfer among them is possible. We also plan to develop methods addressing WRSNs with mobile sensor nodes. Furthermore, recent advances in magnetic resonant coupling show that multiple nodes can be charged at the same time. This enables us to consider new design alternatives for the charging problem. Finally, we plan to implement selected protocols in small/medium scale real experiments (e.g. with robotic elements and wireless charging technology).

## References

1. Angelopoulos, C.M., Nikoletseas, S., Raptis, T.P., Raptopoulos, C., Vasilakis, F.: Efficient energy management in wireless rechargeable sensor networks. In: MSWiM (2012)
2. Chatzigiannakis, I., Nikoletseas, S., Spirakis, P.: Smart dust protocols for local detection and propagation. In: POMC (2002)
3. Efthymiou, C., Nikoletseas, S., Rolim, J.: Energy balanced data propagation in wireless sensor networks. Wirel. Netw. (2006)
4. Fu, L., Cheng, P., Gu, Y., Chen, J., He, T.: Minimizing charging delay in wireless rechargeable sensor networks. In: INFOCOM (2013)
5. Garey, M.R., Johnson, D.S.: Computers and Intractability. W. H. Freeman and Company (1979)
6. Gnawali, O., Fonseca, R., Jamieson, K., Moss, D., Levis, P.: Collection tree protocol. In: SenSys (2009)
7. Gupta, P., Kumar, P.R.: Critical power for asymptotic connectivity in wireless networks. In: Stochastic Analysis, Control, Optimization and Applications (1998)
8. Heinzelman, W.R., Chandrakasan, A., Balakrishnan, H.: Energy-efficient communication protocol for wireless microsensor networks. In: HICSS (2000)
9. Jarry, A., Leone, P., Powell, O., Rolim, J.: An optimal data propagation algorithm for maximizing the lifespan of sensor networks. In: DCOSS (2006)
10. Kang, B., Ceder, G.: Battery materials for ultrafast charging and discharging. Nature **458**, 190–193 (2009)
11. Li, K., Luan, H., Shen, C.C.: Qi-ferry: Energy-constrained wireless charging in wireless sensor networks. In: WCNC (2012)
12. Li, Z., Peng, Y., Zhang, W., Qiao, D.: J-roc: A joint routing and charging scheme to prolong sensor network lifetime. In: ICNP (2011)
13. Madhja, A., Nikoletseas, S., Raptis, T.P.: Efficient, distributed coordination of multiple mobile chargers in sensor networks. In: MSWiM (2013)
14. Peng, Y., Li, Z., Zhang, W., Qiao, D.: Prolonging sensor network lifetime through wireless charging. In: RTSS (2010)
15. Penrose, M.: Random Geometric Graphs. Oxford University Press (2003)
16. Shi, Y., Xie, L., Hou, Y.T., Sherali, H.D.: On renewable sensor networks with wireless energy transfer. In: INFOCOM (2011)
17. Wang, C., Li, J., Ye, F., Yang, Y.: Multi-vehicle coordination for wireless energy replenishment in sensor networks. In: IPDPS (2013)

18. Xie, L., Shi, Y., Hou, Y.T., Lou, W., Sherali, H.D., Midkiff, S.F.: Bundling mobile base station and wireless energy transfer: modeling and optimization. In: INFOCOM (2013)
19. Xie, L., Shi, Y., Hou, Y.T., Sherali, H.D.: Making sensor networks immortal: an energy-renewal approach with wireless power transfer. IEEE/ACM Trans. Netw. **20**(6), 1748–1761 (2012)
20. Zhang, S., Wu, J., Lu, S.: Collaborative mobile charging for sensor networks. In: MASS (2012)
21. Zhao, M., Li, J., Yang, Y.: Joint mobile energy replenishment and data gathering in wireless rechargeable sensor networks. In: ITC (2011)

## **Part IV**

# **Energy Flow**

# Chapter 19

## Collaborative Mobile Charging

Sheng Zhang and Jie Wu

**Abstract** Wireless power transfer attracts significant attention from both academia and industry. While most previous studies have primarily focused on optimizing charging sequences and/or durations for one or more mobile chargers, we concentrate on collaboration between mobile chargers. In this context, what we mean by “collaboration” is that chargers can exchange energy. We will first show the collaboration benefit in terms of charging coverage and energy usage effectiveness, then we will show how to design collaboration-based scheduling algorithms using a simple yet representative setting. Finally, we will demonstrate several extensions in which previous assumptions are relaxed one by one. We also use simulations to evaluate our theoretical findings and investigate the effects of important design parameters.

### 19.1 Introduction

Wireless power transfer [1] provides a promising means of replenishing battery-powered devices in ad hoc communication networks, and thus supports various novel applications. Armed with wireless power transfer, many existing studies [2–4] have envisioned employing mobile vehicles, robots, and even helicopters carrying high volume batteries as *mobile chargers* to periodically deliver energy to rechargeable devices in target areas. The optimization goals of these studies include maximizing the lifetime of the underlying network [5], optimizing the efficiency of charging scheduling [3], energy provisioning [6], minimizing total charging delay [2], optimizing the coordination of multiple mobile chargers [7], minimizing maximum radiation point [8], etc.

---

S. Zhang (✉)  
State Key Laboratory for Novel Software Technology,  
Nanjing University, 163 Xianlin Avenue, Nanjing 210023, China  
e-mail: sheng@nju.edu.cn

J. Wu  
Department of Computer and Information Sciences,  
Temple University, 1925 N. 12th Street, Philadelphia, PA 19122, USA  
e-mail: jiewu@temple.edu

© Springer International Publishing AG 2016  
S. Nikoletseas et al. (eds.), *Wireless Power Transfer Algorithms, Technologies and Applications in Ad Hoc Communication Networks*,  
DOI 10.1007/978-3-319-46810-5\_19

However, we found that most of the existing work has hardly considered the limited energy of mobile chargers, and has usually assumed that a mobile charger has a sufficient amount of energy to not only replenish an entire target network, but also to make a round-trip back to the base station. This model is invalidated when a dedicated charger (even that with a full battery) cannot reach a particularly remote area.

In this chapter, we introduce a novel charging paradigm, i.e., collaborative mobile charging paradigm [9], which allows energy transfer between mobile chargers. By careful selection of the location of and the amount of energy transferred at each rendezvous point, not only is the energy usage effectiveness improved, but the charging coverage is also enlarged.

We will first discuss related work in Sect. 19.2, and show the collaboration benefit in terms of charging coverage and energy usage effectiveness in Sect. 19.3, then we present how to design collaboration-based scheduling algorithms using a simple yet representative setting in Sect. 19.4. Finally, we demonstrate several extensions in which previous assumptions are relaxed one by one in Sect. 19.5, where we also use simulations to evaluate our theoretical findings and investigate the effects of important design parameters. Concluding remarks are given in Sect. 19.6.

Nikola Tesla (July 10, 1856—January 7, 1943) conducted the first experiments in wireless power transfer as early as the 1890s: an incandescent light bulb was successfully powered using a coil receiver that was in resonance with a nearby magnifying transmitter [10]. Recently, Kurs et al. experimentally demonstrated that energy can be efficiently transmitted between magnetically resonant objects without any interconnecting conductors, e.g., powering a 60 W light bulb, which is 2 m away, with approximately 40 % efficiency [1]. This technology has led to the development of several commercial products, e.g., Intel developed the wireless identification and sensing platform (WISP) for battery-free monitoring [11]; 30+ kinds of popular phones are beginning to embrace wireless charging [12]; and even vehicles [13] and unmanned planes [14] are now supporting wireless charging. It is predicted that the wireless charging market will be worth \$13.78 billion by 2020 [15].

## 19.2 Related Work

There are a number of approaches that are useful in extending the sustainability and applicability of battery-power devices, e.g., sensors, RFIDs, and vehicles. These methods can be classified into two broad types: energy harvesting and energy conservation. The former extracts environmental energy for supporting energy-hungry

devices, and the latter resorts to energy-aware mechanisms for conserving energy during normal operations of devices.

For example, in energy harvesting, Kansal et al. [16] incorporated proactive learning on environmental parameters into performance adaption, and also provided performance-aware systematic methods to systematically utilize environmental energy [17]; solar energy harvesting was taken into consideration when making routing decisions [18]; Cammarano et al. [19] developed accurate prediction models for solar and wind energy harvesting.

With regard to energy conservation, Wang et al. [20] proposed using resource-rich mobile nodes as sinks/relays to balance the unbalanced energy usages; Dunkels et al. [21] took cross-layer information-sharing into consideration; Bhattacharya et al. [22] proposed caching mutable data at some locations to control the data retrieval rate, for the purpose of slowing down the energy consumption rate. Note that, a combination of energy conservation and wireless power transfer can further improve the energy usage effectiveness.

Wireless power transfer has been a viable topic in the area of wireless networks and mobile computing in recent years. A practical wireless recharge model is derived in [6] on top of WISP. The performance of multi-device simultaneous charging is investigated in [23]. For stationary chargers, a charger placement framework is proposed in [6] to ensure that each device receives sufficient energy for continuous operation; a joint optimization of charger placement and power allocation is considered in [24]; how to obtain the maximum electromagnetic radiation point in a given plane is studied in [8]; quality of energy provisioning for mobile nodes, given their spatial distribution, is investigated in [25].

For mobile chargers, existing studies have considered various decision variables and objectives. To maximize network lifetime, charging sequence and packet routing are optimized in [5, 26], while charger velocity is optimized in [27]; to maximize the ratio of the charger's vacation time (i.e., time spent at the home service station) over the cycle time, travelling path and stop schedules are optimized in [3, 4]; to maximize energy usage effectiveness, collaboration between mobile chargers is optimized in [28, 29]; to minimize the total charging delay, stop locations and durations are optimized in [2]; NDN-based energy monitoring and reporting protocols are designed in [30] with a special focus on scheduling mobile chargers for multiple concurrent emergencies; to simultaneously minimize charger travel distance and charging delay, synchronized charging sequences based on multiple nested tours are optimized in [31]; given heterogenous charging frequencies of sensors, how to schedule multiple charging rounds to minimize total moving distance of mobile chargers is studied in [32].

### 19.3 Motivation

The motivation of our design is to illustrate the benefits of collaboration in terms of charging coverage and energy usage effectiveness.

### 19.3.1 Notations

In order to clearly present the motivational examples, we first introduce a few necessary notations.

We consider  $N$  stationary sensor nodes distributed along a straight line. These nodes are uniformly distributed, i.e., a unit distance apart. A base station is located to the left of the wireless sensor network (WSN). The base station also serves as the service station that replenishes mobile chargers. Without loss of generality, we denote the sensor nodes from left to right by  $s_1, s_2, \dots$ , and  $s_N$ . The battery capacity of each sensor node is  $b$ . Each node consumes energy for sensing, data reception, and transmission. We represent the average energy consumption rate of each sensor node as  $r$ . The recharging cycle of a sensor node is defined as the time period during which a sensor node with a full battery can survive without being charged. Letting  $\tau$  be the recharging cycle of each sensor node, we have  $\tau = b/r$ .

We assume that mobile chargers are homogeneous: for every charger, the battery capacity is  $P$ , the travelling speed is  $v$ , and energy consumed by travelling one unit distance is  $c$ . Both travelling and wireless charging share the same battery of a mobile charger. The  $i$ -th mobile charger is denoted by  $C_i$ . A mobile charger starts from the base station with a full battery; after it finishes its charging task, it must return to the base station to be serviced (e.g., recharging its own battery).

As the wireless power transfer efficiency decreases rapidly when the distance between charger and rechargeable device increases [6], we assume that a charger can transfer energy to a sensor node only when they are very close to each other; in this case, we assume that the wireless power transfer is perfect, i.e., there is no energy loss during energy transfer. We denote by  $C_i \xrightarrow{e} C_j$  (resp.  $C_i \xrightarrow{e} s_j$ ) the event that charger  $C_i$  transfers  $e$  units of energy to charger  $C_j$  (resp. sensor  $s_j$ ).

### 19.3.2 Collaboration Benefit

**Coverage.** Figure 19.1 shows an example of scheduling chargers without collaboration, where there are 6 sensor nodes and the distance between two consecutive nodes is 1 m. The battery capacities of each node and each charger are 2 and 40 J (J for Joule), respectively; the travelling cost is 3 J/m. In the figure, two chargers are used:  $C_1$  charges  $s_1$  to  $s_4$  and returns to the base station, and  $C_2$  charges  $s_5$  to  $s_6$  and returns to the base station.

We note that even given an infinite number of chargers, the maximum coverage cannot exceed 6 sensors, since any charger must return to the base station for the next round of scheduling (i.e.,  $\frac{P}{2c} = \frac{40}{2 \times 3} < 7$ ). However, we will shortly see in Theorem 19.2 that, the coverage of well-designed collaboration-based scheduling can be infinite.

**Energy usage effectiveness.** The energy consumed in replenishing target networks can be classified into three categories: *payload energy*, which is the energy eventually

**Fig. 19.1** Time-space view of scheduling chargers without collaboration, where  $b = 2 \text{ J}$ ,  $P = 40 \text{ J}$ , and  $c = 3 \text{ J/m}$

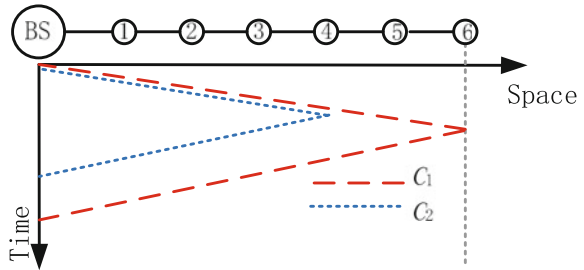
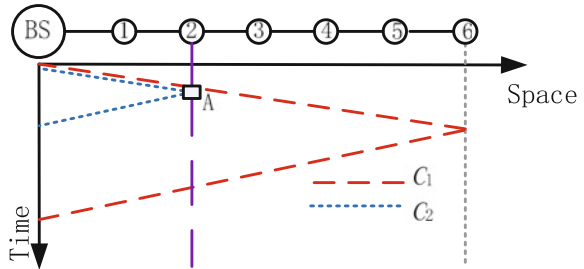


**Fig. 19.2** Time-space view of scheduling chargers with collaboration, where  $b = 2 \text{ J}$ ,  $P = 40 \text{ J}$ , and  $c = 3 \text{ J/m}$



obtained by rechargeable devices, *movement energy*, which is the energy used by mobile chargers for moving, and *loss energy*, which is the energy loss during wireless energy transfer. The energy usage effectiveness (EUE) is thus defined as the ratio of the amount of payload energy to the total energy.

In Fig. 19.1, the payload energy is 12, the movement energy is 60, and the loss energy is 0, and hence the EUE is  $\frac{1}{6}$ . In fact, this is also the highest EUE a scheduling without collaboration can achieve in this example. To delivery energy to  $s_6$ , one charger ( $C_1$  in the example) must travel to  $s_6$ ; due to capacity constraint,  $C_1$  cannot charge more than two nodes (since  $40 < 6 \times 2 \times 3 + 2 \times 3 = 42$ ); therefore, another charger ( $C_2$ ) must travel to at least  $s_4$ .

However, collaboration can improve EUE, as shown in Fig. 19.2.  $C_2$  charges  $s_1$  to  $s_2$ , charges  $C_1$  to its full battery at  $s_2$ , and returns to the base station. We can similarly calculate that, the EUE of this scheduling is  $\frac{1}{5}$ .

## 19.4 Design

In this section, we present the design of collaboration-based scheduling algorithms for a simple yet representative setting. First, we introduce problem formulation in Sect. 19.4.1 and scheduling examples in Sect. 19.4.2, then we present PushWait, an algorithm that achieves the highest EUE in Sect. 19.4.3, and lastly we give some notes in Sect. 19.4.4.

### 19.4.1 Problem Formulation

The scheduling of chargers is equivalent to deciding the time-space trajectories of chargers. In a feasible scheduling, any rechargeable device should not run out of energy, and every charger should be able to return to the base station. The *scheduling cycle* of a feasible scheduling is the time interval between two consecutive time points when each sensor has the same battery level. To evaluate the long-term energy efficiency of a scheduling, we only have to consider the energy usage in a scheduling cycle. In a scheduling cycle, we denote by  $E^{pl}$ ,  $E^{mm}$ , and  $E^{ls}$  the amounts of payload energy, movement energy, and loss energy, respectively. The EUU is thus defined as

$$EUE = \frac{E^{pl}}{E^{pl} + E^{mm} + E^{ls}}. \quad (19.1)$$

Given these settings, our goal is to maximize the EUU.

For simplicity of presentation, we discuss our designs under two assumptions:

- *Short Duration (SD)*: the time for charging a sensor node to its full battery is negligible compared to the recharging cycle;
- *Long Cycle (LC)*: the recharging cycle of a sensor node is longer than a charging round, i.e., any two consecutive charging rounds have no intersections. Thus, mobile chargers can always accomplish a charging round, return to the base station, and wait for another charging round.

Our designs can be applied to settings without these two assumptions, see remarks in Sect. 19.4.4.

### 19.4.2 Scheduling Examples

We introduce three scheduling examples to motivate the algorithm design.

Suppose we have only 3 mobile chargers with  $P = 80 \text{ J}$ ,  $c = 3 \text{ J/m}$ , and the battery capacity of each sensor node is  $b = 2 \text{ J}$ . Since the total energy is fixed, and is  $80 \text{ J} \times 3 = 240 \text{ J}$ , EUU is maximized when  $E^{pl}$  is maximized. Therefore, in the following, we try to see how to cover the greatest number of sensor nodes using 3 chargers.

Figures 19.3, 19.4, and 19.5 show the time-space views of three simple scheduling heuristics. In the figures, we use  $L_i$  ( $1 \leq i \leq 3$ ) to represent the farthest distance that  $C_i$  travels away from the base station. We also let  $L_4$  be 0 for compatibility.

- *EqualShare*: each sensor node is jointly charged by all chargers. In our example, each mobile charger transfers  $2/3$  unit of energy to each sensor node. Thus, 12 sensors can be covered, as shown in Fig. 19.3.
- *SolelyCharge*: each charger is responsible for a set of consecutive sensor nodes, and each sensor node is assigned to one distinct charger. In our example,  $C_3$  charges

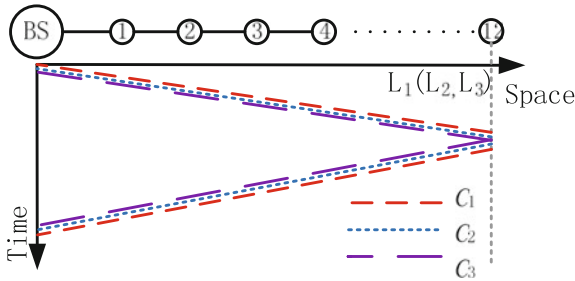


**Fig. 19.3** EqualShare,  $L_3 = L_2 = L_1 = 12$

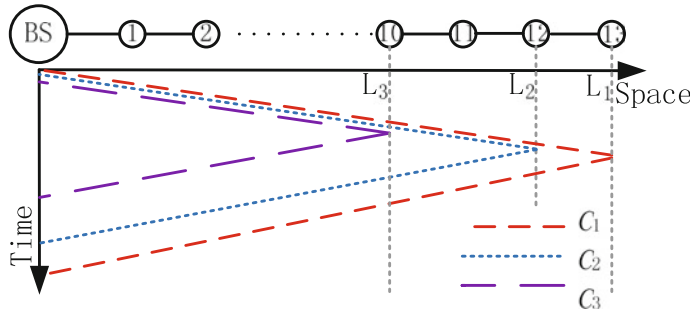


**Fig. 19.4** SolelyCharge,  $L_3 = 10, L_2 = 12, L_1 = 13$ .  $C_2$  has 4 J residual energy

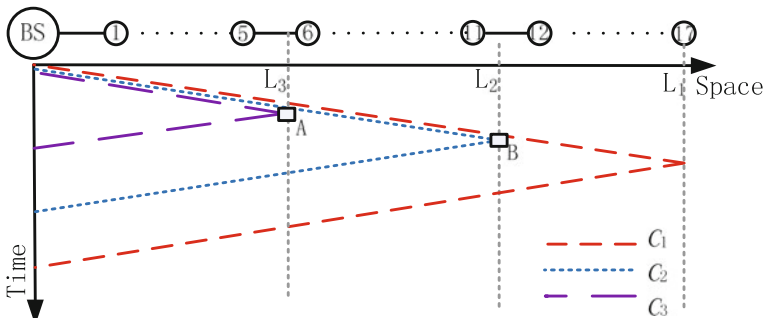


**Fig. 19.5** CLCharge,  $L_3 = 5\frac{5}{6}, L_2 = 11\frac{4}{9}, L_1 = 17$ .  $C_1$  has  $\frac{1}{3}J$  residual energy

sensor nodes from  $L_4$  to  $L_3$ ;  $C_2$  charges sensor nodes from  $L_3$  to  $L_2$ ; and  $C_1$  charges sensor nodes from  $L_2$  to  $L_1$ . The variables  $L_3$ ,  $L_2$ , and  $L_1$  are carefully chosen, so that each charger returns to the base station with exactly zero energy. Figure 19.4 demonstrates that 13 sensors can be covered.

- **CLCharge:** each charger is responsible for a set of consecutive sensor nodes, each sensor node is assigned to one distinct charger, and energy transfer between chargers are utilized. In our example,  $C_3$  charges sensors from the base station to  $L_3$ , then

transfers some energy to  $C_2$  and  $C_1$  at  $L_3$ , and finally returns to the base station. Here,  $L_3$  is carefully chosen, such that (i)  $C_2$  and  $C_1$  have full batteries after  $C_3$  transfers energy to them, and (ii)  $C_3$  returns to the base station with exactly zero energy. In Fig. 19.5, 17 sensors can be covered.

In these scheduling examples, we make the following key observation that may provide some insight into the design of an optimal scheduling algorithm in the next subsection: when the extent of collaboration increases, the coverage increases. In EqualShare, chargers do not cooperate with each other, and they just charge sensor nodes one by one from the base station; in SolelyCharge, each charger is restricted to replenishing a set of consecutive nodes, and the target network is partitioned into disjoint intervals; finally, in CLCharge, intentional energy transfer between chargers is utilized to further enlarge the coverage.

### 19.4.3 PushWait

For a given target network, the payload energy is fixed, i.e.,  $E^{pl}$  is fixed,; since we assume wireless power transfer is perfect, i.e.,  $E^{ls} = 0$ , we can maximize EUU through minimizing the sum of distances travelled by chargers, i.e., minimizing  $E^{mm}$ .

How might we minimize the sum of the distances travelled by chargers? The key observation is that, we can let as few mobile chargers as possible carry the residual energy of all chargers, and move forward. CLCharge in Fig. 19.5 reflects this intuition:  $C_3$  turns around at  $L_3 = 5\frac{5}{6}$ , which is smaller than 13 in Fig. 19.4. Therefore, the sum of the total travelling distances in CLCharge is less than that in SolelyCharge, leading to a higher EUU. The reason that we can safely let  $C_3$  turn around at  $L_3 = 5\frac{5}{6}$  is that  $C_2$  and  $C_1$  can carry the residual energy and move forward, instead of having all of the three not-full-battery mobile chargers move forward.

Can we improve CLCharge? We notice that, in Fig. 19.4, when  $C_2$  (resp.  $C_1$ ) reaches  $L_3$  on its way back to the base station, it has a positive amount of residual energy for safely returning to the base station. In other words,  $C_2$  (resp.  $C_1$ ) carries this particular part of energy during its travelling from  $L_3$  to  $L_2$  (resp.  $L_1$ ), and finally to  $L_3$  again. How about letting  $C_3$  stop moving forward at a place  $L'_3$  which is closer to the base station than  $L_3 = 5\frac{5}{6}$ ? In doing so,  $C_3$  can wait at a place with sufficient energy to support  $C_2$  and  $C_1$ 's travelling from  $L'_3$  to the base station.

We therefore design PushWait, the optimal scheduling algorithm that achieves the highest EUU. Formally, suppose that we require  $M$  chargers to cover a given WSN, then each charger  $C_i$  in PushWait follows the iterative process below.

1.  $C_i$  starts from the base station with a full battery; it then gets fully charged at locations  $L_M, L_{M-1}, \dots$ , and  $L_{i+1}$ .
2.  $C_i$  charges sensor nodes between  $L_{i+1}$  and  $L_i$ . When it arrives at  $L_i$ , it charges  $C_{i-1}, C_{i-2}, \dots$ , and  $C_1$ , such that these  $(i - 1)$  chargers' batteries are full.
3.  $C_i$  waits at  $L_i$ . When all of  $C_1, C_2, \dots$ , and  $C_{i-1}$  return to  $L_i$ , it evenly distributes its residual energy among these  $i$  chargers (including  $C_i$  itself).

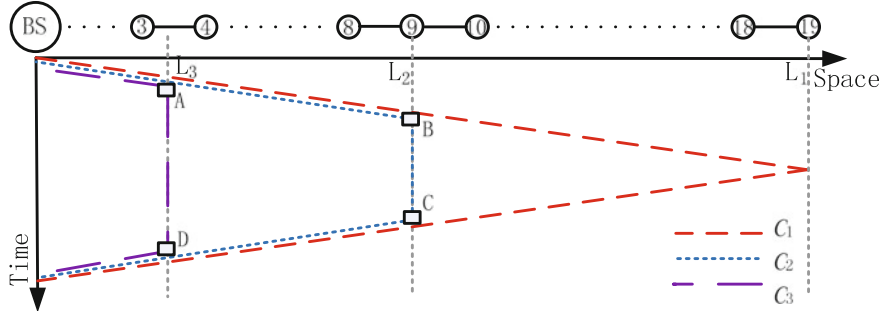


**Fig. 19.6** Time-space view of PushWait with the same settings as in Figs. 19.3, 19.4, and 19.5. We have  $L_3 = 3\frac{1}{3}$ ,  $L_2 = 9$ ,  $L_1 = 19$ .  $C_3$  has 14 J residual energy

4. On  $C_i$ 's way back to the base station, it gets charged at locations  $L_{i+1}, L_{i+2}, \dots$ , and  $L_M$ , which makes it have just enough energy to return to the base station.

The reason for naming this scheduling after “PushWait” is clear: each charger “pushes” some other chargers to move forward, and “waits” for their returns.

Figure 19.6 shows the time-space view of PushWait with the same settings as in Figs. 19.3, 19.4, and 19.5. The running details are as follows. Mobile chargers  $C_1$ ,  $C_2$ , and  $C_3$  start from the base station with  $P = 80$  J energy. At  $L_3 = 3\frac{1}{3}$ , both  $C_1$  and  $C_2$  have  $80 - 3 \cdot L_3 = 70$  J energy, while  $C_3$  has  $80 - 3 \cdot L_3 - 2 \times 3 = 64$  J energy, because it charges nodes  $s_1$ ,  $s_2$ , and  $s_3$ . Then, we let  $C_3 \xrightarrow{10} C_2$  and  $C_3 \xrightarrow{10} C_1$ . After this,  $C_3$  waits at  $L_3$  with 44 J energy. Similarly, after  $C_2$  charges nodes from  $s_4$  to  $s_9$ , and charges  $C_1$  to its full battery at  $L_2 = 9$ ,  $C_2$  waits at  $L_2$  with 34 J energy. When  $C_1$  returns to  $L_2$  after charging nodes from  $s_{10}$  to  $s_{19}$ , as the reader can verify, it has exactly 0 energy. Then, we let  $C_2 \xrightarrow{17} C_1$ . Note that, 17 J energy is just enough for  $C_1$  or  $C_2$  to move from  $L_2$  to  $L_3$ . At  $L_3$ , we let  $C_3 \xrightarrow{10} C_2$  and  $C_3 \xrightarrow{10} C_1$ . Again, note that, 10 J energy is just enough for  $C_1$  or  $C_2$  to move from  $L_3$  to the base station. When they return to the base station, only  $C_3$  has 14 J residual energy. PushWait covers 19 sensor nodes.

#### 19.4.3.1 Parameters

We present how to determine  $L_i$  ( $1 \leq i \leq M$ ) to maximize EUE in this subsection. Remember that, sensor nodes are uniformly distributed, and therefore, we make the following approximation: given  $d'$  distance, we have approximately  $d'/d$  sensors.

Let us analyze the interval between  $L_{i+1}$  and  $L_i$ .  $C_i$  gets fully charged at  $L_{i+1}$  and reaches  $L_{i+1}$  with 0 energy on its way back to the base station. The full battery  $P$  is used up for the following reasons: (i)  $C_i$  charges sensors between  $L_{i+1}$  and  $L_i$ , (ii)  $C_i$  moves from  $L_{i+1}$  to  $L_i$ , (iii)  $C_i$  transfers some energy to  $C_1, C_2, \dots$ , and  $C_{i-1}$  at  $L_i$  for the first time. Note that these  $i-1$  chargers are fully charged at  $L_{i+1}$ , and

thus the energy transferred to them at  $L_i$  is exactly the energy consumed by their travellings from  $L_{i+1}$  to  $L_i$ ; (iv)  $C_i$  transfers some energy to  $C_1, C_2, \dots$ , and  $C_{i-1}$  at  $L_i$  for the second time, which is just enough for them to travel from  $L_i$  to  $L_{i+1}$ , and (v)  $C_i$  moves from  $L_i$  to  $L_{i+1}$ . Combining the above reasons together, we have the following equations.

$$2icd(L_i - L_{i+1}) + b(L_i - L_{i+1})/d = P(1 \leq i < M) \quad (19.2)$$

$$2Mcd(L_M - 0) + b(L_M - 0)/d \leq P \quad (19.3)$$

The second formula is an inequality, since PushWait cannot always use up exactly the total energy of  $M$  chargers. We then have:

$$L_1 = Nd \quad (19.4)$$

$$L_i = Nd - \sum_{j=1}^{i-1} \frac{Pd}{2cd^2j + b} (2 \leq i \leq M) \quad (19.5)$$

The number of chargers  $M$  can be determined by:  $L_M > 0, L_{M+1} \leq 0$ . We further have  $E^{pl} = Nb$  and  $E^{mm} = 2cd \sum_{i=1}^M L_i$ . The duration of a charging round is  $Nd/v$ , and the scheduling cycle is equal to the recharging cycle, i.e.,  $\tau$ .

#### 19.4.3.2 Properties

**Theorem 19.1** (Optimality of PushWait) *For the settings described in Sect. 19.4, PushWait is optimal in terms of EUE.*

*Proof* Denote by  $Distance(alg)$  the sum of travelling distances by all mobile chargers in a scheduling algorithm  $alg$ . As we mentioned before, it is sufficient to prove that  $Distance(PushWait)$  is the minimum. Suppose that PushWait requires  $M$  mobile chargers to replenish the given WSN. We prove the theorem by mathematical induction on  $M$ .

$M = 1$ .  $Distance(PushWait) = 2L_1$ , where  $L_1$  is the length of the given WSN. We note that any scheduling algorithm  $anyalg$  must have at least one charger to charge the farthest sensor node in the WSN, therefore,  $Distance(anyalg) \geq 2L_1 = Distance(PushWait)$ .

$M = 2$ . (By contradiction) Suppose that PushWait is not optimal, and the optimal scheduling algorithm is  $OPT_2$ . Since one charger cannot cover the entire WSN, there are at least two chargers in  $OPT_2$ . One of them, say  $C'$ , must charge the farthest sensor, and thus it moves at least  $2L_1$  distance. By definition, we should have  $Distance(OPT_2) < Distance(PushWait) = 2L_1 + 2L_2$ . Therefore, all the other chargers in  $OPT_2$  cannot travel as far as  $L_2$ . However, according to our calculation of  $L_2$  in PushWait, a charger with a full battery at  $L_2$  can only charge the sensors between  $L_2$  and  $L_1$  and return to  $L_2$  with 0 energy; then we know  $C'$  in  $OPT_2$  can, by

no means, reach  $L_1$ : a contradiction! Therefore, no such  $OPT_2$  exists, and PushWait is optimal.

I.H.: PushWait is optimal for any  $M < n$ .

$M = n$ . (By contradiction) Suppose that PushWait is not optimal, and the optimal scheduling algorithm is  $OPT_n$ . Imagine that a virtual base station  $BS'$  is located at  $L_n$ , then,  $OPT_n$  and PushWait require  $Q$  and  $(n - 1)P$  energy, respectively, to cover the sensors between  $L_n$  and  $L_1$ . By the induction hypothesis,  $Q > (n - 1)P$ . Then, the task of  $OPT_n$  is to cover the sensors from the base station to  $L_n$  and to deliver  $Q$  energy to  $L_n$ . It is then straightforward to see that  $OPT_n$  requires at least  $n$  chargers to reach  $L_n$ ; otherwise, the total residual energy of less than  $n$  chargers at  $L_n$  is definitely less than  $(n - 1)P$ . Since  $Q > (n - 1)P$ ,  $OPT_n$  consumes more energy than PushWait: a contradiction! No such  $OPT_n$  exists, and PushWait is optimal.  $\square$

**Theorem 19.2** (Coverage) *The maximum coverages of EqualShare, SolelyCharge, CLCharge, and PushWait are  $P/2c$ ,  $P/2c$ ,  $P/c$ , and infinity, respectively.*

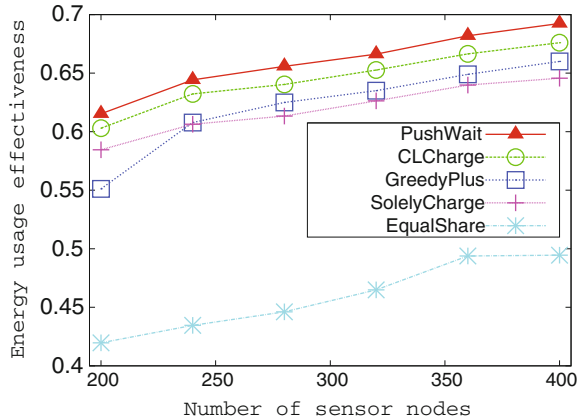
The detailed proofs of Theorems 19.2, 19.3, 19.4, and 19.5 can be found in [9, 29].

Our problem resembles the banana-eating camel problem [33] to a limited extent. A farmer has 3,000 bananas that will be sold at a market 1,000 miles away. He has only a camel that can carry at most 1,000 bananas at a time but will eat 1 banana to refuel for each mile it walks. Is there any method to delivery any bananas to the market? If yes, how? There are two major differences between our problem and this one: first, energy can only be exchanged between chargers, while bananas could be placed on the ground; second, only one camel is involved, implying there is no collaboration.

#### 19.4.3.3 Performance

Following similar settings in [5], we assume that sensor nodes are powered by a 1.5 V 2000 mAh Alkaline rechargeable battery, then the battery capacity ( $b$ ) is  $1.5 \text{ V} \times 2 \text{ A} \times 3600 \text{ s} = 10.8 \text{ KJ}$ . The battery capacity of a mobile charger ( $P$ ) is 2000 KJ; the moving speed of a charger ( $v$ ) is 1 m/s; the charger's moving power consumption rate is 50 W, thus, the moving cost of a charger ( $c$ ) is 50 J/m. We assume that sensor nodes are uniformly deployed over a 10 Km straight line. By default, the number of sensor nodes ( $N$ ) is 400; the wireless charging efficiency ( $\eta_1$ ) is 1.5 %; the charging efficiency between mobile chargers ( $\eta_2$ ) is 30 %. We compare PushWait with EqualShare, SolelyCharge, CLCharge, and GreedyPlus [5]. The original version of GreedyPlus does not consider multiple chargers, and we tailored it to our scenarios: multiple mobile chargers are seen as one large charger, which adopts binary search to

**Fig. 19.7** Performance comparisons by varying the number of sensor nodes



find a suitable target network lifetime. Note that, a sensor may be recharged several times in a charging round in GreedyPlus.

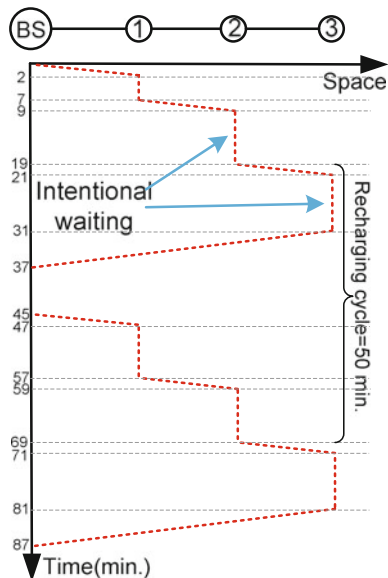
Figure 19.7 shows the performance comparisons in scenario K1K2K3 by varying the number of sensor nodes. When the number of sensor nodes increases, since they are restricted to the 10 km long line, the density of sensor nodes also increases. This is so that mobile chargers can transfer energy to more sensor nodes without incurring much moving cost. According to this, all of the five algorithms perform better when the number of sensor nodes increases. The main reason for the relatively low EUE of EqualShare is that, every charger in EqualShare has to move to the farthest sensor node, and thus, the increase in the number of sensor nodes leads to an increase in the amount of overhead energy. In summary, as we theoretically demonstrated earlier, PushWait achieves the highest EUE among the five algorithms. CLCharge takes advantage of collaboration between chargers, and so has the second highest EUE. GreedyPlus greedily selects the next charging target, outperforming SolelyCharge and EqualShare. EqualShare has the worst performance. Comparisons between EqualShare, SoleCharge, and CLCharge can be found in [28].

#### 19.4.4 Remarks

We now show how to apply PushWait to contexts without the short duration (SD) and low cycle (LC) assumptions.

**Without SD.** When the time for charging a sensor node to its full battery is not negligible compared to the recharging cycle, we use the first charging round to synchronize the battery levels of all sensor nodes. The purpose of synchronization is to make sure that, each sensor node  $s_i$  would require exactly  $b$  amount of energy when the mobile charger approaches it in the following charging rounds. Since the energy

**Fig. 19.8** Without the SD assumption. The first charging round (0 to 37 min) synchronizes the battery levels through intentionally waiting. In the figure, the distance between two consecutive sensor nodes is 10 m,  $b = 2 \text{ J}$ ,  $P = 200 \text{ J}$ ,  $c = 3 \text{ J/m}$ ,  $v = 5 \text{ m/min.}$ , and the charger can transfer 0.2J to a node in 1 min



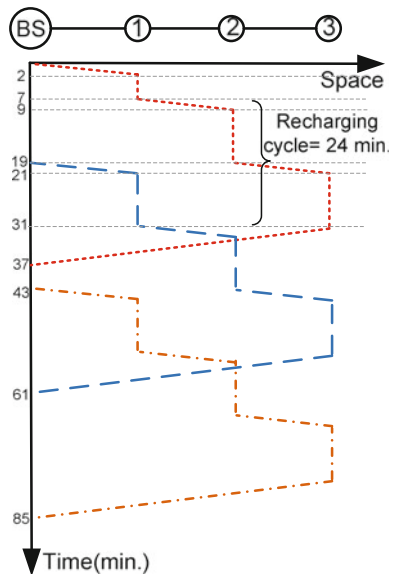
transfer rate is fixed, we can modify our scheduling algorithms by intentionally adding a fixed duration at each sensor node.

We use Fig. 19.8 for further explanation, where 3 sensor nodes are 10 m apart. The battery capacity of each node is 2 J, and the recharging cycle of each node is 50 min. Therefore, the energy consumption rate is 0.04 J/min. The charger can transfer 0.2 J energy to a node in 1 min. Therefore, it takes 10 min to transfer 2 J to a node.

Suppose that when the charger arrives at  $s_1$  for the first time, it has 1.2 J residual energy; since  $(2 - 1.2)/(0.2 - 0.04) = 5$ , it takes 5 min for the charger to replenish  $s_1$  to its full battery. When the charger arrives at  $s_2$ , it also has 1.2 J residual energy. Although the charger could finish charging  $s_2$  in 5 min, *the charger should intentionally wait another 5 min before heading for  $s_3$* . This should be done for the purpose of synchronizing energy levels among sensor nodes, as shown in Fig. 19.8. In doing so, in the following charging rounds, each sensor node will have exactly 0.4 J energy when the charger begins to recharge it, implying that it would take the same amount of time (i.e., 10 min) for the charger to recharge each node to its full battery. For instance,  $s_1$ ,  $s_2$ , and  $s_3$  have full batteries at the 7th, 19th, and 31st min, respectively; in the second charging round, they become fully charged at the 47th, 59th, and 71st min, respectively. We see that, the corresponding time interval for every sensor is 50 min, which is the recharging cycle of each sensor node.

**Without LC.** Generally speaking, when the recharging cycle of a sensor node is not longer than a charging round, we can adopt a pipeline-like solution. Figure 19.9 shows an example. Since the recharging cycle is 24 min, the 2nd (resp. 3rd) charging

**Fig. 19.9** Without the LC assumption. Pipeline-like periodic charging rounds are scheduled to cope with short recharging cycle (24 min < 42 min). In the figure, the distance between two consecutive sensor nodes is 10 m,  $b = 2$  J,  $P = 200$  J,  $c = 3$  J/m,  $v = 5$  m/min., and the charger can transfer 0.2J to a node in 1 min



round has to start at the 19th (resp. 43rd) minute. It is not hard to see that, pipeline-like PushWait can still achieve optimality. An additional requirement of such a solution is that, it needs more chargers, e.g., 2 chargers are required in Fig. 19.9.

## 19.5 Extensions

Three main assumptions that are made in Sect. 19.4 include: (*K1*) all sensor nodes are distributed along a one-dimensional (1-D) line; (*K2*) the recharging cycles of all sensor nodes are the same; (*K3*) there is no energy loss during any energy transfers. In this section, we consider several scenarios that remove these conditions one by one, and finally investigate the mobile charging scheduling problem in general 2-dimensional (2-D) WSNs. We use  $\bar{K}_j$  to indicate that  $K_j$  does not hold,  $j \in \{1, 2, 3\}$ . For example,  $K1K2\bar{K}3$  represents the scenario in which *K1* and *K2* hold, while *K3* does not hold.

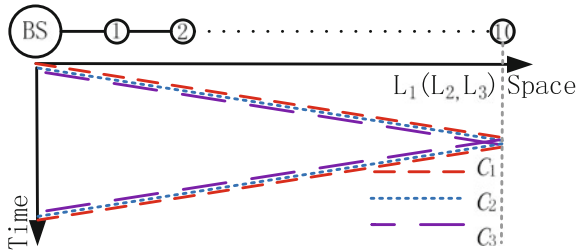
The recharging cycle of  $s_i$  is denoted by  $\tau_i$ . We denote by  $\eta_1$  the wireless charging efficiency between a charger and a sensor node, i.e., a charger  $C$  consumes one unit of energy while a sensor can only receive  $\eta_1$  units of energy. Similarly, denote by  $\eta_2$  the efficiency between two chargers. For example, if  $C_i \xrightarrow{e} C_j$  (resp.  $C_i \xrightarrow{e} s_j$ ), then  $C_j$  (resp.  $s_j$ ) receives only  $\eta_2e$  (resp.  $\eta_1e$ ) units of energy.

### 19.5.1 Energy Loss

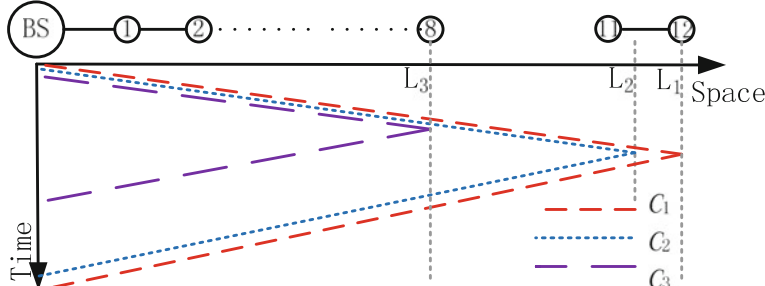
We first study the scenario where  $K3$  does not hold. Mobile chargers' collaboration helps PushWait achieve optimality; however, when energy loss during energy transfer is not negligible, collaboration increases  $E^{ls}$ , and hence, may impair the EUE of PushWait. We use the following example to illustrate this observation.

Figures 19.10, 19.11, 19.12 and 19.13 show the time-space views of four scheduling algorithms. The farthest distance that  $C_i$  moves away from the base station is determined via the same analysis as before. The settings are similar to those in Figs. 19.3, 19.4, 19.5 and 19.6, except that  $\eta_1 = 0.5$  and  $\eta_2 = 0.25$ .

Taking Fig. 19.10 for example,  $C_3$  can cover only 8 sensors, because  $8c + 8c + 2 \times 8\eta_1 = 80$ ;  $C_1$  can cover only  $s_{12}$ , because it cannot return to the base station if it

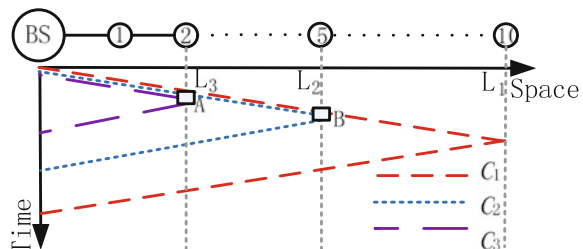


**Fig. 19.10** EqualShare,  $L_3 = L_2 = L_1 = 10$



**Fig. 19.11** SolelyCharge,  $L_3 = 8, L_2 = 11\frac{1}{3}, L_1 = 12$ .  $C_1$  has 4 J residual energy

**Fig. 19.12** CLCharge,  
 $L_3 = 2, L_2 = 5, L_1 = 10$ .  $C_1$   
has 4 J residual energy



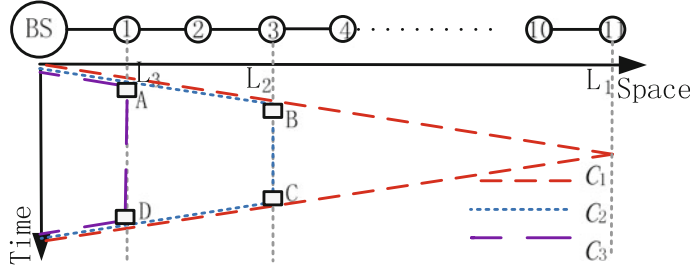


**Fig. 19.13** PushWait,  $L_3 = 1$ ,  $L_2 = 3$ ,  $L_1 = 11$ .  $C_3$  has 10 J residual energy

covers  $s_{13}$  as well. When all three chargers return to the base station, only  $C_1$  has 4 J residual energy. The numbers of sensor nodes that can be covered in four algorithms are 10, 12, 10, and 11, respectively; their EUEs are  $\frac{10 \times 2}{240 - 20} \approx 0.091$ ,  $\frac{12 \times 2}{240 - 4} \approx 0.102$ ,  $\frac{10 \times 2}{240 - 4} \approx 0.085$ , and  $\frac{11 \times 2}{240 - 10} \approx 0.096$ , respectively.

### 19.5.1.1 $\eta$ PushWait

Recall that PushWait is optimal for scenario  $K1K2K3$ ; however, in scenario  $K1K2\bar{K}3$ , due to the energy loss between chargers, its EUE is only the second highest, while SolelyCharge achieves the highest EUE. This example suggests to us that SolelyCharge may perform better than PushWait for  $K1K2\bar{K}3$ .

**Theorem 19.3** (Optimality of SolelyCharge) *If collaboration among chargers is not permitted, SolelyCharge is optimal in terms of EUE for  $K1K2\bar{K}3$ ,*

Though SolelyCharge is optimal if collaboration is not allowed, it has limited coverage (see Theorem 19.2). PushWait is not optimal for scenario  $K1K2\bar{K}3$ , but it can cover a 1-dimensional WSN of infinite length.

We therefore propose combining SolelyCharge with PushWait to construct our solution  $\eta$ PushWait, which is better than either of them individually. Denote by  $cg(alg, M)$  the coverage of a scheduling algorithm  $alg$  with  $M$  mobile chargers. For example, in scenario  $K1K2\bar{K}3$ , if we assume that,  $\forall 1 \leq i \leq N$ ,  $b_i = b$  and  $x_i = i \cdot d$ , following a similar analysis as in Sect. 19.4.3, we have

$$cg(\text{SolelyCharge}, M) = \sum_{i=1}^M \frac{\eta_1 db^{i-1} P}{(2\eta_1 cd^2 + b)^i} \quad (19.6)$$

$$cg(\text{PushWait}, M) = \sum_{i=0}^{M-1} \frac{\eta_1 \eta_2 d P}{\eta_2 b + 2\eta_1 cd^2(\eta_2 + i)} \quad (19.7)$$

Given a WSN and mobile chargers that satisfy  $K1K2\bar{K}3$ , let  $M'$  be the largest value of  $M$  that ensures  $cg(\text{SolelyCharge}, M) \geq cg(\text{PushWait}, M)$ , i.e.,

$$M' = \arg \max_{cg(SolelyCharge, M) \geq cg(PushWait, M)} M. \quad (19.8)$$

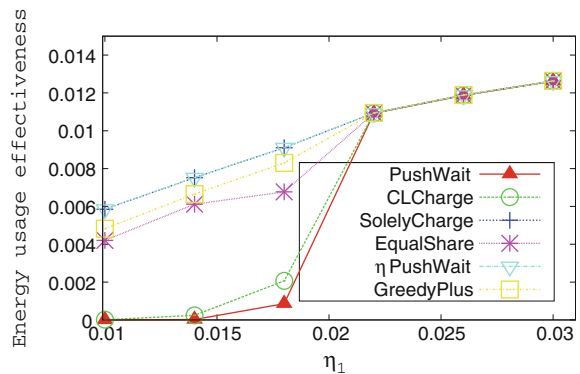
Then,  $\eta$ PushWait can be constructed as follows. If the length of the given WSN is not greater than  $cg(SolelyCharge, M')$ , we use SolelyCharge. Otherwise, we have the following strategy: we use SolelyCharge to charge sensors between the base station and  $cg(SolelyCharge, m)$ , and use PushWait to charge the remaining sensors, where  $m$  ( $1 \leq m \leq M'$ ) is a positive integer that maximizes the EUE of such a strategy.

### 19.5.1.2 Performance

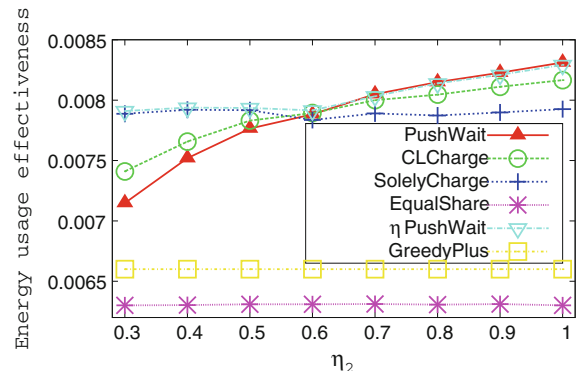
We evaluate the impact of charging efficiencies in this subsection. Figure 19.14 shows the case where  $\eta_2$  is fixed, i.e., the charging efficiency between chargers is fixed. When we increase  $\eta_1$ , the energy loss during wireless charging becomes smaller, so the EUE of each algorithm gets larger.

Figure 19.15 shows the case where  $\eta_2$  is fixed. There are three interesting observations. First, since there is no energy transfer between chargers in SolelyCharge,

**Fig. 19.14** Performance comparisons in scenario  $K1K2K3$  by varying  $\eta_1$  while keeping  $\eta_2 = 0.3$



**Fig. 19.15** Performance comparisons in scenario  $K1K2K3$  by varying  $\eta_2$  while keeping  $\eta_1 = 0.015$



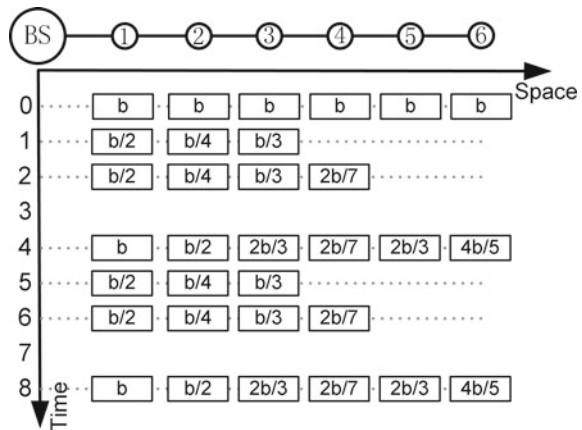
GreedyPlus and EqualShare, their EUEs remain unchanged when  $\eta_2$  increases. Second, CLCharge has a higher and lower EUE than PushWait when  $\eta_2 \leq 0.6$  and  $\eta_2 \geq 0.6$ , respectively. The rationale behind this phenomenon is that, the total energy exchanged between chargers in CLCharge is less than that in PushWait. Thus, CLCharge may perform better than PushWait if  $\eta_2$  is small. Third,  $\eta$ PushWait always has the best performance, because it takes advantage of SolelyCharge when  $\eta_2 \leq 0.6$ , and takes advantage of PushWait when  $\eta_2 > 0.6$ .

### 19.5.2 Different Recharging Cycles

We consider  $K1\overline{K2}K3$  in this subsection. When sensor nodes have different recharging cycles, a scheduling cycle may include multiple charging rounds, which greatly complicates the scheduling problem. Figure 19.16 shows a scheduling example in scenario  $K1\overline{K2}K3$ . There are six sensor nodes in the WSN:  $\tau_1 = 2$ ,  $\tau_2 = 4$ ,  $\tau_3 = 3$ ,  $\tau_4 = 7$ ,  $\tau_5 = 6$ , and  $\tau_6 = 5$ . All sensor nodes are initialized to their full batteries at time 0. At time 1, we plan to charge  $s_1$ ,  $s_2$ , and  $s_3$ . Since  $\tau_2 = 4$  and  $s_2$  has a full battery at time 0,  $s_2$  needs only  $b/4$  energy at time 1. So we employ PushWait to deliver  $b/2$ ,  $b/4$ , and  $b/3$  energy to  $s_1$ ,  $s_2$ , and  $s_3$ , respectively, at time 1. In the scheduling example, there are also charging rounds at time points 2 and 4. From time 5, the three charging rounds between time points 1 and 4 are repeated. Two important questions can be raised for such a scheduling example.

First and foremost, how are we to go about characterizing long-term EUE? Since the scheduling cycle is 4, we can use the EUE within a scheduling cycle to exactly represent the long-term EUE. Second, how might we define the scheduling cycle? As we mentioned before, it is defined as the time interval between two consecutive time points when all sensors are fully charged. For example, the WSN in the figure is fully charged at time points 0, 4, 8, and so on, so the scheduling cycle is 4.

**Fig. 19.16** A scheduling example for  $K1\overline{K2}K3$  where  $\tau_1 = 2$ ,  $\tau_2 = 4$ ,  $\tau_3 = 3$ ,  $\tau_4 = 7$ ,  $\tau_5 = 6$ , and  $\tau_6 = 5$ . For instance, at time 2, we use PushWait to deliver  $b/2$ ,  $b/4$ ,  $b/3$ , and  $2b/7$  energy to  $s_1$ ,  $s_2$ ,  $s_3$ , and  $s_4$ , respectively. The scheduling cycle of this example is 4



Second, when should we plan to make a charging round? The next theorem tells us that, we only need to start a charging round when there is at least one dying sensor node. For example, the charging round at time 1 in Fig. 19.16 is redundant, since no sensor nodes will run out of energy if the charging round is cancelled.

**Theorem 19.4** (Necessary condition) *Given a node  $s$  that is  $x_s$  distance away from the base station, the battery capacity of  $s$  is  $b$ ; using PushWait to deliver  $b$  energy to  $s$  one time achieves a higher EUE than using PushWait twice.*

At one extreme, when we plan to recharge a sensor node, we want to transfer as much energy as possible to it, so as to increase the payload energy. Based on this intuition, we start a charging round only when there is at least one dying sensor node, and in this charging round, we only charge the dying sensor nodes. With the same settings as in Fig. 19.16, Figure 19.17 shows such an example: a sensor node is charged only when it is dying. At another extreme, when there is a charging round, we want to charge as many sensor nodes as possible, so as to increase the payload energy. Figure 19.18 demonstrates this extreme case.

In fact, these two design options compete with each other; thus, we strive to strike a balance between them, and propose our solution ClusterCharging( $\beta$ ).

### 19.5.2.1 ClusterCharging( $\beta$ )

We first sort sensor nodes in decreasing order of their recharging cycles, then we divide them into groups such that the ratio of the maximum recharging cycle to the minimum recharging cycle in each group is not greater than a given threshold, say  $\beta$ . Then, we start a charging round only when there is at least one dying sensor node, and in this charging round, we employ PushWait to charge all sensor nodes in a group on the condition that this group contains at least one dying sensor node. Note that, in each charging round, different sensor nodes may need different amounts of energy, e.g.,  $s_1$ ,  $s_2$ , and  $s_3$  require  $b/2$ ,  $b/4$ , and  $b/3$  energy, respectively, at time 1 in Fig. 19.16. Remember that PushWait can still achieve its optimality in each round, due to Theorem 19.1.

Let us take Figs. 19.17, 19.18, 19.19 and 19.20 for example. “ $\beta = 1$ ” represents the extreme case in Fig. 19.17, where each sensor node, itself, forms a group. Similarly, “ $\beta = +\infty$ ” represents the other extreme case in Fig. 19.18, where all sensor nodes form a single group. In Fig. 19.18, we consider sensor nodes in decreasing order of their recharging cycles, i.e.,  $s_1$ ,  $s_3$ ,  $s_2$ ,  $s_6$ ,  $s_5$ , and  $s_4$ . First,  $s_1$  forms a group  $\{s_1\}$ ; we then attempt to put  $s_3$  into  $\{s_1\}$ , since  $\tau_3/\tau_1 = 1.5 < \beta = 2$ , it is feasible for them to be in the same group; the group  $\{s_1, s_3\}$  can also accommodate  $s_2$ ; when we want to put  $s_6$  into  $\{s_1, s_3, s_2\}$ , as  $\tau_6/\tau_1 > \beta$ ,  $s_6$  forms a new group, and so on. In Fig. 19.19,  $\beta$  is set to 3, resulting in two groups, i.e.,  $\{s_1, s_2, s_3, s_5, s_6\}$ , and  $\{s_4\}$ .

Different values of  $\beta$  lead to different EUEs of ClusterCharging( $\beta$ ), and the optimal value of  $\beta$  varies with the parameters of a given MCS problem. Therefore, for a given MCS problem that satisfies  $K1\bar{K}2K3$ , we maximize the EUE

**Fig. 19.17**  $\beta = 1$ , there are six groups; each sensor, itself, forms a group.  
 Illustrations of ClusterCharging( $\beta$ ) for  $K1\bar{K}2K3$  with the same settings as in Fig. 19.16

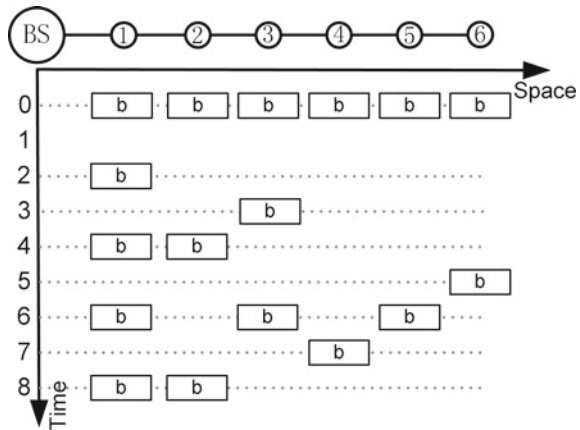


**Fig. 19.18**  $\beta = 2$ , there are two groups:  $\{s_1, s_2, s_3\}$ , and  $\{s_4, s_5, s_6\}$

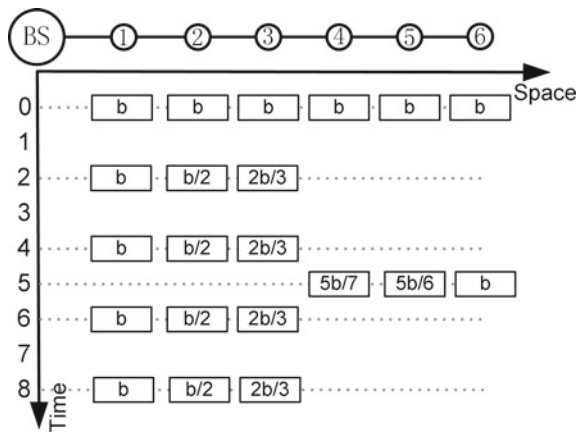


**Fig. 19.19**  $\beta = 3$ , there are two groups:  
 $\{s_1, s_2, s_3, s_5, s_6\}$ , and  $\{s_4\}$

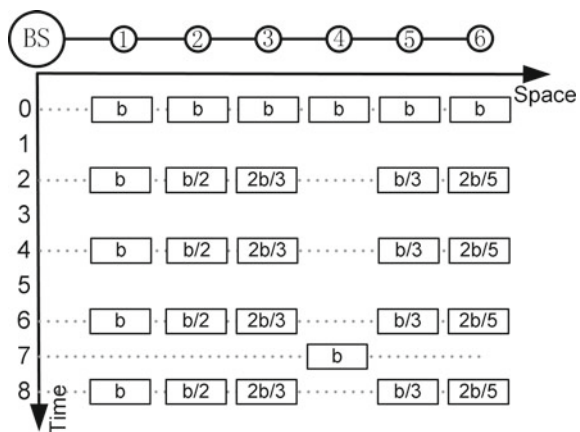
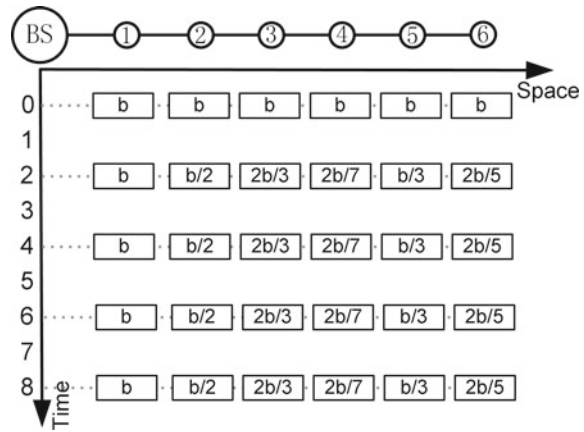


**Fig. 19.20**  $\beta = +\infty$ , there is one group that contains all sensors



of ClusterCharging( $\beta$ ) by searching the optimal  $\beta$  in range  $[1, \frac{\tau_{max}}{\tau_{min}} + 1]$ , where  $\tau_{min} = \min_{1 \leq i \leq N} \tau_i$ , and  $\tau_{max} = \max_{1 \leq i \leq N} \tau_i$ .

**Theorem 19.5** (Performance guarantee of ClusterCharging( $\beta$ )) *The approximation ratio of ClusterCharging( $\beta$ ) for K1K2K3 is*

$$\frac{b_{min}(2cx_N + \sum_{i=1}^N b_i)}{P\tau_{max}k \sum_{i=1}^N b_i} \quad (19.9)$$

where  $b_{min} = \min_{i=1}^N b_i$ , and

$$k = \operatorname{argmin}_{(\sum_{i=1}^k \frac{1}{i} \geq \frac{2cx_N \tau_{max} + b_{min}}{P\tau_{max}})} k \quad (19.10)$$

For scenario K1K2K3, we design an algorithm called  $\eta$ ClusterCharging( $\beta$ ), in which sensor nodes are divided into groups in a similar way as ClusterCharging( $\beta$ ). However, in each charging round, we employ  $\eta$ PushWait instead of PushWait to replenish sensor nodes.

### 19.5.2.2 Performance

We evaluate ClusterCharging( $\beta$ ) under different values of  $\beta$ :  $\beta = 1$  to 5 in Fig. 19.21 and  $\beta = 1$  to 3 in Fig. 19.22. We notice that, ClusterCharging( $\beta$ ) with three different  $\beta$ 's perform almost the same in Fig. 19.21, while ClusterCharging(3) outperforms the other two algorithms in Fig. 19.22. The main reason is that, the relative gap between recharging cycles in Fig. 19.21 is large, while the relative gap in Fig. 19.22 is small. For example, if we use ClusterCharging(5) to replenish the WSN in Fig. 19.21, then the energy we have to transfer to each sensor node varies from 1.8 KJ ( $b/6$ ) to 10.8 KJ ( $b$ ). We can see that, some sensor nodes just need a small amount of energy.

**Fig. 19.21** Performance comparisons in scenario  $K1\bar{K}2K3$  when all  $\tau_i$ 's are uniformly generated between 1 and 6

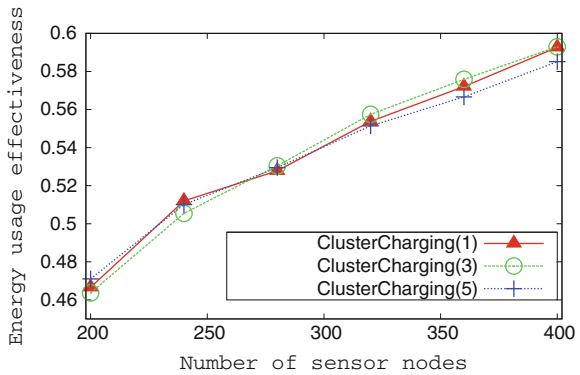
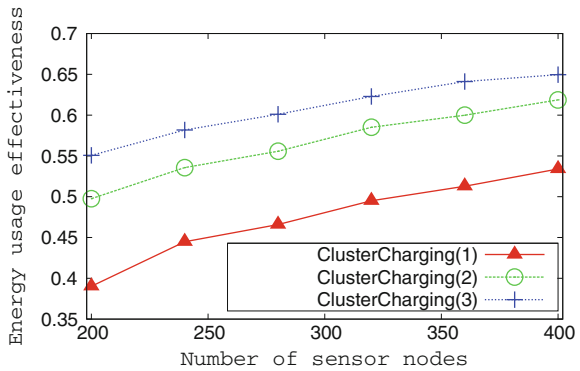


**Fig. 19.22** Performance comparisons in scenario  $K1\bar{K}2K3$  when all  $\tau_i$ 's are uniformly generated between 3 and 8



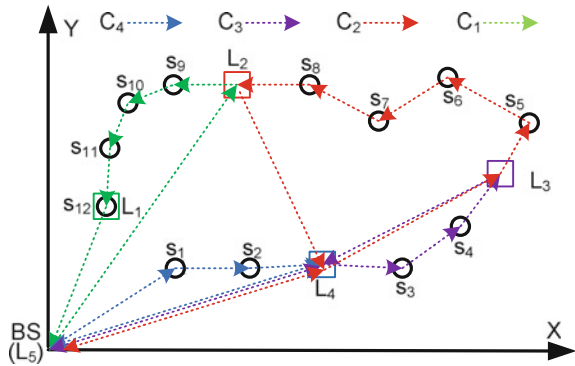
However, if we use ClusterCharging(5) to replenish the WSN in Fig. 19.22 (note that, ClusterCharging(5) is equivalent to ClusterCharging(3) for the setting in Fig. 19.22), then the energy we have to transfer to each sensor node varies only from 4.05 KJ ( $3b/8$ ) to 10.8 KJ ( $b$ ). Therefore, ClusterCharging(5) can have the best performance in Fig. 19.22.

### 19.5.3 2-D Networks + Different Recharging Cycles + Energy Loss

Different recharging cycles force us to divide sensor nodes into groups, and energy loss makes us combine SolelyCharge with PushWait. What challenges does 2-D pose to us? The answer is that, given a set of sensor nodes to be replenished in a charging round, we must discover how to determine the charging sequence, so as to minimize the overhead energy.

Before presenting our design, we introduce some notations. In a charging round, denote by  $S$  the set of sensor nodes that are going to be charged. We construct

**Fig. 19.23** Mobile chargers are no longer restricted to moving along a Hamiltonian cycle; they can take shortcuts to improve EUE when possible



a complete graph  $G[S]$  with vertices being  $S \cup \{BS\}$ , and edge weights being the Euclidean distance between two corresponding vertices.

We denote the minimum weight Hamiltonian cycle of  $G[S]$  by  $H$ . Denote by  $d_H(P_1, P_2)$  the sum of Euclidean distances of line segments between two positions  $P_1$  and  $P_2$  on  $H$ . For example,  $d_H(L_4, L_3) = d(L_4, s_3) + d(s_3, s_4) + d(s_4, L_3)$  in Fig. 19.23.

### 19.5.3.1 $H\eta$ ClusterCharging( $\beta$ )

In  $H\eta$ ClusterCharging( $\beta$ ), we first divide sensor nodes into groups, and plan a charging round when there is at least one dying sensor node; in each charging round, we try to find the minimum weight Hamiltonian cycle in the complete graph on the corresponding set of sensors and the base station. Lastly, we apply  $\eta$ PushWait to the Hamiltonian cycle, and further improve the results through shortcutting. More specifically,  $H\eta$ ClusterCharging( $\beta$ ) works as follows:

1. Sort sensor nodes in decreasing order of their recharging cycles, then divide sensor nodes into groups with respect to a threshold  $\beta$ , as in ClusterCharging( $\beta$ ).
2. Decide the charging round plan, that is, decide the set of sensor nodes  $S$  that should be replenished in each charging round. We apply the following steps, i.e., 3–5, to each charging round.
3. Construct a complete graph  $G[S]$  and use the minimum spanning tree-based heuristic [34] to generate a Hamilton cycle  $H$  in  $G[S]$ .
4. Randomly choose a direction for  $H$ . Suppose that we start from the base station and visit sensor nodes following the chosen direction along  $H$ . Without loss of generality, denote the sequence of sensor nodes we visit by  $s_1, s_2, \dots$ , and  $s_{|S|}$ . We apply  $\eta$ PushWait to  $H$ , which can be seen as a 1-dimensional manifold [35], and thus, we can obtain the number of required chargers  $M$  and the farthest positions that chargers will reach, i.e.,  $L_1, L_2, \dots$ , and  $L_M$ . Again, without loss of generality, we let  $L_{M+1} = (0, 0)$ . (Note that, since we apply  $\eta$ PushWait to this 1-D manifold, each  $L_i$  will be located on an edge between two consecutive sensor nodes or at

the location of a sensor node; particularly,  $L_1$  is located at the same location with the farthest sensor node, i.e.,  $s_{|S|}$ .)

5. We improve  $\eta$ PushWait through shortcutting. In this step, we only present how chargers take shortcuts and do not elaborate on the energy transfers between mobile chargers, for the sake of presentation brevity.

- a. For charger  $C_M$ , it charges the sensor nodes between the base station and  $L_M$ , transfers energy to the other chargers at  $L_M$ , and waits at  $L_M$  for the other chargers' return. When  $C_M$  finishes its charging task, it can take a shortcut: it directly returns to the base station.
- b. For charger  $C_i$  ( $1 \leq i \leq M - 1$ ), denote the current position of  $C_i$  as  $L_g$ . Before it finishes charging the sensor nodes between  $L_{i+1}$  and  $L_i$ 
  - i. When  $i + 2 \leq g \leq M + 1$ , it directly takes a shortcut to  $L_{j_{min}}$ , where  $j_{min}$  satisfies:

$$j_{min} = \operatorname{argmin}_{(d(L_g, L_j) \leq d_H(L_{i+1}, L_j), i+1 \leq j \leq g-1)} j \quad (19.11)$$

- ii. When  $g = i + 1$ , it begins to charge the sensor nodes between  $L_{i+1}$  and  $L_i$ .
- iii. After this, on its way back to the base station: for  $i \leq g \leq M$ , it directly takes a shortcut to  $L_{j_{max}}$ , where  $j_{max}$  satisfies:

$$j_{max} = \operatorname{argmax}_{(d(L_g, L_j) \leq d_H(L_g, L_{g+1}), g+1 \leq j \leq M+1)} j \quad (19.12)$$

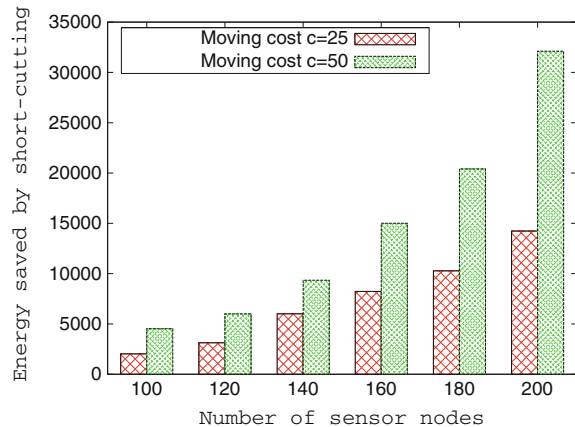
### 19.5.3.2 Running Example

Figure 19.23 shows when and how a charger can take a shortcut. Suppose that we have to replenish 12 sensor nodes in a charging round. Without loss of generality, the Hamiltonian cycle  $H$  we find is  $BS - s_1 - s_2 - \dots - s_{12} - BS$ . After applying  $\eta$ PushWait to this cycle, we know that, this round requires four chargers, and the farthest position of each charger is  $L_i$  ( $1 \leq i \leq 4$ ).

$C_4$  is responsible for replenishing sensor nodes between  $L_5$  (base station) and  $L_4$ . It can only take a shortcut after it completes its task, and thus, its trajectory is  $BS \rightarrow s_1 \rightarrow s_2 \rightarrow L_4 \Rightarrow BS$ , where “ $\rightarrow$ ” denotes a path segment along  $H$ , and “ $\Rightarrow$ ” denotes a shortcut.

When  $C_3$  starts from the base station, since  $g = 5$ , the situation satisfies case 5.2.1 in  $H\eta$ ClusterCharging( $\beta$ ), and we can determine  $j_{min} = 4$ , so it directly moves to  $L_4$ . Then, the situation satisfies case 5.2.2, and thus,  $C_3$  charges sensor nodes between  $L_4$  and  $L_3$ . The situation begins to satisfy case 5.2.3 when it arrives at  $L_3$ , as  $d(L_3, L_5) > d_H(L_3, L_4)$ , it does not have enough energy to move directly to the base station. (Please keep in mind that, according to  $\eta$ PushWait, if  $C_3$  moves along  $H$  to  $L_4$ , it would have 0 energy at  $L_4$ .) Thus, the trajectory of  $C_3$  is  $BS \Rightarrow L_4 \rightarrow s_3 \rightarrow s_4 \rightarrow L_3 \Rightarrow L_4 \Rightarrow BS$ .

**Fig. 19.24** The benefit of shortcircuiting



Following a similar argument, we can have the trajectory of  $C_2$ :  $BS \Rightarrow L_4 \Rightarrow L_3 \rightarrow s_5 \rightarrow s_6 \rightarrow s_7 \rightarrow s_8 \rightarrow L_2 \Rightarrow L_4 \Rightarrow BS$ .

When  $C_1$  is at  $L_5$ , since  $d(L_5, L_2) < d_H(L_3, L_2)$ , we have  $j_{min} = 2$ , and it takes a shortcut to  $L_2$ . After charging sensor nodes between  $L_2$  and  $L_1$ , it arrives at  $L_1$ . As  $d(L_1, L_5) < d_H(L_1, L_2)$ , we have  $j_{max} = 5$ , thus, it directly returns to the base station. The trajectory of  $C_1$  is  $BS \Rightarrow L_2 \rightarrow s_9 \rightarrow s_{10} \rightarrow s_{11} \rightarrow s_{12} \Rightarrow BS$ .

### 19.5.3.3 Performance

We are interested in investigating how much benefit shortcircuiting brings about. The results are shown in Fig. 19.24. When the moving cost of a mobile charger ( $c$ ) is fixed, if the number of sensor nodes increases, the energy saved by shortcircuiting also increases. This is reasonable, since an increase in the number of sensor nodes results in another increase in the number of mobile chargers required. Because of this, more chargers may take shortcuts when necessary. When the moving cost doubles, we find that the energy saved also doubles, or even triples. This is because, when moving cost increases, the number of chargers required also increases.

## 19.6 Concluding Remarks

In this chapter, we mainly present some recent work on collaborative mobile charging. Research results in this area can potentially be used in several mobile applications, including DARPA flying robots, and Google WiFi balloon. Through presenting this content, we aim to inspire readers to recognize the usefulness and importance of collaboration, incorporate it into their designs, and further elevate it.

**Acknowledgments** Jie Wu was supported in part by NSF grants CNS 1629746, CNS 1564128, CNS 1449860, CNS 1461932, CNS 1460971, CNS 1439672, CNS 1301774, and ECCS 1231461. Sheng Zhang was supported in part by NSFC (61502224, 61472181, 61472185), China Postdoctoral Science Foundation (2015M570434, 2016T90444), CCF-Tencent Open Research Fund (AGR20160104), Jiangsu NSF (BK20151390), and Collaborative Innovation Center of Novel Software Technology and Industrialization.

## References

1. Kurs, A., Karalis, A., Moffatt, R., Joannopoulos, J.D., Fisher, P., Soljačić, M.: Wireless power transfer via strongly coupled magnetic resonances. *Science* **317**(5834), 83–86 (2007)
2. Fu, L., Cheng, P., Gu, Y., Chen, J., He, T.: Minimizing charging delay in wireless rechargeable sensor networks. In: Proceedings of IEEE INFOCOM 2013, pp. 2922–2930
3. Shi, Y., Xie, L., Hou, Y., Sherali, H.: On renewable sensor networks with wireless energy transfer. In: Proceedings of IEEE INFOCOM 2011, pp. 1350–1358
4. Xie, L., Shi, Y., Hou, Y.T., Lou, W., Sherali, H.D., Midkiff, S.F.: On renewable sensor networks with wireless energy transfer: The multi-node case. In: Proceedings of IEEE SECON 2012, pp. 10–18
5. Peng, Y., Li, Z., Zhang, W., Qiao, D.: Prolonging sensor network lifetime through wireless charging. In: Proceedings of IEEE RTSS 2010, pp. 129–139
6. He, S., Chen, J., Jiang, F., Yau, D.K., Xing, G., Sun, Y.: Energy provisioning in wireless rechargeable sensor networks. In: Proceedings of IEEE INFOCOM 2011, pp. 2006–2014
7. Madhja, A., Nikoletseas, S., Raptis, T.P.: Distributed wireless power transfer in sensor networks with multiple mobile chargers. *Comput. Netw.* **80**, 89–108 (2015)
8. Dai, H., Liu, Y., Chen, G., Wu, X., He, T.: Safe charging for wireless power transfer. In: Proceedings of IEEE INFOCOM 2014, pp. 1105–1113
9. Zhang, S., Wu, J., Lu, S.: Collaborative mobile charging for sensor networks. In: Proceedings of IEEE MASS 2012, pp. 84–92
10. Cheney, M., Glenn, J., Uth, R.: Tesla: Master of lightning. Barnes & Noble Publishing (1999)
11. Sample, A.P., Yeager, D.J., Powledge, P.S., Mamishev, A.V., Smith, J.R.: Design of an RFID-based battery-free programmable sensing platform. *IEEE Trans. Instrum. Meas.* **57**(11), 2608–2615 (2008)
12. Androidcentral. <http://www.androidcentral.com/these-android-phones-can-handle-wireless-charging/>
13. Tesla motors. <http://www.teslamotors.com/>
14. SHARP. <http://www.friendsofcrc.ca/Projects/SHARP/sharp.html>
15. Wireless charging market. <http://www.marketsandmarkets.com/PressReleases/wireless-charging.asp>
16. Kansal, A., Srivastava, M.B.: An environmental energy harvesting framework for sensor networks. In: Proceedings of IEEE ISLPED 2003, pp. 481–486
17. Kansal, A., Hsu, J., Zahedi, S., Srivastava, M.B.: Power management in energy harvesting sensor networks. *ACM Trans. Embedded Comput. Syst.* **6** (2007)
18. Voigt, T., Ritter, H., Schiller, J.: Utilizing solar power in wireless sensor networks. In: Proceedings of IEEE LCN 2003, pp. 416–422
19. Cammarano, A., Petrioli, C., Spenza, D.: Pro-energy: a novel energy prediction model for solar and wind energy-harvesting wireless sensor networks. In: Proceedings of IEE MASS 2012, pp. 75–83
20. Wang, W., Srinivasan, V., Chua, K.C.: Using mobile relays to prolong the lifetime of wireless sensor networks. In: Proceedings of ACM MobiCom 2005, pp. 270–283
21. Dunkels, A., Österlind, F., He, Z.: An adaptive communication architecture for wireless sensor networks. In: Proceedings of ACM SenSys 2007, pp. 335–349

22. Bhattacharya, S., Kim, H., Prabh, S., Abdelzaher, T.: Energy-conserving data placement and asynchronous multicast in wireless sensor networks. In: Proceedings of ACM MobiSys 2003, pp. 173–185
23. Tong, B., Li, Z., Wang, G., Zhang, W.: How wireless power charging technology affects sensor network deployment and routing. In: Proceedings of IEEE ICDCS 2010, pp. 438–447
24. Zhang, S., Qian, Z., Kong, F., Wu, J., Lu, S.: P<sup>3</sup>: Joint optimization of charger placement and power allocation for wireless power transfer. In: Proceedings of IEEE INFOCOM 2015, pp. 2344–2352
25. Dai, H., Wu, X., Chen, G., Xu, L., Lin, S.: Minimizing the number of mobile chargers for large-scale wireless rechargeable sensor networks. *Comput. Commun.* **46**, 54–65 (2014)
26. Li, Z., Peng, Y., Zhang, W., Qiao, D.: Study of joint routing and wireless charging strategies in sensor networks. In: Proceedings of WASA 2010, pp. 125–135
27. Shu, Y., Yousefi, H., Cheng, P., Chen, J., Gu, Y., He, T., Shin, K.: Optimal velocity control for time-bounded mobile charging in wireless rechargeable sensor networks. *IEEE Trans. Mobile Comput.* **PP(99)**, 1–1 (2015). doi:[10.1109/TMC.2015.2473163](https://doi.org/10.1109/TMC.2015.2473163)
28. Wu, J.: Collaborative mobile charging and coverage. *J. Comput. Sci. Technol.* **29**(4), 550–561 (2014)
29. Zhang, S., Wu, J., Lu, S.: Collaborative mobile charging. *IEEE Trans. Comput.* **64**(3), 654–667 (2015)
30. Wang, C., Li, J., Ye, F., Yang, Y.: NETWRAP: an NDN based real-time wireless recharging framework for wireless sensor networks. *IEEE Trans. Mob. Comput.* **13**(6), 1283–1297 (2014). doi:[10.1109/TMC.2013.2296515](https://doi.org/10.1109/TMC.2013.2296515)
31. Fu, L., He, L., Cheng, P., Gu, Y., Pan, J., Chen, J.: ESync: Energy synchronized mobile charging in rechargeable wireless sensor networks. *IEEE Trans. Veh. Technol.* **PP(99)**, 1–1 (2015). doi:[10.1109/TVT.2015.2481920](https://doi.org/10.1109/TVT.2015.2481920)
32. Xu, W., Liang, W., Lin, X., Mao, G.: Efficient scheduling of multiple mobile chargers for wireless sensor networks. *IEEE Trans. Veh. Technol.* **PP(99)**, 1–1 (2015). doi:[10.1109/TVT.2015.2496971](https://doi.org/10.1109/TVT.2015.2496971)
33. Bentham, J.: An introduction to the principles of morals and legislation. Courier Corporation (2007)
34. Vazirani, V.V.: Approximation Algorithms. Springer (2003)
35. Lee, J.M.: Introduction to Topological Manifolds. Springer (2000)

# Chapter 20

## Assigning Hierarchy to Collaborative Mobile Charging in Sensor Networks

Adelina Madhja, Sotiris Nikoletseas and Theofanis P. Raptis

**Abstract** Wireless power transfer is used to fundamentally address energy management problems in Wireless Rechargeable Sensor Networks (WRSNs). In such networks, mobile entities traverse the network and wirelessly replenish the energy of sensor nodes. In recent research on collaborative mobile charging, the mobile entities are also allowed to charge each other. In this chapter, we enhance the collaborative feature by forming a hierarchical charging structure. We distinguish the Chargers in two groups, the hierarchically lower, called Mobile Chargers, that charge sensor nodes and the hierarchically higher, called Special Chargers, that charge Mobile Chargers. We define the Coordination Decision Problem and prove that it is NP-complete. Also, we propose a new protocol for 1-D networks which we compare with a state-of-the-art protocol. Motivated by the improvement in 1-D networks, we design four new collaborative charging protocols for 2-D networks to achieve efficient charging and improve important network properties. Our protocols are either centralized or distributed, and assume different levels of network knowledge. Extensive simulation findings demonstrate significant performance gains, with respect to non-collaborative state-of-the-art charging methods. In particular, our protocols improve several network properties and metrics, such as the network lifetime, routing robustness, coverage, and connectivity. A useful feature of our methods is that they can be suitably added on top of non-collaborative protocols to further enhance their performance.

---

A. Madhja (✉) · S. Nikoletseas · T.P. Raptis

Department of Computer Engineering and Informatics, University of Patras and  
Computer Technology Institute and Press “Diophantus” (CTI), Patras, Greece  
e-mail: madia@ceid.upatras.gr

S. Nikoletseas  
e-mail: nikole@cti.gr

T.P. Raptis  
Institute of Informatics and Telematics, National Research Council, Moruzzi Str 1,  
56124 Pisa, Italy  
e-mail: theofanis.raptis@iit.cnr.it

## 20.1 Introduction and Contribution

In wireless sensors networks (WSNs), the sensor nodes are equipped with small batteries and thus, the lifetime of the network is limited. Although there are several approaches that try to address this fundamental problem, the proposed solutions are still limited since the energy that is replenished is either uncontrollable (such as environmental harvesting approaches) or require the nodes to be accessible by people or robots in a very accurate way (such as battery replacement approaches).

However, the breakthrough of wireless power transfer technology (see e.g., [9]) combined with rechargeable batteries with high energy density and high charge/discharge capabilities ([8]), has managed to directly address energy management and led to the paradigm of Wireless Rechargeable Sensor Networks (WRSNs). In such networks, special entities (called Chargers) are able to charge sensor nodes wirelessly. Thus, the limited available energy can be managed in a controllable and more efficient manner. This option introduced some new aspects that need investigation such as how Chargers should be deployed, how much energy each Charger should transfer to each sensor node or what is the minimum number of required Chargers in order to improve network properties such as lifetime, connectivity, and coverage.

Wireless charging may address more efficiently the problem of limited energy with respect to network properties if we use Mobile Chargers instead of simple Chargers. Mobile Chargers are called the devices which are able to both charge sensor nodes wirelessly and move throughout the network. This new capability introduced some additional options that need investigation such as how Mobile Chargers can coordinate or which is the trajectory that each Mobile Charger should follow.

The collaborative mobile charging approach proposed in [18] offers even more useful options. In this new charging method, Mobile Chargers are allowed to charge not only sensor nodes but also other Mobile Chargers. This new capability has been proven very important, since it provides better exploitation of the potentially limited available energy supplies.

**The Problem.** Let a WRSN comprised of stationary sensor nodes and Mobile Chargers that can either charge the nodes or charge each other (collaborative charging). The transformation of the flat collaborative charging scheme to a hierarchical one (hierarchical, collaborative charging) imports new challenges for the network energy management. We design efficient protocols for the Mobile Chargers' coordination and charging procedure, in order to efficiently distribute and manage the available finite energy, prolong the network lifetime, and improve key network properties such as coverage, routing robustness, and network connectivity.

**Our Contribution.** Since collaboration provides an efficient energy management potential, we envision collaboration in a hierarchical structure. More specifically, we propose a partition of Chargers into two groups, the hierarchically lower Mobile Chargers, that are responsible for transferring energy only to sensor nodes and the hierarchically higher Special Chargers that are responsible for transferring energy to Mobile Chargers. Using our hierarchical charging model, we first propose a protocol for 1-D networks that achieves a better performance ratio than known state-of-the-art protocol, when the available energy supplies are limited.

Motivated by the improvement in 1-D networks we propose four protocols for 2-D networks as well. Our protocols differ on the available network's knowledge level (2-level knowledge, 1-level knowledge and no knowledge) as well as on their coordination procedure (distributed or centralized). Our No Knowledge No Coordination (NKNC) protocol actually serves as a performance lower bound since it assumes no network knowledge and does not perform any coordination. In contrast, our 2-Level Knowledge Centralized Coordination (2KCC) protocol assumes 2-level knowledge and performs centralized coordination. In between, our 2-Level Knowledge Distributed Coordination (2KDC) and 1-Level Knowledge Distributed Coordination (1KDC) protocols both perform distributed coordination but, since they assume different knowledge level, their coordination and charging procedures differ.

Moreover, the hierarchical solution that we provide can be easily added on top of non-collaborative protocols to further improve their performance (by applying the necessary transformations which depends on the existing charging model). In particular, we enhance a known state-of-the-art protocol that does not use any collaboration, by adding a hierarchical collaborative charging structure and we show the added value of hierarchy.

## 20.2 Related Work and Comparison

Wireless power transfer technology inspired a lot of researchers to investigate how to exploit it in WSNs efficiently. In [14], the authors used a realistic scenario where the sensor nodes are mobile and the Chargers are stationary. They proposed two protocols to address the problem of how to schedule the Chargers activity so as to maximize either the charging efficiency or the energy balance. Also, they conducted real experiments to evaluate the protocols' performance. In [17], the objective was to find a Charger placement and a corresponding power allocation to maximize the charging quality. They proved that their problem (called  $P^3$ ) is NP-hard and proposed two approximation algorithms for  $P^3$  (with and without fixed power levels) and an approximation algorithm for an extended version of  $P^3$ .

However, the exposure on the electromagnetic radiation that is caused by wireless power transfer may lead to undesired phenomena for human health. That is why there are a lot of works that investigate this aspect and try to control the electromagnetic radiation. More specifically, in [13] the authors studied the Low Radiation Efficient Charging Problem in which they optimized the amount of “useful” energy that is transferred to nodes with respect to the maximum level of imposed radiation. In [3], the authors investigated the charging efficiency problem under electromagnetic radiation safety concern. More specifically, they formulated the Safe Charging Problem (SCP) of how to schedule the Chargers in order to increase the received power while there is no location in the field where the electromagnetic radiation exceeds a threshold value. They proved the hardness of SCP and proposed a solution which outperforms the optimal one with a relaxed threshold. Also, to evaluate the effectiveness of their solution, they conducted both simulations and real experiments.

The same research group in [4] studied the Safe Charging with Adjustable PowEr (SCAPE) problem which refers on how to adjust the power of the Chargers in order to maximize the charging utility of the devices while assuring that electromagnetic radiation intensity at any location on the field does not exceed a threshold value. They also proposed an  $(1-\varepsilon)$ -approximation algorithm for the problem and conducted simulations and real experiments to evaluate the algorithm's performance.

Although all above works have studied a variety of problems caused by wireless power transfer and try to maximize the received power by the sensor nodes under various constraints, the usage of stationary Chargers does not exploit all the capabilities of the technology. The hardware device that is able to send energy wirelessly can be easily placed on top of a mobile robot and thus transformed to a new mobile entity called Mobile Charger. Mobile Chargers are able to move throughout the network and charge the sensor nodes. The main difference between our work and all mentioned state-of-the-art studies is that we use Mobile Chargers instead of stationary Chargers.

There has been considerable research work using a single Mobile Charger. In [11] the authors proposed a practical and efficient joint routing and charging scheme, where there are periodical information exchanges between nodes and the Charger on which the latter is based to schedule its charging activities. The approach in [19] proposed to utilize mobility for joint energy replenishment and data gathering. In [1], the authors studied the impact of the charging process to the network lifetime for a set of routing protocols by proposing a protocol that locally adapts the circular trajectory of the Mobile Charger to the energy dissipation rate of each subregion of the network. In [2], the authors proposed distributed and adaptive protocols that use limited network information for efficient recharging. In [6], individual sensor nodes request charging from the Mobile Charger when their energy runs low.

All above works do not take advantage of the network capability to support more than one Mobile Chargers. Such approach is vital for the lifetime prolongation of large networks that consist of several thousand nodes (their maintenance is not feasible using only one Mobile Charger). In contrast to previous works, we use multiple Mobile Chargers in order to further exploit the network capabilities.

In the state of the art there are proposed solutions with multiple Mobile Chargers. More specifically, in [15] the authors leveraged concepts and mechanisms from Named Data Networking (NDN) in order to design energy monitoring protocols that deliver energy status information to Mobile Chargers in an efficient manner. In [12], the authors studied how multiple Mobile Chargers can periodically coordinate and partition the sensor nodes in a balanced manner, according to their energy and adapt to network energy consumption. The proposed protocols were either distributed or centralized and used varying levels of network knowledge. In [5], the authors consider the minimum number of Mobile Chargers problem in a general 2-D network so as to keep the network running forever. More specifically, they partitioned the sensor nodes in subsets, one for each Mobile Charger such that any Mobile Charger, at each own period, visits its corresponding sensors, charges them, and then gets back to the base station to recharge its own battery.

In [16] the authors studied the recharging schedule that maximizes the recharge profit. Although there are a lot of works that make the realistic assumption of Mobile Chargers' battery constraints, in this work, the authors also introduce an other realistic assumption, that of Mobile Chargers' movement cost.

The usage of multiple Mobile Chargers without collaboration also does not exploit all capabilities of WRSNs. There is a work in the state of the art (in [18]) where the authors introduce a new charging paradigm, that of collaborative mobile charging, where Mobile Chargers are allowed to charge each other. They investigate the problem of scheduling multiple Mobile Chargers which collaboratively charge nodes over 1-D WRSNs, to maximize the ratio of the amount of payload energy to overhead energy, such that no sensor runs out of energy. However, in contrast to our work, they restrict their algorithms only in 1-D networks.

### 20.3 The Model

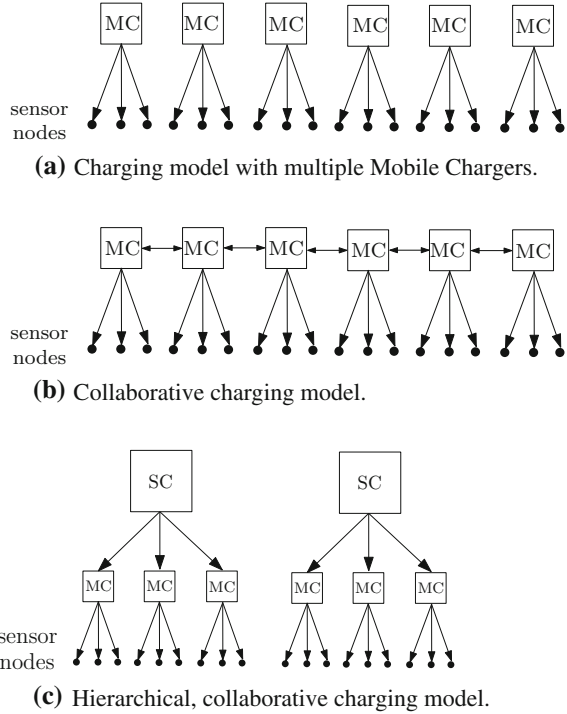
Our model features four types of devices:  $N$  stationary sensor nodes,  $M$  Mobile Chargers which charge sensor nodes,  $S$  Special Chargers which charge Mobile Chargers and a single stationary Sink. The sensor nodes of wireless communication range  $r$  are uniformly distributed at random in a circular area of radius  $R$ . The Mobile Chargers and the Special Chargers are initially deployed at the center of circular area. The Sink serves only as data collector.

In our model, we assume that neither the Mobile Chargers nor the Special Chargers perform any data gathering process. Figure 20.1 depicts the energy flow in *three different charging models*, including simple charging in WRSNs using multiple Mobile Chargers (Fig. 20.1a), collaborative mobile charging (Fig. 20.1b) and our hierarchical collaborative charging model (Fig. 20.1c). The arrows abstract the energy flow from one device to another. The hierarchy of the charging model we propose is shown in Fig. 20.1c in which the Special Chargers that are the highest devices in terms of hierarchy can charge the Mobile Chargers and the Mobile Chargers can charge the sensor nodes. More specifically, the approach in Fig. 20.1a where each Mobile Charger charges its corresponding sensor nodes may lead to non-efficient energy management since if there is a Mobile Charger that consumes its energy with higher rate than others (e.g., its area is more critical), then the network will be disconnected despite the fact that there is still an amount of unused energy available to the network. In Fig. 20.1b, there is an improvement on energy management since Chargers may charge each other and so critical ones will be charged by others avoiding network disconnection. However, in Fig. 20.1c there is a more efficient energy utilization since it both provides a balanced energy consumption rate between Chargers and captures critical aspects of the network, e.g., reduce the amount of energy used for movement.

We denote by  $E_{total}$  the total, finite, available energy in the network. Initially,

$$E_{total} = E_{sensors} + E_{MC}(t_{init}) + E_{SC}(t_{init}),$$

**Fig. 20.1** Energy flow models



where  $E_{sensors}$  is the total amount of energy shared among the sensor nodes,  $E_{MC}(t_{init})$  is the total amount of energy shared among the Mobile Chargers and  $E_{SC}(t_{init})$  is the total amount of energy shared among the Special Chargers. The maximum amount of energy that a single node, a single Mobile Charger, and a single Special Charger may store is  $E_{sensor}^{max}$ ,  $E_{MC}^{max}$  and  $E_{SC}^{max}$ , respectively. Energy is uniformly split among the sensor nodes and the Chargers as follows:

$$E_{sensor}^{max} = \frac{E_{sensors}}{N}, \quad E_{MC}^{max} = \frac{E_{MC}(t_{init})}{M} \quad \text{and} \quad E_{SC}^{max} = \frac{E_{SC}(t_{init})}{S}.$$

At first, we deploy the sensor nodes uniformly in the circular network. Then, we divide our network into  $M$  equal sized slices, one for each Mobile Charger. Thus, every Mobile Charger is responsible for charging nodes that belong to its slice. We denote by  $\mathcal{D}_j$  the set of sensor nodes that belong to slice  $j$ , i.e., to the  $j$ th Mobile Charger's group. Finally, we divide the Mobile Charges into  $S$  groups, one for each Special Charger. Thus, each Special Charger is responsible for charging the Mobile Chargers that belong to its group, denoted as  $\mathcal{C}_k$  (for  $SC_k$ ). Initially, these  $S$  groups are equally sized, i.e.,

$$|\mathcal{C}_k| = \frac{M}{S} \quad (1 \leq k \leq S)$$

and the Mobile Chargers that belong to each group are given by the following formula:

$$\mathcal{C}_k = \left\{ j : j \in \left[ (k-1) \frac{M}{S} + 1, k \frac{M}{S} \right] \right\}, \quad (1 \leq k \leq S)$$

These groups may change during the protocol's coordination phase. More specifically, the Special Chargers communicate with each other and decide, according to their energy status, if they are still able to be in charge of the Mobile Chargers that belong to their group or they should delegate some of them to other Special Chargers.

The network operates under a quite heterogeneous data generation model. The energy consumption due to data generation is nonuniform between the nodes. Moreover, the underlying routing protocol is the multihop one (e.g., [7]) and so, the energy consumption for transferring the data to the Sink is also different between the nodes. In our model, the charging is performed point-to-point, i.e., only one sensor node may be charged at a time from a Mobile Charger, by approaching it at a suitably small distance so that the charging process is conducted with maximum efficiency (charging efficiency  $\approx 1$ ). Also, one Special Charger can charge one Mobile Charger at a time by approaching it very close. The time that elapses during the Charger's movement is considered to be very small compared to the charging time.

## 20.4 The Coordination Decision Problem (CDP)

**Definition 20.1** Consider a set  $\mathcal{S}$  of  $S$  Special Chargers. For each  $SC_k$  ( $1 \leq k \leq S$ ), we denote by  $\mathcal{E}_k$  the percentage of its current energy level to the total amount of energy of all Special Chargers, i.e.,

$$\mathcal{E}_k = \frac{E_{SC_k}}{\sum_{i=1}^S E_{SC_i}} \quad (1 \leq k \leq S).$$

Also, consider a set  $\mathcal{M}$  of  $M$  Mobile Chargers. For each  $MC_j$  ( $1 \leq j \leq M$ ), we define  $E_{MC_j}^{lack} = E_{MC_j}^{max} - E_{MC_j}$  the amount of energy that Mobile Charger  $j$  can receive until it is fully recharged and denote by  $\varepsilon_j$  the percentage of its energy lack to the total energy lack of all Mobile Chargers, i.e.,

$$\varepsilon_j = \frac{E_{MC_j}^{lack}}{\sum_{i=1}^M E_{MC_i}^{lack}} \quad (1 \leq j \leq M).$$

*The Coordination Decision Problem (CDP)* is to determine whether there exists a partition of the Mobile Chargers into  $S$  disjoint subsets, i.e.,  $\mathcal{X} = (\mathcal{X}_1, \dots, \mathcal{X}_S)$  with

$$\bigcup_{k=1}^S \mathcal{X}_k = \mathcal{M}$$

such that

$$\sum_{j \in \mathcal{X}_k} \varepsilon_j = \mathcal{E}_k \quad (1 \leq k \leq S).$$

In other words, the problem is to determine whether there exists a partition of Mobile Chargers in  $S$  groups, one for each Special Charger, such that every Mobile Charger belongs to the group of exactly one Special Charger and for every Special Charger, the sum of percentages of the Mobile Chargers that belong to its corresponding group equals its percentage of current energy.

**Theorem 20.1** *CDP is NP-complete.*

*Proof* (1) Given a partition  $\mathcal{Y} = (\mathcal{Y}_1, \dots, \mathcal{Y}_S)$  of Mobile Chargers into  $S$  groups, we can verify in polynomial time whether, for this partition, the groups are pairwise disjoint and the sum of percentages  $\varepsilon_j$  in a group equals the percentage of the corresponding Special Charger for every group. More precisely, for every Mobile Charger, we check all groups and verify if it belongs to exactly one group. If there is at least one Mobile Charger that does not belong to any group or belongs to more than one group then the given partition is incorrect. This takes  $O(M)$  time and for all Mobile Chargers takes  $O(M^2)$  time. Also, we examine for every group  $k$  if  $\sum_{j \in \mathcal{Y}_k} \varepsilon_j = \mathcal{E}_k$ . This computation takes at most  $O(M)$  time. So, given a partition we can answer in  $O(M^2)$  time if the partition is correct or not. Therefore  $CDP \in NP$ .

(2) Assume a special case of the CDP where all Mobile Chargers have the same percentage of energy  $\mathcal{E}_k = \mathcal{E}$ . If this special case is NP-hard then the generic CDP is also NP-hard. In order to prove the hardness of CDP, we reduce the *Bin Packing Decision Problem* (BPD) to it. An instance of the BPD is the following:  $k$  is the number of bins,  $V$  is the capacity of each bin,  $Z$  is the number of items and  $x_i$  ( $1 \leq i \leq Z$ ) is the size of each item. We create an instance of CDP as follows:  $S = k$  is the number of Special Chargers,  $\mathcal{E} = V$  is the percentage for every Special Charger,  $M = Z$  is the number of Mobile Chargers and  $\varepsilon_j = x_j$  are the percentages of every Mobile Charger. A solution to this instance of CDP would provide an answer to the solution of *Bin Packing Decision Problem* which means that  $BPD \leq_m CDP$ .  $\square$

## 20.5 The Protocols

We present a new protocol operating in 1-D networks and four new protocols operating in 2-D networks. Our protocols use hierarchical collaborative charging. Since there is plenty of research on how multiple Mobile Chargers can charge sensor nodes we focus on how we can efficiently use the available Special Chargers. In all protocols we investigate the following three design aspects:

**Coordination:** A Special Charger consumes its energy according to the energy depletion on its area, i.e., the energy consumed by the sensor nodes and the Mobile Chargers. This may lead to a non-balanced energy consumption between Special

Chargers. For this reason, they should periodically change the area that they are responsible of by increasing or decreasing the number of the Mobile Chargers that belong to their group. This procedure may be distributed or centralized. In the centralized case, the computation is performed by a computationally powerful network entity, e.g., the Sink. In contrast, in the distributed case, each Special Charger locally communicates with its neighbors to learn about their energy status and then calculates the coordination action. In the distributed case, we assume that two adjacent Special Chargers can exchange one of their border Mobile Chargers. More specifically, imagine that  $SC_k$  is in charge of the following group of Mobile Chargers:  $\mathcal{C}_k = \{MC_1, \dots, MC_i\}$  and the  $SC_{k+1}$  has:  $\mathcal{C}_{k+1} = \{MC_{i+1}, \dots, MC_{i+c}\}$ ,  $c > 0$ . After computation, if there is going to be a coordination action then either  $MC_i$  will change group and go under  $SC_{k+1}$ 's responsibility, or  $MC_{i+1}$  will be under  $SC_k$ 's responsibility.

**Trajectory:** Every Special Charger has a group of several Mobile Chargers that it can charge. However, some of its corresponding Mobile Chargers may be more critical than others, so it should decide which one should be charged next in order to manage efficiently the available energy.

**Charging Policy:** When a Special Charger has estimated which Mobile Charger should be charged, then it estimates how much energy should be given to it.

### 20.5.1 *Protocols for 1-D Networks*

#### 20.5.1.1 *The Model in 1-D Networks*

In 1-D networks we compare our protocol to a state-of-the-art protocol ([18]). In order to conduct a fair comparison in 1-D networks, we assume a quite identical model (and not the one described in Sect. 20.3). More specifically, we consider  $N$  sensor nodes that are uniformly distributed, unit distance apart, along a one-dimensional line network. All sensor nodes have the same energy consumption rate and the same battery capacity, denoted by  $b$ . Also, there are  $K$  Mobile Chargers of battery capacity  $B$  which consume  $c$  amount of energy per unit distance. Moreover, the Sink serves as data collector as well as an energy source. The only difference is that we assume that the Sink has finite energy supplies denoted as  $E_{total}$  in contrast to the proposed model in [18] where the Sink has unlimited energy supplies.

#### 20.5.1.2 *PushWait Algorithm*

The PushWait algorithm ([18]) assumes that the Mobile Chargers start from the Sink with full batteries, charge sensors, finally come back to the Sink, and then get themselves charged by the Sink. Both the movement of the Mobile Chargers and the process of wireless charging share the same pool of energy. Also, there are  $K$  rendezvous points denoted as  $L_i$  ( $1 \leq i \leq K$ ) where in each one a Mobile Charger

stops moving forward. A noticeable point is that all Mobile Chargers return to the Sink after each scheduling cycle (in order to make the network able to run forever, i.e., in each scheduling cycle they have exactly the same performance).

PushWait follows two main steps:

- $MC_i$  charges sensors between  $L_{i+1}$  and  $L_i$  to their full batteries. At  $L_i$ ,  $MC_i$  transfers energy to the rest Mobile Chargers,  $MC_{i-1}, MC_{i-2}, \dots, MC_1$  until they are at their full energy capacity. Then  $MC_i$  waits at  $L_i$ , and all of the other  $i - 1$  MCs keep moving forward.
- After  $MC_{i-1}, MC_{i-2}, \dots, MC_1$  return to  $L_i$  where  $MC_i$  waits for them,  $MC_i$  evenly distributes its residual energy among  $i$  MCs (including  $MC_i$ ). This will make them just have enough energy to return to  $L_{i+1}$ .

The above algorithm needs a specific number of Mobile Chargers in order to charge in a round all  $N$  sensors. This is provided via a linear system that, given the number of sensors  $N$ , computes the number of necessary Mobile Chargers.

### 20.5.1.3 1-D No Knowledge No Coordination (1D-NKNC)

In our hierarchical protocol, we use the same number of chargers that are used in PushWait, for a fair comparison. If  $K$  is the number of Mobile Chargers used in PushWait algorithm, given that network contains  $N$  sensor nodes, in our protocol, we separate them into two groups (Mobile Chargers and Special Chargers) as follows:

$$M = q \cdot K \text{ and } S = (1 - q) \cdot K$$

where  $q \in (0.75, 1)$  since we assume that the number of Special Charger is significantly lower than the number of Mobile Chargers.

Note that *only* in this special case of 1-D network deployment, all Chargers (Mobile and Special) have the same battery capacity  $B$ . We divide the line network into  $M$  equal sized segments, one for each Mobile Charger. Each Mobile Charger is responsible for charging the sensor nodes in its area. We group the Mobile Chargers in  $S$  groups, one for each Special Charger. Each Mobile Charger charges the sensor nodes in its area sequentially over the line graph and when it arrives at the last node, it follows the opposite direction in order to reduce movement overhead. When the energy level of a Special Charger is low enough, i.e., its energy is enough for just moving to the Sink, it visits the Sink and gets charged. Mobile Chargers do not roam out of their region. Since the number of Special Chargers is significantly lower than the number of the Mobile Chargers, the energy consumed for movement is much lower and our protocol improves the efficiency ratio.

**Coordination:** There is no coordination between Special Chargers. In this protocol the Special Chargers do not change the Mobile Chargers initially assigned to them.

**Trajectory:** Each Special Charger charges its corresponding Mobile Chargers sequentially. When it arrives to the last one, it changes direction and charges them in reverse order. Also, when it arrives at the first one, it changes direction again and so on. When its energy drops under a specific level, it visits the Sink, gets recharged and then returns back to its previous position.

**Charging Policy:** Since in 1-D networks we assume a uniform consumption rate between nodes, there is a uniform consumption rate between Mobile Chargers. Thus, in order to reduce the movement overhead, Special Chargers charge each Mobile Charger at a maximum level.

In sensor networks with a limited amount of initial energy (stored in the Sink) it is important to exploit this energy optimally. The energy is consumed both for the Chargers' movement and for sensing activities. In this case, (1-D networks), in order to improve the efficiency ratio, our goal is to reduce the energy consumed for movement, denoted by  $E^{overhead}$  and increase the amount of energy obtained by the nodes denoted by  $E^{payload}$ . The efficiency ratio is defined as follows:

$$\text{efficiency\_ratio} = \frac{E^{payload}}{E^{overhead}}$$

The PushWait algorithm proposed in [18] assumes that the Sink has unlimited energy supplies and so the authors investigated how many Mobile Chargers are needed to charge all sensor nodes in a scheduling cycle. In each cycle, Mobile Chargers charge all the sensor nodes and come back to the Sink without residual energy (only one Mobile Charger may have a small amount of residual energy). This algorithm ensures that the movement is minimized and thus, the achieved *efficiency\_ratio* is optimal. In this work, we assume that the Sink has limited amount of energy and thus the PushWait algorithm runs for a specific number of scheduling cycles. Unlike PushWait, we do not have cycles and we compute the overall *efficiency\_ratio* which is the rate of the total amount of energy obtained by sensor nodes over the total amount of energy consumed for both movement of Special Chargers and Mobile Chargers.

For instance, if we run PushWait algorithm with input  $E_{total} = 2000\text{J}$ ,  $B = 80\text{J}$ ,  $b = 2\text{J}$ ,  $N = 29$ ,  $c = 3\text{J/m}$ , then the output is  $K = 7$  and  $\text{efficiency\_ratio} = 0.11$ .

After that, we run 1D-NKNC with input:  $E_{total} = 2000\text{J}$ ,  $B = 80\text{J}$ ,  $b = 2\text{J}$ ,  $N = 29$ ,  $c = 3\text{J/m}$ ,  $q = 0.75$  and thus,  $M = 5$  and  $S = 2$ . The output is  $\text{efficiency\_ratio} = 0.15$ , which is higher.

If in our method we change the model and apply a nonuniform battery capacity deployment, i.e., equip the Special Chargers with larger battery capacity but reduce the battery capacity of the Mobile Chargers such that the total battery capacity maintains the same  $K \cdot B$ , the efficiency ratio can become higher. That is because the Special Chargers will reduce the amount of times that they return to the Sink to get recharged and so reduce the energy consumed for movement. Actually, the efficiency ratio has a threshold behavior as shown in Fig. 20.2. The efficiency ratio is higher only when the battery capacity of each Special Charger takes a value lower than the threshold which is normal since if the battery capacity of the Special Chargers is

**Fig. 20.2** Efficiency ratio over the Special Chargers' battery capacity

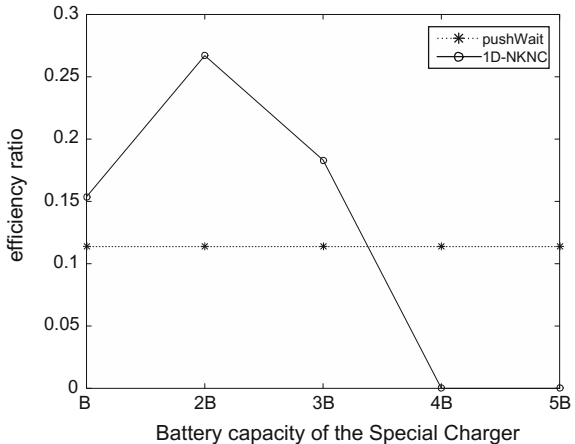
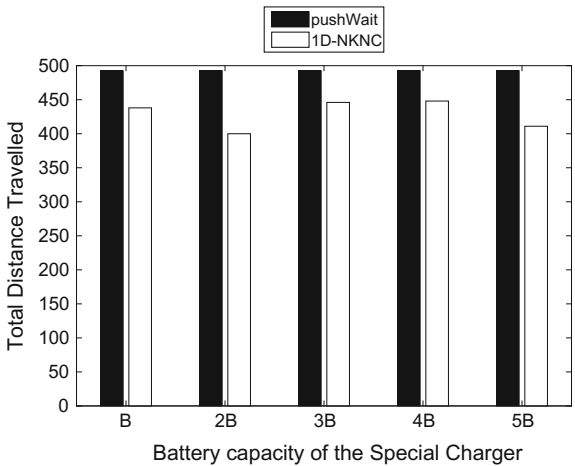


**Fig. 20.3** Distance traveled by all chargers



higher than that, the battery capacity of the Mobile Chargers drops below a specific level, and they will not be able to charge sensor nodes any more. So, the efficiency ratio will be zero.

The total distance traveled by all chargers is a metric that indicates that our hierarchical protocol achieves better performance. More specifically, in the 1D-NKNC protocol, the distance traveled metric refers to the total distance that both the Mobile Chargers and the Special Chargers have covered during the whole process; recall that the PushWait algorithm only uses Mobile Chargers and, we only estimate the total distance traveled by them. Figure 20.3 depicts the simulation results. The distance traveled when using the 1D-NKNC protocol is always lower than the distance traveled when using the PushWait algorithm.

Motivated by this demonstration of the potential power of the hierarchical approach, we propose hierarchical protocols for 2-D networks where Special Chargers have a little larger battery capacity than the Mobile Chargers.

## 20.5.2 Protocols for 2-D Networks

### 20.5.2.1 No Knowledge No Coordination Protocol (NKNC)

The NKNC protocol is a generalization of 1D-NKNC protocol with the difference that the Special Chargers have higher battery capacity than the Mobile Chargers ( $E_{SC}^{max}$  and  $E_{MC}^{max}$ , respectively). This fact does not violate any model assumptions, since the available initial total energy remains the same, independently of the Chargers' battery capacity. More precisely:

**Coordination:** There is no coordination between Special Chargers.

**Trajectory:** Each Special Charger charges the corresponding Mobile Chargers sequentially. When it arrives to the last Mobile Charger of its group, it changes direction and charges them again in a reverse order this time and so on, as shown in Fig. 20.4.

**Charging policy:** Each Special Charger, charges each Mobile Charger in its group until its battery level is  $E_{MC}^{max}$ .

### 20.5.2.2 1-Level Knowledge Distributed Coordination Protocol (1KDC)

The 1KDC protocol performs a distributed coordination among Special Chargers, i.e., every Special Charger  $SC_k$  can communicate with its left and right neighbors

**Fig. 20.4** NKNC trajectory

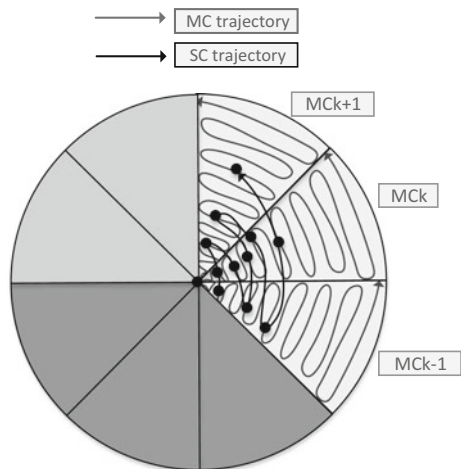
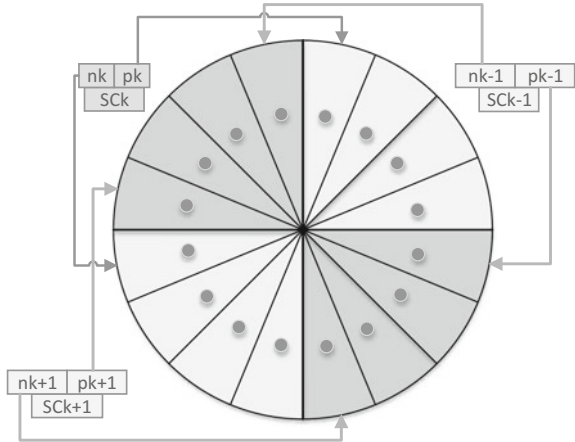


**Fig. 20.5** Distributed coordination



( $SC_{k-1}$  and  $SC_{k+1}$ ) and with the two Mobile Chargers that are on the boundaries of its region (and do not belong to its group). Also, this protocol assumes 1-level knowledge of the network, i.e., in order to perform the coordination it can use information only about Mobile Chargers' energy status (and not about the sensors' which lie one level lower).

**Coordination:** In distributed coordination, we assume that a Special Charger knows which are the adjacent Mobile Chargers on the boundaries of its region. We call next the first Mobile Charger that belongs to the  $SC_{k+1}$  and previous the last Mobile Charger that belongs to  $SC_{k-1}$  as shown in Fig. 20.5. More specifically,

$$n_k = \min_{j \in C_{k+1}} \{j\} : \text{next Mobile Charger (belongs to } SC_{k+1})$$

$$p_k = \max_{j \in C_{k-1}} \{j\} : \text{previous Mobile Charger (belongs to } SC_{k-1})$$

During the coordination procedure, each Special Charger estimates its new region, i.e., the group of Mobile Chargers that it will be responsible of. In the distributed coordination case, as we already mentioned in Sect. 20.5, each Special Charger  $SC_k$  communicates with the Mobile Chargers  $n_k$  and  $p_k$  to get informed about their energy level. After that, the Special Charger estimates how much residual energy it would have by including  $n_k$  or  $p_k$  in its group, using the following equations:

$$e_k^p = E_{SC_k} - \sum_{j \in \mathcal{C}_k} E_{MC_j}^{lack} - E_{MC_{p_k}}^{lack} \quad (20.1)$$

$$e_k^n = E_{SC_k} - \sum_{j \in \mathcal{C}_k} E_{MC_j}^{lack} - E_{MC_{n_k}}^{lack} \quad (20.2)$$

where  $E_{MC_j}^{lack} = E_{MC}^{max} - E_{MC_j}$  is the amount of energy that  $MC_j$  can receive until it is fully charged.

---

**Algorithm 15:** Coordination between  $SC_{k-1}$  and  $SC_k$ 


---

```

1 if  $e_k^p > e_{k-1}^n$  then
2    $\mathcal{C}_k = \mathcal{C}_k \cup \{MC_{p_k}\}$ 
    $\mathcal{C}_{k-1} = \mathcal{C}_{k-1} \setminus \{MC_{p_k}\}$ 
3 else if  $e_k^p < e_{k-1}^n$  then
4    $\mathcal{C}_{k-1} = \mathcal{C}_{k-1} \cup \{MC_{n_{k-1}}\}$ 
    $\mathcal{C}_k = \mathcal{C}_k \setminus \{MC_{n_{k-1}}\}$ 
5 else
6   | There is not any exchange of Mobile Chargers
7 end if

```

---



---

**Algorithm 16:** Coordination between  $SC_k$  and  $SC_{k+1}$ 


---

```

1 if  $e_k^n > e_{k+1}^p$  then
2    $\mathcal{C}_k = \mathcal{C}_k \cup \{MC_{n_k}\}$ 
    $\mathcal{C}_{k+1} = \mathcal{C}_{k+1} \setminus \{MC_{n_k}\}$ 
3 else if  $e_k^n < e_{k+1}^p$  then
4    $\mathcal{C}_{k+1} = \mathcal{C}_{k+1} \cup \{MC_{p_{k+1}}\}$ 
    $\mathcal{C}_k = \mathcal{C}_k \setminus \{MC_{p_{k+1}}\}$ 
5 else
6   | There is not any exchange of Mobile Chargers
7 end if

```

---

After this procedure, each Special Charger  $SC_k$  communicates with its neighbors ( $SC_{k-1}$  and  $SC_{k+1}$ ) to get informed about their residual energy. More specifically, the Special Charger  $SC_{k-1}$  sends the  $e_{k-1}^n$  value that represents its residual energy if it includes to its group the  $SC_k$ 's first Mobile Charger. The Special Charger  $SC_{k+1}$  sends the  $e_{k+1}^p$  value which refers to its residual energy if it includes to its group the  $SC_k$ 's last Mobile Charger.

Between two adjacent Special Chargers the one with the higher energy supplies takes the other's boundary Mobile Charger in its group. Thus, the Special Charger with lower energy supplies is responsible for a smaller area. In the case that their energy supplies are the same they do not exchange any Mobile Chargers. More precisely, the coordination algorithm is the following:

**Trajectory:** Special Charger  $k$  should determine which Mobile Charger will be the next that will be charged prioritizing a Mobile Charger based on minimum energy and minimum distance. Considering this,  $SC_k$  chooses to charge  $MC_m$  where

$$m = \arg \min_{j \in \mathcal{C}_k} \left\{ \left( 1 + \frac{E_{MC_j}}{E_{MC}^{max}} \right) \cdot \left( 1 + \frac{d_{k_j}}{2R} \right) \right\}.$$

**Charging policy:** A Special Charger charges a Mobile Charger  $j$  according to its energy consumption rate  $r_{MC_j}$ . More specifically, a Mobile Charger with higher consumption rate (compared to the rest Mobile Chargers that belong to the Special Charger's group) should be charged with a higher amount of energy. Motivated by that, if by  $MC_m$  we denote the Mobile Charger that Special Charger  $k$  chose to charge, then the amount of energy that the Special Charger will give to it is  $e = c_m \cdot (\min\{E_{MC_m}^{lack}, E_{SC_k}\})$  where

$$c_m = \frac{r_{MC_m}}{\sum_{j \in \mathcal{C}_k} r_{MC_j}}.$$

### 20.5.2.3 2-Level Knowledge Distributed Coordination Protocol (2KDC)

In contrast to previous protocols, the 2KDC assumes 2-level knowledge and thus, each Special Charger  $k$  compute  $e_k^p$  and  $e_k^n$  using information about both the Mobile Chargers and the sensor nodes, as follows:

**Coordination:**

$$e_k^p = E_{SC_k} - \sum_{j \in \mathcal{C}_k} \sum_{i \in \mathcal{D}_j} E_i^{lack} - \sum_{i \in \mathcal{D}_{p_k}} E_i^{lack}$$

$$e_k^n = E_{SC_k} - \sum_{j \in \mathcal{C}_k} \sum_{i \in \mathcal{D}_j} E_i^{lack} - \sum_{i \in \mathcal{D}_{n_k}} E_i^{lack}$$

After that, the coordination algorithm presented in 1KDC protocol's coordination phase is used.

**Trajectory:** Each  $MC_j$  stores a list  $l_j$  of sensor nodes the energy level of which is lower than  $E_{threshold}$ . Special Charger  $k$  defines which Mobile Charger is more critical by making a query to each Mobile Charger in its group on the size of its list. A Special Charger should assign high priority to a Mobile Charger that has a large number of sensor nodes of energy lower than  $E_{threshold}$ . Thus,  $SC_k$  selects to charge  $MC_m$  where

$$m = \arg \max_{j \in \mathcal{C}_k} |l_j|.$$

**Charging Policy:** Since each Special Charger assumes 2-level knowledge, it computes the percentage of energy to transfer, according to the lack of energy in the slice of the selected Mobile Charger compared to the total energy lack in all slices that this Special Charger is responsible for. More precisely, Special Charger  $k$  transfers to  $MC_m$  an amount of energy  $e = c_m \cdot (\min\{E_{MC_m}^{lack}, E_{SC_k}\})$  where

$$c_m = \frac{\sum_{i \in \mathcal{D}_m} E_i^{lack}}{\sum_{j \in \mathcal{C}_k} \sum_{i \in \mathcal{D}_j} E_i^{lack}} \in (0, 1)$$

where  $E_i^{lack} = E_{sensor}^{max} - E_i$  is the amount of energy that sensor  $i$  can receive until it is fully charged.

#### 20.5.2.4 2-Level Knowledge Centralized Coordination Protocol (2KCC)

The 2KCC protocol performs centralized coordination and assumes 2-level network knowledge. It assigns to each Special Charger a set of Mobile Chargers according to their residual energy. More precisely:

**Coordination:**

$$\mathcal{E}_k = \frac{E_{SC_k}}{\sum_{i=1}^S E_{SC_i}} \quad (1 \leq k \leq S), \quad |\mathcal{C}_k| = \mathcal{E}_k \cdot M.$$

**Trajectory:** Since each Special Charger assumes 2-level network knowledge, it takes into account information from both Mobile Chargers and sensor nodes in order to find good trajectories. Thus,  $SC_k$  prioritizes  $MC_m$  where

$$m = \arg \min_{j \in \mathcal{C}_k} \left\{ \alpha \cdot \frac{E_{MC_j}}{E_{MC}^{max}} + (1 - \alpha) \cdot \frac{\sum_{i \in \mathcal{D}_j} E_i}{|\mathcal{D}_j| \cdot E_{sensors}^{max}} \right\}$$

with  $\alpha \in (0, 1)$  a constant allowing to select the weight of each term in the sum.

**Charging Policy:** Same as 2KDC.

## 20.6 Performance Evaluation

The simulation environment for conducting the experiments is MATLAB 7.12. The Sink is placed at the center of the circular area. The number of sensor nodes is set to 2000, the number of Mobile Chargers to 15, and the number of Special Chargers to 3. In the simulations, the number of the Mobile Charges in non-collaborative protocols equals to the sum of the Mobile Chargers and the Special Chargers in the hierarchical protocols, so, in protocols that do not use Special Chargers, the number of Mobile Chargers is set to 18. Our simulations include 4000 generated events. For statistical smoothness, we apply several times the deployment of nodes in the network and repeat each experiment 100 times. For each experiment, we simulate large numbers of data propagations and the average value is taken. The statistical analysis of the findings (the median, lower and upper quartiles, outliers of the samples) demonstrate

very high concentration around the mean, so in the following figures we only depict average values.

In our simulations, we compare the performance of our 2-D protocols to a variation of the state-of-the-art protocol (CC) proposed in [12] which is designed for 2-D networks as well, and divides the network into slices (one for each Mobile Charger) like our protocols. However, this protocol is non-collaborative, i.e., the Mobile Chargers do not charge each other and we label it as “non-collaborative” in our simulation figures.

We focus on the following performance metrics: (a) **alive nodes over time**, that is the number of nodes with enough residual energy to operate, during the progress of the experiment, (b) **connected components over time** which indicates the number of strongly connected components of the network graph throughout the experiment, (c) **routing robustness** and **average routing robustness**, in terms of the nodes’ average alive neighbors during the progress of the experiment, (d) **coverage aging**, that is the average coverage number (number of sensors having the point in their range) of 1000 randomly selected points in the network over time, and (e) **communication overhead** which refers to the number of messages transmitted between the network devices (Special Chargers, Mobile Chargers, sensor nodes, and the Sink) in order to perform the various protocols’ procedures (coordination, trajectory, and charging policy).

### **20.6.1 Fine-Tuning of 2KCC Protocol**

One important performance metric is the network lifetime. We use it to decide which is the appropriate value of parameter  $\alpha$  in 2KCC protocol. As shown in Fig. 20.6 the value that achieves the most prolonged lifetime is  $\alpha = 1$ . This is natural because, despite the fact that energy will eventually be obtained by the sensor nodes, a Special Charger charges only the Mobile Chargers and so, it should take into account only their energy status and not the sensor nodes’. If the nodes of a slice do not have high energy supplies but the corresponding Mobile Charger has, the Special Charger may select it but the energy that will transfer will be very small (since its battery is not discharged very much). So, it would be better to take into account solely the Mobile Chargers’ battery and decide to charge the one that has the smallest amount of energy. Thus, we set  $\alpha = 1$  in all following simulations.

### **20.6.2 Protocols’ Impact on Network Properties**

(i) The charging protocols that we propose manage to prolong **network lifetime** (i.e., alive nodes over time) as shown in Fig. 20.7a. As expected, the 2KCC outperforms the other protocols since it provides a centralized coordination algorithm which implies the most fair partition of Mobile Chargers among Special Chargers. Despite the

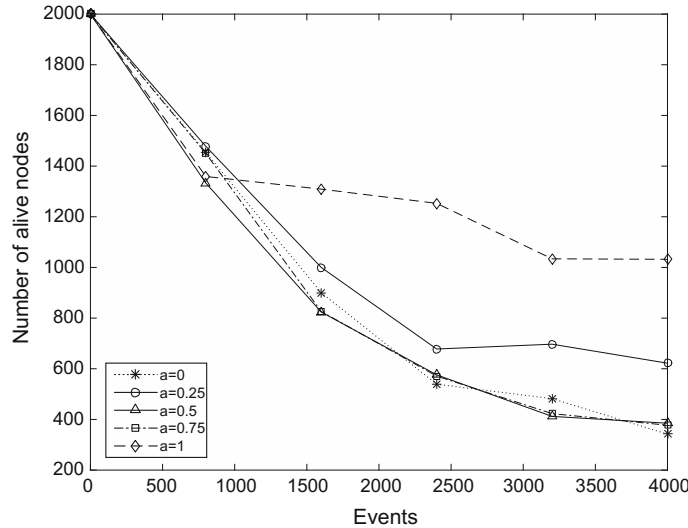


Fig. 20.6 Alive nodes over time (Varying  $\alpha$ )

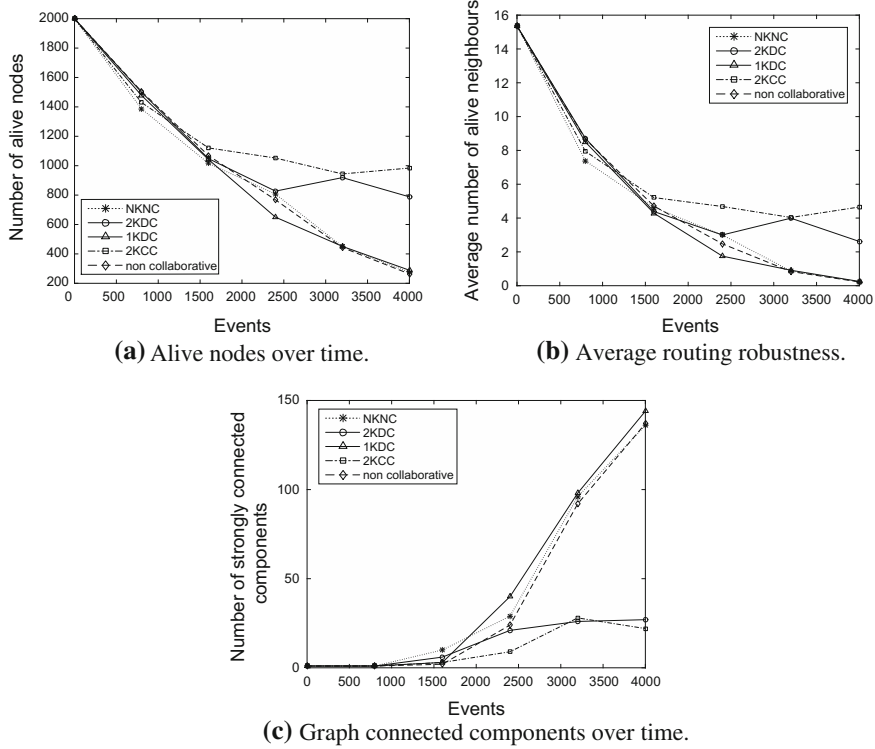


Fig. 20.7 Performance metrics

fact that 2KDC may not achieve the best partition since its coordination procedure takes into account only adjacent Special Chargers its performance is quite close to 2KCC's. We also observe that NKNC has quite the same performance with the non-collaborative case, since it does not perform any coordination or any sophisticated trajectory procedure.

(ii) **Routing robustness** is critical to ensure that all the generated data will arrive to the Sink. It is important that at least one path from each node to the Sink is maintained. A measure of routing robustness is counting the number of alive neighbors of each sensor node, because the greater this number is the lower the disconnection probability of the corresponding node is. Figure 20.7b depicts the average routing robustness for our protocols. We observe that it follows the same pattern as network lifetime. This is natural since the reduction of alive nodes implies the reduction of alive neighbors. We also provide a more detailed routing robustness metric which is shown in Fig. 20.8. We investigate (for each protocol and various number of events) the quality of routing robustness. More specifically, we investigate four cases, the number of nodes that have  $<7$  alive neighbors, the number of nodes that have  $\geq 7$  and  $<13$  alive neighbors, the number of nodes that have  $\geq 13$  and  $<15$  alive neighbors and finally, the number of nodes that have  $\geq 15$  alive neighbors. Of course, it is desirable for each node to have as much alive neighbors as possible and consequently, a high white bar and a low black bar. As we can see in Fig. 20.8, NKNC and non-collaborative protocols' white bar is decreasing with a high rate in contrast to the 2KDC and 2KCC protocols which achieve a better routing robustness.

(iii) Another connectivity metric is the number of **strongly connected graph components**. Two different connected components cannot communicate with each other. This may lead to failures on delivering messages to the Sink. It is important to maintain a small number of connected components. Figure 20.7c depicts the number of strongly connected components over time. As we can see, the 2KCC and 2KDC protocols outperform all others and maintain a small number of connected components for a large number of events. This is because sensor nodes are dying with low rates and the connections are maintained. Unlike 2KCC, the NKNC and 1KDC increase their number of connected components rapidly.

(iv) **Point coverage**. This metric captures the assurance that some selected points in the network are covered by an adequate number of sensor nodes. This is an important aspect if we consider that in some applications, there are some selected points of the network that produce crucial sensing data that should be captured by nearby sensors. A point is  $k$ -covered if there are  $k$  sensor nodes that cover it, i.e., it is inside their communication range. We deploy 1000 random points in the network and examine how many of them are less than 2-covered, 2-covered, 3-covered, or greater than 3-covered over 4000 generated events. In Fig. 20.9 we can observe that the NKNC, non-collaborative and 1KDC rapidly decreases the number of greater than 3-covered points. 2KDC and 2KCC achieve good performance, since they decrease the number of covered points in a very low rate.

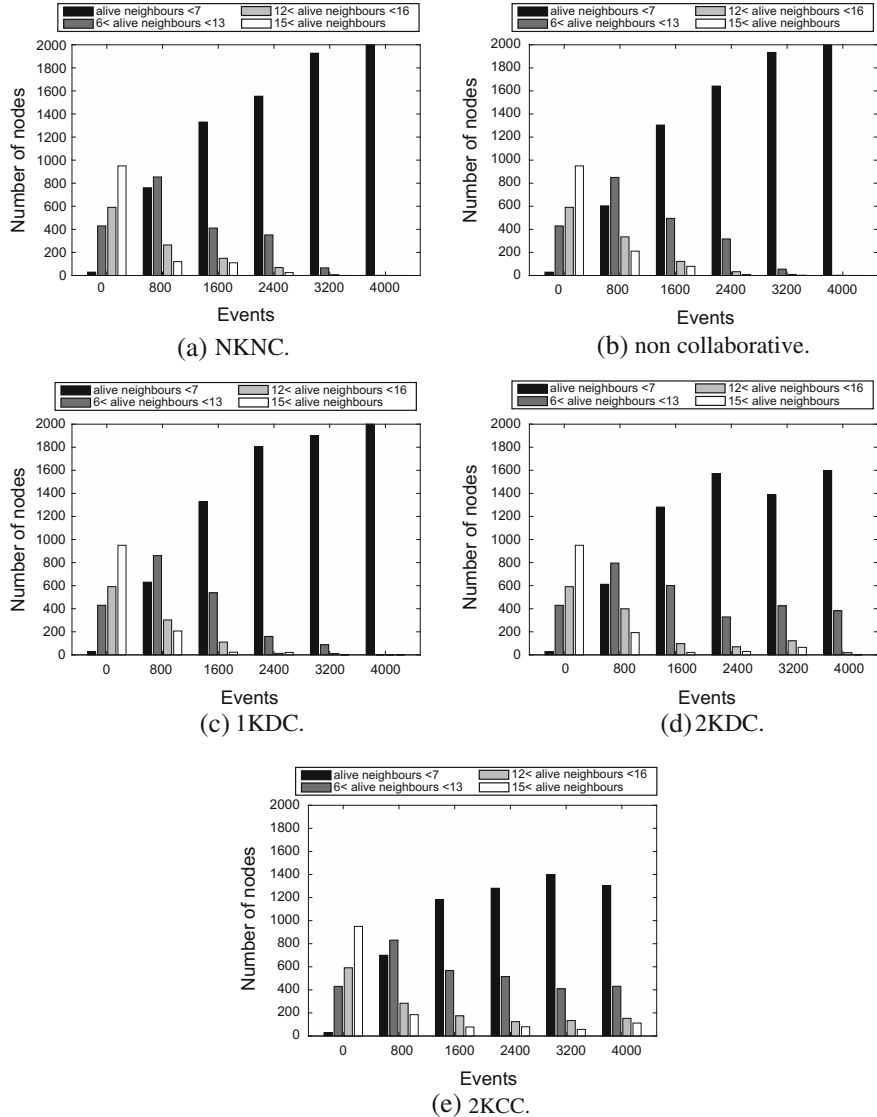


**Fig. 20.8** Routing robustness

### 20.6.3 Communication Overhead

Since the data, generated by sensor nodes, should be transferred to the Sink, we do not take into account the routing communication overhead, as it is decoupled from the charging process for each and every one of the presented protocols. On the

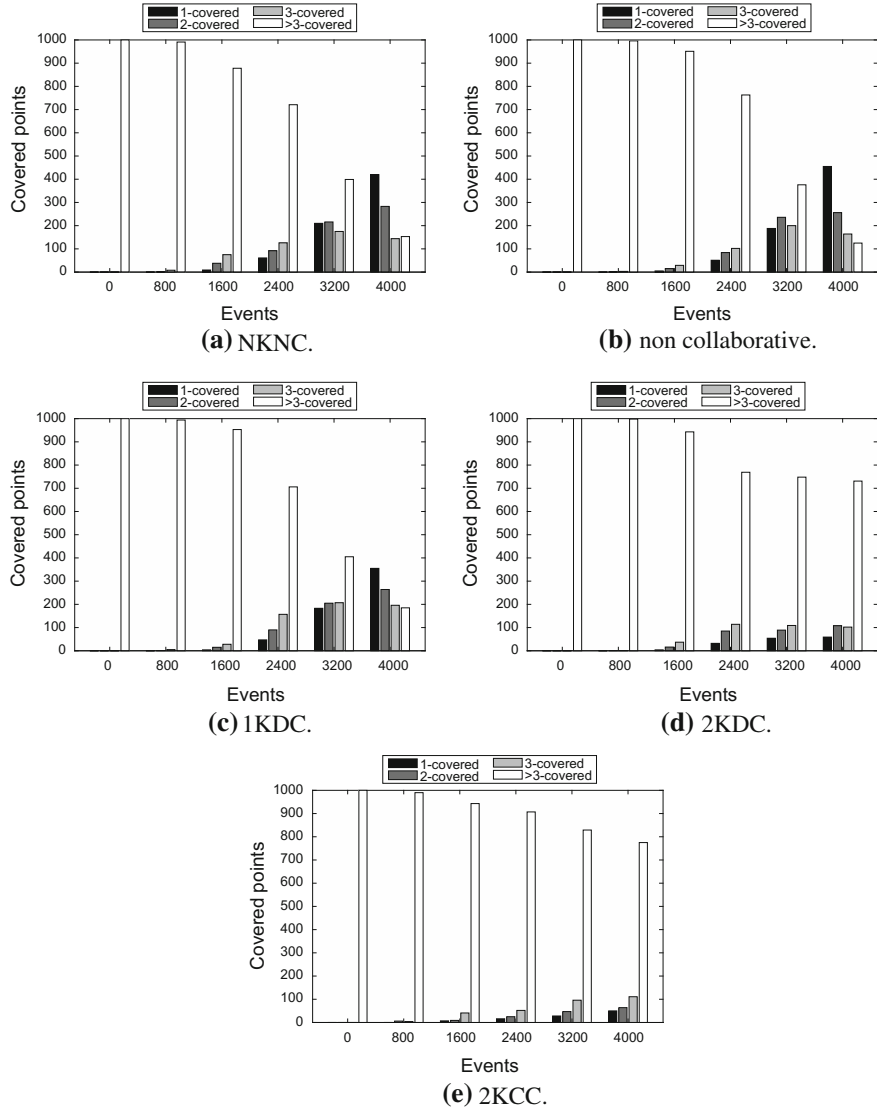
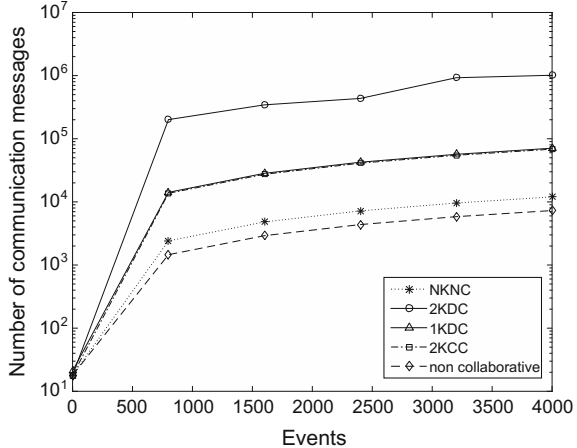


**Fig. 20.9** Coverage aging

contrary, for each of our protocols, the communication overhead is defined as the total number of messages transferred between the network devices for the execution of the protocol, i.e., the number of messages exchanged between the nodes, the Special Chargers, the Mobile Chargers, and the Sink in order to perform the coordination, the trajectory and the charging policy procedures. As depicted in Fig. 20.10, the NKNC and non-collaborative protocols have the lowest communication overhead which is

**Fig. 20.10** Communication overhead



normal since they do not have a coordination phase. Although the 2KCC protocol is a centralized one and one would expect to have the highest communication overhead, this is actually not true. On the contrary, it has lower overhead than the 2KDC protocol. Since they both have the same charging policy procedure, the overhead difference is due to the coordination and trajectory procedures. Although they differ in the trajectory procedure, the overhead is similar because in the 2KCC protocol each Special Charger communicates only with its corresponding Mobile Chargers; observe that we have set  $\alpha = 1$ . In the coordination procedure of 2KDC, each Special Charger communicates with all sensor nodes of its region and with the sensor nodes that belong in the slices of the Mobile Chargers that are on the boundaries of its region and belong to the adjacent Special Chargers. In contrast, in the 2KCC protocol, each Special Charger communicates only with the Sink to calculate its region.

#### 20.6.4 Impact of Knowledge

By observing the performance of the above protocols, we conclude that the amount of knowledge is one of the most determinant factors. 2KDC always outperforms 1KDC and also the NKNC that has no knowledge at all. Since the coordination procedure depends on the amount of knowledge, this difference in performances indicates that the greater the amount of available knowledge the better the protocol's performance. However, as depicted in Fig. 20.10, the level of knowledge also induces communication overhead.

### 20.6.5 Adaptivity of Our Hierarchical Protocols

A notable additional value of hierarchical collaborative charging is that it can easily be added on top of the non-collaborative charging protocols and further improve their performance. Figure 20.11 depicts the improvements in terms of lifetime, of a state-of-the-art protocol proposed in [15]. We transform their algorithm by converting some Mobile Chargers to Special Chargers and applying hierarchy using one of our hierarchical protocols (2KCC) to achieve performance improvement. Then, we compare the proposed non-collaborative algorithm with our hierarchical, as shown in Fig. 20.12.

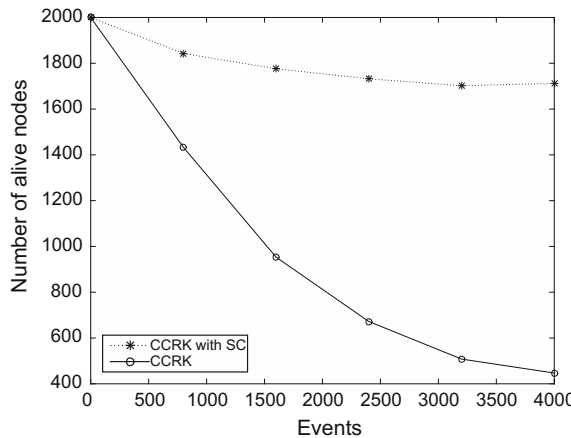


**Fig. 20.11** Alive nodes over time

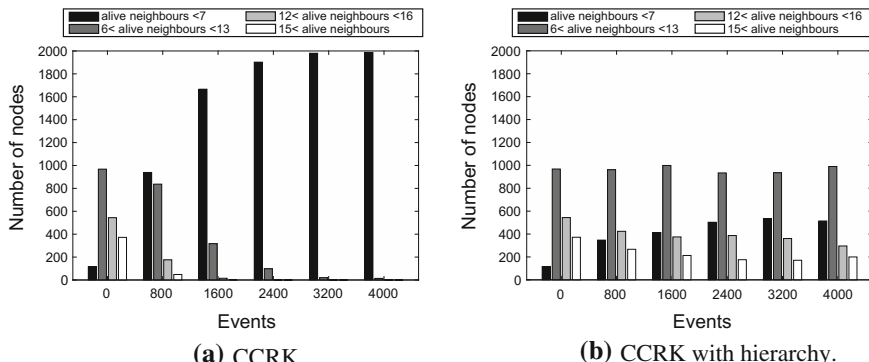


**Fig. 20.12** Adaptivity of hierarchy: Routing robustness

### 20.6.6 Partition of the Chargers

We recognize that the problem of finding the best partition of chargers into Special Chargers and Mobile Chargers needs investigation and we plan to address it in future work. However, we can provide an intuition of the effect of the partition on our 2KDC protocol performance. At first, we divide 25 chargers in two different ways. In the first case, there are 5 Special Chargers and 20 Mobile Chargers and in the second case, the Special Chargers are set to 10 and the Mobile Chargers are set to 15. As depicted in Fig. 20.13, the 2KDC protocol's performance with respect to the alive nodes over time metric is different. After that, we conduct simulations where we keep the number of one kind of chargers fixed and set various values on the other one. More specifically, in Fig. 20.14a, we set the number of Special Chargers to 3

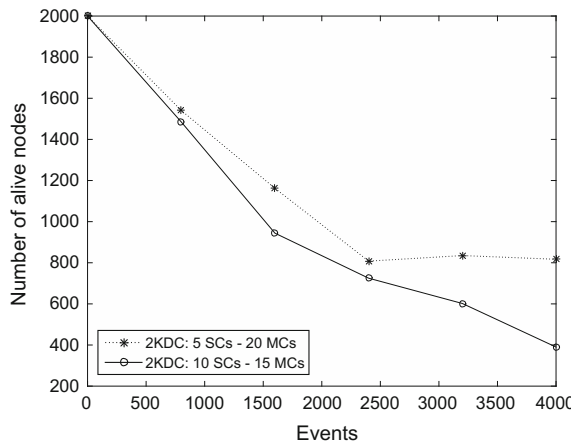


**Fig. 20.13** Alive nodes over time: same number of chargers

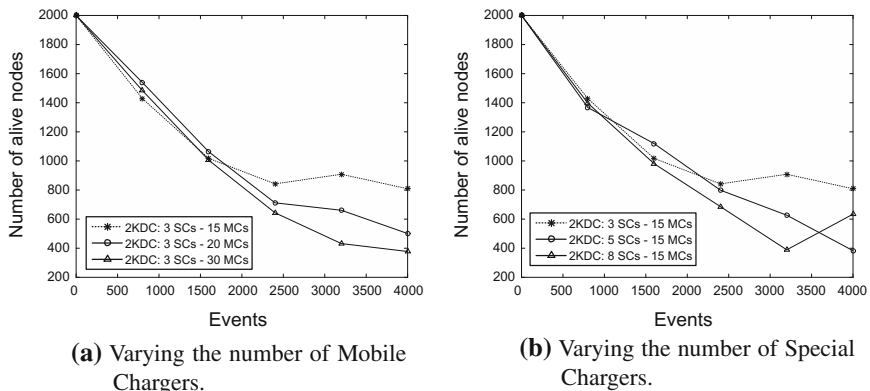


**Fig. 20.14** Alive nodes over time of 2KDC protocol

and the number of Mobile Chargers to 15, 20, and 30, respectively. We observe that, as the number of Mobile Chargers is increasing, the number of alive nodes over time is decreasing. This is logical, since each Special Charger is responsible for more Mobile Chargers and is not able to charge them in due time. On the second case, we set to 15 the number of Mobile Chargers and vary the number of Special Chargers (3, 5 and 8). As we observe in Fig. 20.14b, the smaller the number of Special Chargers is, the better the protocol's performance becomes.

## 20.7 Conclusion and Open Problems

In this work we study the problem of efficient collaborative wireless charging in Wireless Sensor Networks. We propose a new design approach, according to which, the set of chargers is partitioned into two groups, one hierarchically higher, called Special Chargers and one hierarchically lower, called Mobile Chargers. The Mobile Chargers are responsible for charging the sensor nodes whereas the Special Chargers charge Mobile Chargers. This hierarchical structure provides a more controllable and balanced energy replenishment of the network. We investigate what are good trajectories that Special Chargers should follow to charge Mobile Chargers, how much energy they should give and what are good coordination procedures to perform. Moreover, we provide a useful hierarchical add-on that can be added on top of non-collaborative protocols in order to enhance their performance.

As an open problem, it could be addressed nonuniform cases of the network deployment, since in many scenarios the network deployments are limited by the underlying terrain. Another direction is to investigate which is the optimal number of Chargers and what is the best partition of them into Special Chargers and Mobile Chargers. Also it would be interesting in the case where a Charger can deliver energy simultaneously to more than one device with high efficiency using the technology developed e.g., in [10].

## References

1. Angelopoulos, C.M., Nikoletseas, S., Raptis, T.P., Raptopoulos, C., Vasilakis, F.: Efficient energy management in wireless rechargeable sensor networks. In: The 15th ACM International Conference on Modeling, Analysis and Simulation of Wireless and Mobile Systems (MSWiM) (2012)
2. Angelopoulos, C.M., Nikoletseas, S.E., Raptis, T.P.: Wireless energy transfer in sensor networks with adaptive, limited knowledge protocols. *Comput. Netw.* **70**, 113–141 (2014)
3. Dai, H., Liu, Y., Chen, G., Wu, X., He, T.: Safe charging for wireless power transfer. In: Proceedings of the 33rd IEEE International Conference on Computer Communications (INFOCOM) (2014)
4. Dai, H., Liu, Y., Chen, G., Wu, X., He, T.: SCAPE: safe charging with adjustable power. In: Proceedings of the 34th IEEE International Conference on Distributed Computing Systems (ICDCS) (2014)

5. Dai, H., Wu, X., Chen, G., Xu, L., Lin, S.: Minimizing the number of mobile chargers for large-scale wireless rechargeable sensor networks. *Comput. Commun.* **46**, 54–65 (2014)
6. He, L., Gu, Y., Pan, J., Zhu, T.: On-demand charging in wireless sensor networks: Theories and applications. In: Proceedings of the 10th IEEE International Conference on Mobile Ad-Hoc and Sensor Systems (MASS) (2013)
7. Heinzelman, W.R., Chandrakasan, A., Balakrishnan, H.: Energy-efficient communication protocol for wireless microsensor networks. In: Proceedings of the 33rd Hawaii International Conference on System Sciences (HICSS). IEEE Computer Society (2000)
8. Kang, K., Meng, Y.S., Bréger, J., Grey, C.P., Ceder, G.: Electrodes with high power and high capacity for rechargeable lithium batteries. *Science* **311**(5763), 977–980 (2006)
9. Kurs, A., Karalis, A., Moffatt, R., Joannopoulos, J.D., Fisher, P., Soljacic, M.: Wireless power transfer via strongly coupled magnetic resonances. *Science* **317**(5834), 83–86 (2007)
10. Kurs, A., Moffatt, R., Soljacic, M.: Simultaneous mid-range power transfer to multiple devices. *Appl. Phys. Lett.* **96**(4) (2010)
11. Li, Z., Peng, Y., Zhang, W., Qiao, D.: J-roc: A joint routing and charging scheme to prolong sensor network lifetime. In: Proceedings of the 19th IEEE International Conference on Network Protocols (ICNP) (2011)
12. Madhja, A., Nikoletseas, S.E., Raptis, T.P.: Distributed wireless power transfer in sensor networks with multiple mobile chargers. *Comput. Netw.* **80**, 89–108 (2015)
13. Nikoletseas, S., Raptis, T.P., Raptopoulos, C.: Low radiation efficient wireless energy transfer in wireless distributed systems. In: Proceedings of the 35th IEEE International Conference on Distributed Computing Systems (ICDCS) (2015)
14. Nikoletseas, S., Raptis, T.P., Souroulagkas, A., Tsolovos, D.: An experimental evaluation of wireless power transfer protocols in mobile ad hoc networks. In: Proceedings of the IEEE Wireless Power Transfer Conference (WPTC) (2015)
15. Wang, C., Li, J., Ye, F., Yang, Y.: Multi-vehicle coordination for wireless energy replenishment in sensor networks. In: Proceedings of the 27th IEEE International Parallel & Distributed Processing Symposium (IPDPS) (2013)
16. Wang, C., Li, J., Ye, F., Yang, Y.: Recharging schedules for wireless sensor networks with vehicle movement costs and capacity constraints. In: Proceedings of the 11th IEEE International Conference on Sensing, Communication, and Networking (SECON) (2014)
17. Zhang, S., Qian, Z., Kong, F., Wu, J., Lu, S.: P<sup>3</sup>: joint optimization of charger placement and power allocation for wireless power transfer. In: Proceedings of the 34th IEEE International Conference on Computer Communications (INFOCOM) (2015)
18. Zhang, S., Wu, J., Lu, S.: Collaborative mobile charging for sensor networks. In: Proceedings of the 9th IEEE International Conference on Mobile Ad-Hoc and Sensor Systems (MASS) (2012)
19. Zhao, M., Li, J., Yang, Y.: A framework of joint mobile energy replenishment and data gathering in wireless rechargeable sensor networks. *IEEE Trans. Mob. Comput.* **13**(12), 2689–2705 (2014)

# Chapter 21

## Improve Charging Distance with Resonant Repeaters

Cong Wang, Ji Li, Fan Ye and Yuanyuan Yang

**Abstract** This chapter discusses opportunities to use the latest multi-hop wireless charging to improve recharge capability. Due to physical limitations, Mobile Chargers (MCs) only recharge one sensor node at a time, which has limited efficiency and scalability. With the short-range wireless charging reaching its maturity, recent advances in multi-hop wireless charging are gaining momentum and ready to provide fundamental support to address this problem. Unfortunately, the existing designs for single-node wireless charging cannot take advantage of such opportunities. In this chapter, we propose a new design that can relay wireless energy in multi-hops. Our method implements resonant repeater coils on sensor nodes. Once the MC is charging one sensor, the sensor can relay wireless energy to its neighbors. First, we present such novel design and discuss a method for estimating multi-hop charging efficiencies. Then we consider how to optimize network performance and achieve a balance between benefit and cost. A two-step approximation algorithm is proposed. We also discover there are more chances to further reduce the total system cost. Thus, we develop post-optimization procedures that can make use of the trade-offs between different types of energy cost. We also demonstrate simulation results to show significant improvements over single-node wireless charging.

---

C. Wang (✉) · J. Li · F. Ye · Y. Yang

Department of Electrical and Computer Engineering, State University of New York,  
Stony Brook, NY 11794, USA  
e-mail: cong.wang@stonybrook.edu

J. Li

e-mail: ji.li@stonybrook.edu

F. Ye

e-mail: fan.ye@stonybrook.edu

Y. Yang

e-mail: yuanyuan.yang@stonybrook.edu

© Springer International Publishing AG 2016

S. Nikoletseas et al. (eds.), *Wireless Power Transfer Algorithms, Technologies and Applications in Ad Hoc Communication Networks*,  
DOI 10.1007/978-3-319-46810-5\_21

561

## 21.1 Introduction

Recently, wireless charging has been exploited in battery-powered Wireless Sensor Networks (WSNs) to extend network lifetime toward perpetual operations. For high charging efficiency, Mobile Chargers (denoted as “MCs” henceforth) are employed to approach sensor nodes in close proximity and provide effective wireless charging. This type of networks is referred as *Wireless Rechargeable Sensor Networks* (WRSNs). Because the charging efficiency decays as an inverse cube of distance, previous works have only considered “short-range” charging where the charging distance is less than the diameter of the coils. It is not very efficient as the MCs have to recharge nodes one by one. For rechargeable batteries that take 1–2 h recharge time, finishing a network with hundreds of nodes can take days or weeks. It also leads to extremely long latencies that some nodes could exhaust energy, stop working and cause service interruption while waiting for the MCs.

With the wireless charging technology growing at the fastest pace ever, we have seen some latest advances in mid-range wireless charging, in which the charging distance is much larger than diameter of the coils. One of the most cost-effective ways is to implement *resonant repeaters* so wireless energy can be relayed in multi-hops and the MCs can recharge multiple sensors simultaneously. Such resonant repeaters can be easily manufactured from copper coils at low costs. For example, a 18 m copper tube quoted for \$30–35 [1] can make a dozen repeater coils (average \$3–5 additional cost per node). Compared to the cost of a sensor node, which normally ranges from \$30–100, the increase of cost is about 10%.

The effectiveness of using resonant repeaters to relay wireless energy is studied in the following works. In [2], significant improvements of charging efficiency from 10 to 46 % are reported by adding resonant repeaters between the source and receiving coils. In [3], it is demonstrated that using 4 resonant repeaters, we can distribute 15mW energy over a distance of 2 m for 6 different loads. It is not even necessary for all the repeaters to be placed in a strict line. In [4], experiments have shown that resonant repeaters can be organized into a domino form to power a 14 W lamp and their calculations indicate up to 70 % charging efficiency after 5–6 hops of energy relay.

In this chapter, we explore how to leverage this technology to enhance network scalability and performance. First, we describe the model used in the analysis and show how to estimate wireless charging efficiency based on laws in physics and electronics [4]. Based on such charging efficiencies, our objective is to minimize both charging and moving costs in the multi-hop recharge scheduling problem. The problem is formulated into a bi-objective location-routing problem [5]. Due to NP-hardness, we develop a two-step approximation algorithm to minimize both MCs’ charging and moving costs. In the first step, we identify a collection of representative sensor nodes (called “anchors”) where MCs should stop and recharge nearby nodes so that charging cost is minimized. Second, we assign recharge routes for different MCs by splitting a complete shortest path based on energy demands, charging cost and recharge capacity. Finally, we propose a method to further optimize system cost

(charging cost plus moving cost) by proposing a post-optimization algorithm. The algorithm can iteratively change nodes with low charging efficiency into anchors and inserts them back into the established routes whenever there is a chance to reduce the overall system cost. Next, we describe the model and a few assumptions that our analysis is based on.

## 21.2 Related Works

### 21.2.1 Single-hop Wireless Charging

Most of the previous works consider single-hop wireless charging. Due to physical limitations, only one sensor node is recharged each time. In [6], an optimization problem is studied to maximize the ratio between MC's idling and working time. In [7], a framework that coordinates MCs based on energy status information is proposed for perpetual network operation. However, the mechanisms proposed in these works are based on single-hop charging model which has limited scalability.

### 21.2.2 Multi-hop Wireless Charging

Multi-hop wireless charging for WRSNs is studied in [8–10]. In [8], a theoretical multi-hop charging model is proposed and the calculation shows that over 50% charging efficiency can be achieved for 4–5 hops of energy relays whereas making use of this technology in WRSNs is not discussed. In [9], multi-hop wireless charging is formulated into energy flow problems that is similar to data flow in the network. In [10], nodes in a network are organized into hexagonal cells and an MC stops at the cell center to replenish all the nodes in the cell. In this chapter, we propose a new and comprehensive framework that takes multi-hop charging efficiency into account.

## 21.3 Network Model and Assumptions

An embedded resonant repeater is added into the charging circuitry on both MCs and sensors. Nodes need to adjust and resonate at the same frequency to successfully relay energy in the neighborhood and we call these nodes *charging set* while they are recharged together. We consider that the MCs and the sensor nodes have identical coils with  $n_r$  rounds and  $r_s$  radius. Sensors are powered by traditional Ni-MH batteries with  $C_b$  capacity and recharge time  $T_r = 78$  mins [11].

To provide an effective charge, the charging efficiency  $\eta$  should be greater than a threshold  $\tau$ , e.g.,  $\tau = 30\%$ ; otherwise, it cannot simulate enough current and stops

**Table 21.1** List of notations

| Notation        | Definition  |
|-----------------|---|
| $N$             | Number of energy request  |
| $T_r$           | Recharge time of sensor's battery from zero to full capacity            |
| $L_{ij}$        | Mutual inductance between node $i$ and $j$                              |
| $\eta_{i,a}$    | Charging efficiency of node $i$ when the MC resides at anchor $a$       |
| $\mathcal{A}$   | Set of anchors where the MCs stop to recharge nodes in the neighborhood |
| $\mathcal{S}_i$ | Effective charging set of node $i$                                      |
| $m$             | Number of MCs   |
| $\tau$          | Charging efficiency threshold   |
| $q_i$           | Recharge delay  |
| $A_i$           | Arrival time of the MC at node $i$                                      |
| $C_b, C_h$      | Battery capacity of sensor nodes and MCs, respectively                  |

relaying wireless energy to other nodes. A number of  $m$  MCs stop at selected sensor locations (called *anchors*) to recharge nodes in the neighborhood. The effective charging range is a variable depending on how many nodes are in the neighborhood (node density) and efficiency threshold  $\tau$ .

We introduce a new metric called *recharge delay*,  $q_i$ . Once a node cannot be recharged on time will deplete energy and stop working. The time when a node stays in nonfunctional status is determined by how long the MC misses its battery deadline (late arrival). Denote MC's actual arrival time at node  $i$  by  $A_i$  and node  $i$ 's lifetime by  $L_i$ .  $q_i$  takes the maximum value of  $A_i - L_i$  and 0. That is, if  $A_i > L_i$ , a late arrival occurs and  $q_i = A_i - L_i$ ; otherwise,  $q_i = 0$ . This metric will be used in the analysis of assigning recharge routes. We summarize important notations in this chapter by Table 21.1.

## 21.4 Estimate Multi-hop Wireless Charging Efficiency

The first challenge is to calculate multi-hop wireless charging efficiency using resonant repeaters. This section describes an approach to estimate charging efficiency  $\eta_n$  after a number of  $n$  relays. A schematic of  $n$ -hop energy relay is shown in Fig. 21.1. In principle, charging efficiency is determined by *mutual inductance*. Let  $L_{ij}$  denote the mutual inductance between repeaters on nodes  $i$  and  $j$ . From [12], we have,

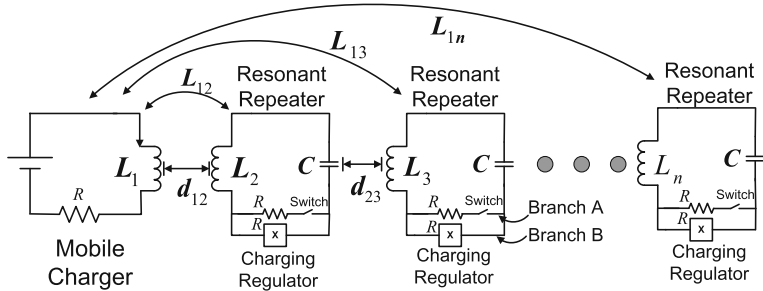


**Fig. 21.1** A schematic of multi-hop resonant repeating circuitries

$$L_{ij} = \kappa_{ij} (n_t L_s)^2 \approx \frac{r_s^3}{2d_{ij}^3} (n_t L_s)^2 \quad (21.1)$$

where  $r_s$  is the coil radius,  $n_t$  is the number of rounds of coil wires,  $\kappa_{ij}$  is the magnetic coupling coefficient between nodes  $i$  and  $j$  ( $0 \leq \kappa_{ij} \leq 1$ ), and  $L_s$  is the self-inductance of coils.<sup>1</sup> The approximation is taken when wireless charging distance  $d_{ij}$  between  $i$  and  $j$  is much larger than the dimensions of coil radius  $r_s$ . Based on Kirchoff's Voltage Law, we can calculate the charging efficiency after  $n$  relays based on the well-established method from [4]. The input voltage from MC's transmitting coil induces currents  $I_2-I_n$  on all sensor coils oscillating at frequency  $w$  and these values can be obtained by solving  $n$  linear equations as shown below.

$$\begin{pmatrix} R + jX & \cdots & jwL_{1n} \\ jwL_{12} & \cdots & jwL_{2n} \\ \vdots & \ddots & \vdots \\ jwL_{1(n-1)} & \cdots & jwL_{(n-1)n} \\ jwL_{1n} & \cdots & R + jX \end{pmatrix} \begin{pmatrix} I_1 \\ I_2 \\ \vdots \\ I_{n-1} \\ I_n \end{pmatrix} = \begin{pmatrix} V_{sc} \\ 0 \\ \vdots \\ 0 \\ 0 \end{pmatrix}$$

$X = wL_s - \frac{1}{wC}$  and  $C$  is the capacitance. In the above calculation, mutual inductance and cross coupling effects between neighboring sensors are accounted. To maximize the utilization of resonant repeaters, nodes finish charging their batteries should still act as energy relays. Suppose the resistance of the charging circuit of branch B is  $R$  in Fig. 21.1. A resistor of the same resistance  $R$  is added to match its resistance with the charging circuit. When a node is being charged, switch at branch A is open so the output load is  $R$ . Once charging is finished, the battery stops charging and makes branch B open. Then we close the switch at branch A so the output load is still  $R$ . In this way, charging efficiencies can stay the same despite some nodes might finish recharging earlier.

<sup>1</sup>  $L_s = \mu_0 r_s (\ln \frac{8r_s}{r_d} - 2)$ ,  $r_d$  is the wire radius and  $\mu_0$  is the permeability constant equal to  $4\pi \times 10^{-7} H \cdot m^{-1}$  (Henry per meter).

We may discover that there could be some inevitable energy cost in this design. Once the battery at a relay node finishes charging, it still needs to keep forwarding energy to others. The energy dissipated at its resistor cannot be ignored in our analysis. The energy cost can be justified from the following two aspects. First, since battery has a low internal resistance [11], the energy dissipated on the resistor is very small. Our model also successfully capture this factor into the calculations of charging efficiency next. Second, since nodes within MC's charging range share similar amounts of traffic load, the variance of recharge time from different nodes is small. Nodes within the same charging set can finish almost at the same time, thereby reducing the energy costs during these time gaps. We will demonstrate the standard deviations of recharge time within MC's charging range by simulations in Sect. 21.7.2.

To account for the energy expenditure at intermediate relaying nodes, we consider the energy dissipated at the  $k$ -th relay -  $I_k^2 R$ ,  $I_k$  is the constant current at branch of the  $k$ -th relay and  $R$  is the resistance. So the efficiency at the  $n$ -th repeater output is,

$$\eta_n = (R I_n^2) / (R \sum_{k=1}^n I_k^2) = I_n^2 / \sum_{k=1}^n I_k^2. \quad (21.2)$$

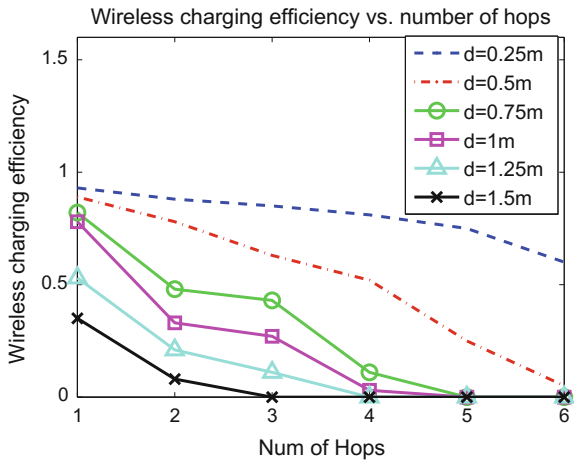
As an example, in Fig. 21.2, we calculate the charging efficiency for up to 6 hops with  $n_t = 300$  rounds and  $r_s = 10$  cm coil radius while changing the hop-to-hop distance  $d$  from 0.25 to 1.5 m. First, we can see wireless charging efficiency decreases with more hops. This matches the intuition that energy relay attenuates rapidly from the source. Second, we observe that the efficiency decreases much faster when  $d$  is larger. This is because that the mutual inductance declines as an inverse cube of distance. For instance, when  $d = 0.25$  m, charging efficiency after 4 hop relay ( $\eta_4$ ) is still 81 %. When  $d = 1.5$  m,  $\eta_2$  has reduced to 8 % and hardly provides any effective charge for sensor's battery. Thus, the charging efficiency depends on the actual number of intermediate nodes relaying energy as well as the distance between them. Based on this method, each node can estimate energy cost during multi-hop charging as if the MC is residing at its position. Since the charging range is usually much less than the communication range, it is not difficult for nodes to gather local information. They can simply propagate requesting packets to all their one-hop neighbors to know their locations.

## 21.5 Recharge Scheduling for Multi-hop Wireless Charging

In this section, we study how to schedule  $m$  MCs for multi-hop wireless charging. A variety of practical factors such as location-dependent charging efficiencies, energy charging cost, MC's energy consumption are brought into our problem formulation.

Our objectives are twofolds: on one hand, we aim to minimize the energy cost in multi-hop charging so it is more desirable to direct the MCs to stop at advantageous

**Fig. 21.2** An example of charging efficiency versus number of relay hops



sensor locations (anchors) and maximize the overall charging efficiencies. On the other hand, we want to minimize MC's moving energy consumption. We discover that our problem is analogous to the classic location-routing problem (LRP) [5]. LRP originates in the area of logistic planning and operation research. It finds the optimal warehouse locations for minimum accessing and distributing costs of transportation routes over demand locations that start and end at warehouses. It encompasses two NP-hard problems, i.e., location and routing problems, and seeks to provide an integrated solution to optimize the overall system cost. However, different from LRP in which vehicles directly visit warehouse locations, our problem involves an additional level of cover problem. That is, the anchors have to ensure that all sensors are "covered," meaning that they are charged either directly or via multi-hops. Based on the energy demands requested at different times, MCs need to calculate anchors adaptively.

To reflect the goals in optimization, we formulate our problem with two objectives. One is to minimize the sum of MCs' charging cost and the other is to minimize their moving cost. Due to the NP-hardness, we propose a two-step approximation algorithm. The first step achieves a ratio of  $\log N$  to the optimal charging cost ( $N$  is the total number of recharge requests). In the second step, given the selection of anchors, the maximum touring cost is bounded by a ratio of  $(\frac{5}{2} - \frac{1}{2k})$  to the optimal solution, where  $k$  is the number of scheduled tours (normally,  $k = m$  and each MC is assigned a recharging route). Finally, we explore subtle relations between the two objectives and combine them into a single-objective problem using the well-known weighted method [13]. A post-optimization algorithm is proposed to further reduce the total system cost by iteratively adding anchors from the original charging sets into the established routes.

### 21.5.1 Problem Formulation

We first formalize our problem. As described in the previous chapter, energy information can be gathered by the MCs on demand in a distributed manner. Consider time  $t$ , denote  $\mathcal{M}$  as the set of  $m$  MCs,  $\mathcal{N}$  as the set of energy requests from sensor nodes,  $\mathcal{A}$  as the set of potential anchors where MCs can stop ( $\mathcal{A} \subseteq \mathcal{N}$ ), and  $\mathcal{I}$  as the set of starting locations of MCs, we formulate the problem as follows.

Consider a graph  $G = (V, E)$ , where  $V_i$  ( $i \in \mathcal{N} \cup \mathcal{I}$ ) is the location of sensor node  $i$ , and  $E$  are edges connecting sensor nodes. The weight of an edge  $E_{ij}$  is the energy cost  $c_{ij}$  traveling on the edge, which is proportional to the distance between nodes  $i$  and  $j$ . Each MC has recharge capacity  $C_h$  corresponding to the sum of energy consumed charging sensor nodes and traveling. For each energy request from node  $i$ , its associated energy demand is  $d_i$  (full capacity minus its residual energy).

Each anchor  $a$  covers a set of nodes  $\mathcal{S}_a$  and the entire covered set of all the anchors should achieve all the requests  $\mathcal{N} (\bigcup \mathcal{S}_{a \in \mathcal{A}} = \mathcal{N})$ . Recharging  $\mathcal{S}_a$  requires  $t_a$  time which is usually determined by the node with the longest recharge time. For a node  $i$ ,  $\eta_{ia}$  denotes the charging efficiency when an MC stops at anchor  $a$ .

Several decision variables are introduced in the formulation.  $x_{ijk}$  is 1 if anchor  $i \in \mathcal{A}$  immediately precedes  $j \in \mathcal{A}$  for MC  $k$ ; otherwise, it is 0. For  $i \in \mathcal{N}, k \in \mathcal{M}, a \in A$ ,  $y_{ia}$  is 1 if node  $i$  can be recharged when a MC resides at  $a \in A$ .  $z_{ik}$  is 1 if node  $i$  is recharged by MC  $k$ .  $u_a$  is 1 if an anchor  $a$  is chosen; otherwise, it is 0.  $v_{ik}$  is the position of anchor  $i$  in the path of MC  $k$ . Our objective is to minimize the multi-hop wireless charging cost,  $F_c$ , and MC' moving cost,  $F_m$ .

$$\mathbf{P1} : \quad \min F = (F_c, F_m) \quad (21.3)$$

where,

$$F_c = \sum_{i \in \mathcal{N}} \sum_{a \in \mathcal{A}} \frac{1 - \eta_{ia}}{\eta_{ia}} d_i y_{ia} \quad (21.4)$$

$$F_m = \sum_{i \in \mathcal{A}} \sum_{j \in \mathcal{A}} \sum_{k \in \mathcal{M}} c_{ij} x_{ijk} + \sum_{i \in \mathcal{I}} \sum_{j \in \mathcal{A}} \sum_{k \in \mathcal{M}} c_{ij} x_{ijk} \quad (21.5)$$

#### Subject to

$$\sum_{i \in \mathcal{A}} x_{ijk} = z_{jk}, j \in \mathcal{A}, k \in \mathcal{M} \quad (21.6)$$

$$\sum_{j \in \mathcal{A}} x_{ijk} = z_{ik}, i \in \mathcal{A}, k \in \mathcal{M} \quad (21.7)$$

$$\sum_{a \in \mathcal{A}} y_{ia} = 1, i \in \mathcal{N} \quad (21.8)$$

$$\eta_{ia} y_{ia} > \tau, i \in \mathcal{N}, a \in \mathcal{A} \quad (21.9)$$

$$y_{ia} \leq u_a, i \in \mathcal{N}, a \in \mathcal{A} \quad (21.10)$$

$$\sum_{i \in \mathcal{N}} z_{ik} (\sum_{a \in \mathcal{A}} d_i y_{ia} / \eta_{ia}) + \sum_{i \in \mathcal{A}} \sum_{j \in \mathcal{A}} c_{ij} x_{ijk} + \sum_{i \in \mathcal{I}} \sum_{j \in \mathcal{A}} c_{ij} x_{ijk} \leq C_h, k \in \mathcal{M} \quad (21.11)$$

$$\sum_{k \in \mathcal{M}} z_{ak} = u_a, a \in \mathcal{A} \quad (21.12)$$

$$2 \leq v_{ik} \leq |\mathcal{N}|, i \in \mathcal{A}, k \in \mathcal{M} \quad (21.13)$$

$$v_{ik} - v_{jk} + (|\mathcal{A}| - |\mathcal{M}|)x_{ijk} \leq |\mathcal{A}| - |\mathcal{M}| - 1, i, j \in \mathcal{A}, k \in \mathcal{M} \quad (21.14)$$

$$x_{ijk}, y_{ia}, z_{ik} \in \{0, 1\}, i, j \in \mathcal{N}, a \in \mathcal{A}, k \in \mathcal{M} \quad (21.15)$$

In the above formulation, constraint (21.6) and constraint (21.7) state the connectivity of the path that an MC stops at an anchor also leaves it. Constraint (21.8) imposes that all the energy requests from nodes are covered by the anchors. Constraint (21.9) ensures an effective charging efficiency for a node from its anchor should be larger than the efficiency threshold. Constraint (21.10) guarantees that a node is assigned to one of the anchors. Constraint (21.11) stipulates that the sum of total demands (including the energy cost) satisfied by the MC plus its moving energy consumptions is within the MC's battery capacity. Constraint (21.12) enforces that each anchor is visited by only one MC. Constraints (21.13) and (21.14) are formed according to [14] to prevent subtours of MCs. Constraint (21.15) forces  $x_{ijk}$ ,  $y_{ia}$  and  $z_{ik}$  to be 0–1 valued. The formulation reflects optimal recharge schedules at time  $t$  based on  $N$  energy requests ( $N$  is an input). For executions at different times, the problem takes corresponding inputs and generates different results (anchors, recharge schedules, etc.).

### 21.5.2 Approximation Algorithms

In this subsection, we develop an efficient algorithm for the NP-hard problem. We first define a *charging set*  $\mathcal{S}_i$  of node  $i$  as its nearby nodes with charging efficiencies larger than  $\tau$  when an MC stops at node  $i$ . Since nodes are static, the charging set can be computed in a distributed fashion by each node at network initialization stage as described in Sect. 21.4. For node  $i$ , its neighbor  $j$  is included in  $\mathcal{S}_i$  only if  $j$ 's charging efficiency is larger than threshold  $\tau$  and the corresponding efficiency is denoted as  $\eta_{j,i}$  ( $j \in \mathcal{S}_i$ ). Our first priority is to find the set of anchors.

#### 21.5.2.1 Adaptive Anchor Selection

The weight of each charging set is defined as the total energy needed to satisfy the recharge demands of these nodes,  $w_i = \sum_{j \in \mathcal{S}_i} (1 - \eta_{j,i})d_j / \eta_{j,i}$ . Then our objectives in Eq. (21.4) is equivalent to minimizing the sum of weights of the selected sets which

belongs to the category of *Set Cover Problem* (SCP) with one difference: while the original SCP allows charging sets to share the same nodes as their members, nodes should be distinct for different charging sets in our problem. In other words, charging sets should be disjoint in our problem. This is because that if a node can be recharged by more than one MCs in different recharge routes, for energy-efficiency concerns, it is always preferred to assign the node to a charging set with higher charging efficiency. This is why our formulation restricts a node to be recharged by only one MC (Eq. (21.12)). Next, we modify the classic greedy approach to fit into our problem.

We use two sets  $\mathcal{A}$  and  $\mathcal{B}$  to record anchors and their covered node sets respectively and both sets are initialized to empty. First, for each node  $i \in \mathcal{N}$ , we compute its average weight,  $\bar{w}_i = \sum_{j \in \mathcal{S}_i} \frac{(1-\eta_{j,i})d_j}{\eta_{j,i}} / |\mathcal{S}_i|$  and search for the set with the minimum  $\bar{w}_i$ . If a node  $k$ 's subset has the least average weight, it becomes an anchor and is added into  $\mathcal{A}$ .  $\mathcal{S}_k$  is put into  $\mathcal{B}$  to be marked as “covered.” This is done by tuning all the nodes in  $\mathcal{S}_k$  to have the same resonant frequency (described next). Since those nodes might be also covered by other sets, we need to remove them from the remaining sets. Their elements are updated accordingly,  $\mathcal{S}_i = \mathcal{S}_i - B, \forall i \setminus k \in \mathcal{N}$ . At this time, if  $\mathcal{B}$  contains all the nodes in  $\mathcal{N}$ , the algorithm terminates. Otherwise, it continues to find the next set among the remaining nodes with minimum average weight until all the nodes are covered ( $\mathcal{B} = \mathcal{N}$ ). Algorithm 17 shows the pseudocode for the adaptive anchor selection algorithm.

---

**Algorithm 17:** Adaptive anchor selection algorithm

---

**Input :** Recharging node set  $\mathcal{N}$ , charging set  $\mathcal{S}_i$ , energy demand  $d_i$ , charging efficiency of node  $j$ .

**Output:** Set of anchors  $\mathcal{A}$  and resultant subsets  $\mathcal{B}$ .

- 1 **while**  $\mathcal{B} \neq \mathcal{N}$  **do**
- 2     Calculate  $\bar{w}_i = \sum_{j \in \mathcal{S}_i} \frac{(1-\eta_{j,i})d_j}{\eta_{j,i}} / |\mathcal{S}_i|$ ;
- 3     Find minimum weight  $k = \arg \min_i \bar{w}_i, i \in \mathcal{N}$ ;
- 4      $\mathcal{A} \leftarrow \mathcal{A} \cup k, \mathcal{B} \leftarrow \mathcal{B} \cup \mathcal{S}_k$ ;
- 5      $\mathcal{S}_i \leftarrow \mathcal{S}_i - B, \forall i \setminus k \in \mathcal{N}$ ;
- 6 **end while**

---

### 21.5.2.2 Resonant Frequency Assignment

After the anchors have been found, we need to assign resonant frequencies in order to distinguish charging sets and avoid mutual interference from the neighboring sets. By tuning to a proper frequency, nodes can “join” or “leave” a set very easily. Given an available frequency range, we divide it into numerous frequency bands and each band should be reused as long as there is no interference between the neighboring charging sets, i.e., we only need to keep the frequency assignment for each charging set and its neighbors to be different. This problem is equivalent to the classic *vertex coloring*

*problem* [15] which tries to color nodes in a graph with as small number of colors as possible such that no two adjacent nodes have the same color. Here, the vertices are anchors and edges are connections represented by energy relays between anchors if the distance between any two elements in their charging sets is less than the maximum charging range  $r_{\max}$ . Unfortunately, vertex coloring is a well-known NP-hard problem and it even turns out that approximation within  $n^{1-\varepsilon}$  is NP-hard ( $0 < \varepsilon < 1, n = |\mathcal{A}|$ ) [16]. For a reasonable balance between computation complexity and optimality, we propose an algorithm that uses at most  $\max_{1 \leq i \leq |\mathcal{A}|} (\Delta_i + 1)$  frequency bands, where  $\Delta_i$  is the degree of anchor  $i$  (between neighboring sets). A set of frequency bands is denoted by  $\mathcal{F} = \{f_1, f_2, \dots, f_n\}$ .

The algorithm starts from an arbitrary anchor in  $\mathcal{A}$  and uses  $f_1$  as its resonant frequency. Then it proceeds to the next anchor and uses available frequency band with the lowest  $f_i$  if it is not used by any of its neighboring anchors. The algorithm terminates when all the anchors in  $\mathcal{A}$  are assigned proper frequency bands. At this point, the anchors, charging sets and their resonant frequencies are determined and these decisions are disseminated to the anchors. Anchors also send out packets carrying their corresponding frequency information within the boundary of their charging sets. Since the maximum charging range  $r_{\max}$  is usually less than sensor's transmission range (e.g. 3–4 m vs. 15 m), the construction of charging sets is done easily by one-hop transmission and the message overhead is  $O(|\mathcal{N} - \mathcal{A}|)$ . The algorithm is summarized in Algorithm 18.

It is worth mentioning that the upper bound of  $\max_{1 \leq i \leq |\mathcal{A}|} (\Delta_i + 1)$  holds because an anchor  $i$  has at most  $\Delta_i$  neighboring anchors and occupies at most  $\Delta_i$  frequency bands (some of the neighboring anchors may have already been assigned frequencies). By the same token, for the anchor with the maximum degree, at most the same amount of frequency bands are needed for its neighbors. Thus, it is not difficult to see the upper bound holds at the maximum degree of anchors. For example, if the maximum degree of charging sets is 5, then only 5 frequency bands are needed to distinguish all the charging sets.

---

**Algorithm 18:** Resonant frequency assignment algorithm

---

**Input :** Set of anchors  $\mathcal{A}$ , set of frequency bands  $\mathcal{F}$ .

**Output:** Frequency assignment  $f_a, \forall a \in \mathcal{A}$ .

- 1 Establish connections among anchors based on  $r_{\max}$ ;
  - 2 **while**  $\mathcal{A} \neq \emptyset$  **do**
  - 3     Check the frequency of anchor  $a$ 's neighbors, denoted by  $\mathcal{F}'$ ;
  - 4     Find available frequency bands,  $\mathcal{F} \leftarrow \mathcal{F} - \mathcal{F}'$ ;
  - 5     Assign frequency  $\min(f_k) k \in \mathcal{F}$  to anchor  $a$ ;
  - 6     Set frequency of nodes in charging set  $\mathcal{S}_a$  to  $f_k$ ;
  - 7      $\mathcal{A} \leftarrow \mathcal{A} - a$ ;
  - 8 **end while**
-

### 21.5.2.3 Recharge Routes

After the set of anchors  $\mathcal{A}$  has been found, we assign the recharge routes for  $m$  MCs based on energy demands, moving cost and multi-hop charging cost. Based on [17], we propose an approximation algorithm to bound MCs' moving energy cost given the choice of anchors. Our approach first utilizes a Traveling Salesman Problem (TSP) algorithm to compute a complete route on  $\mathcal{A}$ , e.g., the 1.5-approximation Christofides algorithm [18]. To facilitate our analysis, we assume that the complete tour starts at the base station and ends at the last node for recharge. If the MC still have ample amount of energy for the next recharge sequence, the starting positions of MCs are the ending positions from the last tour. The recharge sequence can be expressed as  $r = (b, 1, 2, \dots, i, \dots, n)$ , where anchor  $i \in \mathcal{A}$ ,  $n = |\mathcal{A}|$  and  $b$  is the base station. To reflect MC's starting position, an extra edge with cost  $c_{i,b}$ ,  $i \in \mathcal{I}$ , can be added to represent the energy cost from MC's starting location  $i \in \mathcal{I}$  to the base station  $b$ . Let  $c_{\max}$  denote the maximum energy cost from any node on the path to the base station,  $c_{\max} = \max_{i \in \mathcal{A} \cup \mathcal{I}} c_{b,i}$ . The TSP algorithm generates a complete route  $r$  that incurs  $c_r$  energy cost.

For multiple MCs, the complete route  $r$  is split into a number of  $k$  tours. We start from an arbitrary direction along  $r$ . For each route  $j$ ,  $1 \leq j \leq k$ , we find the last anchor along the complete tour  $r$  that makes the traveling energy cost no greater than  $\frac{j}{k}(c_r - c_{\max}) + 2c_{\max}$ . Here, the term  $2c_{\max}$  is the maximum energy cost from MC's starting position to the base station plus the cost from the base station to the first anchor on the recharge path. Then  $r$  will be split into  $k$  tours. Let  $a_i^j$  and  $a_l^j$  represent the  $i$ -th and the last nodes in the  $j$ -th tour, respectively. The  $j$ -th tour is then obtained as  $(\mathcal{I}_j, b, a_1^j, a_2^j, \dots, a_l^j)$ .

The actual  $k$  depends on MCs' battery energy (constraint in Eq. (21.11)). We check whether an equal division of  $m$  MCs from the total energy cost  $(\sum_{i \in \mathcal{A}} \sum_{j \in \mathcal{I}_i} \frac{(1-\eta_{j,i})d_j}{\eta_{j,i}} + c_r - c_{\max})/m + 2c_{\max}$  is less than MC's energy capacity  $C_h$ . There are two cases:

**Case 1:** If an equal division of  $m$  among the total cost is less than MC's capacity  $C_h$ ,  $k = m$ . In this case,  $m$  MCs are sufficient to cover all the nodes in one shot.

**Case 2:** Otherwise,  $k = \lceil (\sum_{i \in \mathcal{A}} \sum_{j \in \mathcal{I}_i} \frac{(1-\eta_{j,i})d_j}{\eta_{j,i}} + c_r - c_{\max})/(C_h - 2c_{\max}) \rceil$  and  $k > m$ . This case usually occurs when the temporary energy demands overwhelmingly exceed MC' battery energy so that they have to take  $\lceil \frac{k}{m} \rceil$  rounds to cover all the routes. At most  $m$  routes can be selected from  $k$  in each round, thus late recharge for some nodes is inevitable. Hence, we want to reduce the recharge delay as much as possible in this case. Let us denote the recharge time for node  $i$  by  $t_i$  and traveling time between nodes  $i$  and  $i + 1$  by  $t_{i,i+1}$  in the recharge sequence. For multi-hop wireless charging, the MC leaves an anchor only after it has fulfilled all the energy requests within its charging set, so the recharge time of  $\mathcal{I}_a$  is  $t_a = \max_{i \in \mathcal{I}_a} (t_i)$ . The total time duration for a route  $j$  is  $T_j = \sum_{a=1}^{l_j} t_a + \sum_{a=1}^{l_j-1} t_{a,a+1}$ . The longest route takes  $T_{\max} = \max_{j=(1,\dots,k)} T_j$  time to finish. For route  $j$ , if it is selected by an MC in the current round, the recharge delay of all the nodes is

$$P_j = \sum_{i \in \bigcup \mathcal{S}_k^j, k \in \mathcal{A}^j} q_i = \sum_{i \in \bigcup \mathcal{S}_k^j, k \in \mathcal{A}^j} \max(A_i - L_i, 0) \quad (21.16)$$

However, if route  $j$  is not selected, the worst case occurs when the node has to wait for the longest route to finish charging. Thus, the recharge delay is

$$P'_j = \sum_{i \in \bigcup \mathcal{S}_k^j, k \in \mathcal{A}^j} \max(A_i + T_{\max} - L_i, 0) \quad (21.17)$$

An increment of

$$\Delta P_j = \sum_{i \in \bigcup \mathcal{S}_k^j, k \in \mathcal{A}^j} (\max(A_i + T_{\max} - L_i, 0) - \max(A_i - L_i, 0)) \quad (21.18)$$

is observed. To keep recharge delay at minimal, we sort  $\Delta P_j$  and select the  $m$  routes with the largest increment in each round so that those routes that would incur longer delay can be recharged at the current round. The pseudocode of the algorithm is shown in Algorithm 19.

### 21.5.3 Approximation Ratios and Complexity

Now we analyze the approximation ratios for the algorithm. For a number of  $n = |\mathcal{N}|$  recharge requests, our algorithm gives a  $\log n$  approximation for the multi-hop wireless charging cost and a  $(\frac{5}{2} - \frac{1}{2k})$  ratio for the traveling cost given the selected anchors, where  $k$  is the number of tours depending on energy demands and MC's energy  $C_h$ .

In the extended greedy algorithm of the Set Cover Problem, we assume the optimal energy cost is  $w^*$ . During computation, when there are  $i$  nodes left to be covered, it incurs at most  $\frac{w^*}{i}$  energy cost per node. The bound is thus  $\sum_{i=1}^n \frac{w^*}{i} = w^* \mathcal{O}(\log n)$ . The equality holds because the summation  $\sum_{i=1}^n \frac{1}{i} = \mathcal{O}(\log n)$  is the  $n$ -th harmonic number.

Although the  $\log n$  bound for energy charging cost seems quite large, it is essentially one of the best polynomial time approximation algorithms: it has been proved in [19] that the Set Cover Problem cannot be approximated in polynomial time within a ratio of  $c \log n$ , for  $c < \frac{1}{4}$ , under general complexity assumptions. Here, a tighter bound is not necessary given the increased complexity and transient nature of energy requests.

Next, we show that the traveling energy cost has an approximation ratio of  $(\frac{5}{2} - \frac{1}{2k})$  regarding  $k$  tours. When  $k > m$ , the  $k - m$  tours are traversed by MCs after they have replaced batteries in the base station. However, the total cost is still the same. For the complete tour, the energy cost is  $c_r$  with the optimal value  $c_r^*$ . Use Christofide's minimum spanning tree approximation to the TSP,  $\frac{c_r}{c_r^*} \leq 1.5$  [18]. Assume that tour

**Algorithm 19:** Route assignment algorithm

---

**Input :** Set of anchors  $\mathcal{A}$ , MCs  $\mathcal{M}$ , energy demand  $d_i$  of node  $i$ , charging efficiency of node  $j$ ,  $\eta_{j,i}$  when MC is at  $i$ . Set of MCs' initial locations  $\mathcal{I}$ , capacity  $C_h$ , base station  $b$ , max energy cost traveling on an edge  $c_{\max}$ .

**Output:** Recharge sequence  $r_j$  for MC  $j$ 's tour.

```

1 if  $(\sum_{i \in \mathcal{A}} \sum_{j \in \mathcal{S}_i} \frac{(1-\eta_{j,i})d_j}{\eta_{j,i}} + c_r - c_{\max})/m + 2c_{\max} < C_h$  then
2   |   k = m,
3 else
4   |   k =  $\lceil (\sum_{i \in \mathcal{A}} \sum_{j \in \mathcal{S}_i} \frac{(1-\eta_{j,i})d_j}{\eta_{j,i}} + c_r - c_{\max})/(C_h - 2c_{\max}) \rceil$ .
5 end if
6 Start with an arbitrary direction on  $r$ ,  $j = 1$ ;
7 while  $r \neq \emptyset$  do
8   |   For tour  $j$ , search for the last node  $a_l^j$  along  $r$ ;
9   |   Satisfying  $c_j \leq \frac{j}{k}(c_r - c_{\max}) + 2c_{\max}$ ;
10  |   Obtain the  $j$ -th tour,  $(\mathcal{I}_j, b, a_1^j, a_2^j, \dots, a_{l_j}^j)$ ,  $1 \leq j \leq k$ ;
11  |   Exclude nodes in  $j$ -th tour from  $r$ .  $j \leftarrow j + 1$ ;
12 end while
13 if  $k = m$  then
14   |   Assign each MC to a recharge route.
15 else
16   |   Find the route with max time duration;
17   |    $T_{\max} = \max_{j=(1,2,\dots,k)} (\sum_{a=1}^{l_j} t_a + \sum_{a=1}^{l_j-1} t_{a,a+1})$ ;
18   |    $\Delta P_j = \sum_{i \in \bigcup \mathcal{S}_k^j, k \in \mathcal{A}^j} (\max(A_i + T_{\max} - L_i, 0) - \max(A_i - L_i, 0))$ ;
19 end if

```

---

$j$  has the maximum energy cost  $c_j$  among  $k$  tours and its optimal value is  $c_j^*$ . The energy cost for tour  $j$  is at most  $\frac{1}{k}(c_r - c_{\max})$  (excluding the edge leaving the base station in the complete tour  $r$ ) plus  $2c_{\max}$  for the two edges connecting the base station to MC's starting position and the first anchor in each tour. Therefore,  $c_j \leq \frac{1}{k}(c_r - c_{\max}) + 2c_{\max} = \frac{1}{k}c_r + (2 - \frac{1}{k})c_{\max}$ . We divide both sides by  $c_j^*$  and have

$$\frac{c_j}{c_j^*} = \frac{1}{k} \frac{c_r}{c_j^*} + \left(2 - \frac{1}{k}\right) \frac{c_{\max}}{c_j^*} \leq \frac{1}{k} k \frac{c_r}{c_r^*} + \left(2 - \frac{1}{k}\right) \frac{1}{2} \leq \frac{5}{2} - \frac{1}{2k} \quad (21.19)$$

The inequality holds because for each MC's route, an edge is added between the first sensor node and the base station,  $c_r^* \leq \sum_{i=1}^k c_i^*$ . If we divide both sides by  $k$  and use the fact that  $\max_{1 \leq i \leq k} (c_i^*) = c_j^*$ , we have  $\frac{c_r^*}{k} \leq c_j^*$ . We take the approximation  $c_{\max} \leq \frac{1}{2}c_j^*$ . The equality holds when the tour has only one node.

The time complexity of the algorithm is analyzed as follows. Denote the number of energy requests by  $N$  and the number of anchors by  $A$ . The time complexity of the adaptive anchor selection algorithm is  $\mathcal{O}(N \log N)$  because if we first sort nodes according to their weights,  $\mathcal{O}(N \log N)$  is required. In each step, we select the node with minimum weight and the number of iterations is bounded by  $\mathcal{O}(N)$ . To assign resonant frequencies for different charging sets, the frequency assignment algorithm needs to go through all  $A$  anchors so its time complexity is  $\mathcal{O}(A)$ . For the route assignment algorithm, if  $k = m$ , the time complexity is  $\mathcal{O}(A^3 + N)$ , i.e., Christofides  $\mathcal{O}(A^3)$  algorithm [18] plus splitting demands over  $N$ . If  $k > m$ , the time complexity is  $\mathcal{O}(A^3 + N + k + k \log k)$  which consists of a series computations in linear time and sorting operations. When  $A^3$  is much larger than  $N$  and  $k$ , both cases have time complexity  $\mathcal{O}(A^3)$  dominated by the Christofides algorithm.

## 21.6 Post-optimization of System Cost

There could be more opportunities to optimize the total system cost from the algorithm. In this subsection, we propose a post-optimization algorithm to explore such opportunities. Since both objectives in Eqs. (21.4) and (21.5) are the energy outputs from the MC's battery, we can combine them into a single objective using the classic weighted method [13],  $F = w_1 F_c + w_2 F_m$ .

Network administrators assign weights  $w_1$  and  $w_2$  to measure the importance of energy charging cost versus moving cost. If  $w_2 > w_1$ , it means that the administrator cares more about MC's moving cost over energy charging cost. For example, if  $w_2/w_1 = 3$ , for total cost  $F$ , reducing the moving cost by 1 J is equivalent to saving energy charging cost of 3 J on MCs. We would expect  $w_2 > w_1$  in most cases as the administrators want to minimize the recharge time by covering more nodes with anchors so a slight increase of energy cost due to multi-hop charging is acceptable.

### 21.6.1 Inserting Anchors

We discover that the optimal system cost  $F$  should achieve a good balance between  $F_c$  and  $F_m$ . In fact, any solution that can minimize  $F$  is said to be *Pareto optimal* when  $w_1, w_2 \neq 0$  [20]. In multi-objective optimization, Pareto optimality describes a state that we cannot further increase the profit of one objective without reducing the profit of the rest objectives. In our problem, it means that we cannot further reduce charging cost without increasing the moving cost on MCs. On one hand, introducing more anchors would potentially increase MCs' moving cost  $F_m$ ; on the other hand, more anchors means fewer energy relays thus less energy charging cost  $F_c$ . Based on this observation, we propose a post-optimization algorithm that exploits marginal benefits by changing a node to an anchor and insert it into the established *charging sets*. However, since such insertion splits the original charging set, it inevitably elongates

the total recharge time of the route. To this end, the algorithm should also ensure that split of charging sets does not cause battery depletion on subsequent nodes in the route. Our solution next suggests a simple, yet effective algorithm in a dynamic network environment.

Initially, for each anchor  $a_i$ , a node with the maximum charging cost is identified in its charging set  $\mathcal{S}_{a_i}$ ,  $\max(\frac{1-\eta_{j,a_i}}{\eta_{j,a_i}} d_j)$  and  $j \in \mathcal{S}_{a_i}$ . Then these selected nodes are sorted in a descending order according to their charging costs.

The MC starts from the first node  $j$  in the list which has the maximum charging cost in the entire route. Tentatively designate node  $j$  as a new anchor because by charging  $j$  directly, charging energy cost can be reduced. We denote node  $j$  as a new anchor  $a'_j$ . The next important step is to see whether we can further reduce energy charging cost by moving some of the elements from  $\mathcal{S}_{a_i}$  to  $\mathcal{S}_{a'_j}$ .

This is because a node  $k$  in  $\mathcal{S}_{a_i}$  may be recharged via the new anchor with a higher efficiency. For each node  $k$  in  $\mathcal{S}_{a_i}$ , we compare if,

$$(1 - \eta_{k,a_i})/\eta_{k,a_i} > (1 - \eta_{k,a'_j})/\eta_{k,a'_j} \quad (21.20)$$

If yes, we move node  $k$  to be covered in  $\mathcal{S}_{a'_j}$  and denote the old  $a_i$  by  $a'_i$  after this operation. This is done by tuning  $k$ 's resonant frequency to be the same as the new anchor  $a'_j$  and  $a'_j$  will select a new frequency band that is not used by its neighbors. We go through all the elements in  $\mathcal{S}_{a_i}$  to examine whether it is beneficial to be included under the new anchor  $a'_j$  or remain with old anchor  $a_i$ . At this point, a new anchor  $a'_j$  is introduced to partition the original charging set whereas their joint coverage still remains the same.

### 21.6.2 Optimize System Cost

The next step is to calculate whether there would be a reduction in the total system cost  $F$ . Denote the changes of moving cost after introducing  $a'_j$  by  $\partial f_m$  and changes of charging cost by  $\partial f_c$ . We assume the new sequence  $(a_1, a_2, \dots, a'_i, a'_j, \dots, a_{l_s})$  has the lowest moving cost so

$$\partial f_m = (c_{a_{i-1}, a'_i} + c_{a'_i, a'_j} + c_{a'_j, a_{i+1}}) - (c_{a_{i-1}, a_i} + c_{a_i, a_{i+1}}) \quad (21.21)$$

and

$$\partial f_c = \sum_{a \in \{a'_i, a'_j\}} \sum_{k \in \mathcal{S}_a} \frac{(1 - \eta_{k,a})d_k}{\eta_{k,a}} - \sum_{k \in \mathcal{S}_{a_i}} \frac{(1 - \eta_{k,a_i})d_k}{\eta_{k,a_i}} \quad (21.22)$$

Then we see whether  $\Delta F = w_1 \partial f_c + w_2 \partial f_m$  is less than zero. If yes, it means a reduction of  $F$  is accomplished. The pseudocode for the post-optimization algorithm is shown in Algorithm 20.

**Algorithm 20:** Post-optimization algorithm for MC  $s$ 


---

**Input :** Recharge sequence  $a_1, a_2, \dots, a_{l_s}$ , set of anchors  $\mathcal{A}_s$ , energy demand  $d_i$  of node  $i$ , charging efficiency of  $j$ ,  $\eta_{j,i}$  if MC is at  $i$ , moving cost  $c_{i,j}$  on edge  $(i, j)$ , time feasibility mark at anchor  $x \leftarrow 0$ , objective weights  $w_1, w_2$ , charging set  $\mathcal{S}_a$  for all anchors.

**Output:** A new recharge sequence consists of anchors.

- 1  $i \in \mathcal{S}_a$ . Sort these nodes in descending order list  $\mathcal{I}$ .  $j \leftarrow 1$ ;
- 2 **while**  $x \neq a_{l_s}$  AND  $\mathcal{I} \neq \emptyset$  **do**
- 3   For  $j > x$ , consider  $j$  as a candidate anchor  $a'_j$  and  $\forall k \in \mathcal{S}_{a_i}$ ;
- 4   **if**  $(1 - \eta_{k,a_i})/\eta_{k,a_i} > (1 - \eta_{k,a'_j})/\eta_{k,a'_j}$  **then**
- 5      $\mathcal{S}_{a'_j} \leftarrow \mathcal{S}_{a_i} - k$ ,  $\mathcal{S}'_{a'_j} \leftarrow \mathcal{S}'_{a'_j} + k$ .
- 6      $\partial f_m \leftarrow (c_{a_{i-1},a'_i} + c_{a'_i,a'_j} + c_{a'_j,a_{i+1}}) - (c_{a_{i-1},a_i} + c_{a_i,a_{i+1}})$ .
- 7      $\partial f_c \leftarrow \sum_{a \in \{a'_i, a'_j\}} \sum_{k \in \mathcal{S}_a} \frac{(1 - \eta_{k,a})d_k}{\eta_{k,a}} - \sum_{k \in \mathcal{S}_{a_i}} \frac{(1 - \eta_{k,a_i})d_k}{\eta_{k,a_i}}$ ;
- 8      $\Delta F \leftarrow w_1 \partial f_c + w_2 \partial f_m$ , new seq. New sequence  $(a_1, \dots, a'_i, a'_j, \dots, a_{l_s})$ ;
- 9     **if**  $\Delta F < 0$  **then**
- 10       For  $A_k - L_k < 0$  in each charging set, find  $k = \arg \max_{k \in \mathcal{S}_{a_i}} (A_k - L_k)$ .
- 11        $\Delta T = \max_{i \in \mathcal{S}_{a'_j}} t_i + \partial f_m/v$ ;
- 12       **for** anchor  $a_i$  from  $a'_j$  to  $a_{l_s}$  **do**
- 13         **if**  $A_{a_i} + \Delta T - L_{a_i} > 0$  **then**
- 14           | When  $a_i > x$ , update mark  $x \leftarrow a_i$ , declare time infeasible, **Break**;
- 15         **end if**
- 16       **end for**
- 17       Insertion of  $a'_j$  is successful,  $\mathcal{I} \leftarrow \mathcal{I} - j$ ,  $j \leftarrow j + 1$ ;
- 18     **end if**
- 19 **end while**

---

### 21.6.3 Complexity of Post-optimization Algorithm

We now analyze the complexity of the post-optimization algorithm. For the number of  $A$  anchors, we need to check at most  $A$  charging sets. Suppose the size of maximum charging set is  $S_m$ . Initially, finding nodes with maximum charging cost for  $A$  anchors requires  $AS_m$  time and the sorting takes  $A \log A$  time. In the worst case, the algorithm iterates through all  $A$  anchors and each iteration requires  $S_m$  for new anchor reassessments and  $AS_m$  time for checking node's lifetime. In sum, the post-optimization algorithm has time complexity  $\mathcal{O}(AS_m + A \log A + A(S_m + S_m A)) = \mathcal{O}(A^2 S_m + A(S_m + \log A))$ .

Although the algorithms are centralized, they can be implemented on the MCs. The MCs have customized high-capacity batteries and orders of magnitude more computing, storage resources than the sensor nodes. In practice, we can implement high-performance *Field-Programmable Gate Array* (FPGA) boards on the MCs. For

example, the latest Xilinx Virtex-7 FPGA contains 1.9 M logic cells, 3600 digital signal processing slices and each one can operate at speed of 1.5 GHz [21]. It is not difficult for them to handle computations for large networks.

## 21.7 Performance Evaluation

We evaluate the performance of the proposed algorithms in a discrete-event simulator. For convenience, we denote the multi-hop wireless charging algorithm by “MH” and compare with the conventional single node wireless charging (denoted as “SN”) [6, 7].

### 21.7.1 System Parameters

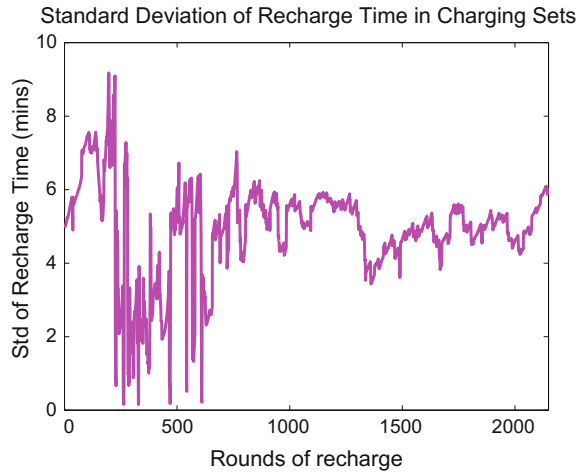
A number of 500 sensor nodes are distributed uniformly randomly in a circular field with radius 50 m. Sensors have identical transmission range of 10 m and consume 20 mJ for transmitting/receiving a packet calculated by the model in [22]. Sensors generate packets following a constant bit rate model of 3 pkt/min and forward them to the base station using the Dijkstra’s shortest path routing algorithm in multi-hops.

If a node’s energy falls below 50 % to the total capacity, it sends out an energy request. Nodes have rechargeable NiMH battery with 780 mAh capacity which takes 78 mins to recharge [11]. The charging efficiency threshold is set to  $\tau = 0.3$ ; any node with smaller charging efficiency will not receive or relay any energy. All the MCs and sensors have identical coils with  $n_t = 300$  rounds and  $r_s = 10$  cm. Multi-hop wireless charging efficiencies are calculated using the procedures in Sect. 21.4. Each MC is equipped with a 12 V battery and 4 Ah battery. While moving at speed of 1 m/s, it consumes 48 J/m. The simulation is set to run for 4 months’ time.

### 21.7.2 Variance of Recharge Time

As mentioned in Sect. 21.4, nodes within MC’s charging range finish charging at relatively similar time. We first evaluate the variance of recharge time within MC’s charging range. Figure 21.3 shows the evolution of standard deviation of recharge time. We can see that it stays around 5 mins at the network equilibrium and the peak value does not exceed 10 mins (vs. total recharge time of 78 mins). Thus, the simulation result further validates that nodes within the same charging set can finish charging at around the same time, and reduce energy cost at intermediate relay nodes.

**Fig. 21.3** Evolution of standard deviations for recharge time in MC's charging range



### 21.7.3 Effectiveness of Post-optimization

Next, let us also validate the effectiveness of post-optimization algorithm. In Fig. 21.4, we evaluate the relations between MC's charging and moving cost when the energy requests are within the range of [50, 120] with  $m = 3$  MCs. As we keep adding new anchors into the recharge route, the total recharge time increases from 600 to 960 mins and the (weighted) moving costs  $w_2 F_m$  of MCs also increase. On the other hand, (weighted) charging cost  $w_1 F_c$  declines as more anchors are introduced to split the original charging sets. The results validate that adding new anchors reduces charging costs whereas increases MC's moving costs. As long as the amount

**Fig. 21.4** Relationships between charging and moving cost when more anchors are introduced

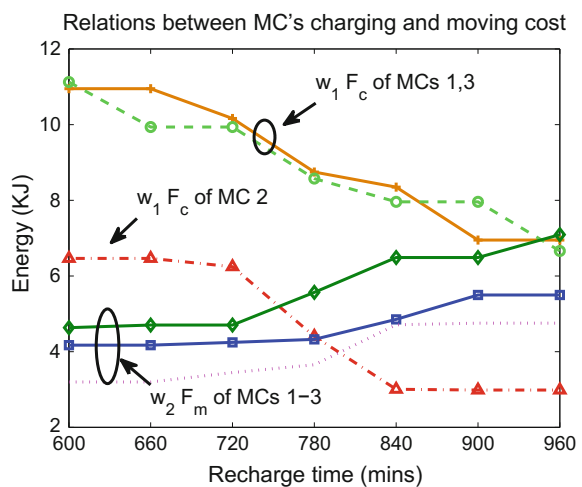
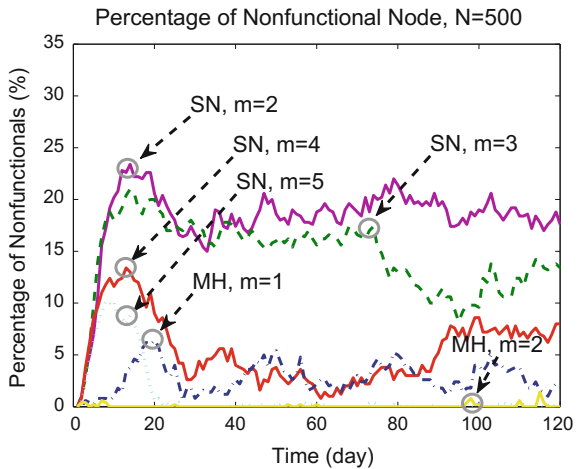


**Fig. 21.5** Number of nonfunctional nodes when  $N = 500$



of reduction from charging cost is less than the increment of moving cost, we can have further savings in the overall system cost.

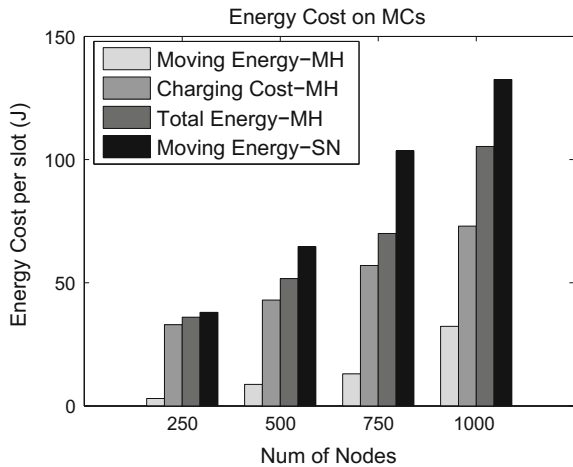
#### 21.7.4 Battery Depletion Rate—Nonfunctional Nodes

We show the advantage of MH by comparing the number of nodes that have depleted energy with SN in Fig. 21.5. Once a node depletes its battery and no MC has arrived yet, it becomes nonfunctional. For SN, 5 MC are needed to keep nonfunctional nodes below 5 %. In sharp contrast, MH only needs 1 MC and 2 MCs can almost eliminate all battery depletions. The surge of nonfunctional nodes around 10–15 days for SN is because the recharge requests have temporarily exceeded MCs' capability. As the network reaches equilibrium, the curves decline gradually. However, this phenomenon does not appear in MH, which represents better robustness even with fewer MCs.

#### 21.7.5 Overall Energy Cost

We compare the energy cost between the two schemes in Fig. 21.6. We assume there is a quality of service requirement to keep nonfunctional nodes under 5 % and examine the relevant energy costs of different schemes. For MH, we show energy costs from both charging and movement, as well as the sum of them and compare with the total cost of SN, while varying  $N$  from 250 to 1000. When  $N = 250$ , the total cost is almost equivalent while increasing  $N$  results in better efficiency for

**Fig. 21.6** Comparison of energy cost to maintain energy depletion rate under 5%

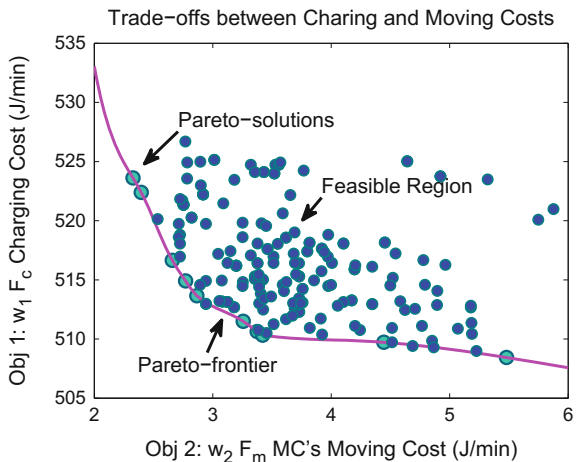


MH. This is because that when node density is higher, more nodes can be recharged simultaneously without the hassle of approaching them one by one.

### 21.7.6 Trade-Offs Between Charging and Moving Costs

Finally, we demonstrate the relations between the two optimization objectives by finding pareto solutions. Note that since the problem is NP-hard and intractable in polynomial time, the pareto solutions found by the algorithm are in fact suboptimal and within the approximation bounds discussed in Sect. 21.5.3. As shown in [20], a minimizer of the weighted combination of objectives in Eqs. (21.4) and (21.5) is a pareto optimal solution to the original bi-objective problem in Eq. (21.3). To explore the solution space, we vary the weights  $w_1$  and  $w_2$  from 1 to 10 in small increments and delineate those solutions of MCs' charging cost and moving cost in Fig. 21.7. The y-axis represents MC's (weighted) charging cost  $w_1 F_c$  (the first objective) and the x-axis represents MC's (weighted) moving cost  $w_2 F_m$  (the second objective). Those choices of different weights allow the MC to explore in the solution space and it has a direct impact on the decision value  $\Delta F$  as well as the recharge routes. In Fig. 21.7, we can see that the points along the *pareto-frontier* form a contour to bound the feasible region. The *pareto-frontier* consists of solutions that cannot be surpassed by any other alternative solutions. As indicated by our analysis, a trade-off is observed between the two optimization objectives. That is, when the MC's moving cost is reduced, the charging cost has to increase and vice versa.

**Fig. 21.7** Trade-offs between MCs' wireless charging and moving cost



## 21.8 Discussion

As we may have realized, the effectiveness of multi-hop wireless charging could be affected by node density. For sparse networks, a node could have no immediate neighbors to relay energy. In this case, our scheme still works, but reduces to the single node recharge method. In practice, due to the declining cost of sensor nodes, they are usually deployed at high density to ensure robustness against node or communication failures. High density is also desired for load balancing purposes. Nodes near the base station are usually deployed in higher density so they can distribute their traffic loads more evenly to extend network lifetime and improve robustness. These networks present opportunities to apply multi-hop wireless charging and our approach can make use of such high density to extend network lifetime.

## 21.9 Conclusion

This chapter introduces a method to use resonant repeaters for improving charging efficiency and scalability in Wireless Rechargeable Sensor Networks. The detailed procedures of how to calculate multi-hop wireless charging efficiency based on the laws in physics and electronics are presented. The new multi-hop recharge scheduling problem is formulated into a bi-objective optimization problem, which is NP-hard. To achieve low-complexity, we propose a two-step approximation algorithm with bounded ratio for each objective followed by a post-optimization algorithm to further reduce the overall system cost. Finally, the extensive simulation results reveal much better network performance of the new scheme and insights for the trade-offs between MCs' wireless charging and moving costs.

## References

1. Price of copper tube: <http://coppertubingsales.com/copper-coils/copper-coils-standard/type-l-copper-coil-astm>
2. Zhang, F., Hackworth, S.A., Fu, W., Sun, M.: The relay effect on wireless power transfer using wireless energy transfer. In: 2010 14th Biennial IEEE Conference on Electromagnetic Field Computation (CEFC), p. 1 (2010). doi:[10.1109/CEFC.2010.5481512](https://doi.org/10.1109/CEFC.2010.5481512)
3. Lee, B.J., Hillenius, A., Ricketts, D.S.: Magnetic resonant wireless power delivery for distributed sensor and wireless systems. In: 2012 IEEE Topical Conference on Wireless Sensors and Sensor Networks (WiSNet), pp. 13–16 (2012). doi:[10.1109/WiSNet.2012.6172148](https://doi.org/10.1109/WiSNet.2012.6172148)
4. Zhong, W.X., Lee, C.K., Hui, S.Y.: Wireless power domino-resonator systems with noncoaxial axes and circular structures. *IEEE Trans. Power Electron.* **27**(11), 4750–4762 (2012). doi:[10.1109/TPEL.2011.2174655](https://doi.org/10.1109/TPEL.2011.2174655)
5. Nagy, G., Salhi, S.: Location-routing: issues, models and methods. *Eur. J. Oper. Res.* **177**(2), 649–672 (2007). doi:[10.1016/j.ejor.2006.04.004](https://doi.org/10.1016/j.ejor.2006.04.004)
6. Shi, Y., Xie, L., Hou, Y.T., Sherali, H.D.: On renewable sensor networks with wireless energy transfer. In: INFOCOM, 2011 Proceedings IEEE, pp. 1350–1358 (2011). doi:[10.1109/INFCOM.2011.5934919](https://doi.org/10.1109/INFCOM.2011.5934919)
7. Wang, C., Li, J., Ye, F., Yang, Y.: Multi-vehicle coordination for wireless energy replenishment in sensor networks. In: 2013 IEEE 27th International Symposium on Parallel Distributed Processing (IPDPS), pp. 1101–1111 (2013). doi:[10.1109/IPDPS.2013.22](https://doi.org/10.1109/IPDPS.2013.22)
8. Watfa, M.K., AlHassanieh, H., Selman, S.: Multi-hop wireless energy transfer in WSNS. *IEEE Commun. Lett.* **15**(12), 1275–1277 (2011). doi:[10.1109/LCOMM.2011.092911.100129](https://doi.org/10.1109/LCOMM.2011.092911.100129)
9. Xiang, L., Luo, J., Han, K., Shi, G.: Fueling wireless networks perpetually: a case of multi-hop wireless power distribution x2217; In: 2013 IEEE 24th Annual International Symposium on Personal, Indoor, and Mobile Radio Communications (PIMRC), pp. 1994–1999 (2013). doi:[10.1109/PIMRC.2013.6666471](https://doi.org/10.1109/PIMRC.2013.6666471)
10. Xie, L., Shi, Y., Hou, Y.T., Lou, W., Sherali, H.D., Midkiff, S.F.: On renewable sensor networks with wireless energy transfer: the multi-node case. In: 2012 9th Annual IEEE Communications Society Conference on Sensor, Mesh and Ad Hoc Communications and Networks (SECON), pp. 10–18 (2012). doi:[10.1109/SECON.2012.6275766](https://doi.org/10.1109/SECON.2012.6275766)
11. Panasonic: ni-mh Battery Handbook. [http://www2.renovaar.ee/userfiles/panasonic\\_ni-mh\\_handbook.pdf](http://www2.renovaar.ee/userfiles/panasonic_ni-mh_handbook.pdf)
12. Mur-Miranda, J.O., Fanti, G., Feng, Y., Omanakuttan, K., Ongie, R., Setjoadi, A., Sharpe, N.: Wireless power transfer using weakly coupled magnetostatic resonators. In: 2010 IEEE Energy Conversion Congress and Exposition, pp. 4179–4186 (2010). doi:[10.1109/ECCE.2010.5617728](https://doi.org/10.1109/ECCE.2010.5617728)
13. Marler, R.T., Arora, J.S.: The weighted sum method for multi-objective optimization: new insights. *Structural and Multidisciplinary Optimization* **41**(6), 853–862 (2010). doi:[10.1007/s00158-009-0460-7](https://doi.org/10.1007/s00158-009-0460-7)
14. Gavish, B.: The formulation of the m-salesman traveling salesman problem. *Manag. Sci.* **22**(6), 704–705 (1976). doi:[10.1287/mnsc.22.6.704](https://doi.org/10.1287/mnsc.22.6.704)
15. Karp, R.M.: Reducibility among combinatorial problems, pp. 85–103. Springer, US, Boston, MA (1972). doi:[10.1007/978-1-4684-2001-2-9](https://doi.org/10.1007/978-1-4684-2001-2-9)
16. Zuckerman, D.: Linear degree extractors and the inapproximability of max clique and chromatic number. *Theor. Comput.* **3**(6), 103–128 (2007). doi:[10.4086/toc.2007.v003a006](https://doi.org/10.4086/toc.2007.v003a006)
17. Frederickson, G.N., Hecht, M.S., Kim, C.E.: Approximation algorithms for some routing problems. In: 1976 17th Annual Symposium on Foundations of Computer Science, pp. 216–227 (1976). doi:[10.1109/SFCS.1976.6](https://doi.org/10.1109/SFCS.1976.6)
18. Christofides, N.: Worst-case analysis of a new heuristic for the travelling salesman problem. Technical report, DTIC Document (1976)
19. Lund, C., Yannakakis, M.: On the hardness of approximating minimization problems. *J. ACM* **41**(5), 960–981 (1994). doi:[10.1145/185675.306789](https://doi.org/10.1145/185675.306789)

20. Bard, J.F., Szidarovszky, F., Gershon, M.E., Duckstein, L.: Techniques for Multiobjective Decision Making in Systems Management (1988)
21. Xilinx virtex-7. <http://www.xilinx.com/products/silicon-devices/fpga/virtex-7.html>
22. Heinzelman, W.R., Chandrakasan, A., Balakrishnan, H.: Energy-efficient communication protocol for wireless microsensor networks. In: Proceedings of the 33rd Annual Hawaii International Conference on System Sciences, 2000, pp. 10, vol. 2 (2000). doi:[10.1109/HICSS.2000.926982](https://doi.org/10.1109/HICSS.2000.926982)

# Chapter 22

## Interactive Wireless Charging for Energy Balance

Sotiris Nikoletseas, Theofanis P. Raptis and Christoforos Raptopoulos

**Abstract** We study how to efficiently transfer energy wirelessly in ad hoc networks of battery-limited devices, toward prolonging their lifetime. In contrast to the state-of-the-art, we assume a much weaker population of distributed devices which are exchanging energy in a “peer to peer”, bi-directional manner with each other, without any special charger nodes. We address a quite general case of diverse energy levels and priorities in the network and study the problem of how the system can efficiently reach a weighted energy balance state distributively, under both loss-less and lossy power transfer assumptions. Three protocols are designed, analyzed, and evaluated, achieving different performance trade-offs between energy balance quality, convergence time, and energy efficiency.

### 22.1 Introduction

Next generation wirelessly networked populations are expected to consist of very large numbers of distributed portable devices carried by mobile agents that follow unpredictable and uncontrollable mobility patterns. Recently, there has been an increasing interest to combine near-field communication capabilities and wireless energy transfer in the same portable device, allowing mobile agents carrying the devices to wirelessly exchange energy. For example, the same antenna, designed to exploit its far-field properties for communication purposes, can be suitably

---

S. Nikoletseas (✉) · T.P. Raptis · C. Raptopoulos  
Department of Computer Engineering and Informatics, University of Patras and  
Computer Technology Institute and Press “Diophantus” (CTI), Patras, Greece  
e-mail: nikole@cti.gr

T.P. Raptis  
Institute of Informatics and Telematics, National Research Council, Moruzzi Str 1,  
56124 Pisa, Italy  
e-mail: theofanis.raptis@iit.cnr.it

C. Raptopoulos  
e-mail: raptopox@ceid.upatras.gr

configured for simultaneously realizing wireless energy transfer via its near-field properties. The near-field behavior of a pair of closely coupled transmitting and receiving dual-band printed monopole antennas (suitable for mobile phone applications) can make it possible to achieve both far-field performance and near-field power transfer efficiency (from 35 to 10 %) for mobile phones located few centimeters apart [5]. Further developments on the circuit design can render a device capable of achieving bi-directional, highly efficient wireless energy transfer and be used both as a transmitter and as a receiver [6, 19]. In this context, energy harvesting and wireless energy transfer capabilities are integrated, enabling each device to act on demand either as a wireless energy provider or as an energy harvester.

Populations of such devices have to operate under severe limitations in their computational power, data storage, the quality of communication and most crucially, their available amount of energy. For this reason, the efficiently distributed cooperation of the agents toward achieving large computational and communication goals is a challenging task. An important goal in the design and efficient implementation of large networked systems is to save energy and keep the network functional for as long as possible [12, 18]. This can be achieved by using wireless energy transfer as an energy exchange enabling technology and applying interaction protocols among the agents which guarantee that the available energy in the network can be eventually distributed in a balanced way.

Inspired by the Population Protocol model of [3, 4], we present a new model for configuring the wireless energy transfer process in networked systems of mobile agents. In contrast with the Population Protocol approach, our model assumes significantly stronger devices with complex wireless energy transfer hardware, not abstracted by computationally restricted finite-state automata.

**Our contribution.** The contribution of this chapter is three-fold:

- We present a new model and a problem statement regarding population weighted energy balance.
- We consider the (quite different) cases of loss-less and lossy wireless energy transfer. We provide an upper bound on the time that is needed to reach weighted energy balance in the population at the loss-less case, and we experimentally investigate via simulations the complex impact of the energy levels diversity in the lossy case; also, we highlight several key elements of the charging procedure.
- We provide and evaluate three interaction protocols which take into account different aspects of the charging procedure and achieve different performance trade-offs; one that is quite fast in achieving weighted energy balance in the loss-less case, another one that achieves weighted energy balance without wasting too much energy in the lossy case and a third one which gradually builds and maintains some knowledge of the energy levels in the network in an on-line manner.

## 22.2 Related Work

Wireless energy transfer applications in networked environments have been lately investigated, especially in sensor and ad hoc networks. Numerous works suggest the employment of mobile wireless energy chargers in networks of sensor nodes, by combining energy transfer with data transmission and routing [8, 9, 23], providing distributed and centralized solutions [2, 20, 21], and collaborative charging schemes [13, 24]. Other works focus on multi-hop energy transfer in stationary networks [17, 22], as well as UAV-assisted charging of ground sensors [7, 10]. Most of those wireless energy transfer applications have also been verified experimentally, using real device prototypes [14–16]. Although all those works provide nice solutions on the efficient charging of networks comprised of next generation devices, none of them investigates the bi-directional charging procedure in populations of mobile agents.

## 22.3 The Model

We consider a population of  $m$  mobile agents  $\mathcal{M} = \{u_1, u_2, \dots, u_m\}$ , each one equipped with a *battery cell*, a *wireless energy transmitter*, and a *wireless energy receiver*. Every agent  $u \in \mathcal{M}$  is assigned to a *weight*  $w_u$  that characterizes the importance or criticality of the agent. Whenever two agents meet (e.g., whenever their trajectory paths intersect), they can interact by exchanging energy between their respective battery cells, according to an *interaction protocol*  $\mathcal{P}$ . We assume that agents are identical, that is they do not have IDs, they have the same hardware and run the same protocol  $\mathcal{P}$ . As a consequence, the *state* of any agent  $u \in \mathcal{M}$ , at any time  $t$ , can be fully described by the *energy*  $E_t(u)$  available in its battery.

More formally, we assume that time is discrete, and, at every time step  $t \in \mathbb{N}$ , a single pair of agents  $u, u' \in \mathcal{M}$  is chosen for interaction. In the most general setting, interactions are planned by a *scheduler* (that satisfies certain fairness conditions ensuring that all possible interactions will eventually occur), which can be used to abstract the movement of the agents. To allow for nontrivial efficiency analysis of our algorithmic solutions, in this chapter, we consider a special case of fair scheduler, namely the *probabilistic scheduler*, that, independently for every time step, selects a single interacting pair uniformly at random among all  $\binom{m}{2}$  pairs of agents in the population.

Whenever a pair of agents  $u, u'$  interact, they are able to exchange energy, by using their wireless energy equipment. Any transfer of energy  $\varepsilon$  induces *energy loss*  $L(\varepsilon)$ , due to the nature of wireless energy technology (e.g., RF-to-DC conversion, materials and wiring used in the system, objects near the devices, etc.). For simplicity, we do not take into account energy loss due to movement or other activities of the agents, as this is besides the focus of the current chapter (see also Sect. 22.3.1). In fact, we assume that most devices can be carried by individuals or other moving entities that

have their own agenda, and thus devices interact when the latter happen to come in close proximity. We will assume that the energy loss function satisfies a linear law:

$$L(\varepsilon) = \beta \cdot \varepsilon, \quad (22.1)$$

where  $\beta \in [0, 1]$  is a constant depending on the equipment. Therefore, if agents  $u, u'$  interact at time  $t$  and, according to the interaction protocol  $\mathcal{P}$ , agent  $u$  should transfer energy  $\varepsilon$  to  $u'$ , then the new energy levels of  $u, u'$  at time  $t$  become

$$E_t(u) = E_{t-1}(u) - \varepsilon \quad \text{and} \quad E_t(u') = E_{t-1}(u') + \varepsilon - L(\varepsilon).$$

Furthermore, the energy levels of all other (i.e., noninteracting at time  $t$ ) agents remain unchanged. Slightly abusing notation, we will write

$$(E_t(u), E_t(u')) = \mathcal{P}(E_{t-1}(u), E_{t-1}(u'), w_u, w_{u'}) = (E_{t-1}(u) - \varepsilon, E_{t-1}(u') + \varepsilon - L(\varepsilon)).$$

### 22.3.1 Problem Definition and Metrics

We will say that a set of agents  $\mathcal{M}$  is in *weighted energy balance* if

$$\frac{E_t(u)}{\sum_{x \in \mathcal{M}} E_x} = \frac{w_u}{\sum_{x \in \mathcal{M}} w_x}, \forall u \in \mathcal{M}.$$

In this chapter, we study the following problem:

**Definition 22.1** (*Population Weighted Energy Balance Problem*) Find an interaction protocol  $\mathcal{P}$  for weighted energy balance at the minimum energy loss across agents in  $\mathcal{M}$ .

In the present chapter, we measure weighted energy balance by using the notion of *total variation distance* from probability theory [1] and stochastic processes [11].

**Definition 22.2** (*Total variation distance*) Let  $P, Q$  be two probability distributions defined on sample space  $\mathcal{M}$ . The total variation distance  $\delta(P, Q)$  between  $P$  and  $Q$  is

$$\delta(P, Q) \stackrel{\text{def}}{=} \frac{1}{2} \sum_{x \in \mathcal{M}} |P(x) - Q(x)|. \quad (22.2)$$

By standard results on total variation distance (see for example [1]), we have the following equivalent expressions, which will be useful in our analysis.

$$\delta(P, Q) = \sum_{x \in \mathcal{M}: P(x) > Q(x)} (P(x) - Q(x)) \quad (22.3)$$

$$= \sum_{x \in \mathcal{M}: P(x) < Q(x)} (Q(x) - P(x)). \quad (22.4)$$

For any time  $t \in \mathbb{N}$ , we define the *energy distribution*  $\mathcal{E}_t$  on sample space  $\mathcal{M}$  (i.e., the population of agents) given by

$$\mathcal{E}_t(u) \stackrel{\text{def}}{=} \frac{E_t(u)}{E_t(\mathcal{M})}, \quad (22.5)$$

for any  $u \in \mathcal{M}$ , where  $E_t(\mathcal{M}) = \sum_{x \in \mathcal{M}} E_t(x)$ . Furthermore, we denote by  $\mathcal{W}$  the *weight distribution*, given by

$$\mathcal{W}(u) = \frac{w_u}{\sum_{x \in \mathcal{M}} w_x}. \quad (22.6)$$

We will say that the population has weighted energy balance at most  $\alpha$  at time  $t$  if and only if  $\delta(\mathcal{E}_t, \mathcal{W}) \leq \alpha$ . It is evident from the definition of our model that  $\delta(\mathcal{E}_t, \mathcal{W})$  is a random variable, depending on the specific distribution of energies in the population and the choices made by the probabilistic scheduler at time  $t$ . Therefore, we are rather interested in *protocols that reduce the total variation distance on expectation with the smallest energy loss*. Furthermore, we measure the efficiency of a protocol  $\mathcal{P}$  by the *total expected energy loss* and the *expected convergence time*<sup>1</sup> needed for the protocol to reach acceptable levels of weighted energy balance.

## 22.4 Loss-Less Energy Transfer

In this section we present a very simple protocol for weighted energy balance in the case of loss-less energy transfer, i.e., for  $\beta = 0$  (Protocol 21). The protocol basically states that, whenever two agents  $u, u'$  interact, they exchange energy so that fraction of their energy to their weight is equal. In particular, if  $E_{t-1}(u), w_u$  (respectively,  $E_{t-1}(u'), w_{u'}$ ) is the energy level and weight of  $u$  (respectively,  $u'$ ) at time  $t - 1$ , then after  $u, u'$  interact at time  $t$ , we have  $\frac{E_t(u)}{w_u} = \frac{E_t(u')}{w_{u'}}$ . Since there is no energy loss due to the transfer, we also have that  $E_{t-1}(u) + E_{t-1}(u') = E_t(u) + E_t(u')$ . Solving this linear system we then get  $E_t(u) = \frac{w_u}{w_u + w_{u'}}(E_{t-1}(u) + E_{t-1}(u'))$  and  $E_t(u') = \frac{w_{u'}}{w_u + w_{u'}}(E_{t-1}(u) + E_{t-1}(u'))$ , as shown in the protocol definition.

In the following Lemma, we show that, when all agents in the population use protocol  $\mathcal{P}_{\text{ows}}$ , the total variation distance between the energy distribution and the distribution of weights  $\mathcal{W} \stackrel{\text{def}}{=} \{\mathcal{W}(u)\}_{u \in \mathcal{M}} = \left\{ \frac{w_u}{\sum_{v \in \mathcal{M}} w_v} \right\}_{u \in \mathcal{M}}$  decreases in expectation. The proof not only leads to an upper bound on the time needed to reach weighted

---

<sup>1</sup>In our setting, the term *time* is used to mean *number of interactions*.

**Protocol 21:** Oblivious-Weighted-Share  $\mathcal{P}_{\text{OWS}}$ 

**Input** : Agents  $u, u'$  with weights  $w_u, w_{u'}$  and energy levels  $\varepsilon_u, \varepsilon_{u'}$

1

$$\mathcal{P}_{\text{OWS}}(\varepsilon_u, w_u, \varepsilon_{u'}, w_{u'}) = \left( \frac{w_u(\varepsilon_u + \varepsilon_{u'})}{w_u + w_{u'}}, \frac{w_{u'}(\varepsilon_u + \varepsilon_{u'})}{w_u + w_{u'}} \right).$$

energy balance (see Theorem 22.1), but more importantly, highlights several key elements of the energy transfer process, which we exploit when designing interaction protocols for the case  $\beta > 0$ .

**Lemma 22.1** Let  $\mathcal{M}$  be a population of agents using protocol  $\mathcal{P}_{\text{OWS}}$ . Assuming interactions are planned by the probabilistic scheduler and there is no loss from energy exchanges, we have that

$$\mathbb{E}[\delta(\mathcal{E}_t, \mathcal{W}) | \mathcal{E}_{t-1}] \leq \left(1 - \frac{1}{\binom{m}{2}}\right) \delta(\mathcal{E}_{t-1}, \mathcal{W}). \quad (22.7)$$

*Proof* We first note that, since we are in the loss-less case, i.e.,  $L(\varepsilon) = 0$ , for any transfer of an amount  $\varepsilon$  of energy, we have that  $E_t(\mathcal{M}) = E_0(\mathcal{M})$ , for any  $t$  (i.e., the total energy amount remains the same).

Define  $\Delta_t \stackrel{\text{def}}{=} \delta(\mathcal{E}_t, \mathcal{W}) - \delta(\mathcal{E}_{t-1}, \mathcal{W})$  and assume that, at time  $t$ , agents  $u, u'$  interact. By a simple observation, since the energy level of every other (noninteracting) agent remains the same, we have that

$$\begin{aligned} \Delta_t = \frac{1}{2} & \left( \left| \frac{w_u(\mathcal{E}_{t-1}(u) + \mathcal{E}_{t-1}(u'))}{w_u + w_{u'}} - \mathcal{W}(u) \right| + \left| \frac{w_{u'}(\mathcal{E}_{t-1}(u) + \mathcal{E}_{t-1}(u'))}{w_u + w_{u'}} - \mathcal{W}(u') \right| \right) \\ & - \frac{1}{2} (|\mathcal{E}_{t-1}(u) - \mathcal{W}(u)| + |\mathcal{E}_{t-1}(u') - \mathcal{W}(u')|) \end{aligned} \quad (22.8)$$

For any agent  $x \in \mathcal{M}$  and time  $t \geq 0$ , set now  $z_t(x) \stackrel{\text{def}}{=} \mathcal{E}_t(x) - \mathcal{W}(x)$ . Let also  $A_t^+ \subseteq \mathcal{M}$  (resp.  $A_t^-$ ,  $A_t^=$ ) be the set of agents such that  $z_t(x)$  is positive (resp. negative and equal to 0).

Depending on relative values of the numbers  $z_{t-1}(x)$ ,  $x \in \mathcal{M}$ , we now distinguish the following cases:

Case I:  $z_{t-1}(u)z_{t-1}(u') \geq 0$ . In particular, if both  $z_{t-1}(u), z_{t-1}(u')$  are nonnegative, notice that  $z_t(u) = \frac{w_u(\mathcal{E}_{t-1}(u) + \mathcal{E}_{t-1}(u'))}{w_u + w_{u'}} - \mathcal{W}(u) \geq \frac{w_u}{w_u + w_{u'}} (\mathcal{W}(u) + \mathcal{W}(u')) - \mathcal{W}(u) \geq 0$ . Similarly,  $z_t(u') \geq 0$ . In the same way we can prove that, if both  $z_{t-1}(u), z_{t-1}(u')$  are negative, then  $z_t(u) < 0$  and  $z_t(u') < 0$ . However, notice that, either if  $z_{t-1}(u), z_{t-1}(u')$  are both nonnegative or if both are positive, from Eq. (22.8) we get that  $\Delta_t = 0$ .

Case II:  $z_{t-1}(u)z_{t-1}(u') < 0$  and  $|z_{t-1}(u)| \geq |z_{t-1}(u')|$ . Assume that  $z_{t-1}(u) > 0$ , so  $z_{t-1}(u') < 0$ . By assumption we then have that  $|\mathcal{E}_{t-1}(u) - \mathcal{W}(u)| \geq$

$|\mathcal{E}_{t-1}(u') - \mathcal{W}(u')|$ , or equivalently  $\mathcal{E}_{t-1}(u) - \mathcal{W}(u) \geq \mathcal{W}(u') - \mathcal{E}_{t-1}(u')$ , and after rearranging we get  $\mathcal{E}_{t-1}(u) + \mathcal{E}_{t-1}(u') \geq \mathcal{W}(u) + \mathcal{W}(u')$ . By multiplying both hand sides of the last inequality by  $\frac{w_u}{w_u + w_{u'}}$  (respectively by  $\frac{w_{u'}}{w_u + w_{u'}}$ ) we get that  $z_t(u) \geq 0$  (respectively,  $z_t(u') \geq 0$ ). Therefore, from Eq.(22.8) we get that  $\Delta_t = \mathcal{E}_{t-1}(u') - \mathcal{W}(u') = z_{t-1}(u')$ .

The situation  $z_{t-1}(u) < 0$  (in which case  $z_{t-1}(u') > 0$ ) is similar, with the inequalities and signs reversed. In particular, we now have that  $z_t(u) \leq 0$  and  $z_t(u') \leq 0$ . Therefore, from Eq.(22.8) we get that  $\Delta_t = \mathcal{W}(u') - \mathcal{E}_{t-1}(u') = -z_{t-1}(u')$ .

Putting it all together, when  $z_{t-1}(u)z_{t-1}(u') < 0$  and  $|z_{t-1}(u)| \geq |z_{t-1}(u')|$ , we have that  $\Delta_t = -|z_{t-1}(u')|$ .

Case III:  $z_{t-1}(u)z_{t-1}(u') < 0$  and  $|z_{t-1}(u)| < |z_{t-1}(u')|$ . This case is symmetrical to Case II, with the roles of  $u, u'$  exchanged. Therefore,  $\Delta_t = -|z_{t-1}(u)|$ .

Since interactions are planned by the probabilistic scheduler, i.e., any specific pair  $u, u'$  of agents is chosen for interaction at time  $t$  with probability  $\frac{1}{{m \choose 2}}$ , by linearity of expectation and Eq.(22.8), we get

$$\begin{aligned} \mathbb{E}[\Delta_t | \mathcal{E}_{t-1}] &= -\frac{1}{{m \choose 2}} \left( \left[ \sum_{x \in \mathcal{M}} |z_{t-1}(x)| \cdot |\{y : |z_{t-1}(y)| \geq |z_{t-1}(x)|, z_{t-1}(x)z_{t-1}(y) < 0\}| \right] \right. \\ &\quad \left. - \left[ \sum_{x \in \mathcal{M}} \frac{1}{2} |z_{t-1}(x)| \cdot |\{y : |z_{t-1}(y)| = |z_{t-1}(x)|, z_{t-1}(x)z_{t-1}(y) < 0\}| \right] \right) \end{aligned} \quad (22.9)$$

where we subtracted  $\sum_{x \in \mathcal{M}} \frac{1}{2} |z_{t-1}(x)| \cdot |\{y : |z_{t-1}(y)| = |z_{t-1}(x)|, z_{t-1}(x)z_{t-1}(y) < 0\}|$  from the above sum, since the contribution  $-|z_{t-1}(x)|$  of agent  $x$  is counted twice for agents  $x, y$  such that  $|z_{t-1}(x)| = |z_{t-1}(y)|$  (once for  $x$  and once for  $y$ ). Notice also that, in the above sum, we can ignore agents  $x \in A_{t-1}^{\neq}$ , since their contribution to  $\mathbb{E}[\Delta_t | \mathcal{E}_{t-1}]$  is 0.

In order to give a formula for  $\mathbb{E}[\Delta_t | \mathcal{E}_{t-1}]$  that is easier to handle, consider a complete ordering  $\sigma_{t-1}$  of the agents  $x \in A_{t-1}^+ \cup A_{t-1}^-$  in increasing value of  $|z_{t-1}(x)|$ , breaking ties arbitrarily. We will write  $x <_{\sigma_{t-1}} y$  if agent  $x$  is “to the left” of agent  $y$  in  $\sigma_{t-1}$ , or equivalently  $\sigma_{t-1}(x) < \sigma_{t-1}(y)$ . We can then see that, the contribution of an agent  $x \in A_{t-1}^+$  (resp.  $x \in A_{t-1}^-$ ) to  $\mathbb{E}[\Delta_t | \mathcal{E}_{t-1}]$  is  $-|z_{t-1}(x)|$  multiplied by the number of agents in  $A_{t-1}^-$  (resp.  $A_{t-1}^+$ ) that are “to the right” of  $x$  in  $\sigma_{t-1}$  (i.e., agents  $y$  such that  $x <_{\sigma_{t-1}} y$ , for which  $z_{t-1}(x)z_{t-1}(y) < 0$ ). Therefore, Eq.(22.9) becomes

$$\mathbb{E}[\Delta_t | \mathcal{E}_{t-1}] = -\frac{1}{{m \choose 2}} \sum_{x \in \mathcal{M}} |z_{t-1}(x)| \cdot |\{y : x <_{\sigma_{t-1}} y, z_{t-1}(x)z_{t-1}(y) < 0\}|. \quad (22.10)$$

Assume now, without loss of generality, that the “rightmost” agent in  $\sigma_{t-1}$  is some  $y^* \in A_{t-1}^+$ . By the above equation, we then have that the contribution  $-|z_{t-1}(x)|$  of every agent  $x \in A_{t-1}^-$  is counted at least once (because of  $y^*$ , since  $x <_{\sigma_{t-1}} y^*$  and

$z_{t-1}(x)z_{t-1}(y^*) < 0$ ). Therefore,

$$\mathbb{E}[\Delta_t | \mathcal{E}_{t-1}] \leq -\frac{1}{\binom{m}{2}} \sum_{x \in A_{t-1}^-} |z_{t-1}(x)|. \quad (22.11)$$

But using a standard result on total variation distance (see for example [1]), we have that

$$\delta(\mathcal{E}_{t-1}, \mathcal{W}) = \sum_{x \in A_{t-1}^-} |z_{t-1}(x)| = \sum_{y \in A_{t-1}^+} |z_{t-1}(y)| \quad (22.12)$$

Therefore, we have that

$$\mathbb{E}[\Delta_t | \mathcal{E}_{t-1}] \leq -\frac{1}{\binom{m}{2}} \delta(\mathcal{E}_{t-1}, \mathcal{W}), \quad (22.13)$$

which completes the proof.  $\square$

It is worth noting that the upper bound of Lemma 22.1 is tight when the distribution of energies is such that there is only one agent  $u$  with energy above or below his weighted average  $\mathcal{W}(u) = \frac{w_u}{\sum_{v \in \mathcal{M}} w_v}$ .

We now use Lemma 22.1 to prove that protocol  $\mathcal{P}_{ows}$  is quite fast in achieving weighted energy balance in the loss-less case.

**Theorem 22.1** *Let  $\mathcal{M}$  be a population of agents using protocol  $\mathcal{P}_{ows}$ . Let also  $\tau_0(c)$  be the time after which  $\mathbb{E}[\delta(\mathcal{E}_{\tau_0(c)}, \mathcal{W})] \leq c$ , assuming interactions are planned by the probabilistic scheduler and there is no loss from energy exchanges. Then  $\tau_0(c) \leq \binom{m}{2} \ln \left( \frac{\delta(\mathcal{E}_0, \mathcal{W})}{c} \right)$ , where  $\delta(\mathcal{E}_0, \mathcal{W})$  is the total variation distance between the initial energy distribution and the distribution of weights  $\mathcal{W} \stackrel{\text{def}}{=} \{\mathcal{W}(u)\}_{u \in \mathcal{M}} = \left\{ \frac{w_u}{\sum_{v \in \mathcal{M}} w_v} \right\}_{u \in \mathcal{M}}$ .*

*Proof* Taking expectations in the upper bound inequality from Lemma 22.1, we have that  $\mathbb{E}[\mathbb{E}[\delta(\mathcal{E}_t, \mathcal{W}) | \mathcal{E}_{t-1}]] \leq \left(1 - \frac{1}{\binom{m}{2}}\right) \mathbb{E}[\delta(\mathcal{E}_{t-1}, \mathcal{W})]$ , or equivalently

$$\mathbb{E}[\delta(\mathcal{E}_t, \mathcal{W})] \leq \left(1 - \frac{1}{\binom{m}{2}}\right) \mathbb{E}[\delta(\mathcal{E}_{t-1}, \mathcal{W})]. \quad (22.14)$$

Iterating the above inequality, we then have that

$$\mathbb{E}[\delta(\mathcal{E}_t, \mathcal{W})] \leq \left(1 - \frac{1}{\binom{m}{2}}\right)^t \delta(\mathcal{E}_0, \mathcal{W}) \leq e^{-\frac{t}{\binom{m}{2}}} \delta(\mathcal{E}_0, \mathcal{W}). \quad (22.15)$$

Consequently, for any  $t \geq \binom{m}{2} \ln \left( \frac{\delta(\mathcal{E}_0, \mathcal{W})}{c} \right)$ , we have that  $\mathbb{E}[\delta(\mathcal{E}_t, \mathcal{W})] \leq c$ , which concludes the proof.  $\square$

## 22.5 Energy Transfer with Loss

In this section we consider the more natural case where every transfer of energy  $\varepsilon$  induces energy loss  $L(\varepsilon) = \beta\varepsilon$ , for some  $0 < \beta < 1$ . The main technical difficulty that arises in this case when considering the total variation distance change  $\Delta(t) = \delta(\mathcal{E}_t, \mathcal{W}) - \delta(\mathcal{E}_{t-1}, \mathcal{W})$  is that any energy transfer between agents  $u$  and  $u'$  affects also the relative energy levels of noninteracting agents  $x$  in comparison with their respective target values  $\frac{w_x}{\sum_{y \in \mathcal{M}} w_y}$ . More precisely, after  $u, u'$  exchange energy  $\varepsilon$  at time  $t$ , we have  $E_t(\mathcal{M}) = E_{t-1}(\mathcal{M}) - \beta\varepsilon$ . Therefore, for any noninteracting agent  $x$  at time  $t$ , we have  $|z_t(x)| \stackrel{\text{def}}{=} |\mathcal{E}_t(x) - \mathcal{W}(u)| = \left| \frac{E_t(x)}{E_t(\mathcal{M})} - \mathcal{W}(u) \right| \neq \left| \frac{E_{t-1}(x)}{E_{t-1}(\mathcal{M})} - \mathcal{W}(u) \right| \stackrel{\text{def}}{=} |z_{t-1}(x)|$ . As a consequence, straightforward generalizations of simple protocols like  $\mathcal{P}_{\text{ows}}$  do not perform up to par in this case.

In particular, there are specific worst-case distributions of energies for which the total variation distance increases on expectation after any significant energy exchange. As a fictitious example, consider a population of  $m$  agents, for some  $m > \frac{2+\beta}{\beta}$  and  $w_u = w_{u'}, \forall u, u' \in \mathcal{M}$ . Furthermore, suppose that agents  $u_i$ , for  $i \in [m-1]$  have energy  $m$ , while agent  $u_m$  has zero energy at his disposal. The total variation distance in this example is  $\frac{1}{m}$ . Without loss of generality, consider now a variation of  $\mathcal{P}_{\text{ows}}$  (adapted from the original version for  $\beta = 0$  to the case of  $\beta > 0$ ) according to which, whenever two agents  $u, u'$  interact, the agent with the largest amount of energy transfers  $\frac{|\varepsilon_u - \varepsilon_{u'}|}{2}$  energy to the other.<sup>2</sup> We now have that, after any significant energy exchange step, i.e., an interaction of  $u_m$  with any other agent, say  $x$ , according to protocol  $\mathcal{P}_{\text{ows}}$ , the new energy level of  $u_m$  becomes  $\frac{m}{2}(1-\beta)$ , the new energy level of  $x$  becomes  $\frac{m}{2}$ , while the energy levels of all other agents remain the same. Therefore, the new total energy in the population becomes  $m^2 - m - \frac{\beta}{2}m$ , and the new total variation distance becomes<sup>3</sup>  $\left( \frac{1}{m} - \frac{1}{2m-2-\beta} \right) + \left( \frac{1}{m} - \frac{1}{2m-2-\beta}(1-\beta) \right) = \frac{2}{m} - \frac{2-\beta}{2m-2-\beta}$ , which is strictly larger than  $\frac{1}{m}$ , for any  $m > \frac{2+\beta}{\beta}$ . We conclude that, in this example, the total variation distance increases also in expectation, as any interaction between pairs of agents that do not contain  $u_m$  does not change the energy distribution.

It is worth noting that, even though the above example is fictitious, our experiments verify our intuition that  $\mathcal{P}_{\text{ows}}$  is not very suitable for weighted energy balance in the case of lossy energy transfer. In particular, it seems that the energy lost with every step does not contribute sufficiently to the reduction of total variation distance

<sup>2</sup>Nevertheless, it is not hard to see that other variations of  $\mathcal{P}_{\text{ows}}$  have similar problems.

<sup>3</sup>The total variation distance consists of 2 terms, since there are only 2 agents with energy levels below the average.

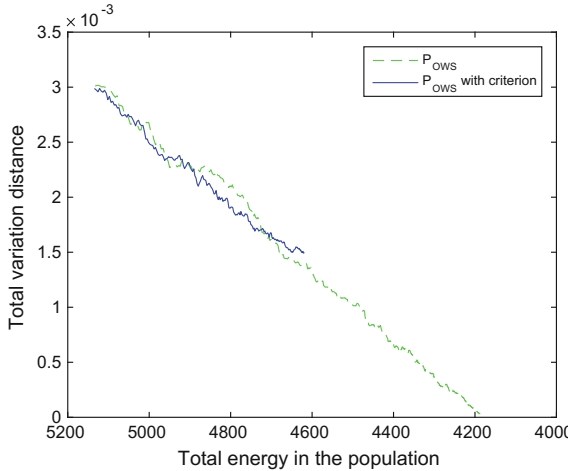


**Fig. 22.1** Efficiency of the  $\mathcal{P}_{\text{ows}}$  protocol applying the criterion that allows transfers between agents with significantly different energy levels, compared to the standard protocol version

between the distribution of energies and the uniform distribution. Our first attempt to overcome this problem was to only allow energy transfers between agents whose energy levels differ significantly. However, this did not solve the problem either (see our experimental results in Fig. 22.1), mainly because of interactions between agents that are both below the average energy. As our main contribution, we present in Sects. 22.5.1 and 22.5.2 two interaction protocols that seem to make the most of the energy lost in every step.

### 22.5.1 The Protocol **Small-Weighted-Transfer** $\mathcal{P}_{\text{SWT}}$

The protocol Small-Weighted-Transfer  $\mathcal{P}_{\text{SWT}}$  (Protocol 22) suggests having only small energy transfers between interacting agents that are proportional to the difference of their relative energies  $\frac{\varepsilon_u}{w_u}$ . In particular we assume that  $d\varepsilon$  is a universal constant known to all agents and corresponds to a very small amount of energy. Whenever agents  $u$  and  $u'$  interact and the relative energy level of  $u$  is higher than the relative energy level of  $u'$ , then  $u$  transfers energy  $\left| \frac{\varepsilon_u}{w_u} - \frac{\varepsilon_{u'}}{w_{u'}} \right| d\varepsilon$  to  $u'$ . The main idea behind  $\mathcal{P}_{\text{SWT}}$  is that pathological energy distributions that lead to increment of the total variation distance  $\delta(\mathcal{E}, \mathcal{W})$  occurs rarely on average. Additionally, by allowing only small energy transfers, we avoid “overshooting” cases where devices below (respectively above) their target energy value are overcharged (respectively transfer more energy than they should). Even though this idea can be wasteful on time, we provide experimental evidence that it achieves weighted energy balance without wasting too much energy.

**Protocol 22:** Small-Weighted-Transfer  $\mathcal{P}_{\text{SWT}}$ 


---

**Input :** Agents  $u, u'$  with weights  $w_u, w_{u'}$  and energy levels  $\varepsilon_u, \varepsilon_{u'}$

- 1 Set
- $$\phi = \left| \frac{\varepsilon_u}{w_u} - \frac{\varepsilon_{u'}}{w_{u'}} \right|$$
- 2 if  $\frac{\varepsilon_u - \phi d\varepsilon}{w_u} \geq \frac{\varepsilon_{u'} + \phi d\varepsilon}{w_{u'}}$  then
- 3 |  $\mathcal{P}_{\text{SWT}}(\varepsilon_u, w_u, \varepsilon_{u'}, w_{u'}) = (\varepsilon_u - \phi d\varepsilon, \varepsilon_{u'} + (1 - \beta)\phi d\varepsilon)$
- 4 end if
- 5 else if  $\frac{\varepsilon_u + \phi d\varepsilon}{w_u} < \frac{\varepsilon_{u'} - \phi d\varepsilon}{w_{u'}}$  then
- 6 |  $\mathcal{P}_{\text{SWT}}(\varepsilon_u, w_u, \varepsilon_{u'}, w_{u'}) = (\varepsilon_u + (1 - \beta)\phi d\varepsilon, \varepsilon_{u'} - \phi d\varepsilon)$
- 7 end if
- 8 else
- 9 | do nothing.
- 10 end if

---

**22.5.2 The Protocol Online-Weighted-Average  $\mathcal{P}_{\text{OWA}}$** 

By the analysis of the expected total variation distance change in Lemma 22.1 for energy transfer without losses, we can see that the total variation distance decreases when the interacting agents have relative energy levels that are on different sides of their respective target values. Using the notation form the proof of Lemma 22.1, if agents  $u, u'$  interact at time  $t$ , then we must either have  $u \in A_{t-1}^+$  and  $u' \in A_{t-1}^-$ , or  $u \in A_{t-1}^-$  and  $u' \in A_{t-1}^+$ , in order for the total variation distance  $\delta(\mathcal{E}_t, \mathcal{W})$  to drop below  $\delta(\mathcal{E}_{t-1}, \mathcal{W})$ . The situation becomes more complicated when there are losses in energy transfers.

In view of the above, an ideal interaction protocol would only allow energy transfers between agents  $u, u'$  for which  $z_{t-1}(u)z_{t-1}(u') < 0$ . In particular, this implies that, at any time  $t$ , each agent  $x$  would need to know the sign of  $z_t(x) = \frac{E_t(x)}{E_t(\mathcal{M})} - \frac{w_u}{\sum_{x \in \mathcal{M}} w_x}$ , which is possible if  $x$  knows (in addition to its own energy level and weight) its target weighted average energy  $\frac{w_u}{\sum_{x \in \mathcal{M}} w_x} E(\mathcal{M})$  in the population. However, this kind of global knowledge is too powerful in our distributed model, since we assume that agents are independent and identical with each other. In particular, in our model, not only are agents not aware of other agents they have not yet interacted with, but also, that they have no way of knowing whether they have met with another agent at some point in the past.

The main idea behind our interaction protocol  $\mathcal{P}_{\text{OWA}}$  (Protocol 23) is that, even in our weak model of local interactions, agents are still able to compute local estimates of their respective target energy levels based on the energy levels and weights of agents they interact with. To do this, every agent needs to keep track of the cumulative

**Protocol 23:** Online-Weighted-Average  $\mathcal{P}_{\text{OWA}}$ 


---

**Input :** Agents  $u, u'$  with weights  $w_u, w_{u'}$  and energy levels  $\varepsilon_u, \varepsilon_{u'}$

- 1 Set  $\text{nrg}(u) = \text{nrg}(u) + \varepsilon_{u'}$  and  $\text{nrg}(u') = \text{nrg}(u') + \varepsilon_u$ .
- 2 Set  $\text{wt}(u) = \text{wt}(u) + w_{u'}$  and  $\text{wt}(u') = \text{wt}(u') + w_u$ .
- 3 **if**  $(\varepsilon_u > \frac{w_u}{\text{wt}(u)} \text{nrg}(u) \text{ AND } \varepsilon'_u \leq \frac{w_{u'}}{\text{wt}(u')} \text{nrg}(u')) \text{ OR } (\varepsilon_u \leq \frac{w_u}{\text{wt}(u)} \text{nrg}(u) \text{ AND } \varepsilon'_u > \frac{w_{u'}}{\text{wt}(u')} \text{nrg}(u'))$  **then**
- 4     Set  $\delta = \left| \frac{w_{u'}\varepsilon_u - w_u\varepsilon_{u'}}{w_u + w_{u'}} \right|$
- 5     **if**  $\frac{\varepsilon_u}{w_u} > \frac{\varepsilon_{u'}}{w_{u'}}$  **then**
- 6          $\mathcal{P}_{\text{OWA}}(\varepsilon_u, w_u, \varepsilon_{u'}, w_{u'}) = (\varepsilon_u - \delta, \varepsilon_{u'} + (1 - \beta)\delta)$
- 7     **end if**
- 8     **else if**  $\frac{\varepsilon_u}{w_u} \leq \frac{\varepsilon_{u'}}{w_{u'}}$  **then**
- 9          $\mathcal{P}_{\text{OWA}}(\varepsilon_u, w_u, \varepsilon_{u'}, w_{u'}) = (\varepsilon_u + (1 - \beta)\delta, \varepsilon_{u'} - \delta)$
- 10   **end if**
- 11 **end if**
- 12 **else**
- 13     do nothing.
- 14 **end if**

---

energy and cumulative weights of agents she comes across.<sup>4</sup> This is accomplished by having each agent  $x \in \mathcal{M}$  maintaining two local registers: (a)  $\text{wt}(x)$  which is used to store the cumulative weight (note that  $\text{wt}(x)$  may include more than once the weight of a particular agent, since agents are assumed identical), and (b)  $\text{nrg}(x)$ , which is used to store the cumulative energy. For each agent  $x \in \mathcal{M}$ ,  $\text{wt}(x)$  is initialized to  $w_x$ , and  $\text{nrg}(x)$  is initialized to  $E_0(x)$ . The exact amount  $\delta$  of energy transfer from agent  $u$  to agent  $u'$ , is calculated from the equation

$$\frac{\varepsilon - \delta}{w_u} = \frac{\varepsilon_{u'} + \delta}{w_{u'}} \quad (22.16)$$

which corresponds to the intended energy exchange when there is no loss.

It is worth noting that  $\mathcal{P}_{\text{OWA}}$  may not perform up to par in the general case where interactions are planned by a potentially adversarial scheduler, because the local estimates kept by agents for the average can be highly biased. On the other hand, in our experimental evaluation, we show that  $\mathcal{P}_{\text{OWA}}$  outperforms both  $\mathcal{P}_{\text{Ows}}$  and  $\mathcal{P}_{\text{SWT}}$  when agent interactions are planned by the probabilistic scheduler. Furthermore, it is much faster than  $\mathcal{P}_{\text{SWT}}$  in terms of the expected number of useful interactions (i.e., interactions that change the energy distribution in the population) needed to reach weighted energy balance.

---

<sup>4</sup>Notice that, by definition, agents cannot store all weights and all energy levels of other agents separately. Indeed, this contradicts our assumption that agents are identical.

## 22.6 Performance Evaluation

We conducted simulations in order to evaluate our methods, using Matlab R2014b. We compared the protocols  $\mathcal{P}_{\text{ows}}$ ,  $\mathcal{P}_{\text{swt}}$  and  $\mathcal{P}_{\text{owa}}$  by conducting experiment runs of 1.000 useful interactions, where the nodes to interact are selected by a probabilistic scheduler. We assign an initial energy level value to every agent of a population consisting of  $|m| = 100$  agents uniformly at random, with maximum battery cell capacity 100 units of energy. We create a highly unbalanced instance of weights distribution by splitting the weights in two categories, very high weights (critical agents) and very low weights (noncritical agents). The constant  $\beta$  of the loss function is set to three different values, as different energy losses might lead to different performance (see Fig. 22.2). For statistical smoothness, we repeat each experiment 100 times. The statistical analysis of the findings (the median, lower and upper quartiles, outliers of the samples) demonstrate very high concentration around the mean, so in the following figures we only depict average values.

### 22.6.1 The Impact of $\beta$

Different loss functions  $L(\varepsilon)$  lead to different performance of the interaction protocols, both when running the same protocol and when comparing different protocols. Regarding the impact of different values of the  $\beta$  constant on the same protocol, an example is shown in Fig. 22.2. The total variation distance w.r.t. the remaining energy in the population is shown. We ran the  $\mathcal{P}_{\text{swt}}$  protocol for values 0.2, 0.4 and 0.6.

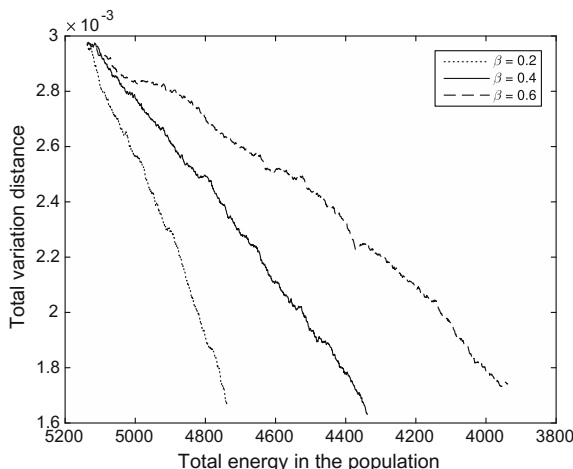


**Fig. 22.2** Performance of  $\mathcal{P}_{\text{swt}}$  for different values of  $\beta$ . Different loss functions affect the performance of the protocol

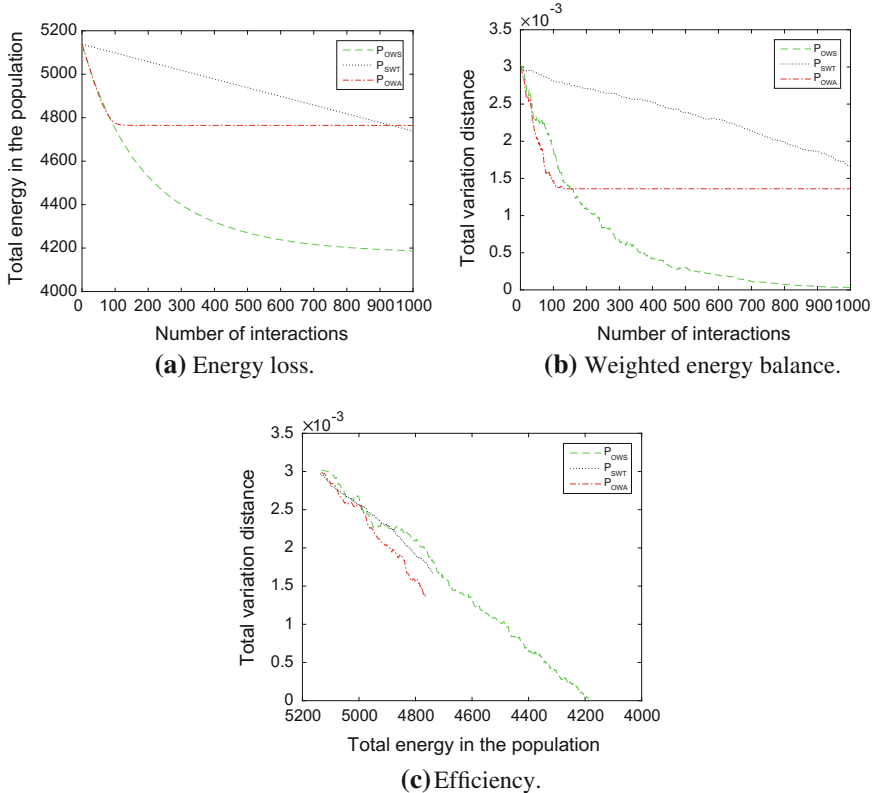


**Fig. 22.3** Comparison of the three protocols for various metrics,  $\beta = 0.2$

The results clearly show that the bigger the  $\beta$ , the larger the total variation distance for a given total level of energy in the population. For this reason, we decided to comparatively evaluate our protocols for different values of  $\beta$ . As for the impact on different protocols, if we observe Figs. 22.3a, 22.4a, and 22.5a carefully, we can see that, for the same total initial energy and number of useful interactions, when the  $\beta$  constant and consequently the energy loss increases, the rate of total energy loss increases as well.

## 22.6.2 Energy Loss

Figures 22.3a, 22.4a, and 22.5a are depicting the total energy of the population over time, for 1.000 useful agent interactions of the three protocols  $\mathcal{P}_{CWS}$ ,  $\mathcal{P}_{SWT}$  and  $\mathcal{P}_{OWA}$ . Each protocol's behavior is similar, regardless of the value of  $\beta$ , but with higher losses when  $\beta$  increases. The energy loss rate for  $\mathcal{P}_{CWS}$  and  $\mathcal{P}_{OWA}$  is high in

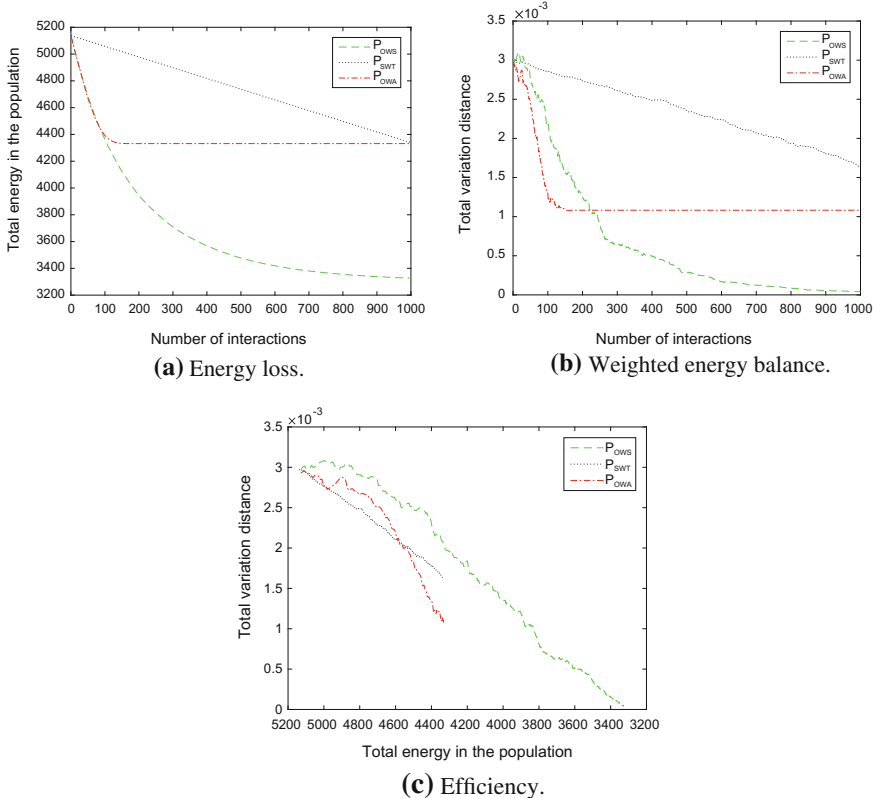


**Fig. 22.4** Comparison of the three protocols for various metrics,  $\beta = 0.4$

the beginning, until a point of time after which it significantly drops. This is explained by the fact that, in the beginning, both protocols perform interactions of high energy transfer amounts  $\varepsilon$  which lead to high  $L(\varepsilon)$ . After this initial phase, interactions with large energy transfers are very rare, and so  $\mathcal{P}_{\text{OWS}}$  and  $\mathcal{P}_{\text{OWA}}$  perform energy transfers of very small  $\varepsilon$ , forcing the energy loss rate to drop.  $\mathcal{P}_{\text{SWT}}$  has a smoother, linear energy loss rate, since  $\varepsilon$  is a very small fixed value.

### 22.6.3 Weighted Energy Balance

Useful conclusions about weighted energy balance of the population can be derived from Figs. 22.3b, 22.4b, and 22.5b, where we can see how total variation distance changes over time. A first remark is that the protocols are balancing the available energy in the population in an analogous rate to the energy loss rate. Since a better weighted energy balance is expressed by lower values of total variation distance, it is

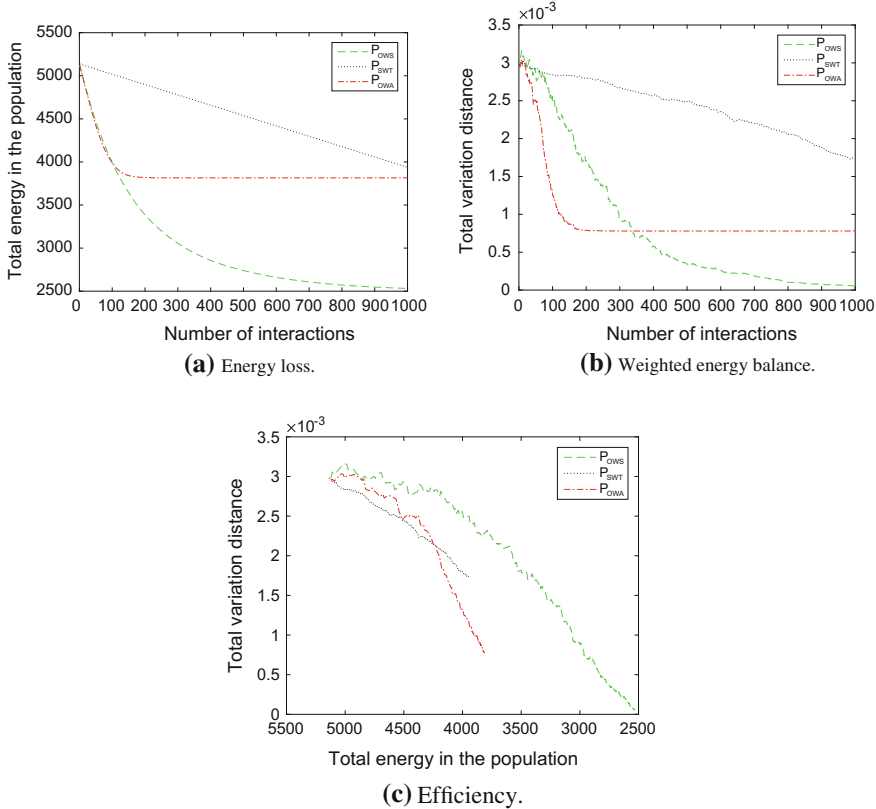


**Fig. 22.5** Comparison of the three protocols for various metrics,  $\beta = 0.6$

apparent that eventually the best balance after 1,000 useful interactions is provided by  $\mathcal{P}_{\text{OWS}}$ . However, note that this is a conclusion regarding only the weighted energy balance, not taking into account the losses from the charging procedure.  $\mathcal{P}_{\text{OWS}}$  eventually achieves weighted energy balance fast, because much energy is being gradually lost by the network and the protocol is managing significantly smaller amounts of energy. Better balance does not necessarily lead to higher overall efficiency, w.r.t. energy loss. If we take a better look at the weighted energy balance figures, we observe that even if the total variation distance follows a decreasing pattern, it is not strictly decreasing. This is natural, since many interactions can temporarily lead to a worse weighted energy balance in the population due to sharp changes in the distribution of total energy (see also the discussion in Sect. 22.5).

### 22.6.4 Convergence Time

The time that each protocol needs for balancing the available energy in the population, is not a negligible factor. Quick balancing leads to transfers of significantly smaller amounts of energy among agents and consequently to lower energy losses. On the other hand, in order to achieve quick balancing, in some cases there has been already much energy loss due to frequent lossy interactions. We can easily observe that  $\mathcal{P}_{OWA}$  is the fastest to achieve a stable level of weighted energy balance in the population, as opposed to  $\mathcal{P}_{SWT}$ , which is wasteful in terms of running time.  $\mathcal{P}_{OWS}$  performance with respect to time lies somewhere in between the two other protocols, since it is able to conduct all types of interactions (unlike  $\mathcal{P}_{OWA}$  in which only some interactions are allowed and  $\mathcal{P}_{SWT}$  which performs only interactions of small  $\varepsilon$ ).

### 22.6.5 Overall Efficiency

We measure the overall efficiency of a protocol by taking into account both energy losses and weighted energy balance in the population. This combination of the two crucial properties is shown in Figs. 22.3c, 22.4c, and 22.5c, where  $\mathcal{P}_{SWT}$  and  $\mathcal{P}_{OWA}$  clearly outperform  $\mathcal{P}_{OWS}$ , most of the time. More specifically, although  $\mathcal{P}_{OWS}$  achieves very good balance quickly, the impact of energy loss affect very negatively its overall performance. This is due to the fact that for the same amount of total energy in the population,  $\mathcal{P}_{SWT}$  and  $\mathcal{P}_{OWA}$  achieve better total variation distance than  $\mathcal{P}_{OWS}$ . It is also clear than eventually,  $\mathcal{P}_{OWA}$  outperforms both  $\mathcal{P}_{OWS}$  and  $\mathcal{P}_{SWT}$  when agent interactions are planned by the probabilistic scheduler. Furthermore, it is much faster than  $\mathcal{P}_{SWT}$  in terms of the number of useful interactions.

## 22.7 Conclusion

In this chapter we apply interactive wireless charging in populations of resource-limited, mobile agents that abstract distributed portable devices. We provide a model in which the agents are capable of achieving bi-directional wireless energy transfer and can act both as energy transmitters and as energy harvesters. We consider the cases of loss-less and lossy wireless energy transfer and, in the former case, we prove a tight upper bound on the time that is needed to reach weighted energy balance in the population. Finally, we design and evaluate three interaction protocols which opt for creating weighted energy balance among the agents of the population.

## References

1. Aldous, D., Fill, J.A.: Reversible markov chains and random walks on graphs (2002). <http://www.stat.berkeley.edu/~aldous/RWG/book.html>. (Unfinished monograph, recompiled 2014)
2. Angelopoulos, C.M., Buwaya, J., Evangelatos, O., Rolim, J.: Traversal strategies for wireless power transfer in mobile ad-hoc networks. In: Proceedings of the 18th ACM International Conference on Modeling, Analysis and Simulation of Wireless and Mobile Systems, MSWiM'15. ACM (2015)
3. Angluin, D., Aspnes, J., Diamadi, Z., Fischer, M.J., Peralta, R.: Computation in networks of passively mobile finite-state sensors. In: Proceedings of the Twenty-third Annual ACM Symposium on Principles of Distributed Computing, PODC'04, pp. 290–299. ACM, New York, NY, USA (2004). doi:[10.1145/1011767.1011810](https://doi.org/10.1145/1011767.1011810)
4. Angluin, D., Aspnes, J., Eisenstat, D.: Stably computable predicates are semilinear. In: Proceedings of the Twenty-fifth Annual ACM Symposium on Principles of Distributed Computing, PODC'06, pp. 292–299. ACM, New York, NY, USA (2006). doi:[10.1145/1146381.1146425](https://doi.org/10.1145/1146381.1146425)
5. Del Prete, M., Berra, F., Costanzo, A., Masotti, D.: Exploitation of a dual-band cell phone antenna for near-field WPT. In: Wireless Power Transfer Conference (WPTC), 2015 IEEE (2015). doi:[10.1109/WPTC.2015.7139132](https://doi.org/10.1109/WPTC.2015.7139132)
6. del Prete, M., Costanzo, A., Georgiadis, A., Collado, A., Masotti, D., Popovic, Z.: Energy-autonomous bi-directional Wireless Power Transmission (WPT) and energy harvesting circuit. In: Microwave Symposium (IMS), 2015 IEEE MTT-S International (2015). doi:[10.1109/MWSYM.2015.7166982](https://doi.org/10.1109/MWSYM.2015.7166982)
7. Griffin, B., Detweiler, C.: Resonant wireless power transfer to ground sensors from a UAV. In: 2012 IEEE International Conference on Robotics and Automation (ICRA), pp. 2660–2665 (2012). doi:[10.1109/ICRA.2012.6225205](https://doi.org/10.1109/ICRA.2012.6225205)
8. Guo, S., Wang, C., Yang, Y.: Mobile data gathering with wireless energy replenishment in rechargeable sensor networks. In: INFOCOM, 2013 Proceedings IEEE, pp. 1932–1940 (2013). doi:[10.1109/INFCOM.2013.6566993](https://doi.org/10.1109/INFCOM.2013.6566993)
9. Guo, S., Wang, C., Yang, Y.: Joint mobile data gathering and energy provisioning in wireless rechargeable sensor networks. *IEEE Trans. Mob. Comput.* **13**(12), 2836–2852 (2014). doi:[10.1109/TMC.2014.2307332](https://doi.org/10.1109/TMC.2014.2307332)
10. Johnson, J., Basha, E., Detweiler, C.: Charge selection algorithms for maximizing sensor network life with UAV-based limited wireless recharging. In: 2013 IEEE Eighth International Conference on Intelligent Sensors, Sensor Networks and Information Processing, pp. 159–164 (2013). doi:[10.1109/ISSNIP.2013.6529782](https://doi.org/10.1109/ISSNIP.2013.6529782)
11. Levin, D.A., Peres, Y., Wilmer, E.L.: Markov Chains and Mixing Times. American Mathematical Society (2006)
12. Luo, J., He, Y.: Geoquorum: load balancing and energy efficient data access in wireless sensor networks. In: INFOCOM, 2011 Proceedings IEEE, pp. 616–620 (2011). doi:[10.1109/INFCOM.2011.5935238](https://doi.org/10.1109/INFCOM.2011.5935238)
13. Madhja, A., Nikoletseas, S., Raptis, T.: Hierarchical, collaborative wireless charging in sensor networks. In: Wireless Communications and Networking Conference (WCNC), 2015 IEEE, pp. 1285–1290 (2015). doi:[10.1109/WCNC.2015.7127654](https://doi.org/10.1109/WCNC.2015.7127654)
14. Naderi, M., Chowdhury, K., Basagni, S., Heinzelman, W., De, S., Jana, S.: Experimental study of concurrent data and wireless energy transfer for sensor networks. In: Global Communications Conference (GLOBECOM), 2014 IEEE, pp. 2543–2549 (2014). doi:[10.1109/GLOCOM.2014.7037190](https://doi.org/10.1109/GLOCOM.2014.7037190)
15. Nikoletseas, S., Raptis, T.P., Souroulagkas, A., Tsolovos, D.: An experimental evaluation of wireless power transfer protocols in mobile ad hoc networks. In: Wireless Power Transfer Conference (WPTC), 2015 IEEE (2015). doi:[10.1109/WPTC.2015.7139128](https://doi.org/10.1109/WPTC.2015.7139128)
16. Peng, Y., Li, Z., Zhang, W., Qiao, D.: Prolonging sensor network lifetime through wireless charging. In: Real-Time Systems Symposium (RTSS), 2010 IEEE 31st, pp. 129–139 (2010). doi:[10.1109/RTSS.2010.35](https://doi.org/10.1109/RTSS.2010.35)

17. Rault, T., Bouabdallah, A., Challal, Y.: Multi-hop wireless charging optimization in low-power networks. In: Global Communications Conference (GLOBECOM), 2013 IEEE, pp. 462–467 (2013). doi:[10.1109/GLOCOM.2013.6831114](https://doi.org/10.1109/GLOCOM.2013.6831114)
18. Rolim, J.: Energy balance mechanisms and lifetime optimization of wireless networks. In: Contemporary Computing. Communications in Computer and Information Science, vol. 168. Springer, Berlin (2011)
19. Schafer, S., Coffey, M., Popovic, Z.: X-band wireless power transfer with two-stage high-efficiency GaN PA/rectifier. In: Wireless Power Transfer Conference (WPTC), 2015 IEEE (2015). doi:[10.1109/WPTC.2015.7140186](https://doi.org/10.1109/WPTC.2015.7140186)
20. Wang, C., Li, J., Ye, F., Yang, Y.: Recharging schedules for wireless sensor networks with vehicle movement costs and capacity constraints. In: 2014 Eleventh Annual IEEE International Conference on Sensing, Communication, and Networking (SECON), pp. 468–476 (2014). doi:[10.1109/SAHCN.2014.6990385](https://doi.org/10.1109/SAHCN.2014.6990385)
21. Wang, C., Li, J., Ye, F., Yang, Y.: Netwrap: an ndn based real-timewireless recharging framework for wireless sensor networks. *IEEE Trans. Mob. Comput.* **13**(6), 1283–1297 (2014). doi:[10.1109/TMC.2013.2296515](https://doi.org/10.1109/TMC.2013.2296515)
22. Xiang, L., Luo, J., Han, K., Shi, G.: Fueling wireless networks perpetually: a case of multi-hop wireless power distribution. In: 2013 IEEE 24th International Symposium on Personal Indoor and Mobile Radio Communications (PIMRC), pp. 1994–1999 (2013). doi:[10.1109/PIMRC.2013.6666471](https://doi.org/10.1109/PIMRC.2013.6666471)
23. Xie, L., Shi, Y., Hou, Y.T., Sherali, H.D.: Making sensor networks immortal: an energy-renewal approach with wireless power transfer. *IEEE/ACM Trans. Netw.* **20**(6), 1748–1761 (2012). doi:[10.1109/TNET.2012.2185831](https://doi.org/10.1109/TNET.2012.2185831)
24. Zhang, S., Wu, J., Lu, S.: Collaborative mobile charging. *IEEE Trans. Comput.* **64**(3), 654–667 (2015)

## **Part V**

# **Joint Operations**

# Chapter 23

## Charging and Routing Activity Scheduling to Prolong Sensor Network Lifetime

Yang Peng, Wensheng Zhang and Daji Qiao

**Abstract** The emerging wireless charging technology is a promising alternative to address the power constraint problem in sensor networks. Comparing to existing approaches, this technology can replenish energy in a more controllable manner and does not require accurate location of or physical alignment to sensor nodes. In this chapter, we present several innovative wireless charging and routing activity scheduling schemes to prolong the sensor network lifetime. Our investigation starts from building a prototype wireless charging enabled sensor network system; then we design several charging activity scheduling schemes to prolong the network lifetime by replenishing sensors that are deficient in energy supply. To fully leverage the strengths of the wireless charging technology, we further design a practical and efficient joint routing and charging activity scheduling scheme, called J-RoC, which can proactively guide the routing activities in the network and deliver energy to where it is needed. To evaluate the performance of the proposed schemes, both testbed experiments in the prototype system and extensive simulations in large-scale networks are conducted. Evaluation results demonstrate that the propose schemes significantly elongate the network lifetime compared to existing wireless charging based schemes under various system configurations.

---

Y. Peng (✉)  
University of Washington Bothell, Bothell, WA 98011, USA  
e-mail: yangpeng@uw.edu

W. Zhang · D. Qiao  
Iowa State University, Ames, IA 50011, USA  
e-mail: wzhang@iastate.edu

D. Qiao  
e-mail: daji@iastate.edu

## 23.1 Introduction

Wireless sensor nodes are powered by small batteries, and the limited energy supply has constrained the lifetime of a sensor network. This has been a long-lasting, fundamental problem faced by sensor networks that are designed for long-term operation. Energy conservation [2, 15], environmental energy harvesting [6, 10, 11, 18], incremental deployment, and battery replacement [24, 26] approaches have been proposed to address the problem. However, energy conservation schemes can only slow down energy consumption but not compensate energy depletion. Harvesting environmental energy, such as solar [6, 11], wind [18], vibration [10], is subject to their availability which is often uncontrollable by people. The incremental deployment approach may not be environmentally friendly because deserted nodes can pollute the environment. The battery or node replacement approach is applicable only for scenarios that sensor nodes are accessible by people or sophisticated robots that can locate and physically touch the sensor nodes.

Since the pioneer adventure of applying resonant magnetic technique to wirelessly transfer and receive energy [13], numerous wireless charging based research investigations have been conducted to study the feasibility of applying the wireless charging technology in different applications [20, 23, 29, 30]. As more and more applications of wireless charging technology have been envisioned, the Wireless Power Consortium [27] has been established to set an international standard for interoperable wireless charging. With electromagnetic radiation technique being commercialized [19], the wireless charging technology has become a promising alternative to address the long-lasting energy constraint problem in sensor networks. Different from energy harvesting technologies, the wireless charging technology, together with more and more mature and inexpensive mobile robots, will make controllable power replenishment possible, with which power can be replenished proactively to meet application requirements rather than passively adapted to the availability of environmental resources. Comparing with sensor node or battery replacement approaches, the wireless charging technology allows a mobile charger to transfer energy to sensor nodes wirelessly without requiring accurate localization of sensor nodes or strict alignment between the charger and nodes.

To leverage the power of wireless charging technology, we build a prototype wireless chargeable sensor network system and design several innovative wireless charging and routing activity scheduling schemes to prolong the network lifetime.

### 23.1.1 Organization

The rest of the chapter is organized as follows. Section 23.2 presents the design and implementation of the prototype system. Section 23.3 formulates the charging activity scheduling problem and presents the design of several scheduling schemes.

Based on the charging activity scheduling schemes, Sect. 23.4 further discusses the design of J-RoC, a joint routing and charging activity scheduling scheme. Finally, Sect. 23.5 concludes the chapter.

## 23.2 A Wireless Chargeable Sensor Network System

Figure 23.1 illustrates a model of wireless chargeable sensor network system composed of three main components: a mobile charger (MC) that is a mobile robot carrying a wireless power charger, a network of sensor nodes each equipped with a wireless power receiver, and a base station (BS) that monitors the energy status of the network and directs the MC to charge sensor nodes.

In this system, each sensor node generates sensory data and sends the data hop-by-hop to the sink periodically. Each sensor node also measures its local energy level, monitors the channel conditions, estimates its energy consumption rate, and reports these information along with the data packet generation rate to the BS. Based on the collected information, the BS schedules future charging activities, and commands the MC via a long range radio to execute the schedule. The MC then travels around the deployment field to charge sensor nodes. The BS also disseminates the schedule to sensor nodes, which may be used in routing path construction. We assume the MC's energy can be replenished at the BS and thus the energy for moving and charging is unlimited.

Based on this model, we have built a prototype system to practically investigate different wireless charging based schemes to prolong sensor network lifetime. In this prototype system, the Powercast wireless power charger and receiver [19] are used as shown in Fig. 23.2a. A Powercast charger is installed on an Acroname Garcia robot [7] to become the MC, and each TelosB sensor is equipped with a Powercast

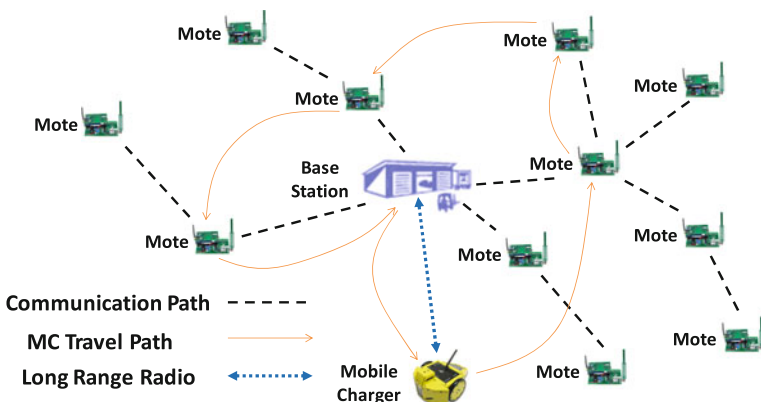


**Fig. 23.1** System overview

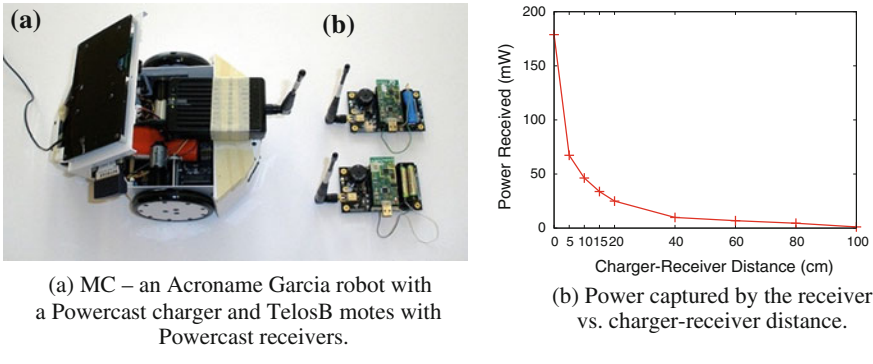


**Fig. 23.2** Prototype system components and charging efficiency

receiver. When the Garcia robot moves at 1 m/s (used in our experiments), its power consumption is about 8 W and the voltage level is in the range of 5.8 to 9 V. The MC communicates with the energy station (a PC in our experiments) via an IEEE 802.11b interface.

Energy charging is carried out in the 903–927 MHz band while sensor nodes communicate in the 2.4 GHz band. When the MC is charging, its power consumption is 3 W. The effective amount of power that can be captured by a receiver varies with the distance between the receiver and the MC. The relation is shown in Fig. 23.2b, which is obtained from our field-test results. The antenna gain is 1.15 for both power charger and receiver. As shown in the figure, the receiver can receive about 45 mW power when it is 10 cm away from the charger, meaning that the charging efficiency is about 1.5 %. As the distance increases, the charging efficiency decreases.

### 23.3 Wireless Charging Scheduling Scheme

As mentioned in Sect. 23.2, sensor nodes perform application tasks such as environment monitoring, generate sensory data, and periodically report the data to the sink. In addition, they also monitor the voltage readings of their own batteries, estimate energy consumption rates, based on which derive their own lifetime, and then report the information to the sink periodically. Upon receiving the energy information, the sink forwards it to the energy station, which runs a *charging activity scheduling algorithm* to plan the charging activities, and then sends a command message to the MC. The command includes the charging plan that the MC should execute. Once receiving the command, the MC starts charging a selected set of sensor nodes sequentially according to the instruction. When the MC receives a new command, it adjusts its charging activities accordingly. To save communication overhead, the energy information can be aggregated when it is forwarded to the sink. Particularly, only the energy information of the  $k$  shortest-lifetime nodes is forwarded while the information of other nodes is dropped, where  $k$  is a system parameter.

In this section, we formally state the *charging activity scheduling problem* that the energy station tries to solve (which is NP-complete) and present two heuristic *charging activity scheduling algorithms* to address the issue. Based on these heuristic algorithms, we will discuss about an advanced design of joint routing and charging activity scheduling scheme in Sect. 23.4.

### 23.3.1 Formulation of the Charging Activity Scheduling Problem

Suppose Graph  $G = (V, E)$  represents the topology of a static sensor network, where each vertex stands for a sensor node and the length of an edge stands for the distance between the nodes connected by it. Suppose all sensor nodes have the same  $E_s$ . Suppose the battery capacity of a sensor node is  $E_s$ . For each sensor node  $i$  ( $i \in V$ ), let  $e_i$  and  $c_i$  denote its residual energy and energy consumption rate, respectively. There is a mobile charger (MC) in the network and its distance to each sensor node is known. The MC carries a battery of capacity  $E_c$ . When the MC charges a sensor node, it consume  $\Lambda_c$  power while the power received by the sensor node is  $\eta \Lambda_c$  where  $\eta$  is called the *charging efficiency*. The MC moves at the speed of  $v$  and the power consumption for its movement is  $\Lambda_m$ .

We study a particular *charging activity scheduling problem* whose goal is to find an optimal charging sequence for the MC, denoted as  $S = \langle (n_1, ct_1), \dots, (n_{|S|}, ct_{|S|}) \rangle$ , where  $\langle n_j, ct_j \rangle$  ( $j = 1, \dots, |S|$ ) represents that node  $n_j$  is charged in the  $j$ th step for a period of  $ct_j$  time, such that the network lifetime is maximized. Here, the network lifetime refers to the time when the first sensor node in the network is out of energy.

Table 23.1 summarizes the notations used in the formulation and analysis of the studied problems in this chapter.

### 23.3.2 NP-Completeness of the Charging Activity Scheduling Problem

By reducing the NP-Complete Traveling Salesman Problem (TSP) to the above charging activity scheduling problem, we can prove that this problem is also NP-Complete. The decision versions of the charging activity scheduling problem and the TSP problem are as follows:

- *Decision version of the charging activity scheduling problem:* Given a network  $G = (V, E)$ , the sensor node behavior (characterized by  $E_s$ ,  $e_i$  and  $c_i$ ), and the MC behavior (characterized by  $E_c$ ,  $\Lambda_c$ ,  $\Lambda_m$ ,  $v$  and  $\eta$ ), the question is whether there exists a charging sequence  $S$  with which the network lifetime can reach at least  $T$ .
- *Decision version of the TSP problem:* Given a network  $G' = (V', E')$ , the question is whether there exists a visiting sequence (i.e., tour) that covers all nodes in  $V'$  and has a length of at most  $D$ .

**Table 23.1** Notations used in this chapter

| Notation        | Meaning  |
|-----------------|--|
| $E_s$           | Battery capacity of a sensor node  |
| $E_c$           | Battery capacity of the MC   |
| $cr_i$          | Energy consumption rate of node $i$  |
| $e_i$           | Residual energy of node $i$  |
| $e_{tx}$        | Energy consumed for transmitting a packet  |
| $e_{rx}$        | Energy consumed for receiving a packet   |
| $\Lambda_c$     | Energy consumed for the MC's charging operation  |
| $\Lambda_m$     | MC's moving power consumption  |
| $\eta$          | MC's charging efficiency   |
| $v$             | MC's moving speed  |
| $T_c$           | Charging activity scheduling interval  |
| $\alpha$        | Charging guiding coefficient   |
| $l_i$           | Charging time allocated to node $i$ in one $T_c$ interval  |
| $r_{i,t}$       | Future sensory data packet generation rate of node $i$ estimated at time $t$                           |
| $\varphi_{i,t}$ | Amount of time that node $i$ has been charged in the current $T_c$ interval at time $t$                |
| $h_{i,t}$       | Charging rate of node $i$ at time $t$  |
| $e_{i,t}$       | Residual energy of node $i$ at time $t$  |
| $c_{i,t}$       | Energy consumption rate of node $i$ at time $t$  |
| $c'_{i,t}$      | Energy consumption rate of node $i$ at time $t$ in transceiving via the energy-minimum routing paths   |
| $\hat{c}_{i,t}$ | Future energy consumption rate of node $i$ estimated at time $t$                                       |
| $P_{i,t}$       | Set of node $i$ 's parents on the energy-minimum path at time $t$                                      |
| $ETX_{i,j,t}$   | Expected number of transmissions needed to send a packet successfully from node $i$ to $j$ at time $t$ |
| $\rho_i$        | Percentage of charging energy that should be allocated to node $i$ in one $T_c$ interval               |

**Theorem 23.1** The decision version of the charging activity scheduling problem is NP-complete.

*Proof* (sketch) Firstly, given a charging sequence  $S$ , we can verify whether the network lifetime can reach  $T$  with  $S$  by simulating each charging operation. This takes  $O(|S|)$  steps. Therefore, the charging activity scheduling problem belongs to NP.

Next, we show that any instance of TSP can be reduced to an instance of the charging activity scheduling problem. Letting  $\langle G' = (V', E'), D \rangle$  be an arbitrary instance of TSP, an instance of the charging activity scheduling problem  $\langle G, E_s, e_i, c_i, E_c, \Lambda_c, \Lambda_m, v, \eta \rangle$  can be constructed as follows<sup>1</sup>

- $G = G'$ ,  $c_i = \delta$ ,  $e_i = (D + |V|) * \delta$ ,  $E_s = e_i + \Lambda_c$ ;
- $\eta = 1$ ,  $\Lambda_m = 1$ ,  $v = 1$ ,  $\Lambda_c = |V| * \delta$ ,  $E_c = \Lambda_m * D + \Lambda_c * |V|$ ;
- $T = D + 2 * |V|$ .

<sup>1</sup>In both instances, the salesman and the MC start from the same position.

Here,  $\delta$  is a small positive value. The following two steps show that these two instances are equivalent.

*Step I:* Suppose there is a tour  $\langle n_1, n_2, \dots, n_m \rangle$  ( $n_i \in V'$ ), which covers all node in  $V'$  and has a length of at most  $D$ , for the above TSP instance. Then, a charging sequence  $S = \langle (n_1, 1), \dots, (n_m, 1) \rangle$ , where node  $n_i$  is charged in the  $i$ th step for one time unit, can be constructed for the above instance of the charging activity scheduling problem. The charging operation is valid due to the facts that (1) the MC's energy capacity  $E_c$  is large enough to support the moving and charging operations; and (2) each node can be charged for one time unit before the capacity ceiling of its battery is reached. With this charging sequence, the lifetime of each node is extended by at least  $\frac{\Lambda_c * \eta * 1}{c_i} = |V|$ . Since the sum of the MC's moving time ( $\frac{D}{v} = D$ ) and the total charging time ( $1 * |V| = |V|$ ) is equal to the initial nodal lifetime ( $\frac{e_i}{c_i} = D + |V|$ ), we know that the network can survive for at least  $T = D + 2 * |V|$  time with the charging sequence. Hence, the above instance of the charging activity scheduling problem also has a positive answer.

*Step II:* Conversely, if there is a charging sequence that extends the network lifetime to  $T = D + 2 * |V|$ , each node must be charged for at least one time unit since the initial nodal lifetime is only  $D + |V|$ . This means that each node must be visited at least once. Excluding the charging energy consumption, the MC has at most  $E_c - \Lambda_c * 1 * |V| = \Lambda_m * D$  energy for moving, which can be used to traverse a distance of at most  $D$ . Therefore, there exists a tour that visits every node and the length of the tour is at most  $D$ .

As the TSP is a well-known NP-complete problem, the charging activity scheduling problem is also NP-complete.

### 23.3.3 Heuristic Charging Activity Scheduling Algorithms

In this section, we present two heuristic algorithms to address the difficult charging activity scheduling problem. As the lifetime of the network is the same as the lifetime of the first sensor node that uses up its battery energy, a *naive algorithm* is to always charge the node with the shortest lifetime to its battery capacity. Unfortunately, this may cause the MC to move back and forth between nodes, which could incur large movement overhead. The proposed *greedy* and *greedyPlus* charging activity scheduling algorithms aim to reduce the movement overhead.

#### 23.3.3.1 Greedy Algorithm

The greedy algorithm is designed to find a charging sequence with which the lifetime of the network can be prolonged as much as possible while incurring less movement than the naive algorithm. It works as follows. All sensor nodes are sorted according to the lifetime in the ascending order. Let us denote the sorted list that contains the  $k$

shortest-lifetime nodes as  $\langle (n_1, l_1), \dots, (n_k, l_k) \rangle$ , where  $(n_i, l_i)$  represents node  $n_i$  with a lifetime of  $l_i$  if it is not being charged, and  $l_i \leq l_{i+1}$  ( $1 \leq i \leq k-1$ ). Clearly,  $l_1$  is the network lifetime if there is no charging. Then, as shown in Algorithm 24, a charging sequence can be found in the following manner:

---

**Algorithm 24:** The greedy algorithm

---

**1 Input:**

- $P$ : position of the MC
- $\alpha$ : remaining energy in the MC's battery
- $\langle (n_1, l_1), \dots, (n_k, l_k) \rangle$ : list of  $k$  shortest-lifetime nodes sorted in the ascending order of their lifetime
- $G = (V, E)$ ,  $E_S$ ,  $A_C$ ,  $A_m$ ,  $v$ ,  $\eta$ ,  $c_i$  ( $i = 1, \dots, k$ ): other system parameters

**Output:** a charging sequence

```

1:  $S^* \leftarrow \emptyset$                                 /* the best charging sequence found so far */
2:  $L^* \leftarrow l_1$                                 /* network lifetime achieved with  $S^*$  */
3: for  $j = 1$  to  $k$  do
4:   if  $j = k$  then
5:      $T \leftarrow \frac{E_S}{\max_{1 \leq i \leq j} c_i}$           /* target network lifetime */
6:   else if  $l_j = l_{j+1}$  then
7:     continue
8:   else
9:      $T \leftarrow l_{j+1}$                                 /* target network lifetime */
10:  end if
11:  for each permutation of  $\langle n_1, \dots, n_j \rangle$ :  $\langle n'_1, \dots, n'_j \rangle$  do
12:     $(\tilde{P}, \tilde{\alpha}, \tilde{e}_{n'_1}, \dots, \tilde{e}_{n'_j}) \leftarrow (P, \alpha, e_{n'_1}, \dots, e_{n'_j})$ 
13:     $S \leftarrow \emptyset, L \leftarrow 0$ 
14:    for  $w = 1$  to  $j$  do
15:       $ChargeTime \leftarrow \lceil (T - l_w) \times c_{n'_w} \rceil / [\eta \times A_C]$ 
        /* time needed to charge  $n'_w$  to extend lifetime to  $T$  */
16:       $NodeCapTime \leftarrow \lceil E_S - \tilde{e}_{n'_w} \rceil / [\eta \times A_C]$ 
        /* time needed to charge  $n'_w$  to full battery capacity */
17:       $MCCapTime \leftarrow \tilde{\alpha} - distance(\tilde{P}, n'_w) \times A_m / v / A_C$ 
        /* maximum time that can be spent to move to and charge  $n'_w$  with the remaining energy at MC */
18:       $DeadTime \leftarrow \min_{w+1 \leq x \leq j} (\frac{\tilde{e}_{n'_x}}{c_{n'_x}} - \frac{distance(n'_w, n'_x)}{v})$ 
        /* maximum time that can be spent to charge  $n'_w$  s.t. no other node dies before MC can charge it */
19:       $t_w \leftarrow \min(ChargeTime, NodeCapTime, MCCapTime, DeadTime)$ 
        /*  $t_w$  is the actual time that MC will charge  $n'_w$  */
20:      if  $t_w < 0$  then
21:        break
22:      end if
23:      Update  $\tilde{P}, \tilde{\alpha}, \tilde{e}_{n'_1}, \dots, \tilde{e}_{n'_j}$ 
24:       $(n'_w, t_w)$  is appended to  $S$ 
25:    end for
26:     $L$  is computed for the charging sequence  $S$ 
27:    if  $L > L^*$  then
28:       $S^* \leftarrow S, L^* \leftarrow L$ 
29:    end if
30:  end for
31:  if (no better charging sequence found in this iteration) then
32:    return  $S^*$ 
33:  end if
34: end for
35: return  $S^*$ 

```

---

- *Loop 1*: The algorithm tries to extend the network lifetime from  $l_1$  towards  $l_2$ . In other words, the target network lifetime is set to  $l_2$ , and if a feasible charging sequence can be found (i.e., without violating the battery capacity of a sensor node, or depleting the battery energy of the MC in the mid of the sequence) to charge node  $n_1$  so that the network lifetime is extended beyond  $l_1$ , the algorithm continues to *Loop 2*; otherwise, it halts. In this algorithm, the charging behavior of the MC is *greedy* in the sense that, once the MC starts charging a sensor node, it keeps charging the node for as long time as possible.
- *Loop j* ( $2 \leq j \leq k$ ): The algorithm tries to extend the network lifetime from  $l_1$  towards  $l_{j+1}$ . Similarly, if a feasible charging sequence can be found to charge nodes  $n_1, n_2, \dots, n_j$  so that the network lifetime is extended beyond  $l_1$ , the algorithm continues to the next loop; otherwise, it halts.

At the end of the above procedure, among all the found feasible charging sequences, the one that extends the network lifetime the most is selected by the algorithm. The complexity of this algorithm is  $O(k^2 k!)$ . Simulation results show that the algorithm can prolong the network lifetime effectively with a relatively small  $k$ , e.g.,  $k = 5$ , while the performance improvement by increasing  $k$  further is not significant. Therefore, the greedy algorithm is simple to implement and effective in practice. Note that when  $k = 0$ , the greedy algorithm reduces to the special case when there is no charging in the network, while when  $k = 1$ , the greedy algorithm is equivalent to the naive algorithm.

One potential issue with the greedy algorithm is that the greedy nature of the algorithm (i.e., the MC keeps charging a sensor node for as long time as possible once started) may degrade the system performance under certain circumstances. Figure 23.3 illustrates an example scenario when the greedy algorithm does not perform well. In this example, at time 0, sensor nodes  $n_1, n_2$ , and  $n_3$  have the residual energy of 1800 J, 1800 J and 7200 J, respectively, and they have the same energy consumption rate of 0.01 J/s. The battery capacity of a sensor node and the MC is 10000 J and 270000 J, respectively. Suppose  $k = 3$ ,  $\Lambda_c = 3$  W,  $\eta = 0.02$ , and the MC movement cost and delay are negligible (i.e.,  $\Lambda_c = 0$  W,  $v = \infty$ ).

As shown in Fig. 23.3a, with the greedy algorithm, the MC starts charging  $n_1$  at time 0 and continues to time 25 h when the residual energy of  $n_1$  becomes the same as that of  $n_3$  (hence they have the same lifetime as they have the same energy consumption rate). This action causes the MC to use up all of its battery energy. As a result, the network lifetime is 50 h when the residual energy of  $n_2$  becomes zero. In comparison, if the MC takes a less greedy approach that charges  $n_1$  for 12.5 h and then charges  $n_2$  for 12.5 h, as shown in Fig. 23.3b, the network can survive much longer for 125 h in total, resulting in a 250 % performance improvement. Motivated by this observation, we revise the greedy algorithm to allow the MC to charge sensor nodes in a more balanced manner. The revised algorithm is named the *greedyPlus algorithm*.

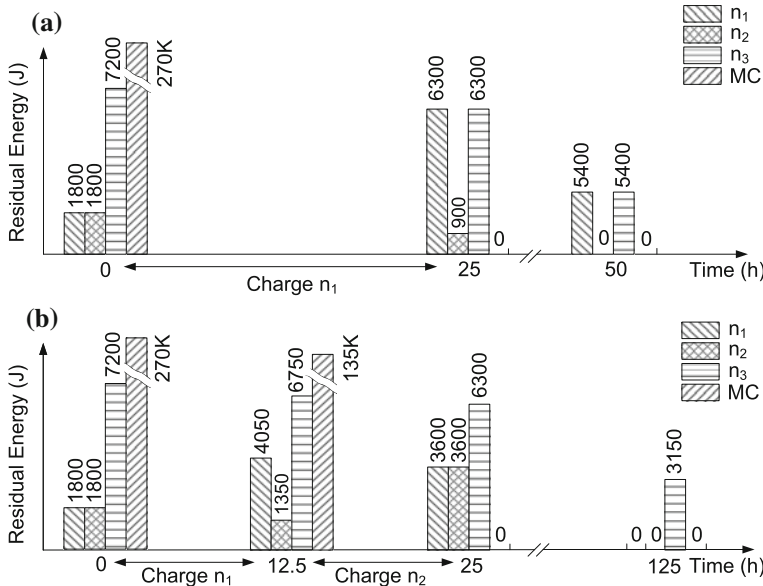


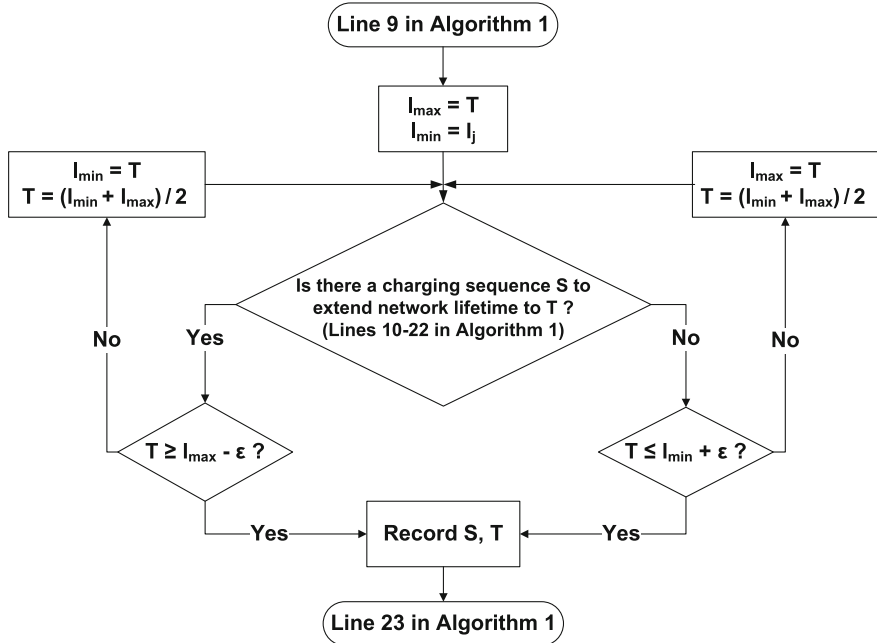
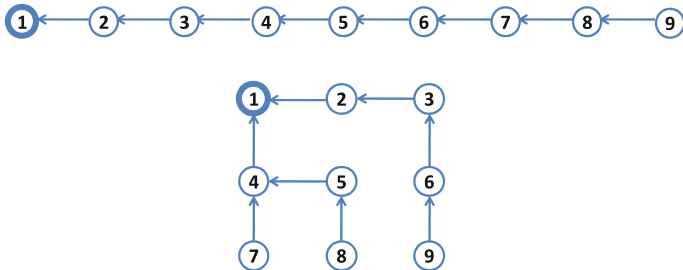
**Fig. 23.3** An example to illustrate that the greedy algorithm could be improved further: **a** network lifetime is 50 h with the greedy algorithm; **b** network lifetime is 125 h with more balanced charging

### 23.3.3.2 GreedyPlus Algorithm

In the greedy algorithm, the MC tends to charge a node in a greedy manner towards the target lifetime  $T$  without considering whether the lifetime of other nodes can also be extended to  $T$ . In fact, as long as one node cannot have its lifetime extended to  $T$ , the network lifetime cannot reach  $T$ , meaning that some of the energy being charged to the current node may be wasted. The greedyPlus algorithm improves upon the greedy algorithm by applying binary search to find a more suitable target network lifetime at each loop, which is a target achievable by all sensor nodes in the network. Figure 23.4 shows the flowchart of the greedyPlus algorithm, which is based on the pseudo-code of the greedy algorithm in Algorithm 24. In the flowchart,  $\varepsilon$  is a small quantity to help define exit conditions for the greedyPlus algorithm.

### 23.3.4 Experiments

Experiments have been performed on the prototype system to evaluate its feasibility and performance of proposed schemes. In the experiments, we measure (1) the initial energy level of individual nodes; (2) the lifetime of the network and individual nodes when there is no energy charging (tagged as *no charge* in the figures) and when the greedyPlus algorithm is used; and (3) the distribution of charging time among

**Fig. 23.4** Flowchart of the greedyPlus algorithm**Fig. 23.5** Experimental topologies

individual nodes. Figures 23.7 and 23.8 show the evaluation results for the line and grid topologies, respectively.

#### 23.3.4.1 Experimental Setup

Nine TelosB sensor nodes are used in the experiments. Each node is powered by two 1.5 V 2000 mAh Alkaline rechargeable batteries, and Fig. 23.5 shows the mapping between the residual energy and battery voltage level. Particularly, 3000 J energy is consumed in the voltage range 3–2.6 V with running time of 8.4 h, 7000 J is

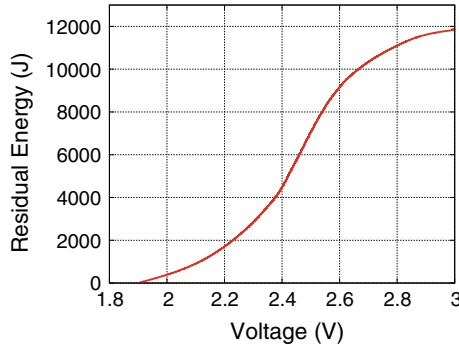


**Fig. 23.6** Battery energy profile

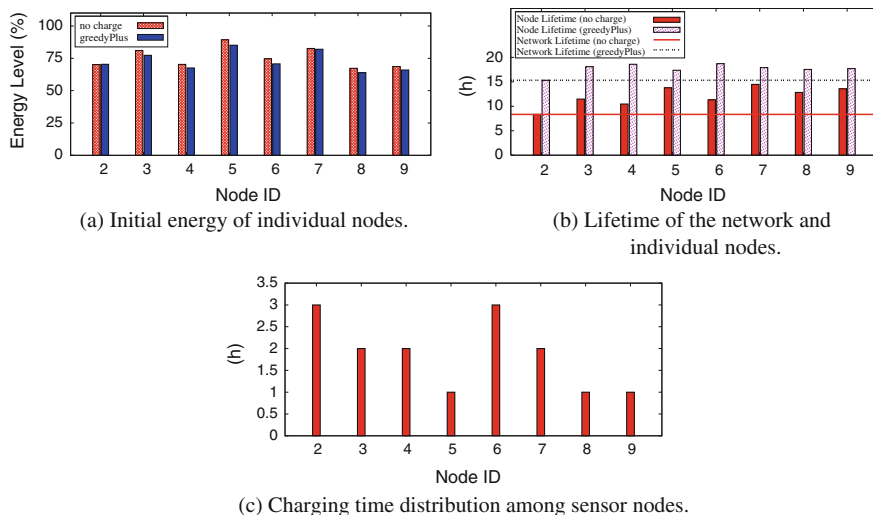


**Fig. 23.7** Evaluation results for line topology

consumed in the voltage range 2.6–2.2 V in a slower pace with 23 h running time and 2000 J is consumed in the voltage range 2.2–1.9 V with 5.3 h running time. The running time is measured with 100 % radio duty cycle. The result is achieved through five trials of experiments with 100 % radio duty cycle. To save experiment time, the batteries on each node are pre-charged to a certain voltage level up to 2.9 V before each experiment (normalized to energy level 100 % in the following figures), and the energy of a mote is assumed to be depleted when the voltage level of its batteries drops to 2.7 V (normalized to energy level 0 % in the following figures).

The power receiver in the node can charge the batteries when it receives energy from the MC, and the charger-receiver distance varies from 5 to 20 cm.

The sensor nodes are deployed in the line or grid topology as shown in Fig. 23.6, where neighboring nodes are two meters apart and the CC2420 radio transmission

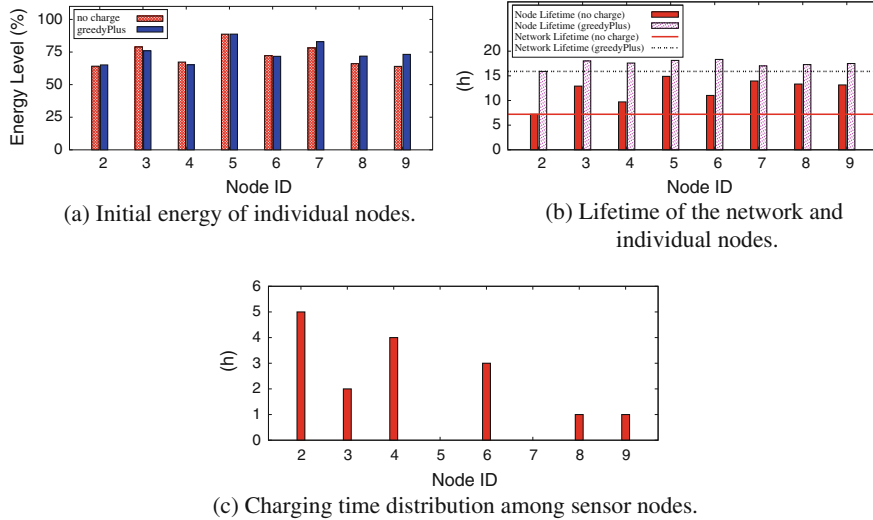


**Fig. 23.8** Evaluation results for grid topology

power is set to level 3 which results in a communication range of about 3.5 m. In both topologies, node 1 works as the sink connected to a PC with stable power supply and therefore it does not need to be charged.

During the experiments, each sensor node sends out a data packet every 16–20 s and an energy report every 10 min. The UPMA-XMAC protocol running on each sensor node sets its low power listening interval to 2 s. Every 10 min, the energy station runs the charging activity scheduling algorithm to adjust the charging plan.

### 23.3.4.2 Evaluation Results for Line Topology

As shown in Fig. 23.7b, the greedyPlus algorithm significantly improves the network lifetime from 8.3 to 15.3 h, an increase of 84 %. This is accomplished by charging more energy to nodes that have shorter lifetime if there were no charging. Particularly, nodes 2, 3, and 4 have higher energy consumption rates than other nodes because they forward more data packets; node 6 has low energy level at the beginning of the experiment. Hence, these nodes have shorter lifetime than others when there is no charging. Their lifetime (especially the lifetime of node 2) becomes the bottleneck of the network lifetime. As shown in Fig. 23.7c, the greedyPlus algorithm charges more energy to these nodes to extend their lifetime and consequently improve the network lifetime.

### 23.3.4.3 Evaluation Results for Grid Topology

For the grid topology, as shown in Fig. 23.8b, the greedyPlus algorithm improves the network lifetime from 7.2 to 15.92 h, an increase of 120 %. Nodes 2, 4, and 6 are charged the most as they have a higher energy consumption rate or a lower initial energy level. Node 5 is seldom charged due to its high initial energy level and node 7 is seldom charged for its being a leaf node with low energy consumption rate. Also being leaf nodes, nodes 8 and 9 however receive more charging than node 7 because they have less initial energy than node 7.

### 23.3.4.4 Discussion

The experiments not only verify the feasibility and effectiveness of our proposed design, but also demonstrate some phenomena that are hard to discover through theoretical derivations or simulations. Such discovery is helpful in enhancing our design and making it more effective in practice. As an example, we present in the following the phenomenon of abnormal voltage level reading which happens during and immediately after a node being charged. We also analyze its effects on the charging performance, and describe our solution to address the issue.

Figure 23.9a displays a charging trace in one experiment. Corresponding to this charging trace, Fig. 23.9b demonstrates the changes of node 2's voltage readings. Figure 23.9c shows the changes of node 2's voltage readings when there is no charging. It can be observed in Fig. 23.9b that, when node 2 is being charged (e.g., during time 25289–26516 s), its voltage reading increases very fast. However, the fast increase is “false” and not stable because, as also shown in Fig. 23.9b, immediately after the charging phase ends (e.g., during time 26516–30491 s), the voltage reading drops much more rapidly than the normal case shown in Fig. 23.9c.

If such instant measurements of energy levels are used directly as the input to the charging activity scheduling algorithm, the algorithm may output less efficient charging decisions. Specifically, a measured fast but false increase of energy level may mislead the algorithm to believe that the currently charged node has been charged with sufficient amount of energy and decide to charge another node; but immediately after the MC leaves, the fast drop of energy level will be measured, which may force the charging activity scheduling algorithm to schedule the MC back to charge the node again. The back-and-forth scheduling of the MC can waste energy and hence degrade the performance of the charging system.

To address this issue, in our design and implementation, when a node is being charged, its energy level that is just measured is not used directly as the input to the charging activity scheduling algorithm. Instead, its energy levels measured during a certain recent time frame (e.g., the past 10 min) are averaged and then scaled down by another certain constant (e.g., 100) to remove the abnormally sharp increase of its voltage reading during the charging time. According to the experiments, the benefit brought by this averaging and scaling technique is significant. Particularly,

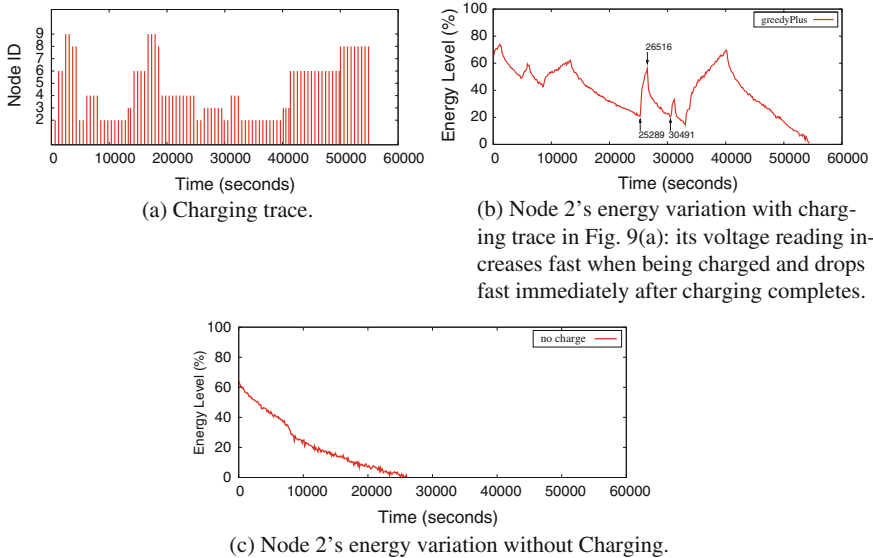


**Fig. 23.9** Abnormal voltage reading during and immediately after a node being charged

the average improvement of network lifetime is about 84 and 120 % for the line and grid topologies respectively when the technique is adopted, while the improvement is only about 40 % if the technique is not used.

### 23.3.5 Simulations

Extensive simulations have been conducted to evaluate the proposed schemes in large-scale networks. In the simulation, the network lifetime of naive, greedy and greedyPlus algorithms are measured and compared under different situations by varying the number of sinks, the system parameter  $k$  and the charging efficiency  $\eta$ .

#### 23.3.5.1 Simulation Setup

The proposed schemes and system are simulated in a custom simulator. In the simulations, 100 nodes are randomly deployed in a  $500 \times 500$  m field. Every sensor node is a data source which reports data packets to the sink at the rate of  $\lambda$ . It also sends one energy report every hour; hence, the energy station runs the charging activity scheduling algorithm once every hour.

The routing algorithm adopted in the simulations uses metric  $C_i = Tr_i * u^{1 - \frac{e_i}{E_s}}$  [16] to select routes. In the metric,  $u$  is a system parameter,  $e_i$

**Table 23.2** Default simulation parameters when evaluating charging activity scheduling algorithms

| Parameter  | Value |
|--|-------|
| Communication range of a sensor node(m)              | 70    |
| Battery capacity of a sensor node: $E_s$ (KJ)        | 10    |
| Battery capacity of MC: $E_c$ (KJ)                   | 2000  |
| Data packet generation rate: $r_i$ (packets/hour)    | 12    |
| The MC's charging power consumption: $\Lambda_c$ (W) | 3     |
| The MC's moving power consumption: $\Lambda_m$ (W)   | 50    |
| The MC's moving speed: $v$ (m/s)                     | 1     |
| The sensor's tx power consumption (J/packet)         | 0.05  |
| The sensor's rx power consumption (J/packet)         | 0.06  |
| System parameter $k$                                 | 5     |
| The MC's charging efficiency: $\eta$ (%)             | 1.5   |
| The number of sinks                                  | 4     |
| The routing metric                                   | ME    |

is node  $i$ 's residual energy and  $Tr_i$  is the sum of energy consumption for transceiving a packet at node  $i$ . This metric is a combination of the minimum energy ( $Tr_{ij}$ ) and max-min residual energy ( $u^{1-\frac{e_j}{E_s}}$ ) metrics. When  $u = 1$ , the metric is reduced to the minimum energy (ME) metric which is used to find the path that can minimize the network-wide energy consumption; when  $u > 1$ , it is reduced to an energy-aware (EA) metric that aims to balance energy consumption among all nodes in the network. We let  $u = 1$  or  $u = 100$  in the simulations. Table 23.2 lists other default simulation parameters.

### 23.3.5.2 Network Lifetime with Varying Number of Sinks

We first measure the lifetime when the number of sinks changes. If there are  $n$  sinks, the whole network field is divided evenly into  $n$  areas and one sink is placed at the center of each area. Figure 23.10a shows that all three algorithms can significantly improve the network lifetime (by at least 80 %) regardless of the number of sinks. Among these algorithms, the greedy and greedyPlus algorithms outperform the naive one as they can significantly reduce energy consumption on MC's movement, which is demonstrated in Fig. 23.10b, and therefore can use more energy to charge sensor nodes.

It is also found that, as the number of sinks increases, less improvement of network lifetime is achieved by the charging activity scheduling algorithms. Particularly, the greedyPlus algorithm extends the network lifetime by 117 % when there is one sink, but the ratio drops to 88 % when there are 9 sinks. This is due to the following reasons. The energy consumption rates of different sensor nodes become more even as the number of sinks increases. With the increase, more sensor nodes need to be charged

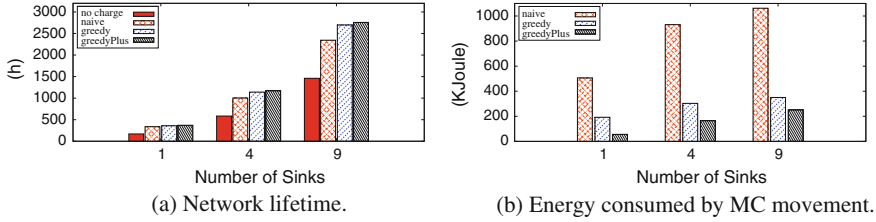


**Fig. 23.10** Effects of the number of sinks

to extend the network lifetime. As the MC's charging capacity and efficiency are bounded, increasing the number of charged sensor nodes decreases the amount of energy charged to each of these nodes. Consequently, the overall improvement in network lifetime decreases. The improvement of network lifetime is further reduced because the MC has to consume more energy in movement as it needs to charge more nodes, which decreases the amount of energy that can be used for charging sensor nodes. The phenomenon indicates that, the less even are the energy consumption rates among sensor nodes, the fewer sensor nodes need to be charged and the better performance can be achieved by the charging activity scheduling algorithms.

### 23.3.5.3 Network Lifetime with Varying $k$

The network lifetime extended by the greedy and greedyPlus algorithms does not increase linearly or significantly as  $k$  increases. This phenomenon is attributed to the following reasons. If the number of bottleneck nodes that constrain the network lifetime is less than  $k$ , increasing  $k$  does not improve the network lifetime as only the energy information about bottleneck nodes is useful for charging planning. If the number of bottleneck nodes is larger than  $k$ , the information of all the bottleneck nodes can still be gradually obtained and considered by the charging algorithms as the algorithms are run once every certain time interval and each running of the algorithm is based on the energy information of the  $k$  shortest-lifetime sensor nodes at the moment. As shown in Fig. 23.11b, a larger  $k$  does help in reducing the movement energy consumption as the information of more nodes is considered in charging planning. However, the benefit brought by increasing  $k$  is not significant and the benefit decreases as  $k$  gets large. In the simulations, we let  $k = 5$  by default.

### 23.3.5.4 Network Lifetime with Varying $\eta$

Due to the relatively low value of  $\eta$  (i.e., 1.5 %) in previous simulations, even when all of  $E_c = 2000$  KJ energy is used by the MC for charging, only 30 KJ can be received by sensor nodes. Hence, the charging efficiency has been a major constraint on improving the network lifetime. Figure 23.12 shows that the network lifetime can

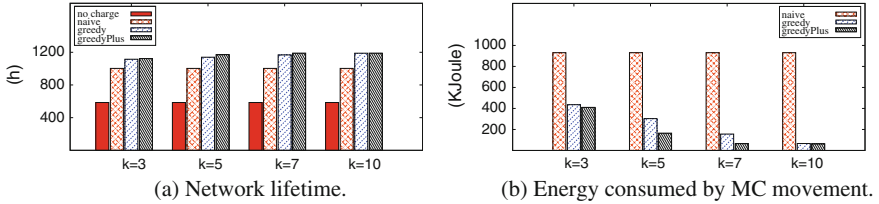
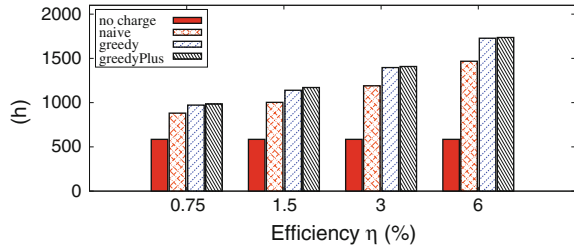


**Fig. 23.11** Effects of system parameter  $k$

**Fig. 23.12** Effects of charging efficiency  $\eta$



be significantly increased as  $\eta$  increases. Particularly, the greedyPlus algorithm can extend the network lifetime by about 100 % with  $\eta = 1.5 \%$  and the extension ratio rises to 200 % when  $\eta = 6 \%$ .

The charging efficiency can be increased through advance in charging technology. In fact, it can be increased through delicate sensor node deployment such as the aggregated sensor node deployment strategy proposed by Tong et al. [25]. Thus, when combined with the aggregated node deployment strategy, the performance of the proposed wireless charging system may be improved further.

### 23.3.5.5 Energy-Efficient Routing Versus Energy-Balanced Routing

When using the ME metric, the routing algorithm adopted in the simulations becomes an energy-efficient algorithm as it tends to find routes that consume the least total energy. When using the EA metric, the routing algorithm becomes an energy-balanced algorithm as it tends to find routes that distribute communication workload among all sensor nodes as evenly as possible. In a non-rechargeable network, the energy-balanced routing algorithm outperforms the energy-efficient algorithm in terms of network lifetime, but this may not be always true when sensor nodes can be charged. Extensive simulations have been conducted to study which of these two types of algorithms is more beneficial to our proposed system.

In our simulations,  $E_c$  (the total amount of energy carried by the MC) and  $\eta$  vary, and the achieved network lifetime is measured by running the greedyPlus algorithm. The results are shown in Fig. 23.13. As shown in the figure, the energy-balanced algorithm (EA) outperforms the energy-efficient algorithm (ME) when  $E_c$  or  $\eta$  is

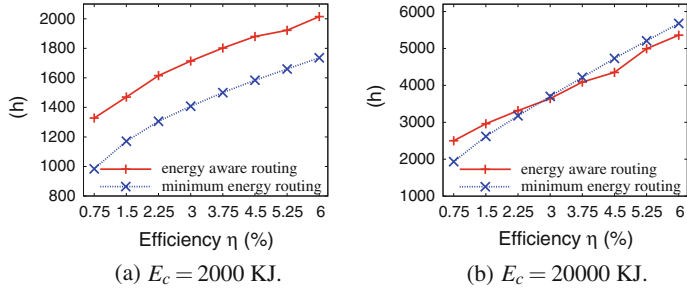


Fig. 23.13 Effects of the routing algorithm

small; however, ME outperforms EA when both  $E_c$  and  $\eta$  are large. The reasons behind the phenomena are as follows.

When the ME routing algorithm is used, nodes that are on multiple routing paths have higher communication overhead and thus become bottleneck nodes. When  $\eta$  or  $E_c$  is small, some of these bottleneck nodes cannot be recharged in a timely manner before their energy is used up though some other nodes may still have lots of energy left, which results in a short network lifetime. On the other hand, the EA routing algorithm tends to balance the energy consumption among nodes. With EA, the energy consumption rates of bottleneck nodes typically are lower than the bottleneck nodes in the network running ME, and hence their lifetime is also longer. Therefore, the network running EA can achieve a longer lifetime.

When  $E_c$  and  $\eta$  are large, bottleneck nodes in the network running ME are likely to be charged promptly. Hence, the charging algorithm can effectively balance the lifetime between bottleneck and non-bottleneck nodes as the EA routing algorithm does. Moreover, the ME algorithm consumes less network-wide energy than the EA algorithm. Resulted from these two effects, the network running ME can achieve longer lifetime than the one running EA.

### 23.3.6 Summary

In this section, we study the charging activity scheduling problem and propose several heuristic algorithms to plan charging activities. The key idea of these schemes is to dispatch a mobile charger to move around the network and charge energy to a selected set of lifetime-bottleneck sensor nodes. Both testbed and simulation experiments have been conducted to evaluate the performance of the proposed algorithms under various configuration parameters. The effectiveness of the algorithms on prolonging the sensor network lifetime has been clearly demonstrated.

As the protocols run by sensor nodes should be simple and localized, the system employs two well-known routing protocols when scheduling charging activities, the energy-balanced routing and energy-minimum routing, both of which are unaware of

wireless charging activities. The charging strategy adopted by the system is simply to charge nodes with the lowest residual nodal lifetime. Hence, the wireless charger only passively makes up for the energy deficiency in the bottleneck nodes caused by the routing activities; that is, the charging activities are passively affected by the routing activities. This may result in the following undesired consequences. If energy-minimum routing is used, nodes on the intersection of multiple energy-minimum routes may be overused even though the charger keeps charging them. When the energy consumption rates of these nodes exceed the charging capability, they deplete their energy quickly and the extension in the network lifetime is limited. Alternatively, if energy-balanced routing is used, the overall energy consumption in the network is increased as routes with longer length (and hence higher energy consumption) are used to bypass low-energy nodes which are on shorter and more energy-efficient routes. Hence, the energy replenished into the network may not be utilized efficiently. To further prolong the network lifetime, we develop advanced joint routing and charging activity scheduling scheme, called J-RoC, which is presented in Sect. 23.4.

## 23.4 Joint Routing and Wireless Charging Scheduling Scheme

To maximize the network lifetime under the constraint of limited charging capability, dynamic and imperfect communication environment, and heterogeneous node attributes, we further propose *J-RoC*, a practical joint routing and charging scheme, in this section. J-RoC aims to employ energy-balanced routing and energy-minimum routing in a balanced way to exploit their strengths while avoiding or mitigating the problems caused by using only one of them. For this purpose, J-RoC requires periodical information exchanges between sensor nodes and the charger. Based on the exchanges, the charger keeps track of the global energy status of the network, schedules its charging activities accordingly, and disseminates the charging schedule to the network. Meanwhile, sensor nodes use a carefully designed *charging-aware* routing metric to estimate their routing costs and make routing decisions; this way, sensor nodes are guided to balance between energy-balanced routing and energy-minimum routing while the protocols run by them remain simple and localized.

### 23.4.1 Overview

As shown in Fig. 23.14, J-RoC works through periodical interactions between the sensor nodes, the base station (BS) and the mobile charger (MC).

Every  $T_c$  time, the BS determines a charging schedule (i.e., charging time  $l_i$  for each sensor node  $i$ ) for the next  $T_c$  interval. As detailed in Sect. 23.4.3, the schedule is decided based on the following information reported by each node: its energy

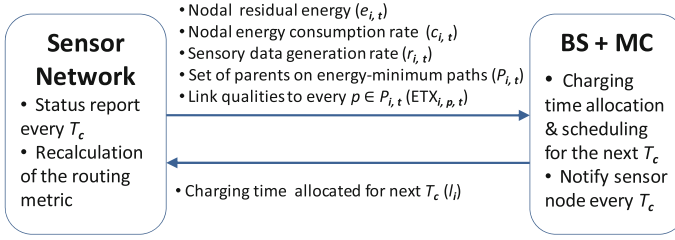


**Fig. 23.14** Overview of the proposed J-RoC scheme

consumption rate, residual energy level, data packet generation rate, set of parents on the energy-minimum paths to the sink, and the qualities of links to each parent. The BS disseminates the schedule to nodes and commands the MC to execute it. To reduce the control message overhead incurred by the periodical interactions between the BS and the network, the interaction interval can be configured to be much larger than the sensor data report interval. This will not compromise the system performance much, because the status of the network likely will not change significantly until a relatively large amount of data have been transmitted and received. For example, the data report interval is 2.5 s in our testbed experiments, and we set the interaction interval to be one hour. Evaluation results in Sect. 23.4.5 show that such a configuration performs well and yields a network lifetime that is reasonably close to the upper bound.

### 23.4.2 Routing Activity Scheduling

The Collection Tree Protocol (CTP) [8] is used as the routing protocol in J-RoC to report sensory data and nodal status to the BS. CTP is the default routing protocol in TinyOS 2.x. It designates a node in the network as the sink node. All other nodes recursively form routing trees rooted at the sink. Nodes periodically broadcast beacons which serve two purposes. First, they contain a field that the link estimator component of TinyOS uses to estimate the expected number of transmissions needed to send a packet successfully (ETX) to a node's neighbor, which roughly reflects the reciprocal of the packet reception ratio ( $\frac{1}{PRR}$ ) over the link. Secondly, nodes embed in these beacons an estimate of the total cost (zero for the sink node and  $\infty$  for others, initially) of routing a data packet to the sink from them. Non-sink nodes then collect the advertised routing costs from their neighbors, add their own one-hop routing costs, and select the neighbors with the lowest total routing costs as their parents. Since the beacons are broadcasted periodically, nodes can dynamically change their parents as routing costs fluctuate.

In J-RoC, each sensor node embeds two types of routing costs in CTP beacons. One contains the total cost of routing a packet to the sink along a charging-aware path. The other one contains the cost of delivering a packet along the energy-minimum path. Here, the energy-minimum path is defined as the path with the minimum total

energy consumption in delivering a packet from a source to a destination. Link quality has been considered in estimating the energy consumption. In J-RoC, all data packets are routed via the afore-mentioned charging-aware paths to the sink. Note that the paths are different from the conventional energy-balanced or energy-minimum ones; as to be elaborated, the selection of the paths considers simultaneously the effects of energy charging, energy balancing and energy efficiency.

### 23.4.2.1 Routing Cost

After receiving the costs from neighbor nodes, sensor node  $i$  calculates its *energy-minimum* routing cost ( $\mathcal{C}'_i$ ) as follows:

$$\mathcal{C}'_i = \min_{j \in N_i} \{\mathcal{C}'_j + ETX_{i,j,t}\}, \quad (23.1)$$

where  $N_i$  is the set of node  $i$ 's neighbor nodes,  $\mathcal{C}'_j$  is the routing cost of node  $j$  and  $ETX_{i,j,t}$  represents the expected number of transmissions needed to send a packet successfully over link  $(i, j)$ . Hence, Eq. (23.1) computes the minimum number of transmissions needed to deliver a packet from  $i$  to the sink successfully. Note that when links are in perfect condition, e.g.,  $ETX_{i,j,t} = 1$  for any  $i$  and  $j$ , the energy-minimum path becomes the shortest path.

The *charging-aware* routing cost at node  $i$  ( $\mathcal{C}_i$ ) is computed as follows:

$$\mathcal{C}_i = \min_{j \in N_i} \left\{ \mathcal{C}_j + u^{1 - \frac{\hat{e}_{i,j,t}}{E_s}} \right\}, \quad (23.2)$$

where  $\mathcal{C}_j$  is the routing cost of node  $j$ ,  $E_s$  is the battery capacity of a sensor node, and  $\hat{e}_{i,j,t}$  in routing metric  $u^{1 - \frac{\hat{e}_{i,j,t}}{E_s}}$  is computed as

$$e_{i,t} + (l_i - \varphi_{i,t})\Lambda_c\eta - t_r * c_{i,\hat{p}_{i,t},t} * \frac{ETX_{i,j,t}}{ETX_{i,\hat{p}_{i,t},t}}. \quad (23.3)$$

In Eq. (23.3),  $\varphi_{i,t}$  denotes how long node  $i$  has been charged in the current  $T_c$  interval,  $t_r$  represents the remaining time in the current  $T_c$  interval and  $\hat{p}_{i,t}$  denotes the parent of node  $i$  on the charging-aware path at time  $t$ . The term  $c_{i,\hat{p}_{i,t},t} * \frac{ETX_{i,j,t}}{ETX_{i,\hat{p}_{i,t},t}}$  estimates the nodal energy consumption rate if  $i$  switches its parent from  $\hat{p}_{i,t}$  to  $j$ . As the nodal energy consumption rate  $c_{i,t}$  is measured when  $\hat{p}_{i,t}$  is  $i$ 's parent, we abbreviate  $c_{i,\hat{p}_{i,t},t}$  to  $c_{i,t}$  in the following sections.

The purpose of using this routing cost is to balance the energy consumption in the possibly lossy wireless environment among sensor nodes in the presence of energy charging. If there is no energy charging, a well-known energy-balanced routing metric [12] is

$$u^{1 - \frac{e_{i,t}}{E_s}}. \quad (23.4)$$

Though the energy-balanced routing extends the network lifetime, different approaches should be adopted when energy charging is available. With energy charging, as much as possible energy should be replenished into nodes on the energy-minimum paths, so that these nodes can live longer and allow others to use them for packet routing, which can improve the energy utilization efficiency and hence prolong the network lifetime. However, as charging takes long time to be accomplished, nodes selected to be charged may not often maintain a high residual energy level, and therefore, energy-minimum paths may not often be chosen by other nodes to route their packets if Eq. (23.4) is used to compute the routing cost. Furthermore, in some environments, particularly in the 2.4 GHz frequency band, links could be highly lossy [22]. Without the knowledge of the link quality, lots of energy may be wasted on packet retransmissions over lossy links.

Our proposed routing metric addresses the above problems by factoring in the effects of charging that has been planned but not executed yet to estimate the routing cost, as well as the real-time link quality. Specifically,  $\hat{e}_{i,j,t}$  estimates node  $i$ 's residual energy at the end of the current  $T_c$  interval when it selects node  $j$  as parent, based on the knowledge of the charging schedule and link quality as in Eq. (23.3). Then,  $\hat{e}_{i,j,t}$  instead of  $e_{i,t}$  is used in the routing metric as in Eq. (23.2). Hence, nodes are led to choose paths to balance their residual energy at the end of the current  $T_c$ .

Figure 23.15 demonstrates how  $\hat{e}_{i,j,t}$  is estimated at time  $t = t_{curr}$ . Note that, in this example, the energy consumption rate of node  $i$  is assumed to be constant from the current time to the end of the  $T_c$  interval to simplify the estimation. Specifically, in Fig. 23.15,  $c_{i,t}$ ,  $e_{i,t}$ ,  $h_{i,t}$  are the energy consumption rate, nodal residual energy and charging rate at time  $t_{curr}$ , respectively.  $\varphi_{i,tcurr}$  is the amount of time that node  $i$  has been charged in this  $T_c$  interval,  $l_i$  is the amount of charging time allocated to node  $i$  in this  $T_c$  interval and  $l_i - \varphi_{i,tcurr}$  is the amount of remaining charging time. Assuming the future energy consumption rate does not change, Eq. (23.3) estimates the residual nodal energy at time  $(n + 1)T_c$ .

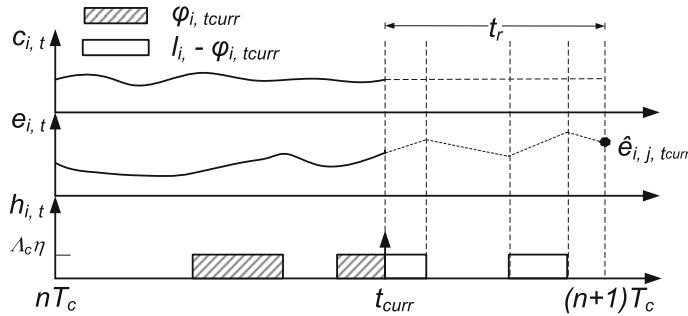


**Fig. 23.15** Computation of  $\hat{e}_{i,j,t}$

### 23.4.3 Charging Activity Scheduling

Every  $T_c$  time, sensor nodes report their nodal status to the BS, including residual energy level ( $e_{i,t}$ ), energy consumption rate ( $c_{i,t}$ ), sensory data packet generation rate ( $r_{i,t}$ ), set of parents on the energy-minimum paths to the sink ( $P_{i,t}$ ), and the expected number of transmissions to deliver a packet successfully to each parent  $p \in P_{i,t}$  ( $ETX_{i,p,t}$ ), based on which the BS schedules the charging activities for the next  $T_c$  interval.  $t$  is the time when node  $i$  reports this information to the BS. The charging activity scheduling algorithm works in two phases. Firstly, it selects a set of sensor nodes that should be charged in the next  $T_c$  interval. Secondly, it determines a sequence in which the sensor nodes are charged so that the movement time is minimized. It also distributes the amount of charging time  $l_i$  for the next  $T_c$  interval to each node in the sequence.

#### 23.4.3.1 Charging Energy Allocation

To allocate charging energy to sensor nodes, the BS first estimates the future nodal energy consumption rate, denoted as  $\hat{c}_{i,t}$ , for every sensor node  $i$ . Let  $\rho_i$  be the percentage of charging energy that should be allocated to sensor node  $i$  in one  $T_c$  interval. To maximize the network lifetime is to maximize

$$\min_i \left\{ \frac{e_{i,t}}{\hat{c}_{i,t} - \rho_i * \Lambda_c * \eta} \right\}, \quad (23.5)$$

where  $0 \leq \rho_i \leq 1$  and  $\sum_i \rho_i \leq 1$ . Algorithm 25 applies the binary search method to solve the optimization problem.

---

**Algorithm 25:** Charging activity scheduling algorithm to maximize the minimal nodal lifetime

---

```

1 Input:  $e_{i,t}$  and  $\hat{c}_{i,t}$  for every sensor node  $i$ 
2 Output:  $\rho_i$ 
1:  $low \leftarrow \min \frac{e_{i,t}}{\hat{c}_{i,t}}$ ,  $up \leftarrow \infty$ 
   /* low/up is the lower/upper bound of the network lifetime */
2:  $target \leftarrow low$ 
   /* target is the maximum achievable network lifetime */
3: while  $up - low > \epsilon$  do
4:   calculate  $\rho_i$  by solving  $target = \frac{e_{i,t}}{\hat{c}_{i,t} - \rho_i * \Lambda_c * \eta}$ ,  $\forall i \in V$ 
5:   if  $\sum_i \rho_i > 1$  then
6:      $up \leftarrow target$ 
7:      $target \leftarrow \frac{low+up}{2}$ 
8:   else
9:      $low \leftarrow target$ 
10:     $target \leftarrow (up = \infty) ? 2 * low : \frac{low+up}{2}$ 
11:   end if
12: end while
13: return  $\rho_i$ 
```

---

Next, we discuss how to estimate  $\hat{c}_{i,t}$ . For a sensor network without energy charging, the energy-balanced routing is favored to extend the network lifetime. The strategy, however, has a side-effect that packets may be routed through less energy-efficient paths to the sink when the energy-minimum paths have nodes with low residual energy. Hence, compared to the energy-minimum routing, the energy-balanced routing consumes more energy in transmitting packets. In a sensor network with wireless charging, the MC is able to charge the energy bottleneck nodes. Therefore, energy-minimum paths should be employed more often to improve the energy utilization efficiency in communication and thus to elongate the network lifetime. Based on this observation, the proposed charging activity scheduling algorithm should intentionally allocate more energy to nodes on energy-minimum paths in order to guide sensor nodes to utilize these paths more frequently. Therefore,  $\hat{c}_{i,t}$  is computed as

$$\hat{c}_{i,t} = \alpha c'_{i,t} + (1 - \alpha)c_{i,t}, \quad (23.6)$$

where  $c_{i,t}$  is the actual energy consumption rate reported by node  $i$ ,  $c'_{i,t}$  is the energy consumption rate of node  $i$  if all sensor nodes use energy-minimum paths, and  $\alpha$  is a value between 0 and 1, called the charging guiding coefficient. In the following, we present how to determine  $c'_{i,t}$  and  $\alpha$ .

Based on the collected  $P_{i,t}$  information from each sensor node, the BS can build a directed acyclic graph. Note that, if sensor node  $i$  has multiple energy-minimum paths towards the sink (e.g., several paths from  $i$  have the same value of Eq. (23.1)), we assume that it transmits packets evenly among these paths. Specifically, if  $i$  has  $k$  energy-minimum paths, it embeds all  $k$  energy-minimum parents and the corresponding link qualities to each parent in the status report to sink. As link qualities are usually stable in a relatively long run [32], we assume that the energy-minimum paths do not change much during one  $T_c$  interval as long as  $T_c$  value is in a reasonable range. Suppose each sensor node generates a packet at rate  $r_{i,t}$  in future, and all sensor nodes use energy-minimum paths to transmit packets. To transmit the packets for itself, the energy consumption rate at sensor node  $i$  is

$$\sum_{s \in S_{i,t}} e_{tx} * ETX_{i,n_{i,t}^s,t} * \frac{r_{i,t}}{|S_{i,t}|}, \quad (23.7)$$

where  $S_{i,t}$  denotes the set of energy-minimum paths from node  $i$  to the sink and  $n_{i,t}^s$  denotes the next hop node of  $i$  on the energy-minimum path  $s$ . To successfully forward packets generated by other nodes, the energy consumption rate at  $i$  is

$$\sum_{j \neq i} \sum_{s \in S_{j,t}} (e_{rx} * ETX_{b_{i,t}^s,i,t} + e_{tx} * ETX_{i,n_{i,t}^s,t}) * \frac{r_{j,t}}{|S_{j,t}|} * I_{i \in s}, \quad (23.8)$$

where  $I_{i \in s}$  is an indicator function whose value is 1 if and only if node  $i$  is on path  $s$  and  $b_{i,t}^s$  denotes the previous hop node of  $i$  on the energy-minimum path  $s$ .  $e_{tx}$  and  $e_{rx}$  are the expected energy consumed to transmit and receive a packet, respectively,

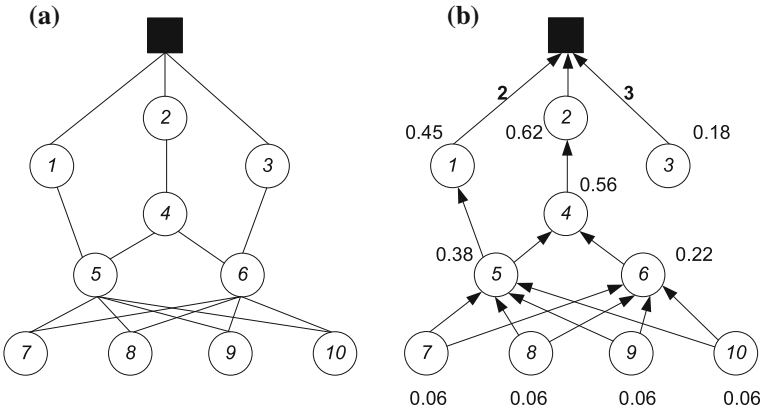


**Fig. 23.16** An example of calculating  $c'_{i,t}$  values

and the values depend on the specific underlying MAC protocols. Hence,  $c'_{i,t}$  can be computed by summing up Eqs. (23.7) and (23.8). Figure 23.16 shows an example of the above procedure. Suppose  $\forall i, j, r_{i,t} = 1$  pkt/s,  $e_{tx} = e_{rx} = 0.06$  J/pkt and  $ETX_{i,j,t} = 1$  except  $ETX_{3,sink,t} = 3$  and  $ETX_{1,sink,t} = 2$ . (a) shows the topology of a network with 10 source nodes and the black square represents the sink. (b) shows the  $c'_{i,t}$  value for each node. All routing paths connecting the sensor nodes and the sink are the energy-minimum ones. As node 4 needs two transmissions to reach the sink while node 3 needs three transmissions, path  $6 \rightarrow 4 \rightarrow 2$  is the energy-minimum path. Take node 4 for instance; for each of the nodes 7, 8, 9, and 10, it has three energy-minimum paths to the sink and two of them pass through node 4; for node 5, it has two energy-minimum paths to the sink and only one of them passes through node 4; for node 6, it only has one energy-minimum path to the sink and it passes through node 4. Therefore, the energy consumption rate for node 4 to relay the packets for nodes 5, 6, 7, 8, 9, and 10 is  $(\frac{2}{3} * 4 + \frac{1}{2} + 1) * (0.06 + 0.06) = 0.5$  J/s, the energy consumption rate for transmitting its own packets is 0.06 J/s; hence we have  $c'_{4,t} = 0.56$  J/s.

The value of the charging guiding coefficient  $\alpha$  is related to two factors. One factor is the relative charging capability of the MC, which is reflected by the ratio between the amount of energy that can be charged per time unit (i.e.,  $\Lambda_c * \eta$ ) and the whole network energy consumption rate (i.e.,  $\sum_i c_{i,t}$ ). When the charging capability is relatively strong, e.g.,  $\frac{\Lambda_c * \eta}{\sum_i c_{i,t}}$  is large, a larger  $\alpha$  values is favorable. This means that the charging scheme should guide more packets to be delivered along the energy-minimum paths as the capability of the MC is strong enough to compensate the energy deficiency in time, and accordingly, more energy should be allocated to nodes on the energy-minimum paths. When the capability is low, a smaller  $\alpha$  value should be used instead. In addition, the  $u$  value also affects the allocation of the chargeable energy. When  $u = 1$ , each sensor node uses a fixed shortest path to route packets, and therefore is not affected by the charging schedule. When  $u > 1$ , each sensor

node selects its path based on the routing metric. As the routing metric in Eq. (23.2) is affected by the charging schedule, the routing decision can be guided by adjusting the charging schedule. Besides, the larger is  $u$ , the more effective is the guidance. Considering both factors, we define  $\alpha$  as

$$\alpha = 1 - u^{-\frac{\Lambda_c * \eta}{\sum_i c_{i,t}}}. \quad (23.9)$$

With this formula, when  $u = 1$ ,  $\alpha$  is equal to 0 and  $c'_{i,t}$  has no impact on the consumption rate estimation. When  $u > 1$ , the stronger is the relative charging capability, the larger is  $\alpha$  and the more weight is given to  $c'_{i,t}$  when computing  $\hat{c}_{i,t}$ .

### 23.4.3.2 Charging Sequence Determination

In practice, the moving speed of a robot is limited [3] (e.g., between 0.2 and 2 m/s). Too frequent movement may waste time that can be used to charge sensor nodes. Hence, given an allocation plan of charging energy, as computed above, it is important to determine a charging sequence to implement the allocation with as little movement as possible.

The procedure of the charging sequence determination works as follows and an example is given in Fig. 23.17. Figure 23.17a shows the positions of 5 nodes and triangle 0 stands for the MC. Figure 23.17b gives a naive charging sequence where the MC visits the nodes in the ascending order of nodal lifetime  $\frac{e_{i,t}}{\hat{c}_{i,t}}$ . The shadow width represents the moving time. Figure 23.17c shows the procedure of merging  $\rho_1$  and  $\rho_4$  into  $\rho_2$ . Figure 23.17d shows the final charging sequence rearranged by the VRPTW solver.

- Given the percentage of the charging energy  $\rho_i$ , the sensor nodes are sorted ascendingly according to their nodal lifetime  $\frac{e_{i,t}}{\hat{c}_{i,t}}$ . For example, Fig. 23.17a illustrates the position and nodal lifetime of 5 nodes where the  $e_i$  values are 750, 300, 150, 750, 900 J and the  $\hat{c}_{i,t}$  values are 0.015, 0.02, 0.03, 0.015, 0.01 J/s. The output of Algorithm 25 produces  $\rho_i$  values as 4, 32, 60, 4, 0 % and *target* as 55714 s assuming  $\Lambda_c \eta = 0.045$  J/s. Figure 23.17b shows the sorting result. It also gives us a naive charging sequence with possibly high movement overhead, e.g.,  $T_e = T_c - T_m^{0,3,2,1,4}$  where  $T_m^{0,3,2,1,4}$  is the total moving time along the trajectory  $0 \rightarrow 3 \rightarrow 2 \rightarrow 1 \rightarrow 4$  and  $T_e$  is the effective charging time.  $\rho_i * T_e$  is the amount of charging time allocated to node  $i$ .
- The  $\rho_i$  value of the maximum lifetime node is iteratively merged to that of the minimum lifetime node until the battery ceiling of the minimum lifetime node is reached, i.e.,  $\frac{E_s - e_{i,t}}{\Lambda_c \eta} < \rho_i * T_e$ . For example, in Fig. 23.17c,  $\rho_4$  is merged into  $\rho_3$  at first. If the updated  $\rho_3$  does not result in a battery ceiling hit, we update  $T_e = T_c - T_m^{0,3,2,1}$  and  $\rho_3 = \rho_3 + \rho_4$ . Then, the algorithm tends to merge  $\rho_1$  into  $\rho_3$ . If the merging leads to a battery ceiling hit, we merge a part of  $\rho_1$  value into  $\rho_2$ . This procedure ends when the maximum nodal lifetime is less than  $T_c$  or only one node exists after merging.

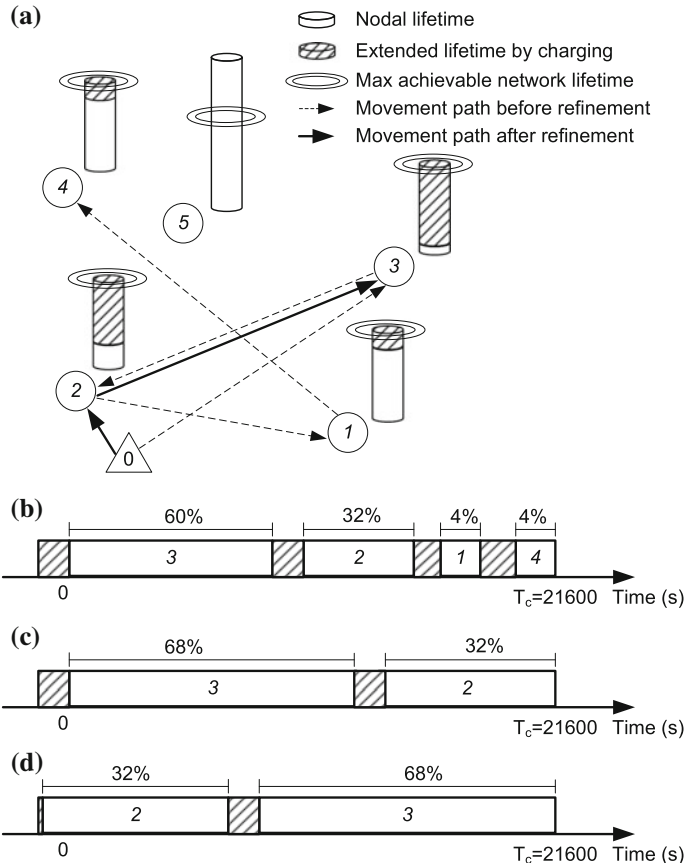


**Fig. 23.17** An example of the movement refinement

- VRPTW solver [9], which solves the vehicle routing problem with time window [14], is called to rearrange the visiting sequence to further reduce the movement time. Here, the nodal lifetime is the deadline for each node to be visited. For example, in Fig. 23.17d, the rearranged sequence has  $T_m^{0,2,3} < T_m^{0,3,2}$  and  $T_e = T_c - T_m^{0,2,3}$ .  $\rho_i * T_e$  is the amount of charging time allocated to node  $i$  and the final charging sequence ready for execution is  $\langle\langle 2, \rho_2 T_e \rangle, \langle 3, \rho_3 T_e \rangle \rangle$ . Obviously, the amount of effective charging time after the movement refinement is much larger than the one before and thus more energy is replenished into the network.

### 23.4.4 Performance Upper Bound of J-RoC

Here, we assume the sensory data packet generation rate  $r_{i,t}$  of a node does not change during the network lifetime and thus  $r_{i,t}$  is denoted as  $r_i$ . When the MC's movement delay is ignored and the link qualities are perfect, the optimal solution can be described by the following linear programming formulation.

$$\max \quad T,$$

s.t.:

$$T * r_i + \sum_{j \in N_i} f_{j,i} = \sum_{j \in N_i} f_{i,j}, \quad (23.10)$$

$$T * \sum_i r_i = \sum_{j \in N_{BS}} f_{j,BS}, \quad (23.11)$$

$$e_{tx} * \sum_{j \in N_i} f_{i,j} + e_{rx} * \sum_{j \in N_i} f_{j,i} \leq E_s + a_i * \Lambda_c * \eta, \quad (23.12)$$

$$\sum_i a_i \leq T, \quad (23.13)$$

$$f_{i,j}, a_i \geq 0. \quad (23.14)$$

Here,  $T$  is the network lifetime.  $f_{i,j}$  is the total number of packets transmitted from nodes  $i$  to  $j$  during the network lifetime.  $a_i$  is the total amount of time that the MC charges  $i$ . Constraints (23.10) and (23.11) reflect the flow conservation requirements. Constraint (23.12) reflects that the energy used for transmission and reception should be smaller than  $E_s$ —the battery capacity of a sensor node—plus the energy charged from the MC. Constraint (23.13) states that the MC could charge one node at a time and thus the total charging time cannot exceed the network lifetime. The output  $\langle f_{i,j}, a_i \rangle$  is the joint routing and charging solution. It specifies the number of data packets transmitted over the link  $(i, j)$  and the total charging time on node  $i$  so that the network lifetime can be maximized.

However, the LP formulation does not take the MC's movement and packet retransmissions into account. Hence, it provides an upper bound of the achievable network lifetime. This formulation is used in both testbed experiment and simulation to evaluate the performance of the proposed J-RoC scheme.

### 23.4.5 Experiments

Experiments have been performed on the prototype system to evaluate the performance of proposed schemes. In the experiments, we evaluate (i) the network lifetime upper bound according to Sect. 23.4.4 and the actually achieved network and nodal lifetime, when the energy-balanced routing is used without charging (tagged as *no charge* in the figures), the energy-balanced routing combined with the greedy-Plus scheme (Sect. 23.3.3.2) is used, and the J-RoC scheme is used, respectively; (ii) the average packet rate (including both the self-generated and the forwarded data packets) of individual nodes; and (iii) the distribution of charging time to individual nodes. As simulation results in Sect. 23.3.5 have shown that greedyPlus scheme performs better with energy-balanced routing than with energy-minimum routing, we only show the results of greedyPlus with energy-balanced routing in the experiment and simulation evaluations. Parameter  $u$  is set to 1000.

#### 23.4.5.1 Experimental Setup

In the experiments, ten TelosB sensor nodes are deployed according to the topology shown in Fig. 23.16a. The neighboring nodes are two meters apart and the CC2420 radio transmission power is set to level 3 which results in a 3.5 m communication range. The sink node is connected to a PC with stable power supply and does not need to be charged. During the experiments, each sensor node generates a data packet every 2.5 s. A modified X-MAC [1] protocol is run on each sensor node with a Low Power Listening interval of 250 ms and default channel checking time of 50 ms. The  $T_c$  length is one hour to reschedule the charging activities.

To save experiment time, the evaluation is conducted when the voltage varies from 3 to 2.6 V, where the energy level is 100 % when the voltage reading is 3 V and the battery is assumed to be completely depleted at voltage level 2.6 V.

#### 23.4.5.2 Overall Evaluation Results of J-RoC

Figure 23.18a shows the network lifetime upper bound and the nodal lifetime of individual nodes. The network lifetime upper bound is 30 h while the achieved network lifetime is 14.9 h (bounded by node 3), 20.5 h (bounded by node 5), and 25.5 h (bounded by node 1) for no charge, greedyPlus and J-RoC respectively. The advantage of J-RoC on prolonging the network lifetime is demonstrated in two aspects in the figure. First of all, compared to the no charge case, the ratio of network lifetime improvement is about 71 % (from 14.9 to 25.5 h); compared to the greedyPlus scheme, the ratio of improvement is about 24 % (from 20.5 to 25.5 h). Moreover, J-RoC achieves 85 % of the network lifetime upper bound (25.5 h out of 30 h). Secondly, the J-RoC scheme helps to reduce the standard deviation of the nodal lifetime which results in more efficient usage of the energy. Specifically, the standard devia-

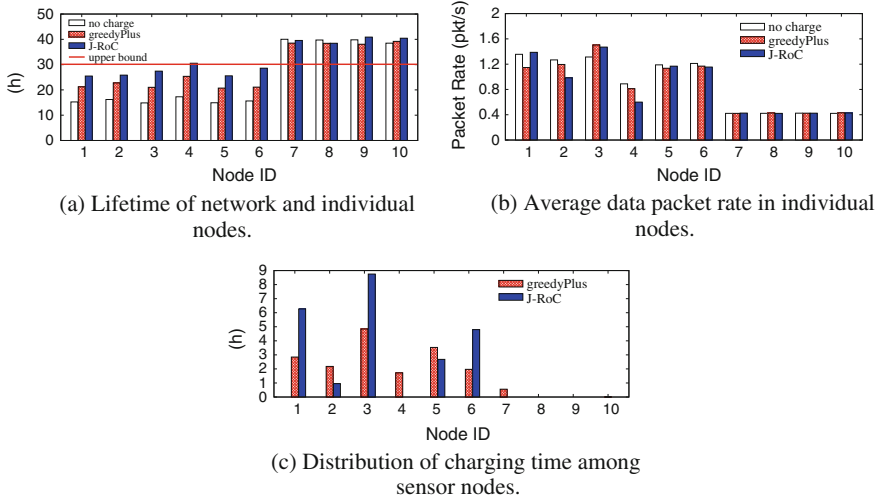


Fig. 23.18 Experimental results

tion of the nodal lifetime is 6.6 h for J-RoC, 8.6 h for greedyPlus and 12.3 h when there is no energy charging.

The improvement in network lifetime shown by Fig. 23.18a is achieved by guiding nodes to use energy-minimum paths more frequently and allocating more charging energy to nodes on these paths. The average packet rate shown in Fig. 23.18b and the charging time allocation depicted in Fig. 23.18c reveals these behaviors in detail.

As shown by Fig. 23.18b, nodes 1, 2 and 3 have forwarded quite different numbers of packets when different schemes are used, though they are all one-hop away from the sink. With no charge, these nodes are equally used and their packet rates are all around 1.3 pkt/s because the energy-balanced routing is used. When J-RoC is used, node 2's packet rate drops to 0.95 pkt/s, which is significantly lower than the packet rates of nodes 1 and 3 (i.e., 1.45 pkt/s and 1.55 pkt/s, respectively). When the greedyPlus scheme is used, node 2's packet rate is approaching 1.3 pkt/s and the packet rate of node 3 is much higher than that of node 1 and node 2 respectively. Figure 23.18c shows that the charging patterns to nodes 2 and 4 are different when different schemes are used. With greedyPlus, both nodes 2 and 4 are charged with 4 h in total, but only node 2 is charged in J-RoC and the charging time is less than 1 h. These differences are attributed to the following reasons. First of all, in greedyPlus, the routing decisions are made without the knowledge of charging activities, and therefore, packets are routed in the energy-balanced manner by using paths through nodes 1, 2, and 3 evenly. The J-RoC scheme, on the other hand, tends to guide nodes to utilize the energy-minimum paths more frequently. Also, if a node has multiple energy-minimum paths that can be used, it is guided to use them in a balanced way. Hence, fewer packets go through node 2, more packets are forwarded by nodes 1 and 3, and the numbers of packets passing nodes 1 and 3 are similar. Second, the charging

decisions made by greedyPlus are simply to balance nodal lifetimes, without considering routing activities in the network. Therefore, both nodes 2 and 4 are charged with a significant amount of energy as they consume a significant amount of energy to forward packets toward the sink. Differently, the J-RoC scheme makes charging decisions through considering two factors in a balanced manner: guiding nodes to use energy-minimum paths more often, and balancing nodal lifetimes. Consequently, nodes 2 and 4 are seldom charged as they are not on energy-minimum paths and they consume less energy to forward packets than nodes 1 and 3.

In general, the differences in the nodes' packet rates and the allocated charging time among individual nodes reveal the principle behind the design of the J-RoC scheme. The experimental results have demonstrated the advantage of J-RoC on improving the network lifetime through proactively guiding the routing activities and delivering the energy to where it is needed. When J-RoC is used, more packets are routed through the energy-minimum paths and more charging energy is allocated to nodes on these paths.

### 23.4.6 Simulations

Extensive simulations have been conducted in a custom simulator to evaluate the performance of J-RoC in large-scale networks. We measure the network lifetimes achieved by the J-RoC scheme, the greedyPlus scheme (Sect. 23.3.3.2), and the upper bound network lifetime derived in Sect. 23.4.4 under different scenarios with varying  $T_c$  interval, routing metric parameter  $u$ , charging efficiency  $\eta$ , data generation rate  $r_i$  and the moving speed of the MC  $v$ . In order to compare with the upper bound network lifetime whose calculation assumes a fix data packet generation rate over time, we assume  $r_{i,t} = r_i$  in the simulation. Note that the calculation of the upper bound of network lifetime does not factor in  $T_c$ ,  $u$  and  $v$ ; hence, its value remains constant as these parameters change. In addition, we also study the effectiveness of the movement refinement strategy described in Sect. 23.4.3 through comparing the J-RoC scheme with its naive version that does not have this refinement (tagged as J-RoC-Naive in the figures).

#### 23.4.6.1 Simulation Setup

In the simulations, 100 nodes are randomly deployed to a  $500\text{ m} \times 500\text{ m}$  field. The base station and the sink are placed in the center of the field. Table 23.3 lists the default simulation parameters. As the charging activity scheduling interval  $T_c$  is much larger than the data report interval (default 6 h compared to 4 min), the overhead of the nodal status information collection and charging activity scheduling information dissemination is neglected in the simulation.

**Table 23.3** Default simulation parameters when evaluating joint routing and charging activity scheduling algorithms

| Parameter   | Value |
|---|-------|
| Communication range of a sensor node (m)                    | 70    |
| Battery capacity of a sensor node: $E_s$ (kJ)               | 10    |
| Energy consumed for MC's charging operation: $A_c$ (W)      | 3     |
| Energy consumed for transmitting a packet: $e_{tx}$ (J/pkt) | 0.05  |
| Energy consumed for receiving a packet: $e_{rx}$ (J/pkt)    | 0.06  |
| The MC's charging efficiency: $\eta$ (%)                    | 1.5   |
| The MC's moving speed: $v$ (m/s)                            | 1     |
| System parameter $u$  | 1000  |
| Data packet generation rate: $r_i$ (packets/hour)           | 15    |
| Charging activity scheduling interval: $T_c$ (h)            | 6     |

### 23.4.6.2 Network Lifetime with Varying $T_c$

In the proposed scheme, the charging activity scheduling happens every  $T_c$  interval, and the length of  $T_c$  affects both the movement overhead of the MC and the amount of energy that an individual node can be charged. To investigate how the scheduling frequency affects the network lifetime, we first evaluate the performance of all the schemes when the  $T_c$  interval changes.

Figure 23.19a shows that the network lifetime achieved by J-RoC outperforms greedyPlus and J-RoC-Naive under various  $T_c$  values and approaches 95 % of the upper bound of network lifetime. In Fig. 23.19a, the lifetimes achieved by both the J-RoC and the greedyPlus schemes decrease slightly as  $T_c$  increases. This is due to the fact that the charging decisions are made based on the prediction of the network status for the  $T_c$  period and they cannot adapt to the network changes effectively if  $T_c$  is long. However, even when  $T_c$  is as long as 24 h in our simulation, J-RoC can still achieve 90 % of the upper bound of the network lifetime.

Figure 23.19a also shows that the difference between the network lifetime achieved by J-RoC and J-RoC-Naive decreases as  $T_c$  increases. This is because the number of nodes to be charged in the J-RoC-Naive scheme is independent of the length of  $T_c$ . When  $T_c$  increases and charging is scheduled less frequently, the MC stays with a node for a longer time and moves less frequently as well. Therefore, the total movement time decreases and more time could be utilized for charging. Finally, J-RoC and J-RoC-Naive achieve the similar lifetime when  $T_c$  is long enough (e.g., 24 h in the simulation).

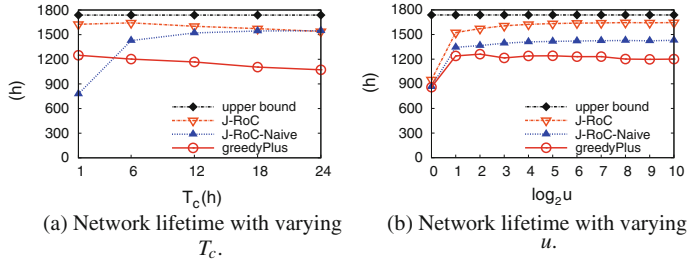


**Fig. 23.19** Achieved network lifetime comparison with varying  $T_c$  and  $u$

### 23.4.6.3 Network Lifetime with Varying $u$

As the value of  $u$  affects both the routing metric and the charging schedules in J-RoC, we vary  $u$  and measure the achieved network lifetime by all schemes. The results are plotted in Fig. 23.19b.

Compared to  $u = 1$ , the performance of all schemes improves significantly once  $u$  is greater than 1, as the energy-balanced routing avoids depleting the energy of a partial set of nodes and hence elongates the network lifetime. Among them, J-RoC outperforms greedyPlus and J-RoC-Naive under various  $u$  values. For instance, when  $u = 1024$ , greedyPlus, J-RoC-Naive and J-RoC achieve 69, 82 and 95 % of the upper bound of network lifetime, respectively.

When the value of  $u$  increases, the performance of J-RoC gradually improves since the charging scheme can guide the routing activities more effectively as described in Eq. (23.9). For example, J-RoC achieves 90 % of the upper bound of network lifetime when  $u = 2$ , and achieves 95 % of the upper bound when  $u \geq 64$ .

### 23.4.6.4 Network Lifetime with Varying $\eta$

Current wireless charging technology has a relatively low charging efficiency which is affected by the distance between the energy transmitter and the receiver. However, the wireless charging efficiency can be increased as the technology advances in the future. In fact, it can also be increased through delicate sensor node deployment [25]. On the other hand, due to the navigation inaccuracy, the distance between the MC and the wireless charging receivers may be relatively long and further decreases the  $\eta$  value. As the energy charging efficiency (e.g.,  $\eta$ ) depends on how close the MC could reach each sensor node, we show the performance of all the schemes as the charging efficiency  $\eta$  varies in Fig. 23.20a.

Compared to other schemes, the network lifetime achieved by the greedyPlus scheme ascends the most slowly when  $\eta$  increases. This is because a larger  $\eta$  value allows more energy to be captured by a sensor node. Once a node is charged by the MC, its high nodal energy attracts more traffic, which easily makes itself the energy depletion hot-spot and thus the MC has to keep charging and saving it from

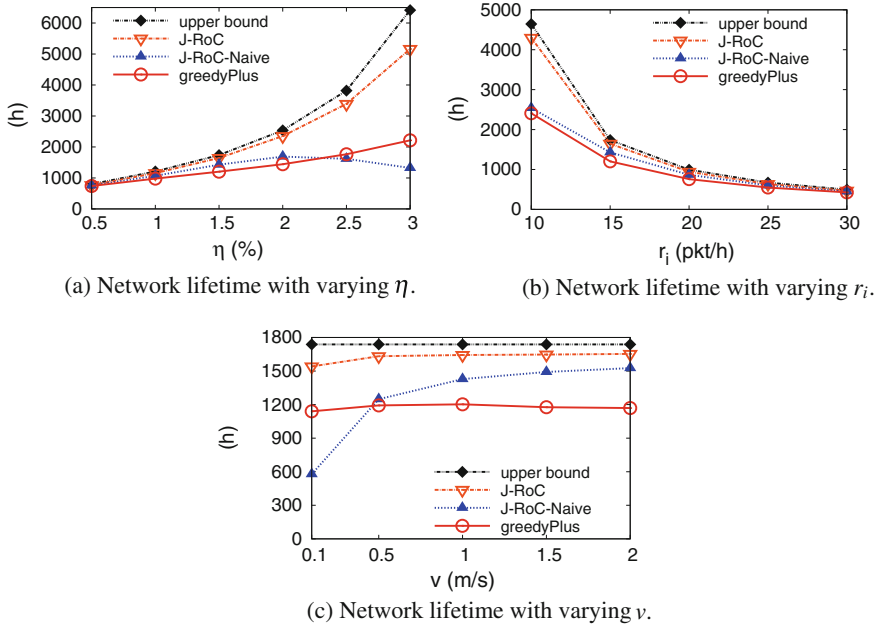


**Fig. 23.20** Achieved network lifetime comparison with varying  $\eta$ ,  $r_i$  and  $v$

being depleted. As the trend continues, the charger is stuck with this node and the opportunities of other nodes to be charged are deprived of. The larger is  $\eta$ , the more intense is this effect. This effect is eliminated in J-RoC which jointly plans the routing and charging activities.

It is also found that the performance of J-RoC-Naive, which does not refine the movement, drops the fastest among all schemes when  $\eta$  is large. This phenomenon can be explained as: the increased  $\eta$  value enables the MC to visit and charge more nodes in one  $T_c$  interval, and the movement time increases accordingly without careful movement planning; the J-RoC scheme, on the other hand, alleviates the increasing movement time problem via the movement refinement procedure and outperforms all other schemes.

#### 23.4.6.5 Network Lifetime with Varying $r_i$

Different sensory data generation rates may result in different network-wide distribution of energy and workload, which may affect the performance of J-RoC. To study the impact, we vary the values of  $r_i$ , measure the network lifetime achieved by all the schemes and plot the results in Fig. 23.20b.

Compared to other schemes, J-RoC performs the best and well adapts to various distribution of energy and workload. It accomplishes around 94 % of the upper bound of network lifetime as the value of  $r_i$  varies widely. On the other hand, both greedyPlus and J-RoC-Naive achieve a smaller fraction of the upper bound when  $r_i$  is small, e.g., only 58 % of the upper bound when  $r_i = 10$  pkt/h. This is due to the following reasons. When  $\eta$  is fixed, the smaller is  $r_i$ , the stronger is the relative charging capability of the MC. J-RoC can make better use of the relatively stronger charging capability to prolong the network lifetime, while the performance of greedyPlus may be degraded because the afore-mentioned effect that the MC is stuck to an energy-depletion hot-spot and J-RoC-Naive may waste time and energy for movement.

### 23.4.6.6 Network Lifetime with Varying $v$

In practice, the moving speed of the MC affects the movement time in all the evaluated schemes and the impact is shown in Fig. 23.20c. Obviously, as the moving speed of the MC increases, less time is wasted on the movement and more energy can be replenished into the network. Therefore, the network lifetime achieved by all schemes improves as  $v$  increases. Since J-RoC conducts the movement refinement, its performance remains almost the same as  $v$  changes and achieves about 95 % of the upper bound of network lifetime when  $v \leq 0.5$  m/s. On the other hand, J-RoC-Naive approaches 88 % of the upper bound when  $v = 2$  m/s while the achieved fraction is only 33 % when  $v = 0.1$  m/s. This result illustrates the effectiveness of the movement refinement in Sect. 23.4.3.

## 23.5 Conclusions

In this chapter, we present the design of a wireless chargeable sensor network system, and several practical and efficient wireless charging and routing activity scheduling schemes to prolong the network lifetime. Both testbed experiments in the prototype system and extensive simulations in large-scale networks are conducted to evaluate the prototype system and proposed scheduling schemes. The evaluation results demonstrate that the propose schemes significantly elongates the network lifetime compared to existing wireless charging based schemes under various system configurations.

Towards the future research, there are more practical issues left open. For example, the geographical conditions may constrain the movement trajectory of the MC and make some nodes inaccessible. This issue shall be factored into the new scheme or protocol design. In addition, how to overcome the limited charging capability of a single mobile charger in the network may be an interesting problem. Efficient coordination and scheduling algorithms among multiple MCs, and jointly with networking protocol design may be posed as practically important research problems.

Finally, it's also worth investigating how to incorporate the wireless charging technology with other energy replenishment or conservation technology such as data aggregation [5, 28, 31], node deployment [4, 25], mobile data collection (mobile sink) [17, 21], solar energy harvesting, etc. A joint design scheme may leverage the strength of multiple techniques while overcoming individual limitations, and the network lifetime can be further prolonged.

## References

1. Buettner, M., Yee, G.V., Anderson, E., Han, R.: X-MAC: a short preamble MAC protocol for duty-cycled wireless sensor networks. In: ACM SenSys (2006)
2. Chang, J., Tassiulas, L.: Energy conserving routing in wireless ad-hoc networks. In: IEEE INFOCOM (2000)
3. Dantu, K., Rahimi, M., Shah, H., Babel, S., Dhariwal, A., Sukhatme, G.S.: Robomote: enabling mobility in sensor networks. In: ACM IPSN (2005)
4. Dutta, P., Hui, J., Jeong, J., Kim, S., Sharp, C., Taneja, J., Tolle, G., Whitehouse, K., Culler, D.: Trio: enabling sustainable and scalable outdoor wireless sensor network deployments. In: ACM IPSN (2006)
5. Fan, K., Liu, S., Sinha, P.: Scalable data aggregation for dynamic events in sensor networks. In: ACM SenSys (2006)
6. Fan, K.W., Zheng, Z., Sinha, P.: Steady and fair rate allocation for rechargeable sensors in perpetual sensor networks. In: ACM SenSys (2008)
7. Garcia: <http://www.acroname.com>
8. Gnawali, O., Fonseca, R., Jamieson, K., Moss, D., Levis, P.: Collection tree protocol. In: ACM SenSys (2009)
9. JOpt.NET: <http://www.dna-evolutions.com>
10. Jose, S.M., Mur-mir, J.O., Amirtharajah, R., Ch, A.P., Lang, J.H.: Vibration-to-electric energy conversion. IEEE Trans. Very Large Scale Integr. (VLSI) Syst. **9**(1), 64–76 (2001)
11. Kansal, A., Potter, D., Srivastava, M.B.: Performance aware tasking for environmentally powered sensor networks. ACM SIGMETRICS Perform. Eval. Rev. **32**(1), 223–234 (2004)
12. Kar, K., Kodialam, M., Lakshman, T.V., Tassiulas, L.: Routing for network capacity maximization in energy-constrained ad-hoc networks. In: IEEE INFOCOM (2003)
13. Kurs, A., Karalis, A., Robert, M., Joannopoulos, J.D., Fisher, P., Soljacic, M.: Wireless power transfer via strongly coupled magnetic resonances. Science **317**, 83–86 (2007)
14. Lenstra, J.K., Kan, A.H.G.R.: Complexity of vehicle routing and scheduling problems. Networks **11**(2), 221–227 (1981)
15. Li, Q., Aslam, J., Rus, D.: Online power-aware routing in wireless ad-hoc networks. In: ACM MobiCom (2001)
16. Lin, L., Shroff, N.B., Srikant, R.: Asymptotically optimal energy-aware routing for multihop wireless networks with renewable energy sources. IEEE/ACM Trans. Netw. **15**(5), 1021–1034 (2007)
17. Luo, J., Hubaux, J.P.: Joint mobility and routing for lifetime elongation in wireless sensor networks. In: IEEE INFOCOM (2005)
18. Park, C., Chou, P.: AmbiMax: autonomous energy harvesting platform for multi-supply wireless sensor nodes. In: IEEE SECON (2006)
19. Powercast: <http://www.powercastco.com>
20. Rao, S., Chiao, J.C.: Body electric: wireless power transfer for implant applications. IEEE Microw. Mag. **16**(2), 54–64 (2015)
21. Shi, Y., Hou, Y.T.: Theoretical results on base station movement problem for sensor network. In: IEEE INFOCOM (2008)

22. Srinivasan, K., Kazandjieva, M.A., Agarwal, S., Levis, P.: The beta-factor: measuring wireless link burstiness. In: ACM SenSys (2008)
23. Toh, W.Y., Tan, Y.K., Koh, W.S., Siek, L.: Autonomous wearable sensor nodes with flexible energy harvesting. *IEEE Sens. J.* **14**(7), 2299–2306 (2014)
24. Tong, B., Li, Z., Wang, G., Zhang, W.: On-demand node reclamation and replacement for guaranteed area coverage in long-lived sensor networks. In: EAI QShine (2009)
25. Tong, B., Li, Z., Wang, G., Zhang, W.: How wireless power charging technology affects sensor network deployment and routing. In: IEEE ICDCS (2010)
26. Tong, B., Wang, G., Zhang, W., Wang, C.: Node reclamation and replacement for long-lived sensor networks. In: IEEE SECON (2009)
27. Wireless Power Consortium: <http://www.wirelesspowerconsortium.com/>
28. Xiang, Q., Xu, J., Liu, X., Zhang, H., Rittle, L.: When in-network processing meets time: complexity and effects of joint optimization in wireless sensor networks. In: IEEE RTSS (2009)
29. Zhang, F., Hackworth, S.A., Liu, X., Li, C., Sun, M.: Wireless power delivery for wearable sensors and implants in body sensor networks. In: Engineering in Medicine and Biology Society (EMBC), 2010 Annual International Conference of the IEEE, pp. 692–695 (2010)
30. Zhang, F., Liu, X., Hackworth, S., Sclabassi, R., Sun, M.: In vitro and in vivo studies on wireless powering of medical sensors and implantable devices. In: Life Science Systems and Applications Workshop (2009)
31. Zhang, J., Jia, X., Xing, G.: Real-time data aggregation in contention-based wireless sensor networks. *ACM Trans. Sens. Netw.* (2010)
32. Zhao, J., Govindan, R.: Understanding packet delivery performance in dense wireless sensor networks. In: ACM SenSys (2003)

# Chapter 24

## Joint Design of Solar Energy Harvesting with Wireless Charging

Cong Wang, Ji Li, Fan Ye and Yuanyuan Yang

**Abstract** Although wireless charging delivers energy reliably, it still faces regulatory challenges to provide high power density without incurring health risks. In clustered Wireless Sensor Networks (WSNs), relatively low energy supplies from wireless chargers cannot meet the rising energy demands from cluster heads. Fortunately, solar energy harvesting provides high power density without health risks whereas its energy supply is subject to weather dynamics. This chapter introduces a new framework with hybrid energy sources—cluster heads can use solar panels to scavenge solar energy and the rest of nodes are powered by wireless charging. The network is divided into three hierarchical levels. On the first level, we study a discrete placement problem of where to deploy solar-powered cluster heads that can minimize overall cost. Then the discrete problem is extended into continuous space for better solutions using the *Weiszfeld algorithm*. On the second level, we establish an energy balance in the network. A distributed cluster head reselection algorithm is proposed to regain energy balance when sunlight is unavailable. On the third level, we first consider the tour planning problem by combining wireless charging with mobile data gathering in a joint tour. We then propose a polynomial-time scheduling algorithm to find appropriate hitting points on sensors' transmission boundaries for data gathering. Our simulation results demonstrate that network with hybrid sources can reduce battery depletion by 20 % and save operating cost by 25 % compared to previous works.

---

C. Wang (✉) · J. Li · F. Ye · Y. Yang

Department of Electrical and Computer Engineering,  
State University of New York, Stony Brook, NY 11794, USA  
e-mail: cong.wang@stonybrook.edu

J. Li  
e-mail: ji.li@stonybrook.edu

F. Ye  
e-mail: fan.ye@stonybrook.edu

Y. Yang  
e-mail: yuanyuan.yang@stonybrook.edu

## 24.1 Introduction

We have seen extensive studies of wireless charging in WSNs. By instrumenting wireless energy transmitters on mobile chargers (MCs) [1–7] or at strategic locations [8–10], sensors can be charged conveniently without wires or plugs. Although wireless charging is a promising technology that can power sensors reliably, rising energy demands in the network also increase the risks of electromagnetic exposure [8]. As a result, energy transmitters must comply with standards from Federal Communication Commission (FCC) and limit their emitting power to human safe power densities ( $<1\text{ mW/cm}^2$  [11]). Nevertheless, nodes at data aggregation points such as cluster heads in a clustered WSN usually consume very high energy (10–100 mW) due to data traffic. Clearly, there is a mismatch between limited energy supply from MCs and rising energy demands from cluster heads so it can potentially cause battery depletion on such nodes and network interruptions.

Another competitive technique that harvest solar energy is risk-free and has much higher power density. As shown in [12], solar harvesting through photovoltaic conversion enjoys power density of  $15\text{ mW/cm}^2$ , which is more than an order of magnitude to wireless charging. A solar panel similar to sensor's size is sufficient to meet the energy demands of cluster heads. However, availability of sunlight is subject to dynamics in the environment. Not only weather conditions would have a direct impact on the harvesting rates, but also a series of spatiotemporal factors such as sunrise, sunset times, locations and their surroundings would affect deployments of harvesting sensors.

After discussing the pros and cons of both technologies, in this chapter, we propose a hybrid framework to make use of their advantages and overcome their drawbacks. In the new framework, a majority of nodes are still wireless-powered nodes (WNs) due to the low costs of charging coils. A small number of solar-powered nodes (SNs) are responsible for aggregating data (cluster heads) due to the relatively higher manufacturing and deploying costs. In normal situations, a fleet of MCs move around the field to serve recharge requests from WNs and collect data from SNs. In contrast to WNs, SNs' energy from the ambient source is self-sufficient.

The hybrid framework provides effective energy replenishment at cluster heads for them to complete high volume data transmissions while the rest of WNs can be recharged by MCs on demand. We first study a placement problem to answer the question: how many SNs are needed and where should we deploy them such that the total cost is minimized. We formulate it into a *facility location problem* [13–16] to minimize the total cost of packet routing and node deployment. Then we further optimize the locations of SNs within a cluster in continuous space and propose an iterative mechanism based on the Weiszfeld algorithm [17]. Second, we find how to regain energy balance in the network when sunlight is unavailable in cloudy/raining days. We discover that a simple and effective way is to use a smaller cluster size so we can reduce energy consumptions. To realize this design in the network, we develop a distributed algorithm to select some WNs as temporary cluster heads until solar energy is available. On the third level, we focus on the question of how to schedule MCs to complete wireless charging and data gathering in the same tour. Different

from previous works that directs the MCs to visit exact SN locations [7], for data gathering, it is only necessary for MCs to move into SN's transmission range. Based on this observation, we develop a polynomial-time route improvement algorithm that can take shortcuts through SN's neighborhood to reduce MCs' moving cost. Next, we start our discussion from the first level of SNs.

## 24.2 Related Works

In this section, we discuss some related works of environmental energy harvesting and tour planning algorithms. Environmental energy harvesting provides an alternative to extend network lifespan. Renewable energy from the environment such as solar, wind, vibration and thermal can be used effectively to power sensor nodes. A majority of previous efforts focus on energy management of sensors [18–20]. In [18], a power management scheme to maximize sensors' duty cycles is proposed. A moving average is used to predict future energy income and sensor's duty cycles are adjusted accordingly. Algorithms from adaptive control theory are adopted in [20] to handle environmental energy dynamics. Joint energy management and resource allocation is considered in [19] for optimizing network performance. A local algorithm is developed to adjust sensors' sampling rates and adapt to the battery states. In [21], a mobile data collector is adopted in solar energy harvesting networks to alleviate possible congestions caused by insufficient ambient energy. However, an inevitable drawback of these networks that purely rely on environmental energy is that the network operations would be interrupted when such ambient energy sources are unavailable (e.g., during cloudy/raining days in a solar harvesting network). In contrast, the hybrid framework in this paper incorporates a combination of hybrid energy sources so that steady network operations can be expected.

Tour planning of mobile vehicles for data collection in WSNs has been studied [22–25]. The problem can be modeled as the well-known Traveling Salesmen Problem with Neighborhood (TSPN) [26–28] in which the salesman aims to find the shortest tour through city neighborhoods (could be arbitrary shapes). For wireless networks, because of the omnidirectional propagation of electromagnetic waves, the neighborhoods are usually assumed to be circles. In [23], the tour planning problem is formulated into a mixed-integer program and a spanning tree covering algorithm is proposed. The algorithm directs the vehicles to visit exact node locations for data gathering. Further cost saving can be achieved if the node's transmission range is considered. In [25], new algorithm is proposed to improve current solutions for TSPN. It first determines the shortest TSP routes among sensors. Then it searches along transmission boundaries to find the best hitting points. In [24], the problem is formulated into a label-covering tour problem. A complete graph is first constructed to represent all possible paths between nodes. The objective is to find an optimal path that covers all the nodes in their transmission ranges. In [22], a progressive tour construction method is proposed. The method exploits the overlaps of transmission ranges of neighboring nodes so that the vehicle can take shortcuts through sensor's

neighborhood. This method works effectively when there exist a significant amount of overlaps among nodes' transmission ranges. Different from all the previous works, a tour consists of both WNs and SNs in our framework so our focus is how to minimize tour lengths by taking advantage of SNs' neighborhoods in a joint wireless charging and data gathering tour.

### 24.3 First Level: Placement of Solar-Powered Sensors

In this section, we formalize the placement problem of SNs and describe an algorithm to solve it. We denote the sets of SNs and WNs by  $\mathcal{S}$  and  $\mathcal{N}$ , respectively. For simplicity, we first study a discrete version of the problem by assuming SNs can only be colocated at WNs' locations,  $\mathcal{S} \subset \mathcal{N}$ . We consider a graph  $G = (V, E)$  where vertices are sensor nodes and edges are connections between them.  $c_{ij}$  is the routing cost between nodes  $i$  and  $j$ , which is the energy consumed for transmitting packets.  $f_i$  is the deploying cost of SN  $i$ , and  $f_i = p_s/l_i$ , where  $l_i$  is the solar strength at node  $i$ .

We scale  $c_{ij}$  by how much the base station has paid for consuming per watt of energy to convert energy units of  $c_{ij}$  into monetary cost. We introduce two decision variables  $x_{ij}$  and  $y_i$ .  $x_{ij}$  is 1 if WN  $j$  is assigned to SN  $i$ ; otherwise, it is 0.  $y_i$  is 1 if we place an SN at  $i$ ; otherwise, it is 0. Initially, all WNs are candidate locations to place the SNs. Our objective is to minimize the total cost by finding the optimal locations for SNs.

$$\mathbf{P1} : \quad \min \sum_{i \in \mathcal{S}} \sum_{j \in \mathcal{N}} c_{ij} x_{ij} + \sum_{i \in \mathcal{S}} f_i \quad (24.1)$$

**Subject to**

$$\sum_{i \in \mathcal{S}} x_{ij} \geq 1; j \in \mathcal{N} \quad (24.2)$$

$$x_{ij} \leq y_i; i \in \mathcal{S}, j \in \mathcal{N} \quad (24.3)$$

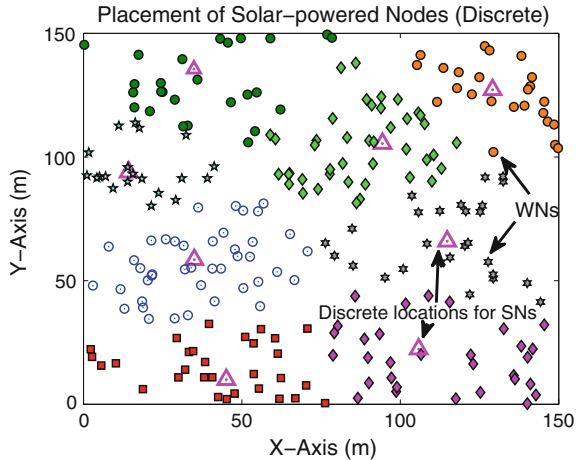
$$x_{ij}, y_i \in \{0, 1\}; i \in \mathcal{S}, j \in \mathcal{N} \quad (24.4)$$

Constraints (24.2) and (24.3) states that each WN is only connected to one SN. We briefly describe an algorithm [14] that can solve the problem efficiently. For each SN  $i$ , we introduce a set  $\mathcal{B}_i$  to represent its connected WNs ( $\mathcal{B}_i \subseteq \mathcal{N}$ ). In each step, the algorithm selects node  $i^*$  with the minimum average cost

$$i^* = \arg \min_{i \in \mathcal{N}} \left( \sum_{j \in \mathcal{B}_i} c_{ij} + f_i - \sum_{j \in \mathcal{B}'_i} (c_{i'j} - c_{ij}) \right) / |\mathcal{B}_i|. \quad (24.5)$$

Node  $i'$  is a deployed SN that WN  $j$  has already connected to.  $\mathcal{B}'_i$  is the set of these already connected WNs which would be benefited by altering their connections to the new SN  $i$  so a saving of routing cost  $\sum_{j \in \mathcal{B}'_i} (c_{i'j} - c_{ij})$  should be deducted from

**Fig. 24.1** An example of SN placements in discrete space (colocate with WNs)



the total cost. To find the minimum average cost for each candidate SN  $i$ , we sort the cost in an ascending order and select the least one so a number of  $|\mathcal{B}_i|$  WNs will be chosen each time. After  $i^*$  is found, we deploy an SN at its location and update all the WNs in  $\mathcal{B}_i \cup \mathcal{B}'_i$  to connect with node  $i^*$ . The iteration continues to add SNs until all WNs are connected to them. The algorithm has  $\mathcal{O}(N^3)$  complexity and is summarized in Algorithm 26. We show an example of finding SNs' locations in Fig. 24.1. A number of 8 SNs are selected to organize 250 WNs into clusters. Their locations are colocated at some WN locations marked by triangles.

---

**Algorithm 26:** SN placement algorithm

---

**Input** : Set of WN  $\mathcal{N}$ .

**Output:** Set of SN  $\mathcal{S}$  and  $\mathcal{B}_i, i \in \mathcal{S}$ .

```

1 while  $\mathcal{N} \neq \emptyset$  do
2   Find  $i^* = \arg \min_{i \in \mathcal{N}} \left( \sum_{j \in \mathcal{B}_i} c_{ij} + f_i - \sum_{j \in \mathcal{B}'_i} (c_{ij} - c_{ij}) \right) / |\mathcal{B}_i|$ ;
3   Deploy  $i^*$ , connect  $\forall j \in \mathcal{B}_i \cup \mathcal{B}'_i$  to  $i^*$ ;
4    $\mathcal{N} \leftarrow \mathcal{N} - \mathcal{B}_i$ ;
5 end while

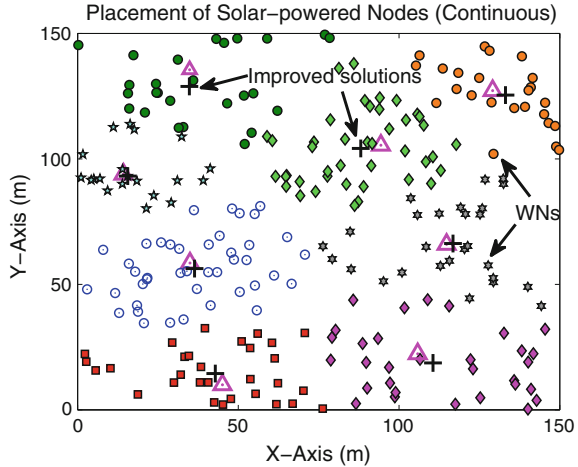
```

---

### 24.3.1 Placement of SNs in Continuous Space

Since MCs enjoy the freedom to place SNs at any feasible location in the field, in this subsection, we explore the placement of SNs in continuous space. Clearly, the continuous problem is much harder than its discrete version. Thus we start from the discrete results and relax them into the continuous domain. Intuitively, the asymptotic behavior of the discrete problem should approach the continuous problem when the

**Fig. 24.2** Improve SN locations in continuous space



number of nodes is infinite. However, in our problem, the number is limited. Thus discrete results provide a feasible, suboptimal solution to the continuous problem.

From the discrete version of the problem, a set  $\mathcal{S}$  is obtained ( $\mathcal{S} \subseteq \mathcal{N}$ ) with the corresponding cluster set  $\mathcal{B}_i, \forall i \in \mathcal{S}$ . Our objective is to minimize the intra-cluster routing cost and this problem is known as the well-known *Weber problem* [17, 29]. In other words, it aims to find the geometric mean for the set of  $\mathcal{B}_i$  nodes. To solve this problem, we apply the widely used Weiszfeld algorithm in each cluster [17]. It is proved in [29] that the Weiszfeld algorithm can converge to an optimum using a recursive function. The operation of the algorithm is illustrated below. First, we initialize SN's location  $x_0$  (from the output of SPP) at node  $i$ 's coordinate. A recursive function  $W(\cdot)$  that computes the  $k$ -th iteration is,

$$W(x_k) = \left( \sum_{j=1}^{|\mathcal{B}_i|} \frac{\alpha_j}{c(x_k, j)} \right) / \left( \sum_{j=1}^{|\mathcal{B}_i|} \frac{1}{c(x_k, j)} \right) \quad (24.6)$$

where  $d(x_k, j)$  is the distance between location  $x_k$  and node  $j$ , and  $\alpha_j$  is the coordinate of node  $j \in \mathcal{B}_i$ . The iteration continues by executing  $x_{k+1} = W(x_k)$  until location changes are less than a small error bound  $\delta$ . The algorithm is summarized in Algorithm 27 (Fig. 24.2).

---

**Algorithm 27:** Extension of Weiszfeld algorithm

---

**Input** : SN's location  $x_0$  obtained in the discrete problem.

**Output:** SN's location in continuous space at convergence.

**1 while**  $x_{k+1} - x_k > \varepsilon$  **do**

**2**     $W(x_k) = \left[ \sum_{j=1}^{|\mathcal{B}_i|} \frac{\alpha_j}{c(x_k, j)} \right] / \left[ \sum_{j=1}^{|\mathcal{B}_i|} \frac{1}{c(x_k, j)} \right];$

**3**     $x_{k+1} = W(x_k);$

**4 end while**

---

## 24.4 Second Level: Wireless-Powered Sensors

In this section, we study the second level which consists of wireless-powered sensors. The objective is to maintain network energy balance on WNs in different weather conditions (i.e. sunny and cloudy days). We first derive network energy balance during sunny days when SNs are fully functional. For convenience, let us denote the number of SNs from the output of SN placement algorithm by  $s = |\mathcal{S}|$  and the maximum hop count from WN to its assigned SN by  $h$ . Second, during cloudy/raining days, SNs cannot effectively harvest enough energy so the energy balance no longer holds. In this case, we further study how to reestablish such balance by refilling the energy gap. We use several WNs to act as temporary cluster heads and derive a numerical range of WN cluster heads first followed by a distributed algorithm to determine which WNs should be selected as new cluster heads. Some of the additional notations used in the following analysis are summarized in Table 24.1.

### 24.4.1 Energy Balance

Energy consumptions in the network is analyzed below. For  $s$  shortest path routing trees originated from SNs, the total energy consumption in  $T$  time is,

$$\begin{aligned}
 E_c &= \sum_{j \in \mathcal{N}} \left( \lambda(e_t + e_s) + \sum_{i \in \mathcal{C}_j} \lambda(e_t + e_r) \right) T \\
 &\leq \sum_{i=1}^h \left( N_i(e_t + e_s) + \sum_{\substack{j=i+1, \\ i \neq h}}^h N_j(e_t + e_r) \right) \lambda s T \\
 &= \left( \left( \frac{2}{3}h^3 - \frac{1}{2}h^2 - \frac{1}{6}h \right) (e_t + e_r) + h^2(e_t + e_s) \right) \pi r^2 \rho \lambda s T
 \end{aligned} \tag{24.7}$$

**Table 24.1** List of notations

| Notation        | Definition   |
|-----------------|--|
| $\rho$          | Node density of uniformly randomly distributed sensors                                   |
| $r$             | Transmission range of sensors  |
| $e_t, e_r, e_s$ | Energy consumptions for sensors to transmit, receive and generate a packet, respectively |
| $m$             | Number of Mobile Chargers  |
| $\sigma$        | Percentage of cloud cover (from weather reports)   |
| $C_h$           | Battery capacity of sensor nodes   |
| $T_r$           | Recharge time of sensor's battery from zero to full capacity                             |
| $v$             | Moving speed of MCs  |

where  $\mathcal{C}_j$  is the set of child nodes of  $j \in \mathcal{N}$ ,  $N_i = (2i - 1)\pi r^2 \rho$ . The inequality holds because (1) clusters can be approximated by circles of radius  $R = hr$  which consists of  $h$  concentric rings [30]; (2) summation of consumptions from all circle-shaped clusters has overlapping areas between neighboring clusters.

The harvested solar energy can be estimated by the empirical model in [31]. The model provides a year-round analysis of solar radiations from weather stations and relates power levels to a quadratic equation on the time  $t$  of the day,

$$E = (a_1(t + a_2)^2 + a_3)(1 - \sigma). \quad (24.8)$$

The shape of the quadratic function from Eq. (24.8) is determined by parameters  $a_1 - a_3$  which vary seasonally for different months. For example, for the month of May,  $a_1 = -1.1$ ,  $a_2 = -13.5$  and  $a_3 = 43.5$ .  $t_1$  and  $t_2$  are the respective time of sunrise and sunset ( $t_1 = -\sqrt{-\frac{a_3}{a_1}} - a_2$ ,  $t_2 = \sqrt{-\frac{a_3}{a_1}} - a_2$ ).  $\sigma$  is the percentage of cloud cover from weather reports. For  $T$  days, energy harvested by SNs is

$$E_s = s \sum_{i=1}^T \int_{t_1}^{t_2} [a_1(t + a_2)^2 + a_3](1 - \sigma_i) dt \quad (24.9)$$

The wireless energy replenished by MCs into the network is governed by the battery charging rates  $C_h/T_r$ . Thus, the amount of wireless energy replenished by  $m$  MCs in  $T$  can be calculated by  $E_w = (mTC_h)/T_r$ ,  $m \neq 0$ . Then network energy balance is achieved when

$$\begin{aligned} E_c &\leq E_s + E_w \\ E_c &< \left[ \left( \frac{2}{3}h^3 - \frac{1}{2}h^2 - \frac{1}{6}h \right) (e_t + e_r) + h^2(e_t + e_s) \right] \pi r^2 \rho \lambda s T \\ &\leq s \sum_{i=1}^T \int_{t_1}^{t_2} [a_1(t + a_2)^2 + a_3](1 - \sigma_i) dt + \frac{mTC_h}{T_r} \end{aligned} \quad (24.10)$$

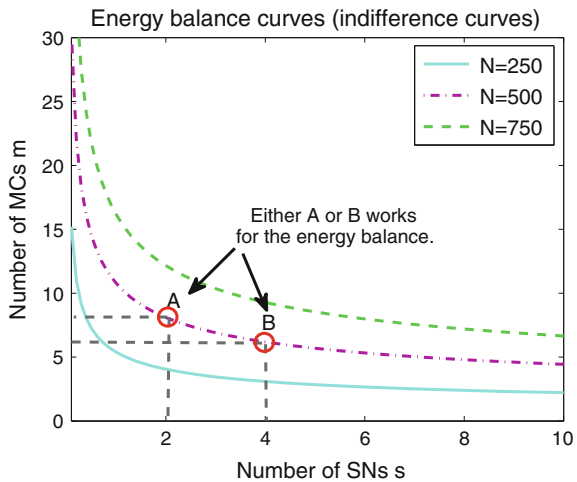
Since  $\pi(hr)^2 s \geq L^2$ , we have  $\sqrt{L^2/(sr^2\pi)} \leq h$ . By plugging it into Eq. (24.10) and taking approximation  $e_t \approx e_r$ , we obtain a relationship between  $s$  and  $m$

$$\frac{LT_r e_t \rho \lambda}{3\sqrt{\pi} C_h r} \left( \frac{4L^2}{\sqrt{s}} - \pi r^2 \sqrt{s} \right) - Xs + \left( \frac{1}{2}e_t + e_s \right) \frac{L^2 \rho \lambda T_r}{C_h} \leq m, \quad (24.11)$$

where  $X$  is

$$X = \left( \frac{T_r}{C_h T} \sum_{i=1}^T (1 - \sigma_i) \right) \left( \frac{a_1}{3} t^3 + a_1 a_2 t^2 + (a_1 a_2^2 + a_3) t \right) \Big|_{t=t_1}^{t=t_2}. \quad (24.12)$$

**Fig. 24.3** Energy balance curves for different network sizes



#### 24.4.2 Energy Balance Curves

The relationship between  $s$  and  $m$  in Eq. (24.11) is better to be explained graphically. Figure 24.3 shows a collection of energy balance curves when  $N = 250\text{--}750$ . Any point on a curve serves the same purpose for balancing network energy and there is no preference between choosing how many SNs or MCs as long as the energy balance holds. In fact, these curves can also be interpreted as the *indifference curves* in microeconomics. An indifference curve shows a collection of different goods between which the consumer is indifferent and every point on the curve results in the same utility. Here, every point on the curve would serve the same purpose of balancing energy demands and supplies. For example, when  $N = 500$ , point A requires two SNs and eight MCs, which is equivalent to point B of four SNs and six MCs. It is interesting to see that the slope of the curve indicates that adding SNs reduces MCs at a diminishing marginal rate. This is because when the number of SNs is small, adding more SNs helps alleviate routing cost significantly (saving energy); however, this benefit gradually diminishes as more SNs are deployed.

#### 24.4.3 Adaptive Reselection of Cluster Heads

A drawback of solar energy is that sunlight is not always available. In particular, during raining seasons, network could experience consecutive cloudy or raining days and SNs are unable to harvest enough energy. To sustain network operation, our framework should adaptively change cluster heads to WNs for aggregating sensed

data. In this section, we first discuss how to maintain energy balance in the absence of solar energy. Then, we propose an algorithm to reappoint some WNs as cluster heads.

#### 24.4.3.1 Maintaining Energy Balance

Because the number of MCs  $m$  has been determined, we cannot expect more energy income from the energy replenishing side. To this end, we consider how to reduce energy consumption in order to restore energy balance. The energy gap during cloudy days should be filled by reducing consumption for at least the same amount. Having more cluster heads in the network can effectively reduce energy consumption because more aggregation points would shorten packet relay paths and traffic loads at intermediate hops. In other words, this is equivalent to having smaller  $k$ -hop clusters ( $k < h$ ). We want to know how many WN cluster heads are needed given  $k$ . The solar radiation model in the previous section indicates the energy harvested peaks when  $\sigma \approx 0$  (perfect weather condition). Let us denote the number of new WN cluster heads by  $s'$  ( $s' > s$ ). The maximum amount of energy harvested is  $E_s^*$  when  $\sigma = 0$  in the ideal case.  $E_c(h)$  is the energy consumption with  $h$ -hop clusters.  $X_c(k)$  is the energy consumption for each  $k$ -hop cluster (plug  $k$  into Eq. (24.7) and omit  $s'$ ). Since  $E_s^* \leq E_c(h) - s'X_c(k)$ , the range of  $s'$  is,

$$\frac{L^2}{\pi(kr)^2} < s' \leq \frac{E_c(h) - E_s^*}{X_c(k)}. \quad (24.13)$$

By fixing  $k$ , any  $s'$  satisfying Eq. (24.13) can make sure energy balance of the network. Next, we develop a distributed algorithm to assign some WNs as cluster heads.

#### 24.4.3.2 Head Reselection Problem

In this subsection, we further explore the *Head Reselection Problem* (HRP) which reduces the cluster size to  $k$  hops with  $s'$  cluster heads satisfying Eq. (24.13). On one hand, the number of such nodes should be kept minimal to save MCs' moving cost since MCs will traverse through WN cluster heads for data collections. On the other hand, for heads to cover all the nodes within  $k$  hops,  $s'$  should be sufficiently large; otherwise, clusters will exceed  $k$  hops and more likely break the energy balance. Hence, our objective is to select a minimum number of heads and ensure that the shortest path from any node to its nearest head does not exceed  $k$  hops.

We leverage the range in Eq. (24.13) as a basis for our analysis. In general, as the number of  $s'$  increases, hop distance from a node to its nearest head should decrease. Thus, we can start from the lower bound and increase  $s'$  iteratively until

all the nodes are covered in  $k$  hops or the upper bound is reached. To find which WNs should become cluster heads, we extend the *furthest first traversal* algorithm proposed in [32]. The algorithm selects the node with the maximum distance from the current node to become the head in the next round. Unfortunately, the algorithm cannot be applied directly to our problem because: (1) it is centralized and not efficient to implement in distributed WSNs at runtime; (2) it may lead to inefficient selections. A new head might be chosen in the vicinity of an established one thereby leaving a large overlap between neighboring clusters. This is not efficient at all and increases the risks to violate Eq. (24.13). Hence, we follow the principle of *furthest first traversal* and propose a new distributed algorithm.

When solar energy is not sufficient to support SNs, the SNs send out a notification to the MCs. Then an MC sends a *head notification* message to any arbitrary WN whose battery has just been replenished and sets a counter to 0. The message specifies the cluster size  $k$  hops.  $k = h - 1$  initially and is decreased by 1 in each trial till  $k = 1$ . Upon receiving the *head notification* message, the WN declares itself as a new head and builds a shortest path tree (e.g., using Bellman-Ford algorithm). Each node also maintains a routing entry to store minimum hop distance to a head. Those entries are updated when a new shortest path tree is formed. If a node  $j$ 's entry indicates the minimum hop distance to a head  $i$  is less than or equal to  $k$ , it sends a *join* message to  $i$  to “join” the cluster as a member. Otherwise, it sends a *resume* message to node  $i$  to let the head selection continue. Within a timeout period, if the head receives a resume message, it means that there still exist some node(s) uncovered and the selection process should continue.

If a *resume* message is received, the head computes a shortest path tree using the Bellman-Ford algorithm. To avoid inefficient head selection, nodes should also report to the head whether they are cluster members or not. Then a new *head notification* message is generated and sent along the shortest path tree to the node with the maximum hop distance and enough battery energy which is not a cluster member yet. The counter is then increased by one. Otherwise, if no resume message is received during the timeout period, the head declares that clustering is successful by sending a *complete* message to all the heads. Upon receiving the complete message, heads report to the MC of cluster information. If the counter exceeds the upper bound in Eq. (24.13), the current  $k$  is not feasible to maintain energy balance so it should be further decreased. In this case, the head will broadcast a message to restart the whole process by selecting a smaller  $k$ . Psuedocode of this algorithm is shown in Algorithm 28. The distributed HRP algorithm can find a set of cluster heads in  $\mathcal{O}(hS)$  rounds and the worst case message overhead is  $\mathcal{O}(hSN^2)$ , where  $S$  is the upper bound in Eq. (24.13). As an example, Fig. 24.4 shows the results from the HRP algorithm to reallocate cluster heads among the WNs. The energy loss in solar energy from the 8 SNs is compensated by introducing 13 WN cluster heads to reduce hop distance.

**Algorithm 28:** Head reselection algorithm for WN  $i$ ,  $i \in \mathcal{N}$ 


---

**Input** : Network consists of SNs, WNs and MCs.

**Output:** The set of WNs selected as new cluster heads.

1 MC sends *HeadMsg* to a WN (with enough energy), counter  $c \leftarrow 0$ , sets *HeadMsg.hop* to  $k$  ( $k < h$ ). Set of cluster heads  $\mathcal{H} \leftarrow \emptyset$ ;

2 **if**  $\text{Recv}(\text{HeadMsg.ID} = i \text{ AND } c \leq \frac{E_c(h) - E^*}{X_c(k)})$  **then**

3      $d_{ij} = \min_{j \in \mathcal{N}} \text{HopCount}(i, j)$  (Bellman-Ford-SPT( $i$ )),  $\mathcal{H} \leftarrow \mathcal{H} + i$ ;

4     Send *new routing msg* regarding new head  $i$  to all the nodes. Set timeout period  $T$  waiting for *resume messages*;

5     **if**  $\text{Recv}(\text{ResumeMsg.ID} = i)$  *within T* **then**

6          $u = \arg \max_{j \in \mathcal{N}} \text{HopCount}(i, j)$ ,  $c \leftarrow c + 1$ . Send *HeadMsg* to  $u$ ;

7     **else**

8         | Clustering is completed and broadcast *complete msg*.

9     **end if**

10 **else if**  $\text{Recv}(\text{NewRoutingMsg.ID is } i) \text{ AND } \min_{j \in \mathcal{H}} \text{HopCount}(i, j) > k$  **then**

11     | Send *ResumeMsg* to the new head;

12 **else if**  $\text{Recv}(\text{NewRoutingMsg.ID is } i) \text{ AND } \min_{j \in \mathcal{H}} \text{HopCount}(i, j) \leq k$  **then**

13     | Send *JoinMsg* to  $u = \arg \min_{j \in \mathcal{H}} \text{HopCount}(i, j)$ . Declare as cluster member of  $u$  ( $\mathcal{B}_u \leftarrow \mathcal{B}_u + i$ ,  $\mathcal{N} \leftarrow \mathcal{N} - i$ );

14 **else if**  $\text{Recv}(\text{HeadMsg.ID} = i \text{ AND } c > \frac{E_c - E^*}{X_c(k)})$  **then**

15     |  $k \leftarrow k - 1$ . Broadcast a *restart message*;

16 **else**

17     | Forward message according to routing entries;

18 **end if**

---

## 24.5 Third Level: Mobile Chargers

Finally, for the third level of mobile chargers, we focus on optimizing their trajectories. Proposed in [7], instrumenting additional radio modules on the MCs realizes joint wireless charging and mobile data gathering. Rather than sending all the data to a static data sink, mobile data gathering can balance energy consumptions in the network [33–35]. This design certainly reduces manufacturing cost of MCs and systems cost.

However, because the effective wireless charging range is very limited (0.5–1m), the method in [7] requires the MC to stop at the exact WN location to perform simultaneous data gathering and recharge. In our new framework, since SNs are powered by solar energy, it is only necessary for the MC to enter the transmission range

or “touch” the transmission boundaries to collect data from SNs. This observation creates opportunities to further optimize MCs’ trajectories.

### 24.5.1 Exhaustive Search

For each MC  $i$ , it calculates a touring sequence using the recharge scheduling algorithms from the previous chapters. The sequence defines an ordered set of nodes that starts from the base station  $b$ , traverses through WNs  $w_i$  and SNs (cluster heads)  $a_j$ ,  $w_i \in \mathcal{N}$ ,  $a_j \in \mathcal{S}$ , and finally returns to the base station for uploading data and recharging MC’s own battery. Normally, the cluster size is larger than one hop ( $h > 1$ ), and the transmission range around SNs form disjoint disks with identical radius. The initial sequence does not distinguish an SN from a WN and stops at the center of SN’s transmission radius. We call it “Initial Center Tour”.

The initial center tour can be further improved if the MCs take shortcuts through the disks. This problem is known as the *Traveling Salesmen Problem with Neighborhoods* and no efficient solution exists [26, 28]. However, in our problem, we can take advantage of WNs in the sequence and greatly reduce computation complexity. For all WNs in a sequence (and the base station), we order them in pairs  $(b, w_1)$ ,  $(w_1, w_2)$ ,  $\dots$ ,  $(w_n, b)$ . For each pair  $(w_i, w_{i+1})$ , there could be at most  $s$  SNs in between. Let us start the analysis with  $s = 1$ . Figures 24.5 and 24.6 show that there are two cases: (1) the path connecting  $w_i$  and  $w_{i+1}$  directly cuts through the disk (Fig. 24.5). In this case, the MC does not need to alter its directions. It only stops for a period of data uploading time (several minutes) in the disk. (2) the disk does not intersect with the path so there should exist a point on the boundaries of the disk that can minimize the path ( $\min(a + b)$  in Fig. 24.6). A naive approach is to divide the disk perimeter

**Fig. 24.4** Restore energy balance by reselecting WN cluster heads

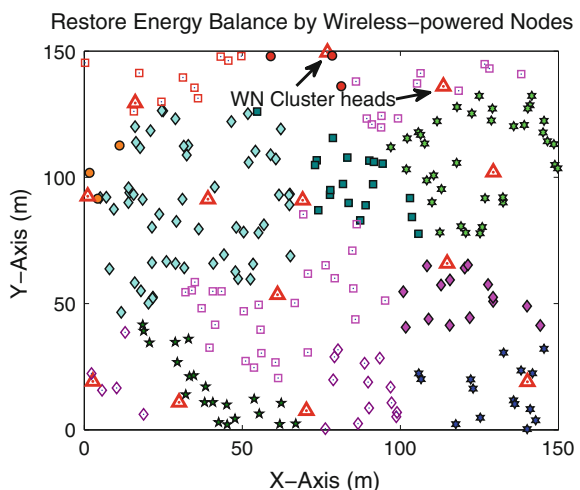


**Fig. 24.5** Case I: the shortest path directly cuts through SN's neighborhood

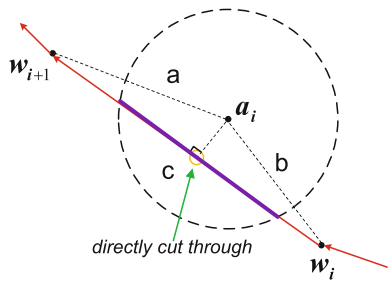
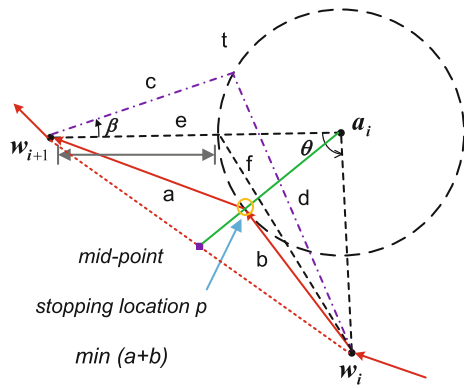


**Fig. 24.6** Case II: the shortest path touches SN's transmission boundary on point  $p$



into  $l$  segments and find out which one yields the minimum distance. The method is used in [25] to find optimal hitting points on disk boundaries and its accuracy is proportional to the number of segments  $l$ .

A closer look at Fig. 24.6 suggests a possible reduction of search space. Let us define the angle between lines connecting  $w_ia_i$  and  $w_{i+1}a_i$  as  $\theta$ . For a point  $t$  on the arc outside the sector, there is an angle  $\beta > 0$  between lines  $w_{i+1}t$  and  $w_{i+1}a_i$ . Clearly,  $c + d > e + f$  so any point  $t$  outside the sector gives an inferior solution compared to a point within the sector of  $\theta$ . Thus, we can narrow down the search space to the points on the arc within angle  $\theta$  between  $w_ia_i$  and  $w_{i+1}a_i$  and examinations of only a fraction  $f = \frac{\theta l}{2\pi}$  points are enough. Although the search space is greatly reduced for finding a point on a single circle, computation complexity of exhaustive search still grows exponentially when there are  $s$  SNs between  $w_i$  and  $w_{i+1}$  with complexity  $\mathcal{O}(f^s)$  so a faster algorithm is needed.

### 24.5.2 Minimizing Sum of Squared Distance

Exhaustive search quickly turns out to be impractical when there are several consecutive SNs in the touring sequence. If the problem can be solved analytically, computational complexity can be greatly reduced. Since the expressions of distance

involving square roots tend to yield intractable computations, we attempt to minimize the sum of squared distance instead. In fact, sum of squared distance has been used in many applications such as the well-known K-means algorithm [36]. We will also evaluate the estimation error to the actual sum of distance by simulations. Likewise, we start our analysis from  $s = 1$ .

As shown in Fig. 24.6, point  $p$  on disk  $a_i$  that minimizes  $d = (|w_i p|)^2 + (|w_{i+1} p|)^2$  is the intersection between line  $w_m a_i$  and the disk, where  $w_m$  is the midpoint between the coordinates of  $w_i$  and  $w_{i+1}$ . Although such discovery seems to be true by visual judgment, a geometric proof is difficult. Thus, we choose another direction to calculate  $p$  in terms of cartesian coordinates. Denote coordinates of  $w_i, w_{i+1}$  and  $p$  as  $(x_i, y_i), (x_{i+1}, y_{i+1}), (x, y)$ , respectively. Assume the origin of coordinate system resides at the disk center. The function of the disk is  $x^2 + y^2 = r^2$ . We use the *Lagrangian multiplier* method to find minimal sum of squared distance. After taking partial derivatives, the variables are

$$\begin{aligned}\frac{\partial L_x}{\partial x} &= 4x - 2(x_i + x_{i+1}) + 2x\lambda, \\ \frac{\partial L_y}{\partial y} &= 4y - 2(y_i + y_{i+1}) + 2y\lambda \\ \frac{\partial \lambda}{\partial \lambda} &= x^2 + y^2 - r^2\end{aligned}\tag{24.14}$$

After some calculations, the coordinates for  $p$  are

$$\begin{aligned}x &= \frac{(x_i + x_{i+1})r}{\sqrt{(x_i + x_{i+1})^2 + (y_i + y_{i+1})^2}}, \\ y &= \frac{(y_i + y_{i+1})r}{\sqrt{(x_i + x_{i+1})^2 + (y_i + y_{i+1})^2}}.\end{aligned}\tag{24.15}$$

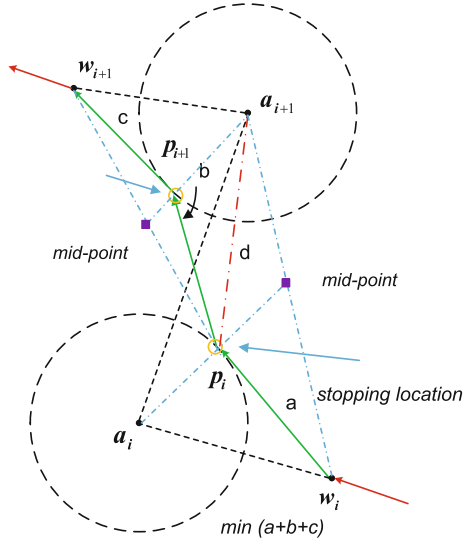
Let us explain the results from the other direction. The coordinates of  $w_m$  are  $(\frac{x_i+x_{i+1}}{2}, \frac{y_i+y_{i+1}}{2})$ . We plug the function of line  $w_m a_i$ ,  $y = \frac{y_i+y_{i+1}}{x_i+x_{i+1}}x$  into the disk function of  $a_i$ , and obtain two intersection points

$$x = \pm \sqrt{\frac{r^2}{(\frac{y_i+y_{i+1}}{x_i+x_{i+1}})^2 + 1}}, y = \pm \sqrt{\frac{r^2}{(\frac{x_i+x_{i+1}}{y_i+y_{i+1}})^2 + 1}}\tag{24.16}$$

We can see one of the solutions in Eq. (24.16) is exactly Eq. (24.15), which validates the midpoint intersection with the circle truly minimizes the square sum of distance.

The next step is to consider the case of  $s = 2$  without a direct cut as illustrated in Fig. 24.7. To use our method, computing each touching point on a disk needs two fixed points. For two disks, since the touching points can change simultaneously, minimization of sum of distance ( $a + b + c$ ) by considering multiple variables is very difficult analytically. Instead, we use the center of  $a_{i+1}$  as the reference point and calculate  $p_i$  on disk  $a_i$  to minimize  $(a + d)$  first. Then, based on  $p_i$ , we calculate

**Fig. 24.7** Two SNs between a pair of consecutive WNs in the recharge sequence



$p_{i+1}$  on  $a_{i+1}$  to  $\min(b + c)$ . In this way, each computation only involves one variable. The method can be easily extended to the case when there are  $s$  SNs between  $w_i$  and  $w_{i+1}$ , so a total of  $\mathcal{O}(s)$  computation is needed, which reduces the exponential- $\mathcal{O}(f^s)$  exhaustive search algorithm to linear time. We summarize the algorithm in Algorithm 29. As an example, Fig. 24.8 shows an initial center tour that covers nine energy requests and 7 SNs for uploading data. The route is then improved in Fig. 24.9 with a saving of 17 % moving energy on the MC.

---

**Algorithm 29:** MC's route improvement algorithm

---

**Input :** Sequence  $\langle b, w_1, \dots, a_i, \dots, w_j, \dots, w_n, b \rangle$ . Set of SNs between  $w_j$  and  $w_{j+1}$ ,  $\mathcal{S}_j$ ,  $\mathcal{S} = \bigcup_{j \in \mathcal{N}} \mathcal{S}_j$ .

**Output:** Coordinates  $(x_i, y_i)$  MC should visit near  $a_i$ .

- 1 **while**  $\mathcal{S}_j \neq \emptyset$  **do**
  - 2   For  $a_i \in \mathcal{S}_j$ , find coordinates of WNs  $w_j, w_{j+1}$  in sequence;
  - 3   **if**  $a_{i+1}$  is also between  $w_j, w_{j+1}$  **then**
  - 4      $x_{j+1} = x_{a_{i+1}}, y_{j+1} = y_{a_{i+1}}$ ;
  - 5   **else**
  - 6      $(x_{j+1}, y_{j+1})$  is set to  $w_{j+1}$ 's coordinates;
  - 7   **end if**
  - 8   Establish cartesian coordinate system originated at center of  $a_i$ ;
  - 9    $x_i = (x_j + x_{j+1})r / \sqrt{(x_j + x_{j+1})^2 + (y_j + y_{j+1})^2}$ ,
  - 10    $y_i = (y_j + y_{j+1})r / \sqrt{(x_j + x_{j+1})^2 + (y_j + y_{j+1})^2}$ ;
  - 11    $\mathcal{S}_j \leftarrow \mathcal{S}_j - a_i$ ;
  - 12 **end while**
-

**Fig. 24.8** Initial centered tour through exact locations of SNs

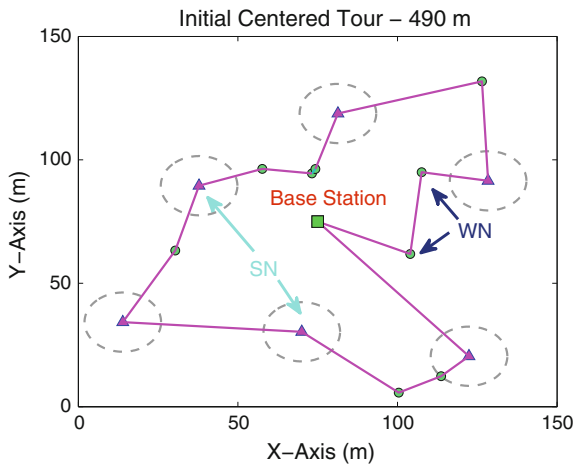
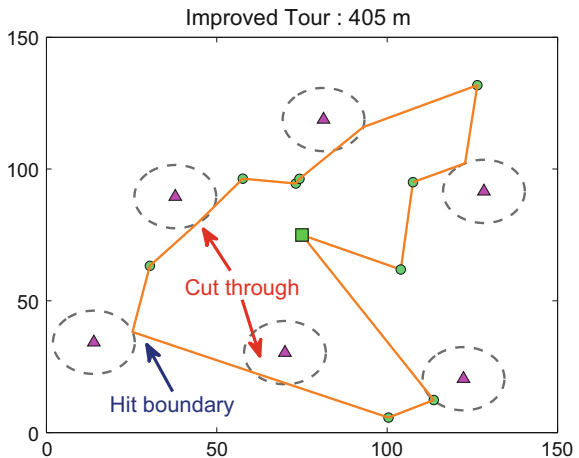


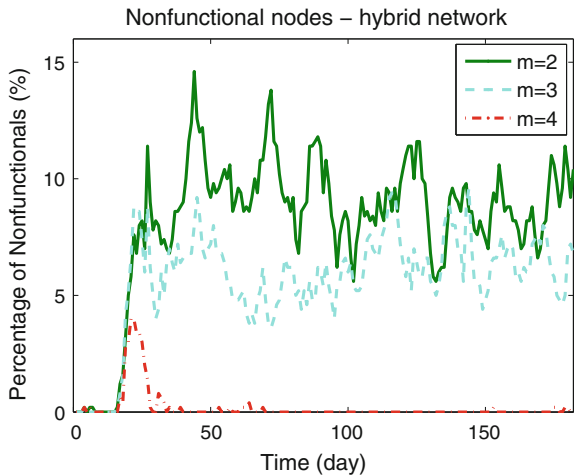
**Fig. 24.9** Improved tour that can take short cuts through SNs' neighborhoods



## 24.6 Performance Evaluation

Finally, we evaluate performance of the framework by a discrete-event simulator and compare it with a network solely relied on wireless energy [6, 7, 9]. In the *wireless-powered network*, all cluster heads are replenished by the MCs. A number of 500 nodes are uniformly randomly distributed over a square field of  $L = 150$  m. Sensors have identical transmission range of  $r = 12$  m, and consume  $e_s = 0.05$  J for generating a sensing packet and  $e_t = e_r = 0.02$  J for transmitting/receiving a packet. Each time slot is 1 min and the traffic follows a Poisson distribution with average  $\lambda = 3$  pkt/min. WNs have battery capacity  $C_h = 780$  mAh and require  $T_r = 78$  min

**Fig. 24.10** Number of nonfunctional nodes in hybrid network

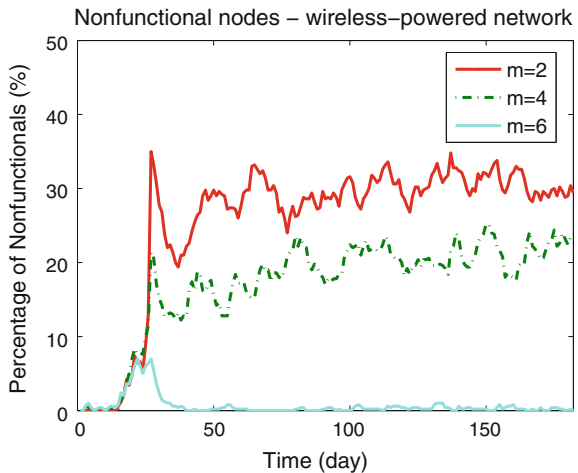


for recharge. SNs have larger capacity of 2150 mAh to store more energy. MC consumes 5 J/m while moving at  $v = 1$  m/s. We use real meteorological trace at Stony Brook, NY from [37], which has a complete archive of weather conditions. The simulation time starts from December and lasts for 6 months.

#### 24.6.1 Nonfunctional Nodes

One of the key performance metrics in the network is to see how many cases of energy depletion have occurred. Once a node's battery is depleted, it stops working and becomes nonfunctional until its battery is replenished. To sustain perpetual operations, nodes should be alive all the time; otherwise, they will degrade sensing qualities and node communications. To compare the performance, we change the number of MCs  $m$ . Figure 24.10 and Fig. 24.11 compare the percentage of nonfunctional nodes between hybrid and wireless-powered networks. From Fig. 24.10, we can see that two MCs can keep the percentage of nonfunctional nodes around 10% and four MCs achieve perpetual network operation at equilibrium. For the wireless-powered network in Fig. 24.11,  $m = 2$  has over 30% nonfunctional nodes and an increase to  $m = 6$  still barely eliminates all battery depletions at equilibrium. These results clearly demonstrate that hybrid approach can improve network performance significantly. This is because the SNs are replenished by solar energy which has much higher power density so MCs have more leverage to take care of the rest of the network. However, for the wireless-powered network, MCs need to visit cluster heads more frequently, which reduces the chances for other nodes to get recharged.

**Fig. 24.11** Number of nonfunctional nodes in wireless-powered framework



### 24.6.2 Energy Efficiency

The cost of network maintenance is another important metric. There are two types of costs in the hybrid network. The first type comes from network maintenance which basically involves energy expenditures at the MCs while moving and charging. We focus on MC's moving cost since charging energy expenditures are necessary. We have evaluated energy efficiency for different types of networks in Fig. 24.12. The energy efficiency is defined as the ratio between the energy replenished into sensors over the total energy consumed. We can see that the hybrid network enjoys higher energy efficiency as more than 90 % energy are used for recharge. The wireless-powered network has lower energy efficiency since the MCs have to move more often to respond recharge request from the cluster heads.

### 24.6.3 Harvested Solar Energy

To validate the proposed algorithms, we present the evolution of SN's energy. We focus on two typical nodes with light and heavy data traffic indicated by their cluster sizes. Figure 24.13 traces SNs' energy under various weather conditions represented by percentage of solar exposure ( $1 - \sigma$ ) obtained in [37]. We can see that through the month of December, energy storage continuously declines due to weak solar strength in winter—there are also several snowing days so SNs are unable to harvest enough energy and reselection of cluster heads among WNs is needed. This gives SNs opportunities to recover their energy (during 40–50 days). For the rest of months, although a few consecutive raining days are observed, the energy gaps are quickly

**Fig. 24.12** Energy efficiency of different networks

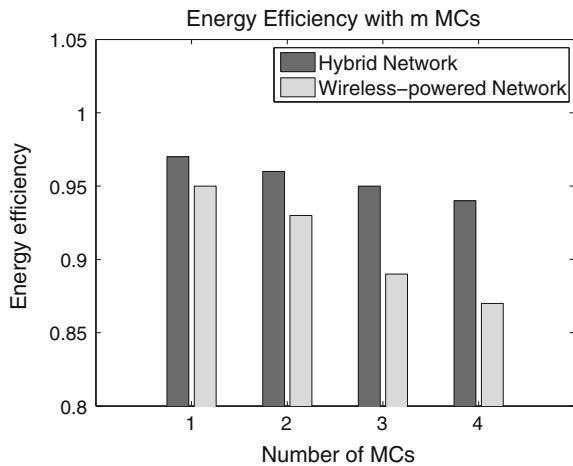
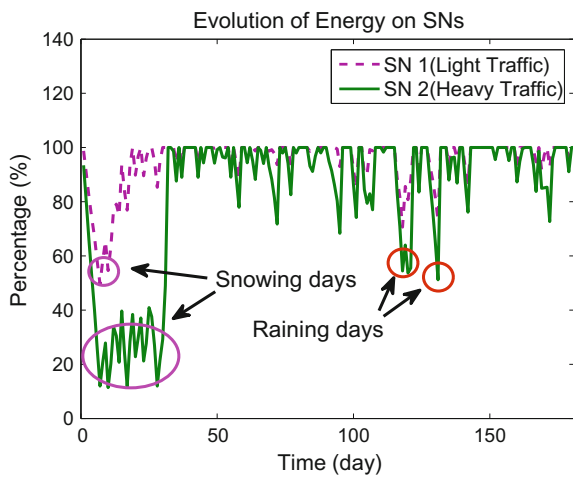


**Fig. 24.13** Energy variations of SNs



filled. This is because that solar radiation has strengthened since spring and energy storage is sufficient to sustain network operations during the raining days.

## 24.7 Conclusion

In this chapter, we combine advantages from wireless charging and solar energy harvesting technologies to form a hybrid network. The network is hierarchically divided into SNs, WNs and MCs levels. On the first level, we study how to minimize the total cost of deploying a set of SNs. The problem is formulated into a facility location problem and an efficient algorithm is proposed in discrete space. Then

the solution is further improved in continuous space. On the second level, energy balance is established and a distributed head reselection algorithm is proposed to designate some WNs as cluster heads when solar energy is not available during raining/cloudy days. The third level studies optimizations of joint tour consisting of both wireless charging and data gathering sites. A linear-time algorithm is proposed to take short cuts through SNs neighborhood for data gathering. Finally, based on real weather data, we evaluate the effectiveness and efficiency of the hybrid framework by comparing to a purely wireless-powered network.

## References

1. Guo, S., Wang, C., Yang, Y.: Joint mobile data gathering and energy provisioning in wireless rechargeable sensor networks (2014). doi:[10.1109/TMC.2014.2307332](https://doi.org/10.1109/TMC.2014.2307332)
2. Li, Z., Peng, Y., Zhang, W., Qiao, D.: J-roc: A joint routing and charging scheme to prolong sensor network lifetime (2011). doi:[10.1109/ICNP.2011.6089076](https://doi.org/10.1109/ICNP.2011.6089076)
3. Peng, Y., Li, Z., Zhang, W., Qiao, D.: Prolonging sensor network lifetime through wireless charging (2010). doi:[10.1109/RTSS.2010.35](https://doi.org/10.1109/RTSS.2010.35)
4. Tong, B., Li, Z., Wang, G., Zhang, W.: How wireless power charging technology affects sensor network deployment and routing (2010). doi:[10.1109/ICDCS.2010.61](https://doi.org/10.1109/ICDCS.2010.61)
5. Wang, C., Li, J., Ye, F., Yang, Y.: Netwrap: An ndn based real-time wireless recharging framework for wireless sensor networks (2014). doi:[10.1109/TMC.2013.2296515](https://doi.org/10.1109/TMC.2013.2296515)
6. Wang, C., Li, J., Ye, F., Yang, Y.: A mobile data gathering framework for wireless rechargeable sensor networks with vehicle movement costs and capacity constraints (2015). doi:[10.1109/TC.2015.2490060](https://doi.org/10.1109/TC.2015.2490060)
7. Zhao, M., Li, J., Yang, Y.: A framework of joint mobile energy replenishment and data gathering in wireless rechargeable sensor networks (2014). doi:[10.1109/TMC.2014.2307335](https://doi.org/10.1109/TMC.2014.2307335)
8. Dai, H., Liu, Y., Chen, G., Wu, X., He, T.: Scape: Safe charging with adjustable power (2014). doi:[10.1109/INFCOMW.2014.6849226](https://doi.org/10.1109/INFCOMW.2014.6849226)
9. He, S., Chen, J., Jiang, F., Yau, D.K.Y., Xing, G., Sun, Y.: Energy provisioning in wireless rechargeable sensor networks (2013). doi:[10.1109/TMC.2012.161](https://doi.org/10.1109/TMC.2012.161)
10. Nikoletseas, S., Raptis, T.P., Raptopoulos, C.: Low radiation efficient wireless energy transfer in wireless distributed systems (2015). doi:[10.1109/ICDCS.2015.28](https://doi.org/10.1109/ICDCS.2015.28)
11. Fcc rules for ism bands, <http://www.afar.net/tutorials/fcc-rules>
12. Raghuathan, V., Kansal, A., Hsu, J., Friedman, J., Srivastava, M.: Design considerations for solar energy harvesting wireless embedded systems (2005). doi:[10.1109/IPSN.2005.1440973](https://doi.org/10.1109/IPSN.2005.1440973)
13. Guha, S., Khuller, S.: Greedy strikes back: improved facility location algorithms (1998). <http://dl.acm.org/citation.cfm?id=314613.315037>
14. Jain, K., Mahdian, M., Markakis, E., Saberi, A., Vazirani, V.V.: Greedy facility location algorithms analyzed using dual fitting with factor-revealing lp (2003). doi:[10.1145/950620.950621](https://doi.org/10.1145/950620.950621)
15. Jain, K., Vazirani, V.V.: Approximation algorithms for metric facility location and k-median problems using the primal-dual schema and lagrangian relaxation (2001). doi:[10.1145/375827.375845](https://doi.org/10.1145/375827.375845)
16. Shmoys, D.B., Tardos, E., Aardal, K.: Approximation algorithms for facility location problems (extended abstract) (1997). doi:[10.1145/258533.258600](https://doi.org/10.1145/258533.258600)
17. Weiszfeld, E., Plastria, F.: On the point for which the sum of the distances to n given points is minimum (2009). doi:[10.1007/s10479-008-0352-z](https://doi.org/10.1007/s10479-008-0352-z)
18. Kansal, A., Hsu, J., Srivastava, M., Raghuathan, V.: Harvesting aware power management for sensor networks (2006). doi:[10.1109/DAC.2006.229276](https://doi.org/10.1109/DAC.2006.229276)
19. Liu, R.S., Sinha, P., Koksal, C.E.: Joint energy management and resource allocation in rechargeable sensor networks (2010). doi:[10.1109/INFCOM.2010.5461958](https://doi.org/10.1109/INFCOM.2010.5461958)

20. Vigorito, C.M., Ganesan, D., Barto, A.G.: Adaptive control of duty cycling in energy-harvesting wireless sensor networks (2007). doi:[10.1109/SAHCN.2007.4292814](https://doi.org/10.1109/SAHCN.2007.4292814)
21. Wang, C., Guo, S., Yang, Y.: An optimization framework for mobile data collection in energy-harvesting wireless sensor networks (2016). doi:[10.1109/TMC.2016.2533390](https://doi.org/10.1109/TMC.2016.2533390)
22. He, L., Pan, J., Xu, J.: A progressive approach to reducing data collection latency in wireless sensor networks with mobile elements (2013). doi:[10.1109/TMC.2012.105](https://doi.org/10.1109/TMC.2012.105)
23. Ma, M., Yang, Y., Zhao, M.: Tour planning for mobile data-gathering mechanisms in wireless sensor networks (2013). doi:[10.1109/TVT.2012.2229309](https://doi.org/10.1109/TVT.2012.2229309)
24. Sugihara, R., Gupta, R.K.: Path planning of data mules in sensor networks (2011). doi:[10.1145/1993042.1993043](https://doi.org/10.1145/1993042.1993043)
25. Yuan, B., Orlowska, M., Sadiq, S.: On the optimal robot routing problem in wireless sensor networks (2007). doi:[10.1109/TKDE.2007.1062](https://doi.org/10.1109/TKDE.2007.1062)
26. Dumitrescu, A., Mitchell, J.S.B.: Approximation algorithms for tsp with neighborhoods in the plane (2001). <http://dl.acm.org/citation.cfm?id=365411.365417>
27. Elbassioni, K., Fishkin, A.V., Mustafa, N.H., Sitters, R.: Approximation algorithms for euclidean group tsp (2005). doi:[10.1007/1152346890](https://doi.org/10.1007/1152346890)
28. Safra, S., Schwartz, O.: On the complexity of approximating tsp with neighborhoods and related problems (2006). doi:[10.1007/s00037-005-0200-3](https://doi.org/10.1007/s00037-005-0200-3)
29. Kuhn, H.W.: A note on fermat's problem (1973). doi:[10.1007/BF01584648](https://doi.org/10.1007/BF01584648)
30. Wu, X., Chen, G., Das, S.K.: Avoiding energy holes in wireless sensor networks with nonuniform node distribution (2008). doi:[10.1109/TPDS.2007.70770](https://doi.org/10.1109/TPDS.2007.70770)
31. Sharma, N., Gummesson, J., Irwin, D., Shenoy, P.: Cloudy computing: leveraging weather forecasts in energy harvesting sensor systems (2010). doi:[10.1109/SECON.2010.5508260](https://doi.org/10.1109/SECON.2010.5508260)
32. Gonzalez, T.F.: Clustering to minimize the maximum intercluster distance (1985). doi:[10.1016/0304-3975\(85\)90224-5](https://doi.org/10.1016/0304-3975(85)90224-5)
33. Luo, J., Hubaux, J.P.: Joint sink mobility and routing to maximize the lifetime of wireless sensor networks: the case of constrained mobility (2010). doi:[10.1109/TNET.2009.2033472](https://doi.org/10.1109/TNET.2009.2033472)
34. Ma, M., Yang, Y.: Sencar: an energy-efficient data gathering mechanism for large-scale multihop sensor networks (2007). doi:[10.1109/TPDS.2007.1070](https://doi.org/10.1109/TPDS.2007.1070)
35. Zhao, M., Yang, Y.: Bounded relay hop mobile data gathering in wireless sensor networks. In: 2009 IEEE 6th International Conference on Mobile Adhoc and Sensor Systems, pp. 373–382 (2009). doi:[10.1109/MOBHOC.2009.5336976](https://doi.org/10.1109/MOBHOC.2009.5336976)
36. MacQueen, J.: Some methods for classification and analysis of multivariate observations. In: Proceedings of the Fifth Berkeley Symposium on Mathematical Statistics and Probability, Volume 1: Statistics, pp. 281–297. University of California Press, Berkeley, California (1967). <http://projecteuclid.org/euclid.bsmsp/1200512992>
37. Weather underground: [www.wunderground.com/history/](http://www.wunderground.com/history/)

## Chapter 25

# Joint Mobile Energy Replenishment with Wireless Power Transfer and Mobile Data Gathering in Wireless Rechargeable Sensor Networks

Miao Zhao, Ji Li and Yuanyuan Yang

**Abstract** Energy replenishment is now experiencing rapid development and great proliferation in rechargeable sensor networks, which has the potential to provide perpetual network operations by capturing renewable energy from external environments. However, the low output of energy capturing devices can only provide intermittent recharging opportunities to support low-rate data services due to spatial-temporal, geographical, or environmental factors. In this chapter, we study the problem of how to provide steady and high recharging rates by employing wireless power transfer and simultaneously achieve optimized data gathering performance in wireless rechargeable sensor networks. We propose to utilize mobility for the joint problem of energy replenishment and data gathering. In particular, a multifunctional mobile entity, called *SenCar*, is employed to serve not only as a mobile data collector that roams over the field to gather data via short-range communication, but also as an energy transporter that charges static sensors on its migration tour via wireless power transfer. Utilizing the control on *SenCar*'s mobility, we focus on the joint optimization on effective energy charging and high-performance data gathering. We first study this problem in generic networks with random topologies. A two-step approach for the joint design is proposed. In the first step, the locations of a subset of sensors are periodically selected as *anchor points*, where the *SenCar* will sequentially

---

M. Zhao (✉)

Department of Computing, The Hong Kong Polytechnic University, Hong Kong, China  
e-mail: csmiaozhao@comp.polyu.edu.hk

J. Li · Y. Yang

Department of Electrical and Computer Engineering, State University of New York,  
Stony Brook, NY 11794, USA  
e-mail: ji.li@stonybrook.edu

Y. Yang

e-mail: yuanyuan.yang@stonybrook.edu

© Springer International Publishing AG 2016

S. Nikoletseas et al. (eds.), *Wireless Power Transfer Algorithms, Technologies and Applications in Ad Hoc Communication Networks*,  
DOI 10.1007/978-3-319-46810-5\_25

667

visit to charge the sensors at these locations and gather data from nearby sensors in a multi-hop fashion. To achieve a desirable balance between energy replenishment amount and data gathering latency, we provide a selection algorithm to search for a maximum number of anchor points where sensors hold the least battery energy, and meanwhile by visiting them, the tour length of the SenCar is bounded by a threshold. In the second step, we consider optimizing the data gathering performance when the SenCar migrates among these anchor points. We formulate this data gathering problem as a network utility maximization problem and propose a distributed algorithm to adjust data rates, link scheduling, and flow routing so as to adapt to the up-to-date energy replenishing status of sensors. Besides the generic networks, we consider a special scenario as well, where sensors are regularly deployed. Correspondingly, we present a simplified solution with lower complexity by exploiting the symmetry of the topology. Finally, extensive evaluations are carried out to validate the effectiveness of the solutions. The results demonstrate that our approaches can maintain perpetual network operations and achieve high network utility on data gathering simultaneously.

## 25.1 Overview

As energy is the paramount factor that constrains the performance of wireless sensor networks, in recent years, extensive research effort has been carried out to prolong network lifetime of wireless sensor networks. In the literature, there are two main categories of strategies that are widely employed. One category involves the conventional solutions to reduce energy consumption from the perspectives of sensors and network routing, such as low-power hardware architecture [1, 2], low-complexity software implementation [3], power-efficient wireless communications [4–6], dynamic routing techniques [7, 8], and mobile data gathering [9, 10]. Although these solutions are effective to some extend, network lifetime is still constrained by the limited battery energy. Another category utilizes the energy harvesting technique to relieve the energy constraint by recharging sensors through capturing mechanical, thermal, photovoltaic, or electromagnetic energy from ambient environments. Different from conventional solutions, the energy harvesting technique makes it possible for sensors to obtain renewable energy when needed, which radically conquers the dilemma that sensors must solely depend on battery supply. Energy harvesting is now considered as a promising approach with the potential to sustain the perpetual operations of the network [11, 12]. However, as the spatial-temporal profiles of ambient energy sources exhibit great variations, the strength of harvested energy is typically low [13–15], and especially sensitive to environment dynamics. For example, in a solar harvesting system, the output power of a sensor is determined by the solar radiation arrived at the equipped solar panel, which drastically varies with time and weather. Statistics show that the difference can be up to three orders of magnitude among the available solar power in shadowy, cloudy, and sunny environments [16]. The low

efficiency and dynamics of energy harvesting impose much difficulty on the design of protocols that must keep sensors from running out of energy while guaranteeing satisfactory network performance.

Recent breakthroughs in wireless power transfer have revealed the possibility of transferring electrical energy with high efficiency [17]. Nowadays, wireless power transfer has already been used to recharge small appliances, such as electric toothbrushes. More-recent progresses further enable the application of non-radiative power transfer over midrange. (Midrange refers to the distance between the transmitter and the receiver longer than the size of devices by a factor of at least 2–3 [18].) It was shown in [18] that through strongly coupled magnetic resonances, the efficiency of transferring 60 W of power over a distance in excess of 2 m can be as high as 40 %. Intel also demonstrated that it is possible to improve transferring 60 W of power over a distance of up to 2–3 feet with efficiency of 75 % [19]. At present, commercial products utilizing midrange wireless power transfer have been available on the market. WiTricity Corp., for example, is delivering WiT-3300 charging system for electric vehicle recharge, which is capable of transferring up to 3.3 kW to the vehicle wirelessly [20]. With the dramatic development of wireless power transfer, it has become an alternative promising and effective solution to replenish the sensors in a sustainable method [21–24]. The situation that sensors only rely on battery supply or energy harvesting on ambient environment would radically change.

In this chapter, we present a joint design of mobile energy replenishment with wireless power transfer and mobile data gathering by exploiting mobility, which is referred to as J-MERDG, in order to provide steady and high-recharging-rate power supplies for sensors, and effectively optimize data gathering performance in parallel [25, 26]. The system architecture of J-MERDG is depicted in Fig. 25.1. In particular, the entire network consists of two types of devices: a multifunctional mobile entity, called *SenCar* that works as energy transporter and data collector, and wireless sensor nodes that perform sensing tasks. The SenCar is equipped with a high capacity rechargeable battery, an oscillator that converts the direct current (DC) from the battery into high frequency alternating current (AC) and a resonant coil as the transmitter. The battery can provide sufficient energy for the operation of the SenCar as well as fully charging the selected sensor nodes. Each sensor has a receiver that consists of a receiver coil tuned to resonate at exactly the same frequency as the transmitting coil on the SenCar, an AC/DC converter which is controlled by the battery charger, and a rechargeable battery with ultrafast charging rate.<sup>1</sup>

---

<sup>1</sup>Ultrafast charging was recently realized in LiFePO<sub>4</sub> by creating a fast ion-conducting surface phase through controlled off-stoichiometry [27]. It inherits and combines the advantages of both conventional Li-ion batteries and supercapacitors, which brings high energy density and can be charged at the rate as high as 400C. C is determined by the nominal capacity of the battery, e.g., for a battery with the capacity of 1000 mAh, i.e., C = 1000 mA. At a rate of 400C, the time to fully recharge a battery can be decreased to 6 s.

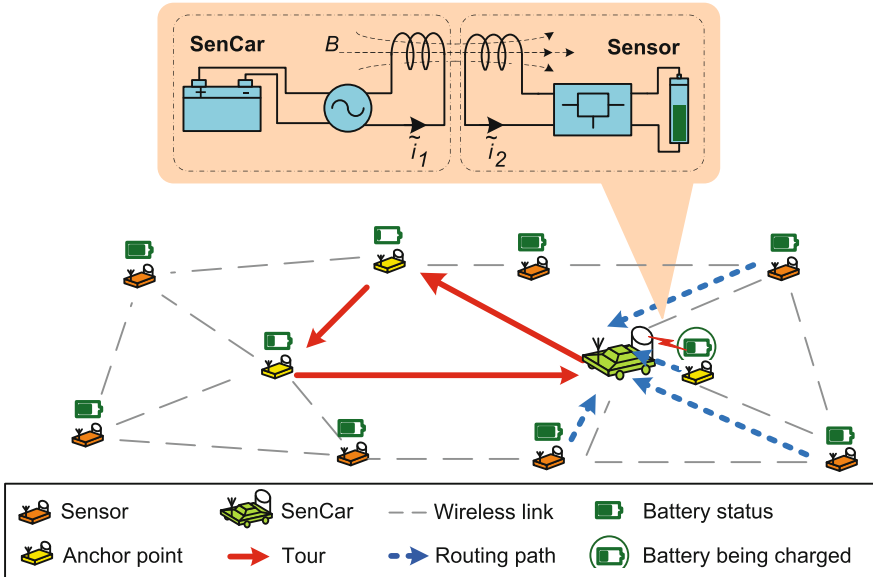


**Fig. 25.1** Architecture of joint mobile energy replenishment with wireless power transfer and mobile data gathering (J-MERDG)

The SenCar periodically chooses a subset of sensors to visit based on their energy status. The locations of those selected sensors are called *anchor points*. When the SenCar arrives at an anchor point, it will quickly charge the sensor located there by wireless power transfer. In particular, the SenCar, as the energy transmitter, feeds alternating current into the transmitter coil and generates an oscillating magnetic field around the coil. An alternating current is then induced in the receiver coil at the sensor side. The sensor battery ultimately get fully charged within a short period of time.

Besides playing as an energy transporter, the SenCar also acts as a data collector to gather the data from nearby sensors with multi-hop routing when it arrives at an anchor point. The SenCar would sojourn at the anchor point for a period of time. The duration of the sojourn time can be manually configured based on the application requirements or scheme design. Since the batteries can be charged in a very short time, which can almost be ignored compared to the sojourn time SenCar spends at each anchor point, we assume that sensor batteries can be instantly fully charged for use. As wireless charging and data gathering are performed by different units in the sensor and work on different frequencies (the coils of wireless power transfer system usually resonate at low frequencies, e.g., 145 kHz for WiT-2000M, while the transceivers for data communication on sensors operate at much higher frequencies, e.g., 2.4 GHz for TI CC2430), these two operations can be performed simultaneously without affecting each other. In a particular time interval, as the SenCar moves over field to visit the selected anchor points in a tour, each sensor has the choices to send

its data to the SenCar when it sojourns at any anchor point along low-cost routes. Moreover, to maximize network utility while maintaining perpetual operations, each sensor employs rate control in order to not only achieve high-performance gain but also avoid draining out of energy budget for the current time interval.

There are many benefits that could be achieved by employing SenCar's mobility in J-MERDG.

- Since sensors receive energy supplement directly from the SenCar, the replenishment will no longer suffer from environmental variations.
- As long as the SenCar moves sufficiently close to sensors, high charging efficiency can be achieved to ensure high-rate data services.
- As the SenCar takes the responsibility of energy delivery, it is commercially appealing that no complex energy harvesting devices are needed at sensors, which significantly reduces the cost of sensors.
- By exploiting controlled mobility, the SenCar can efficiently perform energy delivery and data gathering simultaneously. This is extremely desirable as such combination makes double contribution to the energy management of the network. On one hand, the SenCar infuses steady and abundant renewable energy into the network almost at no additional cost. On the other hand, mobility alleviates the routing burden at sensors for data uploading so that great energy can be saved to further leverage the refilled energy.

The work discussed in this chapter aims to design an adaptive solution that jointly selects the sensors to be charged and finds an effective data gathering scheme, such that network utility can be optimized while maintaining perpetual operations of the network. To that end, a two-step approach for the joint design is proposed. In the first step, we determine the mobility pattern of the SenCar for each time period, that is, where the SenCar will move to charge the located sensors and gather data from the neighborhood. In the second step, the strategies on how to achieve optimal data gathering performance are carefully studied when the SenCar migrates among different anchor points, considering the up-to-date energy replenishing status of sensors. We formulate this problem as a network utility maximization problem and adjust data rates, link scheduling and flow routing to achieve the target. We also study a special scenario where the sensor nodes are regularly deployed. By taking advantage of the symmetry of the topology, we can provide an approach with lower complexity for J-MERDG, where the SenCar's moving pattern and sensor's data gathering scheme can be preset with a deterministic solution.

## 25.2 J-MERDG in Wireless Sensor Networks with Random Topologies

In this section, we consider the generalized case of J-MERDG, where the sensor nodes are randomly deployed. As each sensor has different energy statuses at different times, it is required for the SenCar to properly make decisions on which sensor gets

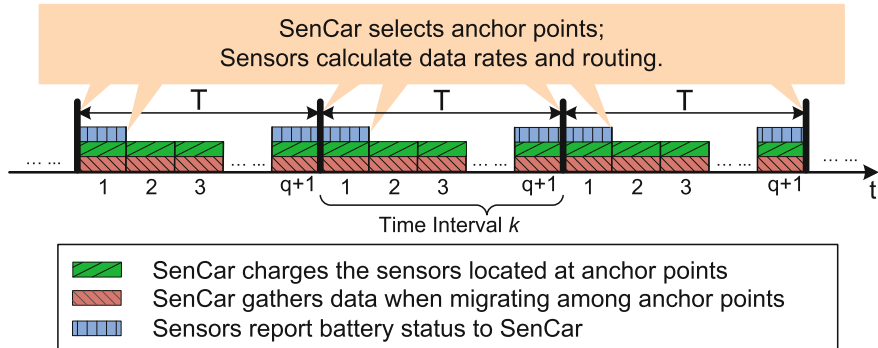


**Fig. 25.2** The time structure of joint mobile energy replenishment with wireless power transfer and mobile data gathering (J-MERDG)

recharged at what time. Due to such time-varying nature of the energy replenishment demand, to facilitate our study, we divide the time into fixed time intervals of length  $T$ . We assume that the possible candidate locations for the SenCar to visit are the locations of all sensors, such that the SenCar can move sufficiently close to charge the sensors in a one-to-one manner with high efficiency. We assume that there are a total of  $q + 1$  migration tours in each time interval, so that the bound for data gathering latency in a tour is determinate if we treat it same for all tours in the interval.<sup>2</sup>  $q$  can be manually configured based on the latency bound for different application needs. In each tour, based on some specific criteria (to be discussed in Sect. 25.2.1), the locations of a subset of sensors, i.e., anchor points, are selected. The SenCar would charge the sensors located at the anchor points and gather the sensing data from nearby sensors. As shown in Fig. 25.2, in each time interval, the SenCar will migrate among the anchor points back and forth. In the first tour, the SenCar would select the sensors with the least residual energy and charge them when it arrives at their locations to provide timely energy replenishment. Meanwhile, the SenCar collects data from surrounding sensors. This tour is referred to as *recharging tour*, or *R-tour*. Considering sensors may not consume energy rapidly, it is unnecessary to frequently recharge the same sensors. In the following  $q$  tours, we can alternatively choose some other anchor points to facilitate the performance optimization on data gathering. Such tours are referred to as *data gathering tours*, or *D-tours*. It is worth pointing out that for both R-tour and D-tours, the SenCar would charge the sensors located at the anchor points and simultaneously collect data from nearby sensors when it sojourns at the anchor points.

<sup>2</sup>For networks we study in this chapter, the data gathering latency refers to the total time of a migration tour, which consists of the data collection time at anchor points as well as the moving time on the trajectory.

Having outlined the basic idea of J-MERDG in random networks, we now provide a two-step approach to efficiently implement the design. In the first step, the SenCar selects the anchor points for R-tour and D-tours based on different principles. In the second step, based on the information of anchor points (i.e., SenCar's sojourn locations) and sensor energy status, each sensor itself determines how to transmit data to the SenCar when the SenCar arrives. Since similar methods are adopted in different time intervals, in the following discussions, unless state otherwise, we only focus on a particular time interval.

### **25.2.1 First Step: Anchor Point Selection**

We treat R-tour and D-tours separately with different criteria on anchor points selection. For R-tour, the principle of anchor points selection falls into the following two aspects. First, the locations of sensors that are selected as anchor points should be those with the most urgent needs of energy supplement. Second, as the SenCar migrates over the anchor points for data gatherings, the length of each migration tour is expected to be short so that the SenCar can spend more time on data collection. To better enjoy the benefit of the energy supply provided by the SenCar, more anchor points should be selected such that more sensors can timely get recharged. However, this would adversely prolong the migration tour and reduce sojourn time for data collection. Thus, there is an inherent tradeoff between the number of sensors to be recharged and the tour length. Based on this observation, the anchor point selection problem for R-tour at a particular time interval  $k$  can be described as follows. Given the up-to-date energy states of sensors obtained by the SenCar at the end of time interval  $k-1$ , find the maximum number of anchor points for R-tour at time interval  $k$  such that the sensors located at these anchor points hold the least battery energy, and meanwhile by visiting these anchor points, the tour length of the SenCar is no more than a threshold. For D-tours, the anchor points are selected with the target to collect more data, leading to high network utility. It is intuitive that the more residual energy a sensor has, the more data it can upload. The SenCar is more likely to be able to collect more data if the surrounding sensors have high battery level. Therefore, the set of anchor points in D-tours can be selected based on the energy status of their neighbors, meanwhile satisfying that the tour length does not exceed the threshold when visiting them sequentially in a tour. It needs pointing out that we handle with a total of  $q$  D-tours as a whole, which means that the selection of anchor points and data collection pattern are the same for each D-tour.

Considering that the possible candidate anchor points are the locations of all the sensors, the anchor point selection problem for R-tour is equivalent to finding a target sensor, such that by visiting the locations of all those sensors whose battery energy is less than or equal to that of the target sensor, the length of shortest migration tour among them is bounded by the threshold. For D-tours, this problem is equivalent to finding a target sensor, such that by visiting the locations of all sensors whose least energy neighbor within  $m$  hops has a battery level higher than or equal to that of the

target sensor, the length of shortest migration tour among them is bounded by the threshold. Motivated by this observation, we propose a selection algorithm to search for the anchor points as shown in Algorithm 30. Given the set of sensors  $\mathcal{S}$ , the set of energy states of sensors at the beginning of R-tour in time interval  $k$ ,  $\mathcal{B}_e^{(k),R}$ , or the set of the least energy of neighbors within  $m$  hops of each sensor at the beginning of D-tours in time interval  $k$ ,  $\mathcal{B}_e^{(k),D}$ , and the tour length bound  $L$ , the algorithm is to find the list of anchor points  $\mathcal{A}^{(k),R}$  or  $\mathcal{A}^{(k),D}$  as follows.

---

**Algorithm 30:** Anchor Point Selection Algorithm

---

**1** //  $\mathcal{S}$  is the set of sensors,  $\mathcal{B}_e^{(k),R}$  is the set of energy states of sensors at the beginning of R-tour in time interval  $k$ ,  $\mathcal{B}_e^{(k),D}$  is the set of the least energy of each sensor's neighbors within  $m$  hops at the beginning of D-tours in time interval  $k$ , and  $L$  is the tour length bound.

**Require:**  $\mathcal{S} = \{1, 2, \dots, N\}$ ;  $\mathcal{B}^{(k)} = \mathcal{B}_e^{(k),R}$  for R-tour in time interval  $k$ , or  $\mathcal{B}^{(k)} = \mathcal{B}_e^{(k),D}$  for D-tours.

**Ensure:** Anchor point list  $\mathcal{A}^{(k)} = \mathcal{A}^{(k),R}$  for R-tour in time interval  $k$ , or  $\mathcal{A}^{(k)} = \mathcal{A}^{(k),D}$  for D-tours in time interval  $k$ ;

**1:** **if** R-tour **then**

**2:** Sort the battery states in  $\mathcal{B}^{(k)}$  in an increasing order and record the result in set  $\mathcal{B}'^{(k)}$ .

**3:** **else**

**4:** Sort the battery states in  $\mathcal{B}^{(k)}$  in an decreasing order and record the result in set  $\mathcal{B}'^{(k)}$ .

**5:** **end if**

**6:** Map  $\mathcal{S}$  to another set  $\mathcal{S}'$  by rearranging the sensors in the sequence corresponding to their respective battery states in  $\mathcal{B}'^{(k)}$ ;

**7:**  $u \leftarrow 1$ ;

**8:**  $v \leftarrow |\mathcal{S}'|$ ;

**9:**  $m \leftarrow 0$ ;

**10:**  $p \leftarrow 0$ ;

**11:** **while** true **do**

**12:**   **if**  $u > v$  **then**

**13:**      $p \leftarrow v$ ;

**14:**     break;

**15:**   **end if**

**16:**    $m = \lfloor \frac{1}{2}(u + v) \rfloor$ ;

**17:**    $\mathcal{A}^{(k)} \leftarrow \{\mathcal{S}'(1), \mathcal{S}'(2), \dots, \mathcal{S}'(m)\}$ ; // We use  $\mathcal{S}'(m)$  to represent the  $m$ th element in  $\mathcal{S}'$

**18:**   Find an approximate shortest tour among the anchor points in  $\mathcal{A}^{(k)}$  and let  $\text{TSP}(\mathcal{A}^{(k)})$  denote its length;

**19:**   **switch**  $\text{TSP}(\mathcal{A}^{(k)})$

**20:**    **case**  $\text{TSP}(\mathcal{A}^{(k)}) < L$ :  $u \leftarrow m + 1$ ;

**21:**    **case**  $\text{TSP}(\mathcal{A}^{(k)}) = L$ :  $p \leftarrow m$ ; break;

**22:**    **case**  $\text{TSP}(\mathcal{A}^{(k)}) > L$ :  $v \leftarrow m - 1$ ;

**23:**   **end switch**

**24:** **end while**

**25:**  $\mathcal{A}^{(k)} \leftarrow \{\mathcal{S}'(1), \mathcal{S}'(2), \dots, \mathcal{S}'(p)\}$ ;

**26:** Find an approximate shortest tour among anchor points in  $\mathcal{A}^{(k)}$ ;

---

For the R-tour, as a pretreatment, the algorithm sorts the sensors with their battery energy in an increasing order. We record this sorted sensor list by  $\mathcal{S}'$  and use  $\mathcal{S}'(i)$  to represent the  $i_{th}$  element in the list. The problem is now converted to finding a target sensor  $\mathcal{S}'(p)$  such that by visiting the sensors with the index no more than  $p$ , i.e.,  $\mathcal{S}'(1), \mathcal{S}'(2), \dots, \mathcal{S}'(p)$ , the tour length is no more than  $L$ . To this end, the algorithm first finds the middle element of  $\mathcal{S}'$ , denoted by  $\mathcal{S}'(m)$  and inspects the shortest migration tour among the locations of the sensors  $\mathcal{S}'(1), \mathcal{S}'(2), \dots, \mathcal{S}'(m)$ . The migration tour can be found by an approximate solution to Traveling Salesman Problem (TSP) [28]. If the migration tour length equals the bound  $L$ , then the target sensor has been found; otherwise, the upper half or the lower half of the list is chosen to further search for the target sensor based on whether  $L$  is greater than or less than the migration tour among  $\mathcal{S}'(1), \mathcal{S}'(2), \dots, \mathcal{S}'(m)$ . The algorithm reduces the number of elements needed to be checked to half each time, which is similar to the binary search algorithm [29]. We use  $[u, v]$  to indicate the search range for the target sensor, where  $u$  and  $v$  are the indices of boundary elements. When there is no valid search range, i.e.,  $u > v$ , it implies that there is no way to find a tour with the length exactly equal to  $L$ . Then  $p$  is set equal to  $v$  and  $\mathcal{S}'(p)$  is selected as the target sensor. By visiting the locations of  $\mathcal{S}'(1), \mathcal{S}'(2), \dots, \mathcal{S}'(p)$ , the tour length will be closest to and less than  $L$ . It is clear that at most  $\lceil \log(|\mathcal{S}'|) \rceil$  rounds are needed to search for the target sensor. In each round, we need to calculate the shortest tour among at most  $|\mathcal{S}'|$  sensors, which can be solved by finding approximate or heuristic solutions to the corresponding TSP problem with  $O(|\mathcal{S}'|^2)$  time complexity. Therefore, the overall time complexity of the selection algorithm is  $O(|\mathcal{S}'|^2 \log(|\mathcal{S}'|))$ .

For D-tours, the sensors are depicted with the least battery energy of their neighbors within  $m$  hops, i.e.,  $\mathcal{B}_e^{(k),D} = \{\min \{b_j^{(k),D} | Dist(i, j) \leq m, j \in \mathcal{S}\} | i \in \mathcal{S}\}$ . Using  $\mathcal{B}_e^{(k),D}$  instead of  $\mathcal{B}_e^{(k),R}$  as the input, and sorting the sensors in terms of their battery energy in an decreasing order as a pretreatment, the anchor points can be selected by executing the algorithm in the similar way as R-tour.

Figure 25.3 shows the examples of anchor point selection algorithm for R-tour and D-tours on a same network with a total of 50 sensors. We set sensor's battery energy following uniform distribution over  $[0, 100]$  and set the tour length bound to 200 m. In Fig. 25.3a, the labeled number next to each sensor stands for the battery level of the corresponding sensor. In Fig. 25.3b, the labeled number next to each sensor alternatively denotes the battery level of the corresponding sensor's one-hop neighbors with the least residual energy. The bold line segments in the figure represent the migration tour of the SenCar. The sensors on the tour are the anchor points to be visited in the current tour. It is evident that for R-tour, the sensors with lower battery level would have higher precedence to be charged than other sensors so as to satisfy the demand for timely energy replenishment. In contrast, for D-tours, the sensors with neighbors having more residual energy are more likely to be selected as anchor points to enable more data uploading to the SenCar.

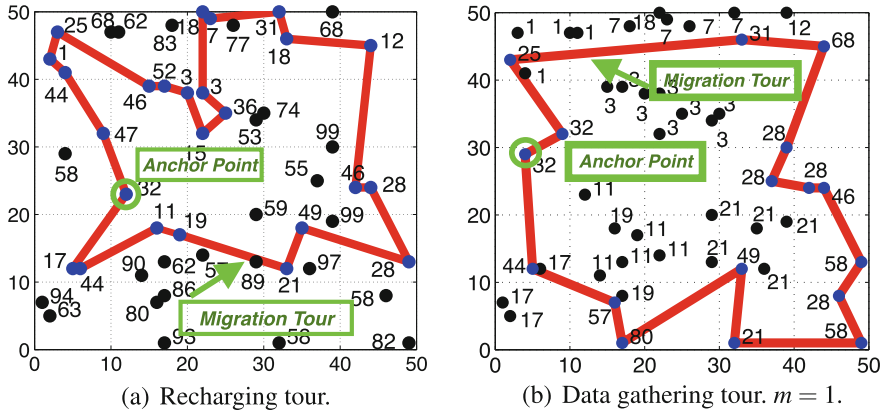


**Fig. 25.3** Example to illustrate the selection algorithm to search for anchor points for recharging tour and data gathering tour. Tour bound  $L = 200$  m

### 25.2.2 Second Step: Optimal Mobile Data Gathering Scheme

Once the anchor points are determined for both R-tour and D-tours, the remaining work is how to gather the data from sensors when the SenCar migrates among the anchor points. We study such a mobile data gathering problem by formulating it into a utility maximization problem based on a flow-level network model. In the following, we first provide the problem formulation for data gathering in R-tour and D-tours, and then propose an optimization-based distributed algorithm for the data gathering problem.

#### 25.2.2.1 Problem Formulation

Given the set of anchor points in a tour, the problem formulation for R-tour and D-tours are actually similar to each other. We first derive the problem formulation for R-tour with details and then directly provide the formulation for D-tours.

For the R-tour in time interval  $k$ , consider a network with a set of static sensors, denoted by  $\mathcal{S}$ , and a set of anchor points, denoted by  $\mathcal{A}^{(k),R}$ . To capture the characteristics of the SenCar movements over different anchor points in the R-tour, we model the sensor network with the SenCar located at an anchor point  $a$  ( $a \in \mathcal{A}^{(k),R}$ ) by a directed acyclic graph (DAG)  $G_a^{(k),R}(V_a^{(k),R}, E_a^{(k),R})$ .  $V_a^{(k),R} = \mathcal{S} \cup \{\Lambda_a\}$ , which represents the set of nodes, including all the sensors and the SenCar at anchor point  $a$  (denoted by  $\Lambda_a$ ).  $E_a^{(k),R} = \{(i, j) | i, j \in V_a^{(k),R}\}$ , which is the set of directed links among the sensors and the SenCar. We assume each sensor, say sensor  $i$ , would send

the sensing data stored in the buffer to the SenCar with a data rate of  $r_{i,a}^{(k),R}$  when the SenCar moves to anchor point  $a$ . The SenCar stays at each anchor point for a same sojourn time  $\tau^{(k),R}$  in the R-tour to collect data routed to it in multiple hops.

The utility function  $U_i(\cdot)$  is used to characterize the impact of the collected data from a sensor on the overall data gathering performance. We define  $U_i(\cdot)$  as a strictly concave, increasing and twice-differentiable function with respect to the total amount of data gathered from sensor  $i$  in R-tour (i.e.,  $\sum_{a \in \mathcal{A}^{(k),R}} r_{i,a}^{(k),R} \tau^{(k),R}$ ). Accordingly, the network utility is defined as the aggregation utility of all sensors.

With the target of maximizing the network utility while maintaining the perpetual operation of the network, the mobile data gathering problem for R-tour in time interval  $k$  can be formulated as follows. For clarity, all the notations used in the formulation are summarized in Table 25.1.

$$\text{MDG: } \max_{\mathbf{r}^{(k),R}, \mathbf{f}^{(k),R}} \sum_{i \in \mathcal{S}} U_i \left( \sum_{a \in \mathcal{A}^{(k),R}} r_{i,a}^{(k),R} \tau^{(k),R} \right) \quad (25.1)$$

Subject to

$$r_{i,a}^{(k),R} + \sum_{j \in \mathcal{C}_{i,a}^{(k),R}} f_{ji,a}^{(k),R} = \sum_{j \in \mathcal{P}_{i,a}^{(k),R}} f_{ij,a}^{(k),R}, \forall i \in \mathcal{S}, \forall a \in \mathcal{A}^{(k),R} \quad (25.2)$$

$$\left( \sum_{a \in \mathcal{A}^{(k),R}} \sum_{j \in \mathcal{P}_{i,a}^{(k),R}} f_{ij,a}^{(k),R} e_i^t + \sum_{a \in \mathcal{A}^{(k),R}} \sum_{j \in \mathcal{C}_{i,a}^{(k),R}} f_{ji,a}^{(k),R} e_i^r \right) \cdot \tau^{(k),R} < \frac{1}{q+1} \sigma b_i^{(k),R}, \forall i \in \mathcal{S} \quad (25.3)$$

$$r_{i,a}^{(k),R} \in \Pi_a^{(k),R}, f_{ij,a}^{(k),R} \in \Pi_a^{(k),R}, \forall i \in \mathcal{S}, \forall j \in \mathcal{P}_{i,a}^{(k),R}, \forall a \in \mathcal{A}^{(k),R} \quad (25.4)$$

where

$$b_i^{(k),R} = \begin{cases} B_i, & \text{if } i \in \mathcal{A}^{(k),R} \\ \check{b}_i^{(k-1),D}, & \text{otherwise} \end{cases} \quad (25.5)$$

$$\tau^{(k),R} = \frac{T/(q+1) - \text{TSP}(\mathcal{A}^{(k),R}) / v_s}{|\mathcal{A}^{(k),R}|} \quad (25.6)$$

The constraints can be explained as follows:

- Equation (25.2) describes flow conservation constraint, which states that at each sensor for each anchor point, the aggregated outgoing link flow rates equal the local data rate plus incoming link flow rates.
- Equation (25.3) describes energy constraint, which enforces the energy cost at each sensor, including the transmitting and receiving energy consumption, in R-tour bounded by its energy budget, which is a portion of available battery energy.

**Table 25.1** List of notations used in mobile data gathering problem in sensor networks with random topology

| Notation                    | Definition  |
|-----------------------------|---|
| $\mathcal{S}$               | Set of sensors, i.e., $\mathcal{S} = \{1, 2, \dots, N\}$  |
| $\mathcal{B}^{(k)}$         | Set of available battery energy of sensors for time interval $k$ , i.e.,<br>$\mathcal{B}^{(k)} = \{b_i^{(k)}   i \in \mathcal{S}\}$   |
| $\mathcal{B}_e^{(k),R}$     | Set of battery energy states of sensors at the beginning of R-tour of time interval $k$ ,<br>i.e., $\mathcal{B}_e^{(k),R} = \{b_i^{(k),R}   i \in \mathcal{S}\}$  |
| $Dist(i, j)$                | The minimal number of hops from sensor $i$ to sensor $j$  |
| $\mathcal{B}_e^{(k),D}$     | Set of the least energy of each sensor's neighbors within $m$ hops at the beginning of<br>D-tours of time interval $k$ , i.e.,<br>$\mathcal{B}_e^{(k),D} = \{\min \{b_j^{(k),D}   Dist(i, j) \leq m, j \in \mathcal{S}\}   i \in \mathcal{S}\}$ |
| $B_i$                       | Battery capacity of sensor $i$  |
| $\mathcal{A}^{(k),R}$       | Set of anchor points for R-tour in time interval $k$  |
| $\mathcal{A}^{(k),D}$       | Set of anchor points for D-tours in time interval $k$   |
| $\mathcal{P}_{i,a}^{(k),R}$ | Set of parent nodes of sensor $i$ for anchor point $a$ in R-tour in time interval $k$ , i.e.,<br>$\mathcal{P}_{i,a}^{(k),R} = \{j   (i, j) \in E_a^{(k),R}\}$   |
| $\mathcal{P}_{i,a}^{(k),D}$ | Set of parent nodes of sensor $i$ for anchor point $a$ in D-tours in time interval $k$ , i.e.,<br>$\mathcal{P}_{i,a}^{(k),D} = \{j   (i, j) \in E_a^{(k),D}\}$  |
| $\mathcal{C}_{i,a}^{(k),R}$ | Set of child nodes of sensor $i$ for anchor point $a$ in R-tour in time interval $k$ , i.e.,<br>$\mathcal{C}_{i,a}^{(k),R} = \{j   (j, i) \in E_a^{(k),R}\}$  |
| $\mathcal{C}_{i,a}^{(k),D}$ | Set of child nodes of sensor $i$ for anchor point $a$ in D-tours in time interval $k$ , i.e.,<br>$\mathcal{C}_{i,a}^{(k),D} = \{j   (j, i) \in E_a^{(k),D}\}$   |
| $\Lambda_a$                 | SenCar located at anchor point $a$  |
| $T$                         | Time length of each time interval   |
| $q + 1$                     | Total number of migration tours in each time interval, including one R-tour and $q$<br>D-tours  |
| $L$                         | Migration tour length bound for the SenCar  |
| $\tau^{(k),R}$              | Sojourn time of SenCar at each anchor point in a R-tour during time interval $k$  |
| $\tau^{(k),D}$              | Sojourn time of SenCar at each anchor point in a D-tour during time interval $k$  |
| $r_{i,a}^{(k),R}$           | Data rate of sensor $i$ when SenCar sojourns at anchor point $a$ in a R-tour during<br>time interval $k$  |
| $r_{i,a}^{(k),D}$           | Data rate of sensor $i$ when SenCar sojourns at anchor point $a$ in a D-tour during<br>time interval $k$  |
| $f_{ij,a}^{(k),R}$          | Flow rate over link $(i, j)$ when SenCar is located at anchor point $a$ in a R-tour in<br>time interval $k$   |
| $f_{ij,a}^{(k),D}$          | Flow rate over link $(i, j)$ when SenCar is located at anchor point $a$ in a D-tour in<br>time interval $k$   |
| $\Pi_a^{(k),R}$             | Feasible region of link capacity variable $f_{ij,a}^{(k),R}$  |
| $\Pi_a^{(k),D}$             | Feasible region of link capacity variable $f_{ij,a}^{(k),D}$  |
| $\sigma$                    | Portion parameter for the energy budget   |

(continued)

**Table 25.1** (continued)

| Notation              | Definition   |
|-----------------------|--|
| $e_i^t$               | Energy consumed by sensor $i$ for transmitting a unit flow                   |
| $e_i^r$               | Energy consumed by sensor $i$ for receiving a unit flow                      |
| $b_i^{(k),R}$         | Residual energy in node $i$ at the beginning of R-tour in time interval $k$  |
| $b_i^{(k),D}$         | Residual energy in node $i$ at the beginning of D-tours in time interval $k$ |
| $\check{b}_i^{(k),R}$ | Residual energy in node $i$ at the end of the R-tour in time interval $k$    |
| $\check{b}_i^{(k),D}$ | Residual energy in node $i$ at the end of the D-tours in time interval $k$   |
| $v_s$                 | Moving velocity of the SenCar  |

- Equation (25.4) describes capacity constraint, which specifies that the flow rate allocated on a link for a particular anchor point must fall in feasible capacity region  $\Pi_a^{(k),R}$ . We employ the node exclusive interference model [11] to characterize the conflict relationship among the links, where a sensor can only communicate with another sensor at a time. Based on the model, a feasible schedule for collision avoidance is equivalent to finding a matching in the corresponding DAG. Thus,  $\Pi_a^{(k),R}$  can be similarly defined as the convex hull of possible rate vectors of the matchings in  $G_a^{(k),R}$ . In fact, as the input to MDG problem,  $\Pi_a^{(k),R}$  can be customized to a specified capacity region that is compatible with the node exclusive interference model for rate optimization based on user or application needs. In the implementation, considering the needs of rate maximization and efficiency enhancement, we can consider all maximal matchings in  $G_a^{(k),R}$  as  $\Pi_a^{(k),R}$ , which can be found in  $O(|E_a^{(k),R}| + |V_a^{(k),R}| + \Delta N)$  time [30], where  $V_a^{(k),R}$  is the vertex set of  $G_a^{(k),R}$ ,  $E_a^{(k),R}$  is the edge set of  $G_a^{(k),R}$ ,  $\Delta$  is the maximum degree in  $G_a^{(k),R}$  and  $N$  is the number of maximal matchings in  $G_a^{(k),R}$ .

In the formulation,  $b_i^{(k),R}$  and  $\tau^{(k),R}$  represent the available battery energy of sensor  $i$  in R-tour for time interval  $k$  and the sojourn time at each anchor point in R-tour during time interval  $k$ , respectively. As the sensors located at anchor points can get fast recharging at the beginning of the R-tour, they are considered to have full battery energy for use, i.e.,  $b_i^{(k),R} = B_i$ , if  $i \in \mathcal{A}^{(k),R}$ . For other sensors,  $b_i^{(k),R}$  is the remaining battery energy from previous time interval.

In the similar way, the mobile data gathering problem for D-tours in time interval  $k$  can be formulated as follows, with the target to maximize the aggregate utility regarding the total data gathered in all D-tours.

$$\text{MDG: } \max_{\mathbf{r}^{(k),D}, \mathbf{f}^{(k),D}} \sum_{i \in \mathcal{S}} U_i \left( \sum_{a \in \mathcal{A}^{(k),D}} r_{i,a}^{(k),D} q \tau^{(k),D} \right) \quad (25.7)$$

Subject to

$$r_{i,a}^{(k),D} + \sum_{j \in \mathcal{C}_{i,a}^{(k),D}} f_{ji,a}^{(k),D} = \sum_{j \in \mathcal{P}_{i,a}^{(k),D}} f_{ij,a}^{(k),D}, \forall i \in \mathcal{S}, \forall a \in \mathcal{A}^{(k),D} \quad (25.8)$$

$$\left( \sum_{a \in \mathcal{A}^{(k),D}} \sum_{j \in \mathcal{P}_{i,a}^{(k),D}} f_{ij,a}^{(k),D} e_i^t + \sum_{a \in \mathcal{A}^{(k),D}} \sum_{j \in \mathcal{C}_{i,a}^{(k),D}} f_{ji,a}^{(k),D} e_i^r \right) \cdot q \tau^{(k),D} < \sigma b_i^{(k),D}, \forall i \in \mathcal{S} \quad (25.9)$$

$$r_{i,a}^{(k),D} \in \Pi_a^{(k),D}, f_{ij,a}^{(k),D} \in \Pi_a^{(k),D}, \forall i \in \mathcal{S}, \forall j \in \mathcal{P}_{i,a}^{(k),D}, \forall a \in \mathcal{A}^{(k),D} \quad (25.10)$$

where

$$b_i^{(k),D} = \begin{cases} B_i, & \text{if } i \in \mathcal{A}^{(k),D} \\ \check{b}_i^{(k),R}, & \text{otherwise} \end{cases} \quad (25.11)$$

$$\tau^{(k),D} = \frac{\frac{q}{q+1} \cdot T - q \cdot \text{TSP}(\mathcal{A}^{(k),D}) / v_s}{q \cdot |\mathcal{A}^{(k),D}|} \quad (25.12)$$

From the formulation, we can see that we treat all  $q$  D-tours as a whole for one-time optimization, i.e., we maximize the network utility with respect to the aggregate data gathered in  $q$  D-tours. This implies that we would follow the same strategies, including anchor points selection, data rates, and flow routing, in all  $q$  D-tours.

### 25.2.2.2 Distributed Algorithm for MDG Problem

Since the MDG problems for R-tour and D-tours have similar formulation, without loss of generality, we describe the solution to MDG for D-tours here as an example for illustration, and the solution to MDG for R-tour can be easily derived in a similar way.

In MDG problem of D-tours, it is observed that the objective function is concave, however, not strictly concave with respect to  $r_{i,a}^{(k),D}$ . This is because  $U_i(\cdot)$  is only strictly concave regarding the linear combination of  $r_{i,a}^{(k),D}$  and the linearity lacks of strict concavity. Directly solving MDG with the dual approach [31] may incur oscillation before the system enters the equilibrium, which is not amenable for practical implementations. Thus, we resort to the proximal optimization algorithm [32], which can be explained as follows.

#### Proximal Approximation-Based Algorithm

It has been proved in [33] that the proximal approximation-based algorithm is effective to such optimization problem with non-strict concavity and can achieve an optimal solution to the problem. Particularly, for our MDG problem, a quadratic term  $-\frac{1}{2c} \|\mathbf{r}^{(k),D} - \mathbf{x}^{(k),D}\|_2^2 = -\frac{1}{2c} \sum_{i \in \mathcal{S}} \sum_{a \in \mathcal{A}^{(k),D}} (r_{i,a}^{(k),D} - x_{i,a}^{(k),D})^2$  is added to the original

objective function to make it strictly concave, where  $\mathbf{r}^{(k),D} = \{r_{i,a}^{(k),D}\}$ ,  $\mathbf{x}^{(k),D}$  is an additional matrix and  $c$  is a positive scalar parameter. The proximal approximation algorithm runs in iterations, which alternatively maximizes the updated network utility over  $\mathbf{r}^{(k),D}$  while keeping  $\mathbf{x}^{(k),D}$  fixed, then over  $\mathbf{x}^{(k),D}$  while keeping  $\mathbf{r}^{(k),D}$  fixed, and repeats. In particular, the  $t$ -th iteration of the algorithm performs the following two steps.

**Step 1:** Fix  $x_{i,a}^{(k),D} = x_{i,a}^{(k),D}[t]$  for all  $i \in \mathcal{S}$  and  $a \in \mathcal{A}^{(k),D}$  and solve the following problem to obtain the optimal  $r_{i,a}^{(k),D}[t]$  and  $f_{ij,a}^{(k),D}[t]$ .

$$\max_{\substack{\mathbf{r}^{(k),D} \\ \mathbf{f}^{(k),D}}} \sum_i U_i \left( \sum_{a \in \mathcal{A}^{(k),D}} r_{i,a}^{(k),D} q \tau^{(k),D} \right) - \frac{1}{2c} \|\mathbf{r}^{(k),D} - \mathbf{x}^{(k),D}\|_2^2, \quad (25.13)$$

subject to constraints (25.2)–(25.4).

**Step 2:** Set  $x_{i,a}^{(k),D}[t+1] = r_{i,a}^{(k),D}[t]$  for all  $i \in \mathcal{S}$  and  $a \in \mathcal{A}^{(k),D}$ .

In the aforementioned two steps of proximal approximation-based algorithm, the main work is to solve problem (25.13). Since it is a strictly concave problem with respect to  $\mathbf{r}^{(k),D}$ , we apply the subgradient method based on dual decomposition for it, which is an efficient technique for convex programs and can naturally achieve the distributed implementation. In the following, we provide the details of the solution to problem (25.13).

**Dual Decomposition:** We relax constraints (25.2) and (25.3) by introducing Lagrangian multiplier  $\lambda_{i,a}^{(k),D}$  and  $\phi_i^{(k),D}$ . Then we can obtain the partial Lagrangian

$$\begin{aligned} L(\mathbf{r}^{(k),D}, \mathbf{f}^{(k),D}, \lambda^{(k),D}, \phi^{(k),D}) = & \sum_i U_i \left( \sum_a r_{i,a}^{(k),D} q \tau^{(k),D} \right) - \frac{1}{2c} \cdot \sum_i \sum_a (r_{i,a}^{(k),D} - x_{i,a}^{(k),D})^2 \\ & - \sum_i \sum_a \lambda_{i,a}^{(k),D} \cdot \left( r_{i,a}^{(k),D} + \sum_j f_{ji,a}^{(k),D} - \sum_j f_{ij,a}^{(k),D} \right) \\ & - \sum_i \phi_i^{(k),D} \left[ q \tau^{(k),D} \cdot (\sum_a \sum_j f_{ij,a}^{(k),D} e_i^t + \sum_a \sum_j f_{ji,a}^{(k),D} e_i^r) - \sigma b_i^{(k),D} \right]. \end{aligned} \quad (25.14)$$

By merging the terms with respect to the same variables and ignoring the constant terms,  $L(\mathbf{r}^{(k),D}, \mathbf{f}^{(k),D}, \lambda^{(k),D}, \phi^{(k),D})$  can be rewritten as follows

$$\begin{aligned} L = & \left[ \sum_i U_i \left( \sum_a r_{i,a}^{(k),D} q \tau^{(k),D} \right) - \frac{1}{2c} \sum_i \sum_a (r_{i,a}^{(k),D} - x_{i,a}^{(k),D})^2 - \sum_i \sum_a \lambda_{i,a}^{(k),D} r_{i,a}^{(k),D} \right] \\ & + \sum_i \sum_j \sum_a \left[ \lambda_{i,a}^{(k),D} - \lambda_{j,a}^{(k),D} - q \tau^{(k),D} \cdot (\phi_i^{(k),D} e_i^t + \phi_j^{(k),D} e_i^r) \right] f_{ij,a}^{(k),D}. \end{aligned} \quad (25.15)$$

By duality, we can alternatively solve the dual problem as

$$\min_{\substack{\lambda^{(k),D} \geq 0 \\ \phi^{(k),D} \geq 0}} g(\lambda, \phi) = \min_{\substack{\lambda^{(k),D} \\ \phi^{(k),D}}} \max_{\substack{\mathbf{r}^{(k),D} \\ \mathbf{f}^{(k),D}}} L, \quad (25.16)$$

subject to constraint (25.4).

From Eq. (25.15), we can see that the dual problem has a good separable property, which can be decomposed into two subproblems. One is the rate control subproblem in terms of rate variables  $\mathbf{r}^{(k),D}$ , and another is the joint scheduling and routing subproblem to find optimal flow variables  $\mathbf{f}^{(k),D}$ .

### Rate Control Subproblem

Given  $\lambda_{i,a}^{(k),D}$ , each sensor solves a local optimization as follows by adjusting its data rates for different anchor points in time interval  $k$ .

$$\max_{r_{i,a}^{(k),D} \geq 0} U_i \left( \sum_a r_{i,a}^{(k),D} q \tau^{(k),D} \right) - \frac{1}{2c} \sum_a \left( r_{i,a}^{(k),D} - x_{i,a}^{(k),D} \right)^2 - \sum_a \lambda_{i,a}^{(k),D} r_{i,a}^{(k),D} \quad (25.17)$$

This local optimization can be solved by a similar approach to that in [34] with the complexity of  $O(|\mathcal{A}^{(k),D}| \log(|\mathcal{A}^{(k),D}|))$ , which is explained as follows.

Let  $\mu_a$  be the Lagrangian multiplier for constraint  $r_{i,a}^{(k),D} \geq 0$ . For each  $a \in \mathcal{A}^{(k),D}$ , the Karush–Kuhn–Tucker (KKT) conditions [31] are given by

$$\mu_a \geq 0; \quad (25.18)$$

$$\mu_a \cdot r_{i,a}^{(k),D} = 0; \quad (25.19)$$

$$U'_i \left( \sum_a r_{i,a}^{(k),D} q \tau^{(k),D} \right) \cdot q \tau^{(k),D} - \frac{1}{c} r_{i,a}^{(k),D} + \frac{1}{c} x_{i,a}^{(k),D} - \lambda_{i,a}^{(k),D} + \mu_a = 0. \quad (25.20)$$

Let  $m_{i,a}^{(k),D} = \frac{1}{c} x_{i,a}^{(k),D} - \lambda_{i,a}^{(k),D}$ . Then, (25.20) can be rewritten as  $U'_i(\sum_a r_{i,a}^{(k),D} q \tau^{(k),D}) q \tau^{(k),D} - \frac{1}{c} r_{i,a}^{(k),D} + m_{i,a}^{(k),D} + \mu_a = 0$ . If we sort the rates in the order that  $m_{i,1}^{(k),D} \geq m_{i,2}^{(k),D} \geq \dots \geq m_{i,|\mathcal{A}^{(k),D}|}^{(k),D}$ , we have that for any  $1 \leq a' \leq a \leq |\mathcal{A}^{(k),D}|$ ,  $r_{i,a'}^{(k),D} \geq r_{i,a}^{(k),D}$ . This result trivially holds when  $r_{i,a}^{(k),D} = 0$ . And when  $r_{i,a}^{(k),D} > 0$ , we have  $\mu_a = 0$  based on (25.19) and  $r_{i,a'}^{(k),D} - r_{i,a}^{(k),D} = c(m_{i,a'}^{(k),D} - m_{i,a}^{(k),D}) + \mu_{a'} \geq 0$ . Therefore, using this result and the KKT conditions, there exists an  $A$ , with  $1 \leq A \leq |\mathcal{A}^{(k),D}|$ , such that

$$r_{i,a}^{(k),D} = \begin{cases} c \left[ q \tau^{(k),D} \cdot U'_i \left( R_i^{(k),D} q \tau^{(k),D} \right) + m_{i,a}^{(k),D} \right] > 0, & a \leq A \\ 0, & a > A \end{cases}; \quad (25.21)$$

where  $R_i^{(k),D} = \sum_{a=1}^A r_{i,a}^{(k),D}$  denotes the sum of data rates for different anchor points. This implies that to find the optimal value for every  $r_{i,a}^{(k),D}$ , we only need to find optimal  $R_i^{(k),D}$  and the  $A$ . As  $r_{i,a}^{(k),D}$  is nonincreasing with  $a$ ,  $A$  can be considered as the dividing line that indicates whether the data rates for the part of anchor points are greater than or equal to zero.

When  $A$  is given,  $R_i^{(k),D}$  can be easily computed by solving the summation of (25.20) for all  $a \leq A$ . In particular, as  $r_{i,a}^{(k),D} > 0$  for all  $a \leq A$ , we have that  $\mu_a = 0$  for all  $a \leq A$  based on (25.19) so that  $R_i^{(k),D}$  is the solution of

$Aq\tau^{(k),D} \cdot U'_i(R_i^{(k),D} q\tau^{(k),D}) - \frac{1}{c}R_i^{(k),D} + \sum_{a=1}^A m_{i,a}^{(k),D} = 0$ . This way, the remaining work becomes finding a proper  $A$ . As aforementioned, since  $r_{i,a}^{(k),D}$  is nonincreasing in  $a$  and  $A$  is the boundary to divide data rates for different anchor points into zero and greater-than-zero parts, we can search for  $A$  from  $|\mathcal{A}^{(k),D}|$  down to 1, and when  $r_{i,A}^{(k),D} = c \left[ q\tau^{(k),D} U'_i(R_i^{(k),D} q\tau^{(k),D}) + m_{i,A}^{(k),D} \right] \geq 0$ , we say  $A$  is found.

For clear presentation, we summarize the details of rate control algorithm for subproblem (25.17) in Algorithm 31.

### Scheduling Subproblem

Given  $\lambda_{i,a}^{(k),D}$  and  $\phi_i^{(k),D}$ , based on Eq. (25.15), the second subproblem can be expressed as following, which aims to provide the solution to the problem of how to schedule the links for data gathering.

---

#### Algorithm 31: Distributed Rate Control Algorithm at Sensor $i$

---

- 1: Sort anchor points in  $\mathcal{A}^{(k),D}$  such that  $m_{i,a}^{(k),D}$  is in the decreasing order;
  - 2:  $A \leftarrow |\mathcal{A}^{(k),D}|$ ;
  - 3:  $M \leftarrow \sum_{a=1}^{|\mathcal{A}^{(k),D}|} m_{i,a}^{(k),D}$ ;
  - 4: **while**  $A \geq 1$  **do**
  - 5:   Solve  $Aq\tau^{(k),D} \cdot U'_i(R_i^{(k),D} q\tau^{(k),D}) - \frac{1}{c}R_i^{(k),D} + M = 0$  for optimal  $R_i^{(k),D}$ ; // Use  $R_i^{(k),D}$  to denote  $\sum_{a=1}^A r_{i,a}^{(k),D}$
  - 6:   Compute  $r_{i,A}^{(k),D} = c \left[ q\tau^{(k),D} U'_i(R_i^{(k),D} q\tau^{(k),D}) + m_{i,A}^{(k),D} \right]$ ;
  - 7:   **if**  $r_{i,A}^{(k),D} \geq 0$  **then**
  - 8:     Compute the data rate for each anchor point as:
  - 9:     
$$r_{i,a}^{(k),D} = \begin{cases} c \left[ q\tau^{(k),D} \cdot U'_i(R_i^{(k),D} q\tau^{(k),D}) + m_{i,a}^{(k),D} \right] > 0, & a \leq A \\ 0, & a > A \end{cases};$$
  - 10:   **else**
  - 11:      $M \leftarrow M - m_{i,A}^{(k),D}$ ;
  - 12:      $A \leftarrow A - 1$ ;
  - 13:   **end if**
  - 14: **end while**
- 

$$f_{ij,a}^{(k),D} \in \arg \max_{f_{ij,a}^{(k),D} \in H_a^{(k),D}} \sum_i \sum_j \left[ \lambda_{i,a}^{(k),D} - \lambda_{j,a}^{(k),D} - q\tau^{(k),D} (\phi_i^{(k),D} e_i^t + \phi_j^{(k),D} e_i^r) \right] f_{ij,a}^{(k),D}. \quad (25.22)$$

If we consider  $\lambda_{i,a}^{(k),D} - \lambda_{j,a}^{(k),D} - q\tau^{(k),D} (\phi_i^{(k),D} e_i^t + \phi_j^{(k),D} e_i^r)$  as the weight of link  $(i, j)$  destined for the SenCar at anchor point  $a$ , the scheduling problem in (25.22) is equivalent to the maximum weighted matching problem under the node exclusive interference model. We can utilize the heuristic distributed algorithms in [35] and [36] to solve this problem in  $O(|E_a^{(k),D}|)$  time.

## Lagrangian Multiplier Update

In each iteration of the subgradient algorithm, sensor  $i$  solves two subproblems in (25.17) and (25.22) with the current Lagrangian multiplier  $\lambda_{i,a}^{(k),D}[n]$  and  $\phi_i^{(k),D}[n]$ . After then, sensor  $i$  needs to update the Lagrangian multipliers as follows and sends them to its direct neighbors to facilitate the computing of  $\mathbf{r}^{(k),D}$  and  $\mathbf{f}^{(k),D}$  in the next iteration.

$$\begin{aligned}\lambda_{i,a}^{(k),D}[n+1] &= \left[ \lambda_{i,a}^{(k),D}[n] + \theta[n] \cdot \left( r_{i,a}^{(k),D}[n] + \sum_j f_{ji,a}^{(k),D}[n] - \sum_j f_{ij,a}^{(k),D}[n] \right) \right]^+, \\ \phi_i^{(k),D}[n+1] &= \left[ \phi_i^{(k),D}[n] + \theta[n] \cdot \left[ q\tau^{(k),D} \left( \sum_a \sum_j f_{ij,a}^{(k),D} e_i^t + \sum_a \sum_j f_{ji,a}^{(k),D} e_i^r \right) - \sigma b_i^{(k),D} \right] \right]^+, \end{aligned}\quad (25.23)$$

where  $[\cdot]^+$  denotes the projection onto the nonnegative orthant and  $\theta[n]$  is a properly chosen scalar stepsize for subgradient iteration  $n$ . In our algorithm, we choose the diminishing stepsizes, i.e.,  $\theta[n] = d/(b + cn)$ ,  $\forall k, c, d > 0$ ,  $b \geq 0$ , where  $b, c$  and  $d$  are adjustable parameters that regulate the convergence speed. The diminishing stepsize can guarantee the convergence regardless of the initial value of  $\lambda$  [31].

## Recovery of Primal Solutions

Since the subproblem of the scheduling subproblem is linear, which implies that the values in the optimal solution of the Lagrangian dual cannot be directly applied to the primal problem. In view of this, we apply the method introduced in [37] to recover the optimal primal values for variables  $f_{ij,a}^{(k),D}$ . When variables  $x_{i,a}^{(k),D}$  converge in the higher level optimization, during the subgradient iterations in the lower level we construct the primal feasible sequences  $\{\hat{f}_{ij,a}^{(k),D}[n]\}$  as follows.

$$\hat{f}_{ij,a}^{(k),D}[n] = \frac{1}{n} \sum_{h=1}^n f_{ij,a}^{(k),D}[h] = \begin{cases} f_{ij,a}^{(k),D}[1], & n = 1 \\ \frac{n-1}{n} \hat{f}_{ij,a}^{(k),D}[n-1] + \frac{1}{n} f_{ij,a}^{(k),D}[n], & n > 1 \end{cases}. \quad (25.24)$$

Sherali and Choi [37] have proved that when the diminishing stepsize is used, any accumulation point of the recovered sequence generated by the method in (25.24) is feasible to the primal problem and it can converge to a primal optimal solution. Thus, optimal flow rates can be obtained when  $\{\hat{f}_{ij,a}^{(k),D}\}$  converges to  $\hat{f}_{ij,a}^{(k),D*}$ . When primal-applicable  $\{\hat{f}_{ij,a}^{(k),D}\}$  is ready, the final value for  $\{r_{i,a}^{(k),D}\}$  can be easily derived by flow conservation constraint.

Finally, we summarize the proximal approximation-based algorithm in Algorithm 32, which is described in the context of sensor  $i$  for time interval  $k$ . As the algorithm is performed by each sensor individually and the information is only exchanged among direct neighbors, the algorithm is fully distributed.

## 25.3 A Simplified Scenario: J-MERDG in Wireless Rechargeable Sensor Networks with Regular Topologies

After studying J-MERDG in generic sensor networks with random topologies, in this section, we consider J-MERDG under the networks with regular topologies. It is quite common in sensor applications that the deployment of sensors is controllable. Some regular network topologies, e.g., equilateral triangle, square, and hexagon, are widely used in practice in order to achieve expanded sensing coverage or ease the network maintenance. The aforementioned algorithms in Sect. 25.2 are assuredly applicable to these cases. However, due to the regularity of the topology, it is possible for us to derive the strategies with less complexity for such networks to meet with our targets. In this section, we will take the square topology as a representative of regular network topologies and explore how to achieve efficient joint mobile energy replenishment and data gathering in a simplified way.

---

### Algorithm 32: Summary of Proximal Approximation-Based Algorithm

---

- 1: Initialize  $\mathbf{x}_i^{(k),D} = \{x_{i,a}^{(k),D} | a \in \mathcal{A}^{(k),D}\}$  to nonnegative values;  
    // iterations for proximal approximation
  - 2: **repeat**
  - 3:   Initialize Lagrangian multipliers  $\lambda_i^{(k),D} = \{\lambda_{i,a}^{(k),D} | a \in \mathcal{A}^{(k),D}\}$  and  $\phi^{(k),D} = \{\phi_i^{(k),D} | i \in \mathcal{S}\}$  to non-negative values;  
    // iterations for subgradient and dual decomposition for (25.13)
  - 4:   **repeat**
  - 5:     Compute  $\mathbf{r}_i^{(k),D}[n] = \{r_{i,a}^{(k),D}[n] | a \in \mathcal{A}^{(k),D}\}$  by solving rate control subproblem (25.17);
  - 6:     Compute  $\mathbf{f}_i^{(k),D}[n] = \{f_{ij,a}^{(k),D}[n] | j \in \mathcal{P}_{i,a}^{(k),D}, a \in \mathcal{A}^{(k),D}\}$  by solving scheduling subproblem (25.22);
  - 7:     Update lagrangian multipliers and send them to the direct neighbors;
  - 8:     **if**  $\mathbf{x}_i^{(k),D}$  get converged in high-level proximal iterations **then**
  - 9:       Compute primal feasible  $\hat{f}_{ij,a}^{(k),D}[n]$  by (25.24);
  - 10:      **end if**
  - 11:     **until**  $\lambda_i^{(k),D}$  and  $\phi_i^{(k),D}$  converge;
  - 12:      $\mathbf{x}_i^{(k),D}[t+1] = \mathbf{r}_i^{(k),D}[t]$  in the  $t$ th proximal iteration;
  - 13: **until**  $\mathbf{x}_i^{(k),D}$  converges and get final optimal  $\mathbf{r}_i^{(k),D}$  and  $\mathbf{f}_i^{(k),D}$
- 

### 25.3.1 Tour Planning for Recharging

Consider a square field covered by  $N^2$  sensors. Each sensor is regularly deployed on a grid, which is apart from its adjacent positions in horizontal and vertical directions with the same distance of  $d$ . To maintain the network connectivity, we assume that each sensor can only reach its adjacent sensors in the horizontal and vertical direc-

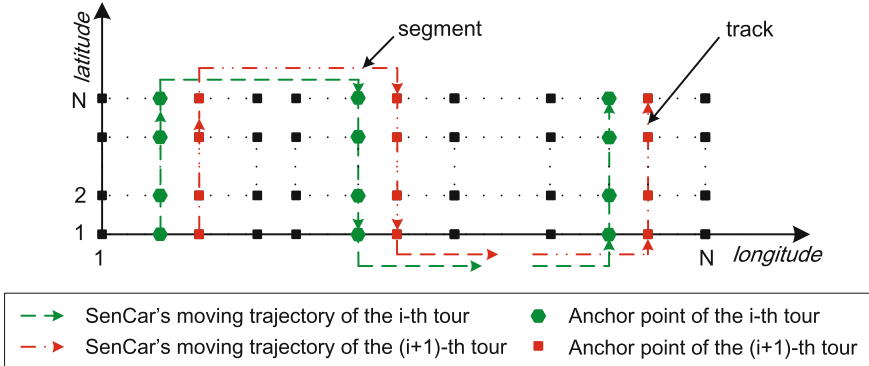


**Fig. 25.4** Joint mobile energy replenishment and data gathering in networks with a square topology

tions, i.e.,  $d \leq r < \sqrt{2}d$ , where  $r$  is the transmission range of sensors. Utilizing the regularity of network topology, we can simplify the migration tour of the SenCar by refining it to move on some parallel straight lines in each tour. The trajectory pattern of each tour can be similar to each other, however, the lines along which the SenCar moves are different from one tour to another so as to ensure the SenCar can have the chance to visit all sensors for energy delivery via wireless power transfer. Specifically, without the loss of generality, we take the first migration tour as an illustrative example. The sensing area is divided into  $p$  regions (denoted as  $1, 2, \dots, p$ ) by  $p$  vertically positioned straight lines. The first line positioned at the left boundary of the area and the  $p$ -th region is bounded by the  $p$ -th line and the right boundary of the area. For this tour, the SenCar moves along these  $p$  parallel virtual tracks (labeled as  $1, 2, \dots, p$ ), traverses the sensors on the track and goes further on  $(p - 1)$  segments that connect the tracks to form a continuous square-wave-shaped path as shown in Fig. 25.4. We use  $w_i$  ( $w_i \in N^+$ ) to represent the width of region  $i$ , i.e., the distance between two adjacent tracks is  $w_i d$ . Since it is expected that the length of each migration tour would not be longer than a threshold  $L$ ,  $w_i$  should be properly set and satisfy the following constraints

$$w_i = \begin{cases} w_1, & i = 1, 2, \dots, t \\ w_2, & i = t + 1, \dots, p, \end{cases} \quad (25.25)$$

where  $w_1, w_2, t$  and  $p$  satisfy the following constraints

$$(tw_1 + (p - t - 1)w_2 + p(N - 1))d \leq L, \quad (25.26)$$

$$tw_1 + (p - t)w_2 = N, \quad (25.27)$$

$$w_1 - w_2 \leq 1. \quad (25.28)$$

The reason why we set two different widths for the regions is because that the side length of the area may not be dividable by only one region width. Equation (25.26) enforces that the tour length is bounded by the given threshold. Equation (25.27)

guarantees that the entire moving trajectory in a tour traverses all area of the network. Equation (25.28) ensures that the regions are separated as evenly as possible in a tour. The positions of the sensors on the tracks are selected as the anchor points, where the SenCar stops for a period of sojourn time to charge the located sensors and simultaneously collect data from nearby sensors via multi-hop routing. In each successive migration tour, the moving trajectory of the SenCar would be shifted to the increasing direction of longitude by 1 unit of  $d$ , and a track which is shifted out of the field would be shifted in from the left and reconnected to the path. In order to reduce energy consumption on packet relay, each sensor is scheduled to transmit data to the SenCar when it visits the nearest anchor point. As the network topology is regular, the routing path for each sensor to the nearest anchor point is a straight line vertical to the track. In other words, each sensor is associated with only one anchor point in each migration tour and the associated anchor point is located on the nearest moving track and has the same latitude of the sensor.

From the above description, we can see that the migration trajectory of the SenCar in a tour is with square-wave type of moving path. The entire trajectory gradually slides along the longitude direction in the subsequent tours so as to cover the entire field for charging. The routing scheme is quite simple and straightforward, which involves limited overhead on forwarding. The reason why we adopt this kind of scheme is to fully utilize the regularity and symmetry of network topology so as to simplify our design. Due to such simplicity, SenCar can easily be aware of its migration tour ahead of time without any complex calculations and meanwhile the tour length bound can be readily ensured by properly setting the width of the region between two consecutive parallel straight lines.

### 25.3.2 Problem Formulation on Data Gathering

As aforementioned migration tour setting and routing scheme, it is shown in Fig. 25.5 that sensors with the same longitude will transmit data in the same pattern. Thus, to find effective data gathering strategies for all sensors can be reduced to the study on data routing among the sensors with the same latitude. Based on this observation, we can classify the sensors into *groups*, each of which consists the sensors with same latitude. In this way, we can simplify the 2-dimensional distribution of  $N^2$  sensors to 1-dimensional distribution of a single group of sensors. Based on the routing pattern, each group can then be further divided into *subgroups*, in which all sensors send data to the same anchor point along horizontal paths. In each subgroup, the sensors are located on the left and right sides of the associated anchor point with complete or partial symmetry. The traffic from the sensors merges to the SenCar at the anchor point along opposite directions. To ease the presentation, in each subgroup, the sensors that are  $i$ -hops away from the anchor point on both sides are denoted as  $i$  and  $i'$ , respectively, the SenCar at the anchor point is denoted as 0, and the sensor located at the anchor point is denoted as  $s_0$ . Correspondingly, a subgroup can be represented as  $\{\dots, i', \dots 2', 1', s_0, 1, 2, \dots i, \dots\}$ . The subgroup and the SenCar can be considered

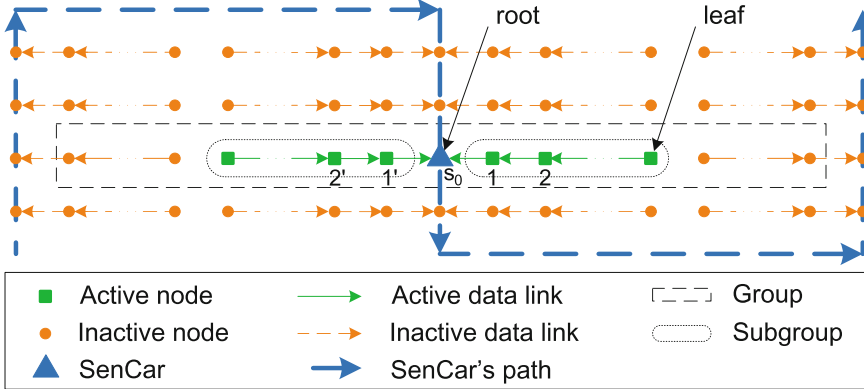


**Fig. 25.5** Each sensor transmits data to the SenCar when it arrives at the nearest anchor point

as a tree, where the SenCar is the *root*. Sensor  $i - 1$  is referred to as the *parent* of sensor  $i$ , and nodes  $0, 1, 2, \dots, i - 1$  are referred to as *ancestors* of sensor  $i$ .

Similar as in networks with random topologies, the design objective of J-MERDG under regular-distribution scenarios is to maximize the network utility in each migration tour. In the square-topology case, it is defined as  $\sum_{\mathcal{G}_j^{(k)}} \sum_{i \in \mathcal{G}_j^{(k)}} U_i(r_i^{(k)} \tau^{(k)})$ , where  $\mathcal{G}_j^{(k)}$  represents subgroup  $j$  in migration tour  $k$ ,  $r_i^{(k)}$  is the data rate of sensor  $i$  in subgroup  $j$  towards its associated anchor point in migration tour  $k$ , and  $\tau^{(k)}$  is the sojourn time at each anchor point in migration tour  $k$ . The utility function  $U_i(\cdot)$  is monotonically increasing, strictly concave, and twice-differentiable with respect to the total amount of data gathered from sensor  $i$  in each migration tour. Since each sensor belongs to a single subgroup and the sensors in different subgroups operate independently, the system-wide optimization can be simplified by maximizing the utility of each subgroup and can be correspondingly formulated as follows. The notations used in the formulation and their definitions are concluded in Table 25.2 for clarity.

$$\max_{\mathbf{r}^{(k)}, \mathbf{f}^{(k)}} \quad \sum_{i \in \mathcal{G}_j^{(k)}} U_i(r_i^{(k)} \tau^{(k)}) \quad (25.29)$$

Subject to

$$r_i^{(k)} + f_{i,i+1}^{(k)} = f_{i,i-1}^{(k)}, \forall i \in \mathcal{G}_j^{(k)} \setminus \{s_0\} \quad (25.30)$$

$$\tau^{(k)}(f_{i+1,i}^{(k)} e_i^r + f_{i,i-1}^{(k)} e_i^t) < \sigma b_i^{(k)}, \forall i \in \mathcal{G}_j^{(k)} \setminus \{s_0\} \quad (25.31)$$

$$r_i^{(k)} < r_{max}, f_{i,i-1}^{(k)} \leq l_{i,i-1}, \forall i \in \mathcal{G}_j^{(k)} \setminus \{s_0\} \quad (25.32)$$

$$r_{s_0}^{(k)} < r_{max}, f_{s_0,0} \tau^{(k)} e_{s_0}^{(k)} < \sigma b_{s_0}^{(k)}, f_{s_0,0} < C_{s_0,0} \quad (25.33)$$

where  $b_i^{(k)}$  is the battery status of sensor  $i$  at the beginning of the  $k$ -th migration tour and would be updated periodically as follows

**Table 25.2** List of notations used in problem formulation for J-MERDG in rechargeable sensor networks with regular topology

| Notation              | Definition   |
|-----------------------|--|
| $\mathcal{G}_j^{(k)}$ | Set of sensors in subgroup $j$ that send data to the same anchor point in the $k$ -th migration tour. The located sensor at anchor point is labeled as $s_0$             |
| $\mathcal{S}_i^{(k)}$ | Set of ancestor nodes of sensor $i$ in the $k$ -th migration tour, i.e., the sensors that help relay data from sensor $i$ towards the SenCar located at the anchor point |
| $B_i$                 | Full battery energy capacity of sensor $i$   |
| $b_i^{(k)}$           | Battery status of sensor $i$ at the beginning of the $k$ -th migration tour  |
| $\mathcal{A}^{(k)}$   | Set of anchor points selected for the $k$ -th migration tour   |
| $L$                   | Tour length bound for the SenCar in each migration tour  |
| $e_i^t$               | Energy consumed by sensor $i$ to transmit a unit flow  |
| $e_i^r$               | Energy consumed by sensor $i$ to receive a unit flow   |
| $r_i^{(k)}$           | Data rate of sensor $i$ destined to its associated anchor point in the $k$ -th migration tour  |
| $r_{max}$             | Maximum data rate for all the sensors  |
| $f_{i,j}^{(k)}$       | Flow rate on link $(i, j)$ in the $k$ -th migration tour   |
| $C_{i,j}$             | Link capacity of link $(i, j)$   |
| $\tau^{(k)}$          | Sojourn time of SenCar at each anchor point in the $k$ -th migration tour  |
| $\sigma$              | Portion parameter of energy budget used for data transmissions in each migration tour  |

$$b_i^{(k)} = \begin{cases} B_i, & i \in \mathcal{A}^{(k)} \\ b_i^{(k-1)} - f_{i+1,i}^{(k-1)} \tau^{(k-1)} e_i^r - f_{i,i-1}^{(k-1)} \tau^{(k-1)} e_i^t, & \text{otherwise.} \end{cases} \quad (25.34)$$

In the above formulation, flow conservation constraint (25.30) states that at each sensor, the aggregated outgoing link flow rates equal to the local data rate plus the incoming link flow rates, energy constraint (25.31) enforces that the energy cost at each sensor for all data gatherings in current tour should be bounded by its energy budget, which is a part of the available battery energy. Constraint (25.32) specifies the upper bound values for data rates and flow rates. Constraint (25.33) separately lists the rate and outgoing flow rate limit for the sensor located at the anchor point. Equation (25.34) describes the sensor energy status, where the sensors located at anchor points would be considered holding full battery capacity and other sensors hold the residual energy from previous migration tour.

### 25.3.3 Deterministic Solution

As indicated above, by utilizing the regularity of the network topology, the routing paths can be predetermined. This makes feasible to derive a deterministic solution and execute the computations in the SenCar so that network operation can be simplified and the overhead introduced by distribution algorithms can be eliminated.

In the following, we first give a theorem and its proof. Then, guided by the theorem, we can determine the optimal data rate allocation for the sensors in a subgroup based on the knowledge of utility functions.

**Theorem 25.1** Let  $\bar{X} = [x_1, x_2, \dots, x_n]$  be an  $n$ -dimensional vector. We have  $\sum_i x_i \leq K$ , where  $K$  is a given constant. Let  $f_i(x_i) = \frac{1}{\alpha_i} \log(x_i)$  and  $g(\bar{X}) = \sum_i f_i(x_i)$ . If we use  $g_{max}$  to denote the maximum value of  $g(\bar{X})$ , then we have  $g(\bar{X}) = g_{max}$  when  $x_i = \frac{\alpha_i}{\sum_j \alpha_j} K, \forall x_i \in \bar{X}$ .

*Proof* Since each  $f_i(x_i)$  is monotonically increasing, it is clear that  $g(\bar{X})$  would achieve its maximum value if and only if  $\sum_i x_i = K$ . Given the Lagrangian multiplier  $\lambda$ , we have the Lagrangian function as follows:

$$\Lambda(\bar{X}, \lambda) = g(\bar{X}) + \lambda(\sum_i x_i - K) = \sum_i f_i(x_i) + \lambda(\sum_i x_i - K). \quad (25.35)$$

Based on the KKT condition, taking derivation of each  $x_i$  and setting the result to zero, we obtain

$$\frac{\partial \sum_i f_i(x_i)}{\partial x_i} + \frac{\partial (\lambda(\sum_i x_i - K))}{\partial x_i} = \frac{\partial f_i(x_i)}{\partial x_i} + \lambda = \alpha_i \frac{1}{x_i} + \lambda = 0, \forall x_i \in \bar{X}. \quad (25.36)$$

Therefore, we have that

$$\alpha_1 \frac{1}{x_1} = \alpha_2 \frac{1}{x_2} = \dots = \alpha_i \frac{1}{x_i} = \dots = \alpha_n \frac{1}{x_n}. \quad (25.37)$$

Jointly considering  $\sum_i x_i = K$ , we have that  $g(\bar{X}) = g_{max}$  when  $x_i = \frac{\alpha_i}{\sum_j \alpha_j} K, \forall x_i \in \bar{X}$ .  $\square$

Let us look back upon the problem formulation. In Eqs. (25.29)–(25.33),  $f_{i,i-1}^{(k)}$  is used to represent the flow rate on link  $(i, i-1)$ , which is the outgoing link originated at sensor  $i$  to its parent sensor  $i-1$ , and  $f_{i+1,i}^{(k)}$  is the flow rate on the incoming link from its child. The maximum possible value for  $f_{i,i-1}^{(k)}$ , denoted as  $\bar{f}_{i,i-1}^{(k)}$ , is determined by the battery status of sensor  $i$  and the link capacity of link  $(i, i-1)$ , which can be approximately estimated as follows:

$$\bar{f}_{i,i-1}^{(k)} = \min \left( \frac{\sigma b_i^{(k)} - \bar{f}_{i+1,i}^{(k)} \tau^{(k)} e_i^r}{\tau^{(k)} e_i^t}, C_{i,i-1} \right). \quad (25.38)$$

If the utility function is in the form of  $U_i = \alpha_i \log(r_i^{(k)} \tau^{(k)})$ , where  $\alpha_i$  stands for the weight of utility at sensor  $i$ , we can directly determine the data rate for each sensor based on Theorem 25.1. Specifically, given the maximum flow rate of the outgoing link of an ancestor  $j$  of sensor  $i$ , i.e.,  $\bar{f}_{j,j-1}^{(k)}$ , the optimal data rate for sensor  $i$  can be calculated as follows:

$$r_i^{(k)} = \min \left( \min_{j \in \mathcal{S}_i \cup \{i\} \setminus \{0\}} \left( \frac{\alpha_i (\bar{f}_{j,j-1}^{(k)} - f_{i,i+1}^{(k)})}{\alpha_i + \alpha_{i-1} + \dots + \alpha_j} \right), r_{max} \right). \quad (25.39)$$

The above equation reveals that data rates should be proportionally allocated to sensors according to their weight of utility while jointly considering the capacity constraint of the bottleneck link on the routing path.

Consider a subgroup with a leaf node being sensor  $i$ . It is clear that there is no incoming flow rate for sensor  $i$ , i.e.,  $f_{i,i+1}^{(k)} = 0$ . Thus, the data rate of the leaf sensor can be first derived. The data rates of the remaining ancestor sensors can then be iteratively induced by updating the incoming flow rate based on the sensors whose data rates have been already determined. The details of the algorithm are described in Algorithm 33, where data rates are calculated for a total of  $K$  migration tours. Inside the inner iterations for a particular subgroup, there are two *for* loops. In the first loop, the maximum possible outgoing flow rates of the sensors in the subgroup are estimated. In the second loop, the data rates are iteratively calculated based on Eq. (25.39). It is worth pointing out that the sensor located at the anchor point needs to be specially handled. This is because it does not need to help relay data packets for others and its data rate only depends on its battery state and its outgoing link capacity. Finally, the available battery energy of each sensor needs to be updated for the use in the calculation of subsequent migration tour.

## 25.4 Performance Evaluation

In this section, we carry out extensive experiments to evaluate the effectiveness of J-MERDG for rechargeable sensor networks with both random and regular topologies.

### 25.4.1 Evaluation on J-MERDG in Rechargeable Sensor Networks with Random Topologies

As indicated in previous discussion, J-MERDG has a distributed nature and the Sen-Car is able to obtain sensor energy states along its migration tour, thus our design is readily applicable to large-scale deployment. Since each sensor runs the exactly same algorithm and only communicates with its neighbors, in this evaluation, we examine the behaviors of 10 wireless rechargeable sensors as an example for demonstration, with the transmission range of 30 m, distributed over a 100 m  $\times$  100 m area. All DAGs,  $G_a^{(k),R}$  and  $G_a^{(k),D}$ , that model the network topology, are constructed by considering the anchor point as the destination and finding the shortest paths from all sensors to the anchor point. The utility function  $U_i(\cdot)$  is defined as  $\alpha_i \log(\sum_a r_{i,a}^{(k),R} \tau^R)$  for R-tour, and  $\alpha_i \log(\sum_a r_{i,a}^{(k),D} q \tau^D)$  for D-tours separately, where  $\alpha_i$  is the weight of

utility at sensor  $i$ . If not specified otherwise, the time interval length  $T$  is set to 1 h and the number of all tours  $q + 1$  in each time interval is 5. We set the diminishing stepsizes for Lagrangian multiplier update as  $\theta[n] = 1/(1 + 10n)$ . For clarity, all other parameter settings are summarized in Table 25.3.

---

**Algorithm 33:** Tour Planning and Data Rate Allocation Algorithm for  $K$  Migration Tours in Networks with Square Topologies

---

**Require:** Full battery status of sensor  $i$ ,  $B_i$ ;  
 Energy consumed by sensor  $i$  to receive and transmit a unit flow  $e_i^r$  and  $e_i^t$ ;  
 Link capacity between a node and its parent  $l_{i,i-1}$ ;  
 Tour length bound  $L$ , sojourn time of SenCar  $\tau^{(k)}$ ;  
 Portion of remaining node energy  $\sigma$ .

**Ensure:** Sensor data rates in each migration tour  $r_i^{(k)}$ ;

- 1: Initialize battery capacity for all sensors:  $b_i^{(1)} \leftarrow B_i$ ;
- 2: Calculate  $w_1$ ,  $w_2$ ,  $t$  and  $p$  to determine the tour trajectory for SenCar based on Eqs. (25.25)–(25.28);
- 3: **for**  $k = 1$  to  $K$  **do**
- 4:   Find a set of anchor points, i.e.,  $\mathcal{A}^{(k)}$ , based on the tour trajectory of SenCar;
- 5:   **for** each subgroup **do**
- 6:     **for**  $i$  in current subgroup except  $s_0$  **do**
- 7:        $\tilde{f}_{i,i-1}^{(k)} = \min\left(\frac{\sigma b_i^{(k)} - \tilde{f}_{i+1,i}^{(k)} \tau^{(k)} e_i^r}{\tau^{(k)} e_i^t}, C_{i,i-1}\right)$ ;
- 8:     **end for**
- 9:     *//Iteratively find data rates of sensors in the subgroup*
- 10:     $m \leftarrow 0$ ;
- 11:    **for** each  $i$  from leafs to 1 (or 1') on either side of anchor point **do**
- 12:       $f_{i,i+1}^{(k)} = m$ ;
- 13:       $r_i^{(k)} = \min\left(\min_{j \in \mathcal{S}_i \cup \{i\} \setminus \{0\}} \left(\frac{\alpha_i (\tilde{f}_{j,j-1}^{(k)} - f_{i,i+1}^{(k)})}{\alpha_i + \alpha_{i-1} + \dots + \alpha_j}\right), r_{max}\right)$ ;
- 14:       $m = m + r_i^{(k)}$ ;
- 15:    **end for**
- 16:    Set the flow rate for each link according to the data rates.
- 17:    Update energy status for all sensors in the subgroup as:  
 $b_i^{(k+1)} = b_i^{(k)} - f_{i+1,i}^{(k)} \tau^{(k)} e_i^r - f_{i,i-1}^{(k)} \tau^{(k)} e_i^t$ ;  
*//Handle the sensor on the anchor point, who gets recharged*
- 18:     $r_{s_0}^{(k)} = \min\left(\frac{\sigma b_{s_0}^{(k)}}{\tau^{(k)} e_{s_0}^t}, C_{s_0,0}\right)$ ;
- 19:     $b_{s_0}^{(k+1)} = B_{s_0}$ ;
- 20:    **end for**
- 21:    Update the moving trajectory of SenCar for next migration tour;

**21: end for**

---

**Table 25.3** Parameter settings for rechargeable sensor networks with random topologies

| Parameter   | Value             | Parameter       | Value        | Parameter | Value |
|-------------|-------------------|-----------------|--------------|-----------|-------|
| $B_i$       | 2100 mAh (3 V)    | $e_i^r, e_i^l$  | 0.3 mJ/Kbit  | $v_s$     | 1 m/s |
| $\alpha_i$  | 100               | $e_i \Lambda_i$ | 0.02 mJ/Kbit | $\sigma$  | 0.9   |
| $\theta(n)$ | $\frac{1}{1+10n}$ | $L$             | 200 m        |           |       |

#### 25.4.1.1 Convergence of Proximal Approximation Algorithm

We first investigate the convergence of proximal approximation-based algorithm. For a particular time interval  $k$ , we assume that each sensor randomly holds 80–100 % of full battery capacity and the anchor points are set to the locations of sensors 1, 2 and 3. Figure 25.6a shows the evolution of data rates  $r_{i,a}^{(k)}$  versus the number of proximal iterations. It is observed that all data rates approach to the stable status after only 10 iterations. Figure 25.6b shows the evolution of recovered flow rates  $\hat{f}_{ij,a}^{(k)}$  on some selected links versus the number of subgradient iterations. It is noticed that the recovered flow rates are well within 5 % of their optimal values after only 300 iterations.

#### 25.4.1.2 Performance of J-MERDG for Rechargeable Sensor Networks with Random Topologies

Now, we examine the performance of J-MERDG varying with the time interval length  $T$  for the networks with random topologies. Figure 25.7a demonstrates the evolution of cumulative network utility in consecutive 24 h under different settings of  $T$ . It is assumed that each sensor initially holds full battery capacity and the number of migration tours  $q + 1$  in each time interval is proportional to  $T$ . It is evident in the figure that higher cumulative network utility can be obtained in the cases with smaller  $T$ 's. This is reasonable since a smaller  $T$  leads to shorter waiting time for the sensors to get recharged so as to be able to spend more energy for data uploading. However, a small  $T$  may cause extra overhead for sensors to frequently optimize their data rates, schedule, and routing. Therefore, a proper setting for  $T$  is actually to explore a good balance between the computation overhead and achievable performance. Figure 25.7b takes sensor 1 as an example to depict battery states evolving with time. It is shown that sensors could timely get recharged to avoid energy depletion. The steps that jump along the lines indicate the recharging chances for sensors. It is apparent that sensors have more chances for energy replenishment under a smaller  $T$ . As an instance, sensor 1 gets recharged for 5 times within 24 h when  $T$  is set to 1 h while it only gets recharged once when  $T$  is set to 6 h.

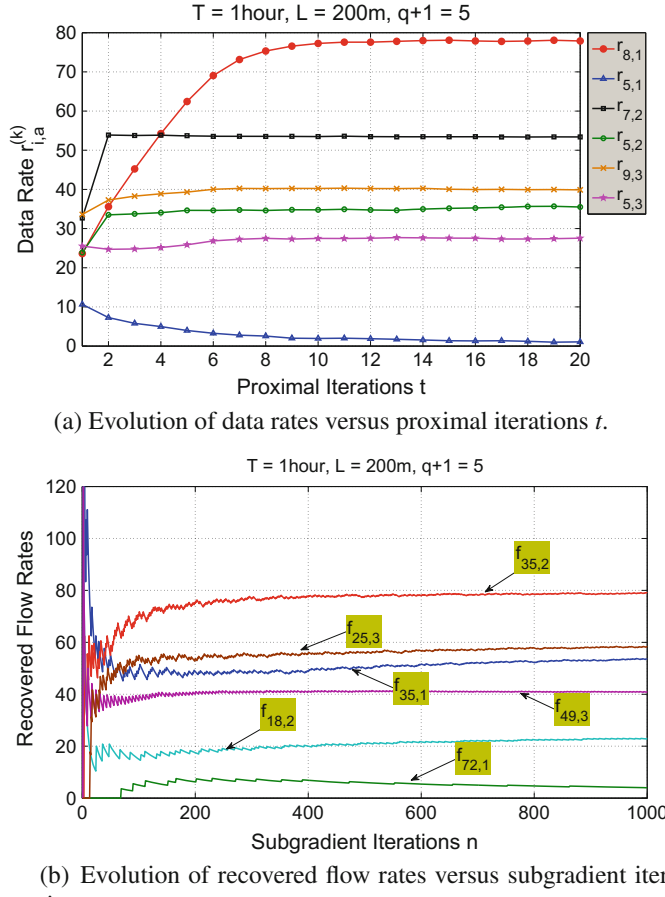
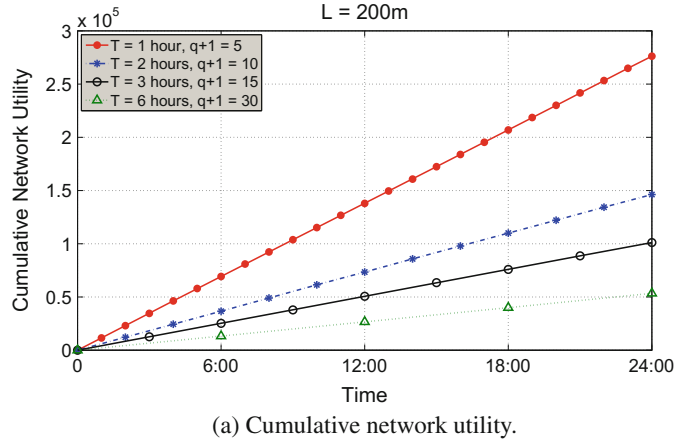


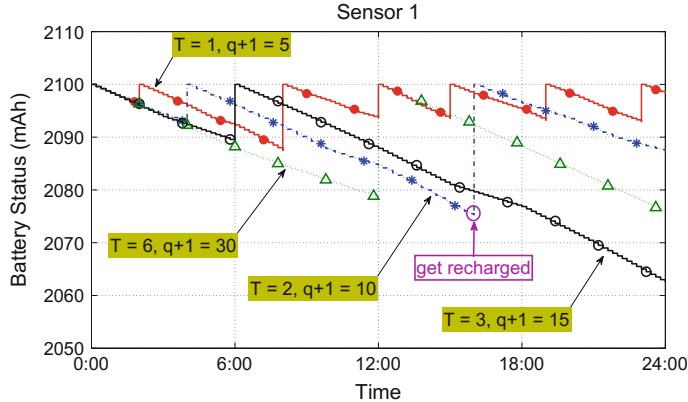
**Fig. 25.6** Investigation on the convergence of the proximal approximation-based algorithm

#### 25.4.2 Evaluation on J-MERDG in Rechargeable Sensor Networks with Regular Topologies

We now come to the position to evaluate the performance of J-MERDG in rechargeable sensor networks with regular topologies, with the goal of providing an instructive guidance on how to select the critical parameters when designing and deploying such a system in practice. We generate a network consisting of 3,600 wireless rechargeable sensors, which are distributed over a  $600\text{ m} \times 600\text{ m}$  square area. The utility function  $U_i(\cdot)$  is still defined as  $\alpha_i \log(r_i^{(k)} \tau)$ . The default values of the main parameters used in the algorithm are listed in Table 25.4. For each parameter setting, we investigate the evolution of network utility in a total of 200 migration tours.



(a) Cumulative network utility.



(b) Battery states of sensor 8.

**Fig. 25.7** Performance of J-MERDG as the function of  $T$ **Table 25.4** Parameter settings for rechargeable sensor networks with regular topologies

| Parameter  | Value         | Parameter      | Value       | Parameter | Value |
|------------|---------------|----------------|-------------|-----------|-------|
| $B_i$      | 2100 mAh (3V) | $e_i^r, e_i^l$ | 0.3 mJ/Kbit | $\tau$    | 60 s  |
| $L$        | 1600 m        | $C_{ij}$       | 250 Kbit    | $\sigma$  | 0.4   |
| $\alpha_i$ | 100           |                |             |           |       |

Figure 25.8a depicts network utility under different settings of tour length bounds. It is clear that the region division is determined by the tour length bound  $L$  as a longer  $L$  makes it possible to divide the areas into more regions and the size of each subgroup becomes smaller. This implies that there would be more sensors on the trajectory of the SenCar in each migration tour and sensors will get recharged in a

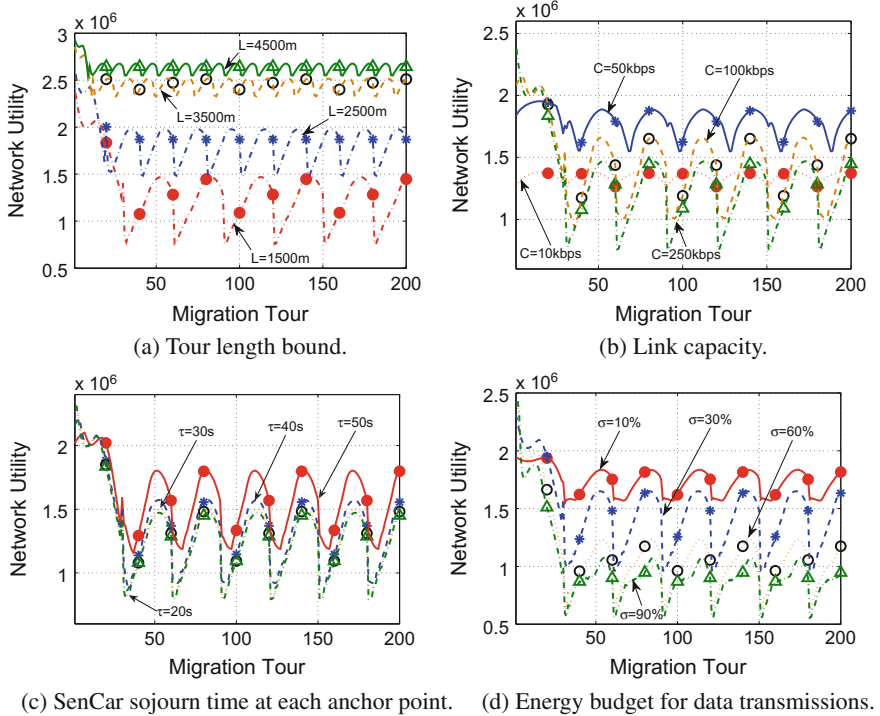


**Fig. 25.8** Network utility evolves with the migration tours as the functions of different parameters in rechargeable sensor networks with a square topology

more timely manner. Moreover, sensors can also reach the SenCar for data uploading with shorter routing paths, which greatly helps save battery energy at sensor side. As a result, these advantages significantly enhance the network utility and effectively dampen the fluctuations due to the fact that sensors would wait less time to get recharged. For example, when  $L$  is set to 450 m, the network utility is about 38 % on average higher than the case with  $L$  set to 1500 m. Meanwhile, the network utility keeps much stable over different migration tours, with variations less than 2 % of the average value.

After the moving trajectory of the SenCar is determined, the data rate of a sensor is calculated based on outgoing link capacity  $C$ , sojourn time  $\tau$  and portion of battery energy for data transmission  $\sigma$ .

Figure 25.8b shows how the link capacity affects network utility. We can see that when the link capacity is small, a limited amount of data would be routed to the SenCar, which leads to less energy consumption. As a result, network utility is relatively low with small fluctuations. In contrast, when the link capacity increases, more data would be gathered from the network in each migration tour and energy consumption increases accordingly. As we have pointed out earlier, the data rate of

a sensor heavily depends on two factors: the first one is the link capacities along the routing path toward the anchor point and the other one is the battery energy of the sensors on the path. As the link capacity becomes large, the link capacity constraint becomes loose and network utility would be mainly determined by the energy state of sensors. Under these circumstances, network utility exhibits intense fluctuations since sensors aggressively use their energy for data transmissions, which leads to drastic variations of battery states in successive migration tours.

Figure 25.8c shows how SenCar's sojourn time at each anchor point impacts on network utility. At the beginning of the simulation, all sensors have sufficient energy to transmit data at high rate. This is demonstrated as that the longer the sojourn time is, the higher the network utility is. Such high data rate transmission leads to more energy consumption, which leads to some sensors becoming bottleneck nodes for data relay as they cannot get timely recharged. This causes significant variations in system-wide performance, which is shown in the figure where network utility decreases rapidly and exhibits intense fluctuations.

**Fig. 25.9** Evolution of sensors' battery status with migration tours under different network parameters

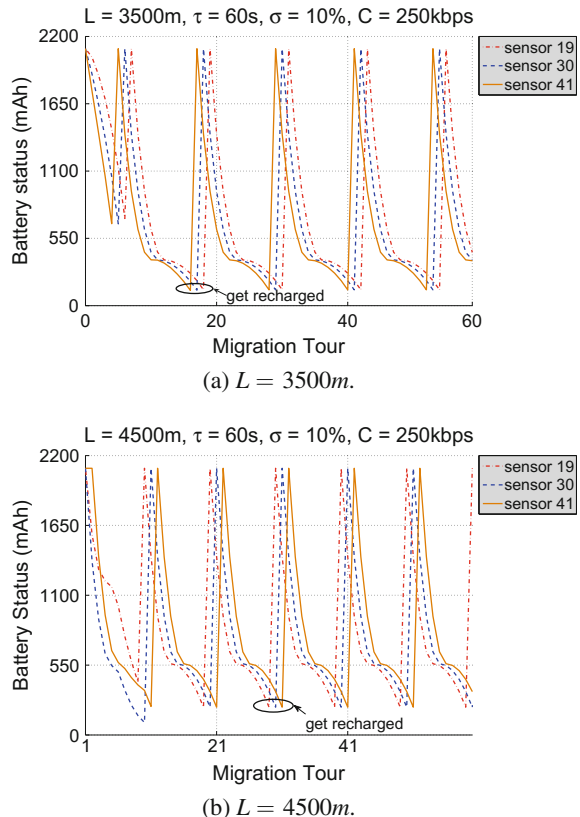


Figure 25.8d illustrates the impact of the portion of energy for data transmissions in each migration tour. A larger portion of sensor energy for data transmission would make more energy available for use in the current migration tour. This accounts for the higher network utility for higher energy budget at the beginning of the simulation. However, a large amount of data transmission drains sensor energy quickly and the remaining energy left for subsequent migration tours would become limited before sensors get recharged. This would result in low network utility with violent fluctuations as shown in the figure.

Figure 25.9a and b exhibit the evolution of sensors' battery status with migration tours under different network parameters. We randomly choose three sensors as the representatives, say, sensors 19, 30 and 41, to examine the changes of their batteries. The positions of those sensors are (19, 1), (30, 1) and (41, 1), respectively. In the figure, the turning points along the curves and the sharp rising slopes indicate the recharging opportunities for the sensors while the falling slopes stand for the discharging process. In Fig. 25.9a, the tour length bound  $L$  is set to 3500 m, while in Fig. 25.9b, the tour length bound is increased to 4500 m. All other parameter settings are the same. Longer tour length bound enables dividing the sensing area into more regions, thus the sensors can get recharged more frequently. Particularly, sensors get recharged every 12 migration tours in Fig. 25.9a, and every 10 migration tours in Fig. 25.9b. For both cases, all the sensors can get timely replenishment before their energy depletes.

## 25.5 Conclusions

In this chapter, we have considered the joint design of mobile energy replenishment with wireless power transfer and mobile data gathering (J-MERDG) in wireless rechargeable sensor networks. Specifically, a SenCar is introduced to migrate among selected anchor points, charges the located sensors via wireless power transfer, and collects data from nearby sensors in multi-hop routing. We first investigated J-MERDG in random networks and proposed a two-step approach for the joint design. In the first step, we proposed a selection algorithm to determine the anchor points, which achieves a desirable balance between the energy replenishing amount and data gathering latency. In the second step, we explored the optimal data gathering performance when the SenCar moves over different anchor points. Each sensor self-tunes the data rate, scheduling, and routing based on the up-to-date energy status such that the entire network utility can be maximized. We also applied J-MERDG to the networks with regular topologies and proposed a simplified solution with lower complexity by taking advantage of the symmetry of network topology. Extensive evaluation results demonstrated that J-MERDG can effectively maintain perpetual network operations and achieve high network utility simultaneously.

## References

1. Alippi, C., Camplani, R., Roveri, M., Viscardi, G.: Netbrick: a high-performance, low-power hardware platform for wireless and hybrid sensor networks. In: IEEE 9th International Conference on Mobile Adhoc and Sensor Systems (MASS) (2012)
2. Pasha, M.A., Derrien, S., Senteys, O.: Toward ultra low-power hardware specialization of a wireless sensor network node. In: IEEE 13th International Multitopic Conference, pp. 1–6 (2009)
3. Dutta, P.K., Culler, D.E.: System software techniques for low-power operation in wireless sensor networks. In: IEEE/ACM International Conference on Computer-Aided Design, pp. 925–932 (2005)
4. Liang, X., Li, W., Gulliver, T.A.: Energy efficient modulation design for wireless sensor networks. In: IEEE Pacific Rim Conference on Communications, Computers and Signal Processing (PacRim), pp. 98–101 (2007)
5. Ye, W., Heidemann, J., Estrin, D.: An energy-efficient MAC protocol for wireless sensor networks. In: IEEE INFOCOM, pp. 1567–1576 (2002)
6. Ma, J., Lou, W., Wu, Y., Li, X., Chen, G.: Energy efficient TDMA sleep scheduling in wireless sensor networks. In: IEEE INFOCOM (2009)
7. Schurgers, C., Srivastava, M.B.: Energy efficient routing in wireless sensor networks. *IEEE Trans. Mob. Comput.* **1**, 357–361 (2001)
8. Ergen, S.C., Varaiya, P.: Energy efficient routing with delay guarantee for sensor networks. *Springer J. Wireless Netw.* **13**(5), 679–690 (2007)
9. Shah, R., Roy, S., Jain, S., Brunette, W.: Data mules: modeling a three-tier architecture for sparse sensor networks. In: IEEE SNPA (2003)
10. Zhao, M., Yang, Y.: Optimization based distributed algorithms for mobile data gathering in wireless sensor networks. *IEEE Trans. Mob. Comput.* **11**(10) (2012)
11. Liu, R.S., Sinha, P., Koksal, C.E.: Joint energy management and resource allocation in rechargeable sensor networks. In: IEEE INFOCOM (2010)
12. Liu, R.S., Fan, K.W., Zheng, Z., Sinha, P.: Perpetual and fair data collection for environmental energy harvesting sensor networks. *IEEE/ACM Trans. Netw.* **19**(4), 947–960 (2011)
13. Roundy, S.J.: Energy scavenging for wireless sensor nodes with a focus on vibration to electricity conversion. Ph.D. Dissertation, Dept. of EECS, UC Berkeley, May 2003
14. Misra, S., Majd, N.E., Huang, H.: Constrained relay node placement in energy harvesting wireless sensor networks. In: IEEE 8th International Conference on Mobile Adhoc and Sensor Systems (MASS) (2011)
15. Gu, Y., He, T.: Bounding communication delay in energy harvesting sensor networks. In: IEEE 30th International Conference on Distributed Computing Systems (ICDCS) (2010)
16. Rahimi, M., Shah, H., Sukhatme, G., Heideman, J., Estrin, D.: Studying the feasibility of energy harvesting in a mobile sensor network. In: IEEE International Conference on Robotics and Automation (2003)
17. Xie, L., Shi, Y., Hou, Y.T., Lou, A.: Wireless power transfer and applications to sensor networks. *IEEE Wireless Commun.* **20**(4), 140–145 (2013)
18. Kurs, A., Karalis, A., Moffatt, R., Joannopoulos, J.D., Fisher, P., Soljacic, M.: Wireless power transfer via strongly coupled magnetic resonances. *Science* **317**, 83 (2007)
19. Intel: Wireless resonant energy link (WREL) demo. <http://software.intel.com/en-us/videos/wireless-resonant-energy-link-wrel-demo/>
20. WiTricity. <http://www.witricity.com>
21. Peng, Y., Li, Z., Zhang, W., Qiao, D.: Prolonging sensor network lifetime through wireless charging. In: IEEE Real-Time Systems Symposium (2010)
22. Li, Z., Peng, Y., Zhang, W., Qiao, D.: J-RoC: a joint routing and charging scheme to prolong sensor network lifetime. In: IEEE ICNP (2011)
23. Xie, L., Shi, Y., Hou, Y.T., Sherali, H.D.: Making sensor networks immortal: An energy-renewal approach with wireless power transfer. *IEEE/ACM Trans. Netw.* (2012)

24. X. Lu, I. Flint, D. Niyato, N. Privault, Performance analysis of simultaneous wireless information and power transfer with ambient RF energy harvesting. In: IEEE Wireless Communications and Networking Conference (WCNC) (2015)
25. Zhao, M., Li, J., Yang, Y.: A framework of joint Mobile energy replenishment and data gathering in wireless rechargeable sensor networks. *IEEE Trans. Mob. Comput. (TMC)* **13**(12), 2689–2705 (2014)
26. Zhao, M., Li, J., Yang, Y.: Joint mobile energy replenishment and data gathering in wireless rechargeable sensor networks. In: The 23rd International Teletraffic Congress (ITC-23), September 2011
27. Kang, B., Ceder, G.: Battery materials for ultrafast charging and discharging. *Nature* **458**, 190–193 (2009)
28. Arora, S.: Polynomial time approximation schemes for Euclidean traveling salesman and other geometric problems. *J. ACM* **45**(5), 753–782 (1998)
29. Cormen, T.H., Leiserson, C.E., Rivest, R.L., Stein, C.: Introduction to Algorithms. MIT Press (2001)
30. Uno, T.: A fast algorithm for enumerating non-bipartite maximal matchings. *NII J.* **3** (2001)
31. Boyd, S., Vandenberghe, L.: Convex Optimization. Cambridge University Press (2004). <http://www.stanford.edu/~boyd/cvxbook/>
32. Bertsekas, D., Tsitsiklis, J.: Parallel and Distributed Computation: Numerical Methods. Athena Scientific (1997)
33. Bertsekas, D.P., Tsitsiklis, J.N.: Parallel and Distributed Computation: Numerical Methods. Prentice-Hall (1989)
34. Lin, X., Shroff, N.B.: Utility maximization for communication networks with multipath routing. *IEEE Trans. Autom. Control* **51**(5), 766–781 (2006)
35. Chen, L., Low, S.H., Chiang, M., Doyle, J.C.: Optimal cross-layer congestion control, routing, and scheduling design in ad hoc wireless networks. In: IEEE INFOCOM (2006)
36. Akyol, U., Andrews, M., Gupta, P., Hobby, J., Sanjeev, I., Stolyar, A.: Joint scheduling and congestion control in mobile ad-hoc networks. In: IEEE INFOCOM (2008)
37. Sherali, H., Choi, G.: Recovery of primal solutions when using subgradient optimization methods to solve Lagrangian duals of linear programs. *Oper. Res. Lett.* **19**(3), 105–113 (1996)

## **Part VI**

# **Electromagnetic Radiation Awareness**

# Chapter 26

## Radiation Constrained Charging Utility Optimization for Human Safety

**Haipeng Dai, Guihai Chen, Yunhuai Liu and Tian He**

**Abstract** Most existing studies for wireless power transfer technology focus on the energy charging efficiency issues, but overlook its threat to human safety due to its high electromagnetic radiation (EMR). Though no study results have generally provided clear evidence of a relationship between EMR and the health impairments, there have been some statistically significant findings in certain positive cases. Exposure to high EMR has been widely identified as a threat to human health. Its potential risks include but are not limited to tissue impairment, brain tumor, and mental diseases. In this chapter, we take the risks of such radiation into consideration, and present the Safe Charging Problem (SCP), aiming at achieving the best trade-off between the charging efficiency and EMR safety. We pay special attention to the following problem: given a set of wireless power chargers and rechargeable devices, how to schedule the chargers so that the devices can obtain more power, while no location exceeds the EMR safety threshold. We prove the hardness of SCP, and propose a near optimal solution. We also present extensive simulation results and testbed results to verify our theoretical findings.

---

H. Dai (✉) · G. Chen

State Key Laboratory for Novel Software Technology, Nanjing University,  
Nanjing 210023, China  
e-mail: haipengdai@nju.edu.cn

G. Chen  
e-mail: gchen@nju.edu.cn

Y. Liu  
Third Research Institute of Ministry of Public Security, Shanghai, China  
e-mail: yunhuai.liu@gmail.com

T. He  
Computer Science and Engineering, University of Minnesota,  
Minneapolis, MN 55455, USA  
e-mail: tianhe@cs.umn.edu

## 26.1 Introduction

In existing studies, researchers focus more on the energy charging efficiency and ubiquitousness, targeting at the minimal number of active chargers with more charging coverage (e.g., [3, 4, 6, 8–10, 16, 18, 19, 21, 28, 30]). In practice, however, this is far from enough. Besides the charging efficiency, a more critical issue is the safety of the electromagnetic radiation (EMR).

Though no study results have generally provided clear evidence of a relationship between EMR and the health impairments, there have been some statistically significant findings in certain positive cases. For example, Olteanu et al. [26] investigated the harmful effect of metallic implant heating resulted from EMR around, which may lead to impairment of tissues. Furthermore, it is reported that heating of tissue that exceeds 1 °C may interfere with behavioral and biological functions [29]. Gandhi et al. [14] found that children’s heads absorb over two times more of RF than adults, and absorption of the skull’s bone marrow can be ten times greater than adults. Tissues of the fetus, such as the central nervous system, seem especially vulnerable to temperature rises caused by high EMR in various time windows, particularly during organogenesis [12]. Changes on gene/protein expression by RF exposure are also investigated. Leszczynskis group performed a pilot study on volunteers and showed that mobile phone radiation might alter protein expression in human skin cells [23]. Nittby et al. [24] found that a large number of genes were altered at hippocampus and cortex using four exposed and four control animals. Though no actual experiments have been conducted concerning the potential harm to people, a plenty of clinical studies such as [17] showed increased risks of high EMR exposure for brain tumors. Besides, the link between RF exposure and mental diseases has also been confirmed. Experiments done on mice [25] showed that EMR causes transient and cumulative impairments in spatial and non-spatial memory.

Concerns about adverse consequences of EMR exposure have resulted in the establishment of exposure limits. These limits are codified in Title 47 of the Code of Federal Regulations (CFR) in the United States [5] and Hygienic Standard for Environmental Electromagnetic Waves GB9175-88 [20] in China, and also contained in standards published by the International Commission on Non-Ionizing Radiation Protection (ICNIRP) [1] in most of Europe. For instance, the maximum allowed power density for frequency 915 MHz, the commonly used frequency band for wireless power transfer, by CFR, GB9175-88 and ICNIRP are  $610 \mu\text{W}/\text{cm}^2$ ,  $40 \mu\text{W}/\text{cm}^2$  and  $457.5 \mu\text{W}/\text{cm}^2$ , respectively. As such, validated wireless charging schemes must comply with these regulations and guarantee the EMR safety in the field. No location should have the EMR value exceeding a certain safety threshold.

In this chapter, we present the *Safe Charging Problem*, attempting to strike the best trade-off between the charging efficiency and EMR safety with the practical and critical concern [7]. Especially, we focus on the following basic problem. Given a set of wireless power chargers and rechargeable devices, we are seeking the charger scheduling scheme so that the devices can obtain more power, while no location exceeds the EMR safety threshold. Though there have been works regarding scenarios

with stationary chargers, but none of them considers the EMR safety. For example, recently Intel developed the wireless identification and sensing platform (WISP) by integrating RFID tags with sensing and computing components. The RFID tags can be wirelessly charged by readers. Buettner et al. explored this technology to recognize human activities in [4], and highlighted applications such as elderly care in [3]. In [16], Powercast developed a wireless power platform to work with wireless sensor network. Their objective was to help monitor temperature and humidity at a zoo without disrupting the animal exhibit. This company also offered a solution for data center environmental monitoring by constructing a network of chargers [21]. He et al. [18] studied the energy provisioning problem, i.e., how to deploy chargers to provide sufficient energy to static/mobile devices in wireless rechargeable sensor networks. In [30], Wicaksono et al. considered the power interference when allocating frequency bands to adjacent stationary chargers.

Safe charging is a quite challenging problem which in general is NP-hard. The challenges are mainly due to the fact that the EMR constraints are imposed on every point in the field, which inevitably results in an infinite number of constraints. In addition, as we will show in later sections, the objective function is a non-convex one, which prevents the classical convex optimization method from applying directly. To overcome these challenges, we design constraint conversion and reduction techniques and apply approximation approaches, which enable us to transfer the problem to a traditional multidimensional 0/1 knapsack problem [13] and a Fermat–Weber problem [22], i.e., to find the optimal activation set of chargers maximizing the overall charging power under a limited number of constraints, and to find the point with the maximum EMR for a given active charger set. The constraints of the first problem are actually derived based on the outputs of the second problem.

The remainder of the chapter is organized as follows. In Sect. 26.2, we give preliminaries and a formal definition of the SCP problem. We introduce a near optimal solution to SCP in Sect. 26.3 based on the theoretical results of maximal EMR point (MEP) computation in the next section. Then, we present an approximation algorithm to MEP computation in Sect. 26.4. Sections 26.5 and 26.6 present extensive simulations and testbed experiments to verify our theoretical results. Section 26.7 concludes the chapter.

## 26.2 Problem Statement

Given the above concerns of the impairments of EMR, a desired charging scheme should strike a balance between the EMR limit and charging efficiency. We assume all the chargers and rechargeable devices are static and deployed in fixed, known locations. In addition, we consider a simplified charger scheduling model in which chargers can be only in either of the on/off states. More complicated deployment schemes (e.g., mobile chargers) and scheduling models (e.g., adjustable charger power) are left for future work.

Ideally, the charging scheme should on one hand maximize the charging efficiency so that more charging energy can be harvested by the rechargeable devices, and on the other hand ensure the safety of the field by limiting the intensity of EMR at every position in the field. To achieve this goal, we will formulate the problem and propose our solutions in the remainder of this chapter. In this section, we will first give the system and charging model, and then provide the formal problem statement. At the end of this section, we will present the main challenges we face when addressing the problem.

### 26.2.1 System and Charging Model

Assume there is a set of  $n$  identical stationary wireless power chargers  $S = \{s_1, s_2, \dots, s_n\}$  deployed on a two-dimensional plane, and we have a set of  $m$  rechargeable devices  $O = \{o_1, o_2, \dots, o_m\}$  in the field. The devices are capable of harvesting the wireless power originated from chargers to maintain their normal working.

In general, both the wireless charging power and the EMR intensity are related to the energy field strength. The received power  $P_r(d)$  by a device can be quantified by an empirical model [18], i.e.,

$$P_r(d) = \begin{cases} \frac{\alpha}{(d+\beta)^2}, & d \leq D \\ 0, & d > D \end{cases} \quad (26.1)$$

where  $d$  is the distance from the charger to the receiver, and  $\alpha$  and  $\beta$  are known constants determined by hardware of the charger and the receiver and the environment. Because of the hardware constraint, the energy field far away from the charger will be too small to be received by a node, and we use  $D$  to denote the farthest distance a charger can reach.

For the charging, we assume the wireless power from multiple chargers to a receiver is additive [18], and define the charging utility to be proportional to the charging power, namely

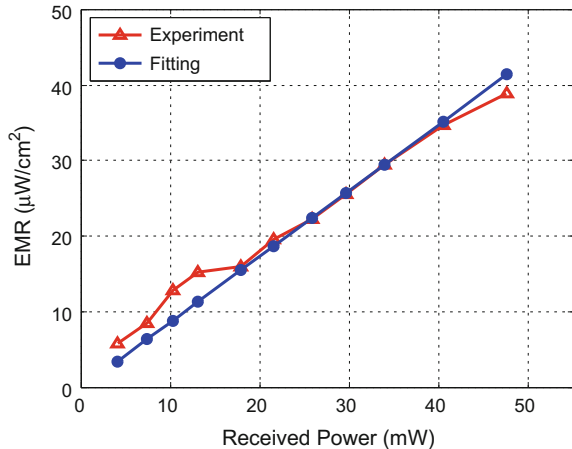
$$u(o_j) = c_1 \sum_{i=1}^n P_r(d(s_i, o_j)) \quad (26.2)$$

where  $d(s_i, o_j)$  is the distance from the charger  $s_i$  to the device  $o_j$ , and  $c_1$  is a predetermined constant.

Similarly, for all rechargeable devices, a charger  $s_i$  can provide charging utility as

$$u(s_i) = c_1 \sum_{j=1}^m P_r(d(s_i, o_j)). \quad (26.3)$$

**Fig. 26.1** EMR versus received power



For the intensity of EMR, intuitively it is proportional to the received power there. The field experiment studies corroborate this intuition. As shown in Fig. 26.1, the EMR is nearly proportional to the received power, which can be modeled by  $e(d) = c_2 P_r(d)$  where  $d$  is the distance and  $c_2$  is the constant to capture the linear relation. Assuming EMR is also additive, the accumulated EMR at a location  $p$  is thus

$$e(p) = \sum_{s_i \in S} e(d(s_i, p)) = c_2 \sum_{s_i \in S} P_r(d(s_i, p)). \quad (26.4)$$

## 26.2.2 Problem Formulation

We start with the following decision problem: given an active charger set  $S$ , is the EMR safety violated? To answer this question, we have to examine every point on the plane to ensure no place will have the EMR exceeding the hard threshold of EMR safety, which we denote by  $R_t$ . Mathematically, we can express the decision problem as follows

$$\forall p \in \mathbb{R}^2, \quad c_2 \sum_{s_i \in S} P_r(d(s_i, p)) \leq R_t.$$

Let  $x_i$  be a binary indicator that denotes whether charger  $s_i$  is active or not. For an active charger set specified by  $x_i$ , the above inequality can be rewritten as follows

$$\forall p \in \mathbb{R}^2, \quad c_2 \sum_{i=1}^n P_r(d(s_i, p)) x_i \leq R_t.$$

This inequality actually serves as the constraint of our problem. On the other hand, our optimization goal is to maximize the overall charging utility from all

the chargers, namely,  $\sum_{i=1}^n u(s_i)x_i$ . The Safe Charging Problem (SCP) can thus be defined as follows

$$\begin{aligned} (\text{SCP}) \quad & \max \quad c_1 \sum_{i=1}^n (\sum_{j=1}^m P_r(d(s_i, o_j)))x_i \\ \text{s.t. } & \forall p \in \mathbb{R}^2, \quad c_2 \sum_{i=1}^n P_r(d(s_i, p))x_i \leq R_t \\ & x_i \in \{0, 1\} \quad (i = 1, 2, \dots, n). \end{aligned} \quad (26.5)$$

where  $x_i$  is a binary indicator that denotes whether charger  $s_i$  is active or not, and  $R_t$  is the hard threshold of EMR intensity safety.

In the above formulation, the objective function  $c_1 \sum_{i=1}^n (\sum_{j=1}^m P_r(d(s_i, o_j)))x_i$  is the summation of charging utility from all the chargers. And the constraints  $\forall p \in \mathbb{R}^2, c_2 \sum_{i=1}^n P_r(d(s_i, p))x_i \leq R_t$  are to ensure no place will have the EMR exceeding the safety threshold. We call a location  $p \in \mathbb{R}^2$  is “safe” if the EMR intensity at this location is below the threshold  $R_t$ , i.e.,  $c_2 \sum_{i=1}^n P_r(d(s_i, p))x_i \leq R_t$ , and is “danger” if otherwise. We will solve SCP by determining  $x_i$  so that the overall charging utility can be maximized while no location is danger; in other words,  $x_i$  is the optimization variable.

To solve SCP, we are mainly facing the following challenges. First, the constraint in SCP is imposed on every point on the plane. In other words, there is indeed an infinite number of constraints, which makes the problem extremely difficult. Second, even if we can reduce the number of constraints to a limited number, we will show later that SCP is in the form of a multidimensional 0/1 knapsack problem, which is NP-hard.

**Theorem 26.1** *SCP is NP-hard.*

Note that due to space limit, we omit all proofs to the theorems and lemmas in this chapter, and refer readers to the journal version of [7] for details.

## 26.3 A Near Optimal Solution

In this section, we will introduce the solution to SCP and show that the algorithm has near optimal performance. We will first depict the roadmap of the solution, and then present the techniques we applied individually in details.

### 26.3.1 Principles and Solution Workflow

As we mentioned before, the major challenge of SCP is the fact that SCP has an infinite number of constraints when optimizing the objective function. To overcome this challenge, we propose two techniques, namely constraint conversion and constraint

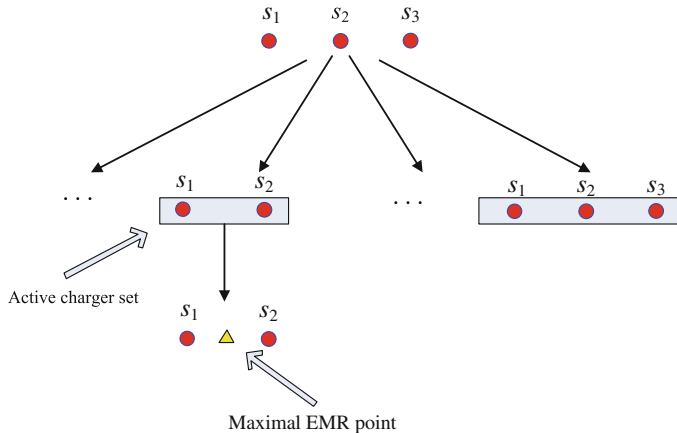


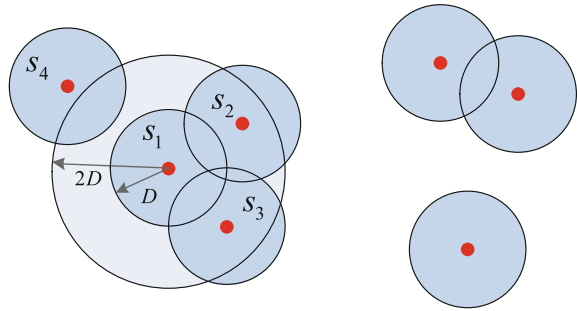
**Fig. 26.2** An illustrative example of constraint conversion. For the set of active chargers  $s_1$  and  $s_2$ , there will be a maximal EMR point (MEP) located between  $s_1$  and  $s_2$ , and a corresponding constraint. Different active charger sets will have different MEPs

reduction, to reduce the number of constraints to a limited and tractable number. By this means, SCP will be reduced to a typical multidimensional 0/1 knapsack problem.

The constraint conversion is based on a simple observation. Given a set of active chargers, there will be one point having the maximal EMR intensity, call Maximal EMR Point (MEP) (if there is a set of points with the same maximal EMR intensity, we can arbitrarily pick one of them without affecting the correctness of our solution). When the MEP does not exceed  $R_t$  and is safe, other locations will be safe too. If the MEP is danger, the constraint is already violated. For example in Fig. 26.2, suppose there are three chargers  $s_1$ ,  $s_2$ , and  $s_3$ . Consider the active charger set of  $s_1$  and  $s_2$  (i.e.,  $s_3$  is inactive). The MEP will be somewhere in between, say location  $p$ . For this case, we only need to check whether  $p$  exceeds  $R_t$  and derive a corresponding constraint. Note that different active charger sets will have different MEPs, and thus for SCP we shall check all the possible combinations of the active charger sets, compute the MEPs under the active chargers, and rewrite the constraints accordingly. With  $n$  chargers, there will be  $2^n$  MEPs and  $2^n$  constraints, which is sufficient. Nevertheless, for practical purposes, we find that the number of effective constraints can be significantly reduced, which will be introduced in a later subsection.

The workflow of our solution is as follows. Given an instance of SCP, we first apply the constraint reduction to list all effective active charger sets, compute the MEP under the charger set, and derive the corresponding constraint. Then, we employ constraint reduction approach to reduce the number of obtained constraints. As such SCP is reformulated to a typical multidimensional 0/1 knapsack problem, we will give the approximation algorithm for MDK. Since the computation of MEP is quite complex, we skip it in this section and describe it separately.

**Fig. 26.3** Active charger set listing



### 26.3.2 Active Charger Set Listing

In the active charger set listing, the input is  $n$  chargers and their locations, and the output is a list of active charger sets used to derive constraints. Intuitively, each possible charger set will have its MEP and each MEP will lead to a corresponding constraint. In the worst case, for  $n$  chargers there will be  $2^n$  active charger sets and thus  $2^n$  constraints as well.

This is, however, neither practical nor necessary for further processing. We desire a lightweight list of active charger sets such that the computational overhead is minimized. We will show that the constraints can be reduced to  $O(n2^{4\rho\pi D^2})$  where  $\rho$  is the charger deployment density, and  $D$  is the farthest distance that a charger can reach in Eq. 26.1, which is much less than  $2^n$ . As shown in Fig. 26.3, since every MEP must lie in the covered region of a certain charger, we only have to investigate the covered region for each charger. For example, for the disk region covered by  $s_1$  with radius  $D$ , an MEP within it can only be charged by chargers with distance less than  $D$ . In other words, only the chargers with distance to  $s_1$  less than  $2D$ , i.e.,  $s_2$  and  $s_3$ , are able to reach the MEP. The number of these chargers is at most  $\rho\pi(2D)^2$ . By enumerating all possible active charger sets for the covered region of each charger, we obtain in total  $O(n2^{4\rho\pi D^2})$  constraints.

### 26.3.3 Constraint Derivation, Reduction, and MDK

For each possible active charger set, we can derive the constraint based on its MEP. In the next section, we will show how to compute an MEP based on a given active charger set. We here use the results directly.

Let  $\Gamma$  denote the lightweight list of effective active charger sets we obtained in the last subsection, and  $S \in \Gamma$  be an active charger set in  $\Gamma$ . Suppose the MEP of  $S$  is at the location  $p$ . The constraint associated with  $S$  is

$$c_2 \sum_{s_i \in S} P_r(d(s_i, p))x_i \leq R_t. \quad (26.6)$$

The obtained constraints by this method can be reduced by removing the following two types of constraints: (i) trivial constraints that can be always satisfied, which means its corresponding active charger set should never lead to an EMR exceeding  $R_t$ ; (ii) redundant constraints that can be safely removed if at least one of the subsets of its corresponding active charger set leads to an EMR exceeding  $R_t$ . For example, if active charger set of  $s_1$  and  $s_2$  has already violated EMR safety, it is needless to include the constraint of its superset of  $s_1$ ,  $s_2$  and  $s_3$ . Actually, the above technique can be applied before the constraint derivation process to reduce the cost of MEP computation.

With the reduced constraints set, which we still denote by  $\Gamma$  for convenience, SCP is reformulated as

$$\begin{aligned} (\text{SCP}) \quad & \max \quad c_1 \quad \sum_{i=1}^n (\sum_{j=1}^m P_r(d(s_i, o_j)))x_i \\ & \text{s.t. } \forall S \in \Gamma, \quad c_2 \sum_{s_i \in S} P_r(d(s_i, p))x_i \leq R_t \\ & \quad x_i \in \{0, 1\} \quad (i = 1, 2, \dots, n). \end{aligned} \quad (26.7)$$

This is a typical MDK problem [13]. When the number of constraint  $|\Gamma| \geq 2$ , there does not exist a fully polynomial time approximation scheme (FPTAS) unless  $P = NP$  [13]. We here apply an algorithm proposed in [15] to obtain an approximation solution.

### 26.3.4 Algorithm Description and Results

In this section, we introduce our approximation algorithm using pseudocode and present the analytical results for the algorithm, demonstrating its near optimal performance.

Algorithm 34 presents the algorithm pseudocode. The input of our algorithm is the set of chargers, devices, and their locations. The output of the algorithm is the binary indicator  $x_i$  to control whether a charger should be active or not. The following theorem describes the performance of Algorithm 34.

**Theorem 26.2** *The time complexity of Algorithm 34 is  $O(n^4(\varepsilon^{-2} + \varepsilon^{-3/2}n) + n(\frac{n}{\varepsilon})^{|\Gamma|})$ . The output of Algorithm 34 is a feasible solution of SCP, and outperforms the optimal solution to SCP with a smaller EMR threshold  $(1 - \varepsilon)R_t$ .*

**Algorithm 34:** Approximation Algorithm for SCP

---

**Input:** A set of  $n$  chargers  $s_i \in S, i = 1, \dots, n$ , and a set of  $m$  rechargeable devices  $o_j \in O, j = 1, \dots, m$

**Output:** Binary indicator  $x_i \in \{0, 1\}, i = 1, \dots, n$

- 1 **for** charger  $s_i$  **do**
- 2     Let  $A$  be the disk area centered at  $s_i$  with radius  $2D$ ; Identify all chargers within  $A$ ; **for** active charger set  $S$  of chargers in  $A$  **do**
- 3         Compute MEP with error threshold  $\varepsilon/2$  based on the active charger set  $S$ ; Derive constraint based on the MEP using Eq. 26.6;
- 4     **end for**
- 5 **end for**
- 6 Conduct constraint reduction; Reformulate SCP based on Eq. 26.7 and modify the EMR threshold  $R_t$  to  $(1 - \varepsilon/2)R_t$ ; Use Algorithm 1 in [15] with error threshold  $\varepsilon/2$  to compute the solution  $x_1, \dots, x_n$  of the reformulated SCP.

---

Generally, for any given small number  $\varepsilon$ , the SCP solution should be better than the optimal solution to SCP with EMR threshold  $(1 - \varepsilon/2)R_t$  if the optimal solution to MDK is available and is applied in Step 6. This is guaranteed by our MEP computation algorithm with bounded error. Nevertheless, as there is no such optimal solution to MDK and instead we use a near optimal algorithm proposed in [15], new error would be introduced but our solution still promises to outperform the optimal solution to SCP with EMR threshold  $(1 - \varepsilon)R_t$ .

For any given small number  $\varepsilon$ , Algorithm 1 in [15] with error threshold  $\varepsilon/2$  guarantees to obtain a near optimal solution which is better than the optimal solution for the MDK problem with its constraints tightened by a factor of  $(1 - \varepsilon/2)$ . On the other hand, despite the approximation error of the MEP algorithm, the modified EMR threshold in Step 6 of Algorithm 34 promises that the optimal solution to the reformulated SCP must be better than the original SCP problem with tightened constraints  $(1 - \varepsilon/2)R_t$ . To sum up, the output of Algorithm 34 outperforms the original SCP problem with threshold  $(1 - \varepsilon/2) \cdot (1 - \varepsilon/2)R_t$ , and therefore outperforms that with threshold  $(1 - \varepsilon)R_t$ .

## 26.4 MEP Computation

In this section, we compute MEP for a given active charger set. This is a major but difficult problem when solving SCP. The challenges are mainly due to the fact that the objective function  $e(p)$  in Eq. 26.4 is non-convex, and thus there is no standard solution to be global optimal. In addition, the search space of MEP is continuous, but the output is a single point. Appropriate discretization method is needed to strike the trade-off between the computation precision and overhead.

In the remainder of this section, we first give the main results, and present the approximation algorithm in details.

### 26.4.1 Main Results

The main results can be summarized as in the following theorem.

**Theorem 26.3** *For any given small number  $\varepsilon$ , the solution  $p^\#$  obtained by our algorithm and the optimal solution  $p^*$  satisfies*

$$(1 - \varepsilon)e(p^*) \leq e(p^\#) \leq e(p^*). \quad (26.8)$$

*The computational time complexity is  $O(\varepsilon^{-2}n^3 + \varepsilon^{-3/2}n^4)$ , and the space requirement is  $O(\varepsilon^{-1/2}n \log n)$  where  $n$  is the number of chargers.*

This shows that the EMR of our solution point  $p^\#$  can be arbitrarily close to that of the optimal one, and the algorithm is thus a fully polynomial time approximation scheme (FPTAS).

### 26.4.2 Algorithm Overview

The key issue in MEP computation is to approximate the non-convex EMR function  $e(p)$  by convex ones so that the problem is transferred into a traditional Fermat–Weber problem [22]. During the approximation, we should guarantee that each step only introduces a bounded error such that the overall algorithm performance can be bounded as well.

The workflow of our algorithm is as follows. We first use a piecewise linear function  $\varepsilon(d)$  to approximate  $e(d)$ . By this means, the covered area of a charger is partitioned to many subareas. Subareas of different chargers will overlap to further partition the area, and each partitioned subarea has a convex objective function. Nevertheless, some subareas may become a non-convex shape, and we thus expand the subareas to convex ones in the third step. By these means, the MEP computation problem can be transferred into a traditional Fermat–Weber problem with norm constraints. The MEP of the whole area is then among these subarea MEPs and easy to find.

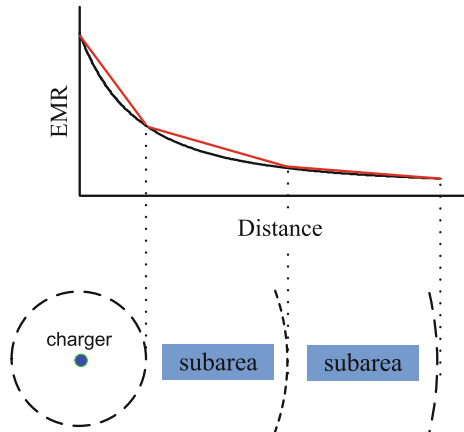
As the goal of each procedure is to convert MEP to the Fermat–Weber problem with norm constraints, we present the formal definition of this problem in advance as follows, in order for a better understanding of these procedures.

**Definition 26.1** (*Fermat–Weber problem with Norm Constraints (FWNC)*) Let  $S = \{s_1, s_2, \dots, s_n\}$  be a set of points in  $\mathbb{R}^2$ , the Weber–Fermat problem is a facility problem that aims to find the point  $p$  such that

$$\begin{aligned} \min \quad & \sum_{i \in n} w_i d(s_i, p) \\ \text{s.t.} \quad & d(s_i, p) \leq C_i, i = 1, 2, \dots, n. \end{aligned} \quad (26.9)$$

where  $w_i$  and  $C_i$  are constants.

**Fig. 26.4** Illustration of piecewise linear approximation



In the remaining subsections of this chapter, we will present the detailed design of these procedures.

### 26.4.3 Piecewise Linear Approximation of $e(d)$

Essentially, we use multiple piecewise linear segments  $\varepsilon(d)$  to approximate the EMR function  $e(d)$  (recall  $e(d) = c_2 P_r(d)$ ), trying to bound the approximation error  $\varepsilon(d) - e(d)$  and the computational overhead.

The basic idea of the approximation  $\varepsilon(d)$  is illustrated in Fig. 26.4. Let the vector  $L = \{\ell_0, \ell_1, \dots, \ell_K\}$  be the end points of  $K$  linear segments in an increasing sequence. The parameter  $K$  is the number of segments that controls the approximation error. In the example of Fig. 26.4,  $K$  is equal to 3. And in general speaking, a larger  $K$  will result in a smaller approximation error but introduces more computation overhead.

**Definition 26.2** Setting  $\ell_0 = 0$  and  $\ell_K = D$ , the piecewise approximation function  $\varepsilon(d)$  can be defined as

$$\varepsilon(d) = \begin{cases} -w_k d + \phi_k, & \ell_{k-1} \leq d \leq \ell_k \ (k = 1, \dots, K) \\ 0, & d > D \end{cases} \quad (26.10)$$

where  $\phi_k = \frac{e(\ell_k)\ell_{k+1} - e(\ell_{k+1})\ell_k}{\ell_{k+1} - \ell_k}$  ( $\phi_k > 0$ ) and  $w_k = -\frac{e(\ell_{k+1}) - e(\ell_k)}{\ell_{k+1} - \ell_k}$  ( $w_k > 0$ ) when  $k \leq K$ , and otherwise  $\phi_k = w_k = 0$ .

**Definition 26.3** To bound the approximation error, we set  $\ell_{k+1}$  (if the obtained  $\ell_{k+1} \geq D$ , set  $K = k + 1$ ,  $\ell_{k+1} = D$ ) sequentially based on  $\ell_k$  ( $\ell_0 = 0$ ) in Eq. 26.10 as

$$\ell_{k+1} = \frac{1}{4}(3x_0 - 2\ell_k + \beta + \sqrt{(3x_0 - 2\ell_k + \beta)(3x_0 + 6\ell_k + 9\beta)}) - \beta \quad (26.11)$$

where  $\beta$  is a constant in Eq. 26.1, and  $x_0$  is one of the roots to the following cubic equation

$$\frac{1-\varepsilon}{(\ell_k+\beta)^2}(x_0+\beta)^3 - 3x_0 + 2\ell_k - \beta = 0$$

that satisfies  $x_0 > \ell_k$ .

By these definitions, we have

**Theorem 26.4** *Setting  $\ell_k$  by Eq. 26.11, we have the approximation errors as*

$$e(d) \leq \varepsilon(d) \leq \frac{e(d)}{1-\varepsilon}. \quad (26.12)$$

**Theorem 26.5** *If  $\varepsilon \rightarrow 0$ , the number of linear segments  $K$  is subject to*

$$\frac{\sqrt{3}}{4}(1 - \frac{1}{(1+D/\beta)^2})\varepsilon^{-1/2} < K < \frac{\sqrt{3}}{4}((1 + D/\beta)^2 - 1)\varepsilon^{-1/2}. \quad (26.13)$$

In other words, we have  $K = \Theta(\varepsilon^{-1/2})$ .

#### 26.4.4 Discretize Solution Space

In this part, we show how to discretize and confine the search space for MEP. The goal is to show that with the approximated EMR function  $\varepsilon(d)$ , the MEP is reformulated as an optimization problem with convex objective function.

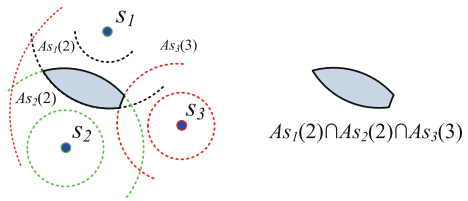
By  $\varepsilon(d)$ , the covered area of a charger  $s$ , denoted as  $A_s$ , is partitioned to  $K$  concentric subareas denoted as  $A_s(k)$ ,  $k = 1, \dots, K$ . Obviously given the active charger set  $S$ , there will be at most  $K|S|$  concentric subareas which may overlap with each other. By computational geometry [11],  $|S|$  chargers will partition the whole plane to at most  $Z$  subarea faces where

$$Z \leq (K|S|)^2 - K|S| + 2 \leq K^2|S|^2.$$

An illustration of such subarea faces with three chargers is depicted in Fig. 26.5. Note that we do not consider the area not covered by any chargers as obviously there has no EMR and MEP cannot be there.

By such partition, MEP for a given active charger set becomes to find MEP from each subarea face, and among these MEPs find the one with the largest EMR. As the second step is straightforward, we here focus on the first step. Denote a subarea face overlapped by several chargers as  $\mathcal{F}(\kappa) = \bigcap_{s_i \in S} A_{s_i}(k_i)$  where  $\kappa = (k_1, k_2, \dots, k_{|S|})$  is a vector indicating the index of concentric subarea that shapes the face. In Fig. 26.5, the face is shaped by  $s_1$ 's second subarea,  $s_2$ 's second subarea, and

**Fig. 26.5** Discretized charging area



$s_3$ 's third subarea, and thus it can be expressed as  $\mathcal{F}(\kappa) = A_{s_1}(2) \cap A_{s_2}(2) \cap A_{s_3}(3)$  where  $\kappa = \{2, 2, 3\}$ . The accumulated EMR approximation for a location  $p$  in  $\mathcal{F}(\kappa)$  is

$$\varepsilon(p) = \sum_{s_i \in S} (-w_{k_i} d(s_i, p) + \phi_{k_i}), \quad p \in \mathcal{F}(\kappa). \quad (26.14)$$

Note  $w_{k_i}$  and  $\phi_{k_i}$  defined in Eq. 26.10 are both constants within the concentric sub-area  $A_{s_i}(k_i)$ . And therefore maximizing  $\varepsilon(p)$  is equivalent to minimizing  $\sum_{s_i \in S} w_{k_i} d(s_i, p)$ . In other words, MEP of an active charger set can be reformulated as

$$\max_{\forall \mathcal{F}(\kappa)} \{\varepsilon(p) | p = \min_{p \in \mathcal{F}(\kappa)} \sum_{s_i \in S} w_{k_i} d(s_i, p)\}. \quad (26.15)$$

#### 26.4.5 Area Expansion

In the last subsection, we can find that MEP is reformulated with a convex objective function  $\sum_{s_i \in S} w_{k_i} d(s_i, p)$ , which allows optimization method to apply. However, by partitions in the last subsection the subarea face  $\bigcap_{s_i \in S} A_{s_i}(k_i)$  may become non-convex (see the example in Fig. 26.5), which will be dealt with in this subsection.

**Definition 26.4** Denoting by  $\Omega_{s_i}(k_i)$  the minimal enclosing disk of  $A_{s_i}(k_i)$ ,  $\Omega_{s_i}(k_i)$  is indeed the union of all concentric subareas no more than  $k_i$ , i.e.,  $\Omega_{s_i}(k_i) = \bigcup_{k \leq k_i} A_{s_i}(k)$ . The expanded area  $\Lambda(\kappa)$  for a subarea face  $\mathcal{F}(\kappa)$  is defined as

$$\Lambda(\kappa) = \bigcap_{s_i \in S} \Omega_{s_i}(k_i) = \bigcap_{s_i \in S} \left( \bigcup_{k \leq k_i} A_{s_i}(k) \right) \quad (26.16)$$

where  $\kappa = \{k_1, \dots, k_{|S|}\}$ .

Figure 26.6 illustrates an example of area expansion based on the example in Fig. 26.5.

**Fig. 26.6** Area expansion



Though  $\mathcal{F}(\kappa)$  is expanded to  $\Lambda(\kappa)$ , the solution to MEP will not change, as the following theorem indicates.

**Theorem 26.6** *Suppose  $p^*$  and  $\bar{p}^*$  are optimal solutions to the reformulated MEP defined in Eq. 26.15 before and after area expansion for each subarea, then  $\varepsilon(p^*) = \varepsilon(\bar{p}^*)$ .*

Note that Theorem 26.6 is not an immediate observation, but a crucial conclusion based on the convexity and monotonic decreasing properties of the EMR function as well as the properties of our piecewise linear approximation.

We further reformulate MEP in each subarea as

$$\begin{aligned} \min & \quad \sum_{s_i \in S} w_{k_i} d(s_i, p) \\ \text{s.t.} & \quad d(s_i, p) \leq \ell_{k_i}, i = 1, 2, \dots, |S|. \end{aligned} \quad (26.17)$$

Notice that the above constraints stem from the definition of expanded area  $\Lambda(\kappa)$ . In the next subsection, we will show how to solve it by a modified Fermat–Weber problem algorithm.

#### 26.4.6 Fermat–Weber Problem with Norm Constraints

Comparing MEP in Eq. 26.17 and the Fermat–Weber problem with norm constraints (FWNC) in Eq. 26.9 we find that they are exactly the same. FWNC is a traditional problem that has been widely studied [22]. There is, however, no standard approximation solution for the problem. Therefore, the approximation algorithm to unweighted Fermat–Weber problem constrained to a polyhedron in [2] can be tailored to our case. The main difference between them lies in the boundary search. The algorithm in [2] simply uses a binary search to find the optimal solution on the line segments of boundaries. In contrast, the adapted algorithm [7] searches all the boundary arcs and adopts Lagrange multiplier method to optimize the objective function.

For the approximation algorithm, we have

**Theorem 26.7** *For any given small number  $\varepsilon$ , our algorithm to FWNC can achieve  $(1 - \varepsilon)$  approximation ratio in deterministic  $O(\varepsilon^{-1}n + \varepsilon^{-1/2}n^2)$  time and  $O(\varepsilon^{-1/2}n \log n)$  space.*

### 26.5 Numerical Results

In this section, we first demonstrate extensive simulations to evaluate our proposed algorithms under different parameter settings, and then reveal insights of the algorithm performance.

### 26.5.1 Evaluation Setup

Assume that there are 12 chargers uniformly deployed over a  $100\text{m} \times 100\text{m}$  2D square area and 100 devices randomly deployed in the area. We set  $\alpha = 100$ ,  $\beta = 40$ , and  $D = 60$  for the charging model, and  $c_1 = 1$  for the EMR model. For the utility model, we simply set  $c_2 = 0.001$ . Moreover, the error threshold of the SCP algorithm is  $\varepsilon = 0.12$ , and the EMR threshold is  $R_t = 150$ . Note that the result is averaged by 100 instances with different random seeds and device deployments.

### 26.5.2 Baseline Setup

In Sect. 26.5.3.1, we compare the MEP algorithm to the particle swarm optimization (PSO) with the number of particles set to be 20 and the loop count be 200. In addition, we use a fine-grained exhaustive search method to find the MEP on the plane, and take its output as the optimal solution.

In Sects. 26.5.3.2, 26.5.3.3, 26.5.3.4, and 26.5.4, we compare the SCP solution to three different algorithms. The first is the optimal solution obtained by enumerating all possible activations of chargers in SCP. Note that here the constraints in SCP are outputs of the optimal solution for MEP used in Sect. 26.5.3.1. The second is the near optimal solution. It is identical to the optimal solution except that its EMR threshold is set to be  $(1 - \varepsilon)R_t$ . The third is a newly designed greedy algorithm for SCP whose constraints are derived based on our approximation algorithm for MEP. Particularly, the greedy algorithm turns on the charger that yields the maximum overall additional utility for all devices while does not violate the EMR safety requirement at each step. Such process repeats until no further activation is possible in terms of the EMR safety.

### 26.5.3 Performance Comparison

In this subsection, we examine the performance of our approximation algorithm for MEP in terms of approximation threshold  $\varepsilon$ , and that for SCP under various designs with different system parameters including the threshold  $\varepsilon$ , the charger number, and the EMR threshold  $R_t$ .

#### 26.5.3.1 Impact of the MEP Threshold $\varepsilon$

To show the efficiency of our MEP algorithm, we consider 50 chargers and 100 devices uniformly deployed over a  $500\text{m} \times 500\text{m}$  2D square area, and investigate the performance of our approximation algorithm for MEP and other two baseline

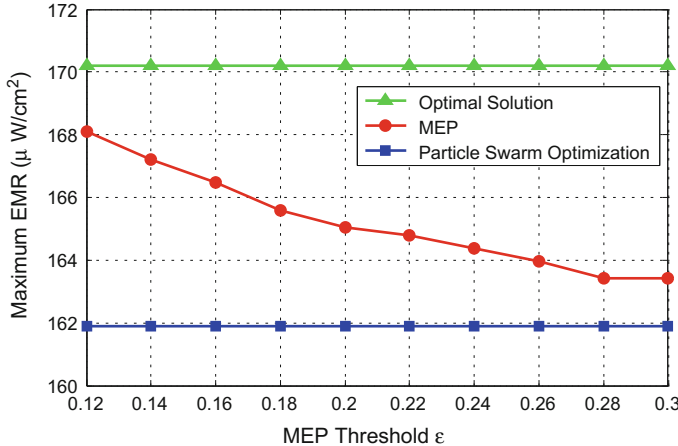


**Fig. 26.7** Maximal EMR versus MEP threshold  $\varepsilon$

algorithms in terms of the MEP threshold  $\varepsilon$ . As illustrated in Fig. 26.7, the outputs of the optimal solution and the PSO are 170.2 and 161.9, respectively, and remain constant. The maximal EMR computed by our algorithm decreases with an increasing  $\varepsilon$ . It is always greater than that of the PSO and is at most 4 % smaller than that of the optimal solution for  $0.12 \leq \varepsilon \leq 0.3$ . This indicates that the approximation bound  $(1 - \varepsilon)$  strictly holds.

### 26.5.3.2 Impact of the SCP Threshold $\varepsilon$

We examine the influence of the SCP threshold  $\varepsilon$  on the overall utility and plot the results in Fig. 26.8. As can be seen, the overall utility of the optimal solution is constant and equal to 12. Our SCP algorithm always outperforms that of the near optimal solution, and the performance gap with the optimal solution diminishes when  $\varepsilon$  decreases and is equal to 6.7 % when  $\varepsilon = 0.1$ . This observation validates our theoretical findings. In addition, the greedy algorithm has the worst performance, which is roughly 34.6 % below that of our SCP algorithm on average.

### 26.5.3.3 Impact of Charger Number

We are also interested in the impact of charger number on overall utility. Figure 26.9 shows that all algorithms have the same performance when the charger number is 4. This is because the activation of all 4 chargers will never damage the EMR safety and thus there is no room for improvement. Besides, the overall utility of every algorithm increases smoothly with the number of chargers, and our SCP algorithm performs

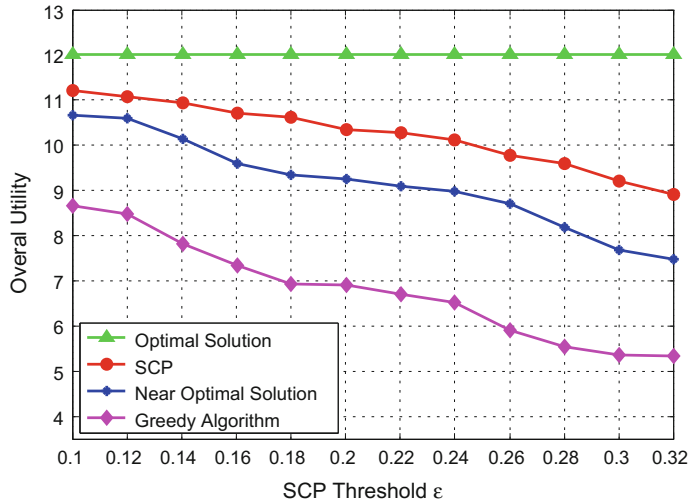


**Fig. 26.8** Overall utility versus SCP threshold  $\epsilon$

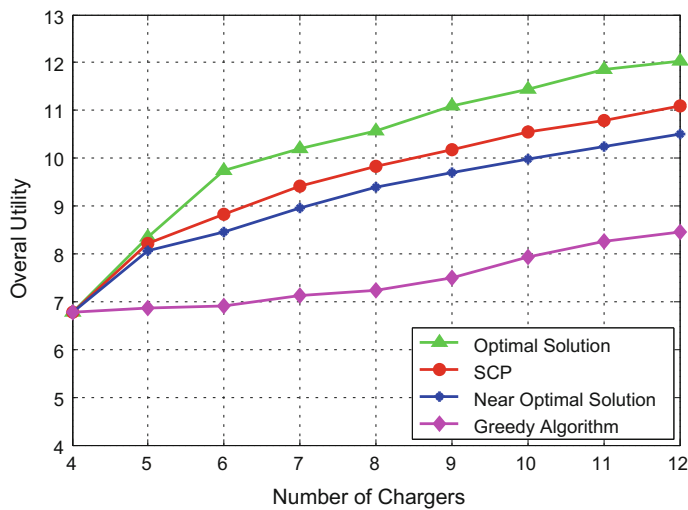


**Fig. 26.9** Overall utility versus charger number

better than the near optimal algorithm, and the performance difference from the optimal one is at most 9.3 %. The gap between the SCP algorithm and the greedy algorithm can be as large as 26.4 %.

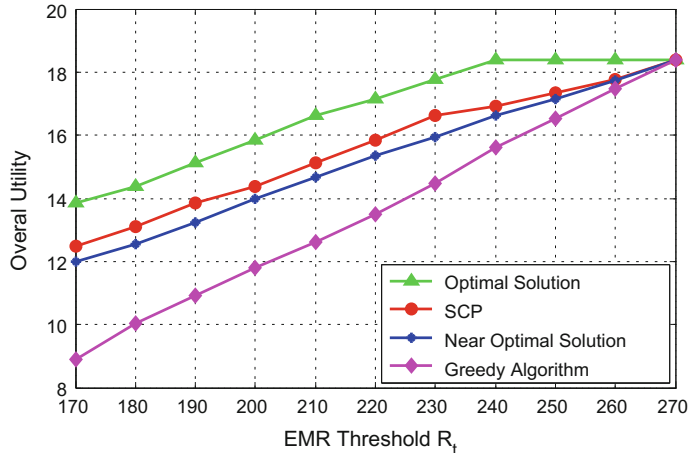


**Fig. 26.10** Overall utility versus EMR threshold  $R_t$

#### 26.5.3.4 Impact of EMR Threshold $R_t$

We study the effect of the EMR threshold  $R_t$  to the overall utility in this subsection. As shown in Fig. 26.10, not surprisingly, the overall utility of all considered solutions grows with an increasing  $R_t$ . The performance of the SCP algorithm also outperforms the near optimal solution. Overall, the optimal solution is nearly 7.7 % higher than that of the SCP algorithm, which in turn enjoys an average performance gain of 14.9 % over the greedy algorithm. Furthermore, when  $R_t$  exceeds 240, the activation of all 12 chargers is allowed for the sake of EMR safety, and thereby the overall utility of the optimal solution reaches the maximum 18.4 and remains constant from then on. The same situation occurs to the other three algorithms when  $R_t$  exceeds 270.

#### 26.5.4 Insights

In this section, we explain why the proposed scheme can obtain a high overall utility gain. Consider the utility of each of 50 devices of a simulation result, as shown in Fig. 26.11. Since the charging utility of a device is proportional to the EMR there (please refer to their definitions in Sect. 26.2.1), the utility distribution of devices actually reflects the EMR distribution for the locations of devices. Intuitively, if all the EMRs at the locations of devices are quite close to the EMR threshold  $R_t$ , which means that the EMRs are balanced among these locations, the overall utility will be high. From the top two sub-figures of Fig. 26.11, we can see that the utility of all 50 devices are nearly uniform, and close to 0.15 and 0.13, respectively, which are

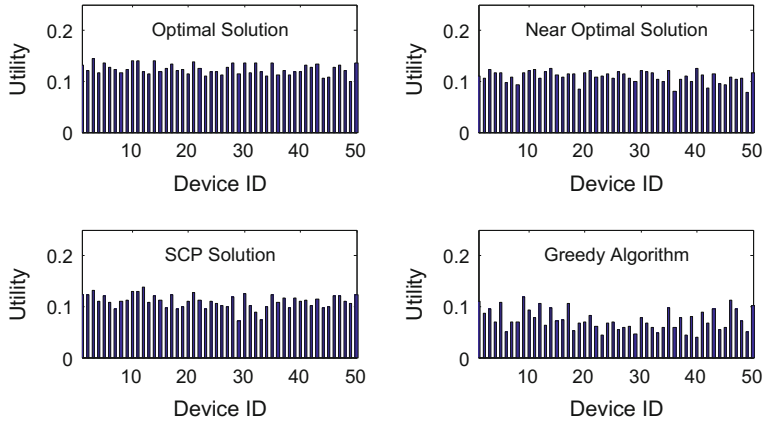


**Fig. 26.11** Utility of devices for four solutions

the theoretical maximum utility constrained by their EMR safety requirements. As for the bottom two sub-figures, the greedy algorithm has utility distribution with a higher variance. This is because the greedy algorithm is conducted in such a way that it totally overlooks the balance of EMR distribution. The EMRs at certain points on the plane shall rise much quickly than others during the greedy process of activating new chargers, and soon approach  $R_t$  and disable further charger activation. Hence, its overall achieved utility is low. Conversely, the SCP solution performs in a reasonable manner so that the utility is balanced among devices and thus is improved significantly.

## 26.6 Field Experiments

In this section, we describe field experiments and show that their results validate our theoretical results.

### 26.6.1 Experimental Testbed

Figure 26.12a shows the indoor experimental testbed. The testbed consists of 8 chargers (TX91501 transmitters produced by Powercast [27]) which are deployed on the vertices and middle points of edges of a  $2.4\text{ m} \times 2.4\text{ m}$  square area. In addition, a wireless rechargeable sensor node (see Fig. 26.12b) is placed at the center of the square area, and another one to the right side of the first one with distance 0.4 m. An RF field strength meter (see Fig. 26.12c) to measure the intensity of EMR.

Note that all the chargers are actually directional. With reasonable precision, their charging region can be modeled as a sector with angle  $60^\circ$  and radius 4. The

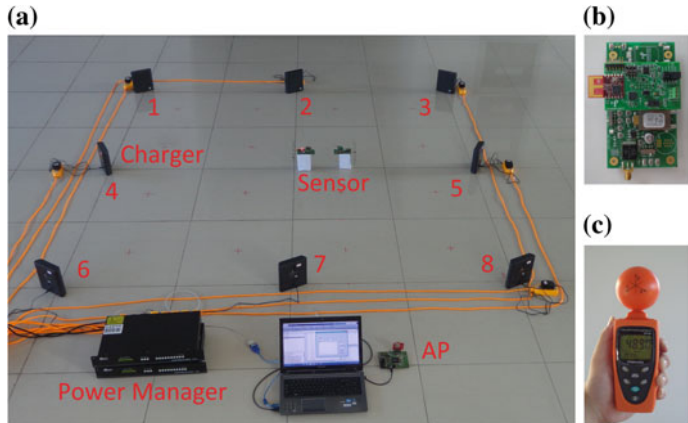


**Fig. 26.12** Field experiment

orientation of chargers should thus greatly impact the EMR distribution of the space. Suppose the chargers are numbered from top to bottom and from left to right as shown in Fig. 26.12a. The chargers are rotated from 1 to 8 such that the angles between their orientation and the positive horizontal line are  $296.56^\circ$ ,  $296.56^\circ$ ,  $243.44^\circ$ ,  $26.56^\circ$ ,  $153.44^\circ$ ,  $63.44^\circ$ ,  $116.56^\circ$ , and  $116.56^\circ$ , respectively, in order to enhance the charging efficiency in the square area.

The computer controls the power supply through a power manager. The sensor nodes record their received power and send the information to an access point (AP) connecting to the computer. The AP then reports the data to the computer for analysis and decision.

### 26.6.2 Adapted Algorithm Description

The following adaptations are made to the SCP algorithm considering real situations. First, the SCP algorithm is adjusted to the case under directional chargers. This can be done by modifying the MEP algorithm. Second, to alleviate the error incurred by modeling of directional chargers, environmental variation, etc., the two sensors sample the charging power from each charger at the beginning of the algorithm. Then, the SCP algorithm is performed based on the sampled values.

### 26.6.3 Experimental Results

As Fig. 26.13 illustrates, we compare the computed utility based on sampling with real utility under three different values of  $R_t$ . Note that in this figure, Node 1 refers to the

**Fig. 26.13** Utility versus EMR threshold  $R_t$

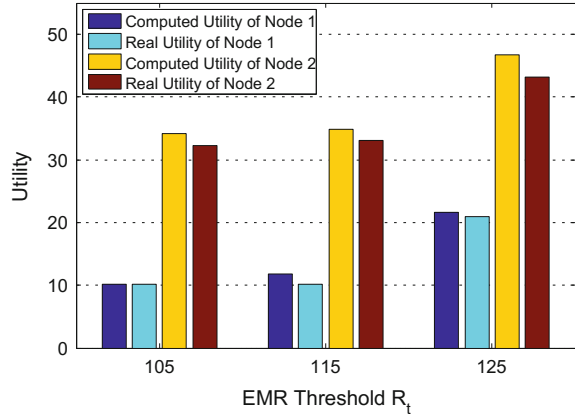
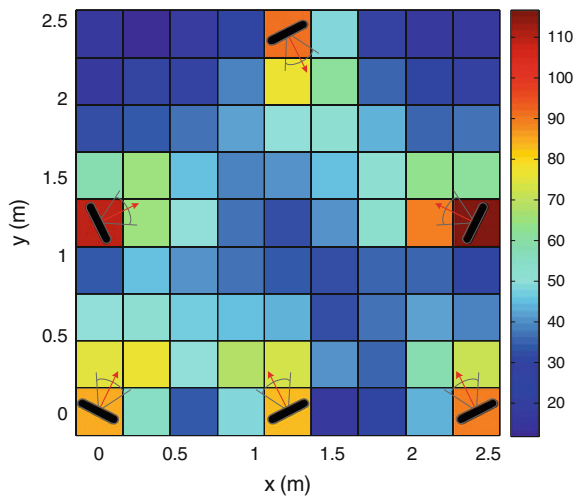


**Fig. 26.14** An example of EMR distribution



node located at the center of the area and Node 2 refers to the other. We can see that the computed utility of both nodes is always larger than the real utility, but the difference between them is quite small and no more than 7.5 %. This observation supports the power additivity assumption and the effectiveness of our sampling approach. Furthermore, the gap between these two solutions tends to increase when the utility grows. This is likely due to the charging property of the capacitors in sensors.

Suppose the EMR threshold  $R_t$  is  $125 \mu\text{W}/\text{cm}^2$ , turn on charger 2, 4, 5, 6, 7 and 8 according to the output of our adapted algorithm. Then measure the EMR values at  $9 \times 9$  grid points of the square region, and plot them in Fig. 26.14 to visualize the EMR distribution of the area in an approximation manner. We observe that the EMR peaks at the location of charger 5 and is equal to  $116.7 \mu\text{W}/\text{cm}^2$  and thus less than  $R_t$ . This fact confirms the correctness of the SCP algorithm.

## 26.7 Conclusion

In this chapter, we first discussed the harmful effect of high EMR to human safety and then presented the Safe Charging Problem. In particular, we studied the problem of maximizing the charging utility under the constraints of EMR safety. We presented a near optimal solution to SCP. In addition, all the extensive simulations and field experiments results corroborated the analytical findings. This solution could be incorporated into many systems to harness the detrimental impact of EMR.

EMR safety, together with charging efficiency, are widely identified as two major barriers for the proliferation of wireless power transfer technology. However, unlike charging efficiency, EMR safety is rarely considered in existing literatures, and the research of safe charging is still at its infancy stage. We hope that this chapter could arouse the interests of scientists in issues of safe charging, and finally contribute to the widespread use of wireless power transfer technology and human safety.

## References

1. Ahlbom, A., Bergqvist, U., Bernhardt, J., Cesarini, J., Grandolfo, M., Hietanen, M., McKinlay, A., Repacholi, M., Sliney, D., Stolwijk, J., et al.: Guidelines for limiting exposure to time-varying electric, magnetic, and electromagnetic fields (up to 300 GHz). international commission on non-ionizing radiation protection. *Health Phys.* **74**(4), 494–522 (1998)
2. Bose, P., Maheshwari, A., Morin, P.: Fast approximations for sums of distances, clustering and the Fermat–Weber problem. *Comput. Geom.* (2003)
3. Buettner, M., Greenstein, B., Sample, A., Smith, J.R., Wetherall, D., et al.: Revisiting smart dust with RFID sensor networks. In: HotNets-VII (2008)
4. Buettner, M., Prasad, R., Philipose, M., Wetherall, D.: Recognizing daily activities with RFID-based sensors. In: Ubicomp (2009)
5. Commission, F.C., et al.: Title 47 of the code of federal regulations. Part **15**, 107–109 (2011)
6. Dai, H., Jiang, L., Wu, X., Yau, D.K., Chen, G., Tang, S.: Near optimal charging and scheduling scheme for stochastic event capture with rechargeable sensors. In: MASS (2013)
7. Dai, H., Liu, Y., Chen, G., Wu, X., He, T.: Safe charging for wireless power transfer. In: INFOCOM, pp. 1105–1113 (2014)
8. Dai, H., Wu, X., Xu, L., Chen, G.: Practical scheduling for stochastic event capture in wireless rechargeable sensor networks. In: WCNC (2013)
9. Dai, H., Wu, X., Xu, L., Chen, G., Lin, S.: Using minimum mobile chargers to keep large-scale wireless rechargeable sensor networks running forever. In: ICCCN (2013)
10. Dai, H., Xu, L., Wu, X., Dong, C., Chen, G.: Impact of mobility on energy provisioning in wireless rechargeable sensor networks. In: WCNC (2013)
11. De Berg, M., Cheong, O., Van Kreveld, M.: Computational Geometry: Algorithms and Applications. Springer (2008)
12. Edwards, M.J., Saunders, R.D., Shiota, K.: Effects of heat on embryos and foetuses. *Int. J. Hyperth.: Off. J. Eur. Soc. Hyperth. Oncol. North Am. Hyperth. Group* **19**(3), 295–324 (2002)
13. Fréville, A.: The multidimensional 0–1 knapsack problem: an overview. *Eur. J. Oper. Res.* **155**(1), 1–21 (2004)
14. Gandhi, O.P., Morgan, L.L., de Salles, A.A., Han, Y.Y., Herberman, R.B., Davis, D.L.: Exposure limits: the underestimation of absorbed cell phone radiation, especially in children. *Electromag. Biol. Med.* **31**(1), 34–51 (2012)

15. Ge, W., Zhang, J., Xue, G.: MIMO-Pipe modeling and scheduling for efficient interference management in multihop MIMO networks. TOVT (2010)
16. Greene, C., Kalp, D., Tauche, W.: Making wireless sensor networks truly wireless using RF power
17. Havas, M., Marrongelle, J., Pollner, B., Kelley, E., Rees, C.R., Tully, L.: Provocation study using heart rate variability shows microwave radiation from 2.4 GHz cordless phone affects autonomic nervous system. Eur. J. Oncol. Library **5** (2010)
18. He, S., Chen, J., Jiang, F., Yau, D.K., Xing, G., Sun, Y.: Energy provisioning in wireless rechargeable sensor networks. In: INFOCOM, pp. 2006–2014 (2011)
19. <http://powercastco.com/PDF/2009SensorsExpo2.pdf>
20. <http://www.moh.gov.cn/zwgkzt/pgw/201212/34317.shtml>
21. <http://www.powercastsensors.com/category/applications/page/2/>
22. Hurter Jr., A.P., Schaefer, M.K., Wendell, R.E.: Solutions of constrained location problems. Manag. Sci. **22**(1), 51–56 (1975)
23. Karinen, A., Heinävaara, S., Nylund, R., Leszczynski, D.: Mobile phone radiation might alter protein expression in human skin. BMC Genomics **9**(1), 77 (2008)
24. Nittby, H., Widegren, B., Krogh, M., Grafström, G., Berlin, H., Rehn, G., Eberhardt, J.L., Malmgren, L., Persson, B.R., Salford, L.G.: Exposure to radiation from global system for mobile communications at 1,800 MHz significantly changes gene expression in rat hippocampus and cortex. Environmentalist **28**(4), 458–465 (2008)
25. Ntzouni, M.P., Skourliakou, A., Kostomitsopoulos, N., Margaritis, L.H.: Transient and cumulative memory impairments induced by GSM 1.8 GHz cell phone signal in a mouse model. Electromag. Biol. Med. **32**(1), 95–120 (2013)
26. Olteanu, M., Marincă, C., Rafiroiu, D.: Dangerous temperature increase from EM radiation around metallic implants. Acta Electrotehn. **53**(2), 175–180 (2012)
27. PowerCast. <http://www.powercastco.com>
28. Shearer, J.G., Greene, C.E., Harrist, D.W.: Power transmission network (2010). US Patent 7,844,306
29. Shkolnikov, Y.P., Bailey, W.H.: Electromagnetic interference and exposure from household wireless networks. In: PSES, pp. 1–5. IEEE (2011)
30. Wicaksono, R.P., Tran, G.K., Sakaguchi, K., Araki, K.: Wireless Grid: enabling ubiquitous sensor networks with wireless energy supply pp. 1–5 (2011)

## Chapter 27

# Efficient Wireless Power Transfer Under Radiation Constraints in Wireless Distributed Systems

Sotiris Nikoletseas, Theofanis P. Raptis and Christoforos Raptopoulos

**Abstract** In this chapter, we follow a new approach in studying the problem of efficiently charging a set of rechargeable nodes using a set of wireless power chargers, under safety constraints on the electromagnetic radiation incurred. In particular, we define a new charging model that greatly differs from existing models in that it takes into account real technology restrictions of the chargers and nodes of the system, mainly regarding energy limitations. Our model also introduces nonlinear constraints (in the time domain), that radically change the nature of the computational problems we consider. In this charging model, we present and study the *Low Radiation Efficient Charging Problem* (LREC), in which we wish to optimize the amount of “useful” energy transferred from chargers to nodes (under constraints on the maximum level of imposed radiation). We present several fundamental properties of this problem and provide indications of its hardness. Finally, we propose an iterative local improvement heuristic for LREC, which runs in polynomial time, and we evaluate its performance via simulation. Our algorithm decouples the computation of the objective function from the computation of the maximum radiation and also does not depend on the exact formula used for the computation of the electromagnetic radiation in each point of the network, achieving good trade-offs between charging efficiency and radiation control; it also exhibits good energy balance properties. We provide extensive simulation results supporting our claims and theoretical results.

---

S. Nikoletseas (✉) · T.P. Raptis · C. Raptopoulos

Department of Computer Engineering and Informatics, University of Patras and Computer Technology Institute and Press “Diophantus” (CTI), Patras, Greece  
e-mail: nikole@cti.gr

T.P. Raptis

Institute of Informatics and Telematics, National Research Council, Moruzzi Str 1,  
56124 Pisa, Italy  
e-mail: theofanis.raptis@iit.cnr.it

C. Raptopoulos

e-mail: raptopox@ceid.upatras.gr

## 27.1 Introduction and Related Work

The beneficial use of Wireless Power Transfer (WPT) in Wireless Distributed Systems (WDS) comes at a price with regards to real life applications. Wireless Power Transfer introduces a new source of *electromagnetic radiation* (EMR) that will co-exist with several other wireless technologies (i.e., Wi-Fi, Bluetooth, etc.). Exposure to high electromagnetic radiation, has been widely recognized as a *threat to human health*. Its potential risks include but is not limited to mental diseases [18], tissue impairment [19] and brain tumor [10]. In addition, there has been solid evidence that pregnant women and children are even more vulnerable to high electromagnetic radiation exposure [6, 7]. We note that particularly the radiation levels created by wireless power can be quite high, due to the strength of the electromagnetic fields created. Even if the impact of electromagnetic radiation can be considered controversial we believe it is worth understanding and control, without, however, compromising the quality of service offered to the user of wireless communications. For such systems, the broader aim would be to come up with radiation awareness in an adaptive manner, by providing design principles and studying key algorithmic and networking aspects of radiation aware wireless networking. The Computer Science research community has already demonstrated relevant interest from an ICT perspective by considering restrictions in the amount of emitted EMR. This creates a new topic in algorithmic network design for WDS.

Research efforts in WDS have already started considering network models that take into account WPT technologies. For instance, wireless rechargeable sensor networks consist of sensor nodes, as well as few nodes with high energy supplies (wireless chargers). The latter are capable of fast charging sensor nodes, by using Wireless Power Transfer technologies. In [2, 3], the authors assume a single special mobile charging entity, which traverses the network and wirelessly replenishes the energy of sensor nodes. Their methods are distributed, adaptive, use limited network information and perform well in detailed experimental simulations. In [14, 15], the authors employ multiple mobile chargers in sensor networks and collaboratively compute the coordination, trajectory, and charging processes. The authors also provide protocols that grant the chargers the ability to charge each other. In [17], the authors propose protocols that focus on charging efficiency and energy balance, and they perform the evaluation through an experimental setting of real WPT devices. In [13], a practical and efficient joint routing and charging scheme is proposed. In [11], the authors consider the problem of scheduling mobile chargers in an on-demand way to maximize the covering utility; the authors formulate the scheduling problem as an optimization one and the authors provide three heuristics. In [20], the authors formulate a set of power flow problems and propose algorithms to solve them based on a detailed analysis on the problem structure. Moreover, the authors further investigate the joint data and power flow problems. In [9], the authors propose a framework of joint wireless power replenishment and anchor-point based mobile data gathering in sensor networks by considering various sources of energy consumption and time-varying nature of energy replenishment.

The attention of researchers from many diverse research fields has been drawn in the field of electromagnetic radiation impact. Consequently, there has also been research on radiation related problems in the WDS context. In [16], the authors study the problem of electromagnetic radiation in wireless sensor networks and more specifically maintaining low radiation trajectories for a person moving in a sensor network area. the authors evaluate mathematically the radiation in well-known sensor network topologies and random geometric graphs. Then, the authors implement online protocols and comparatively study their performance via simulation. Those heuristics achieve low radiation paths which are even close to an off-line optimum. In [1], the authors focus on the problem of efficient data propagation in wireless sensor networks, trying to keep latency low while maintaining at low levels the radiation cumulated by wireless transmissions. The authors first propose greedy and oblivious routing heuristics that are radiation aware. They then combine them with temporal back-off schemes that use local properties of the network in order to spread radiation in a spatio-temporal way. The proposed radiation aware routing heuristics succeed to keep radiation levels low, while not increasing latency. In [12], the authors consider the problem of covering a planar region, which includes a collection of buildings, with a minimum number of stations so that every point in the region is within the reach of a station, while at the same time no building is within the dangerous range of a station. However, those approaches are oriented toward network devices radiation, not addressing wireless chargers.

Some limited research has also been conducted in the cross-section of Wireless Power Transfer and electromagnetic radiation in networking settings. In [4], the authors study the problem of scheduling stationary chargers so that more energy can be received while no location in the field has electromagnetic radiation (EMR) exceeding a given threshold. The authors design a method that transfers the problem to two traditional problems, namely a multidimensional 0/1 knapsack problem and a Fermat-Weber problem. The method includes constraint conversion and reduction, bounded EMR function approximation, area discretization and expansion, and a tailored Fermat-Weber algorithm. In order to evaluate the performance of their method, the authors build a testbed composed of 8 chargers. In [5], the authors consider the problem of scheduling stationary chargers with adjustable power, namely how to adjust the power of chargers so as to maximize the charging utility of the devices, while assuring that EMR intensity at any location in the field does not exceed a given threshold. The authors present an area discretization technique to help reformulating the problem into a traditional linear programming problem. Further, the authors propose a distributed redundant constraint reduction scheme to cut down the number of constraints, and thus reduce the computational efforts of the problem. Although thematically, [5] is related to our current work, nevertheless, our treatment of the subject of low radiation efficient charging is radically different. Indeed, this is due to the different charging model that we define, which takes into account hardware restrictions of the chargers and nodes of the system (energy and capacity bounds). These constraints introduce a nonlinearity in our problems that did not appear in the treatment of [5].

In this chapter, we follow a new approach for radiation aware charging in wireless settings. In particular, as our first contribution in this chapter, we define a *new charging model* that greatly differs from existing models in that it takes into account hardware restrictions of the chargers and nodes of the system. More precisely, we assume (a) that chargers have *finite initial energy supplies*, which restricts the amount of energy that they can transfer to nearby nodes, and (b) that every node has *finite battery capacity*, which restricts the total amount of energy that it can store. It is worth noting that previous works have only considered the problem of maximization of power (i.e., the rate of energy transfer) from the chargers to the nodes, thus ignoring such restrictions. However, new technological advances on Wireless Power Transfer via Strongly Coupled Magnetic Resonances suggest that such restrictions are already in the heart of efficient energy management problems in such systems.

**Our contribution.** An important consequence of the energy and capacity restrictions in our model, which sets it apart from other models considered in the literature thus far, is that they introduce *nonlinear constraints* that radically change the nature of the computational problems we consider. In fact, our charging model implicitly introduces the notion of *activity time* in the (radiation aware) charging process, which is the time that a wireless entity (i.e., charger or node) can “affect the system.”

As our second contribution, we present and study the *Low Radiation Efficient Charging Problem* (LREC). Rather than the maximization of the cumulative power on nodes, the objective function that we wish to optimize in LREC is the amount of “useful energy transferred from chargers to nodes (under constraints on the maximum level of radiation caused because of the Wireless Power Transfer).” We present several fundamental properties of our objective function that highlight several obstacles that need to be overcome when studying LREC. Furthermore, we present an algorithm for computing the value of the objective function, given the configuration of the system at any time point, which runs in linear time in the number of chargers and nodes.

As our third contribution, we present a relaxation of the LREC problem, namely the *Low Radiation Disjoint Charging Problem* (RLDC), which simplifies the computation of the maximum electromagnetic radiation inside the area where chargers and nodes are deployed (i.e., the area of interest). We prove that, even this seemingly easier version of our basic problem is NP-hard, by reduction from the Independent Set Problem in Disc Contact Graphs. Furthermore, we present an integer program for finding the optimal solution to RLDC. We approximately solve this integer program by using standard relaxation and rounding techniques and we use the computed (feasible) solution to assess the performance of our iterative heuristic solution to LREC.

In view of hardness indications for LREC, we propose an iterative local improvement heuristic `IterativeLREC` which runs in polynomial time, and we evaluate its performance via simulation. The most important feature of our algorithmic solution is that it decouples the computation of the objective function from the computation of the maximum radiation. Furthermore, our algorithmic solution is independent of the exact formula used for the computation of the point electromagnetic radiation. This is especially important, because due to the fact that the effect that multiple radiation sources have on the electromagnetic radiation is not well understood in

our days. Finally, we provide extensive simulation results supporting our claims and theoretical results. We focus on three network metrics: *charging efficiency*, *maximum radiation*, and *energy balance*.

## 27.2 The Model

We assume that there is a set of  $n$  rechargeable *nodes*  $\mathcal{P} = \{v_1, v_2, \dots, v_n\}$  and a set of  $m$  wireless power *chargers*  $\mathcal{M} = \{u_1, u_2, \dots, u_m\}$  which are deployed inside an area of interest  $\mathcal{A}$  (say inside  $\mathbb{R}^2$ ). Unless otherwise stated, we will assume that both nodes and chargers are static, i.e., their positions and operational parameters are specified at time 0 and remain unchanged from that time on.

For each charger  $u \in \mathcal{M}$ , we denote by  $E_u^{(t)}$  the *available energy* of that charger that it can use to charge nodes within some *radius*  $r_u$  (i.e., we assume that the initial energy of charger  $u$  is  $E_u^{(0)}$ ). The radius  $r_u$  for each charger  $u \in \mathcal{M}$  can be chosen by the charger at time 0 and remains unchanged for any subsequent time (hence the nondependence of  $r_u$  from  $t$  in the notation). Furthermore, for each node  $v \in \mathcal{P}$ , we denote by  $C_v^{(t)}$  the *remaining energy storage capacity* of the node at time  $t$  (i.e., the initial energy storage capacity of node  $v$  is  $C_v^{(0)}$ ).

We consider the following well established *charging model*: a node  $v \in \mathcal{P}$  harvests energy from a charger  $u \in \mathcal{M}$  with *charging rate* given by

$$P_{v,u}(t) = \begin{cases} \frac{\alpha r_u^2}{(\beta + \text{dist}(v,u))^2}, & \text{if } E_u^{(t)}, C_u^{(t)} > 0, \text{dist}(v, u) \leq r_u \\ 0, & \text{otherwise.} \end{cases} \quad (27.1)$$

$\alpha$  and  $\beta$  are known positive constants determined by the environment and by hardware of the charger and the receiver. In particular, the above equation determines the rate at which a node  $v$  harvests energy from any charger  $u$  that has  $v$  within its range, until the energy of  $u$  is depleted or  $v$  is fully charged. We stress out here that, besides its dependence on the geographic positions of  $v$  and  $u$ , the charging rate  $P_{v,u}(t)$  is also a function of time  $t$ . Indeed, for any node  $v \in \mathcal{P}$  within distance  $r_u$  from charger  $u$ , it is equal to  $\frac{\alpha r_u^2}{(\beta + \text{dist}(v,u))^2}$  in a time interval  $[0, t_{u,v}^*]$  and 0 otherwise. By Eq. (27.1), the time point  $t_{u,v}^*$  at which the value of  $P_{v,u}(t)$  drops to 0 is the time when either the energy of  $u$  is depleted or  $v$  is fully charged (which also depends on other chargers that can reach  $v$ ). Consequently, the exact value of  $t_{u,v}^*$  may depend on the whole network (see also the discussion after Definition 27.1 in Sect. 27.3), i.e., the location, radius, and initial energy of each charger and the location and initial energy storage capacity of each node. As a matter of fact, it seems that there is no “nice” closed formula for  $t_{u,v}^*$ . Nevertheless, the value of  $t_{u,v}^*$  can be found by using the ideas of Sect. 27.4 and, more specifically, using a trivial modification of Algorithm `ObjectiveValue`.

Another crucial assumption on our charging model (which is also widely accepted by physicists) is that the harvested energy by the nodes is additive. Therefore, the total energy that node  $v$  gets within the time interval  $[0, T]$  is

$$H_v(T) = \sum_{u \in \mathcal{M}} \int_0^T P_{v,u}(t) dt. \quad (27.2)$$

One of the consequences of our charging model (and in particular Eqs. (27.1) and (27.2) above) is that  $\sum_{u \in \mathcal{M}} E_u \geq \sum_{v \in \mathcal{P}} H_v(T)$ , for any  $T > 0$ . This means that the total energy harvested by the nodes cannot be larger than the total energy provided by the chargers. As yet another consequence, we have that  $\sum_{v \in \mathcal{P}} C_v \geq \sum_{v \in \mathcal{P}} H_v(T)$ , for any  $T > 0$ , i.e., the total energy harvested by the nodes cannot be larger than the total energy that can be stored by all nodes.

To complete the definition of our model, we will make the assumption that the *electromagnetic radiation (EMR)* at a point  $x$  is proportional to the additive power received at that point. In particular, for any  $x \in \mathcal{A}$ , the EMR at time  $t$  on  $x$  is given by

$$R_x(t) = \gamma \sum_{u \in \mathcal{M}} P_{x,u}(t), \quad (27.3)$$

where  $\gamma$  is a constant that depends on the environment and  $P_{x,u}(t)$  is given by Eq. (27.1). We note that, even though this is the usual assumption concerning electromagnetic radiation, the algorithmic solutions that we propose here could also be applied in the case of more general functions for  $R_x(t)$  (as long as some quite general smoothness assumption are satisfied; see also Sect. 27.5). We feel that this is especially important, because the notion of electromagnetic radiation is not completely understood in our days.

We finally note that the existence of an energy (upper) bound for each charger, and a capacity bound for each node greatly differentiates our model from other works in the literature. Indeed, not only can chargers decide on the length of their charging radius (a slight variation of which has been proposed in [5]), but once each charger has made its decision, all chargers begin charging nodes within their radius until either their energy has been depleted, or every node within their radius has already reached its energy storage capacity. Furthermore, this characteristic radically changes the nature of the computational problem that we consider (see Sect. 27.3).

### 27.3 Problem Statement and First Results

In general, we would like to use the chargers as efficiently as possible, but we would also like to keep radiation levels within acceptable levels. In particular, we are interested in the following computational problem which we refer to as Low Radiation Efficient Charging (LREC):

**Definition 27.1** (*Low Radiation Efficient Charging (LREC)*) Let  $\mathcal{M}$  be a set of wireless power chargers and  $\mathcal{P}$  be a set of rechargeable nodes which are deployed inside an area of interest  $\mathcal{A}$ . Suppose that each charger  $u \in \mathcal{M}$  initially has available energy  $E_u^{(0)}$ , and each node  $v \in \mathcal{P}$  has initial energy storage capacity  $C_v^{(0)}$ . Assign to each charger  $u \in \mathcal{M}$  a radius  $r_u$ , so that the total usable energy given to the nodes of the network is maximized and the electromagnetic radiation at any point of  $\mathcal{A}$  is at most  $\rho$ . We assume that all chargers start operating simultaneously at time 0 and charging follows the model described in Sect. 27.2.

Let  $\mathbf{r} = (r_u : u \in \mathcal{M})$ ,  $\mathbf{E}^{(0)} = (E_u^{(0)} : u \in \mathcal{M})$ , and  $\mathbf{C}^{(0)} = (C_v^{(0)} : v \in \mathcal{P})$ . In essence, the *objective function* that we want to maximize in the LREC problem is the following:

$$\begin{aligned} f_{\text{LREC}}(\mathbf{r}, \mathbf{E}^{(0)}, \mathbf{C}^{(0)}) &\stackrel{\text{def}}{=} \sum_{v \in \mathcal{P}} \left( \lim_{t \rightarrow \infty} C_v^{(t)} \right) \\ &= \sum_{u \in \mathcal{M}} \left( E_u^{(0)} - \lim_{t \rightarrow \infty} E_u^{(t)} \right). \end{aligned} \quad (27.4)$$

The last equality follows from the fact that we are assuming loss-less energy transfer from the chargers to the nodes (obviously this easily extends to lossy energy transfer, but we do not consider such models in this chapter). In fact, we only need to consider finite values for  $t$ , because the energy values  $E_u^{(t)}$  will be unchanged after time  $t^* \stackrel{\text{def}}{=} \max_{v \in \mathcal{P}, u \in \mathcal{M}} t_{u,v}^*$ , where  $t_{u,v}^*$  is the time point at which the value of  $P_{v,u}(t)$  drops to 0 (i.e., the time when either the energy of  $u$  is depleted or  $v$  is fully charged). Therefore

$$f_{\text{LREC}}(\mathbf{r}, \mathbf{E}^{(0)}, \mathbf{C}^{(0)}) = \sum_{v \in \mathcal{P}} C_v^{(t)} = \sum_{u \in \mathcal{M}} (E_u^{(0)} - E_u^{(t)}), \quad (27.5)$$

for any  $t \geq t^*$ . The following Lemma provides an upper bound on the value of  $t^*$ , which is independent of the radius choice for each charger.

**Lemma 27.1**  $t^*$  can be at most

$$T^* = \frac{(\beta + \max_{u \in \mathcal{M}, v \in \mathcal{P}} \text{dist}(v, u))^2}{\alpha (\min_{u \in \mathcal{M}, v \in \mathcal{P}} \text{dist}(v, u))^2} \max_{u \in \mathcal{M}, v \in \mathcal{P}} \{E_u^{(0)}, C_v^{(0)}\}.$$

*Proof* Since  $t^* \stackrel{\text{def}}{=} \max_{v \in \mathcal{P}, u \in \mathcal{M}} t_{u,v}^*$ , we only need to provide an upper bound on  $t_{u,v}^*$ . To this end, without loss of generality, we assume that there is a charger  $u_0$  and a node  $v_0$  such that  $u_0$  can reach  $v_0$  (hence also  $r_{u_0} \neq 0$ ) and  $t^* = t_{u_0,v_0}^*$ . Furthermore, we need to consider two cases, depending on whether  $t_{u_0,v_0}^*$  is equal to (a) the time when the energy of the charger  $u_0$  is depleted, or (b) the time when  $v_0$  is fully charged.

In case (a), by the maximality of  $t_{u_0, v_0}^*$ , we have that

$$E_{u_0}^{(0)} = \sum_{v \in \mathcal{P}} \int_0^{t_{u,v}^*} P_{v,u}(t) dt \geq \int_0^{t_{u_0,v_0}^*} P_{v_0,u_0}(t) dt = t_{u_0,v_0}^* \frac{\alpha r_{u_0}^2}{(\beta + \text{dist}(v_0, u_0))^2} \quad (27.6)$$

where in the first and last equality we used the fact that in case (a)  $t_{u_0, v_0}^*$  is the time when the energy of the charger  $u_0$  is depleted (hence  $v_0$  has not yet exceeded its energy storage capacity).

In case (b), by Eq. (27.2) and the maximality of  $t_{u_0, v_0}^*$ , we have that

$$\begin{aligned} C_{v_0}^{(0)} &= H_{v_0}(t_{u_0, v_0}^*) = \sum_{u \in \mathcal{M}} \int_0^{t_{u_0,v_0}^*} P_{v,u}(t) dt \\ &\geq \int_0^{t_{u_0,v_0}^*} P_{v_0,u_0}(t) dt = t_{u_0,v_0}^* \frac{\alpha r_{u_0}^2}{(\beta + \text{dist}(v_0, u_0))^2} \end{aligned} \quad (27.7)$$

where in the first and last equality we used the fact that in case (b)  $t_{u_0, v_0}^*$  is the time when  $v_0$  is fully charged (hence the energy of  $u_0$  has not been depleted yet).

By Eqs. (27.6) and (27.7), we have that

$$t_{u_0, v_0}^* \leq \max\{E_{u_0}^{(0)}, C_{v_0}^{(0)}\} \frac{(\beta + \text{dist}(v_0, u_0))^2}{\alpha r_{u_0}^2} \quad (27.8)$$

which completes the proof.  $\square$

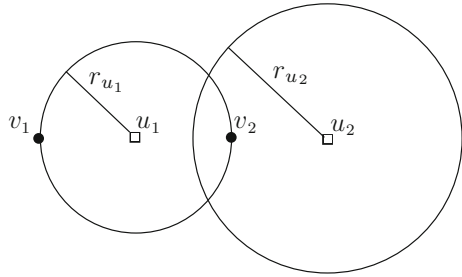
It is worth noting here that, given  $\mathbf{r}$ ,  $\mathbf{E}^{(0)}$  and  $\mathbf{C}^{(0)}$ , the exact value of  $f_{\text{LREC}}(\mathbf{r}, \mathbf{E}^{(0)}, \mathbf{C}^{(0)})$  can be computed by using Algorithm `ObjectiveValue` in Sect. 27.4.

We now prove a Lemma that highlights some of the difficulties that we face when trying to find a solution to LREC. Furthermore, it sets LREC apart from other computational problems studied so far in the literature.

**Lemma 27.2** *Let  $\mathbf{r} = (r_u : u \in \mathcal{M})$ ,  $\mathbf{E}^{(0)} = (E_u^{(0)} : u \in \mathcal{M})$ , and  $\mathbf{C}^{(0)} = (C_v^{(0)} : v \in \mathcal{P})$ . The objective function  $f_{\text{LREC}}(\mathbf{r}, \mathbf{E}^{(0)}, \mathbf{C}^{(0)})$  is not necessarily increasing in  $\mathbf{r}$ . Furthermore, the optimal radius for a charger is not necessarily equal to the distance from some node.*

*Proof* Consider a network consisting of 2 chargers  $u_1, u_2$  and 2 nodes  $v_1, v_2$  all of which are collinear and  $\text{dist}(v_1, u_1) = \text{dist}(v_2, u_1) = \text{dist}(v_2, u_2) = r_{u_1} = 1$  (see Fig. 27.1). Furthermore, assume for the sake of exposition of our arguments that  $E_{u_1}^{(0)} = E_{u_2}^{(0)} = C_{v_1}^{(0)} = C_{v_2}^{(0)} = 1$ . Finally, assume that the parameters for the charging rate in Eq. (27.1) are  $\alpha = \beta = 1$ , the electromagnetic radiation parameter in Eq. (27.3) is  $\gamma = 1$  and that the upper bound on the radiation level is  $\rho = 2$ .

**Fig. 27.1** A network with 2 chargers  $u_1, u_2$  and 2 nodes  $v_1, v_2$ . All 4 points are collinear and  $\text{dist}(v_1, u_1) = \text{dist}(v_2, u_1) = \text{dist}(v_2, u_2) = r_{u_1} = 1$



We will show that the optimal solution to the LREC problem in this network is when  $r_{u_1} = 1$  and  $r_{u_2} = \sqrt{2}$ . To see this, first note that the electromagnetic radiation is maximum when  $t = 0$ , i.e., when chargers are all operational. Furthermore, since there are only 2 radiation sources (namely chargers  $u_1$  and  $u_2$ ), it is not hard to verify that the electromagnetic radiation is maximized on the charger locations, i.e.,  $\max_{x,t} R_x(t) = \max\{r_{u_1}^2, r_{u_2}^2\}$ . Consequently, since  $\rho = 2$ , the radius of each charger can be at most  $\sqrt{2}$ . On the other hand, to achieve an objective function value that is larger than 1, both  $r_{u_1}$  and  $r_{u_2}$  must be at least 1. In fact, if  $r_{u_1} = r_{u_2} \in [1, \sqrt{2}]$ , then, by symmetry,  $v_2$  will reach its energy storage capacity at the exact moment that the energy of  $u_1$  is depleted. Therefore, the objective function value will be only  $\frac{3}{2}$ , since both  $u_1$  and  $u_2$  will have contributed the same amount of energy to fully charge  $v_2$ . To do better,  $v_2$  must reach its energy storage capacity without using too much of the energy of  $u_1$ , which happens when  $r_2 > r_1$ . In this case,  $v_2$  will reach its energy storage capacity before the energy of  $u_1$  is depleted, and so  $u_1$  will use the remaining energy to further charge  $v_1$ . In particular, when  $r_2 > r_1$ , we have that  $t_{u_2, v_1}^* = t_{u_2, v_2}^*$  and also

$$1 = C_{v_2}^{(0)} = t_{u_2, v_1}^* \frac{r_{u_1}^2 + r_{u_2}^2}{4}. \quad (27.9)$$

The remaining energy of  $u_1$  at time  $t_{u_2, v_1}^*$  will then be

$$E_{u_1}^{(0)} - 2t_{u_2, v_1}^* \frac{r_{u_1}^2}{4} = 1 - 2 \frac{r_{u_1}^2}{r_{u_1}^2 + r_{u_2}^2}. \quad (27.10)$$

Since  $1 \leq r_1 < r_2 \leq \sqrt{2}$ , this is maximized for  $r_{u_1} = 1$  and  $r_{u_2} = \sqrt{2}$ , in which case  $E_{u_1}^{(t_{u_2, v_1}^*)} = \frac{1}{3}$ . In that case, when  $v_2$  reaches its energy storage capacity,  $u_1$  will have  $\frac{1}{3}$  energy units more to give solely to  $v_1$ ; the other  $\frac{2}{3}$  units will have been split evenly between  $v_1$  and  $v_2$ . This means that the objective function value is  $\frac{5}{3}$  and it is maximum.

Now this example shows that not only the radius of chargers are not necessarily equal to the distance from some node (since to achieve the optimum we must have  $r_{u_2} = \sqrt{2}$ ), but also increasing  $r_1$  will result in a suboptimal objective function value.  $\square$

## 27.4 Computing the Objective Function

In this section, we provide an algorithm for computing the value of our objective function (i.e., the amount of energy given by the chargers to the nodes), given the radii of the chargers, the capacities of the nodes and the available energies of the chargers. More precisely, assume that at some time  $t$ , each charger  $u \in \mathcal{M}$  has remaining energy  $E_u^{(t)}$  and each node  $v \in \mathcal{P}$  can store  $C_v^{(t)}$  energy. The tuple  $\Sigma^{(t)} = (\mathbf{r}, \mathbf{E}^{(t)}, \mathbf{C}^{(t)})$ , where  $\mathbf{r} = (r_u : u \in \mathcal{M})$ ,  $\mathbf{E}^{(t)} = (E_u^{(t)} : u \in \mathcal{M})$  and  $\mathbf{C}^{(t)} = (C_v^{(t)} : v \in \mathcal{P})$ , will be called the *configuration of the system at time t*. For each  $u \in \mathcal{M}$ , we denote by  $\mathcal{P}_u^{(t)} \stackrel{\text{def}}{=} \{v : \text{dist}(v, u) \leq r_u, C_v^{(t)} > 0\}$  the set of nodes within distance  $r_u$  from  $u$  that have not reached their storage capacities at time  $t$ . Furthermore, for each  $v \in \mathcal{P}$ , we denote by  $\mathcal{M}_v^{(t)} \stackrel{\text{def}}{=} \{u : v \in \mathcal{P}_u^{(t)}, E_u^{(t)} > 0\}$  the set of chargers that can reach  $v$  and have not depleted their energy at time  $t$ . Finally, denote by  $\mathcal{M}_{\emptyset}^{(t)} \stackrel{\text{def}}{=} \{u \in \mathcal{M} : E_u^{(t)} = 0\}$  the set of chargers that have depleted their energy by time  $t$ . Similarly, denote by  $\mathcal{P}_{\emptyset}^{(t)} \stackrel{\text{def}}{=} \{v \in \mathcal{P} : C_v^{(t)} = 0\}$  the set of nodes that have reached their energy storage capacity by time  $t$ .

The value of the objective function can be computed by the following algorithm. The main idea is that given the configuration of the system at any time  $t$ ; we can find which will be the next charger (or node respectively) that will deplete his energy (resp. will reach its energy storage capacity) and when. The algorithm stops when no node can be charged any more, which happens either when they have reached their total capacity (i.e.,  $C_v^{(t)} = 0$ ), or all chargers that can reach it have depleted their energy (i.e.,  $\sum_{u \in \mathcal{M}_v^{(t)}} E_u^{(t)} = 0$ ).

Notice that, in every iteration, algorithm `ObjectiveValue` sets to 0 the energy level or the capacity of at least one charger or node. Therefore, we have the following:

**Lemma 27.3** *Algorithm `ObjectiveValue` terminates in at most  $n + m$  while-iterations.*

## 27.5 Computing the Maximum Radiation

One of the challenges that arises in our model is the computation of the maximum radiation inside the area of interest  $\mathcal{A}$ , as well as the point (or points) where this maximum is achieved. Unfortunately, it is not obvious where the maximum radiation is attained inside our area of interest, and it seems that some kind of discretization

**Algorithm 35:** ObjectiveValue

---

**Input :** Initial configuration  $\Sigma^{(0)} = (\mathbf{r}, \mathbf{E}^{(0)}, \mathbf{C}^{(0)})$

- 1 Set  $t = 0$
- 2 **while**  $\left[ \bigcup_{v \in \mathcal{P}} \left\{ \left( C_v^{(t)} > 0 \right) \text{ AND } \left( \sum_{u \in \mathcal{M}_v^{(t)}} E_u^{(t)} > 0 \right) \right\} \right]$  **do**
- 3   Let  $t_{\mathcal{M}} = \min_{u \in \mathcal{M} \setminus \mathcal{M}_{\emptyset}^{(t)}} \{t' : t' \sum_{v \in \mathcal{P}_u^{(t)}} P_{v,u}(t) = E_u^{(t)}\}$
- 4   Let  $t_{\mathcal{P}} = \min_{v \in \mathcal{M} \setminus \mathcal{P}_{\emptyset}^{(t)}} \{t' : t' \sum_{u \in \mathcal{M}_v^{(t)}} P_{v,u}(t) = C_v^{(t)}\}$
- 5   Let  $t_0 = \min\{t_{\mathcal{M}}, t_{\mathcal{P}}\}$
- 6   For all  $u \in \mathcal{M} \setminus \mathcal{M}_{\emptyset}^{(t)}$ , set  $E_u^{(t+1)} = E_u^{(t)} - t_0 \sum_{v \in \mathcal{P}_u^{(t)}} P_{v,u}(t)$
- 7   For all  $v \in \mathcal{P} \setminus \mathcal{P}_{\emptyset}^{(t)}$ , set  $C_v^{(t+1)} = C_v^{(t)} - t_0 \sum_{u \in \mathcal{M}_v^{(t)}} P_{v,u}(t)$
- 8   Set  $t = t + t_0$  and update  $\mathcal{M}_{\emptyset}^{(t)}$  and  $\mathcal{P}_{\emptyset}^{(t)}$
- 9 **end while**

**Output:**  $\sum_{u \in \mathcal{M}} (E_u^{(0)} - E_u^{(t)})$

---

is necessary. In fact, in our experiments, we use the following generic MCMC procedure: for sufficiently large  $K \in \mathbb{N}^+$ , choose  $K$  points uniformly at random inside  $\mathcal{A}$  and return the maximum radiation among those points. We note also that the computation of the electromagnetic radiation at any point takes  $O(m)$  time, since it depends only on the distance of that point from each charger in  $\mathcal{M}$ .

One of the main drawbacks of the above method for computing the maximum radiation is that the approximation it achieves depends on the value of  $K$  (which is equivalent to how refined our discretization is). On the other hand, it does not take into account the special form of the electromagnetic radiation in Eq. (27.3). In fact, our iterative algorithm `IterativeLREC` in Sect. 27.6 does not depend on the specific form of Eq. (27.3), and this could be desirable in some cases (especially since the effect that multiple radiation sources have on the electromagnetic radiation is not completely understood).

## 27.6 A Local Improvement Heuristic for LREC

We now present a heuristic for approximating the optimal solution to LREC. To this end, we first note that for any charger  $u \in \mathcal{M}$ ; we can approximately determine the radius  $r_u$  of  $u$  that achieves the best objective function value, given the radii  $\mathbf{r}_{-u} = (r_{u'} : u' \in \mathcal{M} \setminus u)$  as follows: Let  $r_u^{\max}$  be the maximum distance of any point in  $\mathcal{A}$  from  $u$  and let  $l \in \mathbb{N}^+$  be a sufficiently large integer. For  $i = 0, 1, \dots, l$ , set  $r_u = \frac{i}{l} r_u^{\max}$  and compute the objective function value (using algorithm `ObjectiveValue`) as well as the maximum radiation (using the method described in Sect. 27.5). Assign to  $u$  the radius that achieves the highest objective function value that satisfies the radiation constraints of LREC. Given that the discretization of  $\mathcal{A}$  used to compute the maximum radiation has  $K$  points in it, and

**Algorithm 36:** IterativeLREC

---

**Input :** Charger and node locations

- 1 **counter** = 1
- 2 **repeat**
- 3     Select u.a.r. a charger  $u \in \mathcal{M}$
- 4     Find (an approximation to) the optimal radius for  $u$  given that the radii of all other chargers are fixed
- 5     **counter** = **counter** + 1
- 6 **until** **counter** =  $K'$

**Output:**  $\mathbf{r} = (r_u : u \in \mathcal{M})$

---

using Lemma 27.3, we can see that the number of steps needed to approximately determine the radius  $r_u$  of  $u$  using the above procedure is  $O((n + m)l + mK)$ . It is worth noting that we could generalize the above procedure to any number  $c$  of chargers, in which case the running time would be  $O((n + m)l^c + mK)$ . In fact, for  $c = m$  we would have an exhaustive-search algorithm for LREC, but the running time would be exponential in  $m$ , making this solution impractical even for a small number of chargers.

The main idea of our heuristic IterativeLREC is the following: in every step, choose a charger  $u$  uniformly at random and find (an approximation to) the optimal radius for  $u$  given that the radii of all other chargers are fixed. To avoid infinite loops, we stop the algorithm after a predefined number of iterations  $K' \in \mathbb{N}^+$ .

By the above discussion, IterativeLREC terminates in  $O(K'(nl + ml + mK))$  steps.

## 27.7 A Relaxation of LREC

The intractability of the LREC problem is mainly due to the following reasons: (a) First, there is no obvious closed formula for the maximum radiation inside the area of interest  $\mathcal{A}$  as a function of the positions and the radii of the chargers. (b) Second, as is suggested by Lemma 27.2, there is no obvious potential function that can be used to identify directions inside  $\mathbb{R}^m$  that can increase the value of our objective function.

In this section, we consider the following relaxation to the LREC problem, which circumvents the problem of finding the maximum radiation caused by multiple sources:

**Definition 27.2** (*Low Radiation Disjoint Charging (LRDC)*) Let  $\mathcal{M}$  be a set of wireless power chargers and  $\mathcal{P}$  be a set of rechargeable nodes which are deployed inside an area of interest  $\mathcal{A}$ . Suppose that each charger  $u \in \mathcal{M}$  initially has available energy  $E_u^{(0)}$ , and each node  $v \in \mathcal{P}$  has initial energy storage capacity  $C_v^{(0)}$ . Assign to each charger  $u \in \mathcal{M}$  a radius  $r_u$ , so that the total usable energy given to the nodes of the network is maximized and the electromagnetic radiation at any point of  $\mathcal{A}$  is at most  $\rho$ . We assume that all chargers start operating simultaneously at time 0 and

that charging follows the model described in Sect. 27.2. Additionally, we impose the constraint that no node should be charged by more than 1 charger.

The following Theorem concerns the hardness of LRDC.

**Theorem 27.1** *LRDC is NP-hard.*

*Proof* The hardness follows by reduction from the Independent Set in Disc Contact Graphs [8]. Let  $G$  be a disc contact graph, i.e., a graph where vertices correspond to discs any two of which have at most 1 point in common. In particular, the set of vertices of  $G$  corresponds to a set of  $m$  discs  $D(u_1, r_1), D(u_2, r_2), \dots, D(u_m, r_m)$ , where  $D(u_j, r_j)$  is a disc centered at  $u_j$  with radius  $r_j$ . Two vertices of  $G$  are joined by an edge if and only if their corresponding discs have a point in common.

We now construct an instance of the LRDC as follows: We place a node on each disc contact point and, for  $j = 1, 2, \dots, m$ , let  $k_j$  be the maximum number of nodes in the circumference of the disc  $D(u_j, r_j)$ . We then add nodes on the circumference of every other disc in such a way that every disc has exactly the same number of nodes (say)  $K$  uniformly around its circumference (notice that this is possible since every disc shares at most  $m$  points of its circumference with other discs). We now place a charger on the center of each disc and set the radius bound for the charger corresponding to  $u_j$  equal to  $r_j$ , for every  $j = 1, 2, \dots, m$ . Finally, we set the initial energy storage capacity of each node equal to 1, the available energy of each charger equal to  $K$  and the electromagnetic radiation bound  $\rho = \max_{j \in [m]} \frac{\alpha r_j^2}{\beta^2}$ .

It is now evident that an optimal solution to LRDC on the above instance yields a maximum independent set in  $G$ ; just pick disc  $D(u_j, r_j)$  if the  $j$ -th charger has radius equal to  $r_j$  and discard it otherwise.  $\square$

We now present an integer program formulation for LRDC (to which we refer as IP-LRDC). To this end, we first note that, for any charger  $u \in \mathcal{M}$ , the distance of nodes/points in  $\mathcal{P}$  from  $u$  defines a (complete) ordering  $\sigma_u$  in  $\mathcal{P}$ . In particular, for any two nodes  $v, v' \in \mathcal{P}$  and a charger  $u \in \mathcal{M}$ , we will write  $v \leq_{\sigma_u} v'$  if and only if  $\text{dist}(v, u) \leq \text{dist}(v', u)$ . For any charger  $u$ , define  $i_{\text{rad}}^{(u)}$  to be the furthest node from  $u$  that can be charged by  $u$  without  $u$  violating the radiation threshold  $\rho$  on its own. Similarly, define  $i_{\text{nrg}}^{(u)}$  to be the furthest node from  $u$  with the property that if  $u$  has radius at least  $\text{dist}(i_{\text{nrg}}^{(u)}, u)$ , then the energy of  $u$  will be fully spent. Assuming we break in  $\sigma$  arbitrarily, nodes  $i_{\text{rad}}^{(u)}$  and  $i_{\text{nrg}}^{(u)}$  are uniquely defined for any charger  $u$ . Our integer program solution is presented below.

$$\max \sum_{u \in \mathcal{M}} \left( E_u^{(0)} x_{i_{\text{nrg}}^{(u)}, u} + \sum_{v \leq_{\sigma_u} i_{\text{nrg}}^{(u)}} (x_{v, u} - x_{i_{\text{nrg}}^{(u)}, u}) C_v^{(0)} \right) \quad (27.11)$$

subject to:

$$\sum_{u \in \mathcal{M}} x_{v,u} \leq 1, \quad \forall v \in \mathcal{P} \quad (27.12)$$

$$x_{v,u} - x_{v',u} \geq 0, \quad \forall v, v' \in \mathcal{P}, \forall u \in \mathcal{M} : \\ v \leq_{\sigma_u} v' \quad (27.13)$$

$$x_{v,u} = 0, \quad \forall v \in \mathcal{P}, \forall u \in \mathcal{M} : \\ v >_{\sigma_u} i_{\text{rad}}^{(u)} \text{ or } v >_{\sigma_u} i_{\text{nrg}}^{(u)} \quad (27.14)$$

$$x_{v,u} \in \{0, 1\}, \quad \forall v \in \mathcal{P}, \forall u \in \mathcal{M}. \quad (27.15)$$

In IP-LRDC, variable  $x_{v,u}$  indicates whether or not the (unique) charger that can reach  $v$  is  $u$ . The existence of at most one charger per node in a feasible assignment of LRDC is guaranteed by constraint (27.12). Constraint (27.13) guarantees that when a node  $v'$  can be reached by  $u$ , then all nodes closer to  $u$  can also be reached by  $u$ . Finally, constraint (27.14) guarantees that the radiation threshold is not violated and also suggests that there is no reason why a charger should be able to reach nodes that are further than  $i_{\text{nrg}}^{(u)}$ .

To understand the objective function that we want to maximize in IP-LRDC, notice that, for any charger  $u \in \mathcal{M}$ , if  $r_u \geq \text{dist}(i_{\text{nrg}}^{(u)}, u)$  (which is equivalent to having  $x_{i_{\text{nrg}}^{(u)}, u} = 1$ ), then the useful energy transferred from  $u$  to the nodes of the network will be exactly  $E_u^{(0)}$ . Indeed, this is captured by our objective function, since  $E_u^{(0)} x_{i_{\text{nrg}}^{(u)}, u} + \sum_{v \leq_{\sigma_u} i_{\text{nrg}}^{(u)}} (x_{v,u} - x_{i_{\text{nrg}}^{(u)}, u}) C_v^{(0)} = E_u^{(0)}$ , when  $x_{i_{\text{nrg}}^{(u)}, u} = 1$ , since, by constraint (27.13), we have that  $x_{v,u} = x_{i_{\text{nrg}}^{(u)}, u}$ , for any  $v \leq_{\sigma_u} i_{\text{nrg}}^{(u)}$ . On the other hand, when  $x_{i_{\text{nrg}}^{(u)}, u} = 0$ , charger  $u$  will not be able to spend all of its energy, since the nodes it can reach cannot store all of it. This is also captured by our objective function, since  $E_u^{(0)} x_{i_{\text{nrg}}^{(u)}, u} + \sum_{v \leq_{\sigma_u} i_{\text{nrg}}^{(u)}} (x_{v,u} - x_{i_{\text{nrg}}^{(u)}, u}) C_v^{(0)} = \sum_{v \leq_{\sigma_u} i_{\text{nrg}}^{(u)}} x_{v,u} C_v^{(0)}$ , when  $x_{i_{\text{nrg}}^{(u)}, u} = 0$ , which is equal to the total energy that the nodes reachable from  $u$  could harvest in total.

In our experimental evaluation, we solve IP-LRDC by first making a linear relaxation and then rounding the solution so that the constraints (27.12), (27.13) and (27.14). It is easy to see that the objective function value that we get is a lower bound on the optimal solution of the LREC problem. We use this bound to evaluate the performance of our iterative algorithm IterativeLREC (see Sect. 27.6).

## 27.8 Performance Evaluation

We conducted simulations in order to evaluate our methods using Matlab R2014b. We compared IterativeLREC, IP-LRDC (after the linear relaxation) and a charger configuration scheme in which each charger  $u$  sets its radius equal to  $\text{dist}(u, i_{\text{rad}}^{(u)})$ . We call this new configuration “ChargingOriented” because it assigns the maximum radius to each charger, without individually violating the radiation threshold. In other words, this configuration provides the best possible rate of transferring energy

in the network and serves as an upper bound on the charging efficiency of the performance of IterativeLREC, but is expected to achieve a poor performance on keeping the radiation low, due to frequent, large overlaps. A snapshot of a uniform network deployment with  $|\mathcal{P}| = 100$ ,  $|\mathcal{M}| = 5$  and  $K = 100$ , is shown in Fig. 27.2. We observe that the radii of the chargers in the ChargingOriented case are larger than the other two cases. In the case of IP-LRDC the radiation constraints lead to a configuration where two chargers are not operational. IterativeLREC provides a configuration in between the ChargingOriented and IP-LRDC, in which some overlaps of smaller size are present.

We deploy uniformly at random  $|\mathcal{P}| = 100$  network nodes of identical capacity,  $|\mathcal{M}| = 10$  wireless chargers of identical energy supplies and  $K = 1000$  points of radiation computation. We set  $\alpha = 0$ ,  $\beta = 1$ ,  $\gamma = 0.1$  and  $\rho = 0.2$ . For statistical smoothness, we apply the deployment of nodes in the network and repeat each experiment 100 times. The statistical analysis of the findings (the median, lower and upper quartiles, outliers of the samples) demonstrate very high concentration around the mean, so in the following figures we only depict average values. We focus our simulations on three basic metrics: charging efficiency, maximum radiation, and energy balance.

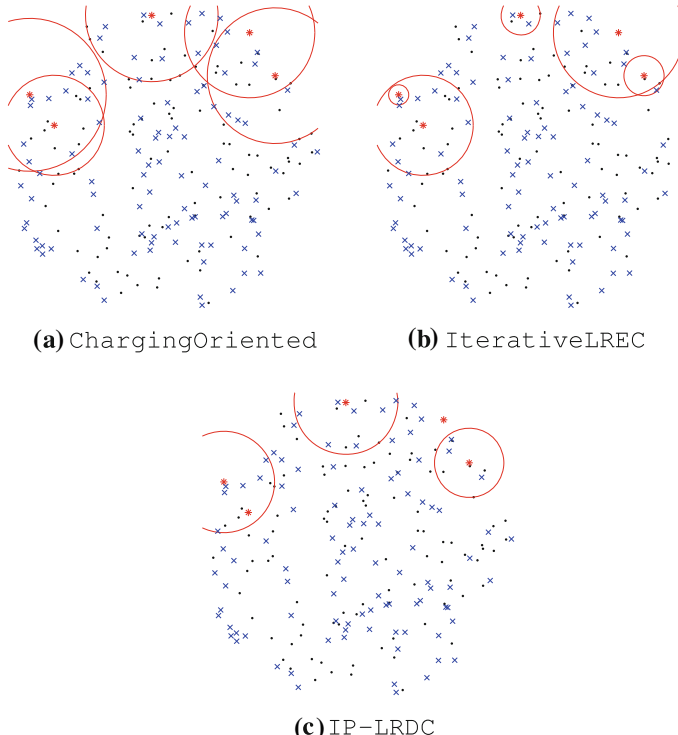


**Fig. 27.2** Network snapshot using 5 chargers

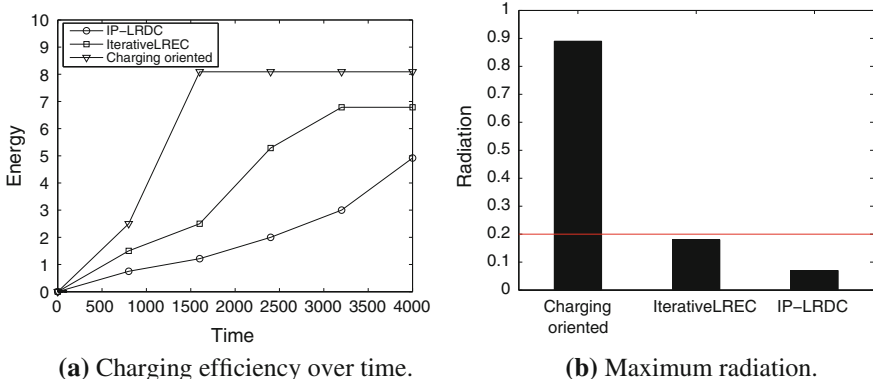
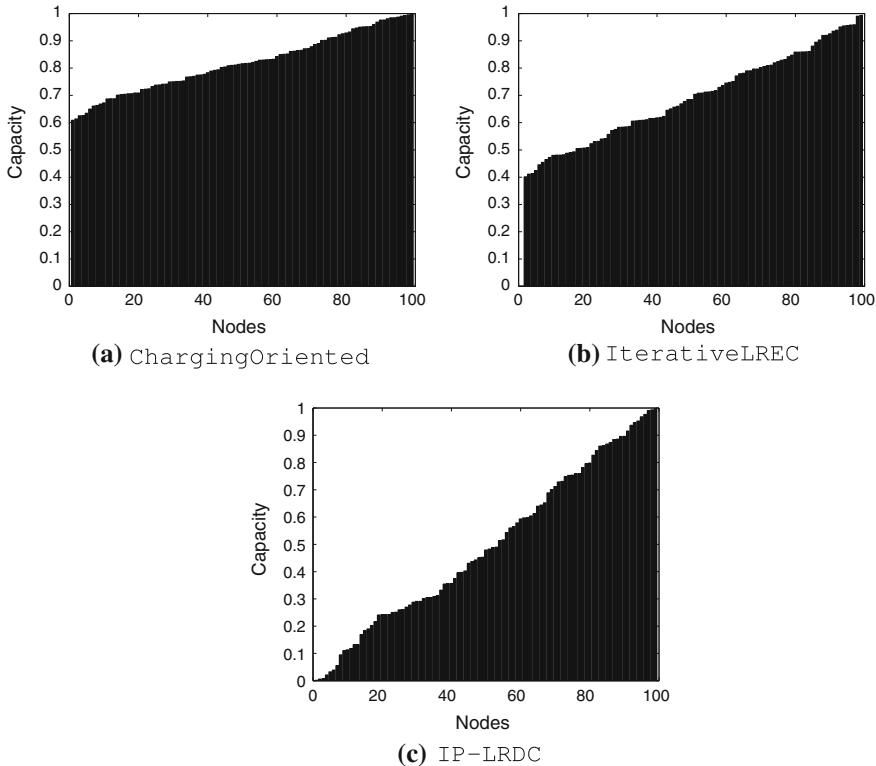


Fig. 27.3 Efficiency and radiation

**Charging efficiency.** The objective value that is achieved as well as the time that is spent for the charging procedure is of great importance to us. The objective values achieved were 80.91 by the ChargingOriented, 67.86 by the IterativeLREC and 49.18 by the IP-LRDC. The ChargingOriented method is the most efficient and quick, as expected but it results in high maximum radiation. As we observe in Fig. 27.3a, it distributed the energy in the network in a very short time. The efficiency of ChargingOriented both in terms of objective value and in terms of time is explained by the frequent charger radii overlaps that are created during the configuration of the chargers (e.g., Fig. 27.2). IP-LRDC achieves the lowest efficiency of all due to the small charging radii and consequently small network coverage by the chargers. Our heuristic IterativeLREC achieves high enough efficiency w.r.t. the radiation constraints. It's performance lies between the performance of ChargingOriented and IP-LRDC, both in terms of objective value and in terms of time.

**Maximum radiation.** The maximum amount of radiation incurred is very important regarding the safety impact of the corresponding charging method. High amounts of radiation, concentrated in network regions may render a method non-practical for realistic applications. This is the case for the ChargingOriented, which in spite of being very (charging) efficient, it significantly violates the radiation threshold (Fig. 27.3). IterativeLREC is performing very well, since it does not violate the threshold but in the same time provides the network with high amount of energy.

**Energy balance.** The energy balance property is crucial for the lifetime of Wireless Distributed Systems, since early disconnections are avoided and nodes tend to save energy and keep the network functional for as long as possible. For this reason, apart from achieving high charging efficiency, an alternative goal of a charging method is the balanced energy distribution among the network nodes. Figure 27.4 is a graphical depiction of the energy provided in the network throughout the experiment. The nodes are sorted by their final energy level and by observing the Figure, we are



**Fig. 27.4** Energy balance

able to make conclusions about the objective value and the energy balance of each method. Our `IterativeLREC` achieves efficient energy balance that approximates the performance of the powerful `ChargingOriented`.

## 27.9 Conclusion

In this chapter, we define a new charging model and we present and study the Low Radiation Efficient Charging Problem, in which we wish to optimize the amount of “useful” energy transferred from chargers to nodes (under constraints on the maximum level of radiation). We present several fundamental properties of this problem and provide indications of its hardness. Also, we propose an iterative local improvement heuristic for LREC, which runs in polynomial time and we evaluate its performance via simulation. Our algorithm decouples the computation of the objective function from the computation of the maximum radiation and also does not depend

on the exact formula used for the computation of the point electromagnetic radiation. We provide extensive simulation results supporting our claims and theoretical results.

## References

- Angelopoulos, C.M., Nikoletseas, S., Patroumpa, D., Raptopoulos, C.: Radiation-aware data propagation in wireless sensor networks. In: Proceedings of the 10th ACM International Symposium on Mobility Management and Wireless Access, MobiWac '12, pp. 11–18 (2012)
- Angelopoulos, C.M., Nikoletseas, S., Raptis, T.P.: Wireless energy transfer in sensor networks with adaptive, limited knowledge protocols. *Comput. Netw.* **70**, 113–141 (2014)
- Angelopoulos, C.M., Nikoletseas, S., Raptis, T.P., Raptopoulos, C., Vasilakis, F.: Improving sensor network performance with wireless energy transfer. *Int. J. Ad Hoc Ubiquitous Comput.* (2015) (in press)
- Dai, H., Liu, Y., Chen, G., Wu, X., He, T.: Safe charging for wireless power transfer. In: INFOCOM, 2014 Proceedings IEEE, pp. 1105–1113 (2014)
- Dai, H., Liu, Y., Chen, G., Wu, X., He, T.: Scape: safe charging with adjustable power. In: 2014 IEEE 34th International Conference on Distributed Computing Systems (ICDCS), pp. 439–448 (2014)
- Edwards, M.J., Saunders, R.D., Shiota, K.: Effects of heat on embryos and foetuses. *Int. J. Hyperthermia* **19**(3), 295–324 (2002)
- Gandhi, O., Morgan, L., de Salles, A., Han, Y., Herberman, R., Davis, D.: Exposure limits: the underestimation of absorbed cell phone radiation, especially in children. *Electromag. Biol. Med.* **31**(1), 34–51 (2012)
- Garey, M., Johnson, D., Stockmeyer, L.: Some simplified np-complete graph problems. *Theor. Comput. Sci.* **1**(3), 237–267 (1976)
- Guo, S., Wang, C., Yang, Y.: Joint mobile data gathering and energy provisioning in wireless rechargeable sensor networks. *IEEE Trans. Mobile Comput.* **13**(12), 2836–2852 (2014)
- Havas, M., Marrongelle, J., Pollner, B., Kelley, E., Rees, C., Tully, L.: Provocation study using heart rate variability shows microwave radiation from 2.4 ghz cordless phone affects autonomic nervous system. *Eur. J. Oncol. Library* **5** (2010)
- Jiang, L., Wu, X., Chen, G., Li, Y.: Effective on-demand mobile charger scheduling for maximizing coverage in wireless rechargeable sensor networks. *Mobile Netw. Appl.* **19**(4), 543–551 (2014)
- Kaklamanis, C., Kirousis, L., Bose, P., Kranakis, E., Krizanc, D., Peleg, D.: Station layouts in the presence of location constraints. *Algorithms and Computation. Lecture Notes in Computer Science*, vol. 1741, pp. 269–278. Springer, Berlin (1999)
- Li, Z., Peng, Y., Zhang, W., Qiao, D.: J-roc: A joint routing and charging scheme to prolong sensor network lifetime. In: Proceedings of the 2011 19th IEEE International Conference on Network Protocols, ICNP '11, pp. 373–382 (2011)
- Madhja, A., Nikoletseas, S., Raptis, T.P.: Distributed wireless power transfer in sensor networks with multiple mobile chargers. *Comput. Netw.* **80**, 89–108 (2015)
- Madhja, A., Nikoletseas, S., Raptis, T.P.: Hierarchical, collaborative wireless charging in sensor networks. In: Proceedings of the IEEE Wireless Communications and Networking conference, WCNC '15 (2015)
- Nikoletseas, S., Patroumpa, D., Prasanna, V., Raptopoulos, C., Rolim, J.: Radiation awareness in three-dimensional wireless sensor networks. In: 2012 IEEE 8th International Conference on Distributed Computing in Sensor Systems (DCOSS), pp. 176–185 (2012)
- Nikoletseas, S., Raptis, T.P., Souroulagkas, A., Tsolovos, D.: An experimental evaluation of wireless power transfer protocols in mobile ad hoc networks. In: Proceedings of the IEEE Wireless Power Transfer Conference, WPWC '15 (2015)

18. Ntzouni, M., Skouroliakou, A., Kostomitsopoulos, N., Margaritis, L.: Transient and cumulative memory impairments induced by gsm 1.8 ghz cell phone signal in a mouse model. *Electromag. Biol. Med.* **32**(1), 95–120 (2013)
19. Oltenau, M., Marincas, C., Rafiroiu, D.: Dangerous temperature increase from em radiation around metallic implants. *Acta Electroteh.* **53**(2), 175–180 (2012)
20. Xiang, L., Luo, J., Han, K., Shi, G.: Fueling wireless networks perpetually: a case of multi-hop wireless power distribution. In: 2013 IEEE 24th International Symposium on Personal Indoor and Mobile Radio Communications (PIMRC), pp. 1994–1999 (2013)